PROCEEDINGS
of the

1993
Battlefield
Atmospherics
Conference

Las Cruces, New Mexico
30 November - 2 December 1993
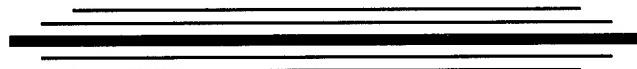
BATTLEFIELD ENVIRONMENT DIRECTORATE
U.S. Army Research Laboratory
White Sands Missile Range
New Mexico

DTIC QUALITY INSPECTED 3

19971215 102

NOTICES

Disclaimers

The findings in this report are not to be construed as an official Department of the Army position, unless so designed by other authorized documents.

The citation of trade names and names of manufacturers in this report is not to be construed as official Government endorsement or approval of commercial products or services referenced herein.

DESTRUCTION NOTICE

When this document is no longer needed, destroy it by any method that will prevent disclosure of its contents or reconstruction of the document.

PROCEEDINGS

of the

1993 BATTLEFIELD ATMOSPHERICS CONFERENCE

30 November – 2 December 1993

Sponsor

Battlefield Environment Directorate
U.S. Army Research Laboratory
White Sands Missile Range, New Mexico

Conference Manager

Mr. Edward D. Creegan
U.S. Army Research Laboratory

Conference Chairman
Mr. John R. Elrick
U.S. Army Research Laboratory

PROGRAM COMMITTEE

Battlefield Environment Directorate
U.S. Army Research Laboratory

       Conference Manager
       Mr. Edward D. Creegan (505) 678-4684

       Conference Chairman
       Mr. John R. Elrick (505) 678-3691

       Conference Advisers
       Dr. Franklin E. Niles
       Dr. Bernard F. Engebos
       Dr. Mary Ann Seagraves
       Mr. Don R. Veazey

Science and Technology Corporation
Meetings Division, Hampton, Virginia

       Conference Administrator
       Ms. Jeanne P. Hawtin

       Conference Coordinators
       Mrs. Judy Cole
       Mr. Keith Hicks

SESSION I: BATTLE WEATHER DATA

SESSION II: SIMULATION AND MODELING

SESSION III: ATMOSPHERIC SENSING

SESSION IV: ATMOSPHERIC ASSESSMENT

SESSION V: MITIGATION AND EXPLOITATION

SESSION III POSTERS: ATMOSPHERIC SENSING

SESSION IV POSTERS: ATMOSPHERIC ASSESSMENT

SESSION V POSTERS: MITIGATION AND EXPLOITATION

APPENDICES

PREFACE

The 1993 Battlefield Atmospherics Conference was held 30 November-2 December 1993 at the Holiday Inn de Las Cruces, Las Cruces, New Mexico, under the sponsorship of the U.S. Army Research Laboratory, Battlefield Environment Directorate, White Sands Missile Range, New Mexico. The Conference included oral presentations, poster and demonstration sessions on five topics: Battle Weather Data, Simulation and Modeling, Atmospheric Sensing, Atmospheric Assessment and Mitigation and Exploitation. The Conference had 211 attendees, including representatives from Denmark, France, Germany, Israel, The Netherlands, and the United Kingdom.

The Conference is the primary forum for usage of and additions to the Electro-Optical Systems Atmospheric Effects Library (EOSAEL) and Tactical Weather Intelligence (TWI) and for comparison of results with measurements and EOSAEL models.

The reader will find the items related to the Conference itself (the agenda and the list of attendees) in the appendices following the papers collected for the proceedings. An author index is also included.

Session I

BATTLE WEATHER DATA

BATTLEFIELD WEATHER DATA SUPPORT FOR THE ARMY

Douglas C. Pearson, Edward L. Bensman and David G. Biggar
Headquarters, 1st Weather Group, Fort McPherson, Georgia 30330-5000

ABSTRACT

Current weather data collection methods are generally sufficient to feed theater-scale atmospheric models. Large, data sparse areas still exist in the world, however, and the data density of indigenous weather sources may not suffice for finer resolution models. The intent of this paper is to describe current sources of meteorological data and envisioned data availability on the battlefield of the future. We believe that models developed for worldwide applications, must account for current and proposed data availability and communications limitations. Because there are regions of the world in which data "density" is insufficient, the application of meteorological models are inadequate to meet combat weather support requirements. We therefore propose a stronger focus on data collection and communication programs. (The views presented in this paper are the opinions of the authors and do not reflect official Air Force or Air Combat Command policy.)

1. INTRODUCTION

A top priority for Army weather support is to provide accurate and timely weather information to the Army commander for success on the battlefield. Communicating observed weather data is one of the most critical aspects in the process of providing weather support to the Army. Any numerical weather prediction program will be ineffective unless accurate weather data can be rapidly and reliably transmitted into and out of the battlefield. Joint doctrine for tactical weather support to the Army is described in Field Manual (FM) 34-81/Air Force Manual (AFM) 105-4. Training and Doctrine Command (TRADOC) Pamphlet 525-21/Military Airlift Command (MAC) Pamphlet 105-3 provides a joint operational concept of environmental support to the Army. These documents state that providing weather intelligence to an Army commander involves a three step process. Step one consists of data collection using manned and unmanned sensors. Step two requires processing and analyzing the collected data, and step three tailors the analysis to produce and disseminate a specific product that satisfies a customer requirement. It is important to understand that each of these three steps in this process is a building block for the next step. Step two can not occur without step one, and likewise step three can not occur without steps one and two. The essential point to be made here is that an accurate product can only be provided after adequate data collection, and weather data collection becomes the foundation for all other weather support. Finally, data transmission is essential and links the entire process together. Observed data must be rapidly transmitted over communication channels to processing

centers. After the data are received and processed, the analyses and customer stated products must be transmitted to users down to the brigade and battalion levels. Thus, the first priority in battlefield weather support to the Army is data collection. Battlefield weather observations have historically been a much needed but difficult piece of information to collect. The wide dispersion of units on the modern battlefield, and the complexity of current and projected highly technical weapon systems, have increased the requirements for timely and accurate tactical weather information. The Secretary of Defense recently outlined the U.S. defense policy as one in which we must be prepared for two Major Regional Conflicts (MRCs) simultaneously. This policy means using force projection to deploy from CONUS to austere locations with leaner fighting forces.

These rapidly deploying forces will initially rely on weather forecasts issued from some centralized facility such as the Air Force Global Weather Central. Depending upon the size of the deployed contingent, the forecast responsibility may shift to a Joint Meteorological and Oceanographic (Metoc) Forecast Unit (JMFU) in theater. This JMFU may work out of a fixed site or may deploy from the CONUS with tactical meteorological and communications equipment. Accurate and timely weather data is a critical factor in ensuring the quality of mesoscale computer models, customer driven tactical decision aids (TDAs), and any weather decision matrix models. In direct correlation to the success of these models is the spatial and temporal density at which these battlefield weather observations are available. It is paramount that weather elements be accurately portrayed and in sufficient density across the entire battlefield so as to give the commander the atmospheric advantage to use weather phenomena as a force multiplier. To logically approach the data collection issue it is necessary to examine the current collection capability. Once this is done, future technologies need to be exploited to provide an adequate battlefield weather data collection capability.

2. CURRENT BATTLEFIELD WEATHER DATA COLLECTION CAPABILITY

The current structure for collecting, analyzing and disseminating weather data on the battlefield is outlined in FM 34-81/AFM 105-4. Weather observations are taken at deployed field locations by trained Air Force weather observers. These observers are doctrinally located with Army corps, divisions, separate brigades, aviation brigades, regiments, and special forces groups. In a military operation the size of Desert Shield/Storm, this equated to approximately 15 Army support data points across the battlefield. Additionally, deployed Air Force, Navy, and Marine units collect and disseminate weather observations. All of these data, plus any indigenous observations, feed into the Automated Weather Network (AWN). This network is a high speed circuit which receives worldwide weather observations and forecasts, and makes them available to anyone with AWN access.

The existing data collection capability must be examined in light of whether these collected data are in support of a mesoscale or synoptic scale analysis or product. Currently, weather data collection can be grouped into surface weather observations, upper air observations, and satellite data. These data must be collected and used by a centralized processor to run forecast models. Running forecast models and gridding data fields are accomplished using data from the AWN and satellite processing capabilities at Air Force and Navy

weather forecast centers. If observed surface and upper air data are not available through AWN/satellite sources, the data can not be considered useful for modeling efforts. Any effort to develop future TDAs, weather decision matrices, or mesoscale models must take into consideration that input surface and upper air data will primarily be that which is available over current or programmed communication systems.

Weather data from the Army's Forward Area Limited Observation Program (FALOP) or its Artillery Meteorological (ARTYMET) soundings do not routinely get entered into the AWN and thus would not currently be considered a reliable data source for modeling purposes. The density of indigenous weather data varies greatly from one country, and one continent, to another. Hellstern and Lott (1989) undertook a project to analyze surface observations from around the world. The purpose of their study was to determine the availability of data worldwide and provide the Air Weather Service with an assessment of data-poor regions. One impact of such a study was that the U.S. knew, prior to initiating Operation Restore Hope, that Somalia was a country which had no reliable weather data. In fact, most African nations (except for a few northern countries) do not report weather observations frequently enough to establish a data base for modeling or for climatological summaries. This also means the deployed weather forces become essential and must create a weather observation network in austere, data-void regions. Table 1 provides a general description of data availability in each region of the world and represents the AWN collection capability for surface data.

REGION	DATA AVAILABILITY
1. United States:	Generally satisfactory. Marginal for coastal Alaska.
2. Rest of N.Amer. plus Greenland:	Satisfactory across southern Canada, but marginal to unsatisfactory over the rest of the region.
3. Central America Caribbean:	Generally marginal, but unsatisfactory in mountainous areas.
4. South America:	Unsatisfactory, except marginal in Uruguay.
5. Western Europe:	Satisfactory, except inland Norway and Spain.
6. Eastern Europe (except USSR):	Satisfactory, except marginal over central and southern Yugoslavia, Albania, and northern Greece.
7. (Former) Soviet Union:	Marginal, but marginal to unsatisfactory for WMO blocks 20 and 21, central and eastern parts of blocks 23 and 28, northern parts of blocks 24 and 25, and eastern parts of blocks 29 and 36.
8. China, Japan Korea:	Marginal, except unsatisfactory for China block 55, and Mongolia, and higher elevations of southeastern Asia. Satisfactory for Japan, North/South Korea, and Taiwan.
9. Middle East, Asia, India:	Unsatisfactory. Marginal on coastal Arabian peninsula.
10. Australia:	Unsatisfactory.
11. Pacific Islands:	Unsatisfactory to satisfactory depending on the island.
12. North/South Pacific, North Atlantic, Indian Oceans, Africa and Antarctica:	All of these areas are unsatisfactory.

TABLE 1. List of Data Availability, Based on Regions of the Globe.

During a contingency, the civilian observing source at some locations may not be available or reliable. Some additional AWN data collection points would be available in a contingency area at locations where the military has

deployed observers with weather teams. The density and quality of weather observations (AWN data), for a particular contingency area, must be examined to determine the capability to produce quality weather analyses. Only reliable and timely data fed into the model will produce good model results. Due to the lack of data in some regions, or termination of indigenous weather observations during a conflict, regional models covering the theater of operations may only have military weather observations as data input. Mesoscale models, which require boundary conditions from regional models, will likely suffer in areas of insufficient data. For this reason, it is critical that model developers include in their model documentation a summary of sensitivity studies and model limitations based on data availability. As Table 1 shows, many areas of the world have a surface data base that can only support synoptic scale analysis, at best. In all of these countries, there are even fewer upper air data locations than surface reporting stations.

Deployed weather teams augment these indigenous sources using a variety of tactical meteorological (TACMET) equipment. The GMQ-33, or Tactical Cloud Height Detector (TCHD), is used to determine ceiling heights for tactical aviation operations. The TMQ-34, or Tactical Meteorological Observing System (TMOS), is used to determine basic weather parameters such as temperature, pressure, wind and humidity. The Belt Weather Kit (BWK) is the most basic form of TACMET and is also used by many deployed weather teams to measure standard weather parameters. Within a division area of operations (AO), there are at most five data points: the division main, aviation brigade tactical operations center (TOC), and three or less mobile observing teams (MOTs). None of these locations regularly report upper air data. Yet, one of the most critical elements in model initialization is a good depiction of upper air patterns. ARTYMET soundings, if regularly transmitted into the AWN, could greatly improve the initialization of any global model. Likewise, upper air data would greatly improve regional modeling and tactical decision aids which require more than just surface weather observations. The biggest problem is not that the data are unavailable. Rather, the problem is that there is no doctrinal requirement for ARTYMET data to be transmitted to U.S. Air Force weather personnel. The result of this is that the division or corps SWO will often get the data, manually transcribed over the phone, or via fax. The SWO's technicians will then plot the data on a thermodynamic diagram (such as a "Skew-T") and analyze it manually. The sounding can be an incredible wealth of information, but it is often not shared outside of the echelon in which it was collected. This is due, largely, to the lack of a well-established protocol to transmit upper air data out of the battlefield.

The Joint Regulation, AR 115-10/AFR 105-3, Meteorological Support for the U.S. Army, defines the communication responsibilities for the Army and the Air Force. The Air Force is responsible for providing communications into and out of the theater of operations from the Defense Communications System (DCS) link in theater. The Army's responsibility moves the data to or from the DCS entry point and connects the weather teams at all Army echelons. If weather information is not flowing down the circuits to the deployed weather teams, then critical weather intelligence is not getting to the Army commanders. Similarly, if weather observations are not processed in a timely manner or are not being transmitted out of theater to the central forecasting facilities, then valuable data will be missing from global atmospheric model runs. One of the lessons learned from Desert Shield/Storm was that during periods of high mobility, the flow of weather information was severely

hampered. This problem was due partly to the constantly changing cryptographic codes and partly due to the loss of data during Army movements. High mobility on the battlefield presents a unique set of problems to Air Force weather teams supporting the Army. Most tactical Air Force units work from fixed facilities and the Navy does not have to set up and tear down for each move. This gives the tactical Air Force and Navy teams the ability to establish communications links which will not change during the course of the battle. The mobile requirements of Army-support weather teams on the battlefield means that communication links will be more difficult to continuously maintain and valuable weather information could be lost. Tactical weather sensors (GMQ-33, TMQ-34 and the BWK) and weather communications equipment (GOLDWING and the European UAWS) do not have an automatic send capability into the AWN. All data must be manually observed, transmitted to a central in-theater location, and then physically transferred to another system for input into the AWN. With its connectivity to the DCS link, the Transportable Automated Weather Distribution System (TAWDS) can be an improved centralized communication terminal for communicating with the AWN. Except for TAWDS, the current tactical systems do not feed battlefield weather data into the AWN in a rapid, automated manner.

3. FUTURE BATTLEFIELD WEATHER DATA COLLECTION CAPABILITY

The success of future battles may very well hinge on the ability to observe, process and rapidly disseminate weather data. Past military operations have demonstrated the need for joint systems that are interoperable and highly automated. Development of regional models and TDAs should account for all sources of weather data available, both in terms of today's technology and from systems which are planned for the future. Future technology upgrades, if fielded, would provide some improvement in data collection and dissemination. Observational data would be collected from the Army's deployment of Automatic Meteorological Sensor Systems (AMSS), use of weather sensors on Unmanned Aerial Vehicles (UAVs), Navy ship data or data from their current Tactical Environmental Support System (TESS), and Air Force deployment of the Tactical Weather Observing System (TWOS). The AMSS will feed data into the Integrated Meteorological System (IMETS) and the TWOS will feed into IMETS and the Air Force's Combat Weather System (CWS). CWS and TWOS will not increase the density of observations since they will be deployed to locations where weather teams would already be located. The Upper Atmospheric Sensor (UAS), part of CWS, would improve upper air data collection. Additional data in the AWN would be available if AMSS, UAVs and ARTYMET data can be ingested into the IMETS.

Future capabilities may enable battlefield weather data to be automatically available to the models through direct satellite communication channels. If models are to successfully use all input data from IMETS, AMSS, TAWDS, CWS, TWOS, UAS, UAVs, Navy ship data, TESS, and ARTYMET, then all data must be properly formatted so model software can recognize the data and properly calculate product results. Whether using the AWN, fiber optics or satellite communication, all of these data sources must be positioned geographically, encrypted and transmitted instantaneously, and formatted to automatically interface with the production of any mesoscale models, TDAs, and weather matrix models. It is critical that all of these systems (TESS, CWS, and IMETS) automatically ingest observed weather data, rapidly transmit the data into available communication systems, and be able to instantaneously access

all theater data. When sizing future dissemination of model output, it is important to consider that communications limitations will likely set time limits or data size limits on the model output. Even the most elaborate model output is thus dependent on the communications system and its inherent restrictions.

4. WHAT IS AN ADEQUATE DATA COLLECTION CAPABILITY ?

The key issue that needs to be resolved is to determine what is an adequate data collection capability for support to mesoscale modeling. Will a TDA or weather matrix provide accurate data at all grid locations over the battlefield if the source of the data is 200nm uniform gridded data fields (UGDFs)? These 200nm UGDFs are developed from synoptic scale surface and upper air data sources, and then reduced to a 25nm grid. Are the interpolation techniques good enough to capture the dynamics of weather changes occurring over time periods of hours and spatial distances of tens of miles as well as an accurate accounting for topographic influences? Will satellite data be automatically ingested and used in developing the model outputs? Anyone who is involved in developing or using a mesoscale model, TDA, or weather matrix, must know the answer to one fundamental question: What is the minimum data density, in time and space, that is needed to support an accurate model output? To answer this it is important to consider what weather parameter is involved, the region of the world, the topography, and the level in the atmosphere. Temperature in the tropics is a much more uniform data field than temperature in the mid latitudes. Upper air data is a more uniform data field than surface data. With complex terrain, surface winds and clouds are not uniform data fields and are very difficult to model in time and space.

The point is that models will do well with uniform data fields, but may not be able to handle the critical parameters that will be important to the customer on the battlefield. We do not have trouble forecasting the uniform data fields, nor are these fields difficult for the models to handle. Highly variable data fields are hard to analyze in total, and difficult for the models to handle. These data fields (e.g. mountain winds, fog, thunderstorms, convective precipitation, diurnal effects, and terrain induced cloud cover) are often the weather elements that have the most impact on battlefield operations and are the most difficult to observe, forecast and model. This paper focuses on a top priority in weather support to the battlefield -- weather data collection and dissemination. Some of the research and procurement resources should be directed towards improving battlefield data collection and communications for data transmission. The great advances in the areas of atmospheric modeling, tactical decision aids, and graphical display will be useless to the forecaster if the problems of data collection and dissemination are not solved.

Surface observations, upper air observations, satellite data, lightning detection data, and if possible weather radar data, all provide a part of the measured three dimensional picture of the atmosphere. Time, as a fourth dimension, is critical in understanding the patterns of weather changes. A data refresh rate of 30-60 minutes is needed to establish surface station trends and satellite cloud changes (looping) for mesoscale applications. Efforts must direct future data collection systems to be fully automated, from the initial sensing of weather on the battlefield, the dissemination of

8

raw data to all users, and finally automatic input to models for analysis and tailored products. Improving the collection, dissemination, and processing of these data must be done to ensure modeling efforts will be successful. If a mesoscale model, TDA, or weather matrix is produced, the developer of that product must determine the minimum data input that is needed for an accurate output. It is essential that the minimum spatial and temporal data density be studied and determined before fielding the software. In addition, the developer must coordinate with the data supplier (AWN) to ensure the model's software will recognize the format and automatically ingest all the observed data. Any limitations or model error in the product must be well documented. The developer must state if the output is valid for all areas of the world and for all weather parameters. The models must be tested under realistic battlefield data input conditions. If there are limitations, the output must highlight areas where the data is insufficient and the resultant analysis is suspect. Thus the research and modeling community must assist in determining what is an adequate data collection capability.

5. CONCLUSION

The Army customer, the Staff Weather Officer and the weather team forecasters must feel confident that they are using a system that displays accurate model output at all grid locations on the battlefield. Lee et al (1991) stated: "The accuracy, timeliness and availability of raw weather data defines how well the Tactical Decision Aids represent the real world environment in which military tactical strategies are performed. The most comprehensive Tactical Decision Aid in the world will produce useless results if its input weather data is out of date, incorrect, or not representative of the area where the Tactical Decision Aid is being applied." The tremendous effort to develop software for weather analysis and tailored product output is dependent on an accurate and complete data base and communications architecture. It is critically important that communications, sized to handle the volume of data at appropriate speeds, be available. There is an entire community of researchers, contractors, communicators, weather personnel and end users working to satisfy the military requirements for weather support. They must ensure that the systems to be fielded over the next five to ten years have a sufficient weather data base input, and a data transmission capability, that will adequately support the model output. It is essential that the Army, Navy, and Air Force strongly advocate programs which are designed to sense, collect and rapidly disseminate observed weather data into and out of a central data bank. The communication of weather intelligence across a constantly changing battlefield will greatly influence the effectiveness of weather support to the U.S. Army.

REFERENCES

Army Regulation 115-10/Air Force Regulation 105-3, 1990: Meteorological Support for the US Army

Field Manual 34-81, 1989: Weather Support for Army Tactical Operations

Hellstern, Frank and Neal Lott, 1989: Surface Observational Data Receipt by Geographical Regions, (Unpublished Report), OL-A, US Air Force Environmental Technical Applications Center (USAFETAC), Asheville, N.C.

Lee, Robert R., Philip Raihl and Sylvia Cossio, 1991: Meteorological
    Observations, Interpolation and Tactical Decision Aids, Proceedings of
    the 1991 Battlefield Atmospherics Conference, pp. 411-419.

TRADOC PAM 525-21/MAC PAM 105-3, 1987: Joint Operational Concept for Weather
    and Environmental Support to Army Operations

DEFINITIONS

SYNOPTIC -- weather parameters measured and analyzed with a resolution on the
order of a few hundred to several thousand kilometers; with a corresponding
time scale of 3 to 12 hours or more.

MESOSCALE -- weather parameters measured and analyzed with a resolution on
the order of a few tens to a few hundred kilometers; with a corresponding
time scale of 1 to 3 hours.

Combat Weather System

Capt Hardwick
HQ AWS/PMA
DSN 576-3268X309

Combat Weather System (CWS)

OVERVIEW

- Purpose

- System Description

- Schedule

- Summary

12

COMBAT WEATHER SYSTEM

PURPOSE

- Meet critical mission to support launch and recovery of aircraft and provide tailored weather support

- Transmit and receive data to and from Command, Control, Computer, Communication, and Intelligence (C4I) systems

- Eliminate deficiencies identified in Desert Storm

13

COMBAT WEATHER SYSTEM

SYSTEM DESCRIPTION

- Small, lightweight, modular, rapidly deployable, and maintainable by operators

- Tactical Weather Observing System (TWOS)

- Tactical Forecast System (TFS)

14

COMBAT WEATHER SYSTEM

SYSTEM DESCRIPTION - TWOS

- TWOS Subsystems

  - Tactical Ground Observing System (TGOS)

  - Manual Observing System (MOS)

  - Upper Atmospheric Sensor (UAS)

  - Expendable Tactical Observing System (TACOBS)

15

AIR WEATHER SERVICE

COMBAT WEATHER SYSTEM

SYSTEM DESCRIPTION - TWOS

- Tactical Ground Observing System (TGOS)

- • Automated, modular, surface-based sensor suite capable of tailored configurations

- • Full and Limited

- • Automatically transmits weather data directly to TFS or hand-held display

16

AIR WEATHER SERVICE

COMBAT WEATHER SYSTEM
SYSTEM DESCRIPTION - TWOS

- Manual Observing System (MOS)

  - Small, lightweight hand-held or ground-mounted sensors

  - Weather teams may use for first-in, stand-alone, or mobile observing capability, and as manual backup to the TGOS

  - Objective weight 10 pounds and less than 2 cubic feet

17

COMBAT WEATHER SYSTEM

SYSTEM DESCRIPTION - TWOS

- Upper Atmospheric Sensor (UAS)

  - • Provides vertical profiles of atmospheric conditions to 40,000 feet

  - • Ground site passively tracks the radiosonde package and transmits data to the TFS or floppy disk in a format ready for long-line transmission

18

COMBAT WEATHER SYSTEM

SYSTEM DESCRIPTION - TWOS

- Tactical Observing System (TACOBS)

  - Increase observation density

  - Placed in data sparse areas to collect and transmit weather observations

19

COMBAT WEATHER SYSTEM

SYSTEM DESCRIPTION - TFS

- Combat Air Forces (CAF) standard work stations with open systems operating system

- • Secret System High

- Minimal, Expanded, and Air Force Component Theater Weather Center (TWC)

- Application software consists of rehosting Automated Weather Distribution System (AWDS) and CAF Weather Software Package (CAFWSP) software

20

AIR WEATHER SERVICE

COMBAT WEATHER SYSTEM

SYSTEM DESCRIPTION - TFS

- Interoperable at TWC level

- Incremental Technology Incertions (ITIs) provide additional capabilities and continuity with fixed AWDS

21

AIR WEATHER SERVICE

COMBAT WEATHER SYSTEM
THEATER DEPLOYABLE COMM - TDC

- Provides all inter and intra-theather communications

- Provides link to C4I systems

- Reach back to CONUS gateway

COMBAT WEATHER SYSTEM
SCHEDULE

- Milestone I — Oct 93

- Rehost Complete — Sep 94

- Request For Proposal (RFP) — Sep 94

- Contract Award — 2FY95

- Initial Operational Capability (IOC) — 4FY96

- Full Operational Capability (FOC) — 4FY00

23

AIR WEATHER SERVICE

COMBAT WEATHER SYSTEM

SUMMARY

The CWS will enhance the effectiveness of combat operations by improving the capability of deployed weather forces to produce mission tailored weather products for battlefield commanders and war fighters via TDC to C4I systems

24

WEATHER DATA REQUIREMENTS FOR
STATE-OF-THE-GROUND TERRAIN ANALYSIS

Franz E. Westermeier
U.S. Army Engineer School
Directorate of Combat Developments
Ft. Leonard Wood, Missouri 65401-6600

Topographic Engineer trafficability/mobility analysis for the Intelligence Preparation of the Battlefield requires analysis and forecasting of the state-of-the-ground. State-of-the-ground includes frost depth; snow cover, depth, drift, and density; ice thickness of rivers and lakes; river stage and flooding; soil moisture; and soil temperature. Weather data inputs will include precipitation, surface temperature, surface wind, as well as other factors. As proponent for state-of-the-ground, the Engineers ask that the research community continue to develop tactical decision aids to model the state-of-the-ground. These tactical decision aids will be used in the Digital Topographic Support System and should use as input data, weather information received through the Integrated Meteorological System. A critical issue will be the development of these programs for remote locations where traditional input data will likely not be available. Therefore, remote sensing is also to be emphasized.

The Mapping, Charting, and Geodesy Branch functions of the U.S. Army Engineer School are located in the Directorate of Combat Developments. Topographic engineers provide expedient maps, geodetic data and terrain analysis information to the commander through the Intelligence Preparation of the Battlefield process. Topographic support covers a very broad range of topics. However, I will focus on terrain analysis which includes determination of mobility factors and identification of mobility corridors. An input to mobility is trafficability, the ability to move over land.

Trafficability includes terrain information such as slope, soil type, tree spacing and tree stem diameter, etc., but it also includes weather effects on terrain.

In 1990-91 the Intelligence School's meteorologists drafted a list of all known Army tactical environmental data requirements. These data needs included weather as well as what we are referring to as "state-of-the-ground" environmental data.

State-of-the-ground data elements include at least (and this list is flexible, we can add or subtract):

River stage/flood forecasting
Frost depth and thickness of frozen layer of soil
Ice thickness on lakes and rivers
Snow cover
Snow drift depth
Snow state (snow density)
Soil moisture
Soil temperature
Water temperature in lakes and rivers

Traditional weather support as outlined in AR 115-10/AFR 105-3 tasks the Air Force only to provide weather information, not information on the weather's effects on terrain. The state-of-the-ground parameters loosely fall under weather effects on terrain and are not been provided through the weather support system. Because they are closely related to the Engineer's trafficability/mobility assessment mission, proponency for them was transferred from the Intelligence School, the proponent for weather, to the Engineer School, the proponent for topography.

There is little, if any, mention of these factors in the military doctrinal literature such as Field Manuals. We know they were, at times, of great importance in World War II and Korea. However, now their measurement and forecasting are largely ignored.

Part of the reason for having ignored these state-of-the-ground parameters may be the difficulty of dealing with them. We have either not had the necessary input data or the manpower to manipulate it through lengthy computations. For example, during World War II we had an eighty-man unit just to forecast the level of the Rhine river; in Korea we had a 24-man unit for river stage forecasting. Now we have one floppy disk.

A maneuver commander has a reasonable right to expect his terrain team and intelligence officers to be able to give him information on these trafficability factors that could limit or even improve his and his opponent's movement. But in most cases the terrain team cannot. Other than a very fine computer program for forecasting streamflow and river stage, there are no established procedures for measuring or forecasting the listed state-of-the-ground factors.

Determination and forecasting weather effects on trafficability by terrain teams in the field is presently restricted mainly to terrain/ precipitation relationships. It may be that precipitation is easier to deal with than the state-of-the-ground parameters. However, the state-of-the-ground factors could be critical and we do not have algorithms for determining or forecasting them, other than flood or streamflow forecasting. Even that is extremely limited by the lack of detailed input precipitation data and the probable lack of opportunity to calibrate the model for the particular watershed. If the terrain analysts are very lucky, they may have information from indigenous sources such as local weather services or agricultural field stations. Otherwise, we have few tactical decision aids (TDAs) for state-of-the-ground.

With the advent of the combination of the Digital Topographic Support System (DTSS), the Terrain Evaluation Module (TEM) of the various command control systems, and the Integrated Meteorological System (IMETS), we are at least approaching the necessary computer power. With satellites, Unmanned Aerial Vehicles (UAVs), and the Automated Meteorological Sensor System (AMSS) we may be able to obtain the input data to either measure or model the state-of-the-ground parameters.

Algorithms already exist or can be developed by the labs and can be inserted into the combination of the Digital Topographic Support System and the Integrated Meteorological System. IMETS should be able to receive and forward to DTSS or TEM the inputs of either remotely sensed data or ground sensed meteorological data. DTSS and TEM should have the power to run computer algorithms for both determination and forecasting of these parameters. Then DTSS or TEM can combine the weather effects and non-weather effects together and the terrain analyst can determine mobility and mobility corridor information to be fed into the Army Command and Control System.

In an effort to improve the state-of-the-ground portion of terrain analysis, the Engineer School established a multi-service working group to discuss these trafficability issues; the first meeting was held in May of this year at Ft. Leonard Wood. We proposed a trafficability Determination Improvement Plan and further working group meetings to identify objective TDA requirements, establish priority of research and development efforts in this area, and monitor progress.

There was considerable enthusiasm to attend the meeting but some reluctance to talk about specific, existent research projects applicable to state-of-the-ground. We will have another meeting next spring with a more focused agenda.

There are aspects of state-of-the-ground in many research efforts. Our challenge is to direct research toward usable state-of-the-ground Tactical Decision Aids (TDAs) and ensure that the Research Plans and directives include state-of-the-ground considerations.

CONCLUSIONS

State-of-the-ground is a new proponency issue for the Engineer School. Traditional weather support will not satisfy these requirements. State-of-the-ground is a complex problem that will require considerable software development. The Army computer systems have now matured sufficiently to begin Tactical Decision Aid development. The challenge is to provide accurate, timely and usable trafficability assessment and predictions for the combat commander.

MOBILE PROFILER SYSTEM IMPROVEMENTS TO THE MET ERROR CONTRIBUTION OF THE ARTILLERY ERROR BUDGET

Abel J. Blanco and James Cogan
U.S. Army Research Laboratory
Battlefield Environment Directorate
White Sands Missile Range, New Mexico 88002-5501 USA

ABSTRACT

All effective artillery fire includes meteorological (met) aiming adjustments to compensate for the variations of wind, temperature, and density. These met uncertainties are due to measurement error, time staleness, distance separation, and terrain classification (type and roughness). When a battlefield target is selected, the commander must use the best met adjustments available to achieve the desired fractional damage. This paper defines the met errors derived from a single met scenario to determine the expected Mobile Profiler System (MPS) met improvements to the accuracy and effectiveness of artillery fire. Using an 84 percentile midlatitude wind scenario, simulated results are presented for the following MPS accuracies:

- Average 1994 — average expected value for the 1994 Technical Demonstration (TD) system;
- Worst Case 1994 — a probable worst case for the 1994 TD System;
- Passive 2000 — an average case for an upgraded system that uses satellite data from passive sensors including upgraded software for satellite data; and
- Active 2010 — the same as for the passive 2000 case, but with data from an active satellite sensor.

When stale met is used for the attack, it will take a larger amount of ammunition to achieve the desired level of effectiveness on the target and render the artillery unit vulnerable to destructive counter attack. The MPS shall provide near real time met data to the battery commander and allow predictive fire effective for long range artillery targets.

INTRODUCTION

In the planning and execution of military operations, weather is an important variable that the commander must consider. He must interpret and act upon information as it is made available to him. In the case of artillery, the resistance of the air to a projectile depends on the met parameters of temperature and density as well as on air motion (wind). Therefore, all effective artillery fire, whether predicted or transferred (adjusted or registered by a forward observer), includes met aiming adjustments that compensate for these atmospheric variables. On the battlefield, the mission of the artillery meteorological section is to provide formatted met messages to the firing units for use in correcting firing data for existing nonstandard weather conditions.

The Meteorological Data System (MDS, AN/TMQ-31)[1] was developed in an attempt to allow nonobserved first-round fire for effect and immediate suppressive fire. The timeliness of the weather information is constrained by the preparation and launch time and by the ascent rate of the balloon which lifts the met sensors. The MPS[2] is being developed to enhance the MDS capability with near real time met data (no balloon in the battlefield). The U.S. Army Research Laboratory (ARL) has also developed algorithms that assess and evaluate the errors and uncertainties in future weather data in order to satisfy the desired artillery requirements. These simulated results demonstrating the different met source error improvements can be utilized by the Artillery Improvement Analysis Working Group[3] in estimating future artillery accuracy and effectiveness.

This paper proposes a methodology that estimates the accuracy of the measured met parameters of wind, temperature, and density. The described procedure can be automated and only requires the following:

- an available met message,
- terrain classification (type/roughness),
- time and space staleness, and
- met sensor type.

Statistical evaluation of the methodology for estimating the met error sources demonstrates a high confidence in these estimated errors.

The expected wind, temperature, and density uncertainties can be computed from ARL algorithms by using an initialization wind profile.[4,5] These expected met errors are derived in units that can be multiplied by the appropriate firing table unit effects for the specific munition and firing range to determine the met aiming adjustments. When a battlefield target is selected, the commander must use the best met adjustments to achieve the desired fractional damage. It will take a larger amount of ammunition to achieve the desired level of effectiveness on the target if stale met is used for the attack.

Simulated results from a rocket-assisted projectile are used to present the met improvement afforded by different MPS configurations (representing current and future sensor accuracies). Future configuration comparisons with MDS results reveal significant met improvements for trajectories with the following apogees: 3, 12, and 19 km. The first and last trajectories reach a 22 km range and the other trajectory represents a long range 30 km application.

The artillery accuracy improvement analysis working group has defined all major contributing errors and presented an artillery cannon error budget with the individual errors assumed to be independent and normally distributed. One of the conditions that significantly affects a projectile after it leaves the tube is the state of the atmosphere through which the projectile passes. The single largest contributor is the wind error. Often a weapon will be fired using a meteorological message containing data that is several hours old acquired from a balloon-borne radiosonde that the prevailing wind carried well away from the firing location. Because of this time staleness, distance separation, and the meteorological instrumentation error, artillery may be aimed and fired using meteorological data that is not entirely correct for the current time and location.

MOBILE PROFILER SYSTEM

Time staleness must be significantly reduced if the artillery commander is to maintain effective predictive fire for future long-range targets. The MPS has been designed to significantly reduce time staleness from battlefield artillery met data. It has a suite of ground-based sensors including a radar wind profiler operating at approximately 924 MHz, a Radio Acoustic Sounding System (RASS) for virtual temperature, and a ground-based microwave radiometer for temperature and pressure. Miers[6] presents information on these types of sensors. The MPS also contains a small terminal/processor for satellite data from polar orbiting satellites. Figure 1 illustrates the overlap region for the wind profiles derived from surface and satellite sensors. Software developed at ARL/Battlefield Environment Directorate (BED), and implemented on the TD system with the assistance of personnel from the Environmental Technology Laboratory (ETL), National Oceanic and Atmospheric Administration (NOAA), merges the sounding data from the several instruments. The same program converts the combined sounding to the format of an Artillery Meteorological Message.[7]
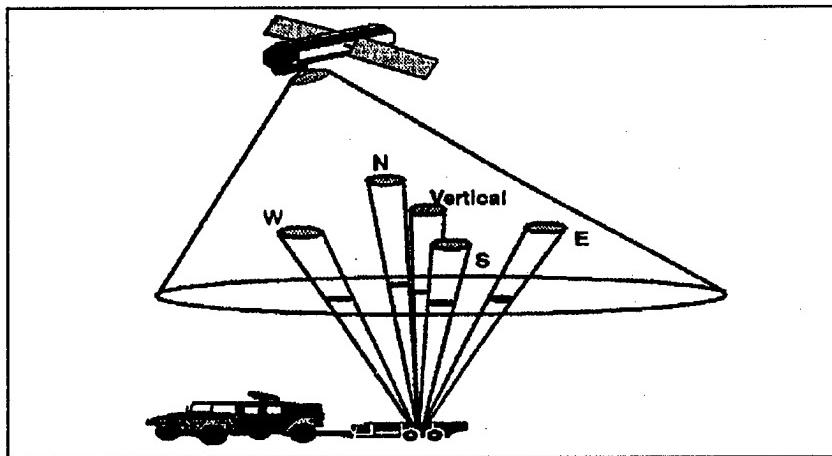
Figure 1.   Sketch of a potential MPS configuration consisting of one vehicle plus trailer showing relation of a five-beam radar profiler to the satellite footprint.

The system is capable of producing a new message every 15 to 30 min, thereby significantly reducing time staleness. The accuracy of the resultant profile of meteorological variables should be compared with data from rawinsonde systems that have time stalenesses of 2 to 4 h. The comparison at these different time stalenesses provides a true comparison of the relative accuracies of the two types of systems for artillery use.

The expected accuracies for the proposed MPS configurations are listed in table 1. The expected met accuracy for the 1994 Technical Demonstration MPS is represented by an average and a worst case for the wind. However, there is only one case for pressure and temperature parameters. These values are based on typical values found in Miers[6] and its literature cited. The "worst case" assumes profiler winds entered only up to 2.5 km, and the satellite wind estimates are degraded from 9 to 10 m/s accuracy. There is no change for the temperature and pressure variables. The temperature accuracies are somewhat to the good side for current technology, but not extreme.

The 2000 MPS case represents an upgraded system that uses satellite data from passive sensors including upgraded software for satellite data. This configuration affords wind and pressure accuracy improvement at the higher altitudes. The improvement here arises from better profiler (wind), improvements to merging algorithm (all variables), and improvement in satellite wind estimates (6 m/s instead of 9 or 10 m/s accuracy). Also, ground-based pressure/height from the microwave radiometer are included.

Table 1. Estimated MPS Measurement Ballistic 1σ Errors

MPS Average 1994

L #	hgt	Wind m/s	Wind bal kts	pres mb	dens bal %	temp K	temp bal %
1	0.2	1.5	2.92	1.0	0.10	1.0	0.35
2	0.5	1.5	2.92	1.0	0.10	1.0	0.35
3	1.0	1.5	2.92	1.0	0.10	1.0	0.35
4	1.5	1.5	2.92	1.0	0.11	1.0	0.35
5	2.0	1.5	2.92	1.0	0.11	1.0	0.36
6	3.0	1.5	2.92	1.0	0.12	1.0	0.36
7	4.0	1.5	2.92	1.0	0.13	1.0	0.37
8	5.0	1.5	2.92	1.0	0.14	1.0	0.37
9	6.0	1.5	2.92	1.0	0.15	1.0	0.38
10	8.0	3.0	4.52	1.0	0.17	1.5	0.38
11	10.0	4.5	5.72	1.0	0.20	1.5	0.38
12	12.0	7.0	7.55	3.0	0.37	1.5	0.38
13	14.0	9.0	9.06	3.0	0.48	2.0	0.38
14	16.0	9.0	9.53	3.0	0.56	2.0	0.38
15	18.0	9.0	9.81	3.0	0.66	2.0	0.38

MPS Worst Case 1994

L #	hgt	Wind m/s	Wind bal kts	pres mb	dens bal %	temp K	temp bal %
1	0.2	1.5	2.92	1.0	0.10	1.0	0.35
2	0.5	1.5	2.92	1.0	0.10	1.0	0.35
3	1.0	1.5	2.92	1.0	0.10	1.0	0.35
4	1.5	1.5	2.92	1.0	0.11	1.0	0.35
5	2.0	1.5	2.92	1.0	0.11	1.0	0.36
6	3.0	3.0	4.75	1.0	0.12	1.0	0.36
7	4.0	3.0	5.04	1.0	0.13	1.0	0.37
8	5.0	6.0	7.81	1.0	0.14	1.0	0.37
9	6.0	6.0	8.54	1.0	0.15	1.0	0.38
10	8.0	10.0	14.02	1.0	0.17	1.5	0.38
11	10.0	10.0	14.54	1.0	0.20	1.5	0.38
12	12.0	10.0	15.05	3.0	0.37	1.5	0.38
13	14.0	10.0	15.45	3.0	0.48	2.0	0.38
14	16.0	10.0	15.62	3.0	0.56	2.0	0.38
15	18.0	10.0	15.62	3.0	0.66	2.0	0.38

Table 1. Estimated MPS Measurement Ballistic 1σ Errors (continued)

MPS Passive 2000

L #	hgt	Wind		pres	dens	temp	
---	---	m/s	bal kts	mb	bal %	K	bal %
1	0.2	1.0	1.94	1.0	0.10	1.0	0.35
2	0.5	1.0	1.94	1.0	0.10	1.0	0.35
3	1.0	1.0	1.94	1.0	0.10	1.0	0.35
4	1.5	1.0	1.94	1.0	0.11	1.0	0.35
5	2.0	1.0	1.94	1.0	0.11	1.0	0.36
6	3.0	1.0	1.94	1.0	0.12	1.0	0.36
7	4.0	1.0	1.94	1.0	0.13	1.0	0.37
8	5.0	1.0	1.94	1.0	0.14	1.0	0.37
9	6.0	1.0	1.94	1.0	0.15	1.0	0.38
10	8.0	2.0	3.01	1.0	0.17	1.5	0.38
11	10.0	3.0	3.81	1.0	0.20	1.5	0.38
12	12.0	4.0	4.65	2.0	0.30	1.5	0.38
13	14.0	4.0	4.94	3.0	0.44	1.5	0.38
14	16.0	5.0	5.44	3.0	0.52	1.5	0.38
15	18.0	6.0	5.85	3.0	0.63	2.0	0.38

MPS Active 2010

L #	hgt	Wind		pres	dens	temp	
---	---	m/s	bal kts	mb	bal %	K	bal %
1	0.2	1.0	1.94	1.0	0.10	1.0	0.35
2	0.5	1.0	1.94	1.0	0.10	1.0	0.35
3	1.0	1.0	1.94	1.0	0.10	1.0	0.35
4	1.5	1.0	1.94	1.0	0.11	1.0	0.35
5	2.0	1.0	1.94	1.0	0.11	1.0	0.36
6	3.0	1.0	1.94	1.0	0.12	1.0	0.36
7	4.0	1.0	1.94	1.0	0.13	1.0	0.37
8	5.0	1.0	1.94	1.0	0.14	1.0	0.37
9	6.0	1.0	1.94	1.0	0.15	1.0	0.38
10	8.0	2.0	3.01	1.0	0.17	1.5	0.38
11	10.0	2.0	3.07	1.0	0.20	1.5	0.38
12	12.0	2.0	3.17	1.0	0.23	1.5	0.38
13	14.0	2.0	3.23	1.0	0.26	1.5	0.38
14	16.0	2.0	3.25	1.0	0.28	1.5	0.38
15	18.0	2.0	3.25	2.0	0.38	2.0	0.38

The 2010 MPS contains relatively minor technological upgrades to the ground-based system compared with the passive 2000 version, but receives data from an active satellite wind sounder. An active wind sounder (for example, space-based lidar) should result in significantly improved wind velocity accuracies. The temperature (from a passive satellite sounder) accuracy for satellite remains as in the passive 2000 scenario.

Demonstration of the 1994 TD MPS is scheduled for April 1994 at White Sands Missile Range, NM. Upon successful demonstration of the system, it will transition to the Project Manager (PM), Electronic Warfare (EW), Reconnaissance, Surveillance, Target Acquisition (RSTA). Current plans call for a preproduction prototype in FY 2000 that will incorporate advances in both software and hardware. Systems produced starting in 2000 through 2005 will use data from improved passive satellite sounders (for example, from DMSP Block 6). Later, relatively minor improvements to the MPS will allow reception and processing of data from active satellite wind sounders expected to come on-line around 2010. Another potential product improvement would be the use of a lower frequency radar profiler (for example, 449 MHz). This upgrade should allow measurement of wind velocities from the radar to a height of approximately 10 to 12 km above the ground depending on, for example, power, antenna aperture, and atmospheric conditions. Expected improvements in antenna design should lead to a lower frequency system that keeps the portability of the higher frequency version.

MODELED WIND, DENSITY, AND TEMPERATURE VARIABILITIES

Blanco[4] presents the methodology for computing wind variability in a formulation that is convenient for artillery applications. The ballistic wind component variability or uncertainty is derived as a function of the following:

- an available scalar wind profile (speed versus height),
- terrain type (flat or complex),
- time staleness,
- distance separation between the wind measurement and artillery firing location, and
- met sensor classification (balloon borne or remote).

An available wind profile provides the scalar wind versus height required to compute the wind variability. Initially, this scalar wind profile is ballistically weighted for surface-to-surface artillery fire using the ballistic weights listed in FM 6-16.[8] This weighting is used to define a single parameter that characterizes the total wind profile.

Originally, the wind variability formula was derived from least squares fits to many sets of experimental data containing wind speed differences with respect to time of measurement. By defining a relationship between the temporal and spatial wind variability, one can compute the distance separation coefficients from the derived time coefficients. For temperate latitudes, the generally accepted relationship between time and space staleness is that 1-h variability is equivalent to a 30-km distance variability.[9] Over fairly level terrain, a message taken 30 km away from a location is considered to give the equivalent accuracy of a 1-h-old message measured at that location. In mountainous terrain and in the proximity of large bodies of water, the valid distance should be reduced. Blanco[4] evaluates the following two terrain types: flat terrain and mountainous/basin border.

Time staleness and distance separation can be selected by the analyst to review accuracy and effectiveness of artillery fire support. The distance between met station and the projectile midpoint trajectory is set by the user; however, the drift of the balloon in the ambient wind will carry the met sensors to a new and significant location from the projectile trajectory.

The measurement errors are dependent on the type of sensor used. The ballistic wind measurement errors for the MDS NAVAIDS mode are listed in ASL-TR-0225[4] and verified by test results in 1988.[10] The accuracy is a function of height and the selected wind profile scenario. To simplify calculations, a maximum measurement error

is used as described by Dudenhoeffer.[11,12] These measurement errors are used to demonstrate the current artillery capability. Four MPS measurement error profiles are defined in the above section and are identified as: Average 1994, Worst Case 1994, Passive 2000, and Active 2010. Table 1 presents the proposed wind, temperature, and pressure errors.

In reality, the artillery commander knows the standard solution for aiming his gun on a selected target. This initial adjustment is based on the U.S. Standard Atmosphere (USSA).[13] Because the USSA does not contain a standard wind, the artillery fire control algorithm assigns a zero value for wind at all heights in computing the initial wind aiming adjustment. The final met correction is then expressed in terms of the measured wind (kts) and the temperature and density departures from the standard conditions.

In order to illustrate the ARL algorithm application (assuming a 155-mm caliber gun, high-explosive round, propellant charge 8, and an 18-km target range) one can determine an aiming elevation angle that will project the shell to within the 4500 to 5000 m layer above the surface or ballistic line 8. Using the met sensor ballistic measurement error and the ballistic wind for line 8, one can compute the wind uncertainty (standard deviation in kts) from the following formula:

Wind Component Variability

$$V = 0.061 (1 + 0.03445 \, S - 0.05846 \, Z)^2 (t + 2 \, d) + Vs \qquad (1)$$

where

- V = ballistic wind component variance (kt^2)
- Vs = met sensor ballistic measurement variance (kt^2)
- S = ballistic wind speed (kt)
- Z = top of ballistic line (km)
- t = staleness (min)
- d = displacement including balloon drift (km).

When estimating the ballistic component wind error for ballistic line 1, equation (1) is modified to include more representative coefficients derived from data collected at the lower (< 200 m) altitudes and short (2 to 8 min) time intervals. For a detailed explanation and equations, see Blanco.[4] Ballistic line 1 results become significant for aiming adjustments in the following applications: rocket, thrusting shell, and wind-sensitive submunitions.

Density and temperature variabilities have received less study than the variabilities of winds. Since density and temperature are scalar quantities, no separation into components is necessary. Density and temperature variabilities as a function of time are higher near the ground and smaller at higher levels. Ballistic temperature [T(Z)] analysis showed a weaker dependence on height (Z) than found for density [D(Z)].

Since the initial density and temperature aiming corrections include the USSA standard density and temperature, the final aiming adjustments are expressed in terms of percent departures from the USSA conditions. Using the met sensor ballistic measurement error and the ballistic line 8 example, one can compute the density and temperature uncertainties (standard deviation in percent) from the following formulas:

Density Variability

$$V = 0.00282 (t + 2 \, d) / Z + Vs \qquad (2)$$

Temperature Variability

$$V = 0.00165 (t + 2 \, d) / Z^{1/2} + Vs \qquad (3)$$

where

V = ballistic variance ($\%^2$)

Vs = met sensor ballistic measurement variance ($\%^2$)

Z = top of ballistic line (km)

t = staleness (min)

d = displacement including balloon drift (km).

These environmental (time staleness and distance separation met errors) algorithms were derived from controlled experiments by the U.S. and NATO countries. ARL has high confidence in these estimates and continues to augment historical data for the purpose of improving the empirical coefficients used in the variability estimation. The described met variability model has been automated to allow rapid computation of artillery accuracy and effectiveness.

Results derived from these wind, density, and temperature algorithms are used to evaluate the worth of the four proposed MPS configurations relative to the MDS. The improvement varies with respect to the trajectory apogee and the initial met conditions. If one derives results from calm conditions, then the expected improvement is minimal.

SIMULATED RESULTS

Using the above described met uncertainties together with the firing table unit effects for each of the met contributors, one can estimate the impact displacement from the met error at stationary targets. Accuracy and effectiveness models can then be parameterized as a function of the met bias error. Assuming the standard expected errors for all other factors in the artillery error budget, the time staleness and distance separation between the met measurement and the midpoint of the projectile trajectory are varied to demonstrate the effect of met on cannon accuracy and effectiveness.

Figure 2 presents the three rocket-assisted M549A1 round trajectories used to compare the proposed MPS configuration improvements over the MDS. This artillery round can reach the 22-km range by either a low or high quadrant elevation. The third trajectory represents a 30-km long range application. Note that these apogees determine the required ballistic met at lines 6 and 15 for the short range and line 12 for the long range.
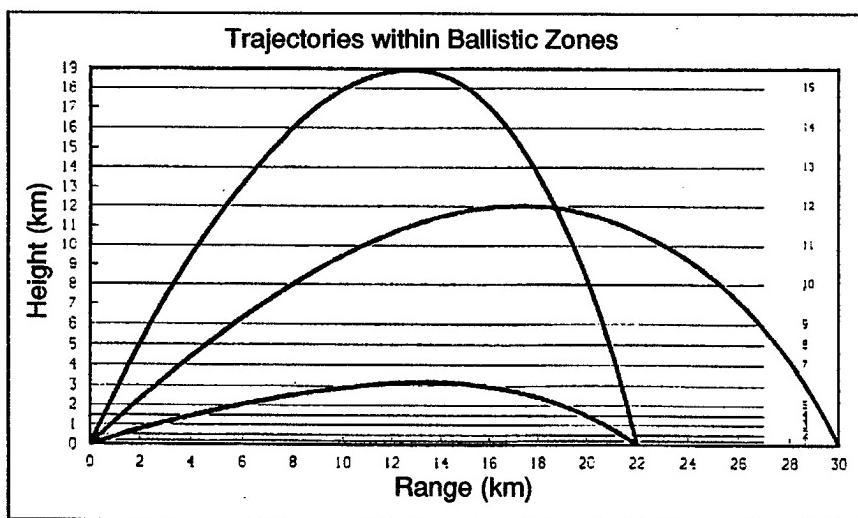
Figure 2. Selected M549A1 rocket-assisted projectile trajectories.

To examine the expected met effects, a weather scenario must be defined. Because of the changing nature of the weather, no fixed rule can be made to standardize a wind profile since the rate of variation of the atmospheric conditions is never absolutely predictable. As a result, a generalized global wind profile is selected; Essenwanger[14] published a set of global scalar wind speed distributions. From a set of Northern Hemisphere data, Essenwanger derived seasonal and annual cumulative frequency distribution wind speed profiles for different regions. He then assumed that these profiles are representative of the corresponding regions (Tropic < 30 N, Subtropic 30 to 45 N, Mid Latitude 45 to 60 N, and Polar > 60 N).

Using the Mid Latitude annual scalar wind profile,[15] one can compute the ballistic wind for the particular artillery firing solution (includes gun caliber, round, propellant charge, and target range). The selected wind profile is also used to derive a resultant balloon drift. Because of radar and satellite technology, all proposed MPS configurations do not have this balloon drift displacement from the point of application. Assuming a battlefield time staleness and resultant displacement between the balloon or MPS site and the midpoint of the shell's trajectory, one can estimate the expected met variability by using equations (1) through (3).

Table 2 lists the Essenwanger midlatitude annual wind speed distribution profiles. The 84 percentile cumulative distribution was selected because it is the closest representation to the one standard deviation wind profile. By this selection the derived met errors can be squared and added to the variances from the other artillery errors (ammunition, survey, muzzle velocity, aiming, and target location) to compute the total artillery error.

Table 2. Windprofiles (annual) for the Midlatitudes
(from Letter Report FARMY-153-5 Dr. Oskar Essenwanger)

| Wind Speed (m/s) Cumulative Percentile | | | | | Wind Direction | |
50%	68%	84%	95%	km	Winter Degree	Summer Degree
3.9	5.1	7.1	10.1	0.	115	317
7.8	9.7	12.9	17.8	1.	332	301
9.3	11.6	15.1	20.4	2.	334	284
10.7	13.3	17.4	23.1	3.	325	280
11.9	14.6	19.4	26.0	4.	326	276
13.0	16.3	21.5	28.9	5.	325	278
15.8	20.1	24.4	32.2	6.	332	281
18.2	22.8	27.5	36.0	7.	327	277
21.0	26.0	31.0	40.0	8.	326	274
22.3	27.7	32.6	42.0	9.	323	275
23.8	29.2	34.6	44.2	10.	314	276
24.0	29.3	34.4	43.5	11.	313	278
22.0	27.2	32.4	40.3	12.	312	280
19.4	23.6	27.8	32.6	13.	309	278
16.0	20.3	23.7	28.2	14.	313	275
12.5	16.2	19.3	22.2	15.	312	275
9.6	12.5	15.0	17.8	16.	315	275
7.8	10.0	12.3	16.8	17.	311	275
7.0	9.0	11.0	14.9	18.	311	274
7.0	8.7	10.7	14.1	19.	310	200
7.0	8.6	10.6	14.1	20.	306	127
7.5	9.4	11.3	15.1	21.	309	110
7.9	10.1	12.4	16.8	22.	308	93
8.2	10.6	13.0	17.4	23.	308	94
8.6	11.1	13.6	18.1	24.	305	96
9.0	11.7	14.5	19.4	25.	304	95

Using the above described algorithms, one can compute the met error for each source (wind, temperature, and density) at the selected line number. An example output listing of the met ballistic errors for the MDS (2 h old and 15 km away) is presented in table 3. These are the wind errors expected from the 84 percentile wind profile, a temperate latitude, and relatively flat terrain. Even though the space separation error is not listed as are the instrument and time staleness errors, it is root-mean-squared to derive the total meteorological error. This MDS met error represents an average for the wind profile selected. For completeness, a best estimate of the computer error is also listed in this table. In computing the expected MPS met errors, no balloon drift is added to the met station separation from the place of application. Note that the three selected ballistic lines (6, 12, and 15) represent minimums and the maximum error within the wind profile.

Table 3. A Standard Deviation of Ballistic met Components

MET STANDARD DEVIATIONS 　(DEN=%,WND=KNOTS,TMP=%)
　　　　　　　　　　　　　　　　(TEM=K,WIN=KNOTS,PRS=mb)
　　　　　　　　　　　　　　　　(WIND=Component Error)

Midlatitude (one standard deviation) wind profile.
Optimized for annual winds (FARMY-153-5)
NAVAIDS (MDS) used for instrument error.

　　　Staleness (hours) = 2.0　　　　　　　Space (km) = 15.0

One-hour time staleness is equivalent to 30 km space separation.
Equivalence factors used for met ballistic lines 1 to 15:

L#	Instrument			Staleness			Total Ballistic			Z#	Total Computer		
	den	wnd	tmp	den	wnd	tmp	den	wnd	tmp		win	tem	prs
1	0.15	1.65	0.25	1.30	4.06	0.99	1.46	6.22	0.78	1	6.2	2.3	3.0
2	0.15	1.04	0.25	0.82	4.22	0.63	0.93	4.84	0.64	2	4.9	1.8	2.3
3	0.15	1.00	0.25	0.58	4.48	0.44	0.67	5.11	0.56	3	5.3	1.6	1.9
4	0.15	1.00	0.25	0.47	4.65	0.36	0.55	5.30	0.52	4	5.6	1.4	1.6
5	0.15	1.00	0.25	0.41	4.77	0.31	0.49	5.44	0.49	5	5.7	1.3	1.5
6	0.15	1.00	0.25	0.34	4.91	0.26	0.41	5.62	0.46	6	5.9	1.3	1.3
7	0.15	1.00	0.25	0.29	5.03	0.22	0.36	5.82	0.44	7	6.0	1.2	1.2
8	0.15	1.00	0.25	0.26	5.11	0.20	0.34	6.00	0.43	8	6.2	1.2	1.1
9	0.15	1.00	0.25	0.24	5.19	0.18	0.32	6.21	0.42	9	6.4	1.1	1.1
10	0.15	1.00	0.25	0.21	5.62	0.16	0.29	6.95	0.41	10	6.5	1.1	1.0
11	0.15	1.00	0.25	0.18	5.76	0.14	0.28	7.54	0.41	11	6.7	1.1	0.9
12	0.15	1.00	0.25	0.17	5.68	0.13	0.28	7.88	0.41	12	7.0	1.0	0.8
13	0.15	1.00	0.25	0.16	5.21	0.12	0.27	7.60	0.42	13	7.7	1.0	0.7
14	0.15	1.00	0.25	0.15	4.63	0.11	0.26	7.01	0.42	14	8.4	1.0	0.7
15	0.15	1.00	0.25	0.14	4.04	0.10	0.26	6.28	0.41	15	9.0	0.9	0.6
										16	9.5	0.9	0.5
										17	9.8	0.9	0.5
										18	9.6	0.9	0.4
										19	8.8	0.9	0.4
										20	7.6	0.9	0.3
										21	6.4	0.9	0.3
										22	5.0	0.9	0.3
										23	3.9	0.9	0.2
										24	3.2	0.9	0.2
										25	2.1	0.9	0.2
										26	1.3	0.9	0.2

Total includes errors due to instrument, staleness, and space.

Using these types of results, one can compare the expected improvement provided by the MPS. Figure 3 presents the comparison of the MDS and the MPS for the three selected ballistic lines. Note that the MDS classifications include 4-, 2-, and 1-h-old data which represent the capability of the equipment in the battlefield. Normally, the available data is 4- or 2-h-old; however, given sufficient logistics and personnel the 1-h MDS is possible for the lower trajectories. For line 6, representing results of met up to 3 km above the surface, the MPS data (starting from the average 1994 case) reveals a significant improvement over the MDS results. For short ranges requiring low apogees, the MPS 1994 average classification improves artillery accuracy. The 2000 passive and 2010 active configurations are identical at these ranges and improve on the 1994 results because of the better surface-based data.
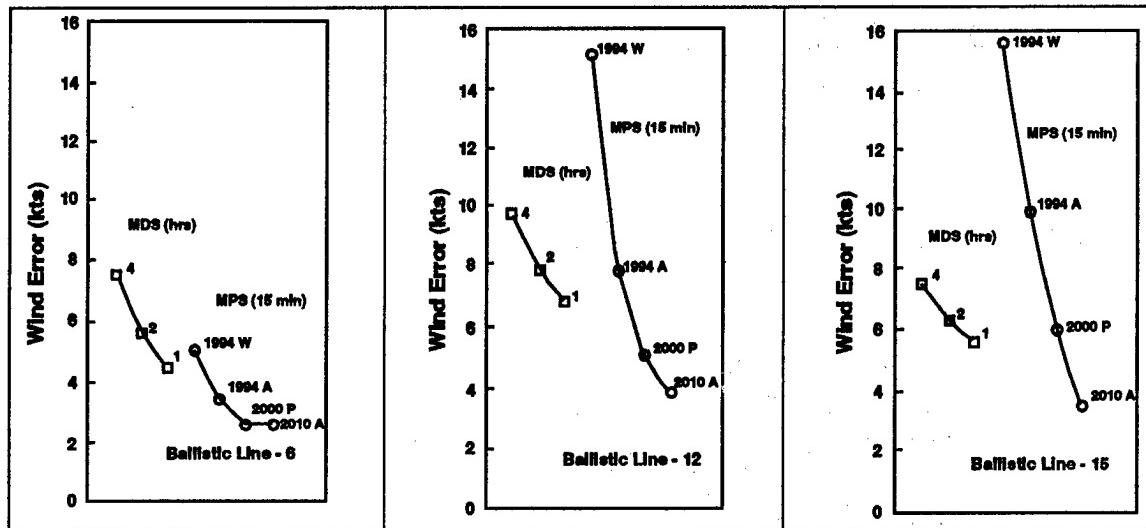
Figure 3. MDS and MPS wind error comparisons for ballistic lines 6, 12, and 15.

The results for the other ballistic lines show no improvement in the 1994 TD MPS because the satellite wind estimates are less accurate than the rawinsonde measurements. However, the passive satellite method expected in 2000 when combined with the improved ground-based system reveals an improvement over the balloon methodology.

Table 4 lists the firing table met unit effects[16] for each ballistic line and can be used to convert the ballistic met data into meters miss on the target. The ARL simulated results (example — table 3) for the following MDS cases:

- a worst 4-h-old and 15 km away,
- the normal 2-h-old and 15 km away, and
- the optimum system capability 1-h-old and 15 km away,

and the following MPS cases:

- an average 1994,
- the passive 2000, and
- the active 2010

are used with the corresponding unit effect from table 4 to derive the expected met parameter error.

The range wind results are cataloged with respect to time staleness and presented in figures 4 and 5. The 15-min data represents the MPS configurations and are not included in the least-squares fit of the MDS data. Both figures illustrate a significant MPS (2000P and 2010A) improvement over the MDS. Note that since a balloon-borne sonde

would require slightly more than 60 min to reach 19 km (line 15; figure 2), a more realistic MDS optimum time is probably around 1.5 to 2 h for a trajectory reaching ballistic line 15. For these two MPS configurations, one can see about 100 m reduction in the expected miss for the long 30 km range target and about 50 m reduction for the 22 km range target. Results from the MPS 1994A comparison reveal a significant improvement only for the low QE 22 km range target. For the other two trajectories, the 1994 measurement errors exceed the expected environmental error due to time staleness, and provide no improvement over the MDS.

Table 4. M549A1 Firing Table Unit Effects

Provisional FT 155-AO-O 155 mm Howitzer M198 Charge 8R Rocket Assisted

range (km)	QE (mil	line #	hgt (km)	cwnd (mil/kt)	rwnd (m/kt)	tmp (m/%)	den (m/%)
22.00	391.5	6.00	3.00	0.53	18.35	29.70	133.15
22.00	1233.2	15.00	18.00	1.37	16.70	35.00	163.20
30.00	886.60	12.00	12.00	0.76	31.90	60.50	221.90
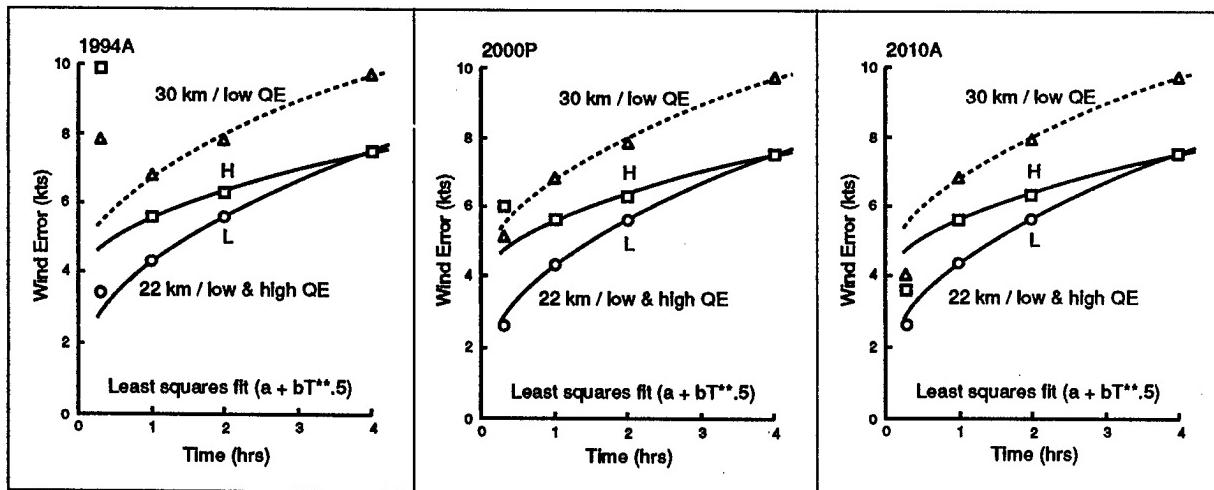
Figure 4. Range ballistic wind MPS and MDS comparisons.
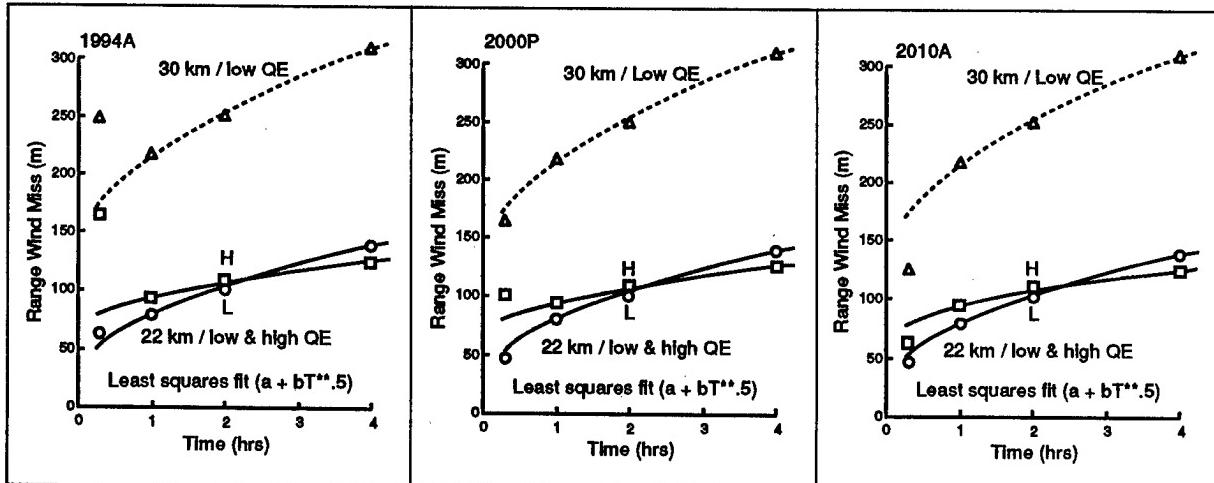
Figure 5. Range wind miss MPS and MDS comparisons.

40

EXTENDED RANGE HOWITZER ERROR BUDGET

From these results, one can now derive the MPS improvements to the met error contribution of the artillery error budget. Reichelderfer[17] presents the most current error budget for the extended range howitzer, mean point impact (MPI) error for the M549A1 at 35-km range, as follows:

Error Source	Range (%)	Deflection (%)
Occasion-to-occasion	40	9
Wind	39	85
Density	7	0
Temperature	1	0
Muzzle velocity	9	0
Rocket	3	0
Aim and position	1	6

Since the simulated results are derived by using the M549A1 firing table (30.1-km maximum range listed), assume that the above error budget is applicable to the analyzed 30-km range. The improvement of the individual met error sources is now derived by the following algebraic expressions:

$$p = W^2 / T^2 \qquad (4)$$

$$T = sqrt(S^2 + W^2) \qquad (5)$$

$$Tn = sqrt(S^2 + Wn^2) \qquad (6)$$

where

the percentage contribution, "p", is given by Reichelderfer,[17]

the wind miss, "W", is read from figure 5,

the total miss, "T", is derived from equation (4), and

the standard deviation for all other error sources, "S", is derived from equation (5).

The new total miss, "Tn", is then derived from equation (6) using "S" and

the improved new wind miss, "Wn", from figure 5.

Following this procedure, an improvement to the total artillery error budget afforded by the MPS 2000P over the MDS 2-h-old data yields a 49-m range and 66-m deflection accuracy improvement.

For the extended range trajectory, the proposed MPS pressure and temperature estimates match the MDS data with 2-h staleness. Based on the simulated results from the above section, there is no improvement. Even if there was an improvement, this would translate to a minor change in the total error budget because of the small 7 and 1 percent density and temperature contributions.

CONCLUSIONS

As long as the met sensor errors are equivalent, it has been demonstrated that fresher met data will always yield more accurate artillery fire. The MPS has the advantage of fresher data and contains no balloon drift. In support of longer range targets, the balloon-borne met sensors must ascend higher and the MDS met data will contain a larger distance separation. The balloon drift results are root-mean-squared with the met station separation. Therefore, using the current MDS for supporting long range firing will contain an increased met error due to space separation. For the MPS, this distance increase is not included because of the remote sensor technology. The lack of balloon drift then becomes another significant factor in the improvement provided by the MPS.

The 1994 MPS classifications do not improve the artillery accuracy for trajectories with apogees greater than ballistic line 12. The MPS met errors at these heights are larger than the balloon with 2-h staleness (see results for ballistic line 15 in figure 3). However, the 1994 technology reveals an improvement for the low QE, 22-km range trajectory. It is not until the 2000 and 2010 classifications that the MPS always provides an improvement over the MDS.

The most important consideration is whether the initial operational capability (IOC) MPS can provide an improved capability for artillery applications. Based on the comparisons presented herein, the MPS (passive 2000) accuracy should exceed that of the MDS for all situations except the theoretical 1-h-old MDS for ballistic line 15. One should consider that balloon sondes rise at approximately 300 m/min, thereby reaching 19 km (figure 2) slightly over 60 min. A more realistic minimum time for that trajectory would be approximately 1-1/2 to 2 h. Thus, for a realistic case, the IOC MPS should exceed the capability of the MDS. MPS range wind results indicate an improvement of about 90 m for the 30-km range trajectory and about 50 m for the 22-km range trajectory. These improvements translate to a 49 m range and 66-m deflection improved total accuracy and to a 25-m range and 50-m deflection, respectively. There was no significant improvement provided by the MPS pressure and temperature estimates. The 15-min stale estimates are as good as the MDS 2-h stale data. Future upgrades (lower frequency radar and active satellite sounder) will produce even better accuracies — significantly better than any projected balloon sonde system.

LITERATURE CITED

1. "Required Operational Capability (ROC) for the Field Artillery Meteorological Acquisition System (FAMAS), Change 1," Department of the Army, Headquarters, U.S. Army Training and Doctrine Command, Fort Monroe, VA (1984).

2. R. E. McPeek and M. A. Seagraves, "Mobile Profiler System (MPS): The Army's Future Target Area Meteorology Data Collection System," Proceedings of the 1992 Battlefield Atmospherics Conference, U.S. Army Research Laboratory, White Sands Missile Range, NM (1992).

3. R. E. Bennett, "Artillery Accuracy Improvement Analysis," U.S. Army Field Artillery School, Fort Sill, OK (1989).

4. A. J. Blanco, "Methodology for Estimating Wind Variability," ASL-TR-0225, U.S. Army Atmospheric Science Laboratory, White Sands Missile Range, NM (1988).

5. "Field Artillery Meteorological Acquisition Systems," TRASANA TR-18-77, U.S. Army TRADOC System Analysis Activity, White Sands Missile Range, NM (1977).

6. B. T. Miers, J. L. Cogan, and R. S. Szymber, "Review of Selected Remote Sensor Measurements of Temperature, Wind, and Moisture, and Comparison to Rawinsonde Measurements," ASL-TR-0315, U.S. Army Atmospheric Sciences Laboratory, White Sands Missile Range, NM (1992).

7. J. L. Cogan, "Battlefield Atmospheric Soundings in Near Real Time Using Satellite and Ground-Based Remotely Sensed Data," Proceedings of the Battlefield Atmospherics Conference, December 1992, pp. 101-110, Battlefield Environment Directorate, U.S. Army Research Laboratory, White Sands Missile Range, NM (1992).

8. Field Manual 6-16, "Tables for Artillery Meteorological (Electronic) Ballistic Type 3 and Computer Message," Headquarters, Department of the Army, Washington, DC (1982).

9. A. S. Jursa, 1985: Handbook of Geophysics and the Space Environment, Air Force Systems Command, Air Force Geophysics Laboratory, Hanscom Air Force Base, Bedford, MA.

10. AN/TMQ-31 Meteorological Data System (MDS) DT Test (1988).

11. A. W. Dudenhoeffer, "Models for Ballistic Wind Measurement Error Analysis," Volume I: Model Formulation, ASL-CR-82-0008-2, U.S. Army Atmospheric Sciences Laboratory, White Sands Missile Range, NM (1982).

12. A. W. Dudenhoeffer, "Models for Ballistic Wind Measurement Error Analysis," Volume II: User's Manual, ASL-CR-83-0008-1, U.S. Army Atmospheric Sciences Laboratory, White Sands Missile Range, NM (1983).

13. 1962: U.S. Standard Atmosphere, National Aeronautics and Space Administration, United States Air Force, United States Weather Bureau (1961).

14. O. M. Essenwanger, "Wind Profiles from Surface to 24 km for Four Climatic Zones," LR-FARMY 153-3, U.S. Army Missile Command, Redstone Arsenal, AL (1990).

15. O. M. Essenwanger, "Wind Profiles (annual) from Surface to 25 km in the Midlatitudes," LR-FARMY 153-5, U.S. Army Missile Command, Redstone Arsenal, AL (1991).

16. "Provisional Firing Table FT 155-AO-O," January 1978, Department of the Army Firing Table, Headquarters, Department of the Army, Washington, DC.

17. M. Reichelderfer, "Methodology and Error Budget Status," Minutes of 22-23 June 1993 JMEM/SS Delivery Accuracy Working Group, Surface Warfare Development Group, Naval Amphibious Base/Little Creek, Norfolk, VA (1993).

COMPUTER-ASSISTED ARTILLERY METEOROLOGY

SYSTEM DESIGN

John B. Spalding and Natalie G. Kellner
Physical Science Laboratory
New Mexico State University
Las Cruces, New Mexico 88003-0002, USA

Robert S. Bonner
U.S. Army Research Laboratory
White Sands Missile Range, New Mexico 88002-5501, USA

ABSTRACT

The Computer-Assisted Artillery Meteorology (CAAM) Phase II system is currently under development at the Physical Science Laboratory under contract with the ARL Battlefield Environment Directorate. The objective of CAAM is to evaluate and demonstrate improvements in reported meteorology (met) for field artillery fire support by integrating, modeling, and disseminating more accurate and timely upper air and target area met data. The CAAM computer is located in an AN/TMQ-31 Meteorological Data System (MDS) van, which allows it to receive and send data with the TACFIRE Fire Direction Center, including computer met messages from other MDS units in the Division area. In the demonstration configuration the other devices that will communicate with CAAM and provide met data are: two remote MDS surrogates (MARWIN upper air systems with laptop PCs) to simulate fielded MDS units, a remote prototype Integrated Meteorological System (to supply special target area met data), a local surface sensor suite, a local Mobile Profiler System (local soundings and met satellite profiles), and a Battery Computer System Simulator for demonstration fire control software. Within CAAM, Ada software modules control all communications, data management, data processing, and user interaction tasks. The improvement in met is accomplished by integrating data from the above sources through a 3-dimensional objective analysis, and then generating forecasts with a meteorological mesoscale model.

1. INTRODUCTION

Since shortly after World War II, the traditional means of providing meteorological support for the U. S. Army Field Artillery has been to rely on balloon-borne radiosonde soundings, usually launched from no more than two locations in friendly territory. These single soundings were

then applied to artillery firing tables for firing solutions in areas where the atmospheric parameters may have been significantly different than the areas where the measurements were actually taken.

When the AN/TMQ-31 Meteorological Data System (MDS) was developed and delivered to Army Artillery Field Units (last deliveries in 1984), the artillery met sections became much more mobile than before and had the added capability of mobile data acquisition through the use of Navigation Aid systems such as LORAN or International OMEGA. These systems added the technique of using a relative positioning calculation with the time of the sonde position, which provides wind speed and direction. However, the principle of balloon-borne soundings from no more than three locations in the friendly area of a division zone of responsibility had not changed from the traditional way of using the met data.

Current technology, through the use of mesoscale models (Yamada and Bunker, 1989), provides a means of projecting measurements taken on the friendly side of the Forward Line of Own Troops (FLOT) to the area of direct application along the trajectories between the guns and their assigned targets. The Computer-Assisted Artillery Meteorology (CAAM) system will have the capability to provide more timely and more spatially applicable meteorological data to the artillery Battery Computer System (BCS), which will then provide more accurate firing solutions to the guns. The CAAM system will also have the capability to provide target area meteorological conditions, as required by the field artillery, in support of smart round/warhead and submunitions deployment.

With the advent of new technology weapons such as the Advanced Field Artillery System (AFAS), Multiple Launch Rocket System (MLRS), and Army Tactical Missile System (ATACMS), come requirements for even more timely, accurate, and directly applicable meteorological measurements. The CAAM system will serve as a developmental platform upon which improvements can be made in model accuracy and resolution and upper air data management to satisfy requirements for these advanced weapons.

2. THE CAAM PHASE II PROJECT

2.1 SCOPE

There are two major goals of the CAAM Phase II effort. The first is to develop an improved CAAM Technology Demonstration Platform. This platform consists of an HP 9000 Series 750 computer housed in an MDS van, where it will gain access to the TACFIRE radio network through the communication capabilities of the MDS. The CAAM computer will run a complex suite of software (written primarily in the Ada programming language) that will manage communications and data, and produce improved composite met messages.

The second goal of this project is to generate documentation to support the transition of CAAM to the Program Manager for follow-on development. To accomplish this, the project is being managed in accordance with DOD-STD-2167A (1985) standards, and a complete set of documents is being produced according to those standards. These documents encompass software and interface requirements and design specifications, test plans, management plans, user's guide,

and others.

Since this is a one-year effort, a platform cannot be developed and evaluated that is ready for the field. An important requirement of this project, however, is to produce a system as similar to an operational configuration as possible. This, plus the DOD-STD-2167A documentation, should allow for more rapid follow-on evaluation and additional software development.

The functions, interfaces, and design of the CAAM Phase II system are discussed below. The demonstration scenarios will take place in an "Area of Operations" (AOP) defined as follows. The section of the battlefield processed by a CAAM system extends across a 60 km section of the FLOT. Perpendicular to the FLOT, it extends 20 km into the friendly side (which contains the artillery and MDS units) and 200 km downrange into the enemy rear. Composite met messages can be produced for any points within this AOP. In the proposed scenarios, however, messages will be produced only for designated gun/target pairs.

2.2 SYSTEM FUNCTIONS

The primary functions of the CAAM Phase II system are:

- ingest and manage met data from both current and future support systems; these data are upper air measurements (rawinsondes, profilers, and met satellite derived profiles) and target area met

- produce "best" MET-CM (computer met message) and MET-TALL (target area low level met entry message) messages for specific gun/target pairs; this requires processing met data through a 3-D objective analysis, mesoscale forecast model (the High Order Turbulence Model for Atmospheric Circulation, HOTMAC), and met message generation sequence; these messages are intended to be used at the midpoint (MET-CM) and at the target (MET-TALL) for these gun/target pairs

- disseminate best MET-CM and MET-TALL messages to the Fire Direction Center

- determine if best MET-CMs have changed since the previous dissemination in a manner that significantly affects artillery and MLRS accuracy; this is used to prevent unnecessary dissemination of met messages, reducing TACFIRE communications traffic

- provide a user interface and executive driver for control of the system

The secondary functions of the CAAM Phase II system are:

- relay met data to the Integrated Meteorological System (IMETS) to enhance its database of upper air information

- accept requests for met messages for specific gun/target pairs from the BCS Simulator, and return best met for these gun/target pairs, as well as observed MET-

CM messages

3. SYSTEM CONFIGURATIONS AND INTERFACES

There are two configurations planned for the devices external to the CAAM system. The Operational Configuration makes use of existing tactical units with the support of a proposed IMETS element. The Demonstration Configuration emulates a more complete set of support devices for the purpose of demonstrating the functions that a future CAAM would perform. Arrows in the following figures indicate the directions of data flow.

3.1 OPERATIONAL CONFIGURATION

Figure 1 shows the Operational Configuration, in which two MDSs (MDS 1 and MDS 2) relay data to the CAAM computer through the Fire Direction Center (FDC). The FDC forwards it to the MDS containing the CAAM system. The AN/UYK-19 computer, which is the System Processor Unit (SPU) of an MDS, communicates with the CAAM computer by direct serial connection.
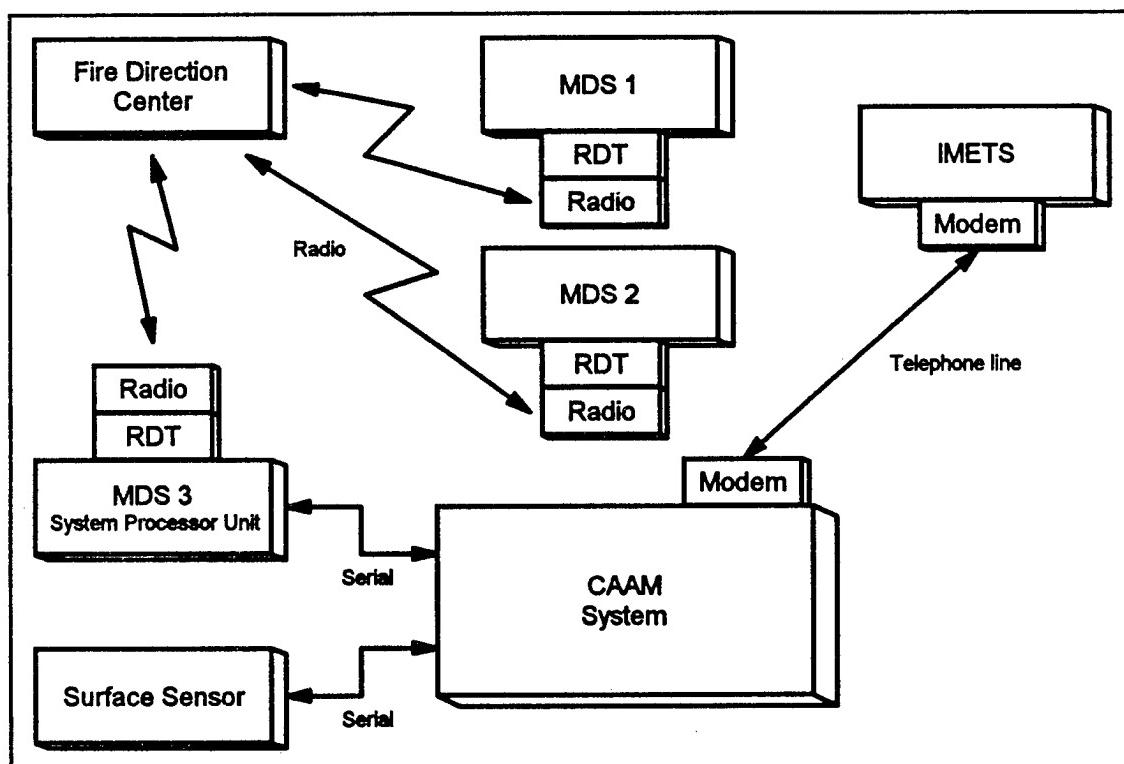
Figure 1. Operational Configuration.

There are two other devices in the Operational Configuration. The surface sensor suite (a modified AN/TMQ-34) measures wind, temperature, pressure, and relative humidity. These values are relayed by the CAAM system to the AN/UYK-19, so that it can incorporate these measurements in line 0 of its MET-CM message. An IMETS is also projected to be part of this configuration. It will provide the met at the target area, which is required by the MET-TALL

48

message. Also, CAAM will relay upper air data to IMETS to supplement its database.

A complete Operational Configuration will not be available during the CAAM Phase II time period, but the capability to receive and process MDS 1 and MDS 2 data through the radio link to the MDS with the CAAM computer is to be provided in the Phase II system. Also, the exchange and use of data with an IMETS are functions of the Phase II system; these functions are exercised in the Demonstration Configuration by including a prototype IMETS.

3.2 DEMONSTRATION CONFIGURATION

Figure 2 shows the Demonstration Configuration, in which the MDS 1 and MDS 2 are surrogates that send data to the CAAM system through a modem. These surrogates are MARWIN upper air systems connected to laptop PCs. The IMETS in this configuration is a Test Exploitation Weather TestBed (TEWTB), which is the prototype IMETS.
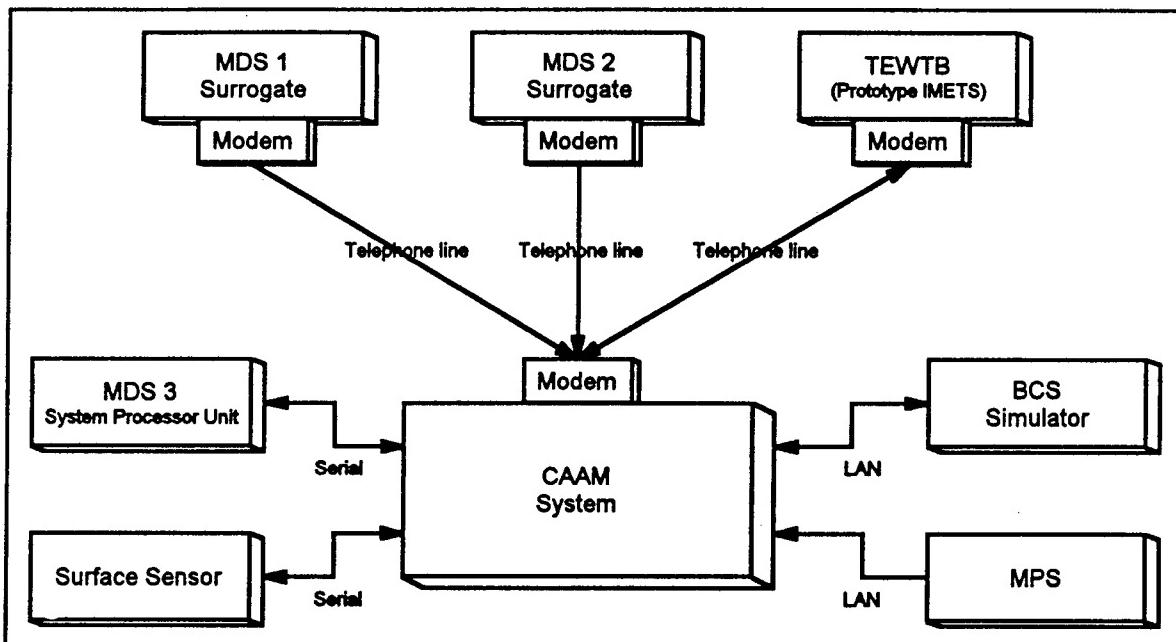
Figure 2. Demonstration Configuration.

There are two additional systems in this configuration. A Mobile Profiler System (MPS) communicates through a Local Area Network (LAN) to provide local upper air profiles and met satellite (METSAT) profiles (Seagraves et al., 1992). The local profiles are provided every 15 minutes, and METSAT every 6-12 hours. A BCS Simulator is also connected to the CAAM computer through a LAN. This system (a PC) contains fire control software and a special application to be developed by the Army Research, Development and Engineering Center (ARDEC) that will simulate the firing of rounds through raw (observed) met and the composite best met produced by the CAAM system for the purpose of demonstrating improved artillery accuracy.

49

3.3 INTERFACES AND DATA FLOW

Figure 3 shows the data flows between the CAAM interface software and the external devices.
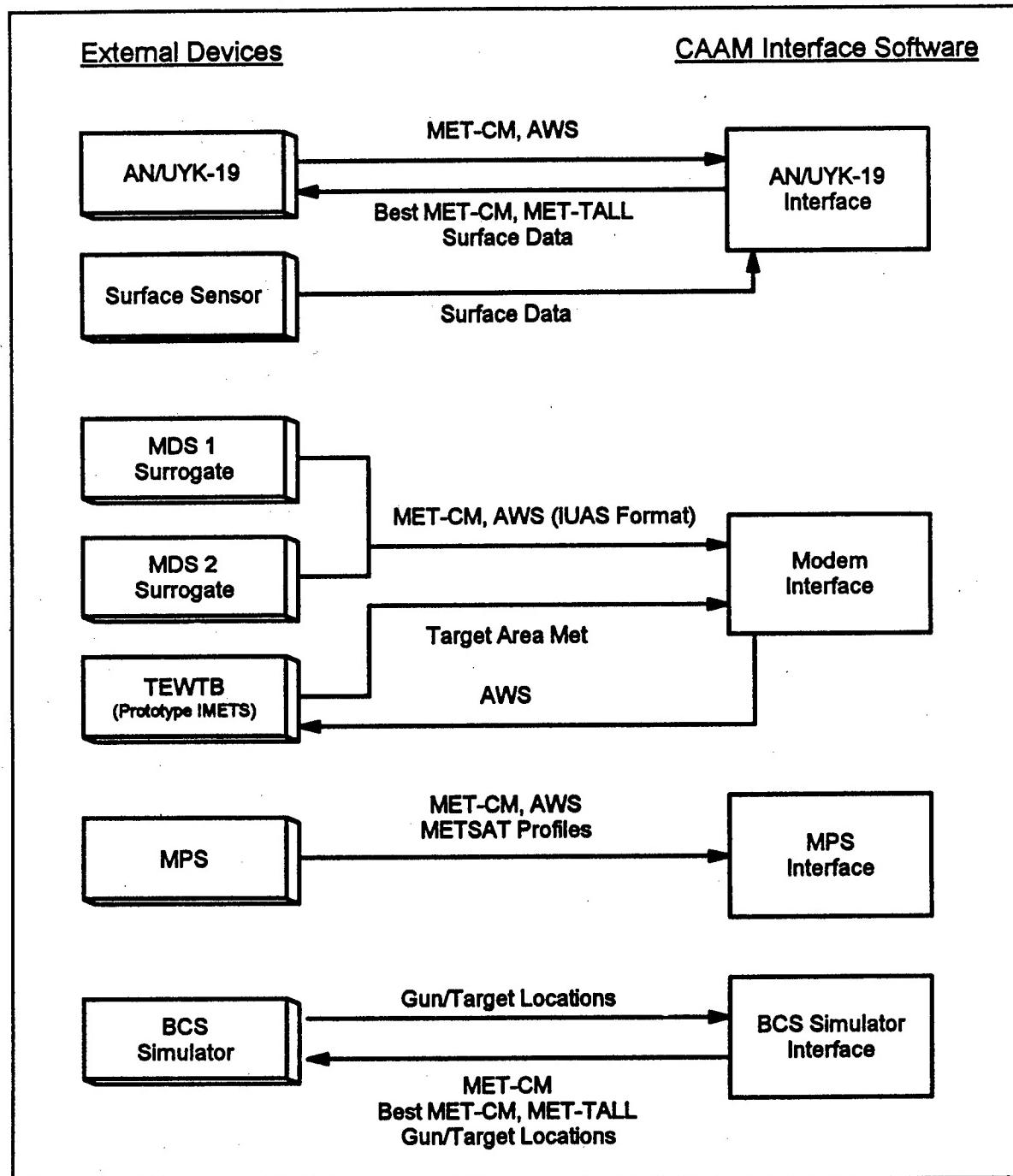
Figure 3. Interfaces and Data Flow.

There are several types and formats of met data that are exchanged between CAAM and these devices:

- MET-CM: computer met message; specifies wind direction and speed, virtual temperature, and pressure from the surface to 20,000 m in 27 layers

- AWS: Air Weather Service met message: specifies wind direction and speed, air temperature, and dew point temperature at mandatory and significant air pressure levels; in the CAAM system, MET-CM and AWS messages are always input as a pair (describing the same sounding or profile)

- MET-TALL: target area low level met entry message; specifies wind direction and speed, air temperature, and relative humidity from the surface to 1,600 m in 17 layers; it also specifies the following values: surface pressure, cloud base height and mean refractive index, and precipitation type and rate

- METSAT profile: meteorological satellite profile; this is a product only of the MPS, and can provide useful air temperature data from about 2 km above the surface to the 10 mb level; it also provides useful dew point temperatures and computed wind speeds and directions in the range between 2 km above the surface to the 100 mb level; at this time, this is the only source of upper air data over the target area

- Surface Data: the surface sensor connected to the CAAM computer reports the following values: pressure, temperature, relative humidity, wind direction and speed; it is not used by CAAM, but rather is relayed to the AN/UYK-19

- Target Area Met: this information is produced by a Staff Weather Officer at the IMETS and is sent to the CAAM system; it specifies the surface pressure, cloud base height and mean refractive index, and precipitation type and rate values that are required for the MET-TALL messages for each of the designated target locations

With two exceptions, all MET-CM, MET-TALL, and AWS messages are transferred and stored in files based on the TACFIRE format. These messages are exchanged with the AN/UYK-19, however, in actual TACFIRE format. The second exception is the receipt of MET-CM and AWS messages from the MDS surrogates in Integrated Upper Air System (IUAS) format. These are converted to TACFIRE-based formatted files within CAAM.

4. SOFTWARE DESIGN

4.1 ADA IMPLEMENTATION

The CAAM Phase II Computer Software Configuration Item (CSCI) has been designed to consist of ten Computer Software Components (CSCs). Some of these CSCs are compute-bound (perform intensive processing and then wait), while others must respond quickly to new data coming into the system or to operator requests. Formerly, systems such as this were written to either periodically stop the compute-bound processing to service other processing, or were coded with interrupts to facilitate the invocation of other processing. These methods are very cumbersome, inject additional complexity into the software, and obscure the implementation of the primary algorithm.

The CAAM CSCI is being coded in the Ada programming language. As such, it has been designed to use the multi-tasking features of Ada. Each CSC, therefore, exists as an Ada task. This tasking approach allows the CSCs to be written as though they were all separate entities; the run-time system handles the swapping of tasks, with tasks assigned relative priorities. This design also allows concurrency, should this system ever be ported to a multiple-CPU platform.

4.2 EXECUTIVE DRIVER

Since multiple tasks are running (effectively) at the same time, their processing must be synchronized. This is done through Ada's rendezvous mechanisms, and the part of the system primarily responsible for this synchronization is the Executive CSC.

The Executive is the "driver" of the CAAM system. It initializes the system by setting state variables and by starting the other tasks. After initialization, the Executive acts primarily as an event handler. At the completion of some type of processing, other tasks notify the Executive. In effect, the Executive sleeps until notified of events by other tasks. This has been implemented as a queue of events to the Executive. The information in the queue includes the source (CSC) of the event, the type of the event, and other pertinent information. Events include operator requests, new data received from an external interface, algorithm completion, and report of output to external interfaces. The Executive performs an orderly termination of the system when requested by the operator.

The Executive CSC also includes the user interface, which runs as an Ada task and is interrupt-driven by operator keystrokes and software events. It consists of four windows: Main Menu, External Interface, Display/Edit, and Message. The Main Menu window displays high-level menu options: AOP definition, Gun/Target Location entry, Sector definition, External Interface Location entry, Dissemination selection, Met Message Display, and Termination. The External Interface window displays the times of most recent data transfer to/from all external interfaces. The Display/Edit window allows the operator to enter and change system control information (such as the location of the AOP), and display CAAM-generated met messages. The Message window displays pertinent messages from other CSCs, including informational messages, warnings, and errors.

4.3 MET PROCESSING SEQUENCE

The sequence of CSCs that process met and produce met messages for dissemination are shown in fig. 4.

The Objective Analysis CSC inputs recent AWS messages and METSAT profiles. The results of the analysis are output in two files that each contain full 3-D descriptions of the atmosphere, but differ in the heights of the data. A pseudo-terrain-following file is generated for HOTMAC; the heights of these data follow elevation contours, leveling out to constant heights at higher altitudes, and go to 12 km above the terrain. A second file that extends from the surface to 20 km is produced that is used as input by the Met Message Generation CSC. In this file, all layers are "horizontal", i.e., at constant heights above mean sea level.

52
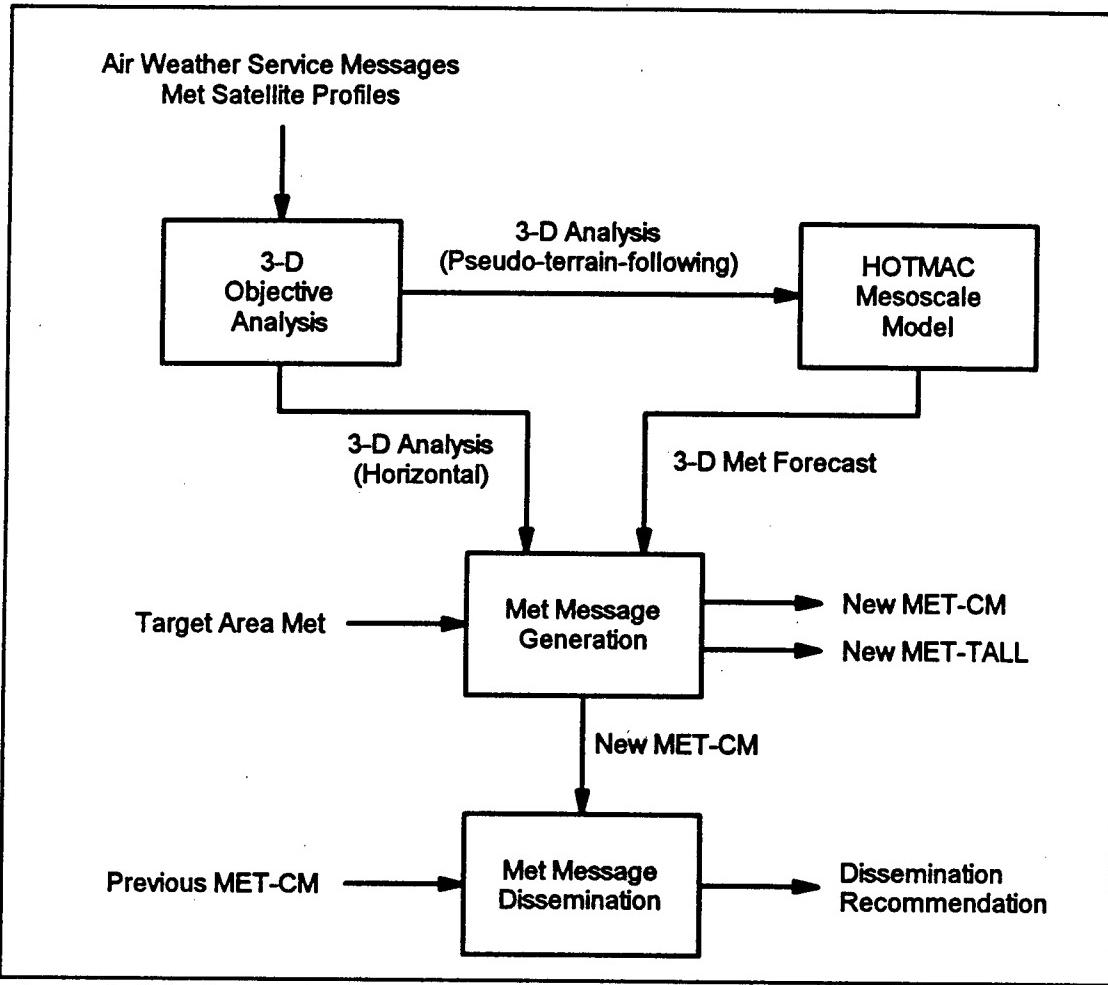
Figure 4. Met Processing Sequence.

The HOTMAC Mesoscale Model CSC uses the 3-D Objective Analysis output and certain other specification files it requires to produce a 3-D met file with forecasts at each hour for a 6-hour forecast period. This model is CPU-intensive, and takes about six minutes to run on the CAAM computer platform.

Met messages are produced by the Met Message Generation CSC. It generates a MET-CM for the designated location by interpolating from both the HOTMAC output file (up to 12 km) and from the 3-D Objective Analysis file (up to 20 km). If HOTMAC fails for some reason, the message is interpolated only from the 3-D Objective Analysis file. A MET-TALL message is generated in a similar fashion, except that it extends only to 1.6 km and uses the target area met data received from the TEWTB to fill in the required surface pressure, cloud base height and mean refractive index, and precipitation type and rate values.

Before the newly generated messages are disseminated, the Met Message Dissemination CSC is invoked to compare the previously disseminated MET-CM with the new one. It uses a combination of Firing Table met effects and a set of rules to determine if the new MET-CM has changed enough from the previous one to significantly affect artillery or MLRS accuracy. The artillery systems to be evaluated are the 155 Rocket Assisted Projectile with M549A1 and 155

Base Burn with M864. This CSC produces a dissemination report to the operator, who makes the final decision on whether to disseminate the new messages to the AN/UYK-19 and the BCS Simulator.

5. CONCLUSIONS

The April 1994 Technology Demonstration for CAAM will show a significant improvement in artillery fire accuracy over the current methods. A series of upper air soundings will be automatically ingested into the CAAM system, where the met processing sequence involving the HOTMAC mesoscale model will provide computer met messages for specific firing missions generated by the BCS Simulator connected to the CAAM system. Actual soundings will be taken at the locations of these met messages in order to make near-real-time comparisons of the data.

The future CAAM will be integrated into the Target Area Meteorological Sensors System (TAMSS) along with the MPS. The TAMSS is planned for full operational capability in 2005.

ACKNOWLEDGMENTS

REFERENCES

DOD-STD-2167A, 1985: Defense System Software Development. Department of Defense, Washington, D.C. 20301.

Seagraves, M. A., R. E. McPeek, and A. A. Grunwald, 1992: The Met Improvement Program: Key to Unlocking Target Area Meteorology. In Proceedings of the 1992 Battlefield Atmospherics Conference, U.S. Army Research Laboratory, White Sands Missile Range, NM 88002-5501.

Yamada, T., and S. Bunker, 1989: A Numerical Model Study of Nocturnal Drainage Flows with Strong Wind and Temperature Gradients. J. Appl. Meteorol., 28:545-554.

EFFECTS OF A PROPOSED CAMM MODEL ON THE IMPACT OF THE MLRS

Edward M. D'Arcy
U.S. Army Research Laboratory
Battlefield Environment Directorate
White Sands Missile Range, New Mexico 88002-5501 USA

ABSTRACT

Because of certain constraints, future Army Artillery will be limited to two families of weapons: the Advanced Field Artillery System (AFAS) and the Multiple Launch Rocket System (MLRS). The MLRS, being a rocket, is acted upon by the wind in a different manner than cannon artillery. Any meteorological (met) system proposed for the future must be able to support both families of weapons. Four proposed candidate models were examined to see what effect they have on the impact of the MLRS through a ballistic simulator and how they differ from one another. The four candidate schemes are the Gandin or PACT model, the National Oceanographic and Atmospheric Administration (NOAA) model, the Time-Space model and the Yamada-Henmi HOTMAC model.

1. INTRODUCTION

With the downsizing of the Army, emphasis has been placed on technology. More must be done with less. This replacement of men and machines with technology is affecting all branches of the Army including the Artillery. In the future, the Artillery will rely on two basic delivery systems: one based on the MLRS platform and one on the 155-mm cannon. Further into the future, there will be the AFAS. In order for these systems to function at their best, all factors affecting their performance, including wind, must be well known. The present method of providing corrections to the wind is inadequate.

At the present time, there are three meteorological sections assigned to a division, although one is usually held in reserve. Each artillery battery is assigned one of these sections as a dedicated section, and this section should be within 30 km of the battery. The recommendation is that the sections try to release balloons alternately so that there will be only one balloon in the air at a time. In normal operation, a battery will use the met message from its dedicated section, even though there may be a newer met message from another met section. It is therefore not unusual for a met message to be between 2 and 4 h old.

Factors other than time that affect the accuracy of a met message are the location of the section in relation to the battery, the terrain surrounding the battery, and the wind direction. In general, the more complex the terrain, the less accurate the met message will be for a given battery. A section upwind from the proposed trajectory will usually provide a more accurate met message for an artillery shell than one that is downwind from the proposed trajectory; however, the MLRS is more sensitive to the low-level winds in the launch area. These and other factors make the use of all available weather data on the battlefield an important function of the technological fire direction center.

This paper will investigate four methods to determine if any improvement in artillery accuracy can be made by better utilization of available met data through a computer-assisted artillery meteorological system (CAAMS). Analysis will be limited to the MLRS and current (less than 1 h old) data.

MODELS

Four models were used in this study. It is beyond the scope of this paper to describe the theory behind or functioning of the models, but three of the models are objective analysis models and the fourth is a prediction model. HOTMAC is the prediction model and has yet to be documented; it was written by Ted Yamada of Yamada Science and Art Corp., 147 Monte Rey Drive South, Los Alamos, NM 87544. The HOTMAC was modified to run on the HP-750 by Dr. Teizi Henmi of Army Research Laboratory (ARL). The NOAA model is an objective analysis scheme written by Dr. Fernando Caracena of the National Oceanographic and Atmospheric Administration National Sever Storms Laboratory (NOAA NSSL) at Boulder, CO.[1,2] The PACT model is an objective analysis scheme based on the Gandin model.[3] The Time-Space model is also an objective analysis scheme written by Abel Blanco of ARL.[4]

There are actually two versions of the Blanco Time-Space model presented. The original model was designed to provide one met message for the launch area and a second met message for the target area. When used with the modified ballistic simulator, the first met message is used on the up-leg of the trajectory and the second met message is used on the down-leg portion of the trajectory. The revised model provides a single met message at the midpoint of the trajectory. The other models also provide a single met message at the midpoint of the trajectory.

DATA

The data used to evaluate the different models were collected during the PASS experiment which was conducted from 1 Nov to 7 Dec 74. Twenty days of data were collected with a total of 662 rawinsonde flights. Due to constraints placed on the data, only 16 days were used with a total of 460 rawinsonde flights. Barnett[5] compiled a complete description of the PASS experiment, and D'Arcy[6,7] provided listings of the rawinsonde data collected.

There are so many ways that one can use this data, that it was difficult to decide on the best way. D'Arcy[8] discusses the effects of varying meteorological parameters along the trajectory and demonstrates how nearly one half of the current dispersion experienced by the MLRS could be caused by this variation. As a result of this investigation, it was decided to use a similar approach here.

Most of the MLRS firings at White Sands Missile Range (WSMR), NM, have been 25-km flights with the launch azimuth to the north west. Two sites in the PASS experiment meet these criterion quite well: TSX(1) and APA(7); they are 24.5 km apart with the azimuth from TSX to APA being 345°. The ballistic simulator was modified so that it could use one met message on the up-leg of the simulation and a different met message on the down-leg of the simulation. Obviously, the met parameters vary in a continuous manner from the launch area to the target area, but this variation can be well represented by individual met messages in each area. This method was used to compute the "truth" — that impact to which all other model results would be compared.

56

A number of different scenarios were run through each of the models to obtain met messages at the midpoint of the simulated trajectory. These met messages were input to the ballistic simulator to provide impacts. These impacts were then differenced with the "truth" to obtain the relative effectiveness of the individual models.

The first scenario consisted of a single station as would be done under the current system. TSX(1) is of course in the launch area and the other four "corps" area stations are between 12 and 20 km from the launch area. Any one of these stations could meet the requirements for a valid corps area met message. The individual met messages were input to the ballistic simulator to provide the basis for comparisons against the current method.

The second scenario consisted of the dedicated station with an addition or an update from one of the other four corps area stations. In these simulations, the profile from the dedicated station can be current (2 or 4 h old). The addition or update is, in all cases, current data. This should allow one to see whether the use of all the data available on the battlefield can increase artillery accuracy.

The third scenario was an attempt to demonstrate the utility of a met message in front of the FLOT. This message could be from a satellite observation, a drop sonde or a report from a remotely piloted vehicle (RPV). Although a met message in the target area or at least upwind from the target area would be preferred, the stations at RAM and HMS (Holloman) were used as the locations of the forward area met messages. These data were used as additions or updates to the second set of scenarios and were, in all cases, current data.

A complete set of scenarios consists of:

- a dedicated station that is current (2 or 4 h old);
- a dedicated station that is current (2 or 4 h old), plus another current corps area station;
- a dedicated station that is current (2 or 4 h old), plus another current corps area station,
    plus a current forward area station.

DISCUSSION

Because of the large amount of data and results from that data, only 2 days will be discussed here. A report detailing the results of the whole data set will be forthcoming. For this paper, the 2 days chosen were the 19th (Day 323) and 20th (Day 324) of Nov 74. November the 19th was chosen because of the large variance in predicted impacts between the dedicated corps area stations (about 600 m). November the 20th was chosen because of the small variance in predicted impacts between corps area stations (about 108 m). The average variance between the five corps area met stations for the 16 days of the study was about 206 m total vector displacement.

A listing of all of the computed impacts from all of the scenarios and all of the models for the 2 days would amount to approximately 45 pages and since our questions can be answered with less data, only the impacts for current data are shown for each day. To understand the data listing:

- The first set of numbers is the day the data were taken and the three-letter alphanumeric is the model used to produce the met message used in the ballistic simulator to provide the predicted impact.

- The next set of numbers consists of the time of the met message and the station ids and flight numbers of the profiles used by the model to produce the met message.

- The next two numbers are the predicted range and cross displacements (in meters) from the target.

- In the lines with two more numbers, these are the algebraic differences between the predicted range and cross displacements and the "truth".

• Following each set of scenarios is a short line of three numbers. These are the averages of the absolute values of the differences of range and cross with the "truth" and the average absolute radial miss.

Therefore, in table 1 (tables are appended at the end of this paper), 19/11/74 PAC 0600,11,21,61 108.87 159.33 85.25 -169.49 shows us that the met message produced by the PACT model for an 0600 launch, using the first flights from stations 1, 2, and 6 on 19 Nov 74 predicted an impact 108.87 m long and 159.33 m right of the target, and if we had corrected for this prediction we would have been 85.25 m long and 169.49 m left of the target. The short line 70.65 161.10 175.91 shows that in the six scenarios above, there was an average miss in range of 70.65 m and in cross of 161.10 m with an average absolute radial miss of 175.91 m. All of the "impacts" are displacements from the no-wind impact which is obtained using a met message with WSMR standard temperature and pressure profiles and no wind.

Let us first look at day 323 (19/11/74) (tables 1 through 5). The "true" impact at 0600 is 23.62 m long and 328.82 m right of the no-wind impact. Individual impacts from the four corps area stations range from 73.68 m long and 308.7 m right of the no-wind to 9.36 m long and 60.70 m left of the no-wind impact. This is a spread of 64.32 m in range and 369.44 m in cross with an average absolute miss of 27.75 m in range and 208.78 m in cross displacement. By 0800 the "true" correction is down to 0.57 m long and 7.23 m right of the no-wind impact while the individual station impacts range from 2.69 m long and 524.20 m right to 20.58 m long and 372.19 m left of no-wind impact. This is a spread of 17.89 m in range and 896.39 m in cross with an average absolute miss of 25.59 m in range and 267.55 m in cross displacement. At 1000 the "true" correction has increased again to 43.17 m short and 323.18 m right of the no-wind impact. At this time, the individual station predictions range from 74.89 m short and 221.21 m left of the no-wind to 78.42 m long and 285.55 m right of the no-wind impact. This is a spread of 153.31 m in range and 506.76 m in cross with an average absolute miss of 67.78 m in range and 205.81 m in cross displacement. As can be seen, in an active weather situation, met messages from any two locations in a corps area can produce very different corrections and unless one knows the "truth" one cannot tell which met message should be used. Of course if one knew the "truth" he would not need the other met messages. Let us now see if the use of multiple soundings will provide any advantage and if so which model provides the greatest advantage.

The PACT model at 0600 using two stations has a spread of 53.94 m in range and 190.80 m in cross with an average absolute miss of 33.35 m in range and 194.14 m in cross displacement. The NOAA model has a spread of 58.95 m in range and 197.30 m in cross with an average absolute miss in range of 47.61 m and 195.01 m in cross displacement. HOTMAC has a spread of 26.07 m in range and 26.07 m in cross with an average absolute miss of 37.92 m in range and 203.13 m in cross displacement. The two-profile version of the Time-Space model has a spread of 63.91 m in range and 192.85 m in cross with an average absolute miss of 23.18 m in range and 201.33 m in cross displacement. The single-profile version of the Time-Space model has a spread of 55.51 m in range and 213.98 m in range with an average absolute miss of 46.58 m in range and 198.83 m in cross displacement.

At 0800, the PACT model using two stations has a spread of 56.72 m in range and 450.25 m in cross with an average absolute miss of 27.21 m in range and 151.11 m in cross displacement. The NOAA model has a spread of 61.30 m in range and 449.10 m in cross with an average absolute miss of 41.25 m in range and 155.99 m in cross displacement. HOTMAC has a spread of 82.75 m in range and 230.65 m in cross with an average absolute miss of 85.91 m in range and 156.17 m in cross displacement. The two-profile version of the Time-Space model has a spread of 52.18 m in range and 454.93 m in cross with an average absolute miss of 24.46 m in range and 158.74 m in cross displacement. The single-profile version of Time-Space has a spread of 52.49 m in range and 416.61 m in cross with an average absolute miss of 43.88 m in range and 147.45 m in cross displacement.

The PACT model at 1000 has a spread of 53.30 m in range and 52.11 m in cross with an average absolute miss of 49.90 m in range and 326.59 m in cross displacement. The NOAA model has a spread of 44.38 m in range and 46.52 m in cross with an average absolute miss of 64.65 m in range and 329.52 m in cross displacement. HOTMAC has a spread of 25.06 m in range and 59.30 m in cross with an average absolute miss of 129.35 m range and 286.58 m in cross displacement. The two-profile version of Time-Space has a spread of 46.95 m in range and 53.35 m in

cross with an average absolute miss of 17.08 m in range and 342.78 m in cross displacement. The single-profile version of Time-Space has a spread of 31.31 m in range and 20.56 m in cross with an average absolute miss of 58.78 m in range and 326.10 m in cross displacement.

As can be seen, the models all have spreads that are less than that of the individual stations but the average absolute miss is not always smaller. Since it is easier to examine the average absolute radial miss than the component miss let us look at this factor. As can be seen by this, at 0600 the PACT model reduces the average radial miss by 6.5 percent, the NOAA model reduces the miss by 4.7 percent and HOTMAC reduces the radial miss by 1.9 percent. The two-profile version of the Time-Space model reduces the radial miss by 3.8 percent while the single-profile version reduces the miss by 3.0 percent.

At 0800, the PACT model reduces the average absolute radial miss by 42.9 percent. The NOAA model reduces the miss by 40.0 percent and HOTMAC reduces the radial miss by 33.7 percent. The two-profile version of Time-Space reduces the radial miss by 40.2 percent while the single-profile version reduces the miss by 42.8 percent.

The 1000 predictions are a different story. Here the use of additional data produces a decrease in accuracy. The PACT model shows an increase in the radial miss of 52.5 percent. The NOAA model increases the average radial miss by 55.0 percent while HOTMAC increases the miss by 45.1 percent. The two-profile version of Time-Space increases the radial miss by 58.4 percent and the single-profile version increases the radial miss by 52.9 percent.

It can be seen that the use of additional information (in these previous cases an additional corps area station) can at times be useful, detrimental, or of no particular value. Let us now see if information obtained from in front of the FLOT will be of any use. There are two stations in front of the FLOT that are used in this analysis. Although an analysis of each station's effect could be made, in this paper they are analyzed together.

At 0600, the PACT model using three stations has a spread of 49.85 m in range and 143.00 m in cross with an average absolute miss of 70.65 m in range and 161.10 m in cross displacement. The NOAA model has a spread of 45.90 m in range and 158.64 m in cross with an average absolute miss of 82.93 m in range and 153.75 m in cross displacement. The HOTMAC model has a spread of 48.69 m in range and 131.30 m in cross with an average absolute miss of 91.41 m in range and 147.18 m in cross displacement. The two-profile version of Time-Space has a spread of 45.35 m in range and 136.99 m in cross with an average absolute miss of 41.40 m in range and 92.13 m in cross displacement. The single-profile version of Time-Space has a spread of 59.09 m in range and 182.55 m in cross with an average absolute miss of 78.35 m in range and 162.91 m in cross displacement.

At 0800, the PACT model has a spread of 66.88 m in range and 329.24 m in cross with an average absolute miss of 49.14 m in range and 161.81 m in cross displacement. The NOAA model has a spread of 69.20 m in range and 328.16 m in cross with an average absolute miss of 63.13 min range and 160.52 m in cross displacement. The HOTMAC model has a spread of 142.91 m in range and 213.86 m in cross with an average absolute miss of 80.26 m in range and 216.44 m in cross displacement. The two-profile version of Time-Space has a spread of 72.95 m in range and 247.67 m in cross with an average absolute miss of 22.55 m in range and 209.41 m in cross displacement. The single-profile version of Time-Space has a spread of 73.68 m in range and 293.99 m in cross with an average absolute miss of 65.71 m in range and 163.06 m in cross displacement.

At 1000, the PACT model has a spread of 43.77 m in range and 39.57 m in cross with an average absolute miss of 60.58 m in range and 242.57 m in cross displacement. The NOAA model has a spread of 38.30 m in range and 54.51 m in cross with an average absolute miss of 73.14 m in range and 243.38 m in cross displacement. The HOTMAC model has a spread of 20.40 m in range and 91.85 m in cross with an average absolute miss of 135.38 m in range and 196.78 m in cross displacement. The two-profile version of Time-Space has a spread of 27.20 m in range and 96.03 m in cross with an average absolute miss of 16.82 m in range and 173.02 m in cross displacement. The single-profile version of Time-Space has a spread of 32.48 m in range and 23.68 m in cross with an average absolute miss of 70.74 m in range and 247.76 m in cross displacement.

If we now look at the average absolute radial miss, at 0600 the PACT model shows a 16.5 percent improvement in accuracy, the NOAA model shows a 17.0 percent improvement and the HOTMAC model shows a 17.8 percent improvement. The two-profile version of Time-Space shows a 52.0 percent improvement while the single-profile version of Time-Space shows a 14.2 percent improvement.

At 0800, the PACT model shows a 37.1 percent improvement in accuracy, the NOAA model shows a 35.8 percent improvement, and the HOTMAC model shows an 14.1 percent improvement. The two-profile version of Time-Space shows a 21.6 percent improvement while the single-profile version shows a 34.6 percent improvement.

At 1000, the PACT model shows a 15.4 percent decrease in accuracy, the NOAA model shows a 17.3 percent decrease, and the HOTMAC model shows a 10.3 percent decrease. The two-profile version of Time-Space shows a 19.8 percent increase in accuracy while the single-profile version shows an 18.9 percent decrease in accuracy.

Let us now turn our attention to day 324 (tables 6 through 10). The "true" impact at 1230 is 171.58 m long and 113.11 m right of the no-wind impact. The four individual corps area stations reporting predict impacts that range from 152.49 to 234.89 m long and from 36.87 to 70.87 m right of the no-wind impact for a spread of 82.4 m in range and 34.0 m in cross. By 1430, the range component of the "truth" has increased to 238.72 m long and the cross component has decreased to 9.64 m right of the no-wind. The five individual corps area stations reporting predict impacts that range from 250.96 to 278.57 m long and from 28.93 m left to 137.22 m right of the no-wind for a spread of 27.61 m in range and 166.15 m in cross. The 1630 "truth" shows little change from 1430 with an impact 233.08 m long and 23.11 m right of the no-wind. The five individual corps area stations predict impacts that range from 237.59 to 289.74 m long and from 70.37 to 115.93 m right of the no-wind for a spread of 52.15 m in range and 45.56 m in cross. As we can see, the vector displacement of the "truth" changes from 205.5 to 234.2 m or only 28.7 m over a 4-h period. There are no wild excursions among the five corps area stations and the spreads are relatively small — all indications of a stable weather situation in the afternoon.

The PACT model at 1230 using two stations has a spread of 42.29 m in range and 15.13 m in cross with an average absolute miss of 37.85 m in range and 60.90 m in cross displacement. The NOAA model has a spread of 51.73 m in range and 15.98 m in cross with an average absolute miss in range of 47.37 and 66. 19 m in cross displacement. HOTMAC has a spread of 61.43 m in range and 13.06 m in cross with an average absolute miss of 198.32 m in range and 61.01 m in cross displacement. The two-profile version of the Time-Space model has a spread of 43.69 m in range and 16.54 m in cross with an average absolute miss of 16.05 m in range and 60.26 m in cross displacement. The single-profile version of the Time-Space model has a spread of 38.74 m in range and 13.59 m in cross with an average absolute miss of 46.98 m in range and 64.92 m in cross displacement.

At 1430, the PACT model using two stations has a spread of 49.94 m in range and 59.81 m in cross with an average absolute miss of 38.00 m in range and 82.35 m in cross displacement. The NOAA model has a spread of 51.55 m in range and 59.78 m in cross with an average absolute miss of 38.83 m in range and 75.56 m in cross displacement. HOTMAC has a spread of 42.89 m in range and 34.55 m in cross with an average absolute miss of 172.74 m in range and 67.86 m in cross displacement. The two-profile version of the Time-Space model has a spread of 48.45 m in range and 68.82 m in cross with an average absolute miss of 17.91 m in range and 86.04 m in cross displacement. The single-profile version of Time-Space has a spread of 49.44 m in range and 55.91 m in cross with an average absolute miss of 41.53 m in range and 78.44 m in cross displacement.

The PACT model at 1630 has a spread of 38.31 m in range and 22.84 m in cross with an average absolute miss of 30.21 m in range and 67.23 m in cross displacement. The NOAA model has a spread of 40.06 m in range and 19.89 m in cross with an average absolute miss of 39.84 m in range and 63.82 m in cross displacement. HOTMAC has a spread of 55.37 m in range and 14.33 m in cross with an average absolute miss of 153.89 m in range and 61 67.19 m in cross displacement. The two-profile version of Time-Space has a spread of 37.89 m in range and 21.58 m in cross with an average absolute miss of 13.91 m in range and 70.46 m in cross displacement. The single-profile version of Time-Space has a spread of 39.34 m in range and 17.31 m in cross with an average absolute miss of 39.35 m in range and 64.14 m in cross displacement.

Again, the spreads in the predicted impacts from the models are generally less than those predicted by the single stations. At 1430, the range spread of the model predictions is greater than the spread for the individual station predictions, but the cross component spread is much less. On the other hand, the average absolute miss is another matter. Almost all cases show an increase in the radial miss. This increase, in most instances, is not large except in the case of HOTMAC where, which for some reason, the increased miss is very large. If we look at these average absolute radial misses, we see that at 1230 the PACT model shows a 2.6 percent decrease in the radial miss, the NOAA model shows a 10.5 percent increase in the radial miss while the HOTMAC model shows a 181.18 percent increase in the radial miss. The two-profile version of Time-Space shows a 15.2 percent decrease in the radial miss while the single-profile version of Time-Space shows an 8.8 percent increase in the radial miss.

At 1430, the PACT model increases the average absolute radial miss by 17.7 percent. The NOAA model increases the miss by 10.2 percent and HOTMAC increases the radial miss by 140.8 percent. The two-profile version of Time-Space increases the radial miss by 14.0 percent while the single-profile version of Time-Space increases the miss by 15.2 percent.

For the 1630 predictions, the use of additional data produces a decrease in accuracy in all cases. The PACT model shows an increase in the radial miss of 4.2 percent. The NOAA model increases the average radial miss by 6.3 percent while HOTMAC increases the miss by 137.3 percent. The two-profile version of Time-Space increases the radial miss by 1.5 percent and the single-profile version increases the radial miss by 6.3 percent.

It can be seen that (for day 324) the use of additional information from additional corps area stations is detrimental in all but one model, although, in most cases the increase in the radial miss is small. Now, let us see if information obtained from in front of the FLOT will be of any use.

At 1230, the PACT model has a spread of 46.92 m in range and 20.57 m in cross with an average absolute miss of 52.32 m in range and 64.76 m in cross displacement. The NOAA model has a spread of 36.70 m in range and 23.56 m in cross with an average absolute miss of 53.57 m in range and 65.78 m in cross displacement. The HOTMAC model has a spread of 45.16 m in range and 25.97 m in cross with an average absolute miss of 190.83 m in range and 59.58 m in cross displacement. The two-profile version of Time-Space has a spread of 34.25 m in range and 36.04 m in cross with an average absolute miss of 13.82 m in range and 73.15 m in cross displacement. The single-profile version of Time-Space has a spread of 30.92 m in range and 23.84 m in cross with an average absolute miss of 54.40 m in range and 65.70 m in cross displacement.

At 1430, the PACT model has a spread of 40.35 m in range and 55.03 m in cross with an average absolute miss of 38.26 m in range and 76.55 m in cross displacement. The NOAA model has a spread of 37.66 m in range and 55.32 m in cross with an average absolute miss of 37.14 m in range and 70.46 m in cross displacement. The HOTMAC model has a spread of 78.74 m in range and 56.02 m in cross with an average absolute miss of 133.47 m in range and 85.47 m in cross displacement. The two-profile version of Time-Space has a spread of 29.91 m in range and 69.81 m in cross with an average absolute miss of 11.94 m in range and 67.34 m in cross displacement. The single-profile version of Time-Space has a spread of 35.64 m in range and 54.80 m in cross with an average absolute miss of 37.02 m in range and 72.18 m in cross displacement.

At 1630, the PACT model has a spread of 39.89 m in range and 45.47 m in cross with an average absolute miss of 39.45 m in range and 58.02 m in cross displacement. The NOAA model has a spread of 37.74 m in range and 47.47 m in cross with an average absolute miss of 42.85 m in range and 53.72 m in cross displacement. The HOTMAC model has a spread of 50.17 m in range and 41.21 m in cross with an average absolute miss of 149.13 m in range and 51.96 m in cross displacement. The two-profile version of Time-Space has a spread of 25.02 m in range and 76.31 m in cross with an average absolute miss of 6.49 m in range and 46.50 m in cross displacement. The single-profile version of Time-Space has a spread of 15.07 m in range and 50.48 m in cross with an average absolute miss of 52.52 m in range and 51.60 m in cross displacement.

If we now look at the average absolute radial miss, at 1230 the PACT model shows a 13.1 percent increase in radial miss, the NOAA model shows a 15.2 percent increase in radial miss and the HOTMAC model shows a 171.5 percent increase. The two-profile version of Time-Space shows a 1.5 percent increase in radial miss while the single-profile version of Time-Space shows a 15.8 percent increase.

At 1430, the PACT model shows an 11.0 percent increase in radial miss, the NOAA model shows a 3.4 percent increase in radial miss, and the HOTMAC model shows an 105.7 percent increase in radial miss. The two-profile version of Time-Space shows an 11.3 percent decrease in radial miss while the single-profile version shows a 5.3 percent increase.

At 1630, the PACT model shows a 0.8 percent decrease in radial miss, the NOAA model shows a 2.9 percent decrease in radial miss, and the HOTMAC model shows a 123.2 percent increase. The two-profile version of Time-Space shows a 33.6 percent decrease in radial miss while the single-profile version of Time-Space shows a 4.0 percent increase.

As can be seen by the above analysis, there can be wide variances from one 2-h period to another and among stations during the same time period. How then do the individual models perform as a function of day and over the entire 16-day test period? These results are shown in tables 11 through 25 which all have the same format. The first line consists of the number of met messages in the set and the mean, variance, and standard deviation of the vector radial miss. The second line consists of the mean, variance, and standard deviation of the range component of the miss. Line three consists of the mean, variance, and standard deviation of the cross component of the miss and the circular probable error (CEP) of the range and cross component misses.

For day 323, tables 11 through 15 show that by using two corps area stations the PACT model decreases the radial miss by 12.1 percent, the NOAA model decreases the radial miss by 10.7 percent, and the HOTMAC model decreases the radial miss by 14.1 percent. The two-profile version of Time-Space reduces the radial miss by 10.6 percent, and the single-profile version of Time-Space reduces the radial miss by 11.8 percent.

When the third observation in front of the FLOT is added, the PACT model reduces the radial miss by 27.7 percent, the NOAA model reduces the radial miss by 26.8 percent, and the HOTMAC model reduces the radial miss by 22. 8 percent. The two-profile version of Time-Space reduces the radial miss by 39.7 percent, and the single-profile version of Time-Space reduces the radial miss by 26 percent.

For day 324, tables 16 through 20 show that by using two corps area stations the PACT model increases the radial miss by 7.5 percent, the NOAA model increases the radial miss by 9.1 percent, and the HOTMAC model increases the radial miss by 158.6 percent. The two-profile version of Time-Space decreases the radial miss by 0.8 percent, and the single-profile version of Time-Space increases the radial miss by 9.9 percent.

When the third observation in front of the FLOT is added, the PACT model increases the radial miss by 5.7 percent, the NOAA model increases the radial miss by 2.5 percent, and the HOTMAC model increases the radial miss by 136.7 percent. The two-profile version of Time-Space decreases the radial miss by 16.9 percent, and the single-profile version of Time-Space increases the radial miss by 5.2 percent.

Tables 21 through 25 show that when the total 16-day sample is considered, the two-station solution for the PACT model shows a 6.5 percent improvement in accuracy, the NOAA model shows a 6.8 percent improvement, and the HOTMAC model shows an 8.0 percent improvement. The two-profile version of Time-Space shows a 9.4 percent improvement, while the single-profile version of Time-Space shows a 7.0 percent improvement.

By adding a third sounding in front of the FLOT, the PACT model increases the improvement to 14.2 percent, the NOAA model increases the improvement to 14.8 percent, and the HOTMAC model increases the gain in accuracy to 12.5 percent. The two-profile version of Time-Space has an increase in improvement to 21.2 percent while the single-profile version of Time-Space has an increase in accuracy of 14.9 percent.

CONCLUSIONS

Before any conclusions can be drawn from the above data and results, one must be cognizant of the attendant caveats.

• First, although the sample size used here is large enough to make statistically significant conclusions for the sample period, the sample period is not large enough so that one could draw the same conclusions for the whole year. Also, all conclusions drawn here can only be applied to data that is less than 1-h old. Ongoing analyses using a combination of new and old data show promising results, but presently no definite conclusions can be made.

• Secondly, since the original analysis, both the NOAA and HOTMAC models have undergone extensive revision. It is assumed that these revisions will increase the accuracy of both of these models; nevertheless, this will have to be investigated.

When two soundings were used by the four methods above, the improvements over the current method range from 6.5 to 9.4 percent for the 16-day test period. Although there are no significant differences between the four models, all gave improvement over the current method — as much as 42.8 percent in one case on day 323. When three soundings were used by the models, the improvements over the current method for the 16-day test period range from 12.5 to 21.2 percent — a significant improvement. One case on day 323 shows a 52.0 percent improvement over the current method. Although there were times when percentage wise the current method did better than the models, this percentage translates to only 10 to 15 m of vector radial miss at 25 km, which is not very significant.

Overall, the two-profile version of Time-Space does best with two soundings as well as with three soundings. On day 323, this version shows the largest percentage increase over the current method, and on day 324 it shows better than the current method during two out of three time periods when the other models do not do as well as the current method. Overall then, the two-profile version of the Time-Space model seems to be the best model. Although this version seems to be the clear winner in most cases, one has to ask if the choice of "truth" has anything to do with the assumed superiority of the model. Would the other models do better if they predicted both a launch and target area profile?

Although some might conclude from the results of the total 16-day sample that a CAAMS is not needed on the battlefield, the author believes that this is a premature and inappropriate conclusion. While it is true that CAAMS would afford only a 10 to 15 percent increase in the accuracy a large portion of the time, battles seem to be waged during weather extremes and this is where a CAAMS would be valuable.

REFERENCES

1. Fernando Caracena, "Analytic Approximation 1992 Annual Report for CAAM," NOAA, Environmental Research Laboratory, National Severe Storms Laboratory, Boulder, CO, contractor report.

2. Fernando Caracena, "The Use of Analytic Approximations in Providing Meteorological Data For Artillery," NOAA, NSSL, Proceedings of the 1992 Battlefield Atmospherics Conference, p. 189, Fort Bliss, TX. (1-3 Dec 92)

3. Ernest B. Stenmark, William D. Ohmstede, and Don R. Veasey, "Proposed AMSA for Corps Tacfire (PACT) - Systems Description," Atmospheric Sciences Laboratory, U.S. Army Electronics Command, White Sands Missile Range, NM, internal report. (Jul 77)

4. Abel J. Blanco, Edward Vidal and Sean D'Arcy, "Time And Space Weighted Computer Assisted Artillery Message," TBP in Proceedings of the 1993 Battlefield Atmospheric Conference.

5. Compiled by Kenneth M. Barnett, "A Description of the Artillery Meteorological Comparisons at White Sands Missile Range, NM, Oct 74 - Dec 74 ("PASS" - Prototype Artillery [Meteorological] Subsystem)," ECOM-5589, Atmospheric Sciences Laboratory, White Sands Missile Range, NM. (Apr 76)

6. Edward M. D'Arcy, " 'PASS' 500mb Rawinsonde Data, Volume I, 1-15 Nov 74," ECOM-DR-77-4, Atmospheric Sciences Laboratory, White Sands Missile Range, NM. (Jun 77)

7. Edward M. D'Arcy, " 'PASS' 500mb Rawinsonde Data, Volume II, 18 Nov 74 to 7 Dec 74," ECOM-DR-77-4, Atmospheric Sciences Laboratory, White Sands Missile Range, NM. (Jun 77)

8. Edward M. D'Arcy, "Target Area Wind Variability and Its Affect on the MLRS Rocket," OSD-1366, Atmospheric Sciences Laboratory, White Sands Missile Range, NM. (Sep 92)

Table 1

DAY 323

19/11/74	PAC	0600,11,71	23.62	328.82			
19/11/74	PAC	0600,11	36.15	172.73	12.53	-156.09	
19/11/74	PAC	0600,21	57.76	59.38	34.14	-269.44	
19/11/74	PAC	0600,41	73.68	308.74	50.06	-20.08	
19/11/74	PAC	0600,51	9.36	-60.70	-14.26	-389.52	
					27.75	208.78	210.62
19/11/74	PAC	0600,11,21	83.10	115.55	59.48	-213.27	
19/11/74	PAC	0600,11,41	58.65	239.64	35.03	-89.18	
19/11/74	PAC	0600,11,51	29.16	48.84	5.54	-279.98	
					33.35	194.14	196.99
19/11/74	PAC	0600,11,21,61	108.87	159.33	85.25	-169.49	
19/11/74	PAC	0600,11,41,61	93.51	244.89	69.89	-83.93	
19/11/74	PAC	0600,11,51,61	69.39	101.89	45.77	-226.93	
19/11/74	PAC	0600,11,21,81	119.24	150.01	95.62	-178.81	
19/11/74	PAC	0600,11,41,81	95.41	241.84	71.79	-86.98	
19/11/74	PAC	0600,11,51,81	79.18	108.34	55.56	-220.48	
					70.65	161.10	175.91
19/11/74	PAC	0800,12,72	.57	7.23			
19/11/74	PAC	0800,12	-10.46	281.43	-11.03	274.20	
19/11/74	PAC	0800,22	20.58	-372.19	20.01	-379.42	
19/11/74	PAC	0800,32	80.09	-145.86	79.52	-153.09	
19/11/74	PAC	0800,42	2.69	524.20	2.12	516.97	
19/11/74	PAC	0800,52	15.83	-6.84	15.26	-14.07	
					25.59	267.55	268.77
19/11/74	PAC	0800,12,22	48.96	-47.98	48.39	-55.21	
19/11/74	PAC	0800,12,32	56.48	64.37	55.91	57.14	
19/11/74	PAC	0800,12,42	4.31	402.27	3.74	395.04	
19/11/74	PAC	0800,12,52	-.24	104.29	-.81	97.06	
					27.21	151.11	153.54
19/11/74	PAC	0800,12,22,62	81.51	35.89	80.94	28.66	
19/11/74	PAC	0800,12,32,62	82.86	115.21	82.29	107.98	
19/11/74	PAC	0800,12,42,62	47.01	346.03	46.44	338.80	
19/11/74	PAC	0800,12,52,62	41.23	139.81	40.66	132.58	
19/11/74	PAC	0800,12,22,82	52.93	45.93	52.36	38.70	
19/11/74	PAC	0800,12,32,82	53.11	144.59	52.54	137.36	
19/11/74	PAC	0800,12,42,82	15.98	365.13	15.41	357.90	
19/11/74	PAC	0800,12,52,82	23.08	159.76	22.51	152.53	
					49.14	161.81	169.11
19/11/74	PAC	1000,13,73	-43.17	323.18			
19/11/74	PAC	1000,13	-74.89	-221.21	-31.72	-544.39	
19/11/74	PAC	1000,23	42.67	232.26	85.84	-90.92	
19/11/74	PAC	1000,33	-11.18	172.89	31.99	-150.29	
19/11/74	PAC	1000,43	78.42	285.55	121.59	-37.63	
					67.78	205.81	216.68
19/11/74	PAC	1000,13,23	29.42	-4.75	72.59	-327.93	
19/11/74	PAC	1000,13,33	-23.88	-28.80	19.29	-351.98	
19/11/74	PAC	1000,13,43	14.66	23.31	57.83	-299.87	
					49.90	326.59	330.38
19/11/74	PAC	1000,13,23,63	23.13	75.66	66.30	-247.52	
19/11/74	PAC	1000,13,33,63	-5.40	61.84	37.77	-261.34	
19/11/74	PAC	1000,13,43,63	25.76	89.86	68.93	-233.32	
19/11/74	PAC	1000,13,23,83	38.37	87.32	81.54	-235.86	
19/11/74	PAC	1000,13,33,83	3.73	67.54	46.90	-255.64	
19/11/74	PAC	1000,13,43,83	18.84	101.41	62.01	-221.77	
					60.58	242.57	250.02

Table 2

DAY 323

19/11/74 NOA 0600,11,71	23.62	328.82			
19/11/74 NOA 0600,11	36.15	172.73	12.53	-156.09	
19/11/74 NOA 0600,21	57.76	59.38	34.14	-269.44	
19/11/74 NOA 0600,41	73.68	308.74	50.06	-20.08	
19/11/74 NOA 0600,51	9.36	-60.70	-14.26	-389.52	
			27.75	208.78	210.62
19/11/74 NOA 0600,11,21	101.41	123.86	77.79	-204.96	
19/11/74 NOA 0600,11,41	69.83	237.43	46.21	-91.39	
19/11/74 NOA 0600,11,51	42.46	40.13	18.84	-288.69	
			47.61	195.01	200.74
19/11/74 NOA 0600,11,21,61	126.46	173.23	102.84	-155.59	
19/11/74 NOA 0600,11,41,61	104.23	256.88	80.61	-71.94	
19/11/74 NOA 0600,11,51,61	80.56	111.00	56.94	-217.82	
19/11/74 NOA 0600,11,21,81	122.07	163.36	98.45	-165.46	
19/11/74 NOA 0600,11,41,81	110.91	247.54	87.29	-81.28	
19/11/74 NOA 0600,11,51,81	95.08	98.24	71.46	-230.58	
			82.93	153.78	174.72
19/11/74 NOA 0800,12,72	.57	7.23			
19/11/74 NOA 0800,12	-10.46	281.43	-11.03	274.20	
19/11/74 NOA 0800,22	20.58	-372.19	20.01	-379.42	
19/11/74 NOA 0800,32	80.09	-145.86	79.52	-153.09	
19/11/74 NOA 0800,42	2.69	524.20	2.12	516.97	
19/11/74 NOA 0800,52	15.83	-6.84	15.26	-14.07	
			25.59	267.55	268.77
19/11/74 NOA 0800,12,22	63.39	-52.27	62.82	-59.50	
19/11/74 NOA 0800,12,32	71.86	78.75	71.29	71.52	
19/11/74 NOA 0800,12,42	10.56	396.83	9.99	389.60	
19/11/74 NOA 0800,12,52	21.48	110.59	20.91	103.36	
			41.25	155.99	161.36
19/11/74 NOA 0800,12,22,62	95.84	27.97	95.27	20.74	
19/11/74 NOA 0800,12,32,62	92.59	127.26	92.02	120.03	
19/11/74 NOA 0800,12,42,62	62.19	335.02	61.62	327.79	
19/11/74 NOA 0800,12,52,62	65.59	142.87	65.02	135.64	
19/11/74 NOA 0800,12,22,82	63.38	59.06	62.81	51.83	
19/11/74 NOA 0800,12,32,82	69.49	139.70	68.92	132.47	
19/11/74 NOA 0800,12,42,82	26.64	356.13	26.07	348.90	
19/11/74 NOA 0800,12,52,82	33.89	154.02	33.32	146.79	
			63.13	160.52	172.49
19/11/74 NOA 1000,13,73	-43.17	323.18			
19/11/74 NOA 1000,13	-74.89	-221.21	-31.72	-544.39	
19/11/74 NOA 1000,23	42.67	232.26	85.84	-90.92	
19/11/74 NOA 1000,33	-11.18	172.89	31.99	-150.29	
19/11/74 NOA 1000,43	78.42	285.55	121.59	-37.63	
			67.78	205.81	216.68
19/11/74 NOA 1000,13,23	45.56	-8.70	88.73	-331.88	
19/11/74 NOA 1000,13,33	1.18	-28.42	44.35	-351.60	
19/11/74 NOA 1000,13,43	17.71	18.10	60.88	-305.08	
			64.65	329.52	335.80
19/11/74 NOA 1000,13,23,63	36.24	76.90	79.41	-246.28	
19/11/74 NOA 1000,13,33,63	14.79	53.46	57.96	-269.72	
19/11/74 NOA 1000,13,43,63	35.62	91.24	78.79	-231.94	
19/11/74 NOA 1000,13,23,83	50.94	82.30	94.11	-240.88	
19/11/74 NOA 1000,13,33,83	12.64	66.93	55.81	-256.25	
19/11/74 NOA 1000,13,43,83	29.59	107.97	72.76	-215.21	
			73.14	243.38	254.13

Table 3

DAY 323

11/19/74 H-M	0600,11,71	23.62	328.82			
11/19/74 H-M	0600,11	36.15	172.73	12.53	-156.09	
11/19/74 H-M	0600,21	57.76	59.38	34.14	-269.44	
11/19/74 H-M	0600,41	73.68	308.74	50.06	-20.08	
11/19/74 H-M	0600,51	9.36	-60.70	-14.26	-389.52	
				27.75	208.78	210.62
11/19/74 H-M	0600,11,21	52.58	135.28	28.96	-193.54	
11/19/74 H-M	0600,11,41	78.65	222.97	55.03	-105.85	
11/19/74 H-M	0600,11,51	53.40	18.81	29.78	-310.01	
				37.92	203.13	206.64
11/19/74 H-M	0600,11,21,6	94.14	193.86	70.52	-134.96	
11/19/74 H-M	0600,11,41,6	112.65	221.24	89.03	-107.58	
11/19/74 H-M	0600,11,51,6	93.03	96.65	69.41	-232.17	
11/19/74 H-M	0600,11,21,8	141.72	184.41	118.10	-144.41	
11/19/74 H-M	0600,11,41,8	141.13	227.95	117.51	-100.87	
11/19/74 H-M	0600,11,51,8	107.53	165.73	83.91	-163.09	
				91.41	147.18	173.26
11/19/74 H-M	0800,12,72	.57	7.23			
11/19/74 H-M	0800,12	-10.46	281.43	-11.03	274.20	
11/19/74 H-M	0800,22	20.58	-372.19	20.01	-379.42	
11/19/74 H-M	0800,32	80.09	-145.86	79.52	-153.09	
11/19/74 H-M	0800,42	2.69	524.20	2.12	516.97	
11/19/74 H-M	0800,52	15.83	-6.84	15.26	-14.07	
				25.59	267.55	268.77
11/19/74 H-M	0800,12,22	103.07	112.43	102.50	105.20	
11/19/74 H-M	0800,12,32	133.22	174.86	132.65	167.63	
11/19/74 H-M	0800,12,42	59.16	298.48	58.59	291.25	
11/19/74 H-M	0800,12,52	50.47	67.82	49.90	60.59	
				85.91	156.17	178.24
11/19/74 H-M	0800,12,22,6	148.86	129.14	148.29	121.91	
11/19/74 H-M	0800,12,32,6	157.31	181.36	156.74	174.13	
11/19/74 H-M	0800,12,42,6	105.14	254.47	104.57	247.24	
11/19/74 H-M	0800,12,52,6	113.60	99.40	113.03	92.17	
11/19/74 H-M	0800,12,22,8	43.70	265.05	43.13	257.82	
11/19/74 H-M	0800,12,32,8	45.06	286.00	44.49	278.77	
11/19/74 H-M	0800,12,42,8	18.58	313.26	18.01	306.03	
11/19/74 H-M	0800,12,52,8	14.40	260.65	13.83	253.42	
				80.26	216.44	230.84
11/19/74 H-M	1000,13,73	-43.17	323.18			
11/19/74 H-M	1000,13	-74.89	-221.21	-31.72	-544.39	
11/19/74 H-M	1000,23	42.67	232.26	85.84	-90.92	
11/19/74 H-M	1000,33	-11.18	172.89	31.99	-150.29	
11/19/74 H-M	1000,43	78.42	285.55	121.59	-37.63	
				67.78	205.81	216.68
11/19/74 H-M	1000,13,23	96.71	47.68	139.88	-275.50	
11/19/74 H-M	1000,13,33	90.17	1.41	133.34	-321.77	
11/19/74 H-M	1000,13,43	71.65	60.71	114.82	-262.47	
				129.35	286.58	314.42
11/19/74 H-M	1000,13,23,6	102.38	96.08	145.55	-227.10	
11/19/74 H-M	1000,13,33,6	100.14	77.88	143.31	-245.30	
11/19/74 H-M	1000,13,43,6	82.91	101.28	126.08	-221.90	
11/19/74 H-M	1000,13,23,8	91.01	169.73	134.18	-153.45	
11/19/74 H-M	1000,13,33,8	94.81	160.92	137.98	-162.26	
11/19/74 H-M	1000,13,43,8	81.98	152.52	125.15	-170.66	
				135.38	196.78	238.85

Table 4

DAY 323

19/11/74	T-A	600	11,71	23.62	328.82			
19/11/74	T-A	600	11	36.15	172.73	12.53	-156.09	
19/11/74	T-A	600	21	57.76	59.38	34.14	-269.44	
19/11/74	T-A	600	41	73.68	308.74	50.06	-20.08	
19/11/74	T-A	600	51	9.36	-60.70	-14.26	-389.52	
						27.75	208.78	210.62
19/11/74	T-A	600	11,21	50.01	113.79	26.39	-215.03	
19/11/74	T-A	600	11,41	17.99	230.76	-5.63	-98.06	
19/11/74	T-A	600	11,51	-13.90	37.91	-37.52	-290.91	
						23.18	201.33	202.66
19/11/74	T-A	600	11,21,61	77.11	188.25	53.49	-140.57	
19/11/74	T-A	600	11,41,61	61.79	250.82	38.17	-78.00	
19/11/74	T-A	600	11,51,61	40.81	149.08	17.19	-179.74	
19/11/74	T-A	600	11,21,81	86.16	272.26	62.54	-56.56	
19/11/74	T-A	600	11,41,81	73.97	286.07	50.35	-42.75	
19/11/74	T-A	600	11,51,81	50.30	273.68	26.68	-55.14	
						41.40	92.13	101.00
19/11/74	T-A	800	12,72	.57	7.23			
19/11/74	T-A	800	12	-10.46	281.43	-11.03	274.20	
19/11/74	T-A	800	22	20.58	-372.19	20.01	-379.42	
19/11/74	T-A	800	32	80.09	-145.86	79.52	-153.09	
19/11/74	T-A	800	42	2.69	524.20	2.12	516.97	
19/11/74	T-A	800	52	15.83	-6.84	15.26	-14.07	
						25.59	267.55	268.77
19/11/74	T-A	800	12,22	14.39	-67.20	13.82	-74.43	
19/11/74	T-A	800	12,32	15.22	85.86	14.65	78.63	
19/11/74	T-A	800	12,42	-36.97	387.73	-37.54	380.50	
19/11/74	T-A	800	12,52	-31.26	108.61	-31.83	101.38	
						24.46	158.74	160.61
19/11/74	T-A	800	12,22,62	42.87	72.57	42.30	65.34	
19/11/74	T-A	800	12,32,62	45.19	156.86	44.62	149.63	
19/11/74	T-A	800	12,42,62	19.98	300.75	19.41	293.52	
19/11/74	T-A	800	12,52,62	14.96	162.30	14.39	155.07	
19/11/74	T-A	800	12,22,82	-1.77	208.45	-2.34	201.22	
19/11/74	T-A	800	12,32,82	-2.05	252.36	-2.62	245.13	
19/11/74	T-A	800	12,42,82	-25.81	320.24	-26.38	313.01	
19/11/74	T-A	800	12,52,82	-27.76	259.57	-28.33	252.34	
						22.55	209.41	210.62
19/11/74	T-A	1000	13,73	-43.17	323.18			
19/11/74	T-A	1000	13	-74.89	-221.21	-31.72	-544.39	
19/11/74	T-A	1000	23	42.67	232.26	85.84	-90.92	
19/11/74	T-A	1000	33	-11.18	172.89	31.99	-150.29	
19/11/74	T-A	1000	43	78.42	285.55	121.59	-37.63	
						67.78	205.81	216.68
19/11/74	T-A	1000	13,23	-12.91	3.32	30.26	-319.86	
19/11/74	T-A	1000	13,33	-59.86	-50.03	-16.69	-373.21	
19/11/74	T-A	1000	13,43	-38.89	-12.10	4.28	-335.28	
						17.08	342.78	343.21
19/11/74	T-A	1000	13,23,63	-13.48	117.75	29.69	-205.43	
19/11/74	T-A	1000	13,33,63	-37.74	97.97	5.43	-225.21	
19/11/74	T-A	1000	13,43,63	-26.24	116.65	16.93	-206.53	
19/11/74	T-A	1000	13,23,83	-16.42	194.00	26.75	-129.18	
19/11/74	T-A	1000	13,33,83	-40.68	187.26	2.49	-135.92	
19/11/74	T-A	1000	13,43,83	-23.52	187.32	19.65	-135.86	
						16.82	173.02	173.84

Table 5

DAY 323

19/11/74 T-S 0600,11,71	23.62	328.82			
19/11/74 T-S 0600,11	36.15	172.73	12.53	-156.09	
19/11/74 T-S 0600,21	57.76	59.38	34.14	-269.44	
19/11/74 T-S 0600,41	73.68	308.74	50.06	-20.08	
19/11/74 T-S 0600,51	9.36	-60.70	-14.26	-389.52	
			27.75	208.78	210.62
19/11/74 T-S 0600,11,21	102.06	127.77	78.44	-201.05	
19/11/74 T-S 0600,11,41	61.98	238.09	38.36	-90.73	
19/11/74 T-S 0600,11,51	46.55	24.11	22.93	-304.71	
			46.58	198.83	204.21
19/11/74 T-S 0600,11,21,61	133.42	188.30	109.80	-140.52	
19/11/74 T-S 0600,11,41,61	105.21	257.08	81.59	-71.74	
19/11/74 T-S 0600,11,51,61	74.33	92.99	50.71	-235.83	
19/11/74 T-S 0600,11,21,81	119.09	148.65	95.47	-180.17	
19/11/74 T-S 0600,11,41,81	105.41	233.91	81.79	-94.91	
19/11/74 T-S 0600,11,51,81	74.34	74.53	50.72	-254.29	
			78.35	162.91	180.77
19/11/74 T-S 0800,12,72	.57	7.23			
19/11/74 T-S 0800,12	-10.46	281.43	-11.03	274.20	
19/11/74 T-S 0800,22	20.58	-372.19	20.01	-379.42	
19/11/74 T-S 0800,32	80.09	-145.86	79.52	-153.09	
19/11/74 T-S 0800,42	2.69	524.20	2.12	516.97	
19/11/74 T-S 0800,52	15.83	-6.84	15.26	-14.07	
			25.59	267.55	268.77
19/11/74 T-S 0800,12,22	61.75	-35.58	61.18	-42.81	
19/11/74 T-S 0800,12,32	68.60	98.28	68.03	91.05	
19/11/74 T-S 0800,12,42	16.11	381.03	15.54	373.80	
19/11/74 T-S 0800,12,52	31.33	89.37	30.76	82.14	
			43.88	147.45	153.84
19/11/74 T-S 0800,12,22,62	98.21	63.41	97.64	56.18	
19/11/74 T-S 0800,12,32,62	93.65	146.72	93.08	139.49	
19/11/74 T-S 0800,12,42,62	70.78	315.46	70.21	308.23	
19/11/74 T-S 0800,12,52,62	72.36	131.47	71.79	124.24	
19/11/74 T-S 0800,12,22,82	64.25	62.52	63.68	55.29	
19/11/74 T-S 0800,12,32,82	68.39	158.40	67.82	151.17	
19/11/74 T-S 0800,12,42,82	24.53	356.51	23.96	349.28	
19/11/74 T-S 0800,12,52,82	38.11	127.86	37.54	120.63	
			65.71	163.06	175.81
19/11/74 T-S 1000,13,73	-43.17	323.18			
19/11/74 T-S 1000,13	-74.89	-221.21	-31.72	-544.39	
19/11/74 T-S 1000,23	42.67	232.26	85.84	-90.92	
19/11/74 T-S 1000,33	-11.18	172.89	31.99	-150.29	
19/11/74 T-S 1000,43	78.42	285.55	121.59	-37.63	
			67.78	205.81	216.68
19/11/74 T-S 1000,13,23	33.31	-10.94	76.48	-334.12	
19/11/74 T-S 1000,13,33	2.00	9.62	45.17	-313.56	
19/11/74 T-S 1000,13,43	11.53	-7.43	54.70	-330.61	
			58.78	326.10	331.35
19/11/74 T-S 1000,13,23,63	35.61	82.55	78.78	-240.63	
19/11/74 T-S 1000,13,33,63	16.55	76.04	59.72	-247.14	
19/11/74 T-S 1000,13,43,63	28.99	89.00	72.16	-234.18	
19/11/74 T-S 1000,13,23,83	46.35	65.32	89.52	-257.86	
19/11/74 T-S 1000,13,33,83	13.89	69.88	57.06	-253.30	
19/11/74 T-S 1000,13,43,83	24.04	69.71	67.21	-253.47	
			70.74	247.76	257.66

Table 7

DAY 324

20/11/74 NOA	1230,11,71	171.58	113.11			
20/11/74 NOA	1230,11	152.49	50.61	-19.09	-62.50	
20/11/74 NOA	1230,21	234.89	57.88	63.31	-55.23	
20/11/74 NOA	1230,31	224.42	70.87	52.84	-42.24	
20/11/74 NOA	1230,51	212.29	36.87	40.71	-76.24	
				43.99	59.05	73.63
20/11/74 NOA	1230,11,21	242.30	46.57	70.72	-66.54	
20/11/74 NOA	1230,11,31	223.98	55.09	52.40	-58.02	
20/11/74 NOA	1230,11,51	190.57	39.11	18.99	-74.00	
				47.37	66.19	81.39
20/11/74 NOA	1230,11,21,61	238.58	49.24	67.00	-63.87	
20/11/74 NOA	1230,11,31,61	224.55	54.38	52.97	-58.73	
20/11/74 NOA	1230,11,51,61	206.93	45.33	35.35	-67.78	
20/11/74 NOA	1230,11,21,81	243.63	47.49	72.05	-65.62	
20/11/74 NOA	1230,11,31,81	226.91	55.56	55.33	-57.55	
20/11/74 NOA	1230,11,51,81	210.32	32.00	38.74	-81.11	
				53.57	65.78	84.83
20/11/74 NOA	1430,12,72	238.72	9.64			
20/11/74 NOA	1430,12	262.14	137.22	23.42	127.58	
20/11/74 NOA	1430,22	278.57	-28.93	39.85	-38.57	
20/11/74 NOA	1430,32	265.89	43.49	27.17	33.85	
20/11/74 NOA	1430,42	250.96	111.83	12.24	102.19	
20/11/74 NOA	1430,52	256.21	73.54	17.49	63.90	
				24.03	73.22	77.06
20/11/74 NOA	1430,12,22	308.64	53.70	69.92	44.06	
20/11/74 NOA	1430,12,32	285.10	80.33	46.38	70.69	
20/11/74 NOA	1430,12,42	257.09	113.48	18.37	103.84	
20/11/74 NOA	1430,12,52	259.36	93.28	20.64	83.64	
				38.83	75.56	84.95
20/11/74 NOA	1430,12,22,62	295.14	64.86	56.42	55.22	
20/11/74 NOA	1430,12,32,62	279.67	88.06	40.95	78.42	
20/11/74 NOA	1430,12,42,62	262.15	107.44	23.43	97.80	
20/11/74 NOA	1430,12,52,62	271.77	97.79	33.05	88.15	
20/11/74 NOA	1430,12,22,82	295.45	52.12	56.73	42.48	
20/11/74 NOA	1430,12,32,82	284.60	70.09	45.88	60.45	
20/11/74 NOA	1430,12,42,82	260.30	84.32	21.58	74.68	
20/11/74 NOA	1430,12,52,82	257.79	76.12	19.07	66.48	
				37.14	70.46	79.65
20/11/74 NOA	1630,13,73	233.08	23.11			
20/11/74 NOA	1630,13	237.99	96.36	4.91	73.25	
20/11/74 NOA	1630,23	261.97	95.43	28.89	72.32	
20/11/74 NOA	1630,33	237.59	71.14	4.51	48.03	
20/11/74 NOA	1630,43	289.74	70.37	56.66	47.26	
20/11/74 NOA	1630,53	255.69	115.93	22.61	92.82	
				23.52	66.74	70.76
20/11/74 NOA	1630,13,23	295.38	90.48	62.30	67.37	
20/11/74 NOA	1630,13,33	259.73	78.77	26.65	55.66	
20/11/74 NOA	1630,13,43	281.26	79.81	48.18	56.70	
20/11/74 NOA	1630,13,53	255.32	98.66	22.24	75.55	
				39.84	63.82	75.24
20/11/74 NOA	1630,13,23,63	293.17	92.36	60.09	69.25	
20/11/74 NOA	1630,13,33,63	272.84	85.27	39.76	62.16	
20/11/74 NOA	1630,13,43,63	281.07	87.19	47.99	64.08	
20/11/74 NOA	1630,13,53,63	263.06	101.23	29.98	78.12	
20/11/74 NOA	1630,13,23,83	286.79	64.33	53.71	41.22	
20/11/74 NOA	1630,13,33,83	270.98	53.76	37.90	30.65	
20/11/74 NOA	1630,13,43,83	284.08	58.15	51.00	35.04	
20/11/74 NOA	1630,13,53,83	255.43	72.31	22.35	49.20	
				42.85	53.72	68.71

Table 6

DAY 324

20/11/74 PAC 1230,11,71	171.58	113.11			
20/11/74 PAC 1230,11	152.49	50.61	-19.09	-62.50	
20/11/74 PAC 1230,21	234.89	57.88	63.31	-55.23	
20/11/74 PAC 1230,31	224.42	70.87	52.84	-42.24	
20/11/74 PAC 1230,51	212.29	36.87	40.71	-76.24	
			43.99	59.05	73.63
20/11/74 PAC 1230,11,21	232.14	56.32	60.56	-56.79	
20/11/74 PAC 1230,11,31	206.31	57.72	34.73	-55.39	
20/11/74 PAC 1230,11,51	189.85	42.59	18.27	-70.52	
			37.85	60.90	71.71
20/11/74 PAC 1230,11,21,61	232.48	56.96	60.90	-56.15	
20/11/74 PAC 1230,11,31,61	221.05	60.32	49.47	-52.79	
20/11/74 PAC 1230,11,51,61	197.81	48.16	26.23	-64.95	
20/11/74 PAC 1230,11,21,81	244.73	39.75	73.15	-73.36	
20/11/74 PAC 1230,11,31,81	230.25	44.42	58.67	-68.69	
20/11/74 PAC 1230,11,51,81	217.09	40.47	45.51	-72.64	
			52.32	64.76	83.26
20/11/74 PAC 1430,12,72	238.72	9.64			
20/11/74 PAC 1430,12	262.14	137.22	23.42	127.58	
20/11/74 PAC 1430,22	278.57	-28.93	39.85	-38.57	
20/11/74 PAC 1430,32	265.89	43.49	27.17	33.85	
20/11/74 PAC 1430,42	250.96	111.83	12.24	102.19	
20/11/74 PAC 1430,52	256.21	73.54	17.49	63.90	
			24.03	73.22	77.06
20/11/74 PAC 1430,12,22	302.83	54.18	64.11	44.54	
20/11/74 PAC 1430,12,32	287.64	94.47	48.92	84.83	
20/11/74 PAC 1430,12,42	252.89	113.99	14.17	104.35	
20/11/74 PAC 1430,12,52	263.53	105.31	24.81	95.67	
			38.00	82.35	90.69
20/11/74 PAC 1430,12,22,62	292.27	68.52	53.55	58.88	
20/11/74 PAC 1430,12,32,62	281.30	91.66	42.58	82.02	
20/11/74 PAC 1430,12,42,62	262.30	110.38	23.58	100.74	
20/11/74 PAC 1430,12,52,62	263.92	101.86	25.20	92.22	
20/11/74 PAC 1430,12,22,82	300.78	55.35	62.06	45.71	
20/11/74 PAC 1430,12,32,82	289.98	75.26	51.26	65.62	
20/11/74 PAC 1430,12,42,82	260.43	101.75	21.71	92.11	
20/11/74 PAC 1430,12,52,82	264.85	84.71	26.13	75.07	
			38.26	76.55	85.57
20/11/74 PAC 1630,13,73	233.08	23.11			
20/11/74 PAC 1630,13	237.99	96.36	4.91	73.25	
20/11/74 PAC 1630,23	261.97	95.43	28.89	72.32	
20/11/74 PAC 1630,33	237.59	71.14	4.51	48.03	
20/11/74 PAC 1630,43	289.74	70.37	56.66	47.26	
20/11/74 PAC 1630,53	255.69	115.93	22.61	92.82	
			23.52	66.74	70.76
20/11/74 PAC 1630,13,23	283.44	93.17	50.36	70.06	
20/11/74 PAC 1630,13,33	258.34	81.77	25.26	58.66	
20/11/74 PAC 1630,13,43	266.27	81.81	33.19	58.70	
20/11/74 PAC 1630,13,53	245.13	104.61	12.05	81.50	
			30.21	67.23	73.71
20/11/74 PAC 1630,13,23,63	292.69	102.70	59.61	79.59	
20/11/74 PAC 1630,13,33,63	263.75	91.25	30.67	68.14	
20/11/74 PAC 1630,13,43,63	278.28	91.20	45.20	68.09	
20/11/74 PAC 1630,13,53,63	259.78	106.01	26.70	82.90	
20/11/74 PAC 1630,13,23,83	287.60	64.75	54.52	41.64	
20/11/74 PAC 1630,13,33,83	266.86	60.98	33.78	37.87	
20/11/74 PAC 1630,13,43,83	278.45	60.54	45.37	37.43	
20/11/74 PAC 1630,13,53,83	252.80	71.64	19.72	48.53	
			39.45	58.02	70.16

Table 8

DAY 324

11/20/74	H-M	1230,11,71	171.58	113.11			
11/20/74	H-M	1230,11	152.49	50.61	-19.09	-62.50	
11/20/74	H-M	1230,21	234.89	57.88	63.31	-55.23	
11/20/74	H-M	1230,31	224.42	70.87	52.84	-42.24	
11/20/74	H-M	1230,51	212.29	36.87	40.71	-76.24	
					43.99	59.05	73.63
11/20/74	H-M	1230,11,21	372.84	44.14	201.26	-68.97	
11/20/74	H-M	1230,11,31	399.15	57.20	227.57	-55.91	
11/20/74	H-M	1230,11,51	337.72	54.96	166.14	-58.15	
					198.32	61.01	207.50
11/20/74	H-M	1230,11,21,6	379.85	44.01	208.27	-69.10	
11/20/74	H-M	1230,11,31,6	388.66	57.12	217.08	-55.99	
11/20/74	H-M	1230,11,51,6	354.78	46.40	183.20	-66.71	
11/20/74	H-M	1230,11,21,8	348.51	63.50	176.93	-49.61	
11/20/74	H-M	1230,11,31,8	359.14	68.07	187.56	-45.04	
11/20/74	H-M	1230,11,51,8	343.50	42.10	171.92	-71.01	
					190.83	59.58	199.91
11/20/74	H-M	1430,12,72	238.72	9.64			
11/20/74	H-M	1430,12	262.14	137.22	23.42	127.58	
11/20/74	H-M	1430,22	278.57	-28.93	39.85	-38.57	
11/20/74	H-M	1430,32	265.89	43.49	27.17	33.85	
11/20/74	H-M	1430,42	250.96	111.83	12.24	102.19	
11/20/74	H-M	1430,52	256.21	73.54	17.49	63.90	
					24.03	73.22	77.06
11/20/74	H-M	1430,12,22	423.92	58.36	185.20	48.72	
11/20/74	H-M	1′70,12,32	433.79	80.56	195.07	70.92	
11/20/74	H-M	1430,12,42	390.90	92.91	152.18	83.27	
11/20/74	H-M	1430,12,52	397.25	78.16	158.53	68.52	
					172.74	67.86	185.59
11/20/74	H-M	1430,12,22,6	414.13	73.46	175.41	63.82	
11/20/74	H-M	1430,12,32,6	406.32	82.91	167.60	73.27	
11/20/74	H-M	1430,12,42,6	375.45	87.61	136.73	77.97	
11/20/74	H-M	1430,12,52,6	404.57	65.14	165.85	55.50	
11/20/74	H-M	1430,12,22,8	347.64	121.16	108.92	111.52	
11/20/74	H-M	1430,12,32,8	345.94	113.20	107.22	103.56	
11/20/74	H-M	1430,12,42,8	335.39	109.76	96.67	100.12	
11/20/74	H-M	1430,12,52,8	348.09	107.65	109.37	98.01	
					133.47	85.47	158.49
11/20/74	H-M	1630,13,73	233.08	23.11			
11/20/74	H-M	1630,13	237.99	96.36	4.91	73.25	
11/20/74	H-M	1630,23	261.97	95.43	28.89	72.32	
11/20/74	H-M	1630,33	237.59	71.14	4.51	48.03	
11/20/74	H-M	1630,43	289.74	70.37	56.66	47.26	
11/20/74	H-M	1630,53	255.69	115.93	22.61	92.82	
					23.52	66.74	70.76
11/20/74	H-M	1630,13,23	390.02	82.39	156.94	59.28	
11/20/74	H-M	1630,13,33	416.38	87.56	183.30	64.45	
11/20/74	H-M	1630,13,43	380.48	96.72	147.40	73.61	
11/20/74	H-M	1630,13,53	361.01	94.55	127.93	71.44	
					153.89	67.19	167.92
11/20/74	H-M	1630,13,23,6	397.39	80.13	164.31	57.02	
11/20/74	H-M	1630,13,33,6	414.32	87.93	181.24	64.82	
11/20/74	H-M	1630,13,43,6	386.27	87.18	153.19	64.07	
11/20/74	H-M	1630,13,53,6	380.46	82.68	147.38	59.57	
11/20/74	H-M	1630,13,23,8	364.15	76.30	131.07	53.19	
11/20/74	H-M	1630,13,33,8	376.97	78.56	143.89	55.45	
11/20/74	H-M	1630,13,43,8	370.30	61.02	137.22	37.91	
11/20/74	H-M	1630,13,53,8	367.79	46.72	134.71	23.61	
					149.13	51.96	157.92

Table 9

DAY 324

20/11/74	T-A	1230	11,71	171.58	113.11			
20/11/74	T-A	1230	11	152.49	50.61	-19.09	-62.50	
20/11/74	T-A	1230	21	234.89	57.88	63.31	-55.23	
20/11/74	T-A	1230	31	224.42	70.87	52.84	-42.24	
20/11/74	T-A	1230	51	212.29	36.87	40.71	-76.24	
						43.99	59.05	73.63
20/11/74	T-A	1230	11,21	193.27	54.59	21.69	-58.52	
20/11/74	T-A	1230	11,31	167.13	60.25	-4.45	-52.86	
20/11/74	T-A	1230	11,51	149.58	43.71	-22.00	-69.40	
						16.05	60.26	62.36
20/11/74	T-A	1230	11,21,61	190.92	55.61	19.34	-57.50	
20/11/74	T-A	1230	11,31,61	176.98	58.80	5.40	-54.31	
20/11/74	T-A	1230	11,51,61	165.19	49.19	-6.39	-63.92	
20/11/74	T-A	1230	11,21,81	199.44	25.83	27.86	-87.28	
20/11/74	T-A	1230	11,31,81	189.23	27.56	17.65	-85.55	
20/11/74	T-A	1230	11,51,81	177.88	22.76	6.30	-90.35	
						13.82	73.15	74.45
20/11/74	T-A	1430	12,72	238.72	9.64			
20/11/74	T-A	1430	12	262.14	137.22	23.42	127.58	
20/11/74	T-A	1430	22	278.57	-28.93	39.85	-38.57	
20/11/74	T-A	1430	32	265.89	43.49	27.17	33.85	
20/11/74	T-A	1430	42	250.96	111.83	12.24	102.19	
20/11/74	T-A	1430	52	256.21	73.54	17.49	63.90	
						24.03	73.22	77.06
20/11/74	T-A	1430	12,22	271.88	57.03	33.16	47.39	
20/11/74	T-A	1430	12,32	247.84	96.13	9.12	86.49	
20/11/74	T-A	1430	12,42	223.43	125.85	-15.29	116.21	
20/11/74	T-A	1430	12,52	224.65	103.69	-14.07	94.05	
						17.91	86.04	87.88
20/11/74	T-A	1430	12,22,62	247.61	74.50	8.89	64.86	
20/11/74	T-A	1430	12,32,62	230.79	96.40	-7.93	86.76	
20/11/74	T-A	1430	12,42,62	217.70	112.62	-21.02	102.98	
20/11/74	T-A	1430	12,52,62	221.35	100.48	-17.37	90.84	
20/11/74	T-A	1430	12,22,82	246.78	42.81	8.06	33.17	
20/11/74	T-A	1430	12,32,82	234.85	57.57	-3.87	47.93	
20/11/74	T-A	1430	12,42,82	223.90	68.53	-14.82	58.89	
20/11/74	T-A	1430	12,52,82	225.16	62.90	-13.56	53.26	
						11.94	67.34	68.39
20/11/74	T-A	1630	13,73	233.08	23.11			
20/11/74	T-A	1630	13	237.99	96.36	4.91	73.25	
20/11/74	T-A	1630	23	261.97	95.43	28.89	72.32	
20/11/74	T-A	1630	33	237.59	71.14	4.51	48.03	
20/11/74	T-A	1630	43	289.74	70.37	56.66	47.26	
20/11/74	T-A	1630	53	255.69	115.93	22.61	92.82	
						23.52	66.74	70.76
20/11/74	T-A	1630	13,23	251.26	96.59	18.18	73.48	
20/11/74	T-A	1630	13,33	221.99	85.42	-11.09	62.31	
20/11/74	T-A	1630	13,43	226.43	85.34	-6.65	62.23	
20/11/74	T-A	1630	13,53	213.37	106.92	-19.71	83.81	
						13.91	70.46	71.82
20/11/74	T-A	1630	13,23,63	250.77	102.14	17.69	79.03	
20/11/74	T-A	1630	13,33,63	234.84	96.67	1.76	73.56	
20/11/74	T-A	1630	13,43,63	239.43	96.80	6.35	73.69	
20/11/74	T-A	1630	13,53,63	228.71	108.60	-4.37	85.49	
20/11/74	T-A	1630	13,23,83	241.71	38.33	8.63	15.22	
20/11/74	T-A	1630	13,33,83	228.73	32.29	-4.35	9.18	
20/11/74	T-A	1630	13,43,83	231.60	34.25	-1.48	11.14	
20/11/74	T-A	1630	13,53,83	225.75	47.79	-7.33	24.68	
						6.49	46.50	46.95

Table 10

DAY 324

20/11/74	T-S	1230,11,71	171.58	113.11			
20/11/74	T-S	1230,11	152.49	50.61	-19.09	-62.50	
20/11/74	T-S	1230,21	234.89	57.88	63.31	-55.23	
20/11/74	T-S	1230,31	224.42	70.87	52.84	-42.24	
20/11/74	T-S	1230,51	212.29	36.87	40.71	-76.24	
					43.99	59.05	73.63
20/11/74	T-S	1230,11,21	238.78	46.51	67.20	-66.60	
20/11/74	T-S	1230,11,31	216.87	55.83	45.29	-57.28	
20/11/74	T-S	1230,11,51	200.04	42.24	28.46	-70.87	
					46.98	64.92	80.13
20/11/74	T-S	1230,11,21,61	237.90	48.77	66.32	-64.34	
20/11/74	T-S	1230,11,31,61	224.84	54.70	53.26	-58.41	
20/11/74	T-S	1230,11,51,61	213.13	47.07	41.55	-66.04	
20/11/74	T-S	1230,11,21,81	241.45	47.40	69.87	-65.71	
20/11/74	T-S	1230,11,31,81	228.01	55.18	56.43	-57.93	
20/11/74	T-S	1230,11,51,81	210.53	31.34	38.95	-81.77	
					54.40	65.70	85.30
20/11/74	T-S	1430,12,72	238.72	9.64			
20/11/74	T-S	1430,12	262.14	137.22	23.42	127.58	
20/11/74	T-S	1430,22	278.57	-28.93	39.85	-38.57	
20/11/74	T-S	1430,32	265.89	43.49	27.17	33.85	
20/11/74	T-S	1430,42	250.96	111.83	12.24	102.19	
20/11/74	T-S	1430,52	256.21	73.54	17.49	63.90	
					24.03	73.22	77.06
20/11/74	T-S	1430,12,22	308.55	57.78	69.83	48.14	
20/11/74	T-S	1430,12,32	289.91	83.42	51.19	73.78	
20/11/74	T-S	1430,12,42	259.11	113.69	20.39	104.05	
20/11/74	T-S	1430,12,52	263.43	97.42	24.71	87.78	
					41.53	78.44	88.75
20/11/74	T-S	1430,12,22,62	289.54	71.37	50.82	61.73	
20/11/74	T-S	1430,12,32,62	272.37	92.15	33.65	82.51	
20/11/74	T-S	1430,12,42,62	272.37	108.44	33.65	98.80	
20/11/74	T-S	1430,12,52,62	265.58	90.30	26.86	80.66	
20/11/74	T-S	1430,12,22,82	295.76	53.64	57.04	44.00	
20/11/74	T-S	1430,12,32,82	287.22	72.66	48.50	63.02	
20/11/74	T-S	1430,12,42,82	260.12	84.89	21.40	75.25	
20/11/74	T-S	1430,12,52,82	262.97	81.14	24.25	71.50	
					37.02	72.18	81.12
20/11/74	T-S	1630,13,73	233.08	23.11			
20/11/74	T-S	1630,13	237.99	96.36	4.91	73.25	
20/11/74	T-S	1630,23	261.97	95.43	28.89	72.32	
20/11/74	T-S	1630,33	237.59	71.14	4.51	48.03	
20/11/74	T-S	1630,43	289.74	70.37	56.66	47.26	
20/11/74	T-S	1630,53	255.69	115.93	22.61	92.82	
					23.52	66.74	70.76
20/11/74	T-S	1630,13,23	296.11	91.80	63.03	68.69	
20/11/74	T-S	1630,13,33	265.25	80.16	32.17	57.05	
20/11/74	T-S	1630,13,43	271.58	79.87	38.50	56.76	
20/11/74	T-S	1630,13,53	256.77	97.18	23.69	74.07	
					39.35	64.14	75.25
20/11/74	T-S	1630,13,23,63	293.51	96.70	60.43	73.59	
20/11/74	T-S	1630,13,33,63	279.42	90.00	46.34	66.89	
20/11/74	T-S	1630,13,43,63	289.83	91.33	56.75	68.22	
20/11/74	T-S	1630,13,53,63	278.44	95.88	45.36	72.77	
20/11/74	T-S	1630,13,23,83	288.16	65.24	55.08	42.13	
20/11/74	T-S	1630,13,33,83	278.44	52.42	45.36	29.31	
20/11/74	T-S	1630,13,43,83	285.21	59.85	52.13	36.74	
20/11/74	T-S	1630,52,33,83	291.76	46.22	58.68	23.11	
					52.52	51.60	73.62

TABLE 11

PAC.323

Current data - 1 dedicated corps station
```
13        245.22  28445.71    168.66
          -30.47   1935.92     44.00
          108.75  77834.10    278.99    260.86
```

Current data - 1 dedicated corps station plus 1 more corps area station
```
10        223.65  16004.35    126.51
          -35.70    724.37     26.91
          106.82  56762.83    238.25    229.20
```

Current data - 1 dedicated corps station plus 1 more corps area station
          plus 1 station ahead of the FLOT
```
20        200.18   6474.27     80.46
          -59.02    452.66     21.28
           56.38  41188.56    202.95    188.48
```

TABLE 12

NOA.323

Current data - 1 dedicated corps station
```
13        245.22  28445.71    168.66
          -30.47   1935.92     44.00
          108.75  77834.10    278.99    260.86
```

Current data - 1 dedicated corps station plus 1 more corps area station
```
10        230.27  14789.85    121.61
          -50.18    719.14     26.82
          106.86  57497.26    239.79    233.00
```

Current data - 1 dedicated corps station plus 1 more corps area station
          plus 1 station ahead of the FLOT
```
20        203.22   5860.08     76.55
          -72.07    422.83     20.56
           54.94  40263.82    200.66    190.83
```

TABLE 13

_H-M.323

Current data - 1 dedicated corps station
```
13        245.22  28445.71    168.66
          -30.47   1935.92     44.00
          108.75  77834.10    278.99    260.86
```

Current data - 1 dedicated corps station plus 1 more corps area station
```
10        230.64   8679.03     93.16
          -84.54   1981.10     44.51
           84.45  49938.49    223.47    224.20
```

Current data - 1 dedicated corps station plus 1 more corps area station
          plus 1 station ahead of the FLOT
```
20        222.06   2601.31     51.00
         -100.14   1941.95     44.07
           16.61  41718.44    204.25    201.41
```

75

TABLE 14

T-A.323

Current data - 1 dedicated corps station
    13   245.22 28445.71   168.66
             -30.47   1935.92   44.00
             108.75   77834.10   278.99   260.86

Current data - 1 dedicated corps station plus 1 more corps area station
    10   228.26 16266.64   127.54
               3.98   668.66   25.86
             114.63   58875.36   242.64   233.30

Current data - 1 dedicated corps station plus 1 more corps area station
              plus 1 station ahead of the FLOT
    20   168.65   5558.94   74.56
             -20.52   606.86   24.63
              -4.22   34428.68   185.55   157.24

TABLE 15

T-S.323

Current data - 1 dedicated corps station
    13   245.22 28445.71   168.66
             -30.47   1935.92   44.00
             108.75   77834.10   278.99   260.86

Current data - 1 dedicated corps station plus 1 more corps area station
    10   226.47 14783.53   121.59
             -49.16   491.60   22.17
             107.06   55859.78   236.35   230.08

Current data - 1 dedicated corps station plus 1 more corps area station
              plus 1 station ahead of the FLOT
    20   206.52   5642.14   75.11
             -71.01   446.90   21.14
              57.98   41244.66   203.09   193.14

TABLE-16

PAC.324

Current data - 1 dedicated corps station
    14   76.43   516.09   22.72
             -26.82   513.89   22.67
             -27.60   4698.11   68.54   71.37

Current data - 1 dedicated corps station plus 1 more corps area station
    11   81.94   201.60   14.20
             -35.13   337.28   18.37
             -37.78   4322.23   65.74   76.75

Current data - 1 dedicated corps station plus 1 more corps area station
              plus 1 station ahead of the FLOT
    22   81.09   222.55   14.92
             -42.53   249.43   15.79
             -31.27   3942.53   62.79   75.45

76

TABLE-17

NOA.324

Current data - 1 dedicated corps station
14	76.43	516.09	22.72	
	-26.82	513.89	22.67	
	-27.60	4698.11	68.54	71.37

Current data - 1 dedicated corps station plus 1 more corps area station
11	83.37	140.23	11.84	
	-41.53	434.97	20.86	
	-32.63	4283.29	65.45	77.84

Current data - 1 dedicated corps station plus 1 more corps area station
plus 1 station ahead of the FLOT
22	78.76	179.91	13.41	
	-43.70	226.67	15.06	
	-27.22	3674.74	60.62	73.17

TABLE-18

H-M.324

Current data - 1 dedicated corps station
14	76.43	516.09	22.72	
	-26.82	513.89	22.67	
	-27.60	4698.11	68.54	71.37

Current data - 1 dedicated corps station plus 1 more corps area station
11	185.61	638.98	25.28	
	-172.87	815.28	28.55	
	-32.47	3688.84	60.74	184.55

Current data - 1 dedicated corps station plus 1 more corps area station
plus 1 station ahead of the FLOT
22	170.92	633.10	25.16	
	-154.81	1071.02	32.73	
	-33.72	3869.87	62.21	168.90

TABLE-19

T-A.324

Current data - 1 dedicated corps station
14	76.43	516.09	22.72	
	-26.82	513.89	22.67	
	-27.60	4698.11	68.54	71.37

Current data - 1 dedicated corps station plus 1 more corps area station
11	75.73	367.78	19.18	
	1.01	346.38	18.61	
	-40.47	4527.25	67.28	70.83

Current data - 1 dedicated corps station plus 1 more corps area station
plus 1 station ahead of the FLOT
22	62.54	790.27	28.11	
	-1.16	163.60	12.79	
	-21.44	4241.07	65.12	59.28

TABLE-20

T-S.324

Current data - 1 dedicated corps station
14   76.43   516.09   22.72
           -26.82   513.89   22.67
           -27.60   4698.11   68.54   71.37

Current data - 1 dedicated corps station plus 1 more corps area station
11   83.72   156.55   12.51
           -42.22   333.99   18.28
           -34.14   4288.99   65.49   78.44

Current data - 1 dedicated corps station plus 1 more corps area station
            plus 1 station ahead of the FLOT
22   80.76   151.64   12.31
           -45.80   193.18   13.90
           -28.44   3745.53   61.20   75.08

TABLE 21

STATS.PAC

Current data - 1 dedicated corps station
232   127.53   10253.83   101.26
       -13.37   2007.92   44.81
       -41.18   22698.02   150.66   137.84

Current data - 1 dedicated corps station plus 1 more corps area station
180   119.48   8491.39   92.15
       -24.93   2060.80   45.40
       -43.63   18246.83   135.08   128.85

Current data - 1 dedicated corps station plus 1 more corps area station
            plus 1 station ahead of the FLOT
340   111.69   6489.34   80.56
       -31.49   1489.79   38.60
       -41.59   14781.59   121.58   118.32

TABLE-22

STATS.NOA

Current data - 1 dedicated corps station
232   127.53   10253.83   101.26
       -13.37   2007.90   44.81
       -41.18   22698.02   150.66   137.84

Current data - 1 dedicated corps station plus 1 more corps area station
180   119.79   8140.16   90.22
       -34.90   2055.32   45.34
       -39.58   17713.34   133.09   128.40

Current data - 1 dedicated corps station plus 1 more corps area station
            plus 1 station ahead of the FLOT
340   111.04   6285.69   79.28
       -38.83   1529.39   39.11
       -36.64   14264.13   119.43   117.46

TABLE-23

STATS.H-M

Current data - 1 dedicated corps station
```
   232    127.53  10253.83    101.26
          -13.37   2007.92     44.81
          -41.18  22698.02    150.66     137.84
```

Current data - 1 dedicated corps station plus 1 more corps area station
```
   180    126.23   6573.56     81.08
          -29.96   7576.74     87.04
          -23.07  13581.54    116.54     126.87
```

Current data - 1 dedicated corps station plus 1 more corps area station
            plus 1 station ahead of the FLOT
```
   340    122.35   5476.70     74.00
          -21.08   7453.93     86.34
          -25.80  11922.77    109.19     120.58
```

TABLE-24

STATS.T-A

Current data - 1 dedicated corps station
```
   232    127.53  10253.83    101.26
          -13.37   2007.92     44.81
          -41.18  22698.02    150.66     137.84
```

Current data - 1 dedicated corps station plus 1 more corps area station
```
   180    115.92   7943.47     89.13
           14.63   1017.02     31.89
          -46.10  18086.04    134.48     124.82
```

Current data - 1 dedicated corps station plus 1 more corps area station
            plus 1 station ahead of the FLOT
```
   340     99.34   6224.95     78.90
            9.61   1208.63     34.77
          -43.75  12901.62    113.59     108.57
```

TABLE-25

STATS.T-S

Current data - 1 dedicated corps station
```
   232    127.53  10253.83    101.26
          -13.37   2007.92     44.81
          -41.18  22698.02    150.66     137.84
```

Current data - 1 dedicated corps station plus 1 more corps area station
```
   180    119.30   8171.20     90.39
          -33.89   1997.77     44.70
          -40.48  17682.87    132.98     128.17
```

Current data - 1 dedicated corps station plus 1 more corps area station
            plus 1 station ahead of the FLOT
```
   340    111.39   6214.46     78.83
          -37.99   1626.52     40.33
          -36.18  14272.63    119.47     117.36
```

TAMDE - THE VARIABILITY OF WEATHER OVER AN ARMY DIVISION SIZE AREA

John T. Grace
U. S. Army Research Laboratory
Battlefield Environment Directorate
White Sands Missile Range, NM 88002-5501

ABSTRACT

The Target Area Meteorological Data Experiment (TAMDE) conducted by the Army Research Laboratory, Battlefield Environment Directorate (BED) in the desert and mountains of southern New Mexico during July - September 1992, was planned and accomplished in response to a U. S. Army Field Artillery School concept of a battle area expanded in size over previous concepts of the battlefield. In the smaller size battle area, an assumption of homogeneity of meteorological conditions was workable. This may not be so in a larger area. TAMDE focused on the variability of weather and weather effects (on weapons and fire control systems) over a 60km X 200km area including White Sands Missile Range (WSMR) and adjacent areas. Emphasis was placed on a 60km X 40km area corresponding to many present tube and rocket artillery systems. There were eight one day episodes of intensive data collection. The meteorological measurement network included eight upper air sites (five soundings a day), twenty-seven automated surface stations, eight meteorological (MET) observers, remote profilers, lightening detection and location system, satellite receiver, weather radar and seven present weather (visibility/forward scatter) systems. Synoptic surface and upper air charts were used to produce a narrative describing the weather conditions of each episode. This paper briefly describes the technical logistics, data and data quality produced by TAMDE and provides information on the availability of data. A few preliminary analyses of the data are also presented.

1. INTRODUCTION

Developments in weapons, communications, intelligence systems, and tactics have recently expanded the depth of the

battlefield for the Army, and in particular, the Field Artillery, Aviation, and Intelligence Branches (as evidenced by both the offensive and defensive operations during Desert Storm). It is widely recognized that to successfully operate and engage targets in this expanded battlefield requires real-time knowledge of the weather in this target area. This situation has led to BED initiatives in a number of programs which seek to provide the Army with Target Area Meteorology (TAM). This paper discusses a data collection exercise that was conducted to provide data for the analysis of target area weather and a means of evaluating potential solutions such as the Computer Assisted Artillery Meteorology (CAAM) System.

The Field Artillery has been taking precision high resolution (vertical) atmospheric measurements on the battlefield for their own use and for other purposes, such as, aviation, chemical and fallout prediction; and for the Air Weather Service (AWS). These atmospheric soundings by rawinsonde are performed from a location behind the guns by the Artillery Meteorology (MET) Section. Through the application to the entire trajectory of fire, there has been applied an assumption of homogeneity, that is, the atmosphere/weather here (behind the guns) is also the same there (out to the target). For a smaller battlefield, the assumption of a homogeneous atmosphere over space has proved workable, even highly successful. It has been demonstrated many times with live fire and measured impact that the MET spatial variability is not as significant as the temporal variability over 40km. The Field Artillery has addressed the time variability with doctrine which requires soundings every two hours. This assumption of a homogeneous atmosphere over space may or may not be valid over an extended target area.

Modern weapon systems in the field now and in various stages of development are proving to be more effected by weather than their predecessors. The very fact that they sense and seek and, in some cases, glide toward the target has made them more susceptible to clouds, precipitation, winds, atmospheric refraction, etc. This, along with the increased ranges of weapons systems means that in the targeting process, knowledge of the weather at the target could be used to advantage to select the attack weapons.

2. ADDRESSING THE TAM ISSUES

The MET Improvement Program in response to the Target Area Meteorological Sensors System Mission Need Statement will provide an enhanced target area meteorology capability with a suite of sensors and software providing weather information and atmospheric measurements in the target area. This area was defined by the U. S. Army Field Artillery School (USAFAS) as 200km forward of the Forward Line of Own Troops (FLOT) when TAMDE was being planned. Since that time the definition has changed to an increased depth out to 500km. This depth anticipates the

future range of systems such as Joint STARS, Apache, and ATACMS, as well as the ranges of some systems of potential adversaries. The TAMDE was planned and conducted to investigate the variability of weather and of specific atmospheric parameters over approximately 200 X 60 km (60km corresponds to a potential Division size front). TAMDE was also designed to provide a data base which could be used to test and validate the CAAM system, competing atmospheric models and potential sensors for the target area.

Recently the USAFAS has refined the Target Area Low Level Message (MET TALL) format for the Multiple Launch Rocket System (ref 4); however, considerations such as location and range of data points, accuracy, and resolution may need to be further defined. In light of the variety of weather/ atmospheric information required in the Target Area (TA) and the various ranges, locations, accuracies and critical thresholds required by different combat systems (refs 1, 2, and 3, see fig 1) (many of which are artillery assets) this further definition seems appropriate. It is expected that information on target area weather from an analysis of the TAMDE data will be useful to this purpose.

3. THE GEOGRAPHY AND CLIMATE OF THE AREA

The measurement network was located in south-central New Mexico extending from Las Cruces at the southwest corner to Orogrande Range Camp WSMR at the southeast corner then north to above Soccoro at the depth (see fig 2). This is desert and mountain country with a base elevation of 4,000 to 5,000 feet for the desert and rugged, rocky mountains with some scrub and little timber rising to 9,000 feet. The San Andreas, Organ, and Oscuro mountains form a range with few gaps north/south through much of the Experiment Area (EA) (NOTE: For the purposes of this study, the Experiment Area is a surrogate Target Area). Other significant features are the "White Sands", an extensive area of gypsum dunes and alkali flats near the center of the area and the volcanic lava flows such as the Malpi. A significant feature to the west of the EA and approaching closely at the northwest corner near Soccoro is the Rio Grande Valley. The soil is sandy over the greater part of the area and the vegetation is sparse with various grasses, creosote bush, cacti, and yucca plants. The climate is semi-arid with approximately eight inches of rain a year. TAMDE began at the end of the spring season which is characterized by warm, dry weather and strong westerly winds corresponding related to the proximity of the jet stream and the terrain. The first episode of TAMDE reflects these spring conditions. During early summer, the winds decrease and temperatures climb into the high 90's, the dry conditions are only occasionally interrupted by thunderstorms. Later in the summer, a monsoonal circulation brings moisture from the Gulf of Mexico and from the Pacific Ocean off of Mexico. Thunderstorms

METEOROLOGICAL DATA TARGET AREA FOR: "ARTILLERY"
(DELIVERY SYSTEMS/SMART AMMUNITIONS/DEEP FIRE)

PRIORITY	PARAMETER	RANGE (SURFACE) in km	HEIGHT (ABOVE GROUND LEVEL)	TIME INTERVALS in hours	ON DEMAND	USER'S MINIMUM ACCURACY REQUIREMENT	CRITICAL VALUES/ REMARKS
P.1	CLOUD BASE (HEIGHT)	5 x 5	2 km	2	YES	± 15 metres	Range to Target up to 200 km for Deep Fire
	VISIBILITY	5 x 5	2 km (and 5 km horizontally)	2	YES	10% of Range	Laser Designator need 4 km horizontally
	WIND SPEED	5 x 5	3 km	2	YES	1 m/sec	Extremely important for the first 300 metres.
	WIND DIRECTION	5 x 5	3 km	2	YES	5°	Gusts of wind above 40 Kts affect flight of RPV and drone.
P.2	CLOUD COVER	5 x 5	1 km	2	YES	1/8	
	HUMIDITY	5 x 5	1 km	2	YES	10%	
	PRECIPITATION/OBSTRUCTION to VISIBILITY	5 x 5	1 km	2	YES		Type/Rate of Precipitation
	STATE OF THE GROUND	5 x 5	surface	12	YES		Vegetation rocks snow frozen earth, moisture level (dry-mud-swamp)
	BACKGROUND IR	5 x 5	surface	2	YES		

P.1 = Priority 1 = REQUIRED (Mission Essential)

P.2 = Priority 2 = Desired (Highly Desirable)

METEOROLOGICAL DATA TARGET AREA FOR : "ELECTRO-OPTICAL"

PRIORITY	PARAMETER	RANGE (SURFACE) in km	HEIGHT (ABOVE GROUND LEVEL)	TIME INTERVALS in hours	ON DEMAND	USER'S MINIMUM ACCURACY REQUIREMENT	CRITICAL VALUES/ REMARKS
P.1	CLOUD COVER	5 x 5	2 km	3	YES	1/8	
	CLOUD HEIGHT (BASE)	•	•	3	YES	50 metres	
	ILLUMINATION	5 x 5 (100x100) (1)	surface	1	YES	Level defined by STANAG	Night level defined FINABEL 1-R-9(Annex 2) (GE Army Aviation requirement 0.1 millilux accuracy)
	PRECIPITATIONS/OBSTRUCTIONS to VISIBILITY	5 x 5 (100x100) (1)	2 km	6	YES		
	VISIBILITY	5 x 5	2 km	3	YES	10% of range	
	ATMOSPHERIC TRANSMISION FACTOR	5 x 5	2 km	3	YES		for Near/Medium/FAR-IR bands
P.2	SOLAR RADIATION	5 x 5	surface	1	YES		
	STATE OF THE GROUND	5 x 5	surface	12	YES		
	TEMPERATURE (GROUND)	5 x 5	surface	3	YES	1°C	
	TURBULENCE	5 x 5	surface to 20 metres	1	YES		20 metres for E/O on helicopters
	IR BACKGROUND	5 x 5	surface	2	YES		
	WIND - SPEED - DIRECTION	5 x 5 •	2 km •	3 •	YES •	2 m/sec 10°	

```
_____;P:__;SB:_/_/_/__/___;C:___;SG:__,__;DT:__,__/__/__/__;ID:_____;A:_;_
T;TALL;DATCDE:_____;ACTCDE:_____;DTI:__/__.__/__;HGT:___;ID:__;
___;POSI:_____;ATMS:___;CBMRI:___/___;PRCTYP:__;PRCRAT:___;
A:__/___/____/__;_,__/____/__;_,__/___/____/__;
B:__/___/____/__;_,__/____/__;_,__/___/____/__;
C:__/___/____/__;_,__/____/__;_,__/___/____/__?
LTTE:_;
```

MET;TALL; | DATCDE:_____;ACTCDE:_____;DTI:__/__.__/__;HGT: ;ID: ;

Figure 1. Top – Tables Excerpted from Basic Meteorological Parameters and Instrumentation on Target Area for all Army Combat and Combat Support Missions. Bottom – Example of MET TALL (Target Area Low Level Meteorological Data Message).

are more frequent and intense with localized heavy rain and strong winds. The majority of the measurement episodes were conducted during the summer. By September when the last episodes occurred, the heat has moderated, and convective activity decreases. During all of these seasons, frontal activity can occur, however it is seldom strong and in some cases may not include the entire TAMDE area. With frontal passage windy conditions usually occur, however the occurrence and intensity of precipitation is determined by the amount of moisture which has recently been advected into the area. This explains the peak in average rainfall during the July and August episodes of the monsoon season.

4. THE MEASUREMENT AND OBSERVATION NETWORK

The location of the experiment was chosen for many reasons chief of which are: 1) the presence of an already existing set of measurement systems belonging to the WSMR MET Team; and 2) The Profiler Test Facility located near a potential FLOT scenario. Additional measurement systems and locations were added to extend the area covered and to fill in gaps or to add new measurement/observation capability. The resultant network is shown in figure 1. The plan was to cover the 60 X 200 km area as densely and uniformly as possible. Factors such as system resources, available trained personnel, financial resources, and terrain limited the network, however, the area was covered well in most cases and better than required for some scenarios of Artillery MET coverage. The network consisted of eight Rawinsonde (RAWIN) systems, Surface Automated Measurement Systems (SAMS) (25 permanent and two portable), a lightening detection and location system, a doppler weather radar, Present Weather Systems (7). Remote radar profiler 924mhz and 404mhz with RASS radio acoustic sounding system, and C-Space satellite receiver for generating soundings using Tiros Operational Vertical Sounder (TOVS) and Defense Meteorological Satellite Program (DMSP). There were eight meteorological observer locations, seven at the RAWIN sites (except for Bldg 305, Meteorological Data System [MDS]) and one at C-Station, with measurements and observation in accordance with Federal Meteorological Handbook (FMH) 1 procedures. In addition, hourly and special observations were taken at C-Station with a laser ceilometer for measured cloud/ceiling height.

Attempts were made to measure temperature, pressure, humidity and wind from an aircraft to simulate the benefit of an Remotely Piloted Vehicle mounted MET sensor; however, due to assorted instrumentation problems, that data proved to be unusable.

5. OPERATIONS

The scope of this paper does not allow detail of operation

Measurement Sites

R - Rawinsonde
O - Observer
P - Radar Profiler
L - Lightning Detection & Location System
WR - Doppler Weather Radar
PS - Portable SAMS
PWS - Present Weather System
F - Forecast Office

SAMS Network

1. "C" Station (CST)
2. Apache (APA)
3. Post-ASD (POS)
4. Northrup Strip (NOR)
5. San Agustin Pass (PAS)
6. Mockingbird Gap (GAP)
7. Ninnerger (NIN)
8. School (SCH)
9. Salinas Peak (SAL)
10. North Oscura Peak (NOP)
11. Denver WIT (DEN)
12. Zurf (ZUR)
13. West C1 (WCI)
14. Oscura Range Camp (ORC)
15. Jallen (JAL)
16. RATSCAT (RAT)
17. Sacramento Peak (SAC)
18. Dirt Site (DRT)
19. Greg Site (GRG)
20. Wilde (WLD)
21. ABC-1 (ABC)
22. Jim (JIM)
23. Yaw Line (YAW)
24. Little Burro (BUR)
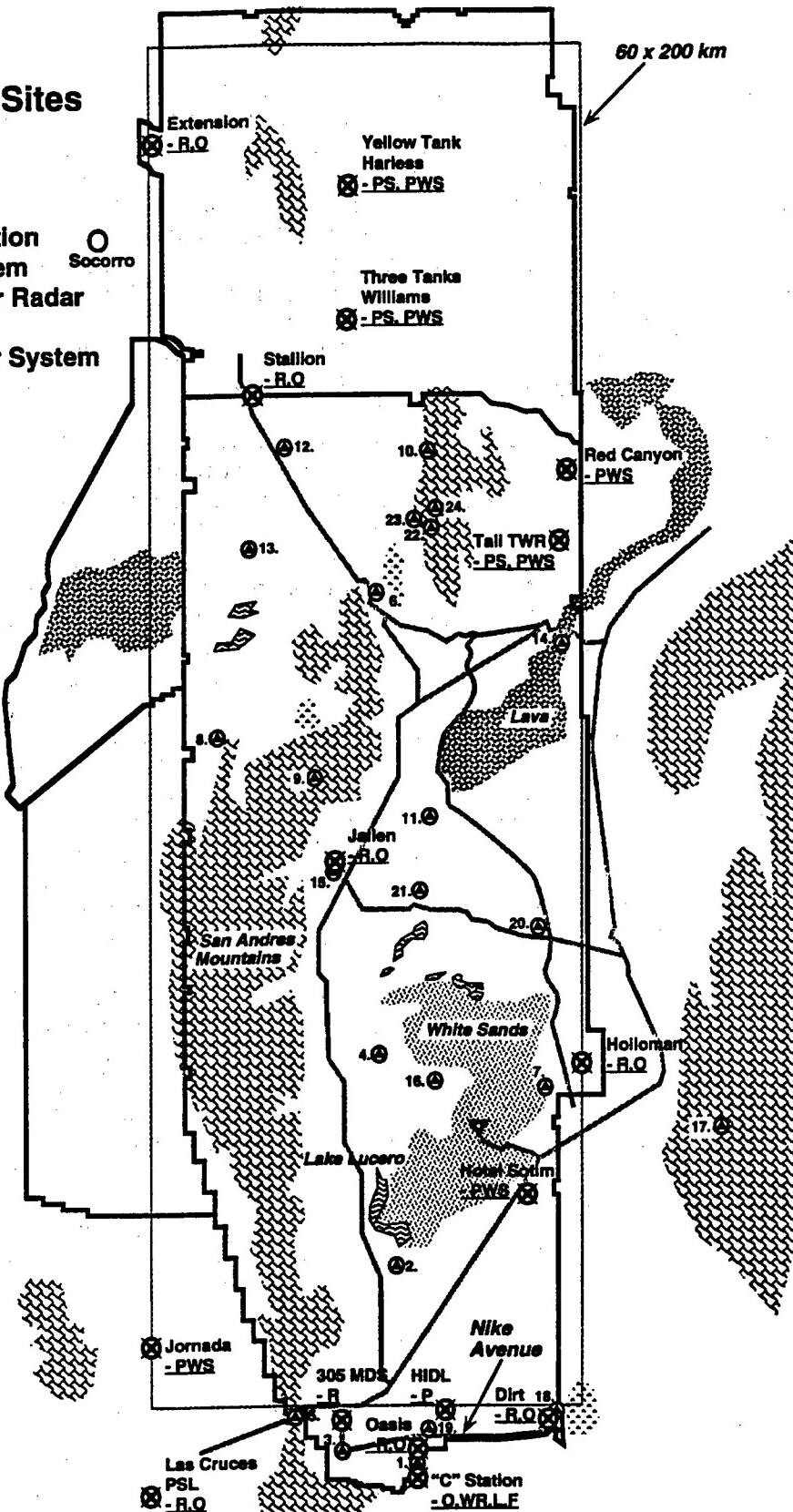
Figure 2. TAMDE Geographic Area and Measurement Network.

86

such as range scheduling, coordination with land owners, emplacement and maintenance of measurement sites and equipment, procedures for measurement and data handling or weather events, however the significant aspects of these will be addressed in general. The data episodes were scheduled to occur on selected Mondays starting on 15 June 1992 through September 1992. Measurement period was 24 hours with five sets of simultaneous RAWIN soundings from seven stations. The MDS RAWIN schedule was offset to provide information on two, four, and six hour time staleness of MET data. SAMS provided hourly data and 15 minute averages. Satellite soundings were dependent on the polar orbit (12 hours revisit to same area). Profiler data was available hourly and in some cases 15 minutes. Lightening detection and location at time of strike occurrence. The PWS data including temperature was recorded every 15 minutes, C-Station observed hourly and specials according to FMH-1.

The plan to react for data collection, to significant weather events determined from a Friday forecast was overcome by exigencies of Range and MET Team schedules, also by reaction time to setup equipment at remote locations. The occurrence of the eight episodes was finally determined by logistical and funding constraints.

The primary tactical scenario that we addressed was a TA extending 200km north from a FLOT running east west parallel to and approximately 5km north of Nike Avenue, WSMR. In this case the data sites south of the FLOT represent potential Artillery MET sites while those to the north are ground truth measurements or may represent possible data from the TA such as dropsonde or satellite data as appropriate. No observer data beyond the FLOT would likely represent a battlefield scenario.

A second scenario is addressed by a subset of the sites running east-west near Nike Avenue, WSMR. This "Lower Range" subset is used with a FLOT running approximately north-south. This scenario corresponds to an artillery rocket or tube trajectory of 50km or less east to west with one or two Artillery MET sites, and the others as ground truth midway through the ballistics trajectory (apogee) or at TA impact point. The lower range subset with the MDS near the FLOT also will address the time staleness of Artillery MET data.

The scenarios outlined above are now being developed in detail for input to the CAAM and the High Order Turbulence Model for Atmospheric Circulation (HOTMAC) model for test and verification of the CAAM Demo.

The juxtaposition of the Profilers at HIDL site to the RAWIN sites at Oasis, Dirt and Bldg 305 is quite opportune for verification of the developmental systems against the atmospheric sounding rawinsonde systems including the MDS. Also opportune is the variety of sensors and windfinding methods available for this verification, e.g., Navigational Aid (NAVAID) at Oasis and Dirt, Radio Direction Finding (RDF) at Bldg 305.

6. DATA HANDLING

A considerable quantity of data was collected. After each episode, the data arrived at the CAAM Team office via modem or hand carried hard drive, disk, and/or hardcopy. It was down loaded, sorted, labeled, and filed prior to quality control (QC) and editing procedures. In preparation of the experiment, samples of data for each system were requested and a directory of flat files had been prepared on the HP9000 computer for each episode and system.

The data from the rawinsonde systems was reviewed first since it was needed to support the evaluation of candidate models for the CAAM program. Over 300 soundings were examined for missing or inconsistent data. The operator's logs were read for any indication of problems that occurred during preflight or during the sounding. The soundings were compared to previous or later ones and to those from adjacent stations. If a problem was detected, the 10 second data points were examined. In cases where editing was required, this was done according to procedures adopted from FMH-3 and written specifically for this experiment using the Integrated Upper Air Systems (IUAS) editor. A Read Me note was added to the data files with information on the QC. In all cases the original data was preserved. This data was then entered into the HP9000 and was available for use in the models usually within three weeks of each episode.

The SAMS data (pressure, temperature, humidity, wind speed and direction, radiation, and ground temperature) was the next priority. It was QC'd, edited, and entered into the HP9000. Calibration information for the SAMS sensors was also entered. The data from other systems was then examined and entered into the directory. The developmental systems offered little, if any, opportunity for QC other than within the operation of the system. Access to the HP9000 TAMDE data, episodes one through eight and a pamphlet "How to Access the Data" is available through Mr. Robert Bonner, AMSRL-BE-W. The radiometer data is available through Dr. Edward Measure, AMSRL-BE-W. A database and a users guide are planned for TAMDE.

7. THE WEATHER

A synopsis of the weather conditions during each episode, produced in conjunction with the C-Station Forecast Office is available along with forecasts and synoptic charts. They are part of the record. As an example, TAMDE 7 (21 September 1992) was chosen for this paper to show the variation of weather across the EA and its effect on TA parameter. It should be noted that TAMDE 7 showed possibly the most variability of conditions during the day and across the EA, hence it will serve as an example by exception.

A low pressure system in south central Canada beyond the Polar Front Jet, coupled to a weak low in the southern United States by a deep trough and the movement of these systems was the primary driver for the weather in the EA on Monday, 21 September 1993. A ridge in southern California was pushing eastward in the direction of northern New Mexico (fig 3).

The movement of the Canadian low toward the east pulled the trough across New Mexico. A weak frontal passage was recorded at C-Station with a Special Observation at 2120MST (fig 4). This frontal passage was accompanied by rapidly rising pressure and a wind shift from West to North. This wind shift was significant at all levels, with speeds 20 - 30 knots at 700 mb and 20 - 35 knots at 500 mb. Clouds moved into the area with scattered clouds at 6,000 feet and a ceiling measured at 12,000 feet (fig 5 and 6). The airmass behind the front was dry and no precipitation was recorded at C-Station. It took approximately three hours for the front to cross the EA from northeast to southwest. After the passage of the front, winds became calm and the skies cleared.

Examination of the data and information of this event shows very specific effects on the TAM parameters defined in references 1, 2, 3, and 4; sequence figures 2a, 2b, and 2c. Wind speed and direction, cloud height and cover, index of refraction and visibility are the parameters chiefly effected in TAMDE 7. The cloud height just meets the criteria of concern for TAM. It is expected then that the effect on terminally guided weapons would not be of great significance, however, knowledge of this condition may be very significant in the targeting process. The strong and gusty winds, and the cloud cover do approach and exceed critical value thresholds for some systems. These transient conditions in the EA could not be detected solely with measurements behind the FLOT. The occurrence and timing of the front was predictable to the forecaster at C-Station, but the degree of effect on TAM critical parameters could only be discerned with the SKEWT analysis of the surrogate dropsonde data at Stallion and the extension site.

Figure 3.   Tuesday, 22 Sept 92
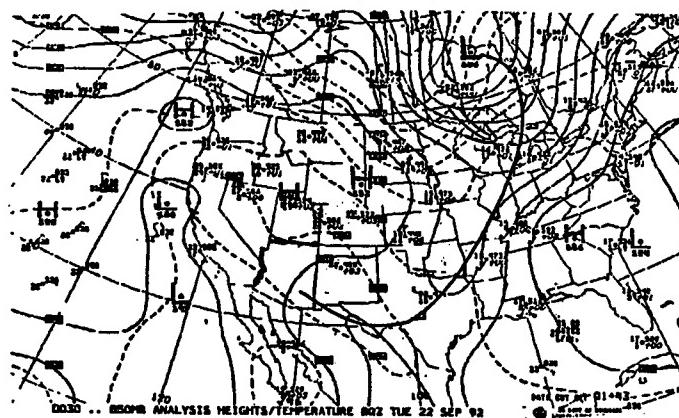
Station: C SITE WHITE SANDS MSR
Date: 09/21/92

```
SA 0050 CLR 20 059/70/51/2806/991 (JW)
SA 0155 CLR 20 062/68/52/E3502/992/ 302 (JW)
SA 0250 CLR 20 060/70/50/3404/993 (JW)
SA 0355 CLR 20 064/70/50/3005/994 (JW)
SA 0450 CLR 30 071/69/51/0000/995/ 210 66 20022 (JW)
SA 0550 CLR 60 084/67/50/2903/996 (JW)
SA 0651 CLR 50 091/63/54/E1201/998 (DN)
SA 0755 CLR 65 088/75/55/0000/999/ 110 (MR)
SA 0855 CLR 65 091/79/52/3306/000 (MR)
SA 0955 CLR 65 091/81/54/3405/001 (MR)
SA 1055 CLR 65 089/82/51/3304/000/CU NW/ 005 1100 58 (MR)
SA 1155 CLR 65 080/84/49/2505/998/CU ALQDS (MR)
SA 1255 CLR 60 077/85/48/3008/997/CU ALQDS (MR)
SA 1355 60 SCT 60 074/87/47/3407/996/ 712 1100 (MR)
SA 1454 60 SCT 60 070/86/46/3606/996 (AK)
SA 1558 60 SCT 60 071/86/49/0306/996 (AK)
SA 1650 60 SCT 60 076/85/45/0306/997/ 302 1100 88 (AK)
SA 1753 CLR 60 086/79/46/0303/998/MDT CU NNE-E FEW SC ALQDS (AK)
SA 1852 CLR 30 102/73/50/E2501/000/FEW SC NW-N-E (AK)
SA 1959 CLR 20 103/71/50/0000/003/SC NE-E AC S-SW/ 217 1470 (AK)
SA 2057 120 SCT 20 114/67/51/E0202/006/PRESRR (AK)
SP 2120 120 SCT 20 0607/009/WSHFT 16 FROPA PRESRR (AK)
SA 2150 M120 BKN 20 124/72/44/0209/010/WND 35V09 (AK)
SA 2254 120 SCT 20 139/65/48/2403/013/ 232 1070 88 (AK)
SA 2351 120 SCT 20 139/65/48/1903/014 (AK)
```


Figure 4. Above – Observation at C Station, LST time. Below – Observation at Stallion, LST time.

Figure 5. Top - SKEW T OASIS 2100 LDT. Bottom - SKEW T Stallion 2100 LDT.

```
IMMMMMMMMMMMMMMMMMMMMMMMMMMMMMMMMMMMMMMMMMMMMMMMMMMMMMMMMMMMMMMMMMMMMMMMMM:
:SKEWT ANALYSIS PROGRAM    STATION:              DATE: 09/22/92   TIME: 2 Z :
LMMMMMMMMMMMMMMMMMMMMMMMMMMMKMMMMMMMMMMMMMMMMMMMMMMMMMMKMMMMMMMMMMMMMMMMMMMMM9
:K INDEX       21.4 deg C :LCL          10296 ft agl:RH SFC-500    32.6 %    :
:V TOT INDEX   34.0 deg C :LFC          * MISSING * :RH 700-500    36.7 %    :
:C TOT INDEX    9.2 deg C :EL(LCL)      * MISSING * :PRECIP WATER  0.58 in   :
:T TOT INDEX   43.2 deg C :CCL          11524 ft agl:                        :
:KO INDEX    * MISSING *  :EL(CCL)      12906 ft agl:CONVECT TEMP  89.1 deg F :
:LIFTED INDEX   3.3 deg C :FREEZING LVL 10559 ft agl:DOWNRUSH TEMP 56.0 deg F :
:SFC LFTD I     0.4 deg C :WB ZERO HGT   8838 ft agl:700-500 LPS R  7.2 C/km :
:BEST LFTD I    0.4 deg C :TROP HEIGHT  53955 ft msl:                        :
:SHOWALTER I    3.4 deg C :                         :FOG STBLTY I  12.4      :
:THOMPSON I    18.1 deg C :1000-850 THK  1432 m     :FOG POINT      0.9 deg C :
:DYNAMIC I      1.3 deg C :1000-700 THK  3094 m     :FOG THREAT    17.3      :
:UPPER LFTD I  13.8 deg C :1000-500 THK  5793 m     :                        :
:MOD LFTD I   * MISSING * :1000-300 THK  9552 m     :HAIL SIZE      0.00 in  :
:SWEAT I       61.4       :850 -700 THK  1662 m     :TSTM GUST     58.2 kt   :
:CAPE        * MISSING *  :850 -500 THK  4361 m     :1000-500 SHR * MISSING * :
:CIN         * MISSING *  :850 -300 THK  8120 m     :850 -700 SHR  13.8 kt   :
:CAP STR I     11.2       :700 -500 THK  2699 m     :850 -500 SHR  26.6 kt   :
:BULK RICH NO * MISSING * :700 -300 THK  6458 m     :850 -300 SHR  26.9 kt   :
:                         :500 -300 THK  3759 m     :700 -400 SHR  39.2 kt   :
LMMMMMMMMMMMMMMMMMMMMMMMMMJMMMMMMMMMMMMMMMMMMMMMMMMMJHMMMMMMMMMMMMMMMMMMMMMMM9
:                                                                            :
HMMMMMMMMMMMMMMMMMMMMMMMMMMMMMMMMMMMMMMMMMMMMMMMMMMMMMMMMMMMMMMMMMMMMMMMMMMM<
```

```
IMMMMMMMMMMMMMMMMMMMMMMMMMMMMMMMMMMMMMMMMMMMMMMMMMMMMMMMMMMMMMMMMMMMMMMMMMMM:
:SKEWT ANALYSIS PROGRAM    STATION:              DATE: 09/22/92   TIME:02 Z :
LMMMMMMMMMMMMMMMMMMMMMMMMMMMKMMMMMMMMMMMMMMMMMMMMMMMMKMMMMMMMMMMMMMMMMMMMMMMM9
:K INDEX       23.3 deg C :LCL           6574 ft agl:RH SFC-500    35.9 %    :
:V TOT INDEX   28.8 deg C :LFC          19590 ft agl:RH 700-500    34.7 %    :
:C TOT INDEX   16.8 deg C :EL(LCL)      19977 ft agl:PRECIP WATER  0.56 in   :
:T TOT INDEX   45.6 deg C :CCL           8888 ft agl:                        :
:KO INDEX    * MISSING *  :EL(CCL)      23364 ft agl:CONVECT TEMP  82.6 deg F :
:LIFTED INDEX   1.4 deg C :FREEZING LVL  9356 ft agl:DOWNRUSH TEMP 52.7 deg F :
:SFC LFTD I     1.3 deg C :WB ZERO HGT   7455 ft agl:700-500 LPS R  7.4 C/km :
:BEST LFTD I    1.3 deg C :TROP HEIGHT  53866 ft msl:                        :
:SHOWALTER I    1.3 deg C :                         :FOG STBLTY I  36.8      :
:THOMPSON I    21.9 deg C :1000-850 THK  1404 m     :FOG POINT      0.7 deg C :
:DYNAMIC I     -1.5 deg C :1000-700 THK  3056 m     :FOG THREAT    18.1      :
:UPPER LFTD I  16.1 deg C :1000-500 THK  5749 m     :                        :
:MOD LFTD I   * MISSING * :1000-300 THK  9507 m     :HAIL SIZE      0.00 in  :
:SWEAT I      154.6       :850 -700 THK  1652 m     :TSTM GUST     54.5 kt   :
:CAPE         -28.7 m2s-2 :850 -500 THK  4345 m     :1000-500 SHR * MISSING * :
:CIN          432.3 m2s-2 :850 -300 THK  8103 m     :850 -700 SHR   6.9 kt   :
:CAP STR I      8.8       :700 -500 THK  2693 m     :850 -500 SHR  27.8 kt   :
:BULK RICH NO  -0.0       :700 -300 THK  6451 m     :850 -300 SHR  12.4 kt   :
:                         :500 -300 THK  3758 m     :700 -400 SHR  43.1 kt   :
LMMMMMMMMMMMMMMMMMMMMMMMMMJMMMMMMMMMMMMMMMMMMMMMMMMMJHMMMMMMMMMMMMMMMMMMMMMMM9
:                                                                            :
HMMMMMMMMMMMMMMMMMMMMMMMMMMMMMMMMMMMMMMMMMMMMMMMMMMMMMMMMMMMMMMMMMMMMMMMMMMM<
```

Figure 6. Top - Analysis OASIS 2100 LDT. Bottom - Analysis
Stallion 2100 LDT.

SUMMARY

The Target Area Meteorological Data Experiment was conducted
to help define meteorological effects in an extended Army
battlefield size area and to provide a reference data base useful
to evaluate competing methodologies for providing weather
information in this area. Temporal and spatial variability of
atmospheric conditions were a focus of this program. This data
set may not be representative of other climates and regions,
however, for the TAMDE in general, the data did not reveal
variability over distance as expected when comparing the 200km
depth to the assumption of homogeneity over a 40km artillery

trajectory. For most episodes, an assumption of homogeneity over distance could to a large degree prove workable.

In conditions of greater weather variability, the driver was synoptic scale weather events which could be discerned by a forecaster such as the Staff Weather Officer (SWO) with the proper guidance and tools. Many of the tools needed for this task are available to the SWO now, such as satellite imagery, synoptic charts, atmospheric sounding, etc. Information not now available on the battlefield, but which showed a correlation to these conditions of greater weather variability were weather radar, atmospheric profiles (deep in TA), and lightening detection and location. An extensive subset of data for intercomparision of various remote profilers, in situ measurements, and satellite soundings is available.

Of the eight episodes conducted, there are four which show some promise of demonstrating (with an in-depth analysis) a variability of weather effects on TAM over a 200km deep TA. Some knowledge to be gained from TAMDE may be applied to a 500km TA, however, specific conclusions can not be extrapolated to a much larger area.

ACKNOWLEDGEMENTS

The CAAM team's key participants in the planning and operation of this experiment were the author, Mr. Robert Bonner and MAJ Arthur Grunwald. Significant participation in the operation by WSMR Met Team, AMSRL-BE-A (Field Support), the Physical Sciences Laboratory (PSL) New Mexico State University, and Naval Oceanographic Laboratory, Pt Mago, California.

The author wishes to thank the following groups for permission to site measurement systems on their land: Department of Agriculture - Jornada Station; National Park Service - White Sands Monument; Williams Ranch - North of Stallion; Harless Ranch - East of Soccoro.

REFERENCES

The framework for this investigation was derived from information on TAM found in the following sources:

Basic Meteorological Parameters and Instrumentation on Target Area for all Army Combat and Combat Support Missions, Meteorology Panel NATO Army Armaments Group, 15 Feb 89, Document AC/225 (page 27).

Field Artillery Weather Data Requirements, Personal Correspondence, 15 Sep 92, CPT Larry L. Letner, U. S. Army Field Artillery School.

MET TALL (Target Area Low Level Meteorological Data Message) extracted from TM 11-7025-289-10-2, TACFIRE Manual (Draft).

Multiple Launch Rocket System (MLRS), Meteorological Target Area Low Level (MET;TALL) message, Memorandum dtd 22 October 1993, Douglas B. Brown, USAFAS.

TECHNIQUES FOR MEASURING TURBULENCE PARAMETERS
FOR ATMOSPHERIC ACOUSTICS

by

John M. Noble
Battlefield Environment Directorate
U.S. Army Research Laboratory
White Sands Missile Range, New Mexico 88002-5501

ABSTRACT

In order to determine the effect of atmospheric turbulence on acoustic propagation, techniques must be devised to measure the turbulence parameters important for atmospheric acoustics. The two important turbulence parameters to be measured are the temperature and wind structure parameters. There are several direct measurement techniques for the measurement of these turbulence parameters including: Sonic Anemometer, Hot-Wire and Hot-Film Anemometer, and temperature structure parameter sensor. These instruments allow for turbulence measurements at high data collection rate (up to 1 kHz). However, these instruments must be mounted on a tower of tethered balloon and provide only point measurements. For measurements above the height of a tower, techniques are being devised to perform remote measurements of the turbulence parameters. Currently, the monostatic SODARs can be used to measure temperature structure parameters. The SODAR provides an integrated and averaged value over the backscattering volume in the atmosphere. Using the direct measurement techniques and the remote sensors, a profile of the turbulence parameters from the surface to several hundred meters can be obtained.

1. INTRODUCTION

As sound propagates through the atmosphere, it is affected by geometrical spreading, temperature gradients, vector wind gradients, molecular absorption, and turbulence. Geometrical spreading is a well understood effect dependent on the geometry of the scenario. The gradients can be measured with tower-based sensors, balloon-based sensors, and remote profilers. The molecular absorption can be calculated from the meteorological measurements. Atmospheric turbulence can dramatically affect an acoustic signal propagating from the source to the receiver.[1] Measurement of

the strength of the turbulence affecting the acoustic propagation can be quite difficult since the sound can travel from 250 m - 2 km above ground level between the source and receiver. To study the effect of atmospheric turbulence on sound, techniques must be developed to measure the strength of the turbulence near the ground surface and higher.

2. SONIC AND HOT-WIRE ANEMOMETERS

A sonic anemometer is used to measure the u, v, and w components of the wind field and temperature with time. A sonic anemometer (fig. 1) consists of a pair of acoustic transceivers spaced from 10 cm to 25 cm apart, that send and receive acoustic pulses at the rate of several hundred times per second. The pulses are averaged to give a data rate of 10 Hz. Sonics provide the wind component and temperature data required for computing fluxes of heat, momentum, and moisture which define the state of the surface layer by the eddy correlation method.
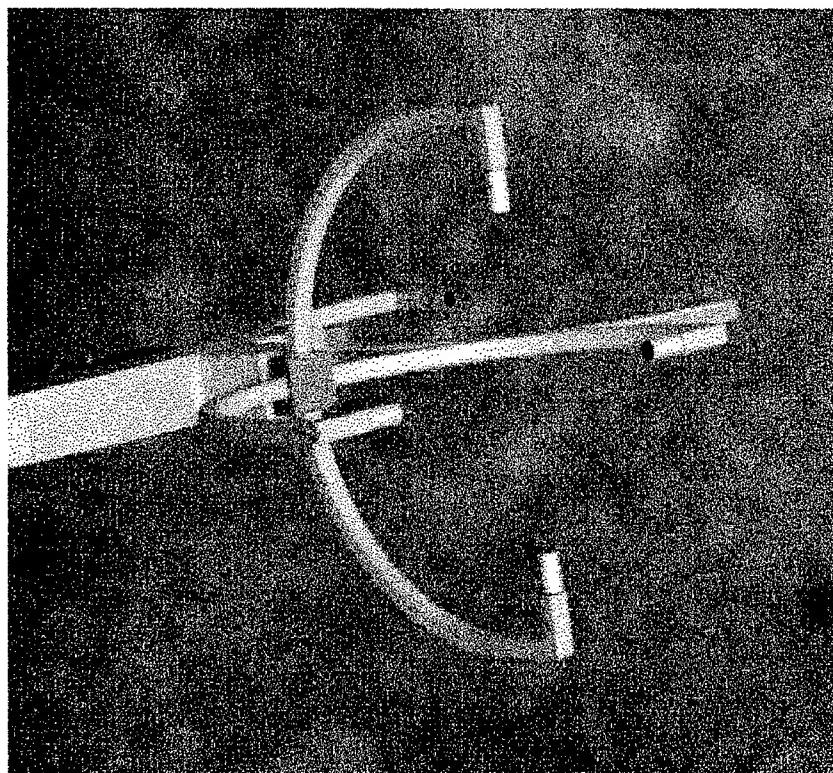
Figure 1. Picture of a three-axis sonic anemometer.

Sonics operate on the principle that the travel time between transmitter and receiver is a function of the speed of sound plus the component of the wind speed in the direction of propagation[2]

$$c(T, \vec{u}) = \sqrt{\frac{\gamma R T}{M}} + \vec{u} \cdot \hat{r}, \qquad (1)$$

where the second term is the projection of the wind vector in the direction of propagation. A sample of data is composed of two pulses: one pulse traveling in one direction and another pulse traveling in the opposite direction. If the two measured speed of sound samples are subtracted, the difference will be twice the component of the wind speed along the axis of the transmitter-receiver since the temperature is independent of the direction of propagation. Two pairs of transceivers will provide the horizontal wind field and three pairs will provide the three-dimensional wind field. The sum of the two measurements will be proportional to the temperature since the wind speed component will be subtracted out due to the vector nature of the wind component in Eq. (1). Figures 2 and 3 shows an example of the output from a sonic anemometer.
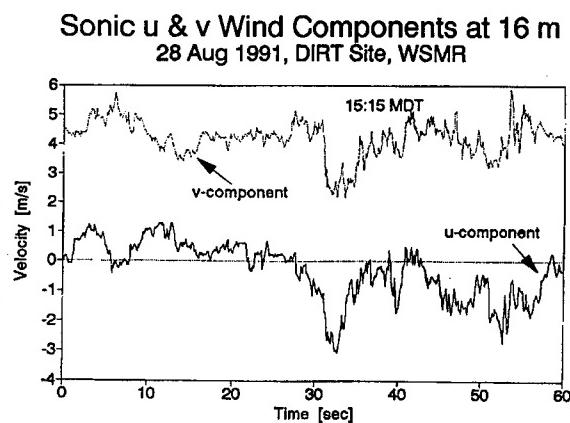
Figure 2. Sonic u and v wind components at 16 m from August 28, 1991 at DIRT Site located at White Sands Missile Range, NM.
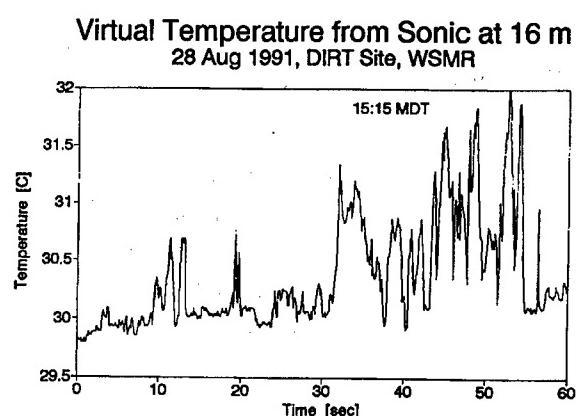
Figure 3. Sonic temperature data at 16 m from August 28, 1991 at DIRT Site located at White Sands Missile Range, NM.

The hot-wire anemometer for years have been used as a device for measuring atmospheric turbulence. There are two types of design: single and dual wire configurations, see fig. 4. The X probe design allows for measurements along two axis while the U probe only allows measurements along one axis. The major advantage of a hot-wire anemometer is the data rate. Depending on the type of wire and the dimensions of the wire[3], data collection rates can range for 1 kHz up to 20 kHz. Commonly available hot-wire anemometers have data collection rates of 1 kHz - 5 kHz. This make them very good for measuring the turbulence characteristics at the lower end of the inertial subrange. The major problems with hot-wire anemometers are the ease of breakage of the wire, the tremendous quantities of data generated, and calibration drift. With the improvements in electronics and new types of compounds for wires, hot-wire anemometers are becoming more reliable.
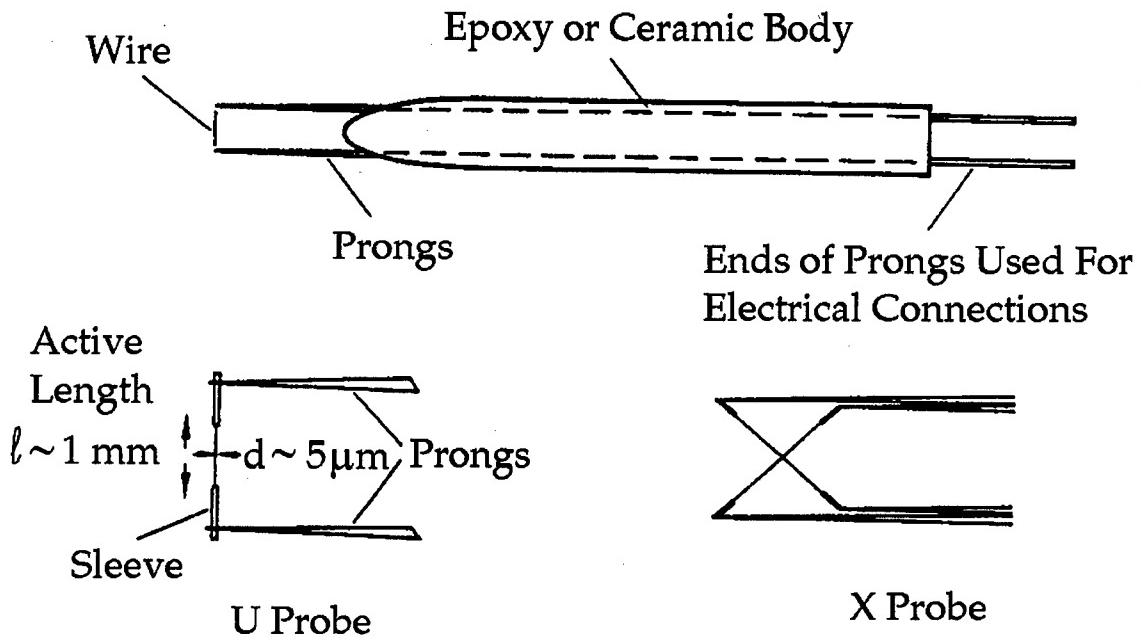
Figure 4. Hot-wire anemometer designs.

From turbulence theory, the structure parameter C_χ^2 in a locally isotropic field is defined by[4,5]

$$C_\chi^2 = \frac{\left\langle [\chi(\vec{r}_1) - \chi(\vec{r}_2)]^2 \right\rangle}{|\vec{r}|^{2/3}} \qquad (2)$$

where $|\vec{r}|$ is the spatial separation distance, $\chi(\vec{r})$ is the measured quantity at each point, and the angle brackets indicate performing an ensemble average. A sonic anemometer makes a measurement at a single point instead of two points separated by a distance r. Typically, two hot-wire anemometers are used separated by a distance r, however, a single probe can be used if the hot-wire anemometer is calibrated to measure the true wind speed. The above equation can be rewritten into a form usable for a single point sensor using Taylor's frozen turbulence hypothesis. Taylor's frozen turbulence hypothesis[6] states that the spatial separation of the turbulence can be calculated from the temporal separation (Δt) times the mean wind speed (u). This allows Eq. (2) to be written as

$$C_\chi^2 = \frac{\overline{[\chi(t_1) - \chi(t_2)]^2}}{(u \, \Delta t)^{2/3}} \qquad (3)$$

where $\chi(t)$ is the fluctuating quantity sampled at two instances with a temporal separation Δt, the overbar indicates a time average, and u is the mean wind speed. This equation allows for the

temperature and wind structure parameters to be calculated from the sonic or hot-wire anemometer data. Figure 5 shows a comparison between 1-minute and 15-minute averages of the wind structure parameters with time derived from sonic anemometer data.

July 25, 1991 20:04 Sonic 1
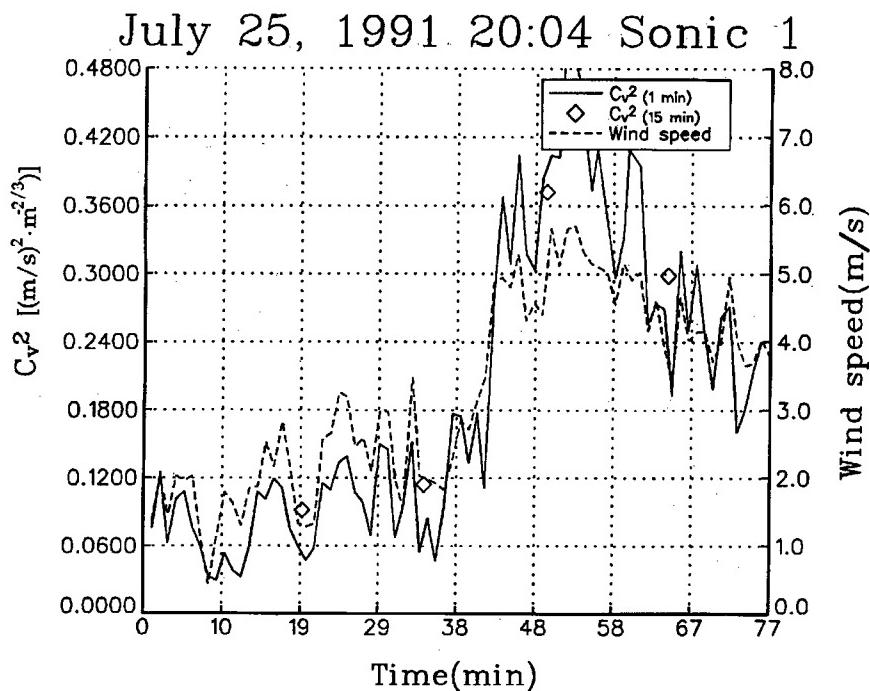
Figure 5. Plot of the 1-minute and 15-minute wind structure parameter along with 1-minute averaged wind speed at a height of 2 m with time.

3. SODAR

Point sensors only allow for measurement of turbulence parameters from a tower or balloon. To measure the turbulence parameters over a larger vertical distance, a remote profiling technique must be used. One technique which have been demonstrated for measuring the temperature structure parameter remotely uses a SODAR. A SODAR is a measurement device used to remotely measure three-dimensional wind speeds. There are several different designs for SODARs, however, they all operate basically the same way. Figure 6 shows a picture of one of the SODARs being used for the C_T^2 measurements. This type of SODAR is a phased array. The multiple acoustic transceivers allow the acoustic beams to be electronically steered along desired directions. The operation of a SODAR is analogous to the wind-profiling radar. The SODAR sends an acoustic pulse into the atmosphere where it is scattered by inhomogeneities in the atmosphere. The movement of the inhomogeneities result in the scattered signal being doppler shifted.
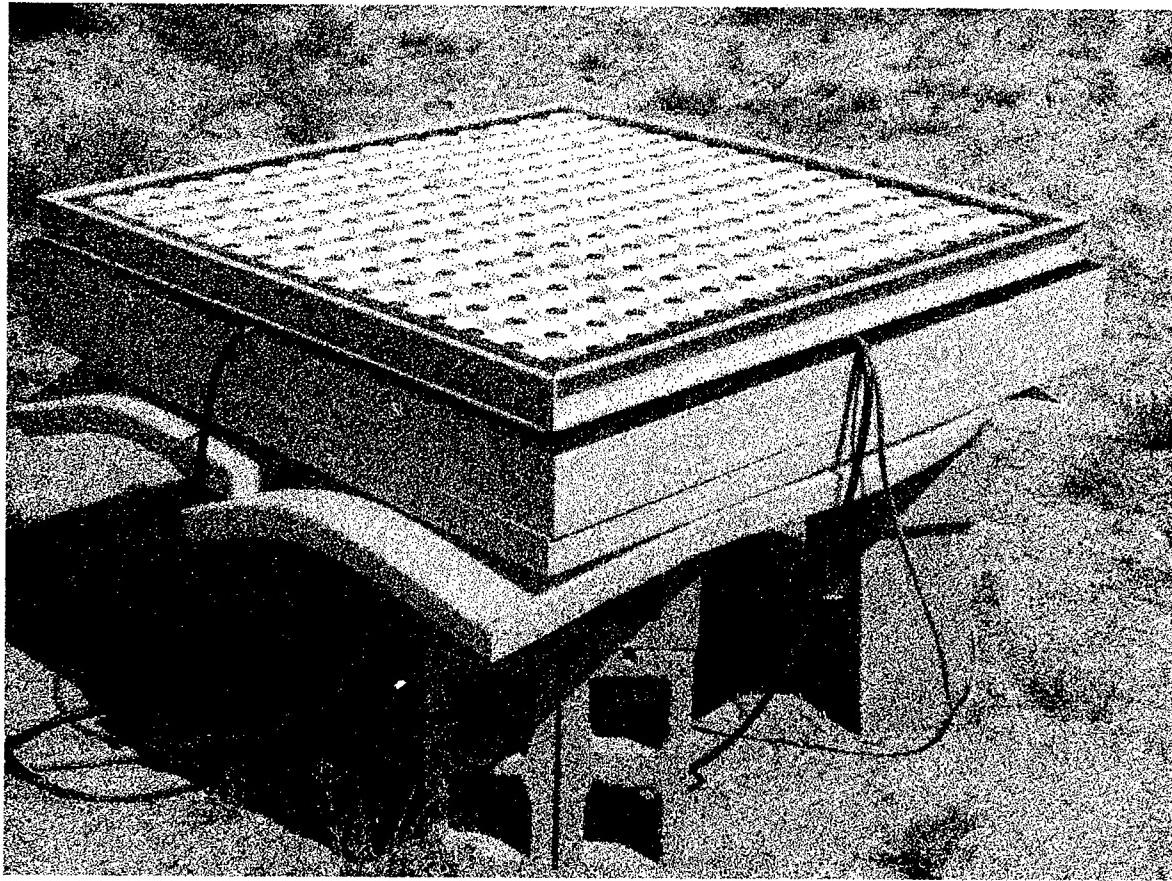
Figure 6. Picture of a phased-array SODAR.

The scattering cross section of an acoustic beam in the atmosphere is given by[7,8]

$$\sigma(\theta) = 0.03\,\kappa^{1/3}\cos^2\theta\left[\frac{C_v^2}{c^2}\cos^2\frac{\theta}{2} + 0.13\,\frac{C_T^2}{T^2}\right]\left(\sin\frac{\theta}{2}\right)^{-11/3}, \tag{4}$$

where κ is the acoustic wave number, θ is the scattering angle, T is the temperature, c is the speed of sound, C_T^2 is the temperature structure parameter, and C_v^2 is the velocity structure parameter. For a mono-static SODAR, the scattering angle is equal to 180°. Substituting this value into Eq. (4) results in

$$\sigma(180°) = 0.0039\,\kappa^{1/3}\,\frac{C_T^2}{T^2}. \tag{5}$$

This provides one with a relationship between the backscattered energy of the acoustic signal and the temperature structure parameter. Unfortunately, a factor is required to calibrate the measurements. The problem can be partially solved by the use of similarity theory. Using similarity theory, the relationship with height of C_T^2 can be obtained for various atmospheric conditions:

100

$$C_T^2 \propto z^{-4/3}, \; Unstable \tag{6}$$

$$C_T^2 \propto z^{-2/3}, \; Stable/Neutral. \tag{7}$$

If a value is known for C_T^2 at one height, then a value for C_T^2 at another height can be estimated by taking the ratio of either Eq. (6) or Eq. (7) depending on the stability class. For the remaining of this paper, the stable/neutral stability class will be used. The ratio of Eq. (7) yields

$$C_T^2(z_2) = C_T^2(z_1) \cdot \left(\frac{z_2}{z_1}\right)^{-2/3}, \tag{8}$$

where z_1 is the height of a known value for C_T^2 and z_2 is the height of the first range gate of the SODAR. This gives the first point needed to calibrate the value of C_T^2 for the first range gate of the SODAR. Using this value of C_T^2 for the first range gate of the SODAR the remaining values of C_T^2 can be calculated by taking a height ratio of Eq. (5):

$$\frac{\sigma_1(z_1)}{\sigma_2(z_2)} = \frac{C_T^2(z_1)}{C_T^2(z_2)} \cdot \frac{T_2^2}{T_1^2} \tag{9}$$

or

$$C_T^2(z_2) = C_T^2(z_1) \cdot \frac{\sigma_2}{\sigma_1} \cdot \frac{T_2^2}{T_1^2}. \tag{10}$$

The unit for temperature in Eq. (10) is kelvin. Since the height difference between range gates for the SODAR is relatively small (25 - 50 m), the difference in temperature between T_1 and T_2 will be very small. This fact allows for the assumption that T_1 is approximately equal to T_2 or the ratio of the temperatures square is one. This allows for Eq. (10) to be reduced to

$$C_T^2(z_2) = C_T^2(z_1) \cdot \frac{\sigma_2}{\sigma_1}. \tag{11}$$

Using Eqs. (8) and (11), a height profile of C_T^2 can be measured from the SODAR and one additional measurement. Usually the additional measurement is from a sonic anemometer mounted on a tower. Figure 7 shows a time-series plot of C_T^2 measured with the SODAR.
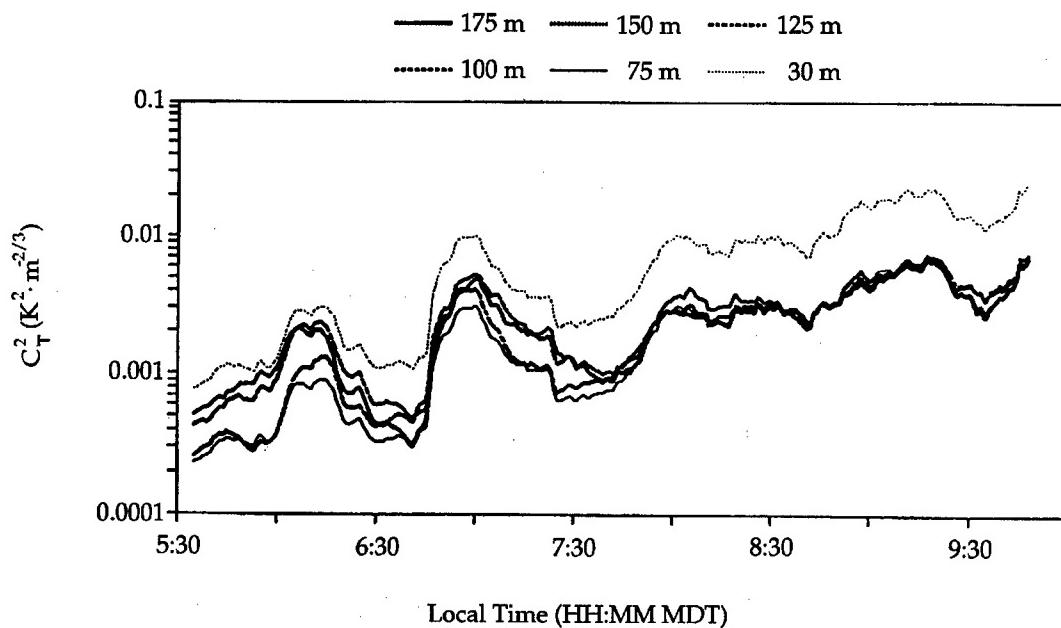
Figure 7. A time-series plot of C_T^2 measured with the SODAR.

4. CONCLUSIONS AND FUTURE DIRECTIONS

The techniques described in this paper provide values of the temperature structure parameter C_T^2 from near the surface of the ground to 30 m using sonic anemometers and from 50 m to a maximum of 700 m using the SODAR. The sonic anemometers provide values of the wind structure parameter C_v^2 from near the surface of the ground to 30 m. These two techniques allow for an improvement in the ability to measure the turbulence parameters over time and height. New techniques are being develop which will extend these capabilities over much larger heights. A new balloon system is available which will hold four sonic anemometers. The balloon can be placed at any height up to about 2 km allowing for extended height measurements using the sonic anemometers. Work is also being conducted which will allow for the SODAR and a 924 MHz Wind Profiling Radar to measure C_v^2. The SODAR will provide C_v^2 from 50 m to a maximum of 700 m. The 924 MHz Wind Profiling Radar will provide C_v^2 for 100 m to a maximum of 2 km. This is very important since the dominate type of turbulence at heights above a couple of hundred meters is the wind structure parameter C_v^2. These future techniques will provide turbulence measurements for near the surface to the top of the Planetary Boundary Layer.

REFERENCES

1. Kenneth E. Gilbert, Richard Raspet, and Xiao Di, "Calculation of Turbulence Effects In An Upward-Refracting Atmosphere," J. Acoust. Soc. Am. **87**, 2428-2437 (1990).

2. Allen D. Pierce, 1981: <u>Acoustics: An Introduction to Its Physical Principles and Applications</u>, McGraw-Hill Book Company, New York, 679 pp.

3. P. Bradshaw, 1971: An Introduction to Turbulence And Its Measurement, Pergamon Press, New York, 215 pp.

4. G.A. Daigle, J.E. Piercy, and T.F.W. Embleton, "Effects of Atmospheric Turbulence on the Interface of Sound Waves Near a Hard Boundary," J. Acoust. Soc. Am. **64**, pp. 622-630 (1978).

5. P. Chintawongvanich and R. Olsen, "Measurements of Temperature and Velocity Structure Parameters From Sonic Anemometers," SPIE Proc., Vol. 1968, Atmospheric Propagation and Remote Sensing II (1993).

6. V.I. Tatarski, 1971: <u>The Effects of Turbulent Atmosphere on Wave Propagation</u>, translated and published by Israel Programs for Scientific Translations Ltd., Jerusalem.

7. C.G. Little, "Acoustic Methods For the Remote Probing of the Lower Atmosphere," Proc. IEEE, Vol. 57, pp. 571-578 (1969).

8. P. Chintawongvanich and R. Olsen, "Experimental Study of Temperature Structure Parameter in the Surface Layer," preprint volume of the 7th Symposium on Meteorological Observations & Instrumentation, pp. 413-418 (1991).

FLUCTUATIONS OF ACOUSTIC SIGNALS SCATTERED BY AN ENSEMBLE OF TURBULES

Harry J. Auvermann
Army Research Laboratory, Battlefield Environment Directorate
White Sands Missile Range, New Mexico

and

George H. Goedecke and Michael D. DeAntonio
Dept. of Physics, New Mexico State University
Las Cruces, New Mexico

Acoustic signals in shadow zones, presumably caused by scattering from turbulence, exhibit great fluctuations. This paper shows that scattering from a structurally described turbulence volume is a possible mechanism for these fluctuations even though the number of scatterers is relatively large. Expressions in terms of the presumed known scattering cross-section of individual objects are derived for the ensemble average single scattering differential cross section and its rms deviation due to a homogeneous collection of N identical objects randomly positioned with no correlations in an observed volume V. For wavelength λ, it is well-known that, if $N\lambda^3/V \leq 1$, there is considerable diffuse scattering, while, if $N\lambda^3/V >>> 1$, the scattering is essentially forward and coherent. Apparently not so well-known is the result that the ratio of rms deviation of the cross section to the cross section itself depends on another parameter $a \equiv C(\theta)N(\lambda^3/V)^{4/3}$, when $C(\theta)$ is a numeric of order unity and depends on scattering angle θ. It is shown that, if $a >> 1$, the ratio goes as $N^{-\frac{1}{2}}$ and is very small, while if $a \leq 1$, then the ratio can approach unity. Results involving numerical simulation of scattering from randomly positioned turbules are presented. A simple simulation of an experimental scenario is shown to recover the essential features of the measured data.

I. INTRODUCTION

Acoustics has become prominent in recent years as a means for Army units to detect and locate enemy assets on the battlefield. Increased understanding of atmospheric effects on acoustic propagation has fostered development of propagation models of increasing sophistication as more and more atmospheric

effects are included. Among those effects that can be included in propagation models are temperature gradients, wind speed gradients, molecular absorption, ground reflections, and certain diffraction effects. Some models are capable of accounting for certain influences of turbulence. Although the inhomogeneities in atmospheric propagation characteristics are relatively small, acoustic signals scattered from turbulent regions can be detected and used for tactical purposes. While the variation of atmospheric parameters with altitude is accounted for in propagation models by approximating this variation with a number of strata within each of which parameters are uniform. Non-uniformity extends to turbulence properties as well. Since temperature turbulence is generated by uneven heating of the ground, intuition says turbulence intensity at altitude is different than at ground level. Since wind speed is zero at the ground, velocity turbulence at altitude is different than at ground level. Experimental evidence supports these intuitive conclusions. For example, it has been shown[1] that temperature and velocity turbulence intensities vary differently with height. Again, spectra change with altitude of the three components of velocity turbulence has been reported[2]. It is then a problem of considerable magnitude to determine the acoustic scattering properties of an atmosphere afflicted by anisotropic inhomogeneous turbulence. This is especially true since present theory[3], referred to here as the statistical model of turbulence, assumes isotropy and homogeneity. Taylor's "Frozen Turbulence Hypothesis" demonstrated by, if nothing else, the fact that instruments employ the phenomenon, indicates that a structural approach to turbulence could be illuminating. To answer the question of what structure to consider, the very success of the statistical approach for isotropic homogeneous turbulence suggests that an eddy could be a first approximation to building a structural model of turbulence. Hence, denominating an isolated eddy as a turbule, the consequences of treating a turbulent region as a collection of turbules of different sizes have been investigated.

The concern of this paper is the fluctuations of the acoustical signal scattered into a detector. In the next section, a "rule-of-thumb" criterion for determining the magnitude of scattered signal fluctuations is developed. In section III, numerical results are presented showing the fluctuations caused by small variations of the positions of a number of isotropic scatterers nominally positioned at three-dimensional grid points. Section IV carries the simulation of acoustical scattering from a moderate number of turbules a step further by including scattering patterns based upon turbule size and motion with the average wind as envisioned by Taylor's hypothesis. Conclusions are presented in section V.

II. DIFFUSE SCATTERING FLUCTUATION CRITERION THEORY

For certain choices of wavelength and scattering volume, it is possible to have wide deviations of the scattered signal for unexpectedly large numbers of scatterers. Derivation of a "rule-of-thumb" criterion for when this occurs is presented in this section. Given N identical scatterers positioned randomly, it is well known that considerable diffuse scattering results when the scattering volume contains more than N volume elements of linear dimension equal to the wavelength.

When the N scatterers are packed into a considerably smaller scattering volume, the scattering is largely coherent and forward. The criterion developed here is different than the above mentioned criterion differentiating diffuse scattering from coherent forward scattering. The derivation is begun by assuming the scatterers are identical and scatter isotropically. The derivation is summarized in the following equations.

$$
\begin{aligned}
&\textit{Number of identical scatterers} \qquad N \\
&\textit{Each scattering amplitude} \qquad f_1(\hat{r}) \\
&\textit{Each localized around} \qquad \vec{r} = \vec{b}_\alpha \\
&\textit{Wavelength } \lambda \qquad \textit{Wavevector} \quad k = 2\pi/\lambda \\
&\textit{Total scattering amplitude}
\end{aligned}
$$

$$
f_N(\hat{r}) = f_1(\hat{r}) \, S_N(\vec{K})
$$

$$
S_N(\vec{K}) = \sum_{\alpha=1}^{N} \exp(-i\vec{K}\cdot\vec{b}_\alpha)
$$

$$
\vec{K} = k(\hat{r} - \hat{k}) \qquad\qquad K = 2k\sin(\theta/2)
$$

The expression S_N is termed the geometric structure factor. The scatterer locations are assumed to have a probability distribution function with the following properties.

$$
\begin{aligned}
&\textit{Stochastic distribution of } \vec{b}_\alpha \qquad p(\vec{b}_\alpha) \\
&\textit{Joint probability distribution is} \quad \Pi_\alpha \, p(\vec{b}_\alpha) \\
&\textit{Fourier transform of} \quad p(\vec{b}_\alpha)
\end{aligned}
$$

$$
P(\vec{K}) = \int d^3 b \; p(\vec{b}) \, \exp(-i\vec{K}\cdot\vec{b})
$$

When the joint probability distribution is a product of the individual distributions as specified above, the distributions of each scatterer location are uncorrelated. The Fourier transform of the distribution will be used in the following. The next step is to restrict all scatterers to be within a spherical volume of radius R. Then an example uniform distribution function can be defined as follows.

$$
p(\vec{b}) = (3/4\pi R^3)\, U(R - b) \qquad U(t) = \begin{cases} 1 & t > 0 \\ 0 & t < 0 \end{cases}
$$

$$
P(\vec{K}) = [3/(KR)^3]\,[\sin(KR) - (KR)\cos(KR)]
$$

$$
P(\vec{K}) \le 3/(KR)^2 = 3/[2kR\sin(\theta/2)]^2, \qquad KR \gg 1
$$

Next, the ensemble average of the cross section and the ensemble average of the cross section squared is calculated.

Ensemble average of cross section

$$\langle \sigma_N(\hat{r}) \rangle = \langle |f_N(\hat{r})|^2 \rangle = \sigma_1(\hat{r}) \langle |S_N(\vec{K})|^2 \rangle = \overline{\sigma}_N(\hat{r})$$

Ensemble average of cross section squared

$$\langle \sigma_N^2(\hat{r}) \rangle = \langle |f_N(\hat{r})|^4 \rangle = \sigma_1(\hat{r}) \langle |S_N(\vec{K})|^4 \rangle$$

From these, the standard deviation of the cross section may be calculated and the ratio of the standard deviation to the mean value of the cross section may be approximated.

Then, for $N \gg 1$ *and* $|P(\vec{K})|^2 \ll 1$

$$\Delta \sigma_N(\hat{r}) = (\langle \sigma_N^2 \rangle - \langle \sigma_N \rangle^2)^{1/2}$$

$$\frac{\Delta \sigma_N(\hat{r})}{\overline{\sigma}_N(\hat{r})} = \frac{(1 + 2N|P(K)|^2)^{1/2}}{1 + N|P(K)|^2}$$

$N|P(K)|^2 \ll 1$	$N|P(K)|^2 \gg 1$
$\Delta \sigma_N \approx \overline{\sigma}_N = N\sigma_1$	$\Delta \sigma_N = (2/N|P(K)|^2)^{1/2} \ll \overline{\sigma}_N$

As indicated above, the criterion is associated with the number of scatterers multiplied by the square of the mean value of the Fourier transform of the position distribution function. When this quantity is calculated for the example uniform position distribution function, the scattering fluctuation criterion expression is

$$\alpha = N |P(K)|^2 = \left(\frac{0.002437}{\sin^4(\theta/2)} \right) N \left(\frac{\lambda^3}{V} \right)^{4/3}$$

Two cases are given below that illustrate the differences in results that may be experienced when the criterion is evaluated. In the table, V is the volume of the scattering region. In case i, the volume density of scatterers, N/V, is that of a solid. In this case, the scattered optical wave will have very small relative fluctuations. The acoustic case ii, on the other hand will have very great relative fluctuations.

Case i) Visible wavelength ‖ *Case ii) Acoustic wavelength*

$$N/V = 10^{22} \text{ cm}^{-3} \qquad\qquad N/V = 10^{-1} \text{ m}^{-3}$$

$$\lambda = 5.0 \cdot 10^{-5} \text{ cm} \qquad\qquad \lambda = 10 \text{ m}$$

$$R = 10 \text{ cm} \qquad\qquad R = 10^3 \text{ m}$$

$$|P(K)| \le 10^{-11} \qquad\qquad |P(K)| \le 10^{-5}$$

$$N|P(K)|^2 \approx 150 \qquad\qquad N|P(K)|^2 \le 0.025$$

$$\Delta\sigma_N \ll \overline{\sigma}_N \qquad\qquad \Delta\sigma_N \approx \overline{\sigma}_N$$

This first principles criterion derivation is applicable to all types of scattering, and depends upon a probability distribution of the positions of the scattering centers within the scattering volume. It was not necessary to postulate a probability distribution for the amplitude or the phase of the sum signal.

III. "STATIONARY" ISOTROPIC SCATTERERS

To illustrate the effect derived in the previous section, the scattered signal from a number of isotropic scatterers was summed coherently. Twenty seven identical scatterers were nominally located on a three dimensional grid. These nominal positions were varied in three dimensions sinusoidally in time. The amplitudes, frequencies, and phases of the sinusoids were chosen randomly with in limits, subject to the condition that the motion of each turbule in a time step constituted a velocity less than a prescribed upper bound. The relative irradiance of the total scattered signal is shown in figure 1. The maximum velocity utilized in the calculation of figure 1 was 8 m$\cdot$s^{-1}. The deep variations predicted by the α criterion of section II is readily apparent. The signal record of figure 1 may be compared with the time history of an acoustical signal recorded in Canada (see acknowledgement below) and shown in figure 2.

The experiment involved a detector located 350 m from a 500 hz source, both near the ground. A wind of approximately 3 m$\cdot$s^{-1} velocity was blowing from the detector towards the source. These circumstances would produce a wind induced shadow zone at the detector resulting in little or no direct signal reaching the detector. Figure 2 shows a segment of the data in the latter quarter of the approximately 1 minute data recording interval. Although figure 1 shows relative intensity and figure 2 shows relative amplitude, the general appearance of the two records is similar. This similarity prompted the investigation of section III where the conditions of the simulation more nearly match those of the experiment.
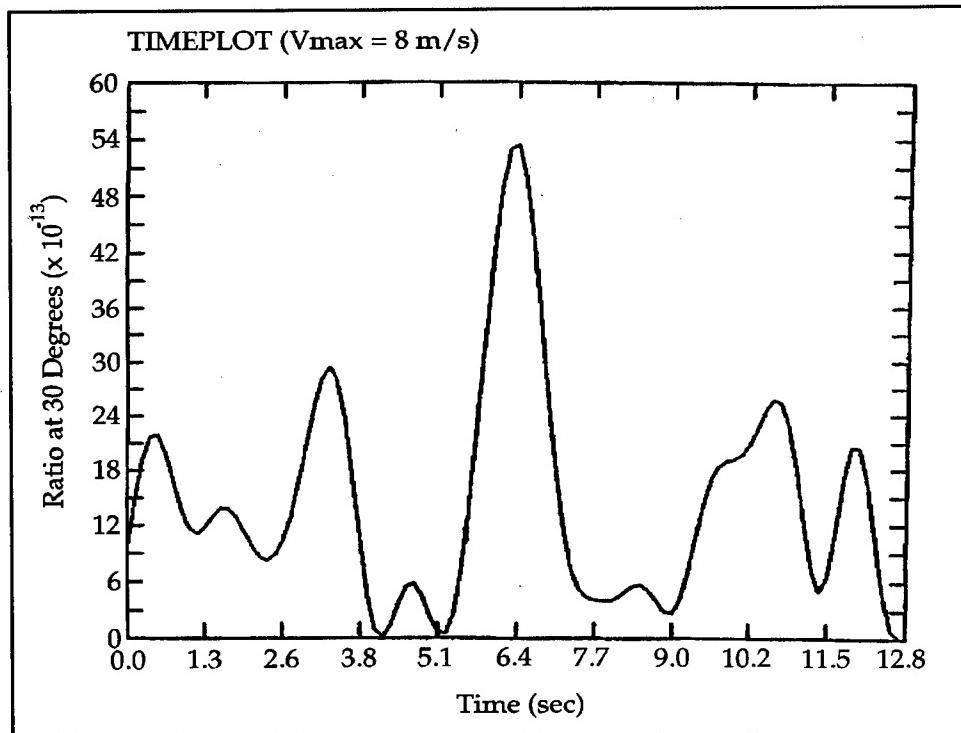
Figure 1. Scattered intensity from 27 turbules.
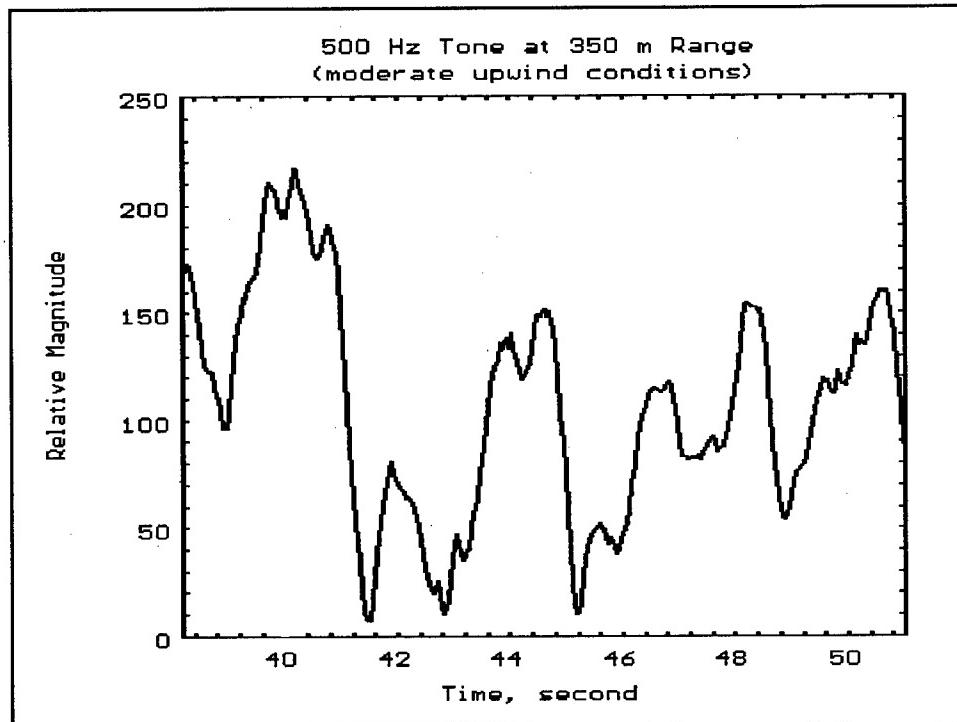
Figure 2. Turbulence scattering experiment signal

IV. WIND DRIVEN ANISOTROPIC SCATTERERS

The next calculation involves coherent summation of the scattered signal from a number of anisotropic scatterers in fixed relative position moving in the direction from detector to source. Nominal positions were specified for 65 turbules spaced 10 m along a horizontal line at an altitude of 10 m. The radius of each turbule, a, was selected randomly between the limits 1.1 m and 3.3 m. The nominal range positions were perturbed randomly within the limits -3.3 m and 3.3 m. The nominal height and the nominal cross wind position was perturbed randomly between the limits 13.3 and 6.7 and -3.3 and 3.3 respectively. The initial positions of the turbules are shown in figure 3.
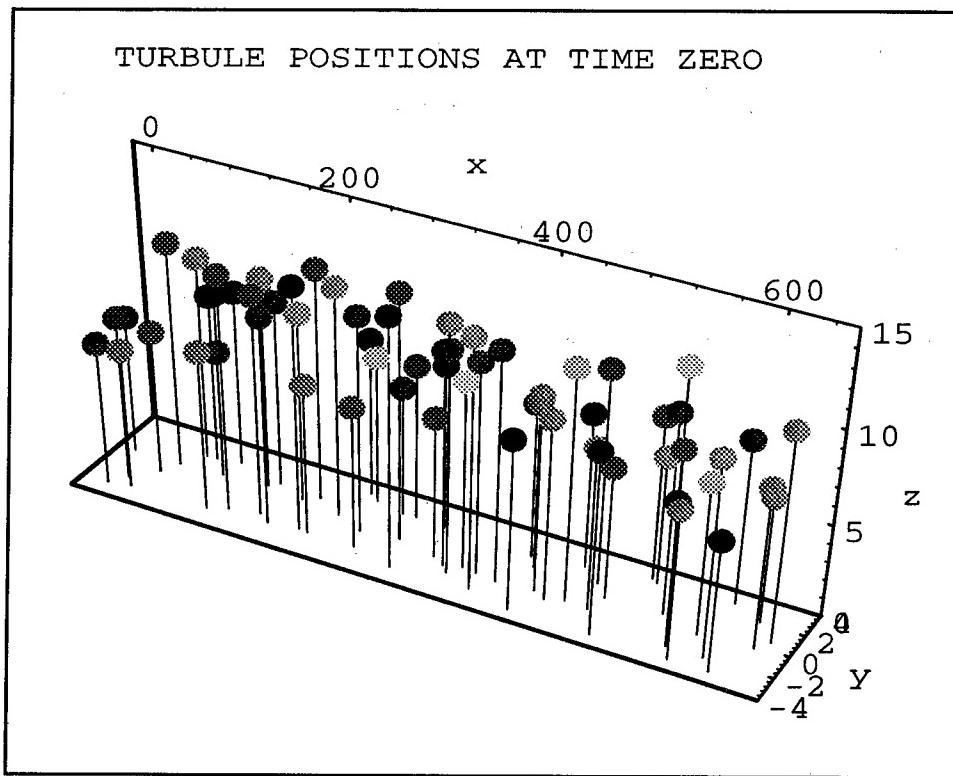
Figure 3. Initial turbule positions

The texture applied to the circles representing the turbules indicates different radii. The vertical lines from each turbule extend to zero height to give a feel for the positions of each.

The signal was calculated each 0.04 s as the collection of turbules moved from right to left at 3 m•s^{-1}. The angular pattern of the scattering amplitude was approximated by the aperture diffraction formula [2 J_1(x)/x] where x is 2 k sin(θ/2), k is (2$\pi a/\lambda$), and θ is the scattering angle. The detector was assumed to respond

to signals generated at ranges between 40 m and 310 m. As each turbule crossed these range limits, the signal was assumed to vary from zero to one according to a sinusoidal pattern while the turbule moved a distance of 2 a. The result is shown in figure 4.
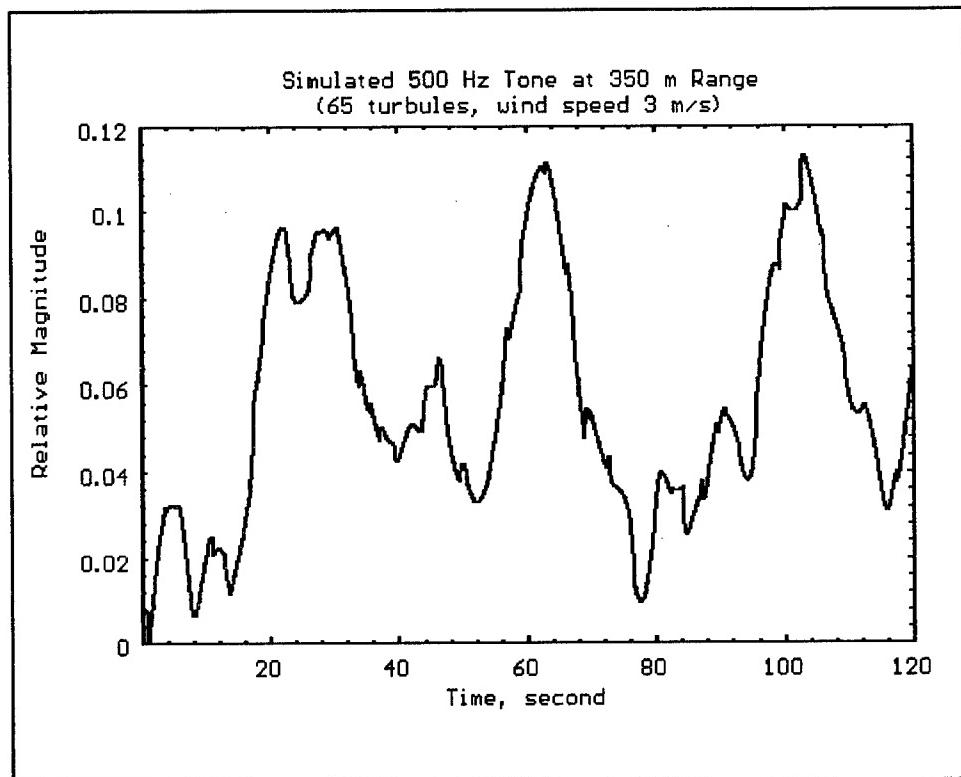
Figure 4. Simulated signal for frozen turbulence

Comparing the simulated signal of figure 4 with the measured signal of figure 2, it is apparent that the simulated signal does not vary as rapidly as the measured one. The deepness of the variations are present, however. The process of attempting to arrive at a distribution of turbules that will more closely produce the signal of figure 2 was carried one step further. Another file of turbule positions was created starting with another random seed. To each turbule entry in the file, six other parameters were added. These parameters were the amplitude, phase, and period of sine waves describing sinusoidal motion of the turbule center in the vertical and cross wind directions. The amplitudes were chosen randomly within the limits 0.0 m to 0.7 m. The phases were chosen randomly within the limits 0.0 to 2π. The periods were chosen randomly within the limits 4.0 s to 12.0 s. Further, the simulation was run for a total of 56.0 s or 1400 points. Figure 5 shows the result of this simulation.

It is seen that the frequency content in figure 5 is apparently more like that of figure 2. To check this out, the spectrum of the signal of figure 5 was calculated, and is shown in figure 6. To compare with this, a 56.0 second segment of the
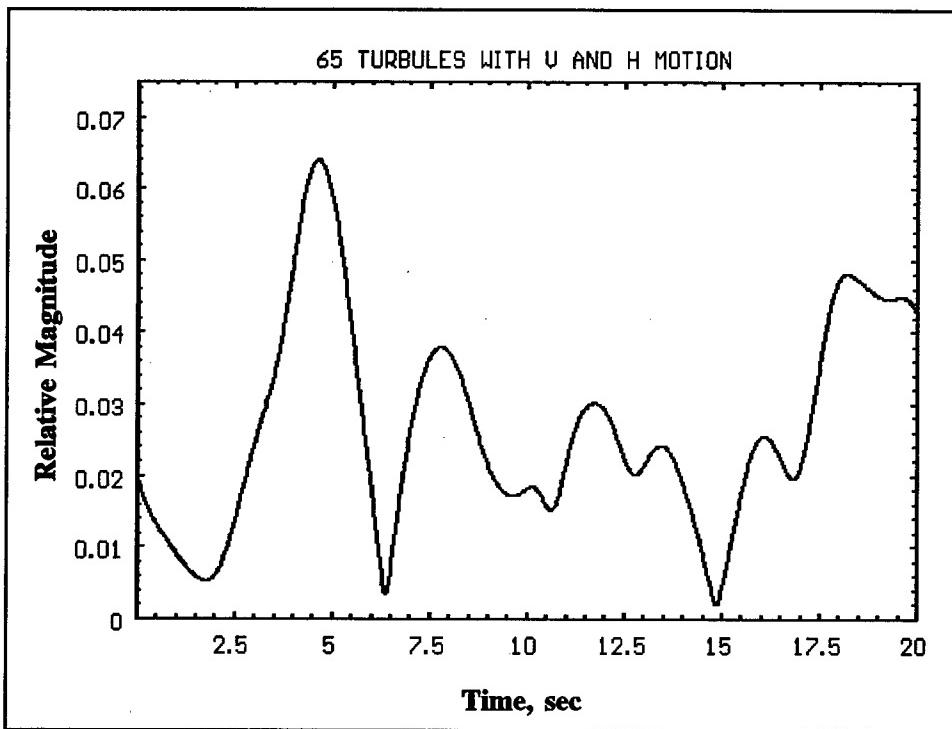
Figure 5. Simulation for moving turbules
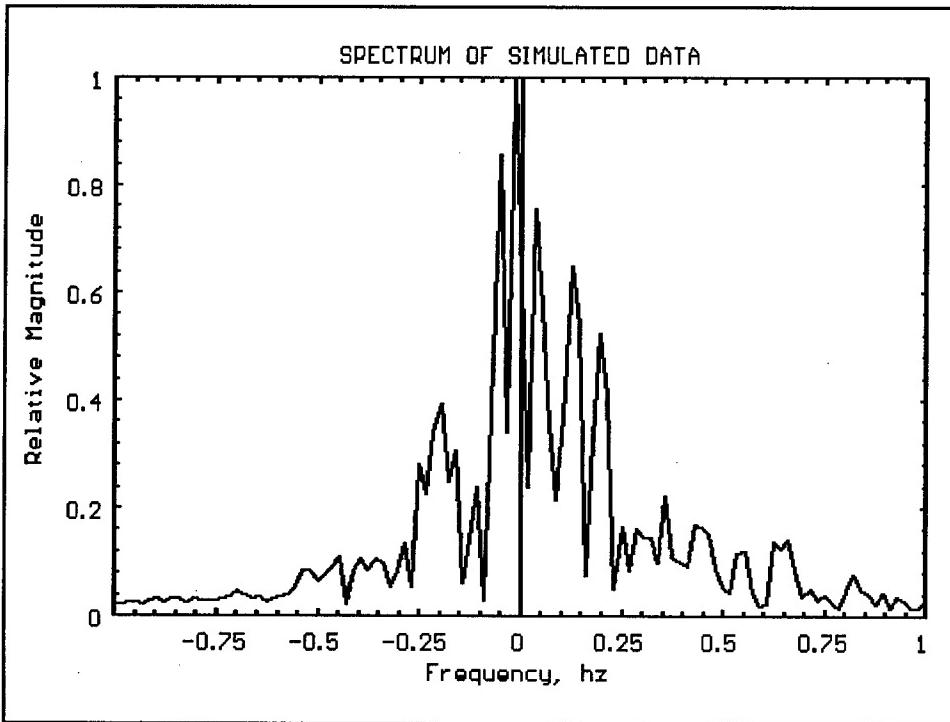
Figure 6. Spectrum of simulated signal

measured signal was analyzed. Figure 7 shows the time history of this segment.

EXTENDED EXPERIMENTAL SIGNAL
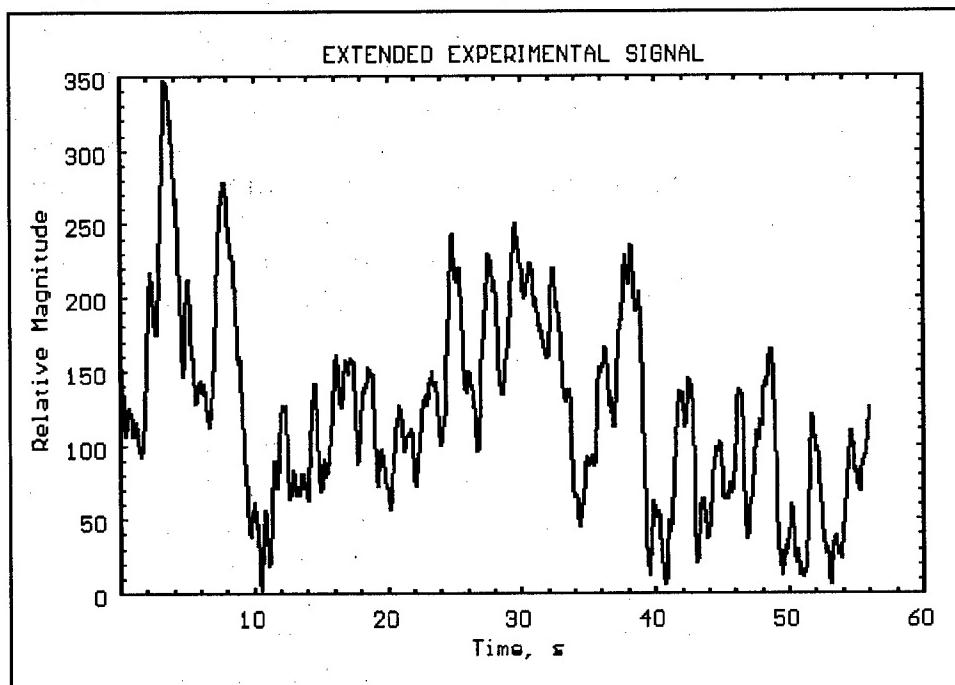
Figure 7. Extended segment of measured signal

The spectrum of this extended segment is shown in figure 8.

SPECTRUM OF EXPERIMENTAL DATA
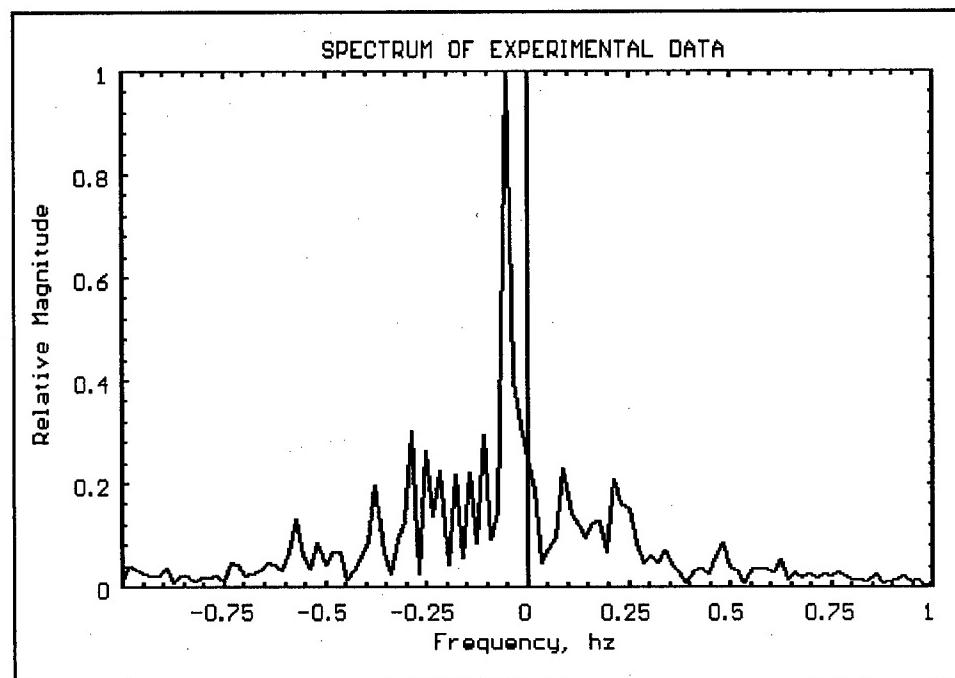
Figure 8. Measured signal spectrum

114

Comparison of figure 6 with figure 8 indicates that the two spectra have the same general character. This is because the period limits of the lateral motions used to generate figure 5 were chosen to accomplish this result. This shows that specification of a reasonable turbulence structure is possible given a measured signal, the experiment geometry, and the atmospheric conditions. To reproduce the measured signal in greater detail by a simulation, a mathematical method of analysis of the measured signal is needed that will infer the structure parameters. Such a mathematical method has not yet been devised. The prominent component of the measured spectrum at about -0.05 hz is believed to be an artifact caused by the source signal frequency being slightly different that 500.0 hz.

V. CONCLUSIONS

The significant points made in this paper are summarized here. A criterion for determining how deep variations are to be expected in a scattering process has been developed. This criterion depends upon the scattering angle, the number of scatterers, and the ratio of the wavelength cubed to the scattering volume, this ratio raised to the four-thirds power. The more familiar criterion which differentiates between diffuse scattering and forward coherent scattering, in contrast, depends only on the number and the first power of the ratio. It has also been shown that a turbulent region modeled as a collection of turbules can exhibit scattering properties similar to that experienced in field measurements.

ACKNOWLEDGMENT

REFERENCES

1. Brown, E. H., and S. F. Clifford, 1976, "On the Attenuation of Sound by Turbulence," J. Acoust. Soc. Am., 60(4), 788-794.

2. Kaimal, J. C., J. C. Wyngaard, D. A. Haugen, O. R. Coté, S. J. Caughey and C. J. Readings, 1976, "Turbulence Structure in the Convective Boundary Layer," J. Atmos. Sci., 33, 2152-2169.

3. Tatarskii, V. I., 1971, The Effects of the Turbulent Atmosphere on Wave Propagation. TT-68-50464, National Technical Information Service, Springfield, VA 22161.

SIMULATION AND MODELING

SIMULATING 3D PHENOMENA OF SMOKE AND CLOUD ON SYNTHETIC AND REAL SEQUENCES OF IMAGES

L. Blondé, Ph.Bordes and J.C.Dusseux
Thomson-CSF/Laboratoires Electroniques de Rennes
Avenue de Belle-Fontaine, 35510 Cesson-Sevigné
FRANCE

Abstract

This article describes the work undertaken at the Thomson-CSF/LER laboratories in simulating clouds and smoke phenomena in 3D scenes.
The purpose was to create realistic scenes in terms of visual rendering and physical measurements.
The cloud models are composed of geometrical shapes and a texture corresponding to the interaction of electromagnetic waves with density.
Illumination calculations use a volumic ray tracing algorithm integrating radiometric parameters along light paths on synthetic or real sequences of images.
This work has been developed within a multispectral image simulation tool to validate and test detection and tracking algorithms.

Introduction

In image synthesis, simulating solid objects is often easier than simulating fuzzy phenomena like clouds or smoke. Solid objects have well defined boundaries surfaces on which spectral properties can be mapped (as reflectivity, directional emisivity, ...). Generally, describing the surface properties of a solid object is sufficient to solve the problems of its integration in a complex scene (illumination calculation of the scene).

However, the 3D phenomena of cloud or smoke cannot be described with such a representation. Because they have fuzzy frontiers, their shape change with time and a normal to the surface cannot be defined. The light rays do not only interact with the object's external layer, but are also subject to reflections and diffusion inside the cloud.

Our work follows and extends previous models from Gardner [1] and Blinn [2] on the simulation of clouds in order to create realistic images in terms of visual rendering and physical measurements.

1.Cloud model presentation

The model presented was first developed for the simulation of clouds. It can be easily extended to smoke, explosions, decoys or plane plumes with some adjustments.

This model represents the clouds as composed of numerous elementary particles. Generally, there are too many particles to consider them individually, consequently the use of statistical models with 3D functions is required.

The structure of the model is independent from the considered spectral band (visible to infrared), only its parameters change according to the spectral band.

Only isolated or heap clouds are simulated. This gives mainly access to the creation of cumulus or nimbus appearances.

First the construction of the cloud start with a geometrical shape that must be close to the general shape of the cloud. This shape can be composed of several elementary geometrical shapes such as ellipsoid. This composed shape constitutes the external 3D boundary of the cloud.

Second a 3D physical function describing the cloud is created: the density (number of particles per unit of volume), defined every where inside the cloud. The density is used to calculate both radiometric (physical measurements) and textural information (visual render) of the cloud, so that the model is coherent.

Rendering is based on a volumic ray tracing algorithm integrating radiometric information along light paths.

1.1. Volumic description

1.1.1. 3D Function of density

The 3D function of density is the main description of the cloud. It allows calculation of the final shape, the texture, the transparency and the radiometric information.

The Gardner's cloud model considers a 3D function $F(x,y,z)$ (x,y,z are expressed in a cloud referential):

$$F(x,y,z) = \sum_{1 \leq k \leq N} c_k.\sin(2.\pi.f_v(k).y+\phi_v(k)).\sum_{1 \leq p \leq N} c_p.\sin(2.\pi.f_h(p).x+\phi_h(p))$$

where:

$$\phi_h(k) = \pi.(\tfrac{1}{2}.\sin(2.\pi.f_v(k-1).y) + \sin(2.\pi.f_v(k-1).z)) + \chi_h(t)$$

$$\phi_v(p) = \pi.(\tfrac{1}{2}.\sin(2.\pi.f_h(p-1).x) + \sin(2.\pi.f_h(p-1).z)) + \chi_v(t)$$

f_v et f_h : vertical and horizontal spatial frequencies.

Note that $F(x,y,z) \in [-1;1]$.

N depends on the image resolution and the distance of the cloud.

$\chi_h(t)$ and $\chi_v(t)$ add temporal disturbance only for the high frequencies so that they do not change the general shape of the cloud.

if k > **Threshold_High_Freq** then: $\chi_h(t) = c_k.\sin(f_v(k).(wt+\psi))$
$\chi_v(t) = c_k.\sin(f_h(k).(wt+\psi))$
else: $\chi_h(t) = 0$
$\chi_h(t) = 0$

The coefficients c_k and frequencies f_v, f_h , are given by the following relationships:

$$c_k = c_{k-1} . 2^{-\frac{1}{2}}$$
$$f_v(k) = 2.f_v(k-1)$$
$$f_h(k) = 2.f_h(k-1)$$

This gives a spectral shaping similar to fractal surfaces. The parameters c_0, $f_v(0)$, $f_h(0)$, N can be adjusted so as to obtain the textural appearance of a particular type of cloud (for example to simulate different kinds of disturbances), or simple texture like smoke.

1.1.2. Boundary of the cloud

A 3D boundary function ε is defined for every point P of the scene. It will give the general shape of the cloud. ε must have the following properties:

$\varepsilon(P) > 0$	if $P \in$ cloud,
$\varepsilon(P) = 0$	if $P \in$ boundary of the cloud,
$\varepsilon(P) = 1$	if $P \equiv$ center of the cloud,
$\varepsilon(P) < 0$	if $P \notin$ cloud.

The choice of a simple analytic function ε will simplify the amount of calculation. For instance, we use the ellipsoid as elementary geometrical shape. Then, we construct a more complex shape with a logical sum of ellipsoids:

$$\varepsilon = \varepsilon_1 + \varepsilon_2 + ... + \varepsilon_N$$

In the case of simulating smoke or explosion, ε can change with time.

In order to have a more realistic cloud shape with a fuzzy boundary, Gardner [1] modulates this function with thresholds. Finally, the 3D density function is expressed as:

$$\rho(x,y,z) = 1 - F(x,y,z) + T_1 + (T_2 - T_1).(1 - \varepsilon(x,y,z))$$

where: T_1 : threshold at the center of the cloud,
T_2 : threshold at the boundary of the cloud.

T_1 and T_2 will be adjusted and ρ will be scaled in order that ρ varies between the desired values.

1.2. Electro-magnetic waves interactions with the cloud

When an electro-magnetic wave interacts with a material, its intensity varies depending on the density and the properties of the material. Three phenomena are considered:

- The first one, called **absorption**, is the transformation of radiant energy from one spectrum to another.
- **Scattering** describes the changes in the direction of the propagation of the light beam, the global energy remaining constant.
- Finally, **transparency** which is the ratio of the light energy transmitted through the material to the total incident light energy.

In the simple model used the absorption and scattering phenomena are not considered individually, but regrouped as a global attenuation.
The corresponding models are derived from the Blinn [2] and Sakas [3] approaches.

121

1.2.1.Transparency Calculation

The transparency can be considered as the probability that a light beam Γ goes through the cloud without encountering any particle:

$$\text{transparency} = e^{-\int_\Gamma \kappa(\lambda,s).\rho(s).ds}$$

where: s : coordinate along the path,

ρ(s) : density in s,

κ(s,λ) : extinction coefficient in s,

$$\kappa(\lambda,s) = \sigma(\lambda,s) + \alpha(\lambda,s)$$

where : σ : scattering coefficient,

α : absorption coefficient.

σ et α are functions of temperature T, wavelength λ and material composition.
In the simulation presented, σ and α are supposed to be constant in the cloud.

$$\kappa(\lambda) = K_0(\lambda,r).\pi.r^2$$

where: r is the average radius of the particles,

If particles are water drops, K_0 is function of the ratio of r to λ:
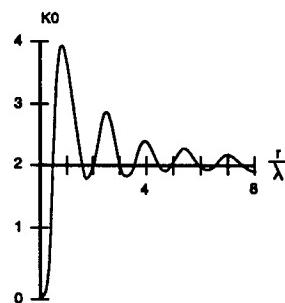
Figure 1: The K_0 coefficient for water drops.

The computations are based on a volumic ray tracing algorithm integrating radiometric parameters along the light paths. The 3D density function is calculated for N points along the beams inside the cloud. N depends on the cloud thickness and on the highest frequency f used in the density formula:

N > 2.f.Thickness

1.2.2.Scattering calculation

A single-scattering algorithm is used. That means that the paths with more than one interaction with particles are not considered. Therefore, this study is restricted to low density clouds with small albedo.

These approximations allows to create realistic scenes with a reasonable amount of calculation.

1.2.2.1.Light source scattering

The scattering of a light source I_{source} is calculated as:

$$I = \int_{s\in\Gamma}(e^{-\int_{(t<s)\in\Gamma}\kappa(\lambda).\rho(t).dt}).\sigma(\lambda).\Phi(\theta,s).\rho(s).(I_{source}.Attenu_{SB}).ds$$

where: $Attenu_{SB} = e^{-\int_{u\in\Gamma T}\kappa(\lambda).\rho(u).du}$ = attenuation(scattering and absorption) between S and B.

$\sigma(\lambda)$: scattering coefficient,
$\Phi(\alpha,\beta,s)$: phase function,
$\rho(s)$: 3D density function.

$\Phi(\alpha,\beta,s)$, called phase function, is the amount of light scattered in the β direction for a beam incident in α direction and interacting with the elementary volume located in s. Blinn [2] suggests various analytical and empirical phase functions.
In the case of several light sources, this single formula will be a sum over all the sources.

If we suppose $Attenu_{SB}$ to be constant $\forall$ (S,B), the equation will simplify [3]:

$$I = I_{source}.\omega(\lambda).\Phi(\theta).(1\text{-transparency}(\Gamma))$$

where $\omega(\lambda)$ is the **albedo**.

Note that I_{source} is the irradiance source at the cloud level, ie already affected by the atmospheric attenuation.

1.2.2.2.Earth irradiation scattering

To calculate the earth contribution scattering one has to integrate over the earth surface under the cloud (assimilated to a plane), the radiance transmitted through the atmosphere up to the cloud. However, M.P.Lévesque [5] suggests to use the following approximation:

$$I_{reçue} = t_{atm}^{3/2}.I_{Earth}$$

where: t_{atm} : vertical atmospheric transmission from the earth to the bottom of the cloud,
I_{Earth} : earth radiance.

Then, the earth contribution scattering is approximated using the light source scattering formulas, with the α direction pointing down to the earth.

1.3.Cloud emitted radiance

The cloud emitted radiance is obtained by calculating the radiance of a black body (Planck's law) at the temperature of the cloud:

$$E_{cloud} = \varepsilon_{cloud}(\lambda).Planck(\lambda,T)$$

where: $\varepsilon_{cloud}(\lambda)$: emissivity of the cloud for the wavelength λ,
$Planck(\lambda,T)$: black body radiance at the temperature T.
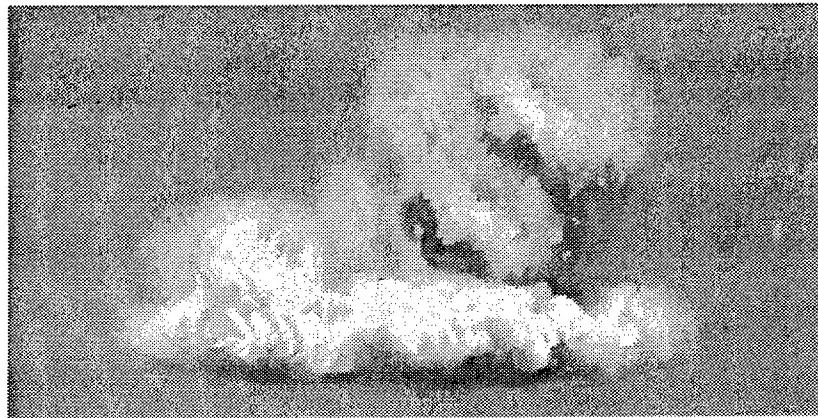
Figure 2: Cloud simulation in the visible band.

2.Scene management with atmosphere

During the illumination calculation, all light exchanges in the scene, including the atmospheric effects, have to be taken into account.

Generally, a classical model to simulate the atmosphere contribution is given by the equation:

$$L_B = Trans_{AB}(\lambda,A,B).L_A + L_{AB}(\lambda,A,B)$$

where: $Trans_{AB}(\lambda,A,B)$ atmospheric transmission between A and B,
$L_{AB}(\lambda,A,B)$ atmospheric path radiance over the path AB,
L_A total radiance of A,
L_B propagated radiance in B.

This model is used for every path between the objects of the scene.

The atmospheric parameters are calculated by exploiting a tabulated atmospheric data referenced in sight, bearing and distance. These data are computed using an atmospheric simulation software exploiting LOWTRAN 7 code.

Two classes of path were defined:
- direct paths,
- indirect paths.

2.1.Direct paths

Direct paths directly relate an object to the viewer. The beams reach the viewer from an object of the scene without being reflected by another.

When calculating the propagated radiance along a path from the cloud to the viewer, one has to sum every radiance component:

- sun component,
- cloud component,
- earth component,
- ground component,
- atmosphere component.
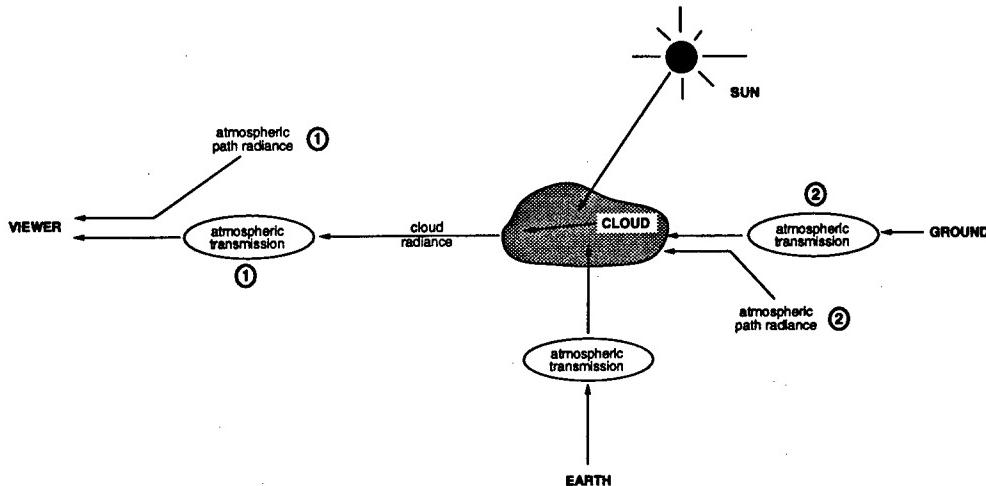
Figure 3: Integration of all components.

The path radiance calculation from the cloud to the viewer (**path 1**) uses atmospheric parameters:

$$Lum_{viewer} = L1_{atm} + Trans1_{atm} \cdot (L_{sun} + L_{cloud} + L_{earth} + L_{ground \to cloud})$$

where: $L1_{atm}$: atmospheric path radiance for **path 1**,
   $Trans1_{atm}$: atmospheric transmission for **path 1**,
   L_{cloud} : cloud emitted radiance,
   $L_{ground \to cloud}$: ground irradiance transmitted through the cloud.

The ground component takes into account the atmosphere along the path from the ground to the viewer (**path 2**):

$$L_{ground \to cloud} = Trans_{cloud} \cdot (L2_{atm} + Trans2_{atm} \cdot L_{ground})$$

where: $Trans_{cloud}$: cloud transparency,
   $Parasite2_{atm}$: atmospheric path radiance for **path 2**,
   $Trans2_{atm}$: atmospheric transmission for **path 2**,
   L_{ground} : ground irradiance.

In the case of using real images (see 4.1.Adding clouds and smokes to real images), for each pixel it is possible to calculate L_{ground} if the weather conditions of the day are available:

$$L_{ground} = (L_{image} - L_{atm}) / Trans_{atm}$$

where: L_{image} : estimated camera irradiance.

2.2.Indirect paths

The indirect paths relate an object to another (but not the viewer). The corresponding beams are used to evaluate the object irradiance.

The indirect effects calculation is a pre-processing step with regard to the direct effects (direct paths).

125

Two classes of cloud indirect effects were defined:

- the cloud transparency indirect effects,
- the cloud emitted radiance indirect effects.

2.2.1.Cloud transparency indirect effects

This concerns the indirect paths passing through one cloud. Then, cloud shadows appear on some objects of the scene.
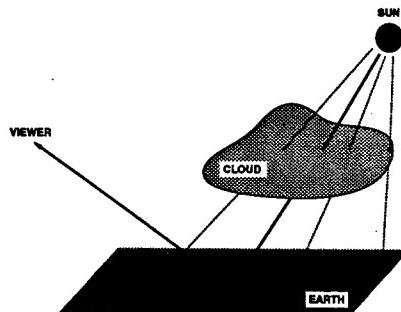
Figure 4: Cloud transparency indirect effect.

A cloud transparency map is constructed for each couple (cloud; light source). These maps are computed following the previous ray tracing algorithm. The source is put in place of the viewer, and we only consider the transparency calculation.
While calculating the illumination results, the shadowing effects are obtained by projecting this map on the scene with the correct geometric parameters.

In the case of distant clouds, the construction of the maps can be simplified using the 3D boundary function with the average cloud transparency.

2.2.2.Cloud emitted radiance indirect effects

The cloud emitted radiance L_{cloud} can be reflected on some objects of the scene. We took this phenomenon into account by considering an invisible light source put in place of the cloud. Then, for each object, the cloud emitted irradiance is L_{cloud} passed through the atmosphere, for the particular path cloud→object.
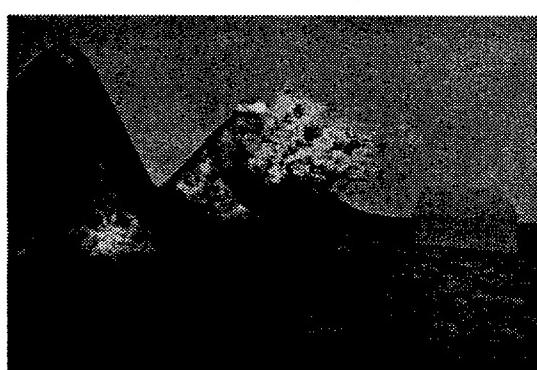
Figure 5: Visible band.
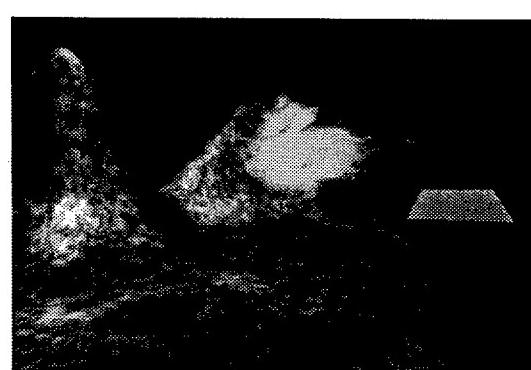
Figure 6: Infrared band.

3. Model extension

The presented models simulate the electro-magnetic waves interactions with cloud of particles. These particles can be water drops (clouds), dust, combustion or explosion waste (smoke). So, we can extend these models to the simulation of smokes, explosions, decoys or plane plumes with some parameters adjustements.

3.1. Simulating smoke

The smokes differs from the clouds in the radiometrical parameters (albedo, higher temperature, ...), in the geometrical shape and in the density.
The boundary limits of smokes move and they can vanish with time.

In the previous models, the ε and F functions depends on time too: for instance, the general shape ε increases while the density F and the temperature decreases with time.
We obtained realistic results by using low frequencies f_v, f_h in the F formula.
Note that ε and F must vary coherently.

3.2. Simulating explosions and decoys

The smoke and cloud model has been extended to the simulation of explosions and infrared decoys by creating a light source in the center of the cloud, corresponding to a hot spot. Then, the light source scattering formula is applied.
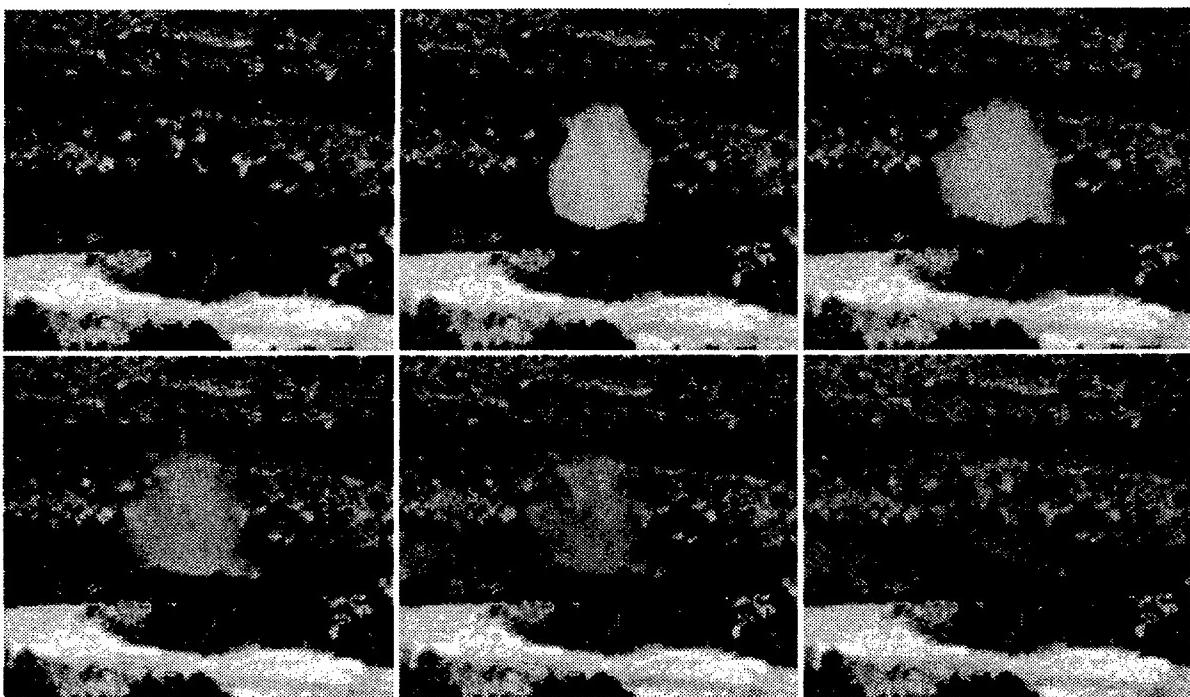
Figure 7: Explosion simulation with wind.

127

4.Images calculation

The image calculation stage manages the illumination informations of solid objects and clouds.

An image synthesis software [7] is used to compute solid objects and indirect effects. A post-processing cloud software is then applied to add clouds phenomena.
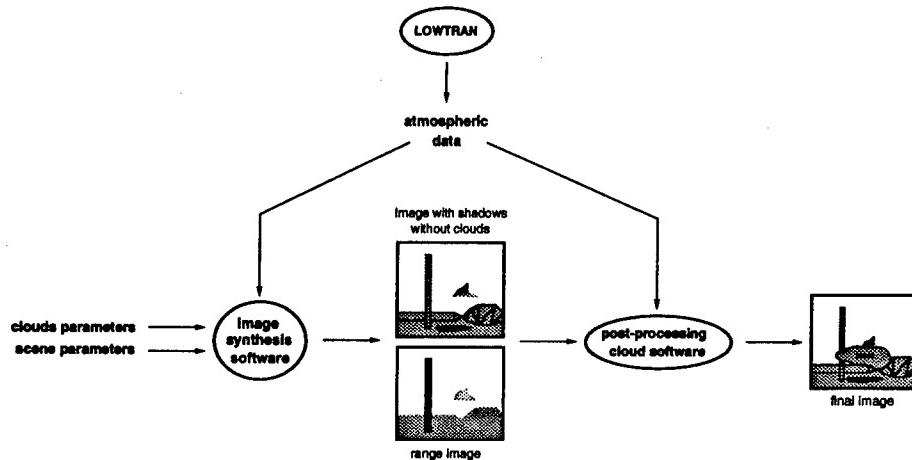
Figure 8: Image construction methodology.

In this configuration, it is possible to use the classical image synthesis software functions: management of dynamic evolution of objects, 3D boundary volumes, light beams exchanges, mapping, ...

The post-processing software is based on the previous volumic ray tracing algorithm using synthetic images and range images computed by the image synthesis software. The transparency maps are pre-processed with the cloud software.

4.1.Adding clouds and smokes to real images

The exploitation of real images requires, first of all, pre-processing steps to get rid of defects or constraints of acquisition: striping noise removal, photonic noise, electronics defects, ...

This pre-processing step includes computation of range data, which will be used by the post-processing software. The sensor can be described by a transfer function between flux and grey level in real image. A calibration of this model will be computed by using reference points (light source, black body, ...). Atmospheric contribution is computed from a simulation of weather conditions of the day of acquisition (LOWTRAN). A range data estimation can be processed with a class segmentation of the real image.

The previously presented images calculation methodology can the be applied.

128

CONCLUSION

Application: simulation tool for image processing validation and testing

This article presents models and a methodology to simulate images including 3D phenomena of smokes and clouds.

They have been developed within a multi-spectral image simulation tool to create realistic scenes in terms of physics measurement, associated with a sensor simulation software.

Thus, the whole set gives access to numerous parameters of scene and sensor definition, allowing full mastery of geometry, dynamics, photometry, meteorology, ...
With this tool, the user can create a lot of testing configurations according to the algorithm under study and validate the developed processing simulating various acquisition conditions and environments.

Offering controlled input sequences to the image processing developer, this tool removes the clasical input data problem and offers more freedom to the user in its study of algorithmetic blocking points. Furthermore, developing a control module (for example driving the line of sight of the simulated system), the user can realise close loop off line simulations at low cost.
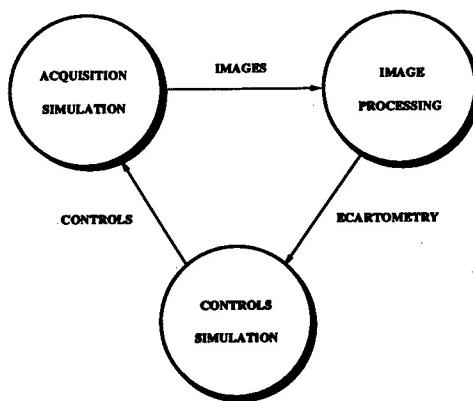
Figure 9: Simulation with feedback of processing.

REFERENCES

[1] Gardner G.Y.: "Visual simulation of clouds", SIGGRAPH'85, Vol. 19, No 3.

[2] Blinn J.F.: "Light reflection functions for simulation of clouds and dusty surfaces", Computer Graphics, Vol. 16, No 3, July 82.

[3] Sakas G.: "Fast rendering of arbitrary distributed volume densities", Eurographics'90, (Sept.), pp519-530.

[4] Gaussorgues G.: "La thermographie infrarouge", Tec-Doc.

[5] Lévesque M.P.:"Generation of IR sky background images", SPIE'91, Orlando, (april).

[6] Blondé L., Viellard T., Bordes ph.: "Simulation de systèmes Optroniques", Revue Technique THOMSON-CSF, Vol. 24, No 4, (Dec.), pp913-936.

[7] EXPLORE software: THOMSON-TDI/WAVEFRONT Technologies Inc.

EFFECTS OF NONUNIFORM AEROSOL FORWARD SCATTERING ON IMAGERY

David H. Tofsted
U.S. Army Research Laboratory
White Sands Missile Range, NM 88002-5501, USA

ABSTRACT

The VIEW and PIXELMOD codes have been developed to modify images for atmospheric transmission, path radiance, and blurring effects. This paper describes the models' method of accounting for aerosol forward scattering effects. The analysis of forward scattering effects begins with the determination of the scattered intensity field at the system entrance aperture, involving the small angle approximation and Gaussian phase functions. This result is then extended to detail the effects of forward scatter at the image plane of a receiver system and includes the effects of inhomogeneous aerosols along the optical path. To modify images, the VIEW code is used to generate the statistics of the forward scattering modulation transfer function (MTF). These statistics are then used in the PIXELMOD program to create a point spread function that is convolved over the image. The salient parameters of the aerosol MTF are the height and width of the low frequency peak. To produce a total atmospheric model, the aerosol scattering MTF and the turbulent MTF must be combined. This step is justified, and comparisons are made between the treatments of aerosol MTF by different researchers.

1. INTRODUCTION

The U.S. Army Research Laboratory's Battlefield Environment Directorate has been investigating the obscuring effects of aerosols on the ability to acquire targets. These studies have focused principally on the importance of transmission and path radiance on target acquisition. Similarly, work has been carried out studying the blurring effects of optical turbulence on imagery. Recent results obtained by Sadot and Kopeika (1993) suggest, though, that turbulence effects are less well pronounced than the effects due to aerosol forward scattering and that traditional emphasis on turbulent blurring has been misplaced. This conclusion has been contradicted by other researchers such as Bissonnette (1992). To help resolve this conflict, or at least to model its impact, it is desireable to develop a model of aerosol forward scattering that can be included in an image modification code being developed to account for atmospheric transmission, path radiance, and turbulent blurring effects.

The driving force for the development of this model is to understand atmospheric effects on target acquisition. This program was initiated as part of the Low Observables program sponsored by the Project Manager - Systems Surviveability. The models developed under this program are being provided to the U.S. Army Tank and Automotive RDEC and the Night Vision and Electronic Systems Directorate (NVESD) of the Communications and Electronics RDEC. The images to be modified are target/background scenes at both visible and infra-red wavelengths.

The means of modifying these images is to use a three-tiered set of computer models. The first tier involves the programs called BLIRB and ATMOS. The BLIRB (boundary layer illumination and radiation balance) model (Zardecki and Wetmore, 1991) requires input information about the atmosphere to be modeled: solar position, atmospheric

vertical profile, the locations of inhomogeneous clouds, etc. The output from this code has been modified to produce a database of radiances reported at regular intervals in a three-dimensional matrix called BLIRB space. The ATMOS code is based on the surface energy budget work of Rachele and Tunick (1991). The code takes input necessary to compute a surface energy budget. It then relates this budget to a vertical profile of the refractive index structure parameter.

Once the first tier is complete, the second tier model called VIEW is run to estimate propagation statistics corresponding to what would be experienced if an observer were located within BLIRB space and were viewing a scene in a specified direction. The output of the VIEW code is a new matrix of results: transmittance, path radiance, turbulence coherence diameter, and aerosol forward scattering MTF information as functions of view direction, range, and propagation wavelength.

The third tier consists of the PIXELMOD (pixel modification) code that modifies images for atmospheric effects. For input the code takes information about the image such as pixel field of view, range to given pixels, and the image orientation relative to BLIRB space. Using this data, the position of every pixel can be determined relative to the VIEW database, and the program can interpolate the atmospheric effects to be applied.

To determine the effects of aerosol forward scattering, a technique was developed, based on the results of Zardecki's forward scattered intensity function analysis (see, e.g., Zardecki and Tam, 1982). Here, this analysis is extended to handle the BLIRB, VIEW, and PIXELMOD model framework and allow image modification for aerosol effects.

2. A MODEL OF AEROSOL SCATTERING

The equation of radiative transfer for an optical beam can be described most generally by the equation (Zardecki *et al.*, 1987)

$$\vec{\Omega} \cdot \nabla I + \sigma_e I = \sigma_s \int_{4\pi} P(\vec{\Omega}, \vec{\Omega}') I(\vec{x}, \vec{\Omega}') d\vec{\Omega}', \tag{1}$$

where I is the radiation intensity in units of W/m^2-sr, a function of 6 parameters of position ($\vec{x}$) and direction ($\vec{\Omega}$); $\vec{\Omega}$ is the unit propagation vector composed of the 3 directional cosines; ∇ is the gradient operator; σ_e is the extinction coefficient, equal to the sum of the scattering coefficient σ_s and the absorption coefficient; and P is the single scattering phase function which depends on the incident and scattered propagation vectors. Normally P is dependent only on the total (scattering) angle between these two vectors.

Calculations of strong forward scattering effects, however, normally do not consider scattering in all directions. If the phase function is forward peaked, then calculations can be simplified by invoking the small angle approximation. In the small angle approximation used here, the nominal direction of propagation is along the positive z axis, and the position coordinates will henceforth use the convention $\vec{x} = (x, y, z) \longrightarrow (\vec{r}, z)$. In this approximation, the components of $\vec{\Omega}$ will also be modified. Normally θ is the zenith angle measured from the z axis and ϕ is the azimuthal angle measured counterclockwise from the x axis. In the small angle approximation, since $\theta \approx 0$, $\cos\theta \approx 1$, and $\vec{\Omega} \approx (\theta\cos\phi, \theta\sin\phi, 1) = (\omega_x, \omega_y, 1)$. The error associated with approximating the cosine by unity will be less than 1 percent as long as the field of view

considered is less than 8 degrees. By simplifying $\vec{\Omega}$, we can write the phase function in terms of $\vec{\omega}$, $P(\vec{\Omega}, \vec{\Omega}') \longrightarrow P(\vec{\omega} - \vec{\omega}')$.

The equation of radiative transfer can then be expressed as

$$\vec{\omega} \cdot \frac{\partial I}{\partial \vec{r}} + \frac{\partial I}{\partial z} + \sigma_e I = \sigma_s \iint_{-\infty}^{\infty} P(\vec{\omega} - \vec{\omega}') \, I(\vec{r}, z, \vec{\omega}') \, d\vec{\omega}', \qquad (2)$$

where we ignore all backscatter.

It will also be convenient to use a 'friendly' phase function similar to that used by Zardecki *et al.* (1987): $P(\vec{\omega}, z) = \alpha^2 \exp(-\pi \alpha^2 \omega^2)$, where $\omega = |\vec{\omega}|$, and α is the phase function width parameter dependent on the type of aerosol which can vary with position z along the optical path. This phase function is 'friendly' because it has a simple Fourier transform (equal to $\exp(-\pi \eta^2/\alpha^2)$, where $\vec{\eta}$ is the transformed coordinate and η is its magnitude, and where the two-dimensional Fourier transform operation defined by Gaskill (1978) is used). Finally, in this model the phase function will not be considered a function of transverse position. This is because scattered energy from a point source that enters a receiver will be contained within a small cylinder centered about the main propagation axis. Beyond a small distance off axis there will be very little energy that will actually enter the receiver. Thus under most conditions the phase function can be assumed to be a function of z only, for a given main propagation axis.

Having a phase function with a simple Fourier transform is helpful because it is easier to solve equation (2) in the Fourier domain. The key element that Fourier transforming equation (2) provides is to convert the convolution on the right-hand side of the equation into a product. Once the solution is found for the Fourier transform of I, an inverse transform can be performed to recover I. Again using Gaskill's definition for the Fourier transform, I can be expressed as

$$I(\vec{r}, z, \vec{\omega}) = \iint_{-\infty}^{\infty} d\vec{\kappa} \iint_{-\infty}^{\infty} d\vec{\eta} \, \hat{\hat{I}}(\vec{\kappa}, z, \vec{\eta}) \exp\left\{ j2\pi(\vec{\kappa} \cdot \vec{r} + \vec{\eta} \cdot \vec{\omega}) \right\}. \qquad (3)$$

Note here a double carat is used to indicate a fourth-order transform.

Performing the quadruple Fourier transform of equation (2) and collecting operators on the left-hand side leads to the equation

$$\left[-\vec{\kappa} \cdot \frac{\partial}{\partial \vec{\eta}} + \frac{\partial}{\partial z} + \sigma_e - \sigma_s \hat{P} \right] \hat{\hat{I}} = 0, \qquad (4)$$

where $\hat{\hat{I}}$ is a function of $\vec{\kappa}$, z, and $\vec{\eta}$, and $\hat{P}$ is a function of z and $\vec{\eta}$.

The Zardecki method of solving for $\hat{\hat{I}}$ now follows an approach to solving partial differential equations from Smirnov (1964). The essence of this approach is to solve equation (4) implicitly by treating $\hat{\hat{I}}$ as a variable along with η_x, η_y, and z. These "variables" are combined in the function $\varphi(\eta_x, \eta_y, z, \hat{\hat{I}}) = C$, where φ is specially constructed such that the equation holds when one substitutes a solution of equation (4) for $\hat{\hat{I}}$. In other words, all functional dependence due to the variables drops out of

the equation whenever the correct relationships exist between the variables. As such, the derivative of φ always equals zero as long as one moves in solution space. Therefore, if x_i and x_j are any two variables, in the solution space we must have

$$\frac{\partial \varphi}{\partial x_i}\partial x_i + \frac{\partial \varphi}{\partial x_j}\partial x_j = 0, \quad \Longrightarrow \quad \frac{\partial x_j}{\partial x_i} = -\frac{\partial \varphi}{\partial x_i}\bigg/\frac{\partial \varphi}{\partial x_j}, \tag{5}$$

which solves for the partial of one variable with respect to another. Zardecki uses this chain rule to recast equation (4) using

$$\frac{\partial \hat{\hat{I}}}{\partial \eta_x} = -\frac{(\partial \varphi/\partial \eta_x)}{(\partial \varphi/\partial \hat{\hat{I}})}, \qquad \frac{\partial \hat{\hat{I}}}{\partial \eta_y} = -\frac{(\partial \varphi/\partial \eta_y)}{(\partial \varphi/\partial \hat{\hat{I}})}, \qquad \frac{\partial \hat{\hat{I}}}{\partial z} = -\frac{(\partial \varphi/\partial z)}{(\partial \varphi/\partial \hat{\hat{I}})}. \tag{6}$$

Placing the definitions given in equations (6) in equation (4) results in

$$-\kappa_x\,(\partial \varphi/\partial \eta_x) - \kappa_y\,(\partial \varphi/\partial \eta_y) + (\partial \varphi/\partial z) + (\sigma_s\,\hat{P} - \sigma_e)\,\hat{\hat{I}}\,(\partial \varphi/\partial \hat{\hat{I}}) = 0. \tag{7}$$

From the Smirnov development, this equation can be related to the so-called characteristic equations of φ. These characteristic equations exist because the use of φ implies an equivalent problem set consisting of 3 differential equations of the form $dy_i/dx = f_i(x, y_1, y_2, y_3)$, $i = 1,3$. From this equation set there are a set of equal differentials: $dx = dy_1/f_1 = dy_2/f_2 = dy_3/f_3$. When one simultaneously solves this equation set, 3 constants of integration are generated. Normally this set of constants is determined explicitly, given the boundary conditions of the equation. But in the Smirnov approach, we assume the constants can be written as explicit functions of x and the y_i. It is postulated that the φ function yields one of these constants when the functional relationships between x and the y_i are introduced. Using the constraints in this parallel problem, Smirnov related the coefficients associated with the partial derivatives (such as $-\kappa_x$ in equation (7)) with the f_i functions. This allowed him to write the characteristic equations where the f_i's are replaced by these coefficients. For our problem, these equations are given as

$$-d\eta_x/\kappa_x = -d\eta_y/\kappa_y = dz = d\hat{\hat{I}}/[(\sigma_s\,\hat{P} - \sigma_e)\,\hat{\hat{I}}]. \tag{8}$$

These characteristic equations can be solved for $\vec{\eta}$ and $\hat{\hat{I}}$ as functions of z: $\eta_x + \kappa_x\,z = C_x$, $\eta_y + \kappa_y\,z = C_y$, and

$$\hat{\hat{I}} = C_I \exp\left\{ \int_0^z [\sigma_s(z')\,\hat{P}(\eta(z'),\,z') - \sigma_e(z')]\,dz' \right\}, \tag{9}$$

where $\vec{\eta}$ in the equation must have a z' dependence given by the previous two equations. Therefore $\vec{\eta}(z')$ must depend on $\vec{\eta}(z)$, $\vec{\kappa}$, and $(z - z')$.

$$\vec{\eta}(z') = \vec{\eta}(z) + (z - z')\,\vec{\kappa}. \tag{10}$$

Also, while C_I in equation (9) is a constant, this constancy is with not with respect to the $\vec{\kappa}$ variable, since the partials in equation (7) do not contain a $\vec{\kappa}$ dependence.

We now introduce boundary conditions and look at some special solutions. For simplicity we chose the initial radiation field as a point source located at the origin. This is denoted by

$$I(\vec{r}, z, \vec{\omega})\Big|_{z=0} = F\,\delta(\vec{r}), \tag{11}$$

where this function has no $\vec{\omega}$ dependence because I is isotropic, and where $\delta(\vec{r})$ is a two dimensional delta function.

Given the initial condition, and a sample case where there is no absorption or scattering, it is possible to show directly from equation (2) that the specific vacuum (V) solution is the equation

$$I^V(\vec{r}, z, \vec{\omega}) = F\,\delta(\vec{r} - \vec{\omega}z). \tag{12}$$

Since I^V can be Fourier transformed to $F\,\delta(\vec{\eta} + z\vec{\kappa})$, if σ_e and σ_s are both set to zero in equation (9), it is found that

$$C_I = \hat{I}^V = F\,\delta(\vec{\eta} + z\vec{\kappa}). \tag{13}$$

And while this function may appear to vary with both z and $\vec{\eta}$, from the constraints given in equation (10) for the solution space, the argument of the delta function is actually a constant.

In a second sample case the scattering coefficient is set to zero. The resulting unscattered (U) solution can then be expressed as

$$I^U(\vec{r}, z, \vec{\omega}) = I^V \exp(-\tau), \tag{14}$$

where $\tau = \int_0^z \sigma_e\,dz$ is the optical depth along the path.

We are now prepared to evaluate equation (9), since $\hat{I} = \hat{I}^U \exp\{\int \sigma_s \hat{P}\,dz'\}$. Here, however, the order in which we perform integrations is significant. It is simpler to evaluate the integration over $\vec{\eta}$, first, because the delta function sifts the integrand, replacing each $\vec{\eta}$ with $-z\vec{\kappa}$. With this substitution the tranformed phase function changes its argument to

$$\hat{P}(\vec{\eta} + \vec{\kappa}(z - z'), z')\Big|_{\vec{\eta} = -z\vec{\kappa}} = \exp(-\pi\,z'^2\,\kappa^2/\alpha^2) = \exp(-\pi\,u^2), \tag{15}$$

where $\kappa = |\vec{\kappa}|$, $u = \kappa z'/\alpha$, and α may be a function of z'.

In the BLIRB model the atmosphere is considered piecewise continuous, composed of cells with constant α. Under this methodology,

$$\tau_s(\kappa) = \int_0^z \sigma_s(z') \exp(-\pi\,u^2)\,dz' = \sum_{i=0}^N \sigma_{s_i}\,\Upsilon_i(\kappa), \tag{16}$$

where σ_{s_i} is the constant scattering coefficient over each interval, and where the form of Υ is based on the error function using a standard definition (see, e.g., Kreyzig (1972)).

$$\Upsilon_i(\kappa) = (\alpha_i/2\,\kappa)\left[\mathrm{erf}\{\sqrt{\pi}\,z_i\,\kappa/\alpha_i\} - \mathrm{erf}\{\sqrt{\pi}\,z_{i-1}\,\kappa/\alpha_i\}\right], \tag{17}$$

where the z_i denote the boundaries of the regions (in particular, $z_0 = 0$ is at the source range and $z_N = z$ is at the receiver). From this result, notice that $\Upsilon_i \geq 0$, since $z_i \geq z_{i-1}$. Also, Υ_i evaluated when $\kappa = 0$ is just the difference in the z_i over that path interval. So, $\tau_s(0)$ is the equivalent of the optical depth calculation, but using the scattering coefficient.

We are now prepared to evaluate the final integral over $\vec{\kappa}$ to obtain I. But notice that the $\vec{\kappa}$ variation within the exponential term is only with the magnitude of $\vec{\kappa}$. Therefore, a Hankel transform can be substituted for the Fourier transform leading to the radially symmetric function

$$G(\rho) = 2\pi \int_0^\infty \left[\exp\left\{ \sum \sigma_{s_i} \Upsilon_i(\kappa) \right\} \right] J_0(2\pi\rho\kappa)\, \kappa\, d\kappa, \tag{18}$$

where $\rho = |\vec{\rho}| = |\vec{r} - \vec{\omega}\, z|$ is used in the Bessel function argument because the sifting property of $\delta(\vec{\eta} + z\,\vec{\kappa})$ in the first half of the inverse transform process replaces $\vec{\eta} \cdot \vec{\omega}$ by $-z\,\vec{\kappa} \cdot \vec{\omega}$, which results in the argument $(\vec{\kappa} \cdot \vec{r} + \vec{\eta} \cdot \vec{\omega})$ in equation (3) being converted into $\vec{\kappa} \cdot \vec{\rho}$. Therefore, the scattered radiation can be written,

$$I^S = F \exp(-\tau)\left[G(\rho) - \delta(\rho) \right]. \tag{19}$$

3. SYSTEM MODEL OF ATMOSPHERIC BLURRING EFFECTS

Now consider what this form for the scattered radiance means when applying this result to a system model of image formation. Let us start by defining the vector $\vec{\omega}_0 = \vec{r}/z$, representing the propagation direction for an unscattered photon emitted from $(0, 0, 0)$ and passing through $(\vec{r}, z)$. Let us also define $\vec{r}_s$ as a vector from $(0, 0, 0)$ to $(x_s, y_s, 0)$, and let $\vec{\omega}_s = (\vec{r} - \vec{r}_s)/z$ be the vector associated with an unscattered photon emitted from $(\vec{r}_s, 0)$ that passes through point $(\vec{r}, z)$. But the $\vec{\rho}$ variable for an incident photon from direction $\vec{\omega}_s$ at point $\vec{r}$ in the transverse plane at z (the receiver plane) is $\vec{\rho} = \vec{r} - z\,\vec{\omega}_s$. Therefore, $\vec{\rho} = \vec{r}_s$!

Thus the scattered field observed at the receiver plane arising from a point source propagated through aerosols is entirely equivalent to a dispersed source distribution propagated through a vacuum. Let us call this altered source distribution I_s. Then

$$I_s(\vec{r}_s) = I_s(r_s) = F \exp(-\tau)\, G(\rho)\Big|_{\rho = r_s}. \tag{20}$$

The question might now be asked — what difference does it make whether we use the five-dimensional intensity function $I(\vec{r}, \vec{\omega}, z)$ or the one-dimensional source intensity function $I_s(r_s)$? — The difference is in how they can be used in further analysis. In virtually all imaging system applications the analysis begins with a known source function intensity or complex amplitude field. The analysis continues by determining the complex amplitude as a function of position in the receiver plane and follows the field through the system to the image plane. Conversely, $I(\vec{r}, \vec{\omega}, z)$ has little use except in scattering theory. Therefore, the construct that allows one to write the scattered field intensity in terms of a modified source function is of great theoretical utility. Also, by using a point source in our test cases, we can immediately determine the aerosol point spread function (PSF): The PSF is given by dividing the energy in the scattered

distribution by the total energy (F) in the original source distribution, and by changing variables to use $\vec{v} = \vec{r}_s/z$, an angular measure in the receiver plane. This yields a nominal aerosol PSF of

$$h_a(\vec{v}) = \exp(-\tau)\, G(z\,|\vec{v}|). \tag{21}$$

We have thus shown that the effect of aerosol forward scattering is equivalent to performing a convolution of the initial energy distribution with a PSF at the object plane. In standard optics texts (e.g., Gaskill (1978)) the imaging process is handled using convolutions, leading to consideration of the MTF as the modulus of the transfer function expressed in angular form. It is logical therefore to use $h_a(\vec{v})$ to model an aerosol MTF that can be applied along with system and turbulent blurring effects to produce overall blurring of a test image. That is, we attribute the overall image degrading effects of the system plus the atmosphere to a net PSF $h(\vec{v})$ that is applied to the image. This process has an analog in the Fourier domain where the output is the product of the transformed input and the total MTF.

$$I_{output}(\vec{v}) = I_{source}(\vec{v}) ** h(\vec{v}) \implies \hat{I}_{output}(\vec{\Psi}) = \hat{I}_{source}(\vec{\Psi})\, H(\vec{\Psi}), \tag{22}$$

where $**$ represents the two dimensional convolution operation and $\vec{\Psi}$ is the Fourier angular frequency vector.

And so, it is now necessary to have some model for combining these three MTFs into a single function. Goodman (1985) has already provided the results for the combination of the system plus turbulent MTFs. It is only necessary to combine in the aerosol MTF. To this end, it is argued that a simple multiplication of the MTFs is a reasonable approach.

$$H(\vec{\Psi}) \rightarrow H(\Psi) = H_S(\Psi)\, H_{Tsn}(\Psi)\, H_A(\Psi). \tag{23}$$

The rationale for this assumption is now given. All that is necessary is to show that the aerosol MTF is relatively independent of the image degrading effects of the system and the turbulence. The independence with respect to system MTF is due to the nature of the development: Since we could replace aerosol blurring through the atmosphere with a change in source intensity distribution, it is impossible for the system to affect the distribution of the energy at the entrance aperture. Furthermore, and perhaps most obviously, all of the image degrading effects of the aerosols occur **outside** the system, while all of the system effects occur within the entrance aperture of the system. Moreover, as should be clear from equation (18) and the definition of $\vec{\rho}$, all of the blurring effects due to aerosols are symmetric about $\rho = 0 \longrightarrow \omega = \vec{r}/z$, or the angle associated with a geometric line of sight between a source point and a point in the system aperture. Since the main effect of the system is to remove this mean divergence ($\vec{\omega}$), therefore, a scaled version of $G(\rho)$ convolved with the system MTF will be formed at the image plane.

To show that the aerosol MTF is independent of the turbulent MTF is a more difficult matter. Arguing on heuristic grounds, first, turbulent and aerosol scatterings are essentially due to different phenomena. Turbulence scattering is due to wave interference effects, where turbulent eddies having very small deviations from the mean refractive index act as weak lenses on the passing wavefront. Aerosol scattering involves individual photons scattering from individual particles which possess refractive indices significantly different from the mean atmospheric value near unity. Second, the atmospheric conditions which generate the two effects tend to exclude one another: optical turbulence

is most prevalent under clear sky conditions while strong aerosol forward scattering is normally connected with precipitation and low visibility, in which case optical turbulence will be suppressed.

Given this independence assumption, the three component MTFs will now be stated. For the system MTF we use the function given by Goodman (1985) for an aberration free imaging system with entrance aperture D_0 and for radiation wavelength λ.

$$H_S(\Psi) = \begin{cases} \frac{2}{\pi} \left[\cos^{-1} u - u \sqrt{1 - u^2} \right], & \text{if } u < 1; \\ 0, & \text{for } u \geq 1; \end{cases} \qquad (24)$$

where $u = \Psi/\Psi_0$ is a dimensionless variable, Ψ is the angular frequency in cycles per radian (due to the form used for the Fourier transform), and $\Psi_0 = D_0/\lambda$ is the high frequency cutoff of the optical system.

Goodman (1985) also provides an equation for the short-term near-field turbulent MTF.

$$H_{Tsn}(\Psi) = \exp \left\{ -3.44 \, (\Psi/\Psi_1)^{5/3} \left[1 - (\Psi/\Psi_0)^{1/3} \right] \right\}, \qquad (25)$$

where $\Psi_1 = r_0/\lambda$ is the ratio of the turbulent coherence diameter to the propagation wavelength.

We have already seen the nominal form for the aerosol PSF in equation (21), but before proceeding to state the aerosol MTF, we need to consider certain aspects of the image modification process and how the aerosol scattering will be handled when non-highly forward scattering aerosols are present along the optical path. These considerations lead to a different aerosol MTF than would be obtained by the direct transform of equation (21). The first of these considerations is the means of applying the scattering/blurring effects in the image modification routine.

When the work began in the fall of 1992 to develop the image modification software that became PIXELMOD, several sample images were obtained from NVESD. These images had significant variations of range to different pixels. As a result, it was decided that a convolution approach should be used whereby different atmospheric blurring PSFs would be used on different parts of the image. But having adopted this approach, it was necessary to limit the size of the convolution kernel to reduce processing time. A typical size for this kernel covers a region of 21 by 21 image pixels. Of course, with a limited size for the scattering kernel, if the aerosol species is not highly forward peaked, only a small amount of the total scattered energy will fall within the scattering kernel. Thus using an image modification method strictly based on equation (22), but using a limited size for the convolution kernel will result in significant losses of energy during the propagation calculation process. To replace this energy it is necessary to have an estimate for the path radiance that is not considered in this kernel.

Therefore, we turn momentarily to the issue of how image modification for aerosols has been attempted in the recent past (Hoock *et al.*, 1992) when aerosol forward scattering effects were not considered. In this approach, we start with a point source brightness I_{source}. Then, using the direct transmittance $(\exp(-\tau))$ and a path radiance due to energy scattered into the optical path from all directions (I_{path}), the observed source brightness is

$$I_{output} = \exp(-\tau) I_{source} + I_{path}. \qquad (26)$$

This is a standard result, though forward scattering effects are absorbed within I_{path} and turbulent blurring effects are not considered. But because it is well known and frequently used, and because we know that equation (22) is only an approximation of multiple scattering and that by limiting the scattering kernel it will be necessary to augment equation (22) in any case, it was decided that the main image processing routine would be based on a modified version of equation (26). This also allowed us to offer the user the capability of turning transmittance, path radiance, and image blurring effects either on or off.

However, to allow these two approaches to be compatible and to replace the energy lost due to the finite kernel, it was necessary to adjust the aerosol PSF. As may be immediately obvious, $\exp(-\tau)$ appears in both equation (26) **and** equation (21). To use a modified version of equation (26) it was necessary to remove the transmittance factor from the aerosol PSF. (This means that what we call aerosol MTF will not be an MTF in the truest sense because it has values greater than unity at zero frequency.)

Second, due to the finite scattering kernel and the fact that I_{path} represents energy scattered into the path from **all** directions, it also means it represents energy scattered into the path from the solid angle represented by the scattering kernel. Therefore, we need to sum the fractional contribution of the scattering kernel to the total path radiance (call it f_F). Once we know this fraction, we must reduce I_{path} by the factor $(1 - f_F)$ so that we are not adding in some energy twice. This aspect becomes especially important as the fraction of forward scattering (f_F) increases.

With the above two considerations made, the final equation for modifying pixel brightness can be written

$$I_{output}(\vec{v}) = \exp(-\tau)\left[I_{source}(\vec{v}) * * h(\vec{v})\right] + (1 - f_F) I_{path}. \tag{27}$$

Here notice that the exact form for the aerosol MTF has still not been stated. This is because the form taken by $G(\rho)$ in equation (18), given the number of approximations made to obtain this result, appears to be unjustifiably complicated. First, a Gaussian phase function was assumed. Next, we assumed a piecewise constant phase function over the optical path. Finally, we assumed aerosol forward scattering effects were independent of turbulence effects. The full aerosol MTF would be

$$H_A(\Psi) = \exp\left\{\sum \sigma_{s_i} \Upsilon_i(\Psi/z)\right\}, \tag{28}$$

where we use Ψ/z as the argument to the Υ_i because the original units of the Υ arguments were in cycles per meter. When Ψ in cycles per radian is the variable, we need to divide by the path length z to convert the radians in the denominator of the unit to distance in the transverse plane at the source.

The problem with the use of equation (28) is that all the z_i and α_i values must be saved to evaluate the Υ_i's. To reduce the complexity of this function, a simplified aerosol MTF is utilized.

$$H_A(\Psi) \approx \exp\left\{\sigma \frac{\sqrt{\pi}}{2} \frac{\Psi_a}{\Psi} \operatorname{erf}\left(\frac{\Psi}{\Psi_a}\right)\right\}. \tag{29}$$

This substitute function carries the main features of the more exact MTF, but with far less cost in memory. The σ parameter is equal to $\tau_s(0)$. This result is due to the form

of the error function chosen: $\text{erf}(x) = (2/\sqrt{\pi}) \int_0^x e^{-t^2} dt$. Following l'Hospital's rule, the indeterminate form of $\text{erf}(x)/x|_{x=0}$ from equation (29) becomes just $2/\sqrt{\pi}$. The σ parameter is computed by the VIEW code as part of the statistics needed to modify the image: $\sigma = \tau_s(0) = \int_0^z \sigma_s(z') \, dz'$.

The second parameter, Ψ_a, is the average width of the low frequency peak of the aerosol MTF. The VIEW program also has been written to evaluate this parameter. The means of computing this parameter in the code is a binary search routine that is seeking to find a Ψ_a that solves the equation

$$\sigma \frac{\sqrt{\pi}}{2} \text{erf}(1) = \sum \sigma_{s_i} \, \Upsilon_i(\Psi_a/z). \tag{30}$$

Given this final form for the total MTF as the product of equations (29), (25), and (24), the convolution kernel must still be evaluated. Since it is only integrated results which are of interest (amount of energy falling within a given pixel), we need to evaluate the total amount of energy falling within an angle v_i of a central point. Call this integrated value I_i, where

$$I_i = 2\pi \int_0^{v_i} G(v) \, v \, dv = 2\pi \int_0^{v_i} \left[2\pi \int_0^\infty H(\Psi) \, J_0(2\pi \, \Psi \, v) \, \Psi \, d\Psi \right] v \, dv. \tag{31}$$

Zardecki indicates this expression can be somewhat simplified using relation 5.56.2 from Gradshteyn and Ryzhik (1981), which states $\int x \, J_0(x) \, dx = x \, J_1(x)$. Using this equality with $x = 2\pi \, \Psi \, v$, we can rewrite I_i as

$$I_i = \int_0^\infty \frac{d\Psi}{\Psi} H(\Psi) \left[x \, J_1(x) \right] \Big|_0^{2\pi\Psi v_i}. \tag{32}$$

Evaluating $x \, J_1(x)$ at 0 and $2\pi\Psi v_i$, and changing variables to $u = \Psi/\Psi_0$, we find

$$I_i = 2\pi v_i \Psi_0 \int_0^1 H(\Psi_0 u) \, J_1(2\pi v_i \Psi_0 \, u) \, du. \tag{33}$$

Note that we have an upper limit of 1 on the integral because of the high frequency cutoff of the system MTF.

In the routine that evaluates the scattering kernel, values of I_i are computed at regular angular intervals of $v_i = \Delta v(i/2 + 1/4)$, where Δv is the angular separation between adjacent pixels, and computations are made every half pixel from the center. These results are then used to approximate the fractional energy falling within a pixel whose center is distance $D/2$ from the kernel center. The means chosen to approximate this fraction was to assume an average pixel at distance $D/2$. For this pixel, it was assumed half of the contribution was from the energy within the band $\Delta v(D/2 - 1/4) < v < \Delta v(D/2 + 1/4)$, and a quarter of the contribution was from each of the two bands

$\Delta v(D/2 - 3/4) < v < \Delta v(D/2 - 1/4)$ and $\Delta v(D/2 + 1/4) < v < \Delta v(D/2 + 3/4)$. The angular weighted result was thus

$$W_A = \frac{I_{D-1} - I_{D-2}}{4} + \frac{I_D - I_{D-1}}{2} + \frac{I_{D+1} - I_D}{4} = \frac{I_{D+1} + I_D - I_{D-1} - I_{D-2}}{4}. \quad (34)$$

But this result must also be weighted with respect to the fraction of the ring that is occupied by the pixel. If the normalized pixel area is considered 1, the fractional area occupied is roughly equal to

$$A \approx \pi \left[\frac{D}{2} + \frac{1}{4}\right]^2 - \pi \left[\frac{D-1}{2} + \frac{1}{4}\right]^2 = \frac{\pi D}{2}. \quad (35)$$

This result leads to a final result for the pixel at position (i, j) of

$$W_{(i,j)} = \frac{I_{D+1} + I_D - I_{D-1} - I_{D-2}}{2 \pi D}. \quad (36)$$

For the central pixel, D equals zero and the results at I_0 and I_1 must be used to interpolate a result. The formula used for this process is

$$W_{(0,0)} = 0.6 I_1 + 0.4 I_0. \quad (37)$$

This method of assigning weights W, while achieving fast computation time, leads to error in its computations because of equations (36) and (37). Also, we do not want to lose energy as a result of turbulent or system blurring effects that spread energy beyond the edges of the convolution kernel. It is therefore necessary to normalized the convolution kernel.

To accomplish this normalization, three summations over the kernel are calculated. The first sum is the net contributions of scatter due to all causes over the kernel. The second sum determines only the contributions to the kernel when system and turbulence MTFs are considered. The third only considers the aerosol portion of the MTF. Once the three results have been computed, the kernel values are divided by the turbulence plus system sum. This normalizes the total energy in the kernel so that there are no losses due to turbulence and system MTFs in the convolution operation caused by the finite extent of the kernel or any error in computing the kernel components. The aerosol portion of the scattering kernel is, of course, also increased as each kernel element is divided by the system plus turbulence effects summation. Therefore, the sum for aerosol effects must also be divided by this sum. This value is then used in equation (27) as f_F.

4. BLURRING SIGNIFICANCE

The primary properties of interest in the aerosol MTF thus derived are the peak at frequency zero and the plateau at high wavenumbers due to the unscattered radiation. Because of this plateau, and because the low frequency peak can be rather narrow, aerosol MTF is seldom accounted for directly. Instead, the low frequency peak is generally ignored, and the energy associated with it is handled as a constant path radiance with no image information content. The plateau region is meanwhile handled through the transmittance, which is the same for every point in the image. This approach has widespread use and appears to be valid under most atmospheric conditions.

141

Given this, it may well be asked whether this model is not sufficient, and if it is not, under what conditions aerosol MTFs should be taken into account.

To investigate this question more clearly, let us rewrite the expression for the full aerosol MTF given by equation (28) by expanding the Υ_i terms.

$$H_A(\Psi) = \exp\left\{ \sum \sigma_{s_i} \left(\alpha_i \, z/2\, \Psi \right) \left[\mathrm{erf}\{\sqrt{\pi}\, z_i \, \Psi/\alpha_i \, z\} - \mathrm{erf}\{\sqrt{\pi}\, z_{i-1} \, \Psi/\alpha_i \, z\} \right] \right\}. \quad (38)$$

Equation (38) provides the best source for gauging the behavior of aerosol effects on imaging. In particular, we are concerned with what situations will lead to a low frequency peak with non-negligible width. This condition will occur whenever one of two conditions is present. Either the α_i are large, or σ_{s_i} is large only when z_i/z is small.

In the first of these cases, when α_i is large, $\Psi/\alpha_i z \ll 1$, and we obtain a contribution from each path segment of approximately $\sigma_{s_i} \Delta z_i$. But since the error function has a maximum of 1 and reaches a value of 0.84 by an argument value of 1, the error function components tend to cancel and $H_A \to 1$ for $\Psi > \alpha_i z$. To avoid this condition, of course, we must have $\alpha_i < \Psi/z$ to large Ψ. The source for large α is large scattering particles. Using the Gaussian phase function at zero angle we have $P(0) = \alpha^2$. With this measure for α we can consider which phase functions have significant forward scattering effects. A preliminary analysis was made of the scattering phase functions incorporated in the EOSAEL PFNDAT phase function library (Shirkey et al., 1987) based on a criteria that a scatterer was judged to have significant effects if there was more than a few percent change in the MTF at the frequency of 4 cycles per milliradian for path lengths on the order of a few kilometers. With this criterion the zero angle phase function value must be at least 10^5.

No haze aerosols met this criterion. Aerosols remaining were: drizzle for $\lambda \leq 1.06$ μm, widespread rain, thunderstorms, and snow for $\lambda \leq 5$ μm.

The second case is where significant amounts of scatterers are only present over the portion of the optical path closest to the source. In this case z_i/z will be small and the error functions will not cancel until higher frequencies. Such a situation could occur due to obscurant near a target position but not along the remainder of the line of sight. In equation (38) let us assume there is only a significant value for σ_e for $z_i/z \leq 0.1$. Then the lower bound on the α values that meet this new criterion is reduced by a factor of 10, meaning the lower bound on the zero angle phase function value is lowered by a factor of 100. This new consideration increases the number of scatterers that could potentially have an effect on image formation. The new scatterers include heavy advection fog for $\lambda \leq 1.06$ μm, all of the previously mentioned cases except now with applicabilities to 12 μm, heavy loading vehicular dust in the visible, and high explosive dust for $\lambda \leq 1.06$ μm.

Of course, it is unlikely that a snow storm or other widespread weather activity will be confined to only a small segment of the optical path. However, for the fog case it is possible to be viewing objects located on the ground from above. In this scenario some forward scattering effects should be detectable.

Overall, the forward scattering effects of aerosols appear to be limited primarily to visible systems, since the situations in which infrared systems are affected are statistically low in natural battlefield situations. Also, haze aerosols have no impact on the MTF because they are not sufficiently forward peaked.

It is interesting to consider for a moment, though, the impact of hot spots. Although the forward peak of most aerosols is not narrow enough to cause edge blurring effects, nevertheless, for a bright object, the energy scattered from this object will still be localized in a halo about the spot. This halo will have a characteristic angular extent approximating the width of the phase function. If this width is large enough to spread over the target there will be an effective decrease in contrast between the different elements of the target itself, but there will be an enhanced contrast between the target and its surroundings.

5. DISCUSSION

The findings of the previous section generally compare favorably with those of existing literature. An overview article by Bissonnette (1992), for example, is typical of comparisons. He discussed the relationship between particle scattering and the size of scattering particles and found that significant aerosol forward scattering was limited to rain and some advection fogs. (He did not consider snow.) He indicated that forward scattering is dependent primarily on having an aerosol with a significant number of scattering particles in the 100 μm range. This criteria is generally met by only rains and snows. However, his considerations were only for uniform atmospheres.

Entirely different results, however, have recently been reported by Sadot and Kopeika (1993). Their results contradict the relationship between phase function and the aerosol MTF established in the analysis given here. Their approach was to measure the overall system plus atmospheric MTF. They then attempted to determine a turbulent MTF independently, and divide through the total MTF by the system and turbulent MTFs to yield the aerosol MTF. But there are serious questions to be asked about the experimental techniques used to verify their findings: Their estimate of the turbulent MTF was made without taking delta-T temperature differential measurements. They also ignored turbulence saturation effects and inner and outer scale effects on their optical measurements that could skew their estimates of the coherence diameter to larger values. Thus when they divided through by the estimated turbulent MTF, they overestimated the effects of aerosol MTF. In some cases they thus found that the aerosol MTF was more significant than the turbulent MTF in image degradation for clear air situations. Moreover, the aerosols present during their experiments must have been in the haze category, and these have negligible particle densities in the 100 μm range, as required by Bissonnette.

Sadot and Kopeika state that the reasons for measuring increased aerosol MTF low frequency peak widths is due to limited field of view and other characteristics of the optical system that interact with the incident radiant field to extend this width. But, as pointed out in detail in section 3, because all the effects of the aerosols can be replaced by a different source function, it does not appear possible for an optical system to influence the aerosol MTF effect.

6. CONCLUSIONS

In this paper the development of an aerosol MTF has been given. The means of modifying images using this MTF in combination with calculations used to evaluate path radiance, transmittance, and the MTFs for the system and turbulence have been given. In obtaining these results a methodology for evaluating the various scatterers' forward scatter effects on imagery has also been developed. The methodology developed is consistent with results of Bissonnette and Zardecki. The results tend to be in conflict with the results of Sadot and Kopeika. It is argued that the experimental methodology

developed by Sadot and Kopeika has led to their assigning greater effects to aerosols than is reasonable given the aerosol types present during their experiments.

REFERENCES

Bissonnette, L. R., 1992, "Imaging Through Fog and Rain," *Optical Engineering*, 31:1045-1052.

Gaskill, J. D., 1978, *Linear Systems, Fourier Transforms, and Optics*, J. Wiley & Sons, New York.

Goodman, J. W., 1985, *Statistical Optics*, J. Wiley & Sons, New York.

Gradshteyn, I. S., and I. M. Ryzhik, 1980, *Table of Integrals, Series, and Products*, Academic Press, Orlando, FL 32887.

Hoock, D. W., J. C. Giever, S. G. O'Brien, and E. J. Burlbaw, 1992, "A Multi-Stream Radiative Transfer Model for Inhomogeneous Three-Dimensional Aerosol Clouds," *Proceedings of the 1992 Battlefield Atmospherics Conference*, R. Lee, chairman, 3-12.

Kreyzig, E., 1972, *Advanced Engineering Mathematics, Third Edition*, J. Wiley & Sons, New York.

Rachele, H., and A. Tunick, 1991, "Energy Balance Model for Imagery and Electromagnetic Propagation," *Proceedings of the 1991 Battlefield Atmospherics Conference*, R. Lee, chairman, 251-260.

Sadot, D., and N. S. Kopeika, 1993, "Imaging Through the Atmosphere: Practical Instrumentation-Based Theory and Verification of Aerosol Modulation Transfer Function," *J Opt Soc Am A*, 10:172-179.

Shirkey, R. C., R. A. Sutherland, and M. A. Seagraves, 1987, *Aerosol Phase Function Data Base PFNDAT, EOSAEL 87, Volume 26*, TR-0221-26, U.S. Army Atmospheric Sciences Laboratory, White Sands Missile Range, NM 88002-5501.

Smirnov, V. I., 1964: *A Course of Higher Mathematics, Volume 2*, Addison Wesley, Reading, MA. (Chap. 2, section 21).

Zardecki, A., and W. G. Tam, 1982, "Multiple Scattering Corrections to the Beer-Lambert Law," *Appl Opt*, 21:2413-2420.

Zardecki, A., S. A. W. Gerstl, and R. C. Shirkey, 1987, *Approximate Multiple Scattering Module ASCAT, EOSAEL 87, Volume 20*, TR-0221-20, U.S. Army Atmospheric Sciences Laboratory, White Sands Missile Range, NM 88002-5501.

Zardecki, A., and A. E. Wetmore, 1991, "Boundary Layer Illumination Radiation Balance Model: BLIRB," *Proceedings of the 1991 Battlefield Atmospherics Conference*, R. Lee, chairman, 261-267.

Hazard Prediction and Assessment Capability and the OMEGA System

M. E. Byers and R. M. Cox
Defense Nuclear Agency, 6801 Telegraph Rd., Alexandria, VA 22310

D. P. Bacon
Science Applications International Corporation, 1710 Goodridge Dr., McLean, VA 22102

The Operational Multiscale Environment model with Grid Adaptivity (OMEGA) is a new atmospheric simulation system that merges state-of-the-art computational fluid dynamics techniques with a comprehensive non-hydrostatic equation set. OMEGA is based upon an unstructured triangular prism grid that permits a horizontal grid resolution ranging from 100 km down to 1 km and a vertical resolution from a few tens of meters in the boundary layer to 1 km in the free troposphere.

Current operational forecast models are scale-specific and have a limit to their resolution caused by their fixed rectangular grid structure. OMEGA, on the other hand, is naturally scale spanning and its unstructured grid permits the addition of grid elements at any point in space and time. This means that OMEGA can readily adapt its grid to fixed surface or terrain features, or dynamic features in the evolving weather pattern. This flexible allows for increased resolution of orographic and land/water boundary features improving the fine scale meteorological simulation. In addition, OMEGA can provide enhanced grid resolution in localized regions such as the battlefield for the assessment of potential hazards like chemical agents.

1. Background

Current operational atmospheric simulation systems (Hoke, *et al.*, 1989; Janjic, 1990; Mesinger, *et al.*, 1988) are scale specific and cannot resolve the full spectrum required for the accurate forecast of local scale phenomena important to the theater Commander. Even with recent advances in computational power (McPherson, 1991), the current architecture and physics of today's generation of atmospheric models cannot simulate the scale interaction of the atmosphere.

The Operational Multiscale Environment model with Grid Adaptivity (OMEGA) was conceived out of a need to advance the state-of-the-art in numerical weather prediction in order to improve our capability to predict the transport and diffusion of aerosols and gases in the theater of operation and provide for increased accuracy of wind forecasts for the use of artillery. The great bulk of releases occur near the surface, are restricted to the planetary boundary layer (PBL), and are strongly influenced by the surface features (Sherman, 1978; Paegle, *et al.*, 1984). OMEGA is based upon an unstructured grid (AGARD, 1992) that makes possible a continuously varying horizontal grid resolution ranging from 100 km down to 1 km and a vertical resolution from a few tens of meters in the boundary layer to 1 km in the free troposphere.

The unstructured grid used in OMEGA is naturally scale spanning and can readily adapt to fixed surface or terrain features, or dynamic features in the evolving weather. OMEGA can provide enhanced grid resolution in localized regions where the theater Commander is interested in accurate wind forecasts needed for the assessment of battlefield hazards. The major advantage of OMEGA over current state-of-the-art models includes the ability to resolve the surface terrain down to scales of 1 km by using the flexibility of the unstructured grid to place vertices only where required. In addition, OMEGA can resolve the local perturbations on the larger scale evolving weather down to the same scale. In order to accomplish this, however, it is necessary to include all of the physical parameters and processes which affect the local flows. These include not only the topography, but the land use, the land/water composition, the vegetation, the soil moisture, the snow cover (if appropriate), and the surface moisture and energy budgets. The inclusion of this additional physics, some of which is only appropriate because of the increased spatial resolution, represents an additional advance in the state-of-the-art.

OMEGA uses a fully non-hydrostatic equation set to describe the dynamics. Cloud formation, growth and precipitation processes are simulated by bulk-water parameterization schemes. A convective parameterization scheme is used in regions where the resolution is insufficient to resolve the convection explicitly. OMEGA incorporates a radiation transport package which approximates the effects of the atmosphere and clouds on the radiation budget. Finally, OMEGA contains an extensive planetary boundary layer package.

In addition, OMEGA has both Eulerian, or grid based, as well as Lagrangian based aerosol and gas transport. This flexibility permits OMEGA to simulate the transport and diffusion of aerosols and gases with high spatial and

temporal fidelity over a wide range of scales.

2. The OMEGA Grid Structure

OMEGA is based on an unstructured triangular prism computational mesh. This mesh is unstructured in the *horizontal* dimension and structured in the *vertical* dimension. The rationale for this mesh is the physical reality that the atmosphere is roughly decorrelated horizontally but correlated vertically. (In fact, this is the reason that most **hydrostatic** forecasting systems work.) While completely unstructured three-dimensional meshes have been used for other purposes (Baum, *et al.*, 1993; Luo, *et al.*, 1994), the benefit of having a structured vertical dimension is a reduction of three orders of magnitude in the computational requirements of the model.

An OMEGA grid element is shown in Figure 1. These elements are stacked vertically in such a fashion that all of the cells in a column have the same projection onto the surface of the Earth (Figure 2). This common projected footprint considerably simplifies the grid generation and provides an extremely simple framework for the radiation transport model.

The underlying mathematics and numerical implementation of unstructured adaptive grid techniques have been evolving rapidly, and in many fields of application there is recognition that these methods are more efficient and accurate than the structured logical grid approach used in more traditional codes. To date, however, unstructured grids and grid adaptivity have not been used in the atmospheric science community (Skamarock and Klemp, 1992). OMEGA represents an attempt to join these two communities.

The adaptation of an unstructured grid takes place through a variety of grid operations. **Vertex addition** is usually followed by a **vertex reconnection** step (Figure 3). The vertex addition step is accomplished by adding a vertex at the centroid of each affected cell and connecting it to the vertices of the cell. The reconnection step then involves the evaluation of each new cell to see if it is possible to create grid cells with a lower aspect ratio by removing an edge and reconnecting the opposite vertices.

The reverse process, **vertex deletion**, coarsens the grid and is also followed by a **vertex reconnection** step. It is important to note that even though the grid adaptation routines may create an apparent **motion** of the grid, it does not, in fact, move; rather the goal is to refine the grid in advance of any important physical process which could require additional grid resolution, and to coarsen the grid behind the region.

Vertex relaxation, in which the vertices are allowed to move as a mass-spring system, and **edge bifurcation**, which is equivalent to vertex addition in the special case of an edge cell, represent additional processes which can be used to refine the grid.

3. Grid Generation

An example of the flexibility of the OMEGA grid is shown in Figure 4. This figure shows a grid generated for the Northeast US in which the grid was adapted to the underlying topography, the land/water boundary, and to the initial weather conditions. The synoptic situation chosen was the Nor'easter of 1992 - December 11, 1992 at 1200 GMT.

In this example, we have broken the grid generation process into different steps for illustration. We have shown a grid generated by adapting to gradients in elevation (refining the grid in mountainous areas), gradients in the land/water index (refining the grid in coastal areas), adapting to the frontal region of the Nor'easter (refining the grid to the initial weather), and, finally, to all of these criteria. The final surface grid consists of 6835 triangles with edges ranging from roughly 4 km to 140 km; more importantly, over 90% of the edges are less than 30 km in length.

4. Conclusions

OMEGA represents a significant change in aerosol transport and diffusion modeling. For the first time, advanced numerical methods developed by the computational fluid dynamics community have been applied to atmospheric simulation. This has permitted the development of an extremely high resolution atmospheric simulation tool. In addition, by embedding the aerosol transport and diffusion model into the atmospheric simulation, the maximum benefit is derived.

As seen in the application of OMEGA to meteorological events like the Nor'easter, a high resolution forecast can be made with a fully coupled system. This allows for increased accuracy both from model output and forecaster derived output; thus, providing the theater Commander with the battlefield weather that is essential to ensuring timely and accurate force employment.

5. Acknowledgments

AGARD (Advisory Group for Aerospace Research and Development), 1992: Special course on unstructured grid methods for advection dominated flows, AGARD-R-787, NATO, Neuilly sur Seine, France.

Anthes, R. A., 1977: A cumulus parameterization scheme utilizing a one-dimensional cloud model. *Mon. Wea. Rev.*, 105, 270-286.

Baum, J.D., H. Luo, and R. Lohner, 1993: Numerical simulation of a blast inside a Boeing 747, AIAA 93-3091, 24th Fluid Dynamics Conference.

Baum, J.D., and R. Lohner, 1993: Numerical simulation of pilot/seat ejection from an F-16. AIAA 93-0783, 31st Aerospace Sciences Meeting and Exhibit, AIAA, Reno, Nevada.

Blackadar, A. K., 1979: High resolution models of the planetary boundary layer, *Advances in Environmental and Scientific Engineering*, Vol. 1, Gordon and Breach, pp. 50-85.

Boybeyi, Z., and S. Raman, 1992: A three-dimensional numerical sensitivity study of convection over the Florida peninsula. *Boundary Layer Meteorol.*, 60, 325-359.

Businger, J. A., J. C. Wyngaard, Y. Izumi, and E. F. Bradley, 1971: Flux-profile relationships in the atmospheric surface layer. *J. Atmos. Sci.*, 28, 181-189.

Charnock, H., 1955: Wind stress on a water surface. *Quart. Jl. R. Met. Soc.*, 81, 639-640.

Deardorff, J. W., 1974: Three-dimensional numerical study of the height and mean structure of a heated planetary boundary layer. *Boundary Layer Meteorol.*, 7, 81-106.

Deardorff, J. W., 1978: Efficient prediction of ground surface temperature and moisture with inclusion of a layer of vegetation. *J. Geophys. Res.*, 83(C4), 1889-1903.

Dietachmeyer, Gary S., and Kelvin K. Drogemeier, 1991: Application of continuous dynamic grid adaption techniques to meteorological modeling. Part I: Basic formulation and accuracy, *Mon. Wea. Rev.*, 120, 1675-1706.

Dudia, J., 1993: A nonhydrostatic version of the Penn State/NCAR mesoscale model: Validation tests and simulation of an Atlantic cyclone and cold front, *Mon. Wea. Rev.*, 121, 1493-1513.

Hoke, J.E., N.A. Phillips, G.J. DiMego, J.J. Tuccillo, and J.G. Sela, 1989: The regional analysis and forecast system of the National Meteorological Center, *Wea. Forecasting*, 4, 323-334.

Janjic, Z. I., 1990: The step-mountain coordinate: physical package, *Mon. Wea. Rev.*, 118, 1429-1443

Kuo, H. L., 1965: On formation and intensification of tropical cyclones through latent heat release by cumulus convection. *J. Atmos. Sci.*, 22, 40-63.

Lin, Y.-L., R. D. Farley, and H. D. Orville, 1983: Bulk parameterization of the snow field in a cloud model. *J. Clim. Appl. Meteorol.*, 22, 1065-1092.

Luo, H., J.D. Baum, R. Lohner, and J. Cabello, 1994: Implicit schemes and boundary conditions for compressible flows on unstructured meshes, AIAA 94-0816, 32nd Aerospace Sciences Meeting and Exhibit, Reno, NV.

McPherson, R., 1991: 2001 - An NMC Odyssey, *Ninth Conf. on Num. Wea. Prediction*, AMS, Boston, MA.

Mesinger, F., Z.I. Janjic, S. Nickovic, D. Gavrilov, and D.G. Deaven, 1988: The step-mountain coordinate: Model description and performance for cases of Alpine lee cyclogenesis and for a case of an Appalachian redevelopment, *Mon. Wea. Rev.*, 116, 1494-1518.

O'Brien, J. J., 1970: A note on the vertical structure of the eddy exchange coefficient in the planetary boundary layer. *J. Atmos. Sci.*, 27, 1213-1215.

Paegle, J., J.N. Paegle, M. McCorcle, and E. Miller, 1984: Diagnoses and numerical simulation of a low-level jet during ALPEX, *Beitr. Phys. Atmos.*, 57, 419-430.

Pielke, R. A., 1974: A three-dimensional numerical model of the sea breezes over south Florida. *Mon. Wea. Rev.*, 102, 115-139.

Sasamori, T., 1972: A linear harmonic analysis of atmospheric motion with radiative dissipation. *J. Meteorol. Soc. Jpn.*, **50**, 505-517.

Schnack, D.D., I. Lottati, Z. Mikic, and P. Satyanarayana, 1993: MHD simulation on an unstructured, adaptive mesh (abstract). EOS, Trans. of Am. Geophys.Union, **74**, SH11A-16 (fall meeting).

Sherman, C. A., 1978: A mass-consistent model for wind fields over complex terrain *J. Appl. Meteor.*, **17**, 312-319.

Skamarock, William C., and Joseph B. Klemp, 1992: Adaptive Grid Refinement for Two-Dimensional and Three-Dimensional Nonhydrostatic Atmospheric Flow, *Mon. Wea. Rev.*, **121**, 788-804.

Smolarkiewicz, P. K., 1983: A simple positive definite advection scheme with small implicit diffusion. *Mon. Wea. Rev.*, **111**, 479-486.

Waugh, D.W., R.A. Plumb, M. Loewenstein, and D.W. Toohey, 1993: Investigation of fine scale structure in stratospheric tracer transport using contour advection with surgery. Fourth International Conference on Southern Hemisphere Meteorology and Oceanography, AMS, Hobart, Australia.
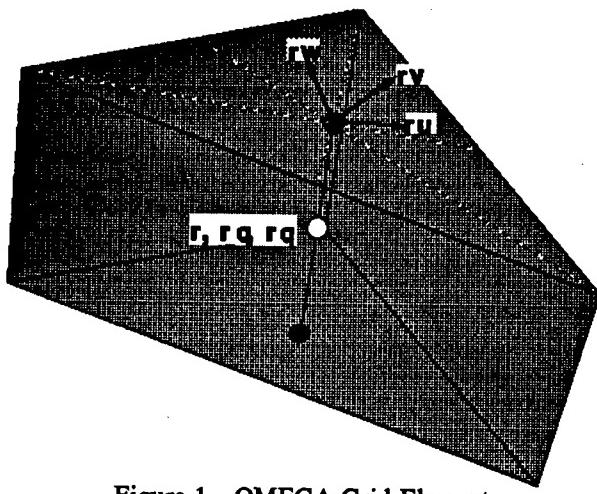
Figure 1. OMEGA Grid Element
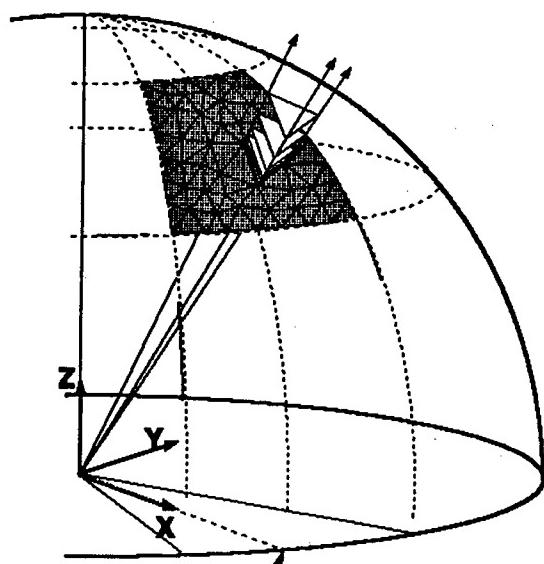
Figure 2. OMEGA coordinate system and Vertical Alignment of OMEGA Grid.

149
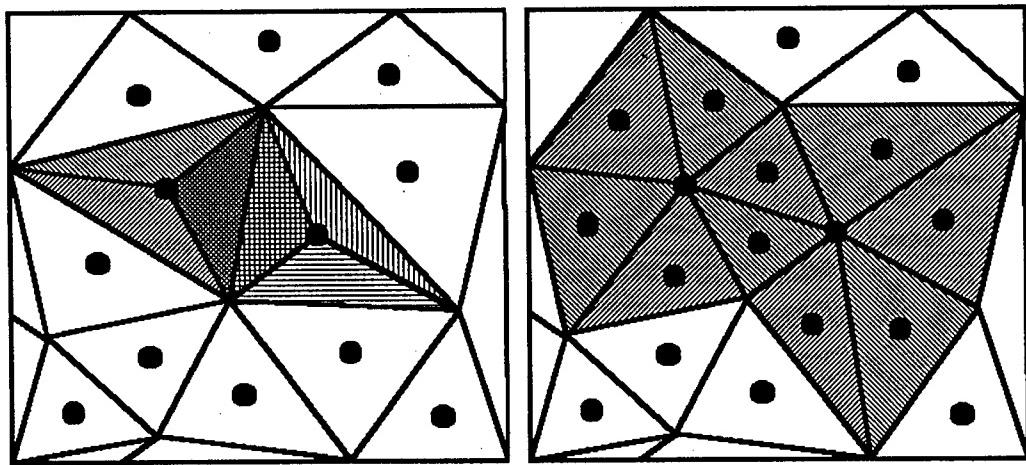
Figure 3. Vertex Addition / Reconnection
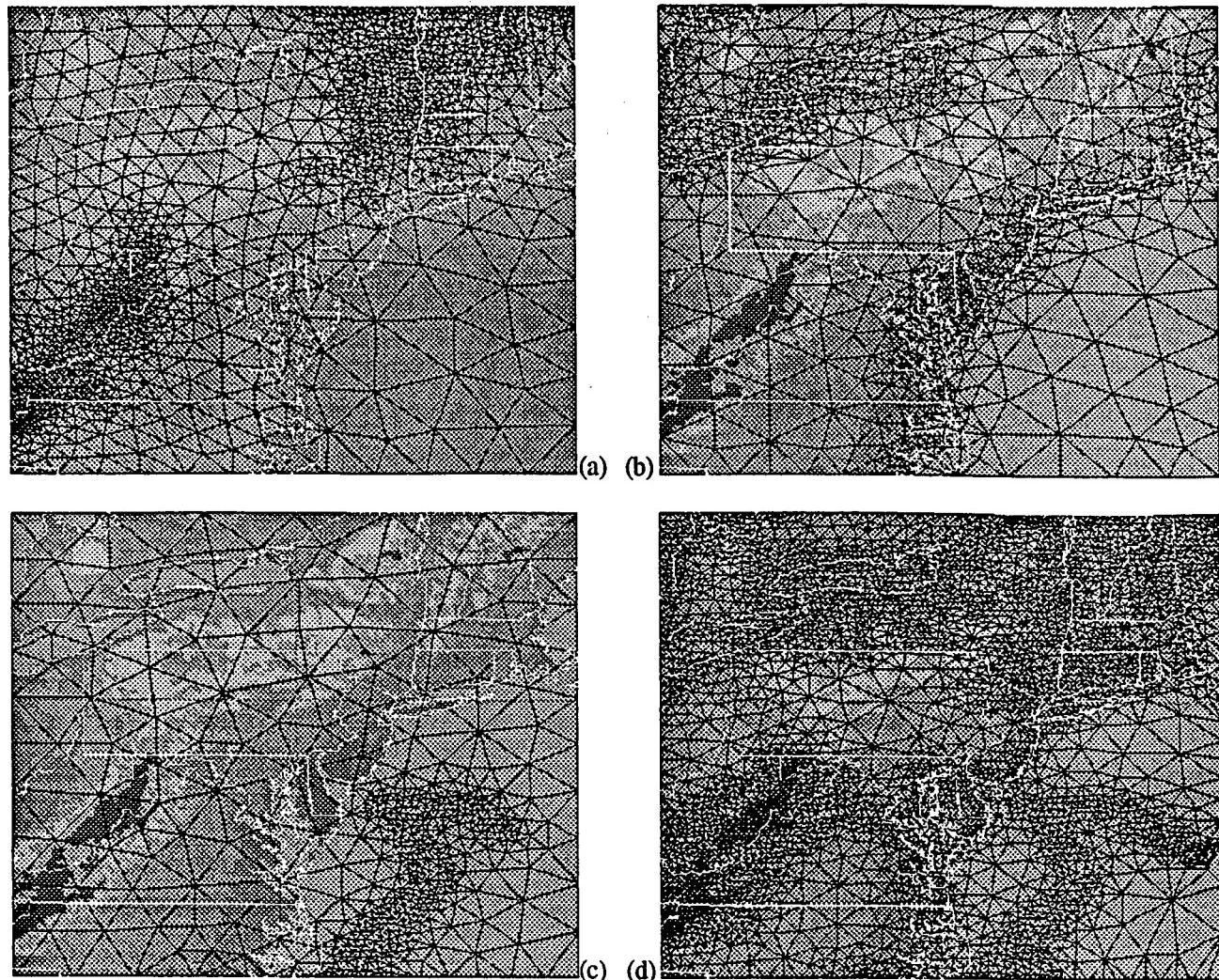
Figure 4. Using an appropriately chosen set of criteria, OMEGA can generate a grid which captures the important physical features. In this example, the OMEGA grid was adapting to: (a) the topography; (b) the land/water boundary; and (c) the weather existing at the time of model initialization. The resulting grid is seen in (d).

150

Development of the Model of Atmospheric Chemical Hazards for Theater Missile Defense

By

Ronald E. Meyers
Keith S. Deacon
Donald Durack

ABSTRACT

The Model of Atmospheric Chemical Hazards for Theater Missile Defense (MACH-TMD) was developed to provide a scientific tool for quickly calculating and visualizing airborne concentrations and ground contamination resulting from interception of a NBC laden missile. The model calculates diffusion in space and time in changing wind fields over complex terrain. The model is operated on a computer workstation by a user who selects meteorological cases, source characteristics, and location. The model works on particle size distributions and vapors resulting from NBC agent releases. In order to calculate the NBC agent transport and dispersion accurately from high altitudes a new diffusion scheme was developed which is both accurate and can adapt to the changing meteorological fields. The adaptive numerical scheme was necessary to achieve maximum efficiency for any given level of accuracy.

INTRODUCTION

The Model of Atmospheric Chemical Hazards for Theater Missile Defense (MACH-TMD) was developed to respond to the problem of determining the airborne and ground contamination resulting from the intercept of a NBC laden missile. The requirements for describing the evolution of concentrations and dosages emitted from an intercepted missile include: 1) realistic changing meteorology, 2) realistic agent physical and chemical properties, 3) accurate diffusion representation and solution visualization, 4) the effects of complex terrain, and 5) a graphical user inter-

face. These items are described in the following paragraphs.

CAPABILITIES

Meteorology and complex terrain

Realistic time varying meteorology and turbulence over complex terrain is vital for modeling the release of agents from an intercepted missile. The first 2 authors developed the AIRSIM meteorological model to compute the velocity, pressure, turbulence statistics, and temperature fields over complex terrain that are used in the diffusion model. The AIRSIM model computes the meteorological fields for up to 72 hours about the release point. Data input to the AIRSIM model can come from local observations or from a larger scale forecast through the data assimilation capability built into the structure of the AIRSIM model.

Agent Properties

Since the releases of agents may take place at high altitudes the thermodynamic properties of the agents become very important. It is possible that an agent release from such an intercept could first vaporize, then condense into liquid or solid, and finally vaporize or liquefy again as it approaches the ground. To solve this problem an advanced agent aerosol research module was developed that incorporates changes of phase.

Diffusion Representation

An adaptive numerical diffusion scheme was developed for this problem to achieve efficiency in computation across the range of scales that can be covered during the evolution of an

152

intercept release. The scheme allows a degree of accuracy to be specified and adapts itself to achieve that accuracy constraint. Furthermore the diffusion itself is based upon the turbulence in the meteorological field, that is both time and space dependent, and not upon some parametrized diffusion coefficient.

User interface

A graphical user interface to the model was developed using POSIX, X11 and Motif standards. The interface is entirely point and click for the selection of the release location and munition/agent types. The graphical display shows 2D contours of dosage, deposition, and concentration, 3D isosurfaces of dosage, and 4D isosurface animations of concentration.

CONCLUSIONS

MACH-TMD provides an increased capability to the Army for predicting the airborne and ground hazard induced by a high altitude intercept of a NBC laden missile. The 2,3, and 4D graphical representations provide the user with a unique perspective on the evolution of such hazards. Finally the speed of the model at a specified degree of accuracy enables it to be used in a near realtime environment and allows a greater number cases to be run in study scenarios for the cost of alternative approaches. At the time of this writing the capabilities of this model have been incorporated into and expanded in the Atmospheric Biological and Chemical Simulation (ABCSIM) system. For further information on these model please contact Ronald E. Meyers at the Army

Research Laboratory, Battlefield Environment Division, White
Sands Missile Range, NM 88002, (505) 678-4037.

ABCSIM 4D CONCENTRATION VIEWER
ISOSURFACE OF COMPUTED AGENT CONCENTRATION
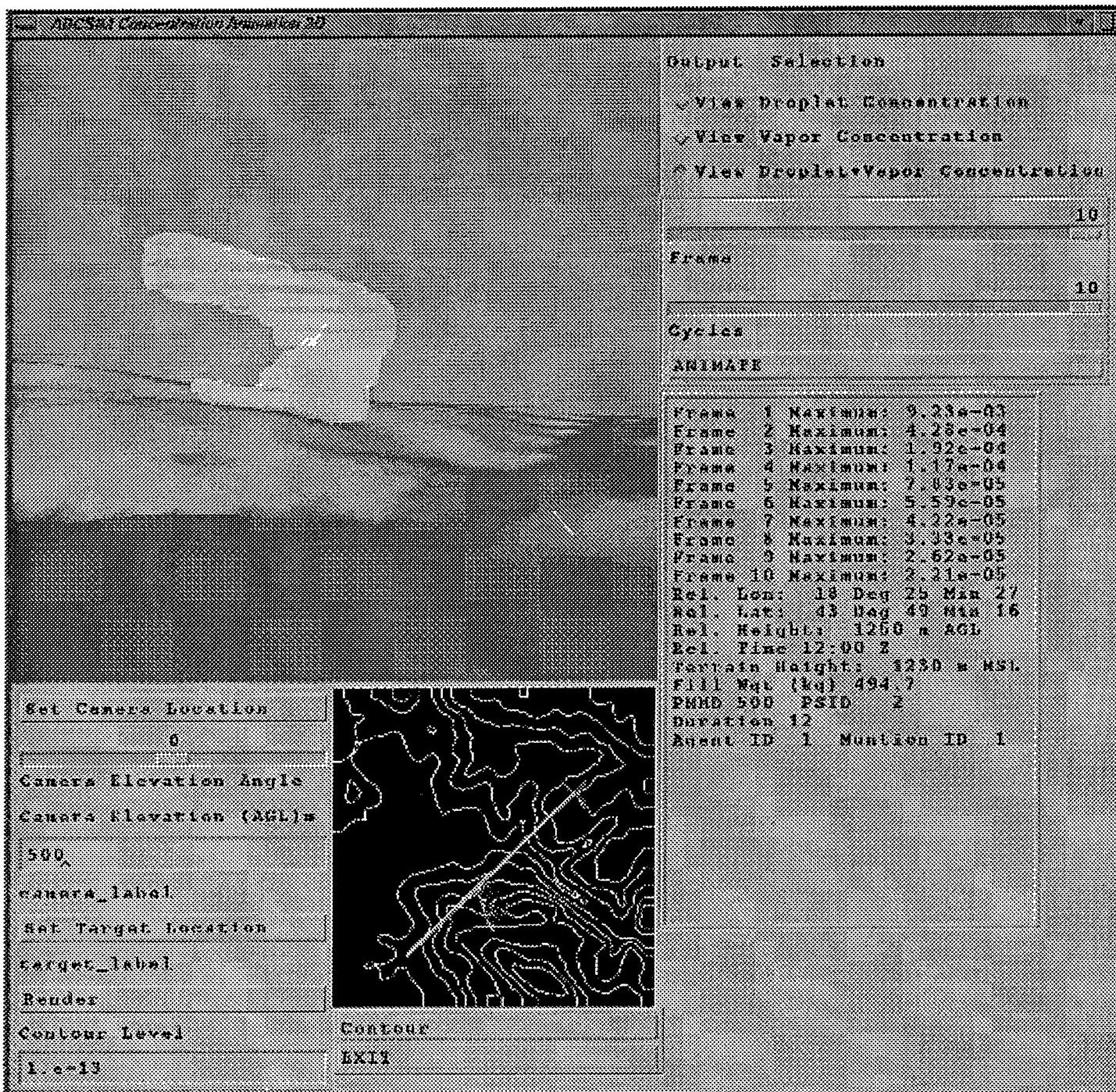
Figure 1.

OVERVIEW OF THE LONG-RANGE OVERWATER DIFFUSION (LROD) EXPERIMENT

James F. Bowers
U.S. Army Dugway Proving Ground
Dugway, Utah 84022-5000

The Long-Range Overwater Diffusion (LROD) Experiment was a Joint Services atmospheric diffusion experiment that was designed and managed by U.S. Army Dugway Proving Ground for the Joint Contact Point and Test (Project DO49). LROD was designed to fill the experimental data gap on the alongwind transport and diffusion (especially at intermediate to long range) of a vapor or aerosol cloud instantaneously released to the atmosphere. LROD consisted of a series of crosswind line source releases of the inert, nontoxic gas sulfur hexafluoride (SF_6). The tracer cloud was sampled by continuous and sequential bag samplers on boats at downwind distances of up to 100 km. Additionally, the cloud was tracked to 100 km using an aircraft-mounted continuous SF_6 analyzer. Meteorological measurements were made from one of the boats and a specially-instrumented research aircraft. Although LROD was conducted primarily to acquire data to assist in defining the operational specifications for biological agent detectors, its data should lead to improvements in the accuracy of many atmospheric transport and diffusion models. This paper describes the LROD experimental design, summarizes the outcome of the field trials, and presents preliminary results.

INTRODUCTION

Current atmospheric transport and diffusion models commonly assume that the alongwind and crosswind diffusion rates are the same because little is known about alongwind diffusion. However, both short-range diffusion experiments[1] and theoretical analyses[2] indicate that this is a poor assumption. Little data exist to characterize alongwind diffusion, especially at distances of more than a few kilometers, because: (1) alongwind diffusion usually is not an issue when modeling continuous sources of air pollution, (2) it is only in recent years that scientists have recognized that concentration exposure histories may be as important as total dosages, and (3) samplers capable of making time-resolved concentration measurements have not been available until recently. The data gap on alongwind diffusion has become a major concern to the Department of Defense (DoD) because accurate predictions of concentration exposure histories are needed to assist in defining the operational specifications for biological agent detectors. In particular, the DoD desires that the response characteristics of biological agent detectors be sufficient to minimize the possibility that U.S. military forces might be subjected to an attack by a lethal dosage of a biological agent without the agent concentration ever reaching the detection threshold.

The primary objective of the Long-Range Overwater Diffusion (LROD) Experiment was to help fill the data gap on alongwind diffusion, especially at intermediate and long range. The experiment's secondary objective was to

document atmospheric transport and diffusion processes over oceans and other large bodies of water. Although LROD was conducted primarily to acquire data to assist in defining the operational specifications for biological agent detectors, the LROD data should lead to improvements in meteorologists' understanding of both the physics of alongwind diffusion and atmospheric transport and diffusion processes over water. A better understanding of alongwind diffusion should in turn lead to improvements in the accuracy of model predictions of the hazards presented by short-term releases of many types of hazardous materials (for example, a transportation accident in which tank cars containing liquified natural gas or chlorine are ruptured).

The LROD experiment was originally scheduled to be conducted during Fiscal Year(FY) 94, but was moved forward to FY93 because of the urgency of acquiring better information on alongwind diffusion. The experiment was designed and managed for the Joint Chemical/Biological Contact Point and Test (Project D049) by the Meteorology Division, U.S. Army Dugway Proving Ground (DPG). LROD participants included the U.S. Air Force 514th Test Squadron, the U.S. Army Research Laboratory Battlefield Environment Directorate (ARLBED), and the National Oceanic and Atmospheric Administration (NOAA) Air Resources Laboratory Field Research Division (ARLFRD) and Atmospheric Turbulence and Diffusion Division (ATDD). The experiment was conducted within the overwater air space of the U.S. Navy Pacific Missile Range Facility (PMRF), Kauai, Hawaii.

EXPERIMENTAL DESIGN

The conceptual design for the LROD experiment[3] called for the crosswind release of the inert, nontoxic tracer gas sulfur hexafluoride (SF_6) from a low-flying aircraft. The recommended length of the disseminated SF_6 cloud was 30-50 km, sufficiently long that diffusion from the ends of the line would not affect the concentration at its center as far as 100 km downwind. The recommended tracer sampling consisted of: (1) continuous sampling by real-time SF_6 analyzers on five boats positioned between the dissemination line and 100 km downwind, and (2) a real-time SF_6 analyzer on an aircraft which would repeatedly traverse through the cloud as it traveled downwind. The suggested location for the experiment was a region where the winds near the surface are highly persistent and define essentially straight-line trajectories over distances of 100 km or longer.

The actual LROD experimental design[4] closely matched the conceptual design. Figure 1 shows the LROD dissemination and sampling lines for the east winds that prevail over the ocean near Kauai during the summer. Depending on the actual mean wind direction during each trial, the dissemination and sampling lines were rotated about the origin of the experiment grid (i.e., the intersection of the two lines) so that the dissemination line was perpendicular to the mean wind direction and the sampling line extended downwind. Because trials were only conducted with easterly trade winds from about 070 to 100°, the sampling line was outside of the disturbances produced in the marine boundary layer by the Islands of Kauai and Niihau. The length of the dissemination line was 100 km, sufficiently long to preclude line-source edge effects on the concentrations at its center even with an allowance for an uncertainty of ±20° in the mean wind direction. The SF_6 tracer was released from an Air Force C-130 flying approximately 91 m above
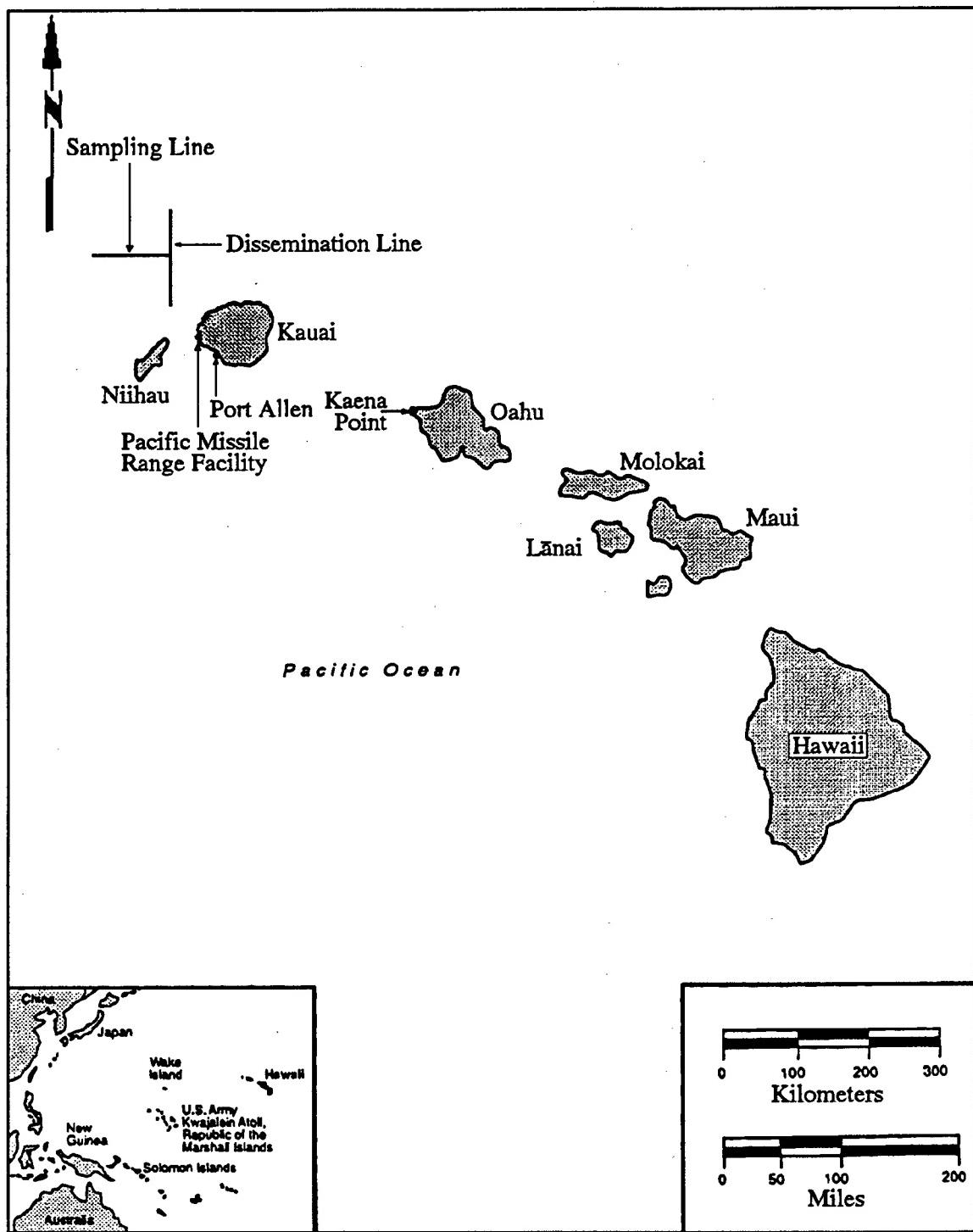
FIGURE 1. Map of the Hawaiian Islands. The Pacific Missile Range Facility
           (PMRF) is on the west side of the Island of Kauai. The nominal
           locations for the LROD experiment's SF_6 dissemination and sam-
           pling lines are shown northwest of Kauai.

mean sea level (MSL). The SF_6 dissemination was controlled by NOAA ARLFRD scientists on the C-130, and the tracer dissemination was documented by recording measurements from a flow meter and Global Positioning System (GPS).

The five sampling boats were chartered commercial fishing and sight seeing vessels which ranged from about 9 to 15 m in length. (Although the conceptual design for LROD had assumed that Navy ships would be used as the surface sampling platforms, the transfer of LROD from FY94 to FY93 did not allow sufficient lead time to schedule operational Navy ships.) Each boat carried a real-time SF_6 analyzer, sequential bag sampler, GPS, data acquisition system, and NOAA ARLFRD scientist to operate the equipment. The bag samplers were added to the experimental design as a backup to the real-time SF_6 analyzers. The LROD test plan called for the five boats to be stationed along the sampling line at downwind distances of 5, 15, 30, 60, and 100 km. However, the downwind distance for the first boat was changed to 10 km immediately prior to the first trial because of NOAA ARLFRD concerns that SF_6 concentrations at 5 km would be so high that the real-time SF_6 analyzer would be saturated.

The sampling aircraft was a twin-engine Cessna 421. It carried a real-time SF_6 analyzer, GPS, data acquisition system, and two NOAA ARLFRD scientists to operate the equipment. Flying at 152 m MSL (the minimum altitude considered by the Cessna's pilot to be safe for flying above the ocean for hours at a time), the sampling aircraft tracked the SF_6 cloud as it traveled downwind by flying a series of overlapping "racetrack" patterns. The sampling aircraft's flight path was always perpendicular to the tracer cloud, (parallel to the mean wind direction) as the aircraft traversed the cloud. The racetrack flight patterns were centered on the sampling line. Based on visual observations of the real-time SF_6 analyzer's analog output, the NOAA scientists on the sampling aircraft transmitted information on the SF_6 cloud's downwind position and alongwind dimensions to the LROD Mission Control Center at PMRF. No attempt was made to adjust these visual observations to account for the response time of the aircraft sampling system or the fact that the aircraft was traversing a nonstationary cloud. The LROD Mission Control Center used the information provided by the sampling aircraft to plot the position of the SF_6 cloud and provide guidance to the sampling boats on when to operate the sequential bag samplers.

LROD meteorological measurements consisted of surface and upper-air observations from one of the sampling boats and measurements by a specially-instrumented NOAA ATTD single-engine Rutan Long-EZ aircraft. The sampling boat assigned to the 10-km downwind position was used as the surface meteorological measurements platform. This boat carried an ARLBED meteorological technician with an OMEGA radiosonde system and the equipment to make surface weather observations. Whenever possible, the low-level winds obtained from a radiosonde sounding 1-2 hours before each trial were used to define the orientation of the experiment grid. The hourly surface weather observations included cloud cover, significant weather, winds, air and sea temperatures, dewpoint, and sea state.

The NOAA ATTD Long-EZ meteorological research aircraft flew parallel to the sampling line approximately 20-25 km from the nearest approach of the

racetrack flight patterns of the sampling aircraft. The Long-EZ began each trial by measuring the vertical profiles of wind speed and direction, temperature, and humidity as it slowly descended from 2,500 m MSL to near the ocean's surface during its flight from the dissemination line to 100 km downwind. The Long-EZ then turned back toward the dissemination line and measured the vertical fluxes of heat, water vapor, and momentum as it flew a single racetrack pattern to the dissemination line and back to 100 km downwind. The Long-EZ flew at approximately 10 m MSL while making these flux measurements. After completing the flux measurements, the Long-EZ again measured meteorological profiles as it slowly ascended from 10 to 2,500 m MSL during its return flight to the dissemination line.

SUMMARY OF EXPERIMENTAL CONDUCT

The LROD experiment was conducted during the period 13 through 26 July 1993. The LROD test plan anticipated that three trials per day could be completed on most days. However, the fatigue suffered by the sampling aircraft's flight crew and NOAA scientists by the end of the first three-trial day was so great that no more than two trials per day were subsequently attempted to ensure the safety of aircraft operations and quality of aircraft sampling data. Primarily because of this reduction in the number of trials per day, only 13 of the scheduled 16 LROD trials could be completed within the window for LROD conduct.

The major problems affecting LROD experimental conduct were poor radio communications with the sampling boats and unseasonably high winds and seas. The communications problems appeared to be primarily attributable to RF interference between the radios and GPS components. Although this interference was reduced by repositioning the GPS antennas and adding shielding, it could not be eliminated on some of the boats. In the case of Boat 1 (the boat assigned to the 10-km downwind position), it was never possible to have simultaneous radio communications and GPS output.

The unusual weather patterns that resulted in unseasonable weather on the U.S. mainland during the summer of 1993 (for example, the heavy rains that caused flooding in the midwest) also resulted in unseasonably high winds and seas in Hawaiian waters. Although the lightest seas of the LROD experiment were encountered during the first trial, all of the NOAA ARLFRD scientists on the sampling boats were incapacitated by seasickness. Consequently, it was necessary to train the boat crews to operate the sequential bag samplers and, to the extent possible, the real-time SF_6 analyzers. NOAA ARLFRD scientists also provided guidance to the boat crews on sampler operation by radio from the LROD Mission Control Center. (The NOAA ARLFRD scientist on Boat 4 (60-km downwind position) volunteered to return to sea after the first trial and was able to remain functional throughout his second stay at sea.) Although the problems with seasickness were mitigated by training the boat crews to operate the samplers, seas were so high during the last week of the experiment that it was generally unsafe for small craft to venture into the open ocean. (The high winds and seas and precipitation during the second week were attributable to the passage over the Hawaiian Islands of the remnants of Hurricanes Dora and Eugene.) The adverse weather restricted the surface sampling (one or more boats) to only six trials. However, because the aircraft operations were only

minimally affected by the weather, the contingency plan of conducting trials with aircraft-only operations allowed an additional seven trials to be completed.

Table 1 summarizes the availability of LROD measurements by trial. The boat numbers used in the table correspond to their relative downwind positions (for example, the assigned position for Boat 5 was at 100 km downwind). Boat 1 was only used for meteorological measurements after Trial 5. Rather than attempt to keep Boat 1 at sea for days at a time, the boat was sent out each day to a position that was far enough south of Kauai to be in open ocean outside of the island's wake. Because of her seaworthiness and the fact that she was kept at sea for less than a day at a time, it was possible to send Boat 1 out on days when high winds and seas kept the other boats in port.

Table 1 identifies several trials with aircraft SF_6 sampling that went beyond the requirements of the test plan. Because the aircraft SF_6 sampling at long downwind distances was far more successful than had been anticipated, the cloud was tracked well beyond 100 km during Trials 9 and 13. (The cloud was not tracked beyond 50 km during Trial 12 because the aircraft GPS failed.) Also, the sampling aircraft attempted to determine the height of the top of the cloud during Trials 9, 10, and 13. Surprisingly, the depth of the cloud at 100 km was significantly less than the depth of the marine boundary layer. The shallow SF_6 clouds help to explain why the measured SF_6 concentrations were much higher than had been anticipated.

PRELIMINARY RESULTS

Table 2 summarizes the Boat 1 surface weather observations taken nearest the start time of each trial when the boat was in open ocean. The cloud cover totals in the table are the totals for all reported cloud layers. Radio communications from the pilots of the sampling aircraft and Long-EZ indicate that significant variations in cloud cover existed at times over the experiment area as well as between the experiment area and the location of Boat 1 when it was south of Kauai. Both conventional overland atmospheric stability classification schemes[5] and overwater stability classification schemes[6] indicate that neutral or slightly unstable conditions (i.e., the Pasquill D or C stability category) existed throughout all of the LROD trials.

Table 3 summarizes the LROD grid orientations and gives preliminary estimates of the SF_6 cloud transport wind directions and speeds. The transport wind directions in Table 3 were estimated from a combination of the Boat 1 radiosonde winds at 300 m MSL and the wind directions estimated by the dissemination and/or sampling aircrafts. When the onsite Long-EZ wind data become available, the preliminary transport wind directions in Table 3 will be refined. The preliminary transport wind speed estimates in the table were inferred from the time and position of the last SF_6 cloud observation reported by the sampling aircraft to the LROD Mission Control Center for each trial. These times and positions are subject to the uncertainties arising from real-time visual observations of analog output, verbal transmission, and manual transcription. Also, it was sometimes difficult for the NOAA ARLFRD scientists in the sampling aircraft to identify the same

TABLE 1

Summary of the Availability of LROD Measurements by Trial

| Trial | Boat SF$_6$ Sampling[a] | | | | | Aircraft SF$_6$ Sampling | | Met. Measurements | |
	1 (10 km)	2 (15 km)	3 (30 km)	4 (60 km)	5 (100 km)	Max. Distance	Cloud Depth ?	Boat 1	Long-EZ
1	GC	--	GC	GC	GC	100 km	No	Yes	Yes
2	--	BS	BS	BS	GC,BS	100 km	No	Yes	Yes
3	BS (partial)	--	--	GC,BS	GC,BS	100 km	No	No	Yes
4	--	BS	--	GC,BS	GC,BS	100 km	No	No	Yes
5	--	BS	--	GC,BS	GC,BS	100 km	No	No	Yes
6	--	--	--	--	--	100 km	No	Yes[b]	Yes
7	--	--	--	--	--	100 km	No	Yes[b]	Yes
8	--	--	--	--	--	100 km	No	Yes[b]	Yes
9	--	--	--	--	--	~120 km	Yes	Yes[b]	Yes
10	--	--	--	--	--	100 km	Yes	Yes[b]	Yes[c]
11	--	--	--	GC,BS	GC,BS	100 km	No	No	Yes
12	--	--	--	--	--	~50 km	No	Yes	Yes
13	--	--	--	--	--	~120 km	Yes	No	Yes

a BS = bag sampler; GC = real-time SF$_6$ analyzer (gas chromatograph).

b Observations taken south of Kauai outside of the island's lee.

c Measurements delayed because of system problems.

TABLE 2

Summary of LROD Surface Weather Observations

Trial	Jul 93 Date/ Start Time (UTC)	Cloud Cover (10th)	Air-Sea Temp. Difference[a] (°C)	Relative Humidity (%)	Wind Direct. (deg)	Wind Speed[b] (m/s)	Wave Height (m)
1	16/1901	-[c]	--	--	--	--	--
2	18/1710	--	--	--	--	--	--
3	18/2225	3	-1.1	81	090	8.2G12.3	1.2-2.4
4	19/1705	--	--	--	--	--	--
5	19/2201	--	--	--	--	--	--
6	20/1602	7	-1.1	77	060	7.7G10.8	1.2-2.4
7	20/2048	5	-0.8	78	060	10.8G13.9	1.8-3.0
8	21/0126	8	1.6	78	060	10.3G13.4	1.8-3.0
9	22/1716	8	-0.3	83	060	10.3G13.4	2.4-3.7
10	23/1806	10	0.7	91	070	5.1G7.7	0.6-1.2
11	24/0009	10	0.1	85	065	10.3G13.9	1.2-2.4
12	24/1700	6	1.3	84	050	11.3G14.4	2.4-3.7
13	24/2115	--	--	--	--	--	--

[a] Negative temperature difference indicates air colder than ocean.

[b] Number following letter G is peak gust.

[c] No data available from Boat 1.

TABLE 3
Summary of LROD Grid Layouts and Preliminary Estimates of
SF_6 Cloud Transport Wind Directions and Speeds

Trial	1993 Date	Grid Layout (wind from)	Estimated Cloud Transport Wind	
			Direction[a]	Speed (m/s)[b]
1	16 Jul	100°	100°	7.6
2	18 Jul	080°	090°	10.0
3	18 Jul	090°	090°	10.0
4	19 Jul	080°	080°	10.5
5	19 Jul	080°	080°	11.2
6	20 Jul	070°	080°	12.3
7	20 Jul	070°	070°	12.0
8	20 Jul	070°	070°	13.1
9	22 Jul	080° [c]	090°	9.9
10	23 Jul	120° [d]	100°	9.9
11	23 Jul	100°	100°	8.8
12	24 Jul	080°	080°	13.0
13	24 Jul	080°	080°	?[e]

[a] Transport directions estimated from Boat 1 radiosonde observations at 300 m and wind estimates by dissemination and/or sampling aircraft.

[b] Transport wind speed estimated from difference between time of last reported aircraft traverse through peak concentration and time of midpoint of tracer dissemination.

[c] Dissemination line displaced 18 km to the south to avoid a thunderstorm.

[d] Dissemination line displaced 7.4 km to the south-southwest to avoid rainshowers.

[e] No cloud positions recorded in logbook because of loss of communications between Mission Control Center and sampling aircraft.

relative positions in the cloud when there were multiple peaks in the concentration profile. Finally, no attempt has been made to correct the logbook entries for the response time of the aircraft sampling system or the fact that it was traversing a nonstationary cloud. Consequently, the preliminary transport wind speeds in Table 3 are also subject to revision after the aircraft real-time SF_6 analyzer measurements have been processed and analyzed.

Figures 2 through 4 show examples of the boat and aircraft SF_6 concentration measurements made during Trial 3. Although all three figures show SF_6 concentration time histories at 100 km downgrid, several points should be kept in mind when comparing the figures. First, there is more than an order of magnitude variation in the length of the time periods covered by the three figures. Second, the bag sampler SF_6 concentrations shown in Figure 2 are in parts per trillion (ppt), whereas the real-time SF_6 analyzer concentrations shown in Figures 3 and 4 are relative concentrations that have not yet been converted to absolute concentrations using the calibration curves established for each analyzer for Trial 3. Third, the lowest relative SF_6 concentration shown in Figure 4 is well above the detection threshold. The times of the highest measured concentrations are indicated on Figures 2 through 4 in Hawaiian Standard Time (HST). These times agree to the nearest minute for the boat and aircraft real-time analyzer measurements and to within 1 min for the boat bag sampler measurements, which have a time resolution of 3 min. Preliminary results also indicate good agreement between the magnitudes of the three different measurements of the peak SF_6 concentration. Thus, the agreement found to date between the boat and aircraft SF_6 concentration measurements has been encouraging.

CONCLUSIONS

The LROD experiment was conducted both to help: (1) fill the data gap on alongwind diffusion, and (2) improve meteorologists' understanding of atmospheric transport and diffusion processes over oceans. In the case of the first objective, preliminary results indicate that the experiment acquired a high-quality data set that is unique in its documentation of alongwind diffusion at intermediate and long range. In the case of the second objective, at least one experimental result appears to contradict current views on modeling diffusion over water. Specifically, the top of the tracer cloud did not extend to the top of the marine boundary layer even at 100 km downwind. It therefore appears that, at least in the subtropical tradewind environment found over open ocean near Hawaii, the depth of the mixed layer is significantly lower than the depth of the marine boundary layer. It is hoped that the high-resolution meteorological data from the NOAA ATDD Long-EZ will provide insight into the reasons for the difference between the depths of the mixed and marine layers.

ACKNOWLEDGMENT

FIGURE 2. Bag sampler SF₆ concentration versus time for Boat 5 (100 km) during Trial 3.
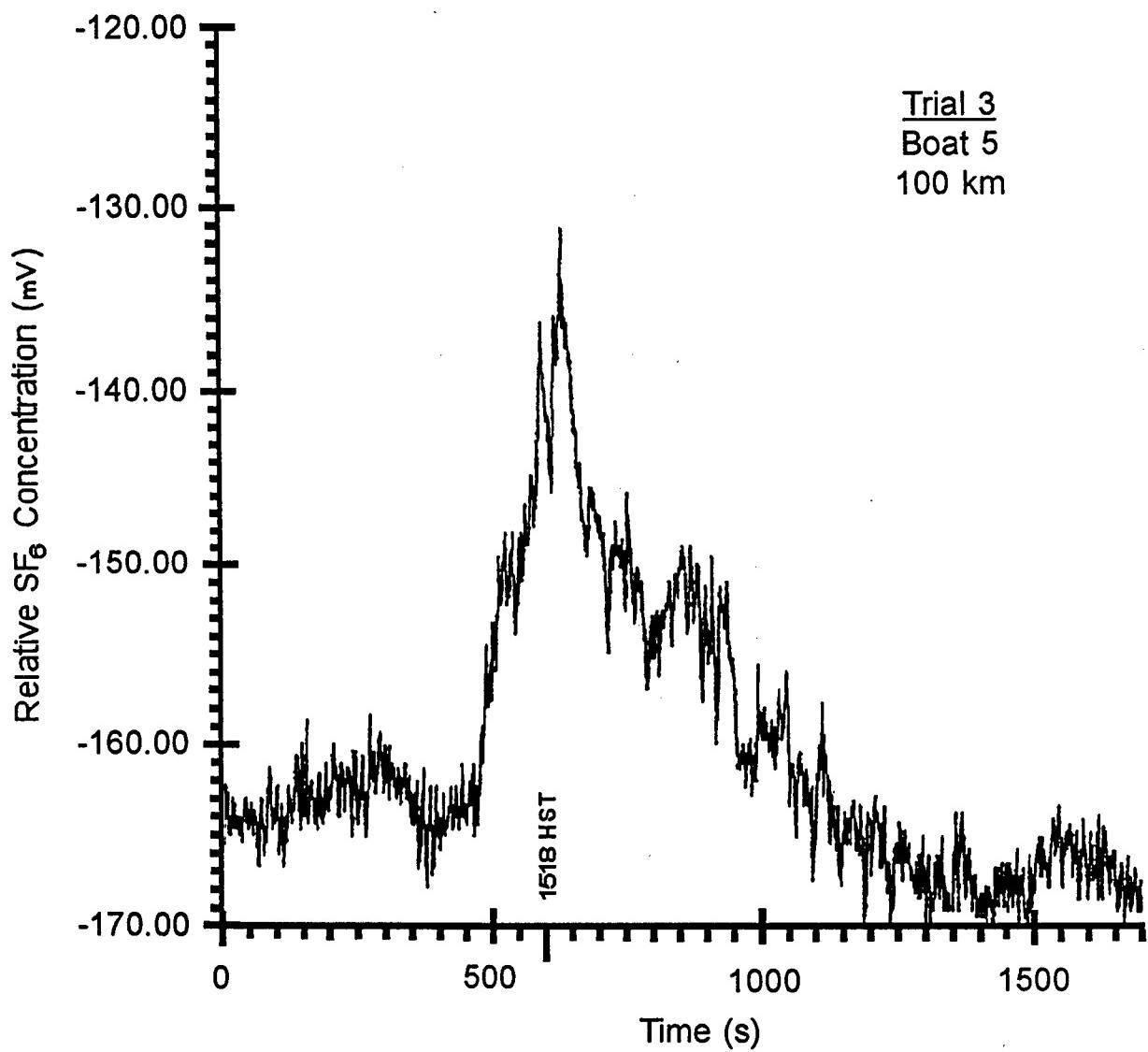
FIGURE 3. Real-time analyzer relative SF_6 concentration versus time for Boat 5 (100 km) during Trial 3.
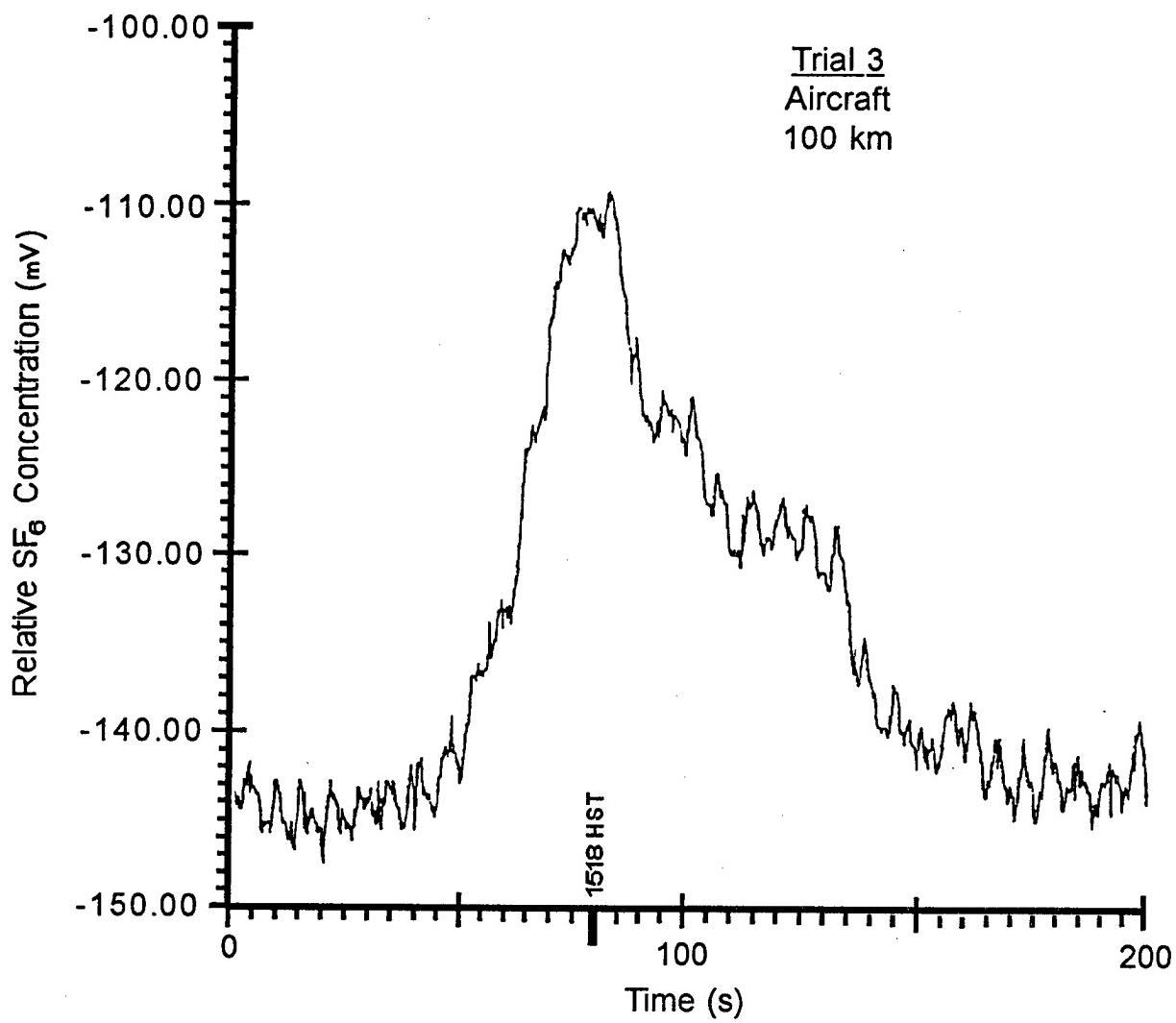
FIGURE 4. Real-time analyzer relative SF$_6$ concentration versus time for an eastbound aircraft traverse through the cloud at 100 km downgrid during Trial 3.

REFERENCES

1. Nickola, P. W., 1971: Measurements of the movement, concentration and dimensions of clouds resulting from instantaneous point sources. <u>Journal</u> <u>of</u> <u>Applied</u> <u>Meteorology</u>, <u>8</u>, 962-973.

2. Wilson, D. J., 1981: Along-wind diffusion of source transcients. <u>Atmospheric</u> <u>Environment</u>, <u>15</u>, 489-495.

3. Bowers, J. F., 1992: Literature review of long-range overwater transport and diffusion. Report No. DPG/JOD-92/036, U.S. Army Dugway Proving Ground, Dugway, UT.

4. Bowers, J. F., 1993: Customer test plan for Long-Range Overwater Diffusion Experiment. Report No. DPG-TP-93-353, U.S. Army Dugway Proving Ground, Dugway, UT.

5. Turner, D. B., 1964: A diffusion model for an urban area. <u>Journal</u> <u>of</u> <u>Applied</u> <u>Meteorology</u>, <u>3</u>, 83-91.

6. Schacher, G. E., D. E. Speil, K. L. Davidson and C. W. Fairall, 1982: Comparison of overwater stability classification schemes with measured wind directions variability. Naval Postgraduate School Report No. NPS-61-82-002 prepared for Bureau of Land Management, Los Angeles, CA.

AIRFLOW INDICES AND CHARACTERISTICS WITHIN AND ABOVE REGULAR AND IRREGULAR ROUGHNESS DOMAINS

Brian L. Orndorff and Ronald M. Cionco

US Army Research Laboratory
White Sands Missile Range, NM 88002

ABSTRACT

To better understand and also model the structure of airflow in the boundary layer and within canopy domains, a variety of boundary layer and canopy indices and characteristics must be calculated and documented. One must know and understand the flow characteristics of your scenario before simulating flow over complex terrain and within, above, and around significant roughness domains such as vegetative canopies. Atmospheric stability, surface roughness effects, effect of wind direction and fetch are a few of the flow features that must be understood. Using the Project WIND data (Phase I), one can analyze and characterize these flow features for a geometrically nice roughness domain such as WIND's orchard as well as for an irregular domain in mountainous terrain such as WIND's coniferous forest. Vertical wind profile structures and indices such as the mixing length and intensity of turbulence are calculated for the ambient flow. Within the canopy domains, vertical profiles and indices of canopy flow, mixing length, canopy coupling ratio, intensity of turbulence, and other factors are calculated to help quantify these domains and their differences.

1. INTRODUCTION

A variety of boundary layer and canopy indices and characteristics can be calculated to characterize the airflow structure in the boundary layer and within canopy domains. Knowledge of these quantifiers and descriptors aid in the understanding and modeling of airflow in the boundary layer and within canopy domains. Atmospheric stability, surface roughness effects, effect of wind direction and fetch are a few of the ambient flow features that must be understood.

Results of analyses of micro-meteorological data from two

171

distinct canopies are presented. Using the Project WIND data (Phase I)(Cionco, 1989a), flow features have been analyzed and characterized for a geometrically regular roughness domain such as WIND's almond orchard (Orchard) as well as for an irregular domain in mountainous terrain such as WIND's ponderosa pine forest (Forest).

Project WIND was a multiple scale field study (Cionco, 1989b) conducted over northern California. The purpose of this study was to evaluate meteorological models and to better understand the structure of micro- and meso-scale airflow in and above the boundary layer and within canopy domains. In this paper, the micro-meteorological data base that was collected over two major high-resolution domains are being analyzed.

The analyses includes vertical wind profile structures and indices calculated for the ambient flow. Within the canopy domains, vertical profiles and indices of canopy flow, mixing length, canopy coupling ratio, intensity of turbulence, and other factors are calculated to help quantify the Orchard and Forest domains and their differences. Initial calculations are showing that values of canopy flow index, coupling ratio, intensity of turbulence, surface roughness etc. differ significantly from the Orchard to the Forest.

2. MEASUREMENTS

The majority of data from Project WIND was obtained within two 5 km by 5 km micrometeorological domains (Cionco, 1989b). One site, called the Orchard, was located on relatively flat terrain with orchard of uniformly spaced almond trees. The other site, called the Forest, was located on complex terrain with a randomly spaced forest. Figure 1 shows the location of the two micrometeorological sites within the mesoscale domain in Northern California.

The vertical structure of the surface layer was documented at the Orchard site by three similar eight-level micrometeorological towers. Four levels were located above the canopy and four levels were located below the tree heights of about 8 m.

Similarly, the vertical structure of the surface layer over the Forest site was also recorded by three eight-level micrometeorological towers. Two levels were located above the canopy and six levels were located below the tree heights of approximately 24 m.

Towers OT-1 and FT-1 were located in the Orchard domain and Forest domain, respectively, within substantial clearings distant from any trees. Towers OT-2 and FT-2 were located just inside of the edge of the Orchard and Forest canopies, and towers OT-3 and FT-3 were located well within the Orchard and Forest canopies, respectively.
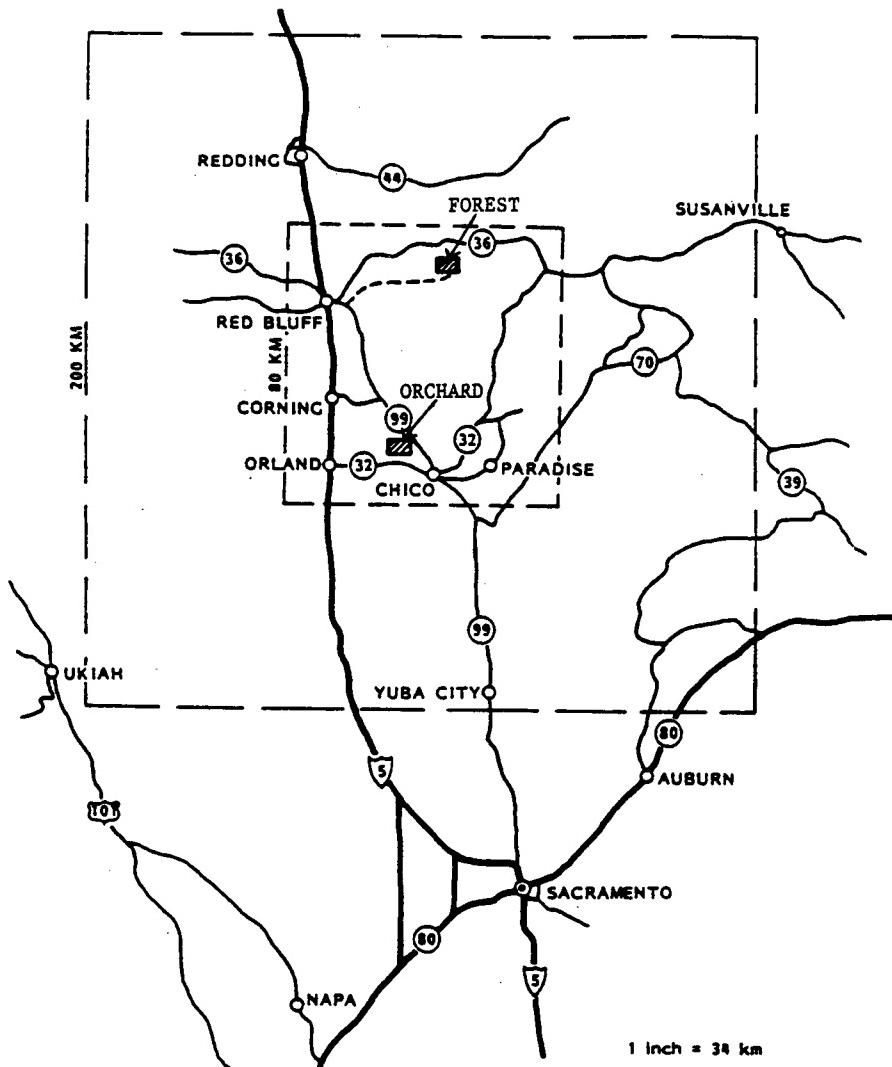
Figure 1. Map of Project WIND domain with locations of Orchard and Forest micrometeorological domains.

All data used in this analysis were acquired from either Orchard tower OT-3 or Forest tower FT-3. Characterization and analyses of the vertical structure of the surface layer were performed for primarily daytime conditions from 0900 to 1500 PST on 24 June 1985.

3. RESULTS

Figure 2 shows the almond tree silhouette next to a normalized composite wind profile during the day on 24 June. As expected, the wind speed above the tree heights displays a logarithmic type of decay. It also demonstrates the greater extraction of momentum that is occurring due to the tree canopies. A semi-log plot indicates that there is an exponential decay of the wind speed within the crown below the tree tops. However, below the main part of the crown the wind speed again slows at a smaller rate.

173
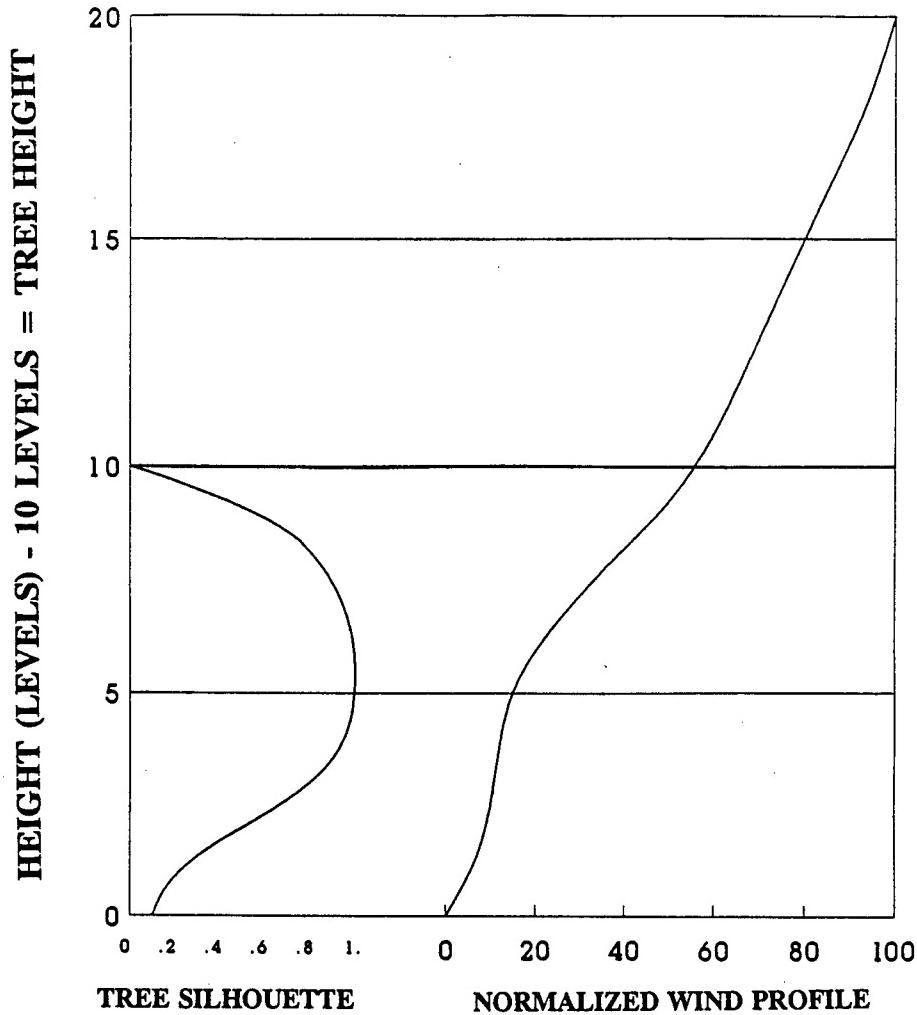
Figure 2. Almond orchard tree silhouette (left) and normalized composite (0900-1600 PST) wind profile (right) at OT-3 to two tree heights. Height is in computation levels where 10 levels equal one tree height (8 m).

In the Forest shown in figure 3, the wind exhibits a similar type of behavior as the Orchard. Above the tree heights the wind speed shows a logarithmic decay and within the crown area the wind speed shows an exponential decay. However, the Forest wind profile differs from the Orchard profile down in the trunk space. Within this region the wind speed increases slightly toward the ground, except when it is close to the ground. The increase is due to the long trunks which result in a large amount of space between the trees from 0 to 5 levels in height.

Figure 4 presents a profile of the composite mixing length for Orchard tower OT-3 during the daytime for 24 June. This figure shows the significantly reduced mixing length or eddy sizes within the Orchard tree crowns between levels 5 and 10. It also displays the expansion of the eddies just below the main tree crowns at about level four.

174
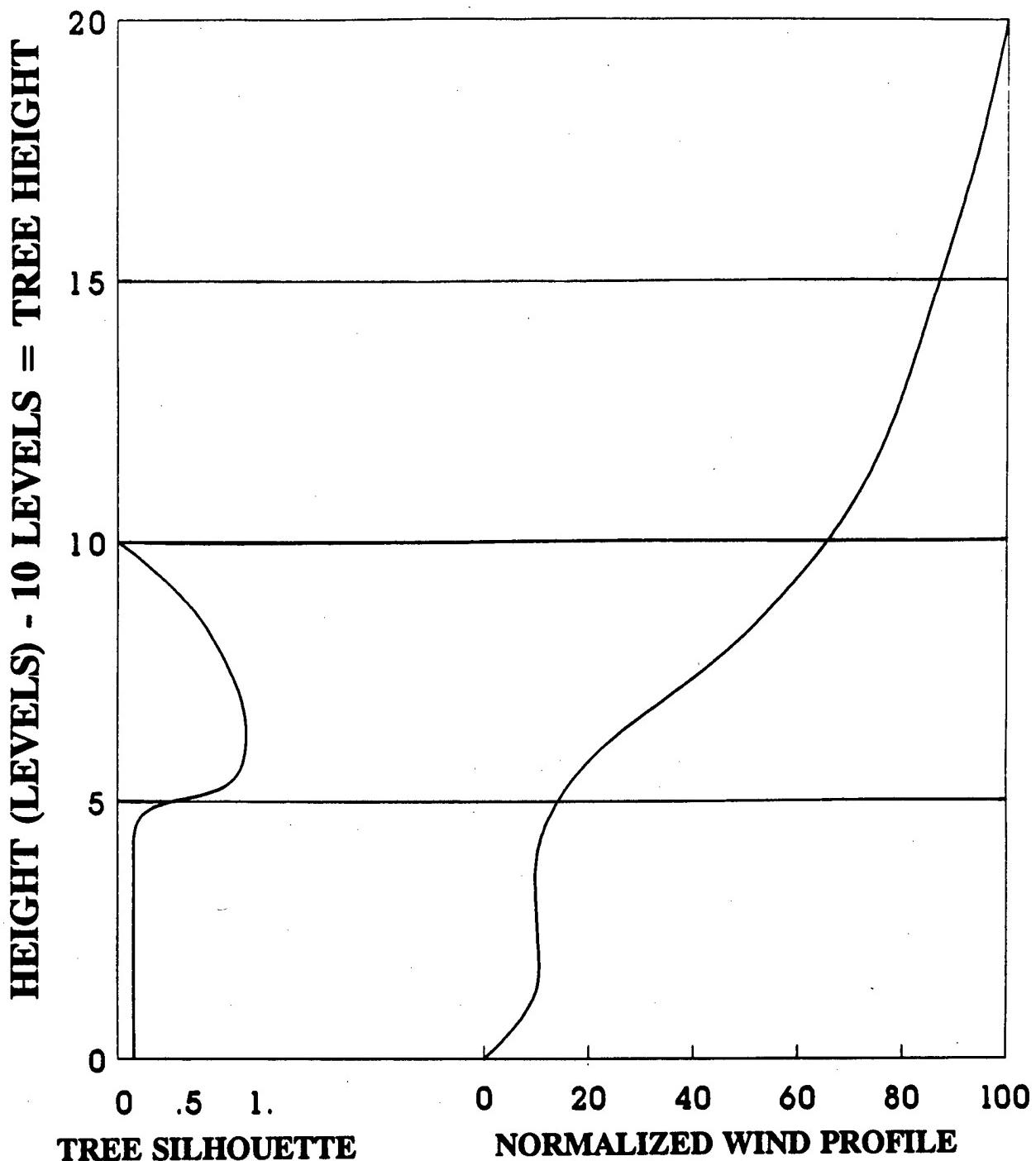
Figure 3. Pine forest tree silhouette (left) and a normalized composite (0900-1600 PST) wind profile (right) at FT-3 to two tree heights. Height is in computation levels where 10 levels equal one tree height (24 m).
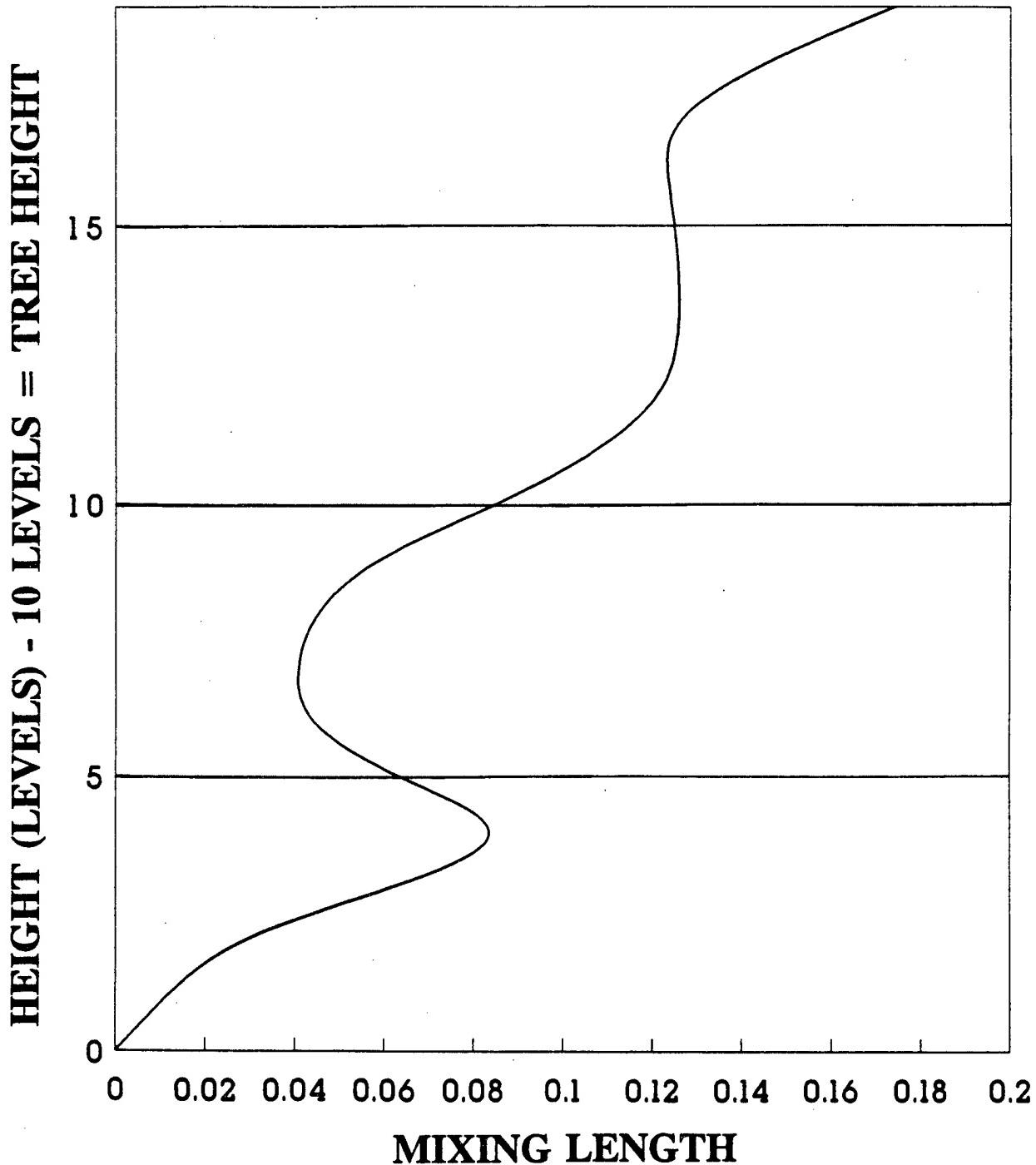
Figure 4. Composite mixing length profile at Orchard site OT-3 on
24 June 1985. Composite is composed of hours 0900-1600 PST.

Figure 5 shows a profile of the composite mixing length for Forest tower FT-3. This figure also indicates that there is a significant reduction in eddy sizes as the winds approach the tops of the pine trees from above. The mixing length also increases just below the main tree crowns at about level 6 indicating expansion of the eddies. The mixing length is not shown below level 5 because the method used for determining mixing length does not work well when the wind profile does not approach the exponential relationship due to the great amount of trunk space in the pine forest.
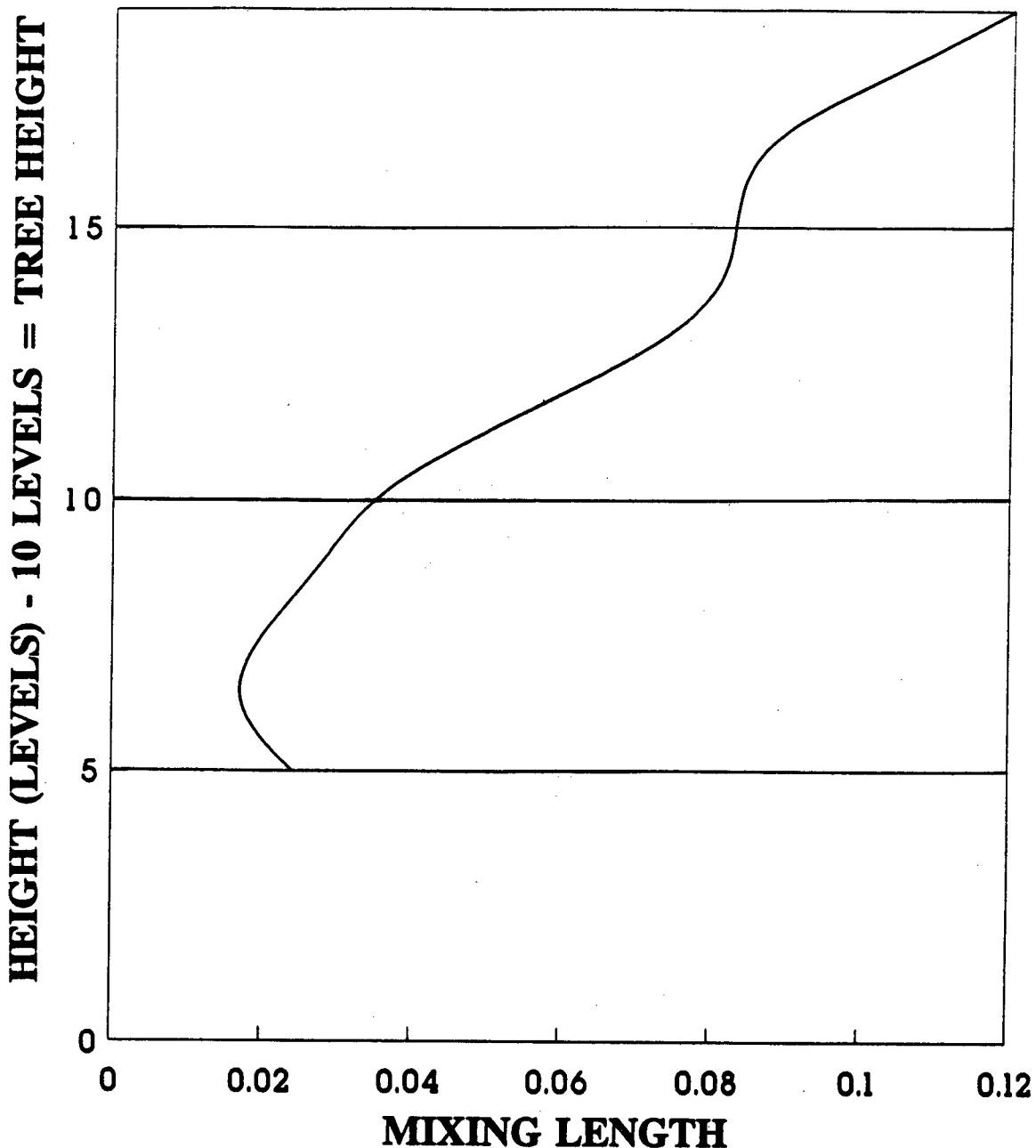
Figure 5. Composite mixing length profile at Forest site FT-3 on 24 June 1985. Composite is composed of hours 0900-1600 PST.

Time PST	ORCHARD				FOREST			
	a	R_c	$I_T(u+v)$ SL/CAN	WS/WDIR M/S Deg.	a	R_c	$I_T(u+v)$ SL/CAN	WS/WDir M/S Deg.
0400		0.07		1.11/23°				
0500		0.06		1.26/65°				
0600		0.06		3.77/336°				
0700		0.10		5.18/336°				
0800		0.09		5.10/334°				
0900	2.18	0.10	0.19/0.37	4.97/330°	4.59	0.18	0.44/0.73	1.66/258°
1000	2.46	0.10	0.18/0.36	4.96/329°	3.84	0.12	0.39/0.90	2.41/259°
1100	2.13	0.11	0.19/0.34	4.98/325°	3.88	0.13	0.32/0.64	3.17/276°
1200	2.46	0.11	0.19/0.41	4.92/320°	2.52	0.11	0.42/0.73	3.11/287°
1300	2.44	0.10	0.20/0.40	4.74/322°	4.19	0.14	0.53/0.83	2.57/305°
1400	2.29	0.12	0.14/0.33	5.75/335°	3.54	0.14	0.49/0.83	2.87/294°
1500	2.48	0.13	0.19/0.33	5.73/340°	5.17	0.16	0.55/1.00	2.48/332°
AVG	2.35	0.11	0.19/0.37	4.85/330°	3.96	0.14	0.45/0.81	2.61/287°

Table 1. Canopy flow index (a), canopy coupling ratio (R_c), intensity of turbulence ($I_{t horizontal}$) in the surface layer (SL) and in the canopy (CAN), wind speed (WS) and wind direction (WDIR) for Orchard tower OT-3 and Forest tower FT-3 during 24 June, 1985. Orchard wind speed and direction are at 1.46 tree heights (11.68 m) while the forest wind speed and direction are at 1.25 tree heights (30.0 m). Average Orchard values for R_c and wind speed and direction are calculated from 0700-1500 PST.

Table 1 presents indices for both the Orchard and Forest locations. The average canopy flow index of 2.35 for the Orchard is significantly less than the index of 3.96 for the Forest. This is due to the shorter, uniformly spaced trees in the Orchard and the taller, nonuniformly spaced pine trees with long trunks in the Forest.

The coupling ratio (Cionco, 1983) is the wind speed at about 0.25 tree heights versus the wind speed at approximately 1.40 tree

heights. The average coupling ratio of 0.11 for the Orchard is different from the coupling ratio of 0.14 for the Forest. The greater coupling ratio of the Forest may be due to the deeper penetration of the ambient flow into the enlarged trunk space of the Forest resulting in greater coupling between the near surface and the surface layer above the pine trees.

Intensity of turbulence is the ratio of the root mean square of the horizontal wind speed fluctuations to the mean horizontal wind speed. Average intensity of turbulence values of 0.19 and 0.37 for the Orchard surface layer and canopy layer, respectively, are also significantly different from the corresponding values of 0.45 and 0.81 for the Forest. These values indicate there is more turbulence within and above the Forest canopy than the Orchard canopy. The overall lower speeds within and above the forest contribute to higher intensity values.

The average wind speed of 4.85 m/s and wind direction of 330° above the Orchard differs considerably from the average wind speed of 2.61 m/s and wind direction of 287° above the Forest. The differences in wind speed and direction are caused by the presence and interaction of the different terrain and tree types. The Orchard is under the influence of well-established valley flow while the Forest is in the slower daytime upslope flow with notable frictional effects.

Transition values (0400-0700 PST) of coupling ratio and wind speed and direction are shown for the Orchard in table 1. A comparison between the winds during the early morning and during daytime hours indicates that the wind flow during transition is disorganized and very light. This is also shown by the very low values of the coupling ratio which averages about 0.06.

4. CONCLUSIONS

Quantifying the differences of the above indicies and characteristics corroborates our expectations. More important is that we are providing two more sets of canopy values to the existing tables of indices and characteristics reported by Cionco (1983) and others.

There are a few similarities between the micrometeorological characteristics and indices for the Orchard and the Forest. Both the Orchard and the Forest appear to have similar wind profiles and mixing length profiles within the tree crowns and above the tree tops.

There are also significant differences between the indices for the Orchard and Forest. For the Orchard, the canopy flow index, coupling ratio and turbulence intensity values are the order of 2.35, 0.11 and 0.37. During the pre-sunrise disorganized flow, the coupling ratio averages 0.06 for the Orchard which is about

179

one-half the daytime magnitude. For the Forest, the canopy flow index, coupling ratio and turbulence intensity values are the order of 3.96, 0.14 and 0.81. Above the Forest, the turbulence intensity values average 0.45 while values for the Orchard average 0.19.

REFERENCES

Cionco, R. M., 1989a: Micrometeorological Measurements of Canopy Domains during PRoject WIND. 19th Conference on Agriculture and Forest Meteorology, American Meteorology Society, Boston, Mass., 165-168.

Cionco, R. M., 1989b: Design and Execution of Project WIND. 19th Conference on Agriculture and Forest Meteorology, American Meteorology Society, Boston, Mass., 156-159.

Cionco, R. M., 1983: On the Coupling of Canopy Flow to Ambient Flow for a variety of Vegetation Types and Densities. Boundary-Layer Meteorology, 6, 325-335.

THE RADIATIVE ENERGY BALANCE AND REDISTRIBUTION (REBAR) PROGRAM

Young P. Yee
Robert A. Sutherland
U.S. Army Research Laboratory
Battlefield Environment Directorate
White Sands Missile Range, NM 88002

Roger Davis
Stephen W. Berrick
Montie Orgill
Science and Technology Corporation
Las Cruces, NM 88011

ABSTRACT

The Radiative Energy Balance And Redistribution (REBAR) program, written in FORTRAN 77, is an integrated set of models to help assess the effects of aerosols on the local meteorology. One research objective is to determine the impact of large-area screening systems on the immediate battlefield. REBAR consists of aerosol, radiative, energy balance, atmospheric stability, and turbulence computer modules that together address important changes in optical and meteorological processes when a large aerosol cloud is present. REBAR gives the user the option of defining natural atmospheric irradiance either through simplified empirical relations or through interfacing with the LOWTRAN module of EOSAEL92. Aerosols may significantly affect electromagnetic propagation through scattering, absorption, and thermal emission depending on the mass density, size distribution, and optical properties of the aerosol cloud. These processes will alter the solar/sky radiation incident on the ground surface thereby changing the surface energy balance budget. Using simplifying relationships and empirical parameterizations, an estimate of the sensible heat flux can be calculated. Meteorological measurements at a reference height can then be used to determine the associated Pasquill categories and the optical turbulence structure parameters. The ARL High Resolution Wind model developed by Cionco will be used to determine wind flow fields and vegetation height and type over a designated complex terrain location.

1. INTRODUCTION

The presence of aerosols in the atmospheric boundary layer can have a significant impact on electromagnetic propagation through the processes of radiation absorption, emission, and scatter. Advection or generation of natural and/or battlefield induced aerosols can alter the local atmospheric stability and the vertical profiles of temperature and humidity. These changes in turn can alter the vertical profiles of optical turbulence and therefore image propagation. Aerosols can have a global impact on the atmosphere and perhaps initiate large scale climate changes. The primary interest here is the short term effects that can occur in the microscale regions. The impact would be most significant in the unique battlefield situation where aerosol loading from various sources involving smokes and dust can be extreme. The aerosols act in two ways, (a) to diminish either by scattering or absorption the amount of radiation reaching the surface and thus alter the surface energy balance, and (b) to increase atmospheric absorption and thermal emissions and thus alter radiative heating and cooling rates in the boundary layer. Sadot and Kopeika (1992) have found statistical evidence that scintillations are affected by aerosols, especially under heavy aerosol loading conditions.

The Sutherland-Hansen-Bach (SHB) stability algorithm is used to determine effects of aerosol loading on the local temperature/humidity profiles and from this we use the Rachele-Tunick method for determining the optical turbulence structure function, C_n^2. Previous calculations have shown that for moderate aerosol loading (optical depth on the order of unity) the radiative effects can alter stability greater than one Pasquill category depending upon the scattering albedo of the aerosol and the existing meteorological conditions (Yee, et al., 1993).

2. THE REBAR PROGRAM CONCEPT

The Radiative Energy Balance And Redistribution (REBAR) program is a set of aerosol related, radiative, energy balance, stability, turbulence, and complex terrain programs to help assess the effects of aerosols on the local meteorology. The REBAR is being developed to assist in the analysis of atmospheric stability and turbulence structure in the local environment when aerosols are introduced into the lower atmosphere. The computer codes are written in FORTRAN 77 and a majority of the programs can be run in stand alone mode. The initial approach is to consider simplified scenarios in which individual computer modules can be called in a logical sequence to minimize the number of user inputs.

Figure 1 is a flow chart overview of the major processes involved in the assessment of atmospheric stability and optical turbulence. The first step in REBAR is the calculation of the atmospheric transmittance either through empirical formulations using the CLEARRAD module or through a more rigorous treatment using the LOWTRAN module. There are two situations to consider; no smoke and smoke case. In the no smoke or no aerosol cloud case,
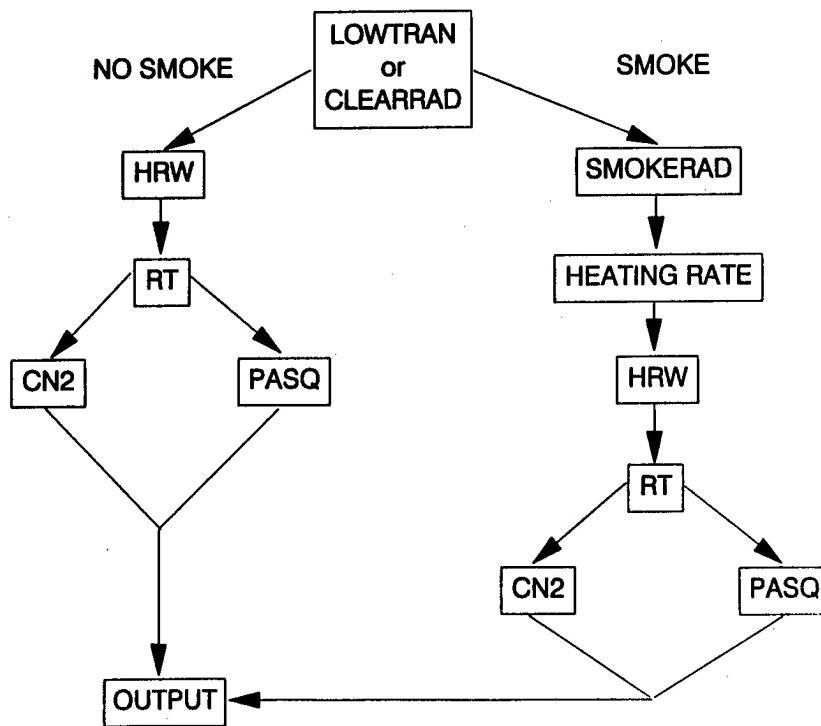
Figure 1. Flow chart overview of the Radiation Energy Balance and Redistribution (REBAR) Program

the high resolution wind (HRW) module is used next to define the current wind field over complex terrain. The wind speed, vegetation height and type, and temperature fields are then passed to the Pasquill (PASQ) and the Rachele/Tunick (RT) module for the calculation of Pasquill category and optical turbulence. In the smoke or aerosol case, the module SMOKERAD computes the downward radiation on the ground surface. After a heat differential term is estimated and used as input into the HRW module, the associated Pasquill category and optical turbulence parameter at each grid point in the terrain map is calculated.

3. DESCRIPTION OF REBAR MODULES

3.1 CLEARRAD Module

The CLEARRAD module (Sutherland and Fowler, 1985) models atmospheric radiation levels at the earth surface for visible wavelengths. The code employs empirical equations to simplify the computations.

INPUTS: Solar Zenith Angle, Day of Year, Solar Irradiance at Top of Atmosphere, Surface Albedo, Atmospheric Single Scattering Albedo, Empirical Constants

OUTPUTS: Direct (Solar) Irradiance, Diffuse (Sky) Irradiance, Reflected (Surface) Irradiance, Global Irradiance (Direct and Diffuse Components)

3.2 LOWTRAN Module

The clear air vertical optical depth can be computed for various meteorological conditions using the atmospheric transmittance code LOWTRAN (Kneizys, et al., 1988). The LOWTRAN module is a computer code that calculates atmospheric transmittance and radiance for horizontal, vertical, and slant paths. The code is capable of providing atmospheric transmittance based on different model atmospheres and aerosol models.

INPUTS: Atmospheric Model, Stratospheric Model, Season Model, Cloud/Rain Model, Solar Zenith Angle

OUTPUTS: Shortwave Downward Irradiance, Longwave Downward Irradiance

3.3 SMOKERAD Module

The SMOKERAD module (Sutherland, 1988) employs generalized methods for obtaining computationally efficient approximations to the radiative transfer equations. Combining both scaling algorithms and precalculated look-up radiative transfer tables, direct and diffuse components of radiation propagated along a path can be estimated. The radiative transfer tables are based upon solutions to the radiative transfer equation obtained in the plane parallel approximation assuming a Henyey-Greenstein form for the phase function. The computer code can account for both single and multiple scattering from the direct solar beam, uniform diffuse skylight, and reflection from the underlying surface.

Part of the downward components of solar and sky irradiance calculated by either CLEARRAD or LOWTRAN will be diffusely reflected upward from the top of an aerosol cloud and some will be transmitted downward through the cloud and some will be absorbed and emit thermal radiation depending on its optical properties and density.

INPUTS: Irradiance at Top of Smoke Cloud, Single Scattering Albedo of Smoke Aerosol, Optical Mass Extinction Coefficient Surface Albedo

OUTPUTS: Shortwave Downward Irradiance from Cloud Bottom, Direct and Diffuse Irradiance

3.4 ENERGY BALANCE Module

Numerous energy balance models are available in the literature varying from simple to complex and requiring from a few to a multitude of inputs. Figure 2 is a typical energy balance scenario in which solar radiation is incident on the ground surface for a clear air case and for one where an aerosol cloud is present.

184
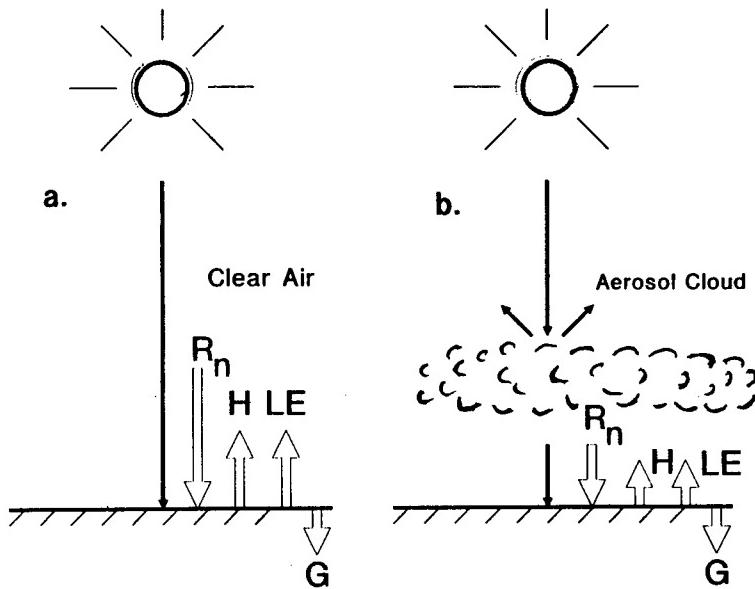
Figure 2. Energy Balance schematic for (a) clear air scenario and (b) aerosol cloud scenario. The net radiation, R_n, is balanced by the sensible heat and latent heat flux, H and LE, and the ground heat flux, G.

During the day, a large area aerosol cloud can substantially decrease the downward net radiation reaching the surface. The net radiation is balanced by the sensible heat flux, the latent heat flux, and the ground soil heat flux. In the initial treatment of the REBAR program, the Bowen ratio method for surface fluxes and the Rachele and Tunick (1992) energy balance model for imagery and electromagnetic propagation were used for beta testing. Although the Bowen ratio can vary with time and weather conditions over any particular site, this approach is simple and the number of input parameters are few. In the Bowen energy balance module the input and output parameters are as follows.

    INPUTS: Net Radiative Flux, Bowen Ratio, Soil Heat Flux

    OUTPUTS: Turbulent Sensible Heat Flux, Latent Heat Flux

3.5 PASQIL Module

The PASQIL module is used to calculate the atmospheric stability using the method proposed by Sutherland et al. (1986). An exponential expression, based upon the Kazanski-Monin stability parameter and modified to account for effects of surface roughness, was formulated to relate wind speed and sensible heat flux density to Pasquill stability class.

    INPUTS: Wind Speed, Sensible Heat Flux, Surface Roughness
               Parameter, Ambient Air Temperature, Reference
               Height, Specific Heat Capacity of Air, Air Density

185

OUTPUTS: Pasquill Stability Category, Friction Velocity, the Monin-Obukhov Parameter

3.6 RACHELE/TUNICK Turbulence Module

The atmospheric environment affects imagery and electromagnetic propagation. An important parameter in assessing atmospheric effects on imaging is the optical turbulence structure parameter. The RACHELE/TUNICK module (Tunick and Rachele, 1991) calculates the optical turbulence structure parameter C_n^2 for visible to mid-infrared wavelengths from estimates of temperature and moisture gradients. The temperature and moisture gradients in turn can be approximated from sensible and latent heat flux estimations which can be obtained from radiation/energy balance equations. In this module, a semiempirical model has been developed to require a minimum number of conventional measurements at a reference level.

INPUTS: Solar Zenith Angle, Reference Height, Specific Heat Capacity of Air, Shortwave Downward Irradiance, Longwave Downward Irradiance, Neutral Point Time, Neutral Point Temperature, Cloud Cover, Surface Roughness Parameter, Wind Speed, Air Density, Ambient Air Temperature, Pressure, Specific Humidity, Surface Albedo, Time of Day, Wetness Factor, Sensible Heat Flux, Latent Heat Flux

OUTPUTS: Monin-Obukhov Length, Friction Velocity, Optical Turbulence Parameter, Temperature and Specific Humidity gradients

3.7 Complex Terrain Module

The HRW complex terrain module is largely based on Cionco's (1985) High Resolution Wind model which determines surface wind fields at sub-mesoscale resolution over complex terrain. The geographically re-locatable analysis exploits detailed topographic information and requires meteorological measurements at only one grid point inside the designated area. Starting from initial estimate of the wind and temperature, a direct variational relaxation is performed to minimize the "constraint" in the sense of Gauss' Principle of Least Constraints (Lanczos, 1962) as applied to fluid flows. The computation uses one constant-thickness layer, the volume between a user selected computation height and the terrain surface. Within the warped computational layer which follows the terrain the wind and temperature fields are adjusted as permitted by terrain geometry and conservation laws to minimize the dynamic constraint. The resulting wind and temperature fields provide an estimate conformable with input information and physical laws. The module uses a sigma coordinate-terrain following system and can model an area as large as 20 x 20 km. Each area can then

186

be subdivided into a maximum of 50 x 50 flux cells. The distance between grid points can be varied from 60 to 400 meters (Byers and Cionco, 1992)

INPUTS: Archived Terrain Data Base that includes the Effective Terrain Elevation, Surface Roughness, Vegetation Height, Vegetation Type; An Upper Air Meteorological Sounding that includes Temperature, Relative Humidity, Wind; A Surface Heating Parameter

OUTPUTS: Relaxed Wind and Potential Temperature Field, Richardson's Number, Friction Velocity, Impaction Vertical Motion, and Wind Power Law Profile

4. PRELIMINARY RESULTS

4.1 Aerosol Effects on Atmospheric Stability

Figure 3 depicts Pasquill stability as a function of solar elevation for several aerosol densities at a wind speed of 6 m/s. At a solar elevation of 90°, the stability changed by one Pasquill category when the optical depth (Tau) increased from 0.5 to 2.0.

PASQUILL STABILITY vs SOLAR ANGLE
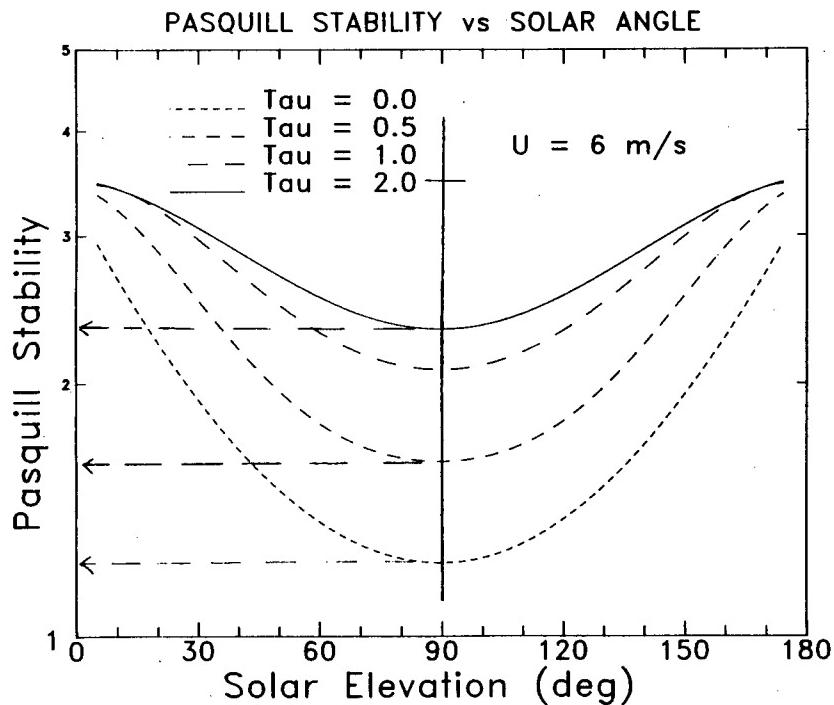
Figure 3. Aerosol induced radiative interactions effect on the atmospheric stability for aerosol optical depths from Tau=0 to 2.0. The wind speed is 6 m/s.

4.2 Aerosol Effects on Optical Turbulence

Figure 4 shows aerosol induced radiative interactions effect on the optical turbulence versus solar elevation for wind speed of 6 m/s. At a solar elevation of 30° the turbulence parameter can change an order of magnitude when the aerosol optical depth varied from 0 to 1.0.

TURBULENCE PARAMETER (E-14) vs SOLAR ANGLE
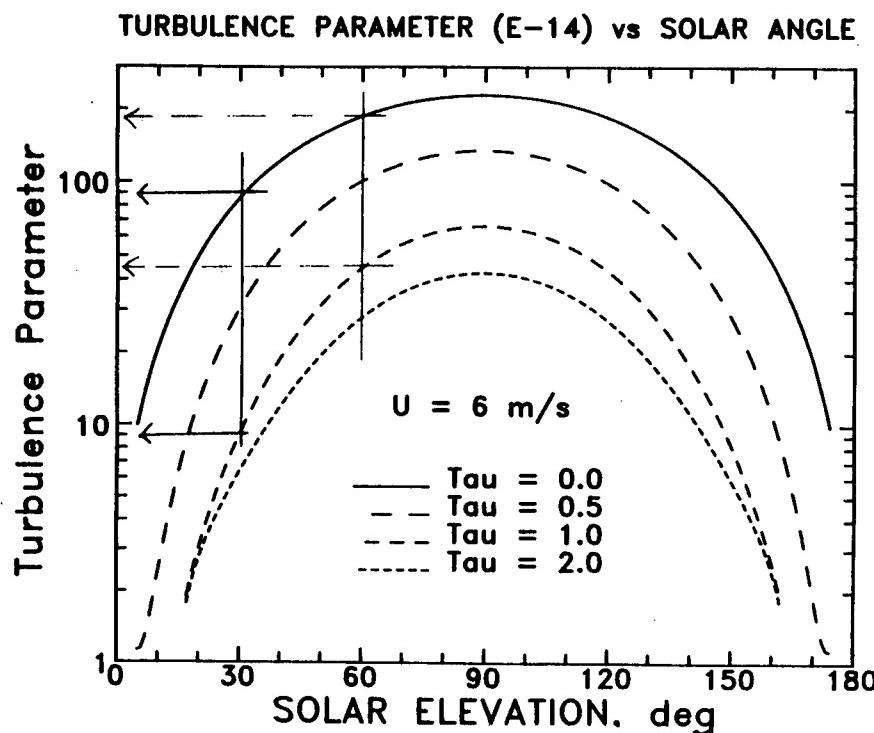
Figure 4. Aerosol induced radiative interactions effect on the optical turbulence parameter C_n^2 for aerosol optical depths Tau=0 to 2.0. The turbulence parameters shown need to be multiplied by 10^{-14} for proper scaling. The wind speed is 6 m/s.

4.3 Aerosol Effects over Complex Terrain

To demonstrate how aerosol interactions can affect atmospheric stability and optical turbulence over complex terrain, terrain data was obtained from the MADONA experiment that was conducted at Porton Downs, United Kingdom (Cionco and Byers, 1993). Figure 5 shows a wind vector field over the test site along with elevation contours. A fog oil smoke cloud is used for illustrative purposes. For the calculations of stability and turbulence fields, the REBAR input parameters used for the test runs are given in Table 1.

TABLE 1
REBAR input parameters used for model simulations.

Meteorological Data:

Ambient Air Temperature: 24 deg C
Relative Humidity: 45%
Atmospheric Pressure: 1013.25 mbar
Air Density: 0.00129 g cm^{-3}
Specific Heat Capacity of Air: 0.2403 cal g^{-1} deg C^{-1}
Wind Speed: 2.828 m s^{-1}

LOWTRAN Data:

Atmospheric Model: Mid-latitude Summer
Haze Model: Maritime
Season Model: Determined Solely by Model
Stratospheric Model: Background Stratospheric Profile/Extinction
Cloud/Rain Model: None

Smoke Data (Fog Oil):

Henyey-Greenstein Asymmetry Parameter: g = 0.875
Single-Scattering Albedo: 0.999
Vertical Optical Depths: 0.0, 0.125, 1.0, 2.0

Scene Data:

Solar Zenith Angle: 25.6 deg
Surface Albedo: 0.2
Surface Roughness Parameter: 0.15 m
Heating Rate (for HRW): 5.0 K
Reference Height: 8 m

4.3.1 Atmospheric Stability Fields

In figure 6, the Pasquill category throughout most of the region was around unity for the no smoke case. A stability value of one is considered extremely to moderately unstable. With an aerosol optical depth of 2.0 (Figure 7) the Pasquill category increased to as high as 3 which is slightly unstable to neutral atmospheric conditions.

4.3.2 Optical Turbulence Fields

Figure 8 depicts the calculated turbulent structure parameter contour field without the presence of smoke. In the smoke case the

189
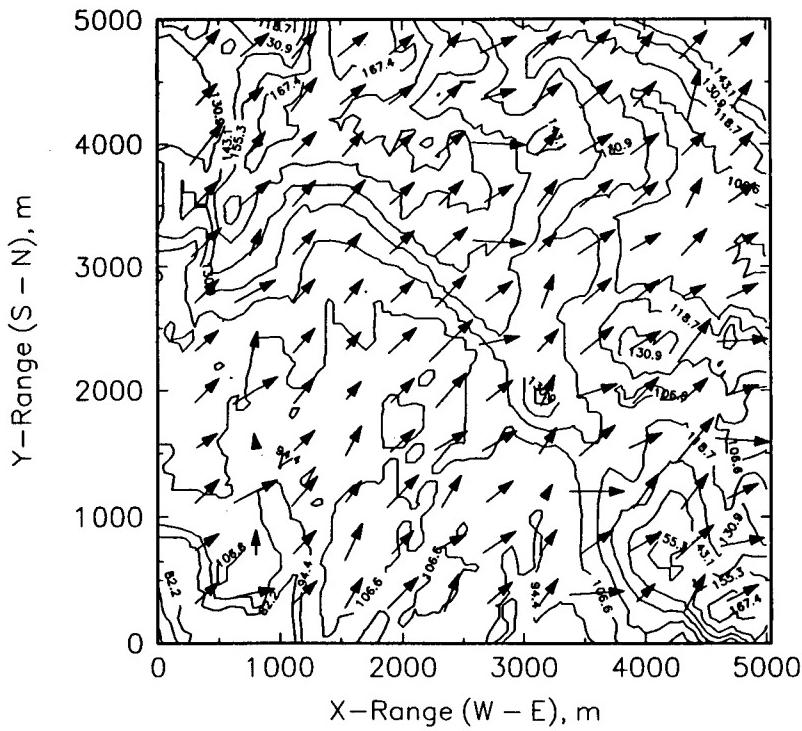
Figure 5. Complex terrain elevation contours (meters) of sample site with wind vector field.

optical depth was 2.0 and the corresponding turbulence field is shown in figure 9. Contour values are scaled logarithmically. Changes in turbulence parameter values between the no smoke and smoke scenarios are as much as two orders of magnitude in certain areas.

5. CONCLUSIONS

The Radiation Energy Balance and Redistribution program is a set of interrelated FORTRAN 77 computer codes to assess the radiative effects of aerosols. The objective of the REBAR is to provide a framework for the analysis of aerosol effects on the energy heat balance at the surface which will affect both the atmospheric stability and turbulence structure. The approach is to consider simplified scenarios in which the various individual computer modules can be invoked in a logical sequence. The computer modules act as building blocks such that input parameters from a particular module may be calculated from a preceding module. In this way the user may not have to obtain a priori input data that may be difficult to measure directly.

Using fog oil as the aerosol cloud, preliminary results have shown changes in atmospheric stability of at least one Pasquill category when aerosol optical depths ranged from 0.5 to 2.0. The aerosol effects mitigated the optical turbulence by at least an order of magnitude in C_n^2 when the aerosol optical depth increased from 0 to 1.0.
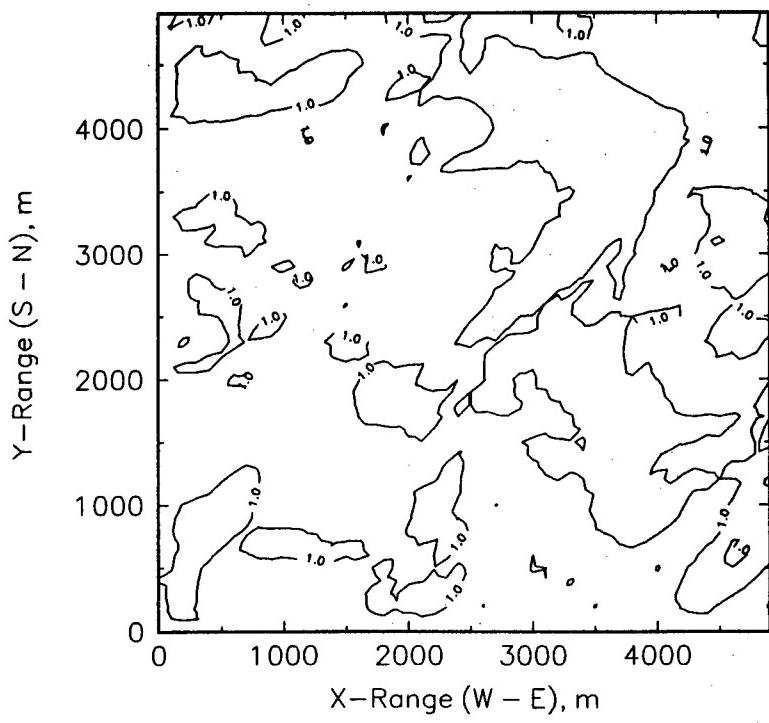
Figure 6. Pasquill stability contours over complex terrain for the no smoke control case.
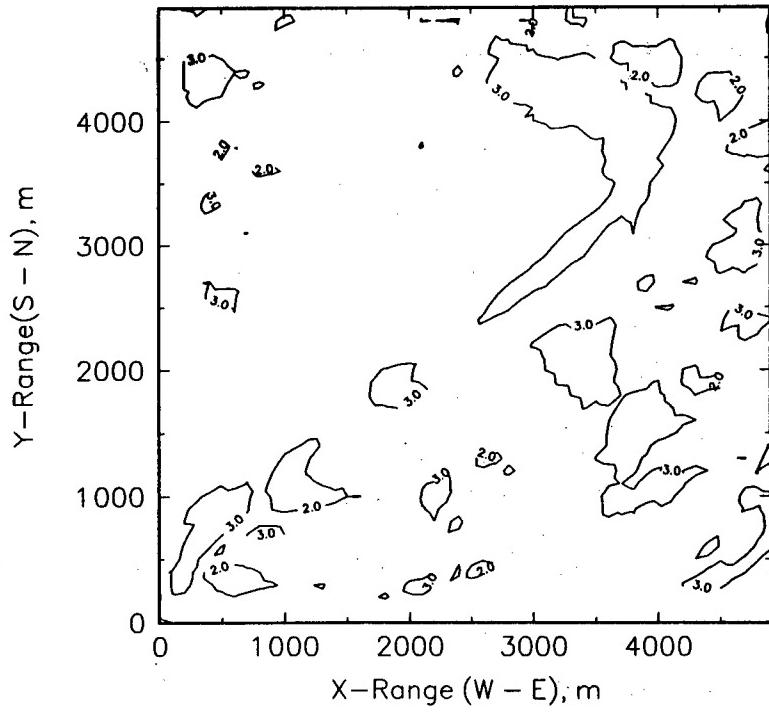
Figure 7. Pasquill stability contours over complex terrain for an aerosol cloud with an optical depth of 2.0.

log(TURBULENT STRUCTURE PARAMETER), m−2/3
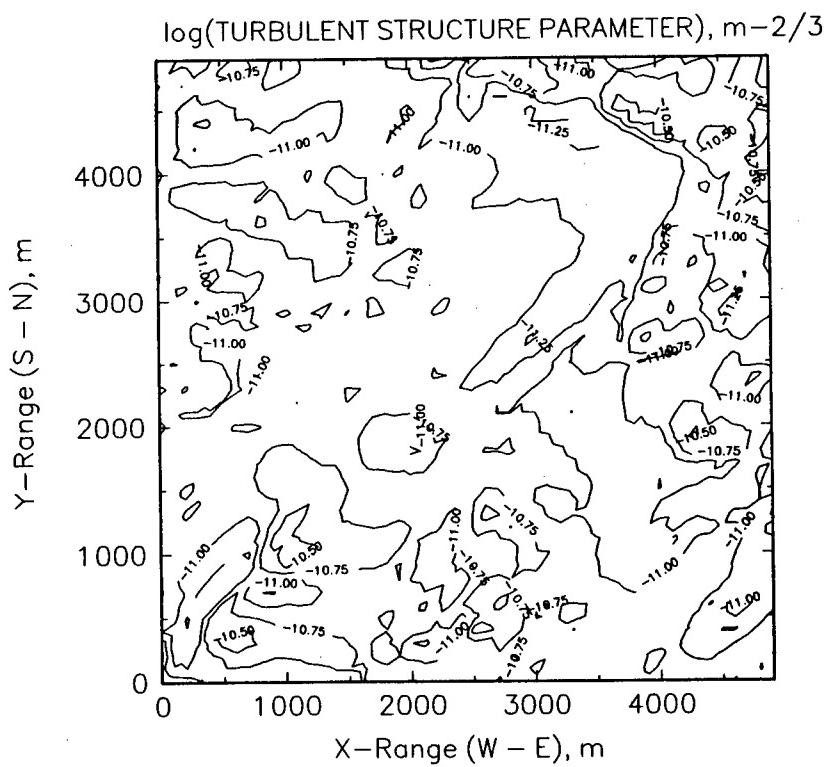
Figure 8. Turbulence structure parameter contours for the no smoke control case. Logarithmaticly scaled values.

log(TURBULENT STRUCTURE PARAMETER), m−2/3
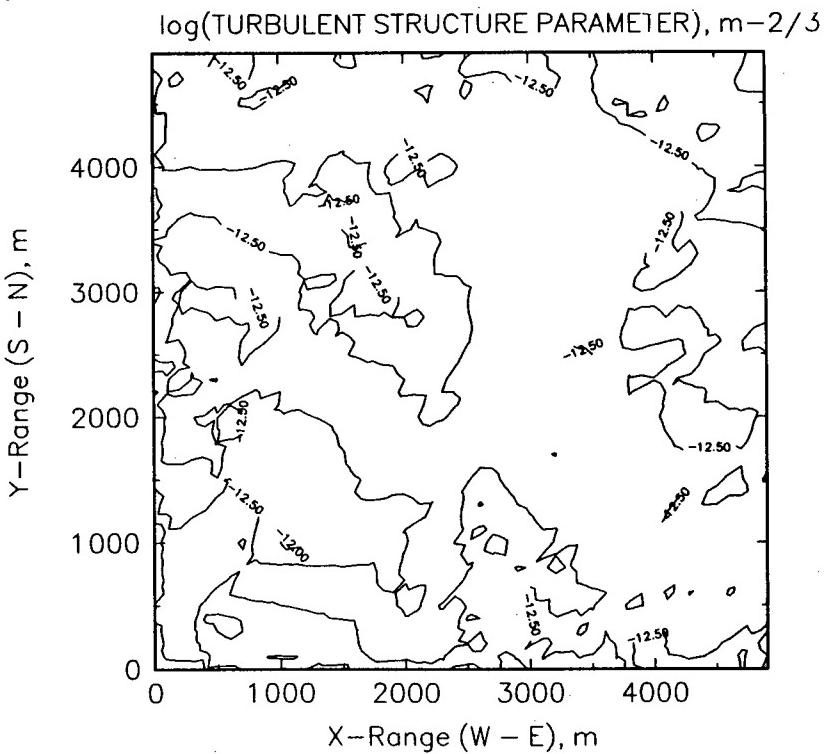
Figure 9. Turbulence structure parameter contours for an aerosol cloud with an optical depth of 2.0. Logarithmicaticly scaled values.

192

For military field operations, two dimensional atmospheric stability and optical turbulence assessment over complex terrain can be invaluable. Incorporation of the ARL High Resolution Wind model into the REBAR program provides this capability. Preliminary results indicated at least one category change in Pasquill stability and up to two orders of magnitude changes in the optical turbulence parameter, C_n^2. Continued research development will include complex terrain interactions over areas as large as 20 x 20 km. Type and height of vegetation over the terrain will be used to calculate two dimensional contours of optical turbulence and atmospheric stability category. These contours maps can then be used in tactical decision aids to estimate image degradation along any line of sight within the defined region.

REFERENCES

Byers, J.H. and R.M. Cionco, Feb 1992: Notes on the Preliminary HRW Code, US Army Atmospheric Sciences Laboratory Report, White Sands Missile Range, NM.

Cionco, R.M., 1985: Modeling Wind fields and Surface Layer Profiles Over Complex Terrain and Within Vegetative Canopies. *Forest-Atmosphere Interactions*, B.A. Hutchinson and B.B. Hicks, editors, D.Reidel Publishing Co., Holland.

Cionco, R.M. and J.H. Byers, 1993: MADONA-An International High-Resolution Meteorology and Diffusion Field Study, Proceedings of the 1993 Battlefield Atmospherics Conference, Las Cruces, NM, 30 Nov-2 Dec, 1993.

Kneizys, F.X., E.P. Shettle, L.W. Abreu, J.H. Chetwynd, G.P. Anderson, W.O. Gallery, J.E.A. Selby, and S.A. Clough, 1988: User's Guide to LOWTRAN 7, AFGL-TR-88-0177, Air Force Geophysics Laboratory, Hanscom Air Force Base, Bedford, MA.

Lanczos, C., 1962, *The Variational Principles of Mechanics*, 2nd edition, University of Toronto Press, Toronto.

Rachele H. and A. Tunick, May 1992: Energy Balance Model for Imagery and Electromagnetic Propagation, *Atmospheric Sciences Laboratory Technical Report #ASL-TR-0311*, White Sands Missile Range, NM.

Sadot, D. and N.S. Kopeika, Feb 92: Forecasting Optical Turbulence Strength on the Basis of Macroscale Meteorology and Aerosols: Models and Validation, *Optical Engineering*, Vol. 31, No. 2, pp 200-212.

Sutherland, R.A. and B.W. Fowler, 1985: Standards for Large Area Screening Systems (LASS) Modeling, Joint Technical Coordinating Group for Munitions Effectiveness (JTCG/ME) Special Report 61 JTCG/ME 85.4.

Sutherland, R.A., F.V. Hansen, and W.D. Bach, 1986: A Quantitative Method for Estimating Pasquill Stability Class from Windspeed and Sensible Heat Flux Density, *Boundary-Layer Meteorology*, **37**, pp. 357-369.

Sutherland, R.A., 1988: Methods of Radiative Transfer for Electro-Optical Obscuration Modeling, *Army Science Conference Proceedings*, Department of the Army, pp. 315-327, 25-27 October 1988.

Tunick, A. and H. Rachele, 1991: Estimating Effects of Temperature and Moisture on C_n^2 in the Damp Unstable Boundary Layer for Visible, Infrared, Radio, and Millimeter Wavelengths, *Proceedings of the 1991 Battlefield Atmospherics Conference*, U.S. Army Laboratory Command, Ft. Bliss, Texas, 3-6 December 1991.

Yee, Y.P., R.A. Sutherland, H. Rachele, and A. Tunick, 1993: Effect of Aerosol Induced Radiative Interactions on Atmospheric Stability and Optical Turbulence, SPIE OE/Aerospace Sensing Symposium, Atmospheric Propagation and Remote Sensing II, Orlando, Florida, 12-16 April 1993.

A FUNCTIONAL RELATIONSHIP BETWEEN BACKSCATTER AND EXTINCTION IN VERY LOW STRATUS CLOUDS AND ASSOCIATED SUBCLOUD REGIONS

Henry Rachele
U.S. Army Research Laboratory, Battlefield Environment Directorate
White Sands Missile Range, New Mexico 88002-5501, USA

Neal H. Kilmer
Physical Science Laboratory, New Mexico State University
Las Cruces, New Mexico 88003-0002, USA

ABSTRACT

The purpose of this study is to obtain one or more algebraic expressions that would approximate the title relationship between backscatter and extinction coefficients. Functions used to fit vertical profiles simulated using a largely theoretically-based microphysics model for very low stratus clouds and associated subcloud regions are combined and solved algebraically for the backscatter coefficient. Another approach leads to a less complicated form, the exponential polynomial form, in which the traditional power law expression is multiplied by the exponential of a polynomial in powers (2 and greater) of the natural logarithm of the extinction coefficient.

1. INTRODUCTION

According to Klett,[1] the volume extinction $\sigma(k)$ and backscatter $\beta(k)$ coefficients resulting from particulate scattering and absorption can be written as

$$\sigma(k) = \pi \int r^2 Q(m, \, kr) \, n(r) \, dr \tag{1}$$

and

$$\beta(k) = \pi \int r^2 Q_\pi(m, \, kr) \, n(r) \, dr \tag{2}$$

where k is the wave number (2π divided by the wavelength), n(r) is the size distribution of particles of radius r (assumed spherical), Q is the extinction efficiency, and Q_π is the backscatter efficiency as determined by Mie theory of scattering. Both Q and Q_π are functions of the complex indices of refraction m and size parameter kr. Klett concludes that the ratio of backscatter to extinction for a given wavelength and complex index is a function of only the shape of the particle size distribution. Consequently, Klett also concludes that, if the spectral shape and composition of the scattering aerosol are spatially invariant, then so will be the proportionality between β and σ. However, if the aerosol spectral form or composition varies with location, β will not be strictly proportional to σ.

The traditional way for expressing the dependency of β on σ is to assume a power law relationship of the form

$$\beta = \kappa \, \sigma^c \tag{3}$$

where κ and c are constants.

Klett proceeds with his analysis by assuming that κ is a function of range (distance) and c is a constant not necessarily equal to 1.

In this study, we wanted to establish a functional form between β and σ resulting from naturally-occurring droplets in very low stratus clouds and their associated subcloud regions, and to judge whether this form is in any way similar to eq. (3).

We initiated this investigation by generating drop size distributions as functions of height using our[2] microphysics model. Mie theory[3] was applied to these simulated drop size distributions to produce vertical profiles of extinction and backscatter coefficients. The extinction and backscatter coefficient profiles were then fit with our R/K (Rachele-Kilmer) optical profile function. An earlier, less extensive form of this function is discussed by Rachele, Manguso, and Kilmer.[4] This function has been modified to assume the form presented in the next section.

2. THE R/K OPTICAL PROFILE FUNCTION

In Kilmer and Rachele,[5] we show that the backscatter coefficient β and extinction coefficient σ profiles simulated using our microphysics model for very low stratus clouds and their associated subcloud regions ("R/K microphysics model")[2] could be represented quite well using the expressions

$$\beta = \beta_1 \left(\frac{\beta_2}{\beta_1} \right)^{M_\beta(z)} \tag{4}$$

$$\sigma = \sigma_1 \left(\frac{\sigma_2}{\sigma_1} \right)^{M_\sigma(z)} \tag{5}$$

where

$$M(z) = \left(\frac{z - z_1}{z_2 - z_1} \right)^{N(z)} \tag{6}$$

In these equations, z is the height above ground level. The form of this function guarantees an exact match at z_1 and z_2; therefore, the points defined by these heights and the values of the extinction or backscatter coefficient at these heights are called "forced match" points. We use this function in two pieces. For the lower piece, the subscript 1 refers to the reference height (2 m above ground level), and the subscript 2 refers to the height of the hinge point, which joins the two pieces. For the upper piece, the subscript 1 refers to the height of that same hinge point, and the subscript 2 refers to the height of the "highest forced match" near the top of the cloud. The hinge point defines the boundary between the function's two pieces. When the R/K optical profile function is to be used to calculate either an extinction or backscatter coefficient profile independent of the other type of profile, the hinge point typically is chosen to be the inflection point at or near the base of the cloud on a ln σ or ln β versus z curve (where ln represents "natural logarithm of") defined by R/K microphysics model data. However, a significant part of the analysis performed in the present work depends on each "forced match" height for backscatter being identical to the corresponding "forced match" height for extinction. Therefore, in this work, the hinge height for both backscatter and extinction is calculated as the arithmetic mean of the two hinge heights determined independently for backscatter and extinction. (These hinge heights typically differ by only a relatively small amount anyway. Their difference was 2 meters or less for 70 percent of the 2376 case-wavelength combinations of profiles simulated in a companion study.[5]) Both pieces are described according to eqs. (4), (5), and (6) but have different values for the constants

and may have different functional forms to describe N(z). N(z) is a function of z and is represented by one of these three equations:

$$N(z) = \exp\left(\sum_{n=0}^{N_E} E_n z^n\right) \qquad (7)$$

$$N(z) = \sum_{n=0}^{N_E} E_n z^n \qquad (8)$$

$$N(z) = A_o + c_1 z + c_2 z^2 + 2\sum_{n=1}^{N_A} A_n \cos\left[\frac{2\pi n(z - z_{F1})}{z_{F2} - z_{F1} + 1}\right]$$

$$- 2\sum_{n=1}^{N_B} B_n \sin\left[\frac{2\pi n(z - z_{F1})}{z_{F2} - z_{F1} + 1}\right] \qquad (9)$$

In these three equations, A_o, the A_n values, the B_n values, the E_n values, c_1, c_2, z_{F1}, and z_{F2} are constants. The combination of eq. (4) or (5), eq. (6), and one of eqs. (7), (8), and (9) is called the R/K (Rachele-Kilmer) optical profile function.

Substituting eq. (6) into eqs. (4) and (5) gives

$$\beta = \beta_1\left(\frac{\beta_2}{\beta_1}\right)^{\left(\frac{z - z_1}{z_2 - z_1}\right)^{N_\beta(z)}} \qquad (10)$$

and

$$\sigma = \sigma_1\left(\frac{\sigma_2}{\sigma_1}\right)^{\left(\frac{z - z_1}{z_2 - z_1}\right)^{N_\sigma(z)}} \qquad (11)$$

Taking the natural logarithms of eqs. (10) and (11) results in

$$\ln\frac{\beta}{\beta_1} = \left(\frac{z - z_1}{z_2 - z_1}\right)^{N_\beta(z)}\ln\frac{\beta_2}{\beta_1} \qquad (12)$$

$$\ln\frac{\sigma}{\sigma_1} = \left(\frac{z - z_1}{z_2 - z_1}\right)^{N_\sigma(z)}\ln\frac{\sigma_2}{\sigma_1} \qquad (13)$$

Taking the natural logarithms of eqs. (12) and (13) gives

$$\ln\left(\ln\frac{\beta}{\beta_1}\right) = N_\beta(z)\ln\left(\frac{z - z_1}{z_2 - z_1}\right) + \ln\left(\ln\frac{\beta_2}{\beta_1}\right) \qquad (14)$$

$$\ln\left(\ln\frac{\sigma}{\sigma_1}\right) = N_\sigma(z)\ln\left(\frac{z - z_1}{z_2 - z_1}\right) + \ln\left(\ln\frac{\sigma_2}{\sigma_1}\right) \qquad (15)$$

When z_1 is identical for the "forced match" points (z_1, σ_1) and (z_1, β_1) and z_2 is identical for the "forced match" points (z_2, σ_2) and (z_2, β_2), then eqs. (14) and (15) can be combined by eliminating $\ln\left(\dfrac{z - z_1}{z_2 - z_1}\right)$, resulting in

$$\ln\frac{\beta}{\beta_1} = \left(\ln\frac{\beta_2}{\beta_1}\right)\left(\frac{\ln\frac{\sigma}{\sigma_1}}{\ln\frac{\sigma_2}{\sigma_1}}\right)^{\frac{N_\beta(z)}{N_\sigma(z)}} \tag{16}$$

For the special case of $N_\beta(z) = N_\sigma(z)$, eq. (16) reduces to

$$\ln\frac{\beta}{\beta_1} = \frac{\ln\frac{\beta_2}{\beta_1}}{\ln\frac{\sigma_2}{\sigma_1}} \ln\frac{\sigma}{\sigma_1} \tag{17}$$

If we let $\dfrac{\ln\frac{\beta_2}{\beta_1}}{\ln\frac{\sigma_2}{\sigma_1}} = c$, then eq. (17) becomes

$$\ln\frac{\beta}{\beta_1} = c\,\ln\frac{\sigma}{\sigma_1} \tag{18}$$

or

$$\frac{\beta}{\beta_1} = \left(\frac{\sigma}{\sigma_1}\right)^c \tag{19}$$

Equation (19) can also be written as

$$\beta = \frac{\beta_1}{\sigma_1^c}\,\sigma^c \tag{20}$$

or

$$\beta = \kappa\,\sigma^c \tag{21}$$

which is the traditional power law relationship between β and σ.

Now, suppose that for a given z, $\dfrac{N_\beta(z)}{N_\sigma(z)} = k^*$.

Then from eq. (16) we can write

$$\ln\frac{\beta}{\beta_1} = \left(\ln\frac{\beta_2}{\beta_1}\right)\left(\frac{\ln\frac{\sigma}{\sigma_1}}{\ln\frac{\sigma_2}{\sigma_1}}\right)^{k^*} \tag{22}$$

or

$$\ln \frac{\beta}{\beta_1} = \frac{\left(\ln \frac{\beta_2}{\beta_1}\right)}{\left(\ln \frac{\sigma_2}{\sigma_1}\right)^{k^*}} \left(\ln \frac{\sigma}{\sigma_1}\right)^{k^*-1} \cdot \ln\left(\frac{\sigma}{\sigma_1}\right) \tag{23}$$

From eq. (23)

$$\beta = \beta_1 \left(\frac{\sigma}{\sigma_1}\right)^{c_1} \tag{24}$$

where

$$c_1 = \frac{\left(\ln \frac{\beta_2}{\beta_1}\right)\left(\ln \frac{\sigma}{\sigma_1}\right)^{k^*-1}}{\left(\ln \frac{\sigma_2}{\sigma_1}\right)^{k^*}} \tag{25}$$

Hence, from eqs. (24) and (25) we see that the relationship between β and σ can still be written in the form of a power law, with the power c_1 a function of z. Later we will also show that k^*, and therefore c_1, can be represented as a function of σ only.

3. β, σ AND $N_\beta(z)/N_\sigma(z)$ RELATIONSHIPS

In this section, we consider the relationship of β versus σ and $N_\beta(z)/N_\sigma(z)$ versus z in terms of eqs. (21)-(25). Using drop size distribution data simulated using our microphysics model[2] and Mie theory,[3] we generated β and σ as functions of height for several cases that depended on input values of air mass type (maritime, rural, or urban), propagation wavelength (0.55, 1.06, 3, 4, 5, 8, 10.6, or 12 μm), and reference height (2 m above the surface) temperature, relative humidity, and visibility. An example showing σ and β as a function of height is presented in fig. 1. All of the figures in this paper were produced using data that had been simulated using the full R/K microphysics model for a maritime air mass, quasi-adiabatic liquid water content, and reference height input values of 99 percent for the relative humidity, 10 km for the visibility, and 15 °C for the ambient air temperature. For this set of input values and a wavelength of 3 μm, we determined c and κ by linear regression of $\ln \beta$ versus $\ln \sigma$ data. Having values of κ and c, we then plotted the $\ln \beta = \kappa + c \ln \sigma$ regression line as long dashes in fig. 2. Finally, we superimposed a plot of $\ln \beta$ vs $\ln \sigma$ as the solid curve in fig. 2 using data (plotted in fig. 1) generated using the full R/K microphysics model.

We observed that there are various degrees of linear tendency between $\ln \beta$ and $\ln \sigma$. There seems to be an especially strong linear relationship in such plots for the wavelength of 3 μm, suggesting that eq. (21) represents a reasonable relationship between backscatter and extinction coefficients for that wavelength. Backscatter coefficient values calculated for this model case and wavelength using eq. (21) are plotted as long dashed lines in the same plot, fig. 3, as backscatter coefficient profile values simulated for the same model case and wavelength using the full R/K microphysics model. (The meaning of shorter dashed lines in some figures, including figs. 2 and 3, will be explained later.) This comparison shows very good agreement for the wavelength of 3 μm. Generally strong long-range linear trends with considerable short-range structure are seen between $\ln \beta$ and $\ln \sigma$ in plots for a wavelength of 0.55 μm. Considerable deviation is seen in such plots for 1.06 μm. In plots for 4 μm, strong linear trends are seen in regions of relatively weak extinction and backscatter; however, in regions of relatively
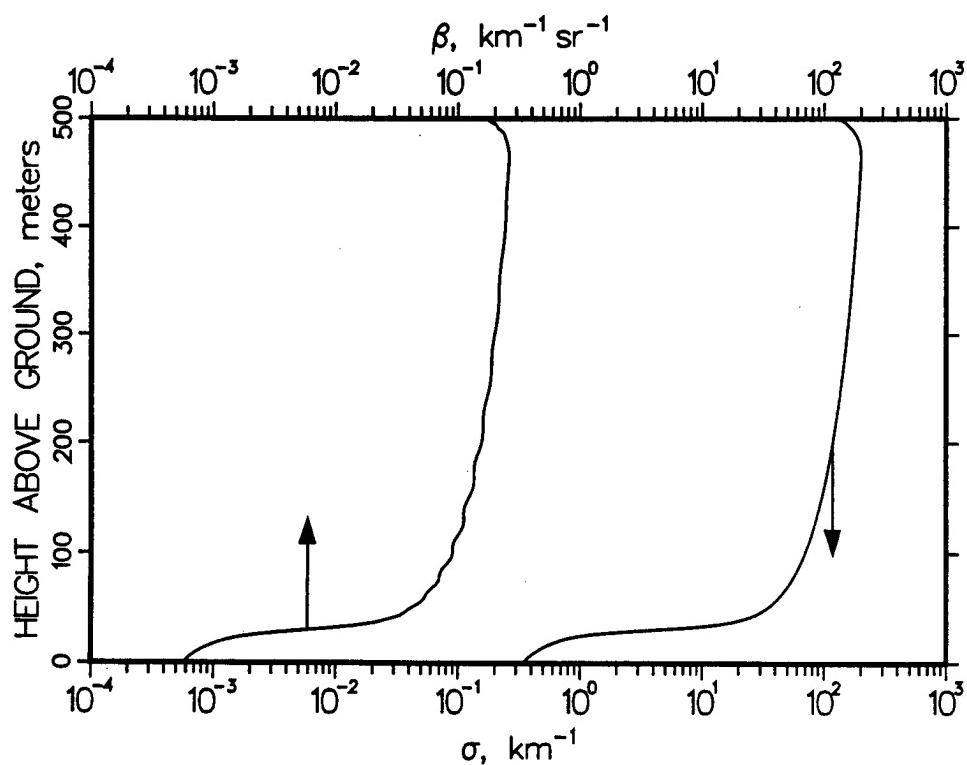
Figure 1.   Backscatter and extinction coefficient profiles simulated for
a wavelength of 3 μm using full R/K microphysics model.
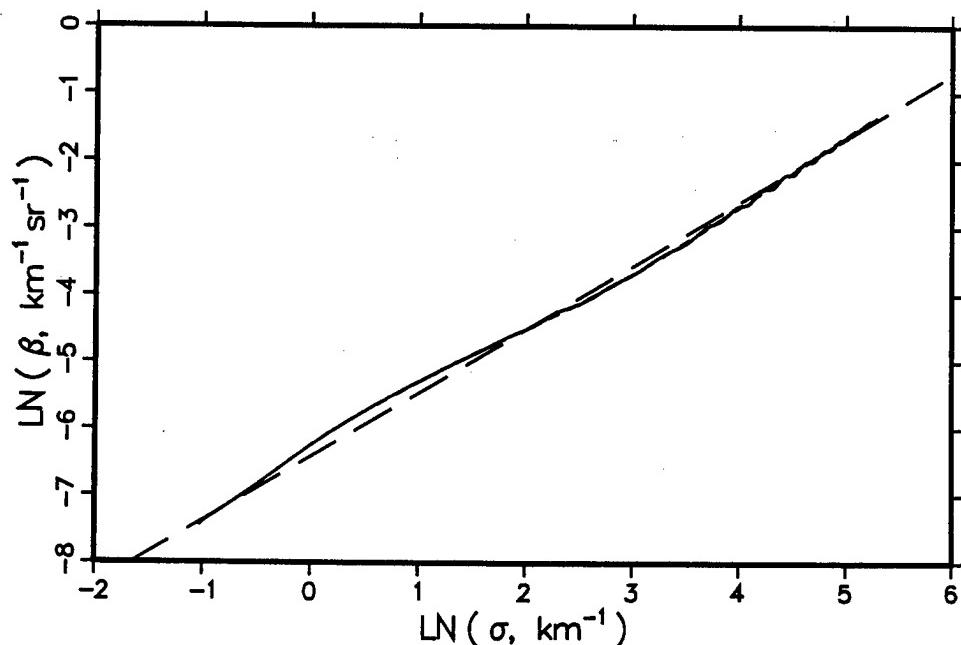
Figure 2.   Ln β simulated for a wavelength of 3 μm using full R/K microphysics
model (solid line) and calculated as a polynomial of degree 12 in ln σ
(medium dashes) and traditional power law expression (long dashes).
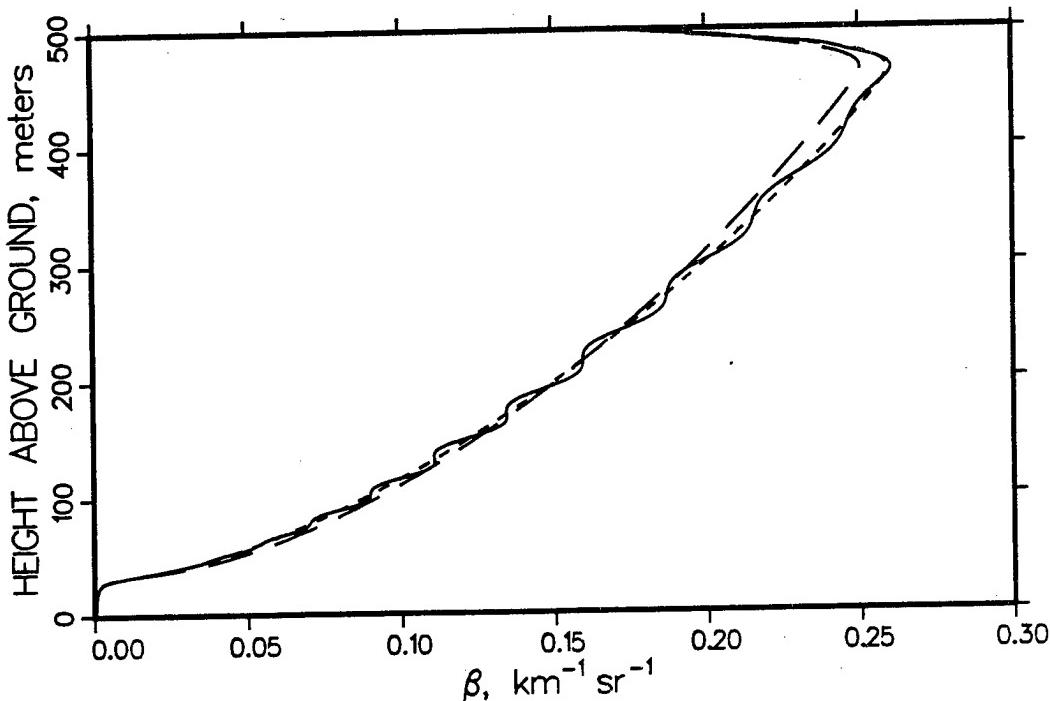
Figure 3. Backscatter coefficient profiles simulated for a wavelength of 3 μm
directly from full R/K microphysics model (solid line) and calculated
using ln σ from full R/K microphysics model in exponentiated
polynomial of degree 12 (medium-length dashes) and traditional
power law expression (long dashes).

strong extinction and backscatter, the character of the relationship deviates much from the earlier linear trends. This may be due largely to the relatively flat long-range trends exhibited by vertical profiles of extinction coefficient for this wavelength for much of the cloud region in some model cases studied. A similar effect is sometimes seen for 5 μm model data also. When this effect is strong, it contributes to poor agreement of the power law versus full R/K microphysics model backscatter coefficient profiles. Curves for the longer wavelengths (λ) modeled ($4\,\mu m \leq \lambda \leq 12\,\mu m$) appear wavy. Inspection of the ln β versus ln σ plots shows that the relationship is nonlinear for mid-values of extinction, with the nonlinearity becoming rather pronounced for longer wavelengths. As such, we fit the ln β versus ln σ with higher order polynomials, i.e.,

$$\ln \beta = \sum_{n=0}^{N_c} a_n (\ln \sigma)^n \qquad (26)$$

Excellent results were obtained when using this form to fit data simulated using the R/K microphysics model[2] and specifying the near-surface (2 m above ground level) relative humidity to be 90 percent. However, such fitting of R/K microphysics model data for a near-surface relative humidity of 99 percent produced results ranging from excellent to poor, depending largely on what wavelength was used in modeling. Using a wavelength of 3 μm led to the excellent results shown in figs. 1-3. As an example of data that are not easy to fit, results for the same case are shown for a wavelength of 0.55 μm in figs. 4-6. (These are analogous to figs. 1-3, except that it was not necessary to attempt any twentieth-degree polynomial fits to show in figs. 2 and 3.)
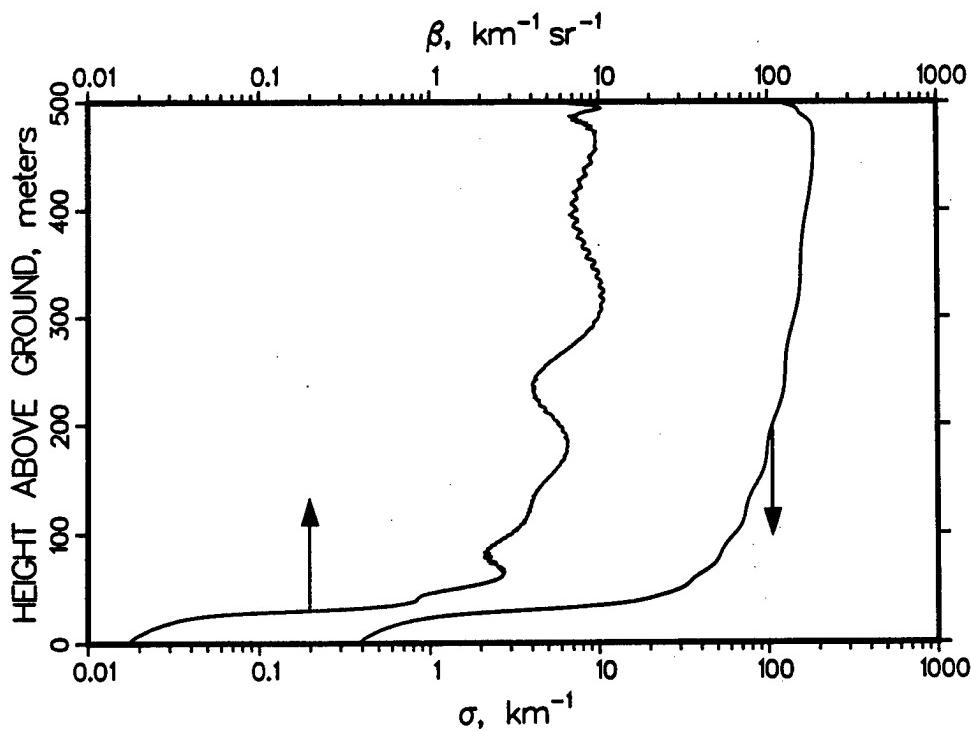
Figure 4. Backscatter and extinction coefficient profiles simulated for
a wavelength of 0.55 μm using full R/K microphysics model.
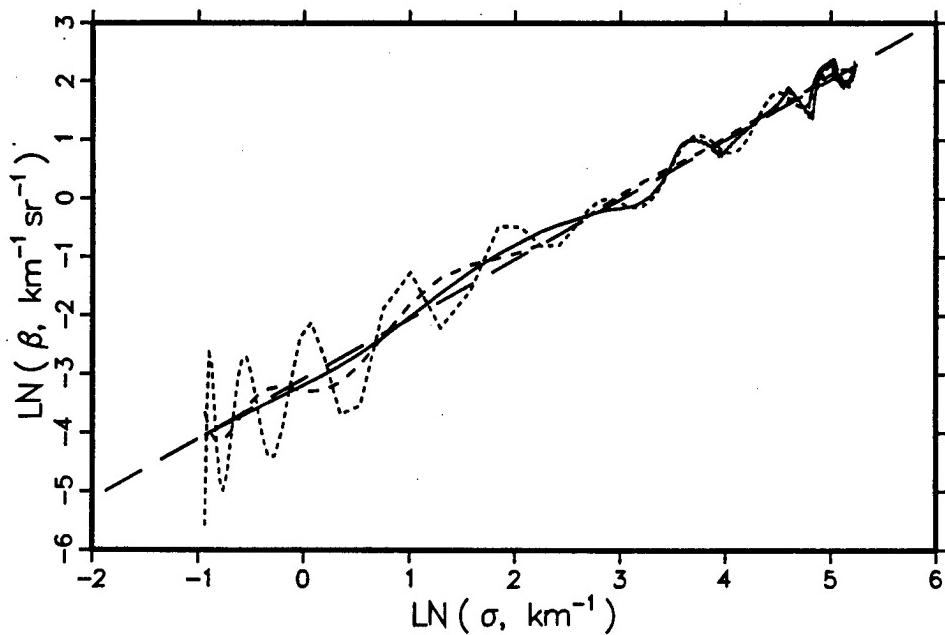
Figure 5. Ln β simulated for a wavelength of 0.55 μm using full R/K microphysics
model (solid line) and calculated as polynomials of degree 12 (medium
dashes) and 20 (short dashes) in ln σ and traditional power law expression
(long dashes).
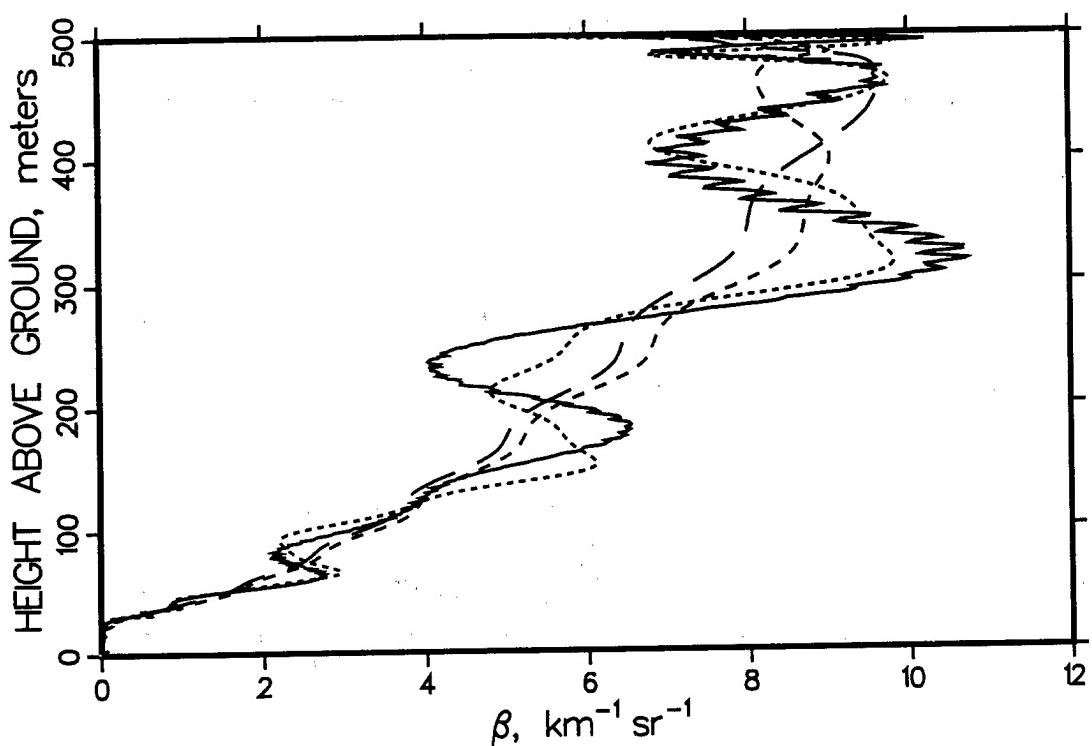
Figure 6. Backscatter coefficient profiles simulated for a wavelength of 0.55 μm directly from full R/K microphysics model (solid line) and calculated using ln σ from full R/K microphysics model in exponentiated polynomials of degrees 12 (medium-length dashes) and 20 (short dashes) and traditional power law expression (long dashes).

Substituting eq. (26) into eq. (22) and solving for k* gives

$$k^* = \frac{\ln\left[\dfrac{\displaystyle\sum_{n=0}^{N_c} a_n (\ln \sigma)^n - \ln \beta_1}{\ln (\beta_2/\beta_1)}\right]}{\ln\left[\dfrac{\ln (\sigma/\sigma_1)}{\ln (\sigma_2/\sigma_1)}\right]} \qquad (27)$$

which is a function of σ only. Substituting eq. (27) into eq. (25) shows that the exponent c_1 of eq. (24) can be expressed as a function of σ. This may be significant in the lidar equation as discussed by Klett.[1]

Simplification of the combination of eqs. (25) and (27) is highly desirable and will be addressed after a brief look at the behavior of k* and c_1. Assume that a profile is to be analyzed for the entire vertical extent of a cloud by applying an equation that includes k*. In such a case, the value of $N_\sigma(z)$ may cross zero somewhere in the profile. From the definition of k* as the ratio $N_\beta(z)/N_\sigma(z)$, it is seen that when $N_\sigma(z) = 0$, k* is infinite or undefined. An example occurs near a height of 235 m in the profile plotted in fig. 7 using data simulated for the otherwise well-behaved case/wavelength combination considered

in figs. 1-3. Figure 8 shows profiles of values of c_1 that were calculated using the same values of k* that were plotted in fig. 7. It is noteworthy that fig. 8 shows no trace of the discontinuity exhibited near a height of 235 m in fig. 7. This behavior suggests that the expression causing the discontinuity in fig. 7 might be eliminated algebraically if the combination of eqs. (25) and (27) were simplified, thus furthering the case for simplification.
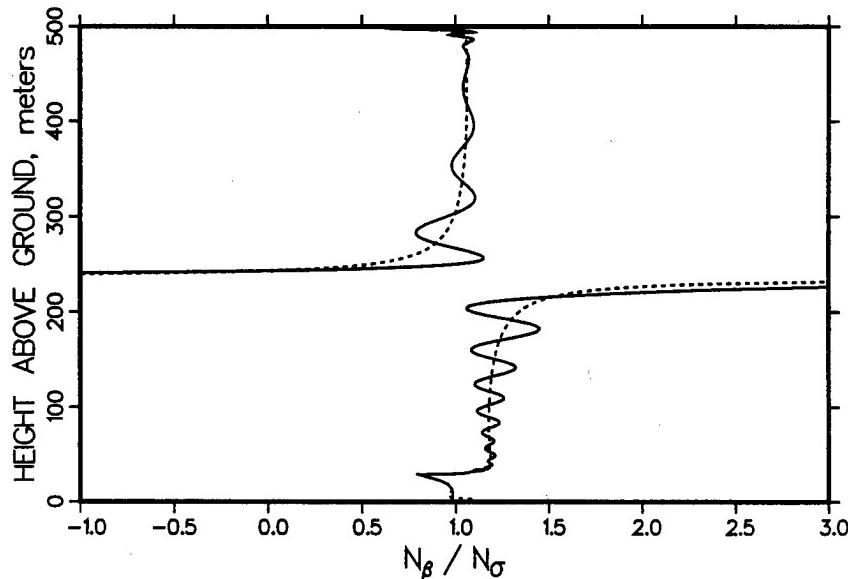
Figure 7. $N_\beta(z)/N_\sigma(z)$ (also called k*) obtained from full R/K microphysics model (solid line) for 3 μm and approximated using eq. (27) (short dashes).
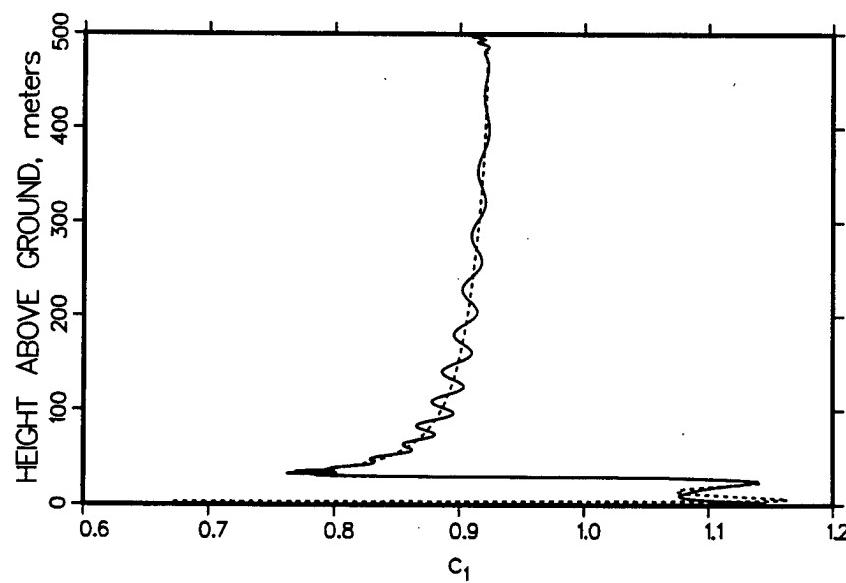
Figure 8. c_1 for a wavelength of 3 μm when $N_\beta(z)/N_\sigma(z)$ (also called k*) is obtained from full R/K microphysics model (solid line) and approximated using eq. (27) (short dashes).

A final observation from figs. 7 and 8 is the goodness of fit attained by using a polynomial approximation for $\ln \beta$. In these figures, solid lines represent values calculated using data directly as simulated using the full R/K microphysics model. Short dashes in these two figures represent values calculated using the fitting constants from eq. (26) with $N_C = 12$. Thus, the values of k^* from eq. (27) were plotted as short dashes in fig. 7, and the values of c_1 calculated according to eq. (25) using k^* values from eq. (27) were plotted as short dashes in fig. 8. The polynomial approximation is seen to produce reasonably smoothed curves in both figures, showing that the major trends of both k^* and c_1 can be approximated as functions of σ only.

The combination of eq. (27) substituted into eq. (25) was simplified algebraically using standard rules for logarithmic and exponential functions. The sometimes troublesome ratio represented as k^* was indeed eliminated, and c_1 was found to be expressed relatively simply as

$$c_1 = \frac{\left[\sum_{n=0}^{N_C} a_n (\ln \sigma)^n \right] - \ln \beta_1}{\ln (\sigma/\sigma_1)} \tag{28}$$

If there had been no interest in exploring the behavior of k^*, then eq. (28) could have been obtained more directly by solving eq. (24) for c_1 and then using eq. (26) to substitute for $\ln \beta$ in the resulting equation.

Both sides of eq. (26) can be exponentiated and the results written as

$$\beta = e^{a_0} \sigma^{a_1} \exp \left[\sum_{n=2}^{N_C} a_n (\ln \sigma)^n \right] \tag{29}$$

The form of the right hand side of eq. (29) is designated the "exponential polynomial form." This form is equivalent to the traditional power law form multiplied by the exponential of the indicated polynomial of powers of $\ln \sigma$. Further, when the values of the fitting constants are available, this form is an example of a more general form given by Klett[1] in his eq. (7). Therefore, this form can be used in Klett's[1] modified lidar inversion solution given by his eqs. (10) through (12) and accompanying text. In that solution, a_1 would be used as Klett's k, and

$$e^{a_0} \exp \left[\sum_{n=2}^{N_C} a_n (\ln \sigma)^n \right]$$

would be used as Klett's B function.

4. RESULTS AND ANALYSIS

Fitting a linear relationship between values of $\ln \beta$ and $\ln \sigma$ simulated using the Rachele-Kilmer microphysics model[2] worked well when the wavelength was 3 μm. For other wavelengths, linear relationships sometimes seemed to be reasonable approximations and sometimes seemed to be very idealized approximations that ignored significant structure. Despite the presence of sometimes very considerable structure, the values estimated for the power law constant c by the slopes of best-fit lines were very encouraging. For the cases considered in this study, we found that c was usually in the range from 0.9 to 1.1, which is well in line with values reported for monochromatic

radiation in the literature, including results from calculations using measured drop size distribution data for fog[6] and previous calculations using measured drop size distribution data,[1,7] which have estimated the power law exponent to be in the range from 0.89 to 1.38. Smaller values, 0.66 and 0.70, were obtained for the power law exponent from previous studies reported by Curcio and Knestrick[8] and by Fenn[9] using data from Barteneva[10] based on actual measurements of electromagnetic radiation spanning a range of wavelengths. However, since the present study does not include calculations for polychromatic radiation, comparison of these smaller values with ours is not appropriate. (Twomey and Howell[11] have compared results from monochromatic and white light.) Superimposing β values from eq. (21) on those produced by the R/K microphysics model shows excellent agreement (with some short-range structure often being smoothed out) for a wavelength of 3 μm. For other wavelengths, superimposing β values from eq. (21) on those produced by the R/K microphysics model often seemed to magnify differences. The differences sometimes were quite considerable, prompting us to try higher order polynomials for fitting ln β versus ln σ.

When we fit ln β versus ln σ with higher order polynomials, we produced better fits of β versus σ than when the simple linear case (corresponding to the traditional power law) was used. The values of β calculated from eq. (29) sometimes agree very well with the profile values from the full R/K microphysics model. Details follow.

Ln β versus ln σ data simulated using our[2] microphysics model were fitted by using polynomials in powers of ln σ. After polynomials of different degrees were tried for selected cases, twelfth-degree polynomials were used for most of the subsequent fitting of this type. Excellent fits were obtained for a wavelength of 3 μm. Examples of results for this wavelength are shown in figs. 2 and 3, in which long dashes represent a traditional power law fit and medium-length dashes represent a twelfth-degree polynomial fit. For the other seven wavelengths (0.55, 1.06, 4, 5, 8, 10.6, and 12 μm) used in simulations, very good fits were obtained for a case for which the reference height (2 m above ground level) relative humidity was 90 percent, and very good agreement was realized between vertical profiles of β simulated using the full R/K microphysics model and corresponding profiles calculated using constants from the aforementioned fits. However, for a case for which the reference height relative humidity was 99 percent, fits and agreement were only fair to good for these seven wavelengths. For a few wavelengths in the latter case, twentieth-degree polynomials were tried with varying degrees of success to improve fits. Examples of traditional power law (long dashes), twelfth-degree polynomial (medium-length dashes), and twentieth-degree polynomial (short dashes) fitting results for the latter case (same case as figs. 1-3 but different wavelength) is shown for a wavelength of 0.55 μm in figs. 5 and 6.

Transferability of ln β versus ln σ polynomial fitting constants was tested by using powers of ln σ with fitting constants determined for the same wavelength of another case, which was similar except that one major input parameter was different. For the cases investigated this way, agreement with β profiles simulated using the full R/K microphysics model was good when the ambient air temperature at the reference height (2 m above ground level) was the different input parameter. However, agreement was not good when some other major input parameter was the one varied. If either the air mass type or else the parameter used to adjust the liquid water content (as a percent of the quasi-adiabatic value for the maximum in the simulated profile) was the one major parameter varied, agreement was only fair to poor. When visibility at the reference height was varied, agreement was horrible for part of the height range of the β profile. That part of this profile occurred where the ln σ values were significantly greater than the largest ln σ value that had been used in determining the polynomial coefficients. Considering that values being compared with β had been calculated using the exponential of a

twelfth-degree polynomial, the very large differences are understandable. This suggests that the range of validity for such fits should not be considered to extend beyond the actual range of ln σ values used in the determination of fitting constants.

CONCLUSIONS

Two algebraic relationships between backscatter and extinction coefficients have been found in functions used to fit vertical profiles simulated using a largely theoretically-based microphysics model for very low stratus clouds and associated subcloud regions. The first relationship results when fitting functions used for backscatter and extinction coefficient profiles are combined and solved algebraically for the backscatter coefficient (β). The resulting expression for the backscatter coefficient can be written in the form of a power function of the extinction coefficient (σ), but the constant power in the traditional power law expression is replaced with an expression that varies with distance (height). A less complicated form, the exponential polynomial form, in which the traditional power law expression is multiplied by the exponential of a polynomial in powers (2 and greater) of the natural logarithm of the extinction coefficient (ln σ), is based on the ability to fit ln β versus ln σ data with polynomials in powers of ln σ. The usefulness of these relationships depends on how well the fitting functions on which these relationships are based fit actual data.

Simulated data, which are not at the mercy of instrumental range limitations, have been treated using these relationships and the traditional power law expression. When results simulated using the R/K microphysics model are fit in accordance with the traditional power law expression, best-fit values obtained for the exponent (constant) are well in line with results from other studies. However, some profiles show considerable deviations from traditional power law behavior. Use of the exponential polynomial form enables better fitting; however, some simulated data sets have been found to resist really good fitting by even this more flexible function. Considering the additional fitting power and flexibility associated with the exponential polynomial form, that form is suggested for further use.

ACKNOWLEDGMENT

REFERENCES

1.	Klett, J. D., 1985: Lidar Inversion with Variable Backscatter/Extinction Ratios. Appl. Opt., 24 (11), 1638-1643.

2.	Rachele, H., and N. H. Kilmer, 1992: Unified Very Low Stratus Cloud/Subcloud Microphysics Model. ASL Technical Report ASL-TR-0309, U.S. Army Atmospheric Sciences Laboratory,[12] White Sands Missile Range, NM 88002-5501.

3.	Miller, A., 1983: Mie Code Agaus 82. ASL-CR-83-0100-3, U.S. Army Atmospheric Sciences Laboratory,[12] White Sands Missile Range, NM 88002.

4. Rachele, H., L. Manguso, and N. H. Kilmer, 1992: A Higher Order Exponential Function for Fitting Nonlinear Curves. ARL Technical Memorandum ARL-MR-24, U.S. Army Research Laboratory, Battlefield Environment Directorate, White Sands Missile Range, NM 88002-5501.

5. Kilmer, N. H., and H. Rachele, 1993: Easy-To-Use Optical Profile Function Program for Modeling Extinction and Backscatter Coefficients in Low Stratus Clouds and Subcloud Regions. In Proceedings of the 1993 Battlefield Atmospherics Conference, U.S. Army Research Laboratory, Battlefield Environment Directorate, White Sands Missile Range, NM 88002-5501 (in press).

6. Tonna, G., 1991: Backscattering, Extinction, and Liquid Water Content in Fog: A Detailed Study of Their Relations for Use in Lidar Systems. Appl. Opt., 30 (9), 1132-1140.

7. Klett, J. D., 1984: Effects of Variations in the Relationship Between Backscatter and Extinction on Lidar Signal Inversions. ASL Contractor Report ASL-CR-84-0093-1, U.S. Army Atmospheric Sciences Laboratory,[12] White Sands Missile Range, NM 88002-5501.

8. Curcio, J. A., and G. L. Knestrick, 1958: Correlation of Atmospheric Transmission with Backscattering. J. Opt. Soc. Am., 48, 686-689.

9. Fenn, R. W., 1966: Correlation Between Atmospheric Backscattering and Meteorological Visual Range. Appl. Opt., 5(2), 293-295.

10. Barteneva, O. D., 1960: Scattering Functions of Light in the Atmospheric Boundary Layer. Bull. Acad. Sci. USSR, Geophys. Ser., (12), 1237-1244. Translation of Izv. Geophys. Ser., 1960, pp. 1852-1865.

11. Twomey, S., and H. B. Howell, 1965: The Relative Merit of White and Monochromatic Light for the Determination of Visibility by Backscattering Measurements. Appl. Opt., 4(4), 501-506.

12. Currently U.S. Army Research Laboratory, Battlefield Environment Directorate, White Sands Missile Range, NM 88002-5501.

Session III

ATMOSPHERIC SENSING

BATTLEFIELD ATMOSPHERIC SOUNDINGS: TEST RESULTS FROM A TECHNICAL DEMONSTRATION MOBILE PROFILER SYSTEM

James Cogan and Dewitt Littell
U.S. Army Research Laboratory
Battlefield Environment Directorate
White Sands Missile Range, NM 88002-5501 USA

Bob Weber, M. Simon, A. Simon, D. Weurtz,
S. King, D. Merritt, and D. Wolfe
Environmental Technology Laboratory
National Oceanographic and Atmospheric Administration
Boulder, CO 80303

ABSTRACT

A near-real-time sounding of the atmosphere from the surface to $\geq$ 30 km over a battlefield may be obtained by combining atmospheric profiles from meteorological (met) satellite (sat) and a ground-based system for remotely sensing wind and temperature. This type of capability is essential for optimum use of Army assets such as artillery and defense against biological and chemical attack. This paper briefly describes the technical demonstration (TD) mobile profiler system (MPS) and the method for merging data from the satellite and ground-based remote sensing systems. Results presented from a month-long field test indicate the capability of the present version of the TD MPS to generate useful atmospheric soundings in the format of an artillery met message and in a variety of other formats and displays. Comparisons made with data from rawinsondes nearly coincident in space and time indicate the accuracy of the data. An intercomparison between two rawinsonde systems on-site suggest possible errors in the rawinsonde data.

1. INTRODUCTION

The mobile profiler system (MPS) is being developed to provide the field artillery with atmospheric soundings in close to real time. The reduction in refresh time from the usual 2 to 4 h with current balloon systems such as the meteorological data system (MDS) to 15 to 30 min will considerably reduce errors due to time staleness. Systems of the type found

211

in the technical demonstration (TD) MPS system are described in Cogan[1] and Miers et al.[6] and their references, Hassel and Hudson,[4] and Strauch et al.[8] This paper briefly describes the TD MPS, outlines the combined sounding technique, and presents examples of actual data in a variety of formats. Comparisons with rawinsonde soundings that are nearly coincident in space and time indicate the accuracy of the system. Due to an unresolved problem in the satellite terminal software (wind speeds from the TIROS operational vertical sounder [TOVS] appear to be in knots, not meters per second as documented), wind comparisons with rawinsonde values were made only for the profiler. The usefulness of rawinsondes as a "standard" is suggested through comparisons of wind velocity soundings from a MARWIN and a cross-chain loran atmospheric sounding system (CLASS) where both systems received data from the same sonde.

2. SYSTEM DESCRIPTION

The TD MPS consists of a 924-MHz radar profiler for wind velocity; a radio acoustic sounding system (RASS) for virtual temperature; a ground-based microwave radiometer for temperature and humidity; a small ground station for temperature, pressure, humidity, and wind velocity; and a receiver/processor for acquisition of satellite sounder data for temperature and humidity. Satellite sounding heights are computed for the standard pressure levels. Wind velocity for the satellite sounding is calculated from gradients of these satellite heights by using the geostrophic assumption. Temperature is converted to virtual temperature as required. Pressure versus height is computed from the measured sounding data and may be measured for the lower part of the sounding by using the microwave radiometer. As of the preparation of this paper the operational parts of the TD MPS were the radar profiler, the RASS, the surface station, and the satellite receiver/processor. The microwave radiometer was being integrated into the system (temperature only). These components of the TD MPS are housed in or on a 9-m (30-ft) trailer with shelter, except for the radar antenna, the four RASS transducers, and the microwave radiometer. The primary processors are a Hewlett Packard (HP) 720 for the satellite terminal and an HP 735 for the ground-based sensors. The HP 735 serves as the primary processor and data manager and handles the data base. Each of three personal computers (PCs) partially run the radar, collect National Weather Service (NWS) weather maps, and operate the microwave radiometer. Up to two balloon systems may be run from the trailer to obtain comparison data; during the test in the Los Angeles, California basin (27 August through 28 September 1993) a MARWIN and CLASS were operated simultaneously. The TD MDS was demonstrated at White Sands Missile Range, New Mexico, in early October 1993 and a "final" technical demonstration is planned for the PM-EW/RSTA (project manager-electronic warfare/reconnaissance, surveillance, and target acquisition) in April 1994.

3. COMBINING METHOD

The merging algorithms are described briefly in Cogan and in more detail in the references therein.[1] Figure 1 shows the basic concept of the method. The ground-based systems provide detailed soundings for the lower troposphere, while the satellite sounder

can cover the atmosphere from around 2 or 3 km up to 30 km. First, profiles from the ground-based systems are combined to form a single multivariable sounding. The satellite sounding is weighted relative to the MPS location and time and then merged with the "ground-based" sounding. Normally, satellite and ground-based profiles will overlap (except temperature when no microwave data are available). If not, the satellite data for each variable are extrapolated down to the uppermost level of each of the ground-based profiles. For each variable, routines within the merging program adjust the satellite profiles, starting at the satellite sounding level immediately above the highest level of each "ground-based" profile. The several merged profiles are entered into a single file to form a combined sounding.
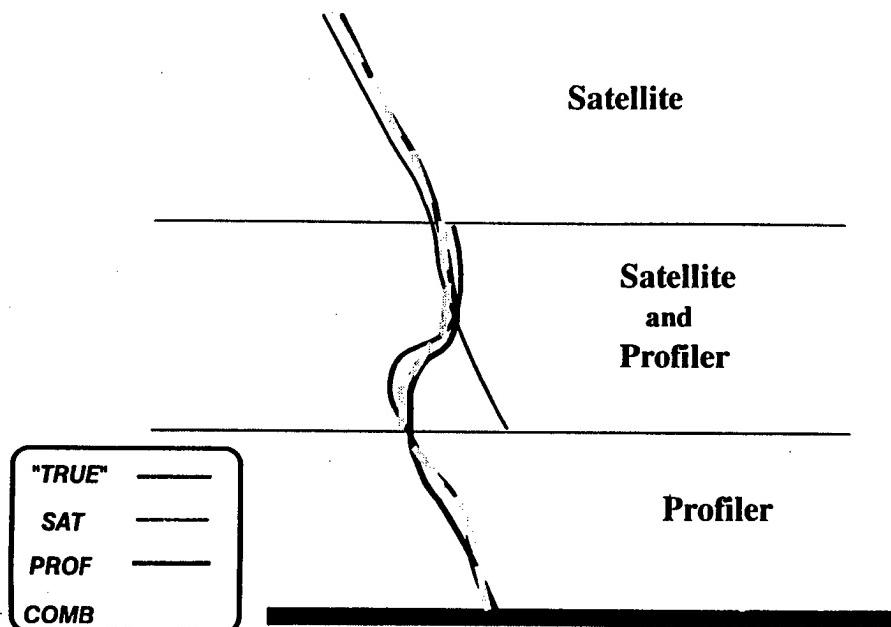
Figure 1. Combined sounding concept. Satellite and ground-based data are merged to form a more accurate sounding for the atmosphere from the surface to the highest satellite sounding level.

The same software package contains "C" functions that convert the combined sounding into two types of meteorological (met) messages, the MET-CM and the Air Weather Service (AWS) (TACFIRE [tactical fire direction system]). These messages are produced every 15 min and in the April demonstration will be sent as ASCII (American standard code for information exchange) files to the CAAMS. For that demonstration satellite sounding files (one per swath) will be sent to the CAAMS as soon as they are received and processed. Details on the specific algorithm for deriving a message in a computer met message format may be found in Cogan.[2] The AWS message essentially is in a standard World Meteorological Organization (WMO) format; no computation of layer values is required.

Miers et al.[6] and Cogan[1] present accuracies of the component systems based on published values in a number of papers such as Strauch et al.,[7] Lawrence et al.,[5] and Weber and Weurtz.[9] The remainder of this paper will present actual samples of MPS data and comparisons with rawinsonde data. Comparison between two rawinsonde systems will give an idea of the potential accuracy of the rawinsonde data (also Fisher et al.[3]).

4. DATA

The combining software produces output in a variety of formats, including MET-CM messages and AWS (TACFIRE) messages. However, the system is capable of producing additional output in alphanumeric text, graphical charts, and imagery. The following examples provide a small sample of the range of output types.

Table 1 shows a combined sounding in the format of a computer met message, except for some change in the heading. The data are in standard artillery format (for example, wind direction in units of tens of mils). The current satellite terminal software calculates geostrophic wind only up to the 100-mbar level, but temperature output reaches up to as much as the 10-mbar level. Future versions of that software will calculate wind to 10 mbar. In this figure wind values appear up to line 18 and temperature up to line 28. Other message formats can be produced, as for example, a message in the MET-CM TACFIRE format.

The system also is capable of producing output in the form of charts and other displays. Figure 2 presents a chart of radar profiler wind velocities in the form of standard wind arrows, except that speeds are in meters per second instead of knots (that is, a full barb indicates 10 m/s). Soundings were made every 15 min, but were displayed every 1/2 h on this chart. The abscissa is time in hours UTC, from 1200, 8 September on the right, to 0330, 9 September 1993 on the left. The included grey shade scale (color in the original) also indicates wind speed. The data were taken during an experiment in the Los Angeles basin during September 1993. Figure 2 shows several interesting meteorological phenomena. The marine boundary layer decreases in thickness from about 2 km at the beginning of the period to around 800 m at about 2100, 8 September (1400 Pacific daylight time [PDT]). Above the boundary layer an easterly flow becomes light and variable for a few hours near 2300, 8 September (1600 PDT), turning westerly up to a height of about 1.5 km. Apparently the marine boundary layer thickened later in the day. The profiler shows the complexity of the flow within the boundary layer and as much as a few kilometers above it.

Figure 3 shows an image of RASS temperatures averaged and displayed each half hour from 1200, 7 September to 0000, 8 September 1993. The grey shade scale below the abscissa indicates temperature in Celsius (original image and scale in color). The early morning inversion persisted until around 1700 to 1800 (1000 to 1100 PDT), with significant heating of the lower part of the boundary layer occurring afterwards. Although some of the temperatures at the far upper left of the image may be spurious (left-most column above

1 km and next column to right above 1.2 km), it appears that an inversion begins to form at around 1 km starting between 2100 and 2200 (1400 and 1500 PDT).

Table 1. Tabular Output from the Combining Software on the TD MPS

Meteorological Message Output

Date/Time 93068 / 131   Lat/Long   40.18 / -104.72

Zone (m)	Line	Wind Dir (10's mils)	Wind Speed (knots)	Temp (1/10 K)	Pressure (mbar)
Sfc	00	373	5	2829	845
200	1	323	5	2862	835
500	2	318	5	2867	810
1000	3	349	4	2836	772
1500	4	460	4	2854	727
2000	5	507	9	2803	685
2500	6	469	15	2767	644
3000	7	460	15	2738	605
3500	8	511	18	2704	568
4000	9	519	29	2664	533
4500	10	515	36	2625	500
5000	11	519	39	2584	468
6000	12	531	48	2523	424
7000	13	538	56	2441	369
8000	14	542	59	2369	320
9000	15	548	61	2300	277
10000	16	557	59	2231	238
11000	17	568	52	2163	204
12000	18	580	43	2099	173
13000	19	-9999	-9999	2065	147
14000	20	-9999	-9999	2071	125
15000	21	-9999	-9999	2078	106
16000	22	-9999	-9999	2083	90
17000	23	-9999	-9999	2088	76
18000	24	-9999	-9999	2099	65
19000	25	-9999	-9999	2114	55
22000	27	-9999	-9999	2144	47
24000	28	-9999	-9999	2183	27

Figure 4 displays combined soundings of wind velocity over a 10-h period, from 1600, 11 September 1993 to 0200 on 12 September 1993. Radar wind profiles appear every 30 min, but satellite wind profiles generally are available only every 2 to 6 h. The adjustment to the satellite winds are only slight as a consequence of the very light and variable wind at uppermost radar heights (below 5 km). In the original color chart, slight changes in wind speed at the lowest three satellite levels show up as minor color variations. A temporary shutdown of the radar produced the gap in data at 2230.
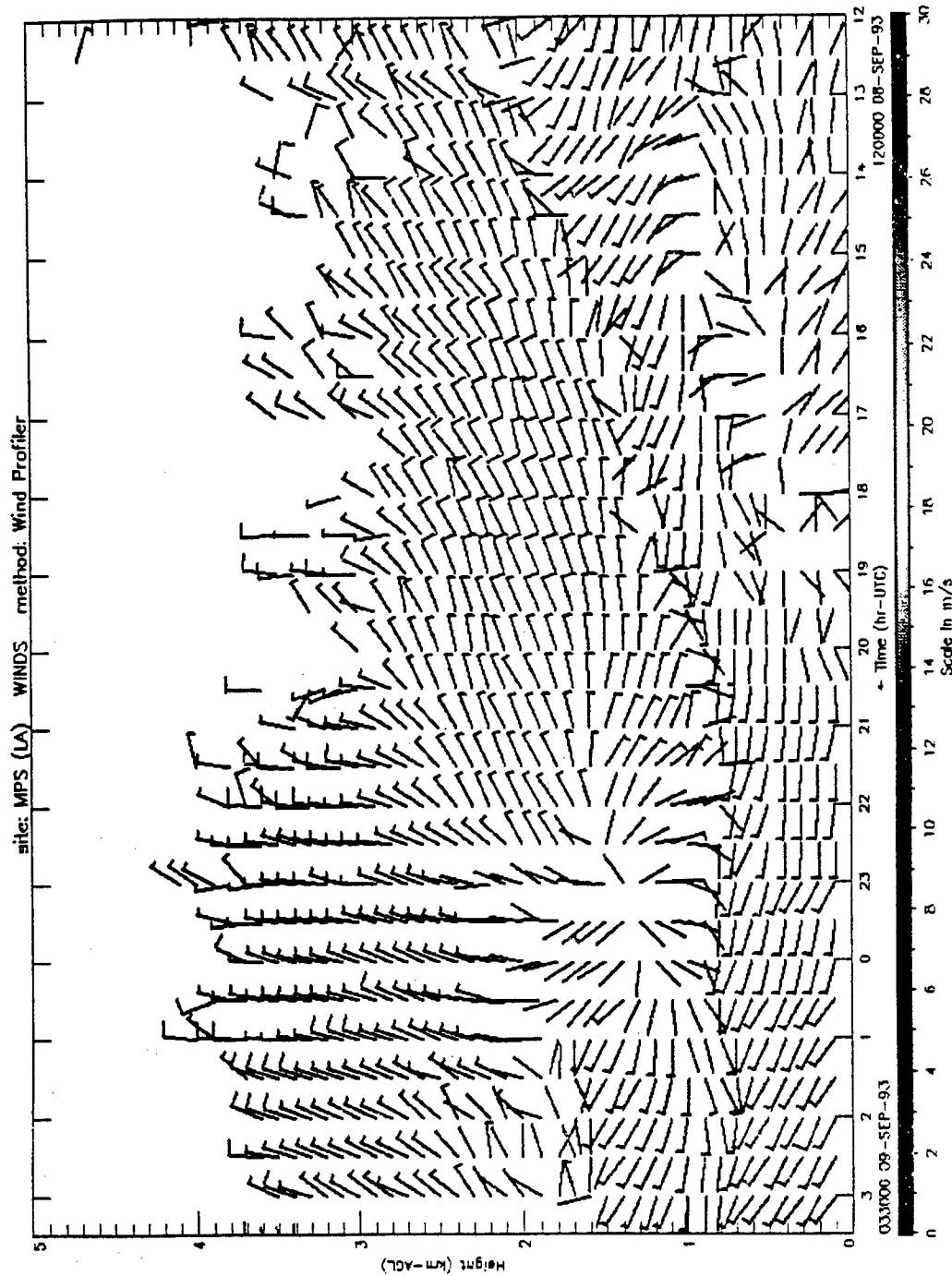
Figure 2. Time-height display of wind velocity profiles from the 924 MHz radar profiler.

Figure 3. Time-height display of virtual temperature from the RASS. Missing data adjacent to the surface were removed by the quality control routine.
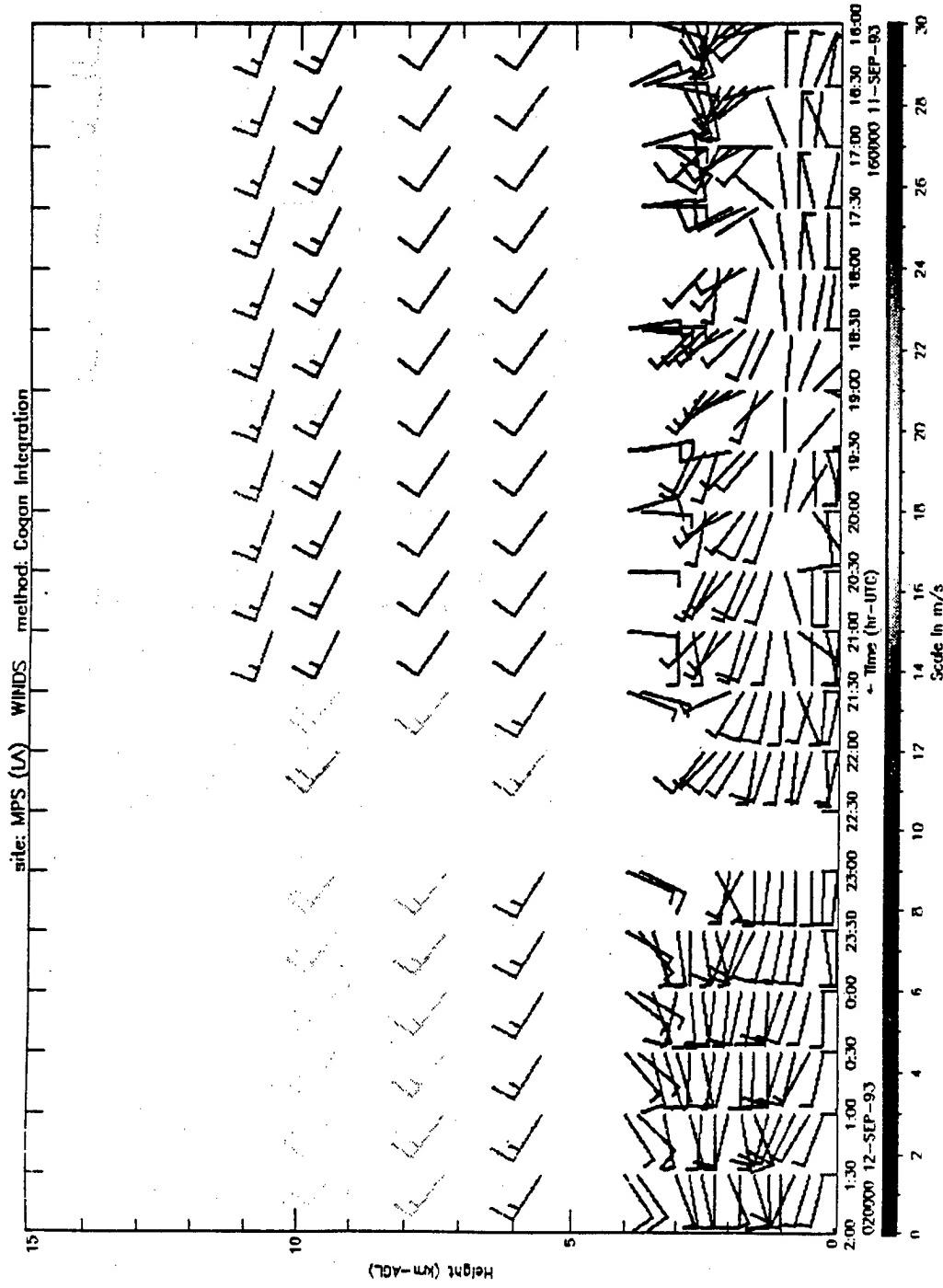
Figure 4. Time-height display of combined wind velocity profiles derived from radar profiler and satellite data.

5. COMPARISONS

Virtual temperature profiles from RASS, satellite, and combined RASS and satellite were compared with soundings from rawinsonde. Figures 5 through 7 show virtual temperature from each of the aforementioned systems plotted against that from rawinsonde. Each figure has several statistics describing the data, including the number of data points. Figure 5 presents the comparison for RASS where MPSB indicates the rawinsonde (balloon) data. Time is given in hours, minutes, and seconds as a six-digit number. Figure 6 has the same type of data for adjusted satellite data. Adjusted data refer to satellite data that were "tied down" in the merging algorithm using the uppermost RASS values. The algorithm modifies the lower three-data levels of the satellite sounding by using the method outlined in Cogan.[1] The standard deviation of the differences for the satellite profile exceeds that for the RASS by slightly more than a factor of 2. The mean difference is about three times as large and of opposite sign. Figure 7 has the comparison for the entire combined sounding. The standard deviation dropped to a value somewhat lower than that for the satellite, but the mean difference fell to a magnitude lower than either the satellite or RASS.

Figure 8 presents the same type of comparison, but for radar profiler wind speeds. The standard deviation was in line with values reported in the literature (Miers et al.[6]). The mean difference was very small, only -0.01 m/s. No attempt was made to compare satellite or merged wind speeds at this time because of a possible error in the units in the commercial software for satellite soundings. The vendor is investigating if the units of speed are knots or meters per second. Another potential source of disagreement between the satellite and rawinsonde could arise when the satellite sounding is far from the balloon location, especially if the launch site is under a ridge or trough. To maximize the possibility of a merged sounding, we set the algorithm to accept the nearest satellite sounding up to a distance of 320 km. Also, the site was under an upper ridge for the period of the data gathered here. Under these conditions large differences could occur between the rawinsonde and satellite wind speeds. Later comparisons between satellite and rawinsonde wind speeds, in a more zonal flow aloft, suggest that this latter explanation may be at least partially the cause of the large differences noted.

To gain an idea of the quality of the rawinsonde data wind, we presented soundings side by side from two similar systems (MARWIN and CLASS) receiving data from one sonde. Figures 9 and 10 show examples of a good and a bad comparison. The soundings were offset from one another on the graphs for clarity of presentation. Fortunately poor matches were not frequent. In figure 9 the wind speeds and directions closely followed one another, generally within 1 m/s and 10°. However, in figure 10 the situation changed. In this case, the wind speeds varied by around 2 or more meters per second at some levels, and wind direction varied considerably below 7 km and around 10 km. A possible partial explanation is that the MARWIN software has more extensive built-in checks and somewhat smooths the data. Nevertheless, caution must be taken when using a rawinsonde sounding as a standard, especially in light winds. The user should make sure each sounding contains valid data and should apply appropriate quality controls.

Virtual Temperature Comparison

130000 10 Sep 93 to 190000 10 Sep 93
Los Angeles, CA npts = 70
Height Range (km-AGL): 0.00 - 0.80
LSF: Slope = 1.00   Intercept = 0.13
Correlation: 0.89
STD DEV of Differences: 0.90 Mean Diff: -0.21
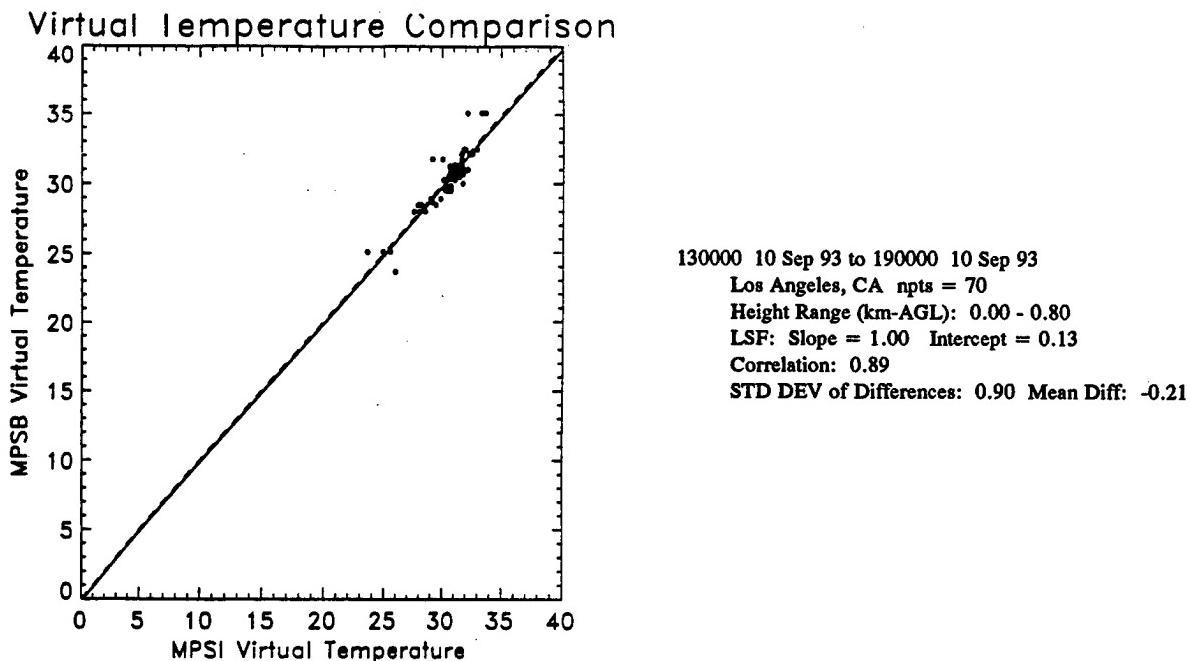
Figure 5. **Virtual temperature comparison between RASS and rawinsonde. MPSB indicates rawinsonde values.**

Virtual Temperature Comparison

130000 10 Sep 93 to 190000 10 Sep 93
Los Angeles, CA npts = 98
Height Range (km-AGL): 5.40 - 13.80
LSF: Slope = 1.03   Intercept = 1.61
Correlation: 1.00
STD DEV of Differences: 1.88 Mean Diff: 0.64
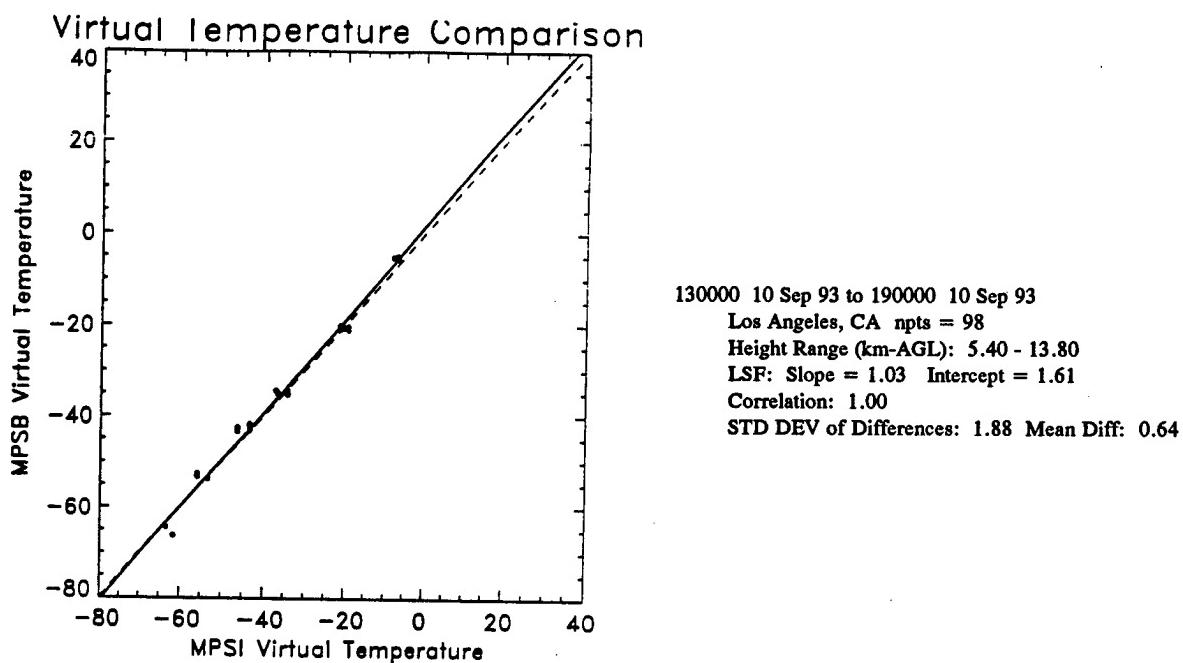
Figure 6. **Virtual temperature comparison between satellite and rawinsonde. The values at the lower three satellite levels (higher temperatures) were adjusted according to the combining algorithm.**

Virtual Temperature Comparison
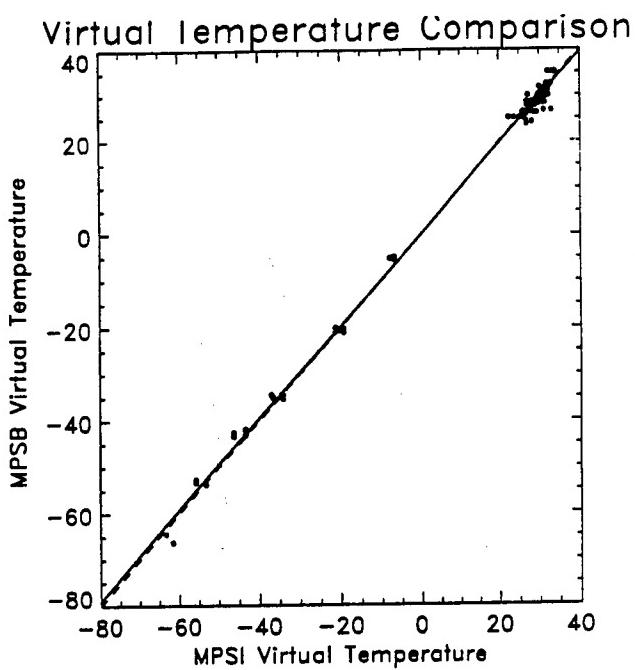
130000 10 Sep 93 to 190000 10 Sep 93
    Los Angeles, CA npts = 237
    Height Range (km-AGL): 0.00 - 13.80
    LSF: Slope = 0.99   Intercept = 0.01
    Correlation: 1.00
    STD DEV of Differences: 1.62 Mean Diff: -0.05

Figure 7. Virtual temperature comparison between the entire combined sounding and rawinsonde.

Wind Speed Comparison
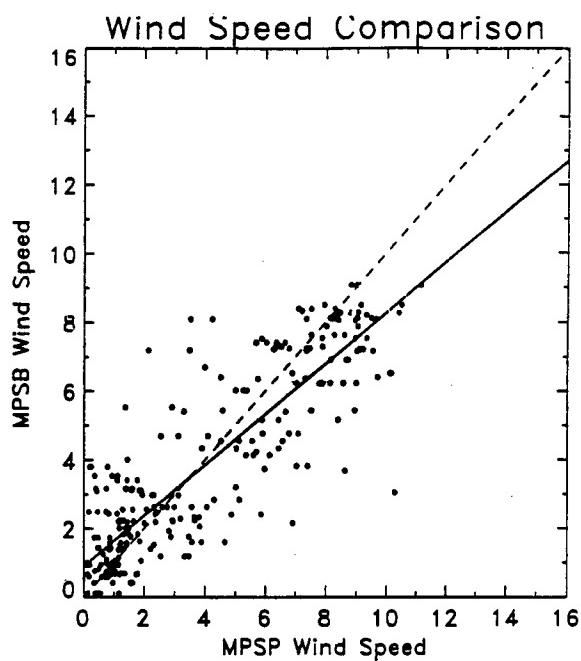
140000 08 Sep 93 to 190000 08 Sep 93
    Los Angeles, CA npts = 269
    Height Range (km-AGL): 0.10 - 3.50
    LSF: Slope = 0.74   Intercept = 0.90
    Correlation: 0.87
    STD DEV of Differences: 1.61 Mean Diff: -0.13

Figure 8. Wind speed comparison between the radar profiler and rawinsonde.

221
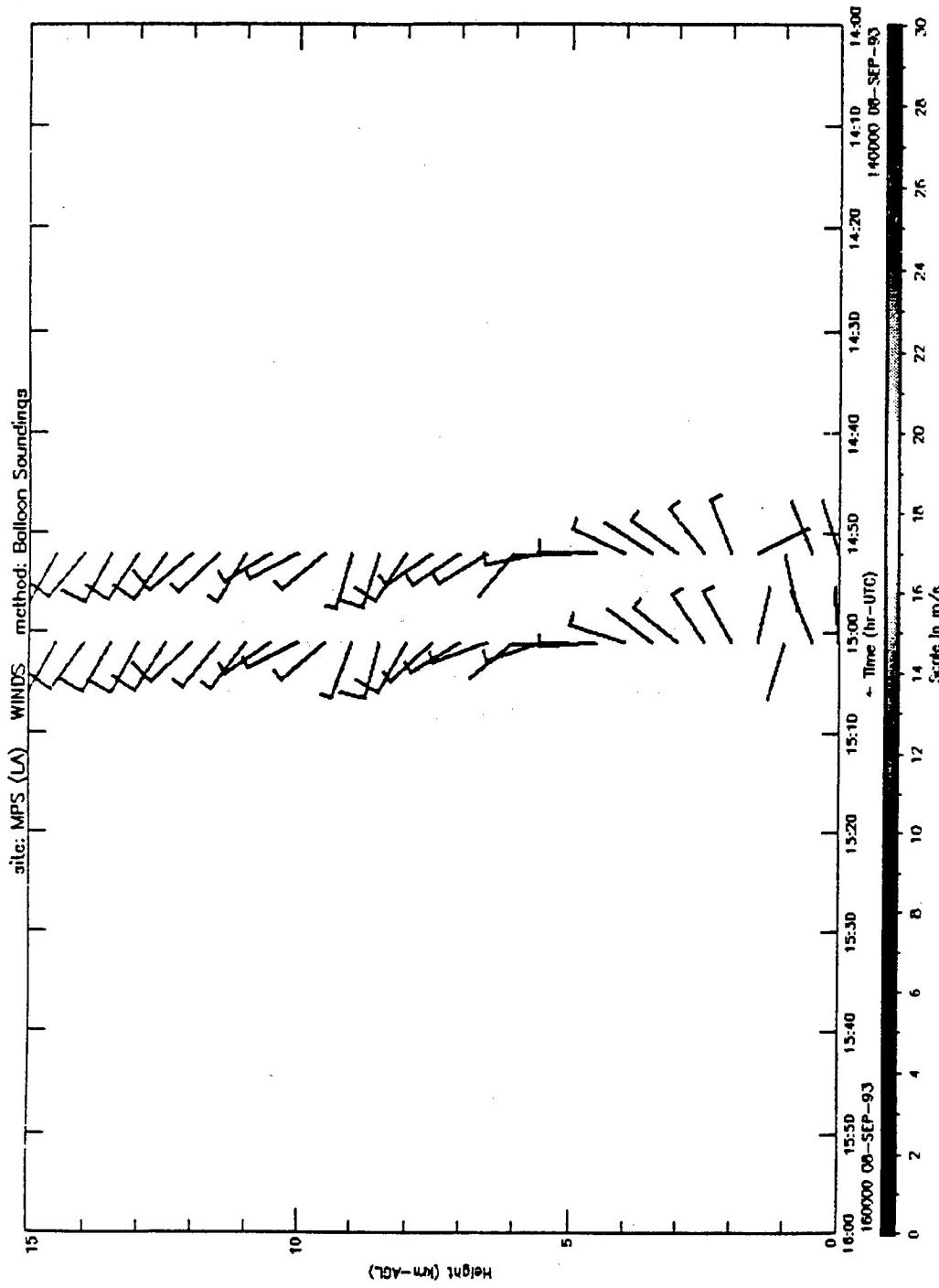
Figure 9. Wind velocity display comparing profiles from two rawinsonde systems, MARWIN (right) and CLASS (left), using the same sonde. The profiles are offset from one another for clarity of presentation. One of the better cases is shown.
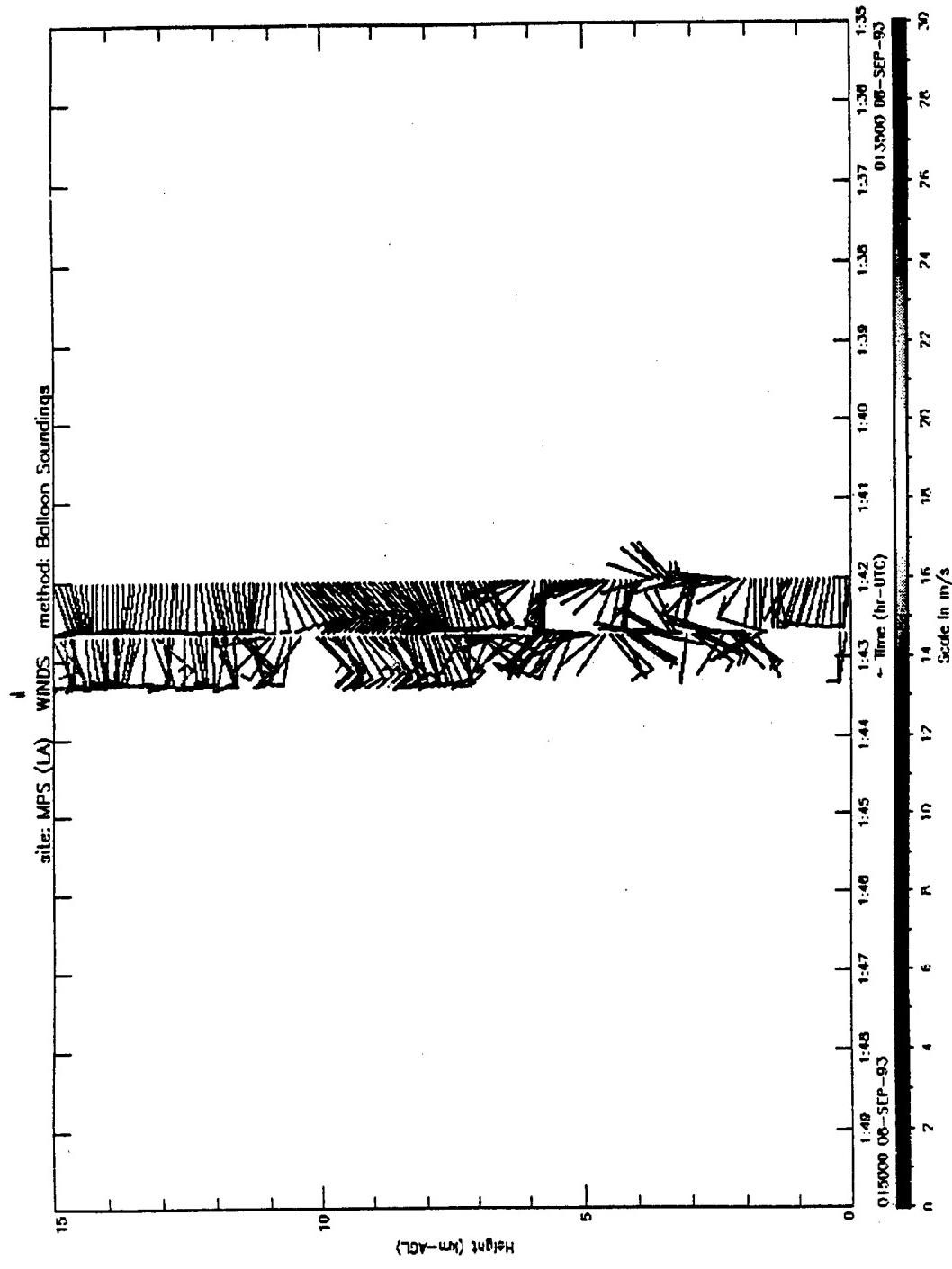
Figure 10. Wind velocity display comparing profiles from two rawinsonde systems using the same sonde, as in figure 9. One of the poorer cases is shown.

6. CONCLUSION

The TD MPS is a mobile system that combines the capabilities of several types of sensing systems to provide atmospheric soundings with a rapid refresh rate that can greatly reduce the error due to time staleness. The MPS when fielded will provide timely atmospheric profiles for fire support and a variety of other Army applications. Examples include biological and chemical defense and support to air mobile operations. It will allow the Integrated Meteorological System (IMETS) to rapidly update models, analyses, and forecasts.

The MPS is a true dual-use system. The data provided by the TD MPS and later versions will have a variety of applications in the civilian world. In a similar manner to the related military application, the MPS can provide timely support for airfield operations, giving, for example, nearly real-time indications of hazardous wind conditions. The ability to generate a picture of very short term flow and virtual temperature patterns can lead to a better understanding of the atmosphere and to better modeling at smaller scales. As the Los Angeles experiment showed, this type of system can be invaluable for pollution studies.

The MPS will be a vital part of the data gathering capability for the "Owning the Weather" concept of operations. It will contribute to making the Army ready to meet the challenges of the coming century.

REFERENCES

Cogan, J., 1992, Battlefield atmospheric soundings in near real time using satellite and ground based remotely sensed data, Second Battlefield Atmospherics Conference, sponsored by U.S. Army Research Laboratory, Battlefield Environment Directorate, White Sands Missile Range, NM 88002, 101-110.

Cogan, J., 1990, A Technique for Computation of Meteorological Variable Profiles for User Defined Heights and Layers. ASL-TMR-0005, U.S. Army Atmospheric Sciences Laboratory, White Sands Missile Range, NM 88002.

Fisher, E. E., F. Brousaides, E. Keppel, F. J. Schidlin, H. C. Herring, and D. Tolzene, 1987, Meteorological Data Error Estimates. Document 353-87, Meteorology Group, Range Commanders Council, White Sands Missile Range, NM 88002.

Hassel, N., and E. Hudson, 1989, The wind profiler for the NOAA demonstration network, Instruments and observing methods, report 35. Fourth WMO Technical Conference on Instruments and Methods of Observation (TE-CIMO-IV), Brussels, WMO/TD, 261-266.

Lawrence, T. R., B. L. Weber, M. J. Post, R. M. Hardesty, R. A. Richter, N. L. Abshire, and F. F. Hall, Jr., 1986, A comparison of Doppler lidar, rawinsonde, and 915 MHz UHF wind profiler measurements of tropospheric winds, NOAA Technical Memorandum, ERL WPL-130, 55 pp.

Miers, B., J. Cogan, and R. Szymber, 1992, A Review of Selected Remote Sensor Measurements of Temperature, Wind, and Moisture, and Comparison to Rawinsonde Measurements. ASL-TR-0315, U.S. Army Atmospheric Sciences Laboratory, White Sands Missile Range, NM 88002.

Strauch, R. G., B. L. Weber, A. S. Frisch, C. G. Little, D. A. Merritt, K. P. Moran, and D. C. Welsh, 1987, The precision and relative accuracy of profiler wind measurements, J Atmos Oceanic Technol, 4:563-571.

Strauch, R. G., D. A. Merritt, K. P. Moran, K. B. Earnshaw, and D. C. Welsh, 1984, The Colorado wind profiling network, J Atmos Oceanic Technol, 1:37-49.

Weber, B. L., and D. B. Weurtz, 1990, Comparisons of rawinsonde and wind profiler measurements. J Atmos Oceanic Technol, 7:157-174.

ANALYSIS OF BISPECTRAL OBSCURANT TRIALS AT SMOKE WEEK XV

Roger E. Davis and Ronald Catherson
Science and Technology Corporation
555 Telshor Blvd., Ste. 200
Las Cruces, NM 88011

ABSTRACT

Smoke Week XV was held at Eglin Air Force Base in May 1993 and bispectral smokes were among the obscurants tested. Bispectral clouds are produced as a mixture of standard visible and infrared screening materials. Analysis of bispectral obscurant optical properties is reported in this paper. Mass ratios of the composite screening materials along an observation line of sight strongly affect the obscurant's effective optical properties. For this reason, standard data reduction and analysis procedures used for single-component smokes have been revised in order to determine bispectral optical constants. Statistical analysis of the multiband transmissometer and nephelometer data is discussed. Mass extinction coefficients and mass extinction coefficient ratios, suitable for use in obscuration models, are determined for the bispectral obscurants.

1. INTRODUCTION

Historically, smokes and obscurants deployed on the battlefield were used to degrade or block only the visible portion of the spectrum. Although the human eye still remains the most prevalent sensor, the modern battlefield environment includes many weapons systems and sensors that operate in a wide variety of spectral regions, ranging from the visible and infrared through millimeter wavelengths. The common deployment and use of systems operating outside of the visible spectral region by military organizations throughout the world has prompted the development of new obscurants. These obscurants have been designed to block either single or multiple spectral regions.

One approach to the development of multispectral obscurants is to mix two obscurants known to be effective in specific spectral regions. The bispectral obscurant examined in this study is composed of fog oil and graphite and is effective in the visible and infrared regions. The mixed obscurant plumes are produced by single generator units. At Smoke Week XV, two different fog oil/graphite generators were used. This paper reports on the optical characteristics, mass extinction coefficient ratios, and mass extinction coefficients for the mixed obscurant determined from the data collected during these bispectral generator trials. The generators used for the trials analyzed can, and did for selected characterization trials, disperse a single obscurant. The optical characteristics of the single-component clouds produced by these generators (fog oil only and graphite only) are also presented.

2. SMOKE WEEK XV BISPECTRAL TRIALS

Smoke Week XV was held at Eglin Air Force Base, FL, from 3 May to 22 May 1993. Smoke Week trials are designed to simulate the "dirty" battlefield as closely as possible in order to assess the performance of obscurants, obscurant dissemination systems, and electro-optical (EO) systems in obscurant environments under realistic atmospheric conditions. Complete descriptions of the test design, experiments conducted, meteorology, obscurants tested, EO systems present, trial documentation, target locations, smoke release positions, and data acquired are found in the Smoke Week XV test plan (Locke et al., 1993), the quick-look report (Ota et al., 1993), and the final report (Ota et al., in preparation).

This section describes instrumentation, trial design, and data collection for bispectral obscurants. This discussion includes not only trials during which the bispectral mixes were released, but also characterization trials in which the individual components of the bispectral smokes were disseminated.

2.1 TEST LAYOUT

Smoke Week XV was conducted on Eglin Air Force Base Test Area C-52A. The grid area is flat, sandy terrain surrounded by forest. Characterization and EO lines of sight (LOS) were established in nominally east-west directions with targets placed at the east end of the grid. Prevailing winds during the trials were generally southerly (sea breeze) and were established by late morning or early afternoon.

The relevant instrumentation for the bispectral obscurant optical properties analysis includes the Research Visible and Infrared Transmissometer (REVIRT) LOSs 4, 5, and 6, and the nephelometer array. These LOSs and the nephelometer locations in the test grid are shown in Fig. 1. REVIRT LOS 4 was 1.77 km long with endpoints at sites S4 and S3. REVIRT LOS 5 was 1.07 km long with endpoints at sites M1 and S3. REVIRT LOS 6 was a short-path LOS of 26.76 m located just north and near the center of the nephelometer array. LOSs 5 and 6 ran parallel to the nephelometer array and approximately 1 m distant from either side of it. Also shown in the figure is the 10-m meteorological tower W2.
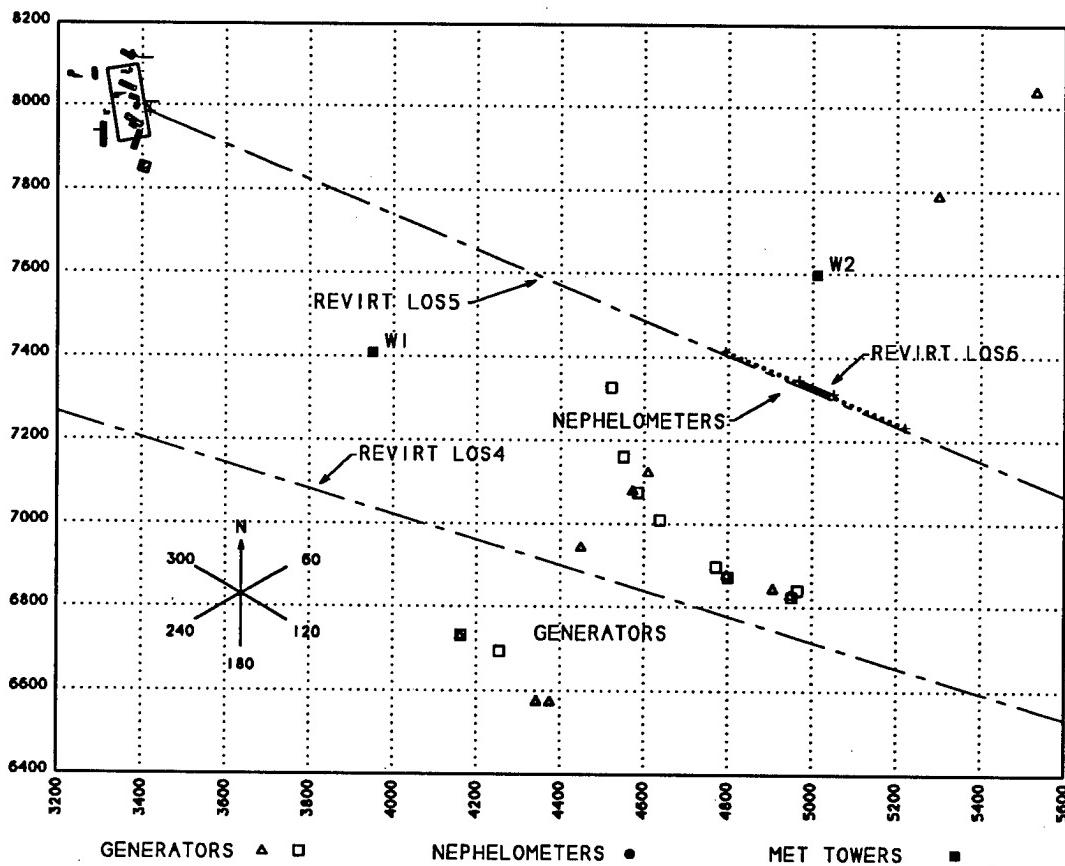
Figure 1. Lines of sight and nephelometer locations for Smoke Week XV.

2.2 BISPECTRAL AND CHARACTERIZATION TRIALS

Obscurants for the bispectral trials at Smoke Week XV were produced by two different generator types, designated in this paper as generator A and generator B. These generators are dissimilar in engineering, producing smokes through somewhat different mechanisms. Information concerning the generators and points of contact in agencies owning them are found in the Smoke Week XV quick-look report (Ota et al., 1993). At Smoke Week XV, data collection using generator A was given higher priority. The same fog oil and pelletized graphite stocks were used in both generators.

Experiments for the bispectral obscurants included characterization trials of the individual obscurant components, fog oil and graphite. A breakdown by generator type and obscurant type of the number of bispectral and characterization trials conducted is provided in Table 1. The total number of trials of each type is given first in each entry. The numbers in parentheses are the number of trials used in the mass extinction coefficient ratio determinations; bracketed numbers indicate the number of trials used in determining mass extinction coefficients (see Section 3 for a description of these calculations). The reason for not using some of the trials in either type of determination was that inadequate data were collected, most often as a result of unfavorable winds. The nephelometer data needed for the calculation of individual obscurant mass extinction coefficients were much more sensitive to capricious winds than were the transmissometer data needed for determining both the coefficients and the ratios.

TABLE 1. SPECTRAL AND CHARACTERIZATION TRIALS AT SMOKE WEEK XV

	FOG OIL	GRAPHITE	BISPECTRAL
GENERATOR A	8 (7) [3]	7 (7) [4]	7 (7) [6*]
GENERATOR B	4 (4) [3]	6 (5) [2]	4 (4) [4*]

*Nephelometer data not required

3. DATA ANALYSIS

The objective of the analysis was to determine mass extinction coefficient ratios and mass extinction coefficients as functions of spectral region for fog oil, graphite, and the bispectral obscurant. The primary assumption made in the analysis of the bispectral obscurant was that there is no chemical or mechanical interaction between the components. That is, no hybrid fog oil/graphite aerosols are formed within the cloud and each aerosol retains its own optical properties. This assumption is certainly debatable but there are currently no data available that would allow for a more sophisticated approach.

3.1 MASS EXTINCTION COEFFICIENT RATIOS

The equation used for determining mass extinction coefficient ratios is Beer's Law, given as follows:

$$T(\Delta\lambda) = e^{-\tau(\Delta\lambda)} \tag{1}$$

where
$\Delta\lambda$ = spectral band bounded by λ_1 and λ_2
$T(\Delta\lambda)$ = transmittance in the spectral band $\Delta\lambda$
$\tau(\Delta\lambda)$ = optical depth of obscurant in spectral band $\Delta\lambda$

Optical depth can be rewritten in terms of the mass extinction coefficient and the path-integrated concentration along the LOS, usually referred to as the concentration length, CL. The mass extinction coefficient has wavelength dependence; CL does not. Hence,

$$\tau(\Delta\lambda) = \alpha(\Delta\lambda)CL \tag{2}$$

where

$\alpha(\Delta\lambda)$ = mass extinction coefficient in spectral band $\Delta\lambda$, $m^2\,g^{-1}$
CL = path-integrated concentration, $g\,m^{-2}$

At a given instant in time, the CL along the LOS is fixed regardless of the spectral band considered and the ratio of the mass extinction coefficients for spectral bands 1 and 2 is given by

$$\frac{-Ln(T(\Delta\lambda_1))}{-Ln(T(\Delta\lambda_2))} = \frac{\alpha(\Delta\lambda_1)CL}{\alpha(\Delta\lambda_2)CL} = \frac{\alpha(\Delta\lambda_1)}{\alpha(\Delta\lambda_2)} \tag{3}$$

In the form presented here, the application of Beer's Law assumes that the mass extinction coefficients of interest are nearly constant across the spectral bands. Problems created by this assumption and correction techniques for broad-band transmittance data have been discussed at this conference in previous years (Sutherland et al., 1989; Davis et al., 1990). Broad-band effects are not a concern in this analysis, however, because most of the collected transmissometer data are narrow band. The exception is the data collected in the visible band on LOS 6 and for one graphite trial on LOS 4. Broad-band effects should be insignificant for the graphite in the visible band but could cause some error in the fog oil visible ratios. The mass extinction coefficient for fog oil varies significantly across the visible band but the variation is smooth and monotonic.

Before Eq. 3 was used to calculate the ratios, the transmittance data were screened. Experience has shown that problems in transmittance ratios occur most often when the obscurant is either very thin or very thick. Under these conditions, Eq. 3 produces very noisy ratios. That is, the ratio expressed in Eq. 3 has arguments near zero when the transmittance is near one (clear air). Small noise fluctuations in this range cause very large fluctuations in the ratio. At the other end of the scale, for optically thick obscurants, the transmissometer source signal becomes more sensitive to noise. Depending on environmental conditions and clear-air settings, transmissometers occasionally reach detection thresholds between 3 and 4 optical depth units. For these reasons, all transmittance data used in this analysis have been screened such that $0.03 < T < 0.90$. This range corresponds to obscurant optical depths between 3.5 and 0.1.

3.2 MASS EXTINCTION COEFFICIENTS

Determining the mass extinction coefficients themselves is more challenging than determining their ratios. Difficulties arise because data from two different instrument types (transmissometers and nephelometers) must be used. Nephelometer sampling of the obscurant is incomplete spatially, the nephelometer measurements are based on scattering theory and determination of a calibration factor, and absolute values rather than ratios are computed. For the case of mixed obscurants, valid nephelometer concentration data are not available. Nevertheless, reasonably consistent mass extinction coefficient values can be obtained for a wide variety of obscurants if care is taken in data collection and analysis.

Unlike the mass extinction coefficients for fog oil or graphite, the effective mass extinction coefficient of the bispectral obscurant should depend on both time and location. This dependence arises when the

230

bispectral cloud is not homogeneously mixed with constant mass ratios of the two constituent materials. This situation requires modification of the usual methods used in determining mass extinction coefficients from field data. Determination of an effective mass extinction coefficient would become even more complicated if the individual components were considered to change chemically and/or physically through interaction with one another. (As already stated, such effects are not considered in this analysis.)

3.2.1 Single-Component Obscurants

The procedure for deriving mass extinction coefficients from trials using fog oil and graphite alone is straightforward. Using Eqs. 1 and 2, the following expression for the mass extinction coefficient is derived:

$$\alpha_t(\Delta\lambda) = \frac{-Ln(T_t(\Delta\lambda))}{CL_t} \tag{4}$$

The numerator on the right-hand side of Eq. 4 is formed directly from the transmittance data for a given spectral band $\Delta\lambda$. The denominator is the path-integrated concentration of the obscurant along the same LOS and at the moment in time t at which the transmittance is observed. The CL is given as

$$CL_t = \int_R \rho_t(r)\, dr \tag{5}$$

where
$\rho(r)$ = obscurant concentration at position r, g m^{-3}
R = distance through obscurant along the LOS, m

At Smoke Week XV, the obscurant concentration was sampled by nephelometers along the LOS. Spacing between nephelometers was approximately 6 m for nephelometers 1 through 11 and 18 through 28. Nephelometers 11 through 18 were spaced approximately 3 m apart. The closer spacing of nephelometers 11 through 18 was established to obtain higher spatial sampling for the short-path LOS 6. Calculations of CL were accomplished using a trapezoid integration, as follows:

$$CL_t = \frac{1}{2}\sum_{i=1}^{m-1} (N_i + N_{i+1})\, \Delta x_i \tag{6}$$

where
N_i = obscurant concentration at time t for nephelometer i, g m^{-3}
Δx_i = distance between nephelometers i and i+1, m
m = total number of nephelometers in array

Although the numerical calculation of CL given by Eq. 6 is straightforward, the determination of CL values has pitfalls. For example, often during a trial, the obscurant plume can miss the nephelometer array either completely or partially. None of the data collected during these time periods can be used to calculate mass extinction coefficients because not all of the mass along the LOS was measured.

A second problem is that occasionally several nephelometers apparently produced spurious signals. To avoid including extra mass in the CL calculations due to spurious clear-air signals, the maximum clear-

air value for each nephelometer was determined and no signal equal to or less than that maximum was used in calculating the CL by Eq. 6. The maximum clear-air value was not subtracted from all data reported by a nephelometer. The reasons are that (1) the signals are not constant, and (2) it is conjectured that for higher obscurant concentrations, the spurious signals will either average out over the trial or be insignificant. Item 2 is debatable but it is a necessary assumption given the way the data were collected.

Additional factors affect the quality of the nephelometer data. These factors include difficulty in measuring low concentrations of graphite due to its low scattering efficiency and high concentrations of fog oil due to its high scattering efficiency, and the determination of calibration "K" factors. While K factor determination is usually not problematic, trial 01079 was not used in the calculation of mass extinction coefficients because the K for this trial was reported to be 50% to 100% greater than those used for all other graphite trials (Tony Spence, Physical Science Laboratory, personal communication).

Obscurant CLs as functions of time were calculated by Eq. 6 using nephelometer data sets screened with the above concerns acknowledged. Mass extinction coefficients as a function of time were then calculated with Eq. 4. An example of these calculations is presented in Fig. 2, where the mass extinction coefficients for trial 04779 are plotted against transmittance for 1.06 μm. Computation of a trial mean was made from this data set.

Several approaches were explored to determine trial means for the mass extinction coefficients. These were (1) simple average using all data points, (2) modified average rejecting data more than some multiple of the standard deviation from the simple average, (3) rejecting data based on a t-test of data skewness, and (4) performing a constrained linear least squares fit of CL versus optical depth. Each approach yielded somewhat different values for the mean. For comparison, results of these approaches for trial 04779 are presented in Table 2.

The data in Fig. 2 indicate that the scatter in mass extinction coefficient values becomes much greater as the obscurant becomes thin, that is, at higher values of transmittance. For the graphite obscurant this result seems reasonable because graphite concentration is difficult to measure by nephelometry when the optical depth is near zero. Therefore, mass extinction coefficients determined under these conditions are likely to be noisy and more subject to error than under denser obscurant conditions. From Fig. 2 it is obvious that computing a simple trial average of all data points would produce a mean that is too high.

To remove the apparently spurious data points occurring primarily under conditions of high transmittance, approaches 2 and 3 described above were explored. Implementing approach 2 using a factor of 2.5 times the standard deviation computed from the entire data set reduced the mean value of the mass extinction coefficient (see Table 4). Choice of the multiplying factor for the standard deviation rejection threshold is arbitrary, however. In an attempt to make the rejection criterion less arbitrary, the skewness, that is, the third moment of the data, was considered, implementing approach 3. A running skewness was calculated beginning with the mass extinction coefficients determined at the lowest transmittance value. The deviation of the data from a Gaussian distribution was then determined for the transmittance level at which the skewness failed the two-tailed t-test at the 99% confidence level. For the data set displayed in Fig. 2, only the data below 50% transmittance passed the test at this confidence level. The data that fulfilled this requirement were averaged and the result is shown in Table 4.
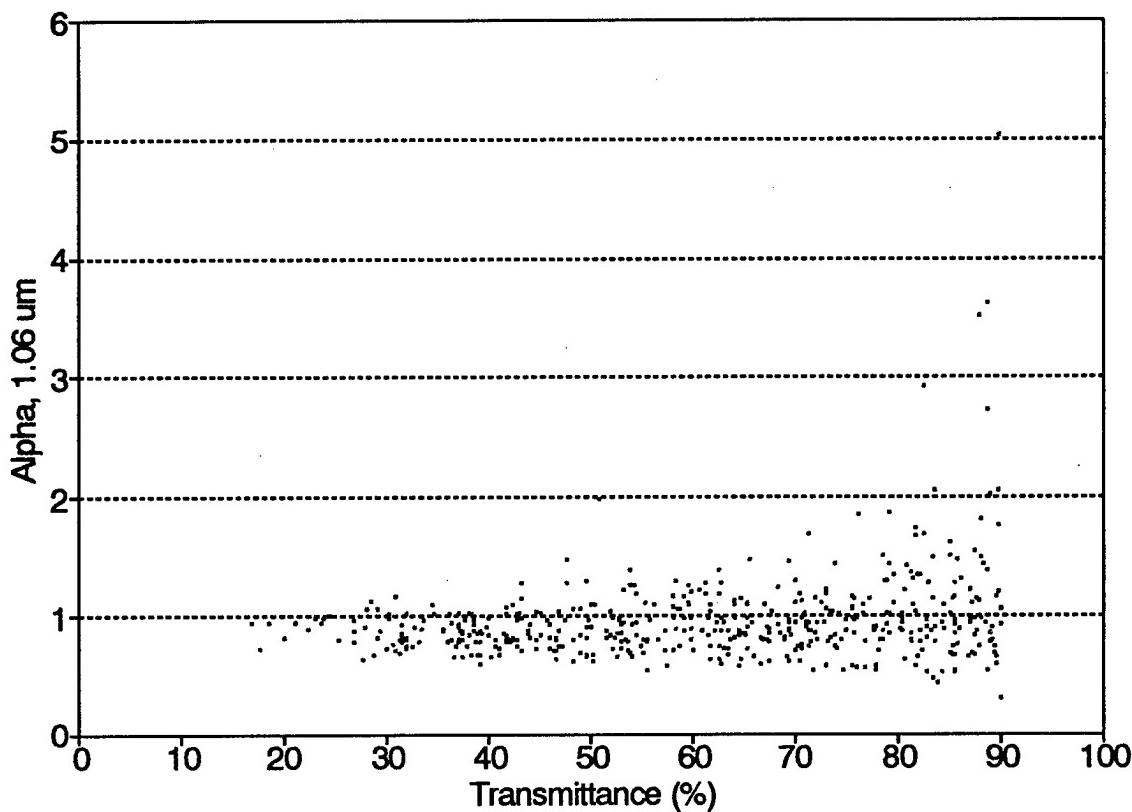
Figure 2. Mass extinction coefficients for trial 04779. Trial means were calculated from this data set using techniques described in the text.

TABLE 2. MASS EXTINCTION COEFFICIENTS, TRIAL 04779

METHOD*	MASS EXTINCTION COEFFICIENT (1.06 μm)
Simple mean (1)	1.03
Modified mean (2)	1.00
Skewness/t-test (3)	0.94
Least squares (4)	0.91

*See text for description of methods

233

Although the skewness approach usually worked well with the graphite trial sets, it did not work so well for fog oil trials. The fog oil CL values showed higher and more erratic scatter than did those for graphite, causing the skewness to fail the t-test at very low transmittance levels. A single widely deviant data point causes the t-test to class the skewness as not statistically Gaussian. This situation was common in the fog oil CL data and caused the rejection of large amounts of valid data.

Problems with the t-test prompted the use of approach 4. In this approach, all data for a trial were used in a linear least-squares fit of CL versus optical depth. The data used to produce Fig. 2 are redisplayed in Fig. 3. The least-squares fit to this data set is shown as a solid line, which was constrained to pass through the origin. From Eq. 4 it is readily recognized that the slope of this line is the mass extinction coefficient. This approach has the advantage that high-transmittance data values have less influence on the trial mean than they do in the other approaches. This approach was adopted as the method for determining trial mean mass extinction coefficients for both the fog oil and graphite trials.

3.2.2 The Bispectral Obscurant

The situation is more complicated for bispectral obscurants because $\alpha(\Delta\lambda)$ represents the mixed obscurants and depends on the CL ratios of the individual obscurants along the LOS at any time. Also, nephelometers are unable to measure valid mass concentrations for obscurant mixtures, so bispectral CL cannot be measured directly. For these obscurants, methods less direct than that of Eq. 4 must be used.
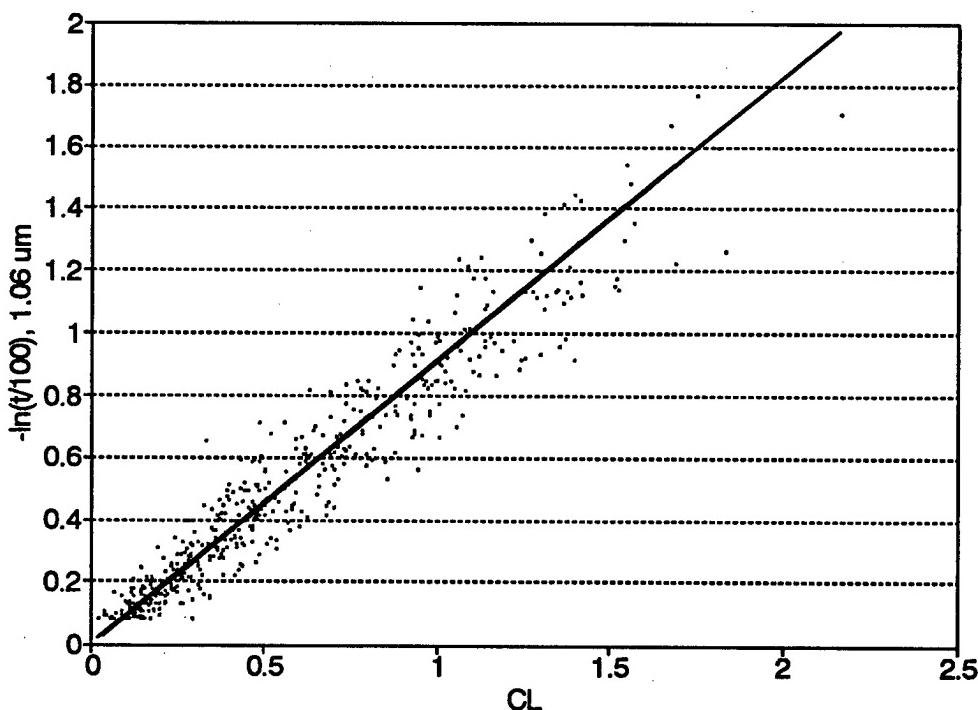
Figure 3. **Optical depth (-ln T) versus CL for trial 04779. The same data used to produce Fig. 2 were used to generate the plot. Parameters for the data set were slope (mass extinction coefficient) = 0.913, correlation coefficient r^2 = 0.914, and average and standard deviation for the data set = 1.038 and 0.382, respectively.**

Assuming that the fog oil (FO) and graphite (G) aerosols maintain their optical properties and that no new aerosol is formed in the obscurant mixture, the bispectral transmittance is expressed as follows:

$$T(\Delta\lambda) = e^{-(\alpha(FO,\Delta\lambda)CL(FO) + \alpha(G,\Delta\lambda)CL(G))} \qquad (7)$$

and

$$-Ln(T(\Delta\lambda)) = \alpha(FO,\Delta\lambda)CL(FO) + \alpha(G,\Delta\lambda)CL(G) \qquad (8)$$

The right-hand side of Eq. 8 could be expressed in terms of an effective mass extinction coefficient for the bispectral smoke such that

$$\alpha_{bi}(\Delta\lambda)CL_{bi} = \alpha(FO,\Delta\lambda)CL(FO) + \alpha(G,\Delta\lambda)CL(G) \qquad (9)$$

where

$\alpha_{bi}(\Delta\lambda)$ = effective mass extinction coefficient for bispectral smoke
CL_{bi} = CL for bispectral smoke

If we allow CL_{bi} to be the sum of the fog oil and graphite CLs, Eq. (9) can be rewritten as

$$\alpha_{bi}(\Delta\lambda) = \frac{\alpha(FO,\Delta\lambda)CL(FO) + \alpha(G,\Delta\lambda)CL(G)}{CL(FO) + CL(G)} \qquad (10)$$

It must be understood that the effective mass extinction coefficient of Eqs. 9 and 10 is not a physical constant. The effective mass extinction coefficient is a function of both the fog oil and graphite CLs, which are temporally and spatially variable within the obscurant cloud. The trial means computed for the effective mass extinction coefficients are only indicators for comparing the bispectral smoke with other obscurants. *Furthermore, if the generator emission rates for the fog oil and/or the graphite are changed or the environmental conditions cause the constituents to mix differently than they did at the Smoke Week XV trials, the mean effective mass extinction coefficients will be different.*

A more meaningful parameter in characterizing the bispectral obscurant is the fog-oil-to-graphite CL ratio as a function of time. This parameter indicates how well the obscurant cloud stays mixed and predicts the expected range in attenuation. Variability of the CL ratios is to be analyzed in future work.

Determining the effective mass extinction coefficient for the bispectral obscurant requires the determination of fog oil and graphite CLs along the LOS. Laboratory data and previous field test measurements show the fog oil mass extinction coefficient at 10.6 μm to be near 0.01 m^2 g^{-1}. The fog oil clouds generated at Smoke Week XV were not dense enough to produce measurable attenuation at 10.6 μm, so no determination of fog oil mass extinction coefficient in this spectral region was possible.

It is reasonable, then, to allow that the attenuation of radiation at 10.6 μm for the Smoke Week XV bispectral trials is due to graphite alone. On this premise, CL for graphite in the mixed cloud is calculated using Eq. 4 rewritten as

$$CL(G) = \frac{-Ln(T(10.6\,\mu m))}{\alpha(G,10.6\,\mu m)} \qquad (11)$$

where the mass extinction coefficient for graphite is determined from the graphite-only trials.

Using the graphite CLs determined from Eq. 11, Eq. 8 is then solved for the fog oil CL, yielding

$$CL(FO) = \frac{-Ln(T(1.06\,\mu m)) - \alpha(G, 1.06\,\mu m)CL(G)}{\alpha(FO, 1.06\,\mu m)} \qquad (12)$$

where the mass extinction coefficients for graphite and fog oil have been determined from the single-obscurant trials.

The CLs for each bispectral trial were calculated using Eqs. 11 and 12 for every second (data collection rate of the instruments) of valid transmissometry. From these data, the bispectral effective mass extinction coefficients as a function of trial time can be computed using Eq. 10. An example of the effective mass extinction coefficient as a function of time is shown for trial 04380 in Fig. 4. Magnitudes of the variations seen in the effective mass extinction coefficient for this trial and bandpass are typical of all the bispectral trials at Smoke Week XV. Unweighted means and standard deviations for the effective mass extinction coefficients were computed for bispectral smokes produced by generators A and B. These values are presented in the next section.

4. RESULTS

Mass extinction coefficients and ratios have been computed using the methods described in Section 3. Means of the trial means were computed and are presented here as functions of obscurant type, spectral band, and generator type. A technical report providing details of data and analyses performed for this study for individual trials and LOSs will be available in early 1994.
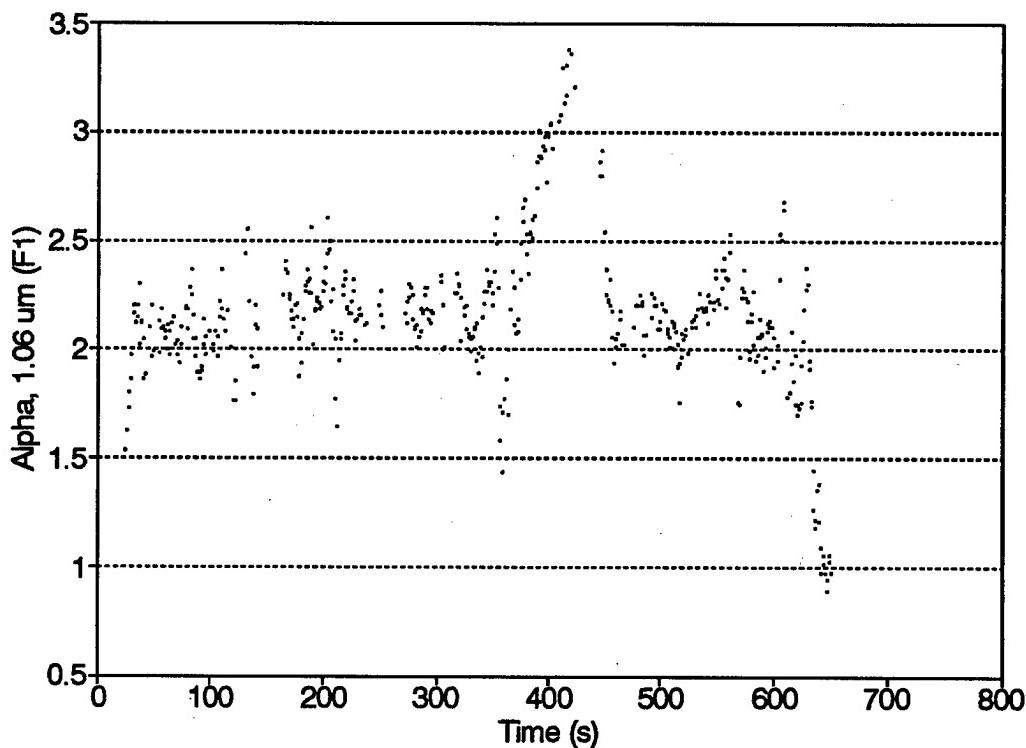
Figure 4. Effective mass extinction coefficient for trial 04380. Mean value for the trial is 2.2 m² g⁻¹.

Mass extinction coefficient ratios and mass extinction coefficients for single-obscurant trials are valid for use by workers required to model fog oil and pelletized graphite clouds disseminated by generator types A and B. Great care should be exercised in using the fog oil/graphite bispectral smoke values because of their dependence on obscurant mass ratios (see Section 3).

4.1 MASS EXTINCTION COEFFICIENT RATIOS

Means of trial mean mass extinction coefficient ratios computed from transmissometry are presented in Table 3 for fog oil, in Table 4 for graphite, and in Table 5 for the bispectral obscurant. Standard deviations of the means of the trial means are given in parentheses and the number of data sets for each spectral region from which the table means were computed are given in brackets. Each data set was for one trial and one LOS; in a few cases data from more than one LOS were available for a single trial. Fog oil released in these generator trials was never dense enough to cause measurable attenuation in the 10.6-μm region.

TABLE 3. MEAN FOG OIL MASS EXTINCTION COEFFICIENT RATIOS

GENERATOR	1.06/VIS (S.D.) [SETS]	1.54/0.532 (S.D.) [SETS]	1.54/1.06 (S.D.) [SETS]
A	0.281 (0.050) [6]	0.201 (0.015) [3]	0.529 (0.070) [6]
B	0.389 (0.020) [4]	0.291 (------) [1]	0.630 (0.065) [3]

TABLE 4. MEAN GRAPHITE MASS EXTINCTION COEFFICIENT RATIOS

GENERATOR	1.06/VIS (S.D.)[SETS]	1.54/0.532 (S.D.)[SETS]	1.54/1.06 (S.D.)[SETS]	10.6/0.532 (S.D.)[SETS]	10.6/1.06 (S.D.)[SETS]	10.6/1.54 (S.D.)[SETS]
A	1.019 (0.017) [7]	1.023 (0.036) [3]	1.030 (0.015) [5]	1.113 (0.071) [3]	1.093 (0.037) [5]	1.080 (0.039) [9]
B	0.998 (0.019) [3]	0.988 (----) [1]	1.016 (0.026) [3]	1.069 (----) [1]	1.112 (0.030) [4]	1.093 (0.015) [5]

TABLE 5: MEAN BISPECTRAL MASS EXTINCTION COEFFICIENT RATIOS

GENERATOR	1.06/VIS (S.D.)[SETS]	1.54/0.532 (S.D.)[SETS]	1.54/1.06 (S.D.)[SETS]	10.6/0.532 (S.D.)[SETS]	10.6/1.06 (S.D.)[SETS]	10.6/1.54 (S.D.) [SETS]
A	0.358 (0.013) [6]	0.300 (0.031) [4]	0.724 (0.056) [7]	0.190 (0.050) [4]	0.446 (0.151) [7]	0.601 (0.150) [11]
B	0.645 (0.040) [4]	0.490 (----) [1]	0.710 (0.056) [4]	0.093 (----) [1]	0.133 (0.014) [4]	0.182 (0.028) [5]

4.2 MASS EXTINCTION COEFFICIENTS

Mass extinction coefficients computed from nephelometry and coincident transmissometry LOSs 5 and 6 are presented in Table 6. The limitations of available transmissometer spectral bands meant that only the 1.06-μm spectral band was common to both LOSs. Visible coefficients were determined using transmissometer LOS 6, while the coefficients for the 1.54-μm and 10.6-μm bands were derived from transmissometer LOS 5. Coefficients for 1.06 μm were determined from transmissometer LOSs 5 and 6.

4.3 DISCUSSION OF RESULTS

Comparison of fog oil mass extinction coefficients and ratios between generator types reveals significant differences in the obscurant cloud optical constants, particularly in the visible spectral region. Analysis of fog oil data from previous Smoke Weeks has shown that this obscurant can exhibit a wide variation in mass extinction coefficient. This variation is apparently dependent upon the method and, most importantly, the temperature used to produce the fog oil aerosol. The fact that generators A and B are mechanically different and that the flow of fog oil through generator B was nearly twice that through generator A may account for the differences seen in optical properties between the resulting fog oil clouds. As analysis of these bispectral trials progresses, generator mechanics and aerosol particle size distributions will be studied.

In contrast to the fog oil results, the graphite mass extinction coefficients and ratios for the two generators are very nearly the same. Mass extinction coefficients for generator A are approximately 5% larger than those calculated for generator B. Only one trial could be used to calculate the coefficients for graphite clouds produced by generator B, however. Given the errors in the measurements, there is no significant difference between the graphite results for the two generators. Future field experiments should be performed to increase the database for generator B in order to confirm this conclusion.

The mass extinction coefficients and ratios for the bispectral clouds, like those for fog oil, show generator-dependent differences. This result is expected because of differences in the fog oil constituent.

A consistency check on the results presented in the above tables can be made by comparing mass extinction coefficient ratios computed from the transmissometry (Tables 3, 4, and 5) with ratios formed from the coefficients in Table 6. The two sets of ratios generally agree within 5% of one another and by no more than 10%. The exception is the generator A fog oil for the visible-to-1.06-μm ratio (over 30%). The visible mass extinction coefficients for generator A fog oil were quite variable. This result could indicate instrument problems and/or real differences in the fog oil from trial to trial. The cause for this variation is being explored.

Analysis of the bispectral trials is continuing. Deposition samples taken for some of the trials are being analyzed in the context of generator efficiency. Although data are sparse, attempts will be made to discern any changes in mass extinction coefficient as a function of distance from generator release locations. The CL ratios as a function of time and downwind distance are also being studied.

TABLE 6. MASS EXTINCTION COEFFICIENTS FOR OBSCURANTS PRODUCED BY BISPECTRAL OBSCURANT GENERATORS

	VISIBLE (S.D) [sets]	1.06 μm (S.D.) [sets]	1.54 μm (S.D.) [sets]	10.6 μm (S.D.)
FOG OIL				
GEN A	11.05 (1.86) [3]	4.09 (0.34) [6]	2.41 (0.43) [3]	---
GEN B	8.32 (----)[1]	3.44 (0.16)[6]	2.28 (0.15)[3]	---
GRAPHITE				
GEN A	0.90 (0.13) [4]	0.94 (0.11)[8]	1.01 (0.06) [4]	1.08 (0.08) [4]
GEN B	0.82 (----) [1]	0.89 (----) [2]*	0.96 (----) [1]	1.04 (----) [1]
BISPECTRAL				
GEN A	---	1.84 (.36) [7]	1.32 (0.20) [7]	0.75 (.12) [7]
GEN B	---	2.61 (0.07) [4]	1.871 (0.18) [4]	0.34 (0.03) [4]

* Calculated from LOSs 5 and 6 for trial 05082

239

ACKNOWLEDGMENTS

REFERENCES

Davis, R.E., S. Berrick, and P.S. Gillespie, 1990: Broad-Band Integrated Transmittances: The BITS EOSAEL Module. *Proceedings of the Eleventh Annual EOSAEL/TWI Conference,* PSL 90/99, U.S. Army Atmospheric Sciences Laboratory (ASL), U.S. Army Laboratory Command, White Sands Missile Range, NM 88002-5501.

Locke, B.A., C.Z. Ota, W. Klimek, and R. Laughman, 1993: *Army Sensors and Countermeasures Obscurants Tests (ASCOT): Smoke Week XV Test Plan.* STC Technical Report 2684, Science and Technology Corporation, 101 Research Drive, Hampton, VA, 23666-1340.

Ota, C.Z., B.R. Bullard, B.A. Locke, S. Gerard, W. Klimek, and R. Laughman, 1993: *Army Sensors and Countermeasures Obscurants Tests (ASCOT)(Smoke Week XV): Quick-Look Report,* STC Technical Report 2725, Science and Technology Corporation, 101 Research Drive, Hampton, VA, 23666-1340.

Ota, C.Z., B.R. Bullard, B.A. Locke, S. Gerard, W. Klimek, and R. Laughman, in preparation: *Army Sensors and Countermeasures Obscurants Tests (ASCOT)(Smoke Week XV): Final Report.* Science and Technology Corporation, 101 Research Drive, Hampton, VA, 23666-1340.

Sutherland, R.A., R.E. Davis, J.C. Crain, and J.L. Sommers, 1989: The Atmospheric Aerosols and Optics Data Library Transmissometer Validation Operator: Theory and Application, *Proceedings of the Tenth Annual EOSAEL/TWI Conference,* U.S. Army Atmospheric Sciences Laboratory (ASL), U.S. Army Laboratory Command, White Sands Missile Range, NM 88002-5501.

LARDS
A Low Altitude Rocket Dropsonde with GPS Windfinding

David B. Call
Atmospheric Instrumentation Research, Inc.
8401 Baseline Road
Boulder, CO 80303

Abstract

The Low Altitude Rocket Dropsonde System (LARDS), includes an expendable, rocket-borne meteorological rawinsonde and ground-based data acquisition system. The system measures pressure, temperature, humidity, wind speed and direction.

LARDS was developed under contract with the Atmospheric Technology Branch of the U.S. Army Test and Evaluation Command's (TECOM) Atmospheric Sciences Division (ASD) at the US Army White Sands Missile Range, NM to satisfy the requirement for high accuracy and high resolution low altitude meteorological data from unmanned, remote locations. The Army's requirement for rapid soundings prepared in advance is satisfied by LARDS without the use of helium balloons.

The Global Positioning System (GPS) is the basis of the wind finding technique employed. GPS technology, first developed by AIR, Inc., for use with GPS radiosondes, was combined with a low altitude rocket to achieve the objectives stated above.

INTRODUCTION

Radiosondes are in daily use in almost every country in the world for upper-air meteorological observations. They consist of a low-cost, light weight, sensor package containing electronic circuitry for measuring pressure, temperature and humidity. This package is carried aloft by a helium filled balloon, measuring the atmosphere as it ascends and transmitting the data to a ground station. Radiosondes are a vital part of the world weather forecast network. Constituencies in aviation, marine, science, agriculture, military, recreation, and industry all depend on accurate and timely weather information derived, in part, from radiosondes. The current World Meteorological Organization (WMO) radiosonde network evolved from technology and instruments developed by meteorological researchers during the 1930's. The equipment and technology was refined and observation networks greatly expanded during WW-II for military weather needs. The WMO network still relies primarily on radar and radiotheodolite tracking for winds in most countries of the world.

Radiosondes are an important component of test systems used on military test ranges to acquire atmospheric data. Routine soundings of the local weather precede every important test that is likely to be affected by the state of the atmosphere. Frequency and intensity of atmospheric sounding increases as the countdown approaches zero. The minutes immediately preceding a test are most critical because the atmosphere is dynamic and unpredictable. Standard radiosondes require personnel at the balloon release point in order to prepare and properly launch. This limits the rate and, hence, the resolution in time and space that upper-level conditions can be measured. A typical radiosonde requires 20 to 30 minutes for

preparation, balloon filling, and release. After release, a radiosonde drifts with the wind for 30 to 90 minutes while its signal is received and processed. If additional soundings are needed, the preparation process must be repeated by meteorological technicians physically located at the launch site. In situations where detailed and very current target area weather data is necessary, it is impractical, from the standpoint of personnel safety, to have MET technicians anywhere near target areas. If radiosondes are to be released in rapid sequence, then separate ground stations are required in order to prepare the radiosonde and track each signal.

The LARDS system addresses the requirement for high accuracy and high resolution data from remote locations. Several rocketsondes can be prepared by technicians hours, or even days, before an important test and installed in launchers located at or near a target site. The receiver and ground station may be located miles away in a more secure position. Each transmitter operates on a preselected crystal frequency so tuning and drift are eliminated. Sensors are factory calibrated and stable without special hermetic packaging or environmental protection. Calibration coefficients and synchronization data are telemetered in digital format from the rocketsonde to the base station automatically when the rocketsonde is powered-on. Since the start-up sequence requires only a few seconds, LARDS rockets can be launched in rapid sequence.

The LARDS system is based on hardware and software developed for a low-cost, commercial GPS radiosonde sounding system, the GPS-700. LARDS electronic circuitry, data format, GPS winds algorithm, and sensor performance are essentially identical to GPSonde™. The ground receiving station receives and processes telemetered data from the LARDS rocketsondes. The method of measuring upper-level winds by tracking a rising balloon or descending parachute using translated GPS radio-navigation signals applies equally.

Within each rocketsonde is a GPS translator that receives and compresses the satellite signals

into a format that can be retransmitted to the ground by narrowband (10 KHz) FM telemetry. This new and innovative technology is the first practical application of GPS to low-cost, windfinding. Based on GPS radiosonde windfinding technology developed by A.I.R., Inc., for its GPSonde™ system, the LARDS system measures atmospheric parameters with high temporal and spacial resolution. LARDS rockets can be prepared for use well in advance and launched to 10,000 foot altitude in rapid sequence by remote control. This flexibility permits the launch and tracking of dropsondes at 10 minute intervals from target areas or at dangerous locations where weather personnel cannot provide conventional radiosonde support.

Only 1.1 inch in diameter and 36 inches long, the rocket body is fabricated of paper and plastic. The rocket motor utilizes a solid propellent that is safe to store and transport. No metal is used in the body or motor construction. Total weight of the rocket vehicle and payload is less than one pound (450 grams). By adapting proven, expendable, GPS radiosonde circuitry to the rocketsonde payload, its commercial price is competitive with conventional radiosonde consumables.

LORAN/OMEGA RADIO-NAVIGATION

Utilization of the radio-navigation signals, LORAN or OMEGA, for radiosonde winds measurement began in the 1970's. Translation of these signals provided an alternative to costly directional antenna tracking techniques used with radar and radiotheodolite radiosonde systems. In this technique, a very simple, inexpensive (<$10), radio-navigation receiver is placed in a radiosonde. This receiver has only the ability to detect and amplify the LORAN or OMEGA signal. Amplified navigation signals are added to the radiosonde's sensor data signal and both are transmitted to the ground station. All cost associated with intelligence and processing of the navigation solution for tracking the radiosonde and computing winds takes place within the ground station.

Radio-navigation offers a level of radiosonde

ground station portability and economy that is not possible with large tracking antennas. Expense for the operation and maintenance of precision tracking antennas is eliminated, as is the problem of transporting large structures. However, a price is paid in system performance when LORAN or OMEGA are used. These systems are not autonomous. They depend on transmitting stations that are located in other countries and at potentially vulnerable or adverse geographic sites. LORAN navigation signal coverage is limited to a fraction of the northern hemisphere: primarily the United States, Europe, Saudi Arabia, and Japan. OMEGA has provided worldwide coverage for many years, but its accuracy is poor and unsuitable for many range and scientific requirements. Its future viability is also in doubt. The DOD has withdrawn financial support from the OMEGA system and committed its navigation resources to GPS. Other compromises that are made for lower ground station cost and complexity are a reduction in winds accuracy and increased sensitivity to radio interference and atmospheric propagation anomalies. LORAN/OMEGA receivers within the radiosonde require a long wire antenna that is susceptible to the effects of lightning and high voltage electrostatic fields in storm clouds. Most of the limitations inherent in any of the other conventional windfinding techniques are absent when GPS radio-navigation techniques are used for radiosonde windfinding.

THE GLOBAL POSITIONING SATELLITE SYSTEM

GPS is the ideal windfinding technology for use with radiosondes and rocketsondes. The constellation of 24 GPS satellites orbit at 12,000 miles above the earth where they provide 24 hour a day worldwide navigation coverage. As a key asset of the U.S. Department of Defence, and with a very large and rapidly expanding civilian constituency, the GPS system is certain to provide secure longevity - at least 30 years - that no other navigation technology can offer. In high orbit, GPS satellites are much more geopolitically secure than earth-based LORAN/OMEGA transmitters. Using radio spread spectrum modulation techniques at a transmission frequency of 1575 MHz, GPS signals are highly resistant to interference and operate in all weather. Low frequency propagation anomalies and spherics do not affect GPS. The antenna necessary for GPS reception is small and contained within the radiosonde/rocketsonde body where it is unaffected by lightning or high voltage in cloud. When GPS is applied to radiosonde tracking it provides superb performance. Accuracy in measuring winds on a rocketsonde is better than 0.5 mph and this matches or exceeds precision tracking radar. GPS is the most accurate and reliable radio-navigation system yet devised.

A GPS radiosonde/rocketsonde system is especially well suited to provide target weather and missile launch site weather at military test ranges. A missile guidance program must have accurate wind profile data and knowledge of upper level wind shear for accuracy and safety. Target weather data is important for forecasting, operations scheduling, sound ranging, particle and gas dispersion predictions, and guidance accuracy evaluation. Passive infrared, lidar, radar, sodar, and optical sensors can all be adversely affected by certain atmospheric conditions.

FREQUENCY BANDWIDTH CONSIDERATIONS

The 400 to 406 MHz meteorological band is heavily used and commercial radiosondes make very inefficient use of the resource. Typical radiosondes require 500 KHz of bandwidth for the signal and an additional 500 KHz to allow for frequency drift of low cost (non-crystal controlled) radio transmitters. In many locations a number of radiosondes can be detected at any one time as a receiver is tuned over the 400 to 406 MHz band. An operator must select a region of the spectrum that is not in use, tune the radiosonde for that frequency, and hope no radiosonde at some other location will interfere. This problem of transmitter drift and frequency interference is significant and increasing, especially in Europe where many countries are using the 400 to 406 MHz band within a relatively small (for radio telemetry) geographic area. Some countries (Germany, Austria, Switzerland) require the radiosonde operate with narrowband, crystal stability,

transmitters. They allow only 20 KHz channel spacing, and neither LORAN nor OMEGA can be used on narrowband crystal stabilized radiosondes. The LARDS narrowband GPS translation technique however will operate easily within this channel spacing limitation. With only a 10 KHz bandwidth and insignificant frequency drift, the LARDS system can accommodate hundreds of radiosondes or rocketsondes within the MET band without interference.

THE ROCKET VEHICLE

The body of a LARDS rocket is fabricated of inexpensive composite material and plastic. It contains no hard metal parts that could be hazardous to personnel or property. The rocket motor case is a fiber wound, phenolic impregnated tube. Its solid fuel is totally insensitive to shock and is classified as a flammable solid, not an explosive. Weight of the rocket and electronic payload is less than 16 ounces. Total fuel weight is less than 112 gram. Under Federal Aviation Administration regulation FAA 101, no special approval is required to launch LARDS rockets. They are classified under the same rules as Hobbyist model rockets. Despite this liberal classification, they are still very high velocity projectiles and accelerate to Mach 1 speeds in 2-3 seconds. Figure 1 shows the configuration of a LARDS rocket.

SENSORS

Due to its fairly rapid descent rate (1000 fpm after parachute deployment), fast response sensors are necessary. Pressure, temperature, and humidity sensors each respond in one second or less. Their accuracy and resolution approaches that of high quality laboratory digital instrumentation. Each sensor is precalibrated at the factory and all calibration coefficient data is stored in microcomputer memory within the LARDS rocketsonde or GPSonde radiosonde. When sonde power is first applied, calibration coefficient data for each sensor is automatically transmitted to the ground station. Specifications for the sensors used in LARDS rocketsondes are

listed in Table 1.

TABLE 1

Sensor Performance Specifications

PRESSURE SENSOR

Type	Aneroid capacitance
Pressure Range	1050 to 600 hPa
Accuracy	1.0 hPa
Resolution	0.01 hPa
Response time	< 0.1 second

TEMPERATURE SENSOR

Type	Bead thermistor
Temperature Range	-55°C to 50°C
Accuracy	0.3°C
Resolution	0.01°C
Coating	None
Nominal Resistance	10 Kohm @ 25°C
Response time	< 1 second

HUMIDITY SENSOR

Type	Capacitance Polymer
Humidity Range	0 to 100% RH
Accuracy	3% RH
Hysteresis	<1% RH
Resolution	0.1% RH
Response time	< 1 second

A small bead thermistor is used for temperature measurement providing high sensitivity, fast response, and long term stability. Pressure is measured by A.I.R., Inc.'s, patented dual differential aneroid capacitance sensor. This sensor offers a very low temperature coefficient of pressure and almost complete insensitivity to shock, vibration, or acceleration. It senses pressure accurately even under the shock and acceleration of 20 to 50 g's at launch.

Relative humidity is measured by A.I.R., Inc.'s, patented HUMAIR[tm] thin polymer membrane capacitance sensor. This sensor is extremely stable and linear. Figure 2 is an example of the test results on a HUMAIR sensor within a precision environmental test chamber. This sensor was exposed to steps of increasing humidity from 5%

to 95% RH in 10% steps then decreasing humidity at the same test points back down to 5%. Linearity and hysteresis were less than 0.5% RH. Even extended exposure to 100% relative humidity has little effect on stability. It provides accurate measurements in cloud as well as above the troposphere where the atmosphere is very cold and dry. HUMAIR has a unique construction. The sensing polymer is 2 microns thick and exposed to airflow on both surfaces. This thinness makes the HUMAIR time constant response to relative humidity fluctuations less than one (1) second.

SONDE MEASUREMENT CIRCUITRY

The LARDS and GPSonde Meteorological Data Encoder (MDE) is microprocessor-controlled. A 6805 single chip microcomputer uses RC oscillators and frequency counting techniques to measure both resistance and capacitance. The MDE produces manchester encoded serial data, with CRC error detection codes. Two spare channels are provided as a standard feature for use with additional optional sensors. For GPSonde, an 8 channel A/D converter circuit card is available and may be plugged into MDE and used with optional sensors for ozone, radioactivity, temperature structure (C_t), etc. This A/D converter measures +/- 2.500 volts with 12 bit accuracy.

GPS receiver circuitry used in both Lards and GPSonde is identical. The receiver requires only 320 milliwatts of battery power and the compressed GPS signal uses only 500 Hz of signal bandwidth in continuous operation. Rocketsonde, GPS receiver and MDE components are surface mounted (SMD) on one side of two 1 x 11 inch printed circuits boards. The two boards are placed back to back and mounted in a one inch diameter by 12 inch long phenolic impregnated fiber tube. This tube forms the body of the LARDS dropsonde. Sensors for temperature and humidity are mounted at one end of the MDE board and exposed in an aerodynamic duct. The GPS volute antenna and parachute line attach to the GPS receiver board at the other end. A 7.5 inch wire forms the 403 MHz transmitter antenna and

is attached to the sensor end of the MDE board. The 403 Mhz antenna wire coils within the rocket nose cone and is attached to it. The nose cone shields the fragile temperature and humidity sensors before parachute deployment. After deployment, the weight of the nose cone pulls the antenna wire down to form a vertically-polarized monopole antenna.

The FM transmitter center frequency is set by crystal selection. The LARDS rocketsonde range is, typically, in excess of twenty (20) miles. The 500 Hz GPS signal and 1000 baud MDE digital signal are combined and modulate the transmitter with 5 KHz deviation.

TABLE 2

Telemetry Performance Specifications

TRANSMITTER

Power Output	30 mW
Frequency Range	395 to 410 MHz
	(Crystal selected)
Modulation	FM (narrow band)
Antenna	1/4 wave monopole
Frequency Stability	+-5 KHz
Deviation	5 KHz
Range	20 miles

DATA FORMAT

MET Data Rate	Manchester, 1000 baud
MET Sample Rate	1 Hz
Error Detection	32 bit CRC
GPS Data	500 Hz bandwidth

TABLE 3

GPS Receiver Specifications

GPS Signal	L1 (1575.42 MHz)
Antenna	1/4 Wave RHCP Volute
Noise Figure	1.5 dB
Velocity Accuracy	0.5 mph
Power	8 volts @ 40 milliamps

THE GROUND STATION

The ground station consists of three elements: UHF Receiver/PTH processor (Model IS-5A-RCR), GPS winds processor (Model 70 atmospheric data processor), and IBM compatible PC. Figure 3 provide a conceptual schematic of the ground station. The PC is an unmodified, commercial, personal computer. Application software was written to run under the IBM OS-2 operating system. OS-2 was selected because its multi-tasking and multi-windowed features allow seamless manipulation of both tabular and graphical real-time processes. A single RS-232 COM port provides the interface between the PC and the system. The decision to eliminate custom cards or special hardware within the PC was intentional and carefully considered. The AIR system avoids subtle compatibility problems with custom PC cards, BIOS, clock speed, addressing, etc., that sometimes occur with "100% IBM compatible PC's". The only compatibility issue for the PC is that it must run OS-2 and include a device driver for the COM port.

The PTH processor within the UHF receiver has two microcomputers that receive and process telemetry data continuously. One (68HC11) converts the manchester-encoded telemetry signal into standard binary data. The second (80186) calculates pressure, temperature, relativity humidity, and time in standard scientific units. The PTH processor is a data concentrator and coordinates serial communication to and from several RS-232 ports. One port supports remote control of the UHF receiver. A second port provides an interface to the winds processor.

The GPS winds processor utilizes a dedicated 486 microcomputer, as well as custom circuitry for digital signal processing. It contains a standard commercial C/A code correlating GPS receiver that is used to derive UTC time, geodetic position, and the GPS constellation almanac.

A GPS receiver, essentially identical to that flown on the rocketsonde, is installed at the base location. Both translated and base reference GPS signals are processed in parallel to derive sonde velocity. The resulting differential solution eliminates the effects of Selective Availability/Anti-Spoofing (SA/AS). The system also operates in autonomous mode, (non-differential) to produce wind data when the base receiver is absent or is moving during the sounding.

The UHF FM receiver was specifically designed for radiosonde telemetry reception. Receiver functions may be controlled through either the RS-232 port or the front panel keypad. The remote control feature enables the ground station computer to scan the meteorological frequency band and warn an operator of potentially interfering signals within the band. With standard coaxial cable, the omnidirectional antenna and preamplifier can be separated from the receiver by up to 100 feet.

TABLE 4

Ground Station Specification
COMPUTER

IBM COMPATIBLE	80486
RAM	16 MB
Hard Disc	210 MB
Floppy Disc	3.5 inch, 1.44 MB
Display	VGA
Operating system	IBM OS-2

UHF RECEIVER/PTH PROCESSOR

IF bandwidth	30 KHz
Detection	FM
AFC	Automatic
Preamp NF	1.0 dB
Sensitivity	0.5 microvolt
Synthesizer	2.5 KHz steps
Antenna	1/4 wave monopole
PTH Processor	500 to 2200 baud
PTH input	50 mV to 1.0 V
PTH output	RS-232, ASCII or binary

ATMOSPHERIC DATA PROCESSOR, MODEL 70

Input channels	4
Processor	80486 SLC

TEST FLIGHT DATA

A.I.R., Inc., has flown dozens of GPS sonde flights to date. These flights include about equal numbers of the RKS-700-4035 rocketsonde and the IS-5A-4035G radiosonde. Figures 4a, 4b, 4c, and 4d are examples of GPS radiosonde flight data received and processed by a Model GPS-700 ground station. Wind speed and direction are calculated once per second by the GPS winds processor and a least squares fit of this data is passed to the PC every 5 seconds. This smoothing removes the motion of the rocketsonde as it swings below the parachute. Pressure, temperature, humidity are measured and calculated every second and correlated to the 5 second wind data. Figure 4e is the same information, but plotted in the graphical format that A.I.R., Inc., developed for editing WMO/NWS mandatory and significant messages.

Figure 5 shows GPSonde wind data produced by the GPS-700 ground station and compared with data simultaneously obtained from a NAVAIR LORAN system. The balloon carrying both sondes achieved an altitude of 80,000 feet. The data presented shows excellent agreement between the two systems.

Figure 6 is a plot of LARDS rocketsonde pressure versus time. It shows the very rapid decrease of pressure as the rocket reaches an altitude of 5200 feet AGL. Shortly after apogee, the ejection charge expels the payload and parachute. A gradual increase of pressure is recorded as the payload drifts with the wind back to the surface. This test rocket utilized a motor with about one half the fuel required for 10,000 foot flights in order to expedite recovery of the payload and rocket for evaluation.

Figure 7 shows the results of a developmental LARDS rocket test flight. Real time PTU and wind data from the GPS-700 is plotted. This profile was made during late morning after the boundary layer inversion had dissipated. Local site altitude was 5,300 feet ASL, pressure 830 hPa, surface wind at 15 miles per hour.

CONCLUSIONS

The Low Altitude Rocket Dropsonde System includes an expendable, rocket-borne meteorological rawinsonde and ground-based data acquisition system. State-of-the-art sensors are combined with advanced microprocessor technology to meet the requirements of the project. The accuracy achieved with the GPS signal translation windfinding technique surpasses any other traditional method. The simple automated design of the LARDS ground station supports the Army's requirements for quick succession launches from remote, unmanned locations without the use of helium balloons. The LARDS rocketsonde is the first meteorological system to make practical (low cost) use of signals from the Global Satellite Positioning system. The PC-based ground station is highly portable, and is useable anywhere in the world.

Other applications for this technology may include artillery ballistics, shipboard weather forecasting, measurement of refractive index to predict radar ducting, sound ranging, chemical and biological dispersion studies, air pollution research, emergency response, and synoptic meteorology.

247

CAPACITIVE SENSORS
93F26M412   JUNE 26, 93

Figure 2 Hysteresis Plot for HUMAIR

LARDS ROCKETSONDE
RKS-700-403.5

Figure 1 Rocketsonde Construction

GPS UPPER AIR SOUNDING SYSTEM
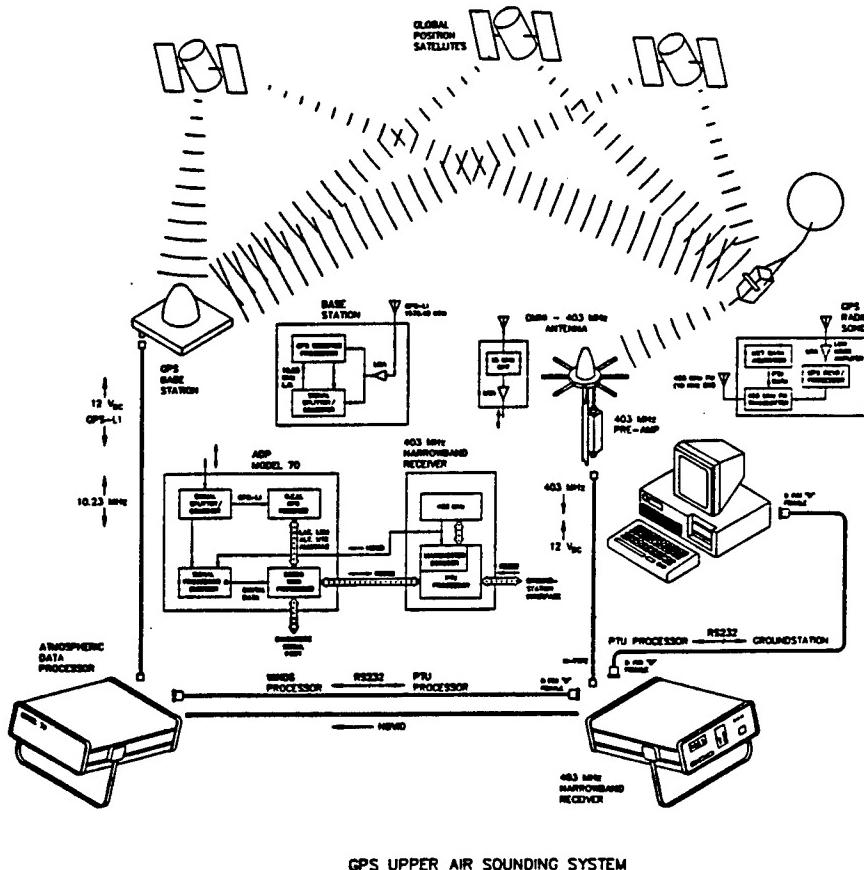
Figure 3 GPS-700 Base Station

248

A.I.R. GPS Data
October 20, 1993

Pressure (hPa)

Temperature (deg C)
-60 -50 -40 -30 -20 -10 0 10
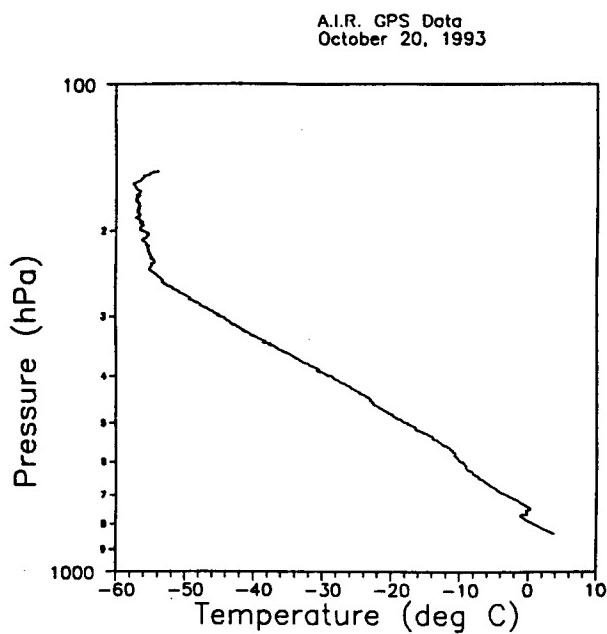
Figure 4a GPSonde Temperature

A.I.R. GPS Data
October 20, 1993

Pressure (hPa)

Percent RH
0 20 40 60 80 100
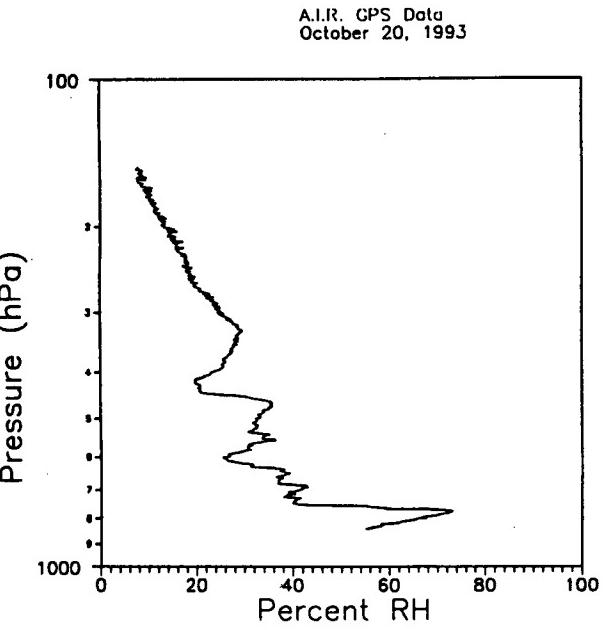
Figure 4b GPSonde Relative Humidity

A.I.R. GPS Data
October 20, 1993

Pressure (hPa)

Wind Speed (m/s)
0 10 20 30
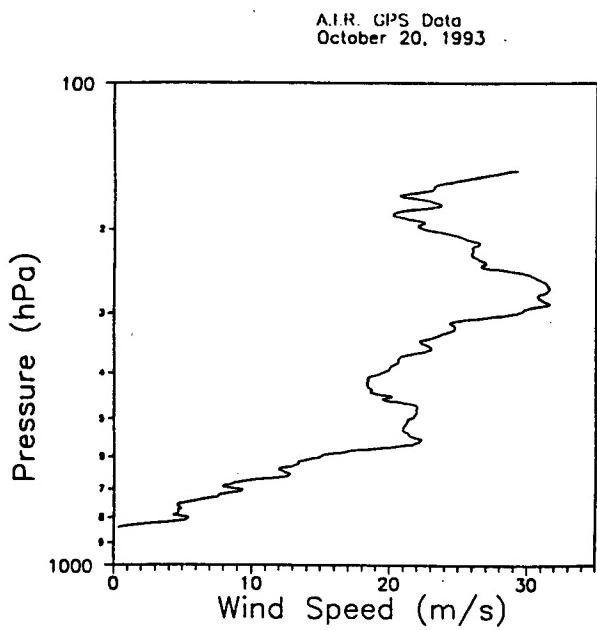
Figure 4c GPSonde Wind Speed

A.I.R. GPS Data
October 20, 1993

Pressure (hPa)

Wind Direction (deg)
0 100 200 300
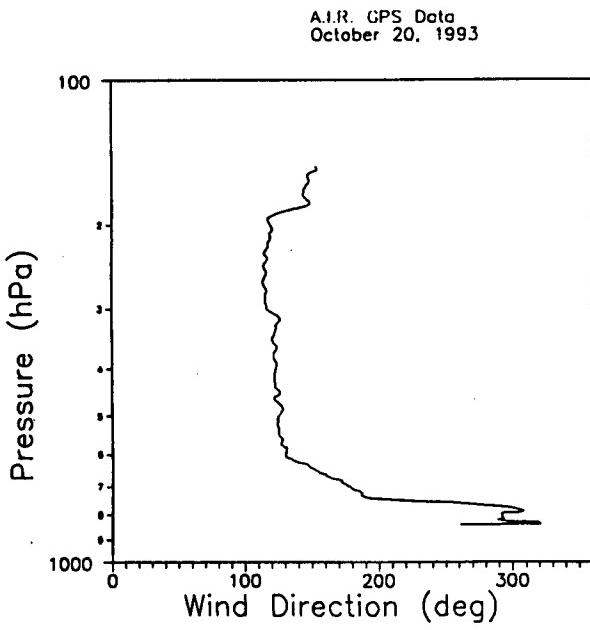
Figure 4d GPSonde Wind Direction
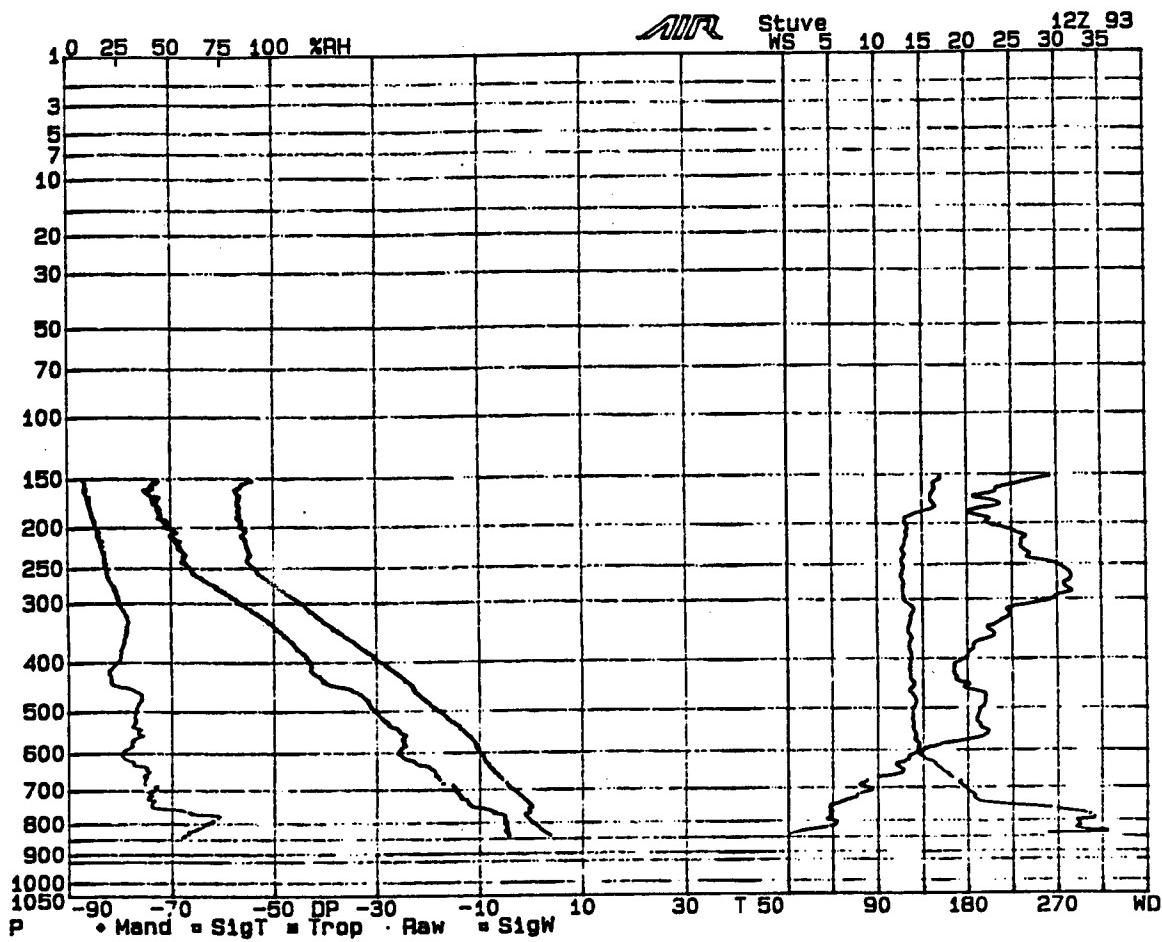
Figure 4e GPSonde Flight Data in WMO Display Format

A.I.R. SOUNDING ROCKET
FLIGHT AIRP6-B   10-28-93
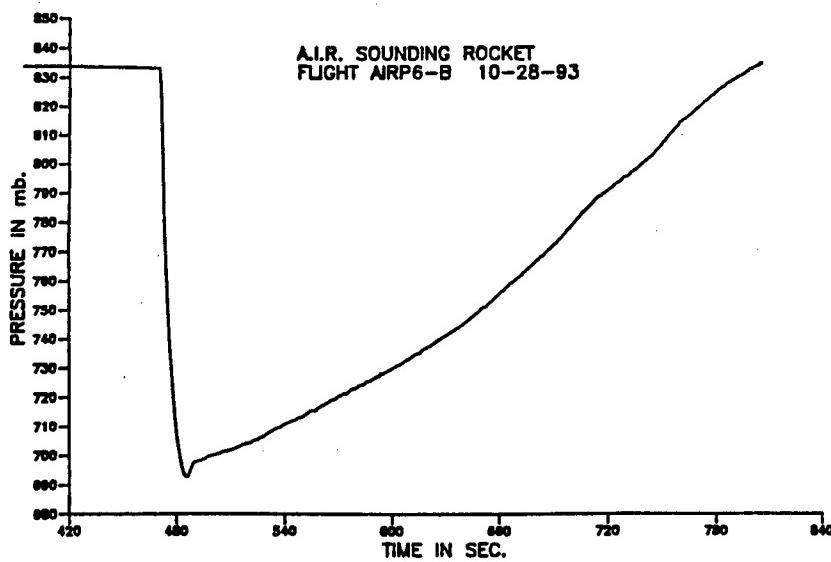
Figure 6 LARDS Rocketsonde Pressure Flight Profile

250

Figure 5 GPS and Loran Radiosondes on Same Balloon
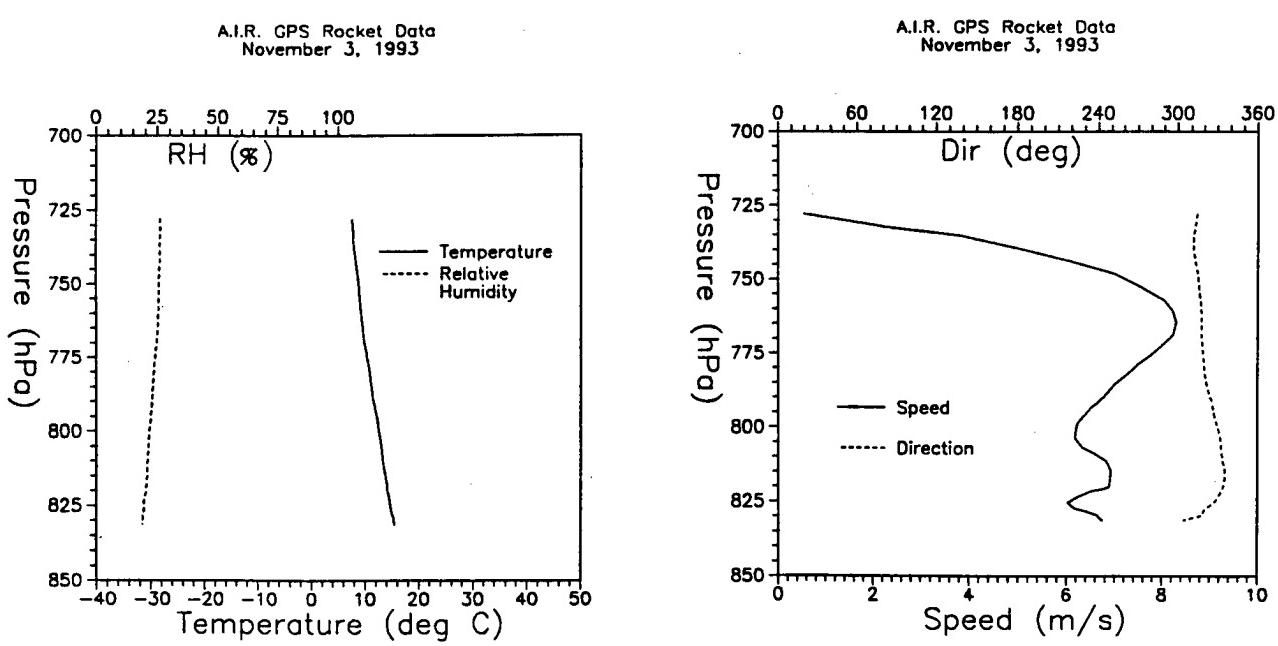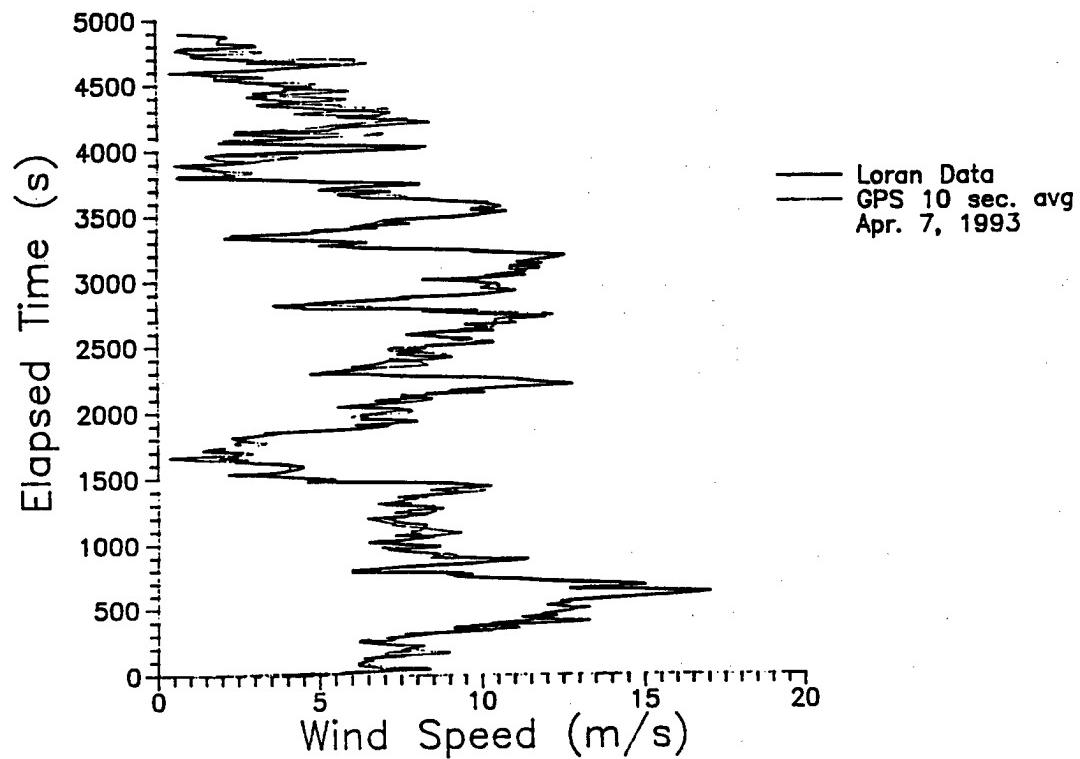
Figure 7 LARDS Rocketsonde Flight Data

NEAR-GROUND SEEING MEASUREMENTS

James J. Drexler, David B. Soules
Lockheed Engineering and Sciences Company,
WSMR, NM 88002-5501

Frank D. Eaton, Scott A. McLaughlin, John R. Hines
US Army Research Laboratory,
AMSRL-BE-W, WSMR, NM 88002-5501

ABSTRACT

Preliminary simultaneous angle-of-arrival measurements for horizontal laser propagation paths from 0.25 m to 5 m above ground level exhibit a distinct increase in angle-of-arrival variance as path height decreases. Random apodization of the image is also shown to increase as the path height approaches ground level. Theoretical calculations are shown to be insensitive to the inner scale of turbulence and to agree with data obtained for paths of 80 m, 150 m and 2.2 km in length.

INTRODUCTION

Fluctuations in the angle-of-arrival (AOA) of light passing through an aperture after propagating through the turbulent atmosphere have been measured for a number of years.[1] The variance of the observed AOA is a direct measure of the seeing quality of the atmosphere and is used routinely by the astronomical community to derive Fried's seeing parameter, r_0, the standard turbulence-related indicator.[2] This parameter has been derived theoretically from the index of refraction structure function, $C_n{}^2$, for weak turbulence,[3] but horizontal paths within the planetary boundary layer typically do not satisfy the prerequisite weak turbulence conditions. Frehlich has developed a strong turbulence description,[4] but it requires knowledge of additional atmospheric parameters, such as the Fresnel scale, the inner scale of turbulence, and the effective scattering radius. Lacking access to independent measurements of these parameters, we have chosen to present the current measurement results in terms of the variance of the measured AOA, rather than as a derived parameter.

It is well known that atmospheric seeing degrades rapidly as path heights approach ground level. Preliminary efforts at quantifying this integrated path effect over short paths within 1 m above ground level (AGL) using simultaneous AOA measurements at four discrete heights are presented along with previous results for longer paths at heights of several meters.

In addition to the more pronounced AOA effects, the stronger turbulence at lower path heights also results in a greater degree of intensity apodization (which is manifested as "image break-up") at the entrance pupil of the receiver. Representative, qualitative examples of this apodization, taken directly from individual frames of digitized camera data, are presented for the two lowest paths. These examples offer an insight into the phenomenon which is otherwise difficult to obtain.

Specialized equipment, including the U.S. Army Research Laboratory's Atmospheric Turbulence Measurement and Observation System (ATMOS), has been developed to perform AOA measurements with adequate precision for existent requirements. This equipment has been used on numerous occasions to characterize the atmospheric "seeing conditions" for astronomical observations and for ground to space laser beam propagation. For the current study, the ATMOS technique was adapted to investigate the effect of atmospheric turbulence on image quality over paths near the ground for the much shorter distances associated with the battlefield environment.

MEASUREMENTS

All of the measurements reported herein were obtained at White Sands Missile Range (WSMR) in southern New Mexico. The optical receivers consisted of 14-inch diameter Schmidt Cassegrain telescopes for light collection and two-dimensional focal plane array CCD cameras for image detection. ATMOS equipment was used to acquire and analyze data from the CCD cameras. The light source in all cases was a 2.5 milliwatt HeNe laser fitted with a 7.5 µm diameter spatial filter. For the 150 m and the 2.2 km paths, the HeNe laser was also fitted with a 50 mm collimating lens.

Short Path Measurements: (80 meters):

For the shorter paths, a wooden stand was constructed to support two of the telescopes, one directly above the other, as depicted in Figure 1. The telescopes were each fitted with an aperture mask containing two vertically aligned 11-cm diameter subapertures (on July 21, 1993, the subapertures were stopped down to 5 cm) with the lowest subaperture located at 0.25 m AGL and the remaining subapertures located at 0.50, 0.75, and 1.00 m AGL. Optical wedges placed over the subapertures separated the two images formed by each telescope. A total of four images of the laser source were formed in this manner. This apparatus was set up just inside the double doors of the west facing entry to a small building. The laser source was placed at a height of 0.25 m AGL in a portable shelter approximately 80 meters west of the telescopes. The terrain between the telescopes and the laser was nominally one half concrete tarmac and one half graded gravel and sand.

Daytime observations of image motion associated with horizontal propagation over the 80 m path were recorded at two minute intervals for several extended periods of time during July of 1993. During each of these observation periods the data acquisition systems were synchronized to ensure that all four images were recorded simultaneously. AOA information was extracted from several hundred individual data sets, each consisting of 300 frames of digitized CCD camera data, by computing the centroid of each image on a frame by frame basis. Only data sets with greater than 80% good frames were retained for inclusion in the results. The primary cause of unacceptable frames was the interruption of the propagation path caused by vehicular and pedestrian traffic during exposure. Assuming that this type of disruption is uncorrelated with turbulence effects, discarding a relatively small number of frames should have a negligible effect on the overall statistics of the data.

Figure 1. Photograph showing the arrangements of the two 14-inch telescopes and the four apertures used for the July 1993 angle-of-arrival measurements.

Our measurements were performed during the early part of the typical summer wet season with atmospheric conditions generally characterized as rainy, cool, and cloudy to partly cloudy, with intermittent periods of rapid solar ground heating. Even though better than normal seeing would be expected under these

TABLE 1

General Measurement Conditions Summary

Day	Weather Conditions	Period	Exposure Time	Comments
7/22/92	Cloudy skys, light breezy to light westerly winds. Dry ground and air S by SE 2.2 km path, 5 m AGL.	22:00--22:09 22:10--22:17	2.0 ms 5.0 ms	5 cm ap. data is part of multi-aperture study.
9/29/92	Clear night skys. Mild breeze from the west. N-S 150 m path, 4 m AGL.	18:40--19:15	2.0 ms	5 cm ap. data is part of multi-aperture study.
7/14/93	Rained >.5 inch during past 2 days. Clear sky and mostly sunny at start of test, but humid with slight breeze. Remained clear to partly cloudy.	< 8:42 >8:42	0.5 ms 0.5 ms	Archiving every 1 minute. Archiving every 2 minutes.
7/16/93	Rained prior night. < 11:00 mostly cloudy, > 11:00 hazy-partly cloudy. 13:00 sunny, but clouds building.	11:09--11:33 11:46--14:26	2.0 ms 3.0 ms	ND=1 filters installed.
7/19/93	Clear and sunny skies prior to test. Clouds start to build at approx 11:45, and soon turns partly cloudy.	11:00--14:30	3.0 ms	Significant ground heating and stable conditions for entire test period.
7/21/93	Clear, bright skies at start of test. Remains bright sunshine and sky remains mostly clear.	9:00--11:14 1:18--13:00	0.25 ms 1.0 ms	11-cm subapertures were stopped down to 5 cm.

conditions, this period afforded us the opportunity to obtain data for a variety of ground heating conditions. The general conditions during each measurement period are presented in TABLE 1.

Longer Path Measurements: (150 meters and 2.2 kilometers)

The measurements associated with the 150 m and 2.2 km path lengths were performed during the summer and early fall of 1992 at a location approximately 15 km east of the site of the 1993 measurements. The data at these longer paths were obtained under separate measurement programs, but each contains AOA data for 5 cm diameter (or larger) subapertures, some of which is deemed useful for qualitative comparison with the shorter path measurements. The equipment arrangement for the 2.2 km path measurements consisted of a single telescope located inside a dome at approximately 5 m AGL, with the laser source mounted atop an earthen embankment at approximately the same height. The observations for the 150 m path were also conducted with a single telescope and camera, with both the source and receiver mounted on outdoor towers at approximately 4 m AGL. The ground surface characteristics for both the 150 m and 2.2 km paths consisted of typical desert terrain, with randomly spaced sand hillocks and moderate to sparse vegetative cover.
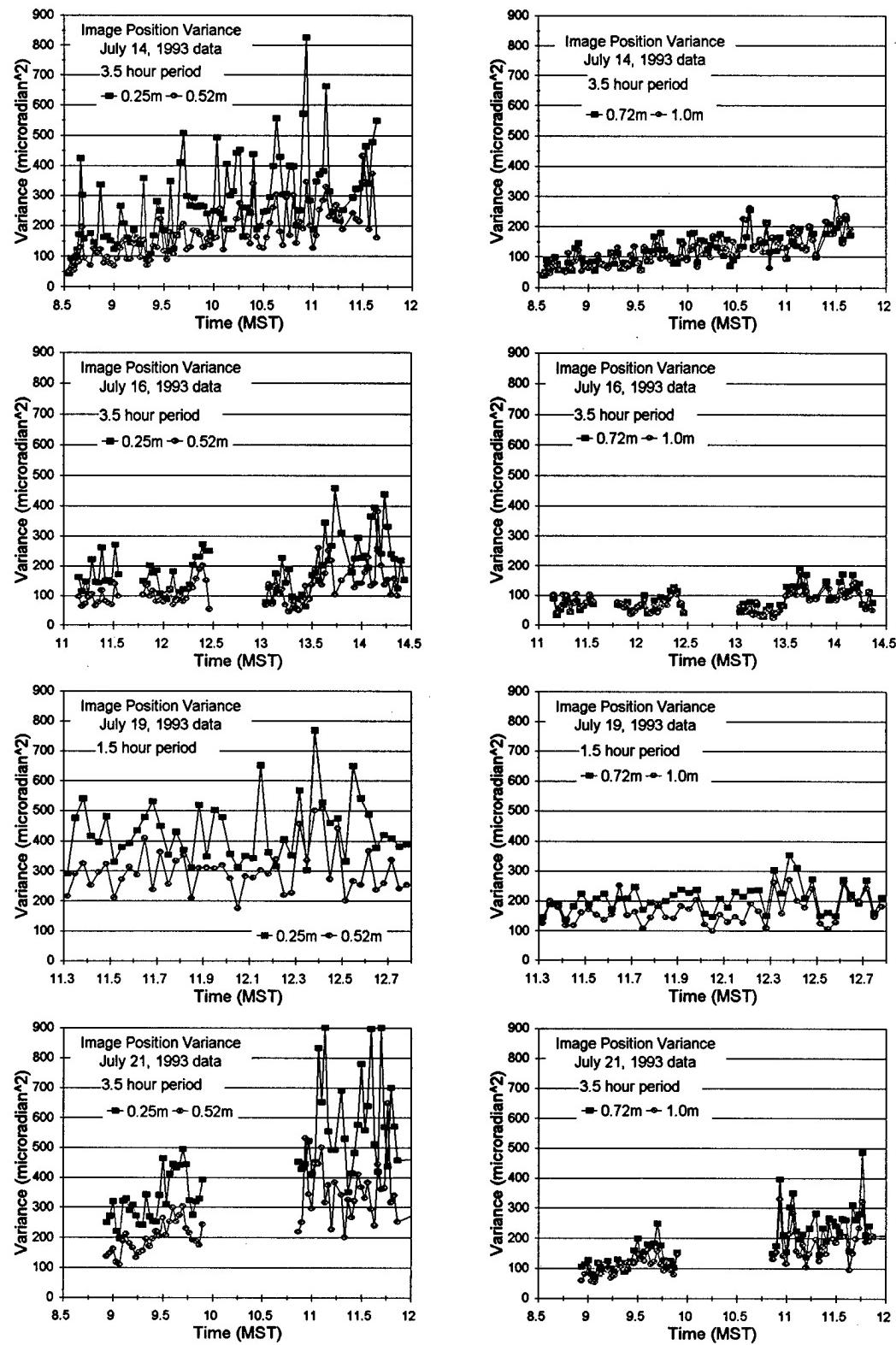
Figure 2. Time history of the angle-of-arrival variance during the four data acquisition periods of July 1993. Each time period is displayed using two plots to better exhibit the data associated with each of the four subapertures.

256

The time history of the AOA variance for the 80 m path configuration for four different measurement periods is shown in Figure 2. The data from the different subapertures are seen to be distinct from each other and to track together over the entire measurement periods, albeit with different sensitivities. The AOA variance distributions for the different subapertures are compared in Figure 3 for each of the four 80 meter path observation periods. These distributions represent the same data presented in Figure 2. Figure 4 is a log-log plot of the same variance data as a function of the average path height between the laser and the aperture. Based on spatial temperature profile measurements near the ground[5] and various optical and radar techniques at greater heights,[6] it was expected that the image motion variance would exhibit a power law dependence on height, ranging from a -4/3 law for local free convection conditions to a -2/3 law under neutral conditions. For the data acquired under the present measurement program, the specific power law relationship varies from -1.27 to -0.93, which clearly falls within the expected limits. Inspection of Figure 4 indicates that this is true over a wide range of turbulent conditions, with image motion variance near the ground ranging from roughly 100 μradians^2 to well over 500 μradians^2. For comparison, stellar observations near zenith through the entire atmosphere typically yield values of AOA variance in the range 10 to 100 μradians^2.

Figure 5 contains individual plots representing the 150 m and 2.2 km path measurements. The low AOA variance values exhibited by the 150 m path are, in part, the result of performing the measurements during (or near) the evening neutral event. The 2.2 km path measurements exhibit a higher variance due primarily to the longer path length. While the differences in test requirements and atmospheric conditions are sufficient to rule out direct comparison of these results with the 80 m path
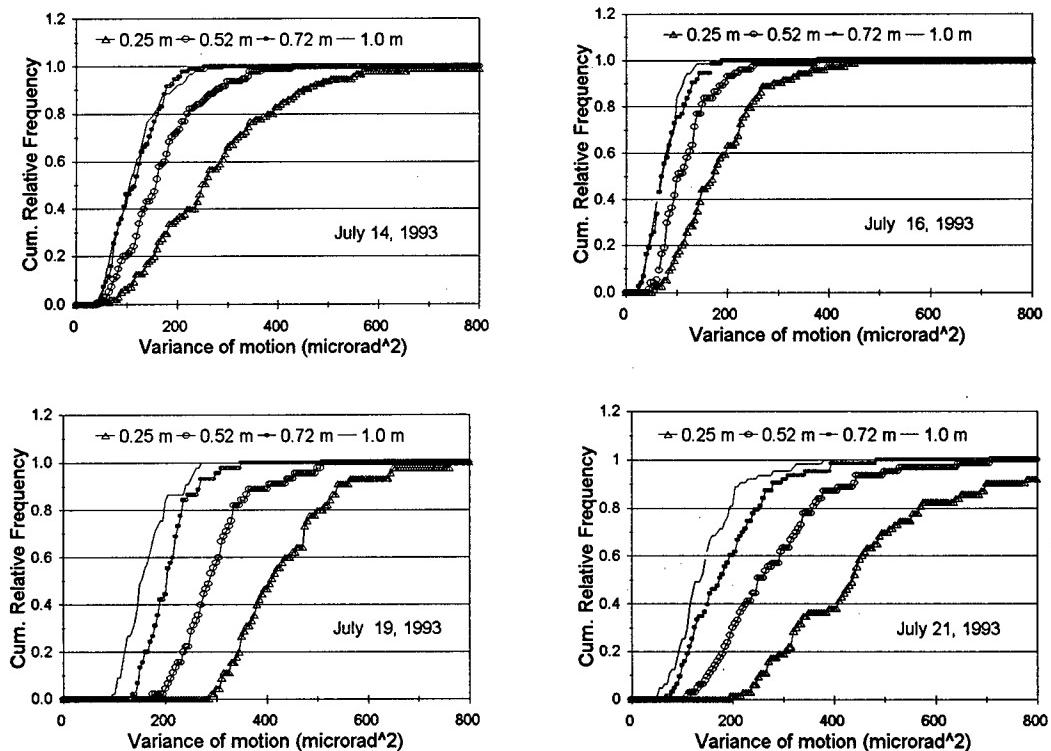
Figure 3. Comparison of the angle-of-arrival variance distributions for each of the four subaperture heights for each of the four measurement periods of July 1993. Each plot shows the cumulative frequency of the variance values.

257
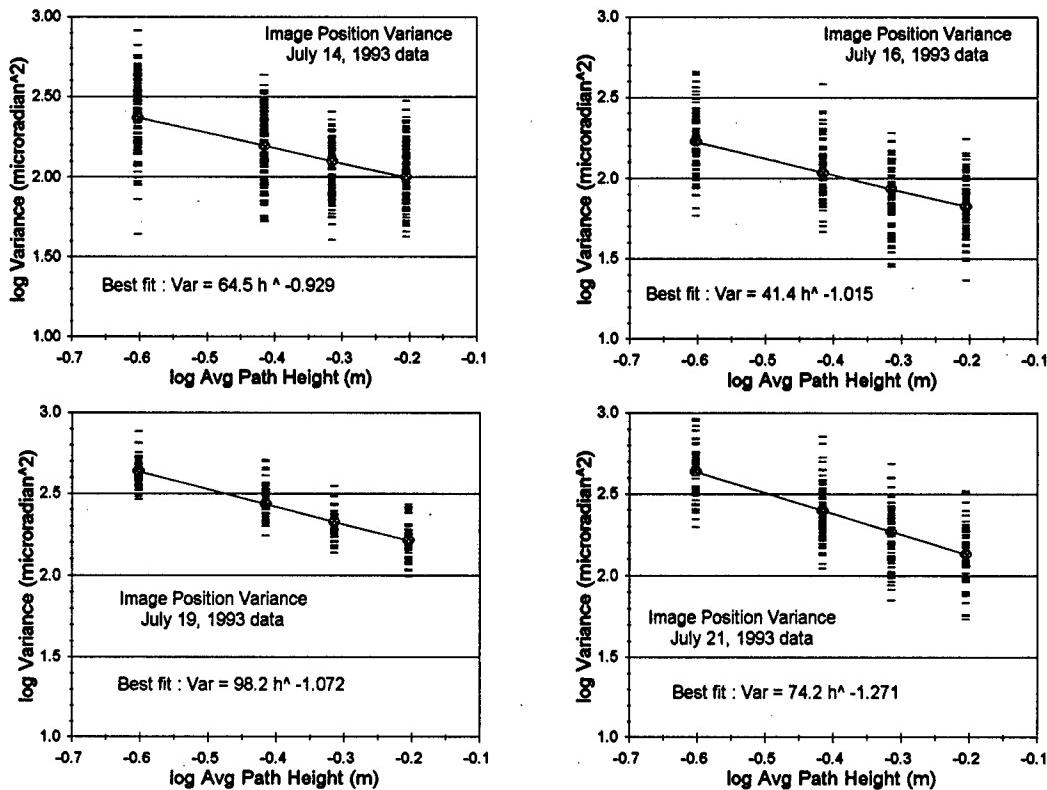
Figure 4. Log-log plots of the angle-of-arrival variance as a function of the average propagation path height for the July 1993 measurements. These plots exhibit the power law dependence of turbulence strength on the path height.

measurements, it is clear from Figure 6 that given the greater path lengths, the turbulence-induced image motion at four to five meters above ground level is significantly less than that at heights below one meter. A later discussion (see Figure 8) will indicate that the AOA variance at these longer path lengths should be decreased by approximately one order of magnitude to compare with 80 meter path values.

Pictorial representations of image apodization are presented in Figure 7. This figure is a reproduction of two frames of data obtained at 12:32 p.m. on July 21, 1993 during a period of rapid path heating by the sun through clear skies. The degree of fragmentation of the image from the lowest aperture (0.25 meters AGL) is typical of approximately ten percent of the frames from that data set. The image from the aperture at 0.50 m AGL also breaks up, but does so much less often and much less severely than the image from the 0.25 m AGL aperture. The images formed through the apertures at 0.75 m and 1.0 m AGL did not exhibit noticeable apodization effects on any of the numerous data sets reviewed.
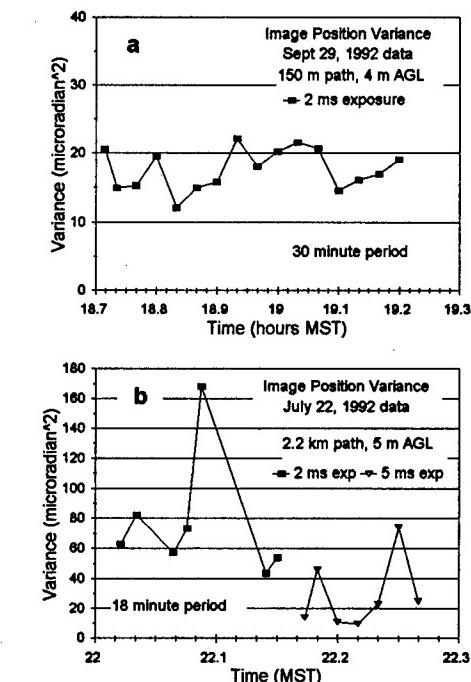
Figure 5. AOA variance for the 150 m path (a) and for the 2.2 km path (b).

258

DISCUSSION

Simultaneous measurements of AOA variance at four different levels over an 80 m horizontal path indicate a clear dependence on path height. AOA measurements made during previous tests over longer paths also indicate a qualitative agreement with these relationships. As shown in Figure 6, the seeing conditions close to the ground improve noticeably as the average path height increases from 0.25 m AGL to 0.7 m AGL and improve further at 4m AGL (even at approximately twice the path length) and at 5 m AGL (at 27.5 times the path length).

In addition to the short term, set-to-set fluctuations in the AOA variance displayed in Figure 2, the data of both July 14 and July 21 show a distinct

Figure 6. Extension of Figure 4 to include the longer path data. This graph shows the average AOA variance with +/- 1 standard deviation ranges indicated. The data have been offset slightly from the actual average path heights for clarity of plotting. The variance for the 4 m and 5 m heights have been adjusted to compensate for the longer paths as discussed in the text (see Figure 8).

Figure 7. Two frames of digitized data obtained with 1 ms exposure on July 21, 1993 from the lower telescope. These two frames were separated by 3.5 seconds and exhibit the apodization typical of approximately ten percent of the images from the lowest two subapertures. The left image in each frame corresponds to the lowest subaperture.

trend toward increasing turbulence as the daily surface heating progresses, while the data of July 16 exhibits a pronounced step function approximately one half hour after continuous solar heating began. On July 19, the conditions were characterized as "significant ground heating and stable ... for the entire test period," which is borne out by the moderately high turbulence levels with no dramatic variations over the entire observation period.

Calculations of the image motion variance based on Frehlich's development[4] yield the theoretical dependence on path length shown in Figure 8 for moderate ranges of path length, C_n^2, and inner scale of turbulence. These graphs each contain eight curves: one curve for each of two values of inner scale (1.0 mm and 3.0 cm) for each of four values of C_n^2. The range of C_n^2 for these plots is based on a compilation of measurements made over a 15-month period during 1988 and 1989 at WSMR at 8 m AGL. The range of 10^{-14} to 10^{-11} then covers a nominal range of average path heights from 0.1 m to 8 m. The inner scale values of 1 mm and 3 cm were chosen to bracket the expected values at WSMR. The two graphs indicate only minor differences due to aperture size or inner scale values, leaving normal variations in C_n^2 as the major contributor to image motion variance. For apertures much smaller than one centimeter, the

259

apodization effects and the increased AOA fluctuations near the ground can be expected to be highly dependent on the inner scale.[7]

Even though the fluctuations in the AOA have been discussed in terms of a receiving system, they also pertain equally to the problem of propagating a laser beam near the ground. The data presented can be expected to characterize the condition of the laser beam at its destination. Beam spreading and beam apodization have been observed[8] over relatively short paths as high as 4 or 5 meters AGL, but the effects of laser parameters such as the diameter of collimating optics or the degree of beam focus were not included in this investigation.

CONCLUSIONS

Image degradation due to turbulence associated with propagation paths close to the ground has been observed and quantified using the AOA variance as a measure of the turbulence strength. The measured dependence of turbulence strength on path height follows a negative 1.1 power law relationship in the lowest meter of the atmospheric boundary layer. Allowing for normal atmospheric variability, this result agrees well with theoretical expectations of a power law between -2/3 and -4/3.

Given the combination of increased image motion and increased image apodization for paths close to the ground, tactical users are inherently subject to turbulence induced limitations both for imaging and for precise laser beam positioning.

Figure 8. Angle-of-arrival variance calculated from Frehlich's equations for apertures of 0.8 cm (a) and 7.6 cm (b). At the shorter paths, inner scale of 1 mm yields the upper curve of each of the line-pairs in a) and the lower curve in b). The second curve of each pair represents inner scale of 3 cm. Lines with a +1 slope (arrows) have been added for reference.

Techniques similar to those described for this preliminary work hold promise of providing in situ atmospheric characterization which, in turn, could be used for rapid selection of propagation paths for specific applications.

Based on Frehlich's development, the inner scale of turbulence is of minor importance for the path lengths, path heights and turbulence parameters likely to be associated with battlefield scenarios if the receiving optical system has an aperture diameter of approximately one centimeter or larger.

ACKNOWLEDGMENTS

REFERENCES

1. David B. Soules, James J. Drexler, Arthur H. Waldie, John A. Qualtrough, Frank D. Eaton, William A. Peterson, John R. Hines, "Temporal Characteristics of Turbulence-Induced Image Motion," *SPIE Proceedings, Propagation Engineering*, Orlando, Florida, **1115**, 224-231. 1989.

2. D.L. Fried, "Statistics of a Geometric Representation of Wavefront Distortion," J. Opt. Soc. Am. **55**, 1427-1435, 1965.

3. F. Roddier, "The Effects of Atmospheric Turbulence in Optical Astronomy," *Progress in Optics*, edited by E. Wolfe, **19**, 283-377, 1981.

4. R.G. Frehlich, "Variance of Focal-Plane Centroids," J. Opt. Soc. Am. A, **7**, 2119-2140, 1990.

5. John C. Wyngaard, "On Surface-Layer Turbulence," *Workshop on Micrometeorology* (Publication of the American Meteorological Society), pp. 101-149, 1973.

6. F.D. Eaton, W.A. Peterson, J.R. Hines, and G. Fernandez, "Isoplanatic Angle Measurements and Associated Atmospheric Conditions," Applied Optics, **24**, 3264-3273, 1985.

7. Frank D. Eaton, John R. Hines, David B. Soules, James J. Drexler, John A. Qualtrough, "Aperture Diameter Effects on Horizontal Path Scintillation," International Meeting for Wave Propagation in Random Media, Poster Paper, Seattle, Washington, August 3-7, 1992.

8. Frank D. Eaton, William A. Peterson, John R. Hines, James J. Drexler, David B. Soules, A. Howard Waldie, John A. Qualtrough, "Morphology of Atmospheric Transparent Imhomogeneities," *SPIE Proceedings. Propagation Engineering*, **1312**, 134-146, 1990.

AN ATTEMPT TO CORRELATE RASS COVERAGE WITH

WIND SPEED AND RELATIVE HUMIDITY

by Wm. H. Hatch

ARMY RESEARCH LABORATORY

White Sands Missile Range, New Mexico

ABSTRACT

The 50 MHz High Performance Radar System, one of the building blocks of the Army Research Laboratory's (ARL) Atmospheric Profiler Research Facility (APRF), has an associated Radar Acoustic Sensing System (RASS) to measure temperature profiles. This system is configured to measure profiles of virtual temperature from 5.42 km to 14.87 km MSL. Although normal coverage is from approximately 6.5 to 11 km MSL, this can vary from no coverage to essentially full coverage over the extreme height range. Correlations of these variations in measurement ranges to wind speed and water vapor content are shown.

INTRODUCTION

The 50 MHz High Performance Radar System is a pulsed, multi-beam 49.25 MHz profiling radar for upper-air atmospheric research. It uses a phased array antenna of 15657 square meters and a peak transmitted power of 250 kilowatts. Nominally designed and built to measure winds and turbulence from 3.22 km to 19.72 km MSL, it has been augmented with acoustic transducers and other hardware and software to implement a temperature measuring capability[1]. Three acoustic transducers and acoustic horns have been placed in the northwest, southwest, and southeast corners of the antenna array to produce sound waves in the range from 94 to 110 Hz.

Radio waves are usually reflected by temperature and humidity fluctuations in the upper atmosphere, quantified as the refractive index structure parameter C_n^2. Eddies approximately 3 meters in size sensed at 50 MHz, are entrained with the wind and thus the Doppler shift in the radar signal can be utilized to measure the radial wind velocity along the path. Radio waves are also reflected by the disturbances produced by acoustic waves, and with a sufficient number of acoustic waves with a wave length one half of the radar wave length, there is enough energy returned to measure the Doppler velocity of the acoustic wave. The temperature profile can be calculated from these measurements since the virtual temperature is related to the speed of sound.

There are 64 channels, or heights, for which data are available from the RASS, with the lowest at 5.42 km and the highest at 14.87 km MSL. Because of antenna problems with the vertical antenna, rarely are there any usable data points below about 6.5 km. After analyzing these RASS data it was observed that RASS coverage rarely exceeded 11 km.

On one spring day the data coverage dramatically increased to the maximum range of 14.87 km. This was attributed to the occurrence of a spring rain, although the exact cause was not immediately apparent. Consultation with experts in the field of RASS led to the conclusion that the increased activity was due to the lessened acoustic attenuation due to the humidity.

A brief survey of the literature[2] confirmed this possibility; namely, that acoustic attenuation tends to peak at the low humidities which are found in the desert environment, and then becomes less as the humidity increases, at least up to a point. It is implied that the attenuation is less for completely dry air, however. This theoretical effect provided the basis for this study.

THE DATA

The RASS data from the 50 MHz High Performance Radar System are collected approximately 2 samples every 30 minutes. This can vary with the operating parameters of the radar, so that there are normally from 1 to 6 samples of RASS data every hour. This data was quality-controlled and analyzed for hourly

intervals with the Weber-Wuertz Continuity Model[3] for consistent patterns which fit within very generous profile limitations. The profiles were imported to a PC where the gate number, from 0 to 64, of the highest valid temperature within each hourly interval was extracted.

Associated in the APRF is the 404 MHz Wind Profiler Radar, part of NOAA's Wind Profiler Demonstration Network. This profiler is augmented with an automated surface meteorological station, providing "ground-truth" surface data of wind speed, wind direction, temperature, dewpoint, relative humidity, and pressure. Hourly averages of these variables were extracted from the database, and were utilized for the analysis.

Originally, it was hoped to be able to use the dewpoint and relative humidity data from RAOB runs, also available on the data base. It soon became apparent that this data was insufficiently populated to perform any meaningful continuous analysis, and therefore the surface data was utilized.

DATA ANALYSIS

Data for the months of April, May, June, July, August, and September, 1993, were extracted from the two sources and combined along time lines for the analysis. Not all of the times contained data from both sources, depleting the amount of useful data considerably. It was also thought that those cases where the RASS height was zero, or the case where no valid data was measured, should also be excluded as probably being due to other circumstances having nothing to do with attenuation. Even so, the total count of analyzable points were 1,753 out of a possible 4,392 for the six months, or almost 40%.

A standard correlation coefficient was calculated using the following formula

$$CC = \sum (x_i - \overline{x}) * (y_i - \overline{y}) / \sigma_x * \sigma_y$$

to compare the RASS heights to wind speed, temperature, dewpoint, and relative humidity. This was done for each month separately, and also for all 6 months (listed as AMJJAS). The averages and sigmas for each of the months, along with the number of valid concurrent points, are presented in table 1, and the correlation coefficients are in table 2.

A plot of the relative RASS heights and the dewpoints versus time for each month and for AMJJAS are presented in figures 1-7.

CONCLUSIONS

There is a very weak negative correlation between surface wind speeds and the relative RASS heights, contrary to that which was expected. Further work may be needed to explain this. The relatively stronger correlation with temperature than with wind might have been expected, given that most attenuation equations include the speed of sound in the denominator.

The stronger correlation of the relative RASS heights with dewpoint agrees with theory, although this must be taken with caution. The two months with the strongest correlations, April and June, not only show large changes in dewpoint values during each month but contain the driest conditions of the six months examined. At times there appears to be a time lag between height coverage and dewpoint. This may be due to the humidity profile changing from top-to-bottom, a phenomenon which is not reflected by the surface measurements alone.

A scatter plot, figure 8, seems to confirm that at low dewpoints, the RASS coverage is low, but it would appear that after the dewpoint is slightly above zero, no further enhancement of coverage is detected.

No quantitative conclusions may be made from this data, as there are too many variables as yet unexamined. The meteorological parameters are almost certainly affecting other components of the system, i.e. the antenna, the acoustic transducers, and the radar beam itself, to name a few. This could be an exhaustive study in and of itself, and may have impact in future attempts to measure humidity through combinations of radar and RASS beams.

REFERENCES

1. Marschall, J. M., A. M. Peterson, and A. A. Barnes Jr., 1972: Combined RADAR-Acoustic Sounding System, Appl. Opt., 11, 108-112

2. Kinsler, L. E., and A. R. Frey, Fundamentals of Acoustics, John Wiley and Sons, Inc, 1962

3. Weber, B. L., and D. B. Wuertz, 1991: Quality Control Algorithm for Profiler Measurements of Winds and Temperatures, NOAA Technical Memorandum ERL WPL-212, Wave Propagation Laboratory, Boulder, CO

	RASS avg/ sd	WIND avg/ sd	TEMP avg/ sd	DEWP avg/ sd	RH avg/ sd
April #86	36.43/ 12.3	3.55/ 1.92	19.72/ 7.37	-4.54/ 8.95	29.45/ 22.43
May #335	44.13/ 9.39	2.68/ 1.71	22.81/ 5.09	3.24/ 4.71	35.56/ 15.30
June #191	41.18/ 12.08	3.14/ 2.15	25.02/ 5.5	-0.71 8.01	27.40/ 18.63
July #247	54.74/ 5.20	2.71/ 1.81	28.71/ 5.01	11.65/ 3.67	43.36/ 19.10
August #552	50.48/ 9.00	2.18/ 1.33	25.57/ 4.86	14.08/ 3.05	57.20/ 20.18
September #343	45.74/ 9.31	2.62/ 1.61	23.30/ 5.62	8.06/ 6.08	46.49/ 19.03
AMJJAS #1753	47.24/ 10.47	2.61/ 1.70	24.70/ 5.73	7.97/ 7.82	44.41/ 21.62

TABLE 1 Averages and Sigmas

Correlation Coefficients of relative RASS heights with;

	wind	temp	dewp	RH
April	-.0161	0.130	0.766	0.632
May	-.009	0.396	0.317	-.060
June	-.268	0.165	0.765	0.536
July	0.024	0.058	-.037	-.021
August	0.062	0.130	-.104	-.127
September	-.07	-.017	0.286	0.175
AMJJAS	-0.119	0.272	0.517	0.175

TABLE 2 Correlation Coefficients

FIGURES
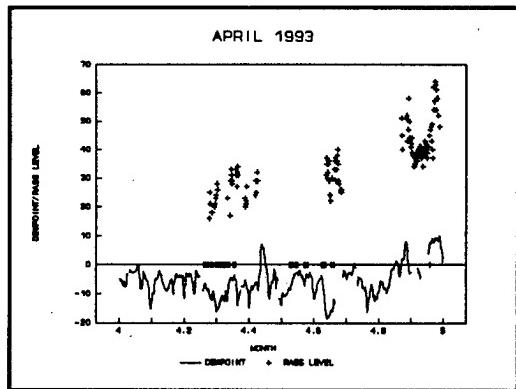
Figure 1 APRIL
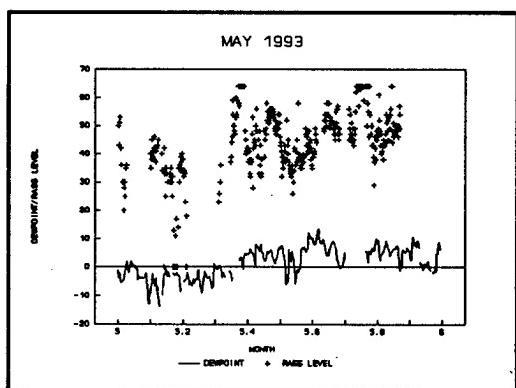
Figure 2 MAY

Figure 3 JUNE

Figure 4 JULY
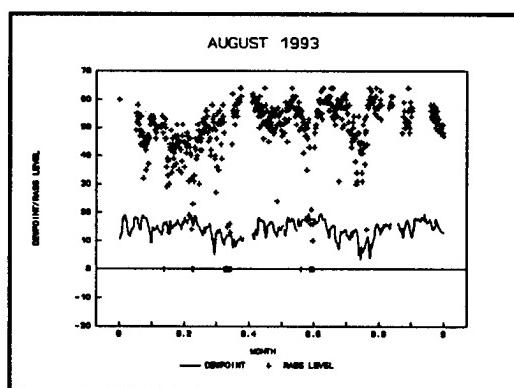
Figure 5 AUGUST
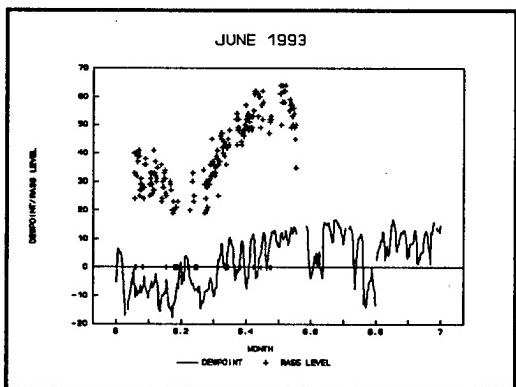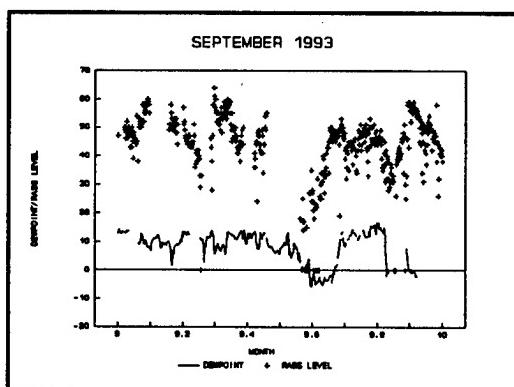
Figure 6 SEPTEMBER
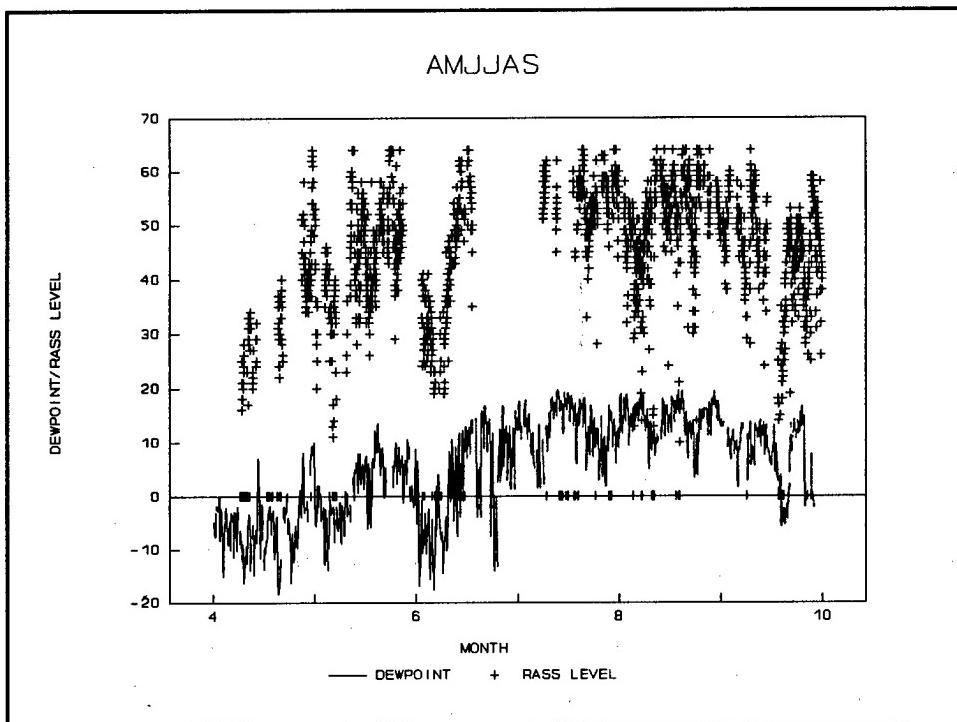
Figure 7 ALL MONTHS
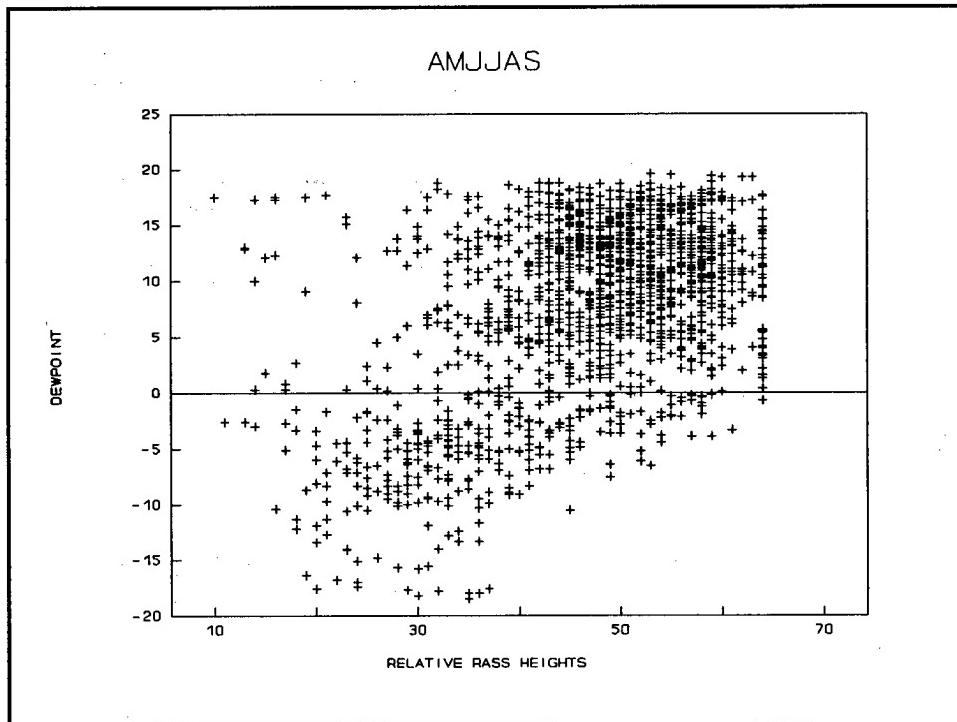
Figure 8 SCATTER - AMJJAS

267

Session IV

ATMOSPHERIC ASSESSMENT

THE DIRTY BATTLEFIELD ENVIRONMENT

Alice L. C. Ruf and Jeff Todd
Dynetics, Incorporated
Huntsville, Alabama 35814-5050

Brian Matkin
Army Materiel Command Smart Weapons Management Office
Redstone Arsenal, Alabama 35898-5500

ABSTRACT

The development, analysis, and evaluation of smart weapon systems and associated sensors and seekers in a clean, countermeasure free, benign battlefield produce unrealistic results and non-responsive systems. To complement previous studies on weather and countermeasures, the dirty battlefield and its components have been defined and interrelationships investigated to determine the remaining factors of the battlefield environment requiring study. These remaining factors, herein called battle by-products, are produced by military operations and may unintentionally impact the performance of smart weapon sensors and seekers. A standardized methodology has been developed to assess this impact. This paper presents the dirty battlefield definition set and the battle by-product assessment methodology developed for an ongoing effort by the Army Materiel Command Smart Weapons Management Office.

1. INTRODUCTION

Observation 1: There are a multitude of phenomena found on the battlefield that may impact weapon system performance. While many of these phenomena can be classified as "weather" or "countermeasures", there are remaining factors that do not belong to either group, such as dust, fires, missile plumes, etc.

The Army Materiel Command Smart Weapons Management Office (AMC-SWMO) has conducted several studies on the realistic battlefield environment. One purpose of these studies was to develop methodologies for quantifying the impact of the battlefield environment on smart weapon system performance. These methodologies are instrumental in the development of system requirements and specifications. These studies focused primarily on weather[1] and countermeasures[2]. To complement these efforts, the remaining elements of the battlefield environment are being examined. However, before these elements can be scrutinized, their unique role must be defined, as well as their relationship to weather and countermeasures. This will be accomplished by an examination, breakdown, and categorization of the entire battlefield environment and development of a standardized battlefield definition set.

Observation 2: The "dirty battlefield" is a term that is often used, but not in a consistent manner.

As part of this battlefield study, the term "dirty battlefield" (or "dirty battlefield environment") will be defined. Although it is often used, no definition could be found for the term, and consistency in use is lacking. It might be appropriate to use it interchangeably with the "realistic battlefield," or perhaps it might apply to the unlabeled set of battlefield elements, or maybe it would be more appropriate for an altogether different application. An important consideration for this definition, as with all the definitions, is that it be as consistent as possible with past usage and accepted by the defense community.

Current and past usage of the term "dirty battlefield" was researched. Both literature searches and interviews with a representative sample of the defense community were conducted. Interviewees were asked how they perceived the term and how they used it. While neither an exhaustive literature search nor interviews with all members of the defense community were possible, sufficient research was conducted to gain historical perspective of usage. The dirty battlefield is consistently used to refer to elements found on the battlefield that impact the performance of weapon systems. Specifics, however, were not so consistent. After the first draft was completed, a large and diverse group consisting of representatives from Army project offices, schools, and laboratories and also the Air Force met to review the entire battlefield definition set (including weather, countermeasures, and other components). Feedback was integrated into the work and a second draft was prepared. At the end of October, a "dirty battlefield committee" composed of representatives from key Army, Air Force, and Navy organizations will finalize the definition set. Due to the timeline of events, however, the second draft will be presented in this paper.

2. THE DIRTY BATTLEFIELD DEFINITION SET

The most appropriate subject of the term "dirty battlefield" was determined to be the *entire* battlefield environment, including all factors that might affect weapon system performance. Therefore, the definition set will be called the dirty battlefield definition set. The dirty battlefield environment and its component interactions will be first be examined, then each of the components will be individually examined. Whenever definitions have been previously developed for a component, they are first reviewed before presenting the definition pertaining to the dirty battlefield.

2.1 Dirty Battlefield

The dirty battlefield environment encompasses all elements of the battlefield environment, both intentional and unintentional, both natural and manmade. The term can be used interchangeably with the "realistic battlefield environment" as well as the "realistic dirty battlefield environment." The three primary components - weather, countermeasures, and battle by-products - can be illustrated by a Venn diagram as shown in *Figure 1*. This illustrates the unique contribution of each component, as well as the interactions. Examples of each category are included in the figure. In addition to the three primary components, there are some additional dynamic battlefield factors that must be considered when examining the dirty battlefield. Because they can impact all three components, they are shown in *Figure 1* encompassing the Venn diagram. These factors are collectively called the "battlespace domain." They include temporal descriptors such as time of year and time of day; spatial elements such as terrain and the celestial dome; and also the battle scenario.

2.2 Weather

There are several established definitions for the term "weather" and use of the term is fairly consistent. Webster's Dictionary[3] defines weather as "the general condition of the atmosphere with regard to temperature, moisture, etc." The DOD approved definition[4] for adverse weather is "weather in which military operations are generally restricted or impeded." The only point of

confusion related to the weather concerns weather's interaction with the environment, such as puddles on the ground from rain, amorphous snow, or solar loading - are these also considered weather? To verify the inclusion of these elements, the weather definition for the definition set is as follows:

WEATHER: The natural state of the atmosphere including its interaction with other elements of the naturally occurring and manmade environment.
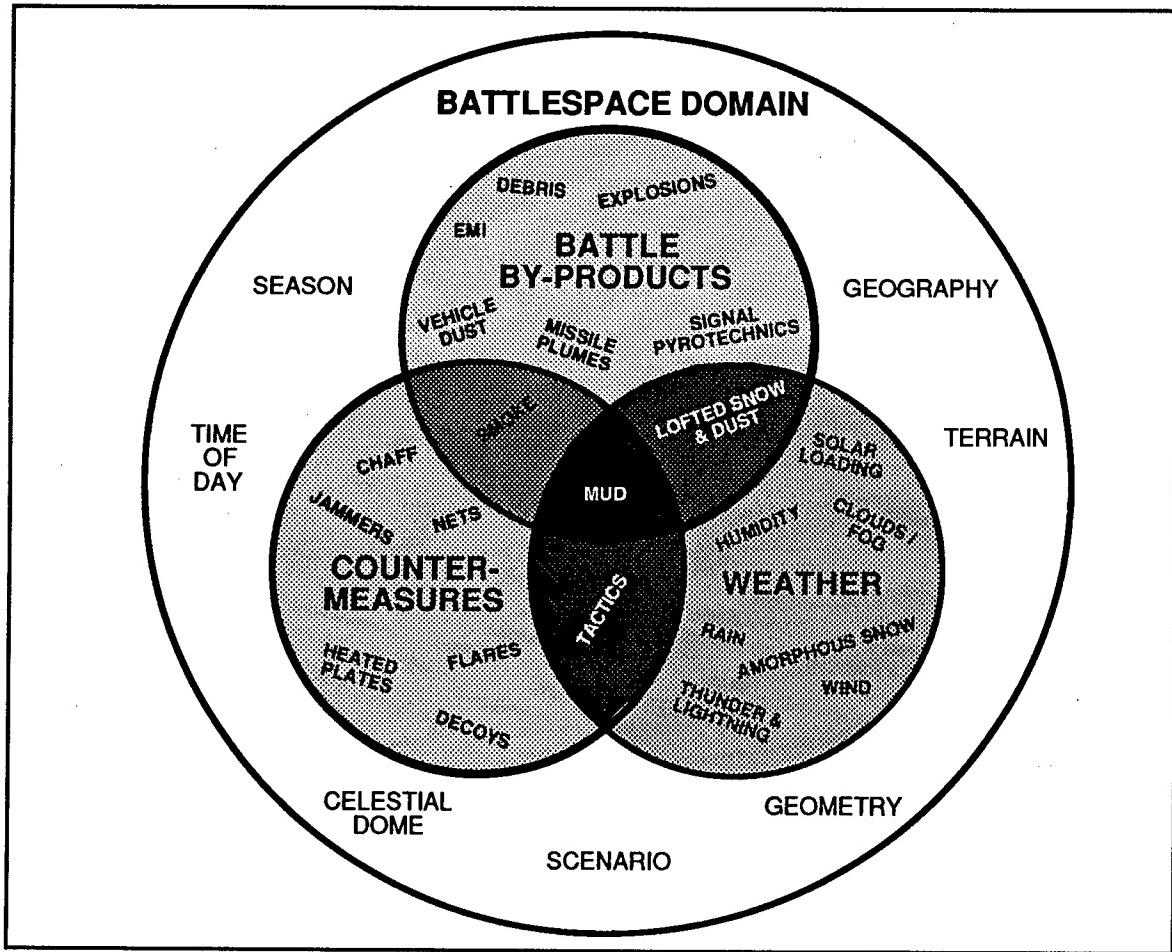
FIGURE 1. The Dirty Battlefield Environment

2.3 Countermeasures

The DOD approved definition[4] for countermeasures is "that form of military science that, by the employment of devices and/or techniques, has as its objective the impairment of the operational effectiveness of enemy activity." The definition found in the SWMO Countermeasures study[2] is "a device, technique, or action that responds to a specific enemy action or capability; designed to reduce an enemy's capability or operational effectiveness." As a point of interest, countermeasures are also subdivided into several different sets of categories to further classify a countermeasure by parameters such as its frequency of occurrence. This level of detail will not be addressed in this paper.

The definition of countermeasures developed for the definition set is very similar to those above. The word "intentional" is added in order to stress the unique role of countermeasures. It is implied in the definitions above through use of the words "objective", "responds", and "designed." Intention is also implied by examining the name "countermeasures" itself - a *measure* taken to *counter* the enemy. The definition is:

> COUNTERMEASURES: Intentional devices, techniques, or actions that are designed and employed to reduce the operational effectiveness of a specific activity or capability.

2.4 Battle By-Products

The name given to the third component of the dirty battlefield is "battle by-products." The definition is as follows:

> BATTLE BY-PRODUCTS: Phenomena produced by military operations that unintentionally reduce the operational effectiveness of an activity or capability.

Note use of the word "unintentional" in the above definition; intention is the primary difference between countermeasures and battle by-products. The same element can be considered a countermeasure or a battle by-product, depending on the intent. White phosphorous smoke is sometimes used as a countermeasure to obscure targets. White phosphorous rounds are also used to produce casualties, with the obscuration produced by the smoke being a battle by-product. Another note on the battle by-product definition is that the "reduction of operational effectiveness" can apply to friendly and/or enemy forces. For example, dirt kicked up by a convoy of vehicles will obstruct the vehicles' view of the road and the enemy, as well as the enemy's view of the convoy.

Example battle by-products are listed in *Table 1.* This is an extensive list, though not exhaustive (an exhaustive list is not possible; for example, a few years ago oil well fires would never have been added). The phenomena have been grouped according to their impact on smart weapon sensors and seekers. The primary effects are attenuation, clutter, and target signature alteration. This type of impact is important to consider when assessing the effect the battle by-product has on a particular sensor.

3. ASSESSMENT METHODOLOGY

The assessment methodology to quantify the impact of battle by-products on sensor systems will now be discussed. This methodology was developed to provide a standardized approach for addressing the effects of battle by-products. These phenomena are produced by complex interactions among many different constituents of the battlefield. The methodology must consider everything on the battlefield which can contribute to and/or be influenced by battle by-products. This standardized methodology can be used to evaluate the effects of battle by-products on various types of smart weapon sensors, including infrared, millimeter wave, acoustic, and laser sensors.

The general assessment methodology consists of four basic steps. This methodology is shown in *Figure 2.* The first step is to define the scenario(s) of interest. This includes engagement specifics, weapon system(s), and the battle by-products (BBP) present. The key battle by-products that need to be addressed in the scenario are determined in the second step. The third step is to evaluate the performance impact of the battle by-products on sensor links in the scenario. The fourth step is to study the overall operational effectiveness of the system with the battle by-product effects included in the evaluation.

TABLE 1.   List of Battle By-product Elements

ATTENUATION	CLUTTER

• SMOKE FROM BATTLEFIELD FIRES
  - VEHICULAR
  - OIL WELLS
  - VEGETATION
  - BUILDINGS
• VEHICLE EXHAUST
• VEHICULAR DUST
• HELICOPTER LOFTED DUST
• HELICOPTER LOFTED SNOW
• DUST FROM EXPLOSIONS
• WHITE PHOSPHOROUS SMOKE
• MISSILE PLUMES
	• BATTLEFIELD FIRES
	  - HEAT, ILLUMINATION, TURBULENCE
	• EMI
	  - RADARS
	  - JAMMERS DIRECTED AT RADARS
	  - COMMUNICATION CENTERS
	  - FIELD RADIOS
	• ACOUSTICAL NOISE
	  - OTHER VEHICLES
	  - EXPLOSIONS
	  - GENERATORS
	• SIGNAL SMOKES / FLARES
	• ILLUMINATION ROUNDS
	• MUZZLE FLASH
	• EXPLOSION DEBRIS
	• TANK HULLS / "DEAD" VEHICLES
	• VEHICLE TRACKS

TARGET SIGNATURE ALTERATION

• MUD ON VEHICLES
• SANDBAGS ON VEHICLES (FOR ARMOR PROTECTION)

FIGURE 2.   Proposed Analysis Methodology

This four step process (or any number of successive steps) can also be applied in the reverse order. If a system needs to achieve a certain operational effectiveness level, the performance degradation due to battle by-products that will cause the system to drop below this level of effectiveness can be determined. Next, the battle by-products that cause that performance degradation can be measured and quantified. If the scenario has been designed to examine a specific battle by-product, it may need to be redesigned if the quantity determined in the second step of the methodology is not that desired. The four basic steps in the assessment methodology will be examined in more detail in the following paragraphs.

The first step in the methodology is to define the scenario and systems to be modeled. The types of sensor technologies employed in the weapon system must be determined. A system typically depends on several different sensor links for a successful performance. Some of the potential sensor links are acquisition, tracking, guidance, and data links from remote sensors. The impact of the battle by-product on each sensor link must be examined to determine the impact on the overall system. The engagement specifics must be addressed in sufficient detail to describe the scenario. These specifics include terrain, climate, geometry, background, etc. The positions and motions of the targets and sensors need to be examined and quantified. Important parameters of each sensor employed by the weapon system of interest must be defined. To summarize, all aspects of defining the scenario and weapon system are addressed in the first step of the assessment methodology.

The second step of the methodology is to determine key battle by-products. This step also includes the quantification of the battle by-products to determine how much of each element exists in the defined scenario. All battle interactions that can create battle by-products should be examined. These battle by-products can then be categorized as either a background effect or an obscurant effect. These effects must then be quantified. One example of this process is using the EOSAEL[5] module COMBIC to determine the amount of vehicular dust that exists in a scenario. Each vehicle in the scenario, to include its motion, must be modeled. All target and observer locations must also be input. The concentration path lengths over various lines of sight to the targets can then be calculated for different aspect angles. This path length can then be used to determine the effect of vehicular dust on transmission over a given waveband.

The third step of the assessment methodology is to evaluate the performance impact of the battle by-products on individual sensor links. The first phase is to model key sensor parameters. The type of sensor being examined determines the parameters of interest. For a millimeter wave sensor, for example, these parameters would include power, frequency, antenna gain, aperture diameter, pulse width, etc. Next, the sensor's measure of performance is identified. This is the performance parameter of the sensor that will be impacted by the battle by-product. *Table 2* contains some measures of performance for various types of sensor technologies. The last phase of this step is to quantify the amount of degradation of sensor performance (i.e. the change in the "measure of performance") due to the battle by-products. This step will need to be repeated if multiple sensor links must be evaluated.

Figure 3 shows a generic process nomogram that illustrates the methodology involved in this step. The upper left graph shows how a key parameter of the system is degraded from its baseline value by a battle by-product. The upper right graph shows how this degradation influences a sensor parameter, or design point. This sensor design point then influences the sensor measure of performance as shown in the bottom right graph. These measures of performance can then be used as inputs to effectiveness models. The generic nomogram also shows how this can be a two-way process; if a desired sensor performance is needed, a quantification of the battle by-product that can be tolerated can then be calculated.

276

TABLE 2. Measures of Performance for Various Sensor Technologies

TECHNOLOGY	IMPLEMENTATION	MOP
Visible	TV DVO Human Eye	Minimum Resolvable Contrast
Active Laser	Laser, Semiactive	SNR, Pdet
IIR	IR TV Thermal Imaging FLIR	Minimum Resolvable Temperature
Non-IIR	EO Tracker Beacon Tracker IR Seekers	SNR, Pdet
Acoustic	Acquisition Sensor	SNR, Pdet
Active MMW	MMW Seekers	SNR, Pdet
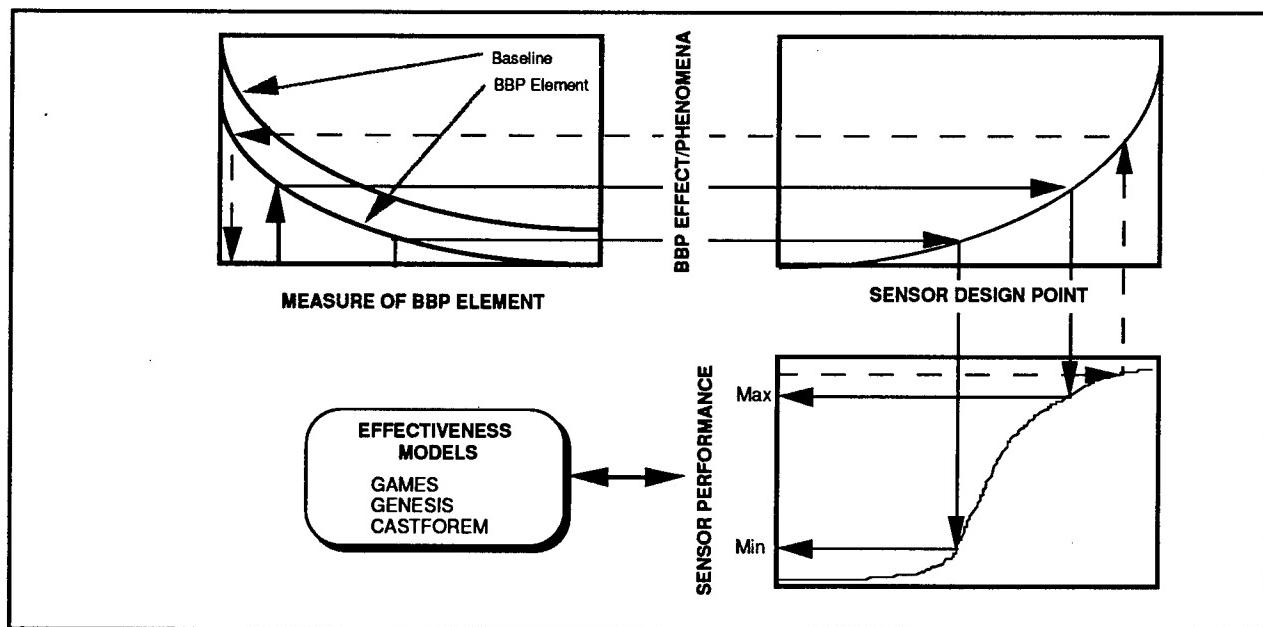
FIGURE 3. Generic Process Nomogram for Methodology

An example of this process nomogram for a non-imaging infrared system is shown in *Figure 4.* In this example, the concentration path length of dust degrades the transmission to the sensor. This transmission degradation influences the signal-to-noise ratio of the sensor. The signal-to-noise ratio in turn affects the system's probability of detection. This example also illustrates the two-way process feature of the assessment methodology. If the probability of detection needed to achieve a required level of operational effectiveness has been determined, the signal-to-noise ratio that corresponds to this probability of detection can be calculated. The transmission necessary to achieve this signal-to-noise ratio can then be calculated. This, in turn, shows the concentration path length of dust that can be tolerated by the system and achieve its required operational effectiveness. Currently, only attenuation effects of battle by-products have been examined in detail, but clutter effects of certain battle by-products are also an important area that must be addressed.
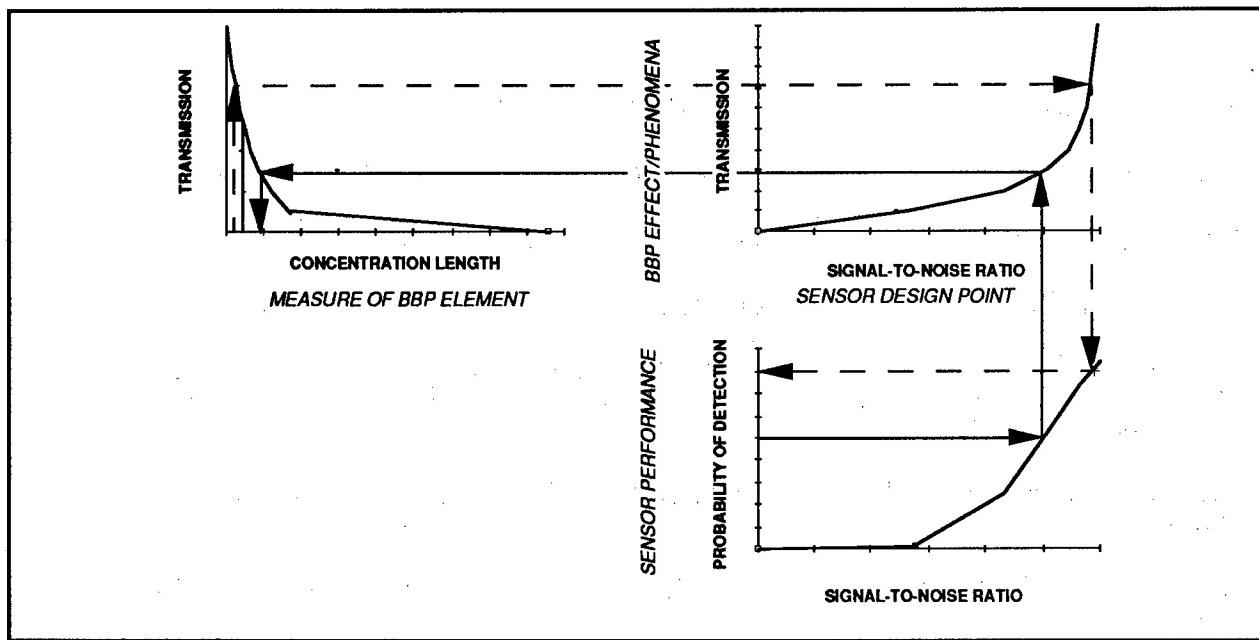
FIGURE 4. Non-Imaging Infrared Process Nomogram

The final step in the assessment methodology is to study operational effectiveness of the weapon system. This can be accomplished with an effectiveness model. For a simple model such as GAMES[6] or GENESIS[7], the inputs that will reflect the impact of the battle by-products are the detection probabilities calculated in the third step of the assessment methodology. More complex models allow for a detailed representation of the battle by-product and sensor parameters. Parametric runs of the effectiveness models enable the user to calculate the minimum probability of detection values at which the system can still achieve a required level of operational effectiveness for a given scenario. Note, the system may still achieve this operational effectiveness with a significant decrease in detection probability. The required operational effectiveness may also be met by compensating for the battle by-product with an operational alteration, such as a different attack azimuth or selection logic. These options can be examined with the use of effectiveness models. After this fourth and final step is completed, the impact of the battle by-product on system effectiveness can then be quantified by comparing the effectiveness of the system both with and without the battle by-products in the scenario.

4. CONCLUSIONS

The draft definition set for the dirty battlefield environment was presented in this paper. Community acceptance of these definitions will lead to a consistent use and a greater understanding of battlefield elements as well as lay the groundwork for consistency in system specifications and testing procedures for battle by-products. The assessment methodology provides a standardized approach for evaluating the impact of battle by-products on smart weapon sensors and seekers. Addressing these battle by-products in addition to countermeasures and weather will lead to more responsive smart weapon systems.

REFERENCES

1. "Smart Weapons Weather Specification Guide," AMC-SWMO, 31 October 1990.

2. "AMC-SWMO Countermeasures Study, Volumes I - IV," AMC-SWMO, January 1990.

3. Webster's New World Dictionary, Merriam-Webster, Inc., Springfield, Massachusetts, 1989.

4. Department of Defense Dictionary of Military and Associated Terms, Joint Chiefs of Staff, 1987.

5. Mason, James B., Ralph G. Steinhoff, Electro Optical Systems Atmospheric Effects Library (EOSAEL) Executive User's Guide, ARL Battlefield Environment Directorate, White Sands Missile Range, New Mexico, 1987.

6. Guided Artillery Munition Effectiveness Simulation (GAMES) User and Programmer Manual, AMSAA, June 1987.

7. Generic Smart Indirect Fire Simulation (GENESIS) Operator's Manual - Version 2.0, GACIAC, December 1991.

ANALYSIS OF INFRARED BACKGROUND SCENES FROM THE GRAYLING I SWOE JT&E FIELD TEST

Max P. Bleiweiss
U.S. Army Research Laboratory
White Sands Missile Range, New Mexico, 88002-5501, USA

Michael Rollins and Charles Chaapel
Science and Technology Corporation
Las Cruces, New Mexico, 88001, USA

ABSTRACT

The Smart Weapons Operability Enhancement (SWOE) Joint Test and Evaluation (JT&E) program is an effort to validate the SWOE process of background scene generation. To this end, images were acquired in the field for comparison with these synthetic scenes. Although a wide variety of measurements were made at this test, which was held at Camp Grayling, Michigan, during September and October 1992, only the mid- and far-infrared imagery acquired by the Battlefield Environment Directorate of the U.S. Army Research Laboratory will be discussed here. The test consisted of 107 2-hr missions extending over the 41-day test period. All of the imagery used in this analysis was acquired of the same scene under a variety of diurnal and meteorological conditions. One image from each of the missions for each band has been processed extensively for the purpose of characterizing these scenes to evaluate a variety of feature metrics as to their dependence on the conditions at the time of measurement. Summaries of these analyses will be presented and discussed.

1. INTRODUCTION

The purpose of the analysis presented in this paper was to review calibration procedures and to characterize mid- and far-infrared images acquired at Grayling I. Due to limitations in time and resources, this analysis should not be considered comprehensive. A brief discussion of the calibration procedures and analysis is presented.

No existing standard can be compared with imagery to determine its "goodness." There are some quantities available (such as mean square error) that could be used for this purpose, but there are neither scales nor standards to compare against. This problem also exists for the comparison of model-generated images to field-acquired imagery. Such analysis is required for a number of activities that use battlefield imagery, including simulation and sensor performance assessment, and in image compression, where fidelity losses must not include relevant information. Several processes can be performed on the imagery to arrive at figures of merit that might be used for comparison purposes. Further review of the literature may yield additional characterization methods. This paper presents a description of some methods that have been used to date with the Grayling I imagery.

The images examined in this study were acquired by the Agema BRUT imaging system. This system includes two infrared cameras, one operating in the mid-infrared waveband (2 - 5.6 μm) and one in the far infrared (8 - 12 μm). The cameras were located on the same instrument platform and operated along virtually the same line of sight. The area E that was used for this study consisted of two subscenes, E_1 and E_2, at the left and right of the scene, with six regions of interest (ROI) defined that

represent types of background important to the SWOE process. These backgrounds included terrain with various types of foliage. The outer edges of E are outside the cameras' fields of view. The algorithms to be applied to the scenes and subscenes are described in the next section. A discussion of how the parameters that result can be used for analysis follows. One possible result of this analysis may be the development of tools for inserting realistic texture into simulated scenes.

2. ANALYSIS PROCEDURES

A description of the sampling, registration, and cropping process follows. The analytical tools used in the study are presented in the remaining paragraphs.

2.1 SWOE GRAYLING IMAGE PREPARATION

Each raw infrared image file produced by the Agema BRUT system consists of an image information header followed by the bitmapped pixel data. The file header contains the date and time of frame capture, scanning mode, and image resolution. The complete file is referred to as a frame and contains four separate segments within the file known as fields. Each field contains a header followed by image data at a resolution of 140 horizontal pixels by 70 vertical pixels, with 16 bits of data for the A/D counts associated with each pixel. Each field header specifies the type of lens and filter used, along with calibration constants for calculation of the apparent temperature for each pixel. The four fields are interlaced, resulting in a raw composite image resolution of 140 pixels horizontally by 280 pixels vertically.

A file conversion routine was written to convert Motorola-based data, which have the most significant byte first, to an Intel format with the opposite byte sequencing. This process resulted in PC-readable files with image information content identical to that of the originals.

After all Grayling image files were converted and saved to diskettes, an image viewer utility was written to display the full image along with header information. A majority of the Grayling images were reviewed, and a reference image was chosen based on its superior feature clarity and contrast. All images processed, which consisted of pairs of simultaneously acquired images in each of the two infrared wavebands of interest, were registered and cropped with this reference image. A utility was written to load and process the reference image and the image to register and crop. After registration with the reference, the raw images were cropped to 128 x 128 pixels such that each scene contained exactly the same elements. This square, power-of-two image dimensionality is required for two-dimensional fast Fourier transform processing and provides a square aspect ratio for each pixel. During the processing of the images, a problem was discovered. The mid-infrared camera lens had an 8% wider field of view than the lens on the far-infrared camera. After an investigation of various interpolation algorithms, a cubic spline-based interpolation process was incorporated into the registration and cropping program as the final step in outputting the 128 x 128 mid-infrared images.

The original images had different horizontal and vertical resolutions. In order to sample at the same resolution in each direction, two of the four vertically interlaced fields were discarded. To allow registration at maximum resolution first, the selection of fields to be retained was made at the last stage of the process, when the image was considered registered and ready for output to the 128 x 128 format.

282

The registration and cropping process resulted in an image data set containing simultaneously acquired images in the two wavebands for each Grayling trial, all of which were registered to the same reference image. Utilities were written for viewing the 128 x 128 format images and performing apparent temperature statistical analyses on the whole image and on six regions of interest within each image.

2.2 HISTOGRAM ANALYSIS

Histograms of apparent temperatures were created for the entire scene and for the six ROIs. From these, the following parameters were calculated (as defined in *Numerical Recipes* [Press et al., 1988]): mean, median, maximum, minimum, variance, standard deviation, absolute deviation, skewness, and kurtosis. These measures have been applied to a variety of targets and backgrounds (King et al., 1992; Ota and Bleiweiss, 1992; Ben-Yosef and Wilner, 1985; Ben-Yosef et al., 1985) and some may be better discriminants of targets in backgrounds that the traditional "delta-T." Other features of the distribution can also be investigated (Jain, 1989).

Another parameter associated with these statistical values is "clutter" (Hetzler et al., 1987), which can make it difficult to distinguish a target from a background. One definition for this quantity is

$$C = \left[\frac{1}{N} \sum_{j=1}^{N} x_j^2 - \frac{1}{N} \left(\sum_{j=1}^{N} x_j \right)^2 \right]^{\frac{1}{2}} \tag{1}$$

or the square root of variance for all N pixels. Another reference (Schmeider and Weathersby, 1983) states that single pixels should not make up the distribution used to compute clutter. Instead, the distribution should consist of cells twice as large as the target. In this treatment, each cell is square, with dimensions of approximately twice the target height. This definition can be expressed as

$$C = \left(\sum_{i=1}^{N} \frac{\sigma_i^2}{N} \right)^{\frac{1}{2}} \tag{2}$$

where σ_i is the radiance standard deviation of the ith cell and N is the number of contiguous cells in the scene (Hetzler et al., 1987).

This definition means that for a scene without a target, the clutter level may be undefined or, instead, can take on a range of values because one can determine a value of C for all reasonable possible target sizes. For this reason, clutter analysis has not been emphasized in this study to date.

2.3 GRAY-LEVEL CO-OCCURRENCE ANALYSIS

Gray-level co-occurrence analysis "... characterizes the microtexture of an image region by measuring the dependence between pairs of gray levels arising from pixels in a specified spatial relation" (Haralick and Shapiro, 1991). This technique may be applied either to the whole image or to a ROI. Although a large number of parameters can be derived from the analysis of co-occurrence matrices, our discussion can be limited to a few that have been shown to provide good discrimination between textures (Wahl, 1987; Ballard and Brown, 1982; Marceau et al., 1990). These parameters are contrast (or inertia), homogeneity (or energy), entropy, and correlation. Other texture analysis techniques are available (He and Wang, 1990; Therrien et al., 1986) but have not been applied in this study because of limited resources. The following paragraphs illustrate the derivation of co-occurrence matrices from images and present the definitions of these four quantities.

The gray-level co-occurrence matrix (GLCM) is a square matrix whose size is based on the number of gray levels in the image under analysis. For example, an image with a possible number of quantization levels of 256 leads to a GLCM of 256 X 256. Since this treatment creates an extremely large matrix, the number of levels is generally reduced to 8 or 16 (Wahl, 1987). In addition, as will be seen shortly in the definition of how the GLCM is formed, it is possible to create a matrix for a large number of angles or orientations as well; this number too is usually limited in practice, normally to 0°, 45°, 90°, and 135°. The matrix is a "distribution" of the number of times certain configurations of brightness levels occur. This approach can best be explained by example (Haralick, 1974).

Shown below are a representation of a simple digitized image with four possible gray levels, along with a generalized representation of the co-occurrence matrix that would be derived from this image for a given pixel pair configuration.

<table>
<tr><td colspan="6" align="center">DIGITAL IMAGE</td><td colspan="5" align="center">GENERALIZED GLCM</td></tr>
<tr><td></td><td></td><td colspan="4">Column</td><td></td><td colspan="4">2nd gray level of pair</td></tr>
<tr><td></td><td></td><td>1</td><td>2</td><td>3</td><td>4</td><td>1st gray level</td><td>j = 0</td><td>1</td><td>2</td><td>3</td></tr>
<tr><td>Row</td><td>1</td><td>0</td><td>0</td><td>1</td><td>1</td><td>i = 0</td><td>#(0,0)</td><td>#(0,1)</td><td>#(0,2)</td><td>#(0,3)</td></tr>
<tr><td></td><td>2</td><td>0</td><td>0</td><td>1</td><td>1</td><td>1</td><td>#(1,0)</td><td>#(1,1)</td><td>#(1,2)</td><td>#(1,3)</td></tr>
<tr><td></td><td>3</td><td>0</td><td>2</td><td>2</td><td>2</td><td>2</td><td>#(2,0)</td><td>#(2,1)</td><td>#(2,2)</td><td>#(2,3)</td></tr>
<tr><td></td><td>4</td><td>2</td><td>2</td><td>3</td><td>3</td><td>3</td><td>#(3,0)</td><td>#(3,1)</td><td>#(3,2)</td><td>#(3,3)</td></tr>
</table>

In the generalized GLCM, #(i,j) is the number of times that the i,j gray-level pair occurs in the digital image in a particular orientation. Specifically, for $\phi = 0°$ (horizontal orientation), a sequence of two zeroes occurs (left/right, right/left) a total of four times in the digital image. At 45°, the pair (0,0), (moving both up and down the 45° direction) occurs four times. The GLCM matrices for horizontal and 45° adjacent pairs are given below.

$$P_{0°} = \begin{pmatrix} 4 & 2 & 1 & 0 \\ 2 & 4 & 0 & 0 \\ 1 & 0 & 6 & 1 \\ 0 & 0 & 1 & 2 \end{pmatrix} \qquad P_{45°} = \begin{pmatrix} 4 & 1 & 0 & 0 \\ 1 & 2 & 2 & 0 \\ 0 & 2 & 4 & 1 \\ 0 & 0 & 1 & 0 \end{pmatrix}$$

Similar matrices can be obtained for distance measures greater than 1 (i.e., for nonadjacent pairs).

For this study, the images were rendered in 16 gray levels to make the generation of the GLCMs more feasible. The matrices were computed for 0°, 45°, 90°, and 135°. The metrics mentioned above were derived from these matrices according to Eqs. 3 through 6.

Contrast or inertia

$$f_2 = \sum_{i=1}^{N_g} \sum_{j=1}^{N_g} (i-j)^2 \frac{P(i,j)}{R} \tag{3}$$

Contrast is greatest when adjacent pixels are very different in gray level.

Homogeneity or energy

$$f_1 = \sum_{i=1}^{N_g} \sum_{j=1}^{N_g} \left(\frac{P(i,j)}{R}\right)^2 \tag{4}$$

Homogeneity is greatest when most of the co-occurrences are for the same two gray levels. It is a measure of how consistently a pattern is repeated in an image.

Entropy

$$f_9 = -\sum_{i=1}^{N_g} \sum_{j=1}^{N_g} \frac{P(i,j)}{R} \, log \left[\frac{P(i,j)}{R}\right] \tag{5}$$

Entropy is a measure of "information" content in the image. It is maximum when all co-occurrence possibilities occur in equal proportion.

Correlation

$$f_3 = \frac{\sum_{i=1}^{N_g} \sum_{j=1}^{N_g} (i-\mu_x)(j-\mu_y)\frac{P(i,j)}{R}}{\sigma_x \sigma_y} \tag{6}$$

Correlation is greatest when the pixels in the (i,j) pair are similar in gray-level value and both values at the same time are either above or below the average values for their respective positions in the pair (μ_x and μ_y).

In Equations 3 through 6,

$P(i,j)$ = the value of the i,j element of the GLCM

R = normalization constant (equal to the number of actual co-occurrences obtained from summing over all the elements in the matrix)

N_g = number of gray levels

μ_x = $\sum_{i=1}^{N_g} i \sum_{j=1}^{N_g} \frac{P(i,j)}{R}$ (average gray level value for first pixel in pair)

μ_y = $\sum_{j=1}^{N_g} j \sum_{i=1}^{N_g} \frac{P(i,j)}{R}$ (average gray level value for second pixel in pair)

σ_x^2 = $\sum_{i=1}^{N_g} (i-\mu_x)^2 \sum_{j=1}^{N_g} \frac{P(i,j)}{R}$ (standard deviation of gray level value for first pixel in pair)

σ_y^2 = $\sum_{j=1}^{N_g} (j-\mu_y)^2 \sum_{i=1}^{N_g} \frac{P(i,j)}{R}$ (standard deviation of gray level value for second pixel in pair)

2.4 TEXTURE DESCRIPTION BASED ON FOURIER ANALYSIS

Texture descriptions based on Fourier analysis can be divided into two groups (Haralick and Shapiro, 1991), the power spectral density (PSD) and the autocorrelation function (ACF). Both the PSD and the ACF were computed for the Grayling images. The PSD is the Fourier transform of the ACF. High PSD at high spatial frequencies indicates fine texture with high contrast. The identification of peaks and the measure of the slope of the PSD can be useful for descriptive purposes (Wahl, 1987). As an example, the PSD for the Grayling reference image used in this study is shown in Fig. 1. The ACF is examined to derive various image parameters, such as coarseness, which is proportional to the width of the ACF (Jain, 1989). Moments can be generated to arrive at other measures. There are other techniques, such as generalized linear filtering (Jain, 1989), that can be applied to a variety of image transforms to arrive at other descriptors. These measures have been applied to infrared backgrounds for analysis by other researchers (Ben-Yosef et al., 1985; Futterman et al., 1991).
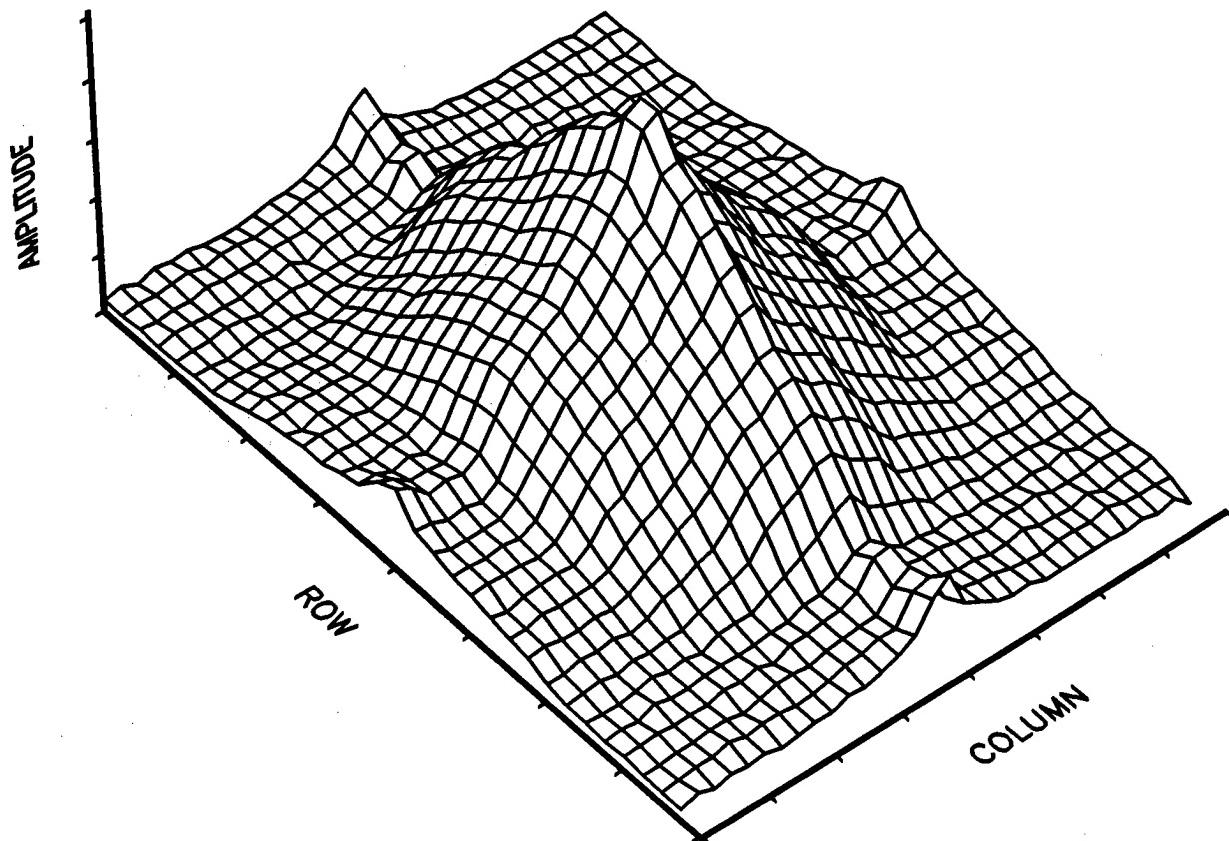
Figure 1. Power spectrum of entire Grayling scene.

In one dimension, the correlation of two functions, $g(t)$ and $h(t)$, is defined to be

$$Corr(g,h) \equiv \int_{-\infty}^{\infty} g(\tau + t)h(\tau)d\tau \qquad (7)$$

and the Fourier transform of $Corr(g,h)$ is given by

$$Corr(g,h) \rightarrow G(f)H(-f) \tag{8}$$

(where capital letters denote the Fourier transform of the lower-case function) so that the Fourier transform of the correlation is the product of the Fourier transforms of the individual functions (Press et al., 1988). Similarly, for the autocorrelation, if g is real,

$$Corr(g,g) \rightarrow G(f) \, G(-f) = G(f) \, G^*(f) = |\, G(f) \,|^2 \tag{9}$$

The above expression is also known as the Wiener-Kinchine Theorem. $|\, G(f) \,|^2$ is the power spectral density, PSD. Parseval's Theorem says that the total power in a signal is the same in the time domain and the frequency domain (Press et al., 1988):

$$Total\ Power \equiv \int\limits_{-\infty}^{\infty} |g(t)|^2 \, dt = \int\limits_{-\infty}^{\infty} |G(f)|^2 \, df \tag{10}$$

and the "one-sided power spectral density" of the function g is

$$P_g(f) \equiv |G(f)|^2 + |G(-f)|^2 \qquad 0 \le f < \infty \tag{11}$$

if g is real,

$$P_g(f) = 2|G(f)|^2 \tag{12}$$

For our analysis, the function $g(t)$ is replaced by the image, $f(x,y)$. Other parameters obtainable from this analysis are scene variance and the correlation length. Variance, σ^2, can be obtained (Futterman et al., 1991) from the integral of the PSD or the ACF evaluated at zero spatial separation. Correlation length, L_C, which is a measure of how gradually changes in gray level occur within a given neighborhood, was evaluated for this study.

$$\sigma^2 = \int\limits_{0}^{\infty}\int\limits_{0}^{\infty} P_f(k,l) \, dk \, dl = ACF(0,0) \tag{13}$$

$$L_C = \frac{1}{\sigma^2} \int\limits_{0}^{\infty}\int\limits_{0}^{\infty} ACF \, dx \, dy \tag{14}$$

2.5 DUAL-BAND PROCESSING

The ratio of the mid-infrared image to the far-infrared image can be formed and the above analyses can be performed on the resulting images. Differenced images can also be created. According to Richards (1986), multiplication of images from two different bands is not as useful. An important consideration here is the registration of images. Depending on the spectral bands and the bandwidths, ratios are useful "... in reducing the effect of topography, as a vegetation index, and for enhancing subtle differences in the spectral reflectance characteristics for rocks and soils" (Richards, 1986). Other arithmetic operations can create still other images for analysis.

One interesting form of dual-band processing involves the creation of plots in which statistical measures obtained for a ROI at different times in one band are plotted against corresponding measures in the other band. Such plots can be created to discern whether or not a variety of information classes exist in the scene. An example of such a plot, for average temperatures in ROI 1 and ROI 2, is shown in Fig. 2.
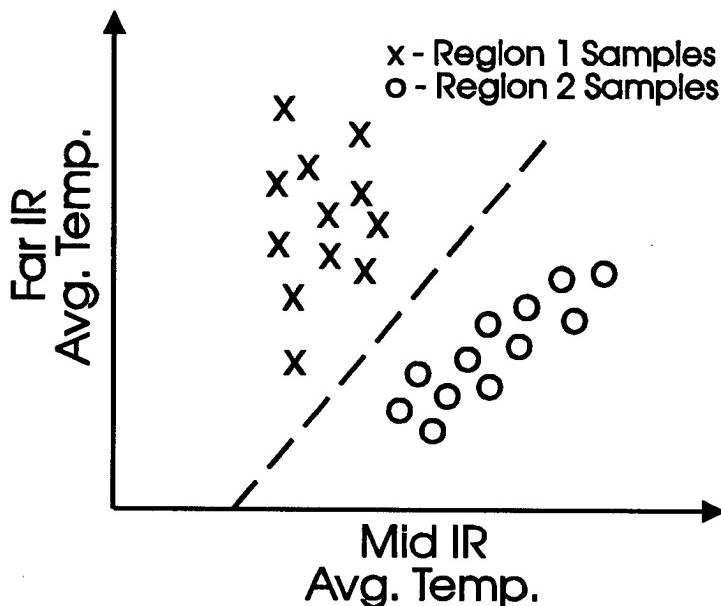
Figure 2. Dual-band plot for average temperatures showing clustering for regions 1 and 2.

It is clear from Fig. 2 that these plots can be used for feature identification and, if there are features that can be defined *a priori*, their movement with time in this pattern space can be displayed. This technique was applied to the imagery used for this study.

2.6 WAVELET ANALYSIS

Other techniques for describing background scenes have been investigated as well. One technique that has received considerable attention in this study is wavelet analysis.

Scene analyses involving power spectra, autocorrelation, and various statistical measures primarily address the textural qualities of a region in an image. These methods are less suited to analyzing discrete objects in terms of size, shape, and location.

A wavelet is a function whose value is very close to zero everywhere except for a specific interval. A basis that can be used to construct any image can be generated from translations and dilations (scaled versions) of a given wavelet (Ruskai, 1992). A wavelet transform of an image is a decomposition of that image in terms of a specific wavelet basis. Size, shape, and position of discrete objects can be inferred from a few wavelet coefficients.

In this study, three wavelet-based parameters were calculated for the small ROIs. These parameters were compaction, horizontal wavelet transform centroid, and vertical wavelet transform centroid. The first parameter, compaction, is a measure of the presence of sudden, discrete patches within the region. The compaction is the variance of coefficient energies about the average. It is maximum when a few coefficients contain most of the energy, widely varying from the average. This pattern can be due to

288

a discrete object such as a vehicle or a bush. The second and third parameters are useful in attributing a rough size and aspect ratio to the main discrete object(s) in the region. The expressions for compaction and horizontal wavelet centroid are given below.

$$Compaction = \frac{\sum\limits_{k=0}^{N-1} \sum\limits_{l=0}^{N-1} \left| W(k,l)^2 - \overline{W(k,l)^2} \right|}{\sum\limits_{k=0}^{N-1} \sum\limits_{l=0}^{N-1} W(k,l)^2} \qquad (k,l) \neq (0,0) \qquad (15)$$

$$Hor.\ cen. = \frac{\sum\limits_{m=0}^{\log_2(N)} \sum\limits_{n=0}^{\log_2(N)} \left(n \sum\limits_{k=INT(2^{m-1})}^{2^m-1} \sum\limits_{l=INT(2^{n-1})}^{2^n-1} W(k,l)^2 \right)}{\sum\limits_{i=0}^{N-1} \sum\limits_{j=0}^{N-1} W^2(i,j)} \qquad (i,j);(k,l);(m,n) \neq (0,0) \qquad (16)$$

where $W(k,l)$ is the wavelet transform coefficient at indices k,l.

Equation 16 partitions the wavelet transform domain into regions (bands, indexed by m and n) of the same wavelet dilation and obtains the energy in each band. The vertical centroid is obtained similarly, using m as the explicit factor rather than n.

Note that in both of these expressions, no pair of indices should be simultaneously zero to avoid considering global brightness offsets (i.e., DC term). The centroid expressions are only valid for the Haar wavelet, which was used in this analysis.

Wavelet transforms are not translationally invariant (Mallat and Zhong, 1992) and these parameters are only appropriate as rough measures. If an object in an image aligns with a particular large wavelet, then approximation of the object may require few coefficients. If the object is "out of phase" with any wavelets of the same size, the object must be approximated by combinations of smaller wavelets, thus spreading the spectrum and affecting the centroids. Compaction appears to be invariant to shifting. Invariance problems can be lessened by using both sine and cosine Gabor functions in a wavelet-related process, since Gabor functions allow for phase differences (Priddy, 1992). (Such a process apparently occurs in biological vision.)

2.7 APPLICATIONS

The descriptors presented in the previous paragraphs can be used for a variety of purposes, including the following:

(1) Scene-by-scene (or ROI-by-ROI) analysis, including

    (a) Comparing measured scene descriptors to modeled scene descriptors

    (b) Comparing measured scene descriptors to compressed, measured scene descriptors for a variety of compression levels to assess compression effects

    (c) Comparing measured scene descriptors between mid- and far-infrared bands

(d) Comparing measured scene descriptors for a variety of slopes and aspects as seen by the different imaging systems participating in SWOE, which have all acquired imagery at different depression angles and azimuths

(2) Ensemble comparison

(a) Comparing the distribution of one descriptor from all scenes or a particular ROI (for example, the mean) to that for the modeled scene to determine whether the variety (distribution) of modeled values appears the same as measured

(b) Investigating differences in descriptors between day and night, for example

(3) Comparing mid-and far-infrared wavebands

3. RESULTS

Results from co-occurrence analysis, autocorrelation analysis, dual-band analysis, and wavelet analysis are presented here. The results are discussed in the light of visual assessment of the regions of interest. The Grayling image scene used for this study is shown in Fig. 3, with the six ROIs marked. In addition to the ROIs, the whole scene was processed.
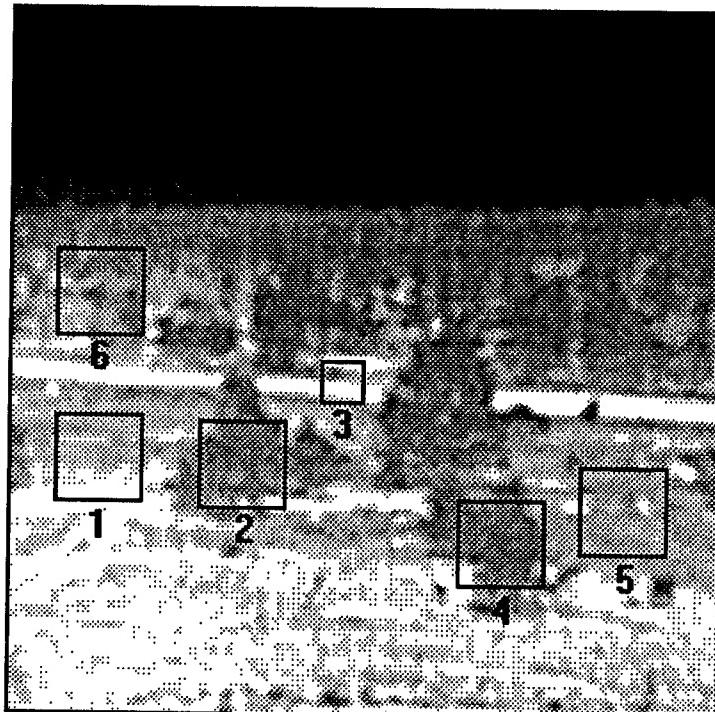
Figure 3. Grayling image with regions of interest framed.

3.1 GRAY-LEVEL CO-OCCURRENCE ANALYSIS RESULTS

Parameters from gray level co-occurrence analysis for each ROI are shown in Table 1. Referring to Fig. 3, it is clear that the contrast measures agree with visual assessment of contrast differences between regions 4 and 5. Region 6 has "rolling" features such that adjacent pixels are usually above or below the average gray scale value at the same time. Looking at the expression for correlation (Eq. 6), one can see why a high correlation would result from this type of feature arrangement. Region 3 has a greater spread of different gray scale co-occurrences than region 5, resulting in about twice the entropy and therefore much lower homogeneity. Less obvious is why region 3 has a lower contrast measure than region 6. The way contrast is measured in the co-occurrence process penalizes region 3 for having small or zero-level changes between pixels anywhere except at the road and light patch boundaries.

3.2 POWER SPECTRUM AUTOCORRELATION ANALYSIS

Correlation lengths were calculated for regions 1, 2, 4, 5, and 6, all of which were of the same pixel dimensions (see Eq. 14). The results are shown in Table 2. Correlation lengths are given relative to the maximum one (region 5) for comparison with visual assessment. Region 5 exhibits the greatest correlation length because its average brightness (and therefore its ACF integral) is large compared to its variance.

TABLE 1. RESULTS FROM CO-OCCURRENCE ANALYSIS OF GRAYLING IMAGE SCENE

Region	Contrast	Correlation	Entropy	Homogeneity
1	0.2917	0.177	2.239	0.2089
2	0.2958	0.132	1.515	0.4255
3	0.2857	0.166	2.402	0.1122
4	0.3417	0.124	1.741	0.3665
5	0.2708	0.126	1.292	0.4226
6	0.3667	0.198	2.259	0.1332

TABLE 2. CORRELATION LENGTHS

Region	Correlation length
1	0.9768
2	0.9754
4	0.9710
5	1.0000
6	0.9853

3.3 DUAL-WAVEBAND ANALYSIS RESULTS

Dual-band plots of the type shown in Fig. 2 were made for this image set using mean, variance, skewness, and kurtosis statistics for the six regions. Because of great variations in environmental conditions over several days, plots using data from all the images acquired in the test did not demonstrate any discernable clustering characteristics for the six regions. For this reason, it was decided to examine plots for specific time blocks, such as early morning, midday, early evening, and so forth. These specific time blocks were still unable to discriminate completely between the regions, however. Plots of skewness for sets of images acquired during early morning and late afternoon-early evening are shown in Figs. 4 and 5.

One interesting result from this analysis was that the higher-order statistics, skewness and kurtosis, seemed to have a larger spread of results over the collection of images for foliage than for more barren terrain. Compare, for example , the points representing region 2 (foliage) and region 1 (primarily grass) in Fig. 4. These outlying values occurred most appreciably during periods of maximum temperature change, showing the difference in thermal inertia between the ground and the foliage. These data are for a period of stable temperature and most sample points are clustered within a small area. During the period represented by Fig. 5, environmental temperatures descended considerably. The foliage regions have less thermal inertia and demonstrate higher skewness (the same result was observed for kurtosis). The small areas of terrain within the scene are still warmer than the foliage, skewing the distribution.

3.4 WAVELET ANALYSIS

The results of wavelet analysis for each of the small regions of interest in the Grayling image of Fig. 3 are shown in Table 3. Note that the wavelet centroid measures detect the large aspect ratio of the road seen in region 3. The concentration of energy in the lower left corner of region 4 registers with a high compaction measure.

TABLE 3. PARAMETERS FROM WAVELET ANALYSIS OF GRAYLING IMAGES

Region	Horizontal Centroid	Vertical Centroid	Compaction
1	0.0831	0.6011	0.8221
2	0.5137	0.9962	1.0080
3	0.0670	0.8477	0.7130
4	0.7058	0.6109	1.0760
5	1.3740	1.4450	0.9130
6	0.3905	0.5952	0.8270

0400 to 0800 hrs
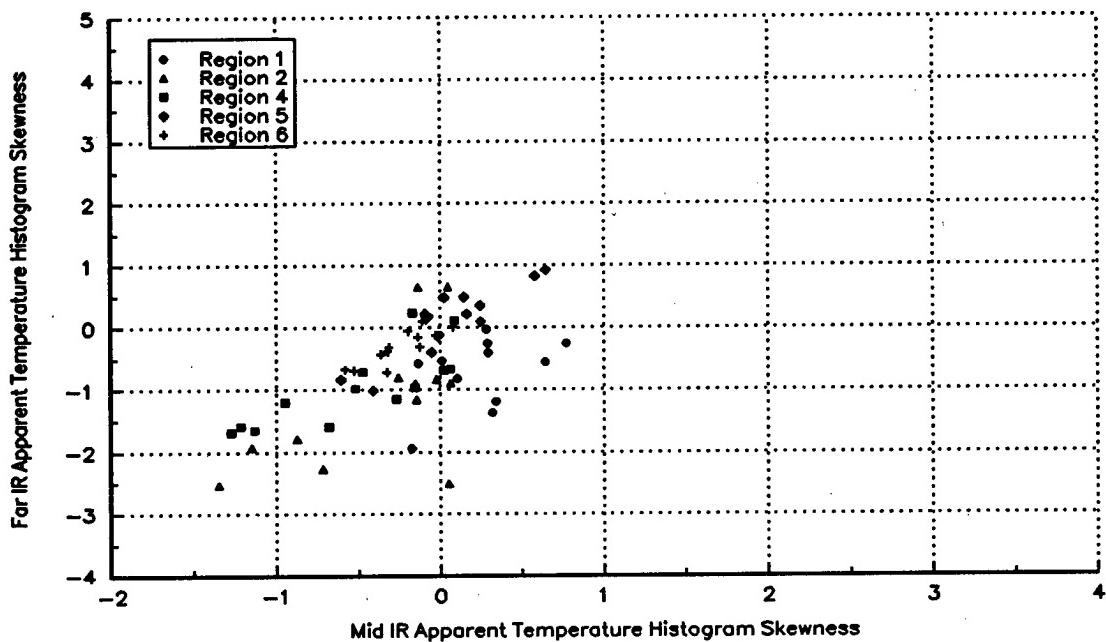
Figure 4. Skewness plot for early morning.

1600 to 2000 hrs
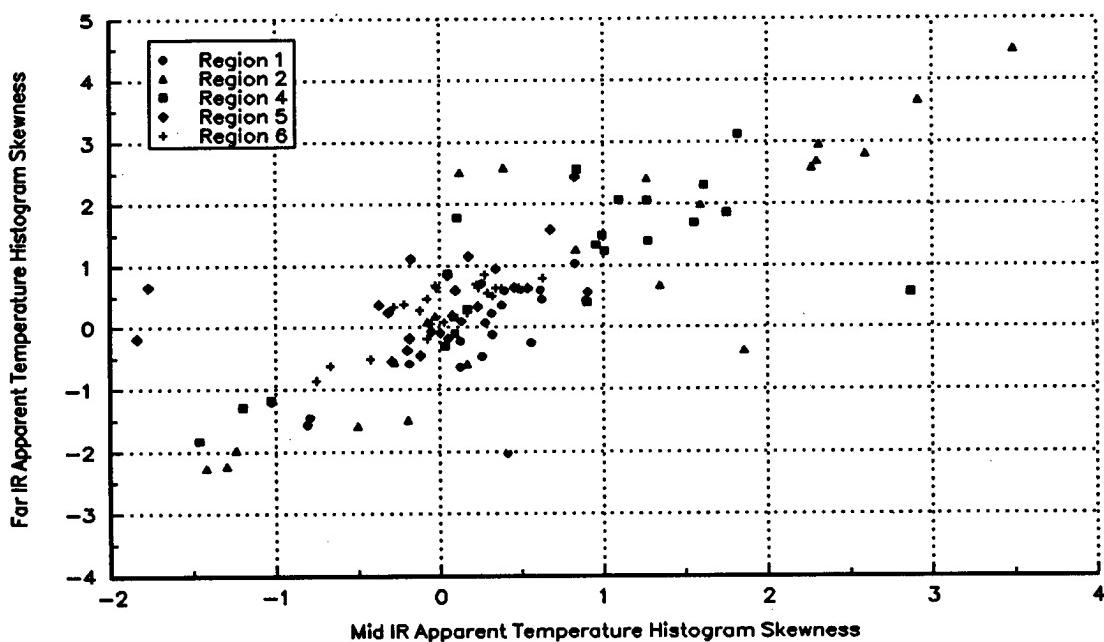
Figure 5. Skewness plot for late afternoon and early evening.

4. CONCLUSIONS

This analysis has brought together a number of independent tools useful in characterizing infrared image textures, structures, and thermal characteristics. Some methods demonstrate better agreement with subjective visual assessment than others. Use of single parameters to characterize complex scenes provides convenient discrimination but only under special conditions. A combination of statistical parameters and transform spectra will be necessary to discriminate fully among regions in terrain images. Further analysis and selection of tools is ongoing, with the goal of developing an objective scene characterization process.

REFERENCES

Ballard, D.H., and C.M. Brown, 1982: *Computer Vision*. Prentice-Hall, Inc., Englewood Cliffs, New Jersey.

Ben-Yosef, N., K. Wilner, I. Fuchs, S. Simhony, and M. Abitol, 1985: Natural Terrain Infrared Statistics: Daily Variation. *Applied Optics, 24*(23), 4167-4171.

Ben-Yosef, N., and K. Wilner, 1985: Temporal Behavior of Thermal Images. *Applied Optics, 24*(2), 284-286.

Ben-Yosef, N., K. Wilner, S. Simhony, and G. Feigin, 1985: Measurement and Analysis of 2-D Infrared Natural Background. *Applied Optics, 24*(14), 2109-2113.

Futterman, W.I., E.L. Schweitzer and J.E. Newt, 1991: Estimation of Scene Correlation Lengths, *Characterization, Propagation, and Simulation of Scenes and Backgrounds*. SPIE V. 1486, 127-140.

Haralick, R.M., and L.G. Shapiro, 1991: Glossary of Computer Vision Terms. *Pattern Recognition, 24*(1), 69-93.

Haralick, R.M., 1974: *Texture-Tone Study With Applications to Digitized Imagery*. Kansas University Center for Research, prepared for Army Engineer Topographic Laboratories, ETL-CR-74-17, AD-A008 030.

He, D.-C., and L. Wang, 1990: Texture Unit, Texture Spectrum, and Texture Analysis. *IEEE Transactions on Geoscience and Remote Sensing, 28*(4), 509-512.

Hetzler, M.C., R.M. Smith, R.C. DuVarney, and J.M. Marks, 1987: A Study of Clutter in Infrared Backgrounds, *Infrared Image Processing and Enhancement*, SPIE V. 781, 10-17.

Jain, A.K., 1989: *Fundamentals of Digital Image Processing*. Prentice-Hall, Inc., Englewood Cliffs, New Jersey.

King, T.A., K.C. Payne, and M.P. Bleiweiss, 1992: MAESTRO—A Target and Background Characterization System for EO Sensors. *Proceedings of the Smoke/Obscurant Symposium XVI*, U.S. Army Chemical Research, Development and Engineering Center, Aberdeen Proving Ground, Maryland.

Mallat, S., and S. Zhong, 1992: Wavelet Transform Maxima and Multiscale Edges. *Wavelets and Their Applications*, Mary Beth Ruskai, ed., Jones and Bartlett, Boston, Massachusetts, 67-104.

Marceau, D.J., P.J. Howarth, J.-M.M. Dubois, and D.J. Gratton, 1990: Evaluation of the Grey-Level Co-Occurrence Matrix Method for Land-Cover Classification Using SPOT Imagery. *IEEE Transactions on Geoscience and Remote Sensing*, **28**(4), 513-519.

Ota, C.Z., and M.P. Bleiweiss, 1992: Apparent Target Temperatures at Smoke Week XIII. *Proceedings of the Smoke/Obscurant Symposium XVI*, U.S. Army Chemical Research, Development and Engineering Center, Aberdeen Proving Ground, Maryland.

Press, W.H., B.P. Flannery, S.A. Teukolsky, and W.T. Vetterling, 1988: *Numerical Recipes: The Art of Scientific Computing*. Cambridge University Press, New Rochelle, New York.

Priddy, K.L. 1992: *Feature Extraction and Classification of FLIR Imagery Using Relative Locations of Nonhomogeneous Regions with Feedforward Neural Networks*. PhD Dissertation, Air Force Institute of Technology, Ohio.

Richards, J.A., 1986: *Remote Sensing Digital Image Analysis*. Springer-Verlag, New York, New York.

Ruskai, M.B., ed., 1992: *Wavelets and Their Applications*. Jones and Bartlett, Boston, Massachusetts, 3-14.

Schmeider, D.E., and M.R. Weathersby, 1983: Detection Performance in Clutter with Variable Resolution, *IEEE Transactions on Aerospace and Electronic Systems*. **AES-19**(4), 622-630.

Therrien, C.W., T.F. Quatier, and D.E. Dudgeon, 1986: Statistical Model-Based Algorithms for Image Analysis, *Proceedings of the IEEE*. **74**(4), 532-551.

Wahl, F.M., 1987: *Digital Image Signal Processing*. Artech House, Boston, Massachusetts.

MICROPHONE WIND NOISE:
IS IT REALLY CAUSED BY WIND ?

David H. Marlin
Army Research Laboratory
Battlefield Environment Directorate
White Sands Missile Range, NM 88002-5501

Since a microphone measures pressure, wind noise is caused by processes which produce pressure fluctuations. Three candidate mechanisms have been proposed: aeroacoustic sources, wake shedding by the microphone housing and turbulence. In most cases, turbulence is the predominant source. The pressure fluctuations at the microphone due to turbulence are not acoustic in nature in the sense that they do not obey any type of wave equation. Turbulence-induced spatial-pressure variations are advected past the microphone by the wind. The effect of a windscreen is to diffuse fluctuations of length smaller than the radius of the windscreen. Wind noise data sampled at 48kHz, with an anti-aliasing cutoff of 20kHz, exhibits some evidence of a low-dimensional chaotic attractor.

Introduction

Acoustics is playing an ever increasing role in battlefield dynamics. Several programs, such as BAT, Wide Area Mine (WAM), Anti-Helicopter Mine (AHM) and Non-Imaging Sensors (NIS) rely on acoustics for detection and classification of targets. Passive arrays are used by scouts and other units for detection and localization of enemy forces. Also, tactical decision aids for these acoustic sensor systems will provide battlefield commanders with information such as predicted detection ranges for helicopters and ground vehicles.

Wind noise can be a limiting factor in the performance of these system. In fact, under moderate surface wind conditions they can be completely disabled. Microphone wind screens have traditionally been used to reduce wind noise, but their effect is frequency dependent. They act as a lowpass filter for the noise, and the larger the screen, the lower the cutoff frequency. Unfortunately, it is low frequency sound, on the order of tens of Hertz, which is of primary interest in detection of helicopters and tanks. In order to be effective at these frequencies, a wind screen would need a diameter on the order of meters. This is clearly unreasonable for most of the systems mentioned above as deployment and concealment would be impractical.

Thus, it becomes necessary to rely on signal processing techniques to further reduce the wind noise. However, wind noise is broad-band, so traditional linear filtering methods do not work well. Some reduction can be achieved through the use of correlations among array elements. Also of some promise are active cancellation techniques using velocity measurements. Another field of interest, the subject of this paper, is the use of non-linear signal processing techniques based on the theory of non-linear dynamics and chaos.

297

The Potential Causes of Wind Noise

Studies of the last few decades have suggested three possible causes of wind noise in unscreened microphones: aeroacoustic noise from disturbances in the flow, wake shedding by the microphone housing (Figure 1) and the advection of turbulence past the microphone by the mean wind (Figure 2). In addition, a further mechanism contributing to windscreened microphones is flow through the windscreen. Note that the microphone wake constitutes turbulence, but in this paper the term "turbulence" refers to the turbulence encountered upwind from the microphone and not the microphone wake.

Various models have been put forth and experiments have been performed to determine the contribution of each effect, with different conclusions drawn by different authors. However, many of the experiments were not conducted under conditions representative of actual outdoor sound measurements in low speed flows. Recent results provide good evidence that turbulence is the predominant cause under many conditions. Before turning to this evidence, a brief description of each effect is given.

Figure 1 - *Aeroacoustic noise and wake shedding as a source of microphone wind noise.*

Aeroacoustic noise is sound which actually radiates from disturbances in the flow. Local interaction of the disturbance with the flow acts as a source, which then radiates acoustic energy. The radiated energy propagates to the microphone at the speed of sound, according to the acoustic wave equation. Thus, aeroacoustic noise is generated by sources which are not "local" to the microphone. This type of noise can be quite significant in flows with a high Mach number.

Figure 2 - *Atmospheric turbulence as a source of microphone wind noise. Turbulent eddies are advected past the microphone by the mean wind.*

In contrast to aeroacoustic noise, wake shedding by the microphone housing induces local pressure fluctuations at the microphone diaphragm. Although the wake continues for some distance downwind, there is no radiation involved. The only pressure fluctuations affecting the microphone signal are those induced by the flow interaction very near the microphone.

Turbulence induced noise exhibits features of both aeroacoustic noise and wake shedding. As with the latter, there is no radiation. The noise is induced by local pressure fluctuations which are not governed by the wave equation and do not propagate at the speed of sound. But the pressure fluctuations are those due to atmospheric turbulence and they are distributed throughout a very large region, being advected past the microphone by the mean wind. Thus, turbulence induced noise possess a non-local character, just as the aeroacoustic noise. The pressure fluctuations are generated far from the microphone by one mechanism and then carried to the microphone diaphragm by another.

The Case for Turbulence

J. Sullivan[1] conducted an experiment to measure the contribution of acoustic and aeroacoustic sources to wind noise in an outdoor flow. He did this by measuring correlations between two sets of microphones and anemometers, in a frequency range between 2 and 50 Hz. First, correlations were measured with no acoustic or aeroacoustic sources present. The correlation peak occurred at time $t=s/U$, where U is the mean wind speed, s is the separation distance and the measurements were taken parallel to the wind direction. The measurements were repeated with a speaker placed on an axis perpendicular to the wind direction, through the mid-point between the two microphones. If the acoustic noise dominates the wind noise, the correlation should occur at $t=0$. This did not occur; the correlation still peaked at $t=s/V$. Next, two aeroacoustic sources were used: the edge of a building and a large van. Both generate large scale turbulence in the flow and should be good aeroacoustic sources. In both cases, no acoustic signal was detected at all. Thus, Sullivan concludes acoustic and aeroacoustic sources do not contribute to wind noise.

This leaves wake shedding and turbulence and, in the case of screened microphones, flow through the windscreen as the possible sources of wind noise in outdoor flows. In a recent study by Morgan[2], strong evidence was found for turbulence as the leading cause in many situations. Morgan analyzed data from two sets of outdoor measurements taken in October 1990 and March 1991. The experimental configuration consisted of screened and unscreened microphones, some paired with hot-film anemometers placed approximately 2 inches upwind from the microphones. Wind screens of various sizes, shapes and porosity were used.

Figure 3 - *Cross correlation between microphone and hot-wire anemometer.*

Figure 3 shows the cross-correlation between an unscreened microphone and associated hot-film anemometer. As with all the data, the correlation peak occurs at a time delay of $t=s/U$, where s is the vector separation between microphone and anemometer, $s=|s|$ and U is the mean wind speed in the direction of s. All the data exhibit correlation peaks between .5 and 1, with the majority in the .7 to .9 range. Since the anemometer is upwind, it is measuring only the incoming atmospheric turbulence, and not the wake turbulence of the microphone. Thus, the strong correlation suggests a close relationship between the microphone noise and the atmospheric turbulence.

Figure 4 - *Power spectra of microphone, hot-wire anemometer probe, and their difference.*

Similarly, the power spectra of the microphones and anemometers exhibit similar shape, as shown in Figure 4. Because the units are different for each device, it is the flatness of the difference curve which is important and not its relative value. Note that the curve begins to roll off above 100 Hz. Morgan attributes this

299

to averaging of smaller fluctuations across the microphone diaphragm. The active measurement area of the hot-film anemometer is much smaller, so averaging will occur at much higher frequency for that device.

More evidence comes from consideration of a quantity proposed by Morse and Ingard[3]. They derive from first principles an expression for pressure fluctuations at a microphone due to turbulent flow advecting past the diaphragm. Their expression is

$$p \sim \rho u U, \qquad (1)$$

where p is the turbulent pressure fluctuations at the diaphragm, u the turbulent velocity fluctuations and U the mean velocity. Note that this expression is for the turbulence upwind of the microphone and does not include the microphone wake. Figure 5, also from Morgan, shows the wind noise data as a function of $(\rho u U)^{1/2}$. The equations for the curves are: October 1990, $p=1.6\rho(uU)^{1.1}$ and March 1991, $p=\rho(uU)^{1.1}$. The variance of the data and the size of the exponent suggest (1) is indeed a good measure of the wind noise and thus atmospheric turbulence is the major source.
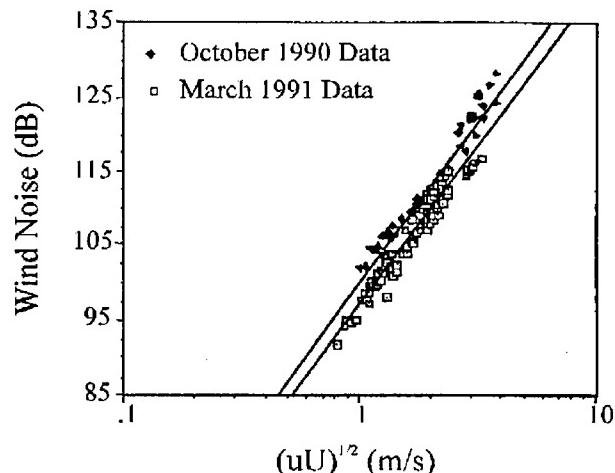
Figure 5 - *Wind noise as a function of $(uU)^{1/2}$. The equations are $p=1.6\rho(uU)^{1.1}$ and $p=1.1\rho(uU)^{1.1}$.*
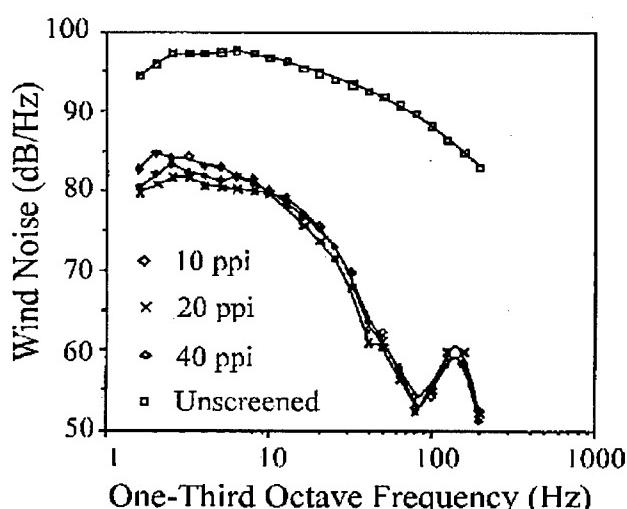
Figure 6 - *Power spectra for an unscreened microphone and three screened microphones. The windscreens are of varying porosity, measured in pores/inch, ppi.*

In the case of screened microphones, flow through the windscreen is also a candidate source for wind noise. Morgan also addresses this. Figure 6 shows the spectra for one unscreened and three screened microphones. The windscreens have the same diameter but varying porosity, which is the primary factor affecting the flow through the screen. The similarity between the spectra suggests flow is not the main cause of noise in a screened microphone. Additional evidence comes from (1). The flow quantities u and U were measured inside a wind screen and the noise estimated using (1). These estimates were several orders of magnitude below realistic levels of wind noise in a screened microphone. Thus, flow through the screen is not the major cause of the noise.

Evidence for the Chaotic Nature of Wind Noise

The understanding of turbulence in fluids is arguably the driving element of the theory of non-linear dynamics and chaos. Although a complete dynamical description of atmospheric turbulence may never be found, great progress has been made in the past two decades in characterizing aspects of the dynamics. Similarly, there has been a rise in the use of non-linear signal processing techniques to separate signals from "deterministic noise." Given that microphone wind noise is induced by the turbulent structure of the atmosphere, one asks whether it is possible to use any of these techniques to improve the microphone signal-to-noise ratio. The first question to ask is whether the wind noise exhibits evidence of a low-dimensional attractor, since this is the key to computationally feasible signal processing techniques.

Any dissipative dynamical system will contract volumes in phase space as the flow progresses in time. In many nonlinear systems, the trajectories will approach a chaotic attractor of non-integral dimension[4] d_A much lower than the dimension of the phase space. This attractor inherits a topology from the phase space and can be viewed as an abstract topological space, distinct from the phase space in which the dynamics evolve. Given only the topological attractor A without knowledge of the original phase space, one can seek to imbed A in $\mathbb{R}^d$, for some d. It has been shown[5] that an attractor A of dimension d_A can be imbedded in any dimension $d > 2d_A$. This gives an upper bound on the minimum imbedding dimension d_E: $d_A \leq d_E < 2d_A$.

Basically, d_E is the smallest dimension in which the attractor can be imbedded without self-intersection. In terms of the dynamics, this is the smallest dimension for which the flow trajectories do not intersect.. We deal here only with autonomous flows, so that in the original phase space, trajectories do not intersect. If trajectories are projected onto a lower dimensional subspace, however, false intersections may occur. Consider for example the harmonic oscillator. In two dimensions, two trajectories are given by $x_1(t) = \cos \frac{t}{T}$, $y_1(t) = -\frac{1}{T}\sin \frac{t}{T}$ and $x_2(t) = 2\cos \frac{t}{T}$, $y_2(t) = -\frac{2}{T}\sin \frac{t}{T}$. These trajectories do not intersect anywhere. But when projected onto the one-dimensional subspace of x, they intersect everywhere on the interval $[-1,1]$. Thus, if one is interested in the dynamics, it is important to find the imbedding dimension. In particular, this is necessary to extract meaningful results using time-delay embedding[6], a technique which attempts to reconstruct phase-space from a scalar time series.

Given a scalar time series $x(n)$, an N-dimensional vector time series

$$x_N(n) = [x(n) \ x(n+T) \ x(n+2T) \ ... \ x(n+(N-1)T)] \tag{2}$$

can be constructed for any time delay $T > 0$. This can be thought of as an approximation to the phase space representation given by the N-1 derivatives of $x(n)$. That interpretation is not necessary. $x_N(n)$ is equivalent to a vector of N state variables, and it's trajectory will exhibit similar behavior. In particular, it will approach an attractor which is in a sense equivalent to the original phase space attractor projected onto the dimension N. The imbedding dimension sets a lower bound on N. If d_E is small enough, then non-linear signal processing techniques can be used to improve signal-to-noise ratio. The definition of small depends on computer number-crunching capability. Currently, $d_E < 10$ is a good working criteria, but this will likely continue to increase dramatically, as it has in the last two decades.

In a recent paper, Kennel and Isabelle[7] were unable to draw a definite conclusion about the existence of a low-dimensional attractor in wind noise. However, the data used in that investigation were sampled at about 2.5

kHz, with an antialiasing filter cutoff of around 500-700 Hz. This is typical of most of the wind data available and it poses two problems: the data rate is probably too low and the anti-aliasing filter distorts the data. Aliasing is a phenomenon associated with linear signal processing. If one wants to do frequency domain processing, then it is absolutely necessary to pre-filter the data to remove aliasing. But this filtering alters the data by smoothing the time series. Nonlinear signal processing does not look at the frequency spectrum of the signal, so aliasing is not an issue. What is needed is a sampled trajectory of the flow and this should not be smoothed by a lowpass filter. Furthermore, it must be sampled at a high enough rate to capture the significant dynamics.

In August 1993, data was gathered at Dirt Site, White Sands Missile Range, N.M., by the author and Dr. John Noble, also with the Army Research Laboratory. This data was sampled at 48kHz using a Teac digital tape recorder. On the Teac, it is not possible to sample without the analog anti-aliasing filter. But by sampling at the highest possible rate, the cutoff was moved up to 20kHz, significantly reducing the smoothing. This data was examined for evidence of a low-dimensional attractor.

The algorithm used, the method of false nearest-neighbors[8] was developed by researchers at the Institute for Nonlinear Science in San Diego. The method uses time delay embedding to determine an upper bound on the imbedding dimension of an attractor. First, an N-dimensional time series is constructed, using (2). For each n, the nearest neighbor $x_N(\tilde{n}_N)$ is then determined:

$$||x_N(n)-x_N(\tilde{n}_N)||_{l2} = \underset{m}{MIN}||x_N(n)-x_N(m)||_{l2} .$$

(3)

Next, $N+1$ dimensional vectors are generated according to (2) and the increase in distance Δ between N-dimensional nearest neighbors is considered:

$$\Delta = \frac{||x_{N+1}(n)-x_{N+1}(\tilde{n}_N)||}{||x_N(n)-x_N(\tilde{n}_N)||} .$$

(4)

Note that $\tilde{n}_N$ is that value of m for which the minimum occurs for the vector $x_N(n)$ and therefore *depends on dimension N*. In general, $\tilde{n}_{N+1} \neq \tilde{n}_N$. If $N < d_E$, then the attractor will intersect itself and result in false neighbors. As the dimension N is increased by one, some of self-intersections will be removed, and the associated false neighbors will move apart. This will result in $\Delta > \Delta_{th}$, a threshold ratio. Once $N \geq d_E$, the attractor will no longer contain self-intersections and there will be no more false neighbors. On the other hand, some neighbors will be true neighbors in that the trajectories actually approach one another even for $N < d_E$. These neighbors will remain neighbors as N is increased, manifested by $\Delta < \Delta_{th}$.

The key to the algorithm is to successively increase N and count the percentage of nearest neighbors which are false at each step. As N passes through d_E, this percentage should drop to zero. Of course there are various limitations to the algorithm. For a given number of points in the scalar data set, the density will decrease as N is increased, so eventually the nearest neighbors will not be very close. This is dealt with by using a second threshold. The increase in distance between these not-very-near nearest neighbors is compared to the overall scale of the attractor. If the points are false neighbors, then they should separate toward extremities of the attractor as it is unfolded in the next dimension. The scale of the attractor is calculated as $\frac{1}{K}\sum_{n=1}^{K}(x(n)-\bar{x})^2$, where K is the number of points in the time series. For a more comprehensive discussion see the reference.
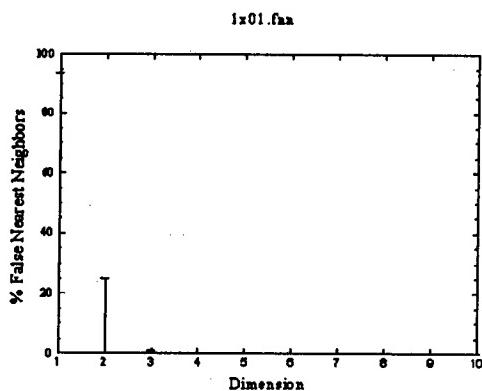
Figure 7 - *False-nearest-neighbors test on original August 1993 data.*

Figure 7 shows the results of the false-nearest-neighbor test on the August 1993 data. It indicates an attractor dimension of three or four. Figure 8 through Figure 10 show the results when the data were subsampled at one of twenty, 100 and 500 points respectively. The embedding dimension appears to increase with subsampling rate. Initially, some increase probably results from the reduction in correlation among adjacent points due to the smoothing of the antialiasing filter. This correlation is artificial, but as the subsampling increases, the natural correlation due to the dynamics will also decrease. Chaotic systems exhibit exponential separation of trajectories along some dimensions and contraction along others. Given enough separation in time, points along a given trajectory will appear to be independent. Figure 11 gives the results for a Gaussian white noise series, showing the effect of uncorrelated samples. Compare this with Figure 10.
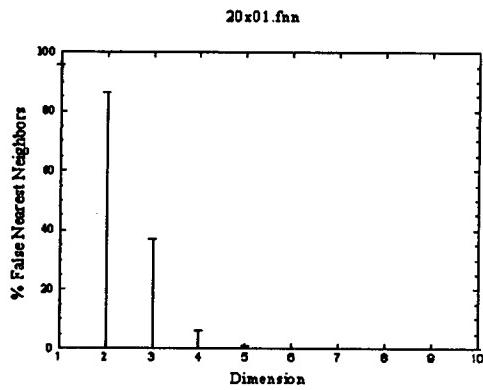
Figure 8 - *False-nearest-neighbors test on August 1993 data, subsampled at one out of twenty points.*
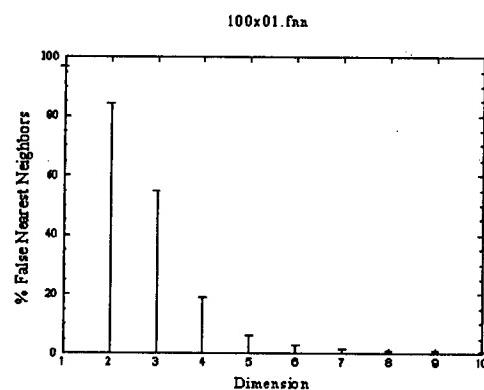
Figure 9 - *False-nearest-neighbors test on August 1993 data, sampled at one out of 100 points.*
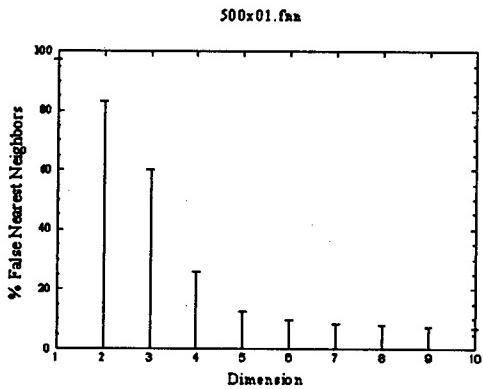
Figure 10 - *False-nearest-neighbors test on August 1993 data, sampled at one out of 500 points.*
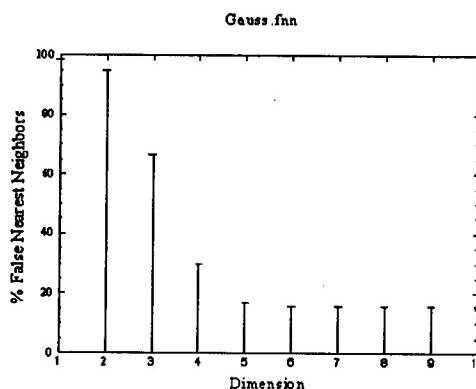
Figure 11 - *False-nearest-neighbors test on Gaussian white noise.*

Average mutual information[9] is usually considered more appropriate than correlation for nonlinear time series. Nevertheless, the arguments of the previous paragraph still apply. The antialiasing filter will affect the mutual information of adjacent samples, and the mutual information will decrease as separation in time increases. Furthermore, samples from uncorrelated Gaussian noise are independent, so their mutual information is also zero.

Thus, the subsampling rate of one out of 500 is probably too high, resulting in too much loss of information between points. On the other hand, the adjacent points in the unsubsampled data will show too much correlation and mutual information. The best choice probably lies with the subsampling rate somewhere between these two extremes. This leads to an attractor dimension in the range of four to eight.

Conclusions

It appears that the primary source of wind noise in most outdoor flows is atmospheric turbulence. The chaotic nature of the turbulence is reflected in the microphone wind noise. An analysis of wind noise data, sampled at a high enough rate, contains evidence of a low dimensional attractor. That dimension appears to be between four and eight for the data considered in this study. This is low enough to make wind noise amenable to nonlinear signal processing techniques for the improvement of signal-to-noise ratio.

However, more analysis is necessary. The method of false nearest neighbors used here should be compared with other techniques based on different properties of attractors and nonlinear dynamics. Agreement with other techniques would boost confidence of the existence of a low-dimensional attractor.

References

1. J. Sullivan, "An Investigation of Wind Noise," Construction Engineering Research Laboratory (unpublished)

2. M. S. Morgan, "An Investigation of the Sources and Attenuation of Wind Noise in Measurement Microphones," Ph.D. Dissertation, University of Mississippi (1993).

3. P.M. Morse and K.U. Ingard, *Theoretical Acoustics*, (Princeton University Press, Princeton, N.J., 1960), p. 701.

4. J. D. Farmer, E. Ott and J.. Yorke, "The Dimension of Chaotic Attractors", Physica 7D, 153 (1983).

5. T. Sauer, J.. Yorke and M. Casdagli, "Embedology", Journal of Statistical Physics, 65, 579 (1991).

6. See ref. 5.

7. M. Kennel and S. Isabelle, "Method to distinguish possible chaos from colored noise and to determine embedding parameters", Physical Review A, 46, 3111 (1992).

8. M. Kennel, R. Brown and H. Abarbanel, "Determining embedding dimension for phase-space reconstruction using geometrical construction", Physical Review A, 45, 3404 (1992)

9. R. Gallager, *Information Theory and Reliable Communication*, (John Wiley and Sons, Inc., New York, 1968), Ch. 2.

SHORT TERM FORECASTING FOR ARTILLERY USING TIME SERIES METEOROLOGICAL DATA

Fernando Caracena
and
Hui Xue Zhang

NOAA, Environmental Research Laboratories
National Severe Storms Laboratory
Boulder, Colorado 80303

ABSTRACT

In its efforts to "own the weather," the Army has been pushing to get high-end workstations into battlefield artillery sites, and to do on-site, short-range weather forecasting; however, due to financial constraints, instead the computers selected may be 486-type personal computers. This battlefield computer will be tasked with providing wind, temperature, and pressure information for artillery. Very short term weather forecasting (less than 3 hr) using numerical prognostic models is already fraught with problems on current, high-end workstations where non-hydrostatic mesoscale models, that use "full physics," generate forecasts at about the pace of real time. A speed up in computation, by sacrificing some of the physics, degrades the quality of forecasts. On a 486-type personal computers the mesoscale modeling capabilities are reduced by at least an order of magnitude over those of workstations , so that numerical, mesoscale modeling of the atmosphere becomes impractical. Modeling of three dimensional winds over complex terrain on a personal computer is still possible, however, in some diagnostic sense, and forecasting can be achieved only through statistical techniques. We are in the process of adapting Analytic Approximation techniques to automate the generation of meteorological messages for artillery guidance using Tamde and PASS data.

1. INTRODUCTION

This paper documents experimental results on now casting and very short term weather prediction, using sparse, mesoscale observations of the atmosphere and diagnostic modeling. We concentrate on the kinematic field which can be diagnosed for terrain effects through a variational analysis that makes minimal adjustments to winds supplied by an initial, unconstrained analysis using the NUATMOS model (See

Ross et al., 1988). Constrained wind diagnoses are compared to corresponding, unconstrained analysis via Analytic Approximation (Caracena, 1992), a scheme described in a previous report

The Army needs computationally cheap now casts and short term predictions (0-3h) of wind, temperature, and other atmospheric variables in the battlefield based on data from a variety of sources. Atmospheric data, encoded as a meteorological message (met message), is essential for the accurate delivery of missiles and projectiles (Blanco and Traylor, 1976).

Sophisticated, numerical, mesoscale models can produce now casts and forecasts using sufficiently powerful computers such as currently available workstations. However, a downsizing of the battlefield computer from a high-end workstation to high-end personal computer (PC) has been proposed to reduce military costs. This would amount to a reduction of computational speed by an order of magnitude. Even small numerical models would not be able to deliver timely output under these circumstances. A model that runs in minutes on a high-end workstation would take a large fraction of an hour to run on a PC. Therefore, we should prepare to use smaller computational schemes to predict the weather and assimilate weather information, should the battlefield computer be downsize.

To this above end, we have developed a number of modules, that can be used in various combinations, to generate automated meteorological (met) messages for artillery, and have tested them using data from PASS and Tamde projects. One module Analytic Approximation (Caracena, 1987) a generalization of objective analysis, was described in a previous report (Caracena, 1992); and was shown to give physically reasonable results in situations where about eight, simultaneous observations were used, but is robust enough to work with much fewer observations.

Blanco (1988) used a time-weighting technique to fill in missing current observations. Blanco and Trayler (1978) also experimented with using a linear least squares fit to past time series of past data to make the best estimate of current data at a non reporting sites. We have used time series of past data to make short term predictions, by extrapolating the linear trend into the future independently for each observing site and each data type, using the latter technique, and applying a mass-continuity constraint to model the effects of complex terrain in refining spatial flow patterns.

2, Mass continuity constraints

In the past, conventional observations of the wind were restricted to its horizontal components, so that the vertical component had to be estimated somehow. Since the vertical component of the wind plays a pivotal role in weather, meteorologists for a long time have been concerned with extracting the vertical component of wind from its observed horizontal components. A related problem is incorporating the effects of complex terrain on atmospheric flows. There area a number of techniques that have been developed to address these twin problems.

One technique developed long ago, was simply to vertically integrate the equation of continuity, estimating the vertical derivative of the vertical wind component from the divergence in the horizontal winds. It soon became obvious that there were large errors in this estimate. Particularly disturbing were the large values obtained for vertical velocities at the top of the troposphere where vertical velocities were expected to be small.

2.1 O'Brien Adjustment and related variational techniques

O'brien (1970) discussed several simple techniques to adjust the wind components so that the vertical wind component would vanish at some upper level in the atmosphere, thereby correcting for systematic errors in the measured winds in a vertical column. A proposed simple technique was to set the vertical wind component to zero at a top level and solve for a corresponding constant correction in the value of divergence in the horizontal winds at all levels. Another technique allowed a linear variation of this correction with height. He also discussed a variational method based in Sasaki's (1958) variational technique. McGinley (1973) also discussed a variational approach that applied the mass continuity constraint to the vertically integrated equation of continuity. The Lagrangian multiplier, a function of the horizontal components only, turned out to be the velocity potential for the field of horizontal wind corrections.

2.2 A variational technique used in modeling flow over complex terrain

Two diagnostic schemes, discussed below, use the same variational technique to impose mass continuity and model airflow over complex terrain. This variational technique is discussed, before going on to describe these diagnostic wind models.

An unconstrained objective analysis initializes the wind vectors v_0 on a three dimensional lattice. Using the equation of continuity as a variational constraint, adjusted wind vectors v are found that departed minimally from the initially analyzed winds. The problem, stated in mathematical notation, is

$$\delta \iiint dx\ dydz\ \{\ \alpha_1^2\ [\ (u-u_0)^2 + (v-v_0)^2\ ] + \alpha_2^2\ (w-w_0)^2 + \lambda\ \nabla \cdot v\} = 0, \tag{1}$$

where the variables α are the Gauss precision moduli. Because the main anisotropy is introduced vertically in the atmosphere by stability effects, there is no loss in generality if we set $\alpha_1 = 1$ and let $\beta = 1 / \alpha_2$. The variation carried out in (1) yields the following solutions:

$$u = 2u_0 + \partial\lambda/ \partial x \tag{2a}$$

$$v = 2\ v_0 + \partial\lambda/ \partial y \tag{2b}$$

$$w = 2\ w_0 + \beta^2\ \partial\lambda/ \partial z \tag{2c}$$

$$\nabla \cdot v = 0 \tag{3}$$

subject to the boundary conditions,

$$\lambda\ n \cdot \delta v = 0, \tag{4}$$

where n is the unit normal at each boundary point. The velocity potential is solved by combing the appropriate first derivatives of (2a-c) with (3), resulting in a modified form of Poisson's equation

$$\partial^2\lambda/\partial x^2 + \partial^2\lambda/\partial y^2 + \beta^2\,\partial^2\lambda/\partial z^2 = -2\,\nabla \cdot \mathbf{v}_0. \qquad (5)$$

As with the variational technique described by McGinley, the Lagrangian multiplier here acts as the velocity potential for the wind field adjustments, and is a solution of Poisson's equation having source term proportional to the three dimensional divergence of the initially analyzed winds. Stability effects are modeled by varying the parameter β. Terrain effects are introduced through solid boundary conditions at the varying ground level (4) by selecting $\mathbf{n} \cdot \delta\mathbf{v} = 0$. At the other boundaries, the flow-through condition $\lambda = 0$ is applied.
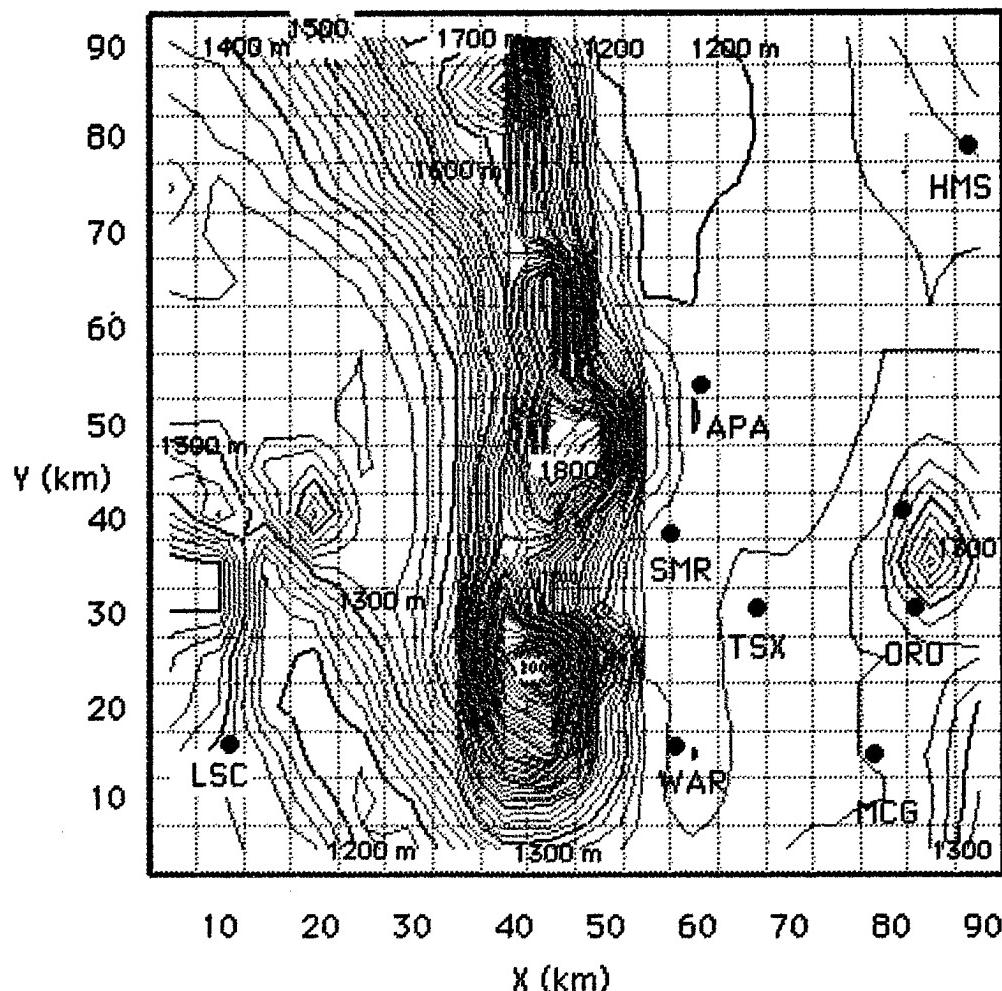
Fig. 1. Map of White Sands area displaying PASS sounding sites and terrain elevation averaged over 5km grid squares (light gray). Contour ntervals are 20 m (light gray) and 100 m (dark gray) as indicated, MSL.

2.2 The MATHEW Model

The MATHEW model (Sherman, 1978) was an early attempt to diagnose air flow over complex terrain by imposing mass continuity as a variational constraint. A bad choice of boundary conditions gave the MATHEW model some poor results,

particularly near the earth's surface. The lower boundary was chosen on the lattice points nearest to ground level. This resulted in a stair-stepped lower boundary where the vertical component of the wind was assumed to vanish. The difficulty with lower boundaries was avoided in the NUATMOS Model by using sigma-z, or terrain following coordinates.

2.3 The NUATMOS Model

The NUATMOS Model (See Ross et al., 1988) is an interactive program written at Monash University, Australia, under partial funding by Rocky Flats and the U.S. Dept. of Energy. It has a built-in, three-dimensional objective analysis scheme that outputs to sigma-z levels, or terrain-following layers to generate an initial three dimensional wind field. The variational analysis portion makes minimal adjustments to the wind on this three dimensional lattice to enforce mass continuity and solid boundary effects.

Sigma-z coordinates define height varying surfaces that asymptotically approach a flat, horizontal surface at the top, and the Earth's surface at the bottom, of the analysis domain. The sigma-z coordinate, which varies from 0 to 1, is a linear interpolator between the varying, lower level (sigma-z = 1) and the flat, top level (sigma-z = 0). Each value of sigma-z defines a corresponding surface lying a sigma proportional in distance between the flat, top level and the varying height of the ground, or bottom level.

In analyzing the three -dimensional, kinematic field, the NUATMOS Model first interpolates each sounding vertically to operator-specified sigma levels, and then performs a series of two-dimensional wind analyses on each sigma level, using an inverse-distance-squared weighting function. Given a single sounding, the model initializes all grid points on a given sigma level with the sounding value for that level.

Adjustments to the initially analyzed winds are computed by a mass-continuity module that modifies both vertical and horizontal winds, using the no-flow-through condition at the Earth's surface $n \cdot \delta v = 0$. The module provides for either compressible, or incompressible flow. As one would expect, the greatest kinematic adjustment happens near the ground, and where the terrain has the greatest relief.

3.0 Analysis of PASS data

A series of analysis of the winds were performed for Nov. 23, 1974, a day during the PASS project when there was a lot of temporal and spatial variability in the winds. The analysis domain is shown in Fig. 1. More general results for this day were presented previously (Caracena. 1992), and this day is revisited here, to compare constrained and unconstrained analysis schemes. Analytic Approximations were applied to the winds for various analysis and forecast times, and the results were compared to flow constrained to conserve mass *incompressibly* (3).

The NUATMOS model was run with PASS data using a 5km x 5km mesh, for which the average terrain elevations were computed for each square. Ten sigma-z layers were defined between the surface (about 1300 m, MSL) and a top level of 5050 m, MSL. corresponding approximately to the artillery levels (0 - 9). Note that over the mountain ridge (> 2000 m, MSL), sigma-z levels should shrink significantly relative to the artillery zones defined over the almost flat desert terrain.

309

3.1 Comparison of two analyses of the kinematic field

Constrained and unconstrained analyses give complimentary results as is demonstrated by comparing the unconstrained Analytic Approximation of surface winds for PASS data taken at 0630, 23 November 1974 (Fig.2a) with a corresponding analysis from the NUATMOS model (Fig. 2b). Where the density of observations is high, the Analytic Approximation more faithfully captures kinematic detail, but where observations are sparse, and there is a great deal of complexity in the terrain, the NUATMOS model gives better results.
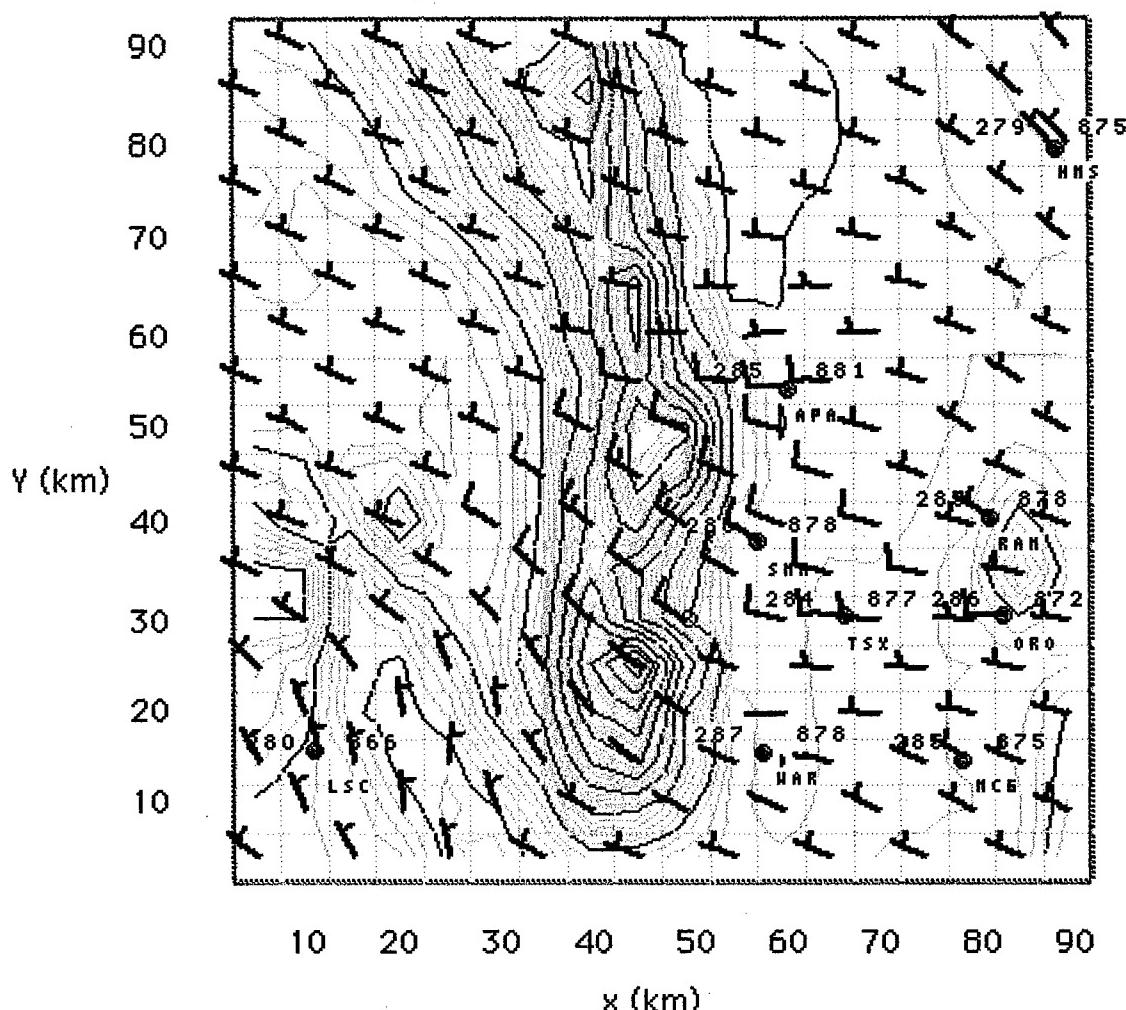
Fig. 2a. Unconstrained Analytic Approximation of surface winds for 0630, 23 Nov. 1974. Black dots indicate the positions of observing sites. Terrain contours are as labeled in Fig.1.

The inversion of Poisson's equation smoothes the initially analyzed winds, smoothing away kinematic features that are easily resolved in an unconstrained analysis. This is

the price one pays for being able to capture the kinematic effects of terrain. Of course, even using mass-continuity, the results improve dramatically with increasing number of observations. For example, an analysis based on a single observation (not shown) simply gives the effects of complex terrain on the otherwise uniform flow.

The comparison between the two analysis schemes can be pushed farther by contrasting a three station analysis (Fig .3a) using the Analytic Approximation, with a corresponding analysis using the NUATMOS model (Fig. 3b). Both analyses capture the large scale trend in the winds supplied by the triangle of observations that encompass the analysis domain, but the NUATMOS model provides additional kinematic details that appear physically reasonable: the wind accelerates and changes direction over mountain ridges, and decelerates and turns in their lee.
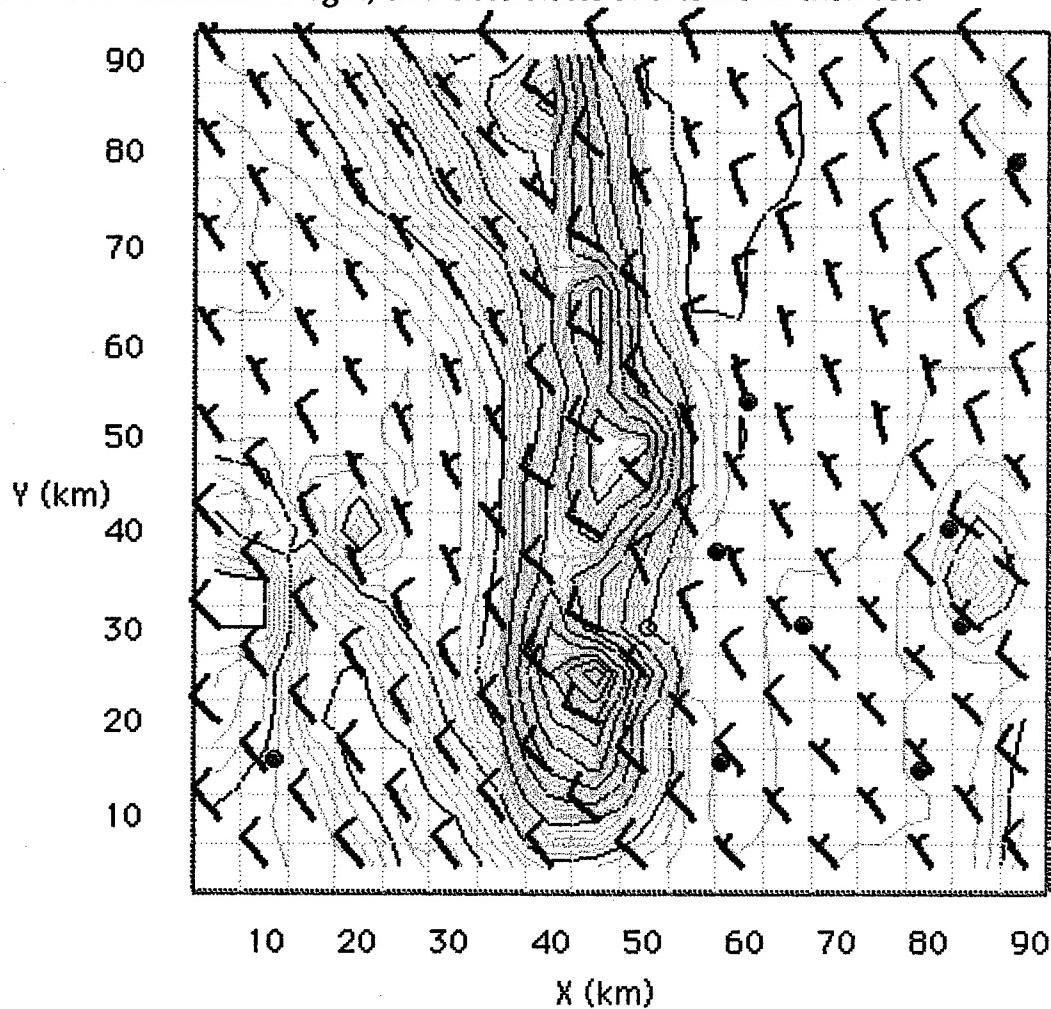
Fig. 2b. Surface winds analyzed for 0630, 23 Nov. 1974, imposing mass-continuity through the NUATMOS model. Terrain contours are as labeled in Fig.1.

3.2 Short term forecasting using time series analysis

We tried Analytic Approximation as a means of analyzing time series of observations and extrapolating the trend into the future; however objective analyses do not extrapolate well beyond data domains without special modifications. The
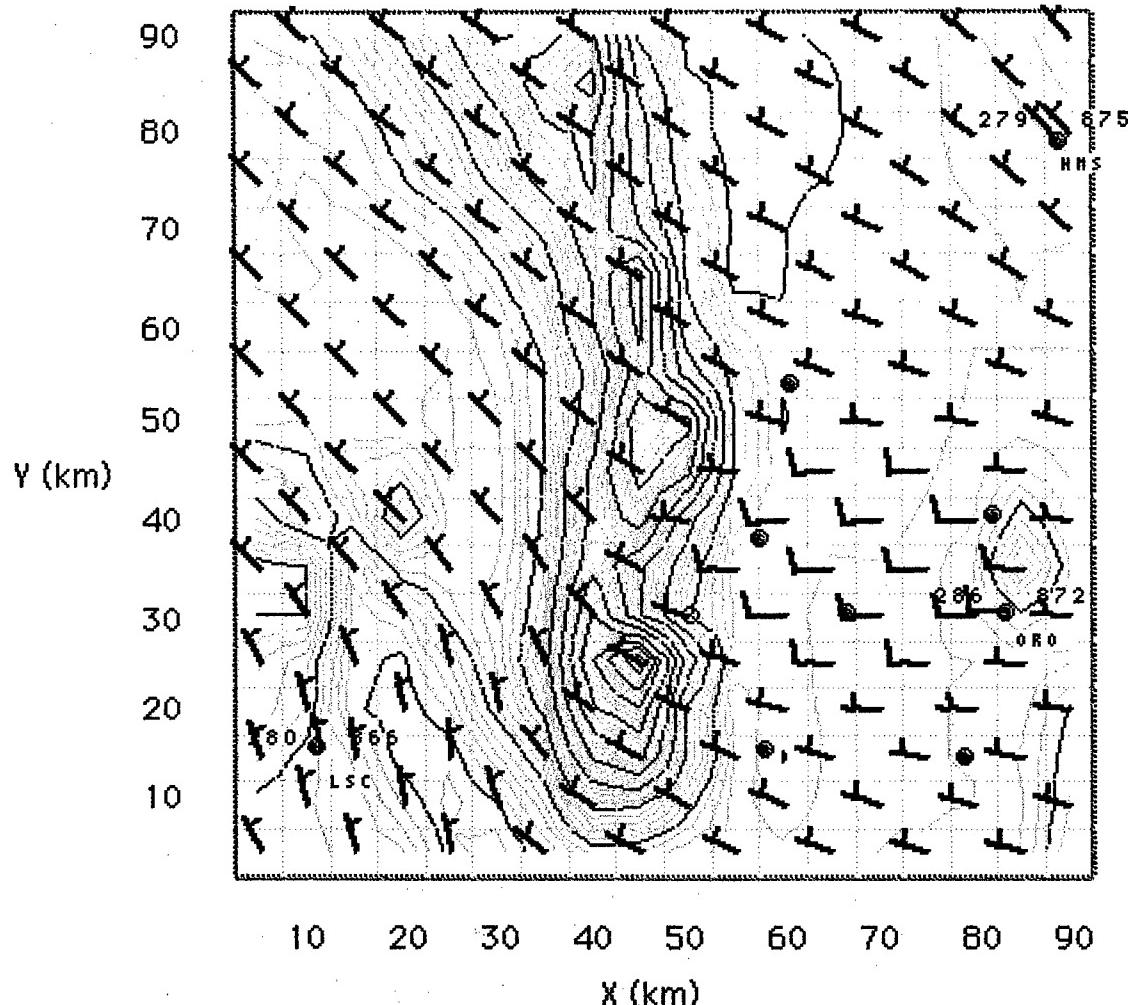
Fig. 3a. As in Fig. 2a, but the analysis is only for the three stations identified in the figure. as LSC, ORO, and HMS.

output values beyond data boundaries tend to approach a constant asymptotic value. In the time domain, the present is one boundary, and extrapolation is simply persistence. A scheme having better extrapolation properties was needed for this task. Since battlefield observations are likely to be sparse both in space and time, we needed to have a very robust scheme that could handle few observations. Were only one sounding to be available, the forecast should default to persistence. A time series consisting of two soundings, could be extrapolated as a straight line. For short time scales on the order of 1-2 h, a linear trend is probably as good a fit as any.

We wrote a short-term forecasting scheme that works by extrapolating a linear trend in observations. A straight line fitted independently to each time series of data for each station, is extrapolated into the forecast time. In this way, a new file of forecast observations is generated in the same format as the original observational data. Subsequently, this new file is inputted either into the Analytic Approximation Scheme

312

(see Fig. 4a), or the NUATMOS model (see Fig. 4b), to arrive at a corresponding spatial analysis of forecast fields. All trends in meteorological observations, whether temperature, pressure or kinematic data are handled in the same way. Since errors in linear extrapolations grow in time, this approach is usable for only very short-term forecasts (0-2h). Even in such short periods, mesoscale features such as fronts and convective systems can significantly change the weather so that a linear extrapolation is unsuitable. As in previous examples, the constrained analysis (Fig. 4b) produces a better portrayal of the winds over ridge tops than the
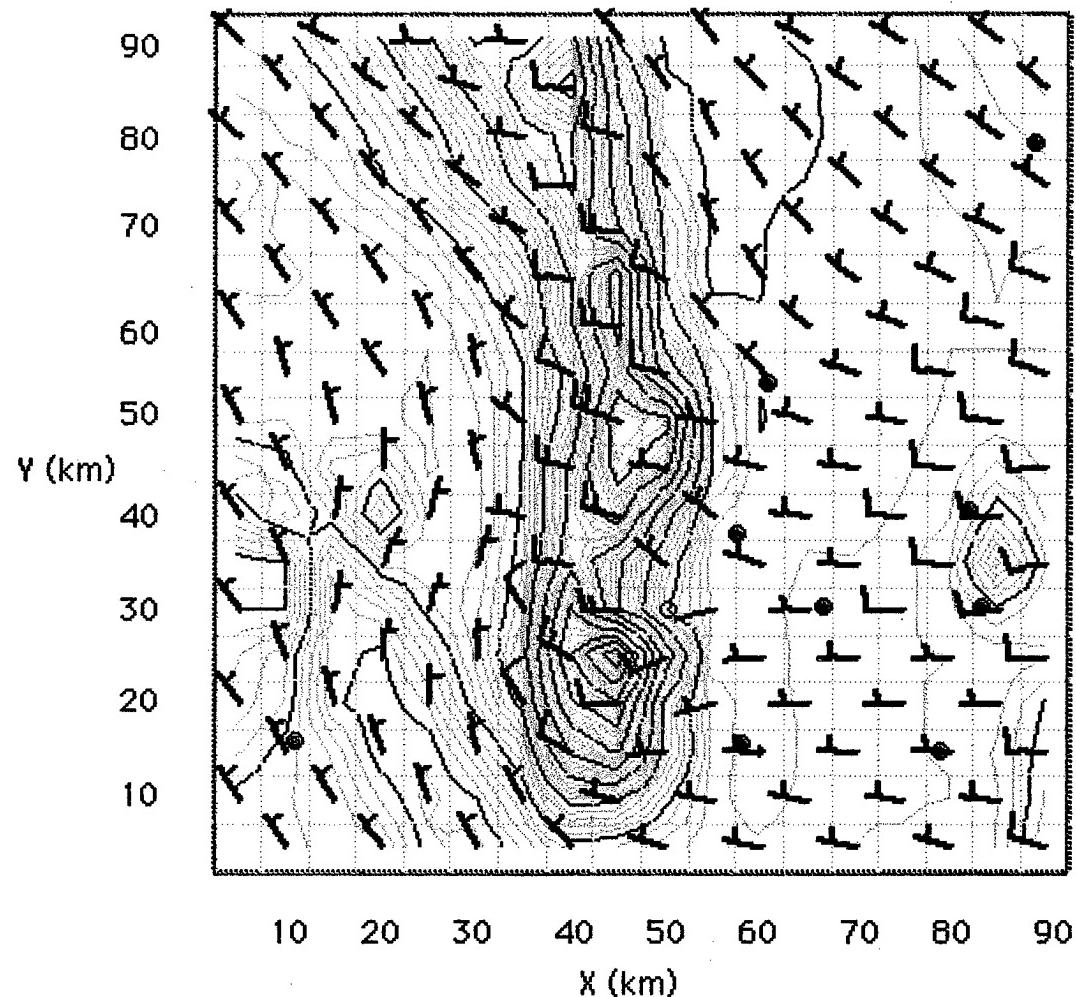
Fig. 3b. Same as in Fig. 1b caption, but for 3 stations indicated in Fig. 2a.

Analytic Approximation, but overly smoothes the analysis where observations would support greater detail. A pair of analyses using current data are presented in Figs. 5 a and b, for verifying the forecasts depicted in Figs. 4 a and b. Note that surface winds were backing and weakening as the day progressed so that the ridge top winds have weakened in both analyses, but mass-conserving flow is still stronger at ridge tops than that of the Analytic Approximation.

3.3 Capturing terrain effects through potential flow

313

A great deal of the computational apparatus used in solving for mass constrained flow goes into obtaining a good estimate of the vertical component of the wind. A small variation in horizontal winds can produce significant changes in the magnitude of the vertical component of the wind. The extra pains taken, result
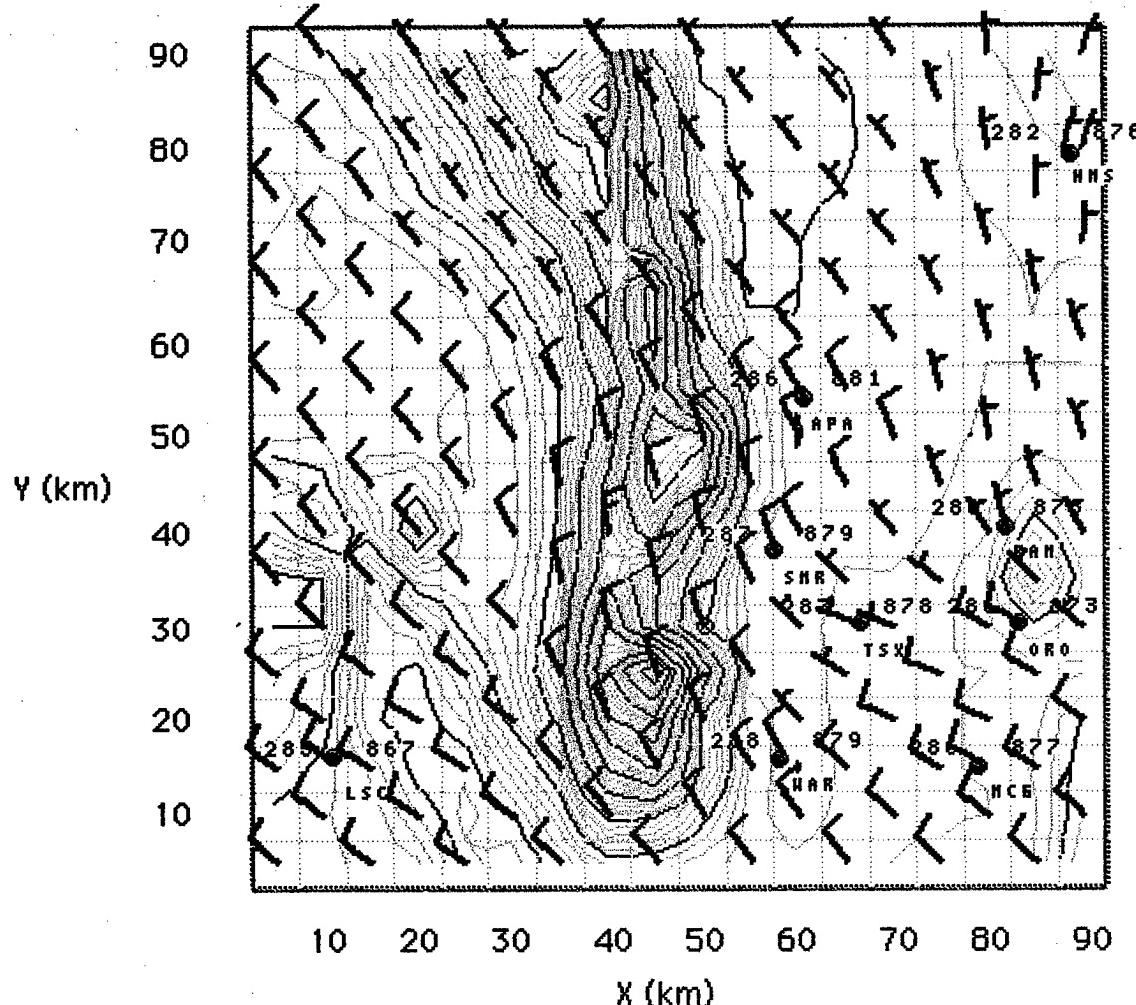
Fig. 4a. Forecast surface winds 40 min. in advance, analyzed without constraints for 1130, 23 Nov. 1974, using Analytic Approximation. Black dots indicate the positions of observing sites. Terrain contours are as labeled in Fig.1. Data ingested prior to 1050 was used in generating the analysis of forecast data for 1130.

in over-smoothing of the winds where there are sufficient observations to warrant greater detail. We are in the process of writing a scheme that would insert terrain effects while still maintaining detailed flow features as revealed by a properly filtered objective analysis. It is a potential flow solution that cancels the normal component of wind at the terrain interface, ignoring the wind divergence in the intervening space. We assume that the horizontal components of the wind vector are already well enough specified, except for the effects of complex terrain. A solution of Laplace's equation suffices to make corrections due to complex terrain. We use a Cartesian grid to solve for the potential flow, using a stepped lower boundary such as is used in the

MATHEW model, but modified so that the boundary values of the wind normal to the terrain are computed from objectively analyzed winds and the local terrain height gradients. A 2-dimensional version of this scheme, and preliminary results are presented in Fig. 6. We are in the process of writing the full three dimensional module, and hope to complete it by the end of the year.
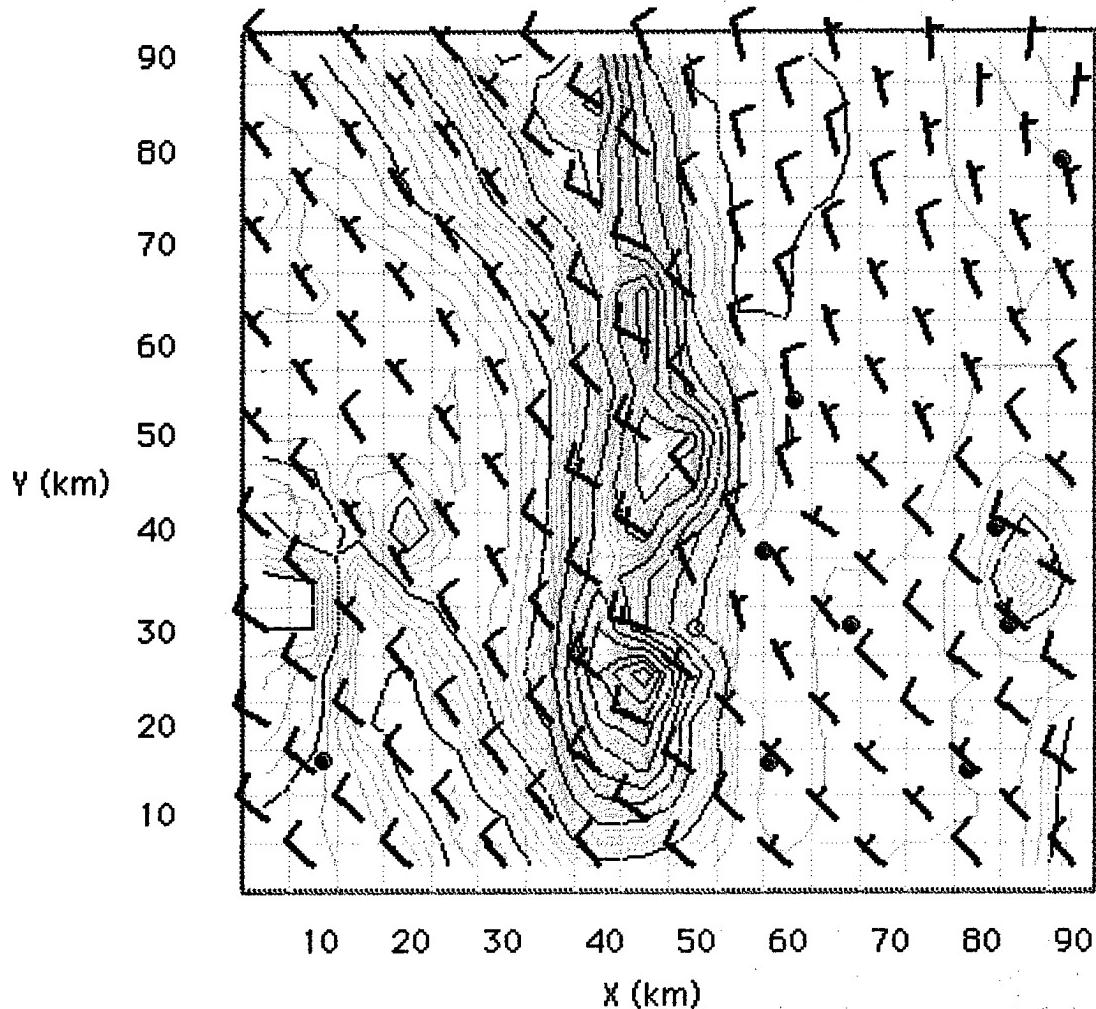
Fig. 4b. Surface wind forecast for 1130, 23 Nov. 1974, using a time series extrapolation from a cut off time 1050 and imposing mass-continuity through the NUATMOS model. Terrain contours are as labeled in Fig.1.

4. CONCLUSIONS

We have proposed a simple forecasting scheme that is robust enough to use sparse data gathered in battlefield conditions. A simple linear, least squares fit of time series data at any location is used to forecast weather conditions at each observational site for short periods by extrapolating observed trends at each site. From these independent, discrete-point forecasts, forecasts are spatially extended by applying either an objective analysis scheme such as analytic approximation or a variational scheme that minimally adjusts the kinematic field, subject to the constraint of mass continuity. Effects of complex terrain are introduced into the flow through no flow-through conditions at solid boundaries. To do this, we have developed a number of modules,
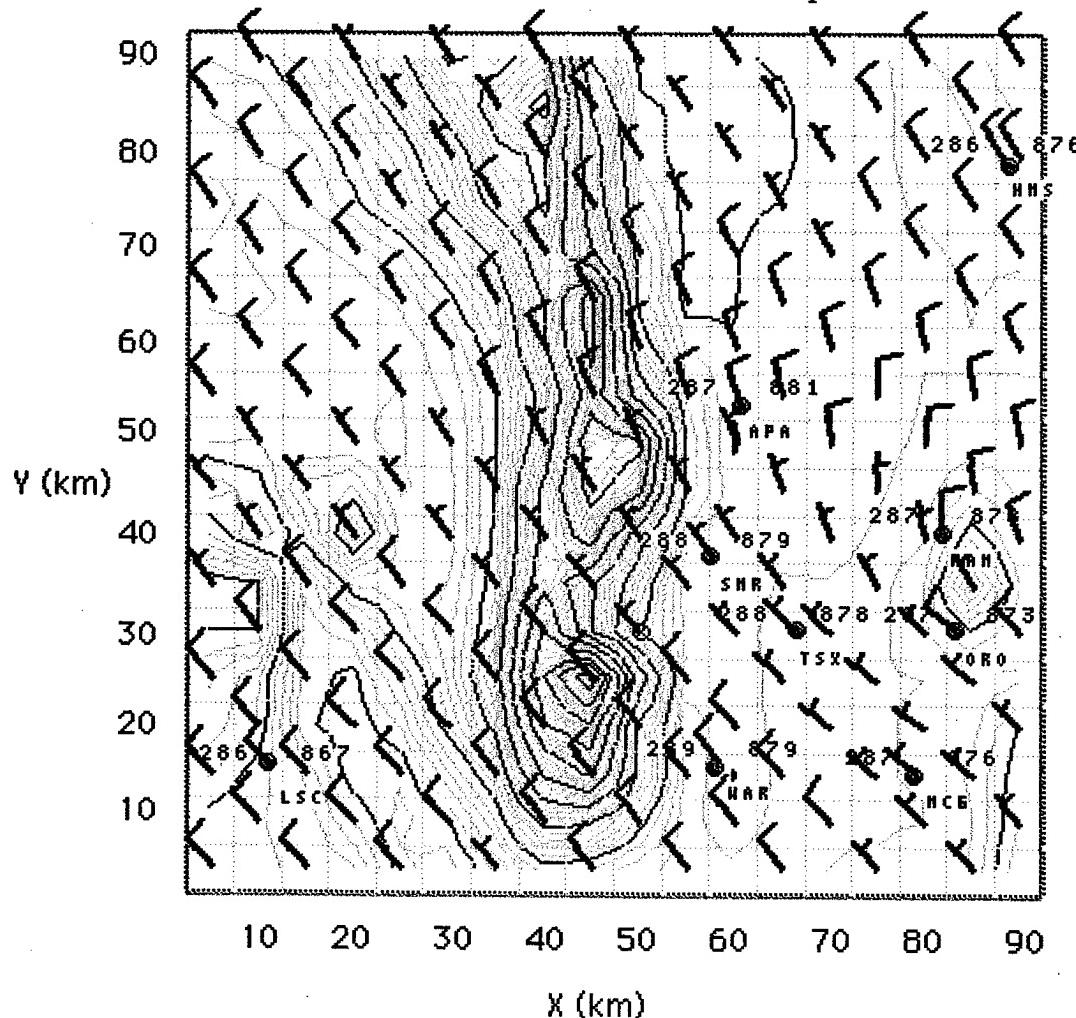
Fig. 5a. Surface winds analyzed without constraints for 1130, 23 Nov. 1974, using Analytic Approximation. Black dots indicate the positions of observing sites. Terrain contours are as labeled in Fig.1.

that used in various combinations, generate automated meteorological (met) messages for artillery, and have tested them using data from the PASS and Tamde projects.

To a limited extent, poor coverage of the domain by observations can be offset by using a mass continuity constraint and a gridded representation of the terrain. In battlefield conditions, the number of observations is likely to be very few (about 3 or less), in which case mass continuity as a constraint on the flow, can add detail.

316

However, should there be a sufficient number of observations, the application of mass continuity could result in loss of detail where more data are available.
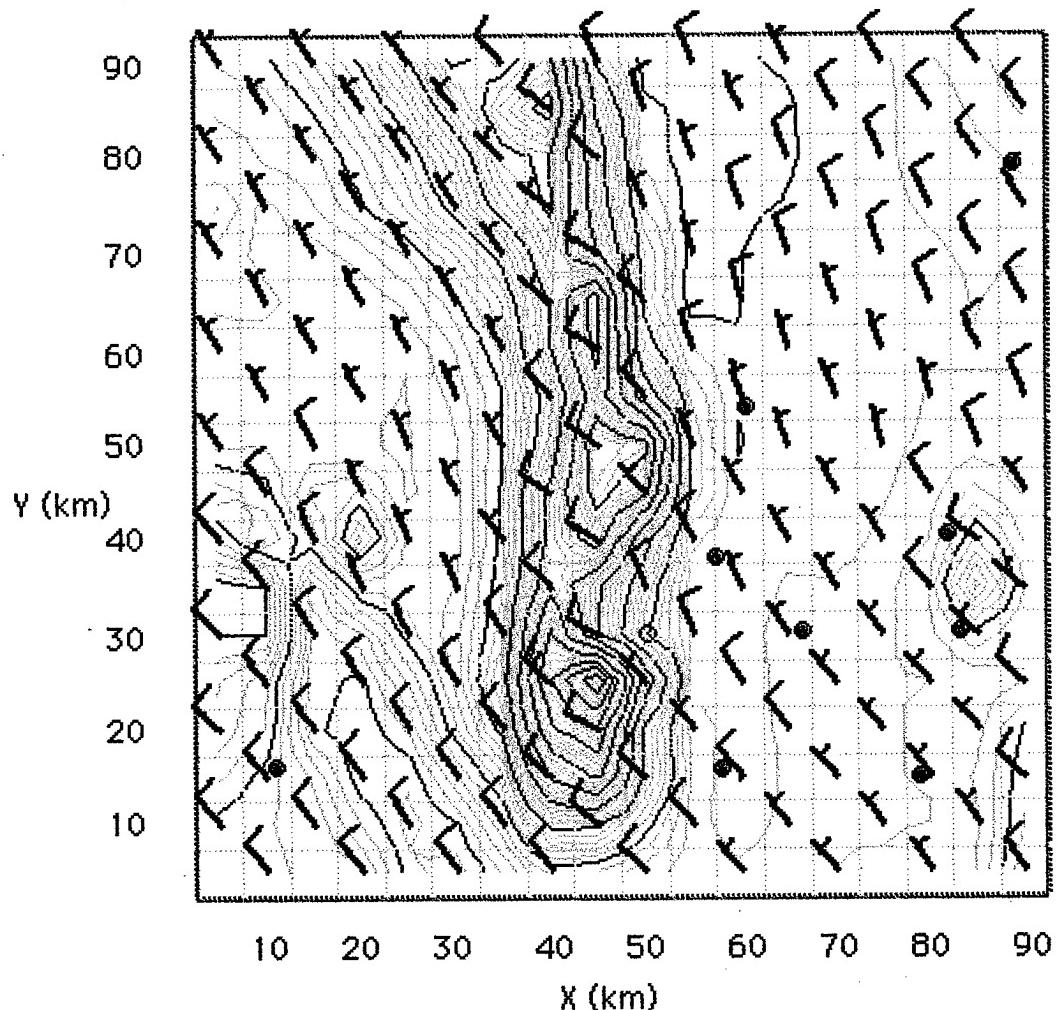
Fi.g 5b. *Same as in Fig. 5a caption , except having mass continuity constraint.*

References

Blanco, A. J., 1988: Methodology for estimating wind variability, ASL-TR-0225, US Army Atmospheric Sciences Lab, WSMR.

Blanco, A. J., and L.E. Traylor, 1976: Artillery meteorological analysis of Project Pass. ECOM-5804, U.S. Army Atmospheric Sciences Laboratory, White Sands Missile Range, NM 88002-5501.

Caracena, F., 1992: The use of Analytic Approximations in providing meteorological data for artillery. Preprints, Battlefield Atmospheric Conference. Ft. Bliss, TX.

Caracena, F., 1987: Analytic approximation of discrete field samples with weighted sums and the gridless computation of field derivatives. J. Atmos. Sci.,44, 3753-   3768.

Mc Ginley, J., 1973: Environmental energy fields associated with severe storms. Master's Thesis. University of Oklahoma.

O'brien, J. J., 1970: Alternative solutions to the classical vertical velocity problem. J. Appl. Metor., 9, 197-203.

Ross, D. G., I. N. Smith, P. C. Manins, and D. G. Fox, 1988: Diagnostic wind field modeling for complex terrain: model development and testing. J. Applied Meteor. 27, 785-796.
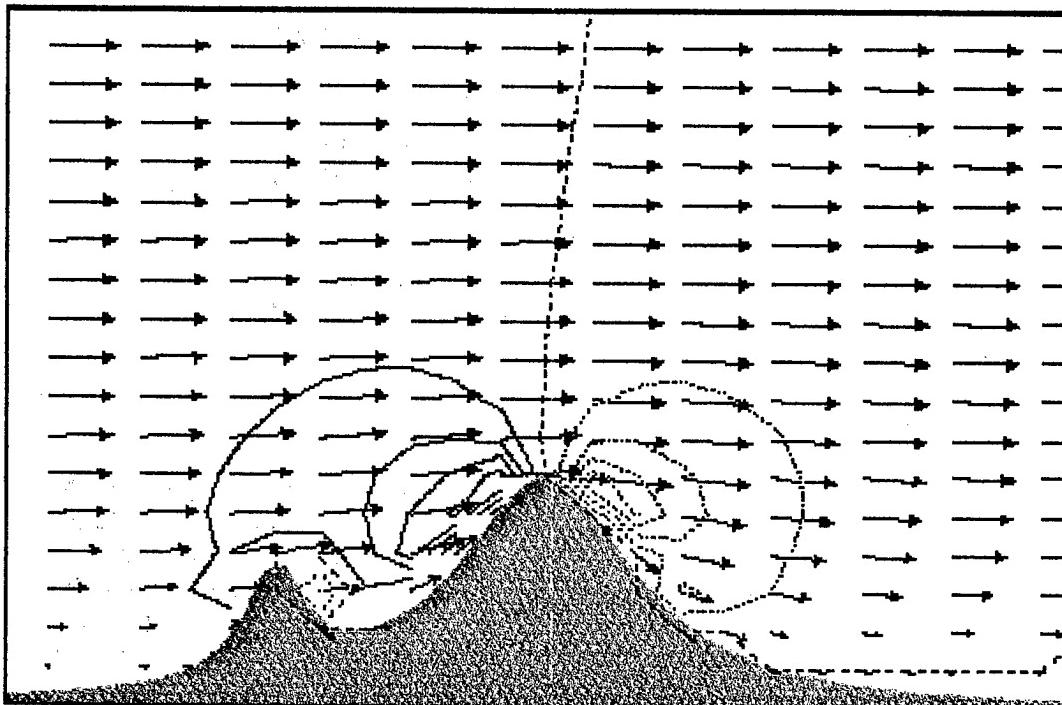
Fig. 6. Flow over complex terrain in 2 dimensions, simulated by imposing only the no-flow-through boundary conditions in Laplace's equation, and otherwise horizontally uniform flow. This solution has the effect of adjusting the winds so that the normal component of wind vanishes at the terrain interface. Contours are for the vertical component of the wind (solid, for upward, and dotted for downward)

Sasaki, Y., 1958: An objective analysis based on the variational method. J. Meteor. Soc. Japan, 36, 77-88.

Sherman, C. A., 1978: A mass-consistent model for wind fields over complex terrain. J. Applied Meteor. 17, 312-319.

MEASURING/ANALYZING CROSSWINDS ALONG A HIGH-ENERGY LASER BEAM PATH

Gail Tirrell Vaucher
Science and Technology Corporation
White Sands Missile Range, New Mexico 88002

Robert W. Endlich
U.S. Army Atmospheric Research Laboratory
White Sands Missile Range, New Mexico 88002

Alan Rishel
Science and Technology Corporation
White Sands Missile Range, New Mexico 88002

ABSTRACT

One of three critical meteorological elements sampled along a free-atmosphere high-energy laser beam path is the crosswind. In 1992-93, at the High-Energy Laser Systems Test Facility (HELSTF), a network of 14 UVW anemometers was installed to characterize the crosswinds along a 1-km beam path. This article describes the anemometer network in terms of sensors, sensor spacing, sampling rate, data acquisition, processing, and real-time display. A statistical summary of the 14 anemometer crosswind measurements is presented, along with recommendations for the real-time application of the crosswind network.

1. INTRODUCTION

One of the critical meteorological measurements affecting high-energy laser (HEL) propagation is cross-beam ventilation. When crosswinds along a laser path are insufficient, the result can be nonlinear propagation, such as thermal blooming. Historically, the High-Energy Laser Systems Test Facility (HELSTF) meteorology laboratory has used measurements from an array of temperature and wind sensors mounted on three fixed towers located a few hundred meters to the west of the HEL beam path. These towers are spaced 500 m apart, and are referred to as the 0-, 0.5-, and 1-km towers (see Fig. 1). The crosswind measurements are derived from the tower's three-component (UVW) Gill polypropylene anemometers mounted at 2, 4, 8, and 16 m above ground level (AGL). The 0- and 1-km towers have additional wind sensors at 32 m AGL. Data from the three towers are sampled every 10 s. In the past, the posttest crosswind measurement was centered on the lase "time-0" and averaged over the time it takes the wind to travel 500 m, the distance between the sensors.

In addition to the tower data, a more direct measure of the crosswind has been taken from "near" and "far" single-propeller Gill polypropylene anemometers mounted at the one-third and two-thirds points of the beam path, at 8 m AGL (see Fig. 1). These individual instruments are oriented such that only the horizontal wind component perpendicular to the beam is sampled. Their readings are displayed on an analog meter and recorded on an analog chart.
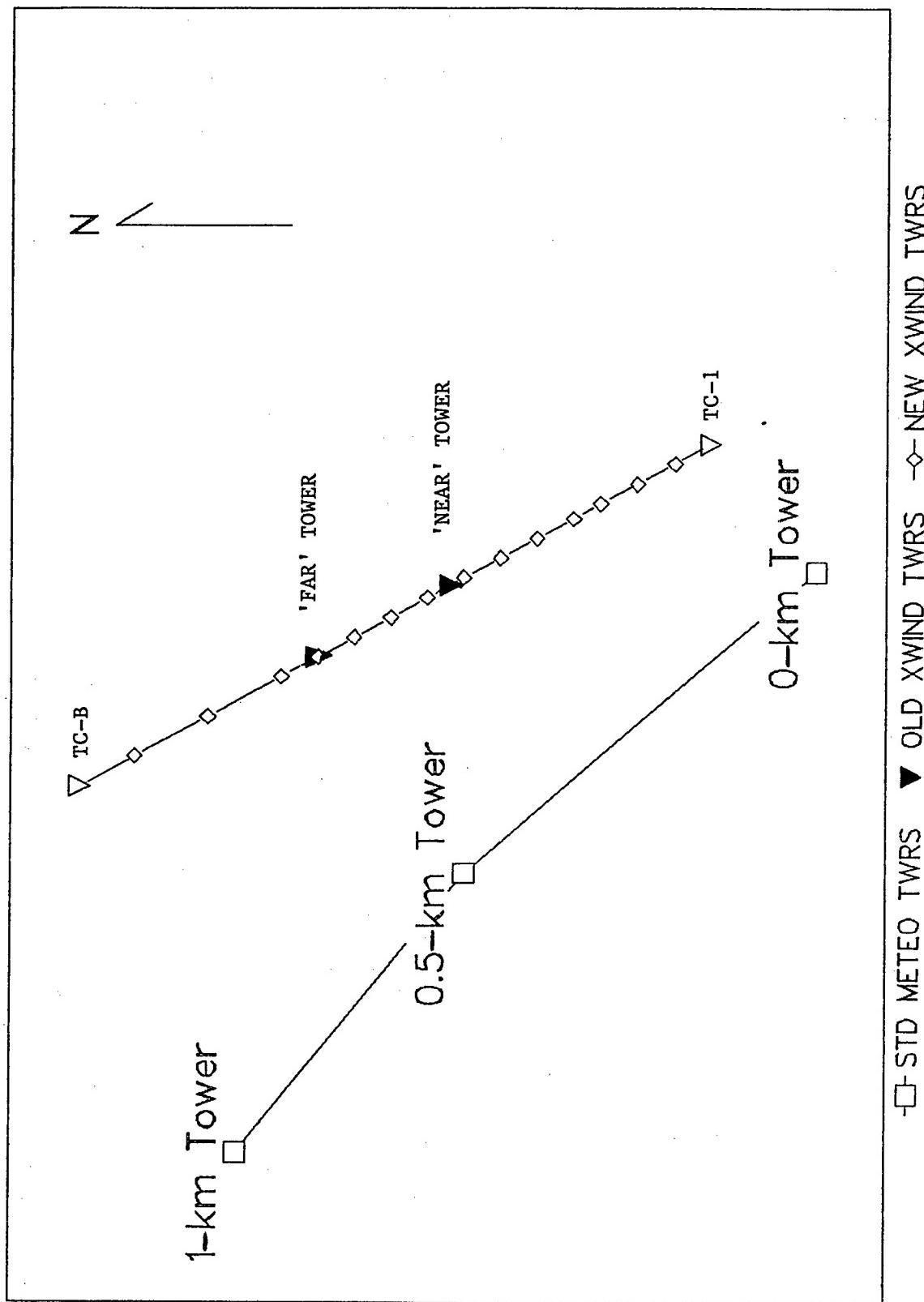
Figure 1. Old and new crosswind towers (HELSTF, NM). Test Cell-1 (TC-1), Test Cell-B (TC-B) indicate the beam path endpoints.

Average crosswinds measured by the anemometers mounted on the 0-, 0.5-, and 1-km towers have differed significantly among themselves as well as differing from the "near" and "far" crosswind measurements. In fact, the "near" and "far" crosswind anemometers themselves have also differed significantly, sometimes having opposite signs. Even when the averaging time was extended to several minutes, the ability of the results to represent crosswinds at all points along the beam path has been a subject for debate (Freeman, 1991). Our proposed solution was to create a network of crosswind measurements giving better spatial and temporal resolution of the winds along the beam path.

In this paper, we describe details of this new crosswind subsystem, including the crosswind sensor, data acquisition, data processing, and user's screen display. We then highlight some of the crosswind characteristics observed from a 24-hr case study conducted in September 1993. Finally, we offer recommendations for improving the crosswind subsystem, as well as for the implementation of this network into high-energy laser missions.

2. CROSSWIND ANEMOMETER NETWORK

In 1992, a network of 14 UVW polypropylene anemometers was installed along the beam path and a graphical, near-real-time display summarizing the measurements was put into operation. The key characteristics of this "new" array of instruments was that (1) the anemometers were placed as close to the beam path as was deemed safe, (2) the density of sensors was increased by a factor of almost three, and (3) the sampling rate was increased from one sample every 10 s to two samples per second. The following sections describe both the hardware and software utilized in this array of sensors.

2.1 CROSSWIND SENSOR

The primary sensor used to measure crosswind is the Model 27106 R. M. Young Gill anemometer. The complete instrument consists of three independent helicoid propeller sensors mounted orthogonally on a common mast. Each sensor provides a direct wind speed measure of the east-west component, U; the north-south component, V; and the vertical component, W. In a previous study (Vaucher and Endlich, 1991), it was found that the starting threshold for this type of polypropylene anemometer was around 0.4 m s^{-1}; the stopping threshold was approximately 0.1 m s^{-1}. Under typical mission conditions, crosswind velocities range between 1 and 2 m s^{-1}.

The linear placement of the 14 UVW anemometers is displayed in Fig. 1. On average, the horizontal separation between the first 12 instruments is 50 m. The remaining sensors have a 100-m horizontal spacing, with 75 m separating the last sensor and the beam path endpoint. All 14 anemometers are mounted on triangular towers positioned approximately 2 m west of the beam path. Though the path's terrain has small irregularities, each instrument is installed at the beam path height, about 8 m AGL.

2.2 CROSSWIND DATA ACQUISITION AND PROCESSING

The voltage signals generated by the anemometer propeller/generator are fed through a series of cables to a multiplexer and A/D board commanded by an Advantech 1610 Industrial 486 PC. The 486 software collates the measurements from the 14 towers and transmits these data through an INMAC 19.2-Kbaud line driver/RS-232 cable to a DEC microVAX II at a 2-Hz rate.

Once the data are in the microVAX II, three FORTRAN 77 programs process them. First, the program INGEST retrieves the data from the RS-232 data line and stores them in a real-time common that holds

5 s of current data. Then the program WRITE_DATABASE reads the data from this buffer and writes them to a disk file. A third program, DISPLAY_WINDS, retrieves the data from the disk file, processes the measurements, and displays the crosswind results on the user's monitor (see Section 2.3).

Before the crosswind magnitudes are calculated, corrections are applied to each of the UVW component values for the propellers' noncosine response to off-axis wind (W. Hatch, U.S. Army Atmospheric Research Laboratory, personal communication). The actual calculation of the perpendicular wind component across the beam path, the crosswind, is then geometrically derived from the corrected UVW Gill anemometer vector components and the beam path azimuth.

A screen display of the processed data is updated every 5 s. The program uses a default average of 20 s of data (40 samples) for its crosswind calculations. This average represents all the data acquired from 10 to 30 s prior to the current time. Thus, the processing of data provides the user with near-real-time bucket averages of the crosswinds along the beam path. Additional details on the crosswind screen display are given in the next section.

The final crosswind measurement display is sent via a VT241 terminal system box's RS-170 composite video output to a CCTV network for the customers to view. In the HELSTF meteorology laboratory, the data display is available on either a DEC VR299 workstation or a DEC VT241. Since the software is device independent, the results can be displayed on several types of graphics screens.

2.3 CROSSWIND SCREEN DISPLAY

When the user first logs into the crosswind account, the screen displays the current status of the ingest and databasing programs, as well as a list of eight options, as shown in Fig. 2. The user initiates the ingest process, then turns on databasing. Finally, after the user has selected the desired crosswind display, the software requests a crosswind threshold value. This interactive menu is automatically replaced by the crosswind display that remains on screen and is actively updated at 5-s intervals until the user indicates otherwise. If the user perceives the need to delete a tower's input from the analysis and display or wishes to generate a real-time tabular printout of data, these real-time options are available.

An example of the processed crosswind measurements, as displayed on the DEC VR299, is shown in Fig. 3. The path endpoints are labelled "TC-1" and "TC-B;" a thin solid center line represents the beam path. Two dashed lines bracket this center path, indicating the user-selected crosswind threshold in meters per second. The near-real-time display places the sample's date and end time, in Mountain Standard Time, in the upper left corner of the screen. (After the data are processed, the date and time appear in the header, as in Fig. 3.) The software centers the x-axis scaling on 0 m s^{-1}. The 14 measurements are graphically displayed as independent horizontal bars stemming from the x axis' zero point. The placement of each bar along the center line is proportional to its tower position along the beam path. Bars indicating winds from the western side of the beam path start at the center line and extend to the right. Bars for winds from the eastern side are drawn to the left of the center line. The length of each bar is proportional to the crosswind magnitude. Three bar colors are utilized, red for measurements ≤ 50% of the threshold, yellow for measurements between 50 and 150% of the threshold, and green for magnitudes ≥ 150% of the threshold. As an option, a triangle can be superimposed on the bar when there are vertical winds greater than 0.1 m s^{-1}. The placement of this triangle along the bar indicates the relative magnitude of the vertical component with respect to the total crosswind and its associated direction. Finally, an average of all 14 crosswind values displayed (using absolute values only) is calculated and printed just below the x axis.

```
                        Cross Winds
                High Energy Laser Network

            Ingest of winds data is currently:   OFF

            Databasing of winds data is currently:   OFF
----------------------------------------------------------------------
Please type in your choice and press <return>:

 A - Set the port to ingest the winds data
 B - Turn on winds databasing
 D - Display 20-second averages of cross winds
 W - Display cross_winds and vertical winds (VR299 terminal only!)
 C - Change a tower's display and averaging status
 T - Tabular display of wind data
 S - Stop ingest of winds data
 E - Exit from this menu




Your choice?
```

Figure 2. Crosswind user's menu.
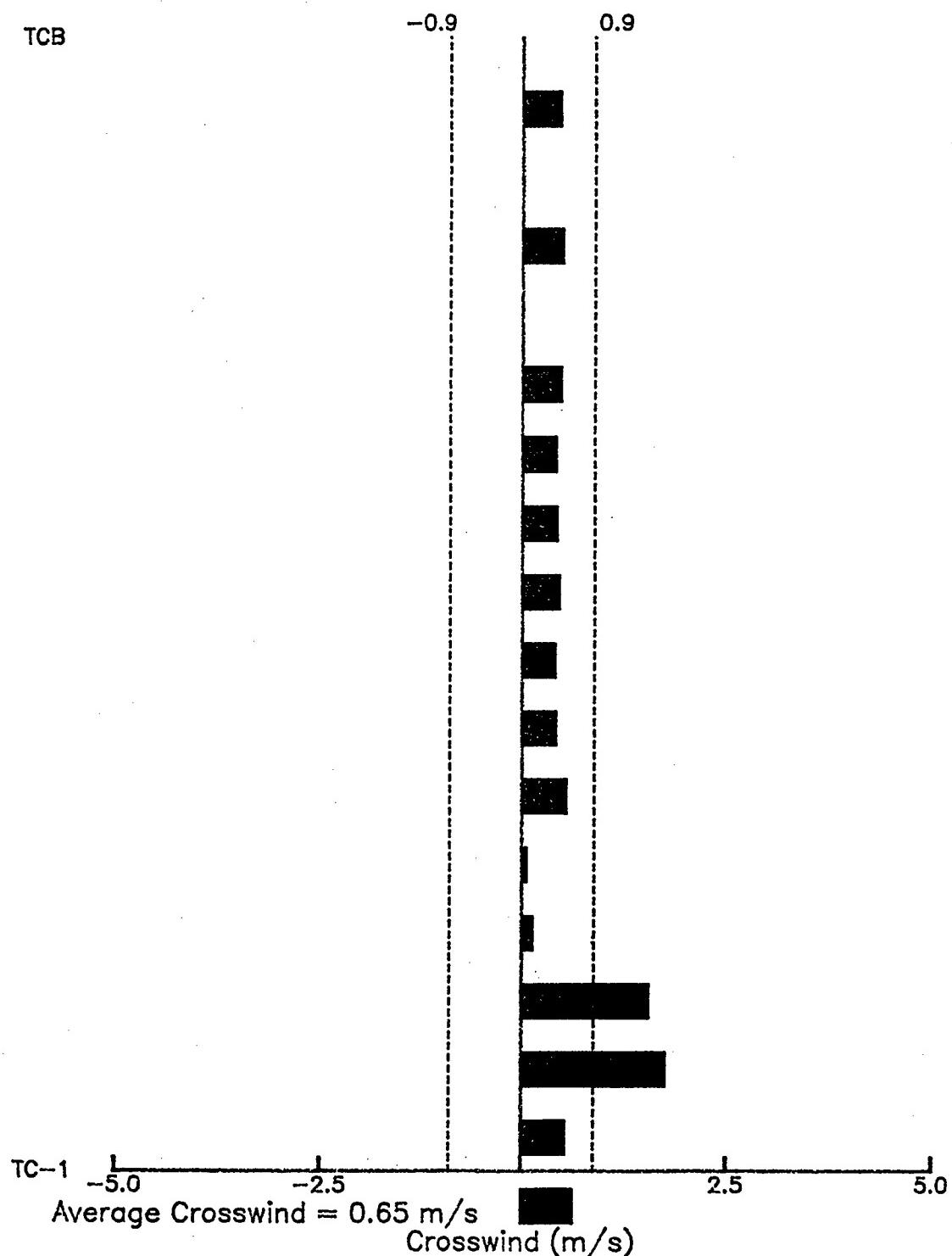
Figure 3. Crosswind data display.

3. CROSSWIND DATA ANALYSIS

The goal of this crosswind analysis was to characterize the crosswinds, using the crosswind subsystem measurements, along the given beam path. Samples were collected from all 14 towers over one representative 24-hr period. The following statistics and discussion are based on the 22 September 1993 case study selected for this project.

3.1 STATISTICS

The statistics used in this study are based solely upon the absolute values of the crosswinds. Hourly averages of the samples taken from the 14 crosswind towers are presented in Table 1. The abundance of numbers found in Table 1 is summarized in Fig. 4 by graphically displaying a subset of these magnitudes, namely those from towers 2 through 5. The data from the remaining 10 towers were far less dynamic than the selected subset; therefore, the hourly averages of these 10 towers were consolidated (averaged) into a single representative array and plotted as a solid line without data markers.

The general compilation found in Table 1 was expanded into individual tables consisting of hourly averages, standard deviations, and maximum and minimum crosswind values, as calculated per tower. Three representative hourly samples from this one-day case study are presented in Tables 2 through 4. These samples are from the two optical turbulence neutral events (sunrise and sunset), and the period of maximum insolation.

3.2 DISCUSSION

The synoptic weather conditions on 22 September 1993 consisted of a warm air mass moving in from the south and subsidence from the existing ridge. This stable atmosphere kept temperatures well above normal. Moisture slowly increased throughout the day. The precipitable water for the southern Tularosa Basin was just over an inch, but no showers or thunderstorms occurred over HELSTF. The Basin's afternoon and evening skies were partly cloudy, with southeasterly winds at less than 7 m s^{-1}.

The hourly averaged crosswinds of 22 September, as shown in Table 1 and Fig. 4, were consistently less than 2 m s^{-1}. The range of individual crosswind magnitudes (independent of direction), however, was from 0 to 3.7 m s^{-1} (Tables 2 through 4). Collating the hourly crosswind summaries shown in the tables with the local weather conditions, additional crosswind characteristics along the beam path come into focus.

First, there is the significant consistency (75% of the 24-hr period) with which the greatest crosswind occurs at the second and third towers. Next, consider the diurnal cycle. Starting with the predawn hours, towers 4 and 5 generated the greatest crosswind magnitudes. Surface winds during the day's first 6 hr were less than 3 m s^{-1} and were from the southeast, east, and northeast. The 8-m level winds were 5 m s^{-1} and less, with wind directions the same as the surface winds. It is important to note that there is a substantial building complex just south and southeast of the beam path. Also noteworthy, as the winds took on an easterly, northeasterly direction (0300-0400 MST), the crosswind averages showed that towers 11, 12, 13, and 14 had equivalent crosswind maximum magnitudes to those of towers 4 and 5.

TABLE 1. 22 SEPTEMBER 1993 CROSSWIND TOWER AVERAGES BY HOUR[*]

HOUR MST	CROSSWIND TOWER													
	1	2	3	4	5	6	7	8	9	10	11	12	13	14
0-1	0.3	0.5	0.6	0.5	0.6	0.2	0.2	0.3	0.3	0.3	0.3	0.3	0.3	0.3
1-2	0.3	0.3	0.5	0.5	0.6	0.2	0.1	0.3	0.2	0.2	0.2	0.2	0.2	0.3
2-3	0.3	0.2	0.2	0.6	0.7	0.3	0.3	0.4	0.4	0.4	0.5	0.5	0.5	0.5
3-4	0.3	0.1	0.2	0.6	0.7	0.3	0.3	0.5	0.5	0.5	0.6	0.6	0.7	0.6
4-5	0.3	0.3	0.4	0.7	0.8	0.2	0.2	0.4	0.3	0.3	0.4	0.3	0.3	0.4
5-6	0.2	0.0	0.1	0.6	0.7	0.3	0.3	0.5	0.5	0.5	0.5	0.5	0.5	0.6
6-7	0.1	0.4	0.4	0.3	0.4	0.2	0.2	0.3	0.2	0.2	0.2	0.2	0.3	0.2
7-8	0.2	0.7	0.6	0.3	0.4	0.2	0.2	0.2	0.2	0.2	0.2	0.2	0.2	0.2
8-9	0.4	1.5	1.4	0.3	0.4	0.4	0.3	0.4	0.4	0.3	0.4	0.4	0.4	0.4
9-10	0.5	1.6	1.4	0.4	0.4	0.5	0.4	0.5	0.5	0.5	0.5	0.6	0.6	0.6
10-11	0.6	1.7	1.5	0.6	0.6	0.7	0.6	0.7	0.7	0.7	0.7	0.8	0.8	0.7
11-12	0.6	1.8	1.6	0.5	0.5	0.6	0.5	0.5	0.6	0.6	0.6	0.6	0.6	0.6
12-13	0.6	1.8	1.6	0.5	0.5	0.6	0.6	0.6	0.6	0.6	0.6	0.7	0.6	0.6
13-14	0.6	1.7	1.5	0.5	0.5	0.6	0.6	0.6	0.6	0.6	0.6	0.7	0.7	0.7
14-15	0.6	1.9	1.7	0.6	0.6	0.7	0.6	0.6	0.7	0.6	0.6	0.7	0.7	0.7
15-16	0.6	1.7	1.5	0.5	0.5	0.6	0.5	0.5	0.6	0.6	0.6	0.6	0.6	0.6
16-17	0.6	1.7	1.5	0.4	0.4	0.7	0.5	0.6	0.6	0.6	0.6	0.7	0.6	0.6
17-18	0.3	1.3	1.2	0.2	0.2	0.5	0.4	0.4	0.4	0.4	0.4	0.5	0.5	0.4
18-19	0.1	0.4	0.4	0.2	0.2	0.2	0.1	0.2	0.2	0.2	0.2	0.2	0.1	0.2
19-20	0.1	0.1	0.1	0.3	0.3	0.1	0.1	0.1	0.1	0.1	0.1	0.1	0.0	0.2
20-21	0.2	0.8	0.7	0.2	0.2	0.4	0.2	0.3	0.3	0.3	0.3	0.3	0.3	0.3
21-22	0.4	1.3	1.0	0.2	0.2	0.4	0.3	0.4	0.3	0.3	0.3	0.4	0.4	0.4
22-23	0.5	1.5	1.3	0.4	0.4	0.7	0.5	0.5	0.5	0.5	0.5	0.6	0.6	0.6
23-24	0.2	0.7	0.6	0.1	0.2	0.2	0.1	0.2	0.1	0.1	0.1	0.1	0.2	0.1

[*]All values in m s⁻¹; highlighted values are the two highest crosswind averages for the given hour.
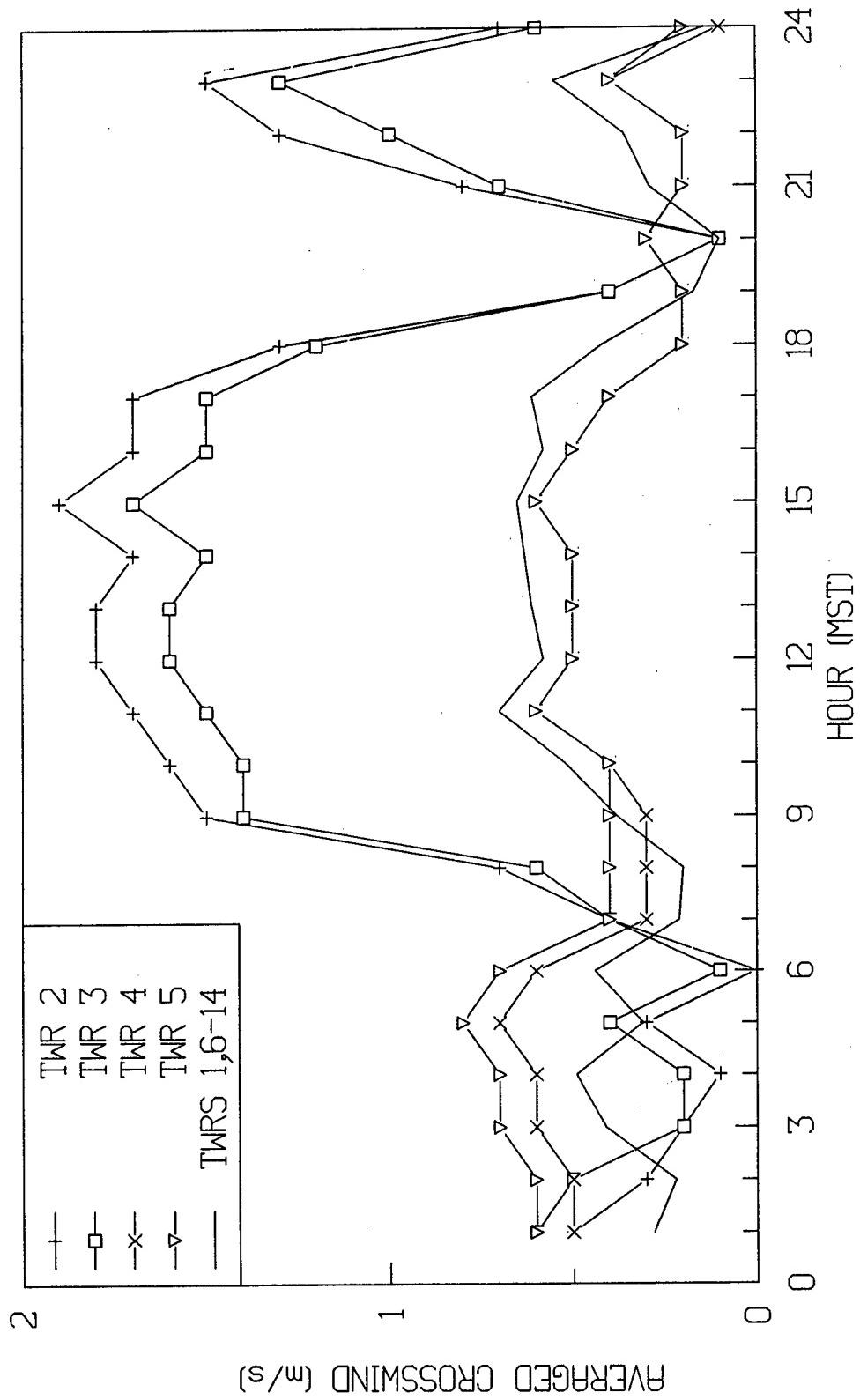
Figure 4. Hourly crosswind averages for 22 September 1993. Crosswind data from towers 2 through 5 show a dynamic diurnal variation. The remaining less variable 10 towers of averages were consolidated into single hourly averages and plotted as a solid line with no markers.

TABLE 2. STATISTICAL SUMMARY OF ABSOLUTE CROSSWIND MAGNITUDES DURING THE SUNRISE NEUTRAL EVENT*

22 September 93, 0600-0700 MST

TOWER	AVERAGE	STD DEV	MAX	MIN	# OBS
1	0.1	0.11	0.6	0.0	7200
2	0.4	0.42	1.7	0.0	7200
3	0.4	0.34	1.5	0.0	7200
4	0.3	0.29	1.3	0.0	7200
5	0.4	0.33	1.5	0.0	7200
6	0.2	0.12	0.6	0.0	7200
7	0.2	0.09	0.5	0.0	7200
8	0.3	0.16	0.7	0.0	7200
9	0.2	0.15	0.7	0.0	7200
10	0.2	0.16	0.8	0.0	7200
11	0.2	0.18	0.8	0.0	7200
12	0.2	0.18	0.7	0.0	7200
13	0.3	0.16	0.7	0.0	7200
14	0.2	0.18	0.9	0.0	7200

*All values in m s^{-1}; highlighted values indicate the towers with the two highest crosswind averages.

TABLE 3. STATISTICAL SUMMARY OF ABSOLUTE CROSSWIND MAGNITUDES DURING MAXIMUM INSOLATION*

22 September 93, 1100-1200 MST

TOWER	AVERAGE	STD DEV	MAX	MIN	# OBS
1	0.6	0.35	2.1	0.0	7076
2	1.8	0.57	3.6	0.1	7076
3	1.6	0.53	3.7	0.0	7076
4	0.5	0.34	1.8	0.0	7076
5	0.5	0.36	1.9	0.0	7076
6	0.6	0.34	1.8	0.0	7076
7	0.5	0.31	1.6	0.0	7076
8	0.5	0.35	1.9	0.0	7076
9	0.6	0.38	2.2	0.0	7076
10	0.6	0.37	2.0	0.0	7076
11	0.6	0.37	1.8	0.0	7076
12	0.6	0.39	2.0	0.0	7076
13	0.6	0.36	1.9	0.0	7076
14	0.6	0.34	1.9	0.0	7076

*All values in m s^{-1}; highlighted values are the towers with the two highest crosswind averages.

TABLE 4. STATISTICAL SUMMARY OF ABSOLUTE CROSSWIND MAGNITUDES DURING THE SUNSET NEUTRAL EVENT*

22 September 93, 1700-1800 MST

TOWER	AVERAGE	STD DEV	MAX	MIN	# OBS
1	0.3	0.19	1.4	0.0	7200
2	1.3	0.41	2.6	0.4	7200
3	1.2	0.40	2.5	0.3	7200
4	0.2	0.17	1.0	0.0	7200
5	0.2	0.18	1.1	0.0	7200
6	0.5	0.19	1.2	0.0	7200
7	0.4	0.17	1.2	0.0	7200
8	0.4	0.17	1.2	0.0	7200
9	0.4	0.19	1.5	0.0	7200
10	0.4	0.19	1.2	0.0	7200
11	0.4	0.22	1.4	0.0	7200
12	0.5	0.23	1.5	0.0	7200
13	0.5	0.18	1.3	0.0	7200
14	0.4	0.22	1.5	0.0	7200

*All values in m s^{-1}; highlighted values are the towers with the two highest crosswind averages.

The morning transitional hour (0600-0700 MST) extended the source of the maximum crosswind averages (towers 4 and 5) to towers 2, 3, 8, and 13. Since the magnitude differentials are so small during this hour, it is difficult to interpret the data. Focusing on the overall trend, however (see Fig. 4), one notes that the maximum crosswind averages appear to indicate a transition from towers 4 and 5 to towers 2 and 3. Surface winds over this period were again light, but this time from the south-southeast. The 8-m winds were 5 m s^{-1} and less, and were also from the south-southeast.

The daylight surface winds were around 4 m s^{-1} and from the south-southeast. The south-southeasterly 8-m winds were just as persistent at approximately 5.5 m s^{-1}. Examining the hourly averaged crosswinds for the 0700-1800 MST daylight hours, all 11 hr of data show the maximum crosswind peaking at the second and third towers. Insolation for this time period shows a typical Gaussian curve, with only two minor interruptions in the mid and late afternoon (probably passing clouds). The C_n^2 time series follows the typical bell-shaped curve, peaking around maximum insolation at about 1200 MST and dipping to minima over the sunrise/sunset time periods. All these results indicate that the strong consistency in crosswind magnitudes is reasonable in the light of the lack of external atmospheric forcing (frontal passages, thunderstorm development, etc.) over the beam path.

The evening transition (sunset) occurred around 1800 MST. As expected, the ambient winds decreased (to about 1 m s^{-1}). The general wind direction over the subsequent hour was southeast, tending towards east-southeast. The average crosswinds responded to this condition by briefly shifting the maxima from the daylight's favored second and third towers to towers 4 and 5. The differential between these average crosswind magnitudes, however, was very small.

329

After insolation had gone to zero again (nighttime), the earlier pattern of finding the greatest crosswind magnitudes at towers 2 and 3 returned. The surface winds were light over the remaining 4 hr. The 8-m winds stayed in the vicinity of 4 m s^{-1}. At both levels, the predominant wind direction was south-southeast.

4. CONCLUSIONS

Based on the placid atmospheric conditions of 22 September 93, representative of a typical diurnal atmospheric cycle with no external forcing, it is fair to say that the maximum crosswind magnitudes along the beam path are a function of wind direction, as moderated by local topography (e.g., building structures and knolls surrounding the path). Three examples of this observation were discussed in the previous section and are summarized below.

When the dominant wind was from the south-southeast, the average crosswind maxima were measured at towers 2 and 3. Under these conditions, the beam path's air flow had to pass over and/or around a multitude of buildings before traversing the path. This trek, no doubt, initiated eddies in the air stream. In terms of the crosswind, the statistical averages and standard deviations imply that these eddies created an influx of crosswind between towers 2 and 3. As an interesting sidelight to this finding, two meteorologists working independent of this study walked the beam path during the 22 September daylight hours. Their specific interest was to determine whether towers 2 and 3 were generating valid data. They not only confirmed the enhanced crosswind around these towers, but they also identified the source of airflow as being a Venturi effect through the open space between the TC-1 and the vacuum chamber buildings (W. Klein, Science and Technology Corp.; R. Endlich, U.S. Army Research Laboratory, personal communication).

When winds gained a more easterly component, towers 4 and 5 mapped the "eddy-enhanced" flow along the beam path. The circulation was presumed to be an eddy due to the 50% (often greater) decrease in average crosswind magnitudes reported by the neighboring towers.

Finally, when the winds shifted to northeasterly, towers 4 and 5 averaged the greatest crosswinds, as did towers 11 through 14. There is a significant knoll to the northeast of the path's far end, as well as some buildings and miscellaneous obstacles north of the path. Therefore, one is led to believe that the strengthened crosswinds of towers 11 through 14 may have been generated by airflow cresting and circumnavigating the local terrain and building complexes. The increase in crosswind magnitude values from towers 11 through 14 would again be a signature of eddies in the airflow.

5. RECOMMENDATIONS

As of this writing, the 14-tower crosswind array has been running for approximately one year. While the start-up bugs have been identified and resolved, there is still room for improvement. The following recommendations are made based on this study:

1. To enhance data quality, a computer algorithm implementing the anemometer calibration slippage correction needs to be developed and installed in the software. Complementing this effort, an anemometer threshold cutoff correction also needs to be incorporated.

2. Three suggestions aimed at assisting the HELSTF meteorologist, and ultimately the HELSTF customers, are the following:

(a) Since the crosswind magnitudes depend heavily on wind direction, a wind barb indicating the ambient wind speed and direction should be derived from the UVW components and added to the user's display. As of this writing, such a feature was being developed and introduced into the user's display.

(b) This study examined signatures from gentle and light winds originating from the eastern quadrants. It is recommended that this analysis be continued, focusing on the eddy air flow as generated under gentle and light winds from the western sectors.

(c) As a second iteration to the above analysis, it is recommended that the crosswind statistics incorporate the positive/negative crosswind directions. This information would not only further characterize the beam path airflow, but would also help isolate the path's major wind-influencing structures, the eddy generators.

3. An algorithm needs to be developed in which the array of crosswind averages is used as input to equations modeling the nonlinear effects generated by insufficient beam ventilation, such as thermal blooming. This is, after all, the ultimate goal of the 14-anemometer crosswind network.

REFERENCES

Freeman, K.P. (Ed.), 1991: *Workshop on Improving Atmospheric Characterizations at the High-Energy Laser Systems Test Facility, White Sands Missile Range, 17-18 December 1991*. Science and Technology Corporation, Washington, D.C., Internal Report.

Vaucher, G. Tirrell., and R. Endlich, 1991: *Improving Atmospheric Characterizations at HELSTF: Wind Analysis, Phase I—Calibrating the R.M. Young Gill UVW Anemometers*. STC Technical Report 6217, Science and Technology Corporation, 101 Research Drive, Hampton, Virginia 23666.

ACKNOWLEDGEMENTS

VARIABILITY OF ATMOSPHERIC TURBIDITY AND THE REFRACTIVE INDEX STRUCTURE PARAMETER (C_n^2)

Frank D. Eaton, Scott A. McLaughlin, John R. Hines
US Army Research Laboratory,
AMSRL-BE-E, WSMR, NM 88002-5501

James J. Drexler, David B. Soules, and John Qualtrough
Lockheed Engineering & Sciences Company,
WSMR, NM 88002-5501

ABSTRACT

Turbidity fluctuations are presented as calculations of Linke's Turbidity Factor from direct beam solar radiation measurements taken with pyrheliometers. The optical device used in this study for measuring variability of optical turbulence is the Atmospheric Turbulence Measurement and Observation System (ATMOS) which measures angle-of-arrival fluctuations through two relatively small apertures. This optical arrangement utilizing a differential measurement technique eliminates system errors produced by tracking errors, vibration and wind loading.

Results shown include daytime thermal activity and wave activity detected from an FM-CW radar and a sodar as time-height "maps". Time series of the refractive index structure parameter, C_n^2, values measured from these two systems are also shown integrated over the ranges sensed and compared to time series of measurements taken with the ATMOS and pyrheliometer. Since the optically derived information is from ground-to-space, the results from the profilers explain the patterns of variability.

1. INTRODUCTION

Variability of atmospheric particulate matter and the refractive index structure parameter (C_n^2) and derived quantities are of considerable interest to many propagation and remote sensing efforts using optical, radio, and acoustic techniques. Fluctuating levels of particulate matter, quantified as turbidity, and turbulence are often suspected for producing intermittent performance of various systems such as " fading." Imagery often shows variations in quality with time when observations are made through long atmospheric paths. Ground-to-space changes in turbidity can be monitored by observing fluctuations in the direct beam solar radiation received at the surface. Since generally most aerosol material is contained in the mixing layer, knowledge of the conditions in the boundary layer are crucial in explaining the patterns and nature of turbidity.

Traditionally optical turbulent effects known as astronomical "seeing" have been examined for selection and evaluation of observatory sites. The formulation of the transverse coherence length (r_o) puts the classical "seeing" problem on a quantitative basis (Fried, 1966). A derived quantity of C_n^2, r_o is defined as:

$$r_o = [0.423k^2 \int_o^\infty C_n^2(Z)\, dZ]^{-3/5}$$

where:

$k = 2\pi/\lambda$ (λ is the wavelength of light), and
$z =$ distance along the path between source and receiver.

Although r_o is an integrated path value, high resolution changes in C_n^2 can be sensed at different altitudes using state-of-the-art clear air radars and acoustic sounders.

2. THEORETICAL BASIS OF THE MEASUREMENTS

Since different techniques are used to measure turbidity, r_o, and profiles of C_n^2, the theoretical basis for each of the different measurement techniques used is discussed separately.

2.1 Atmospheric Turbidity

The direct beam solar radiation incident on a given surface depends on the attenuation due to various atmospheric components such as water vapor and particulate matter which can be in forms including natural background aerosol, dust, haze, or smoke. Simple measurements of solar radiation intensity would be meaningful to obtain extinction values only if made at the same solar elevation angle and optical depth.

Extinction of solar radiation may be shown as:

$$I = \frac{1}{S} \int_o^\infty I_o e^{-A(\lambda)\, d\lambda}$$

where:

$I_o(\lambda) =$ the extraterrestrial solar radiation
$S =$ the radiation factor for mean solar distance
$e^{-A(\lambda)} =$ the transmission of the whole atmosphere
$I =$ the measured radiation intensity

$A(\lambda)$ is composed of three components:

$$A(\lambda) = A_R(\lambda) + A_D(\lambda) + A_W(\lambda)$$

where:

$A_R(\lambda) =$ the extinction in clear dry air due to Rayleigh scattering as product of the optical air mass and the extinction coefficient

$A_D(\lambda)$ = the product of the relative air mass and
haze extinction coefficient, and
$A_W(\lambda)$ = the product of the relative air mass and
the coefficient of selective absorption
by water vapor

Linke(1922,1929) defined the Turbidity Factor,T, as the number of pure, dry (Rayleigh) atmospheres that produce the same attenuation as that of a measured atmosphere by comparing the complex extinction coefficient (a_R) with the extinction to a Rayleigh atmosphere for all wavelengths as:

$$I = \frac{1}{S} I_o \exp\{-T \cdot a_R(m) \cdot m\}$$

This complex extinction coefficient varies with air mass due to the shifting of the optical center of gravity of radiation with m. Turbidity values are also adjusted for sea level so that intercomparisons at different sites can be made directly.

2.2 Transverse Coherence Length (r_o)

"Seeing" conditions have been incorporated for over 50 years using various experimental techniques such as sensing image spread and wander by photography or photoelectric devices (Whitford and Stebbins,1936;Couder,1936). Technology developments naturally have been incorporated into seeing monitors such as replacing film techniques with linear array CCD's to obtain the line spread function. Analysis of such information to obtain r_o from the modulation transfer function as well as the technique used in this study are documented in Eaton et al.(1988).

In this study a telescope equipped with two subapertures is used to sense the relative distance between the centroids of two stellar images. Image motion is produced by fluctuations of the phase front of the received light. The relationship used in this study to calculate r_o is:

$$r_o = \{\frac{27.5\ F^2}{k^2\ d^{1/3}\sigma_r^2}\ [1 - \frac{25}{36}\ (\frac{d}{\mu})^{1/3}]\}^{3/5}$$

where:
F = the focal length of the receiving telescope
d = the diameter of each subaperture
μ = center-to-center separation of the
subapertures, and
σ_r^2 = mean-square of the relative distance between the
centroids of the two images.

2.3 FM-CW Radar Derived C_n^2

Radar returns of the clear air for determining C_n^2 predominantly depend on reflections that are one-half the transmitted radar wavelength. Ottersten(1969) showed the relationship of backscatter, η, with C_n^2 for an isotropic inertial subrange as:

$$\eta \ (m^{-1}) = 0.38\lambda^{-1/3}C_n^2$$

where:

$\lambda =$ the radar transmitted wavelength.

Combining this relationship with the standard radar equation and incorporating the effect of two side-by-side antennas gives:

$$C_n^2 = 4.061 \frac{P_r R^2}{P_t R_G (\frac{D}{R})}$$

where:

$P_r =$ the received power
$P_t =$ the transmitted power
$R =$ the radar range

$R_G \ (\frac{D}{R}) =$ the antenna autocorrelation function

Due to the antenna configuration, below 100m the weighting function goes to zero. The antennas may be aligned differently to cover lower ranges, but an empirical calibration is necessary for data collected below 180m since this is the near field regime.

2.4 Sodar Derived C_n^2

Sodar (sonic detection and ranging) detects the temperature structure function (C_T^2) and ultimately provide C_n^2 through calculations using simultaneous sampled ambient temperature and pressure values. The sodar equation used is:

$$C_T^2 = \frac{P_r T_o^2 e^{2\bar{\alpha}R} L_e}{E_r[P_t \cdot E_t][(\frac{c\tau}{2})(\frac{A}{R^2} \cdot G)][0.0039k^{1/3}]}$$

where:

$T_o =$ surface temperature
$\alpha =$ molecular and classical adsorption
$E_r =$ receiver efficiency
$E_t =$ transmitter efficiency
$c =$ speed of sound
$\tau =$ pulse length
$A =$ antenna area
$G =$ antenna directivity
$L_e =$ excess attenuation coefficient

By accounting for the various terms in this relationship, the sodar is calibrated using a first principles approach.

3. INSTRUMENTATION

The instrumentation used in this study includes a Normal Incidence Pyrheliometer, an Atmospheric Turbulence Measurement and Observation System (ATMOS), an FM-CW Radar, and a sodar. Each type of instrumentation is discussed separately.

3.1 Normal Incidence Pyrheliometer

A pyrheliometer is an instrument for measuring "the intensity of direct solar radiation" (World Meteorological Organization, 1965). The pyrheliometer used in this study is a Normal Incidence Pyrheliometer made by Eppley Laboratory. A fast response wire-wound plated copper-constantan multijunction thermopile is used as the sensing unit joined to a 9mm-diameter receiver coated with Parson's optical black lacquer. The sensor is stabilized using a temperature-compensated circuit. A 1-mm thick quartz window seals the instrument and provides all-weather capability. A series of diaphragms within the tubular body limits the aperture to a circular cone of full angle 5° 41′ 30". The instrument was mounted in an equatorial mount driven by an electric motor for automatic tracking.

3.2 Atmospheric Turbulence and Observation System (ATMOS)

The ATMOS uses a differential angle-of-arrival approach by collecting light from a single star with two subapertures (11-cm diameter) on a 35.5cm (14 in) diameter telescope. The subapertures have optical glass wedges so that the two images can be separated and be focused onto a 2-D charged-coupled device (CCD) camera placed at the focal plane. Two nearly parallel paths of turbulence are measured at 23.5cm separation. The method eliminates common system errors caused by tracking errors, vibration, and wind loading since such effects will display identical image motion and not be included in the variance of centroid differences. The ATMOS includes a frame grabber that can vary exposure time and frame rates up to in excess of 300 fps. The CCD camera is intensified and uses an electronic shutter capable of 20 μsec exposure time.

3.3 FM-CW Radar

The FM-CW Radar used in this study was designed for studying the planetary boundary layer and cloud physics. It is an ultrasensitive system (-165dBm) which has a height resolution of 2m. The highly linear FM is generated with a frequency synthesized source instead of a YIG-tuned transistor oscillator as was used in previous generation systems. A low noise 200 MHz sweep over 50 ms as a "sawtooth" wave is centered at 2.9GHz. The system is also capable of sensing near the ground and has accurate calibration for C_n^2. The system consists of two trailers; one for the antennas, the other for the electronics.

3.4 Sodar

The sodar used is an Echosonde model three-axis system manufactured by Radian Corporation. The three antennas are 5 ft (1.5m) diameter. The sodar is typically operated at 1850 Hz and 86 W transmitted power using a 40 ms pulse length. Backscatter (for deriving C_T^2) is averaged every 30 sec in 200 range gates for obtaining C_n^2 from 18-275m AGL. Some researchers obtain C_T^2 values from sodar by comparing the backscattered values to those obtained by in situ measured values from tower sensors.Calibration of the sodar used in this study was accomplished by a first principles approach.

4. RESULTS AND DISCUSSION

4.1 Turbidity

Figure 1 shows calculations of Linke's Turbidity Factor, T , from 0700 to 1700 MST. The direct beam solar radiation was sampled at 10sec intervals and averaged for 1 min for the calculations. From 0700 to 0930 MST there is a general increase in turbidity but the pattern is relatively smooth.The late morning and afternoon show many rapid changes in turbidity. This enhanced activity agrees with times of strong convective activity as typically seen as "thermals" in sodar records. The early morning is a time of surface heating and developing thermal activity.

Figure 2 displays the 0700-0800 MST results. A slowly varying pattern is seen with little structure. In contrast, the pattern for 1500-1600 MST seen in Figure 3 shows considerable fluctuations, presumably due to thermal activity raising large quantities of particulate matter. The random nature of the peaks is predicted from the convective patterns.

4.2 ATMOS

A 24-hr plot of differential image motion variance measured on Oct 8,1991 with the ATMOS is shown in Figure 4. The 24-hr r_0 values calculated from these measurements are shown in Figure 5. The evidence of a weak morning "neutral"event at 0800 MST and a strong evening event near 1700 MST is displayed. The greatest variability and highest values of variance are from mid-morning to evening, while nighttime values show slowly varying patterns with less short-term fluctuations.

One-hour plots of the measured variances and calculated r_0 values are shown in Figures 6 and 7 for 1100 to 1200 MST.

The variances change from slightly below 1 to over 5 μrad^2. Figure 8 and 9 show similar parameters as for the previous two figures but for the neutral event period between 1650 and 1750 MST. The r_0 values are several times higher than found for midday conditions. Figures 10 and 11 show one hour variance measurements and r_0 values for nighttime conditions starting at 2000 MST. The r_0 pattern is wavy in nature and shows values between midday and the evening neutral event.

4.3 Sodar

Figure 12 shows typical sodar obtained results during midday with clear skies. Surface solar radiational heating produces pronounced convection or thermal activity. There is a random pattern of strong backscatter where a thermal is sensed and intermittent periods of low backscatter during atmospheric subsidence conditions. Figure 13 shows typical nighttime sodar results with several layers and wave patterns. Integrated path daytime and nighttime C_n^2 values are seen in Figures 14 and 15. The patterns shown agree with the ATMOS high speed measurements taken at the same times.

4.4 FM-CW Radar

Figure 16 shows a classical Kelvin-Helmholtz instability induced wave sensed with the FM-CW Radar on 3 April 1992. Time runs from left to right from 0845 to 0945 GMT. The C_n^2 values sensed within the wave are about 2 orders of magnitude higher than the background C_n^2. However, the integrated path values seen in Figure 17 show much less variability since the wave pattern is continuous.

5. SUMMARY AND CONCLUSIONS

Under moderate to strong surface convective conditions, both direct beam solar radiation and angle-of-arrival measurements show pronounced fluctuations occurring randomly several times in an hour. These effects are seen in time series of atmospheric turbidity calculations (Linke's Turbidity Factor) and of angle-of-arrival variances or r_0 using stellar sources. These patterns are verified as being caused by thermals by examining sodar daytime results. Integrated path C_n^2 values from sodars display similar patterns as seen in the ground-to-space measurements. Occasionally the sodar shows very low C_n^2 values which are under subsidence conditions between rising thermals. Although the average "seeing" conditions are the poorest during midday of a diurnal cycle, these short times of low turbulence provide "seeing" values comparable to many of the nighttime periods. The use of various systems influenced by excessive particulate matter or turbulence could take advantage of these time periods.

Nighttime sodar data displays wave patterns and multi-layers. The integrated C_n^2 values show slowly varying changes, unlike the strong intermittent daytime results. These patterns agree with those found from angle-of-arrival data. "Seeing" does vary to a moderate degree and some systems may operate near the thresholds. As predicted, the "seeing" is best during the evening neutral event. If low turbulent conditions are required for special testing or communications, neutral periods are the best times to operate.

Other atmospheric features create C_n^2 at layers higher than sensed by the sodar. Radar can identify such features and quantify the effects. In general such features are slowly varying in integrated path effects. Remote sensors are useful in defining the levels and nature of C_n^2 in the atmosphere. This information is needed to explain the C_n^2 contributions at different altitudes of ground-to-space integrated path measurements.

6. REFERENCES

1. Couder,A,"Optique asmospherique-measure photographique de l'agitation des images stellaries," C.R. Acad. Sci. Paris 205: 609-611 (1936).

2. Eaton,F.D., W.A.Peterson, J.R.Hines, J.J.Drexler, A.H.Waldie, and D.B.Soules, "Comparison of two techniques for atmospheric seeing", Proceedings of the SPIE Meeting, Orlando, FL, vol. 926, pp.319-334, April 1988.

3. D.L.Fried, "Optical resolution through a randomly inhomogeneous medium for very long and short exposures", J. Opt. Soc. Am. 567: 1372-1379 (1966).

4. Linke,F., "Transmissionkoeffizient und Trubungsfaktor". Beitr. Phys. frei. Atmos. 10,91 (1922).

5. Linke,F., "Messengen der Sonnenstrahlung bei vier Freiballonfahrten." Beitr. Phys. frei. Atmos. 15,176 (1929).

6. Ottersten,H. "Atmospheric Structure and Radar Backscattering in Clear Air," Radio Science, 4, 12, 1179-1193 (1969).

7. Whitford,A.E., and J.Stebbins, "Photoelectric measurement of scintillation of stars," Publ. Am. Astron. 8:228 (1936).

8. World Meteorological Organization (1965). Measurement of radiation and sunshine. In "Guide to Meteorological Instrument and Observing Practices," 2nd ed., W.M.O. No. 8, (1961).
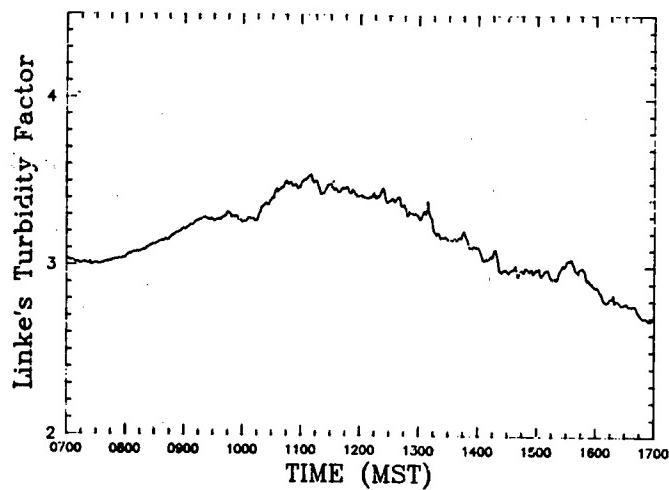
Figure 1 Calculations of Linke's Turbidity Factor, T, for 8 Oct. 1991
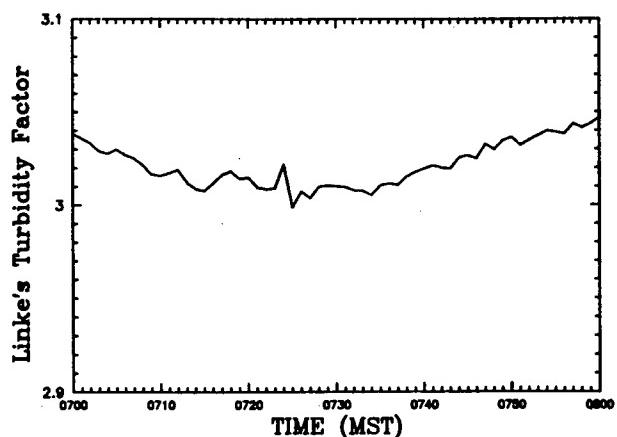
Figure 2 Linke's Turbidity Factor, T, for one hour in early morning.
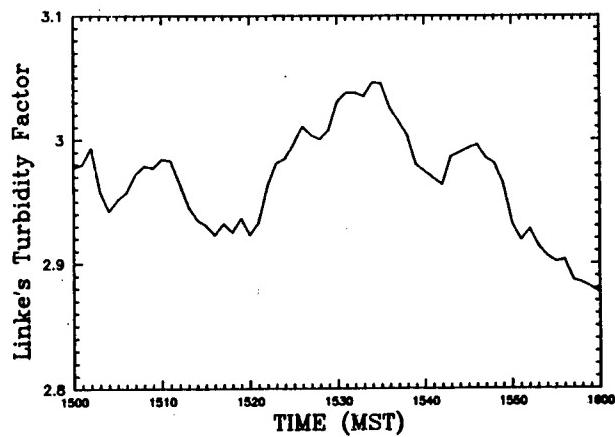
Figure 3 Same as Figure 2 except for mid-afternoon.

340
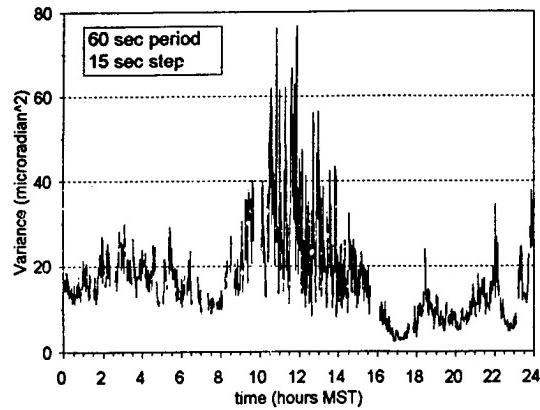
Figure 4 Diurnal cycle of differential image motion measured on 8 Oct 1991.
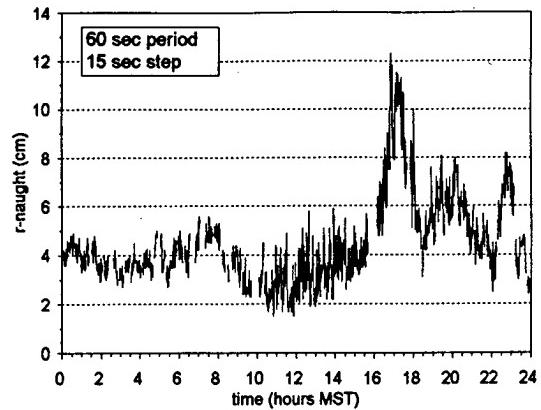
Figure 5 Diurnal cycle of r_o values calculated from the results shown in Figure 4.
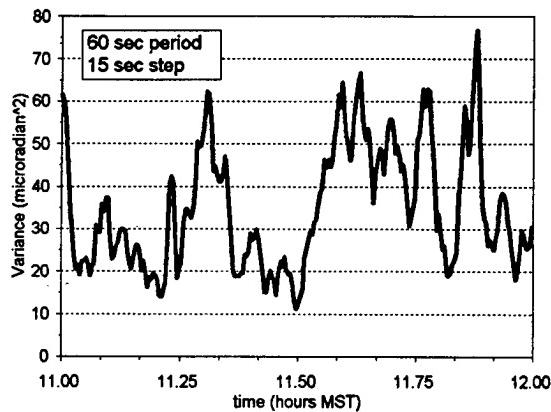
Figure 6 One-hour plot of measured differential motion for 1100 to 1200 MST.
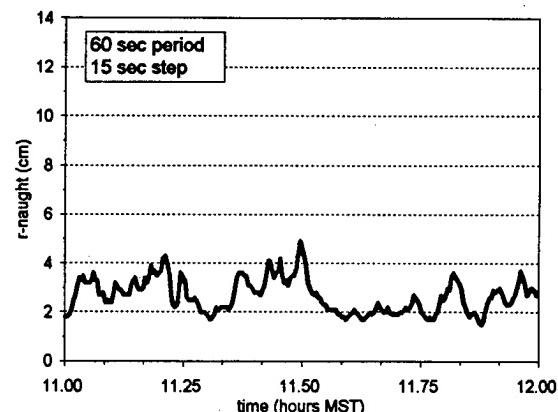
Figure 7 Calculated r_o values from the results in Figure 6.
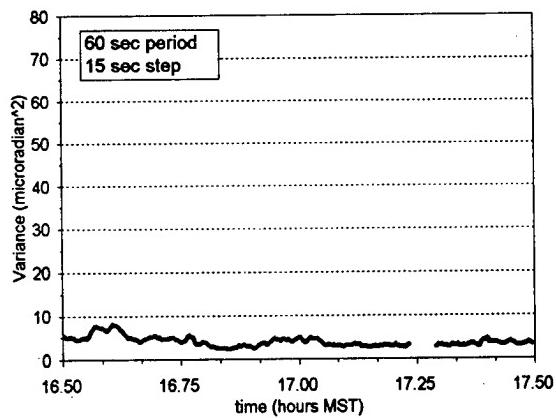
Figure 8 Same as Figure 6 except for 1650-1750 MST.
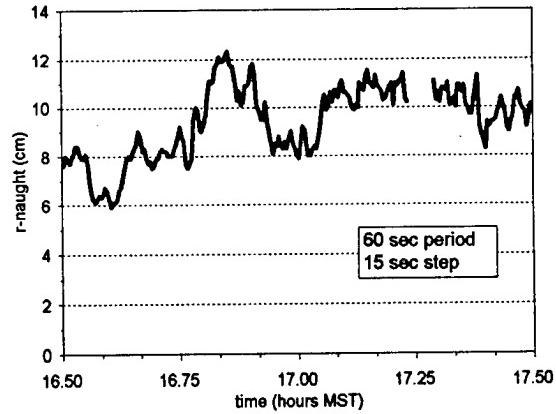
Figure 9 Same as Figure 7 except for 1650 to 1750 MST.
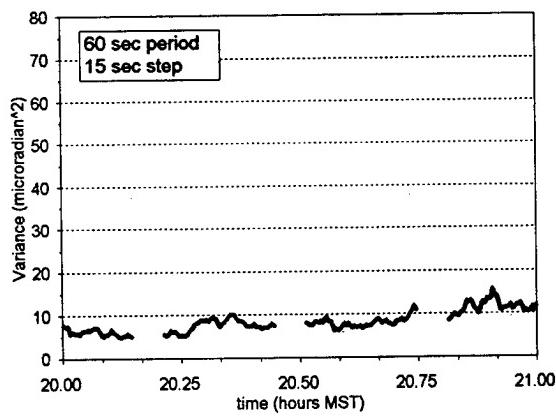
Figure 10 Differential image motion measurements for 2000 to 2100 MST.
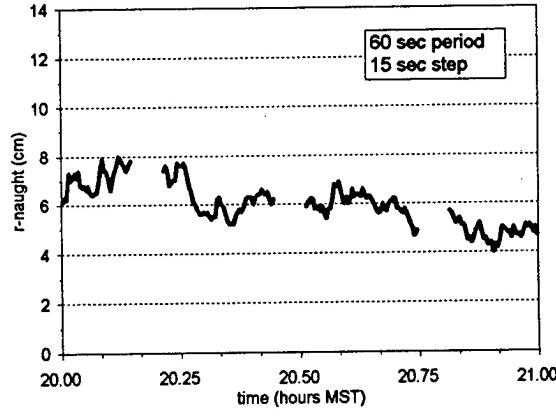
Figure 11 Calculated r_o values from the results in Figure 10.
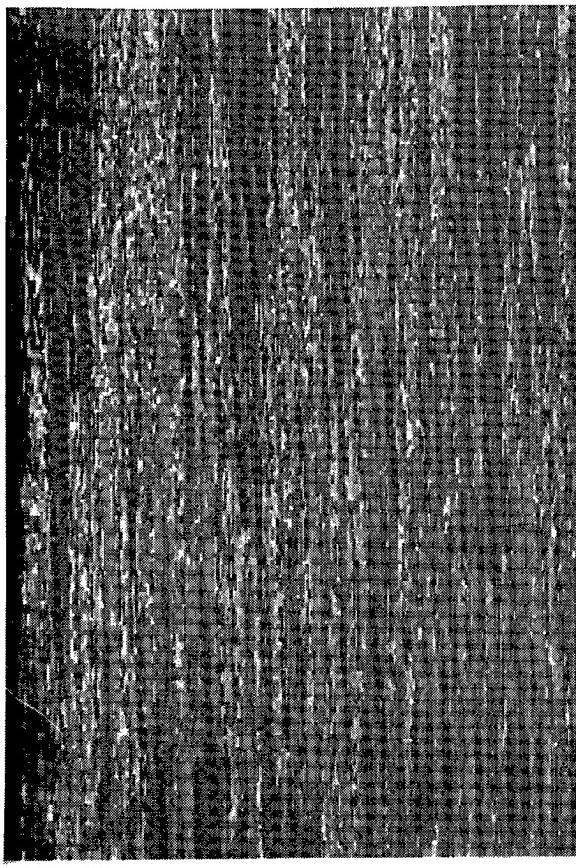
Figure 12 Sodar obtained backscatter during midday.
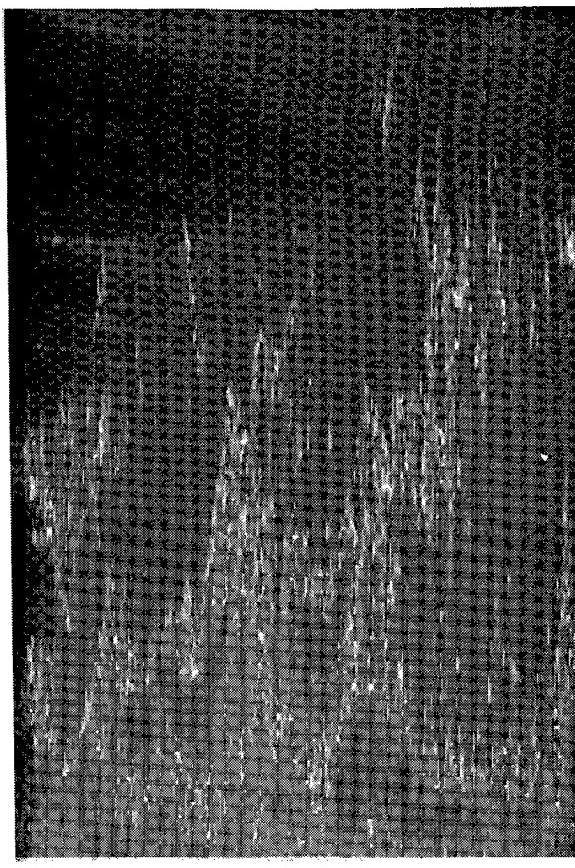
Figure 13 Sodar obtained backscatter during nighttime.
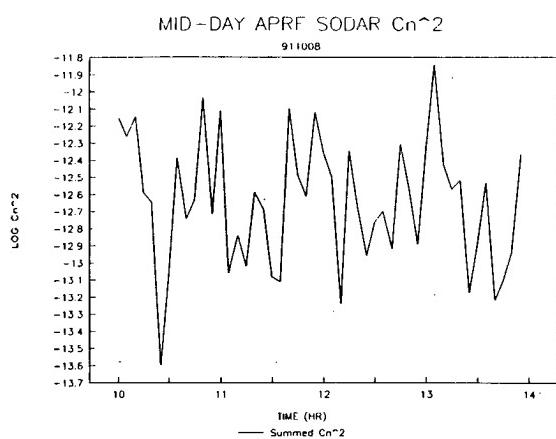
Figure 14 Integrated vertical path C_n^2 values measured with a sodar during daytime.
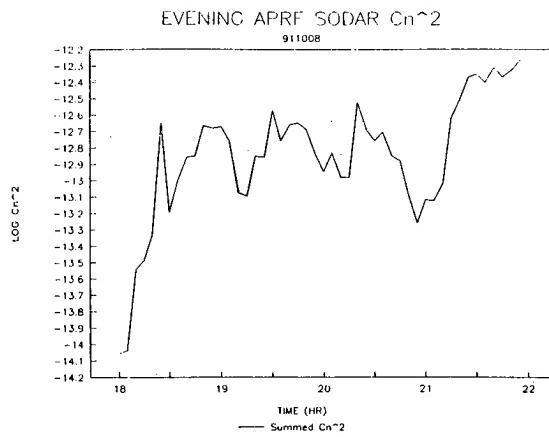
Figure 15 Integrated vertical path C_n^2 values measured with a sodar during nighttime.

343
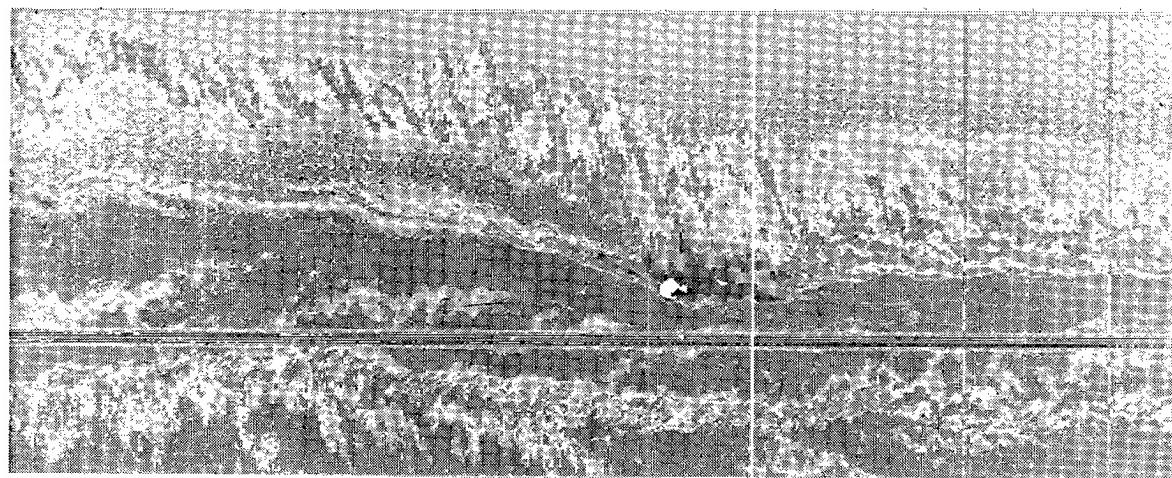
Figure 16 Example of a Kelvin-Helmholtz instability induced wave from 0845-0950 GMT on 3 April 1992.
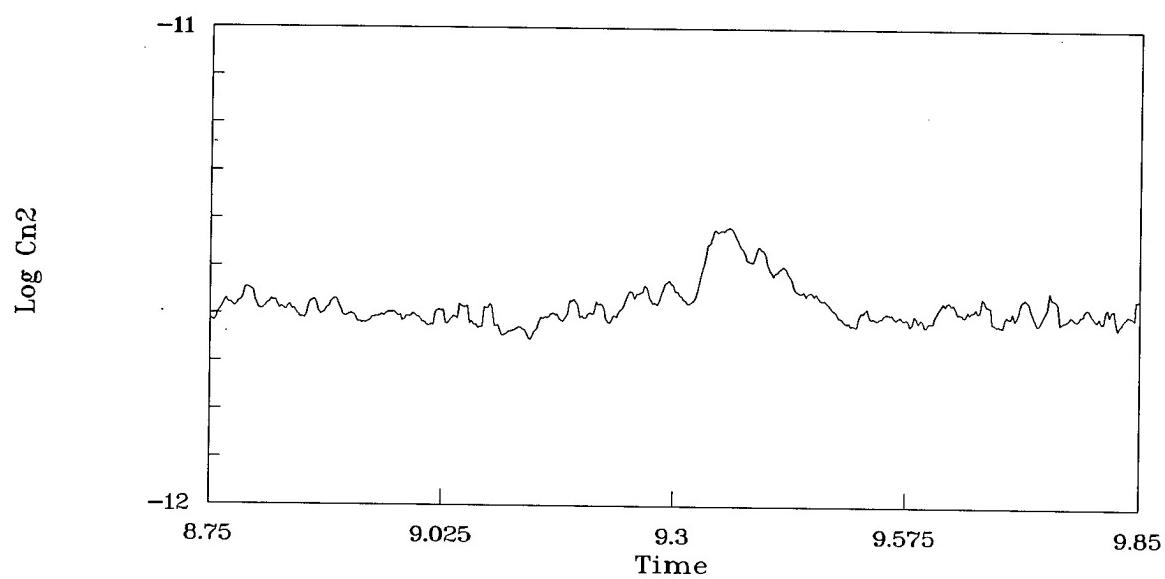
Figure 17 Integrated path C_n^2 values from the data shown in Figure 16

344

ASSESSMENT OF THE PERFORMANCE OF WIND PROFILERS
AT WHITE SANDS MISSILE RANGE

John Hines
Battlefield Environment Directorate
U. S. Army Research Laboratory
White Sands Missile Range, New Mexico 88002-5501

and

Linda Parker-Sedillo
Science and Technology Corporation
Las Cruces, New Mexico 88005

ABSTRACT

Wind profiling radars are being used at White Sands Missile Range (WSMR) to obtain vertical profiles of the wind from the boundary layer into the stratosphere. Such measurements are based on turbulence-induced backscattering from refractive index fluctuations and are adversely affected by RF noise, echoes from unwanted targets (airplanes, birds, insects and ground clutter) and certain meteorological factors such as precipitation, convective activity and gravity waves. This paper addresses the resultant necessity for editing data from the wind-profiling radars and describes the techniques used to edit the wind data from the 924-, 404-, and 50-MHz profilers currently in use at WSMR.

I. INTRODUCTION

The Atmospheric Profiler Research Facility (APRF) was established in 1990 by the U.S. Army Atmospheric Sciences Laboratory (ASL) at White Sands Missile Range (WSMR) in close association with the National Oceanic and Atmospheric Administration (NOAA) Wave Propagation Laboratory (WPL). The facility was designed to monitor three primary atmospheric parameters: wind (speed and direction), refractive index structure parameter (C_n^2), and virtual temperature from 50 m to 20 km above ground level (AGL). (Hines et al., 1992)

The APRF currently provides a continuous, overlapping profile of wind speed and direction from 120 m AGL to 18.5 km AGL with 924-, 404.37-, and 49.25-MHz radar profilers. Data from these profilers can be contaminated with RF noise and interference, echoes from unwanted targets, and precipitation (Wuertz and Weber, 1989). These contaminants produce "fliers," points or clusters of "bad" data that do not accurately reflect the atmospheric flow. An example of such fliers is shown in figure 1. Another example in figure 2 has several fliers at the top of the 404-MHz (low mode) profiler's range. Fliers of this type are very likely due to a low signal-to-noise ratio.

Before profiler data can be effectively used, these fliers must be flagged through a quality control, or

345

editing, process. Two methods used for flagging such fliers are discussed here. One is consensus averaging, whereby vertical wind profiles are temporally compared. The second is a continuity method that looks for consistency over both time and height, using pattern recognition to flag fliers. The main purpose of this paper is to describe in detail the continuity method being used at the APRF; the consensus method is first briefly discussed to establish a point of comparison.

II. INSTRUMENTATION

The profilers use three beams to estimate horizontal wind speed and direction as a function of altitude, a vertical beam and two oblique beams set at 90 degrees to each other and at a high elevation angle to have sampling volumes relatively close to each other. Figure 3 shows the beam configuration for the 50-MHz profiler. The vertical beam is used to measure the vertical wind speed and to compute the horizontal wind speed components from the radial speeds along the oblique beams. The three profilers have different beam settings (table 1) and vertical resolutions (table 2). Further details are provided by Hines et al., 1993.

TABLE 1. BEAM CONFIGURATIONS FOR THE 924-, 404-, AND 50-MHZ PROFILERS.

Profiler	Beam Width	Oblique Beam angle	Oblique Beam direction
924 MHz	10.0°	20°	N & E
404 MHz	4.0°	16.1°	N & E
50 MHz	3.3°	15°	S & W

TABLE 2. SPATIAL AND TEMPORAL SETTINGS FOR THE 924-, 404-, AND 50-MHZ PROFILERS.

Profiler	Vertical Range	Vertical Resolution	Temporal Resolution
924 MHz	150 - 4000 m	100 m	1.5 min
404 MHz (low) 404 MHz (high)	500 - 9250 m 7.5 - 16.2 km	375 m 1 km	6 min 6 min
50 MHz	2 - 18.5 km	150 m	3 min

Wind speed and direction measured by these profilers can be portrayed graphically over time and height using wind barb graphs. In these graphs, the orientation of the barbs indicates wind direction, and markings on these barbs indicate wind speed. The barb points in the direction the wind is moving. For example, the wind barb in figure 4 represents a wind moving from the south to the north at 15 to 20 m/s. A legend for wind barb to wind speed conversion is displayed in figure 5.

III. CONSENSUS METHOD

The consensus method of quality control averages the raw profiler data (1.5-, 6-, or 3-min) at a given height into hourly averages based on two criteria: (1) The data points used in the average must be

within a certain range of each other and (2) in that hour, there must be a specified number of those points that fit into the range. If in an hours worth of data points, that predetermined number of data points can be found within the specified range of each other, then those points are vector averaged and presented as hourly data. A shortcoming of the consensus method is that it only looks for consistency over time.

IV. CONTINUITY METHOD

The Weber-Wuertz continuity method of quality control (WW method) was developed by Weber and Wuertz at NOAA in Boulder, CO (B. Weber et al., 1991.) The WW method uses an editing technique of pattern of recognition in the data to flag discontinuous data points, or fliers, in the raw (1.5-, 6-, or 3-min) profiler data before an hourly average is calculated. It is controlled by five parameters. These control parameters allow a generalized model that can be applied to any type of continuous data to become a specific and specialized continuity model. The five parameters as applied to profiler measurement are:

dx(h) - vertical width for neighboring points. (The height difference allowed for two points to still be neighbors.)

dx(t) - temporal width for neighboring points. (The time difference allowed for two points to still be neighbors.)

dy - the maximum difference in the data (wind, temperature, or C_n^2) allowed per each dx(h) and dx(t).

gd - gross difference. Used to minimize computation time by allowing entire branches to be flagged all at once instead of point by point.

nmin - the size of the smallest allowable pattern detected by pattern recognition.

The parameters currently in use at APRF for quality control run on the u and v components of the wind speed (924-, 404-, and 50-MHz profilers) are listed in table 3.

TABLE 3. WEBER-WUERTZ PARAMETERS CURRENTLY IN USE AT APRF FOR WIND COMPONENT (U AND V) DATA.

Profiler	dx(h)	dx(t)	dy	gd	nmin
924 MHz	(2 gates) 200 m	30 min	3.5 m/s	35 m/s	10
404 MHz low mode	(2 gates) 750 m	12 min	5.0 m/s	50 m/s	25
404 MHz high mode	(1 gate) 1000 m	12 min	6.0 m/s	60 m/s	25
50 MHz	(2 gates) 300 m	6 min	4.0 m/s	40 m/s	30

The WW method assumes that the data are continuous over time and altitude and applies a pattern recognition technique to determine continuous and noncontinuous points. The method consists of two main parts: pattern recognition and quality control. The procedure can best be visualized by thinking of the data as a tree of continuous data. Points connected to other points they are continuous with

347

form a single branch in that tree. Two branches may connect to each other at a node[1] until the data are represented by several trees (patterns), each tree consisting of a stream of continuous data over time and altitude. Two non-neighboring points may not be continuous with each other but may be in the same pattern if they are connected by continuous data points. Therefore, an easterly wind in the morning may gradually shift to a westerly wind in the afternoon. But, if the data in between remain continuous, both winds may be in the same pattern. A comparison of the consensus method and WW method is shown in figure 6.

A. PATTERN RECOGNITION

In pattern recognition, the individual data points are checked to find their neighbors (those points within dx(h) and dx(t) of each other). The neighbors (designated as n_1 & n_2) then have their "connectivity" value (the degree to which their points are connected or continuous with each other, 0 to 10 is considered to be connected, 11-100 not connected) calculated according to the following two step formula:

$$connectivity = \frac{10}{dy} \times (n_1 - n_2)$$

$$IF\ n_1 - n_2 < MIN(n_1, n_2),\ THEN\ connectivity = connectivity \times \frac{n_1 - n_2}{MIN(n_1, n_2)}$$

This definition of connectivity has the advantage of being independent of the magnitude of the data and is not overly sensitive to the user selected dy. The algorithm allows for the fact that a 4 m/s difference in wind speeds between 18 m/s and 22 m/s is not the same as a 4 m/s difference in wind speeds of 1 m/s and 5 m/s.

Next, data points are designated a "node" or a "branch" based on the connectivity of their neighbors. Nodes are added to branches they are continuous with until every data point is included in a branch and the data are represented by many branches of continuous data. A new measure of connectivity is now added by using the formula below to calculate the branch connectivity of each branch to each other (0 to 10 connected, 11 to 100 not).

$$branch\ connectivity = \frac{\sum connectivity\ between\ branch\ points}{\sum number\ of\ neighbors\ in\ two\ branches}$$

Branches are then put into larger "patterns" consisting of branches that are interconnected. The branch connectivity is also used in the quality control phase.

B. QUALITY CONTROL

The first step of the quality control phase is intended to minimize run time by cutting entire branches.

---

[1] Nodes are those points continuously connected to two or more points which are discontinuous with each other.

348

The branches of each pattern are checked against the branches of the other patterns. If the two branches' connectivity is greater than a set value (gqc) defined by:

$$gqc = MIN(100, 10 \times \frac{gd}{dy}) \ ,$$

then the branch in the smaller pattern is cut (all points in the branch are given a QC value of 100, discontinuous from the "good" data).

Next, the QC values are set by checking point discontinuities in a certain order. First, smaller patterns are checked for discontinuities by checking the point against the interpolated value from its neighbors. Its QC is set by the formula:

$$QC = MAX[oldQC, connectivity(point, interpolated \ value \ of \ point)]$$

Secondly, branches with the worst branch connection are checked for discontinuities using the same QC formula. Lastly, any patterns smaller than nmin have the QC for it's points set equal to 100.

It should be emphasized that the five parameters currently in use at APRF were determined using trial and error as opposed to a set formula. Parameters can be set to either minimize type I (deleting good data) or type II (accepting bad data) errors. While not wanting to delete any good data, our main goal was the elimination of bad data before calculating hourly averages. An important point here is that we have not altered any raw data, merely assigned each datum a quality control factor. We then use those points having a good quality control factor to calculate hourly averages. Figure 7 shows a sample of data before and after running the WW method.

C. PROBLEMS WITH THE WW METHOD

This method is not without problems. The algorithm does not work correctly with data that have a large number of "bad" points and is unable to be used with realtime data acquisition.

The WW method examines the data to find the largest number of data points that are considered continuous. If the "bad" data outnumber the "good" data and those "bad" data points are found to be continuous with each other, the algorithm will keep the "bad" data and cut the "good". We found such a problem with the 50 MHz profiler temperature data. It consistently included bad data with the good data.

To get around this problem, we employed a method suggested by W. Hatch of ARL. In this case, climatological data on the temperature extremes as a function of altitude were used to set limits on the temperature at each altitude.[2] The 50 MHz profiler data were then checked against these limits and only the fitted data sent on for QC. The other data was assumed to be "bad" and assigned a QC of 100.

---

[2]Equations determining the upper and lower limits for the air temperature at each gate were calculated using radiosonde data acquired at Oasis Site, WSMR, from January 1992 through March 1993. The differences between the absolute maximum temperature and the 15-month mean temperature and the absolute minimum temperature and the 15-month mean temperature were plotted as a function of altitude. Those curves were then fit with straight lines and the lines shifted outside the curves until all points on the curve would be included inside the two lines. Those lines formed the equations for the upper and lower limits on the temperature.

The WW method was designed to be used with a set amount of data, whether a days or an hours worth. Possibly extensive work will be needed to change the code for realtime use. The algorithm also uses an enormous amount of CPU run time due to the large amount of working memory needed for the data arrays. This can be a real problem when running the quality control on a VAX. We found that the Microvax II with 16 Mbytes RAM takes two minutes to process one hours worth of data while our HP 9000-Apollo 730 with 112 Mbytes RAM takes only a few seconds. This run time problem also interferes with realtime processing.

CONCLUSIONS

In conclusion, automatic editing of wind data for fliers can be successfully achieved through the Weber-Wuertz continuity method. Currently, we are running the WW method on a days worth of data at a time. There is a requirement for near realtime quality controlled data for the different profilers for producing composite vertical wind profiles for internet access. (An example of 12 consecutive, composite, hourly profiles is shown in figure 8.) This will require that the algorithm be extended to dealing with data as they come in so that the data may be quality controlled, the edited data sent to a file, and the data points' parameters "remembered" for use with the next batch of data.

ACKNOWLEDGEMENTS

REFERENCES

John R. Hines, Frank D. Eaton, William Hatch, and Scott McLaughlin, "The U. S. Army Atmospheric Profiler Research Facility: A Preliminary View," *Proceedings of the SPIE meeting, Orlando, FL,* vol 1688, pp. 225-236, April 1992.

John R. Hines, Scott A. McLaughlin, Frank D. Eaton, and William H. Hatch, "The U. S. Army Atmospheric Profiler Research Facility: Introduction and Capabilities," *Eighth Symposium on Meteorological Observations and Instrumentation, Anaheim, CA,* pp. 237-242, January 1993.

David B. Wuertz and Bob L. Weber, "Editing Wind Profiler Measurements," *NOAA Technical Report ERL 438-WPL 62,* 78 pp, August 1989.

Bob L. Weber and David B. Wuertz, "Quality Control Algorithm for Profiler Measurements of Winds and Temperatures," *NOAA Technical Memorandum ERL WPL-212,* 32 pp, October 1991.

25 May 1993
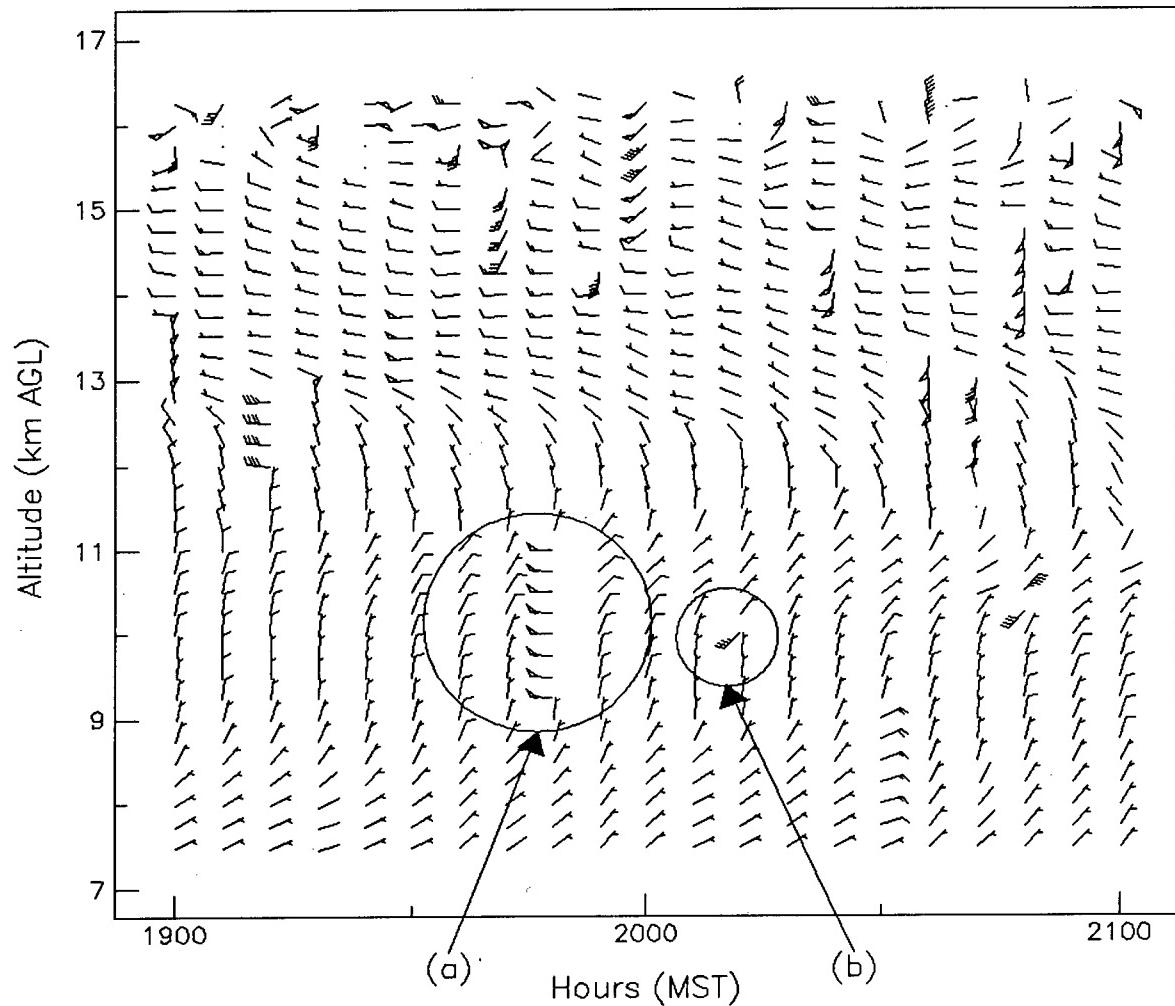
Figure 1. Raw data including "fliers" from a 404-MHz (high mode) wind profiler. (a) An example of a cluster of non-continuous data points. (b) An example of a single point of non-continuous data.

17 May 1993
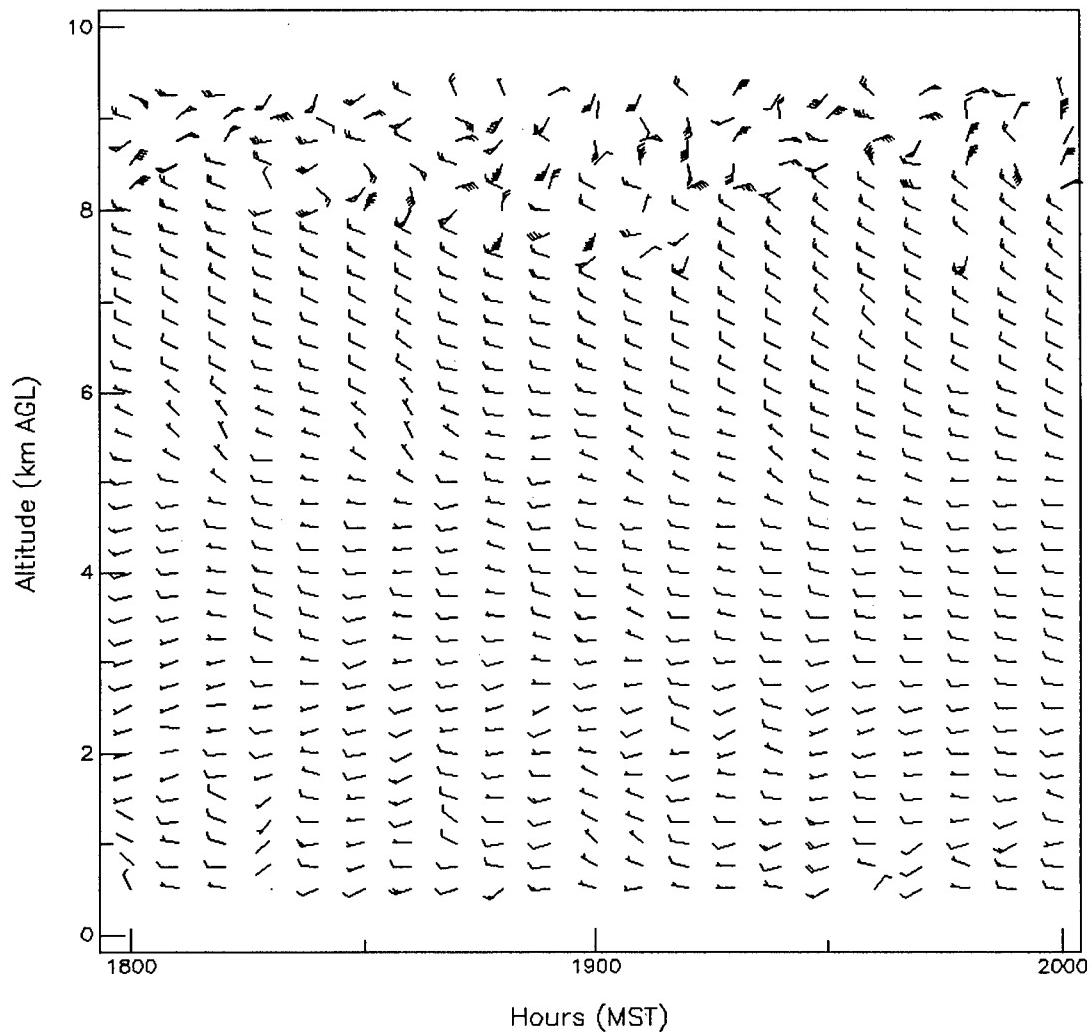
Figure 2. Six—minute average vertical profiles of wind speed and wind direction, as measured with a 404—MHz (low mode) wind profiler.
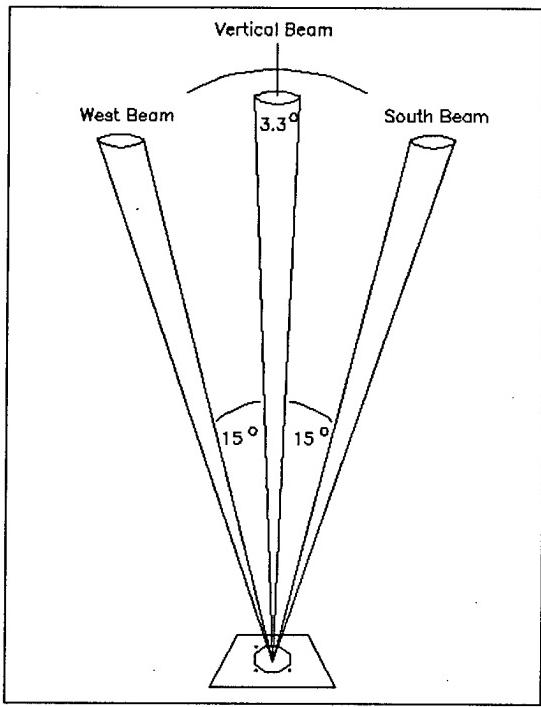
Figure 3. Beam Configuraton for the
50–MHz wind profiler.
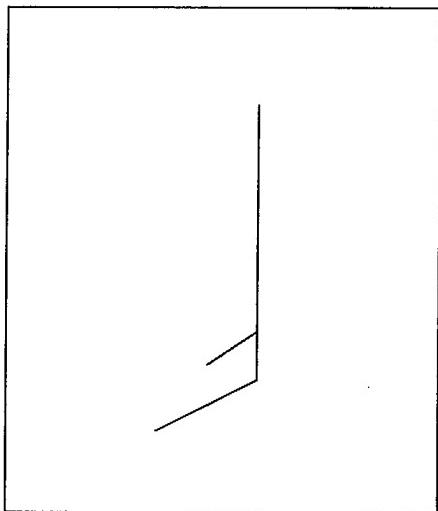
Figure 4. Wind barb example. Wind from
the South heading North, speed
15 to 20 m/s.
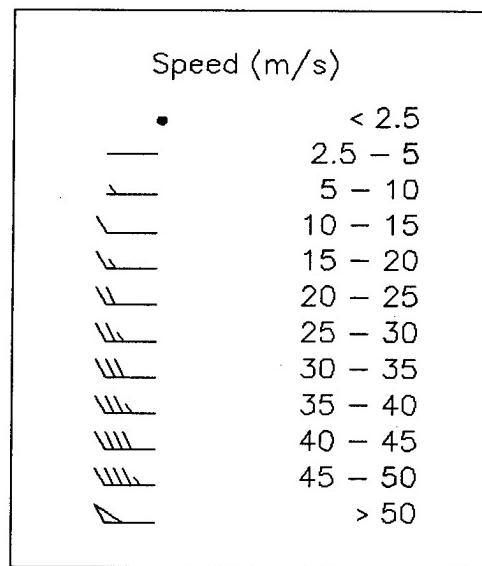
Figure 5. Wind barb to wind speed
conversion legend.

Concensus Averaging QC

Time

Height

1 2 3 4 5 6 7 8 9 10

Compare all time periods (1 hour) at the same time. At least X must be within Y of each other. These are the points used to find the hourly average.

X = the number of data points in concensus necessary to find an hourly average.

Y = the maximum difference for two points to still be in concensus.

WW Method QC

Time

Height

1 2 3 4 5 6 7 8 9 10

dh = 1   dt = 2

Check each point individually to see if it is continuous with it's neighbors (those points within dh and dt of it.) All the continuous points in that hour are used to find the average.

Figure 6. Comparison of the two different methods of quality control currently used on data at APRF, WSMR.

354

16 May 1993
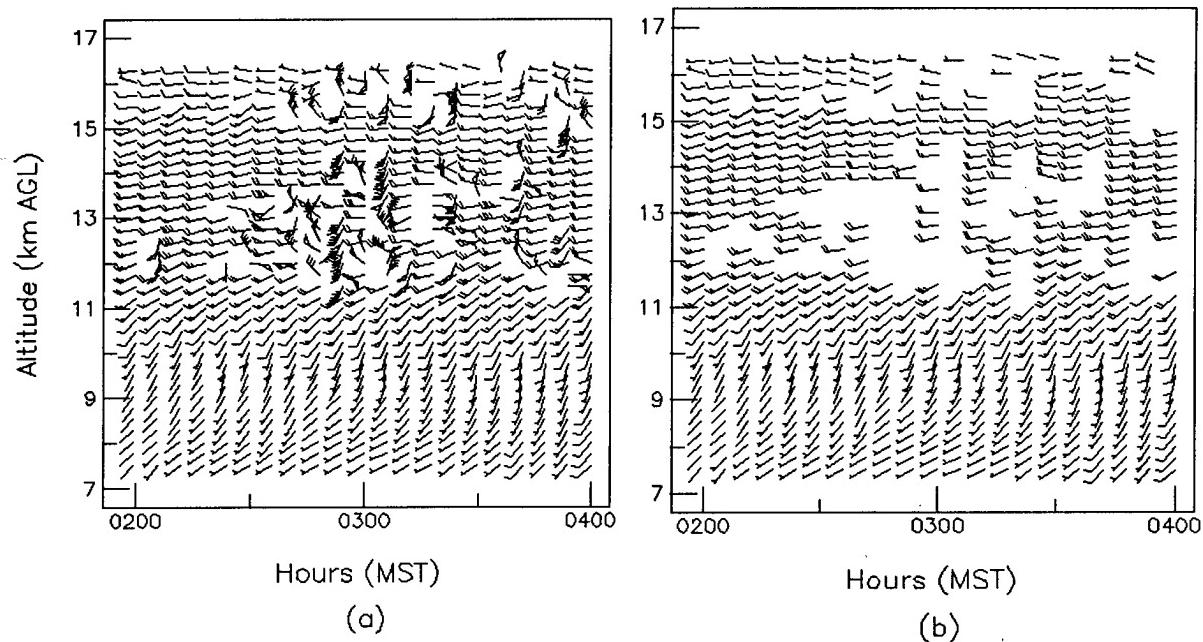
Figure 7. Six—minute average vertical profiles of wind speed and wind direction, as measured with a 404—MHz (high mode) wind profiler. (a) Raw data, no quality control. (b) The same raw data, after applying the Weber—Wuertz continuity method of quality control.

17 May 1993
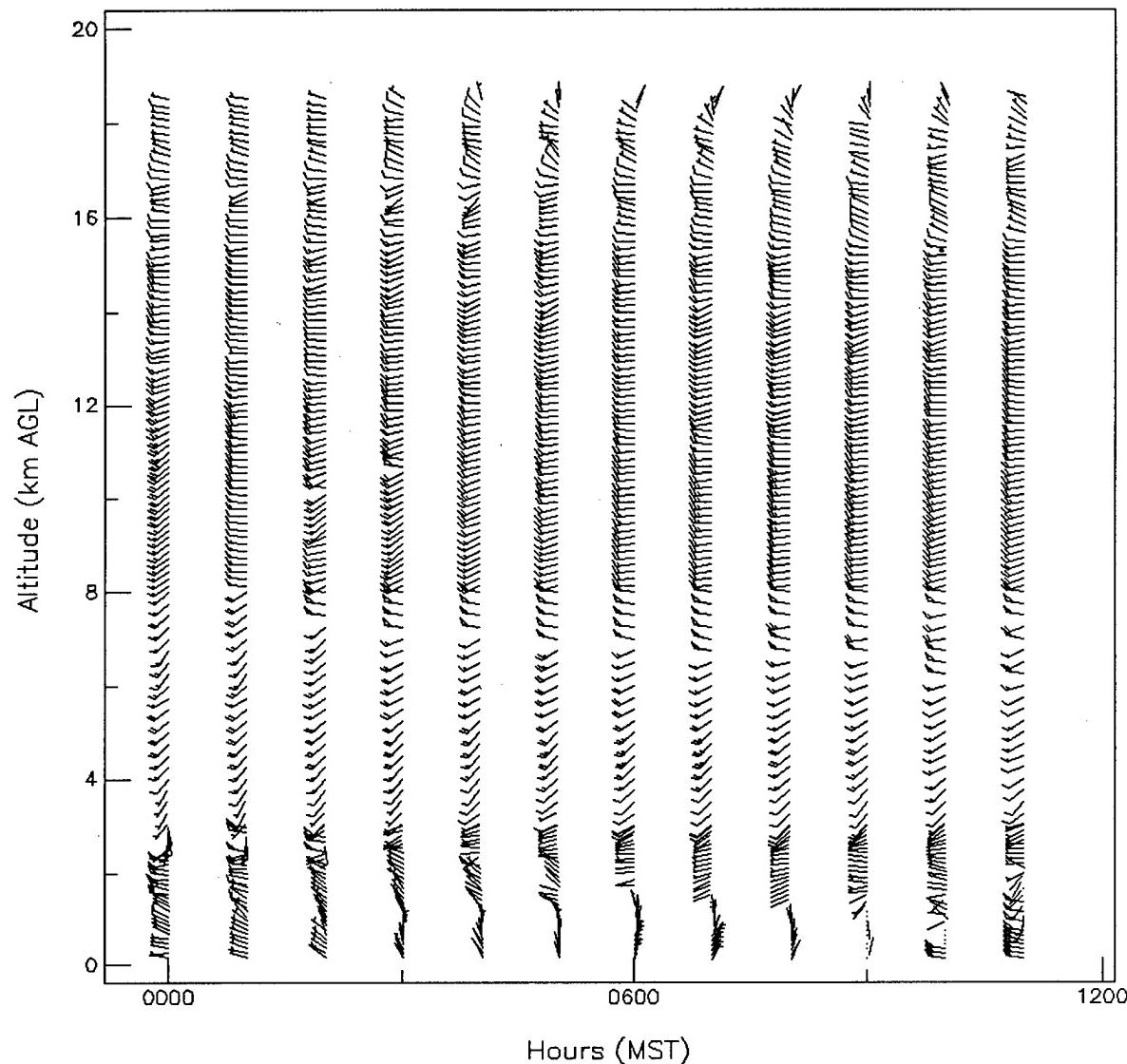
Figure 8. Composite profile of winds provided by the 924—, 404—, and 50—MHz wind profilers, 17 May 1993, at APRF, WSMR.

SATELLITE ANALYSIS OF KUWAITI OIL SMOKE PLUMES

Jan L. Behunek, John M. Forsythe and Thomas H. Vonder Haar
STC-METSAT
Fort Collins, Colorado, U.S.A.

ABSTRACT

The Kuwait Oil Field Fire Experiment (KOFFE) is a study of several aspects of the oil smoke plume created by the Kuwait oil well fires. *STC*-METSAT is participating in the KOFFE analysis by extracting parameters describing the smoke plume from satellite data. These parameters include smoke plume edge location, plume optical depth, plume movement and the generation of mesoscale temperature and wind fields. The main satellite data sources are NOAA AVHRR and TOVS, and METEOSAT. These satellite-derived analyses are important for the study of obscurant location and optical characteristics, as well as input to or validation of transport and dispersion numerical models.

1.0 INTRODUCTION

The Kuwait oil field fires started by the Iraqi Army during the Persian Gulf War early in 1991 generated a smoke plume of unprecedented proportions. Although these fires represented a great environmental and economic disaster, they also created a very unusual opportunity for scientific research relating to characterization of the battlefield atmosphere. The oil smoke plume emanating from the fires traced mesoscale transport and dispersion processes over greater distances than previously observed. The dark smoke also absorbed significant amounts of solar radiation, leading to speculation that the plume might self-loft into the upper reaches of the atmosphere.

A data collection and analysis effort called the Kuwait Oil Field Fire Experiment (KOFFE) was undertaken in order to study this unique event. The data collection phase of KOFFE included data from satellite, aircraft, upper air data and surface radiometer and state parameter data. The large physical dimensions of the plume, and the high contrast between the relatively dark smoke and the bright desert background

in the visible spectrum made satellite observations of the plume possible. The satellite data were particularly valuable for their spatial coverage of the extensive plume, which contrasted with the point measurements made by other instruments.

The following smoke plume characteristics were analyzed from satellite data: plume boundary location, plume optical depth, plume movement, and wind and temperature field in the plume environment. Plume location from satellite is useful either for initialization or validation of transport and dispersion models of the plume. The associated plume boundary data are being used in a fractal analysis of turbulence effects on plume dispersion (e.g. Gifford, 1991). The optical depth analysis essentially gives a measure of smoke (optical) mass distribution within the plume. It is useful for transport model input and validation, simulation of plume lofting due to solar radiation absorption, and assessment of surface or low-altitude object obscuration by the smoke. The 3-dimensional wind and temperature fields derived from satellite data supply transport model input or validation. Geostationary METEOSAT data provides an overview of mesoscale circulation effects on plume movement.

2.0 DATA

The comprehensive data sets collected during KOFFE help make that experiment unique in terms of ability to characterize contaminant transport and dispersion over relatively large spatial scales. Much of the satellite, aircraft, surface and upper air data collected during KOFFE are maintained as part of the Kuwait Data Archive (KuDA) at the National Center for Atmospheric Research (NCAR). STC-METSAT has obtained a subset of satellite and other data from KuDA to support our studies. We also have obtained additional, independent satellite data sets for this work. Satellite data from the polar-orbiting TIROS-N (NOAA), Defense Meteorological Satellite Program (DMSP), LANDSAT and geostationary METEOSAT platforms were examined. Results presented here rely primarily on NOAA and METEOSAT data. The cases studied were 26 May, 29 May, 30 May and 1 June 1991.

2.1 NOAA AVHRR

The Advanced Very High Resolution Radiometer (AVHRR) carried aboard the TIROS-N (NOAA) satellites is a five channel imaging radiometer. The main spectral channel utilized during this study was the visible channel (#1, 0.58 - 0.68 μm). Other AVHRR channels cover the near-infrared, mid-infrared and IR (11 μm) window channels. AVHRR channel 1 was emphasized because it had the greatest sensitivity to this particular smoke plume. The very small particles that the plume was composed of scattered visible radiation much more efficiently than they interacted with infrared radiation by absorption/emission processes. AVHRR channel 1 has a horizontal resolution of 1.1 km at nadir, which degrades with distance scanned by the instrument

away from nadir. Although three NOAA satellites were in operation at the time of the KOFFE, our focus was on the midday pass of NOAA-11 because of the favorable solar illumination at that time. All images from AVHRR were coregistered so that any particular earth location was represented by the same pixel location regardless of the image date and time. This process removed variations caused by the satellite's orbit.

2.2 NOAA TOVS

The TIROS Operational Vertical Sounder (TOVS) instrument is a suite of three multispectral scanning radiometers designed to measure atmospheric vertical temperature and moisture profiles. These instruments operate in the infrared and microwave portions of the spectrum. The maximum horizontal resolution of the IR data is 17.4 km (footprint size), with 42 km between samples. We utilized TOVS data and the vertical profiles generated from them from the morning passes (approximately 0400 UTC) of NOAA-10 and NOAA-12, and the midday pass of NOAA-11. The radiance data collected by satellite were converted to temperature and moisture profiles by a method known as sounding retrieval (Smith, 1983). Further details on the TOVS are contained in Kidwell (1991).

2.3 METEOSAT

The primary METEOSAT platform is geostationary above the Greenwich Meridian. The main advantage of METEOSAT data is the 30-minute interval between images of a particular region. METEOSAT receives radiation in the visible (0.4-1.1 μm), water vapor absorption (6.7 μm), and IR window (11.5 μm) spectral channels. The visible channel data were the most valuable for study of the Kuwait oil smoke plume, as with the NOAA satellite data. Sequences of these images were used to evaluate the movement of the smoke plume. This analysis helped assess the validity of plume transport simulations and to what extent plume transport was affected by changing mesoscale circulations. The METEOSAT data used in the study either had 2.5 by 5 km resolution or 10 km nominal resolution depending on the case in question.

3.0 ANALYSIS METHODS

3.1 Surface Albedo

Knowledge of surface albedo characteristics was required for successful plume boundary and optical depth analyses. A surface albedo map was created by compositing five digital AVHRR image files from five days other than those on which smoke characteristics were studied. Those days, 25 May, 11 June, 12 June, 13 June, and 14 June 1991, were characterized by atypical wind and plume transport directions. The surface was visible from the satellite perspective on those days in areas where it usually could not be seen. All five images were from the midday pass of NOAA-11.

Therefore, the solar zenith angle and incoming solar insolation varied little. The smoke-free surface was represented by the brightest pixel at each location from the five coregistered input images. Water clouds were excluded from the analysis by use of a 30 percent albedo brightness threshold. All pixels brighter than that threshold were not considered eligible to represent the surface. Very few water clouds were observed in this region at this time of year.

3.2 Plume Boundary

The plume boundary analysis from satellite data had several objectives. One objective was to determine where smoke effects such as reduced solar radiation and obscuration of the surface from air and space-borne assets occurred. Another objective was to provide initialization or validation information for the plume transport and dispersion models being used by other members of the KOFFE analysis team. Model validation was the more important of these applications, in which the satellite observations of plume location were compared with simulated plume locations based on knowledge of the plume source, the wind field, and the turbulence characteristics of the atmosphere. Plume edge data derived from satellite also are being applied in a fractal analysis of turbulence effects on plume dispersion.

The plume boundary analysis was accomplished by image processing edge detection techniques. Gradient edge detection was employed, in which the gradient operator was applied to nine pixels centered on the pixel of interest. This computation was accomplished for each pixel in an image, except those on the very edge of the image. The image gradient gave an indication of all boundaries in the image, including smoke plume and surface features. Separation of smoke features from surface features was achieved by subtracting the gradient of the surface albedo map from the gradient of the image containing smoke. Values of this gradient difference that exceeded zero indicated the edge of the smoke plume.

3.3 Smoke Optical Depth

Estimates of the Kuwait oil smoke plume optical depth from satellite data gave an indication of the smoke particle mass distribution within the plume. These estimates were based on measurements and radiative transfer modeling of scattered and transmitted solar radiation. NOAA AVHRR channel 1 data were used for this work. Satellite measurements of radiance backscattered from the plume were compared with the model solution, which depended on the plume optical depth, the optical properties of the smoke particles, and the sun-smoke-satellite geometry. Measurable contrast, or difference in the radiance received at the satellite, between the smoke-free background and the smoke plume was required in order to obtain the optical depth estimate. This contrast typically was observed between the smoke plume and the bright desert of the Arabian Peninsula. The radiative transfer model converted radiance reduction by the smoke into an optical depth estimate.

The radiative transfer model used for this work was a doubling model (Greenwald and Stephens, 1988) solution of the radiative transfer equation, expressed as:

$$\mu \frac{dI(\tau, \mu, \phi)}{d\tau} = -I(\tau, \mu, \phi) + \frac{\omega_0}{4\pi} \int_0^{2\pi} \int_{-1}^{1} P(\tau, \mu, \phi) I(\tau, \mu, \phi) d\mu d\phi + J(\tau, \mu, \phi)$$

where I = radiant intensity, τ = optical depth
          ω_0 = single scatter albedo P = phase function
          μ = cosine of zenith angle ϕ = azimuth angle

The doubling model solved for optical depth by iterating scattered intensity and optical depth until the observed intensity was obtained. In practice, the doubling model was used to build a lookup table relating satellite-observed radiance to smoke optical depth for given smoke optical properties and sun-satellite geometry, i.e. conditions specific to the case. Optical depth was then rapidly calculated at each pixel containing smoke. This procedure avoided lengthy radiative transfer calculations at roughly 10^5 smoke-filled pixels. Smoke particle optical properties were specified by single scatter albedo (ω_0) and asymmetry parameter (g).

Typical values were:

$$\omega_0 = 0.55, \quad g = 0.$$

based on aircraft particle probe and radiometer data (Weiss and Hobbs, 1992; Baumgardner, et al., 1993).

3.4 Wind and Temperature Fields

Knowledge of the 3-dimensional wind field in the vicinity of the smoke plume is important for assessing its future movement. One method of predicting that movement is with mesoscale transport and dispersion models. Vertical temperature profiles are important for diagnosing atmospheric stability, which influences the self-lofting ability of the plume due to solar heating. The 3-D wind and temperature structure of the atmosphere was obtained from NOAA TOVS data. Vertical temperature profiles were estimated from the 23 infrared and four microwave spectral channels measured by TOVS. The sounding retrieval process required inversion of the radiative transfer equation to get equivalent radiating temperatures from the observed radiances. These temperatures applied to specific levels in the atmosphere because of different atmospheric transmittance values in those spectral channels. The geopotential height field was calculated from temperatures using the hydrostatic approximation, and winds were calculated using the geostrophic approximation. Additional details are contained in Smith (1983).

3.5 Plume Movement

Observation of the Kuwait oil smoke plume every 30 minutes by METEOSAT allowed plume motion to be evaluated. This part of the study was accomplished by man-computer interactive analysis of METEOSAT image time sequences. The analysis was essentially a qualitative evaluation of plume location changes and transport based on plume appearance in these sequences.

4.0 RESULTS

Results have been generated for all of the products described in section 3 for all four case studies. Selected results are presented here.

4.1 Plume Boundary

The AVHRR visible (channel 1) image from 26 May 1991 at 1056 UTC is shown in Figure 1. The oil smoke plume is readily seen over the desert near the Persian Gulf. It is noteworthy that thin western portions of the plume over the Saudi Arabian desert are more difficult to distinguish, as is the plume boundary in that region. The smoke plume is invisible over the Persian Gulf because of the very low contrast between the water and the dark smoke. The plume boundary analysis is shown in Figure 2. This analysis is designed for definition of the plume edge (outer white boundary) rather than details of the plume interior. An estimate of the boundary location over water also is shown (white line at right). The boundary was not detectable over water by the gradient difference method described above. This boundary was defined by a manually selected brightness threshold in channel 1 in order to compare observed and modeled plume width. The plume boundary can be identified downwind to about 800 km from the source in Figure 2. This is considerably further than distances observed in previous studies for continuous plumes in the lower troposphere. Therefore, this product is quite valuable for the study of mesoscale circulations and turbulence effects on contaminant dispersion.

4.2 Plume Optical Depth

Plume optical depth was analyzed where AVHRR channel 1 showed that smoke was present over land. Results for 26 May 1991 at 1056 UTC are depicted in Figure 3, in which optical depth values are displayed as gray shades. Those gray shades represent optical depth values ranging from 0.1 to 1.4. For reference, smoke with an optical depth of 1.0 extinguishes 63.2 percent of the incident radiation. The optical depth map reveals considerable interior plume structure not seen in the plume boundary analysis.
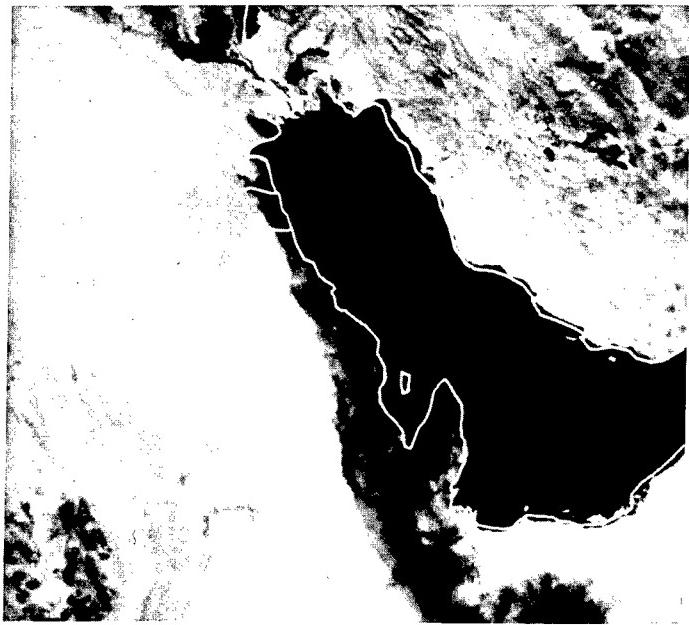
Figure 1. AVHRR visible channel image for 26 May 1991 at 1056 UTC. The oil smoke
plume is seen near the Persian Gulf coast of Kuwait and Saudi Arabia.
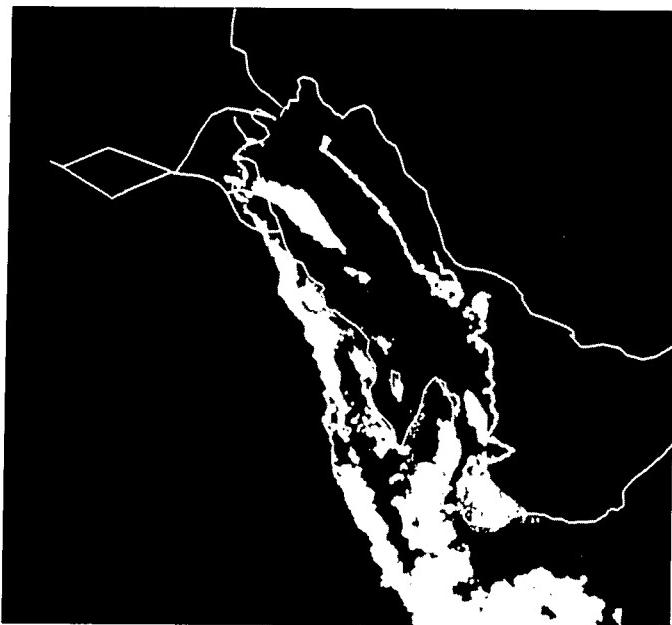
Figure 2. Smoke plume boundary analysis corresponding to the image data in
Figure 1. The western (left) plume edge is depicted in solid white. The
eastern (right) edge is over water and is partially outlined in white.
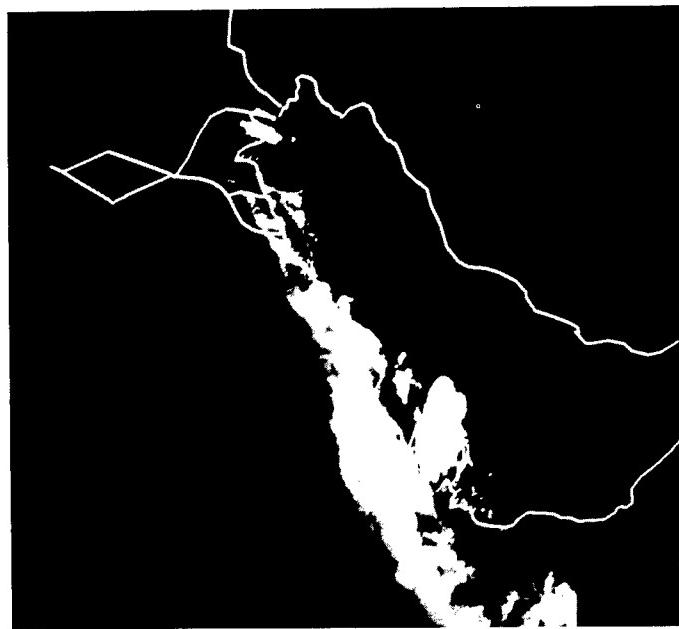
Figure 3. Plume optical depth analysis corresponding to the image data in Figure 1. Gray shades indicate optical depth ranging from 0.1 (dark gray) to 1.4 (white).
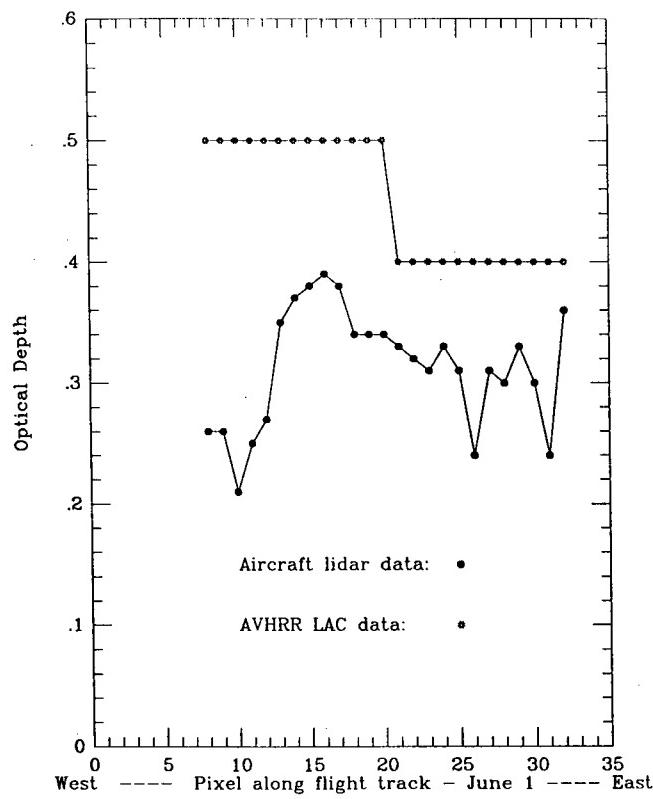
Figure 4. Intercomparison of smoke optical depth derived from satellite and aircraft-borne lidar for 1 June 1991 at 0953 UTC. Satellite-derived values are plotted with stars and lidar values are solid dots. The units of the abscissa are satellite pixels counted along the aircraft flight track.
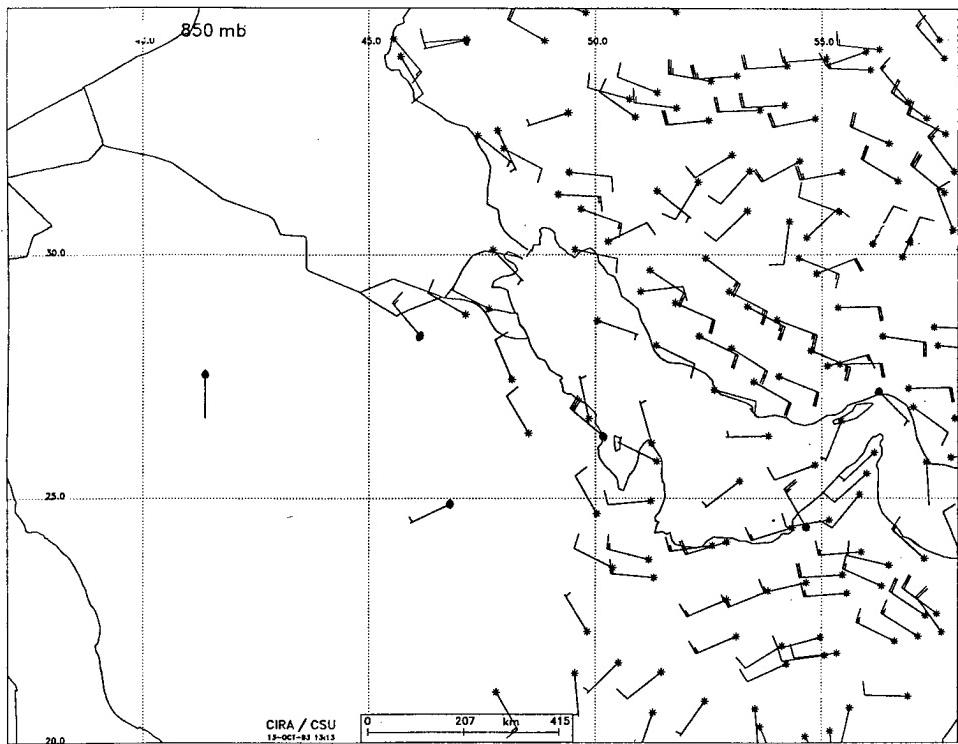
Figure 5. Wind field at 850 mb from TOVS (asterisks, valid at 1027 UTC) and from
rawinsonde (solid dots, valid at 1200 UTC) for 29 May 1991. Short barbs
denote 2.5 m/s, long barbs are 5 m/s.
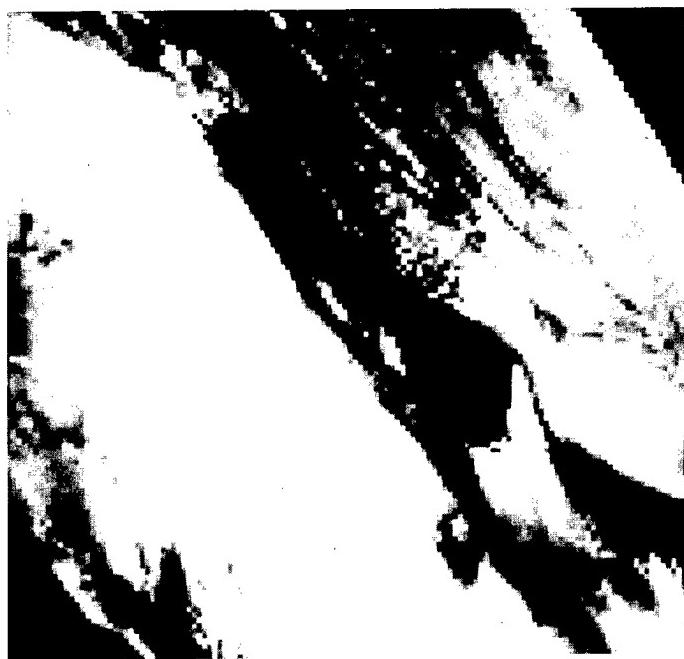
Figure 6. METEOSAT image sequence of the smoke plume for 26 May 1991 at:
(a) 0530 UTC

(b) 0830 UTC
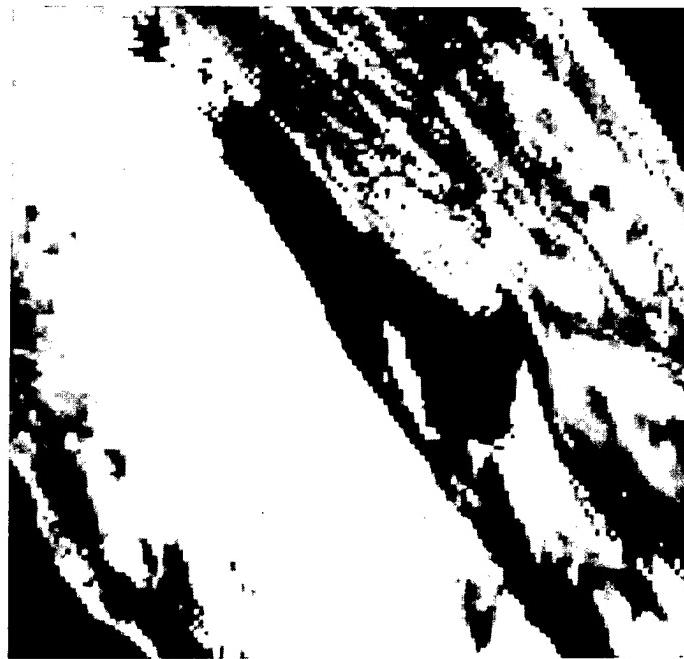
(c) 1130 UTC
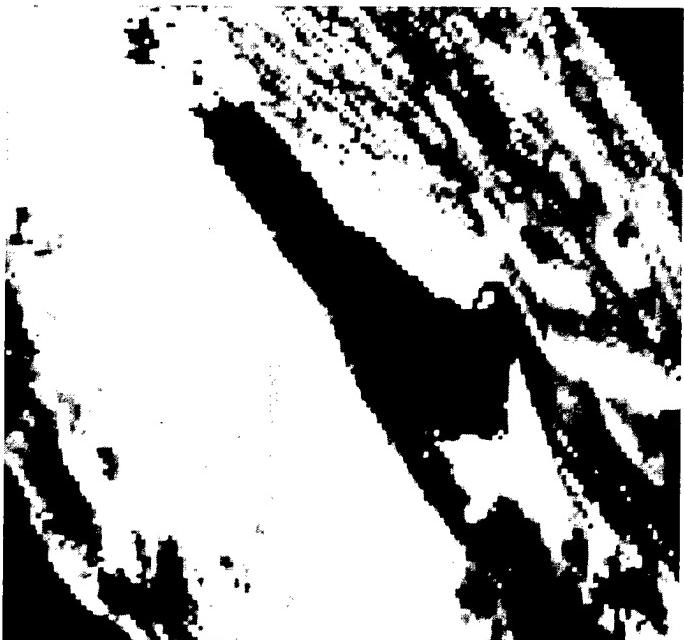
Figure 6 (continued). METEOSAT image sequence of the smoke plume for 26 May 1991 at: (b) 0830 UTC, (c) 1130 UTC.

Intercomparison of satellite-generated estimates of plume optical depth with aircraft lidar measurements was accomplished from 1 June 1991 data. Optical depth values from those sources are plotted in Figure 4. The lidar and satellite measurements are not directly comparable for several reasons, including the inability of the lidar to transmit through the entire thickness of the plume. Nevertheless, relatively good agreement is seen between these estimates from different instruments. It is estimated that the lidar beam penetrated approximately 75 percent of the plume thickness on that date, which is consistent with the slightly lower lidar optical thickness compared to the satellite estimate. Additional intercomparisons and validation are recommended, although opportunities are limited to relatively infrequent coincidences of appropriate data sets.

4.3 Wind and Temperature Fields

Figure 5 shows an example of the 850 mb wind field derived from TOVS retrievals for 29 May 1991 at 1027 UTC. This constant pressure surface level corresponds to about 1500 m Above Sea Level. Wind barbs from the small number of available rawinsonde stations also are plotted in that figure. It can be seen that the satellite-derived winds greatly increase the spatial coverage and horizontal resolution of the wind field analysis. Intercomparison of the satellite and rawinsonde winds shows relatively good agreement in wind directions and fair agreement in speeds over the Persian Gulf area. Wind and temperature fields also were generated at other levels in the vertical, including 700, 500, 400, 300, 250, 200, 150, and 100 mb.

4.4 Plume Movement

A sequence of three visible channel images from METEOSAT is shown in Figure 6 for 26 May 1991. Each of those images is three hours apart, which gives an overview of the plume movement on that day. The northern part of the plume shows very constant location and transport. Variations are noted farther south near the Qatar Peninsula as thicker smoke elements are transported from over the Persian Gulf. These variations also are seen even farther south over the Arabian Peninsula.

5.0 CONCLUSIONS

This study of the Kuwait oil smoke plume used satellite data to detect and characterize that plume. The study is important because it demonstrates how at least some battlefield contaminants can be detected and analyzed remotely, when *in situ* data sources may not be available or offer sufficient spatial coverage. We have shown how the plume boundaries can be identified, and how the (optical) mass of the plume can be estimated remotely. These capabilities can identify where and to what degree battlefield objects and events can be detected by other remote sensing assets. They also provide valuable input and validation to research efforts that seek to better

understand and simulate the transport and dispersion of contaminants in battlefield and other mesoscale environments. Estimates of the 3-dimensional wind field and how the smoke plume actually moved in response to it are examples of how the satellite analyses can contribute.

Enhancements to the current satellite analysis capabilities for smoke and similar aerosols are planned. One improvement will seek to estimate particle optical properties directly from satellite data. The resulting elimination of the need for *in situ* measurements, such as by aircraft, will allow spatial variations in those optical properties to be included in the calculation of optical depth. This will reduce the uncertainty of these estimates. Another planned enhancement is an investigation of the representativeness of the Kuwaiti oil smoke plume transport and satellite analysis methods for other geographic regions.

6.0 ACKNOWLEDGMENTS

7.0 REFERENCES

Baumgardner, D., K. Laursen, and B. Morley, 1993: Optical properties of the Kuwait oil fire smoke plume. NCAR Technical Note (in preparation), National Center for Atmospheric Research, Boulder, CO.

Gifford, F.A., 1991: The structure of atmospheric diffusion at regional scales. Final Report to U.S. Army Research Office under Contract No. P-27096-GS-S, 39 pp.

Greenwald, T.J., and G.L. Stephens, 1988: Application of a doubling-adding model to visibility problems. CIRA Report, Colorado State University, Ft. Collins, CO, 89 pp.

Kidwell, K.B., 1991: NOAA polar orbiter data users guide. NOAA, U.S. Dept. Commerce, Washington, D.C.

Smith, W.L., 1983: The retrieval of atmospheric profiles from VAS geostationary radiance observations. J. Atmos. Sci., 40, 2025-2035.

Weiss, R.E., and P.V. Hobbs, 1992: Optical extinction properties of smoke from the Kuwait oil fires. J. Geophys. Res., 97 (D13), 14537-14540.

REMOTE SENSING OF VISIBILITY OVER MONTEREY BAY

Arunas P. Kuciauskas and Andreas K. Goroch
Naval Research Laboratory
7 Grace Hopper Avenue
Monterey, CA 93943-5502

ABSTRACT

Several techniques are available to relate satellite visible radiance to surface aerosol concentrations, and subsequently values of visible range. A particular method using the two visible channels of the NOAA Advanced Very High Resolution Radiometer (AVHRR), has undergone preliminary validation tests in the Mediterranean Sea[1] and the North Arabian Sea[2], but with limited ground truth data. The Naval Research Laboratory (NRL) is continuing validation of the algorithm in the Monterey Bay region. NOAA AVHRR data are being collected and used with the two channel algorithm to provide estimates of atmospheric optical depth and surface visibility. To provide a validation for this algorithm, NRL is developing an objective technique for measuring visibility by image analysis of photographs taken across the bay. Although detailed correlations of visibility between the two channel algorithm and photographic output are not yet available, this paper presents preliminary comparisons of the visibility parameter from day to day.

1. INTRODUCTION

There are current requirements in the Navy to provide continuous visibility measurements over open water regions throughout the world. An adequate assessment of visibility is important for the conduct of various naval operations, such as at-sea replenishment and search and rescue, as well as being vital to predict the performance of various electro-optical sensors onboard Navy vessels. Unfortunately, in situ measurements of these optical properties are not routinely available. To offset this void, models have been developed to convert radiance from polar orbiting satellite sensors to atmospheric extinction parameters. One such model, SATVIS[3], converts upwelling optical radiance measured by the AVHRR sensor to optical depth values for the marine boundary layer. Preliminary validation work has been conducted by Mineart et al.[2] and Haggerty et al.[1], but the limited ground truth data warrants further studies.

This paper investigates an alternate method of validating satellite optical depth (or equivalently visible range) retrievals to ground truth data. In this method, photographs taken across Monterey Bay are matched in time with satellite passes sensing the same region. Photographic imagery is digitized and contrast at several landmarks is then used as a measure of contrast transmittance. Comparisons are then made to optical depth values obtained from satellite data and processed by using the two channel algorithm, henceforth termed SATVIS. This simple technique allows the observer to relate an objective interpretation of visibility to output from SATVIS. Eventually, refinements of this technique as well as additional information from other land-based instruments will provide direct validation criteria to the SATVIS model.

2. TECHNICAL BACKGROUND ON SATVIS

The SATVIS Meteorological Range Estimation Model[1] ingests and processes satellite data from NOAA's Advanced Very High Resolution Radiometer (AVHRR) sensor. Of the 5 channels within the AVHRR instrument (Table 1) SATVIS uses visible wavelengths (channels 1 and 2) for the optical depth inference and an infrared wavelength (channel 4) for cloud detection. Its output consists of a variety of atmospheric extinction parameters, one of which is optical depth. Several inherent characteristics of the satellite retrieval process limit the applicability of this model. First, SATVIS only operates in cloud-free regions and outside of sunglint regions. Second, SATVIS assumes a uniform aerosol size distribution characteristic of clear marine air conditions with scattering characteristics described by the Henyey-Greenstein phase function. Third, the model includes only single scattering, this being strictly applicable to the low total particle densities.

Table 1. Wavebands of the Advanced Very High Resolution Radiometer (AVHRR)		
Channel	Wavebands (μm)	Center Frequency (μm)
1	0.58 - 0.68	0.63
2	0.73 - 1.10	0.83
3	3.55 - 3.93	3.7
4	10.30 - 11.30	11.0
5	11.50 - 12.50	12.0

Given these assumptions, a brief description of the conversion from satellite sensed radiance to optical depth calculations follows. The upwelling radiance sensed by satellite can be related to the aerosol size distribution in the atmosphere by

$$L_A = \frac{\omega_o F_o}{4\mu} p(\theta) \tau_A ,$$

where L_A is backscattered solar radiance due to aerosol scattering, τ_A is optical depth due to aerosol scattering, ω_o is the single scattering albedo, μ is the cosine of the satellite zenith angle, $p(\Theta)$ is the scattering phase function, where Θ is the scattering angle, and F_o is incoming solar radiative flux. Therefore, optical depth τ_o is a linear function of radiance. The scattering phase function is approximated by the two-term Henyey-Greenstein parameterization[4]. The coefficients of the Henyey-Greenstein formula are parameterized by the ratio of channels 1 and 2 of the AVHRR data. A more complete description of this equation is found in Durkee et al.[4] and Haggerty et al..[2]

370

3. METHOD

The visibility analysis is conducted over the Monterey Bay region which is shown in broad and closeup views in Figure 1. Monterey Bay extends 42 km along a north-south axis between Monterey and Santa Cruz and 16 km across the east-west axis. The NRL site is located in Monterey and is 2.62 km southeast of the Monterey Bay shoreline. The Monterey Bay region provides a particularly favorable study environment since the photographed landmarks occur at a variety of ranges from the NRL sites, so that a range of contrast transmittances can be observed. Photographs of the region were obtained from the roof of the building. Case studies were collected when cloud free conditions existed over Monterey Bay and distant mountain terrain across the bay was not totally obscured. The following describes the products acquired from the satellite and photographic measurements.

3.1 Collection of satellite data and SATVIS data

AVHRR data are routinely collected and archived by NRL in High Resolution Picture Transmission (HRPT) format which samples data at a nadir resolution of 1 km per pixel and includes the five channels listed in Table 1. For this study, two daily passes, morning and afternoon, were collected and archived at NRL. The satellite data were processed using a commercial satellite image processing and display software package on a workstation. Raw data were ingested, calibrated (using standard AVHRR tables), navigated, edited, and finally transformed onto a 64 X 64 km box centered within Monterey Bay (Figure 1).

The algorithm ingests channels 1, 2, and 4 from processed satellite data and produces optical depth values in either image or ASCII data format. For this paper, three distinct measurements of optical depth values were averaged within a 5 X 5 pixel box amid points 1, 2, and 3 as indicated within a line segment in Figure 1. This technique permitted a general assessment of typical optical depth conditions within Monterey Bay during that particular time period.

3.2 Photography

Photographs of the Santa Cruz mountain range were obtained with a single lens reflex camera with a 40 mm lens using high resolution 6 cm X 6 cm color negatives. The camera was positioned on a tripod at a fixed position on the roof of the NRL building at a height of 43 m above sea level. The field of view encompassed four prominent peaks from the Santa Cruz mountain range north of Monterey Bay (Figure 1). For each feature, the heights in mean sea level coordinates as well as distances from NRL are shown. Pictures were taken when the operator could visually detect any portion of the targeted Santa Cruz mountain range under scattered or cloud-free conditions.

The film was processed in color, then digitized onto a 256 level scale. Vertical cross sections were then obtained over four individual mountain peaks as described in Figure 1. Each cross section consisted of a line segment 50 pixels long extending vertically from the sky immediately above the mountain feature, then extending down across the profile of the mountain and finally ending over the bay below the terrain. From this cross section, an assessment of visibility can be made by calculating gradients of brightness between the sky and mountain terrain as well as from the mountain terrain and the bay. The following sections describe a particular comparison of SATVIS and photography, and a summary of five separate occasions.
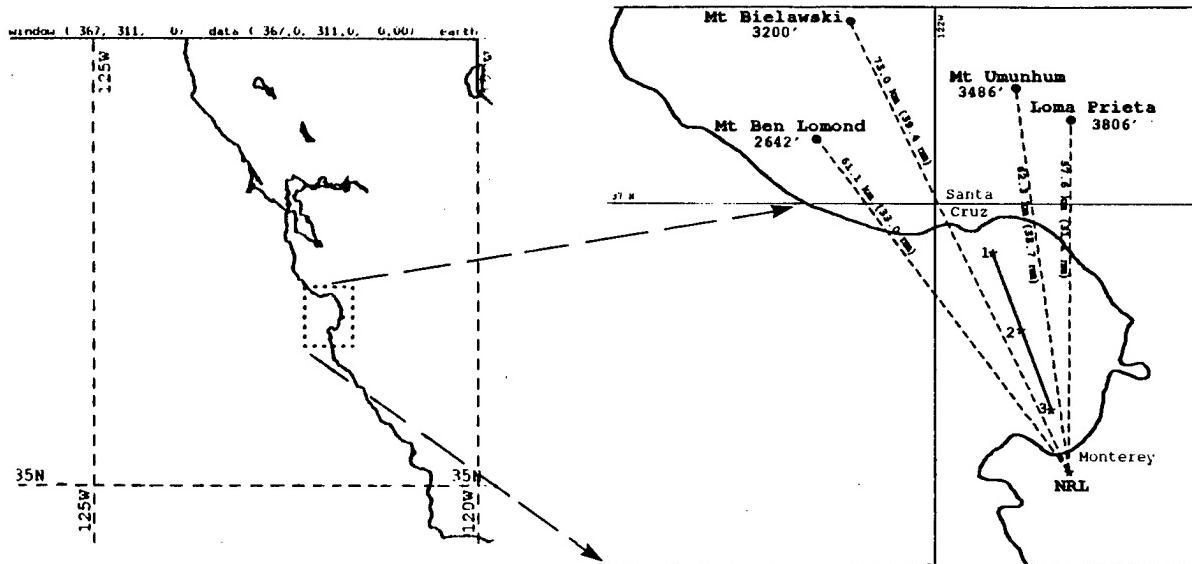
Figure 1. Map of California coast and an insert (dashed box) which details the study region around Monterey Bay. Points within the line segment annotated across the bay shows where optical depth values from the AVHRR were calculated.

4. RESULTS

4.1 Case Study, March 22, 1993

A high pressure system dominated the eastern Pacific Ocean during the day. A visible satellite image at 23:51 UTC (15:51 PST) (Figure 2) displays a clear region off the California coast. The Monterey Bay is cloud free providing suitable conditions for both satellite data and photography across the bay.

Figure 3 displays the optical depth field over Monterey Bay during the time of the satellite pass. Throughout the bay, the optical depth field varies between 0.13 to 0.15, indicative of fairly low aerosol amounts and thus high visibility. The higher optical depth shadings shown in white along the eastern edge of the bay are probably due to contamination of data resulting from shallow water depths which cause enhanced reflectivities.[2]
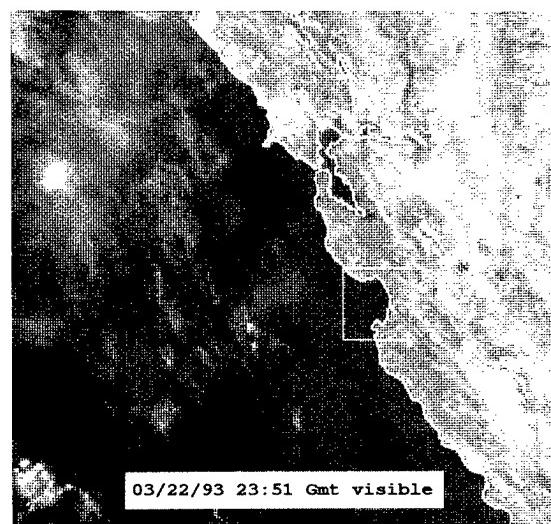
Figure 2. Visible satellite image off the California coast on 22 March 1993 at 23:51 UTC.

03/22/93 23:51 Gmt

Santa Cruz

optical depth legend

dark gray: < .13
middle gray: .13 - .15
white: > .15
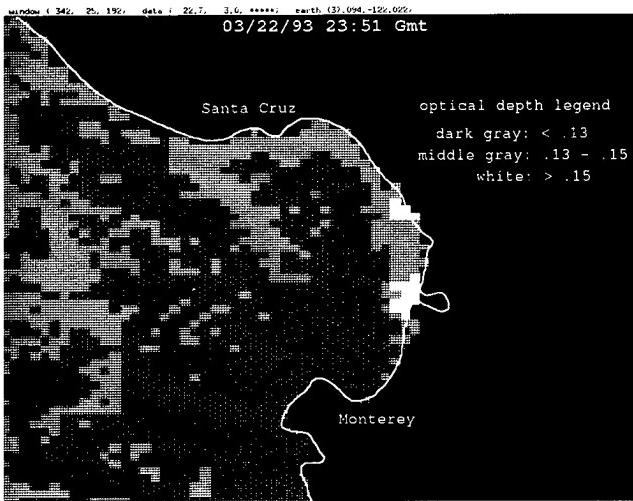
Monterey

Figure 3. *Image of optical depth shadings within the Monterey Bay region for 30 March 1993 at 23:51 UTC.*

Figure 4. *Vertical cross section of brightness intensity across Mt Ben Lomond.*

During the time of the satellite pass, a photograph was taken across Monterey Bay as described in Figure 1. From the processed film, a vertical cross section over one of the mountain peaks, Mt Ben Lomond, is presented in Figure 4. The profile in the figure shows three distinct brightness regions: the sky contains the highest brightness levels (pixels 0 to 25) followed by moderate brightness levels across the terrain (pixels 25 to 32) and finally dark shades associated with Monterey Bay below the terrain (pixels 32 to 50). Of interest in this study are the brightness gradients (contrast) associated with the interface between sky, terrain and water features. Visually, visibility across the bay was designated as moderate. Conditions with poor visibility are noted by weak or no brightness gradients between sky, terrain and water.

4.2 Composite of 5 case studies

Figure 5 focuses on the region between the sky and terrain as well as the terrain and water across Mt Ben Lomond.

Figure 5. *Composite of brightness gradients along profile of Mt. Ben Lomond for 5 case study days.*

The profile has been filtered so that only contrast greater than 10 brightness counts between adjacent pixels are plotted. For the sky-terrain interface, only 3 days were detected to produce an appreciable contrast. The other days showed no appreciable difference because

of either haze or scattered stratus clouds on top of the peak. All 5 days depicted significant contrast levels between the terrain-water interface.

Figure 6 represents the average terrain-water contrasts for all 5 days over Mt Ben Lomond and is related to the optical depth measurements obtained from SATVIS calculations over the three points in Monterey Bay (see Figure 1). From the vertical scales on the graph, it would be expected that an inverse relationship would exist in the plots during clear conditions, when the contrast from photographs is high, optical depth values would be low. This condition only appears to be true for 22 March 1993. Some of the discrepancy can be attributed to aerosol amounts existing above the boundary layer, which would distort SATVIS calculations. However there is undoubtedly significant uncertainty in the use of the difference of only two pixels to estimate contrast transmittance. New efforts currently under review analyze statistics of the gradient region with somewhat more consistency.

5. CONCLUSIONS

A technique for validating SATVIS has been applied. A parameter related to contrast transmittance was obtained from photographs taken across Monterey Bay and related to optical depth measurements calculated by SATVIS. From the 5 case study days analyzed, the optical depth values derived from SATVIS and the photographic contrasts across Monterey Bay show that a statistical analysis may be appropriate to reduce errors associated with feature location, changes of background albedo, and photographic processing. However, the results are preliminary until a larger data set is collected.

Photo Contrast vs SATVIS
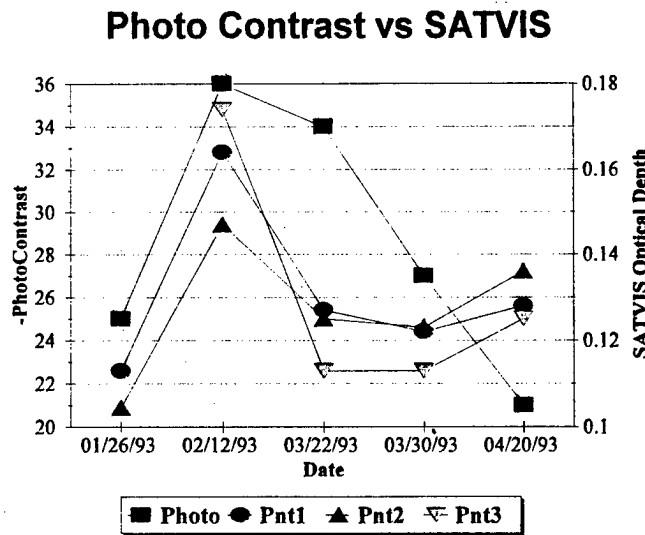
Figure 6. Contrast from photographs between the terrain-water interface vs SATVIS output on Monterey Bay for 5 case days.

NRL is continuing the collection of data from satellite and ground-based sensing instruments for validation of the SATVIS model. These techniques are being supplemented by a pair of multifrequency rotating shadowband radiometers (MFRSR) which provide an automated measurement of total optical depth of the atmospheric column between the sun and the earth surface. These instruments are collocated on the roof of the NRL building. Data collected from these instruments should provide an accurate assessment of local atmospheric extinction parameters which will further bolster ground truth measurements to be compared with SATVIS data.

6. ACKNOWLEDGMENT

7. REFERENCES

1. Haggerty, J. A., P. A. Durkee, and B. J. Wattle, 1990: A comparison of surface and satellite-derived aerosol mea-surements in the western Mediterranean. J. Geoph. Res., 95, 1547-1557.

2. Mineart, G. M., J. C. Hinz, T. F. Lee, and J. Haggerty, 1991: Validation of the SATVIS Meteorological Range Estimation Model in the North Arabian Sea. NRL TN 190, Naval Research Laboratory, Monterey, CA, 59 pp.

3. Durkee, P. A., D. R. Jensen, E. E. Hindman, and T. H. Vonder Haar, 1986: The relationship between marine aerosol particles and satellite-detected radiance. J. Geophys. Res., 91, 4063-4072.

4. Kidwell, K. B., 1991: NOAA Polar Orbiter Data (TIROS-N, NOAA-6, NOAA-7, NOAA-8, NOAA-9, NOAA-10, NOAA-11, and NOAA-12) Users Guide. National Oceanic and Atmospheric Administration, NESDIS, Washington, D. C.

Session V

MITIGATION AND EXPLOITATION

A REVIEW OF MODEL EVALUATIONS FOR TARGAC

Patti Gillespie
Battlefield Environment Directorate
U.S. Army Research Laboratory
White Sands Missile Range, NM 88002–5501

ABSTRACT

The EOSAEL target acquisition model TARGAC has undergone at least ten completed model evaluations. The discussion in this paper covers two aspects: (1) the structure of the submodules within TARGAC and its contribution to overall error, and (2) the results of completed model evaluations. All of the ten model evaluations mentioned above are for the overall TARGAC model prediction. Some attention will be given to the evaluation of sub–models used within TARGAC. These models have been subject to separate model evaluation. Preliminary recommendations for the overall validation, verification, and accreditation process for TARGAC will also be discussed.

INTRODUCTION

One of the six steps in the validation, verification, and accreditation (VV&A) procedure defined for EOSAEL models[1] is the comparison of model results. The EOSAEL model TARGAC integrates a sensor performance model[2] with a target–background contrast model and with several atmospheric modules, most of which are EOSAEL models[3]. This paper will discuss primarily the overall TARGAC model evaluations, and then cite and review results of the model evaluations done for the separate atmospheric modules used by TARGAC. Thus this paper does not present any new results, but draws together a variety of studies done on TARGAC into one document. This paper does attempt to make modest recommendations about future direction for the Army target acquisition model for EOSAEL and the Integrated Meteorological Systems (IMETS).

TARGAC COMPARISON OF MODEL RESULTS

TARGAC is a target acquisition model based on the Night Vision Sensor Performance Model with extensive atmospheric and battlefield effects folded into the acquisition range calculations. TARGAC uses several EOSAEL modules to make its environmental calculations, and itself an EOSAEL module[3]. Environmental, scenario, and sensor information is input to TARGAC, and detection and recognition ranges are produced as output from TARGAC.

TARGAC consists of three major model components: a sensor performance model, a target and background contrast model, and the atmospheric effects model. The section in this paper on comparison of TARGAC to measurements (observer data) is an overall comparison of these three model components combined into a single

prediction to actual acquisition results. If any of the three components are weak for a given circumstance, the entire model may appear to give erroneous results. All models are approximations to reality, and thus will not always compare favorably to measurement. The TARGAC Users Guide will attempt to detail cases for which TARGAC may give less than optimum results[3].

The sensor performance model in TARGAC is the Night Vision Sensor Performance Model, also known as ACQUIRE and FLIR92[2]. The VV&A of that model is under the purview of the CERDEC Night Vision Electro–OpticsSensors Directorate (NVESD). Targets and backgrounds are characterized with different models for the infrared and visible wavebands. The visible target–background model is based on the reflectances of surfaces, and most of these reflectances are derived from measurements. The thermal target and background model is a mixture of an empirical and a first principles model. The simple version of this model that is incorporated in TARGAC is based on models like GTSIG and PRISM[4].

A detailed VV&A plan for TARGAC is not presented here, but rather a brief survey of model evaluations and comparison to data that can be used as a basis of the VV&A is presented. A VV&A six–stepplan has been detailed for EOSAEL[1]. Step four in the EOSAEL VV&A plan is a comparison of model results. The comparisons to models for TARGAC described in this paper will fulfill item 4 in the list for the EOSAEL General Plan for V&V process.

Experimental data from at least eleven field tests have been used in the evaluation of the TARGAC model. These eleven tests are listed in Table 1. None of these tests were conducted for the explicit purpose of evaluating TARGAC, or any specific target acquisition model. These tests were conducted to study the effects of battlefield smokes and aerosols on military systems. Work has been completed for ten of these studies. These validations are for the overall predictions of the TARGAC model. Other validations for submodules of the TARGAC model have been conducted, but are not included here. TARGAC includes sensor options for four types of sensors; thermal, direct view optics (DVO), image intensifiers (NVG), and silicon televisions. The validation studies cited here in Table 1 are for the thermal and DVO sensors only. Much of the validation for DVOs can be extended to image intensifiers and silicon televisions for the atmospheric part of the model.

TABLE 1. Description of model evaluation for TARGAC

Test Name	Sensor	Study Date	Test Site
SNOW III West	Thermal	1987,1987, 1989	Camp Grayling, MI
BEST ONE	Thermal & DVO	1987,1989	Oldebroek, Netherlands
Smoke Week V–B	Thermal & DVO	1987,1989	Fort Huachuca, AZ
Smoke Week VII	Thermal	1986	Fort Sill, OK
Smoke Week VIII	Thermal & DVO	1987,1989	Eglin AFB, FL
Smoke Week X	Thermal	1990	Fort Huachuca, AZ
Smoke Week XI	Thermal	1990	Valcartier Range, Quebec, Canada
Smoke Week XII	Thermal	1991	Eglin AFB, FL
Smoke Week XIII	DVO	1992	Eglin AFB, FL
Smoke Week XIV	Thermal	1993	Eglin AFB, FL
BEST TWO	Thermal	late 1993	Camp Mourmelon, France

When model and experimental acquisition ranges are compared, the model is generally said to either under–predict or over–predict the acquisition ranges. This means simply that the model either predicts shorter or longer acquisition ranges than those found in experiment. Whether this is good or not depends on the use of a tool such as TARGAC. If TARGAC is used for planning by our forces using our sensors and threat targets, then ideally the model should predict acquisition ranges as close to the actual ones as possible. Predicting shorter acquisition ranges means that the user will be alerted to look for a target sooner than it actually appears. Conversely, if the model predicts longer acquisition ranges than actually occur, the targets will appear sooner than expected. If TARGAC is used to determine at what range our forces will be detected, over–or under–prediction of acquisition ranges takes on a different meaning. Considering these factors, accurate prediction of acquisition ranges is the best outcome, and understanding the circumstances under which under– and over–prediction take place is the next best occurrence.

The model evaluation studies have been conducted by a variety of groups over the last seven years. Unfortunately, the techniques used in all these studies are not uniform. The later studies, from Smoke Week X to present, incorporate standard techniques used in perception testing. This includes observer screening and training and formal observer testing of images. Another observation is that most tests have pointed out a limitation of the model or an effect that is not accounted for. The general conclusions of each test is outlined in the paragraphs below.

Thermal Model Comparisons

The results for the thermal model are presented first. The analysis of the first five tests in Table 1 are not as quantitative as conclusions drawn from Smoke Weeks X through XIV. These results are still very important because they can point out weaknesses in the model, therefore, the results for the first five tests are summarized more briefly than later results. The thermal model was evaluated using data from the SNOW–III West test[5,6,7,8]. The SNOW III West test was held at Camp Grayling, MI by the U.S. Army Cold Regions Research and Engineering Center during the winter of 1984–85 for the purpose of comparing military acquisition sensors under winter obscuring conditions. The model was found to make accurate thermal contrast predictions, but the model under–predicted performance. This was probably due to motion cuing. Motion is not accounted for by TARGAC since it uses a static performance model. Petzko[6] reported that the thermal model for the contrast of exercised tanks contrasted against undisturbed snow gave accurate results, however, the changes in temperature of the targets when going from off to idle to exercised seemed incorrect. This thermal model has since been replaced by the first principles model TCM2[4] that is a more accurate representation of target thermal signatures.

The BEST ONE test was conducted in September 1985 in the Netherlands. One of the major reasons for conducting this tests was to study burning targets. TARGAC is designed to predict target acquisition through clear air, weather, and smoke; and so video data from before the ignition of the fires was used in this comparison. The BEST ONE experimental thermal data produced results that were so mixed that no specific results could be concluded[7,9]. Environment conditions during BEST ONE were sometimes foggy and low contrast, and this may have impacted the results[10].

Smoke Week V–B was held at Ft. Huachuca, AZ during October and November 1983. This was a dynamic search tests with one purpose being to provide data for the analysis of probability of detection and recognition of target moving in and out of defilade in clear and obscured environments. The test grid was rolling desert terrain in which targets could be hidden while moving through the terrain. The thermal model consistently under–predicted the recognition ranges from Smoke Week V–B thermal data[7,9]. There were fewer correct responses for detection than recognition. It is believed that this was due to low contrast conditions most of the time during the test.

Smoke Week VII was conducted at Ft. Sill, OK with the primary aim of the test being the evaluation of simulated threat artillery–delivered smoke screens. The site was grassy, gently rolling terrain with scattered, small clumps of trees. The targets were stationary, but idling. TARGAC had a tendency to under–estimate thermal contrast for the thermal data from Smoke Week VII[8]. There was a great deal of scatter in that data.

Smoke Week VIII was conducted at Eglin AFB, FL during May 1986 with the stated goal of evaluating the performance of thermal imagers in detecting five stationary targets and one moving target in an obscured environment. Smoke Week VIII thermal data produced moderately accurate results compared to TARGAC, with low contrast cases causing some problems[7,9]. The initial look at the data showed that although the targets were often warmer than the background, the model often predicted the opposite. The choice of background in the model did have a profound, and unexpected effect on the model results. The low contrast cases resulted in the model over–predicting the acquisition range; that is, predicting a longer acquisition range than an experiment would show.

Observer data from Smoke Weeks X through XIV were obtained through the use of the then Edgewood Research, Development, and Engineering Center (ERDEC) (now Army Research Laboratory (ARL)) Personnel Response Evaluation System for Target Obscuration (PRESTO) both during the field test and later in the laboratory. The TARGAC model was evaluated by comparing the model's predicted detection probabilities or ranges to the measured detection responses from observers viewing the target with laser goggles and as measured by the PRESTO system. Meteorological conditions for all of these tests were measured by the Atmospheric Sciences Laboratory (now ARL) Transportable Atmospheric Characterization Systems (TACS) team. Additional transmission data were obtained using either the ERDEC MultiPath Transmissometer/Radiometer (MPTR) or the ARL Research Visible and Infrared Transmissometer (REVIRT). For these later Smoke Week tests the targets were stationary at a fixed and known distance. For this reason, observer data from these tests were compared to probabilities of detection at the known target distance.

Smoke Week X was conducted at Ft. Huachuca, AZ at the U.S. Army Electronic Proving Ground West Range during late September and early October of 1988. Trials were held in clear air and with smoke screens having fronts from 0.5 to 1.0 km in length at ranges of approximately 0.5 to 1.0 km from the sensors. The obscurant materials included fog oil, phosphorus, kaolin/silica, brass, and graphite. Targets for all trials moved through natural arroyos that provided some defilade positions. All targets were M35 (2.5–ton–trucks). The thermal data from Smoke Week X had targets with unique hot spots, resulting in obvious cuing from the hot spots. In this case, the acquisition ranges were under–estimated by TARGAC[11].

Smoke Week XI was conducted at Valcartier Range in Quebec, Canada during February and March of 1989. The thermal predictions for this test fall into three categories. For the high visibility, high transmission cases, TARGAC over–predicted the acquisition range compared to the experimental data. Under moderate visibility TARGAC under–predicted acquisition ranges; that is, predicted shorter acquisition ranges than the experimentally determined ones. Finally under low visibility conditions (falling snow), TARGAC was accurate. Locke concludes[11] that the contradictions between model and measurement are not due to problems with the estimate of target contrast by the model. The model contrast predictions were comparable to the values measured at Smoke Week XI. The model does over–estimate the probabilities of recognition compared to observer results. The differences between model predictions and observer responses, when they occurred, are perhaps due to differences in performance parameters (imager or observer characterization)[11]. This test is the only evaluation of TARGAC for snow conditions during Smoke Week tests.

Smoke Week XII was conducted at Eglin AFB during May of 1990. The test grid was located on flat, sandy terrain surrounded by a U.S. southern pine forest. Ground cover on the test grid was burned and removed before the trials began. Obscurants disseminated during Smoke Week XII included fog oil, brass, phosphorus, graphite, aluminum, diesel smoke, and dust. The targets for this test were T–62 tanks and a M–60 tank. The Smoke Week XII thermal data included a number of low contrast situations. TARGAC under–estimated the observers ability to detect targets for the thermal (observer) data from Smoke Week XII[12]. Both measured and predicted thermal contrasts on the order of 1 K for many of the experiments at Smoke Week XII, and the noise for these measurements was on nearly the same order. The range between the target and observer was no greater than 3 km, and the short ranges may have contributed to the problems with low contrast conditions in making acquisition predictions[12].

Smoke Week XIV was held during May of 1992 at Eglin AFB at Range C52–A. The range was prepared

in a similar manner as for Smoke Week XII. Obscurants disseminated during this Smoke Week were fog oil, brass, phosphorus, graphite, aluminum, and dust. A tactical vehicle was used as the target. Smoke Week XIV data were used to compare the thermal contrast models in TARGAC past and present. The thermal contrast model originally in TARGAC is known as TCM, and the new thermal contrast model is known as TCM2. TCM2 is a first principles model that makes contrast predictions for a menu of targets and backgrounds. The target menu includes a variety of tanks, APCs, and other tactical targets. Backgrounds are generalized descriptions such as growing/dormant or sparse/moderate/dense. Some TCM backgrounds (empirical backgrounds) are still available in TCM2. The user may also input target and background temperatures in TARGAC using the generic target/background feature. For the purposes of this discussion, the two versions of TARGAC are known as TARGAC (with TCM) and TARGACxTCM2.

TARGAC and TARGACxTCM2 predicted the PRESTO probability of detection within 0.1 when the transmittance values were 20% or higher. When the transmittance values were between 0% and 5%, however, TARGAC and TARGACxTCM2 predictions were as much as 50% higher than the probability of detection experienced by PRESTO observers. This difference appears to be caused by the models's over–estimation of target contrast [13]. This means that the model computed values of the target contrast to background were noticeably higher that the values derived from measurements made a Smoke Week XIV. The measurement of apparent contrast for this analysis was done by the ARL Multispectral Acquisition and Evaluation System for Target Research Origination (MAESTRO). Further comparison of clear air apparent contrasts showed that the two models had good agreement between predictions, but there was significant disagreement between model and measurement of apparent contrast, especially for the low transmission cases [13]. Eventually, a total of eight (8) different backgrounds were used in the TARGACxTCM2 model. Since the two models gave similar predictions, only the newer TARGACxTCM2 model was used in these additional calculations. All of the eight backgrounds could have described the environment at Eglin during the time of the test. These backgrounds are tall grass growing, tall grass dormant, mowed grass growing, mowed grass dormant, trees, dry plowed field, standard sand, and growing and sparse foliage. One of these backgrounds gave good agreement with the MAESTRO data for apparent contrasts. The contrasts for MAESTRO and one of the backgrounds (dormant tall grass) were about 1 or 2 K, whereas target to background contrasts using some of the other backgrounds were as large as 7 to 10 K. The target–background contrast for the original choice of background (growing tall grass) was about 4 K. Thus the choice of background from the menu can be crucial for making accurate acquisition predictions with TARGACxTCM2 (or TARGAC) [13].

Thermal data from BEST TWO and comparisons to TARGAC are still in progress [14] at this time. This comparison has indicated, at least informally, that TARGAC can make reasonable predictions, but with some caveats. This evaluation is the subject of another paper at this conference, "Evaluation of Target Acquisition Model TARGAC Using BEST TWO Observer Performance Data".

Direct View Optics (Visual) Comparisons

Early comparisons of the visual model to experiments were done with data from BEST ONE and Smoke Week V–B. Visible imagery from these tests was examined by Burlbaw and Gale[7]; later visible imagery from Smoke Week VIII was studied by Burlbaw, Matise, and Bean[9]. The visible imager was a color video camera used as part of the SMART (Simultaneous Multi–spectral Absolute Radiometric Transmission) System. The reports by Burlbaw[7,9] used a different scheme for evaluating the observer performance than the one used in the later Smoke Week tests (as discussed earlier). In the Burlbaw reports[7,9] targets were characterized as easily detected, barely detected, possibly detected, and not detected. These codes were used because of some of the special conditions for these tests. As a result, the information derived from this scheme can be interpreted as follows: a not detected score for an event for which the target was beyond the model predicted detection distance only confirms that the model is not over–predicting the detection range. Similarly, an easily detected score for an event for which the target was closer than the model predicted detection range confirms that the model is not under–predicting the acquisition range, that is, predicting an acquisition range that is shorter than measured. Although this is not a standard method by which observer responses are recorded in psychophysics, an interesting set of information was derived from these tests. Burlbaw[7] reported that the NVESD performance methodologies generally under–predicted the systems performance of all the electro–optic systems at the SNOW

383

III West test with this most probably due to target motion aiding the observers detecting the targets further away than the model predicts.

The BEST ONE visible data were examined by Burlbaw and Gale. The data from this test showed that for trucks and armored personnel carriers, the model was 100% successful in predicting the acquisition ranges for the targets. For tanks and personnel the model varied between a 79 and 93% success rate.[7] Results of comparing Smoke Week V-B data with model calculations showed similar results to the BEST ONE data comparison. Further reflections on these work showed that the majority of the "successes" were for easily detected and not detected cases for which there was a larger discrepancy between model predicted acquisition ranges and actual target ranges, which provides little information about the model. The "failures" were generally for borderline cases where the most information about the actual detection distance would be available. In general, the model tended to over-predict the detection and recognition ranges.[7] Characterization of the visible imagers and the associated optics may have contributed to some of these discrepancies. The second Burlbaw report[9] concludes that the DVO model of TARGAC does a good job of predicting acquisition ranges.

Visible data from the Smoke Week VIII data were also used in a model evaluation. The TARGAC model successfully predicted detection most of the time for the visible model for this test. A closer look reveals that when targets were predicting acquisition out to four km, the targets were actually at distances of less than one km.[9]

Smoke Week XIII produced data that was compared to the photopic or visual wavelength model in TARGAC. Smoke Week XIII was conducted at Eglin Air Force Base during 3-17 May, 1991. The test site on the range was C-52A, which is flat, sandy terrain surrounded by a U.S. southern pine forest. The test site was prepared in a manner similar to the ones for Smoke Weeks XII and XIV. The six targets used in Smoke Week XIII included armored tactical vehicles. Obscurants disseminated during the test included fog oil, brass, phosphorus, graphite, aluminum, and dust. Since obscurants played such an important part in the data from this test, the smoke model in TARGAC was exercised for all pertinent scenarios.

Two important model limitations were identified in this analysis. The first was a problem in interpolation in the sensor performance model section of TARGAC[15]. Since TARGAC is currently being upgraded to include the new CERDEC (Night Vision) sensor performance model, the final resolution to this problem is on hold. The other problem has to do with calculations in the atmospheric model using visibilities greater than 50 km[15]. Since most instruments do not accurately measure visibility above 50 km, and the "problem" probability of detections occurred for high visibility coupled with smoke conditions, when the maximum allowed visibility was limited to 50 km and no further problems with model predictions occurred.

TARGAC generally predicted PRESTO results. The difference in the probability of detection of TARGAC and PRESTO was 0 (zero) for 28% to 48% of the time; while 66% to 80% of the time, TARGAC predictions were within ± 0.1 of PRESTO results[14]. The main concerns with TARGAC that cause any of the deviations between model and measurement are the two discussed in the paragraph above. One of these is an interpolation problem, and the other has to do with how the visibility model works above 50 km visibility. The visibility can easily be limited to 50 km.

SUB-MODULE COMPARISON TO DATA

The physical models for atmospheric effects used in TARGAC to model extinction, contrast, smoke, and climatology are either based on data, or have undergone some evaluation or comparison to data. In this section each of these models is briefly examined, and the type of evaluation is mentioned. The weather and battlefield effects models used in target to model the environment are discussed briefly in the paragraphs below. This discussion is included to demonstrate that a relatively complicated model like TARGAC can be validated on several levels, and there are pitfalls in each type of validation.

Extinction is modeled in TARGAC through a combination of the use of XSCALE to provide aerosol scattering (attenuation)[16], and a parameterization of LOWTRAN[17] to provide the molecular absorption.

XSCALE is for the most part, based on empirical models, developed to mimic closely, at least one set of actual data. These data sets are cited in the XSCALE Users Guide[16]. The rain, ice fog, blowing snow, and slant path infrared models in XSCALE have not been compared to data[16]. When a model is used outside the region of its applicability, XSCALE writes messages concerning the error and does not continue computation.

XSCALE has been compared to data[18] for the case of the vertical structure algorithm. The vertical structure algorithm is an attempt to quantify the visible extinction in a vertical extent, and is based on data obtained at two field tests in Europe (Meppen and Cardington). That model was modified to obtain better computer run times and improve agreement with specific data sets[19,20]. Data from Meppen and Cardington, as well as data from a third test in Sprakensehl, were compared to the four types of profiles computed in XSCALE: cloud, sub-cloud,haze, and clear air. Data were available for only a limited number of altitudes, but comparisons with data show that the haze and stratus clouds were particularly well represented in XSCALE[18].

The XSCALE horizontal path model has been evaluated with data also[10,16]. The fog and haze models were evaluated with BEST ONE data. This studied concluded that actual fogs were difficult to parameterized as a single type of fog, and that other contaminants, such as pollution might impact the resulting propagation of radiation. Neither the fog nor haze data were good matches to the XSCALE model, but on the average, the XSCALE model was not a bad approximation[10]. The XSCALE Users Guide[16] contains a summary of the model evaluations done for XSCALE. A study by Shirkey and Hutt that is described in the Users Guide determined that XSCALE calculations for snow and fog agreed with data well for visible wavelengths, and not as well for infrared wavelengths. This difference between calculations and measurements was attributed to off-axis forward scattering that is not accounted for in the XSCALE model. This shortcoming in the XSCALE model results in XSCALE calculating less transmission than might actually occur.

LOWTRAN 7 is parameterized for use in TARGAC because it provides an alternative to the more accurate, but much slower LOWTRAN 7 for predicting broadband gaseous transmittance along a path through the atmosphere. Fiegel comments in the conclusion of his report on the parameterization of LOWTRAN 7 that the parameterization agrees with actual LOWTRAN calculations to within 7% on the average, although some cases may exhibit a much larger discrepancy[17]. LOWTRAN calculations should definitely be used when resolution needs are 5 cm^{-1} or smaller, but TARGAC applications are for lower resolution cases. LOWTRAN itself is based on measurements and the high resolution, first-principlesmodel FASCODE. LOWTRAN is considered to be the industry standard for low resolution atmospheric transmission calculations. These models have been compared to data for many cases. These models also assume that only natural atmospheric gases are present in the typical amounts for a given elevation above sea level. Other gases that might provide absorption are not accounted for by the LOWTRAN, and therefore the parameterized model.

The visible contrast calculations (delta Eddington (DE) model) that produce a sky to ground ratio used in the contrast transmittance, has been evaluated both by comparison to a more exact model[21] and by comparison to data[22]. More exact radiative transfer models are not used because of the computer time and code size burden. In the past an empirical model with some very grave limitations that this DE does not have, was used to calculate sky-to-groundratios.

Davis finds that the model performs well for the calculation of the apparent contrast of an object against the sky, but displays some error for the apparent contrast of the object against the ground. The model does not calculate the inherent radiance of the object well due to the approximate nature of the treatment of the reflection of diffuse radiances, especially for targets whose outward normal is nearly horizontal. Despite this shortcoming, the model does show the ability to track the apparent contrast against the ground into the limiting ranges of near zero visibility. The DE model was evaluated for its ability to calculate contrast transmittance for a variety of scene parameters. The model evaluates the contrast transmittance within 10-15%of the results generated by

Monte Carlo calculations, except for lines of sight in the direction of the sun and for scenes with low surface reflectance[21].

In the comparison to data, the scenarios are all high visibility cases and model demonstrated good agreement with data, especially when compared to the older empirical model, formerly used for sky to ground ratio calculations. Sky to ground ratios as calculated by the DE model varied about 10% from the measured values, as compared to 66% variation between the older model and measurement for cases when the observer is nearly looking at the sun[22]. When the line of sight is not in the direction of the sun, both the older model and the DE model did under-predict the sky to ground ratio by as much as 38%. To see these predictions in a more realistic light, the lines of sight nearly looking at the sun generated sky to ground ratio measurements of 7.5 in some cases and the DE model predicted 6.7, and the older model predicted 2.5. For the lines of sight looking away from the sun, measurements of sky to ground ratio were 3.0 in some cases, and the DE model gave 1.8 and the older model 1.8[22]. The DE model reproduces the behavior of real data sufficiently with so little computational overhead that the use of this approximate model is justified.

Smoke modeling in TARGAC is done through a greatly simplified parameterization of COMBIC[3]. COMBIC has many options for various smokes, making the validation of the model extremely difficult. Ayres [23] has summarized the COMBIC evaluations in the Users Guide for COMBIC. The model has been qualitatively evaluated for several typical smokes of military interest[23] showing reasonable results.

The climatology option in TARGAC uses the EOSAEL model CLIMAT. This model is derived from climatological data obtained from all over the world. As more data is available, CLIMAT has been updated. An evaluation study has not been done for this model. The User Guide for CLIMAT gives the limitations of the climatology database[24].

SUMMARY

The physical models that underlie the weather and battlefield effects portion of the TARGAC have been compared to data in various circumstances. Since most of these models are either approximate or empirical, the most important feature to understand is that these can breakdown for specific circumstances or have limited application. The TARGAC model does not do extensive error checking to insure that sensible and consistent inputs are used throughout. Inputs are checked to insure that they are within a stated range for a given variable. The user of a model like TARGAC should use common sense when interpreting the results of such a model, however, the User Guide[3] attempts to point out inappropriate uses of the model and shortcomings of the model.

One suggestion for the completeness of the VV&A process would be a sensitivity study of major submodules for TARGAC. For example, perception variation among individuals might give rise to uncertainties in the sensor performance model that overwhelm all other uncertainties in the sensor performance model. Similarly, visibility variation may overwhelm uncertainty in temperature or relative humidity. These questions are unanswered at as yet, but are outside the scope of this study. To conduct such a study using only the TARGAC model, one would decide upon several parameters that are basic to each sub-model such as visibility, aerosol type, humidity, and temperature for the weather effects model; and then vary these parameters and examine the variability of the calculated acquisition ranges. For the background-target model, one would simply examine the effect of the different targets and background, including changing the size of the targets, holding the weather effects and sensors constant. For the sensor performance model, one would examine the differences among the different sensor types (direct view optics or thermal imagers, for example) as well as the differences among the specific sensors in a given sensor type holding the weather effects and target-background models constant. The permutations for this study are almost endless for a model like TARGAC, therefore a careful and thoughtful choice of parameters to vary would be necessary. This type of study would determine the area of the model that would be most important to improve in the future.

One type of test that has not been done with TARGAC is a field test with side by side sensors from the four

types of sensors included in the TARGAC model. This type of test would allow the user to determine for a given set of conditions how well the model performed for all sensor types. All of the test data used with TARGAC thus far have required that the user define his own sensor. Obtaining sensors that are included in the menus for each of the four sensor types from Army inventory for use in such a test would be the first step in such a test. Before pursuing such a goal, updating TARGAC to include the latest version of the sensor performance model as developed by NVESD, as discussed below, is recommended.

Ongoing efforts to include additional atmospheric effects in TARGAC include calculations for turbulence, clutter, emissive sources, target shadows, and scene shadows. Also the sensor performance model is being updated to include the new sensor performance model developed by NVESD. As models become more complicated and offer many options, codes can become convoluted. As resources permit, a modularization of TARGAC is recommended to facilitate future updates of physical models. The first step in modularization would be to develop a design document and flowchart.

To summarize the results of the TARGAC overall model evaluations conducted over the last several years we can make some general comments. For the thermal model in TARGAC the acquisition ranges were under-predicted for six of the evaluations, over-predicted acquisition ranges for two of the evaluations, provided mixed results for which no specific conclusions about over or under-prediction could be made in two of the cases, and made accurate predictions of the acquisition ranges for two of the evaluations. Looking at the low contrast cases (four evaluations) separately, the acquisition ranges were predicted accurate for one evaluation, over-predicted for one of the evaluations, and under-predicted for two of the evaluations. Motion and hot spot cuing are two very important factors in acquisition using thermal devices. The TARGAC model does not account for either phenomena. The DVO or visible sensor model made accurate predictions for the four evaluations done, with the caveat of being careful of results computed using very high visibilities (>50km). These model evaluations are to be the basis of a future VV&A for TARGAC. This VV&A will be undertaken in the near future.

ACKNOWLEDGMENT

REFERENCES

1. Gillespie, Patti, Alan Wetmore, and James Williams, 1993, The Validation, Verification, and Accreditation of EOSAEL Models, Proceedings of the Fourth Annual Ground Target Modeling and Validation Conference, 24–26 August 1993, Houghton, MI.

2. Users Manual FLIR90 version 0, 1990, C2NVEO Thermal Imaging Systems Performance Module FLIR90, U.S. Army CECOM Center for Night Vision and Electro-Optics Report M5008986.

3. Gillespie, Patti, 1993, TARGAC Users Guide, U.S. Army Research Laboratory Technical Report, in editorial review, available in draft version from author.

4. Johnson, Keith, Leonard Rodriguez, 1990, Target/Background Models for TCM2, Georgia Tech Research Institute Interim Report for Period August 1988–July 1990 for the Avionics Laboratory of Wright Research and development Center, Air Force Systems Command.

5. Lacombe, J., B.K. Matise, D.R. Petzko, J.W. Petraska, J.E. Rice, E.J. Burlbaw, T. Chenault, E.S. Stallings, and W.M. Farmer, 1988, SNOW III West Field Experiment Report, Volume I, Special Report 88–28, U.S. Army Corps of Engineers, Cold Regions Research and Engineering Laboratory, Hanover, NH.

6. Petzko, David R., Jeffrey W. Petraska, and James E. Rice, 1987, Comparison of TDA Predicted Inherent Thermal Signatures with SNOW III West Measured Signatures, OMI–203, OptiMetrics, Inc.

7. Burlbaw, Edward J., and John Gale, 1987, Target Acquisition Model Evaluation, OMI–247, OptiMetrics, Inc.

8. Crain, John N., Edward J. Burlbaw, and W. Michael Farmer, 1986, Target Acquisition Model: Validation, Sensitivity Studies, and Modification, STC Technical Report 2125, Science and Technology Corporation.

9. Burlbaw, Edward J., Brian K. Matise, and Brent Bean, 1989, Evaluating the Target Acquisition Model: Final Report for WAO 8809–Task 2, OMI–349, OptiMetrics, Inc.

10. Gillespie, Patti S., 1987, BEST–ONE Data Analysis and Comparison, OMI–237, OptiMetrics Technical Report, Las Cruces, NM.

11. Locke, Brian A., 1990, Evaluation of the Target Acquisition Model in Smoke Weeks X and XI, STC Technical Report 4017, Science and Technology Corporation, Hampton, VA.

12. Berrick, Stephen W., Brian Locke, Lori Fuentes, and Ronald Catherson, Target Acquisition Model Evaluation With Smoke Week XII Data, 1991, STC Technical Report 6214, Science and Technology Corporation.

13. Catherson, Ronald L., and Brian Locke, 1993, Evaluation of TARGAC and TARGACxTCM2 Using Far Infrared Target Detections from Smoke Week XIV, STC Technical Report 6238, Science and Technology Corporation.

14. Bijl, Piet and J. Mathieu Valeton, 1993, Evaluation of Target Acquisition Model "TARGAC" Using BEST TWO Observer Performance Data, Proceedings of the 1993 Battlefield Atmospherics Conference, 30 November–2 December 1993, Las Cruces, NM.

15. Catherson, Ronald L., and Brian Locke, 1992, Evaluation of TARGAC Using the Photopic Target Detections from Smoke Week XIII, STC Technical Report 6229(B), Science and Technology Corporation.

16. Duncan, L.D., M.A. Seagraves, and M.G. Heaps, 1987, Natural Aerosol Extinction Module XSCALE, ASL–TR–0221–7, U.S. Army Laboratory Command, Atmospheric Sciences Laboratory, White Sands Missile Range, NM. New Version (to be released): Fiegel, Robert P., 1993, Natural Aerosol Extinction Module XSCALE, Army Research Laboratory Technical Report, in editorial review.

17. Fiegel, Robert P., 1990a, Parameterization of LOWTRAN 7 for Broadband Gaseous Transmittance, ASL–TR–0270, U.S. Laboratory Command, Atmospheric Sciences Laboratory, White Sands Missile Range, NM.

18. Fiegel, Robert P., 1990b, Comparison of XSCALE 89 Vertical Structure Algorithm with Field Measurements, Proceedings of the Eleventh Annual EOSAEL/TWI Conference, 27–30 November 1990, Physical Sciences Laboratory, New Mexico State University, Las Cruces, NM.

19. Fiegel, Robert P. and M.G. Heaps, 1989a, A Comparison of LOWTRAN7 and XSCALE Transmittance in the 0–2 km Boundary Layer, Proceedings of the Twelfth Annual Review Conference on Atmospheric Transmission Models, E.P. Shettle and F.X. Kneizys, editors, Geophysics Laboratory, Hanscom AFB, MA.

20. Fiegel, Robert P. and M.G. Heaps, 1989b, XSCALE 1989 Update, Proceedings of the Tenth Annual EOSAEL/TWI Conference, Physical Science Laboratory, New Mexico State University, Las Cruces, NM.

21. Davis, John M., 1991,An Evaluation of the Delta Eddington Contrast Transmission Model, Atmospheric Environment, Vol. 25A, No. 8, pp. 1679–1687.

22. Gillespie, Patti, 1989,Preliminary Comparison of Delta Eddington Model Calculations of Contrast to Measurements, Proceedings of the Tenth Annual EOSAEL/TWI Conference, 28–30 November, Physical Sciences Laboratory, New Mexico State University, Las Cruces, NM.

23. Ayres, Scarlett, Donald Hoock, 1993,COMBIC Users Guide, U.S. Army Research Laboratory Technical Report, White Sands Missile Range, NM.

24. Avara, Elton P., 1993,CLIMAT Users Guide, U.S. Army Research Laboratory Technical Report, White Sands Missile Range, NM.

EVALUATION OF TARGET ACQUISITION MODEL 'TARGAC'
USING OBSERVER PERFORMANCE DATA

Piet Bijl and J. Mathieu Valeton

TNO Institute for Human Factors
PO Box 23   3769 ZG Soesterberg   The Netherlands

ABSTRACT

The TARGAC model predicts target acquisition performance for a variety of sensors in the visible and thermal infrared. Its predictions are compared with the actual performance of observers with a thermal imaging system, using imagery collected during a field trial. TARGAC systematically under-estimates observer performance and it does not predict the large variance in the observer data. The 95% confidence interval of the predictions spreads from 0.9 to 3.6 times the predicted acquisition range. TARGAC can predict overall mean performance, but a correction factor of 1.80 should be used. For individual cases range predictions may be off by a factor between 0.5 and 2.0. The conclusions of this evaluation may also hold for other models based on the Johnson criteria.

1. INTRODUCTION

Target acquisition models predict the range at which a target can be detected, recognized or identified with an optical or electro-optical viewing device, in a given scene, under given atmospheric conditions. These models are used e.g. as tactical decision aids (TDA's), in war games, and as a tool to compare performance of competing sensor systems for a specific task.

TARGAC is a comprehensive target acquisition model that was developed at the U.S. Army Research Laboratory, Battlefield Environment Directorate. It is part of the Electro Optical Systems Atmospheric Effects Library (EOSAEL). In this paper we evaluate the TARGAC model by comparing its predictions with a large body of actual observer performance data, that were collected on imagery recorded during the NATO AC243/Panel4/RSG.15 field trial BEST TWO that was held in France in 1990.

The evaluation of target acquisition models is of interest because the reliability and accuracy of their predictions is not always known. These models are however used frequently and the absence of knowledge about their accuracy often leads to the effect that the predictions are treated as being exactly correct. This effect is known as the *false precision problem*. The present study aims to further the understanding of target acquisition model application.

The evaluation is carried out in four steps:
1. The TARGAC predictions are calculated for the BEST TWO situation. To be able to do this, extensive meteorological data for the BEST TWO situation, data on the BEST TWO target set, and the MRTD curve for the FLIR system that was used to record the imagery was collected and fed into the model.
2. A sensitivity analysis is performed because not all of the input information was available with a high degree of accuracy. This analysis shows the extent to which changes in each input parameter influences the model output. Parameters for which the model is not very sensitive need not be specified with great accuracy, while parameters for which a high sensitivity is found must be provided with high precision.
3. The TARGAC predictions are plotted as probability of a correct recognition response *vs.* target range in graphs that also contain the observer data. A graphical comparison gives a first impression of the

quality of the predictions.

4. The observer data are normalized by re-scaling to allow an assessment of the mean and variance of the difference between the prediction and the individual observer data points.

This paper is organized as follows. In section 2, a short description of TARGAC will be provided and section 3 contains an outline of the BEST TWO field trials and the observer experiments that were carried out. In section 4, we present the results of the sensitivity analysis and in section 5 the predictions made by TARGAC for the BEST TWO situation are compared with the actual observer performance data. A discussion of the results is presented in section 6.

2. TARGAC

2.1 General

TARGAC predicts the probability of detection- and recognition of (military) targets as a function of range, for a variety of sensors. The model is freely available, and runs on a PC. There also exists a version for a HP minicomputer. An extensive overview of the model is given in the TARGAC User Guide[1]. The model basically consists of three parts:

2.1.1 Inherent contrast calculation

The first stage of the model calculates the inherent contrast (i.e. the contrast at the location of the target) between target and background, given the characteristics of target and background, and the meteorological conditions. For the case of thermal imaging, the inherent contrast is calculated by a Thermal Contrast Model (TCM2), and is expressed in terms of temperature difference. It is possible to by-pass this module and directly input the inherent contrast.

2.1.2 Atmospheric effects calculations

TARGAC contains an extensive atmospheric effects module. This module calculates the contrast transmittance through the atmosphere for various wave bands, based on meteorological input data. It yields the apparent contrast of a target as seen by a sensor, as a function of range.

2.1.3 System performance calculation

The actual probability of acquisition is calculated using the NVESD Static Performance Model[2,3], in which target acquisition performance is described using the well known 'Johnson criteria'. These criteria link target acquisition performance with the ability to resolve dark bars of a certain spatial frequency and contrast against a uniform background. For example, recognition is modelled by stating that if a target is at such a range that a human observer with the viewing system is just able to resolve four line pairs over the effective, i.e. minimum, dimension of the target, the recognition probability is 50%. The higher the resolution of the viewing device, or the larger the target, the longer the range at which four line pairs can be resolved. For a 50% detection probability the resolution of 1 line pair is required, for identification this number is 6.4. These relationships between the number of line pairs that must be resolved and the corresponding acquisition performance levels are called the Johnson criteria.

In practice, the Johnson criteria are applied using a threshold performance curve of the viewing device that gives the contrast required to resolve a 4-bar pattern as a function of spatial frequency. For visible light devices this is called the Minimum Resolvable Contrast (MRC)-curve; infrared devices are characterized by a Minimum Resolvable Temperature Difference (MRTD)-curve.

2.2 TARGAC version

The TARGAC model is 'currently defined as being in the developmental stage of software'[1]. This means that regularly new versions are released. The TARGAC version that was used for the present evaluation, was released in June, 1992 (PC version). During the sensitivity analysis (see section 4) a number of software errors were found and most of the bugs were fixed in consultation with Dr. P. Gillespie of ARL. This means however that results presented in this paper were obtained with an improved version,

and not with the standard distribution version. Since the latter still contains a number of errors, we recommend to contact ARL before using the program.

2.3 TARGAC input

2.3.1 Built-in choices
TARGAC has a number of built-in choices for viewing devices, targets and backgrounds. For viewing device, there are 14 visible sights, 4 Image Intensifiers and 5 thermal sights, and the corresponding MRC or MRTD curves are built into the program. There are 24 built-in targets, for example a T62 and T72 tank, a number of ZIL trucks and BRDM-2 anti-tank vehicles. Many of these are available in 'off', 'idle' and 'exercised' conditions. For background, there are 29 choices, like: 'tall grass -- growing', 'dirt road', and 'coniferous trees -- dormant', etc.

2.3.2 User specified inputs
When predictions must be made for a viewing device that is not built in, the user must specify an MRC or MRTD curve, in the form of the coefficients of a sixth order polynomial fit to the MRC or MRTD data. For the present analysis, MRTD measurements for the Philips UA9092 thermal were provided by FEL-TNO[4].

It is not possible to enter user-specified targets and backgrounds. The target information is used both for the contrast calculation and to determine the 'effective dimension' for the application of the Johnson criteria. If predictions must be made for non built-in targets and backgrounds, one can circumvent the contrast calculation by entering values for target and background temperature directly into the program. Such information may, for example, be available from direct measurement in the field. Since 'target size' can not be entered as such, one must use one of the built-in targets that best matches the target that is studied. For the present analysis a number of these options for user specified data entry were used because the built-in choices did not cover the BEST TWO situation.

TARGAC was used in 'batch mode', which means that the choice of target and background, meteorological data, the geographical situation, date, time, and the viewing device MRTD were entered as a data file.

2.3.3 Meteorological data
Meteorological input data for a large number of BEST TWO target approaches were supplied by Dr. P. Gillespie, who compiled the information from data provided several nations that participated in BEST TWO.

2.3.4 Target and background temperatures
The TCM2 module in TARGAC was used to calculate inherent target contrast from target and background characteristics and meteorological data. Field measurements of target signatures provided by Denmark[5] were used to check the calculations.

2.5 TARGAC output
The program produced detection and recognition ranges for five probability levels: 10%, 30%, 50%, 70% and 90%. (The standard version of TARGAC only calculates 3 probability levels). Ranges are specified with a precision of 0.1 km. TARGAC also provides several results of intermediate calculation stages, such as the inherent target contrast, when the Thermal Contrast Model (TCM2) is used.

3. BEST TWO FIELD TEST AND LABORATORY EXPERIMENTS

During BEST TWO, recordings were made of single stationary or moving target vehicles approaching from a distance of 4000 m to a distance of 1000 m. Image sequences, recorded from a Philips UA9092 (8-12 µm) thermal imager, were used in laboratory experiments to measure observer performance for target recognition and identification. The experiments are described extensively in a number of TNO re-

ports[6,7,8].

In two experiments, observer performance was measured for a total of 38 different target approaches (runs). These runs differ in target type, approach route, date and time (recordings were made during day and night). Six different targets were used, three of which were camouflaged during some of the runs. Sequences of images containing a single target were presented to observers. The observer's task was similar to the target acquisition task in a practical military situation: after each presentation, they were first asked to indicate whether they were able to identify, recognize or only detect the target, after which they had to name the target. Two ways of presenting the target images were used: 'pop-up' and 'approaching'. In the 'pop-up' presentation, a randomly chosen target, was presented at a random distance. In the 'approaching' condition, the images from a single target approach were presented as an ordered sequence, simulating a target approach from 4 km on down. Search was explicitly avoided. In one experiment, performance was measured for 15 runs, for both the 'pop-up' and 'sequential' targets. Recognition scores for a selection of these runs are presented in the Appendix. In a second experiment, performance was measured for 33 runs, for 'pop-up' presentation only (10 of these approaches were also used in the first experiment).

TARGAC will be evaluated against three data sets. Data set A contains observer performance data for all (38) runs, for 'pop-up' targets. Data set B contains the data for 15 runs, presented as an ordered sequence. Data set C, which is a subset of data set A, contains the data for the same 15 runs, now presented as 'pop-up' targets. This set will be used for a direct comparison of the results of the evaluation for the two types of presentation order.

4. TARGAC SENSITIVITY ANALYSIS

Two 'standard' situations were defined to test the sensitivity of TARGAC output for variations of a number of input parameters. Input files for a 'typical' afternoon and a night session were put together. An exercised T62 tank was chosen as target and the background was a 'grass field'. TARGAC predictions were made for a range of input values of a test parameter, while keeping all other parameters constant. This sensitivity analysis is fully described in a TNO report[9]; in this paper only the main results will be presented.

4.1 The effect of time and date
The probability *vs.* range predictions, for both detection and recognition, are almost identical for the two standard situations. TCM2 predicts a thermal contrast of 9.2 K for the afternoon situation and 8.7 K at night, and the influence of the difference of these values on the raange predictions is negligible.

4.2 The effect of acquisition level: transmission losses
The effects of transmission losses through the atmosphere can be assessed by comparing the predicted ranges for recognition and detection. According to the Johnson criteria, the number of line pairs required for target recognition at a given probability level, is four times the number of line pairs required for detection at the same probability level. This means that, if atmospheric effects are negligible, the ratio between detection and recognition ranges will be 4:1. Atmospheric contrast reduction will reduce this ratio.

The ratio between detection and recognition range was calculated for all probability levels and it was found to be 4.0 at all probability levels except at the 10% level, where it was 3.6. This means that, for the BEST TWO situation, the effects of transmission losses on the predictions are negligible, at least when target inherent thermal contrast is high.

4.3 The effect of target type
There are two target parameters that affect the predictions: target temperature and effective target dimension. Predictions for several different built-in targets were compared with the 'standard' T62, see Table 1, where target inherent contrast and 50% recognition range are presented for both standard situ-

ations. Each target is calculated for both the 'exercised' and 'off' states in order to be able to asses the effect of inherent target contrast.

4.3.1 Thermal contrast

Table 1 shows that thermal contrast varies over a wide range (between -0.29 and 10.6 K), but it has only has a small effect on predicted acquisition range. For each target, the four predicted acquisition ranges are very similar, which means that for the BEST TWO situation the inherent thermal contrast will not be the limiting factor for the predicted acquisition range.

TABLE 1: Effect of target type on TARGAC predictions.

target type	target height (m)	inherent contrast (K)		50% recog. range (km)	
		afternoon	night	afternoon	night
T62 (tank), off	2.2	2.6	1.5	1.5	1.2
T62, exercised		9.2	8.7	1.5	1.5
ZIL (Truck), off	2.6	3.3	-0.29	1.8	1.8
ZIL, exercised		5.8	2.2	1.8	1.7
T72 tank, off	2.3	2.9	3.6	1.6	1.5
T72, exercised		10.6	11.3	1.6	1.6
BRDM-2 (APC), off	2.1	2.0	1.3	1.4	1.3
BRDM-2, exercised		3.8	3.3	1.4	1.4

4.3.2 Target effective dimension

When atmospheric effects are negligible, predicted range is expected to be proportional to the effective, or minimum, dimension of the target (because a number of line pairs has to be resolved across the target effective dimension). For ground-to-ground target acquisition, the minimum dimension is target height. In Table 1, target height can be compared with recognition range (e.g. columns 2 and 5). Dividing these two columns yields values between 1.4 and 1.5, which means that the expected proportionality is there. Effective target dimension thus seems to be a parameter that has a large influence on the model output.

4.4 Background type

The test field in Mourmelon mainly consisted of dry grass with bushes. However, due to the frequent use of the approach routes, bare soil came up and hot tracks appeared during the test, which were seen as white lines on the thermal imagery. At the longest ranges, the targets were seen against a background of wood. Several background types from the TARGAC menu were chosen to assess the possible influence of background type on the predicted ranges. Although the temperature is different for different backgrounds (target contrast varies between 5.0 and 12.0 K), there is no influence of background type on recognition range.

4.5 MRTD curve

If apparent target contrast is high, as seems to be the case in the BEST TWO situation, the acquisition threshold will be determined in the high contrast - high spatial frequency region of the MRTD curve, and acquisition range may be expected to be *proportional to* the cut-off frequency of the MRTD-curve. Predicted ranges were calculated for the 'standard situation', for different MRTD-curves, and were indeed found to be proportional to the cut-off frequency. Hence, the second parameter that has a large influence on the model output is the MRTD curve cut-off frequency.

4.6 Conclusions

The results of the sensitivity analysis for the BEST TWO situation can be summarized as follows:

1. Due to the excellent atmospheric conditions, predicted recognition range is almost independent of

time or day.

2. For the same reason, recognition range is almost independent of target and background temperature. Therefore, it is not necessary to have an accurate estimate of target and background temperature. For the calculations it makes no difference whether target and background temperatures calculated by TCM2 are used, or those measured during the trials.

3. There are only two parameters that significantly influence the TARGAC predictions: the effective target dimension and the cut-off frequency of the MRTD curve of the viewing device. As a consequence, inaccuracies in the values of these parameters directly influence the model evaluation.

4. Because the influence of thermal contrast and atmosphere on recognition range are negligible, only the routine that describes electro-optical and human visual system performance can be tested with the BEST TWO material. This routine is based on the Johnson criteria. This means that the results of the present evaluation may also apply to other models that are based on the Johnson approach.
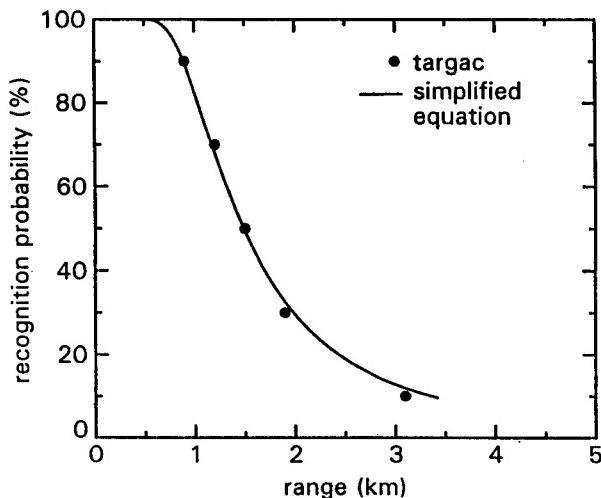
Fig. 1.   Comparison of the results of the simplified equation (solid line) with the TARGAC predictions (filled circles) for the BEST TWO standard situation.

5. TARGAC EVALUATION

5.1   Simplified equation

In section 4 it was shown that, due to the excellent atmospheric conditions during the BEST TWO trials, predicted recognition range depends significantly on only two parameters: effective target dimension and cut-off frequency of the MRTD curve of the viewing device. This makes it possible to carry out the evaluation with a simplified equation that describes the TARGAC predictions for the BEST TWO situation. It can be shown[9] that the TARGAC predictions for the BEST TWO situation are accurately described by:

$$P_{\text{Targac}} = 2^{[-4r/(f_{MRTD} \cdot D_{\text{Target}})]^s} \times 100\%, \tag{1}$$

or, inversely:

$$r_{\text{Targac}} = (f_{\text{MRTD}} \cdot D_{\text{Target}} / 4) \cdot [-^2\log(P / 100\%)]^{1/s}, \tag{2}$$

where:

P = is the acquisition probability (%), r = acquisition range, f_{MRTD} = cut-off frequency of the MRTD curve, D_{Target} = target effective dimension, s = steepness of the curve. The steepness s was set to 2.32 for an optimal fit of the curve to the predicted points. Fig. 1 shows that the TARGAC predictions (filled

396

circles) are described very well by equation (1). This equation is a so-called Weibull function, which is a relation that is frequently used to describe human visual threshold behaviour.

5.2 Range predictions for the BEST TWO targets

Equation 4 can be used to calculate the TARGAC range predictions for the specific target vehicles that were used in the BEST TWO trials. The results are presented in Table 2, where the BEST TWO targets and their effective dimension (target height) are shown together with the predicted recognition range. The bottom row gives a 50% recognition range for a 'mean BEST TWO target', which will be used in one of the analyses below. Note that the probability *vs.* range relationship is the same for each target, except for a single factor that is determined by the effective target dimension.

TABLE 2: Target effective dimensions and predicted recognition ranges for the targets used in BEST TWO.

target type	target height (m)	50% recognition range (km)
Leopard 2	2.50	1.8
AMX-30	2.30	1.6
PRI	2.60	1.8
PRAT	2.60	1.8
AMX-10	1.90	1.3
Truck	2.80	1.9
mean target	2.45	1.7

5.3 Qualitative comparison for individual target approaches

An overview of the results of the observer target recognition experiments is shown in the Appendix, where a selection of the recognition data is shown together with the corresponding TARGAC predictions. Three typical examples from this set are presented in Fig. 2. In all three cases, TARGAC under-estimates observer performance. In Fig. 2, panel A, measured recognition performance gradually decreases with target range, which is what the model also predicts. In Fig. 2, panel B, the observer recognition performance is roughly constant at probability level better than 80% for ranges up to 4000 m, which is very different from the model prediction. Fig. 2, panel C, shows an example where recognition performance does not simply decrease with target range, but instead changes rapidly with the position of the target. This is not due to noise in the observer measurements, but to the local structure and contrast of the target background. This behaviour is termed 'target-terrain interaction'[7], and it cannot be described satisfactorily with a monotonously decreasing function. On average, predicted performance is again far too low.

These three examples show that:
- TARGAC predictions are in general too conservative; for individual points the deviation can be considerable.
- The monotonously decreasing performance curve that TARGAC predicts, is found only in a number of cases.
- In cases where large target-terrain interactions are present, a probability *vs.* range relationship does strictly not exist. Such behaviour is not predicted by the model.
- TARGAC is not suitable for predicting performance for individual targets.

5.4 Comparison with overall mean observer performance

Since TARGAC does not appear to be suitable to predict performance for individual targets, its predictions will now be compared with the overall mean performance of observers over a large number of targets and runs. This seems to be a reasonable approach because originally the Johnson criteria were

397

also based on mean acquisition performance over a large number of conditions.

The data sets A, B, and C, defined in section 3, will be used and the comparison with TARGAC prediction for the 'mean' BEST TWO target (see Table 2) is shown in Fig. 3. Using the prediction for a 'mean' target makes sense because all targets in the set were presented to the observers roughly equally often, and predicted ranges for the six targets do not differ considerably. Filled circles represent mean observer performance (averaged per distance). The solid line indicates the TARGAC predictions for the BEST TWO mean target. The dashed line represents the best fit of equation 1 (see 5.1) to the observer data and will be shown to correspond to range predictions increased by a factor of 1.80 (see 5.5).
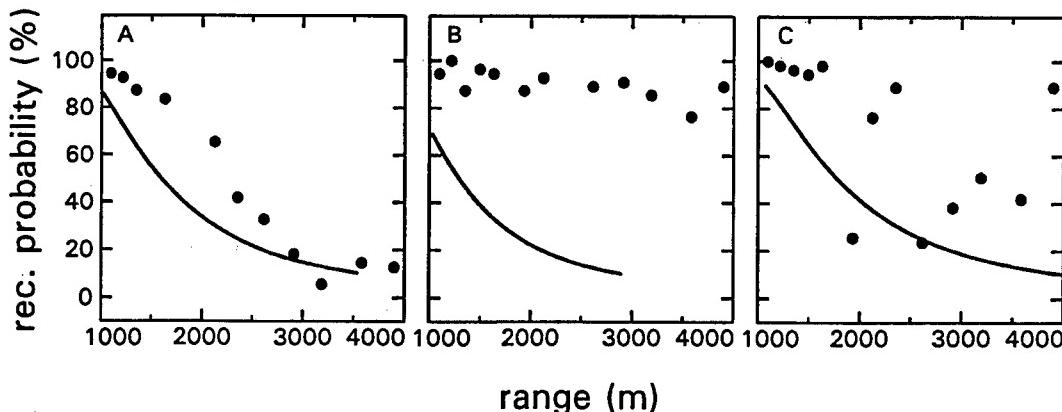
Fig. 2   Comparison of observer performance vs. target range and the corresponding TARGAC predictions for three typical examples. Filled circles: observer recognition scores. Solid lines: TARGAC predictions.

Data set A was recorded with 'pop-up' targets. It is based on a large number of observations and shows the overall mean behaviour. Data set B and C were selected to illustrate the difference between 'pop-up' targets and 'approaching' targets. Set C is a subset of A and represents the 'pop-up' targets. Set B was recorded with the same images that were used in set C, but now in approaching order.
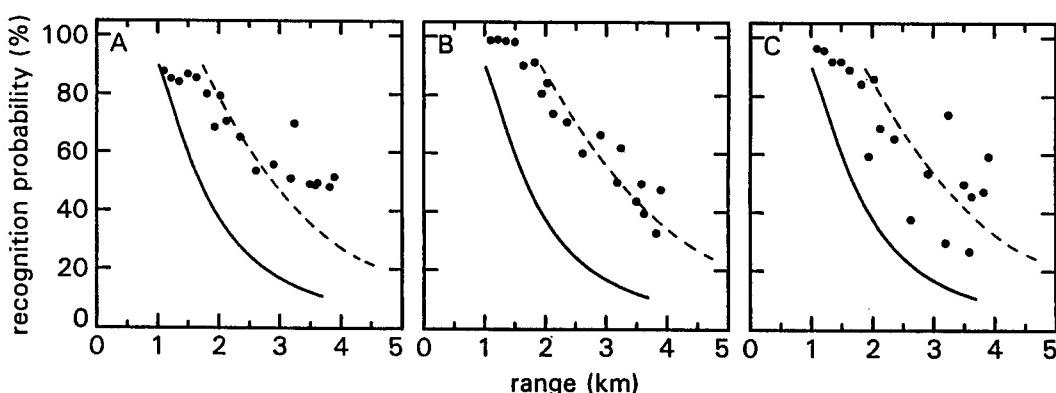
Fig. 3   Comparison of overall mean observer performance (filled circles) and TARGAC predictions (solid lines) for the three data sets A, B and C. Dashed line: best fit of equation 1 (see 5.1) to the data.

Figure 3 shows that:
- TARGAC predictions are indeed far too conservative, for all mean conditions.
- For data sets A and B, the overall mean probability decreases with target range, which was not the case for the scores for individual target approaches (Fig 2). This is caused by the averaging over many target approaches, which diminishes the effects of target-terrain interactions. The results for

398

set C show more residual terrain interactions because it is a small subset of A.

- Comparison of data sets B and C shows that for approaching targets (B) the data conform much better to a monotonously decreasing function than for 'pop-up' targets (C). This is because the accumulation of information during a target approach helps to reduce the effects of the target-terrain interactions[7].
- The mean recognition probability for the observers is never below about 50% correct, even at the longest target range (4 km). This means that the shape of the probability $vs.$ range relationship is not known for lower probabilities.
- The slope of the prediction curves is steeper than rate of decrease of the observer data, especially for the 'pop-up' targets. The difference is much smaller or non existent for the 'approaching targets'. This might suggest that the model should be made to accommodate these different target behaviours.

5.5 Comparison with individual data points

In the previous sections, it was shown that overall *mean* recognition performance can be described reasonably well as a monotonously decreasing function of target range. It seems that the fit of the model to the mean observer data could be much improved by applying a single correction factor and possibly a small change in the steepness s, see equations (1) and (2). Apart from the *mean* performance, it is worthwhile to know how well TARGAC predicts the performance for *individual cases*: targets and runs. The previous sections have shown that there is a lot of variation in the observer data, but the model predicts only a single curve, with an unknown confidence interval.

In order to determine the unexplained variance in the observer data, these will be regarded as a large set of single points, and a point by point comparison will be made between data and model predictions. This analysis will yield a distribution which gives the unexplained variance in the data due to all parameters that were varied in the experiments (including the effects of local conditions). This variance provides an indication of the accuracy of the model for individual predictions.

5.5.1 Procedure

Each data point represents a probability of correct recognition P for a target at range r. At this probability level P, the model predicts a target range r' . For each data point in the set, a ratio r/r' between actual and predicted range is calculated. If the model makes a correct prediction, the ratio $r/r' = 1$. If the predicted range for a given point is too short, the ratio will be larger than 1, if it's too large, the ratio is smaller than 1. It is convenient to transform the r/r' values to a log scale, because correct predictions are centred at 0, and an over- or underestimates of the range by the same factor are equally shifted in opposite directions along the axis.

Mean and variance of the log (r/r') distribution directly provide a measure of the accuracy of the model. If the model correctly predicts most of the variation in the data (e.g. due to target type, part of day, probability level, etc.), all ratios r/r' will be approximately equal to 1, and a narrow distribution around log $(r/r') = 0$ will be found.

The *mean* of the log (r/r') distribution, defined as «log (r/r')», is the distance between 0 and the location of the center of the distribution, and can be used as the range correction factor that will make the model predict overall mean performance correctly.

The *variance* of the log (r/r') distribution is in fact the variance in the observer data that is not explained by the model. A wide distribution means that the model is not able to make reliable predictions for individual conditions. The 95% confidence interval (the interval that contains 95% of the data) is given by [«log (r/r')» - 2σ , «log (r/r')» + 2σ].

5.5.2 Graphical representation

The predicted relation between acquisition performance and target range is the same for each run, except for a single factor that is determined by the effective dimension of the target (see equation 1, section 5.1). This factor may be expressed as r_{50}, the range for which 50% correct recognition is predicted. To enable correct comparison of all individual data points, both the *predicted* and all *observed* recognition ranges are normalized by dividing all ranges by r_{50}, . This procedure yields a single pre-

dicted probability *vs. relative* range curve through $(r, P) = (1, 50\%)$, for all targets. The normalized observed target recognition ranges for all targets can now be plotted in a single graph, together with the normalized prediction curve, see e.g. Fig. 4, panel A. If the model predictions would be perfect, this would result in a set of data points that are distributed near the (single) predicted curve $(r/r' \approx 1)$. In practice, prediction errors will results in normalized data points that are scattered away from the curve.

5.5.3 Results

The normalized results for data set A are plotted in Fig. 4, panel A. The solid curve is the TARGAC prediction and the large scatter of individual data points shows that the model is by no means able to explain the variance in the observer data. Even if we only consider the data points with a recognition probability between 20% and 80% (at very high or very low probabilities, r/r' may take unrealistic values), r/r' ranges from about 0.6 to about 3.6.

Fig. 4, panel B, presents a histogram of the distribution of log (r/r')-values, based on the 230 data points with a probability between 20%-80% in Fig 5A. The mean of the distribution is 0.23 and thus, on average, the predicted range is $10^{-0.23} = 1/1.70$ times the observed recognition range. The standard deviation is 0.17, on a log scale. Thus, the 95% confidence interval is (-0.11, 0.57). On a linear scale, this interval is (0.8, 3.7), spanning a factor of almost 5! In words, if you make a TARGAC prediction for an individual case, there is a probability of 95% that the actual range falls between 0.8 and 3.7 times the predicted range. Even after correction for the overall mean acquisition range, the actual range may be more than twice, or less than half, the predicted range. The mean of the distribution is plotted as a dashed line in Fig. 5A and the 95% confidence region is indicated by two dotted lines.
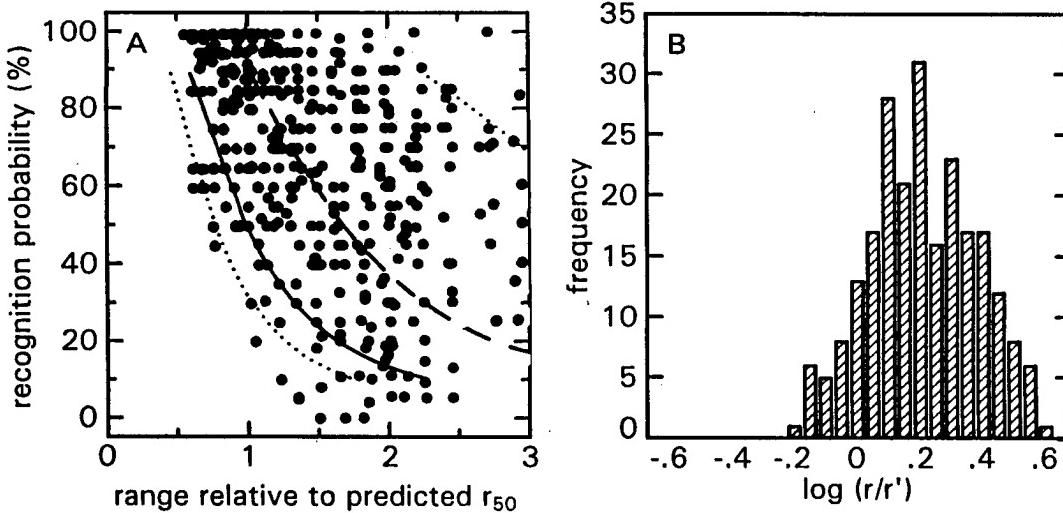
Fig. 4   Panel A: Point by point comparison between measured and predicted recognition performance for data set A. Solid line: model predictions; filled circles: observer data. Dashed line: mean of the log(r/r') distribution. Dotted lines: boundaries of the 95%-confidence interval.

Panel B: Histogram of the log(r/r') distribution. Mean is 0.23; $\sigma = 0.17$.

Fig. 5A and B show the normalized data and prediction curves for data set B (15 runs 'approaching' targets) and C (15 runs, 'pop-up' targets). Symbols are as in Fig. 4A. The results for these data sets are similar to those for data set A. The mean shift between the data and the TARGAC predictions is 0.23 for B and 0.28 for C on a log scale, which corresponds to an underestimate of the observed recognition range by factors of 1.70 and 1.90 respectively. The confidence interval is very large in both cases, spanning a factor of about 4 for the 'pop-up' targets and a factor 3.3 for the 'approaching targets'. The smaller interval for the latter case is due to the more stable responses that are obtained using this presentation order.

400
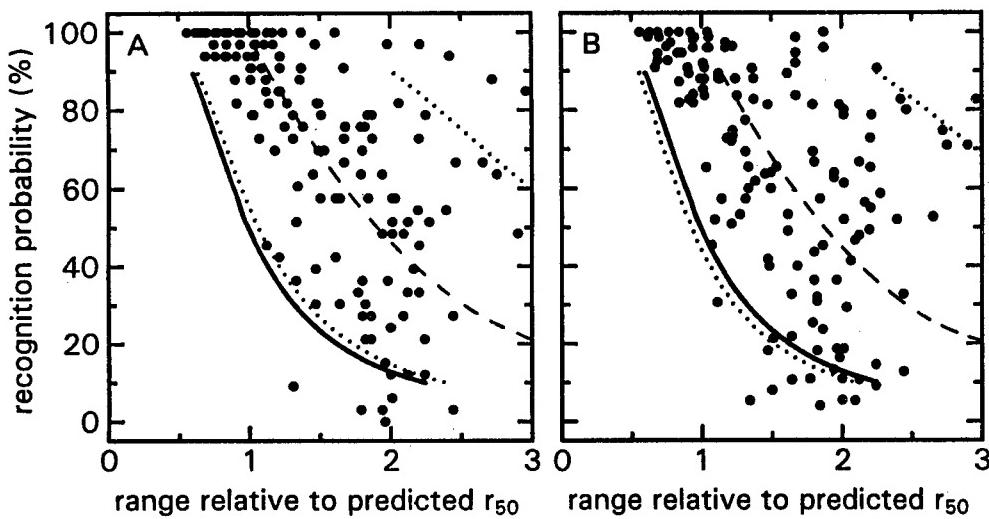
Fig. 5   Point by point comparison between measured performance and TARGAC predictions for data set B (left) and data set C (right). Symbols as in Fig. 4.

5.5.4 Further analyses

Part of the variance that is found in the log(r/r')-distribution, could be due to statistical errors in the observer scores. This was checked[9], but the variance on the observer scores is very much smaller than the variance in the log(r/r')-distribution, and hence, this variance must be ascribed to incorrect model predictions. Only observer data between 20% and 80% correct were used in these analyses. It was checked[9] that extending this range does not significantly influence the log(r/r')-distribution.

6. DISCUSSION

The main findings of this paper are that (1) the present version of TARGAC under-estimates the mean overall observer performance for the BEST TWO situation by a factor of about 1.8, and (2) that TARGAC is not able to predict performance for individual target runs: the 95% confidence interval is the region between roughly 0.90 - 3.6 times the predicted acquisition range, thus spanning a range of a factor 4.

6.1   Mean acquisition performance

The under-estimation of the mean acquisition performance may in part be due to errors in the data that are input to the model. The sensitivity analysis showed that the model output is directly proportional to the MRTD curve cut-off frequency, and hence uncertainties in the MRTD will be translated into errors in the predictions. We checked the methods that were used to measure the MRTD curve of the Philips FLIR that was used in the observer experiments[4], and found that the uncertainty in the cut-off frequency is about 20%. This is not enough to explain the observed variance, and the short-fall of the model must be ascribed to the Static Performance Model as it is incorporated in TARGAC. The implemented version uses Johnson criteria relative to the minimum target dimension, and is in fact 1-dimensional. A newer version of the Static Performance Model is 2-dimensional (ACQUIR 90), and uses target area. This model was compared with the BEST TWO data and gave better predictions: the acquisition ranges was underestimated less than 30%.

6.2   Acquisition performance for individual cases

There does not seem to be an easy solution to the problem of modelling individual target recognition performance, in the sense of possible corrections to the model. A model can only do better when more

401

detailed information on the target- and local background signatures is available. Such a model can be built, but would be become rather complex and require extensive and detailed input.

The TARGAC user interface suggests that predictions are indeed made for individual targets, but this is not really correct because the underlying human performance model uses the Johnson criteria and these are based on mean observer performance over a large number of conditions. It would seem appropriate (1) to explain to the user that the predictions are valid only for mean overall performance and (2) to present as output a statement that indicates the accuracy of the prediction, such as the 95% confidence interval, instead of presenting only a single number for acquisition range per probability level.

CONCLUSIONS

The target acquisition model TARGAC was evaluated using BEST TWO observer performance data for target recognition. Due to the excellent atmospheric conditions during the BEST TWO trials, recognition performance predictions are determined solely by the system performance module of TARGAC, which is equivalent to the 1-dimensional NVESD Static Performance Model. The main results of the evaluation are:
1. The model predictions are too conservative. On average, TARGAC underestimates recognition range by a factor 1.8. This ratio is similar for 'pop-up' targets and approaching targets.
2. TARGAC is unable to make accurate predictions for individual cases. The analysis shows that the 95%-confidence interval roughly ranges from 0.90 to 3.6 times the predicted acquisition range, thus spanning a range of a factor 4.
3. The TARGAC predictions for overall mean performance can be improved by incorporating the 2-dimensional version of the Static Performance Model.
4. It is suggested that TARGAC predictions are not only presented as single numbers for acquisition probability *vs.* target range, but that some indication is given of the accuracy of the results, preferably in the form of a 95% confidence interval.

ACKNOWLEDGEMENTS

REFERENCES

[1] Gillespie, P. (1991) TARGAC user guide. U.S. Army Research Laboratory, Battlefield Effects Directorate, White Sands Missile Range, NM, USA.

[2] Johnson, J. (1958). Analysis of image forming systems. Image Intensifier Symposium, Warfare Vision Branch, Electrical Engineering Dept., U.S. Army Engineer Research and Development Laboratories, Fort Belvoir, VA, 249-273.

[3] Ratches, J.A., Lawson, W.R., Shields, F.J., Hoover, C.W., Obert, L.P., Rodak, S.P. and Sola, M.C. (1981). Status of Sensor Performance Modelling at NV&EOL. Night Vision & Electro-Optics Laboratory, Fort Belvoir, VA 22060, USA.

[4] Jong, A.N. de, Janssen, Y.H.L, Roos, M.J.J. & Kemp, R.A.W. (1991) Infrared and Electro-Optical experiments during Best Two by Research Group Infrared. Report No. FEL-91-A252, TNO Physics and Electronics Laboratory, The Hague, The Netherlands.

[5] Andersen, E. (1991) BEST TWO Infrared signatures of the vehicles participating in the trial, Report No. DDRE N-7/1991, Danish Defence Research Est. Copenhagen, Denmark (NATO Confidential).

[6] Valeton, J.M. and Bijl, P. (1992). Observer experiments with BEST TWO thermal images, Part 1: De-

sign, training and observer selection. Report No. IZF 1992A-33, TNO Institute for Human Factors, Soesterberg, The Netherlands.

[7] Bijl, P. and Valeton, J.M. (1992). Observer experiments with BEST TWO thermal images, Part 2: Terrain interactions and target motion. Rep. IZF 1992A-34, TNO Institute f.or Human Factors, Soesterberg, The Netherlands.

[8] Bijl, P. and Valeton, J.M. (1992). Observer experiments with BEST TWO thermal images, Part 3: Reliability of observer responses. Rep. IZF 1992A-35, TNO Institute for Human Factors, Soesterberg, The Netherlands.

[9] Bijl, P. and Valeton, J.M. (in preparation). Evaluation of the target acquisition model TARGAC with BEST TWO observer performance data. Report No. IZF 1993A-..., TNO Institute for Human Factors, Soesterberg, The Netherlands.

APPENDIX

A selection of observer data taken from previous reports[7,8]. Recognition scores (filled circles) and TARGAC predictions (solid lines) for 15 BEST TWO runs with 'pop-up' targets. Target names have been removed because some data are confidential .
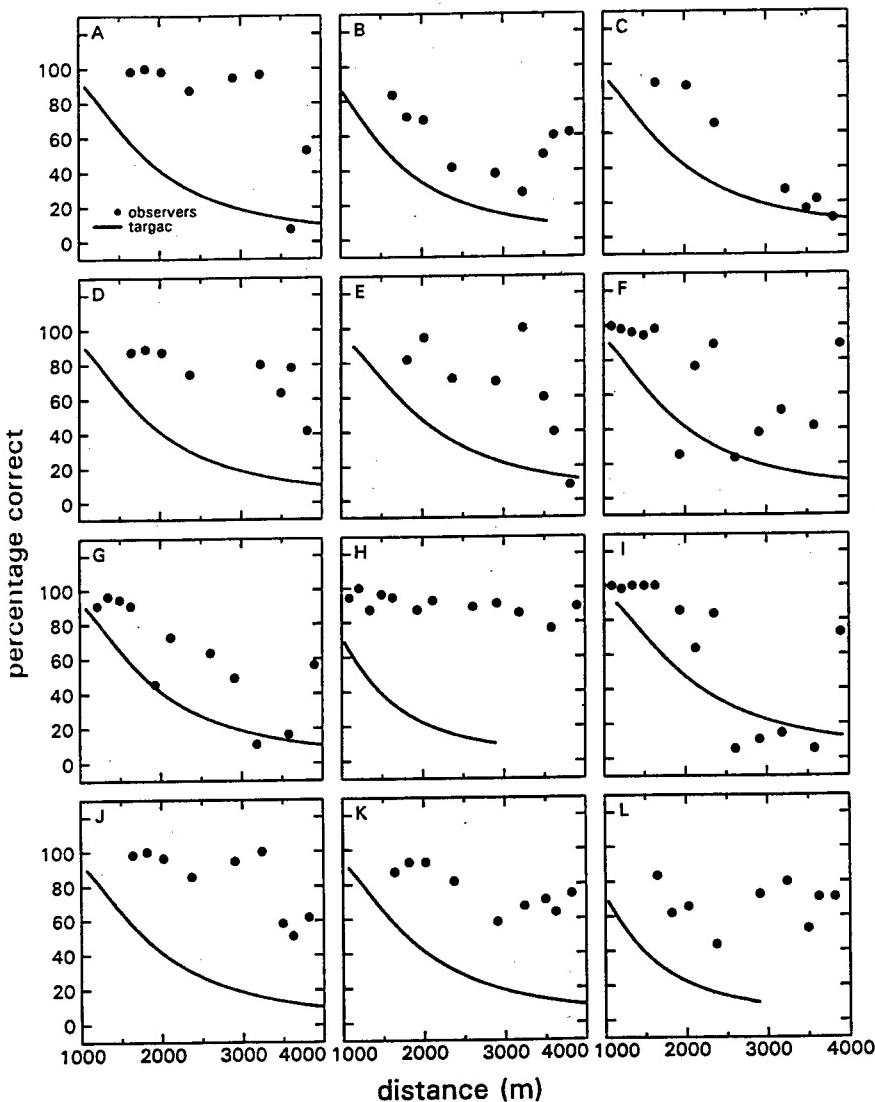
METHODS FOR REPRESENTING THE ATMOSPHERE IN INTERACTIVE SCENE VISUALIZATIONS

Donald W. Hoock
Battlefield Environment Directorate
U.S. Army Research Laboratory
White Sands Missile Range, NM 88002-5501

John C. Giever
Physical Science Laboratory
New Mexico State University
Las Cruces, NM 88003-0002

Soon it will be commonplace for "combatants" on separate computers to share a virtual environment in which they can interactively train together, develop tactics and test new weapons concepts. Differences in Computer Image Generator (CIG) virtual environments, however, must not become critical as correlation, fidelity or fair fight issues. This is especially true when the emphasis is on combatant inter-visibility or reciprocal line-of-sight differences in sensor performance. Consistency will require physically accurate atmospheric representations and atmospheric effects across the network. These are the subject of this paper. For example, the physically correct propagation description for haze and fog is compared to typical CIG methods for "atmospheric fading". The CIG definition is tested through simulation against the actual definition of meteorological visibility and a conversion from visibility to CIG input parameters is derived. A fast, efficient and accurate radiative transfer model for haze and fog radiance, tailored to visualization applications, is described and verified. CIG implementation methods for pseudo-random structures such as clouds and smoke plumes are discussed with respect to tradeoffs in two-dimensional versus three-dimensional fluctuation fields. Examples are shown of simulated scenes to illustrate the various methods.

1. INTRODUCTION

Improving computer graphics hardware and widespread demand for more realistic synthetic scenes are driving computer simulations to include atmospheric propagation, weather and illumination effects for training and augmentation of field testing. The U. S. Army Research Laboratory's Battlefield Environment Directorate is therefore upgrading its atmospheric and propagation models to meet these more demanding needs. Focus is partly to exploit computer advances to allow better use of "research-grade" models in routine atmospheric effects applications. For example, we are including more physically correct and accurate electromagnetic propagation effects of ambient illumination and battlefield aerosols on signatures, weapon systems effects and for the visualization of both natural and combat-induced environments.

At the same time, however, we are also approaching the problem from the other end. Today's sophisticated Computer Image Generators (CIG's) provide many hardware functions for rendering a scene. There is a large community of users that will make use of practical application software and physically-based parameters that can be easily interfaced with the CIG. We are therefore

placing some effort on asking how our models can be improved to work more closely and efficiently with these functions, what techniques can be used to approach real-time simulation, and what are the tradeoffs in accuracy for speed. This paper explores some of these issues.

Perhaps the simplest and most direct CIG applications of radiative transfer theory can be made in the areas of: simulating atmospheric visibility; modeling the illumination environment; modeling natural features such as clouds and fog; and simulating the dynamic (now termed "embedded") processes such as dust, smoke plumes, detonations, and fires. We begin by examining standard scene rendering techniques that rely on parameters for "fog functions", blending by transparency and pixel brightness. Often these parameters are chosen based purely on subjective qualities of the final scene. However, many parameters actually have an underlying physical basis that allows them to be quantified in a scientifically meaningful and instructive way.

As a supporting application, we detail an accurate radiative doubling algorithm tailored for visualization use. The method can efficiently calculate tables for haze, fog and solar illumination parameters both off-line as precalculations and (in principle) on the fly during the rendering process. The present 2-D (plane-parallel) version uses the diffuse radiance interaction approach of the 3-D Battlefield Emission and Multiple Scattering (BEAMS) model[1] to determine the multiple scattering effects of uniform aerosol slabs for 17 upward and 17 downward solid angles. This doubling code is most applicable to viewing above, below and within uniform aerosol layers near the terrain surface. In the future we will replace or enhance this basic model with the Boundary Layer Illumination and Radiation Balance (BLIRB) model[2] and its propagation scenario code VIEW. The latter codes treat extended inhomogeneous aerosols, near-surface propagation environments, and initial scene illumination. We also examine how radiative transfer parameters can be used to support the simulation of other realistic atmospheric fluctuations implemented in the main processor cpu as 2-D or 3-D fields or within the CIG as 2-D texture overlays.

2. COMPUTER IMAGE GENERATOR (CIG) FUNCTIONS AND PROPAGATION

The Graphics Language (GL) software[3] used to drive Silicon Graphics imaging systems is representative of techniques commonly used by many simulators to off-load scene processing into hardware graphics processors. Propagation modeling is affected by and affects these functions:

o viewing transformations - the CIG translates world coordinates x-y-z to viewport coordinates, thus relieving the user from generating a 2-D image (screen) projection from 3-D geometries. The user is still responsible for defining the size of the viewport, the eyepoint coordinate, the field of view orientation and size, and the maximum and minimum ranges from the eye that will be considered. The CIG internally computes range from eye to object.

o rendering - the CIG connects user-provided x-y-z points (vertices) to form surfaces (polygons) and fills in the resulting surfaces with pixels (points on the screen) with interpolated colors and intensities based on some shading model. The user is relieved of generating the individual image pixels, but must still provide the vertex locations, their color and intensity, any special data for surface curvature, and must work within the limits of the CIG shading interpolation model. Some CIG's accept vertex lists as "objects" which are either rendered as a group or ignored as a group. While the resulting image is geometrically correct, the CIG does not automatically provide any change in color or intensity due to an intervening atmosphere.

o color and intensity - the CIG drives the display color and brightness of each pixel. The user can provide 3-color (red-green-blue) data, usually as integers 0-255 for each color component, or can provide a single number (typically 0-255) that points to a color in a look-up table (palette). Other values (such as alpha transparency below) can modify the color value. The CIG maintains a gamma calibration table designed to produce non-linear voltages to the display to maintain a linear change in perceived intensity. The user application must work within the

capability of the display to meet some industry color standard, must contend with the gamma corrections for different displays, must work within or define a suitable color palette where applicable, and must deal with the limits of a 3-color, typically 8-bit, precision. Wavelength-dependent propagation must be in the context of averages for the overlapping 3-color bands.

o range-dependent ordering - the CIG may support alternative rendering approaches to assure that objects nearer the eyepoint properly appear in front of farther objects. The method may be as simple as back-to-front rendering so that, if rendered from farthest to nearest, nearer object pixels replace those of more distant objects. The user application has the responsibility to pass vertices or objects in range-sorted order, which can be inefficient if many rendered details are then covered by nearer objects. Another common option is z-buffered rendering. The CIG produces and maintains an array (buffer) of integer distances (viewport z coordinate) for every pixel in the viewport. Only objects producing a (typically) smaller z value have that pixel rendered and their z data updated. The user application can thus pass object and vertex locations to the CIG in any order without regard to sorting. However, without regard for sorting, the results can be incorrect if an object is semi-transparent because later background objects behind it will not be rendered. Since the eyepoint receives propagated intensities, the atmosphere must either be rendered as an "object" or must modify vertex properties in a physically correct manner.

o blending - the CIG may implement a transparency channel (sometimes called an "alpha" value) and one or more methods for partly combining an incoming pixel color and intensity with an existing pixel color and intensity. The user is responsible for defining the transparency blending factor and the blending method for every vertex. Typically the shading model interpolates the blending factor as well as the color and intensity when rendering surfaces between vertices. This is probably the greatest asset the CIG maintains to support propagation effects.

o hidden surface removal - the CIG may implement methods to avoid rendering surfaces that point away from the eyepoint. A typical method is back-face elimination in which the order that vertices are provided by the user to define surface edges determines the surface orientation (right-handed versus left-handed ordering). The user can be required to provide the direction of surface normals or to pass all vertices of each polygon in the same order (say counter-clockwise with respect to viewing the surface). Depending on optical thickness and method of rendering, clouds and aerosols may or may not also possess a hidden surface requirement.

o texturing - the CIG may implement a built in 2-D table look-up that ties some property of the vertex (position, color, alpha channel, etc.) to a place in the table. The CIG modifies an attribute at the vertex (for example color or intensity) by blending or replacing it with the value in this texture table. As the surface is shaded, the CIG interpolates spatially within the texture table corresponding to the spatial interpolation of pixels being generated to form the surface between the vertices. Typical applications are photo texturing in which the texture table (itself a pixel image) is mapped on to the rendered surface, "shrink-wrapping" the photo on to the surface. Other texture approaches provide patterns or modify pixel properties to modulate filled-in pixel appearance. The user must provide the texture table and must provide explicit information for where each vertex passed to the CIG points to in the texture table. Innovative use of texture tables to represent transparency and aerosol scattering (path radiance) has great potential for off-loading the overhead of propagation effect interpolations from the CPU into the CIG.

o Mip-maps - the CIG may implement a series of texture maps to provide different levels of detail or resolution depending on object size in the viewport. These are called mip-maps (from the Latin term for many things in a small place). The CIG chooses between these 2-D tables to reduce rendering requirements. It also interpolates map to map through filters that magnify and blend values. The user must set up these tables if they are used. Mip-maps can provide a challenge to propagation corrections when each represents an object seen at a different range, but potentially could also provide transitions between different levels of detail of propagation effects.

o _illumination_ - the CIG may implement virtual illumination sources. Each rendered pixel intensity is modified based on distance of the surface to this source or, perhaps, on whether a ray from the surface being rendered connects to the light source without encountering a surface. The latter implements a z-buffer to the light source. The user must define the light source and its properties. If proper shadowing is required, the user must consider range-sorted ordering front-to-back from the light source as well as back-to-front toward the eyepoint. Generally the lighting functions are difficult to quantify radiometrically, and propagation losses from light source to scene objects may not be implemented as a CIG function.

It must also be understood that the CIG is separate from and complements but does not replace the host computer central processor (CPU). For example, the CIG can internally determine if an object will be too small in the viewport to be worth rendering (called culling) or falls outside the viewport (called pruning), and then skips further processing of that object. But these processes do not prevent or replace the user's responsibility within the application program in the CPU to also address this possibility. Without some care, the user's application can spend considerable time computing and passing information to the CIG that will not appear on the screen. Likewise, the CIG performs many arithmetic operations and mathematical transformations, such as sophisticated texture mapping. However, it may use integer arithmetic of low precision in many of these operations and thus can not or at least should not be used as a substitute for the floating point precision calculations available in the main CPU. Similar comments apply to implementing inherently 3-D propagation effects into the 2-D CIG world of surfaces. Aerosol effects can be made to show against rendered surfaces, but otherwise will not appear unless rendered themselves.

The richness of the available techniques defined above should make it clear that there can be as many different approaches as there are user simulations. The implications to providing any type of "standard" propagation models across simulations are correspondingly a challenge. For example, in using propagation codes to properly modify the CIG _inputs_ to produce the correct output scene for aerosol transmission (transparency of objects through an atmosphere) and aerosol scattering (the appearance of haze, clouds, etc., themselves), one must consider whether a transparency channel is accessible, the order used for object rendering, the color values and display gamma response, and possible interactions with values in the texture tables. It is unlikely that any single "propagation" module can be designed to plug into what is typically a very "object-oriented" environment. Rather, the propagation codes should be designed to provide relevant CIG _parameters_ and _tables_ along with the equations that define the _modifiers_ for both user application _outputs sent to the CIG_ as well as those that can be implemented directly _in the CIG itself_. Above all, the simulation designer should be educated to think in terms of how real-world illumination and propagation environments should affect the application's design and approach to ordering of commands and data sent to the CIG. As a good example, we next consider the specific example of haze and fog parameters that can be provided to the Silicon Graphics CIG.

3. FADING, FOG AND COLOR BLENDED RENDERING

The Silicon Graphics (SGI) fog function, also known on other CIG's as the fading function, is provided to simulate a loss in visibility with range. The relevant form for haze and (with proper use) for fog is documented as a hardware blending of two colors $C_{original}$ and C_{fog}:

$$C_{fogged} = C_{original} [1 - F_{og}] + C_{fog} F_{og} \quad and \quad F_{og} = 1 - e^{5.5 * Z_{eye} * D_{ensity}} \quad (1)$$

where F_{og} is an interpolating value from 0 to 1 that blends the current pixel color (or intensity) $C_{original}$ into a value C_{fog} at long range, Z_{eye} is distance in world units (meters) from the eyepoint into the scene (always a negative number in the eye viewport where x is left to right, y is bottom to top and z is toward the eye); and "D_{ensity}" is a fall off factor that defines how rapidly the effect takes place over range. The user inputs C_{fog} and D_{ensity}. The CIG computes Z_{eye} and F_{og}.

Physically, the radiative transfer equation that transforms a radiance $L(0,\Omega)$ (w m^{-2} sr^{-1}) propagating in angular direction Ω into a radiance $L(s,\Omega)$ over a distance ds along the path is:[4]

$$\frac{dL(s,\Omega)}{ds} = -K_{ext}\left[L(0,\Omega) - \omega \int_{4\pi} P(\Omega,\Omega') L(\Omega') d\Omega' \right] \tag{2}$$

where the phase function $P(\Omega,\Omega')$ is the scattering pattern produced when incoming radiance $L(\Omega')$ from direction Ω' is scattered by the aerosol into direction Ω, K_{ext} is the volume extinction coefficient for the aerosol, and ω, the single scattering albedo, is the ratio of scattering to extinction. Under the condition that the pattern of incoming radiance $L(\Omega')$ is uniform in angular pattern over a path of length s, then the integral can be performed to produce:

$$L(s,\Omega) = L(0,\Omega) \, T(s,\Omega) + L_s(\Omega) \, [\, 1 - T(s,\Omega) \,] \tag{3}$$

$$\text{where} \quad L_s(\Omega) = \omega \int_{4\pi} P(\Omega,\Omega') \, L_{in}(\Omega') \, d\Omega' \tag{4}$$

is called the limiting path radiance, and T is the direct (Beer's Law) transmittance over the path. For a horizontal layer of aerosol of thickness b and an incoming path with direction having a cosine of μ with the vertical, then the transmittance and the extinction coefficient K_{ext} can be determined from the meteorological visibility V_{is} using the Koschmieder equation:

$$T_{Beer's}(s,\Omega) = e^{-\tau(b)/\mu} = e^{-K_{ext} b /\mu},$$

$$\text{where} \quad s = b/\mu, \quad \text{and} \quad K_{ext} = \frac{3.912}{V_{is} \, (in \; units \; of \; s)} \tag{5}$$

Thus, the direct (Beer's Law) transmittance is $e^{-\tau}$ and the optical depth (or optical thickness) τ is the dimensionless product of the aerosol extinction per unit distance times distance over the path.

The similarity of Eq. 3 to Eq. 1 is obvious if one makes the connections:

$$D_{ensity} \, (in \; m^{-1}) = \frac{K_{ext}}{5500} = \frac{3.912}{5500 \, V_{is} \, (in \; km)} \, , \tag{6}$$

$$F_{og} = 1 - T(s) \quad \text{and} \quad C_{fog} = L_s(\Omega)$$

Thus, the CIG parameters do have a physical basis that can be quantified and assigned.

4. CORRELATING THE CIG FOG/HAZE FUNCTION TO VISIBILITY

The interesting factor of 5.5 in the internal F_{og} function of Eq. 1 is described in its documentation[3] as (paraphrasing) "sufficient to convert the incoming pixel C_{pixel} to the fog value C_{fog} over a unit range if D_{ensity} is assigned a value of one". We conjecture that the value of 5.5 was arbitrarily chosen so that the effective transmittance of $e^{-5.5} = 1/244$ will insure that a full 8-bit intensity of 255 will be reduced to a value very near 1. In any event, it is next worthwhile to perform a verification test to confirm the physical connection implied by Eq. 6.

Fortunately, this can be done objectively, without requiring subjective observation to judge if an object on the screen is just visible against its background. Meteorological visibility is very explicitly defined:[5] a black object, large enough to be easily resolved, is placed against the horizon sky. The visual range, or meteorological visibility, is that distance at which the contrast of the black target against this background fades to 0.02 of its initial value of -1, where contrast is defined as the difference in target and background radiances divided by background radiance.

A Silicon Graphics VGXT 310 computer was used to simulate a scene with a sky background. The fog function was turned on. For various values of C_{fog} between 100 and 255 and for an eyepoint above the surface with a 60 degree field of view, a rendered black target square was progressively moved out in distance. The intensity values of both the target and the background were monitored directly until the contrast fell to 0.02 of its initial value. Results are shown in Table 1. Intensity values were monitored at the CIG output rather than at the display to avoid the individual display's characteristics and gamma correction. Table 1 shows that the SGI function Eq. 1 with the physical connection, Eq. 6, does meet the objective criteria for meteorological visibility. Figures 1 through 4 show example scenes of clear air, the basic SGI fog function using Eq. 6, test target in the scene, and radiometrically corrected scene using models of later sections.

TABLE 1. Simulation Data Comparing SGI Fog Function with Meteorological Visibility							
C_{fog}	Assumed V_{is} (km)	Target Range (km)	Measured Contrast	C_{fog}	Assumed V_{is} (km)	Target Range (km)	Measured Contrast
255	2 km	1.0	-0.1412	175	7 km	7.0	-0.020
"	2 km	2.0	-0.020	"	15 km	7.5	-0.1428
"	7 km	3.5	-0.1412	"	15 km	15.0	-0.020
"	7 km	7.0	-0.020	100	2 km	1.5	-0.140
"	15 km	7.5	-0.1412	"	2 km	2.0	-0.020
"	15 km	15.0	-0.020	"	7 km	3.5	-0.140
175	2 km	1.0	-0.1428	"	7 km	7.0	-0.020
"	2 km	2.0	-0.020	"	15 km	7.5	-0.140
"	7 km	3.5	-0.1428	"	15 km	15.0	-0.020

Figure 1. Example Clear Air Scene.   Figure 2. Test of Visibility with SGI Fog.
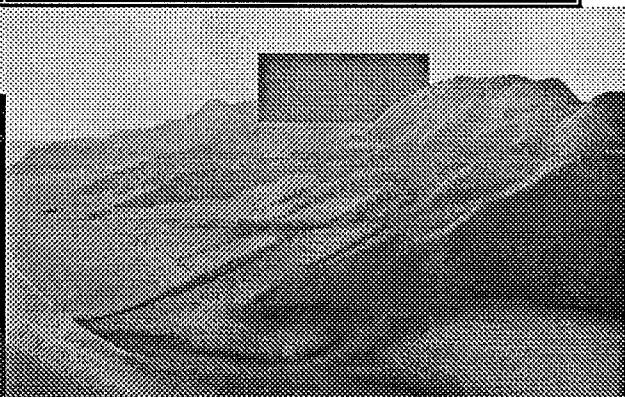
Figure 3. Scene with SGI Fog, Eq. 7.
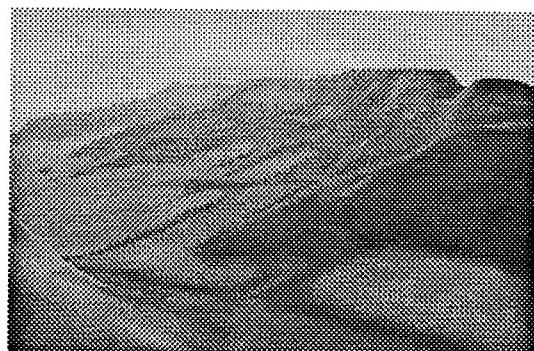
Figure 4. Corrected Haze with Radiative Model.

In addition, however, there are geometric errors in the SGI fog function for perspective projection views. In the simulation, the error was observed to increase from the center of the viewport towards its edges up to 15% over a 30° angular change. The cause of this error is simple. The CIG should really use range R_{eye} from eye to vertex rather than Z_{eye}, which is the z-buffer perpendicular distance from the eye viewport to a parallel plane that contains the vertex (i.e., the orthographic projection). This can be corrected by dividing D_{ensity} by $\mu_{(vertex-eye)}$, the dot product of the direction cosines of the eye viewing direction (center of the viewport) and the direction of the vertex with respect to the eye. One might ask, if the eyepoint is some distance above the layer in clear air, then how can we even use the fog function? As shown in Fig. 5, a geometric correction to D_{ensity} is b / H where b is the thickness of aerosol above the vertex and H is the eye height above the vertex. Thus:

$$D_{ensity}\,(in\,m^{-1}) = \frac{K_{ext}\,b}{5500\,H_{eye}\,\mu_{(vertex-eye)}} = \frac{3.912\,b}{5500\,V_{is}\,(in\,km)\,H_{eye}\,\mu_{(vertex-eye)}} \quad (7)$$

Effective Extinction Coefficient

$$K_{eye} = K_{ext}\,\frac{Layer\ Height}{Eye\ Height}$$

Eyepoint Height above Terrain

Layer Height
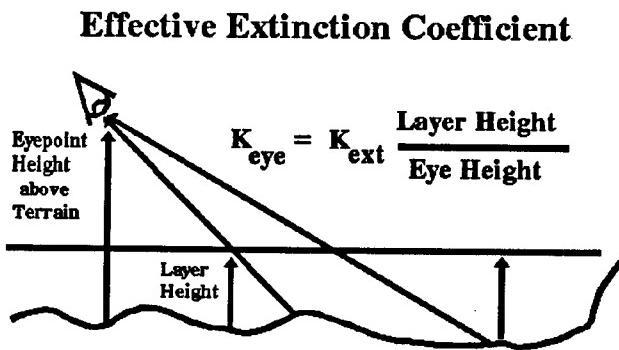
Figure 5. Defining an Effective Extinction Coefficient for Eyepoints Above the Layer.

$R = R_1 + T_1 R_2 T_1 + T_1 R_2 R_1 R_2 T_1 +$

Incoming Radiance

Layer #1

Layer #2

$T = T_2 T_1 + T_2 R_1 R_2 T_1 + T_2 R_1 R_2 R_1 R_2 T_1 +$
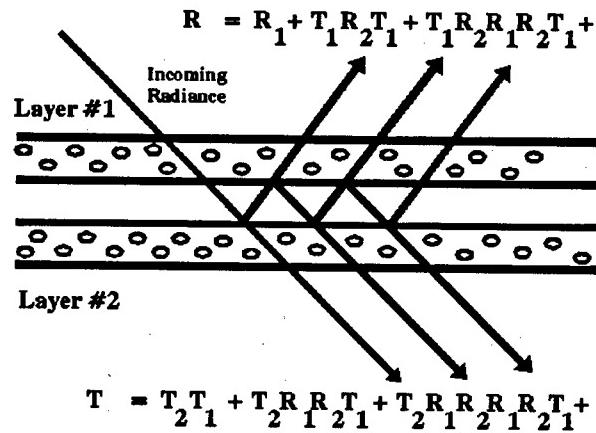
Figure 6. Multiple Scattering Between Layers in Terms of Transmissions and Reflections.

Having determined K_{ext} from the desired visibility, and D_{ensity} from K_{ext}, we now turn to the more difficult problem of picking a value for $C_{fog} = L_s(\Omega,r)$. Contrast depends critically on the scattering factor L_s. Without it, all aerosols and even white fog would appear dark, and the background behind the aerosol would always darken. It is somewhat surprising to learn that visibility, which is defined in terms of contrast, actually tells us nothing about the value of L_s. Given no other information, a reasonable choice for $L_s(\mu=0,\phi)$ is the measured brightness (and color value) of unobstructed horizon sky, where μ is the cosine of the viewing angle from zenith

411

and ϕ is the viewing azimuth (compass heading). This is because the radiance of the horizon sky is entirely due to scattering. A trivial looking, but instructive, result for viewing the horizon sky (through a uniform haze of horizontal extent at least as great as the visibility) at 0 and s is:

$$L_{sky}(s) = T(s) L_{sky}(0) + [1 - T(s)] L_s, \quad thus \quad L_s = L_{sky} \tag{8}$$

Thus, objects near the horizon such as hills, structures or trees should also appear to fade (as they approach the visual range) toward the brightness (and color) of the horizon sky. Of course from a modeling and visualization standpoint this is a somewhat circular argument, since the brightness (and color) of the horizon sky should be computed based on L_s.

At non-horizontal viewing angles there is no recourse but to compute the value of L_s. A first approximation is to compute L_s from Eq. 4 using the ambient sunlight, skylight and terrain light that are incident on the haze or fog layer as inputs to the integral. This is sufficient for small optical depths. At larger optical depths, however, multiple scattering up and down within the layer greatly modifies this result, as shown in Fig. 6. A radiative transfer model to determine an effective L_s efficiently for CIG use is given in the next sections.

5. SINGLE-SCATTERING INITIALIZATION WITH THE BEAMS PHASE FUNCTION

The BEAMS[1] radiative transfer approach treats diffuse radiances averaged within a finite number of solid angles. BEAMS normally treats diffuse radiant energy transfer between elements of different concentration and optical properties on a 3-D cubic lattice. Solid angles are centered on rays projecting from the center of each cubic element to the centers of its 26 nearest neighbors. The solid angles are not equal in size. They are pyramidal cones defined to cover the full 4π sr in direction without gaps or overlap. The drawback to using BEAMS directly in simulations is its large memory requirement and a very long run time imposed by repeated iterations of element to element interactions to convergence. For simpler situations, such as uniform haze or fog layers, the problem reduces to the simpler and extensively treated 2-D plane-parallel aerosol problem.

Reduction to 2-D uniform aerosol geometries permits one to treat the radiative interactions by the well-known invariant embedding or doubling method. The main improvements we make here are: using the BEAMS averaging and integration of diffuse radiance over solid angles which can then be combined as matrices rather than integrals; and grouping operations so that diffuse sky operators do not need to be recalculated when direct beam (sunlight) conditions are changed.

To overcome the chronic problem in plane-parallel solutions of scattering along the horizontal, the 8 BEAMS solid angles in the horizontal plane are broken in half into 8 upward-projecting and 8 downward-projecting components. Thus, radiances are sought for 17 upward projecting solid angles and 17 downward projecting solid angles. The BEAMS initialization of the resulting 17x17 radiative transfer matrices is still used. These matrices, denoted as P_{ij}, are integrations and averages of the single scattering phase function $P(\Omega,\Omega')$ over incoming and outgoing solid angles:

$$P_{ij} = \frac{\displaystyle\int_{\Delta\Omega_i} \left[\int_{\Delta\Omega_j} P(\Omega_i,\Omega'_j)\, d\Omega'_j \right] d\Omega_i}{\displaystyle\int_{\Delta\Omega_i} d\Omega_i} \tag{9}$$

Note that the transformation of the phase function into a finite number of discrete solid angles requires that we integrate incident radiance over the incoming solid angle and average the radiance over the outgoing solid angle to conserve the phase function normalization.

412

This one-time calculation completely defines the optical scattering properties of a given aerosol type for one distribution of particle sizes per unit concentration at the radiation wavelength. It is performed off-line in 5 to 10 minutes on a 60 MHz 80486 PC or equivalent.

6. MATRIX FORMULATION FOR RADIANCE FROM AEROSOL LAYERS

The basic form of the radiative transfer operator is a matrix multiplication that transforms incident radiances $L^{dn}(0)$ at the top of a layer and $L^{up}(b)$ at the bottom of the layer into outgoing radiances $L^{dn}(b)$ from the bottom of the layer and $L^{up}(0)$ from the top of the layer:

$$
\begin{bmatrix} L^{dn}(b) \\ L^{up}(0) \end{bmatrix} = \begin{bmatrix} T^{dn} & R^{dn} \\ R^{up} & T^{up} \end{bmatrix} \begin{bmatrix} L^{dn}(0) \\ L^{up}(b) \end{bmatrix}
\tag{10}
$$

In the present method the individual transfer entities R and T are actually 17x17 matrices and the radiances L are 17 element vectors for the 17 solid angle incoming and outgoing directions.

Transfer matrices can be combined for the total effect of a single layer as in Fig. 6. Total transmission downward through layer 1 of optical depth b and layer 2 of optical depth c is:

$$
T(b+c) = T_2(c) \left[1 + R_1(b) R_2(c) + R_1(b) R_2(c) R_1(b) R_2(c) + \cdots \right] T_1(b)
$$
$$
= T_2(c) \left[1 - R_1(b) R_2(c) \right]^{-1} T_1(b)
\tag{11}
$$

where the negative exponent implies a matrix inversion. Total reflection is:

$$
R(b+c) = R_1(b) + T_1(b) \left[1 + R_2(c) R_1(b) + R_2(c) R_1(b) R_2(c) R_1(b) \right.
$$
$$
\left. + \cdots \right] R_2(c) T_1(b)
\tag{12}
$$
$$
= R_1(b) + T_1(b) \left[1 - R_2(c) R_1(b) \right]^{-1} R_2(c) T_1(b)
$$

Equations for total upward transmission and total downward reflection for radiance incident from below the layers are similar, with substitutions $R_1(b)$ for $R_2(c)$, $T_1(b)$ for $T_2(c)$ and vice versa.

This provides a particularly efficient and convenient method for building up the multiple scattering between layers by doubling the optical depth at each iteration:

$$
T^{up}(2b) = T^{up}(b) \left[1 - R^{up}(b) R^{dn}(b) \right]^{-1} T^{up}(b)
\tag{13}
$$

$$
R^{up}(2b) = R^{up}(b) + T^{up}(b) \left[1 - R^{up}(b) R^{dn}(b) \right]^{-1} R^{up}(b) T^{dn}(b)
\tag{14}
$$

and similarly for downward operators. Matrices are initialized by the exact solution for a layer of optical depth r, sufficiently thin that single scattering dominates, based on Eq. 4. Subscript conventions used are modified from the BEAMS 26-solid angle integrated phase function $P(\Delta\Omega_{in}, \Omega'_{out})$. The present transfer matrix is P_{ij} such that j is the incoming radiance and i is the outgoing radiance, and stored such that $P_{(35-i)j}$ has outgoing radiance opposite in direction to that of i. Initial T_{ij} and R_{ij} are then:

$$T_{ij} = \delta_{ij}\, e^{-\tau/\mu_i} + (1 - e^{-\tau/\mu_i})\, \omega\, P_{ij} \left.\begin{array}{c} \\ \\ \end{array}\right\} \quad \begin{array}{l} i = 1 \ to \ 17 \\ j = 1 \ to \ 17 \ downward \\ and = 18 \ to \ 34 \ upward \end{array} \qquad (15)$$
$$R_{ij} = (1 - e^{-\tau/\mu_i})\, \omega\, P_{(35-i)j}$$

The formalism thus far applies to diffuse radiance entering and emerging over the 17 solid angle element directions. It is also necessary to include an incident direct (parallel) beam radiance term L_{dir}, such as sunlight. This can be done by defining separate transfer matrices T_{dir} and R_{dir} for the <u>diffuse radiance</u> resulting only <u>from the direct beam</u> interaction with the aerosol slab. These are distinguished from the previously defined transfer matrices T_{dif} and R_{dif} resulting from incident diffuse radiation L_{dif}, such as skylight and terrain radiance, by:

$$\begin{bmatrix} L_{dif}^{dn}(b) \\[2mm] L_{dir}^{dn}(b) \\[2mm] L_{dif}^{up}(0) \\[2mm] L_{dir}^{up}(0) \end{bmatrix} = \begin{bmatrix} T_{dif}^{dn} & T_{dir}^{dn} & R_{dif}^{dn} & R_{dir}^{dn} \\[2mm] 0 & e^{-\tau} & 0 & 0 \\[2mm] R_{dif}^{up} & R_{dir}^{up} & T_{dif}^{up} & T_{dir}^{up} \\[2mm] 0 & 0 & 0 & e^{-\tau} \end{bmatrix} \begin{bmatrix} L_{dif}^{dn}(0) \\[2mm] L_{dir}^{dn}(0) \\[2mm] L_{dif}^{up}(b) \\[2mm] L_{dir}^{up}(b) \end{bmatrix} \qquad (16)$$

This method is particularly convenient. It allows all the transfer matrices to be precomputed (for a particular sun angle) and then applied to whatever ambient illumination conditions L_{dif} and L_{dir} are present in the scenario. To further facilitate computations, the matrix interactions can be separated so that only T_{dir} and R_{dir} need to be recomputed (or pre-computed) for different sun angles, while the diffuse transfer matrices T_{dif} and R_{dif} remain unchanged. Doubling equations for diffuse components (and similarly for reversed up and down directions) results in:

$$T_{dif}^{dn}(2b) = T_{dif}^{dn}(b)\left[1 - R_{dif}^{dn}(b)\, R_{dif}^{up}(b)\right]^{-1} T_{dif}^{dn}(b) \qquad (17)$$

$$R_{dif}^{up}(2b) = R_{dif}^{up}(b) + T_{dif}^{up}(b) * \qquad (18)$$
$$\left[1 - R_{dif}^{up}(b)\, R_{dif}^{dn}(b)\right]^{-1} R_{dif}^{up}(b)\, T_{dif}^{dn}(b)$$

$$T_{dir}^{dn}(2b) = T_{dir}^{dn}(b)\, e^{-\tau(b)} + T_{dif}^{dn}(b)\left[1 - R_{dif}^{dn}(b)\, R_{dif}^{up}(b)\right]^{-1} * \qquad (19)$$
$$\left[T_{dir}^{dn}(b) + R_{dif}^{dn}(b)\, R_{dir}^{up}(b)\, e^{-\tau(b)}\right]$$

$$R_{dir}^{up}(2b) = R_{dir}^{up}(b) + T_{dif}^{up}(b)\left[1 - R_{dif}^{up}(b)\, R_{dif}^{dn}(b)\right]^{-1} * \qquad (20)$$
$$\left[R_{dif}^{up}(b)\, T_{dir}^{dn}(b) + R_{dir}^{up}(b)\, e^{-\tau(b)}\right]$$

Although they appear formidable, these matrix terms can be precomputed, combined and stored as sets of 17x17 coefficients for a series of optical depths. These can then be used as weights and applied to whatever combination of ambient incoming radiances represent the

illumination conditions of a particular scenario. The resulting output values of L^{up} and of L^{dn} for each optical depth then give a reasonably compact data set for the diffuse scattered radiation from aerosol slabs of different thickness and in each of 17 directions. These can be rapidly interpolated in both layer thickness and angle to give vertex radiance values for direct scene rendering. Or they can be converted into equivalent L_s values for use in the CIG blending and fog functions.

For cases where we are inside the aerosol layer, the results can be combined for two layers, one above and one below the observer. Let an upper layer 1 of optical depth b have transfer matrices T_{dif1}, T_{dir1}, R_{dif1} and R_{dir1}, and a lower layer 2 of optical depth c have transfer matrices T_{dif2}, T_{dir2}, R_{dif2} and R_{dir2}. After multiplication, downward and upward diffuse radiances are:

$$L_{eff}^{dn} = \left[1 - R_{dif1}^{dn}(b)\, R_{dif2}^{up}(c) \right]^{-1} \left\{ R_{dif1}^{dn}(b)\, T_{dif2}^{up}(c)\, L_{dif}^{up}(b+c) + \right.$$

$$\left[R_{dif1}^{dn}(b)\, T_{dir2}^{up}(c) + R_{dir1}^{dn}(b)\, e^{-\tau(c)} \right] L_{dir}^{up}(b+c) + \qquad (21)$$

$$\left. T_{dif1}^{dn}(b)\, L_{dif}^{dn}(0) + \left[T_{dir1}^{dn}(b) + R_{dif1}^{dn}(b)\, R_{dir2}^{up}(c)\, e^{-\tau(b)} \right] L_{dir}^{dn}(0) \right\}$$

$$L_{eff}^{up} = \left[1 - R_{dif2}^{up}(c)\, R_{dif1}^{dn}(b) \right]^{-1} \left\{ R_{dif2}^{up}(c)\, T_{dif1}^{dn}(b)\, L_{dif}^{dn}(0) + \right.$$

$$\left[R_{dif2}^{up}(c)\, T_{dir1}^{dn}(b) + R_{dir2}^{up}(c)\, e^{-\tau(b)} \right] L_{dir}^{dn}(0) + T_{dif2}^{up}(c)\, L_{dif}^{up}(b+c) \qquad (22)$$

$$\left. + \left[T_{dir2}^{up}(c) + R_{dif2}^{up}(c)\, R_{dir1}^{dn}(b)\, e^{-\tau(c)} \right] L_{dir}^{up}(b+c) \right\}$$

Again, parts of these equations can be precomputed and stored as 17x17 tables as a function of optical depth. Interpolation in optical depth for the partial slab above and partial slab below the observer can be performed. And, until the output data set becomes unmanageably large, these radiance vectors can either be precomputed and stored or recomputed on the fly.

7. VERIFYING THE DOUBLING METHOD FOR BEAMS PHASE TRANSFER MATRICES

The doubling method with the BEAMS initial diffuse transfer matrix P_{ij} compares extremely well with exact results for anisotropic scattering from finite layers published by Van de Hulst[6]. Figures 7 through 11 compare transmitted and reflected radiance from uniform aerosol layers of optical depths ranging from almost transparent ($\tau=0.0625$) to opaque ($\tau=32$). In each case a radiance of flux $0.24\,\pi$ is incident downward, perpendicular to a uniform aerosol layer having an anisotropic, conservative ($\omega=1$), single scattering Henyey-Greenstein phase function with asymmetry factor $g = 0.5$. The factor $0.24\,\pi$ for incident flux is the solid angle of the normal-incidence BEAMS solid angle. Thus, the incident radiance is unity (1 w m^{-2} sr^{-1}), and the figure vertical axes of the outgoing radiance (w m^{-2} sr^{-1}) are for directions and optical depths τ shown.

Exact values for transmitted radiance are shown as solid lines and computed data as points for outgoing angles of 0° (straight through), 45°, 55°, 77°, and 90° (grazing) at the bottom of the layer. Exact values for reflected radiance are shown as dashed lines and the computed data as points for outgoing angles of 180° (straight back), 135°, 125°, 103°, and 90° (grazing) at the top of the layer.

For nearly every outgoing angle and optical depth, the doubling code is within 5% of the exact value, with some exceptions. At optical depths between 0.5 and 2 and 0° outgoing direction (Fig. 7) the predicted transmitted radiances are 10% too low. The data include only diffusely scattered radiance and do not include the directly transmitted (Beer's Law $e^{-\tau}$) radiance which varies from

415

0.586 w m^{-2} sr^{-1} at a τ of 0.5 to 0.117 w m^{-2} sr^{-1} at a τ of 2. Error when the direct transmittance is added is 5% or less.

Worst agreement is for radiance emerging at 90°, parallel to the aerosol layer surface (Fig. 11). Plane parallel radiative transfer models usually have problems at angles from about 87° to 93°, because the emerging ray has experienced large multiple scattering along almost infinite paths through the aerosol. Model outputs at 90° are linearly extrapolated from those at 77.424° and 79.168° which are the mean angles for BEAMS transfer matrix solid angles that include 90°. The error is nearly a factor of 2 at low optical depths and 10% to 15% at optical depths above 0.25.

BEAMS 2-D Radiative Transfer
Case: 0° In; 180° (Reflectance) and 0° (Transmittance) Out
H-G Phase Function, g=0.5, omega=1
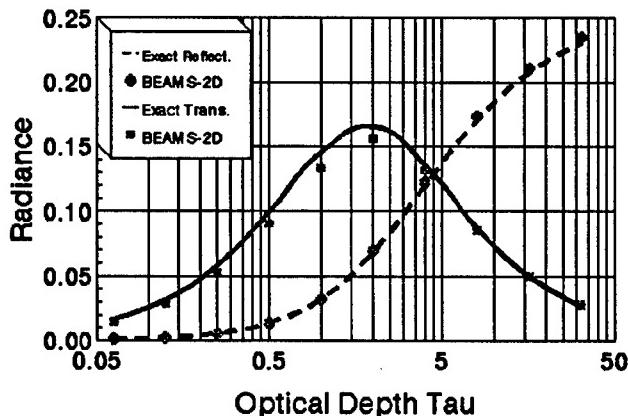
Figure 7. Comparison of Exact Radiance (Van de Hulst) with Doubling Method. Diffuse Forward and Backward Scattering from Uniform Aerosol Layer.

To pass as a C_{fog} parameter to the CIG hardware, radiance values must be converted to the effective value of $L_s(\Omega)$ of Eq. 3. The limiting path radiance $L_s(\Omega)$ is also that required for the direct blending of an existing background when $\alpha = 1 - T$ is used as a blending factor. The $L_s(\Omega)$ are as easy to tabulate with τ as L is itself, based on the conversion:

$$L_s^{dn}(\tau, \Omega_i) = \frac{L_i^{dn}(\tau) - L_i^{dn}(0)\, e^{-\tau/\mu_i}}{1 - e^{-\tau/\mu_i}} \qquad (\textit{similarly for } L_s^{up}) \tag{23}$$

Figures 12 through 15 show converted radiances L_s for the Van de Hulst comparison data sets. Note the improvement at 90° by extrapolating L_s values rather than L values to 90°. Computer times to generate a complete doubling set of L or L_s are on the order of a few seconds given the initial P_{ij} as starting values for Eq. 15. Curves are smooth enough to linearly interpolate in τ.

BEAMS 2-D Radiative Transfer
Case: 0° In; Edge (135° Reflectance and 45° Transmittance) Out
H-G Phase Function, g=0.5, omega=1

Figure 8. Comparison of Exact and Doubling Method for 45° Scattering.

BEAMS 2-D Radiative Transfer
Case: 0° In; Corner (125° Reflectance and 55° Transmittance) Out
H-G Phase Function, g=0.5, omega=1
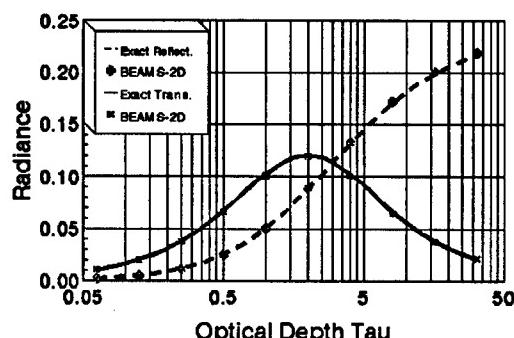
Figure 9. Comparison of Exact Radiance with Doubling Method for 55° Scattering.

416

BEAMS 2-D Radiative Transfer
Case: 0° In; Side (103° Reflectance and 77° Transmittance) Out
H-G Phase Function, g=0.5, omega=1

BEAMS 2-D Radiative Transfer
Case: 0° In; Grazing(90° Reflectance and 90° Transmittance) Out
H-G Phase Function, g=0.5, omega=1
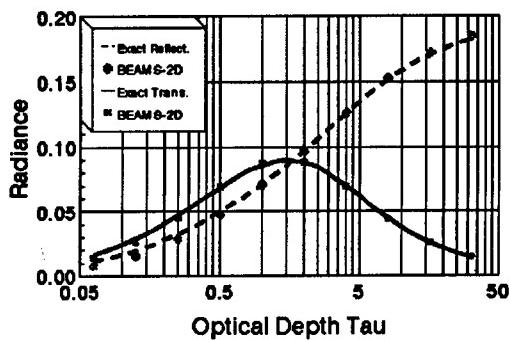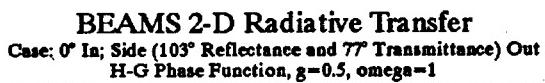
Figure 10. Comparison of Exact Radiance with Doubling Method for 77° Scattering.
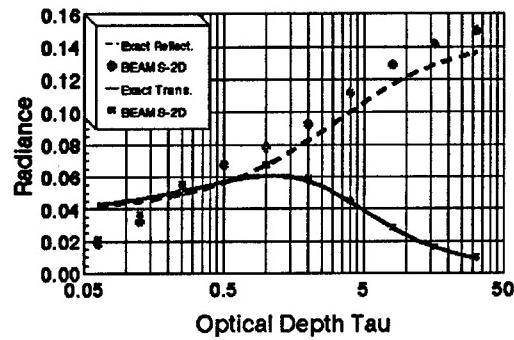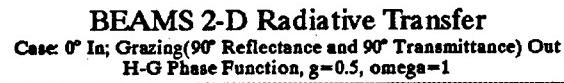
Figure 11. Comparison of Exact Radiance with Doubling Method at 90° (Grazing).

BEAMS 2-D - Converted Ls Values
Case: 0° In; 180° (Reflectance) and 0° (Transmittance) Out
H-G Phase Function, g=0.5, omega=1

BEAMS 2-D Converted Ls Values
Case: 0° In; Corner (125° Reflectance and 55° Transmittance) Out
H-G Phase Function, g=0.5, omega=1
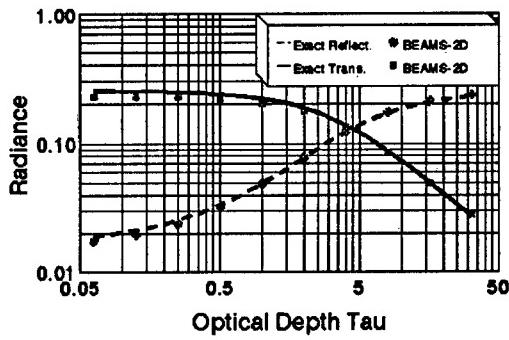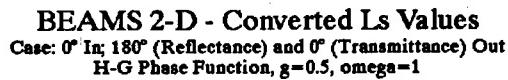
Figure 12. Converted Ls Values for 0 and 180 deg.
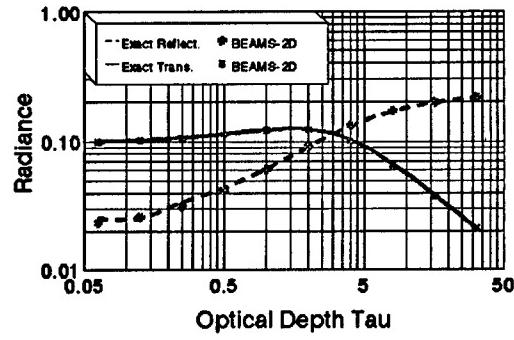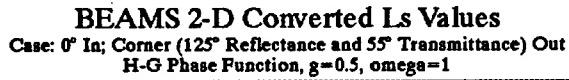
Figure 13. Converted Ls Values at 55 deg.

BEAMS 2-D Converted Ls Values
Case: 0° In; Side (103° Reflectance and 77° Transmittance) Out
H-G Phase Function, g=0.5, omega=1

BEAMS 2-D Converted Ls Values
Case: 0° In; Grazing(90° Reflectance and 90° Transmittance) Out
H-G Phase Function, g=0.5, omega=1
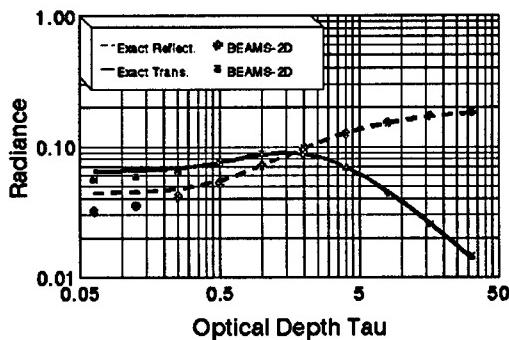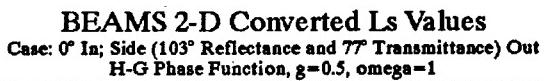
Figure 14. Converted Ls Values for 77 deg.
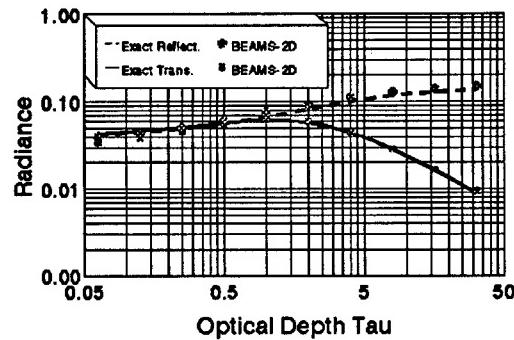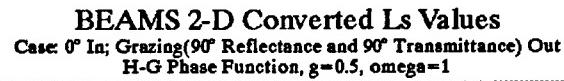
Figure 15. Converted Ls Values at 90 deg

417

8. ONGOING EFFORTS ON FINITE, INHOMOGENEOUS CLOUDS

The approach to inhomogeneous haze and fog and to finite smoke and dust plumes is similar to that for aerosol layers. However, the fog function is less likely to be an efficient choice of CIG function. Rather, use can be made of a combination of alpha-blending and texture mapping. The physical parameters required are: a physically based model of inhomogeneity and fluctuations in concentration[7]; optical depth determined through use of mass extinction (extinction per unit concentration) rather than volume extinction (extinction per unit distance)[8]; a phase function relevant to the particles and wavelength of interest[9]; a source model for the transport, diffusion and mean mass distribution of the cloud[8]; and a radiance model for computing $L_s(\Omega,r)$ [1]. Most of these elements have been described previously. The connection to the CIG is in the rendering.

Successful models for scene generation with obscurants have been produced[10]. The tradeoffs are in the volume rendering of internal elements within the cloud versus approximating the statistics and appearance as 2-D textures mapped on to either curved surfaces or multiple perpendicular planes. Required time dependence of clouds adds additional overhead.

Physically-based pseudo-random fluctuation fields can be generated from portable random number generators to provide the same 3-D volumes or 2-D texture maps in a networked environment. Use of Fast-Fourier Transforms (FFT) can provide a 256x256 texture that contains 8 additional bands along the third dimension in approximately 2 seconds on a fast 80486 equivalent cpu. These are sufficient for most 2-D textured fluctuation fields such as that shown in Fig 16. Time-dependent evolution of eddies in a dust or smoke plume takes place as they transport down wind. However, the larger eddies do not significantly evolve into smaller eddies over periods less than two or three seconds. Thus, the same texture can be transported over those periods. Pre-computation of multiple sets of textures can be effective since movement from disk to memory is faster than recalculation from scratch. However, there is a penalty paid each time a new texture is required to be "bound" into texture map memory. The generation of full 3-D fluctuation fields by 3-D FFT can be very time consuming. Once formed, the rendering of a 3-D volume of concentration elements is proportional to the number of planes in the third dimension.
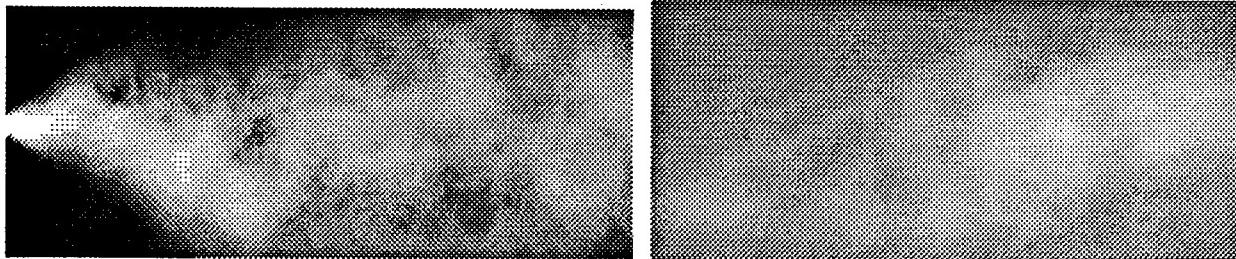
Figure 16. 2-D Texture Times Mean Cloud.   (Fog Oil Left, Explosive Dust Right)

Thus, while the best physics is probably provided by 3-D cloud volumes, current technology limitations favor the 2-D approach. The 2-D approach involves texture mapping of fluctuations about the mean on to a smooth mean field value for concentration. The mean field can be easily described as a path-integrated concentration through the plume, usually gaussian in the lateral directions. Alpha blending, using the alpha channel to vary the transparency (i.e. $\alpha = 1 - T$), and using the color or intensity channels to provide the value(s) of L_s is thus effectively:

$$L_{out}(x_i,y_j) = L_{background}(x_i,y_j) \left[1 - \alpha(x_i,y_j) \right] + L_s(x_i,y_j)\, \alpha(x_i,y_j) \qquad (24)$$

The L_s field, like the mean, path-integrated concentration, changes with position more smoothly than transmittance fluctuations. In the case of L_s, this is because the diffuse radiance participating in the scattering comes from many different directions. Its integration smooths out some fluctuations in incoming radiance. The transmittance $(1-\alpha)$, however, is computed over

418

individual rays that encounter far fewer eddies within the cloud and thus experience less averaging through the eddies. Optical depth dependence of L_s is very similar in form to that shown in Figs. 12 through 15. The main differences are that radiation escapes from the sides of finite clouds, whereas it is "trapped" in the plane parallel layers discussed earlier. Since detailed radiance calculations of L_s for specific snapshots of 3-D concentrations are so lengthy and require large memory arrays, one must at present settle for "typical" distributions from representative calculations. Thus, while the CIG is provided with L_s distributions similar to those shown in Figs. 12 through 15, they must in general be solely from pre-processed parametric curves or stored data rather than computed on the fly. Work is in progress to develop these representative data sets.

9. CONCLUSIONS

The drive towards increased computer simulation of combat and weapon engagements through advances in Computer Image Generators includes the need for greater realism of the battlefield environment. We have shown some of the U.S Army Research Laboratory's ongoing efforts to incorporate physically correct propagation and radiance into scene visualization. Our approach begins with low-level requirements for off-loading image processing from central processors to CIG hardware and to work backwards to determine how detailed physics models can best be produced to meet these requirements. In this paper we have shown that the CIG fog and fading functions have a physical basis that can be quantified and predicted. The haze function for one CIG has been verified with physics. A highly accurate and efficient algorithm for treating layers of aerosols and fog has been described. The extension of the methods to the rendering of other forms of clouds through other functions such as pixel blending and surface texturing are ongoing.

10. REFERENCES

1. Hoock, Donald , John Giever, Sean O'Brien and Edward Burlbaw, 1992; "A Multi-Stream Radiative Transfer Model for Inhomogeneous, Three-Dimensional Aerosol Clouds", U.S. Army Research Laboratory Proceedings of the 1992 Battlefield Atmospherics Conference, Ft. Bliss TX, pp. 3-12.
2. Wetmore, Alan E., 1993; "The Boundary Layer Illumination and Radiation Balance Model BLIRB", Proceedings of the Cloud Impacts on DoD Operations and Systems (CIDOS) 1993 Conference, 16-19 Nov 93, Ft. Belvoir, VA, in press.
3. Silicon Graphics, Inc, 1991; Graphics Library Programming Guide, Document Number 007-1201-040, Silicon Graphics, Inc., Mountain View, CA.
4. Hoock, Donald W., 1991; "Modeling Time Dependent Obscuration for Simulated Imaging of Smoke and Dust Clouds", Proceedings of the SPIE Vol. 1486, pp. 164-175.
5. Hoock, D., J. Giever and S. O'Brien, 1993; "Battlefield Emission and Multiple Scattering (BEAMS), a 3-D Inhomogeneous Radiative Transfer Model", Proceedings of the SPIE Vol. 1967, Characterization, Propagation and Simulation Conference, Orlando, FL, pp. 268-277.
6. Van de Hulst, Hendrik C., 1980; Multiple Light Scattering Tables, Formulas and Applications, Volumes 1 and 2, Academic Press, New York.
7. Hoock, Donald W., 1991; "Theoretical and Measured Fractal Dimensions for Battlefield Aerosol Cloud Visualization and Transmission", U.S. Army Research Laboratory Proceedings of the 1991 Battlefield Atmospherics Conference, Ft. Bliss TX, pp. 46-55.
8. Hoock, D., R. Sutherland and D. Clayton, 1987; EOSAEL 87, Volume 11, Combined Obscuration Model for Battlefield Induced Contaminants COMBIC, U.S. Army Research Laboratory Battlefield Environment Directorate (formerly Atmospheric Sciences Laboratory) report TR-0221-11, White Sands Missile Range, NM.
9. Pollock, David, 1993; The Infrared and Electro-Optical Systems Handbook, Volume 7, SPIE Optical Engineering Press, Bellingham Washington, Chapter 6.
10. Gardiner, Geoffrey, and G. Mike Hardaway, 1992; "Visualization of Multiple Battlefield Obscurants", U.S. Army Research Laboratory Proceedings of the 1992 Battlefield Atmospherics Conference, Ft. Bliss TX, pp. 13-22.

Comparison of the BEAMS 2.2 Radiative Transfer Algorithm with other Radiative Transfer Methods

Sean G. O'Brien
Physical Science Laboratory
New Mexico State University
Las Cruces, New Mexico 88003-0002

ABSTRACT

This paper describes the Battlefield Emission and Multiple Scattering (BEAMS 2.2) model, a 26-stream radiative transfer algorithm for the prediction of diffuse radiation in finite 3-dimensional clouds. Results are presented for several comparisons of the BEAMS 2.2 model with other, independent, methods for computing radiance from homogeneous cuboidal and semi-infinite plane-parallel clouds. The radiative transfer methods and results from the literature that are compared to BEAMS 2.2 results include both Monte Carlo solutions for cuboidal-shaped clouds and spherical harmonics solutions for plane-parallel cloud types. Aerosol phase functions used in these comparisons varied from a sharply forward-peaked Deirmendjian water cloud (C1 function) to Henyey-Greenstein phase functions with small asymmetry parameters and broad forward peaks. In most cases, the BEAMS 2.2 algorithm results compare closely with those reported for the other methods. The present BEAMS 2.2 radiative transfer model also agrees well with the other methods at larger optical thicknesses. This improvement over the BEAMS algorithm as described at last year's conference is discussed.

1. INTRODUCTION

Recent improvements in computer hardware capability and concerns about future military training budgets have made the simulation of battlefield sensor imagery a very active DOD research area. Much recent work has been directed at the realistic simulation of terrain elements, vehicle signatures, obscurant dissemination, and weather effects. Radiative transfer effects have usually been simulated in rudimentary ways, with path transmission and single scattering path radiance effects representing the normal level of sophistication. This degree of realism is adequate for most optically thin atmospheric conditions, but when dense artificial or natural obscurants are present, a treatment that includes multiple scattering effects must be employed.

Multiple scattering visualization treatments are usually impractical and rare. Execution times and storage allocation for full multiple scattering analysis are restrictive for spatial arrays with granularities approaching those used to simulate terrain scene elements. The speed and memory capabilities of current computers used in scene visualization do, however, allow for multiple scattering calculations to be performed on coarse grids that are fine enough to show small-scale spatial variations of multiply scattered radiance. Though such grids are more coarse than those used for normal scene elements, they at least provide a more accurate picture of radiance that may be mapped into more detailed grids.

A multistream model for the calculation of multiple scattering radiance within aerosol obscurant clouds was described at last year's Battlefield Atmospherics Conference[1]. This model, called the Battlefield Emission and Multiple Scattering (BEAMS) model, maps a coarse multiple scattering radiance grid into a fine transmission grid. The BEAMS 2.2 model described below differs

from the version (BEAMS 2.0) described last year in three significant respects. BEAMS 2.2 partitions diffuse scattered radiance into 26 equally sized solid angle streams rather than the non-uniformly sized streams of BEAMS 2.0. Another difference is that BEAMS 2.2 uses a single scattering approximation for cell-to-cell radiation transfer, unlike the more elaborate two-stream eigenvalue solution applied to rows of cells in BEAMS 2.0[1]. In its reliance on uniform stream sizes and microscale single scattering, BEAMS 2.2 resembles the original 6-stream BEAMS (Version 0) code more than either of the later BEAMS 1.0 or 2.0 versions. BEAMS 2.2 differs from all previous versions in its use of a multiple scattering phase matrix. The construction and meaning of the multiple scattering phase matrix will be outlined below.

As a check on the accuracy and domain of applicability of the BEAMS 2.2 model, several comparisons were made between the BEAMS 2.2 model and other radiative transfer results available in the literature, from private communications with other investigators, or from independent in-house models. These comparisons are organized around the shape of the aerosol obscurant cloud that occupies the computational grid.

2. THEORY

2.1 THE BEAMS 2.2 MULTISTREAM APPROACH

The BEAMS numerical solution of the radiative transfer problem is performed for a three-dimensional array of cubical elements enclosing a region of multiply-scattering aerosol obscurant. Each array element exchanges radiant power with its 26 nearest neighbor cells or the enclosing boundary via 26 transfer streams. Figure 1 illustrates the points where the stream centerlines intersect the surface of a cubical element and their orientation relative to the cartesian coordinate system used in the BEAMS 2.2 radiative transfer model.
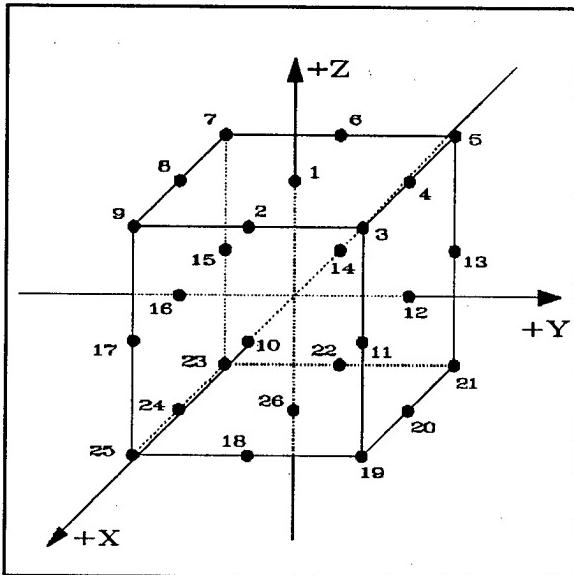
Figure 1. BEAMS 2.2 multistream geometry for an individual array element.
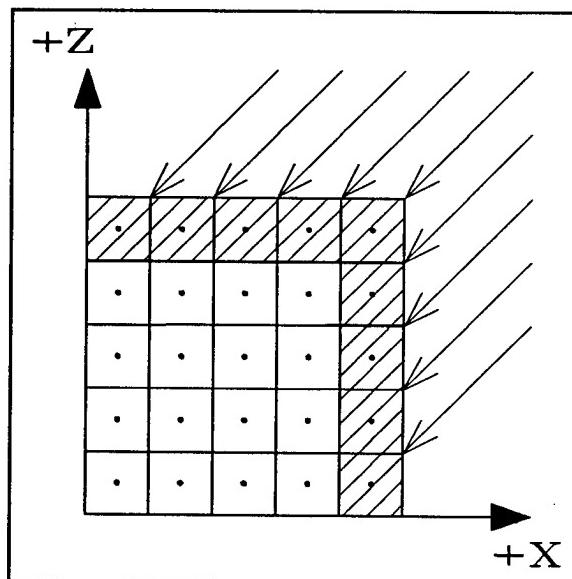
Figure 2. XZ section of 5x5x5 definition region showing echelon of initial illumination.

The external boundary of the problem definition region may be illuminated by one or any combination of the following: 1) a collimated infinite beam simulating clear sky solar illumination, 2) isotropic diffuse illumination simulating skylight from above and/or diffuse ground plane reflection from below,

422

or 3) finite beam illumination from collimated sources. Of these possibilities, only the infinite beam case will be considered here. Figure 2 shows an X-Z layer section of a 5x5x5 definition region initially illuminated by an infinite collimated beam incident in the X-Z plane at a zenith angle of 45 degrees. The hatched echelon of cells shows the zone where streams deliver power to the center of each cell. The radiative transfer approximation used here assumes that, for each propagation step, power transfer between cells is a single scattering process between cell centers. This is a reasonable simplification for finely-gridded and optically thin clouds. In this regime, the transfer of radiation by scattering from stream i to stream j is represented as a product of propagation factors:

$$P_j = P_i \left[e^{-k_{abs} r_{ij}} (1-e^{-k_{sca} r_{ij}}) \, p_{ij} \right] , \tag{1}$$

where P_j is the output power along stream j, P_i is the input power along stream i, k_{abs} is the volume absorption coefficient, r_{ij} is the length of the path from the entry point of stream i through the cell center to the exit point of stream j, k_{sca} is the volume single scattering coefficient, and p_{ij} is the phase matrix element for scattering from the stream i direction into the stream j direction. The exponential factor involving absorption in Eq. 1 reflects that fraction of the incoming power that survives absorption. The fraction of incoming unabsorbed power that is scattered is given by the absorption factor multiplied by the (1-exp($-k_{sca}$ r_{ij})) scattering factor. Finally, the fraction of the scattered power that transfers from stream i to stream j is represented by the phase matrix element p_{ij}.

Multiple scattering effects are simulated in the BEAMS 2.2 algorithm by allowing cells to emit and receive power from their adjacent neighbors in successive propagation steps. The BEAMS propagation step consists of a two phase output/input calculation cycle. The first phase calculates the 26 output stream powers for each cell in the definition array, based upon incoming power at the cell boundary. These output power values are then summed with the contents of an accumulator array and stored in that array. The second phase of the propagation step calculates the input stream values at the boundary of each cell. Figures 3-6 schematically show two propagation cycles for the initial conditions of Fig. 2.
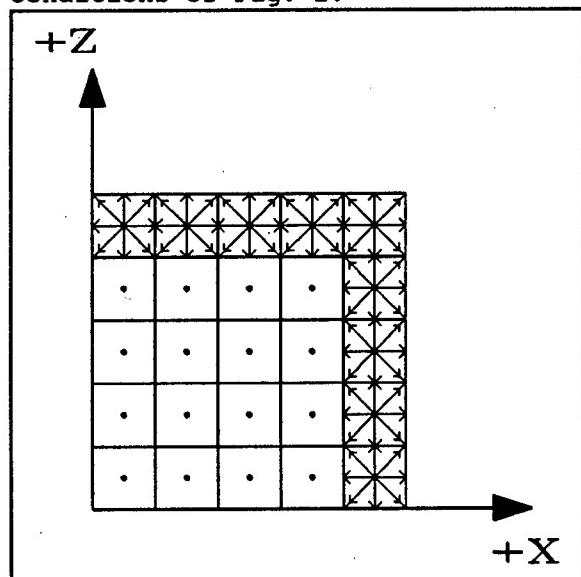
Figure 3. Radiant output calculation phase at beginning of first propagation step for initial conditions of Fig. 2.
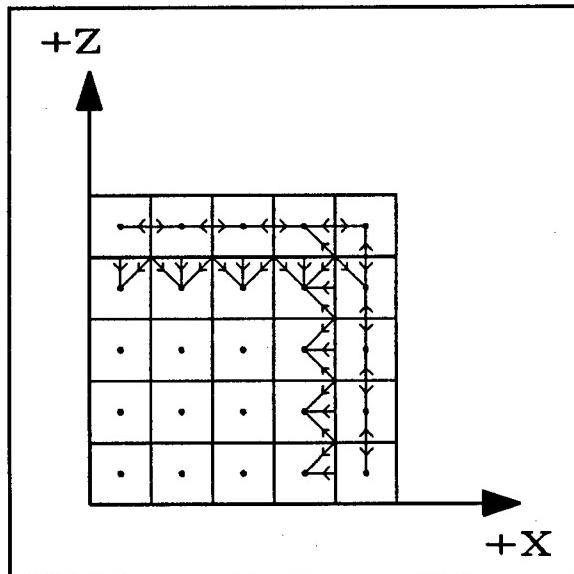
Figure 4. Second phase of first propagation step: calculation of incoming scattered power along active streams.
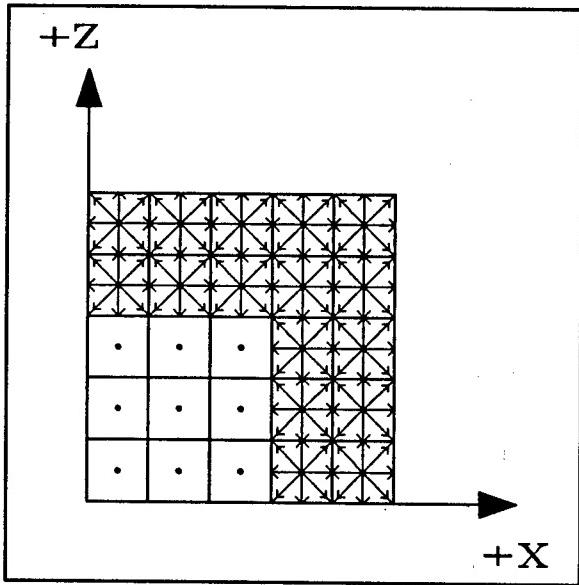
Figure 5. First phase of second propagation step: calculation of active cell output streams.
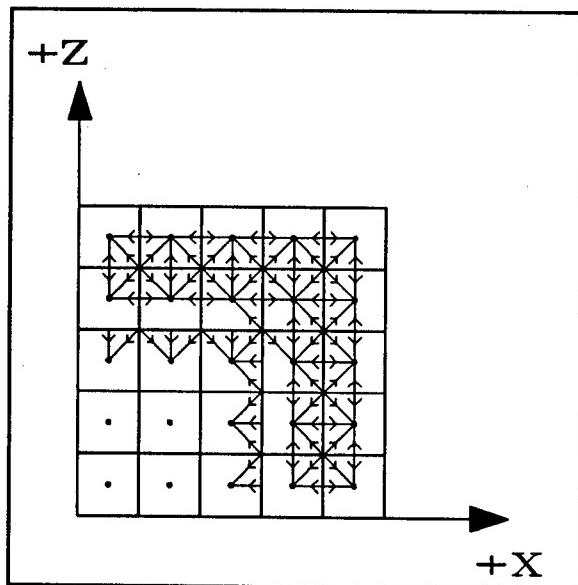
Figure 6. Second phase of second propagation step: calculation of incoming power along active streams.

The output accumulator power values at the boundary of the enclosing definition array are then summed to yield a value of the total output power. This total power is differenced with the total power from the previous propagation step. If the absolute value of the difference exceeds a set convergence value, another propagation step is performed. In order to avoid spurious early convergence, propagation stepping is enforced for the first N steps, where N is the maximum number of cells along any of the XYZ axes of the definition array. When the cloud aerosol single scattering albedo is less than or equal to unity, convergence is guaranteed due to losses at the definition array boundary.

BEAMS 2.2 can also examine cloud geometries with periodic lateral boundary conditions, as in the case of plane-parallel layers of infinite lateral extent. This is accomplished by feeding the lateral streams of cells at the edge of the definition array back into themselves at each propagation step. Allowance for radiative losses only at the top and bottom of the definition array generally makes convergence much slower in this case than for non-periodic boundary conditions.

After convergence of total output power from the definition array has been achieved, the results are processed in forms suitable for use by the BEAMS visualization algorithms or comparison with other radiative transfer models. Cubic spline interpolation between output streams was used to generate much of the intensity or detected power versus angle data shown in the results below. In cases where collimated illumination is not incident along one of the 26 BEAMS stream directions, lack of information about the forward and backward scattering peaks will cause some inaccuracy of the interpolation. This is especially true in situations where the aerosol scattering phase function is sharply peaked and the aerosol cloud is optically thin. Developmental versions of BEAMS 2.2 attempted to minimize this problem by estimating forward and backward enhancements of the scattered power. The multiple scattering phase matrix was used to weight extrapolations in the forward and backward directions from nearby stream values. This technique met with mixed success, working well in optically thin problems and creating non-physical artifacts at larger optical depths. Improved estimation of the cubic spline fitting function second derivative has largely eliminated the need for the phase matrix extrapolation technique, which is not used in the results given below.

2.2 PHASE MATRIX CALCULATION

Before the BEAMS 2.2 radiative transfer model is run, a 26 x 26 stream phase matrix must be constructed from available phase function data for all aerosols present in the definition array. Each matrix element p_{ij} represents the value of the aerosol phase function for output stream i and input stream j. Thus, each column of the phase matrix is a normalized three-dimensional phase function for radiation incident upon the cubical array element from the j-stream direction. Polarized radiation scattering is readily simulated by this phase matrix computational scheme for phase functions that lack azimuthal symmetry. Because none of the comparison sources used below considers polarization, only the unpolarized 26 x 26 phase matrix is treated in this paper.

BEAMS 2.2 represents an improvement over previous versions in its use of a multiple scattering phase matrix. This is important because the bulk optical characteristics and geometry of each cubical cell element must be considered in modeling center-to-center scattering interactions. In general, for a given aerosol type, the angular form of the phase matrix for a given cubical cell element will vary with optical depth τ. At small optical thicknesses, the phase matrix resembles a point particle single scattering phase function sampled at each of the output stream directions and integrated over the solid angle subtended by each stream. Increasing optical depths in an elemental cell cause angular broadening of the phase matrix and enhance departures of the phase matrix from that of a point particle due to the cubical shape of the cell. One shape effect seen at large optical depths is a smaller value of the forward scattering phase matrix element for collimated illumination incident upon one of the cubical cell's faces. For example (referring to the stream numbering of Fig. 1), the $p_{26,1}$ (face-incident) forward scattering phase matrix element is considerably smaller than either the $p_{22,2}$ or $p_{23,3}$ (edge or corner-incident) forward scattering elements at larger optical depths. The face-incident radiation (direct and scattered) must traverse uniformly larger optical depths than radiation incident from any other direction. A portion of the incident collimated radiation parallel to either a cube edge (e.g. stream 2) or cube corner (e.g., stream 3) will traverse optically thin regions near cube edges and will give rise to larger forward scattering and direct transmission.

A phase matrix used by BEAMS 2.2 may be constructed through two different methods. The first method creates a true multiple scattering phase matrix using a thin cloud single scattering phase function as a starting point. A modified version of the BEAMS model then performs multiple scattering calculations over a non-uniformly spaced grid of optical depths τ_n for homogeneous cubical definition arrays. The resulting far-field (face-averaged) radiances then define a multiple scattering phase matrix for each optical depth n. The results are stored in a phase matrix database for later re-use by the full BEAMS 2.2 model. Inhomogeneous, non-cubical cloud scattering problems may thus be treated using cubical element results from the multiple scattering phase matrix database.

The above technique works well in most cases, though it does take a great deal of computer time to generate a phase matrix database for each aerosol. A second, more approximate method generates a phase matrix without the use of BEAMS and is appreciably faster. The single scattering phase function is first defined at each stream direction as the integral of the phase function over the solid angle subtended by the stream. For each incident stream direction, a single scattering ray trace integration over the volume of the elemental cube is then performed. This integration uses the solid angle-averaged phase function in its calculation of the radiance scattered into output stream directions. The resulting radiances are then renormalized to yield a phase matrix at a given optical depth.

The second method for computing a set of optical depth-dependent phase matrices displays reasonable accuracy over a wide range of optical thicknesses. It reproduces the "silver lining" forward scattering phenomenon described above with acceptable fidelity. In the BEAMS 2.2 results that follow, the second method is used.

3. RESULTS

3.1 SEMI-INFINITE LAYERS

Many numerical and analytical radiative transfer results for plane-parallel cloud layers are available in the literature. BEAMS 2.2 was checked against three sources of such results, two of which are from the literature. The most extensive reference is due to Lenoble, where plane-parallel results from different radiative transfer models are compared[2]. In the second literature source, van de Hulst provides multiple scattering results for a plane-parallel medium composed of Henyey-Greenstein scatterers[3]. Private communications with A. Zardecki of Los Alamos National Laboratory supplied comparisons with a discrete-ordinates model (DOM) used as part of the Boundary Layer Illumination and Radiation Balance (BLIRB) model[4]. Zardecki's DOM model uses eight streams to simulate three dimensional radiative transport. In order to provide a common point of comparison, the BEAMS and BLIRB models treat a scenario that van de Hulst also considers.

Lenoble compares net fluxes and scattered intensities for five cases involving uniform plane-parallel atmospheres illuminated by a collimated infinite beam at a wavelength of 0.7 μm. The incident flux is set at π W m^{-2} for the cases reported here. A BEAMS 5x5x5 definition array composed of cubical cells with 1 meter edges is employed for this case and for the rest of this paper. The BEAMS incident flux level is assumed to be 1 W per m^2 at normal incidence. Net flux values calculated by the BEAMS code must therefore be multiplied by a factor of $\pi/25$ when directly comparing them with Lenoble results.

Table 1 shows how the net flux results from BEAMS compare with spherical harmonics model calculations reported in the Lenoble paper. It is stated in the Lenoble report that the spherical harmonics code results are probably the most accurate of the codes examined. The results shown here are given for three of the five cases, all of which pertain to a plane-parallel layer of Deirmendjian Haze L pure water aerosol with an optical depth of 1.0. Case 1 has the incident illumination normal to the layer and the scattering albedo of the aerosol set at 1.0. The only difference between Case 2 and Case 1 is that the Case 2 single scattering albedo is set to 0.9. Case 3 differs from Case 2 only in the 60° incident illumination zenith angle that it assumes.

Table 1. Comparison of Lenoble spherical harmonics flux results with BEAMS 2.2.

	Case 1		Case 2		Case 3	
	Lenoble	BEAMS	Lenoble	BEAMS	Lenoble	BEAMS
Flux up	0.1736	0.1791	0.1236	0.1214	0.2255	0.2796
Flux down	2.9682	3.1592	2.6712	2.8194	1.0158	1.0072
Flux down (scattered)	1.8124	2.0035	1.5155	1.6637	0.8032	0.7946
Net flux (top)	2.9680	2.9625	3.0180	3.0200	1.3452	1.2912
Net flux (bottom)	2.9682	3.1592	2.6712	2.8194	1.0158	1.0072

The "Flux up" quantity in Table 1 is the upward-directed flux at the top (illuminated side) of the layer. The "Flux down" is the downward-directed flux at the bottom (opposite the illuminated side) of the layer. The "Flux down (scattered)" quantity is the "Flux down" minus the direct (unscattered) beam flux. The "Net flux (top)" quantity is the incident flux value (equal to π times the cosine of the incident illumination angle) minus the "Flux up" value. The "Net flux (bottom)" quantity is the "Flux down" value minus any flux upwelling from beneath the aerosol layer. No such flux was treated in any of the cases here, so "Net flux (bottom)" and "Flux down" are always equal.

The Table 1 flux comparison generally shows very good agreement between BEAMS and Lenoble except for the "Flux down" and "Flux down (scattered)" quantities. The disparity appears to revolve around the scattered downward flux, because the difference between BEAMS and Lenoble is nearly the same for either the flux down or the scattered flux down. The calculation of the direct beam contribution by BEAMS and Lenoble is thus essentially the same.

The fundamental output of the BEAMS 2.2 model consists of direct and scattered power values carried by each of the 26 output streams. These may be converted to radiant intensities to provide another comparison with spherical harmonics results from Lenoble. Output stream i carrying power P_i is assumed to have an intensity I_i given by

$$I_i = \frac{P_i}{\frac{25 \times 4\pi}{26}} \quad W \ m^{-2} \ ster^{-1} \ , \qquad (2)$$

where unit incident flux is assumed (1 W m^{-2}), the factor 25 m^2 is the surface area of a 5 cell by 5 cell face of the 5x5x5 definition array considered in this comparison, and the $4\pi/26$ steradian factor is the solid angle subtended by each stream cone. The intensity I_i calculated above must be further multiplied by π to allow direct comparison to the Lenoble results, which used an incident flux of π W m^{-2}.

Figures 7-11 show comparisons of the scattered intensity calculated by BEAMS with those from Lenoble for each of the three cases. Note that the Case 3 results shown in Figs. 9-11 were calculated using input illumination that was partitioned between two streams. This division was necessitated by the fact that the incident illumination direction did not coincide with any of the 26 stream directions.
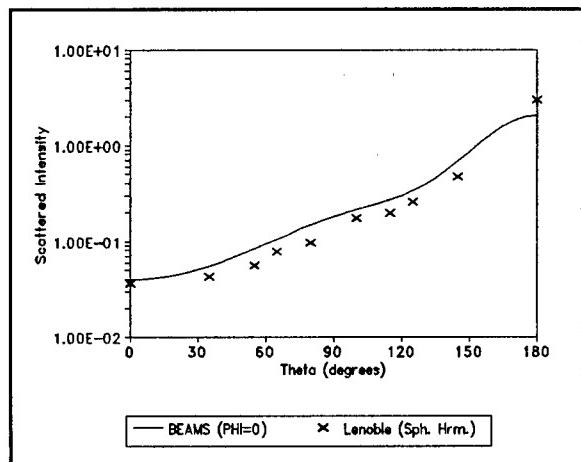
Figure 7. Comparison of intensities predicted by BEAMS 2.2 with those predicted by a spherical harmonics code: Lenoble Case 1.
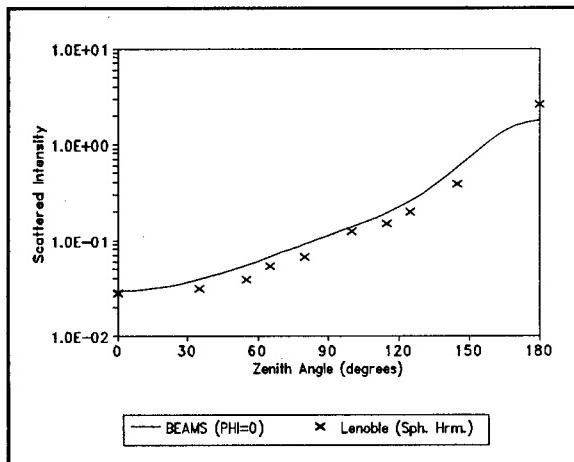
Figure 8. Comparison of intensities predicted by BEAMS 2.2 with those predicted by a spherical harmonics code: Lenoble Case 2.

427
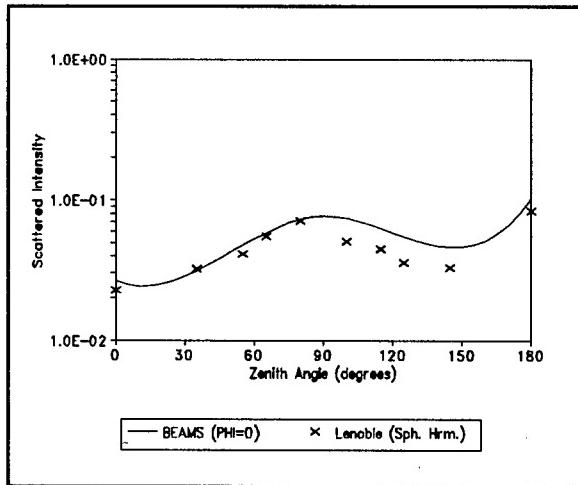
Figure 9. Comparison of intensities predicted by BEAMS 2.2 with those predicted by a spherical harmonics code: Lenoble Case 3, $\phi = 0°$.
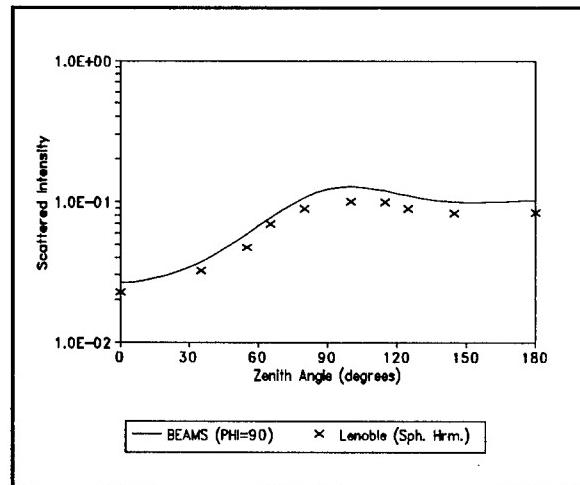
Figure 10. Comparison of intensities predicted by BEAMS 2.2 with those predicted by a spherical harmonics code: Lenoble Case 3, $\phi = 90°$.
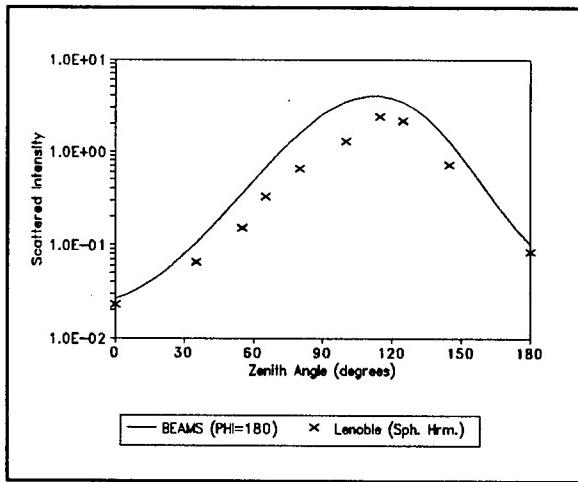
Figure 11. Comparison of intensities predicted by BEAMS 2.2 with those predicted by a spherical harmonics code: Lenoble Case 3, $\phi = 180°$.

For the normally incident beam of Cases 1 and 2 (Figs. 7 and 8), the BEAMS and Lenoble intensities agree reasonably well in form, although the BEAMS results are in general slightly higher. The Case 3 results also show good agreement for the $\phi = 90°$ half-plane (Fig. 10). The results do not agree quite as well for the $\phi = 0°$ and $\phi = 180°$ half-planes (Figs. 9 and 11, respectively). The cause of this disparity is essentially the same as that mentioned above: the grid of 26 stream directions used by BEAMS did not coincide with either the forward or backward scattering direction. When combined with an interpolation technique that does not incorporate phase function weighting in the near-forward and near-backward directions, the lack of an "anchor point" on the grid of stream directions will lead to some degree of inaccuracy for sharply peaked phase functions.

Two cases were examined where BEAMS 2.2 scattered flux results were compared with those provided by Zardecki and van de Hulst for the plane-parallel geometry. In the first case, a double Henyey-Greenstein phase function is used[5]:

$$p(\theta) = \frac{b\,(1 - g_1^2)}{(1 + g_1^2 - 2g_1\cos(\theta))^{1.5}} + \frac{(1 - b)\,(1 - g_2^2)}{(1 + g_2^2 - 2g_2\cos(\theta))^{1.5}} \tag{3}$$

where θ is the scattering angle, $b = 0.98$, $g_1 = 0.89$, and $g_2 = -0.66$. This phase function represents an analytic approximation to the Deirmendjian water cloud C.1 phase function at a wavelength of 0.45 μm[6]. The single scattering albedo is set to a value of 0.9 for this example. The coordinate system is oriented such that the cloud layer is in the XY plane and the positive Z axis points upward. The optical depth of the layer (i.e., along the Z axis) is set at a value of 5.

428

Zenith angles of 0° and 60° for the infinite beam illumination are used. Table 2 lists the results of this comparison. The "fractional flux" quantity is the ratio of the flux out of the top or bottom of the infinite slab to the incident flux. The upward-directed component is labelled as "P(+z)" and the downward component is denoted by "P(-z)".

It is apparent from Table 2 that both the upward and downward fractional fluxes are lower in the BEAMS results. BEAMS may be predicting stronger absorption losses due to multiple scattering than does the BLIRB DOM model in this instance.

Table 2. Comparison of BEAMS 2.2 with BLIRB DOM fractional fluxes.

	0 Deg. Zenith Angle		60 Deg. Zenith Angle	
	BEAMS	BLIRB	BEAMS	BLIRB
P(+z)	0.0795	0.1119	0.1581	0.1999
P(-z)	0.4853	0.5788	0.2637	0.3579

In a second case, BEAMS and BLIRB were compared with results given by van de Hulst for a plane-parallel layer of Henyey-Greenstein scatterers with an asymmetry parameter g = 0.75[3]. The vertical optical thickness of the layer is set at 4, and the single scattering albedo is again 0.9. The infinite beam is normally incident (0° zenith angle) upon the cloud layer in this case. Table 3 lists the results.

Table 3. Comparison of BEAMS 2.2 fractional fluxes with BLIRB DOM and van de Hulst.

	BEAMS	BLIRB	van de Hulst
P(+z)	0.1245	0.1279	0.1416
P(-z)	0.4900	0.4330	0.3973

BEAMS and BLIRB compare fairly closely in this case, but both show somewhat lower upward (back) scattering and higher downward (forward) fluxes than the van de Hulst results.

3.2 UNIFORM CUBICAL CLOUDS

Radiative transfer of infinite collimated beam illumination from homogeneous cubical clouds has been studied by many investigators in the literature. This is largely due to the importance of such studies to interpretation of remote sensing data in which either stratiform or cumuliform clouds are present. McKee and Cox[7] used a Monte Carlo technique to examine scattered radiances from a uniform cubical cloud composed of Deirmendjian water cloud C.1 aerosol at a wavelength of 0.45 μm[6]. The axial optical depth of the cube is 9.8 and the infinite collimated "solar" illumination is incident at zenith angles of 0° and

60° upon the cloud cube. BEAMS 2.2 simulated these cases after an appropriate phase matrix was constructed. As for the Lenoble study above, a conventional right-handed cartesian coordinate system is employed, with the Z-axis vertical and the Y-axis at an azimuth angle ϕ of +90° from the X reference axis. Figures 12-14 show a comparison of McKee and Cox results with those from BEAMS 2.2. For the 60 degree zenith angle case, the azimuth from which the incident solar beam originates is ϕ = 180°. The terms "anti-solar side" and "solar side" refer to the azimuthal planes (ϕ = 180° and ϕ = 0°, respectively) at which the scattered radiances are observed. In this geometry, the anti-solar side contains the forward scattering direction and the solar side contains the backscattering plane.
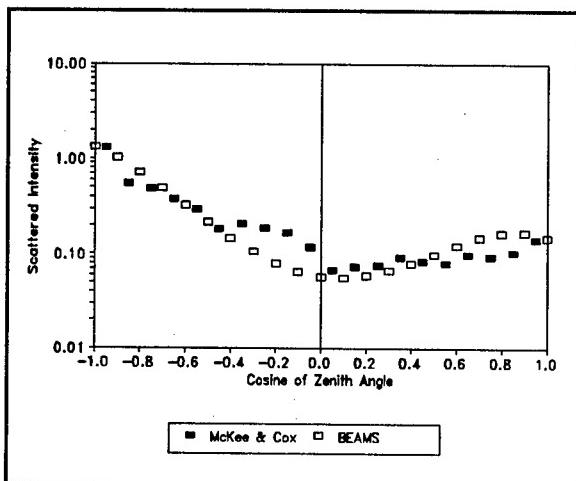
Figure 12. Comparison of BEAMS 2.2 intensity values with McKee and Cox: anti-solar side of cloud, normal incidence.
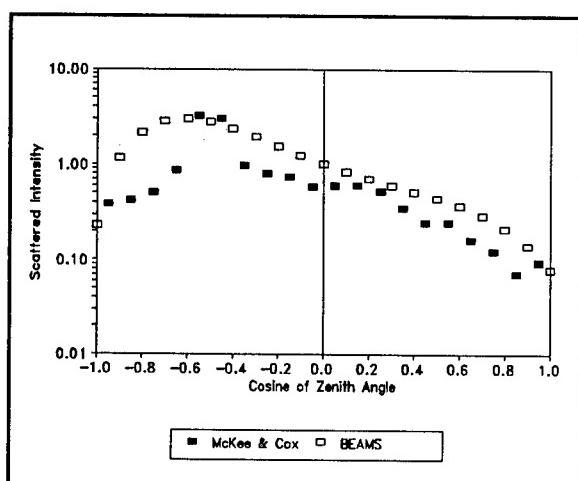
Figure 13. Comparison of BEAMS 2.2 intensity values with McKee and Cox: anti-solar side of cloud, 60 degree incidence angle.
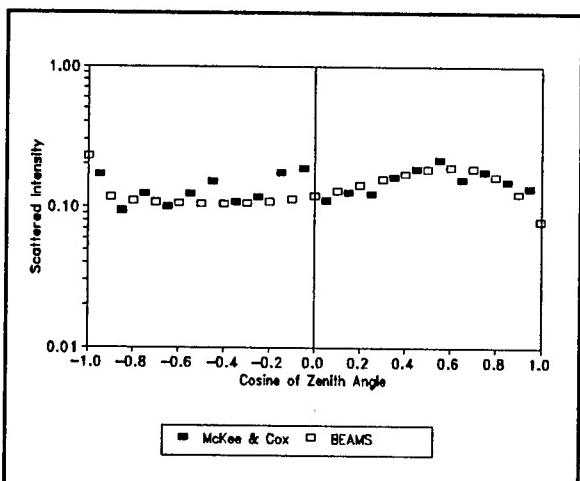
Figure 14. Solar side of cloud and 60 degree solar incidence angle.

In Fig. 13, the McKee and Cox results display a sharper forward radiance peak than does BEAMS. Inferior BEAMS angular resolution due to the relatively small number of output streams is the probable cause of this disparity. Otherwise, the BEAMS 2.2 results compare reasonably well with McKee and Cox.

A modified version of another Monte Carlo code named MSCAT[8] was compared with BEAMS 2.2 for Henyey-Greenstein phase functions at axial optical depths of 1 and 10. Incident illumination is normal to the top of the cube and 25 W of radiant power is intercepted by the cloud top. A total of 20,000 photon histories are used to generate each of the MSCAT data points. Figures 15 and 16 show the scattered power intercepted by a 1 m^2 detector surface located 20 km from the cloud center. Asymmetry parameter g is 0.5 for these cases, representing a broadly forward-peaked phase function. A more sharply-peaked phase function (g = 0.875) produced the results shown in Figures 17 and 18. These results show that the MSCAT random numerical noise is quite substantial in the optical depth 10 cases.

430

For the g = 0.5 Henyey-Greenstein phase function, BEAMS and MSCAT agree within the limits of MSCAT numerical fluctuations. The sharply-peaked g = 0.875 phase function again shows that the lower angular resolution of BEAMS does not closely track the forward scattering power peak seen by MSCAT for the thin cloud of Fig. 17. The thicker cloud of Fig. 18 does indicate, however, that the angular behavior of the scattered power is adequately tracked by BEAMS.
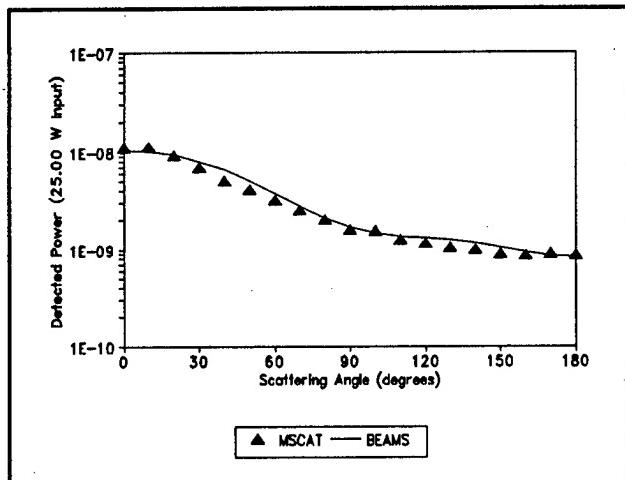
Figure 15. Far-field detected power for Henyey-Greenstein cube, g = 0.5, optical depth = 1.
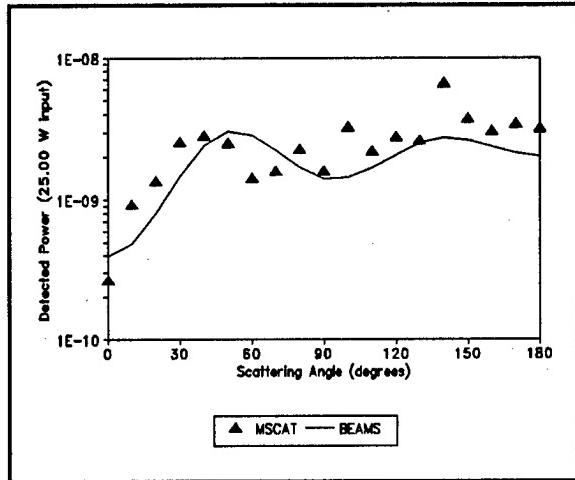
Figure 16. Far-field detected power for Henyey-Greenstein cube, g=0.5, optical depth = 10.
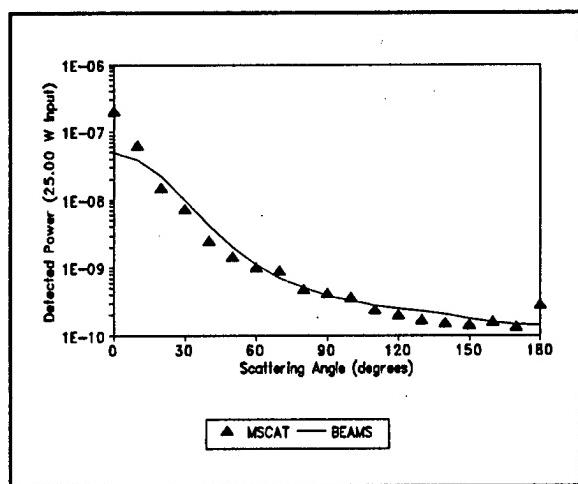
Figure 17. Far-field detected power for Henyey-Greenstein cube, g=0.875, optical depth = 1.
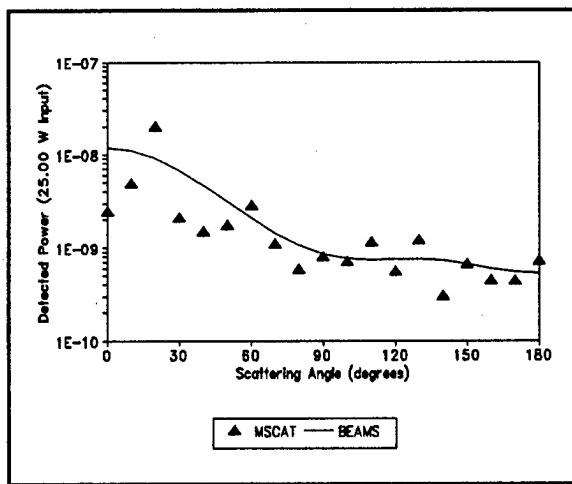
Figure 18. Far-field detected power for Henyey-Greenstein cube, g=0.875, optical depth = 10.

BEAMS 2.2 results for scattered power out of the cube top as a fraction of total incident power are compared with multimode analytical model calculations[9] and Monte Carlo results[5] in Figure 19. The aerosol phase function used for these comparisons is the double Henyey-Greenstein function of Eq. 3. The cloud has an axial optical depth of 5 and an aerosol single scattering albedo of 1.0. The three different radiative transfer methods are in good agreement in this example.

431
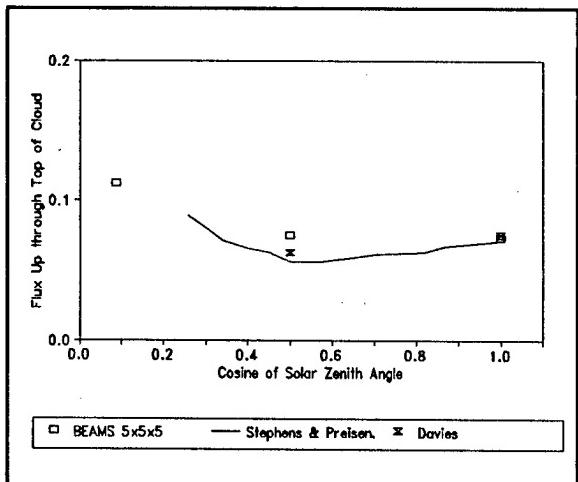
Figure 19. Comparison of BEAMS 2.2 upward fractional flux for Henyey-Greenstein cube with Stephens-Preisendorfer and Davies.

A final cubical cloud comparison was performed between BEAMS 2.2 and the BLIRB DOM model of Zardecki. A Henyey-Greenstein g = 0.75 phase function and axial optical depth of 5 are used in this case. The total fractional scattered radiant power exiting each of the cube faces provides the basis for comparison in Table 4. Zenith angles of 0° (μ = 1) and 84.3° (μ = 0.5) for incident collimated illumination are shown. Agreement between the two models is excellent in this instance.

Overall, the comparison results for cubical clouds show that BEAMS 2.2 correctly predicts multiple scattering fluxes and radiances for this geometry. The new method for calculating an optical depth-dependent phase matrix evidently provides significantly better accuracy for multiple scattering radiance than did the simpler thin cloud phase matrix described last year[1].

Table 4. Comparison of BEAMS 2.2 with BLIRB DOM fractional fluxes for cubical Henyey-Greenstein cloud, g=0.75, axial optical depth = 5.

	0 Deg. Zenith Angle		84.3 Deg. Zenith Angle	
	BEAMS	BLIRB	BEAMS	BLIRB
P(+x)	0.1111	0.1166	0.0427	0.0576
P(−x)	0.1111	0.1165	0.2771	0.2749
P(+y)	0.1111	0.1164	0.1029	0.1067
P(−y)	0.1111	0.1167	0.1029	0.1064
P(+z)	0.0442	0.0628	0.1047	0.1025
P(−z)	0.2832	0.2683	0.1432	0.1569

3.3 NON-CUBICAL RECTANGULAR PRISM CLOUDS

A more critical test of the BEAMS 2.2 model may be made if the homogeneous scattering cloud is a non-cubical rectangular box rather than the cube of the previous section. BEAMS 2.2 and Monte Carlo results[5] were compared for the case of a "bar" shaped cloud composed of the double Henyey-Greenstein phase function aerosol of Eq. 3 with a single scattering albedo of 1.0. The XYZ axial optical depth values are 50 x 50 x 200 for this cloud. Figure 20 shows how closely the results compared for three zenith angles of the incident collimated illumination. Figure 21 depicts a comparison of BEAMS 2.2 with Monte Carlo[5] and multimodal[9] models for the "flat" cloud case where the XY axial optical depths are equal and larger than the Z-axis optical depth. Aspect ratios of 2.5 to 1 (500 x 500 x 200 XYZ axial optical depths) and 10 to 1 (50 x 50 x 5) were examined. The aerosol phase matrix and albedo are the same as those used for Fig. 20.

432

The bar-shaped cloud case has very good agreement between the BEAMS and Monte Carlo models, even though the optical depth of 5 in each cell in the 10x10x40 definition array is rather large. The agreement for the flat cloud cases is best described as qualitative.
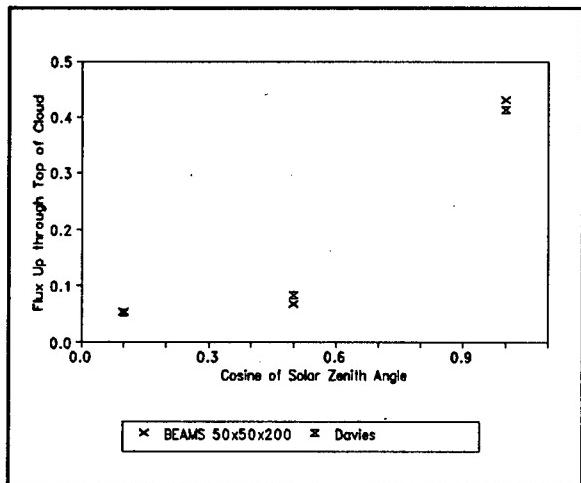
Figure 20. Comparison of BEAMS 2.2 with Davies for bar-shaped cloud.
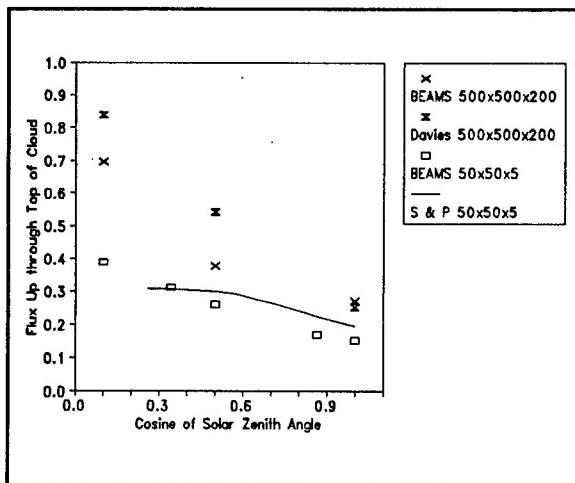
Figure 21. Flat cloud comparison among BEAMS 2.2, Stephens and Preisendorfer, and Davies.

Comparisons were also made with the Zardecki BLIRB model for the 50 x 50 x 5 flat cloud case at two incident illumination zenith angles. Results for g = 0.75 and the double Henyey-Greenstein phase functions are shown in Tables 5 and 6, respectively. The single scattering albedo is 0.9 for both cases.

The BEAMS fractional fluxes are systematically lower than those predicted by BLIRB. Possibly, the BEAMS model indicates substantially larger absorption losses during the multiple scattering process.

Table 5. Comparison of BEAMS 2.2 with BLIRB DOM fractional fluxes for flat-shaped Henyey-Greenstein cloud, g=0.75, axial optical depths = (50 x 50 x 5).

	0 Deg. Zenith Angle		60 Deg. Zenith Angle	
	BEAMS	BLIRB	BEAMS	BLIRB
P(+x)	0.0127	0.0212	0.0124	0.0237
P(-x)	0.0127	0.0212	0.0387	0.0693
P(+y)	0.0127	0.0212	0.0128	0.0194
P(-y)	0.0127	0.0212	0.0128	0.0194
P(+z)	0.0846	0.1939	0.1439	0.2625
P(-z)	0.3908	0.4551	0.2435	0.2849

Table 6. Comparison of BEAMS 2.2 with BLIRB DOM fractional fluxes for flat-shaped Davies double Henyey-Greenstein cloud, g=0.75, axial optical depths = (50 x 50 x 5).

	0 Deg. Zenith Angle		60 Deg. Zenith Angle	
	BEAMS	BLIRB	BEAMS	BLIRB
P(+x)	0.0076	0.0148	0.0122	0.0121
P(-x)	0.0076	0.0148	0.0459	0.0799
P(+y)	0.0075	0.0148	0.0094	0.0152
P(-y)	0.0075	0.0148	0.0094	0.0152
P(+z)	0.0768	0.0974	0.1113	0.1728
P(-z)	0.4501	0.5374	0.2555	0.3252

3.4 NON-UNIFORM CLOUDS

From the scene visualization standpoint, one of the important BEAMS 2.2 features is its ability to treat rectangular box shape regions that are not cubical and are not uniform. Unfortunately, not many other models with which BEAMS may be compared for this geometry are readily available. Zardecki[4] proposed a non-uniform cloud BEAMS-BLIRB comparison case for a g = 0.75 Henyey-Greenstein aerosol. A 5x5x5 cubical definition array as defined for this case is shown in two orthogonal cross sections in Figure 22. The axial optical depth for hatched cells is 1.0 and is 0.1 for the unhatched cells. Collimated infinite beam illumination zenith angles of 60° and 84.3° are used in this test. As can be seen in Table 7, the two methods agree quite well.
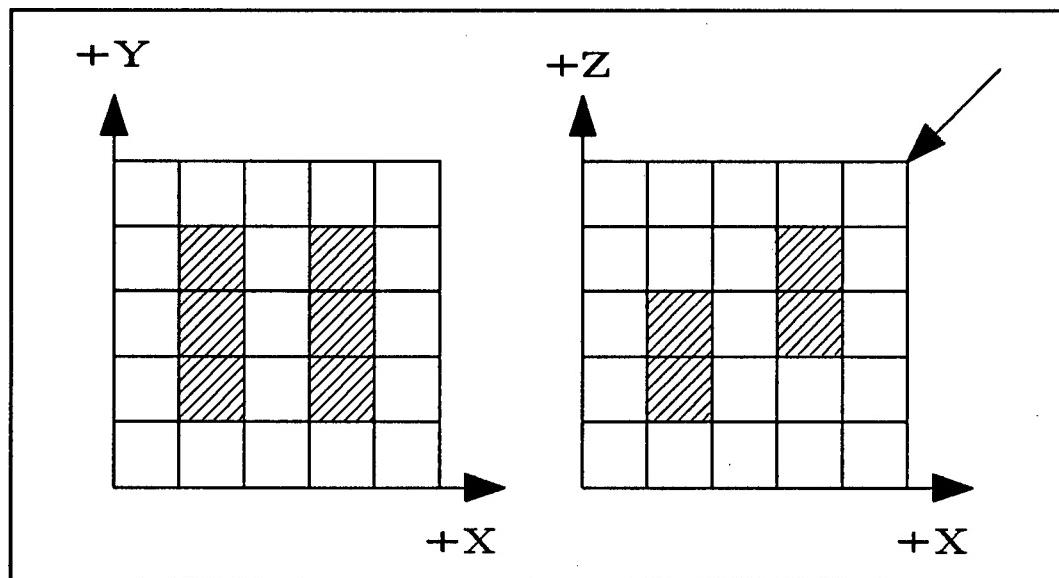
Figure 22. Geometry of embedded thick clouds in tenuous medium. Hatched areas indicate dense medium. Arrow at upper right indicates 45 degree zenith angle for incident radiation.

Table 7. Comparison of BEAMS 2.2 with BLIRB DOM fractional fluxes for two small, dense clouds embedded within a tenuous cubical Henyey-Greenstein cloud, g=0.75.

	60 Deg. Zenith Angle		84.3 Deg. Zenith Angle	
	BEAMS	BLIRB	BEAMS	BLIRB
P(+x)	0.0134	0.0160	0.0140	0.0145
P(-x)	0.4890	0.4932	0.6777	0.6853
P(+y)	0.0363	0.0326	0.0447	0.0382
P(-y)	0.0363	0.0326	0.0447	0.0383
P(+z)	0.0242	0.0231	0.0437	0.0358
P(-z)	0.3412	0.3526	0.1318	0.1227

4. CONCLUSIONS

BEAMS 2.2 radiance and flux predictions did differ somewhat from those of other methods for flat, high aspect ratio clouds. The cause of this disparity is not yet apparent. One possibility is that for such cloud shapes, BEAMS does not make enough propagation steps along the thin axis of the cloud to achieve proper numerical convergence. Future work will attempt to determine the exact nature of this phenomenon.

The results given above indicate that the basic algorithm of the BEAMS radiative transfer model is valid and produces reasonably accurate results using appropriate phase matrix data. Because it is a good compromise between speed and accuracy, the BEAMS 2.2 radiative transfer algorithm is a realistic means to incorporate multiple scattering effects into a visualization model.

REFERENCES

1. Hoock, D.W., J.C. Giever, S.G. O'Brien, and E.J. Burlbaw, 1992: A Multi-Stream Radiative Transfer Model for Inhomogeneous, Three-Dimensional Aerosol Clouds, in Proceedings of the 1992 Battlefield Atmospherics Conference, Ft. Bliss, TX, pp. 3-12.

2. Lenoble, J., 1977: Standard Procedures to Compute Radiative Transfer in a Scattering Atmosphere, Radiation Commission, International Association of Meteorology and Atmospheric Physics (IAMAP), published by National Center for Atmospheric Research, Boulder, CO.

3. van de Hulst, H.C., 1980: Multiple Light Scattering, Tables, Formulas, and Applications, Volume 2, Academic Press, NY.

4. Zardecki, A., 1993: private communication.

5. Davies, R., 1978: The Effect of Finite Geometry on the Three-Dimensional Transfer of Solar Irradiance in Clouds, Journal of the Atmospheric Sciences, September 1978, pp. 1712-1725.

6. Deirmendjian, D., 1969: Electromagnetic Scattering on Spherical Polydispersions, Elsevier, NY.

7. McKee, T.B., and S.K. Cox, 1976: Simulated Radiance Patterns for Finite Cubic Clouds, Journal of the Atmospheric Sciences, October 1976, pp. 2014-2020.

8. O'Brien, S.G., 1984: Volume 18, Aerosol Multiple Scattering Module MSCAT, Technical Report TR-0160-18, U.S. Army Atmospheric Sciences Laboratory, White Sands Missile Range, NM.

9. Stephens, G.L., and R.W. Preisendorfer, 1984: Multimode Radiative Transfer in Finite Optical Media. II: Solutions, Journal of the Atmospheric Sciences, March 1984, pp. 725-735.

COMPUTER MODELING OF TIMELINES AND TACTICS FOR USE OF THE XM81 GRENADE

Joseph L. Manning and William G. Greenleaf
Computer Sciences Corporation
Huntsville, Alabama

Jeffrey S. Moore
US Army Edgewood RD&E Center
Aberdeen Proving Ground, Maryland

ABSTRACT

The XM81 is a bispectral obscurant grenade that is designed to provide a quick obscurant screen for a vehicle under imminent missile attack. XM81 grenades may be launched by VIDS, an on-board threat alarm system that responds to laser, radar, and acoustic signals. The vehicle must then move to make the best use of the obscurant cloud. A computer model has been developed to evaluate the effectiveness of the obscurant and to determine tactics to optimize the obscurant effectiveness. The code is a one-on-one engagement model with a gaussian puff model to simulate the transport, diffusion, and dispersion of the obscurant according to atmospheric conditions. Time histories of missile-seeker-to-target line-of-sight transmittance, and perspective-view transmittance maps as seen from the missile, are used to assess the effectiveness of the obscurant. Timelines are critical, because in many cases there are only a few seconds between the VIDS alarm and the missile impact. The code has been used to model XM81 deployment scenarios against several blue missile systems, including Javelin, Hellfire, Longbow, and MLRS/TGW.

1. INTRODUCTION

The XM81 bispectral obscurant grenade is under development as a countermeasure to be used by armored vehicles against anti-tank guided missiles. XM81 is typically deployed in an eight-round salvo when the vehicle commander believes the vehicle is under imminent attack. The obscurant provides a relatively short duration, dense obscurant screen intended to defeat the missile's infrared or millimeter-wave guidance system. A VIDS system (Vehicle Integrated Defense System),[1] which is mounted on the vehicle to provide quick detection and countermeasure response to threats, may be used to detect the threat, determine the bearing of the attack, and deploy the grenades in the appropriate direction.

SSSMKMAP is a one-on-one engagement model that includes scenario geometry for XM81 deployment and a gaussian puff transport and diffusion model. SSSMKMAP uses the self-screening smoke subroutines from MICOM's Battlefield Environment Weapon System Simulation force-on-force model, BEWSS.[2] These subroutines were developed over a number of years and have been used primarily to model the effects of the L8A1-type munitions on infrared systems.[3] An earlier version of these subroutines formed the basis of the EOSAEL module GRNADE,[4] although the BEWSS and EOSAEL versions have evolved along somewhat different paths since then.

SSSMKMAP can be used to simulate attack and predict the effectiveness of the countermeasure against various types of missiles, and to determine if the effectiveness can be improved by evasive motion after

grenade deployment. Timelines associated with the attack and countermeasure deployment can be established. Other applications include determining the effects of meteorological conditions on the obscurant and on its effectiveness, and investigating modifications in the deployment pattern to enhance effectiveness.

The SSSMKMAP engagement model was used to predict the effects of XM81 grenade deployment against several blue systems as surrogate threats: Hellfire, which uses an infrared laser designator; Longbow, which employs an on-board millimeter-wave radar; Javelin, which uses an infrared imaging tracker; and MLRS/TGW, which searches for a target and then tracks its target using millimeter-wave radar.

2. DESCRIPTION OF THE CODE

2.1 Scenario Description and Geometry

In a typical XM81 deployment scenario, the vehicle commander is notified by the VIDS system that he is under attack (for example, VIDS has detected infrared laser or millimeter-wave radiation indicating that the vehicle is being designated or tracked by a missile system). The turret is turned to face toward the threat, and eight grenades are deployed in an arc around the vehicle. The targeted vehicle may then take evasive action such as moving toward the smoke, or it may try to move out of the area, or it may hold still.

SSSMKMAP calculates the transmittance between the missile and the target as the missile moves along its trajectory, the target moves after countermeasure deployment, and the obscurant clouds grow, merge, drift downwind, and disperse, as illustrated in the diagram in Figure 1.

The SSSMKMAP code allows flexibility in the number and placement of the grenades; for example, the user may choose to deploy only the upwind four grenades, or only the central four. The throw distance and mean burst height may be varied. The height of each actual grenade burst above or below the mean burst height may be specified, or may be set by

Figure 1. SSSMKMAP calculates the time history of the missile-target line of sight.

the code using a normally-distributed random draw. These options give the cloud a more realistic appearance.

2.2 Transport and Diffusion

SSSMKMAP uses a gaussian puff model for transport and diffusion of smokes and obscurants. This method includes the effects of atmospheric stability and wind speed on the movement, growth, and dispersion of the smoke. The "puff" generated by each grenade is characterized by the coordinates of its center, which moves horizontally with the wind and moves downward at the settling speed, and by its "sigma" values which represent the distances from the center at which its concentration falls by a factor of 1/e in the downwind, crosswind, and vertical directions. The sigmas increase with time depending on wind speed and stability. Calculations are done separately for each puff, so that the size and shape of the obscurant cloud at any time depends on the locations and sizes of each of the puffs.

A fraction of the smoke particles that strike the surface are reflected back into the air. Gaussian models treat this by folding the portion of the puff that would be below the surface back up to an equivalent position above the surface. The fraction of particles that are reflected in this way is a model input. The ground therefore is not a complete sink for particles unless the fraction of reflected particles is input as zero.

The algorithm for cloud growth consists of two phases. The first models the explosive growth during the first fraction of a second after the grenade bursts. In this phase sigma increases linearly between two user-specified values. The second phase represents cloud growth due to atmospheric turbulence, and the equation for sigma in the downwind direction has the form

$$\sigma_x = \sigma_{x,ref}\left(\frac{A+x}{x_{x,ref}}\right)^{\gamma}$$

where x is distance downwind that the puff has moved. Similar equations describe the crosswind and vertical sigmas as functions of x. The reference distance $x_{x,xref}$, the reference sigma $\sigma_{x,xref}$, and the curvature parameter γ are inputs, and parameter A is determined by the code from the user-input sigma for the beginning of this phase. The cloud growth inputs include the initial sigma, sigma at the transition from explosive to atmospheric growth, the reference sigma, the reference distance, and the curvature parameter, for the downwind, crosswind, and vertical directions, a total of fifteen parameters. This provides a great deal of flexibility but also poses a problem when trying to simulate realistic conditions, since none of the parameters relates directly to Pasquill category or to measured turbulence parameters. For purposes of this study, the inputs were selected to provide cloud growth equivalent to that obtained from the COMBIC code[5] for Pasquill categories A (very unstable), B (moderately unstable), and D (neutral) for the M76 grenade.

Cloud growth as described by the above equation is a function of downwind distance rather than of time. Growth therefore scales with wind speed: at a distance x downwind the puff has a certain width independent of how long it took to get there. For low wind speed it takes a long time to get there, and therefore the rate of growth of the cloud is low. This is a characteristic of most gaussian models, including COMBIC. This sometimes causes confusion because, intuitively, it is easy to think of cloud growth as being a turbulence effect and cloud transport as a wind effect; in fact, in most gaussian models the growth rate varies with the wind speed as well as the turbulence or stability. At zero wind there is zero growth.

The initial smoke cloud from an XM81 grenade is not spherical. It is torroidal, with a random orientation that depends on the orientation of the grenade when it bursts. If a single burst were being modeled, this could be represented by selecting the initial sigmas so that the initial cloud was an ellipsoid, with the orientation and shape selected to resemble the orientation and shape of the torroidal cloud. We did not do this for XM81 deployment simulations, since all eight of the initial clouds would have had the same orientation; such choreography would diminish rather than enhance realism. Including a model to allow treatment of the initial clouds as randomly-oriented disk-like ellipsoids has been left for a future version of the code.

2.3 Treatment For Multispectral Obscurants

SSSMKMAP treats each component of a bispectral or multispectral obscurant separately. Parameters such as extinction coefficient, fill weight, settling velocity, and surface reflection coefficient are input for each obscurant component, rather than for the combined obscurant. The primary reason for this is that it is easier to find input data for the individual components than for the combined obscurant. For each grenade burst, the model creates a separate puff for each component, initially the same size and in the same location. These puffs could separate over time if the settling velocities and reflection coefficients for the components were sufficiently different. This is not the case for XM81, however; the components from each grenade burst continue to occupy the same space over the lifetime of the countermeasure.

3. SAMPLE ANALYSIS USING SSSMKMAP

In the analysis that follows, the missile system inputs, including the trajectory, and some of the obscurant properties were fabricated for this unclassified paper.

A vehicle detects that it has been targeted by a laser designator system and it responds by turning the turret toward the perceived direction of the threat, which is crosswind as shown in Figure 2, and deploying obscurant grenades in an arc. The actual missile attack is offset by 15° from the designation direction, as shown. The missile's flight time is 30 seconds. This type of missile can be defeated by blocking the designator beam for one second during the final five seconds of its flight. The wind speed is 3 m/s, and atmospheric stability is neutral. The two questions we will address are:

- When is the optimum time, relative to the missile launch, to deploy the obscurant grenades?

- What should the vehicle do after deployment to make the best use of the screen?

To determine the best time to deploy the obscurant, SSSMKMAP was first run for two different paths, one representing the path from the ground designator to the vehicle and the second representing the missile's approach path. Blocking of either of these paths with the obscurant would disrupt the designator beam. Two motion strategies are examined:

Figure 2. Sample analysis scenario.

1. The vehicle remains stationary after deploying the obscurant;

2. The vehicle moves 25 m into the obscurant pattern and then moves downwind with the cloud.

Figures 3 and 4 show the transmission histories for the designator-vehicle path and the missile approach path, respectively, for the stationary vehicle. The calculation for the missile approach path is done for a line of sight between the vehicle and the missile's location three seconds before impact. These calculations are done to establish times at which the cloud blocks these two stationary lines of sight, regardless of where the missile actually is. The missile's motion as it approaches the cloud and the vehicle will be accounted for later. The total transmittance at any time for a laser designator beam being reflected off the vehicle and transmitted along the missile approach path is the product of the transmittances from Figure 3 and Figure 4 for that time.

Figure 5 shows the transmission history for the missile approach path if the vehicle moves after deploying the grenades. The total transmittance for the designator beam at any time is the product of the transmittances from Figure 3 and Figure 5 for that time.

Figure 3. Transmission history calculated by the computer model for the designator-vehicle path, stationary vehicle (time axis represents time since grenade deployment).
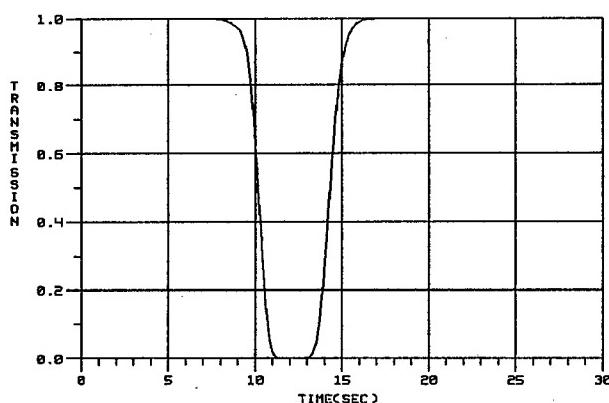
Figure 4. Transmission history calculated by the computer model for the missile approach path, stationary vehicle (time axis represents time since grenade deployment).
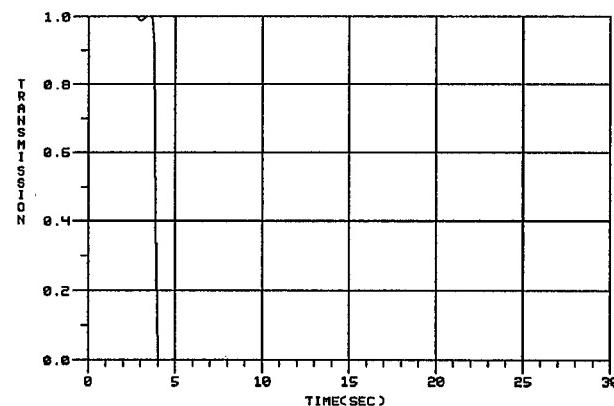
Figure 5. Transmission history calculated by the computer model for the missile approach, vehicle moves toward the obscurant and then moves downwind (time axis represents time since grenade deployment).

441

From these plots, the obscuration times (time period where the beam is blocked along either the designator-target or target-missile path) are:

OBSCURATION TIMES
(seconds from deployment of obscurant grenades)

	obscuration begins	obscuration ends
stationary vehicle	3.2	13.2
vehicle moves 25 m and moves downwind	3.5	30.0

These values include the time the grenades are in the air before they burst. For the stationary vehicle, the end of obscuration is the time that the 3-m/s crosswind blows the cloud past the vehicle.

The "deployment window" is the range of time after missile launch during which the obscurant grenades can be deployed and be effective. The timeline for latest deployment is illustrated in Figure 6.

Figure 6. Timeline for latest deployment of obscurant grenades.
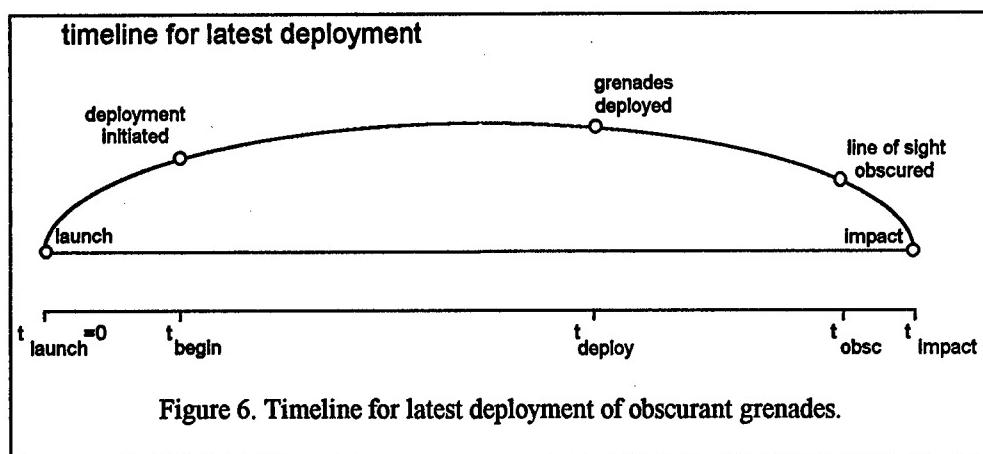
For the stationary vehicle, t_{impact}=30 sec and t_{obsc}=29 sec (the beam must be blocked for a one second duration) and it takes 3.2 seconds after deployment for the smoke to block the beam path, so t_{deploy}=25.8 seconds after missile launch.

The timeline for earliest deployment is shown in Figure 7.

Figure 7. Timeline for earliest deployment of obscurant grenades.
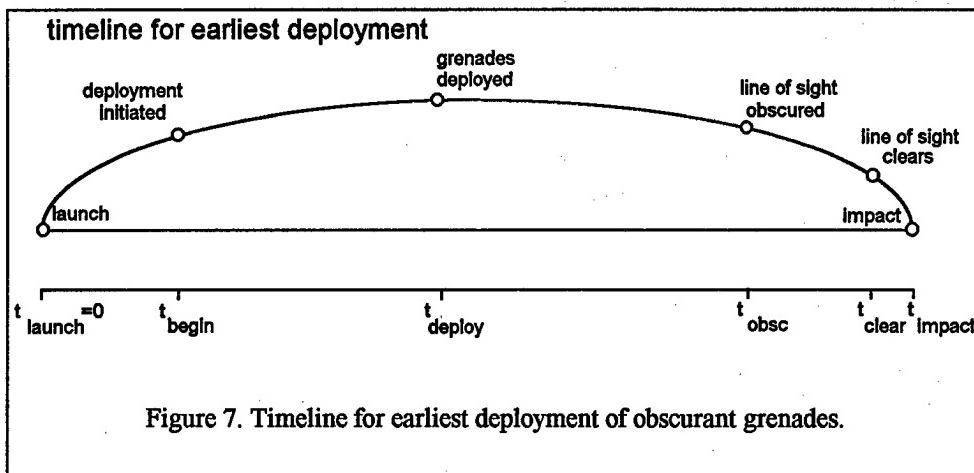
For the stationary vehicle, t_{impact}=30 sec and t_{clear}=26 sec, since the beam path is to be obscured for one second of the final five seconds of the missile's flight. The obscurant is blown clear of the beam path at 13.2 sec after grenade deployment by the 3-m/s wind, so t_{deploy}=12.8 sec. The deployment window for the stationary vehicle is 12.8 to 25.8 seconds after missile launch; if the obscurant is deployed before that window it will clear while the missile is still in flight, and if it is deployed after that window the cloud will not have time to develop before the missile arrives. The deployment times for both motion strategies are:

DEPLOYMENT WINDOW
(seconds from missile launch, for a 30 second flight time)

	starting time	ending time
stationary vehicle	12.8	25.8
vehicle moves 25 m and moves downwind	0.0	25.5

This result shows that the vehicle will be screened during the critical period, the final five seconds of the missile's flight, regardless of whether it moves. The only advantage to vehicle motion after countermeasure deployment, for this particular scenario, is that it removes the possibility that the smoke would be deployed too early and would clear before the arrival of the missile. There are other scenarios where maneuvering after countermeasure deployment increases the effectiveness of the countermeasure. Whether or not moving after deployment is advantageous depends strongly on the threat missile system.

Now we can calculate the transmission histories from the designator to the vehicle and the vehicle to the missile as the missile moves along its trajectory, for a selected countermeasure deployment time. Figure 8 shows the transmission history from the actual missile position to the target, for the case in which the vehicle deploys the obscurant grenades at 18 sec after missile launch and remains stationary. Figure 9 is the transmission history from the ground designator to the vehicle. The missile's view of the target is not completely blocked until about a second before projected impact. However, it does not see its designation signal because the beam is blocked before it reaches the target.
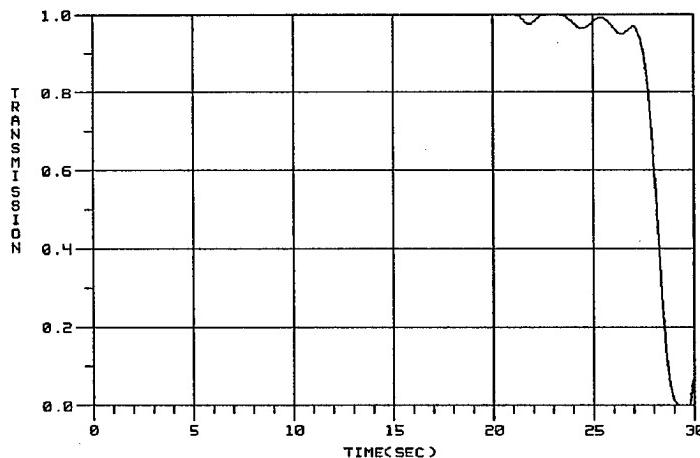
Figure 8. Missile-target transmission history calculated by the computer model for obscurant deployment at 18 seconds after missile launch (time axis represents time since missile launch).

This result is illustrated graphically in Figures 10 and 11. These figures are perspective view transmission maps at 4 sec and 2 sec before projected impact, for grenade deployment at 18 sec after missile launch (12 sec before projected impact). The targeted vehicle is always at the center of these figures, at the intersection of the horizontal and vertical lines, regardless of the bearing of the missile. Figure 10 shows the view seen from the approaching missile; as the missile approaches, its line of sight to the vehicle passes through the top of the obscurant cloud. The smoke deployment was fairly late in this example; had it been slightly earlier, the cloud would have grown to sufficient height to completely block the missile-target path. Figure 11 shows the view from the designator location; the path to the vehicle is completely blocked by the obscurant cloud. The end of the cloud can be seen in Figure 11 as the wind blows the obscurant to the left, but the projected missile impact time will have passed before the cloud clears the vehicle.
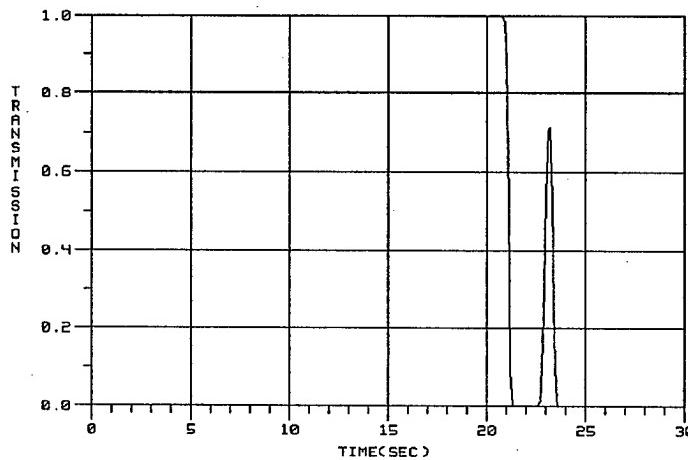
Figure 9. Designator-target transmission history calculated by the computer model for obscurant deployment at 18 seconds after missile launch (time axis represents time since missile launch).

444

Figure 10. Transmission maps as viewed from the missile, with the vehicle remaining stationary.

a) 4 sec before projected impact
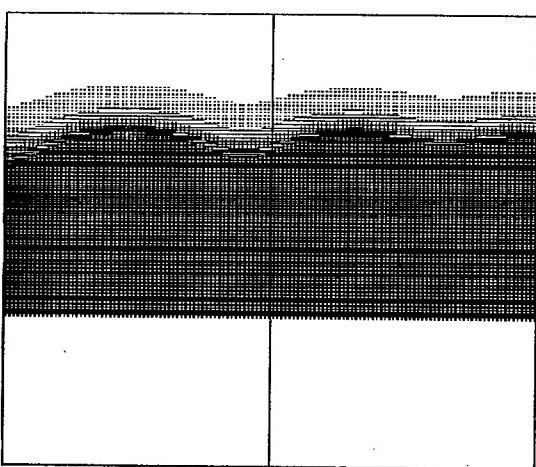
b) 2 sec before projected impact
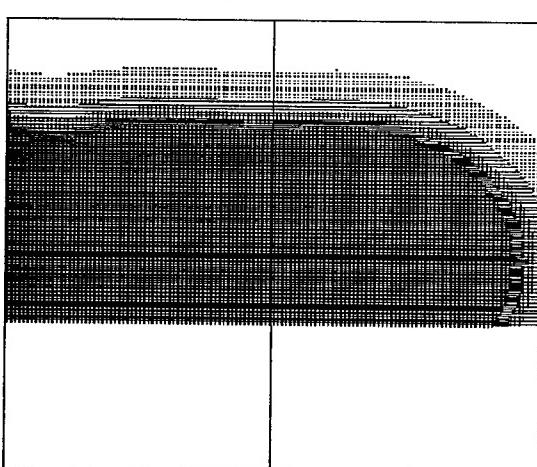
Figure 11. Transmission maps as viewed from the ground designator, with the vehicle remaining stationary.

The atmospheric stability for this example was neutral. In an unstable atmosphere, the cloud would have exhibited faster vertical growth and would have blocked the missile approach path sooner and for a longer period. Higher wind speed would also have resulted in faster vertical growth but would also have moved the clouds past the target faster, making target motion strategy more important. Meteorological conditions have a strong influence on the success of the countermeasure and on the strategy required to take best advantage of it, and SSSMKMAP provides a modeling tool for quantifying these effects.

4. SSSMKMAP CODE VERIFICATION

Data from grenade tests conducted at Eglin AFB in June of 1992 were used to verify that the SSSMKMAP code predicts realistic appearance and transmission values. The comparisons were done primarily with results measured by the ATLAS system.[6] ATLAS creates transmittance maps of the obscurant clouds by comparing infrared images of the clouds at each time step to a clear air image taken just before the grenades are detonated. The ATLAS transmission maps for the first second or two are inaccurate because of thermal emission from the obscurant, which is heated by the blast. After the obscurant cools to near ambient temperature the maps are accurate to within 10%.

Figure 12 shows ATLAS transmission contours and a SSSMKMAP transmission map at one second after burst in a test in which eight grenades were detonated in an arc. The SSSMKMAP field of view and view direction were set to be the same as for ATLAS and the instrument coordinates, launcher coordinates, and launch direction for the code run were taken from the site survey. The fact that the puffs are arranged in an arc is not immediately apparent from the figure, since the look direction is nearly horizontal. In the calculated figure, the outermost puffs appear to overlap while the central puffs are distinct, a result of the arc deployment; the outermost puffs are actually almost behind their neighboring puffs. In the measurement figure, the regions of lowest transmission are near the ends of the cloud, where the lines of sight must pass through puffs that are behind those in front. Wind speed and direction and stability class were reported at a nearby met site; the wind blows almost exactly right-to-left in the figures. The SSSMKAP transmission map displays low transmittance as high print density, while the ATLAS data are presented as transmittance contours, so an exact correlation is not expected between the figures; such correlation would not be expected in

TIME = TO + 1.0 SECS
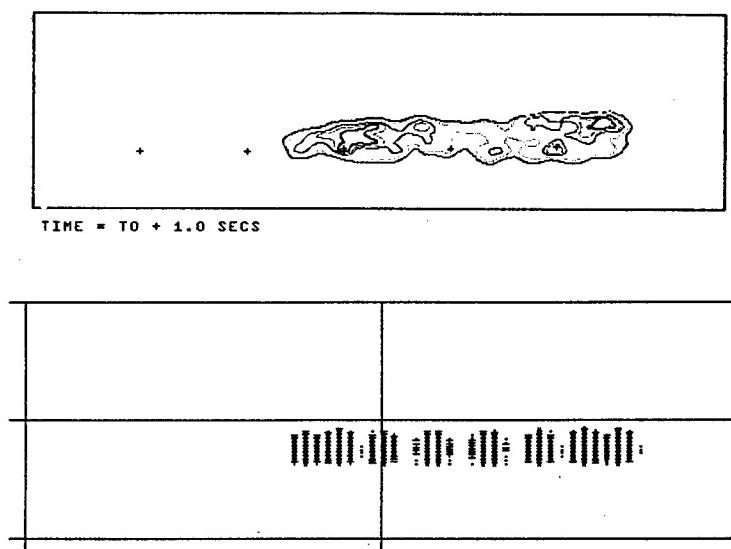
Figure 12. ATLAS transmission map (above) and SSSMKMAP prediction at one second after detonation.

any case because the structure in the real clouds, gaps and holes and eddies, is not predicted by a gaussian model. The figure does illustrate that the location, size, and shape of the cloud is predicted well by the code.

Figure 13 shows the measured and calculated transmission maps for the same cloud at nine seconds after detonation of the grenades. Once again, the size, shape, and location of the cloud is predicted well by the code. The measured transmission maps show the cloud moving slightly downward in the field of view over time, indicating that there was a slight wind component toward the sensor. This is not seen in the predictions because the wind data from the met site we used (and three other nearby sites) showed a small wind component away from the sensor.

One dominant feature of the measured cloud that is not represented by the model is the tail of obscurant near the ground that follows behind when most of the obscurant has cleared. This is probably due to two factors: transport near the surface is slowed because of wind shear near the ground (the wind speed approaches zero at the surface), and particles may be slowed by capture and later reentrainment from the surface. Neither of these phenomena can be treated in this type of model without greatly complicating it. The model, like most gaussian models, treats the transport of the entire puff at one wind speed, and has no provision for shear. Capture and reentrainment is treated as simple reflection, with no delay.

Figure 14 shows results of another trial at four seconds after detonation. In this trial, only the central four grenades of the pattern were fired. In the code inputs, the burst heights of the four grenades were adjusted to simulate the unevenness seen in the measured transmission maps.

Comparisons such as those shown here were performed for three trials from the time of the initial burst until the cloud moved out of the field of view (about 20 seconds). In all cases the size of the predicted cloud as the puffs merged and moved downwind and the progression of the cloud in the downwind direction compared well with the data.

TIME = TO + 9.0 SECS
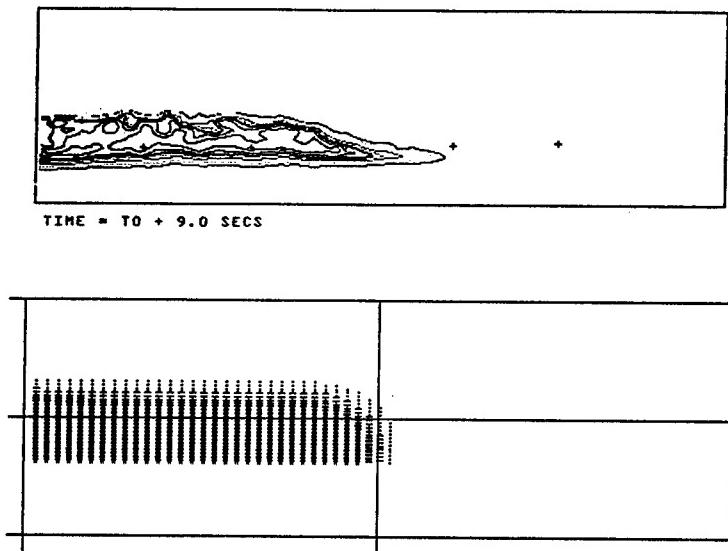
Figure 13. ATLAS transmission map (above) and SSSMKMAP prediction at nine seconds after detonation.

447

TIME = T0 + 4.0 SECS
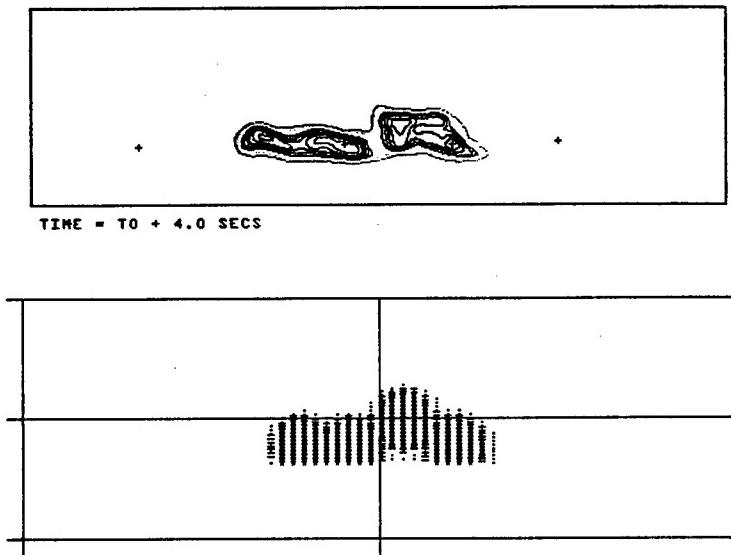
Figure 14. ATLAS transmission map (above) and SSSMKMAP prediction at four seconds after detonation in a four-grenade test.

5. CONCLUSIONS

The SSSMKMAP code provides a tool for predicting the effects of obscuration countermeasures in one-on-one engagements. Efficient application of gaussian puff transport and diffusion methodology provides realistic cloud size, density, and motion, and allows transmission histories to be calculated in scenarios where both ends of the line of sight are moving. The code has been used to model the effectiveness of XM81 bispectral obscurant grenades in one-one scenarios against surrogate-threat blue missile systems, although it is not limited to XM81 grenades nor to missile engagements. The transport and diffusion model in the code has been verified against field test data.

REFERENCES

1. J.C. Campbell, "Vehicle Integrated Defense System Demonstration," *Proceedings of the Smoke/Obscurants Symposium XVII*, US Army Edgewood Research, Development and Engineering Center, Edgewood, Maryland, 1993.

2. R.E. Alongi, D. Scalf, and A. Lee, *Battlefield Environment Weapon System Simulation (BEWSS) Users Guide*, Technical Report CR-RD-GC-91-1, Guidance and Control Directorate, US Army Missile Command, Redstone Arsenal, Alabama, March 1991.

3. R.E. Alongi and W.G. Greenleaf, *Development of a Self-Screening Smoke Model (SMKSCRN)*, Special Report RG-83-8, U.S. Army Missile Command, Redstone Arsenal, Alabama, 1983.

4. R.E. Davis and R.A. Sutherland, *Self-Screening Applications Module GRNADE*, EOSAEL 87, Vol. 14, TR-0221-14, U.S. Army Atmospheric Sciences Laboratory, White Sands Missile Range, New Mexico, October 1987.

5. D.W. Hoock, R.A. Sutherland, and D. Clayton, *Combined Obscuration Model for Battlefield Contaminants, COMBIC*, EOSAEL Vol. 11, TR-0221-11, U.S. Army Atmospheric Sciences Laboratory, White Sands Missile Range, New Mexico, October 1987.

6. M.P. Bleiweiss, R.A. Howerton, K. Payne, and T.A. King, "ATLAS Transmission Maps," *Proceedings of the Smoke/Obscurants Symposium XV*, US Army Chemical Research, Development and Engineering Center, Aberdeen Proving Ground, Maryland, 1991.

INTEGRATED WEATHER EFFECTS DECISION AID (IWEDA)

Carl H. Chesley, Jerry S. Johnson, Wilbert G. Maunz[†], and Andrew R. Spillane
Science and Technology Corporation
Hampton, Virginia 23666
and
Franklin Niles, Robert Lee, and David Sauter
U.S. Army Research Laboratory Battlefield Environment Directorate
White Sands Missile Range, New Mexico 88002

[†]Wilbert G. Maunz, who was a major contributor to the development of IWEDA, died unexpectedly on May 29, 1993.

ABSTRACT

The Integrated Weather Effects Decision Aid (IWEDA) was initially designed for use by the staff weather officer (SWO) in the provision of weather effects information to tactical customers. Ultimately it will be used on the Integrated Meteorological System and Army tactical C^2 systems to provide weather effects information. The IWEDA system makes use of vertical connectivity for tracing weather impacts from the mission level down to the lowest component levels. The IWEDA system is comprised of a number of software modules, including a knowledge-based expert system containing over 360 rules for 41 systems. All software was custom developed in the ANSI C and C++ programming languages.

Through the use of this program, IWEDA users will find answers to these six basic weather support questions:

▶ *Who?*	Support commanders, planners, staffers, and SWOs
▶ *What?*	Provides weather impacts on missions, systems, subsystems, and components
▶ *When?*	Displays weather impacts with respect to time
▶ *Where?*	Overlays weather effects onto maps
▶ *Why?*	Provides detailed explanations on weather impacts
▶ *What-If?*	Allows quick look at alternative mission or system setups and weather conditions

The IWEDA v1.0 has completed beta-testing. Design of the IWEDA v2.0 will begin early in 1994.

BACKGROUND

Wherever called upon, the Army must be prepared to win by using all available combat power throughout each dimension of the battlefield. Combat power depends on much more than troops and weapons systems. It depends on logistics, security, intelligence, and communications with other types of combat support services. Any of these factors may prove decisive in battle, and commanders can manipulate and control them to achieve a tactical advantage. Weather is the sole decision factor over which the commander has little or no control, yet it may be the most significant factor to be considered.

Despite the increased lethality of fire power, aviation assets, and artillery, the Army is still at the mercy of adverse weather, and because of the sophistication of today's high-tech weapon systems, weather affects the Army's mission all the more. However, when it comes to the actual planning and utilization of systems, weapons, and tactics on the battlefield, weather is often ignored. So called all-weather systems have been developed, but for a weapons system to be truly all-weather capable would mean that its mobility, logistical support, mission capabilities, and human operators are totally unaffected by adverse weather. Clearly few, if any, weapons in the U.S. Army meet these criteria. Adverse weather frequently degrades the accuracy and effectiveness of complex weapons and support systems. Weather affects virtually every operation, every piece of equipment, and every person on the battlefield.

Although commanders have virtually no control over the weather, they can take advantage of it or at least minimize its effects through the use of weather tactical decision aids (TDAs) to ensure proper planning and decision making. Weather TDAs are techniques that assess the tactically significant effects of both the current and forecast state of the weather. The TDAs depict weather effects as either simple, easily understood messages or as graphical depictions that enable the commander to evaluate the weather's impact on weapons system effectiveness, to determine the advantages of one system over another, and to anticipate how operations will be degraded or improved during engagements. The TDAs do not make decisions but rather supplement the tactical commander's knowledge and provide guidance during the decision-making process by providing information useful in the formulation and execution of operations. The TDAs enhance the commander's ability to plan operations in a dynamic tactical situation and allow for the use of weather as a force multiplier.

CURRENT SUPPORT PROCEDURES

The requirement and the need for providing tactical or weather decision aids is identified in Army/Air Force joint regulation AR 115-10/AFR 105-3, "Meteorological Support for the U.S. Army." This regulation assigns responsibilities to both the Air Force and the Army. The Air Force is to provide an assessment of current and forecast weather conditions, in light of critical threshold values provided for Army operations, weapon systems, and equipment, and provide TDA information in general formats such as *favorable, marginal,* or *unfavorable.* The Army, on the other hand, is to provide weather effects information to the Air Weather Service as either critical values or TDAs defining weather elements and their weather effects critical threshold values that affect mission areas and battlefield operations systems.

To provide weather effects, the U. S. Air Force Staff Weather Officer (SWO) must first prepare a weather forecast for the unit's area of interest—which for a division, would cover a 48- to 72-hour forecast period. Once the forecast is prepared, the SWO then prepares a weather effects (or weather impacts) chart that becomes part of the weather briefing to the tactical commander and staff. This chart can also be posted and/or sent to subordinate units.

To meet the Army's requirement in the joint regulation, the Army Research Laboratory's Battlefield Environment Directorate (ARL/BED) developed three separate and distinct modules: the Weather Effects Matrix (WEM), the Tactical Weather Effects Messages (TWEM), and the Consolidated Weather Effects Decision Aid (CWEDA). The WEM automatically took a terminal aerodrome forecast, compared it against critical parameters, and depicted the resultant weather impacts in a color-coded matrix against 10 types of fixed Army mission operations. The green, amber, and red color codes used by WEM corresponded to the requirement of specifying favorable, marginal, and unfavorable conditions, respectively. The WEM served an extremely useful purpose by providing the tactical commander and/or staff with an overview of the forecast weather that may impact various missions. The TWEM concept was to use weather impact messages to provide tactical users a reasonable amount of detail about weather and environmental effects on Army systems. The user selected a system and weather elements and received limited weather-impact information pertaining to that system. The

CWEDA was very similar to the TWEM except that it depicted weather impacts on the subsystems of five selected major systems.

Science and Technology Corporation (STC) was asked to evaluate these three modules and concluded that the concepts used to develop them were sound and attempted to address requirements of both the user (i.e., the SWO) and joint regulation AR115-10/AFR105-3. However, STC also concluded that the implementation of these TDAs was problematic. Based on this evaluation, STC was tasked to design the Integrated Weather Effects Decision Aid (IWEDA) software program by building upon the early concepts developed by BED.

INTEGRATED WEATHER EFFECTS DECISION AID

In response to the requirement for providing an automated weather effects decision aid, STC designed and later developed a functional prototype of the Integrated Weather Effects Decision Aid, known as IWEDA v1.0. This software was alpha tested by STC and ARL/BED and beta tested by Detachment 14, 1st Weather Group (USAF) and the 1st Cavalry Division at Fort Hood, Texas.

INITIAL IWEDA DESIGN

As mentioned, Army and Joint Service regulations mandate the requirements for weather-oriented TDAs. However, current weather support procedures are not automated, and the Army Science and Technology Master Plan has identified several environmentally related Science and Technology objectives to resolve these shortcomings. Moreover, Army commanders are typically more concerned with weather effects (or weather impacts) than they are with actual weather forecasts, and frequently say, "Don't tell me what the weather is going to be—tell me what effect it is going to have on my mission." The IWEDA system was custom designed by ARL/BED and STC to meet the needs of the SWO as defined in the Joint Service regulations.

The initial design of IWEDA envisioned a single software system that would be used by all Army commanders, SWOs, and their staffs to produce clearly and easily understood weather effects products. The initial concept of operations for IWEDA's deployment envisioned Army users (commanders and staff principals and planners) on the Army Tactical Command and Control System nodal points within a tactical unit, (e.g., all the G-3s in a division and its brigades and battalions), and the SWO located in the Integrated Meteorological System (IMETS) as the primary users. The IMETS performs the environmental data collection effort from various sources and provides the environmental data as input to IWEDA. The role of the SWO is (1) to ensure that the environmental database in IMETS is current, accurate, and complete; (2) to run TDAs to determine the impacts that may occur if and when weather conditions change, and (3) to brief the tactical commander on the output of the TDAs.

It was envisioned that IWEDA would be integrated into each user's own software and/or hardware. With IWEDA being on the user's standard workstation and containing a knowledge base of critical weather values, IWEDA would thus encourage the users to be more reactive to the potential weather impacts and take the timely and necessary actions to minimize environmental effects on systems and/or operations. Although each organization's version of IWEDA would have the same capabilities for producing, displaying, and disseminating weather effects products, each would also have specific weather information scaled to its area of operations and be limited to systems that are authorized in its modified table of organization and equipment (MTOE).

The following major assumptions were identified in the IWEDA preliminary design document. It was envisioned that other Army hardware and/or software systems would provide the information needed.

- Automated four-dimensional, gridded environmental input data fields would be available for observations, forecasts, and climatology for the battlefield area.
- Terrain, mobility, and vegetation data would be available.

- Software to produce a gridded area of interest boundary, with geographical references (i.e., rivers, cities, and magnetic orientation), would be available.
- Map backgrounds including terrain, organizational features, and geopolitical boundaries would be available for producing software overlays of IWEDA products.

Given the above underlying assumptions, it was decided that a fully functional prototype should be developed as a proof-of-principal. To produce this prototype, STC used a rapid-prototyping software engineering methodology. The prototype objective was to aid the SWO in producing weather effects briefing products. The IWEDA development team, consisting of STC meteorologists, systems engineers, and software developers and scientists from BED, investigated the needs and desires of SWOs at various echelons from brigade through corps. The end result of this research was the IWEDA v1.0 software system, which contains a weather effects library based on operational characteristics of systems used by the III Corps and the 1st Cavalry Division.

CURRENT IWEDA CHARACTERISTICS

Artificial intelligence is at the core of the IWEDA reasoning mechanism. Specifically, IWEDA can be categorized as an intelligent knowledge-based decision aid. The knowledge contained within IWEDA takes the form of rules. These rules contain critical values for weather parameters, as well as detailed explanations of the weather effects. For a division-sized unit, IWEDA v1.0 currently has approximately 360 such rules based on approximately 41 weather parameters. The IWEDA system compares and contrasts the critical values contained within its knowledge base against current weather observations and/or forecasts. The results of this reasoning process are then presented to the user via a highly interactive graphical user interface.

The IWEDA system was designed and developed by STC to run in the Microsoft Windows operating environment on an IBM PC-compatible microcomputer. This microcomputer is the most common computer platform in existence—making IWEDA potentially available to the vast majority of Army units. The IWEDA v1.0 was designed for a specific unit—namely the 1st Cavalry Division. This software can be used by other divisions if the knowledge base is updated to include weather impacts on the specific equipment in their MTOE. The user log-on screen to IWEDA is shown in Figure 1.

The IWEDA system uses a custom model developed by STC to represent tactical Army missions, systems, subsystems, and components, as shown in Figure 2. In the IWEDA knowledge representation, missions are at the highest level and are defined as collections of systems. Systems, in turn, contain subsystems, which themselves are comprised of components. By structuring knowledge in this fashion, STC engineers have eliminated the need for rule redundancy, while increasing usability, reliability, and maintainability. Moreover, users of IWEDA can ascertain,
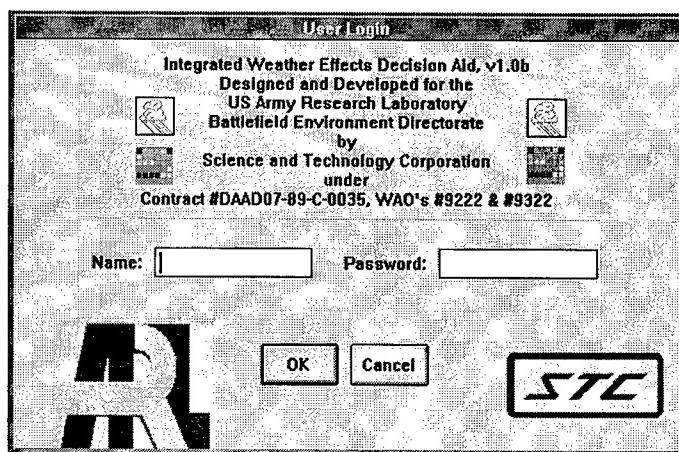
Figure 1. IWEDA v1.0 Title Screen.
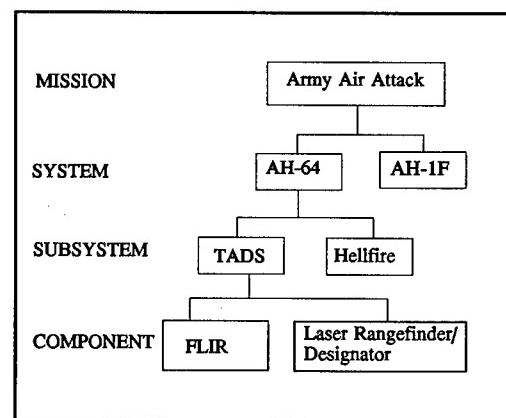
Figure 2. Custom IWEDA Model.

454

down to the subsystem and component levels, exactly which elements of a mission are impacted by the weather and why.

The IWEDA system was designed by STC to aid in the translation of weather data into weather effects intelligence tailored to the Army commander and to provide answers to such common intelligence briefing questions as *who*, *what*, *when*, *where*, and *why*. The IWEDA system also allows for contingency planning, simulation, and training by addressing the *what-if* queries made by the user. The following paragraphs summarize the functionality of IWEDA v1.0 as designed by STC.

WHO

The IWEDA v1.0 system has built-in support for three types of users: commanders, staffer-planners, and staff weather officers. Support for the corps, division, brigade, separate brigade, special forces, and echelons-above-corps is envisioned, although IWEDA v1.0 is tailored toward the division. Each type of user has unique capabilities. For example, only the SWO has access to the forecast or observation entry modules and only the commander can define missions that are accessible by staff members. Additionally, the detailed weather effects explanations generated by IWEDA are tailored specifically toward the type of user. The IWEDA v1.0 screen where this information is entered is shown in Figure 3.

WHAT

As already mentioned, IWEDA produces weather effects on missions and systems, as well as on the subsystems and components contained within them. An effective point-and-click interface allows the user to tailor equipment for a particular purpose, as indicated in Figure 4. For example, the user can choose to deactivate the component VT Fuze from the Munitions Subsystem when computing weather effects on the M109 SP Howitzer. Of course, IWEDA has the intelligence to require that certain subsystems and components remain active at all times. These items are graphically denoted on screen as mandatory elements.
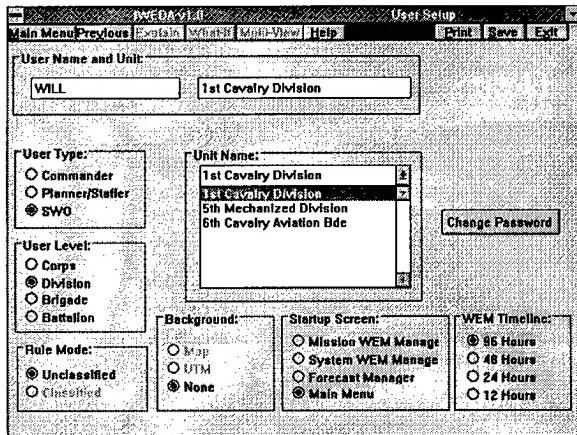
Figure 3. IWEDA v1.0 User Setup Screen.
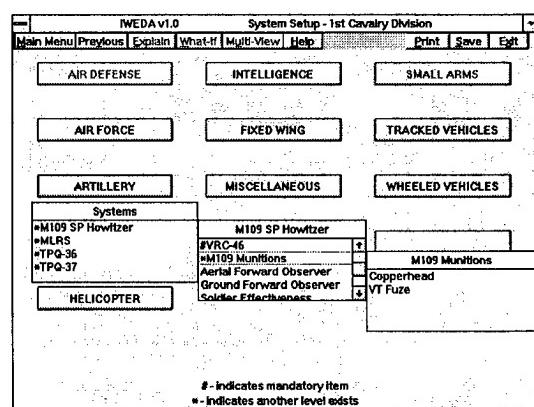
Figure 4. IWEDA v1.0 System Setup Module.

At present, IWEDA distinguishes between two types of missions: those defined by the commander and those defined by other staff members. The commander's missions are fixed, ensuring that all users will be able to access weather effects on these missions but will not be able to alter their definitions in any way. Therefore, all members of the commander's staff will know what is being briefed to the commander.

User-defined missions are created using the same straightforward point-and-click interface used to configure systems, subsystems, and components. The user simply selects an unused button and enters

455

the name of the mission that is to be created. Then IWEDA allows the user to assign systems to the new mission from any of the available system categories. Again, the flexible IWEDA reasoning mechanism designed by STC allows the same system to be assigned to multiple missions simultaneously. And naturally, the user can save a custom-defined mission so that it may be instantly retrieved in future sessions.

WHEN

Depending upon the preference of the user, IWEDA is capable of producing weather effects at the mission or system level. A similar user interface is used in either case. At the topmost level, IWEDA presents the user with a WEM that replaces the weather effects flimsy traditionally produced manually by the SWO. There is one row in the WEM for each mission or system of interest to the user. Again, flexibility was a major STC design criteria—IWEDA allows the user to position the missions or systems in any desired order and save the WEM configuration for future sessions.

Figure 5. IWEDA v1.0 WEM.

The WEM screen, as shown in Figure 5, contains a wealth of information to aid the tactical decision maker. Weather impacts over time are represented with GREEN, AMBER, and RED blocks, indicating favorable, marginal, and unfavorable weather conditions, respectively. Additionally, IWEDA is capable of computing weather effects due to prevailing and intermittent forecast weather conditions.

The weather effects matrix itself shows a high-level depiction of mission or system weather effects versus time. The IWEDA system can use either Zulu or local time. The user has control over the length of time displayed on the WEM. For example, certain users may prefer 48-hour time lines, whereas others, perhaps at higher echelons, may require 96 hours.

Condensed phrases that inform the user of problematic weather conditions can be instantly obtained by positioning the pointer on any AMBER or RED block. The first two such impacts appear directly below the WEM timeline. When IWEDA has determined that more than two impacts are present, the user can, if desired, display a complete listing by positioning the pointer over the desired block and depressing a single key. The WEM was designed by STC so that it could be printed for hard copy dissemination, faxed by internal IWEDA hardware, or stored in computer files for later retrieval by third party software such as word processors.

WHERE

Despite the high informational content on the WEM screen, certain commanders and planners will require further detail to produce optimal decisions. To aid these users, IWEDA can produce geographical depictions of weather effects over a given area of operation or area of interest. The user highlights up to four blocks from the WEM and selects the Multi-View button. Then IWEDA constructs the desired weather effect presentations and displays them, as shown in Figure 6. The same familiar GREEN, AMBER, and RED coloring
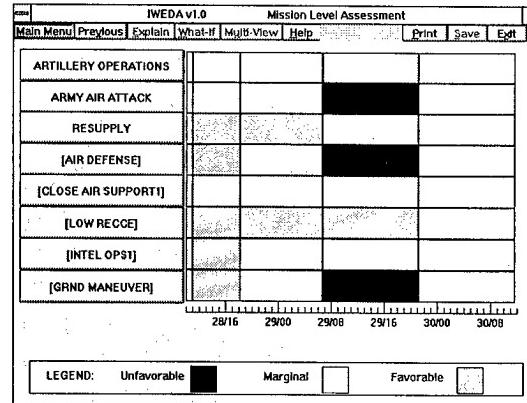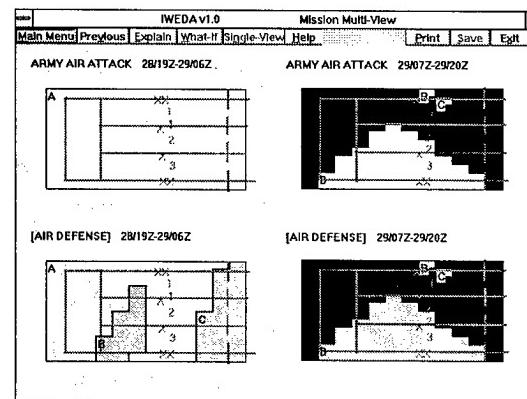
Figure 6. IWEDA v1.0 Multi-View Screen.

scheme from the WEM is used. This screen explicitly shows the user *where* impacts occur for a specific timeframe.

WHY

The Explain Module enables the user to determine *why* a given weather effect region has been labeled marginal or unfavorable. Because of the vertical connectivity of its reasoning mechanism, IWEDA is unique in its ability to propagate weather effects from the lowest component up through the mission level. The structural organization of knowledge within IWEDA is thus transformed into a powerful decision aiding tool for the tactical analyst.

In the Explain Module, the user sees a detailed geographical depiction of weather effects on that mission or system on the left and a condensed breakdown of the selected mission or system on the right. Using the pointer, the user can query down into lower levels to see the effect of subsystems and components on various systems. This capability allows the staffer and planner to tailor their operations so as to minimize the effect of climate or weather, which was perhaps the single most critical design objective of the STC development team.

In a fashion consistent with that used on the WEM screen, the user can position the pointer onto any AMBER or RED impact block to obtain additional information. Here, the user is provided textual explanations of conditions for the given forecast period, as shown in Figure 7. As determined by the user's setup configuration, IWEDA constructs explanations that are tailored to the user's type. For example, a SWO is given a more detailed explanation from that given to a commander. This is yet another example of the flexibility and power of the IWEDA design created by STC.

Figure 7. IWEDA v1.0 Explain Screen.

WHAT-IF

The IWEDA v1.0 system also has a What-If Module, as shown in Figure 8. The module allows the SWO user to incrementally alter the forecast and immediately see the repercussions with respect to weather effects. This capability is of obvious merit in training the SWO to understand the impact of the forecast upon the unit. It is also an invaluable tool when weather conditions are in a state of flux and the SWO desires to ascertain quickly the effects of rapidly changing meteorological conditions.

The non-SWO user, while not having access to manipulating weather forecasts, is able to view efficiently the results of altering mission and/or system configurations. The What-If Module allows, for example, the user to compare and

Figure 8. IWEDA v1.0 What-If Module.

contrast the effect of substituting one type of helicopter for another, or selecting different missiles. The What-If Module highlights the tradeoffs between systems, subsystems, and components with respect to the forecast weather and its impending effects.

CONCLUSIONS

To date, it has been shown that the IWEDA concept is functional and is highly desired by the SWOs in the field. The initial work on IWEDA has reinforced the known need for mesoscale 4D weather data and also reinforced the need for an Army-wide critical value database of weather effects.

The IWEDA v1.0 system underwent a beta (end-user) test by the 1st Cavalry Division at Fort Hood from July to September 1993. A revision of the software that takes into consideration the comments received by the beta testers will be completed by 31 December 1993. The IWEDA v2.0 system is expected to be designed and developed beginning in early 1994. Planned enhancements to IWEDA include but are not limited to

- Terminal aerodrome forecast (TAF) or other point forecast support
- Use of terrain data
- Use of climatology data
- Use of derived weather elements
- Addition of a Weather Warning Module
- Production of enhanced sensitivity messages
- Enhanced printing capability
- Capability to support classified information
- Addition of an inverse What-If Module (i.e., a mission planner)
- Tighter integration with IWEDAs running at subordinate units
- Support of weather effects on threat systems
- Production of gridded output for use by other TDAs

CONFIGURATION MANAGEMENT
FOR THE TECHNOLOGY EXPLOITATION WEATHER TESTBED

John R. Elrick
U.S. Army Research Laboratory
Battlefield Environment Directorate
White Sands Missile Range, New Mexico 88002-5501 USA

ABSTRACT

The U.S. Army Research Laboratory (ARL), Battlefield Environment (BE) Directorate, has initiated a configuration management program designed to oversee its Technology Exploitation Weather TestBed (TEWTB) and its related research and development (R&D) efforts. Through this endeavor, consistent state-of-the-art products are controlled in all phases of their evolution through actual delivery to the final customer. The initial customer for TEWTB commodities was the program director (PD), Integrated Meteorological System (IMETS). The BE Directorate has successfully and smoothly transitioned its Block I IMETS software to PD IMETS by the application of proven configuration management discipline. The Block I IMETS transition provided valuable lessons learned that will be incorporated into future IMETS Block II and III releases.

1. INTRODUCTION

The formal use of configuration management principles for military applications came in the years following World War II.* The rapid advancement of science and technology during this period has made the need for adequate accounting of research and development activities a must in both the U.S. civilian and military communities. The U.S. Air Force spearheaded the implementation of rules, regulations, and requirements for effective resource management. These principles have been applied to both commercial and military organizations in this dynamic environment. The U.S. Army Research Laboratory (ARL),

---

*The Elements of Configuration Management, Course Notes, Course Sponsored by Technology Training Corporation, 9-10 Nov 92, San Jose, CA, presented by Mr. John M. Roberts.

Battlefield Environment (BE) Directorate, identified a need for effective configuration management in the development of their Technology Exploitation Weather TestBed (TEWTB) thrust, and this need has extended to other projects within the directorate. Effective implementation of configuration management discipline will ensure consistency of product releases to customers requiring state-of-the-art processed weather information to support simulated or real battlefield operations.

2. BACKGROUND

The BE Directorate has been developing state-of-the-art software to support U.S. Army tactical battlefield operations for many years. Accurate weather support is a necessary ingredient to successful mission planning; knowledge of the weather and its effects on Army systems and day-to-day operations can be used to assemble a sensible weapons mix or to actually use meteorological conditions as a force multiplier.

Early on, the U.S. Army Atmospheric Sciences Laboratory, predecessor of the BE Directorate, developed a computer hardware and software suite to support the airland battlefield environment (ALBE) concept. These efforts were incorporated into a system known as the Integrated Meteorological System, or IMETS. IMETS is a system that operates on Army Tactical Command and Control System (ATCCS) common hardware and software to provide modern weather support techniques to the U.S. Air Force Staff Weather Officers. These officers furnish weather support to the U.S. Army at all organizational levels from corps through separate brigades and in peacetime as well as in times of conflict. In early 1993, the IMETS transitioned to the program manager, Program Executive Office Command and Control Systems, and is managed by the program director (PD), IMETS. Since then, BE Directorate efforts have continued in a program called the Technology Exploitation Weather TestBed (TEWTB) designed to continue support to PD IMETS and other Army customers in the varied battlefield functional areas (BFAs) that require accurate weather information for mission accomplishment.

Through the evolutionary process delineated above, numerous hardware platforms and software packages have been used. These multiple actions coupled with rapid advances in electronics and computer technology have made the tracking and standardization of systems difficult. The BE Directorate has adopted modern configuration management discipline through proven techniques and established government standards so that their current system status, interoperability, and future configurations can be accurately monitored and effectively implemented to ensure consistent internal efforts and a usable, timely, quality product for a widening variety of customers.

Contractual efforts to develop a viable configuration management scheme and implementation strategy were through the Physical Science Laboratory (PSL) at New Mexico State University in Las Cruces, New Mexico. PSL personnel have provided several documents outlining configuration management practices and procedures as they apply to the TEWTB effort. The initial test of the configuration management program was the effective transition of the Block I IMETS weather decision aid software to PD IMETS. The

process was assessed and valuable lessons were learned that should streamline future BE Directorate releases to a wide variety of Army users.

3. LESSONS LEARNED

Throughout the development and implementation of the configuration management practices tailored to the BE Directorate R&D, several valuable lessons have been learned. Problems that were identified in the BE Directorate scheme need to be addressed and corrected wherever possible. Inherent problems that cannot be corrected because of organizational structure or personnel limitations need to be understood and recognized in the future.

Because there is a definite Army need to demonstrate future weather support concepts, TEWTB systems have been "loaned" to organizations at remote (from White Sands) locations. Upgrades to system software and identification of specific system discrepancies become problems because of personnel and budgetary limitations. The personnel who operate the systems at these locations are, for the most part, inexperienced in using computers and in accurately interpreting meteorological processes involved in applying programs that reside on these systems. Therefore, many software and physical process problems go unnoticed and are never reported to the developers. Even if skilled scientists and programmers working off-site for the BE Directorate note problems, often knowledgeable BE Directorate or contractor personnel must correct these problems on-site. Too often, these remote systems become "out-of-sight, out-of-mind," and the need to correct problems is easily ignored. These problems can be corrected by expensive on-site visits; at any rate, they should be corrected as soon as practical to maintain system integrity.

When the Block I IMETS was fully tested and baselined, it was delivered to the IMETS integration contractor with a list of known software discrepancies that were noted and documented during acceptance testing, but whose correction was not deemed critical to the release and therefore were not corrected. These discrepancies are now being corrected by the IMETS contractor and the BE Directorate developers independent of one another. There is a very real danger that two separate versions of the same applications software could be simultaneously active. The IMETS contractor has promised to provide the developers the software changes made, with full documentation of corrective actions taken to correct the Block I IMETS. These contractor changes must be identified, tested, and a new baseline established before another IMETS release.

Short notification requests for capabilities demonstrations have caused some configuration management headaches and software compatibility problems to surface. In one instance, the demonstration system and the developmental system had different operating systems. This is a problem related to both system integrity and configuration management. Adequate notification of support requirements with the appropriate documented changes that are needed to ensure system interoperability will preclude this from happening in the future.

Since Configuration Management Working Group (CMWG) meetings were not being held regularly, several system problems were not being voiced and, therefore, not corrected.

Meetings are now being held monthly with representatives from affected work units. Meeting minutes are distributed to all concerned scientists, programmers, and engineers whether or not they attend the meeting. Several ancillary meetings have spun off from these CMWG meetings to discuss issues related to a particular task that was not necessarily of interest to the whole group. Regular meetings have produced a healthy trend and have been ingrained into people's schedules and should continue with positive results.

Finally, there was no central location for configuration management information and documentation. Developers and contractors could not get easy access to TEWTB-related publications pertaining to the system or its configuration. New furniture and a new floor plan at the BE Directorate computer facility have eliminated this problem. All manuals and publications related to a specific system now reside in a reference library collocated with the computer systems that they support.

4. TEWTB DOCUMENTATION

The following is a list of documents that specifically evolved as a result of the BE Directorate configuration management efforts.

Document Report for Configuration Management, PSL-91/55, Nov 91, K. L. LaValle

Document for Configuration Management, PSL-91/61 (Rev.1), Mar 92, K. L. LaValle and C. O. Alvillar

Technology Exploitation Weather TestBed (TEWTB) User's Guide and Technical Reference for the Block I Integrated Meteorological System (IMETS), PSL-92/60, Nov 92, Authors from both PSL and the BE Directorate

Functional Description for the Technology Exploitation Weather TestBed (TEWTB), PSL-92/68, Dec 92, M. H. Dubbin, J. R. Elrick, C. E. Lewis, and L. E. Roth

Configuration Management General Information and Processing Procedures for the Technology Exploitation Weather TestBed (TEWTB), PSL-93/13, Feb 93, K. L. LaValle, C. O. Alvillar, L. E. Roth, and C. E. Lewis

Additionally, as a result of the Block I weather decision aids software release, documentation was released as a baseline report that contains all relevant information about the released software and testing information.

Finally, current TEWTB software and hardware are accounted for with a database (DBASEIII) program. Configuration status is updated as it changes and is controlled by PSL.

5. SUMMARY

Rapid advances in science and technology have made accurate accounting practices for computer hardware and software a necessity. The use of modern, tested configuration management practices makes this accounting possible. Configuration management techniques are being used and modified by the BE Directorate to meet their internal needs and the needs of a modern, dynamic Army. This process will ensure that consistent, tested products are delivered to support Army users at all levels requiring specialized or routine weather information.

Session I Posters

BATTLE WEATHER DATA

MODELED CLIMATOLOGY (MODCLIM)

Captain Robert J. Falvey
United States Air Force Environmental Technical Applications Center
Simulation and Techniques Branch
Scott AFB, Illinois
618-256-5412/DSN 576-5412/Fax x-3772

ABSTRACT

Climatological data is a valuable tool that typically requires large amounts of manipulation and computer storage space. Compressing such data reduces the amount of storage space needed and makes it more accessible to smaller computer systems. Modeling frequency distributions of climatological data using numerical methods is an effective data compression technique. The increased use of the personal computers (PCs) by the Department of Defense has led to an effort at the United States Air Force Environmental Technical Applications Center (USAFETAC) to develop PC-based modeled climatological databases. One such effort is called "Modeled Climatology" (MODCLIM).

1. Introduction. MODCLIM consists of two microcomputer programs. Modeled Ceiling and Visibility (MODCV) provides conditional, unconditional, and joint ceiling and visibility probabilities out to 72 hours. Modeled climatological Curves (MODCURVES) provides diurnal and annual curves of temperature, dew point, relative humidity, altimeter setting, and pressure altitude.

2. MODCV. USAFETAC has created cumulative frequency distributions of ceiling and visibility observations covering a 20 year period of record for over 600 reporting locations around the world (Kroll and Elkins, 1989). Surface observations from all hours are binned into 3-hour groups so that airways and synoptic reporting stations can be used. Since ceiling and visibility data are not normally distributed, the Weibull family of curves is used to produce theoretical estimates of the cumulative probability distribution. The Weibull curve is used because it has a great variety of shapes and is flexible enough to fit most distributions (Nelson, 1982). The use of the Weibull curve for modeling visibility is well documented in Somerville, Bean, and Falls (1979) and Whiton and Berecek (1979). The Weibull curve is expressed by the equation:

$$P = 1 - exp \left(- \alpha X_t^\beta \right)$$

where α and β are the modeling coefficients, X_t is some threshold visibility in statute miles, and P is the probability the visibility will be less than X_t. A slightly different form of the Weibull

curve is used to fit ceiling data. The Reverse Weibull curve is similar to the Weibull but takes the form:

$$P = exp \left(- \alpha X_t^\beta \right)$$

where α and β are as described above, X_t is some threshold ceiling in feet, and P is the probability the ceiling is less than X_t. In both cases, α and β are determined from the empirical distributions.

For most mid-latitude stations in the United States and western Europe, the distributions display a gradual "stairstep" increase in the cumulative probability as the ceiling and visibility values increase. This gradual increase makes it relatively easy to estimate the theoretical distribution. Cumulative distributions for stations in the tropics and non-western nations, however, frequently exhibit large "jumps" at certain cloud heights and visibilities, and then show no increase across the remaining range of ceiling or visibility values. The cause of these "jumps" in the tropics is likely due to the relative low frequency of sustained low ceiling and visibility. The reason for the "jumps" in the data from the non-western nations is not as easily explained, but may be due in part to a lack of adherence to World Meteorological Organization (WMO) standards. The erratic nature of these distributions creates some problems when fitting the Weibull curve to the observed distribution. Knowing the nature of these observed cumulative probability distributions allows careful thresholding of the ceiling and visibility observations which are then used to construct a modeled distribution. Weibull coefficients are calculated and stored for use with the MODCV software. The software uses these coefficients, along with current conditions and serial correlations, to produce conditional and unconditional probability forecasts of ceiling and visibility, and joint ceiling and visibility probabilities. The output consists of bar graphs or tables of ceiling and visibility probabilities for eight user-selected forecast times up to 72 hours in the future. Figure 1 is an example showing a joint probability forecast for Oslo, Norway.
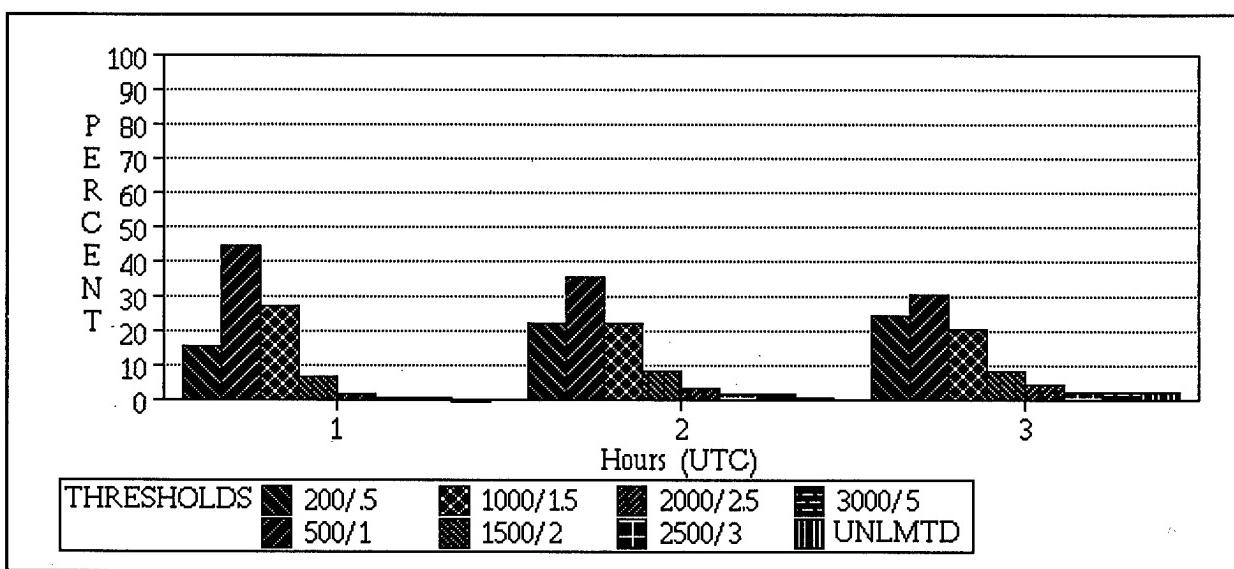
Figure 1. Sample MODCV output for Oslo, Norway, showing joint probability forecast for November.

The verification data for the 3- and 24-hour forecasts was collected for 11 stations for the month of February 1987. Table 1 shows the Brier Skill (P) Scores for the Wind Stratified Conditional Climatology (WSCC) tables of ceiling (WC) and visibility (WV) and for MODCV ceiling (MC) and MODCV visibility (MV). Brier Skill Scores range from 0 (perfect) to 2 (worst). They are calculated using:

$$P = \frac{1}{N \left[\sum_{j=1}^{r} \sum_{i=1}^{N} (f_{ij} - E_{ij})^2 \right]}$$

where r is the number of forecast categories, N is the number of days, f is the probability forecast of the event occurring in that category, and E takes the value of one or zero according to whether the ceiling or visibility occurs in that category.

Table 1. Forecast Verification Results (P-Scores) for 11 Stations

	Morning								Afternoon							
	3 Hours				24 Hours				3 Hours				24 Hours			
	WC	MC	WV	MV	WC	MC	WV	MV	WC	MC	WV	MV	WC	MC	WV	MV
Ramstein	.62	.52	.66	.63	.83	.76	.82	.84	.50	.53	.60	.47	.77	.72	.79	.72
Mildenhall	.53	.60	.26	.45	1.5	.78	.60	.61	.64	.69	.38	.37	.72	.75	.43	.48
Cannon	.22	.41	.29	.29	.42	.55	.38	.43	.25	.38	.12	.12	.21	.48	.25	.26
Lajes	.18	.23	.07	.07	.26	.34	.00	.00	.26	.49	.00	.14	.47	.45	.14	.14
Osan	.01	.11	.27	.30	.08	.09	.42	.28	.16	.09	.51	.64	.28	.27	.47	.50
McChord	.30	.32	.21	.17	.35	.39	.18	.21	.09	.11	.00	.05	.11	.18	.01	.02
Shemya	.40	.42	.26	.27	.69	.66	.47	.46	.52	.51	.35	.33	.56	.62	.55	.48
Eglin	.21	.31	.20	.27	.51	.45	.29	.27	.30	.23	.25	.18	.49	.53	.3	.32
Shaw	.27	.24	.26	.21	.66	.42	.25	.26	.30	.34	.31	.33	.66	.36	.22	.20
Minot	.53	.62	.33	.42	.68	.67	.20	.21	.51	.46	.11	.14	.69	.64	.34	.29
Clark	.00	.00	.01	.00	.01	.00	.00	.00	.00	.00	.11	.00	.00	.00	.00	.00

The P-scores in Table 1 show a wide range of results. For example, Mildenhall's afternoon ceiling 3-hour verification (MC=.69) was The P-scores in Table 1 show a wide range of results. For example, Mildenhall's afternoon ceiling 3-hour verification (MC=.69) was not as good as WSCC's (WC=.64). But Osan's morning MODCV visibility verified at 24 hours (MV=.28) is better than the WSCC's visibility (WV=.42). Therefore, a paired t-test was used to determine if the differences between MODCV and the WSCC P-scores were statistically significant. The result was there is no significant difference between the P-scores for the WSCC forecasts and the P-scores for the MODCV forecasts. MODCV shows good skill when compared to the WSCC tables.

3. MODCURVES. USAFETAC also created climatological diurnal and annual curves of five weather variables from 20 years of weather station observations. A Fourier series is used to describe diurnal and annual curves of temperature, dew point, relative humidity, altimeter setting, and pressure altitude. Since the first three harmonics, coupled with the mean, account for between 95 and 98 percent of the variance (Panofsky and Brier, 1968), the Fourier series is truncated after the third harmonic. Although this prevents the exact replication of the original curve, the truncation of the higher frequency oscillations eliminates the unwanted "noise" in the data and reduces the original data by about 46 percent, allowing Fourier coefficients for individual observations sites to be placed in separate compact data files. The Fourier coefficients from the analysis are uses by the MODCURVES program to regenerate the curves.

Since not all meteorological variables are normally distributed, MODCURVES uses the 5th, 50th, and 95th percentiles to represent the minimum, median, and maximum values of the variables. The use of percentiles eliminates the extreme values from the data, thus giving a more representative climatological view. These percentile values are placed in a time series to examine their diurnal or annual behavior. This technique gives forecasters access to information from large databases quickly and easily through a user-friendly pull-down menu system. Users can specify five wind categories (north, east, south, west, or all), three sky cover categories (clear/scattered, broken/overcast, and all) and three percentile categories ($5^{th}\approx$minimum, $50^{th}\approx$median, and $95^{th}\approx$maximum) to examine unconditional and conditional climatologies. The output is in the form of time-series diagrams depicting the diurnal and annual cycle of the selected variable. The user can also choose a modified climatology by entering the initial value of the variable to which the curve is adjusted. This adjustment provides a climatological curve which is tailored to the current conditions and allows a more accurate forecast for any time during that 24-hour period.

In order to determine the usefulness of MODCURVES, a simple accuracy study was conducted. Data sets of Fourier coefficients for Eglin AFB, Eielson AFB, McChord AFB, and Scott AFB were generated. The mean monthly values in the Climatic Summaries (RUSSWO) were compared to the 50th percentile (median) values from MODCURVES. Since the RUSSWO's do not contain monthly mean altimeter and pressure altitude, only temperature, dew-point temperature, and relative humidity could be examined. The mean absolute errors for all 12 months combined (|MODCURVES value - RUSSWO value|) are listed in Table 2.

Table 2. Mean absolute difference between MODCURVES and RUSSWOs.

Location	RUSSWO POR	MODCURVES POR	Temp	Dew Point	RH
Eglin	1939-86	1973-90	0.51°F	2.24°F	5.95%
Eielson	1944-87	1973-90	1.21°F	1.84°F	4.91%
McChord	1940-81	1973-90	0.44°F	0.88°F	3.88%
Scott	1938-85	1973-90	0.86°F	1.35°F	1.56%

Figures 2 and 3 are examples of the Enhanced Graphics Adapter (EGA) and Color Graphics Adapter (CGA) resolution output, respectively.
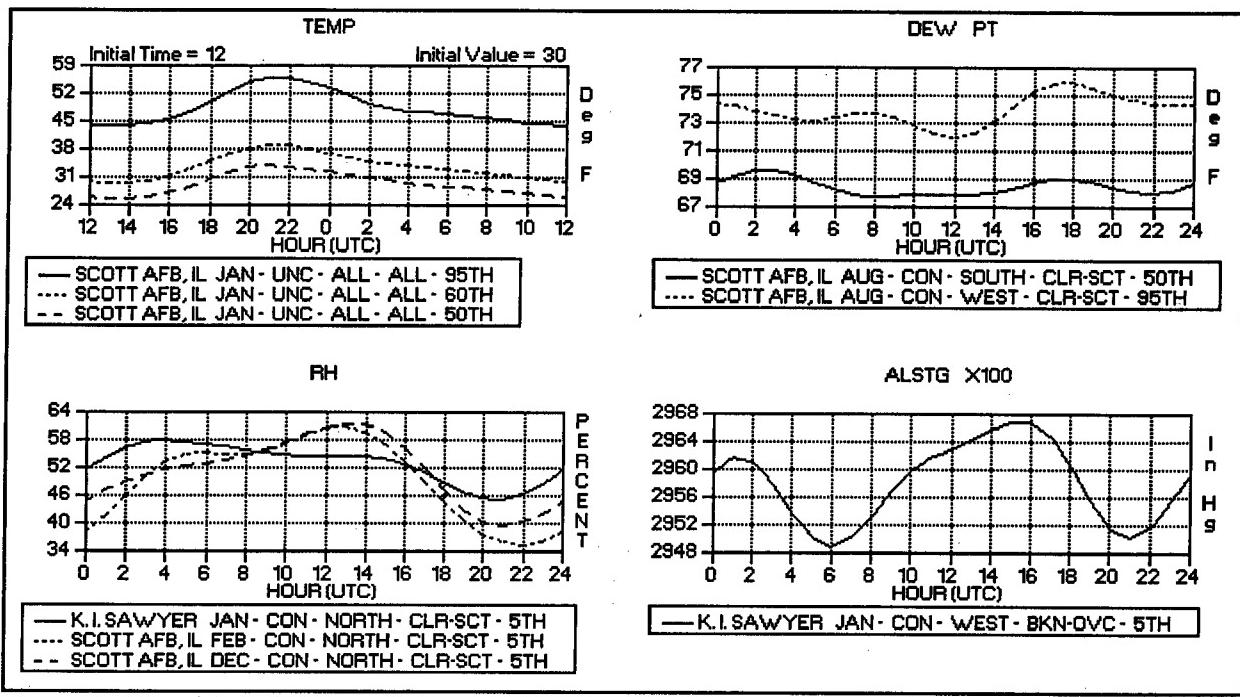
Figure 2. Example EGA 4-panel plot showing the use of the overlays and initial conditions for diurnal curves of temperature, dew-point temperature, relative humidity, and altimeter setting.
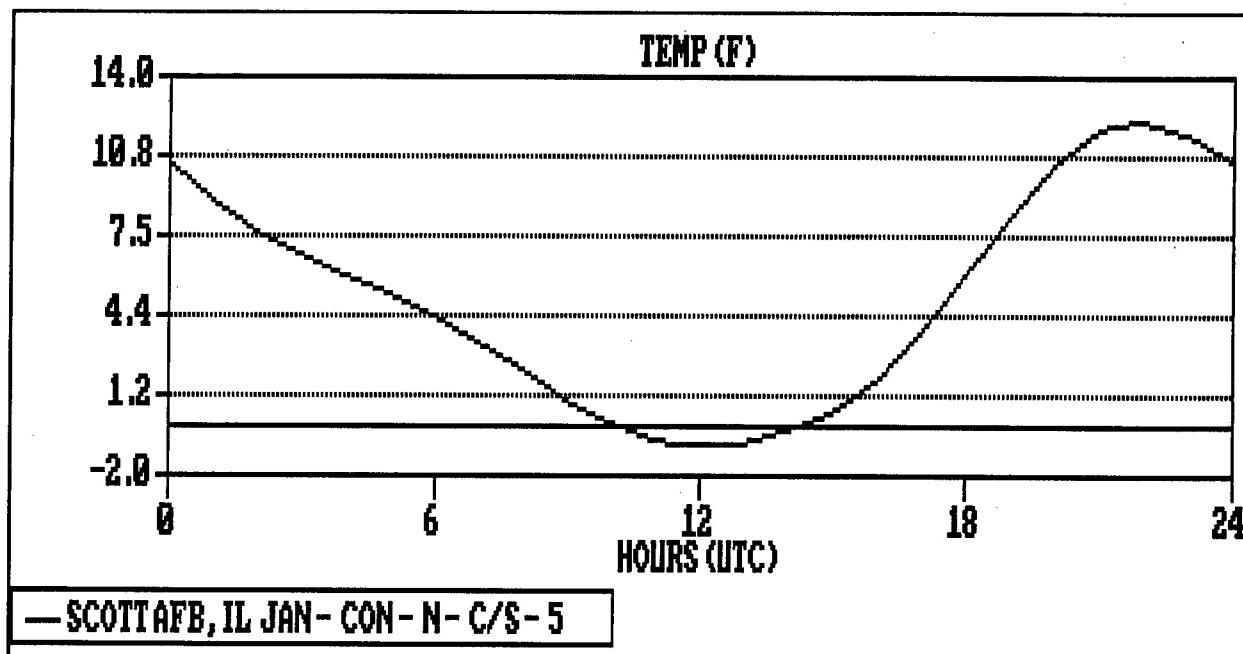
Figure 3. Example CGA plot of temperature for Scott AFB in January with north winds and clear/scattered skies for the 5th percentile (lowest 5%).

471

CONCLUSIONS

USAFETAC developed PC-based MODCLIM products to make climatological data easier to access and use. The user-friendly MODCV and MODCURVES programs allow quick access to a station's climatological database. Since both programs run on laptop computers, the latest climatology is available in electronic form for forecasters at base weather stations as well as to those deployed to the field.

REFERENCES

Kroll, James T. and Harold A. Elkins, *The Modeled Ceiling and Visibility (MODCV) Program*, USAFETAC/TN-89/001, United States Air Force Environmental Technical Applications Center, Scott AFB, IL, January 1989.

Nelson, Wayne, *Applied Life Data Analysis*, John Wiley & Sons, Inc., New York, 1982.

Panofsky, Hans A. and Glen W. Brier, *Some Applications of Statistics to Meteorology*, The Pennsylvania State University, University Park, PA, 1968.

Somerville, P.N., S.J. Bean, and S. Falls, *Some Models for Visibility*, AFGL -TR-79-0144, Air Force Geophysics Laboratory, Hanscom AFB, MA, 1979.

Whiton, Roger C. and Emil M. Berecek, *Basic Techniques in Environmental Simulation*, USAFETAC/TN-82/004, United States Air Force Environmental Technical Applications Center, Scott AFB, IL, July 1982.

A COUPLE OF LOCKHEED'S
METEOSTAR™ ENVIRONMENTAL SYSTEMS

James L. Hatch, T. Steven Barker and Robert L. Scheinhartz

Lockheed Missiles and Space Company, Inc.
Austin, Texas

1. INTRODUCTION

Timely warning of weather hazards for both air traffic controllers and pilots is essential for safe and efficient flight operations. Weather and environmental effects are also important factors in allocation and employment of military forces. Despite demanding requirements for environmental support for military and civilian operations, funds to develop and procure systems to meet the requirements have grown scarce. Cost-effective systems are needed which meet both civilian and military requirements. These systems must acquire and process meteorological data from all available conventional sources, as well as from geostationary and polar orbiting meteorological satellites. Satellite sounding data and special sensor microwave imagers are particularly important for obtaining weather information in data sparse areas. Conventional data, combined with multi-spectral processing of visible, IR, and other spectral data from the TIROS, DMSP, GOES, METEOSAT, and GMS, can provide the basis for accurate analysis over most areas of the earth. Low-cost integration of satellite data, local sensor suites, and WMO observations and forecasts provides the basis for an extremely powerful weather analysis and forecast capability.

The development of highly advanced systems that meet most meteorological user needs has been the goal of Lockheed Austin Division's Environmental Systems Team for the past two years. To begin this process, Lockheed applied the principles of Quality Function Deployment to establish system requirements. Extensive user inputs from trade shows, interviews, briefings, and more than 15 system specifications for civil and military meteorological systems worldwide were analyzed. Composite requirements were derived which meet the needs of most users.

Corresponding author address: James L. Hatch, Lockheed Austin Division, 6800 Burleson Road, Bldg 320 Orgn T2-30, Austin, TX 78760-7100

To satisfy the composite requirements, new capabilities were developed and merged with capabilities selectively transitioned from existing military environmental systems. The result was a series of commercial meteorological products known as Lockheed MeteoStar™ Environmental Systems. The functionality discussed may be considered a base set of requirements for meteorological systems today.

2. THE LOCKHEED APT/WEFAX WEATHER SYSTEM (LAWS)

The Lockheed MeteoStar™ LAWS is a Commercial-Off-The-Shelf (COTS), personal computer-based system. It is designed to support both military and civilian operations at fixed, land-based locations throughout the world and in mobile configurations, including onboard ships and aircraft. The system provides automatic, unattended acquisition, processing, and display of (1) real-time, low-resolution, Automatic Picture Transmission (APT) imagery from U.S. NOAA and Russian METEOR polar-orbiting satellites, and (2) weather facsimile (WEFAX) products from U.S. GOES, European Space Agency METEOSAT, and Japanese GMS geostationary weather satellites.

The Lockheed MeteoStar™ LAWS acquisition subsystem includes both an omni-directional and a parabolic dish antenna for the receipt of polar-orbiting and geostationary meteorological satellite data. It also includes a pre-amplifier/filter for the polar-orbiting data, a pre-amplifier/down-converter for the geostationary data, and a computer-controlled VHF receiver. The Lockheed

473

MeteoStar™ LAWS processing and display subsystem includes, at a minimum, a 386-based IBM-compatible personal computer with math co-processor, 4 MBytes of random access memory (RAM), and 80 MByte hard disk for the processing and storage of the satellite data. It includes a fourteen-inch, high-resolution Super VGA color monitor for the display of the satellite imagery, and an optional color printer. The proprietary Lockheed Weather Satellite Interface Card resides in one of the computer's full-size expansion slots. This card prepares the satellite analog data for processing by the computer.

The DOS- or Windows-based Lockheed MeteoStar™ LAWS software is composed of COTS packages fully integrated with "SatMapper" software developed by Lockheed. The SatMapper software automatically acquires the polar-orbiting satellite data using an internally created schedule of passes. Following completion of a pass, the data are processed, time-tagged, and stored for later viewing by the operator. The SatMapper software automatically creates an accurate latitude/longitude grid and geopolitical map for overlay on the processed NOAA satellite imagery (the Russian METEOR imagery is not currently gridded). For the automatic acquisition of WEFAX products, the Lockheed MeteoStar™ LAWS is pre-loaded with a master acquisition schedule for each of the geostationary satellites. The operator edits the appropriate master schedule to select only those products desired. User-friendly menus are used for all interactions between the operator and the system. Imagery can be displayed in either a visible or infrared mode and magnified up to twenty times. When infrared data are displayed, a readout of cursor-position latitude, longitude, and temperature is displayed along with the imagery. For image enhancement, the operator may either adjust the displayed gray-shades for better contrast or activate up to three palettes of seven colors each to bring out more detail in the displayed imagery. WEFAX products can be displayed either singularly or in animated form. These products can also be annotated. NOAA APT data can be earth located and displayed with background maps, as well as with color enhancements and user added annotation. METEOR data can be displayed, color enhanced, and annotated, but cannot be overlaid with background maps.

3. THE LOCKHEED ENVIRONMENTAL ANALYSIS AND DISPLAY SYSTEM (LEADS)

The Lockheed MeteoStar™ LEADS is a COTS system for receipt and processing of meteorological conventional and satellite data, integration of all data types, and interactive generation and display of tailored weather support products. The Operator-Machine Interface (OMI) is easy-to-use, powerful and extremely responsive to operator requests. Meteorological products can be produced without difficulty; the user can create almost any weather product that can be imagined. Lockheed MeteoStar™ LEADS software runs on workstations which adhere to UNIX, X-Windows, Motif and Open Network Computing Remote Procedure Calls standards. In addition, LEADS architectures share the following common features: all can be procured as "starter" systems and expanded as needed; all provide sufficient CPU and memory to ensure near-instantaneous response to operator requests for data, interactive operations, and displays; all provide great flexibility in the number and type of external interfaces that can be accommodated; all provide the software for integration of a large variety of meteorological data types; all can include options for satellite ingest and RADAR interfaces; all can be configured with an optional suite of meteorological sensors; all are relatively inexpensive; and all can be easily adapted to meet specific customer requirements. The functionality of the Lockheed MeteoStar™ LEADS software is summarized in the following paragraphs.

3.1 Area Definition.

The user may define many areas of interest (AOIs), where North is at the top of each area and the distance horizontally across each area is the same as the distance vertically from the top of the area to the bottom. The system can be operational with dozens of AOIs defined simultaneously. All data types are mapped to these AOIs on retrieval; therefore, all data types properly overlay when displayed together. Thus LEADS can perform as a meteorological workstation at a command and control center where many regions must be analyzed simultaneously or in a mobile configuration where the AOI is continually changing. Intuitive OMI is provided to define the projection (Lambert Conformal, Mercator, Polar Stereographic, Earth Normal, and Orthographic) and real-earth extent of each AOI. The system

provides high-resolution worldwide background maps and worldwide topography with a resolution 5 NM.

3.2 Grid Field Handling.

The Lockheed MeteoStar™ LEADS decodes grids from external sources and stores the decoded fields in an internal format. External grids which arrive in sections are "pieced together" internally to provide a composite grid database. Therefore, gridded data can even be retrieved across boundaries introduced into external gridded fields to optimize transmission. These data may be retrieved by element, level, forecast hour, gridded data source (the weather central which initially produced the gridded field), model, and base time over any AOI previously defined by the user. The grid point density retrieved over an AOI is user definable; therefore, the user has control of "scale of analysis". That is, the density of grid points mapped to an AOI may be greater or less than the density of stored grid points from an external grid, since extraction uses interpolation. After extraction and projection, the AOI will contain a 32 X 32, 64 X 64, or 128 X 128 grid. By properly selecting the AOI real-earth size and the extracted grid density, the user maintains control of the scale of analysis (e.g., microscale, mesoscale, or macroscale).

Gridded fields are also generated by the system from observation data on pressure, height or potential temperature surfaces. These grids can contain errors present in the input observation data, just as gridded fields from external sources may contain transmission induced errors. A grid editor is provided to correct errors in gridded data. The user may interactively select bad grid points in displayed data, and replace bad values with "null" or other values. If the user changes a displayed grid, a reanalysis can be accomplished to fill in null areas and to smoothly merge any user added grid values into the remainder of the grid.

3.3 Observation Handling

The system receives, decodes and stores Global Telecommunication System (GTS) observation data. Automatic quality control includes message header checks, syntax checks and gross error checks. The system provides functions to edit messages which fail quality control checks, and to read undecoded message data at any time. A minimum of 48 hours of "raw" message data, 24 hours of decoded surface and upper air data, and 1000 hours of bathythermograph data are retained in the system. Decoded data can be plotted, gridded and contoured. Automated surface observing systems which report in GTS format are easily interfaced to the system. Observation data can also cause alerts to be generated by the system. Alerts are issued based on arrival of user identified data, thresholding surface observation data within a user defined area, and encountering "key words" in arriving messages. For alert on threshold, any number of Meteorological Watch (METWATCH) areas can be user defined, with up to three thresholds specified for each area.

3.4 Imagery Handling

Satellite radio frequency hardware and data processing options are available for high-resolution (HRPT, DMSP, GOES, METEOSAT and GMS) and/or low-resolution (APT and WEFAX) satellite data. Following ingest, "sectors" of satellite data are projected into requested AOIs. Since satellite data are mapped to the same AOI projections as all other data types, the imagery may be overlaid by other data and backgrounds. Functions are provided for creation of composite imagery from multiple polar satellite passes. Options for receipt and processing of RADAR imagery will be included in the system by early 1994. By mid-1994, options for producing gridded fields from DMSP special sensor microwave imagery will also be included in the system.

3.5 Communications

Multiple Lockheed MeteoStar™ LEADS may be interconnected with Local Area Networks (LANs) and Wide Area Networks (WANs) to enable exchange of data and products. The MeteoStar™ LEADS software is configurable to meet specific customer communications requirements and varying levels of fault tolerance.

3.6 Product Building

The LEADS provides a "toolbox" of meteorological functions. Using these tools, product building can be accomplished interactively by a user, or by executing macros. The system provides macros to automatically

475

generate objective analysis fields, derived grids and products for display. To build a macro, the user places the software in "learn" mode, in which menu selections are recorded by the system. After a product has been generated, the list of menu selections used to create the product may be saved as a macro under a user specified name. A macro can be executed by schedule, or manually by the user. The tools provided by LEADS are discussed below.

3.6.1 Retrieve and Store

Data are mapped to the projection associated with a user specified AOI when retrieved. This provides the mechanism by which different data types overlay when displayed together. Data may be retrieved on pressure, height or potential temperature surfaces. The store function provides the capability to store products, intermediate product steps, and displays.

3.6.2 Plot, Grid and Contour

The plot function creates plots of grids and observations under control of user-defined or WMO standard plot models. Custom plot models may be defined or edited interactively. Plot models accommodate both symbolic (wind barbs, cloud cover, past weather, etc.) and alphanumeric characters. When plot models are applied to observation data, the user may also specify up to three thresholds which allow the data to be screened on plotting; only data meeting the specified thresholds is plotted. Plotting of station data is controlled by user defined/selected station plot models and a Station Priority List. Menus are provided for user modification of the Station Priority List. If two stations would overplot at a given zoom level, only the station with the highest priority is plotted. Plot models for gridded data are defined at the time the data are displayed. Each cell of a gridded data plot model may be a different color, as defined by the user. Plotting of upper air data is provided on pressure, height and potential temperature surfaces. Since plotted data at one location is not allowed to overwrite plotted data at another location, all data are not generally plotted at 1:1 zoom. However, when plotted data are zoomed, plots not displayed at a lower zoom levels (e.g., 1:1) are displayed at higher zoom levels (e.g., 1:4).

The grid function uses a Cressman or Barnes analysis to grid observation data. Options are provided for full or partial interpolation (outside or inside the domain of observations locations), for specifying the radius of influence for the analysis, and for stating the desired output grid point density.

The contour function creates isopleth displays from gridded data. All contour lines are properly labeled, and the user may select the number of decimal points to be used for labels. The base contour level and the contour interval, as well as the color and line style to be used for contouring, are user selectable; default values can also be used.

3.6.3 Sounding Data

Skew-T Log-P, bathythermograph soundings and cross sections are provided to display the vertical structure of data in the database. Cross section elements include wind speed, temperature, dewpoint depression, relative humidity and wind barbs. Any cross section element may be converted to an image and displayed as the background for the cross section. The Skew-T Log-P function creates a thermodynamic diagram from upper air data. The displayed diagram includes wind barb plots and stability analysis. This function provides a graphical interface which displays the location of all possible upper air stations in the selected AOI. The user interactively selects stations for which Skew-T Log-P diagrams are to be generated. Multiple selections of the same station cause display of Skew-T Log-P diagrams for different valid times for the same station. A tabular listing of layer stability, various stability indices and sounding data is also provided. The bathythermograph function presents an OMI nearly identical to the Skew-T Log-P function, except the bathythermograph function displays temperature with ocean depth.

3.6.4 Derived Fields

Grid and image calculator functions provide arithmetic and logical operations (add, subtract, multiply, divide, constant, less than, less than or equal to, greater than, greater than or equal to, equal, OR, AND, NOT, merge, and mask). Using the calculator function, the user may construct such products as height change and time change

fields, or a grid can be thresholded before contouring. Gridded fields and imagery output from the calculator functions can be used as input to other system functions, including the calculator functions themselves. Rule-based merging enables compositing of satellite imagery, RADAR data and gridded fields. Other derived fields include streamline, vorticity, advection, divergence and convergence.

3.6.5 Display

This function provides the capability to display selected data. Multiple overlays for the same AOI may be selected for simultaneous display. One image and any number of graphics may be selected for display. Special displays are also supported, such as gridded fields converted to imagery by interpolating grid point values to image pixels. On the resulting "grid-to-image" display, each color or gray shade represents an interpolated value from nearby grid points. Grids may also be displayed in a 3-dimensional isometric view, where the vertical axis represents the value of grid points in the displayed gridded field. The units of any displayed data may be changed at any time, and an interrogate function is provided which gives the latitude and longitude of the cursor on any displayed, earth-located, image. The value of the pixel beneath the cursor is also displayed, as is the element value associated with the pixel value (e.g., the temperature associated with an IR pixel value). The system automatically labels and manages overlays displayed by the system. Displayed data may be interacted with by the user in one of two ways. One mechanism provides the OMI to control the default appearance of the displays, such as contour line colors, contour interval, and starting contour value (although the system enables the user to override defaults at any time). A second mechanism provides for direct, interactive manipulation of displayed data.

3.6.6 Colors

The system provides (1) color and gray scale enhancement of displayed imagery (including imagery generated from topography), (2) selection and modification of the background color, (3) selection and modification of background map colors, and (4) selection and modification of colors used for all displayed graphics and text. Color and/or gray scale color tables are created

interactively; all enhancement table changes are simultaneously reflected on any displayed image. The ability to save and subsequently use defined color tables is provided. The user may also interactively select the size of a circle, ellipse or parallelogram to be displayed on the screen, which may subsequently be filled with a user selected color and pattern. The geometrical shapes generated by these functions are useful for weather warning areas, and can be used to highlight text warnings. The user may also select any displayed object and color the object with a user selectable highlight color.

3.6.7 Drawing and Modifying Lines and Symbols

A draw function provides the capability to interactively draw smooth, cubic spline lines and line-symbols (including multi-colored lines such as stationary fronts). The capability to draw both labeled and unlabeled lines is provided. Labeled lines have a value attribute associated with each line, so labels can be dynamically located on the display when graphics data are zoomed or displayed. This prevents labels from being lost (i.e., moved off the display) during zoom. All properly colored WMO meteorological line symbols (e.g., upper air and surface fronts) are provided. Lines, line-symbols and contours are easily modified at any zoom level. It is possible to zoom in on a specific area of analysis, modify a line at the higher zoom factor, then zoom back to a standard level (e.g., 1:1 zoom). Changes made at the higher zoom level are retained at all lower zoom levels. The system also allows the user to define multiple sizes of line symbols and line thickness. Five sizes of all WMO weather symbols are also provided. The user may select the symbol and size from a menu, and drop the symbol anywhere on the display. Functions are provided for selecting a displayed object and "dragging" the object to another location on the screen, and deletion of lines and displayed objects is fully supported. The user may also define alphanumeric labels and place these labels on the screen at any desired location.

3.6.8 Zoom

The zoom function operates in a context sensitive way, depending on the data currently displayed. When more than one data type is displayed, the rules for each data type are followed individually. For example, if a graphics chart is

displayed over an image, the image is first zoomed (pixel replication zoom), then any background maps are re-drawn at the new zoom factor, and finally the graphics chart is re-displayed; all contour lines are automatically relabeled at the new zoom level.

3.6.9 Animate and Sequence

Using the mouse, a user may select multiple products or images to be included in animation sequences. Animation at rates of 14 to 28 frames per second is supported (the higher rates are provided on high-end workstations). Any product that can be displayed can be animated. The function also provides the capability to sequence through a preselected list of products, one frame at a time, making it ideal for presenting briefings. The number of frames that may be included in a briefing sequence or an animation loop is dependent on the amount of system memory provided with the system.

4. FUTURE CHALLENGES

The next decade should see an explosion in the amount and availability of weather data. Deployment of the Automated Surface Observing System (ASOS), the Next Generation Weather Radar (NEXRAD), wind profilers, acoustic sounders, lidar, and aircraft-mounted sensors are among those systems adding increased temporal and spatial resolution of many atmospheric parameters. The modern high-speed information highway ensures all of this data can be available. Message traffic of image data will be facilitated by automatic compression schemes. These can be tailored to provide lossless or levels of degradation in the transmission. A system receiving all of this data may be required to forward specific types of messages to certain platforms on a local or wide area network. Lockheed has begun work on a product called the Lockheed MeteoStar™ Rapid Information Management System (RIM) which is weather switching software that manages multiple interfacing weather circuits and receives and forwards weather message traffic.

A second challenge is to develop algorithms which maintain a coherent, dynamically consistent database. Quality control procedures on received and decoded data will have to undergo stringent consistency and priority checks before being merged into a database system. Although interactive quality control will still be a major feature of future systems, the need is to eliminate as much of it as possible so that this wealth of data can be exploited to achieve operational objectives. Deadlines are always a certainty.

Furthermore, this wealth of information will change the way weather data is viewed. Traditional analyses at synoptic times on constant surfaces will be augmented or replaced by sophisticated visualization techniques consisting of volumetric displays at any time, perhaps to the nearest minute.

INTEGRATION OF A HEAT STRAIN PREDICTION MODEL WITH ARMY WEATHER DATA RESOURCES

William T. Matthew
U.S. Army Research Institute of Environmental Medicine
Natick, MA

Richard E. McNally
Science Applications International Corporation
Joppa, MD

Gary B. McWilliams and Steve F. Kirby
U.S. Army Research Laboratory
White Sands Missile Range, NM

Heather D. Pfeiffer
Computer Science Department
New Mexico State University, Las Cruces, NM

ABSTRACT

We have begun integration of the U.S. Army Research Institute of Environmental Medicine (USARIEM) Heat Strain Prediction Model with an image-oriented weather/terrain data processing system. Components of the USARIEM model will be linked with the TWIST (Terrain and Weather IPB Software Toolkit) system, currently under development by the U.S. Army Research Laboratory (USARL). In a preliminary evaluation, using archived weather data for a 178 X 112 km section of the Los Angeles basin as input to the heat strain model, we produced map-overlays which illustrate striking variability in heat injury risk across the region.

INTRODUCTION

Weather Effects on the Soldier

In spite of remarkable changes in the global geo-political community which continue to shape the role of U.S. military forces, the effective performance of the

deployed combat soldier is likely to remain a critical determinant of mission success. The operational "envelope" of the most sophisticated and essential component of our military system is bounded by finite physiological limits which can be approached or exceeded by mission demands. For the dismounted infantry soldier, the physical performance of a basic task such as movement over terrain in extremely hot or cold environments, or at high terrestrial altitude is constrained in ways that can now be quantified in the context of mission scenario, weather, and terrain. The near real-time ability to anticipate and even exploit these constraints for tactical advantage is a key element of Intelligence Preparation of the Battlefield (IPB).

Heat Strain Models

Even in temperate climates, air temperature, humidity, wind speed, and solar radiation may interact with mission requirements for heavy physical effort and/or chemical protective postures to create significant heat injury risk. Recognition of the potential impact of heat stress induced injury and performance degradation on the combat mission, as well as the potential burden to the combat casualty care system, has led to the expenditure of considerable effort to develop a practical thermal strain prediction model suitable for use in military applications. The U.S. Army Research Institute of Environmental Medicine (USARIEM) has developed a heat strain prediction model with modest computational demands and well defined input requirements[1,2]. The U.S. Army Chemical School, under the "Physiological and Psychological effects of the NBC environment and sustained operations in Combat"(P^2NBC^2) program has supported enhancement and translation of the USARIEM heat strain prediction model into an Ada language version known as the "P^2NBC^2 Heat Strain Decision Aid"[3,4].

Spatial Variation in Heat Stress Effects

Previous work using the USARIEM heat strain model and surface weather station data from Southwest Asia has shown that, across a Mesoscale region, there may be substantial point-to-point variation in prevailing heat injury risk[5]. The ability to map the boundaries of physiologically significant risk zones or "thermal features" in near real-time would provide extremely useful IPB in an operational setting. A highly automated image oriented computational platform and surface level weather data at high spatial resolution are required to implement this capability.

The TWIST Project

The U.S. Army Research Laboratory, Battlefield Environments Directorate (USARL-BED) is developing the Terrain and Weather IPB Software Toolkit (TWIST). This software system incorporates the weather and terrain data handling capabilities of Mercury[6] and WADIF[7], and will ultimately be linked to the Army's Integrated Meteorological System (IMETS)[8]. The overall function is to integrate terrain information with weather parameters derived from global models, surface weather stations, and satellites using heuristic reasoning methodologies to improve accuracy and effectively maximize the spatial resolution. The gridded weather parameters are then available to support a broad range of near real-time map overlay type IPB products.

OBJECTIVES AND SCOPE

The overall objective of this effort is to develop and demonstrate a highly automated, terrain map overlay IPB product which assesses prevailing environmental injury risk and soldier performance limitations in a spatial context relevant to military operations. The specific objectives of this paper are to describe our approach to implementation and provide results of a preliminary case study evaluating the spatial contrast in thermal strain effects on soldiers across a typical coastal region. Scope is limited to consideration of heat stress effects for healthy young soldiers wearing standard military chemical protective clothing and performing at moderately heavy work rates, typical of many military tasks.

APPROACH

The approach is to develop and implement the software interfaces required to effectively integrate the USARIEM Heat Strain Prediction Model with TWIST. A contract task to accomplish this work was awarded to Science Applications International Corporation (SAIC) in late April 1993. Software interfaces are being written to automate input of Mercury's gridded air temperature, wind speed, humidity, and solar radiation estimates to an Ada computational module which re-uses selected components of the P^2NBC^2 Heat Strain Decision Aid. A simplified user input facility for selecting scenario-specific settings for soldier acclimatization status, physical work load, and clothing type is being developed. Data file structures for each of the four output products will be compatible with TWIST display capabilities. To accommodate the image-oriented map overlay display format, model outputs for heat injury risk, maximum safe work time, hourly drinking water requirements, and optimal work/rest cycles will be classified into three broad categories of risk or performance limitation for display: green, amber, and red overlays represent areas of low, moderate, and severe environmental health/performance conditions respectively. As part of the preliminary effort to evaluate predictive model default options and practical thermal strain classification thresholds for use with TWIST, spatial and temporal variation in heat stress model outputs across the Los Angeles basin over a 24 hour period were investigated.

METHODS

Weather Data Set
The weather data set was retrieved from the AZephyr Weather Line and consisted of hourly air temperature, dew point, and wind speed measurements for 27 May 1991 from an average of 17 weather stations located in a 178 X 112 km section of the Los Angeles basin.

Scenario-Related Inputs
For this analysis, all troops were considered to be unacclimatized, performing tasks requiring moderate to heavy physical effort (525 Watts), wearing standard issue

Battledress Overgarment (BDO) in the Military Operational Protective Posture, category 4 (MOPP-4) chemical protection configuration.

Procedures

The required variables were extracted from the weather data set and processed through the thermal strain prediction model. Results for heat casualty risk, maximum safe work time, and optimal work/rest cycle times were then processed through a gridding program to interpolate to a 1 km grid spacing. The gridded results were then contoured using a topological program, and those results overlaid on a map of the Los Angeles area.

RESULTS

Results are reported for the 0400 and 1700 GMT observation periods. In all locations at those hours, the predicted thermal strain levels were above threshold and soldier performance was constrained. Map overlays for predicted maximum safe work

FIGURE 1   **FIGURE 2**

Maximum safe work time, 0400 GMT.   **Maximum safe work time, 1700 GMT.**
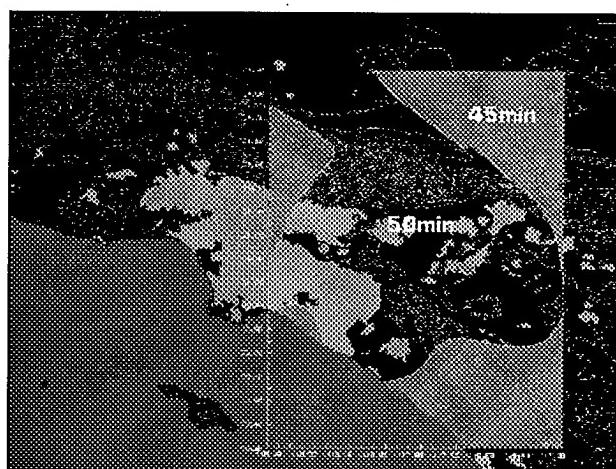
time, optimal work/rest cycle limits and heat casualty risk for the Los Angeles basin data are shown in Figures 1 through 6.

Figures 1 and 2 illustrate the predicted maximum safe continuous work time in minutes for the defined soldier task at 0400 and 1700 GMT. Total contrast in maximum safe work time across the region was only 10 minutes at 0400 and 5 minutes at 1700. In addition, despite the 13 hour difference in observation periods, the maximum safe work times are generally comparable.

Figures 3 and 4 show the predicted optimal work/rest cycle schedules needed to sustain some level of activity on the task with minimum heat injury risk. The cycles are

FIGURE 3

Optimal work/rest cycle, 0400 GMT.
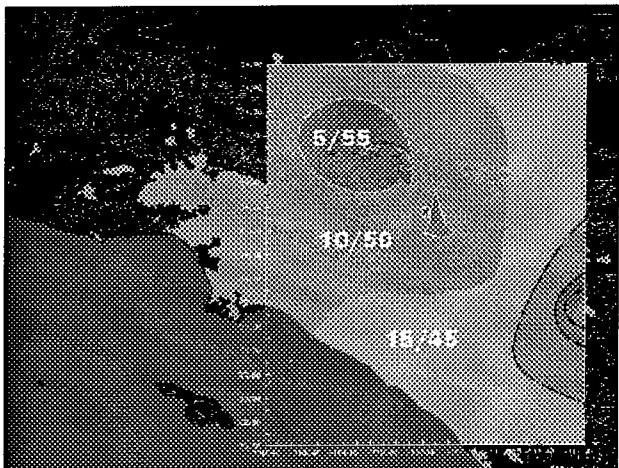
FIGURE 4

Optimal work/rest cycle, 1700 GMT.
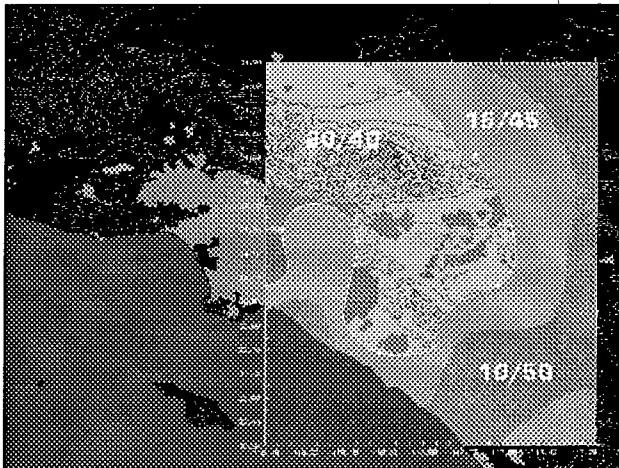
FIGURE 5

Heat casualty risk, 0400 GMT.
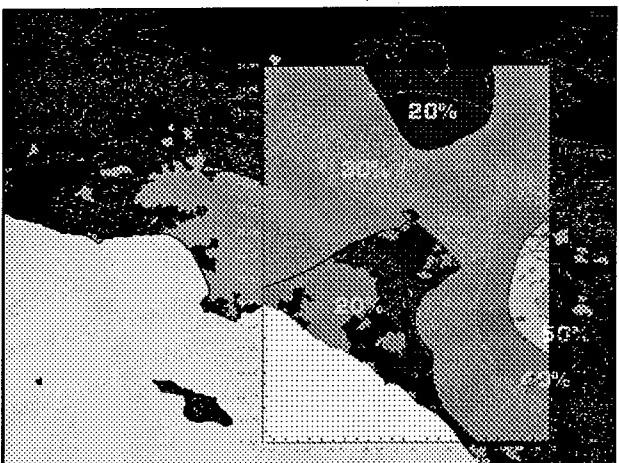
FIGURE 6

Heat casualty risk, 1700 GMT.
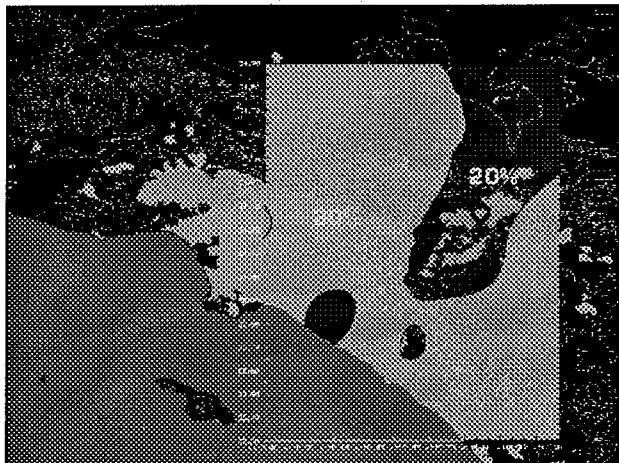
dominated by the long rest periods required to cool down in MOPP-4. At both 0400 and 1700 GMT, some locations allowed doubling or tripling of work time over worst case locations.

Figures 5 and 6 show the predicted heat casualty probability overlay which assumes no action is taken to adhere to either the maximum safe work time or optimal work/rest cycle guidance.

Because the 0400 GMT (2100 PDT) and 1700 GMT (1000 PDT) observation times represent mid-points rather than extremes in the diurnal cooling and heating cycle, overall differences in the magnitude of predicted limits for these two time periods are not

483

great. Nevertheless, our results suggest that even at these times, significant soldier performance constraints may exist, and local differences in the severity of those constraints can be visualized effectively in a map overlay format. It should be noted that the relatively heavy work rates, MOPP-4 chemical protection clothing, and absence of heat acclimatization we programmed in this analysis are circumstances that far exceed anything the resident civilian population would encounter in the course of normal daily activities.

DISCUSSION

The practical application of map-overlay representations of heat injury risk or soldier-system limitations is critically dependent upon the availability of reliable air temperature, humidity, wind speed, and solar radiation data. In a spatial domain of tens of thousands of square kilometers, the accuracy to which available meteorological observations can be interpolated to a grid establishes the baseline reliability of the predictive model output products. Other investigators working with the Ballistics Research Laboratory (BRL) TCOR model and surface level weather data for a 80 X 160 km desert area found substantial sensitivity of that model to RMS errors in interpolated weather values[9]. Although our predictive model is likely to manifest similar sensitivity to input errors, it is anticipated that the heuristic interpolation strategies implemented in TWIST will help minimize RMS errors for the gridded weather parameters.

This preliminary off-line analysis demonstrates the potential look of soldier performance related map overlay products and illustrates the kind of variation in predicted thermal strain effects that may occur across a coastal area. Nevertheless, the ability to apply appropriate methodologies to interpolate the input meteorological parameters, prior to processing, is critical to proper application of the predictive model. The final integration of the Ada components of the USARIEM Heat Strain Model with TWIST will provide an important capability to test and validate model sensitivity to clothing and work rate factors in the context of real-world weather and terrain.

CONCLUSIONS

We conclude that potentially significant point-to-point differences in weather effects on dismounted soldiers can occur within a 178 X 112 km coastal region, and that the integration/re-use of existing soldier performance related Ada software components with TWIST will provide a cost effective capability to quantify, depict, and ultimately exploit those differences in a tactical setting. This approach leverages prior investments in predictive model software development and documentation, improves configuration management of the thermal strain model within TWIST, and should facilitate the ultimate transition to an operational environment.

ACKNOWLEDGMENT

REFERENCES

1. Pandolf, K.B., L.A. Stroschein, L.L. Drolet, R.R. Gonzalez, and M.N. Sawka, 1986: Prediction Modeling of Physiological Responses and Human Performance in the Heat, Comput. Biol. Med., 16, 319-329.

2. Gonzalez, R.R. and L.A. Stroschein, 1991: Computer Modeling: Predicting the Soldier's Heat Transfer and Work Capabilities in MOPP. In Proceedings of the 23rd Annual Military Testing Association Conference, San Antonio, Texas.

3. SAIC, 1993: P^2NBC^2 Heat Strain Decision Aid Users Guide. Contract # DAAL02-90-C-0071, Science Applications International Corporation, Joppa, Maryland.

4. SAIC, 1993: Enhancement and Support of the P^2NBC^2 Heat Strain Decision Aid, Final Report. Contract # DAAL02-90-C-0071, Science Applications International Corporation, Joppa, Maryland.

5. Matthew, W.T. and W.R. Santee, 1991: Potential Heat Casualty Risk Assessment in Southwest Asia: Weather Data Requirements in the Spatial Domain. In Proceedings of the Eleventh Annual EOSAEL/TWI Conference, Las Cruces, New Mexico, 315-324.

6. McWilliams, G. and S. Kirby, 1990: Mercury: A System for Fusing Mesoscale Meteorological Data. In Proceedings of the Tenth Annual EOSAEL/TWI Conference, Las Cruces, New Mexico, 228-235.

7. McWilliams, G., 1992: Integrating Battlefield Weather and Terrain Data for IPB Through Automated Techniques. In Proceedings of the 1991 Battlefield Atmospherics Conference, Fort Bliss, Texas, 405-410.

8. Brown, R.C. and J.E. Harris, 1990: The United States Army's Proof-of-Concept Integrated Meteorological System. In Proceedings of the Tenth Annual EOSAEL/TWI Conference, Las Cruces, New Mexico, 228-235.

9. Lee, R.L., P. Raihl, and S. Cossio, 1992: Meteorological Observations, Interpolation, and Tactical Decision Aids. In Proceedings of the 1991 Battlefield Atmospherics Conference, Fort Bliss, Texas, 411-420.

FORECASTING CLEAR AIR TURBULENCE USING A SINGLE SOUNDING

Jeffrey E. Passner
Battlefield Environment Directorate
U.S. Army Research Laboratory
White Sands Missile Range, NM 88002-5501 USA

ABSTRACT

An effort was made to improve forecasting of clear air turbulence (CAT) in situations where weather data is restricted. A computer program was generated to predict layers of CAT based on a single sounding. The algorithm synthesizes the influences of the vector wind shear, the wind speed of the layer, and the Richardson number. Program output indicates zones and intensity of turbulence throughout the sounding. The study uses 0000 universal time coordinated data from 11 February through 15 April 1993 to "nowcast" the weather to predict turbulence. Results show that none of the methods was very useful in predicting where turbulence was occurring. Of the three methods tested, the Richardson number showed the highest skill.

1. INTRODUCTION

In recent years, the Battlefield Environment Directorate (BED) has generated numerous forecaster decision aids (FDAs) that will provide the staff weather officer (SWO) with reliable information to strengthen the effectiveness of weapons systems and troops in military conflict. Much of the information used to devise these FDAs incorporate large-scale and synoptic data reports. The large-scale data includes both surface- and upper-air data and is used to develop the FDAs.

Many times in military situations the synoptic data is not available; thus, the only obtainable data may be an upper-air sounding released locally. The upper-air skew T - log P diagram presents the temperature, moisture, wind, and heights of the atmosphere from the surface to a level typically around 50,000 ft. This diagram furnishes a vertical estimate of the main atmospheric variables and displays information that can assist in making a weather forecast.

One FDA developed by BED uses only a single-station upper-atmospheric sounding to assist the SWO in predicting weather hazards, thunderstorms, and other severe weather events that might degrade the performance of weapon systems and troops in the field. One such weather feature that might be a hazard to operations is low-level turbulence. The single sounding is used to forecast turbulence in an effort to provide guidance for Army aircraft operations.

2. METHODS OF FORECASTING TURBULENCE

Turbulence is generally a state of fluid in which there are irregular velocities and apparently random fluctuations (Glossary of Meteorology 1959). These oscillations in the atmosphere (the fluid) can adversely affect flight paths and endanger Army aircraft operations. Turbulence is present in and near thunderstorms, as can be expected, based on the dramatic updraft and downdraft speeds. Typically a thunderstorm is a warning sign that turbulence will be present and that pilots need to adjust their flight plans based on the local weather.

However, forecasting clear air turbulence (CAT) is much more difficult. Rammer (1973) related several synoptic flow patterns to observations of CAT. He noted that CAT is often found in curved jet streams associated with troughs, ridges, and upper-air lows. Ellrod and Knapp (1992) listed several mesoscale environments where significant CAT was found to be prevalent. These environments included regions of vertical wind shear, regions of horizontal wind shear, regions of wind convergence, regions of horizontal deformation, areas on the skew T - Log P diagram that displayed temperature lapse-rate discontinuities, and areas with strong horizontal thermal gradients.

Techniques to forecast CAT have usually centered on forecasting wind shear or using the gradient Richardson number (Ri). Ellrod and Knapp (1992) associated a broader physical understanding of atmospheric properties by including vertical wind shear, deformation, and convergence into a single index. Lake (1956), and more recently Black and Marroquin (1993), used efforts to calculate kinetic energy to forecast turbulence. Other forecasters simply apply certain synoptic conditions and flow patterns to the forecast of CAT.

Both theoretical studies and empirical evidence have associated CAT with Kelvin-Helmholtz (K-H) instabilities. Miles and Howard (1964) indicate that the development of K-H instabilities requires the existence of a critical $Ri < = .25$. The Ri can be expressed as a ratio of the buoyancy resistance to the energy available from the vertical shear (Keller 1990). Thus once the turbulent eddies have occurred in the stably stratified atmosphere, they can be maintained only as long as the work required to overcome the buoyancy resistance is less than that available from the shear of the layer.

Since the only data source being used in this study is a single sounding, several of the above methods are not possible to forecast turbulence. Use of a single sounding to find horizontal wind shear, areas of wind convergence, regions of horizontal deformation, and

regions of strong horizontal thermal gradients is not feasible. Based on these limitations, the approach in this study was to apply methods of using wind speed, vertical wind shear, and the gradient Richardson number. The gradient Richardson number is written as

$$Ri = (g/\theta) \left(\frac{d\theta}{dz}\right) \Big/ \left(\frac{dV}{dz}\right)^2 \qquad (1)$$

where g is the acceleration due to gravity, $d\theta/dz$ is the change of potential temperature with height, and $(dv/dz)^2$ is the vector wind shear occurring over the vertical distance.

3. DATA AND VERIFICATION

Data for this study consisted of 0000 universal time coordinated (UTC) soundings from 13 days between 18 February through 15 April 1993 at Little Rock, Arkansas; Centreville, Alabama; Jackson, Mississippi; and Nashville, Tennessee. This study used 0000 UTC sounding to "nowcast" the weather in an effort to find a technique that would be useful to forecast turbulence. Data were quality controlled by the single-station program and then examined manually to ensure accuracy. The output for each 0000 UTC sounding gave values of turbulence for each available sounding level from the surface to 400 mbar. Since Army aircraft operations and other military operations rarely involve weather conditions above 20,000 ft, there was no effort in this study to verify data in the higher levels of the troposphere.

Pilot reports for verification include reports of both turbulence levels and intensity and reports of no turbulence in the area surrounding the four soundings tested for each data set.

A contingency table was used to make conclusions about the forecasting methods since this type of statistical analysis provides a method of displaying results about YES/NO types of questions. Derived from the contingency table were a probability of detection (POD), false alarm rate (FAR), a correct nonoccurrence, a critical success index (CSI), a true skill score (TSS), and bias.

4. FORECASTING TURBULENCE USING A SINGLE SOUNDING

4.1 Empirical Method

The empirical method for forecasting turbulence was derived from AFGWC/TN-79/001 (Air Weather Service 1984). This CAT prediction is obtained from a simple chart that is a combination of the vertical wind shear and the mean wind speed for each level of the sounding. The values for this chart were coded into the sounding program and displayed in chart form. Table 1 shows the chart used to forecast CAT in this method.

Table 1. Chart Used to Forecast CAT*

Wind speed   Vector wind shear s^{-1} (knots/1000 ft)

Knots	5-7	7-10	10-20	20-30	30-50	50+
40-60	NEG	LGT	LGT-MOD	MOD	MOD-SVR	SVR
60-120	LGT	LGT-MOD	MOD	MOD-SVR	SVR	SVR-EXT
120+	LGT	LGT-MOD	MOD	MOD-SVR	SVR	EXT

*Empirically derived forecast of turbulence and intensity based on wind speed and shear. Columns are vector wind shear in knots/1000 ft. Rows are measured wind speed in knots. "NEG" indicates no turbulence, "LGT" indicates light turbulence, "MOD" indicates moderate turbulence, "SVR" indicates severe turbulence, and "EXT" indicates extreme turbulence.

Table 2 shows an example of a case using the sounding of 0000 UTC 09 March 1993 at Nashville, Tennessee. The empirical chart method was used, but pilot reports were available at only the four levels listed.

Table 2. Results for 09 March 1993 0000 UTC Turbulence Nowcast for Sounding Heights From Surface to 18,000 ft (MSL)

Height (ft)	Turbulence Forecast	Pilot Report
1008	None	
2557	None	
3000	None	MDT
4500	None	
8000	None	MDT
9841	LGT	
10000	LGT	MDT-SVR
12000	None	
13000	Light	
14000	Light	LGT-MDT
18000	None	

Results for this empirical method are shown in table 3. Based on 62 data samples, this method displays little skill in nowcasting CAT. The probability of detection was only 0.16 and the true skill score was 0.04. These values indicate that this method was not much better than a "coin flip" forecast or a "guess." In addition, this technique clearly underforecasts turbulence as seen by a bias of 0.24. Using this chart often requires that wind speeds must be greater than 40 kn for any turbulence to occur. Because of the requirements of this empirical method, this method is not of much value for forecasting turbulence in the lower and middle layers of the troposphere where wind speeds are not usually greater than 40 kn. In addition, of the 37 reported cases of turbulence, the empirical method correctly nowcasted the turbulence intensity only 5 percent of the time. The results shown in the table are based on 62 sample 0000 UTC soundings from 18 February through 15 April 1993 over the Southeastern United States.

Table 3. Results for Empirical Method of Nowcasting Turbulence

Empirical Method Results
POD = 0.16
FAR = 0.33
Correct Nonoccurrence = 0.88
CSI = 0.15
TSS = 0.04
BIAS = .24

4.2 Vertical Shear Method

The second method to forecast turbulence was to factor out the effects of vertical shear alone, where vertical shear is defined simply as the vertical gradient of wind speed. The definition of vertical shear by Harrison (1959) and George (1960) was used for the criteria for vertical shear as listed in table 4.

Table 4. Classification of Turbulence Intensities Based on Vertical Shear Alone

Vertical Shear
3-5 kn/1000 ft --- light turbulence
6-9 kn/1000 ft --- moderate turbulence
10-15 kn/1000 ft --- severe turbulence
> 15 kn/1000 ft --- extreme turbulence

All 62 soundings were tested for this method, and the results are presented in table 5.

Table 5. Results of Vertical Shear Method

<div style="text-align:center">

Results of Vertical Shear Method
POD = 0.43
FAR = 0.41
Correct nonoccurrence = 0.56
CSI = 0.33
TSS = -0.01
Bias = 0.73

</div>

The results actually show negative skill for this method when using the TSS. There is still a tendency to underforecast turbulence as well as a low probability of detection of the event. Totally, 22 percent of the turbulence intensities were nowcasted correctly. Based on these results, the effects of vertical wind shear alone are not adequate for forecasting CAT in this study.

4.3 Richardson Number Method

The final method evaluated for forecasting turbulence is calculating the Richardson number for each layer of the sounding by using equation (1). Any level where the Ri was calculated to be less than or equal to 0.25 was considered to be a level where turbulence was forecasted. An example of the output is shown in table 6.

Table 6. Richardson Number Test for Sounding of 0000 UTC 11 March 1993 at Nashville, Tennessee[*]

Height (ft)	Richardson Number	Pilot Report
600	0.48	
2000	0.09	
2500	0.33	LGT
3000	0.10	
3500	0.00	LGT
4500	1.13	
6000	1.07	
7000	2.45	
8000	2.05	
10000	2.85	NEG
12000	9.22	LGT-MDT
14000	0.27	

[*]Ri numbers $< = .25$ indicate a nowcast for turbulence. Verified pilot reports are in the right column. "NEG" indicates no turbulence, "LGT" indicates light turbulence, "MDT" indicates moderate turbulence.

In the above table, based on the Richardson number values, many of the lower levels of the atmosphere near Nashville are turbulent since the Ri $< = .25$. Above 4500 ft MSL the Ri values are above .25; thus these layers of the atmosphere are not expected to have much turbulence. Verification using pilot reports was available at only four levels during the 6-hour period from 2100 UTC to 0300 UTC. Results for the Ri method of nowcasting turbulence are shown in table 7. The results are based on 62 sample 0000 UTC soundings from 18 February through 15 April 1993 over the Southeastern United States.

Table 7. Results for the Ri Method

POD = 0.13
FAR = 0.00
Correct Nonoccurrence = 1.00
CSI = 0.13
TSS = 0.16
BIAS = .13

Results of this Ri method of turbulence nowcasting again show only very little skill. The FAR rate is 0.00; however, this may be more a result of the serious underforecasting problem as noted by the bias of .13.

CONCLUSIONS

Several methods were used to nowcast turbulence using a single-station program. Verification from actual pilot reports over the Southeastern United States were used to measure the skill of each of these methods. Results indicate that none of the methods was very useful in predicting where turbulence was occurring. In addition, the nowcasts were strongly biased towards the nonevent, which resulted in low FAR rates and high prediction rates of the nonevent. Of the three methods tested, the one applying the Richardson number showed the highest skill. This trend agrees with results derived by McCann (1993).

Based on these results, none of these methods can be applied with much confidence for Army applications below 20,000 ft. This conclusion might be expected since the tested methods of turbulence forecasting have generally been designed to work best in the higher levels of the atmosphere in the vicinity of the jet stream. In addition, this study does show that the nature of forecasting turbulence is difficult because turbulence is often a small-scale phenomenon that is short-lived and difficult to verify. Knapp and Dumais (1993) have investigated a technique to forecast turbulence by using a mesoscale model. This trend of making short-term forecasts using the predicted wind fields shows much promise in improving the skill of forecasting turbulence.

Note that the sample size for this study is relatively small and is restricted to only the Southeastern United States. Further studies will investigate the use of the sounding program over different areas and different weather environments. There will also be an attempt to forecast turbulence over a mesoscale grid using hourly plots of the wind.

ACKNOWLEDGMENTS

Thanks to Captain Dave Knapp for his beneficial advice on how to verify turbulence reports and for his efforts to produce correlation factors on the turbulence forecasts.

REFERENCES

Air Weather Service, 1984, Clear Air Turbulence Forecasting Techniques. AFGWC/TN - 79/001 (Rev).

Black, T. L., and A. Marroquin, 1993, "Preliminary Results of Turbulence Predictions for Use in Aviation Weather Forecasting," Preprint of the Fifth International Aviation Weather Systems, Vienna, VA, American Meteorological Society, Boston, MA.

Ellrod, G. P., and D. I. Knapp, 1992, "An Objective Clear-Air Turbulence Forecasting Technique: Verification and Operational Use," Weather Forecasting, 7, 150-165.

George, J. J., 1960, "A Method for the Prediction of Clear Air Turbulence," Eastern Airlines, Atlanta, GA.

Harrison, H. T., 1959, "The Use of Horizontal Shear in Forecasting High Level Clear Air Turbulence," United Airlines Meteorological Circular No. 49, Denver, Colorado.

Huschke, R. E., ed., Glossary of Meteorology, American Meteorological Society, Boston, MA.

Keller, J. L., 1990, "Clear Air Turbulence as a Response to Meso- and Synoptic-Scale Dynamic Processes," Monthly Weather Review, 118, 2228-2242.

Knapp, D. I., R. Dumais, and T. J. Smith, 1993, "Evaluation of Low-Level Turbulence Indices on a Mesoscale Grid," In Proceedings of the 1993 Battlefield Atmospherics Conference, U.S. Army Research Laboratory, White Sands Missile Range, NM.

Lake, H., 1956, "A Meteorological Analysis of Clear Air Turbulence," Geophys. Res. Pap. No. 47, Air Force Cambridge Research Center, Cambridge, MA.

McCann, D. W., 1993, "An Evaluation of Clear-Air Turbulence Indices," Preprint of the Fifth International Conference on Aviation Weather Systems, Vienna, VA, American Meteorological Society, Boston, MA.

Miles, J. W., and L. N. Howard, 1964, "Note on a Heterogeneous Shear Flow," J. Fluid Mech., 20:331-336.

Rammer, W. A., 1973, "Model Relationship of CAT to Upper Wind Flow Patterns," National Meteorological Center Aviation Weather Forecast Branch Note, 14 pp.

TWO RECENT CLIMATOLOGICAL DATA INITIATIVES AT USAFETAC

Captain Christopher A. Donahue
United States Air Force Environmental Technical Applications Center (USAFETAC)
Simulations and Techniques Branch
Scott AFB, Illinois
(618) 256-4107/DSN 576-4107/FAX x-3772

ABSTRACT

Two recent initiatives at USAFETAC are described: lightning strike climatologies and the use of Uniform Gridded Data Field (UGDF) format for climatology data. The UGDF climatologies will be used during testing of command and control systems as these systems are developed, as well as for mission planning once these systems are operational. The database of cloud-to-ground lightning strikes has proven useful for such applications as site selection for construction projects, and mission planning purposes.

1. Introduction. The United States Air Force Environmental Technical Applications Center (USAFETAC) has been working to find new applications for its world-wide climatological database. This paper describes two recent initiatives involving lightning strike climatologies and the use of Uniform Gridded Data Field (UGDF) format for climatology data.

2. Uniform Gridded Data Fields. A UGDF is simply a data set in which weather elements are arranged in a regularly spaced, gridded format. A complex set of product identification and data description "headers" are included so the data set can be ingested and displayed by interactive graphics, and command and control systems. The UGDF format was originally developed to transmit real-time weather data from Air Force Global Weather Central (AFGWC) to the Automated Weather Distribution System (AWDS) sites, but the format has been adopted for use by several other interactive weather analysis systems. USAFETAC follows this format as closely as possible, but some modifications have been necessary in order to include unique elements which are not included in the UGDF format documentation.

The data contained in USAFETAC's UGDFs are produced by two of AFGWC's models: the High Resolution Analysis System (HIRAS) and the Real Time Nephanalysis (RTNEPH). HIRAS contains data on a 2.5 X 2.5 degree grid, with values at standard levels between the surface and 10 mb. Elements available are temperature, dewpoint depression, height, U- and V-components of the wind, relative

and specific humidities, precipitable water, and vorticity. HIRAS data is interpolated to an eighth mesh grid for inclusion in the UGDFs. The RTNEPH database contains cloud base, top, type, and amount for four cloud layers, as well as present weather type, and visibility data. RTNEPH data is already in eighth mesh format, so no interpolation is necessary.

The UGDF products prepared by USAFETAC have included monthly mean values for several weather elements, as well as "best/worst" case conditions for a given area. All UGDFs provided by ETAC are for window regions which cover 65 X 65 eighth-mesh grid points. Data points are referenced by i, j coordinates, beginning with the bottom-left grid point.

Among the shortfalls of these data sets is the fact that the model output has no visibility data in regions that are far removed from surface observation sites. A second deficiency is the use of simple bilinear interpolation to achieve eighth-mesh resolution for the HIRAS output. No allowance is made for the effects that changing elevations and varying surface features have on data for the lower levels of the atmosphere. In the near future, USAFETAC hopes to develop "climate spreading" techniques that will incorporate these effects.

3. Cloud-to-Ground Lightning Climatologies. USAFETAC maintains a six year (1986-1991) data set of cloud-to-ground lightning strike information. The data set contains information on the time, latitude, longitude, polarity, and peak current of over 30 million lightning strikes across the continental U.S. The data was purchased from GeoMet Data Services (GDS) of Tucson. GDS estimates detection efficiency is 70 percent for strikes within 215 nautical miles of the detection finders. Strikes can be detected beyond 215 miles, but at a lower efficiency. Strike location accuracy depends on the distance of the strike from the detector, the number of detectors that record the strike, and the distance between detection finders. GDS estimates the accuracy is normally within 3 to 5 miles.

USAFETAC has received widespread interest in its our graphical method of displaying climatologies of cloud-to-ground lightning strike data. Using this database, personal computer (PC) programs were developed that graphically display lightning data for the area surrounding a given location, typically a 10° by 10° region surrounding an Air Force base. The software uses bar graphs and contour charts to display summarized lightning data. To create these displays, the area of interest is divided into grid boxes, each about 10 minutes per side. The lightning data is stratified by month, hour, and 700 mb wind direction, and a final data set containing the average strike count for each grid box is produced.

Figures 1 and 2 provide examples of two types of output available from the PC program developed for Eglin AFB (on the Florida panhandle). Figure 1 shows the average number of lightning strikes per hour when easterly winds are observed, for the

area shown by the grid boxes in the upper-left portion of the figure. Figure 2 shows the average number of strikes at 1900 UTC for each wind sector for the same region.

Figure 1. Average number of lightning strikes per hour for August when easterly winds are observed (for the region indicated by the grid boxes in the upper-left).
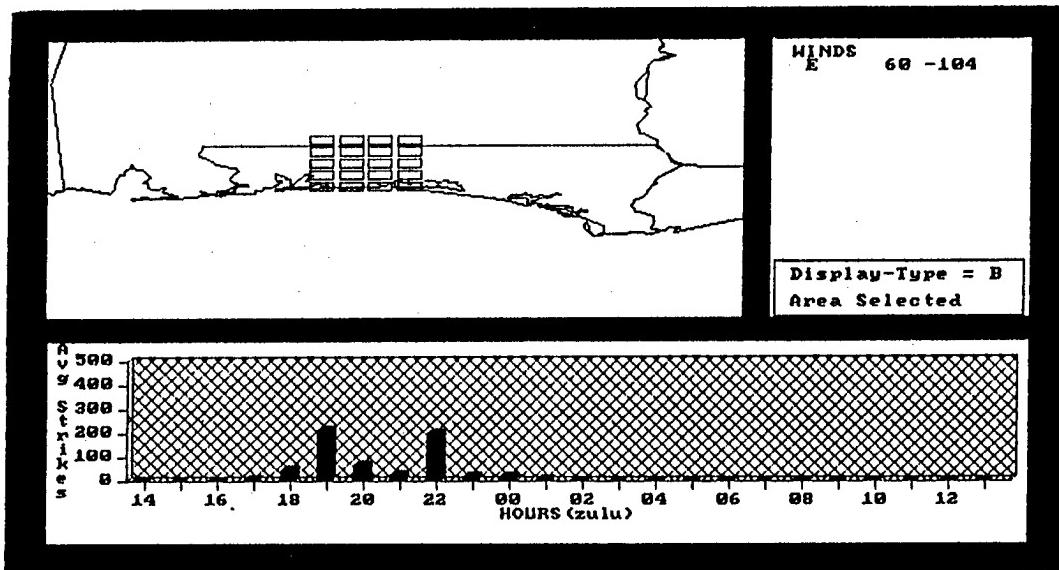
Figure 2. Average number of lightning strikes during August at 1900 UTC for each wind sector (for the region indicated by the grid boxes in the upper left).
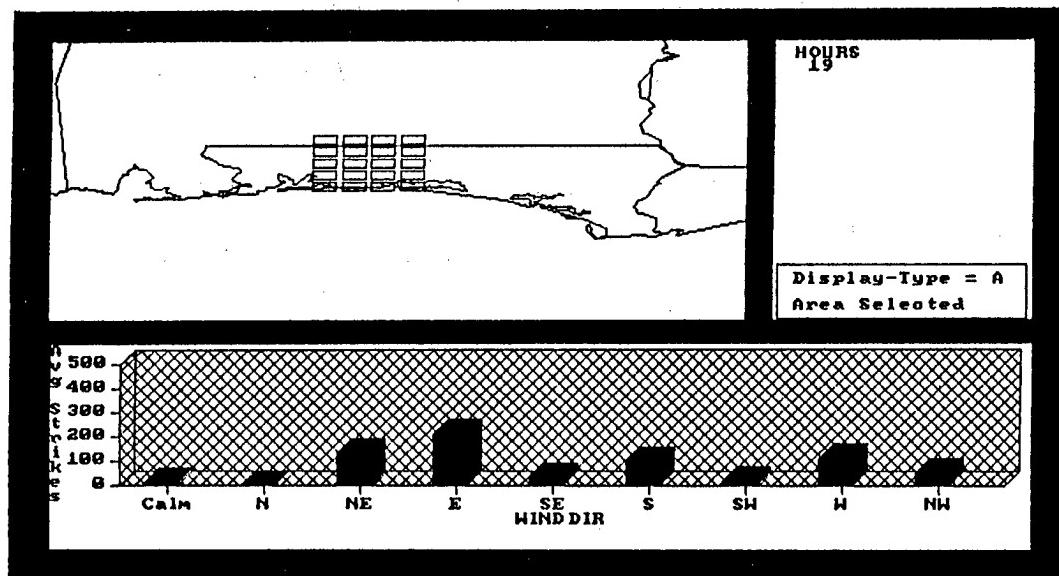
CONCLUSIONS

USAFETAC is constantly striving to support the needs of its DoD customers. Climatological UGDFs have proven useful for development and testing of command and control systems. Lightning strike climatologies can assist with site selection for construction projects. Both of these tools can be useful in many aspects of mission planning. Future initiatives will focus on the issue of "climate spreading", which will provide a better method of interpolating data to finer resolutions by incorporating the effects of changing elevations and surface features.

REFERENCES

Automated Weather Distribution System Pre-Planned Product Improvement Interface Control Document for Command and Control Systems (Draft), ESD/AVD, Hanscomb AFB MA, August 1991.

HIRAS User's Handbook No. 5, USAFETAC/UH-88/001, USAF Environmental Technical Applications Center, Scott AFB IL, October 1988.

RTNEPH, User's Handbook No. 13, USAFETAC/UH-86/001, USAF Environmental Technical Applications Center, Scott AFB IL, September 1986.

EVALUATION OF LOW-LEVEL TURBULENCE INDICES
ON A MESOSCALE GRID

Captain David I. Knapp and MSgt Timothy J. Smith
Operating Location N, Headquarters Air Weather Service

Robert Dumais
U.S. Army Research Laboratory
White Sands Missile Range, NM 88002-5501

ABSTRACT

Three objective upper-level clear air turbulence indices were studied in lower levels to determine their effectiveness for determining areas of low-level turbulence. Mesoscale model grid point values of Turbulent Kinetic Energy and the gradient Richardson Number were compared to turbulence reports. Correlation coefficients derived for these indices from comparisons with corresponding turbulence intensity reports were well below .20. The Turbulence Index, the vertical wind shear multiplied by the sum of horizontal deformation and convergence, was also evaluated and found to produce correlation coefficients greater than .60 for levels below 7000 feet above ground level.

The Turbulence Index was further examined as a simple yes/no turbulence indicator. The Probability of Detection for the index was .63 for all levels below 14,000 feet above ground level, with a corresponding False Alarm Ratio of .18. Case studies led to dividing the Turbulence Index into independent terms to determine the most significant terms at different levels. High correlation coefficients led to developing an improved index. This Regression Turbulence Index produced correlation coefficients which outperformed the Turbulence Index and each of its separately treated independent terms.

1. INTRODUCTION

The U.S. Army depends on accurate low-level turbulence analyses and forecasts for its aviation missions. New advancements in the use of "smart" munitions and unmanned aerial vehicles sensitive to turbulence make these forecasts even more important to mission accomplishment. Unfortunately, the science of identifying and forecasting low-level turbulence has advanced slowly. Forecasters generally rely on empirical low-level turbulence forecast rules that have been used for years, resulting in the habit of consistently underforecasting or

overforecasting suspected turbulence areas.

Objective turbulence indices have been developed in an attempt to depict areas of upper level turbulence. The gradient Richardson number (Ri) has been shown to accurately indicate the development of Kelvin-Helmholtz instabilities and turbulence occurrence when values of Ri are less than or equal to .25 (Miles and Howard, 1964). Marroquin and Nickerson (1993) summarize the findings of other work which reveal that turbulence can exist for values of Ri greater than 2.0.

Turbulent Kinetic Energy (TKE) has been examined as a possible indicator of atmospheric instability and turbulence occurrence by Lake (1956). More recent case studies using high resolution model data completed by Marroquin and Nickerson (1993) and Black and Marroquin (1993) further enhance TKE's potential use as a turbulence forecasting tool. Cases investigated included such phenomena as turbulence in the vicinity of breaking gravity waves and upper-tropospheric jet-front systems.

Upper-level instabilities can also be approximated using the components of Petterssen's (1956) frontogenesis equation. Mancuso and Endlich (1966) found that the deformation and vertical wind shear components of this equation were independently correlated with the frequency of moderate or severe turbulence. Ellrod and Knapp (1992) went further by deriving a turbulence index (TI) based on certain assumptions to Petterssen's equation. Assuming that frontogenesis results in an increase in vertical wind shear (VWS), horizontal deformation (DEF), and horizontal convergence (CVG), a similar increase in turbulence occurrence should also be expected. For a given layer, the index is simply stated as:

$$TI = VWS \times (DEF + CVG), \qquad (1)$$

where

$$VWS = \frac{\sqrt{\Delta u^2 + \Delta v^2}}{\Delta z} \qquad (2)$$

$$DEF = \sqrt{(\partial u / \partial x - \partial v / \partial y)^2 + (\partial v / \partial x + \partial u / \partial y)^2} \qquad (3)$$

$$CVG = -(\partial u / \partial x + \partial v / \partial y) \qquad (4)$$

The range of TI values associated with turbulence occurrence were found to be model-dependent (Ellrod and Knapp, 1992) based on grid resolution and other physical and dynamic parameter calculations unique to every model. Typical TI values ranged from 1.0 to 12.0 $(x10^{-7}s^{-2})$.

At levels below upper-level jet stream maxima, Ellrod and Knapp found the TI's performance to be unreliable. This was attributed to coarse synoptic scale model grid-point resolution that missed the more subtle features in low-level wind fields contributing to turbulence occurrence. The resolution problem is solved by deriving the TI from mesoscale model grid data. Comparisons of Ri and TKE calculations to the TI using this same high resolution data would be useful.

At the Army Research Laboratory (White Sands Missile Range, NM), these three upper-level turbulence indices are being applied to levels below 14,000 ft above ground level (AGL). This study is designed to find the most accurate objective low-level turbulence forecast technique for future use by Air Force Staff Weather Officers supporting the U.S. Army.

2. MODEL AND TURBULENCE TECHNIQUE DESCRIPTIONS:

The Higher Order Turbulence Model for Atmospheric Circulations (HOTMAC) was used to provide a mesoscale nowcast analysis of meteorological variables using observed upper-air and surface data reported at rawinsonde locations. This analysis is produced by horizontally interpolating observed rawinsonde wind data onto the mesoscale grid with a resolution of 20 km. In the vertical, wind observations are interpolated to predefined levels. Utilizing a transformation to a terrain-following vertical coordinate system, 22 staggered levels are retained to allow for high resolution (Yamada and Bunker, 1989), with eight levels within the first 1000 feet AGL, five levels from 1,000-5,000 feet AGL, and eight levels from 5,000-16,000 feet AGL. (NOTE: Hereafter, levels AGL will be in hundreds of feet, i.e., 010-050, 050-160, etc.) Rawinsonde data reported from 00 UTC provide the raw input to the mesoscale objective analysis for this study.

HOTMAC automatically calculates TKE and Ri values at every grid point for each model level. TKE values are calculated from the Mellor-Yamada second order turbulence closure scheme as described by Black and Marroquin (1993). The TKE and Ri values are then interpolated to the base and top of each user-prescribed layer, and a layer average is calculated for each horizontal grid point. The TI is calculated from HOTMAC's u and v wind components at each grid point in the horizontal and vertical. As for TKE and Ri calculations, layer average values of VWS, DEF, and CVG are used for the final TI calculation at every grid point for each prescribed layer.

3. TECHNIQUE VERIFICATION

The turbulence techniques have been tested using data in the Huntsville AL mesoscale region for twenty 00 UTC cases during February, March, and April 1993. Point verification was used to verify the effectiveness of each technique using pilot reports (PIREPs) from 22 UTC to 02 UTC for each case studied. PIREP data included reports of turbulence level(s) and intensity, as well as reports of no turbulence for each case. (NOTE: If a PIREP did not contain any turbulence remarks, it was not counted as a valid report) A program was written to extract values for each technique at the grid point closest to each verifying report. Turbulence reports in the vicinity of thunderstorms were not included in the verification process. Data from the National Lightning Detection Network were used to filter out these reports in or near active cloud-to-ground lightning strikes during the times studied.

Turbulence reports were assigned numerical values based on intensity to establish correlation coefficients when compared to grid point output from each of the techniques. Intensities and corresponding numerical values were assigned as follows:

       0 = no turbulence
       1 = light
       2 = light-moderate
       3 = moderate
       4 = moderate-severe
       5 = severe
       6 = severe-extreme
       7 = extreme

Verification results indicated that correlation coefficients for TKE and Ri values were much less than .20, generally too low to be of any significance. These results are similar to those of Marroquin, et. al. (1992), who found that these indices are generally very small from the top of the boundary layer to just below the levels of upper-level jet stream maxima. They explain that this is due to the mixing length in HOTMAC's Mellor-Yamada formulation being set to a constant above the boundary layer. Additionally, the poor performance of TKE and Ri may be due to HOTMAC's vertical resolution being insufficient to resolve the conditions contributing to TKE and Ri values indicative of turbulence in shallow low- and mid-level layers. For this study, the vertical resolution was set at 22 levels for efficient computational speed when the model was run. Where the Ri and TKE fail to be useful predictors of low-level turbulence, however, the TI was found to be accurate up to 070. Correlation coefficients were .69 for the 010 to 040 layer (29 PIREPs) and .63 from 040 to 070 (22 PIREPs).

To further examine the accuracy of the TI, statistics were calculated to determine its effectiveness as a simple yes/no indicator of turbulence occurrence. Probability of Detection (POD), False Alarm Rate (FAR) and the True Skill Statistic (TSS) or Hanssen-Kuipers' Determinant were calculated for each layer studied and for all layers combined. Once again, point verification was used as described above. If the TI at the grid point closest to a pilot report was found to be at least 1.0 $(x10^{-8}s^{-2})$, then turbulence would be expected. Results are summarized in Table 1 and show that the TI is most accurate from 010 to 040, with a gradual reduction in accuracy in higher layers to 100. Above 100, however, the TI is unreliable. This drop in accuracy with height is due to HOTMAC's high lower-level vertical resolution which drops off significantly above 040. We can safely assume that if the same resolution were used above this level, verification statistics would remain roughly the same as in the lowest levels.

4. TI CASE STUDY

A significant low-level turbulence event in the Huntsville AL, region occurred during the 00 UTC 16 Feb 1993 verification period. Four reports of moderate to extreme turbulence from 010 to 040 were reported ahead of an approaching winter storm system. The synoptic features at 00 UTC and the 00 UTC RAOB locations used to derive the mesoscale wind fields are presented in Fig 1. Derived TI contours, grid-point values, and verifying PIREPs from 010 to 040 show that three of the four reports in this layer fell in or near the highest TI values (Fig 2).

The 010 wind field at each model grid point is plotted in Fig 3, with corresponding pilot reports transposed from Fig 2 for reference. A well-defined cyclone center is located just to the west of the extreme turbulence report in northern Mississippi (Figs 2 and 3). The moderate-severe report in northeastern Alabama occurs just to the south of a confluent axis near the Alabama-Tennessee border. At 040, the extreme turbulence report lies along a well-defined trough axis with rapid horizontal shearing in a line bisecting the report location from west to east (Figs 2 and 4). Note the significant vertical wind shearing at this point from Fig 3 to Fig 4, as well as at the location of moderate-severe turbulence in northeastern Alabama.

Grid point values and contours of VWS and DEF+CVG are presented in Figures 5 and 6, respectively. The extreme turbulence report in northern Mississippi is located in an area of relatively low VWS along an axis of high DEF+CVG, whereas the moderate-severe report in northeastern Alabama falls in a relatively higher area of VWS along an axis of moderate DEF+CVG.

5. AN IMPROVED TURBULENCE INDEX

In the case study presented, the turbulence reports occurred in regions of varied VWS and DEF+CVG. No distinctive pattern from either term could be consistently seen as dominating the other. Based on this case, and on the 19 other cases examined for the Huntsville mesoscale region, correlation coefficients were calculated for the TI and independently for each of its terms (VWS and DEF+CVG). These coefficients are summarized in Table 2. In lower levels, DEF+CVG correlated better with turbulence intensity than did VWS. However, this trend was reversed in layers above 070.

Further comparisons of the correlation coefficients for the TI's two independent terms with the complete TI equation led to other interesting findings. Considering all layers combined, the TI had the highest correlation coefficient. Yet when breaking accuracy down into the layers studied, DEF+CVG was highest from 010 to 040, and VWS highest above 070.

The TI's two terms were treated as independent variables and combined into one regression equation, based on the strength of each term's individual correlation coefficients compared with the TI's. The results indicate a potentially new and more accurate turbulence tool than either the TI or its independent terms treated separately. The new Regression TI (RTI) is simply:

$$RTI = A(VWS) + B(DEF+CVG) + C \qquad (5)$$

where A and B are the regression coefficients for each of the independent variables, and C is the regression constant. Correlation coefficients for the RTI are the highest of any of the other techniques studied, peaking at .73 from 010 to 040, with values of .39 and .54 from 070 to 100 and 100 to 140, respectively (Table 2).

McCann (1993) studied numerous turbulence techniques and determined correlation coefficients for upper-level data objectively interpolated in 50mb increment levels. Correlation coefficients relating these techniques to turbulence intensity were most significant for lnRi and TI (without the convergence term) with values of -0.346 and 0.219, respectively. McCann used lnRi to show the details of high turbulence potential/low Ri environments. Note that these values are for upper-level data where jet stream maxima are generally well defined, and the vertical dynamics leading to turbulence occurrence are much easier to detect than in the lower levels. Comparing McCann's upper-level coefficients to those in lower levels (Table 2) clearly show the improved objective index accuracy when using mesoscale model grid data.

Using data solely from the 20 cases in the Huntsville region, the new index would be:

$$RTI = .0434(VWS) + .0276(DEF+CVG) + .3070 \qquad (6)$$

VWS and DEF+CVG input values are in units as depicted in Figs 5 and 6, respectively. The output, RTI, corresponds to expected turbulence intensity on a scale of 0-7 as previously described.

6. CONCLUSIONS

Three previously validated upper-level aircraft turbulence detection tools were studied using mesoscale model gridded analysis data in an effort to find a useful objective low-level index for use by military forecasters. The Ri, TKE, and TI were examined using data from 20 cases in a mesoscale region surrounding Huntsville, AL. Correlation coefficients relating reported turbulence intensity to grid point values for each of these techniques show that the TI far outperforms the Ri and TKE in lower levels. The TI was further studied to determine grid point accuracy for simple yes/no turbulence nowcasts. High probabilities of detection and low false alarm rates from 010-070 prove the usefulness of this index using high resolution model grid point data.

A TI case study examining the specific contributions of each term of the TI was accomplished. Turbulence occurrence and intensity for each pilot report were independently correlated with each term of the TI, as well as with the TI as a whole. DEF+CVG outperformed VWS below 070, with the opposite holding true above 070. Finally, a new multi-variable linear regression version of the TI, or RTI, was studied and compared to the TI and its independent terms. The RTI's correlation coefficients for turbulence intensity were better than any of the other turbulence indicators studied. This new index will be further studied using mesoscale data from regions centered on Chicago IL and Denver CO. With positive results, the RTI can then be implemented as an accurate objective low-level turbulence indicator for use with mesoscale data.

TABLE 1. TI Verification Statistics.

LAYER	POD	FAR	TSS
ALL	.63	.18	.40
010-040	.73	.06	.59
040-070	.62	.20	.40
070-100	.57	.11	.43
100-140	.33	.75	-.10

(For simple yes/no turbulence expectation: If $TI > = 1 \times 10^{-8} s^{-2}$, expect turbulence).

TABLE 2: Correlation Coefficients.

Layer	ALL	010-040	040-070	070-100	100-140
# of PIREPs	82	29	22	21	10
TI	.59	.69	.63	.05	.00
VWS	.47	.34	.52	.38	.50
DEF + CVG	.57	.72	.62	.02	.25
RTI	.63	.73	.68	.39	.54

Layer altitudes are in hundreds of feet AGL. 010-040 represents the layer from 1000-4000 feet AGL.
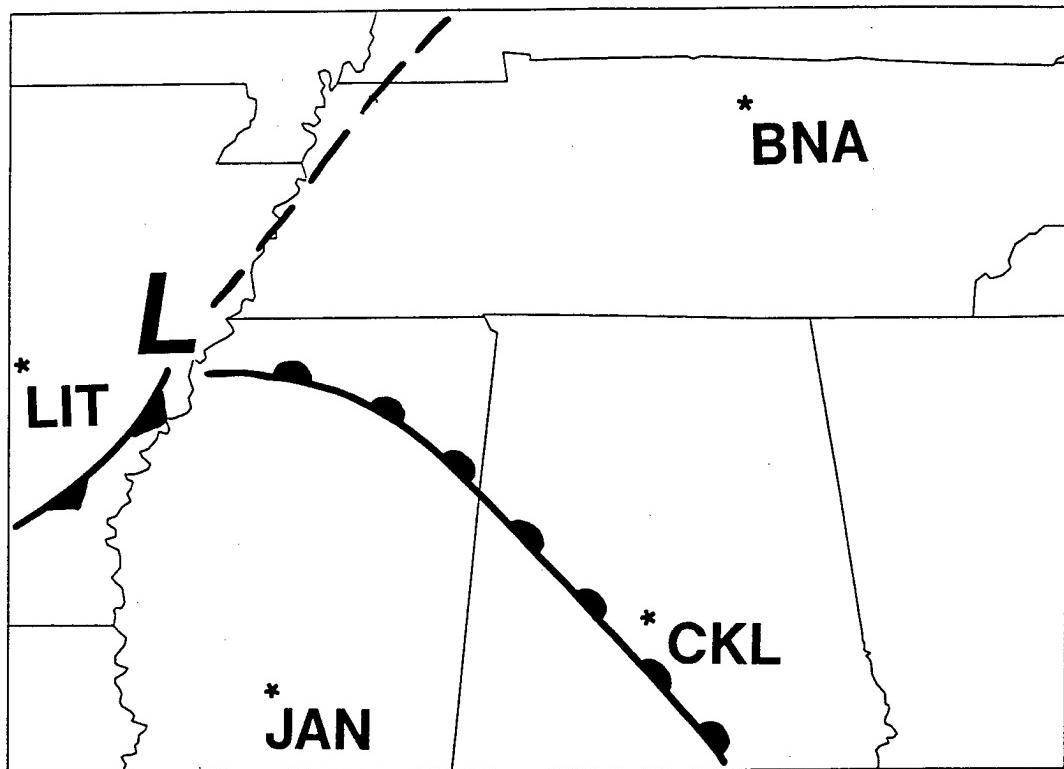
Figure 1. Huntsville, AL, mesoscale region with 16 Feb 1993 00 UTC synoptic features and RAOB locations (*) used to derive HOTMAC gridded wind fields.
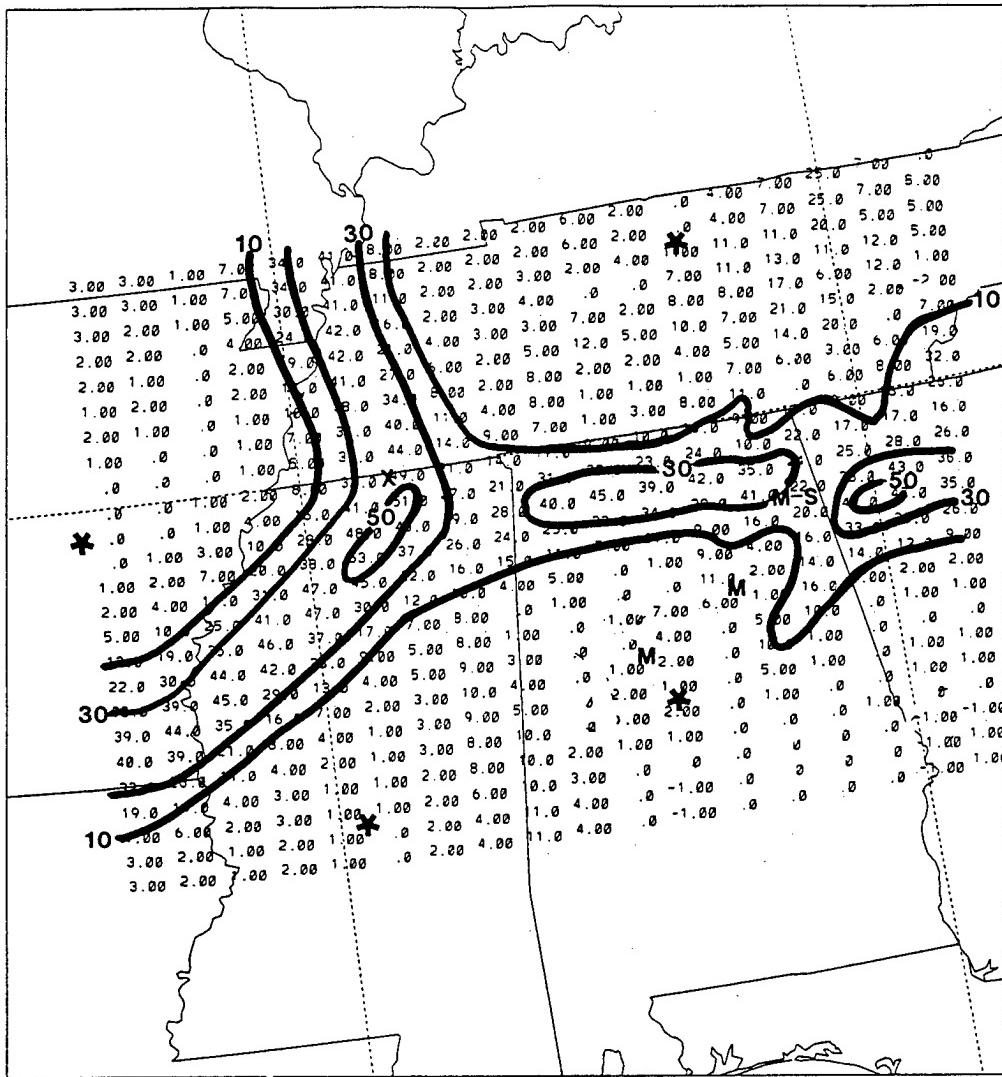
Figure 2.   TI grid point values and contours for the 1000-4000 foot layer (in units of $10^{-8}s^{-2}$) at 00 UTC 16 Feb 1993.   Turbulence reports in this layer were reported from 15 Feb 22 UTC to 16 Feb 02 UTC and are indicated by intensity (M=Moderate, M-S=Moderate-Severe, and X=Extreme).   RAOB data locations are also indicated (*).
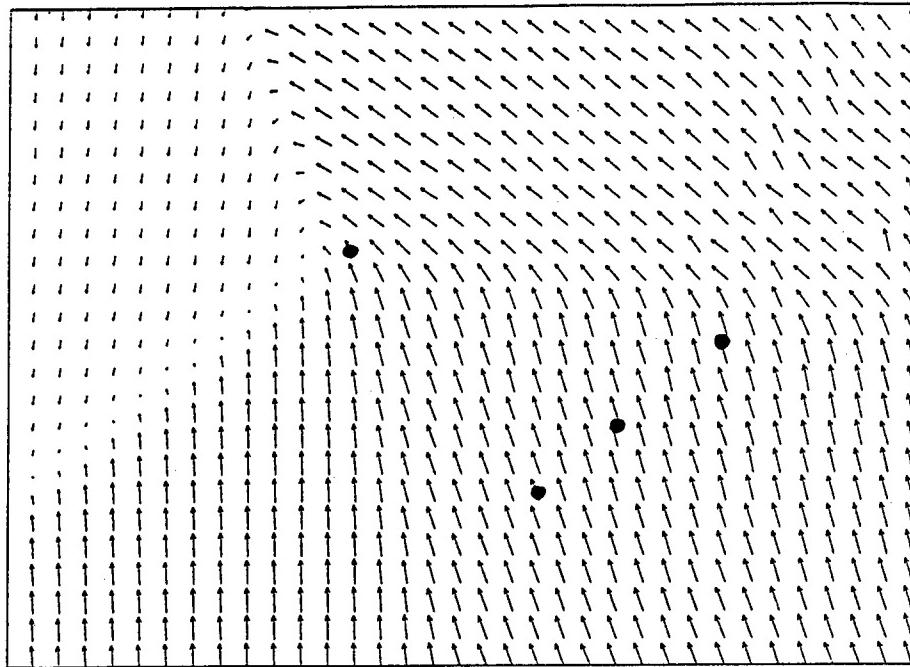
Figure 3. HOTMAC grid point wind vectors at 1000 ft AGL, 00 UTC 16 Feb 1993. Dots indicate pilot reports as depicted in Fig 2.
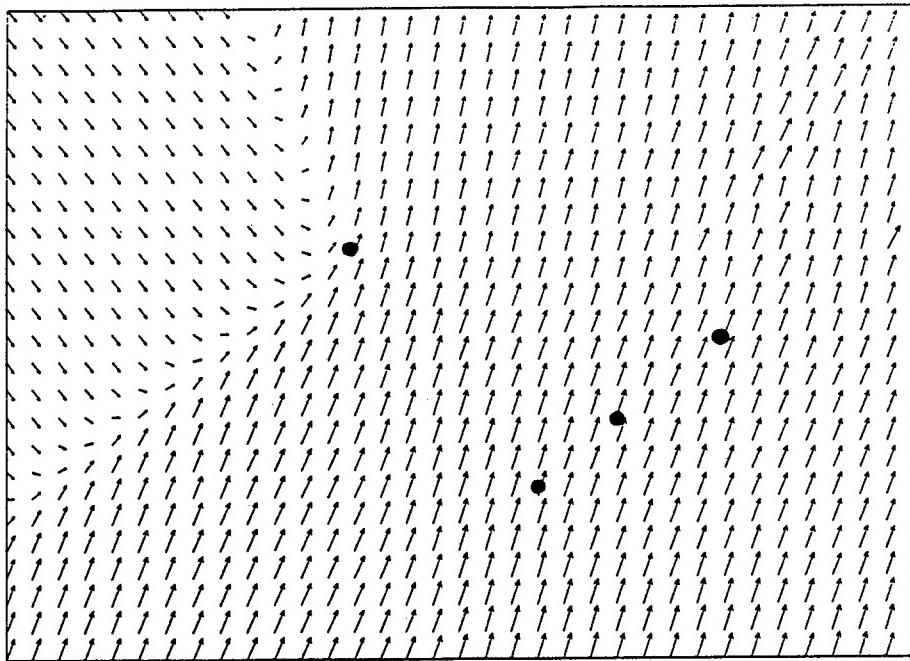
Figure 4. Same as Fig 3, for the level at 4000 ft AGL.
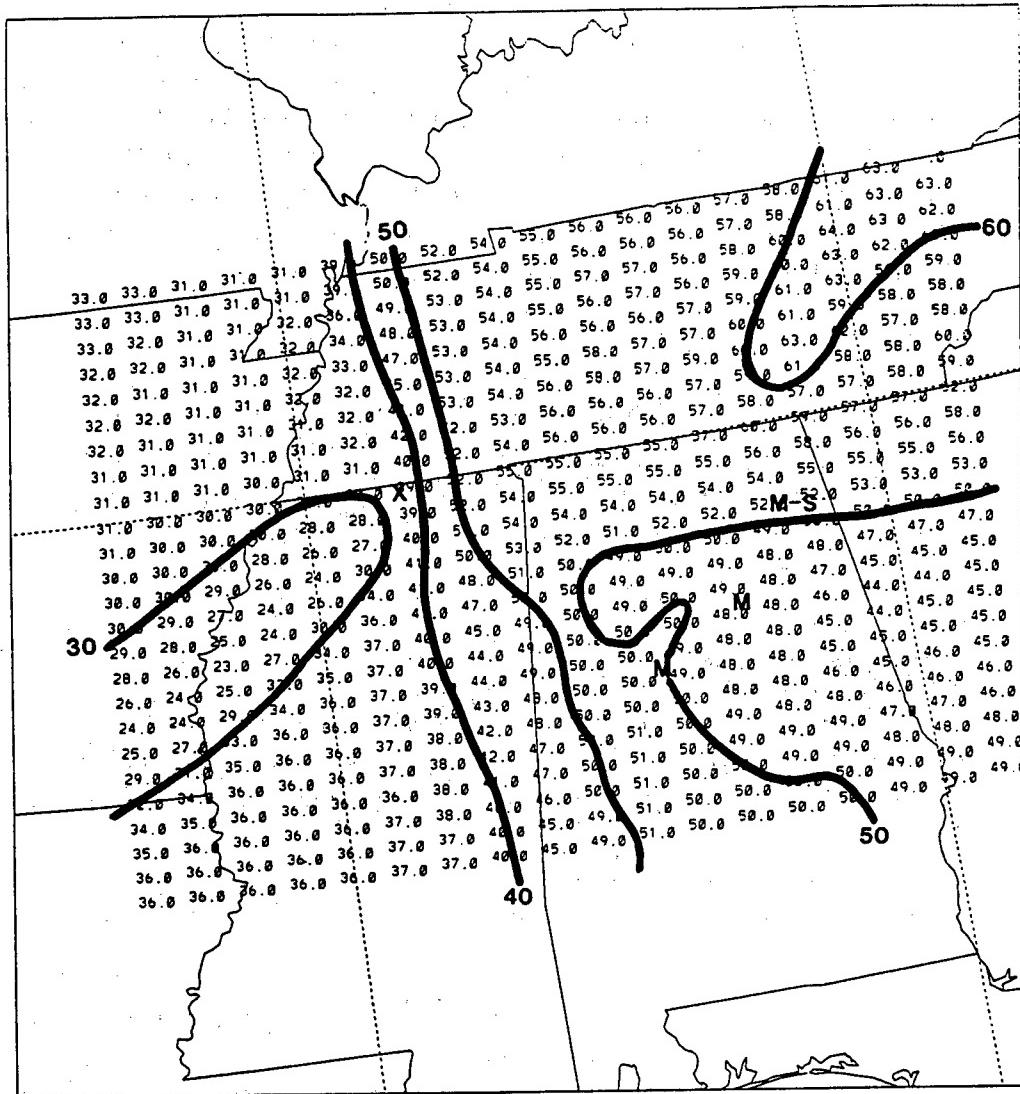
Figure 5. VWS grid point values and contours (in units of $10^{-4}s^{-1}$). Valid time, layer, and PIREPs are the same as in Fig 2.
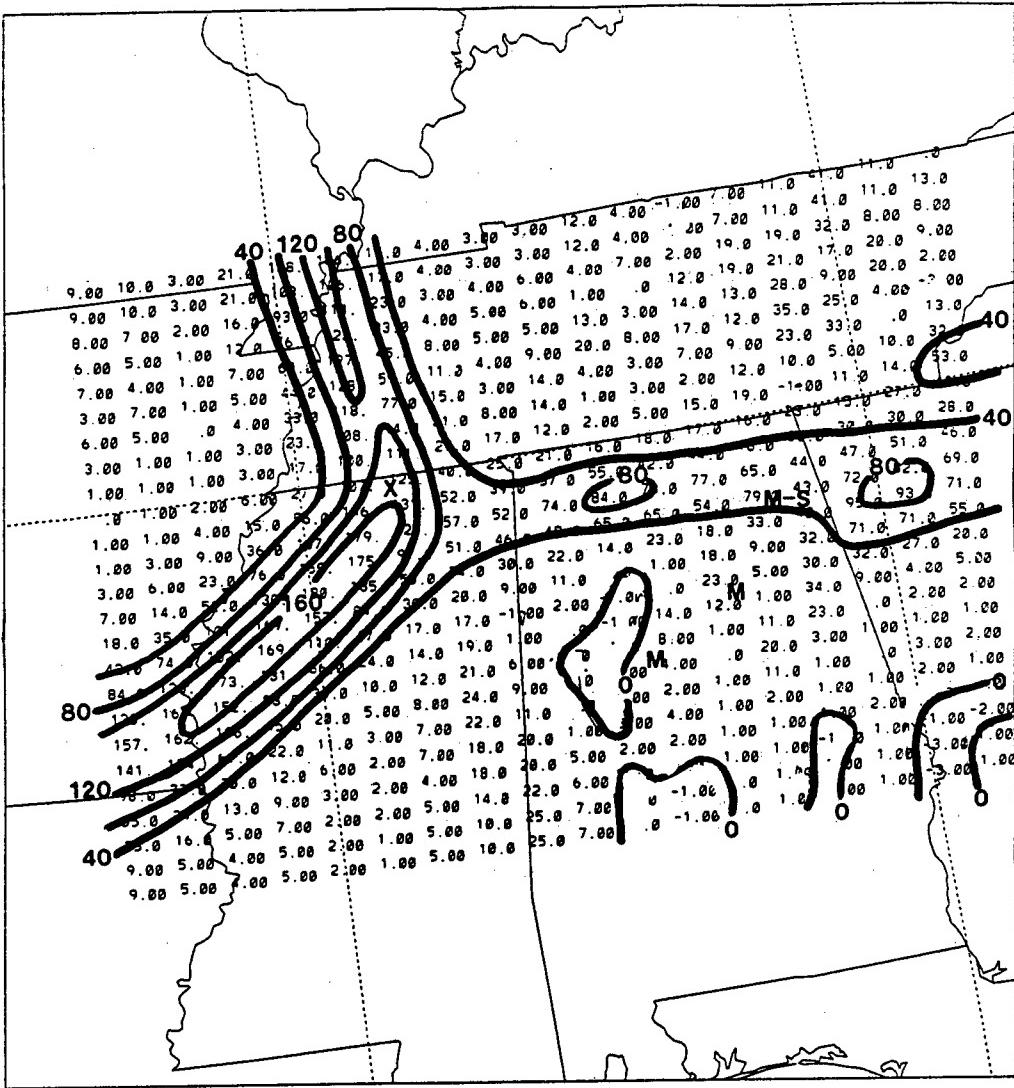
Figure 6. DEF+CVG grid point values and contours (in units of $10^{-3}s^{-1}$). Valid time, layer, and PIREPs are the same as in Fig 2.

REFERENCES

Black, T.L., and A. Marroquin, 1993: Preliminary results of turbulence predictions for use in aviation weather forecasting. *5th International Conference on Aviation Weather Systems*, Vienna, Virginia, Amer. Meteor. Soc., 461-462.

Ellrod, G.P., and D.I. Knapp, 1992: An objective clear-air turbulence forecasting technique: Verification and operational use. *Wea. Forecasting*, **7**, 150-165.

Lake, H., 1956: A meteorological analysis of clear air turbulence. *Geophys. Res. Pap. No. 47*, Air Force Cambridge Research Center, 63 pp.

Mancuso, R.L., and R.M. Endlich, 1966: Clear air turbulence frequencies as a function of wind shear and deformation. *Mon. Wea. Rev.*, **94**, 581-585.

Marroquin, A., G.K. Greenhut, B. Jamison, J.L. Mahoney, B.Schwartz, and C. M.I.R. Girz, 1992: Modeling and forecasting clear air turbulence using a mesoscale numerical model. *10th Symposium on Turbulence and Diffusion*, Portland, Oregon, Amer. Meteor. Soc., 346-349.

Marroquin, A., and E. Nickerson, 1993: Testing of TKE parameterizations in numerical models for clear-air turbulence forecasting. *5th International Conference on Aviation Weather Systems*, Vienna, Virginia, Amer. Meteor. Soc., 308-312.

McCann, D.W., 1993: An evaluation of clear-air turbulence indices. *5th International Conference on Aviation Weather Systems*, Vienna, Virginia, Amer. Meteor. Soc., 449-453.

Miles, J.W., and L.N. Howard, 1964: Note on a heterogeneous shear flow. *J. Fluid Mech.*, **20**, 331-336.

Petterssen, S., 1956: *Weather Analysis and Forecasting, Vol 1*. McGraw-Hill Book Co., 428 pp.

Yamada, T., and S. Bunker, 1989: A numerical model study of nocturnal drainage flows with strong wind and temperature gradients. *J. Appl. Meteor.*, **28**, 545-553.

DEVELOPMENT OF RULE-BASED TECHNIQUES FOR THE

MANAGEMENT OF METEOROLOGICAL MESSAGE DISSEMINATION

IN THE COMPUTER-ASSISTED ARTILLERY METEOROLOGY SYSTEM

Arthur W. Dudenhoeffer and Donald D. Bustamante
Physical Science Laboratory
New Mexico State University
Las Cruces, New Mexico 88003-0002

ABSTRACT

The Computer-Assisted Artillery Meteorology (CAAM) System, which is under development for the U. S. Army Research Laboratory, will employ rule-based computer techniques that assist in the management of artillery Meteorological (MET) Message Dissemination. In the CAAM System the battlefield area of operations is divided into sectors. For a given sector the rule-based techniques yield a recommendation on whether a newly generated computer MET message (MET-CM) should be disseminated. The rules are based on the sensitivity of projectile trajectories to changes in MET parameters from one message to the next. This paper discusses the development of the rule base for MET message dissemination. The role of firing tables and computer simulations in the analysis of trajectory sensitivity is addressed. Nominal firing scenarios are investigated for representative weapon systems.

1. INTRODUCTION

The Computer-Assisted Artillery Meteorology (CAAM) Phase II project is a technology demonstration effort for the purpose of demonstrating anticipated improvements in long-range artillery accuracy through integration of various aspects of battlefield meteorology. These aspects include meteorological (MET) databases, modeling, MET message generation and dissemination functions, executive and user interfaces, displays and communications interfaces (Seagraves et al., 1992).

The primary functions of the CAAM system include the following (Spalding et al., 1993): ingest and manage MET data from upper air measurements; process MET data through a three dimensional objective analysis and a mesoscale forecast model, the High Order Turbulence Model for Atmospheric Circulation (HOTMAC); use the results to generate a "best" MET message; determine whether the message should be disseminated to the Fire Direction Center; and provide a user interface and executive driver for control of the system. This paper discusses the development of the Computer Software Component (CSC) involving MET Message

Dissemination.

The management function of MET Message Dissemination involves making a recommendation on whether a newly generated MET message should be disseminated to supplant a previously disseminated message. Two broad approaches are feasible here: (1) recommend dissemination of every new message because it contains the most up-to-date information available; (2) recommend dissemination of a new message only if it is "sufficiently different" from the previous message, so that lack of it would degrade artillery accuracy. The purpose of the second approach is to help alleviate the anticipated high density of communications traffic on the battlefield. This approach requires the establishment of difference criteria on which the recommendation can be based.

Rule-based techniques will be used in arriving at a dissemination recommendation consistent with the second approach noted above. The rules should incorporate information on the sensitivity of artillery trajectories to changes in MET from a previously disseminated message to a new message.

2. RULE-BASED TECHNIQUES

A rule-based system (RBS) is a computer application program that utilizes inferencing procedures in conjunction with specific expert knowledge in order to solve problems in a particular domain of interest. The domain knowledge resides in the rule base (or knowledge base), which is an organized assembly of facts and production rules. The most basic representation of a production rule is the condition-action pair of clauses:

    IF [condition] THEN [action].

More generally the IF-clause may contain multiple conditions and the THEN-clause multiple actions. Depending on the inferencing tools used, an ELSE-clause may also be possible. The rule base may utilize information and data from various sources.

Superficially the structure of rules in an RBS resembles the structure of conditional statements in conventional programming languages such as Ada or Fortran. For software written in conventional languages, the programmer must pay close attention to the placement of the action branches of conditional statements; the program determines the sequence in which the branches are accessed. In an RBS the rules may be placed in any order. The activation of any particular rule depends on (among other things) its content, not necessarily its location in the rule base. Thus a rule may conveniently be added to or removed from the rule base in any order, so long as its interactions with other rules are considered.

The overall execution of an RBS is governed by one of two fundamental control strategies: backward chaining or forward chaining. In backward chaining the truth of one or more goals defined in the action clauses of particular rules is assumed. The system then attempts to establish the truth of the condition clauses by invoking other pertinent rules. This process chains backward until facts or previous results eventually provide support or non-support for the goals. While backward chaining is goal driven, forward chaining is data driven. In forward chaining,

data or other knowledge are matched with rule condition clauses to determine rule applicability. The actions of applicable rules are then matched with the conditions of other rules. This process continues until one or more goals or conclusions are reached or until all relevant rules are exhausted.

An RBS is one type of knowledge-based or expert system. The development and maintenance of such systems can be facilitated through the use of an Expert System Development Tool (ESDT). A typical ESDT contains a user interface and an inference engine that is independent of the actual knowledge on which it operates. Harmon et al. (1988) and Bustamante and Dudenhoeffer (1990) contain useful information on various commercial ESDTs.

The ESDT proposed for use with the Met Message Dissemination CSC is the Ada version of the C Language Integrated Production System (CLIPS). CLIPS was originally developed for the National Aeronautics and Space Administration (NASA) Software Technology Branch, Lyndon B. Johnson Space Center, Houston, and is available for use on government contracts. The basic control strategy used in CLIPS is forward chaining. Additional information is available in the product manual (Giarratano, 1991).

3. SECTOR DEFINITION

The CAAM project defines a rectangular battlefield Area of Operations (AOP) that is 220 km deep by 60 km wide. The AOP may be oriented an any azimuth and is situated such that the Forward Line of Troops (FLOT) is located 20 km forward of the rear of the AOP. Artillery fire is directed from the area behind the FLOT toward targets located forward of the FLOT.

A sector of the AOP is defined by the locations of a gun area and a target area. In general a gun area location refers to some mean position of a grouping of artillery pieces, not the precise location of a single weapon. Likewise the target area location generally refers to a grouping of targets, not necessarily an individual target. The system operator enters the locations as latitudes and longitudes. From these coordinates a range and an azimuth can be established for the sector.

Each sector is defined dynamically. As battle conditions change, old sectors may be eliminated and new ones established. The CAAM system can accommodate a maximum of six sectors to be defined at any one time.

For each defined sector CAAM generates a Target Area Low-Level MET Message (MET-TALL) and a Computer MET Message (MET-CM). MET Message Dissemination uses only the MET-CM, which is generated for the mid-range point of the sector. The header of this message specifies location, surface elevation, date, time, and other information. The body of the message contains MET data for 27 atmospheric zones, numbered 0 (surface) through 26 (20000 m above the surface). Values of the following MET parameters are given for each zone: wind direction (Army mils); wind speed (knots); temperature (K); pressure (mb). Detailed information on the zone structure and the MET-CM message is given in Technical Manual TM-11-7440-241-10-5 (1990).

As far as CAAM is concerned, there is no restriction on the types of weapons associated with a given sector. In fact the CAAM system is not informed of the actual weapons that are in use. Consequently the Met Message Dissemination CSC is based on the use of predetermined weapon systems.

4. TRAJECTORY CONSIDERATIONS

Trajectory is dependent on (among other things) the properties of the projectile and the charge used in firing it. The CAAM system does not receive information on the specific weapons that are deployed for a particular sector. Therefore it is proposed that MET Message Dissemination consider several representative weapons systems currently in use, including: 155 mm Howitzer Rocket-Assisted Projectile (RAP) with M549A1 (7R and 8R charges); 155 mm Howitzer Base Burn with M864 (7R and 8R charges); and the Multiple Launch Rocket System (MLRS). The maximum range for these systems is approximately 30 km. Both low-angle and high-angle fire may be considered where appropriate.

For a given range, the trajectory of a projectile is influenced by both MET (as contained in the MET message) and non-MET factors (such as rotation of the earth). MET Message Dissemination concentrates on the effect of the change in MET from one message to the next. Unlike the MET factors, which may undergo continual change, non-MET factors like earth rotation remain constant for a given sector.

In determining MET effects, the information in a MET-CM message is not used directly in its raw form. The following transformations need to be carried out for each zone. The wind direction and speed are decomposed into range wind (parallel to the firing azimuth) and cross wind (perpendicular to the firing azimuth). Atmospheric density is computed from temperature and pressure using the Ideal Gas Law. Also, for temperature and density, percentage departures from the International Civil Aviation Organization (ICAO) Standard Atmosphere values are found. Range effects due to MET are dependent on range wind and temperature and density departures from the ICAO Standard Atmosphere. Deflection effects due to MET are dependent on cross wind.

The zonal sensitivity of range and deflection effects to individual MET parameters can be determined from computer simulations. For a given range the parameter of interest is changed from a standard value in a particular zone, while standard values are maintained in the other zones. The simulator then computes a new range and deflection. The changes in range and deflection from the standard case can then be determined. Figure 1 shows several range-wind zonal sensitivities determined in this manner for a 155 mm Base Burn Projectile for a range of 25 km. The slope of each line (in units of m/knot) is the first-order sensitivity (or unit effect) for the for the particular zone under consideration. The GTRAJ3 simulator (BRL GTRAJ3, 1991) was used to produce the results shown in the figure.

Tabular firing data (Firing Table FT-155-AO-0, 1978; Firing Table FT-155-AU-PAD, 1989) for the 155 mm Howitzer contain MET effects for a variety of ranges (up to approximately 30 km) and charges. In particular, unit effects for range wind, cross wind, and temperature and
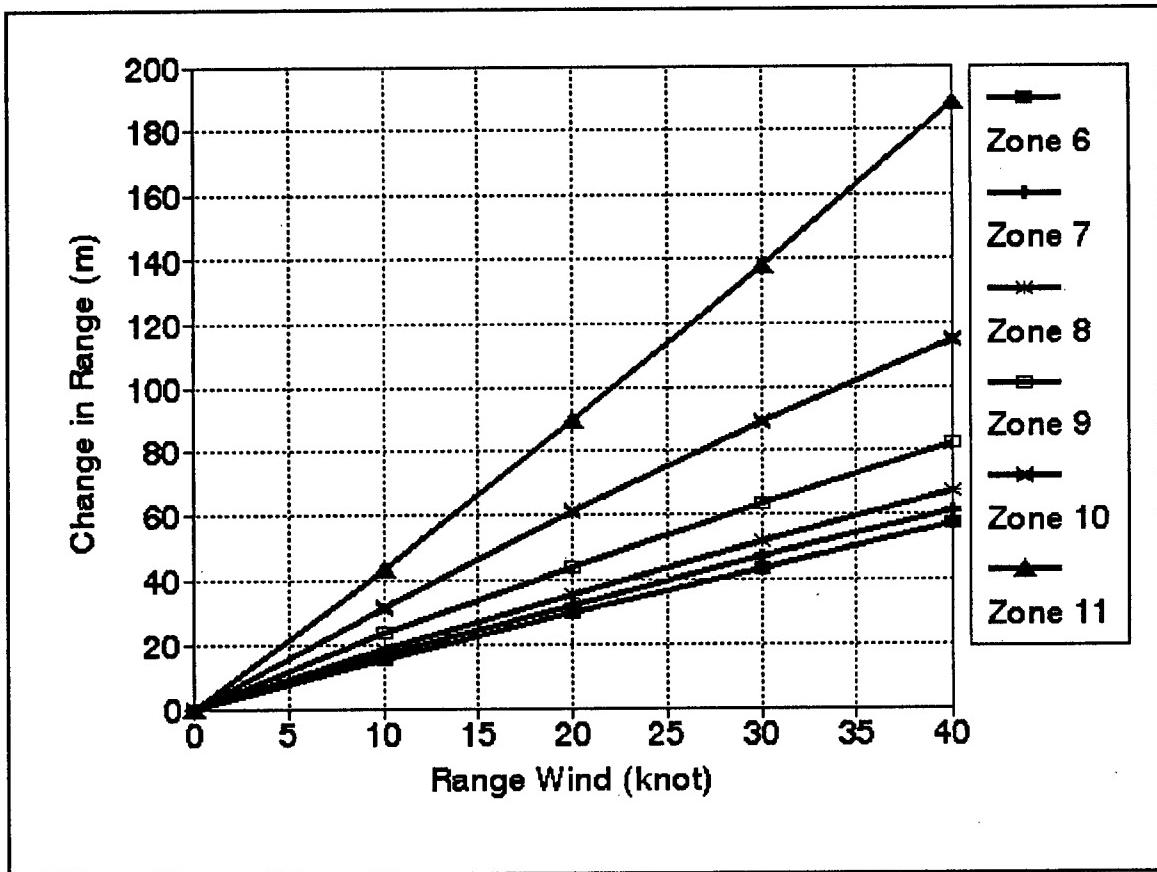
Figure 1. Zonal sensitivity of range to range wind for zones 6 - 11, 155 mm Howitzer Base Burn (8R charge) at a range of 25 km.

density percentage departures from ICAO standard values are given in the tables. Each unit effect must be multiplied by the ballistic value of the appropriate MET parameter to find the net effect on the trajectory. Figure 2 shows the range-wind unit effect as a function of range for the 155 mm Howitzer Base Burn with M864 (charge 8R).

The ballistic value of a MET parameter is obtained from a weighted sum over the zonal values of the parameter for a given ballistic line. The ballistic zone structure used in obtaining ballistic MET values differs from the MET-CM zone structure (Field Manual FM-6-15, 1992; Field Manual FM-6-16, 1982). Thus in order to use the tabulated unit effects, it is first necessary to convert the MET-CM zone values to ballistic zone values. A method of weighted averages (Blanco,1993) may be used to accomplish this. Finally the overall ballistic value is computed using the weighted sum of ballistic zone values.

Tabulated unit effects are not available for the MLRS. A zonal sensitivity analysis (similar to that described previously) using the Fire Control System (FCS) simulator can be used to find the zonal unit effects. If desired, ballistic techniques can be used to develop "ballistic-type" weighting factors for the MET-CM zones.
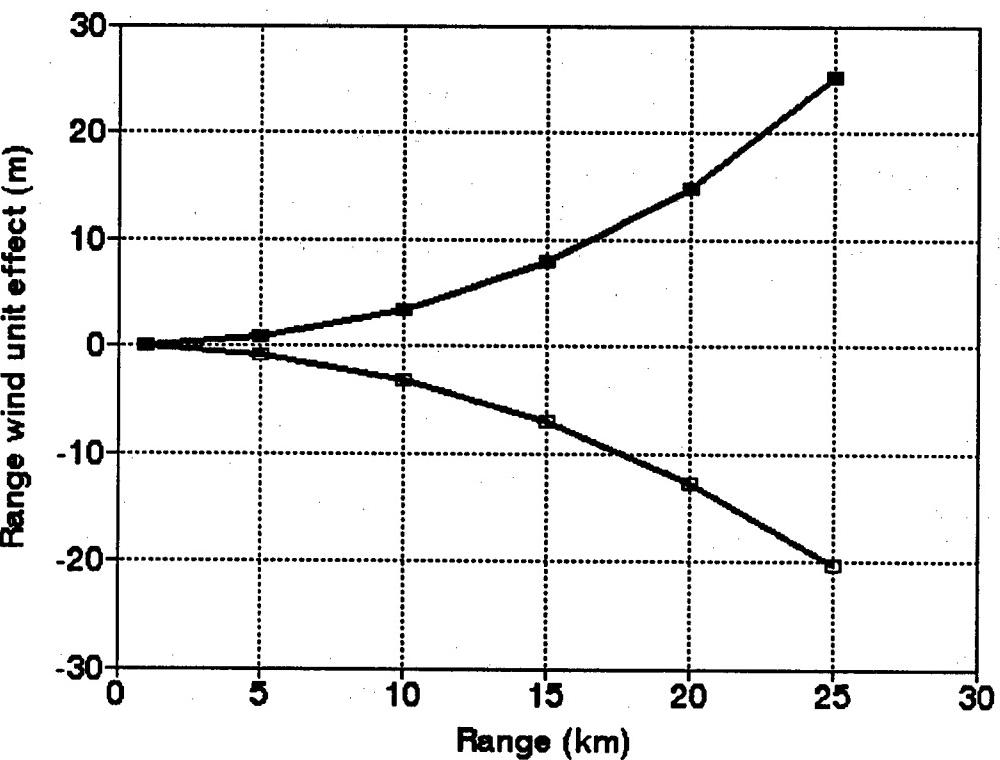
Figure 2. Range correction unit effects for ballistic head wind (upper branch) and ballistic tail wind (lower branch), 155 mm Howitzer Base Burn (8R charge), as a function of range. (After FT-155-AU-PAD, 1989)

5. RULE BASE CONSIDERATIONS

As of this writing, the rules that govern MET Message Dissemination for CAAM are still under development. The final rule base will incorporate the considerations noted in this section.

For a particular sector, input to the RBS includes the change in trajectory range and deflection due to changes in MET values from the previously disseminated message to the new message. These changes are computed for each of the representative weapons and charges considered in the system. For each weapon it is necessary to establish accuracy criteria in the form of critical cut-off values for change in range and deflection. Such values define an ellipse about the impact point in the target area.

One candidate for the choice of critical values for a given weapon involves the use of the probable errors (or a multiple thereof) stated for range and deflection in the firing tables. These errors increase with range. For example, for the 155 mm Howitzer Base Burn using charge 8R, the range probable error increases from 27 m at 10 km to 89 m at 28 km, while the deflection probable error increases from 3 m to 15 m (Firing Table FT-155-AU-PAD, 1989).

Internally the rule base can determine a dissemination recommendation for each of the representative weapons under consideration. This includes individual recommendations relevant to the specific firing charges used and to the separate cases of low-angle and high-angle fire. However, for a particular sector only a single overall recommendation is returned to the Executive. The derivation of the overall recommendation is straightforward for the extreme situations: recommend to disseminate the message if the dissemination advice is "yes" for all the individual cases; recommend not to disseminate the message if the advice is "no" for all the individual cases. Ultimately the rules must be able to provide an overall recommendation when the individual advice differs from case to case.

6. STRUCTURE OF THE MET MESSAGE DISSEMINATION CSC

The Executive CSC controls the overall operation of CAAM, invoking other individual CSCs as necessary. Each CSC is invoked as an Ada task. All external information needed by MET Message Dissemination is received from the Executive or read from files. After the MET Message Dissemination CSC executes, a dissemination report for all defined sectors is returned to the Executive.

The MET Message Dissemination CSC is modularized into three Computer Software Units (CSUs) in accordance with MIL-STD-2167A requirements, as follows:

- The Dissemination Control (DISSCON) CSU acts as the interface between the Executive CSC and the MET Message Dissemination CSC. This CSU receives a run command and AOP data from the Executive, computes sector range and azimuth, controls data flow between the other CSUs, and returns output to the Executive. The primary output is a dissemination report covering all defined sectors.

- The Message Processor (DISSMES) CSU receives derived range and azimuth values for a given sector from the DISSCON CSU. For the designated sector it reads the previously disseminated MET-CM message and the new candidate MET-CM message from file and decodes them. It also computes values of required derived MET parameters. It returns the decoded and derived MET information to the DISSCON CSU.

- The Rule-Base Processor (DISSRB) CSU receives AOP data and decoded and derived met parameter values from the DISSCON CSU. It computes ballistic MET values and uses tabular information and/or predetermined sensitivity knowledge to determine the effect on trajectory due to differences between the new and the previously disseminated MET-CM messages. It utilizes an RBS to determine a recommendation on whether to disseminate the new message for the sector. It returns the dissemination recommendation to the DISSCON CSU.

For each defined sector the DISSCON CSU first invokes the DISSMES CSU and then the DISSRB CSU. In this fashion it builds up the dissemination recommendation report. Figure 3 depicts the structure of the CSC.
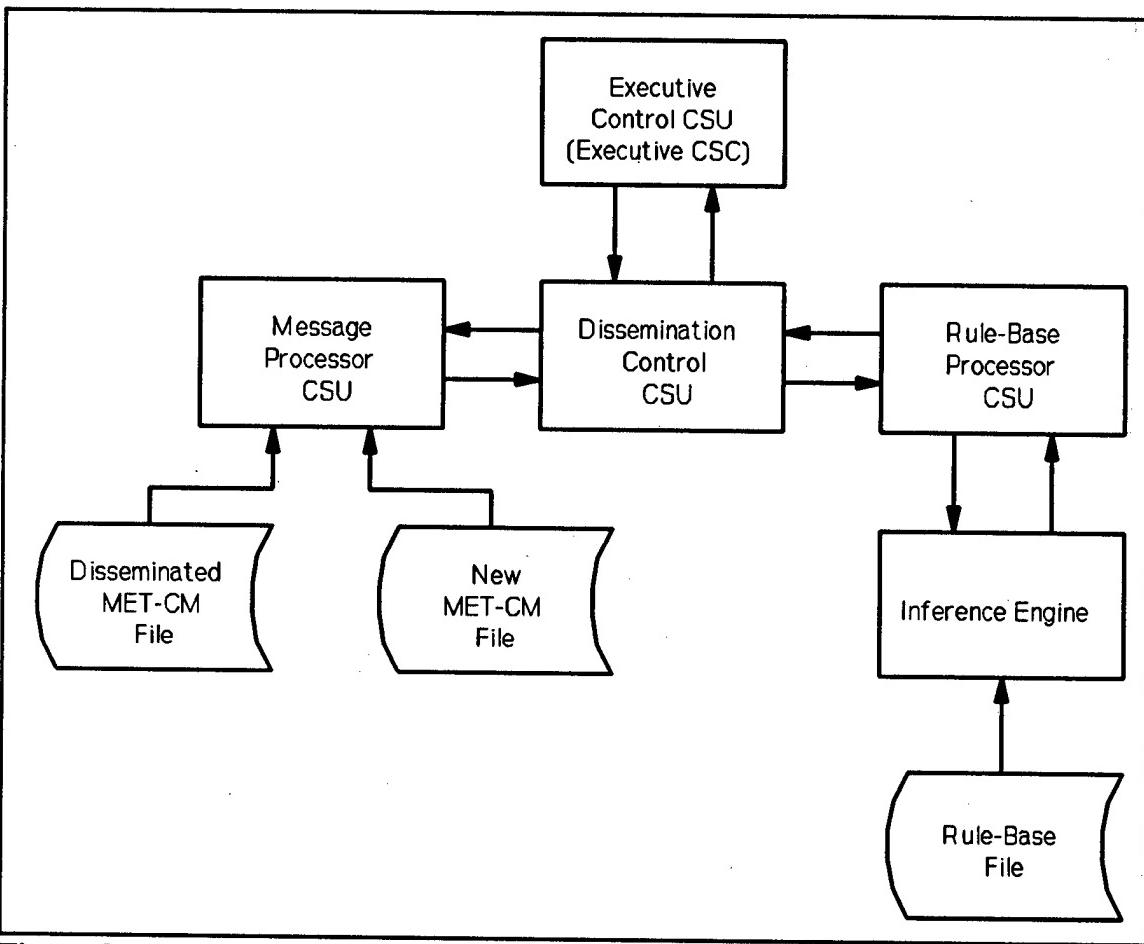
Figure 3. Structure of the MET Message Dissemination CSC.

7. CONCLUSIONS

As is the case with the other CSCs in the CAAM system, MET Message Dissemination is currently undergoing development. The general framework for the approach has been established regarding the following items: data transfer to and from the Executive and within the CSC; MET message processing; computation of MET effects on the trajectories of the representative weapon systems; interface to the CLIPS inference engine to execute the rule base. Research is ongoing concerning the detailed content of the rule base.

The next developmental phase will include coding of each of the constituent CSUs in the Ada language. It will also include the construction of specific production rules in a format compatible with the CLIPS inference engine. Ultimately, the MET Message Dissemination CSC, including the rule base, will undergo testing to assure that it operates as expected in the CAAM System and yields realistic advice consistent with available data.

ACKNOWLEDGMENT

REFERENCES

Blanco, A., 1993: Personal communication.

BRL GTRAJ3, 1991: User's Guide for the General Trajectory Program (GTRAJ3). U. S. Army Ballistic Research Laboratory, Aberdeen, MD.

Bustamante, D. B., and A. W. Dudenhoeffer, 1990: A Survey of Artificial Techniques for Processing Meteorological Satellite Data. PSL-90/102, Physical Science Laboratory, P. O. Box 30002, Las Cruces, NM 88003-0002.

Field Manual FM-6-15, 1992: Tactics, Techniques, and Procedures for Field Artillery Meteorology. Headquarters, Department of the Army, Washington, DC.

Field Manual FM-6-16, 1982: Tables for Artillery Meteorology (Electronic) Ballistic Type 3 and Computer Messages. Headquarters, Department of the Army, Washington, DC.

Firing Table FT-155-AO-0, 1978: Provisional Firing Tables for Cannon, 155MM, Howitzer, M185. U. S. Army Ballistic Research Laboratory, Aberdeen, MD.

Firing Table FT-155-AU-PAD, 1989: Provisional Aiming Data for Cannon, 155MM, Howitzer, M185. U. S. Army Ballistic Research Laboratory, Aberdeen, MD.

Giarratano, J. C., 1991: CLIPS User's Guide. JSC-25013, NASA, Lyndon B. Johnson Space Center, Information Systems Directorate, Software Technology Branch, Houston, TX.

Harmon, P., R. Maus, and W. Morrissey, 1988: Expert Systems Tools and Applications. John Wiley & Sons Inc., New York, 289 pp.

Seagraves, M. A., R. E. McPeek, and A. A. Grunwald, 1992: The Met Improvement Program: Key to Unlocking Target Area Meteorology. In Proceedings of the 1992 Battlefield Atmospherics Conference, U. S. Army Research Laboratory, White Sands Missile Range, NM 88002-5501.

Spalding, J. B., N. G. Kellner, and R. S. Bonner, 1993: Computer-Assisted Meteorology System Design. In Proceedings of the 1993 Battlefield Atmospherics Conference, U. S. Army Research Laboratory, White Sands Missile Range, NM 88002-5501.

Technical Manual TM-11-7440-241-10-5, 1990: Technical Manual, Operator's Manual, Fire Direction Center, Artillery. Headquarters, Department of the Army, Washington, DC.

TIME AND SPACE WEIGHTED
COMPUTER ASSISTED ARTILLERY MESSAGE

Abel J. Blanco, Edward Vidal, and Sean D'Arcy
U.S. Army Research Laboratory
Battlefield Environment Directorate
White Sands Missile Range, New Mexico 88002-5501, USA

ABSTRACT

An analytic time and space weighted approximation is derived as a composite of artillery meteorological (met) messages from available balloon borne met observations. Many times the current doctrine of utilizing data from a dedicated met station is not representative of the actual wind, temperature, and pressure effects experienced by unguided projectiles. Based on modeled ballistic met variability functional relationships with time staleness and space separation between the measurement and the application, normalized weighted sums of artillery computer zone data are used to define an automated technique that can enhance the met artillery first-round-hit probability by 30 percent in the average and as much as 70 percent during active weather conditions. Pseudocode defining this weighted approximation is presented and the algorithm is automated into a firmware that has demonstrated enhancement of existing artillery as well as future artillery systems.

1. INTRODUCTION

The classical mechanics for predicting unguided projectile trajectories is well known and automated at artillery fire control centers. Under standard conditions, this simulation science is considered to be exact. However, since the variables affecting artillery accuracy are not constant, the accuracy of aiming artillery is degraded. For the present artillery ranges this current accuracy is acceptable because the warhead lethal radius is larger than the artillery accuracy. For long-range applications this degraded accuracy cannot meet the required future artillery performance standard. In a joint effort under the direction of a U.S. Army Research Laboratory (ARL) focus program on advance artillery technology near- and long-term accuracy improvements are being proposed. A recent study[1] revealed that the muzzle velocity (MV) and the meteorological (met) variables are the major contributors to the total artillery accuracy error budget. There are concurrent programs investigating

proposals that can allow the required future artillery accuracy. Only through a joint improvement of both MV and met can the future artillery requirement be satisfied. This paper proposes an automated analytical technique that provides the U.S. Army Field Artillery with a computer-assisted artillery methodology that produces the best artillery met message for a designated battlefield area from available met observations. This derived message enhances the first-round-hit probability for current and future artillery fire systems. Aiming adjustments are made available to accurately deliver carrier projectiles and to compensate for met effects on parachute delivered submunitions, scan and search patterns, chemical bursts, and wind gliding warheads.

Since the atmospheric conditions are rarely standard, the U.S. Army Field Artillery deploys met teams to measure atmospheric conditions within the battle area. These teams are dedicated to specific users; and based on the freshness and location of the measurements, a user may adjust artillery fire with met data that is 1 to 4 h old and/or collected 20 to 30 km away from the point of application. The met teams are not collocated with the artillery fire systems, and the balloon borne sensor may drift away or towards the point of application, depending on the general wind flow within the battle area. Seagraves et al. (1992) describe ARL, Battlefield Environment Directorate proposals on how ARL plans to retrieve, analyze, and disseminate an improved computer met message known as a computer-assisted artillery message (CAAM). This paper documents the first version of CAAM with the firmware application that is generic and can support the current as well as future artillery systems.

The current practice of adjusting artillery fire for the actual met effect is unacceptable in meeting future long-range artillery accuracy requirements. A less expensive and effective technique for automating a more representative met correction is defined as the composite of available artillery computer met messages. First, all battlefield messages are retrieved through existing equipment. The available data is then cataloged with respect to time staleness and space displacement from the point of application. Established time and space met variability relations are used to compute a weighted approximation for each computer zone. By pooling all available computer met messages, the artillery system aimed with stale and largely displaced data may receive updated corrections from other met team stations. The immediate improvement is experienced by the commander using greater than 2 h old data from his dedicated met station. Since time staleness is more important than space displacement[3], this methodology can enhance the first-round-hit probability. This proposed algorithm provides the commander with data from other met stations that allow significantly more representative data than that provided from his dedicated met team.

Artillery cannon simulated results are used to evaluate the range of improvement allowed by the time/space firmware solution of automating the first version of CAAM. Project PASS data reported by Blanco and Taylor (1976) is used to demonstrate the effectiveness of this firmware solutions. A general statement derived from the analysis of the simulated impacts is that the current met contribution to the total artillery cannon

accuracy may be improved by 30 percent during average conditions of a winter season at White Sands Missile Range (WSMR), New Mexico. An improvement of 70 percent was experienced during a few days that contained more active weather variability.

2. TIME/SPACE MET VARIABILITY

Simulated and actual firing ballistic data analysis reveals that the older the met message the larger the artillery met accuracy error contribution. The ballistic wind error that normally contributes the single largest artillery bias is a function of the time staleness (t) and the space separation (s) raised to a power "p." The Air Force Handbook of Geophysics and the Space Environment (1985) presents the following relationships:

$$\sigma(t) = K_t t^p \qquad (1)$$

$$\sigma(s) = K_s s^p \qquad (2)$$

where

K_t = time staleness coefficient,

sigma(t) = variability during the time staleness (t),

K_s = space staleness coefficient, and

sigma(s) = variability due to the space separation (s).

The exponent "p" depends on the correlation coefficient between winds separated by the time and space interval. A suitable exponent generalization for the temperate zone is 0.5. The K coefficient values are a function of the global regions, terrain environments, and climatic seasons. For midlatitudes and under a flat terrain environment, literature results indicate that the space separation contributes a smaller expected error than the time staleness. Under these conditions single rawinsonde balloon measurements are representative of a large area. On the other hand if the terrain is complex the single sounding is only representative of the immediate area. For this example, it would be an error to apply these met observations at largely displaced distances.

The current doctrine allows an artillery commander to use a single wind profile to represent an entire area assuming negligible spatial variability within that area. The commander is aware that the atmosphere is not spatially homogeneous and has established a met relationship between time and space. During its annual 1974 meeting, the North

527

Atlantic Treaty Organization (NATO) Meteorology Panel XII postulated that the generally accepted relationship be that 1 h variability is equivalent to a 30 km distance variability. Over fairly level terrain, a message taken 30 km away from a location is considered to give the equivalent accuracy of a 1 h old message measured at that location. This "30 km ~ 1 h" equivalence is a compromise between reported variability equivalence of as much as "46 km ~ 1 h" to as little as "10 km ~ 1 h." In mountainous terrain and in the proximity of large bodies of water the valid distance should be reduced.

Although this empirical relationship is an acceptable average, the K_t and K_s coefficients actually depend on the wind speed, which is a function of the global region, terrain, season, and altitude. Simple algebraic formulas defined by Blanco (1988) accurately describe the expected wind, temperature, and density variabilities for a selected time staleness and space separation. Figure 1 demonstrates the relationship between time staleness at a given location and the space displacement at different locations contained within a midlatitude and relatively flat terrain environment. The variability presented is applicable for a 68-percentile wind-speed profile representing annual condition at WSMR, New Mexico. A wind-speed profile is used to initialize the empirical variance formulas that provide the balloon drift as well as the influence in deriving the environmental variance. The results are applicable for any trajectory whose apogee is approximately 1 km above the surface. Appropriate figures may be prepared for apogees as high as 20 km. Using this methodology to compute the expected atmospheric variances, one can define normalize weights to automate the first version of CAAM.
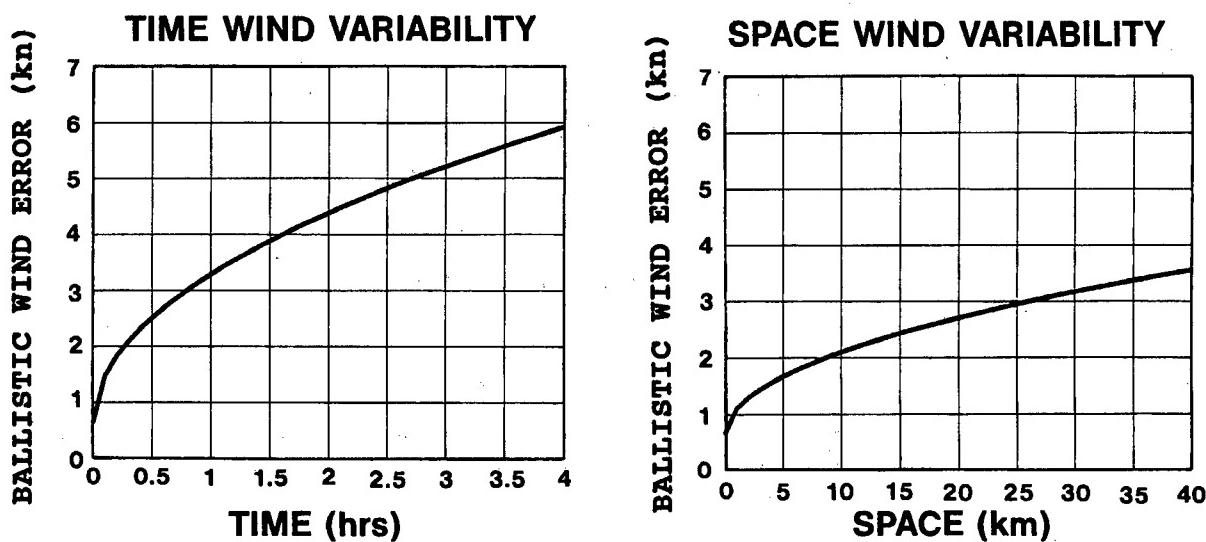
Figure 1. Ballistic wind time staleness and space variability.

3. ALGORITHM DEFINITION

The improvement allowed by this proposed approximation is dependent on the number of observations used to derive the composite message. Under actual tactical operations there may be no forward area met team soundings because of security or wind flow drifting balloon borne sensors further into friendly areas. Figure 2a illustrates a common scenario revealing that the location of observations and area of application are significantly displaced in space, and by knowing the release time one can understand the time staleness of the data at the time of fire. The time/space approximation will provide the best composite message when interpolating results as presented in figure 2b. Future CAAM versions plan to use rocketsonde, dropsonde, and satellite data in the forward area to allow optimum approximations for any location within the battle area. The complexity of the CAAM estimating algorithm will also increase to include terrain parameters perturbing the initial estimated wind, temperature, and pressure contours. There is on-going ARL research to tailor available mesoscale atmospheric models to represent long-term future versions of CAAM.

The application of CAAM is focused on the artillery computer met message. This is a standard artillery formatted data communication. Table 1 lists the atmospheric zone structure and identifies the zone thicknesses. Note that the zones are not uniform with thicker zones as you deviate from the surface. In coding this methodology, the computer zone represents the height. The algorithm then takes a weighted average of the available computer zone values using the inverse expected met parameter variance. The improved time/space relation described in the above section is applied in deriving the expected ballistic wind component uncertainty from the following formula:

(a)   (b)
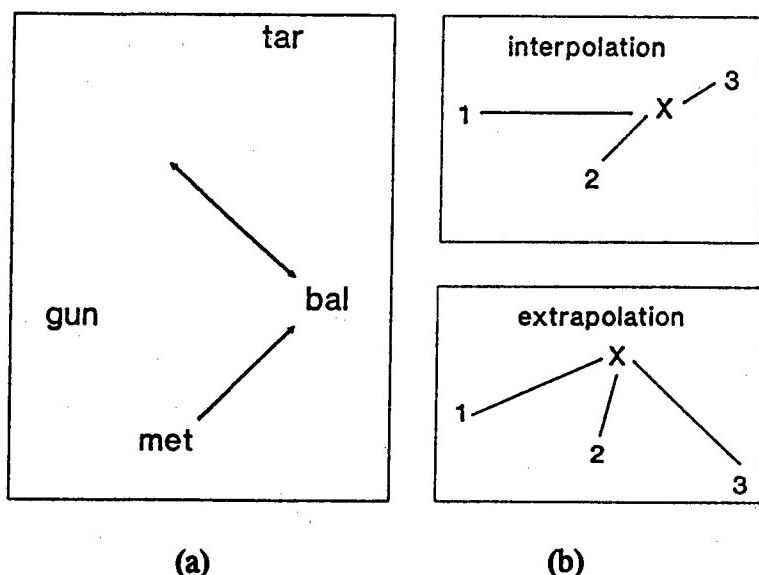
Figure 2. Common scenario illustrating gun, target, met station, and balloon locations.

Table 1. Artillery Computer met Message Zones

Zone No.	0	1	2	3	4	5	6	7	8	9	10	11	12
Height (km)	.0	.2	.5	1.	1.5	2.	2.5	3.	3.5	4.	4.5	5	6

Zone No.	13	14	15	16	17	18	19	20	21	22	23	24	25	26
Height (km)	7	8	9	10	11	12	13	14	15	16	17	18	19	20

$$Var = .0611(1+.03445V_b-.05846Z_b)^2(time+2dis)+Var(sensor) \quad (3)$$

where

Var = ballistic wind component variance (kn^2),

Vb = ballistic wind speed (kn),

Zb = top of ballistic line (km),

time = staleness (min), and

dis = displacement including balloon drift (km).

The wind variability increases with an increase of wind speed; however, there is a balance with the negative coefficient of the height parameter. As time staleness and space displacement increase so does the expected wind variance.

In contrast to the wind, density and temperature are scaler quantities and no separation into components is necessary. Density and temperature variabilities as a function of time are higher near the ground and smaller at higher computer zones. The ballistic temperature analysis shows a weaker dependence on height than found for density. The density and the temperature uncertainties are derived from the following formulas:

$$Dvar = .00282(time+2dis)/Z_b+Var(sensor) \quad (4)$$

$$Tvar = .001659(time+2dis)/\sqrt{(Z_b)}+Var(sensor) \quad (5)$$

where

Dvar = ballistic density variance ($\%^2$),

Tvar = ballistic temperature variance ($\%^2$),

Zb = top of ballistic line (km),

time = staleness (min), and

dis = displacement including balloon drift (km).

The weight assigned to each computer zone data is the inverse of the total variance due to time staleness (min) and space separation (km). The staleness is defined as the difference between the measurement time and the firing time. The space separation is the distance between the measurement and the application (as shown in figure 2). Using cartesian coordinates this displacement is defined as

$$(dis^2)_i = (x - x_i)^2 + (y - y_i)^2 \qquad (6)$$

where

dis$_i$ = space separation at the ith location,

x_i = easting location of measurement at the ith location,

y_i = northing location of measurement at the ith location,

x = easting location of point of application, and

y = northing location of point of application.

In the case of the same air mass moving through the battle area (constant flow) and using the same type of upper air sonde (fixed sensor variance), the total variance is expressed as

$$Tol = \sigma^2(t) + \sigma^2(s) \qquad (7)$$

Following these assumptions and normalizing the weights, the total variance is simplified by the following:

$$Tol = time(\text{min}) + 2dis(km) \qquad (8)$$

531

The weights are now defined as the inverse of the total variance. For one station, the scheme estimates constant wind, temperature, and pressure at the corresponding computer zone. To describe the estimates for greater than one met station, we define the explicit value of the individual weights.

$$wgt_i = 1/tol \qquad (9)$$

The normalized weights are then expressed by equation (10).

$$wgt_i = (1/Tol)/(\Sigma(1/Tol)) \qquad (10)$$

When the application point is equidistant from all measured points and when it is located very far away from all observation points, the value of the approximation reduces to the arithmetic mean. Since the time will never be a real-time measurement, the defined weighing scheme is well behaved with no possibility of a discontinuity or nonconvergence. The larger the total variance the less weight is given to that observation. The most influential observations are then the ones containing the most recent and closest met measurements.

The same weights are used in estimating the best wind components (U,V), temperature, and pressure values. Having defined the normalized weights as a function of the expected met parameter variances, the time/space weighted approximation is expressed by the following:

$$\langle U \rangle_j = \Sigma wgt_{ij} U_{ij} \qquad (11)$$

where

$< U >$ represents the time/space weighted approximation for any met parameter,

n = the number of observing stations,

j = the selected computer zone,

i = the available met observation, and

wgt = the particular weight for the ith observation at the jth zone.

This algorithm is automated and applied through a firmware operation. In the present configuration it is very portable and improvements in weight definition can readily be incorporated. As ARL refines the algorithm new firmware may easily be distributed.

4. FIRMWARE DEVELOPMENT

Currently the firmware is coded on a Z80 based microprocessor. The design of the processor is such that it is on a 7.75 by 3.75 in printed circuit board. The major functions of the module include the following: 16 KBytes Random Access Memory (RAM), 32 KBytes Electronic Programmable Read Only Memory (EPROM), 2 Serial Input/Output ports, 2 Paraellel Input/Output ports, 2 Counter Timer Circuits (CTC), and Programmable Real Time Clock (RTC). The vast majority of the code is done in a high level language C, and there is only a small portions coded in assembly level language. The unit can be connected to a dumb terminal to provide the operator with prompts or to machine to machine connection where the prompting is suspended.

The time-space technique is applied by met level (computer zone) in the CAAM code. Initially, the code establishes the time staleness and space location of available met messages and the time and location of the composite target area message. For the available messages at each met level, the movement of the balloon is calculated by using the wind velocity and the time of rise between levels. This horizontal displacement is then added to its previous location and the time of rise from the previous level is added to its time. In this manner the distance and time staleness for each message level is derived for defining the time/space weights. After all messages have been weighted, the data is summed and normalized by the sum of the weighing factors, giving the proposed CAAM for that level of the computed message (equation (11)). This process is repeated for each met message level, proceeding from the lowest level to the highest level.

The CAAM version 1 c code has been defined and will be published as a separate users guide report because of this proceeding's paper page limitations. For completeness of the CAAM code description table 2 lists the pseudocoding for the time/space weighted "caamts3.c."

When operating in areas near a UTM grid zone boundary, it is possible to have met stations in different grid zones. This can complicate matters when the met stations must be compared on a common grid, because the standard UTM grid cannot be used. To compensate, a procedure has been developed to find station coordinates on a common grid. This procedure works by translating the coordinates from one UTM grid zone to an adjacent zone. The translation is limited to one zone, but this should be adequate for any reasonable situation, as each grid zone covers 6° longitude. The translation is accomplished by computing a vector from the location of interest to a known point on the grid zone boundary. This boundary point has the same UTM northing value as the point of interest. The boundary point easting is computed using a simplified formula for the zone width as a function of UTM northing at the zone boundary. The zone width is also calculated at points north and south of the main boundary point. The difference of these widths, divided by the distance between their boundary points, gives the sine of the angle between grid lines at the boundary. The vector for translation is the combination of this grid differential angle with the easting distance between the point of interest and the zone boundary. This vector is simply converted from polar to rectangular coordinates and added to the coordinates of the boundary reference point. Table 3 lists the pseudocoding for caamzone.c.

Table 2. Pseudocoding for "caamts3.c."

A. "TIMSP( )"

Initialize internal variables to zero.
REPEAT-FOR each station
| Initialize message time staleness and balloon coordinates-"STNINIT( )"
| REPEAT_FOR LEVEL, from highest level of met data found (zero for
| first station) to highest level of met data possible (MAX_LVL).
| | IF temperature > 0 and pressure > 0 and temperature < 399
| | and pressure < 1999
| | | highest level of met data found = LEVEL.
| | ENDIF
| END REPEAT-FOR
END REPEAT-FOR
REPEAT-FOR each met level from zero to highest level of met data found
| Compute time-space message line for this met level- "COMPUT( )"
END REPEAT-FOR
Calculate temperature and pressure from last met level calculated.
REPEAT-FOR each met level from highest level of met data found to highest
level of met data possible (MAX_LVL)
| Compute predicted met data for this level- "METEXT( )"
END REPEAT-FOR

B. "COMPUT( )"

Initialize met data summation variables to zero- "WTINIT( )"
REPEAT-FOR each station
| Set met values and adjust balloon location for drift- "SETWIND( )"
| Calculate distance from balloon to target coordinates- "SPACE( )"
| Calculate weighted met data values, and add to met data summation
| values- "WEIGHT()"
END REPEAT-FOR
Normalize weighted met data sums- "CALC( )"

C. "STNINIT( )"

Convert time of application to minutes.
Convert time of message to minutes.
Calculate time staleness of message (for level 0).
Initialize balloon easting coordinate to message easting coordinate.
Initialize balloon northing coordinate to message northing coordinate.

Table 2. (cont)

D. "SETWIND( )"

Convert wind data from speed and direction to easting and northing components.
Extract temperature and pressure from input message.
IF level is greater than zero
| Set time for previous level.
ELSE
| Set time for previous level to zero.
ENDIF
Add easting wind drift to balloon easting coordinate.
Add northing wind drift to balloon northing coordinate.

E. "SPACE( )"

Subtract easting coordinate of target from easting coordinate of balloon.
Subtract northing coordinate of target from northing coordinate of balloon.
Calculate distance from delta easting and delta northing.

F. "WTINIT( )"

Initialize met data summation variables to zero.
Initialize met data normalization variables to zero.

G. "WEIGHT( )"

IF level = 0
| Add weighted met datum plane to met datum plane sum.
| Add MDP weighting factor to met datum plane normalization sum.
ENDIF
Calculate weight factor for met data.
IF wind velocity data exists
| Add weighted easting wind component to easting component sum.
| Add weighted northing wind component to northing component sum.
| Add weight factor to wind normalization sum.
ENDIF
IF temperature data exists
| Add weighed temperature to tumperature sum.
| Add weight factor to temperature normalization sum.
ENDIF
IF pressure data exists
| Add weighted pressure to tumperature sum.
| Add weight factor to pressure normalization sum.
ENDIF

Table 2. (cont)

IF weight factor < 0
| Set error flag.
ENDIF

H. "CALC( )"

Initialize output values to default of 0.
IF level = 0 and MDP normalization sum is not = 0
| Output met datum plane equals MDP sum divided by normalization sum.
ENDIF
IF wind normalization sum is not 0
| Normalize easting wind component sum.
| Normalize northing wind component sum.
| Calculate output wind direction from components.
| Calculate output wind speed from components.
ENDIF
IF temperature normalization sum is not 0
| Normalize temperature sum.
| Set output temperature to normalized temperature value.
ENDIF
IF pressure normalization sum is not 0
| Normalize pressure sum.
| Set output pressure to normalized pressure value.
ENDIF

Table 3. Pseudocoding for "caamzone.c."

A. "ZONECHK( )"

Initialize multiple zone flag to 1.
REPEAT-FOR each station
| IF gridzone of message is not same as gridzone of target
| | Increment multiple zone flag.
| ENDIF
END REPEAT-FOR
IF multiple zone flag > 1.
| Find primary zone for translation- "ZONE_TRANS( )"
| IF primary zone < 61
| | REPEAT-FOR each station
| | | IF station gridzone is not primary gridzone
| | | | Translate station coordinates to
| | | | primary gridzone- "COORD_TRANS( )"
| | | ENDIF
| | END REPEAT-FOR
| ENDIF
ENDIF

B. "ZONE_TRANS( )"

Initialize low and high gridzone to target gridzone.
REPEAT-FOR each station
| IF station gridzone < low gridzone
| | Set low gridzone to station gridzone.
| ENDIF
| IF station gridzone > high gridzone
| | Set high gridzone to station gridzone.
| ENDIF
Calculate difference in gridzones from low gridzone to high gridzone.
IF difference in gridzones = 1
| Set primary gridzone to target gridzone.
ENDIF
IF difference in gridzones = 2
| IF central gridzone is target gridzone
| | Set primary gridzone to target gridzone.
| ELSE
| | Set primary gridzone to 999 (error flag).
| ENDIF

Table 3. (cont)

ENDIF
IF difference in gridzones > 2
| Set primary gridzone to 999 (error flag).
ENDIF

C. "COORD_TRANS( )"

Find difference of new gridzone from old gridzone (+1 or -1).
IF zone difference = +1 or -1
| Calculate gridzone width/2 at 25 km south of northing coord.
| - "ZONEW()"
| Calculate gridzone width/2 at 25 km north of northing coord.
| - "ZONEW()"
| Calculate angle between grids of adjacent zones, from gridzone
| widths above and below station coordinates.
| Calculate gridzone width/2 at station northing coord.- "ZONEW()"
| Calculate distance from easting coord. to gridzone boundary,
| from width.
| Adjust northing coord. by northing component of distance.
| Calculate easting coord at gridzone boundary, from width, and add
| easting component of distance, to get new easting coord.
| Set station gridzone to new gridzone.
ENDIF

D. "ZONEW( )"

Calculate distance between gridzone boundary and central meridian, at a
given northing coordinate (half of the gridzone width at that northing).
Return distance calculated.

The firmware also includes the vertical extension of the CAAM results to contain
derived met data up to 30 km above the surface. The last observed wind is applied as
constant direction and speed at all higher altitudes. And the last observed temperature and
pressure are used to compute the departure from standard conditions to derive estimates for
the corresponding parameters up to 30 km. The pseudocoding for the extension of the
computer met message to 30 km is included in table 4.

Table 4. Pseudocoding for "extmet.c."

A. "METEXT( )"

Initialize height of met levels.
Calculate altitude from level and met datum plane.
Get standard temperature and density for altitude- "TEMDEN( )"
Calculate standard pressure from standard temperature and density.
IF level is last level of met data
| Calculate temperature departure from standard.
| Calculate pressure departure from standard.
ELSE
| Set output wind data to values at last level of data.
| Calculate output temperature from standard temperature and departure.
| Calculate output pressure from standard pressure and departure.
ENDIF

B. "TEMDEN( )"

IF altitude $<=$ 11019.068 meters
| Calculate temperature and pressure for alt $<$ 11019 meters.
ELSE
IF altitude $<=$ 20063.124
| Calculate temperature and pressure for alt $>$ 11019m. and $<$ 20063m.
ELSE
IF altitude $<=$ 32161.903
| Calculate temperature and pressure for alt $>$ 20063m. and $<$ 32161m.
ENDIF

As an added feature the firmware module has the capability to injest a met surface sensor. The module is configured to accept a modified AN/TMQ-34 surface sensor that measures wind speed, wind direction, temperature, barometric pressure, and relative humidity. This data is transferred to the module through a serial RS-232 connection and the communication parameters are 1200 baud, 8 data bits, 1 stop bit and no parity. The module transmits a request for the surface sensor readings and then reads the string of data. It is believed that these near-real-time met readings can be incorporated as software enhancement to the CAAM profiles for improving time staleness effects at the time and location of application.

5. QUICK LOOK CAAM EVALUATION

Selected days from the PASS experiment[4] are used to present a preliminary evaluation of CAAM version 1. This data consists of met messages collected from nine met stations over 20 days in the fall of 1974, at WSMR, NM. The messages were collected simultaneously at 2 h intervals, over a time period of 6 to 10 h, with the start and ending times varying with each day.

The evaluation process derives the met variability for a given met station. These results represent the current artillery met accuracy. Using up to three met stations, CAAM derives a met message for a designated station (TSX). A balloon schedule is assumed to define a battlefield firing scenario where the stations follow a 2 h staggered rawinsonde release. An example for Julian day 327 contains the first release at 0615 from TSX station 1, the second release at 0815 from ORO station 2, and the third release at 1015 from MCG station 3. Six h later (1215), station 1 initiates the schedule again. This scenario allows fresh data every 2 h providing CAAM with the latest available designated met station message augmented with the latest available messages from the other two stations. With the constraint of the three latest messages, CAAM derives a tailored message for the designated station at a selected time when the designated station is not on schedule for releasing a rawinsonde. The evaluation is then concerned with the comparison between the composite message and the actual release for the station that was not available during the define scenario. This scenario is representative of actual battlefield experiences where commander are using 4 to 6 h old met data. Yes, the met team has the capability of releasing every hour but because of logistics and manpower they can not sustain this rate.

A computer batch job was prepared so that an operator can select from the above scenario a combination of available computer met messages and enter the desired time and location of the application to automatically derive a composite time/space weighted message. This met message is then prepared into the format required by the General Trajectory Model (GTRAJ3).[6] Cannon simulated rocket assisted firings at 28 to 29 km ranges are then derived for each computer met message. The apogee for these trajectories is contained within computer zone 12 (6 km). Met data from station 1 represents the "truth" and CAAM results are then compared to demonstrate the improved artillery met accuracy.

The GTRAJ3 simulator is used as an indicator measure of the computer met message effects on a rocket assisted shell fired at this extended range. The simulator output (range and deflection impact) is used to determine the worth of proposed CAAM results. When CAAM reproduces the data at the designated met station the delta impact comparison yields a zero difference illustrating that CAAM does improve the met artillery error budget. Figure 3 presents the range and deflection comparisons for data scenario Julian day 327. This figure displays the root-mean-square one standard deviation miss versus the met data time staleness (hours). The solid curve represents the current met artillery accuracy at the extended range. If one aims with 4 h stale met data one can expect some 350 m miss due to the range wind, temperature, and pressure. However, using CAAM technology even if your dedicated met message is 4 h old one experiences a bit over 200 m miss. This miss is equivalent to about 2 h stale data using the current artillery technology. For the case of one having 2 h old data, CAAM provides the equivalent 1 h stale current technology artillery met accuracy. The deflection comparison represents the effect due the cross wind with little second order effects from the other met parameters.

Analyzing a more homogeneous data collected on PASS Julian day 305 reveals CAAM results providing worst met range accuracy than the current method of aiming artillery. This day contains three simultaneous release sets; therefore, the sample statistic is too small for making a general conclusion about CAAM. For completeness figure 4 presents the comparison for a day when met variability is at a minimum. All the met accuracies (at 28 to 29 km range) are well within the lethal radius of the delivered round. On-going research shall determine the cause of this range effect and identify which met parameter is responsible. From the deflection results one may assume that the range wind is no the cause.
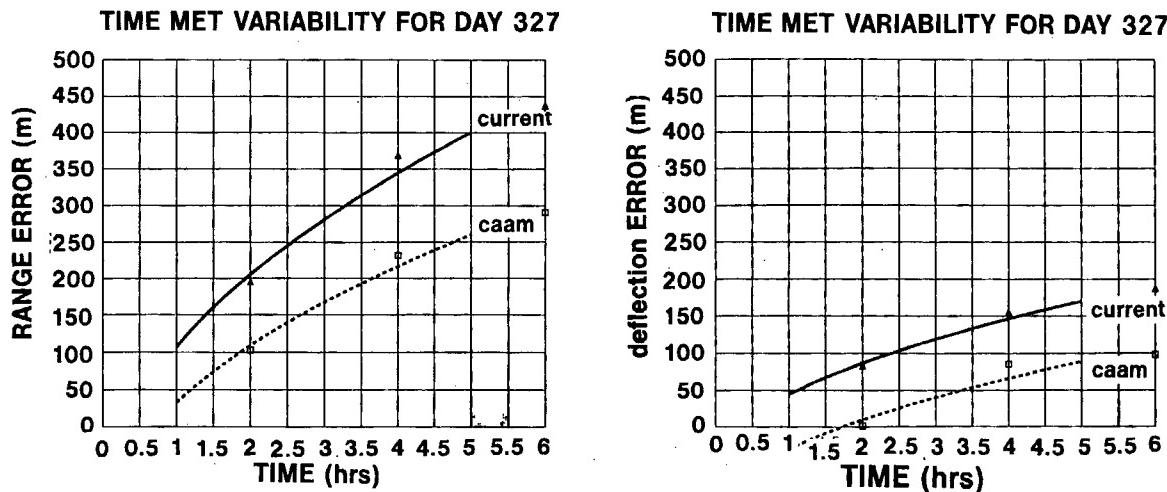
Figure 3. Rocket assisted round, M549A1, met accuracy at 28 to 29 km range.
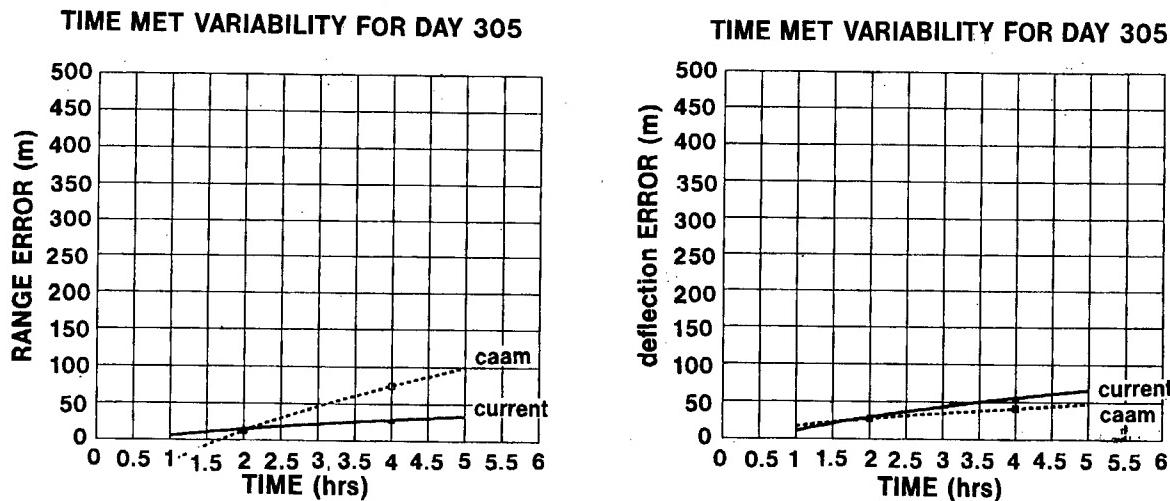
Figure 4. Rocket assisted round, M549A1, met accuracy at 28 to 29 km range.

541

Another observation in the interpretation of the quick look evaluation reveals that there may be an advantage when limiting CAAM input data to a selected staleness. For example, using all available stalenesses during Julian day 327 reveals a most impressive percent reduction of the variance met error. The range and deflection improvements are computed as 56 and 99 percent for the commander whose dedicate met data is 2 h stale. If ones met data is 4 h old as illustrated in figure 3 the percent variance reduction for range and deflection are 46 and 78 percent. Our analysis show, that when current data (during this most variable day) is always used to represent the CAAM output, the comparison reveals less improvement than using up to 4 h stale input CAAM data. There were some occasions when using up to 2 h stale produced the best results, but no general conclusions are stated at this time because of the limited sample size.

CONCLUSIONS

The time and space weighted algorithm has been defined and developed into a firmware. The initial evaluation reveals a most impressive result. For a strong met variability day, CAAM allows an artillery unit using 4 h old data to gain the met accuracy of 2 h old data. CAAM affords the artillery unit using 2 h old data the 1 h stale met accuracy. Farther improvement is expected when the available staggered release schedule is 1 h. By simply integrating all available met data and extrapolating a composite message at the desired time and location, the artillery met team can significantly upgrade met aim adjustments. Except for one event, the percent variance reduction for the two analyzed PASS days include a range from 0 (as good as the current technology) to 99% improvement.

Future plans include investigations for demonstrating that CAAM will not degrade the current artillery met accuracy. CAAM should always provide met accuracies that are as good as or better than the current capability. CAAM can be improved to limit the staleness of input data given base rules dictating scenarios that have consistently provided significant improvements. Another proposed investigation addresses the use of a surface met sensor that can adjust or nudge CAAM results to coincide with the near real time available surface sensor data.

REFERENCES

1. Lillard, Robert, et al, 1990, Personal Communication, Artillery Accuracy and Effectiveness Working Group, TRADOC, U.S. Army Field Artillery School, Fort Sill, OK.

2. Seagraves, M.A., R.E. McPeek, and MAJ A. Grunwald, 1992, "The met improvement program: key to unlocking target area meteorology," Proceedings of the Battlefield Atmospherics Conference, Fort Bliss, Texas.

3. Blanco, Abel J., 1988, "Methodology for estimating wind variability," ASL-TR-0225, U.S. Army Atmospheric Sciences Laboratory, White Sands Missile Range, NM.

4. Blanco, A. J., and L. E. Traylor, 1976, "Artillery Meteorological Analysis of Project PASS," ECOM-5804, U.S. Army Atmospheric Sciences Laboratory, White Sands Missile Range, NM.

5. Jursa, Adolph S., 1985, <u>Handbook of Geophysics and the Space Environment</u>, Air Force System Command, Air Force Geophysics Laboratory, Hanscom Air Force Base, Bedford, MA.

6. Miller, Jon, 1991, Personal Communication, U.S. Army Ballistic Research Lab's "User's Guide for the General Trajectory Program (BRL GTRAJ3)", U.S. ARDEC, Fire Support Armaments Center, Fire Control Division, Firing Tables Branch, Aberdeen Proving Ground, MD.

WIND FIELD VARIABILITY IN THE CAAM (COMPUTER-ASSISTED ARTILLERY MET) MODEL VALIDATION

Juan R. Quezada, John T. Grace, and Abel J. Blanco
U.S. Army Research Laboratory
Battlefield Environment Directorate
White Sands Missile Range, New Mexico 88002-5501, USA

ABSTRACT

During the target area meteorological data experiment (TAMDE) June-September 1992 and the prototype artillery (meteorological) subsytem (PASS) November-December 1974, data were collected from different upper-air sites located inside and outside White Sands Missile Range (WSMR) boundaries. Another available data set containing simultaneous upper-air releases from different sites is the Yuma data (1988-1992). These data bases provide support to the computer-assisted artillery meteorological (met) (CAAM) model development and evaluation in validating improvements to artillery fire accuracy. The purpose of this paper is to identify the public access data bases and software codes that graphically display the observed winds at artillery computer zones throughout the experiment area. Selected data that demonstrate significant wind field variability are presented for model validations. This variability shows the effects of terrain and mesoscale weather events.

1. INTRODUCTION

Computer software packages written in FORTRAN77 were developed to read, interpret, and display wind fields from TAMDE,[1,2] PASS,[3] and Yuma[4] artillery met computer messages. To make the data base more manageable and more meaningful for ballistic applications, all flights are reduced into the artillery computer and ballistic message formats. The met messages for the three data bases reside in these reduced formats in public-access directory /u4/contrib of White Sands Missile Range HP9000 C system. These packages provide the capability to display data in a single level or all levels of the rawinsonde soundings that demonstrate wind field variability due to the effects of terrain and mesoscale weather events.

These displays of wind conditions are used to evaluate CAAM modeling proposed to improve artillery fire accuracy. Currently, the U.S. Army Field Artillery uses a dedicated tactical met station methodology and assumes that the collected upper-air data is homogeneous and applicable anywhere in the battle area.[5] A good understanding of upper-atmospheric observations at different times and locations allows for improvement of artillery accuracy in the testing of artillery systems. CAAM proposes significant improvement of met support for the aiming adjustment of artillery systems.

2. DATA BASES

All available data bases include the following met parameters: wind direction and speed, virtual temperature, and pressure. The reduced artillery met messages can be used in analyses that aid in artillery accuracy studies.[4] The artillery met message zones and their varying thicknesses are listed in table 1.

Met data averaged into the artillery zones are recorded in the ballistic and computer met message formats. Since the computer met message is a record of actual measured weather conditions, it is more likely to show drastic changes not noticed on the original data or on the Ballistic met message.[5] For example the Field Artillery Meteorological Manual FM 6-15[5] lists the following quality checks:

- Wind speeds and directions should be fairly uniform with proportional changes in altitude. Large changes in wind direction (1,000 mils) or abrupt increases or decreases in wind speeds (10-15 kn) should be investigated.

- Temperature accuracy, because of erratic changes in temperature, is difficult to evaluate. Any severe increase or decrease in temperature (for example, +20 K) should be questioned.

- Pressure decreases logarithmically with height.

These and other quality control checks listed in the Federal Meteorological Handbook No. 3[6] are used to edit the data bases providing good data for CAAM evaluations. The format and units of the computer met message are shown in table 2, and examples of actual messages are presented in figure 1.

Table 1. Artillery Computer and Ballistic met Message Zones

Standard height (meters)	Zone structure Ballistic	Zone structure Computer
surface	0	0
200	1	1
500	2	2
1000	3	3
1500	4	4
2000	5	5
2500		6
3000	6	7
3500		8
4000	7	9
4500		10
5000	8	11
6000	9	12
7000		13
8000	10	14
9000		15
10000	11	16
11000		17
12000	12	18
13000		19
14000	13	20
15000		21
16000	14	22
17000		23
18000	15	24
19000		25
20000		26

Table 2. Computer Met Message Format

COMPUTER MET MESSAGE

For use of this form see FM 6-15; the proponent agency is United States Continental Army Command

IDENTIFICATION	OCTANT	LOCATION $L_1L_2L_3$ or xxx	$L_oL_oL_o$ or xxx	DATE	TIME (GMT)	DURATION (HOURS)	STATION HEIGHT (10's M)	MOP PRESSURE MU's
METCM	O			YY	$G_oG_oG_o$	G	hhh	$P_dP_dP_d$

METCM

LINE NUMBER	ZONE VALUES WIND DIRECTION (10's M)	WIND SPEED (KNOTS)	TEMPERATURE (1/10°k)	PRESSURE (MILLIBARS)
ZZ	ddd	FFF	TTTT	PPPP

METCM1328061	METCM1328061
151500125873	022010125877
0037300629990873	0048001030590877
0137901529770860	0150901030330865
0240201429530836	0249100929950841
0342001329150796	0349700829560803
0445101728760751	0450501029090759
0545302228380709	0550301428610713
0644702728170666	0651601828230673
0744903427960625	0749901427990634
0845303727670588	0853001427640595
0945504027280553	0955801727260560
1045304026930521	1053301926870527
1145104226620490	1151602326530493
1244704926010444	1251602526010447
1346006025280390	1351703025290392
1445207124440339	1451002824500342
1545606923760294	1551203523670297
1645807323020255	1651504022810256
1745207322180219	1752804221940220
1846608121490187	1853304821190188
1947108720860160	1950004521080160
2046907620530136	2051603520820136
2145906320470115	2150402420480115
2246902720720097	2247101720540098
2356500920420082	2352101220840083
2415300221210070	2440900721040071
2524400521430060	2549100321200060
2612600621440051	2607900521410051

Figure 1. Examples of actual met messages: TAM1_09 and TAM5_14 at Holloman site.

TAMDE DATA

TAMDE artillery met data resides in directory /u4/contrib/TAMDE of WSMR HP9000 C system. Data were collected for eight different days during June-September 1992, from the following eight different upper-air sites: Holloman (hm), Jallen (ja), Oasis (oa), Dirt (dr), MDS (md), and Stallion (st) inside WSMR boundaries, and outside WSMR at the Physical Science Laboratory (PSL [ps]) at New Mexico State University, Las Cruces, New Mexico, and Extended range (et). There are eight subdirectories under /u4/contrib/TAMDE that correspond to the days for which data were collected. Figure 2 lists the directory structure for the TAMDE data.

Each of these subdirectories contains all the data in computer met message format taken during the day of the sounding at the sites where the upper-air system was available at times 0600, 0900, 1400, 1800, and 2100 for each day.

As an example, directory u4/contrib/TAMDE/TAM1 contains files 'TAM1_06', 'TAM1_09', 'TAM1_14', 'TAM1_18', and 'TAM1_21'. These subdirectories also contain the following Fortran77 codes: mapts12.f, and tamde.f, which display wind vectors at available stations. Software code mapts12.f displays wind vectors for single computer zones, and tamde.f displays wind vectors for all zones of the soundings at the different stations of the experiment area. Output plots of program tamde.f are shown in figures 3a and b. The purpose of these plots is to display wind variability over the entire rawinsonde sounding. Note that for TAM3_09 in figure 3a, the wind field is light and calm with the displacement of the balloon at each station moving only a short distance.

Figure 3b TAM1_09 displays data in figure 1. The wind field is somewhat uniform with stronger winds showing the displacement of the balloon moving a considerable distance. TAM7_09 reveals strong direction change as seen from the reversal balloon displacements at the upper zones.

Output plots of program mapts12.f are presented in figures 4a, 4b, and c to display different types of wind variability taking place at computer zones 1, 3, 5, 7, 9, and 13 in TAM5_14. The wind vectors displayed at these zones can be verified with the met message in figure 1.

During this day the general weather picture featured upper ridge continued with drying and hence little convective activity. Variable high cloudiness throughout the range, featuring autocumulus and cirrus, and only a .1 cumulus reported uprange in midafternoon. Average 5-10 kn, peak 15-30 kn depending on location. Downslope winds from lee trof responsible. Temperature ranged into mid 90's max and 60's min downrange; and upper 80's-lower 90's max and upper 40's-lower 50's min uprange.

```
                    _____TAM1 (15 Jun 92)
                    |_____TAM2 (20 Jul 92)
                    |_____TAM3 (10 Aug 92)
                    |_____TAM4 (28 Aug 92)
u4_____contrib_____TAMDE____|_____TAM5 (02 Sep 92)
                    |_____TAM6 (11 Sep 92)
                    |_____TAM7 (21 Sep 92)
                    |_____TAM8 (28 Sep 92)
```
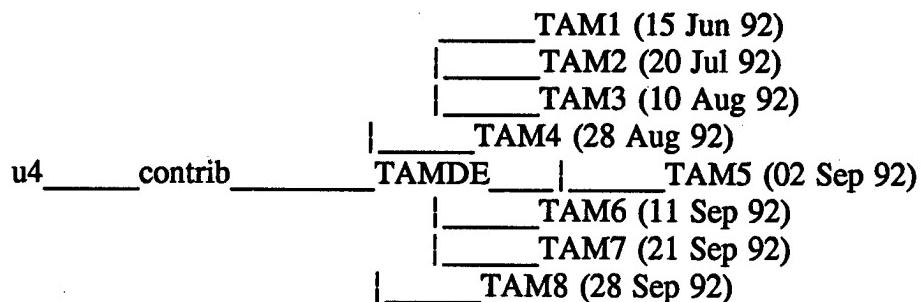
Figure 2. TAMDE directory structure.
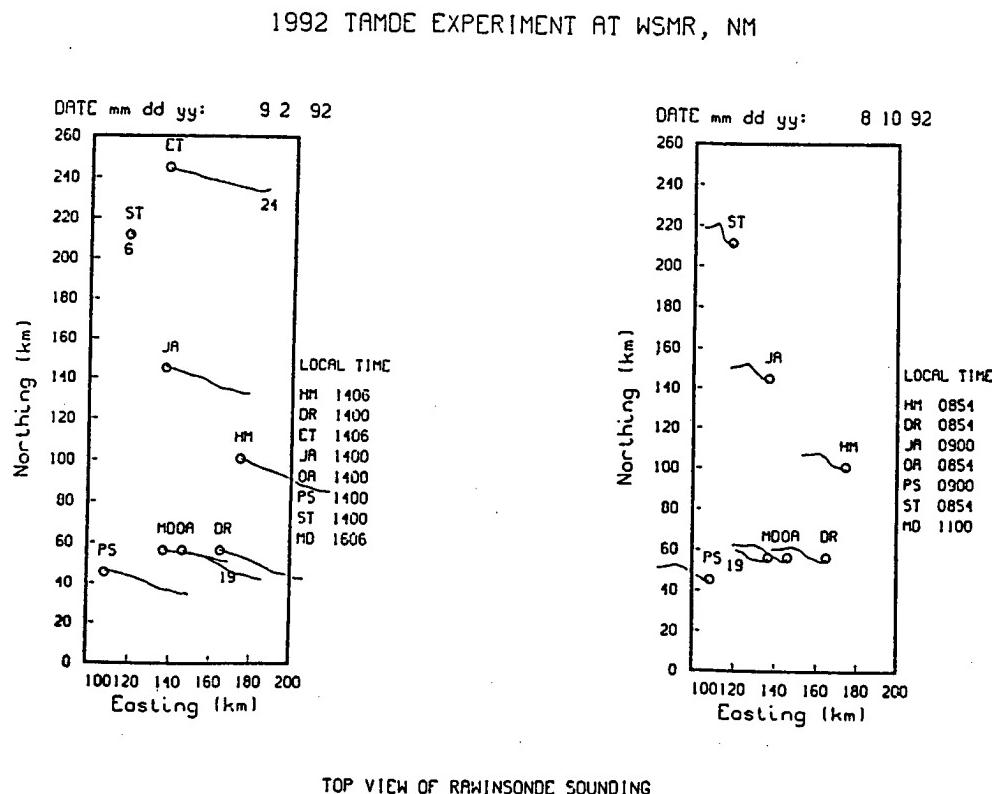
Figure 3a. tamde.f output display using TAM5_14, and TAM3_09 data.
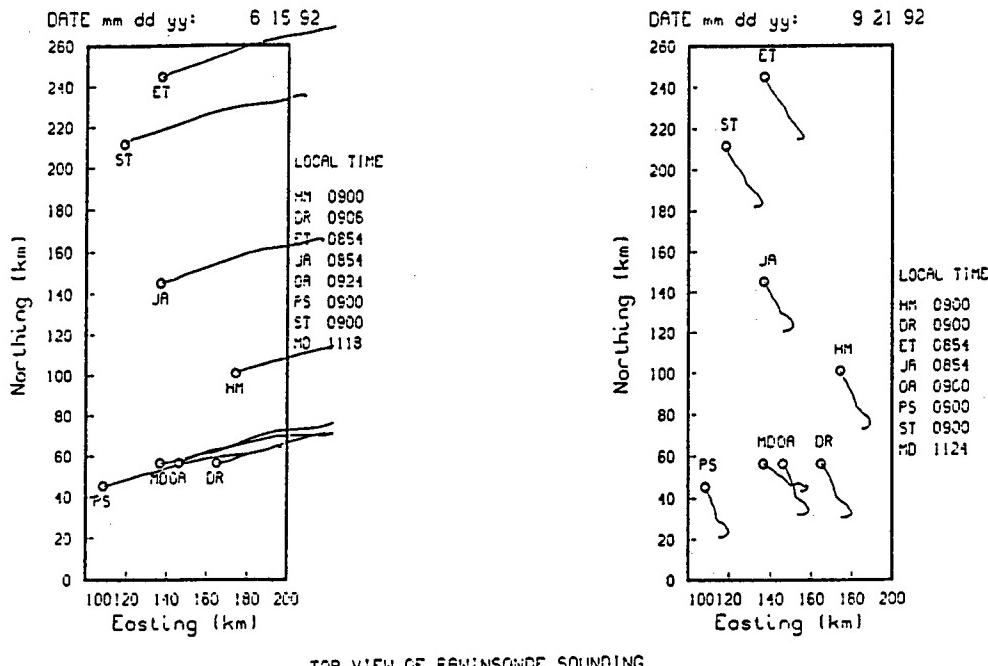
Figure 3b. tamde.f output display using TAM1_09, and TAM7_09 data.
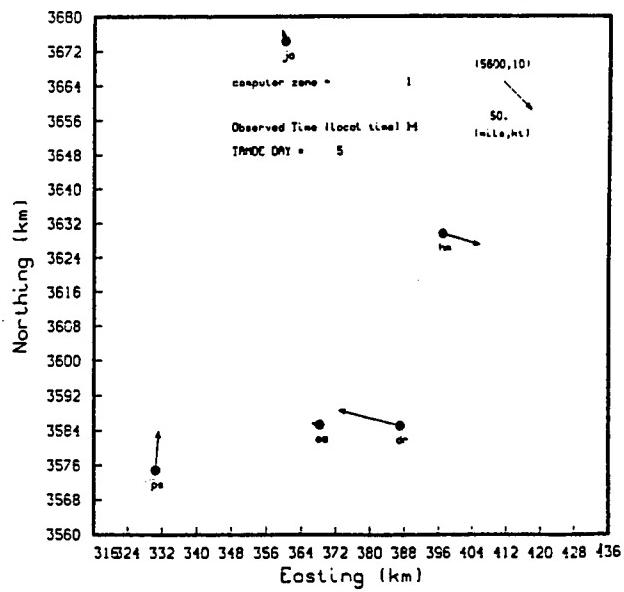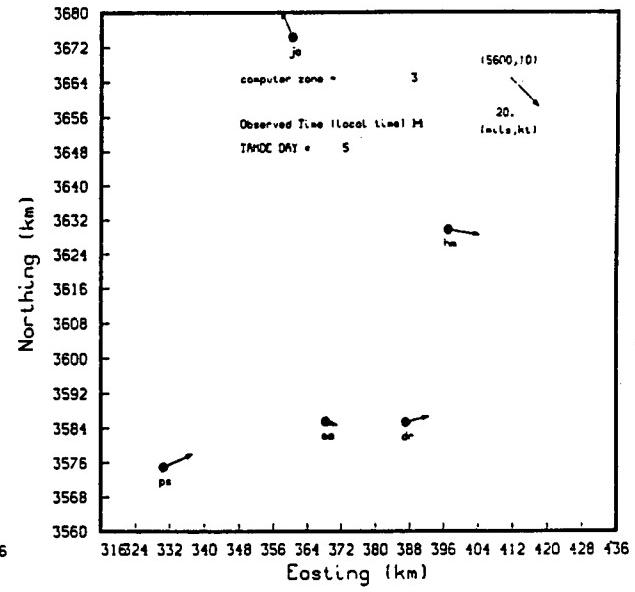
Figure 4a. mapts12.f output display of computer zones 1 and 3 using data TAM5_14.

551
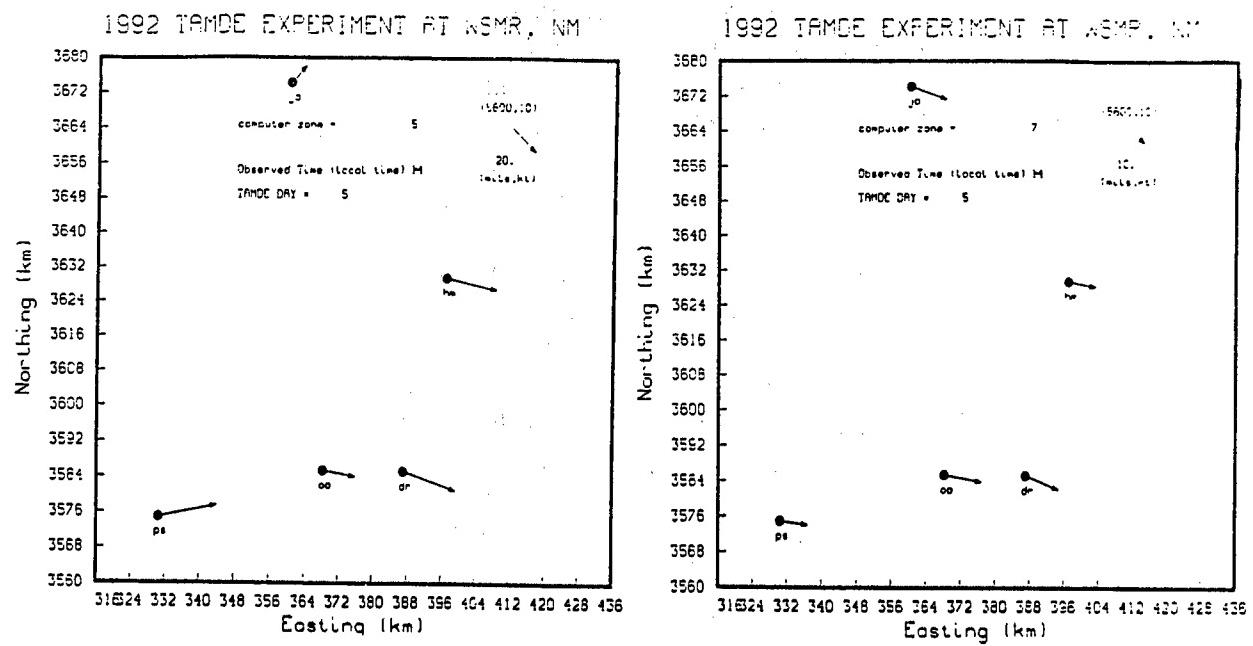
Figure 4b. mapts12.f output display of computer zones 5 and 7 using data TAM5_14.
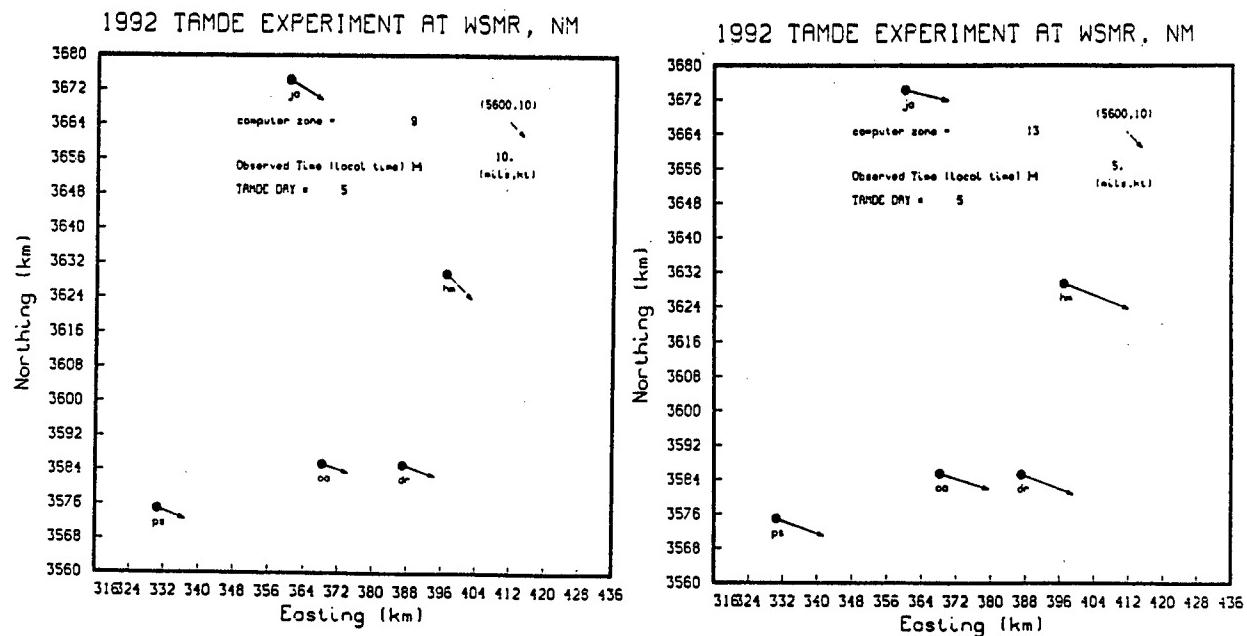
Figure 4c. mapts12.f output display of computerzones 9 and 13 using data TAM5_14.

552

Figure 3 shows a whole picture of the rawinsonde soundings although it is difficult to examine what happens between zones at different sites. Software code mapts12.f then allows one to have a clear view of the wind variability between computer zones. In an analogous situation, mapts12.f "cuts" the atmosphere in slices and takes "snapshots" of the wind variability present at different sites. From figure 4a computer zone 1, we can distinguish a circular wind flow that seems to have a pivot point between Holloman and Dirt.

Also note that winds are stronger at PSL, Holloman, and Dirt than at Oasis and Jallen. Another observation that can be appreciated is a clockwise whirlwind motion at Jallen site between computer zones 3 and 7 and a similar situation at PSL between computer zones 1 and 7. Notice that the winds seem to be more persistent after computer zone 7. As an example of a drastic change in wind direction we can look at Oasis site between computer zones 1 and 3. Although there is not much change in speed, wind changed direction almost 180° from west to east. As a final observation we see that the wind was at an almost constant direction and speed at Holloman between zones 1 and 7.

PASS DATA

The PASS data reside in directory /u4/contrib/PASS of WSMR HP9000 C system. Like TAMDE, this data base is recorded in the computer met message format. However, julian dates 327, 337, 339, and 341 are the only days available at the time of finalizing this paper. Upper-air data were collected from the following sites: TSX, Oro Grande, McGregor, War Road, Small Missile Range, Ram Site, Apache, Holloman, and Las Cruces. Data were simultaneously collected at 2-h intervals, over a time period of 6 to 10 h, with the start and ending times varying with each day. As an example file names pass327_0615 through pass 327_1415 contain data from julian date 327 at times 0615, 0815, 1015, 1215, and 1415. Included is a software code, 'pass.f', which allows displaying wind vectors for all zones of the rawinsonde soundings. Output of this program is shown in figure 5.

1974 PASS EXPERIMENT AT WSMR, NM
DATE mm dd yy: 12 7 1974
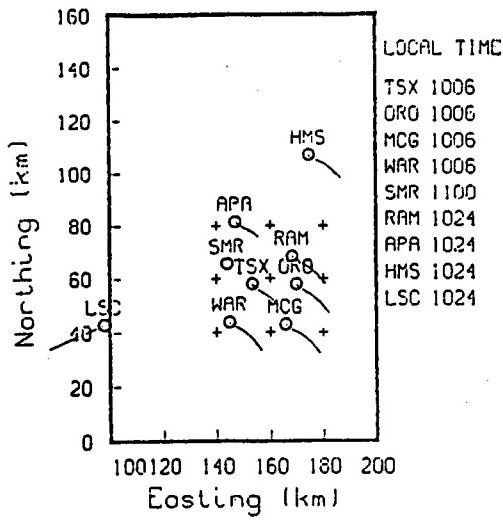
TOP VIEW OF BALLOON DRIFT

Figure 5. Output from pass.f using input file pass341_1015.

YUMA DATA

The Yuma Proving Ground Data can be accessed by logging into the WSMR HP9000 C system public-accessed directory /u4/contrib/yuma. There are two subdirectories ("rstation" and "tstation"), each containing five subdirectories pertaining to years 1988 through 1992. The subdirectories are called "1988," "1989," "1990," "1991," and "1992." Each of these contains 12 subdirectories pertaining to the 12 months of the year, and their names are the first three letters of the month ("jan," "feb," and so forth). Figure 6 lists the directory structure for the Yuma data. Each of these 12 subdirectories contains all the raw data files for the upper-air soundings collected during that month of the year at that particular station (files have extension ".raw"). These subdirectories include a filename called "file" that lists the names of the ".raw" files for the soundings in order of time and the computer met message data file for all the soundings. The name of the file that contains the computer met message corresponds to the site, month, and year at which the data were collected; for example, the name of the file with the computer met message data collected at the R station in june of 1991 is r_jun_1991.

554

The data was set up in the manner discussed above to make it easier on the user to access the data for a particular station, year, and month. For example, the path to access the data for the R station taken in March of 1992 will be: "/u4/contrib/yuma/rstation/1992/mar." This directory will contain 91 files with extension ".raw," a filename called "file," and a file called "r_mar_1992." The files with extension ".raw" contain the raw data taken at a particular day and at a particular time in March of 1992. For example, file "r14mar9206.raw" contains the raw data that was taken at R station, 14 March 1992 at 6 o'clock local time. The filename called "file" just contains the 91 names of all these ".raw" data files in order of time. The "r_mar_1992" file contains the computer met message for all the 91 ".raw" data files in the same order they are contained in "file." For example the third computer met message contained in "r_mar_1992" corresponds to "r03mar9205.raw," namely, the third ".raw" name in "file." In this arrangement, it is easy to match the computer met message with the raw data, since all the messages in "r_mar_1992" are numbered. So if one looks at the 50th computer met message in "r_mar_1992" and wishes to review the raw data for that message, one would go to the 50th line in "file" and that identifies the ".raw" data file.
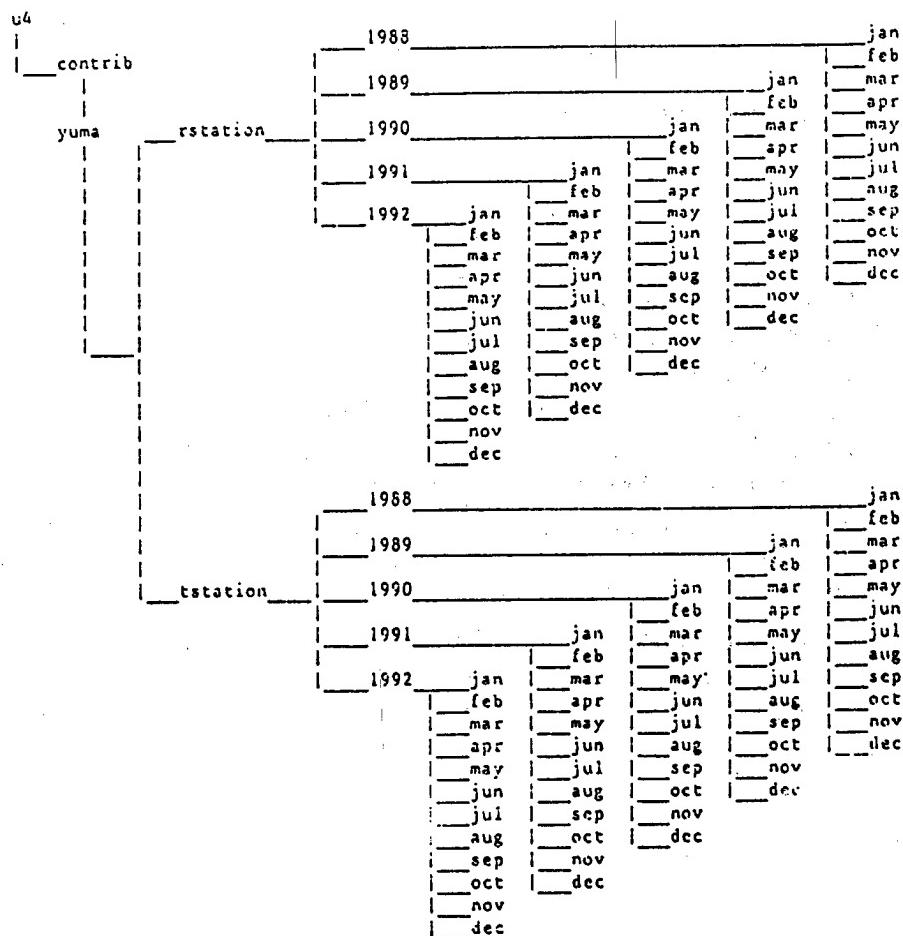
Figure 6. Yuma Directory Structure.

555

SUMMARY

Available field data have been reduced and arranged into public access data bases for the use of validating CAAM. To allow artillery met improvement evaluations, all data bases are presented in the artillery computer met message formats. Procedures to acquire available data have been presented and access to different software codes has been described. The uniqueness of these data bases is that they contain simultaneous upper-air releases from stations covering up to 100 x 260 km experimental area. Proposed CAAM results can be compared to measured data for evaluating worth of proposed met improvement algorithms.

LITERATURE CITED

1. Bonner, Robert, 1993: How to Access TAMDE Data.

2. Grace, John T., 1993: TAMDE-The Variability of Weather Over an Army Division Size Area. U.S. Army Research Laboratory, White Sands Missile Range, NM.

3. Blanco, Abel, and Larry Traylor, 1976: Artillery Meteorological Analysis of Project PASS, ECOM-5804, U.S. Army Atmospheric Sciences Laboratory, White Sands Missile Range, NM.

4. Blanco, Abel, and Juan Quezada, 1993: Time/Space Ballistic Meteorology Analysis of Yuma Proving Ground Data. U.S. Army Research Laboratory, Battlefield Environment Directorate, White Sands Missile Range, NM.

5. Field Artillery Meteorology Manual FM 6-15, 1992

6. Federal Meteorological Handbook no. 3 (FMH-3)

TWIST: REASONING WITHIN THE COMBINED MERCURY AND WADIF SYSTEMS

Heather D. Pfeiffer

Computer Science Department

New Mexico State University

Las Cruces, New Mexico, 88003-8001 U.S.A.

ABSTRACT

The Mercury heuristical objective analysis weather system and the Weather and Doctrinal Information Fusion (WADIF) system have been combined into the Terrain and Weather IPB Software Toolkit (TWIST). TWIST uses Artificial Intelligence (AI) techniques in order to analyze together terrain, weather and doctrinal information for automated templating which is performed as part of the aerial intelligence preparation of the battlefield (AIPB) process[10]. A range of AI techniques are used within TWIST in order to allow the most relevant information to be analyzed efficiently. This twisting technique has performed well for determining Air Avenues of Approach for AIPB. The overall goal of TWIST is to be able to reason over multiple areas of interest using terrain and weather effects, and then applying that information when solving many difficult problems which arise within the AIPB process.

1. INTRODUCTION

The Army Research Laboratory (ARL) Battlefield Environment Directorate (BED) along with the U. S. Army Space Technology and Research Office (ASTRO) and the U.S. Army Topographic Engineering

557

Center (TEC) are currently working in cooperation with New Mexico State University (NMSU) to develop an automated aerial intelligence preparation of the battlefield (AIPB) process[10]. ASTRO's program is providing the 'start-up' money for prototyping the TWIST system; TEC's expertise is in terrain data collection, updating and analysis; while BED's responsibilities include 1) developing weather analysis[1], 2) integrating terrain and weather effects[8] and 3) developing AIPB process as effected by the twisting of terrain and weather effects with doctrinal information for defined area of interest[9]. NMSU both through the Computer Science Department (CS) and the Physical Sciences Laboratory (PSL) are providing weather effects expertise, and expertise in the use of appropriate AI techniques for analysis throughout the AIPB process. Through this work tactical command and control is automate by utilizing ground data and space resources.

Since database functionality and information processing is not enough to integrate all these different aspects of the IPB process, NMSU has incorporated Artificial Intelligence (AI) techniques to accurately and efficiently process operations-level decisions[2]. These technics provide a means of specifying and organizing domain "rules-of-thumb" (heuristics) for explanation and prediction. With these heuristics automation of the battlefield becomes more of a possibility.

2. BASIC REASONING METHODOLOGIES

There are different types of basic reasoning methodologies[6]. Two of the methodologies available are *Quantitative* and *Qualitative* reasoning[11]. Quantitative reasoning is known as the ``*Mathematical Models of Numeric Processing*''. With quantitative reasoning the amount of data necessary for processing is very important. If the standard database tables (or incoming terrain/weather data) have sufficient information, a straight query from those tables (data) may be adequate. However, if not all information is available, sometimes the data can be numerically computed from available data. Therefore quantitative reasoning may or may not be heuristical depending on whether or not heuristics are needed for computing numeric thresholds.

However, a new situation arises when some of the data item's information is missing or can not be directly computed from factual information. In this situation, a quantitative methodology may not be appropriate and an incremental approach may be taken by using qualitative methodologies.

Qualitative reasoning is based on *relationship* decisions. These decisions are considered artificial in nature so are referred to as AI techniques. When data is missing from the database tables or incoming data, relationships between items and their components, or items and other items may assist in computing the needed information or in helping the computer to give back an answer. The following are a few of the relationships that may be used in answering a query:

A. Temporal - the relationship between time and other factors, or the time spacing between values of the same elements.
B. Spatial - the relationship of the object locations between elements.
C. Causal - the relationship between cause and effect of events.
D. Heuristic - the relationship between two objects or concepts.

In qualitative reasoning these and other relationships may be used to fill or evaluate possible value for missing data. The kind of reasoning to use depends on the data missing; also, the kind of technique to use depends on the relationship between that data and other available data[11].

3. CURRENT REASONING IN TWIST

Within TWIST there are two subsystems, Mercury and WADIF. Mercury is an AI-based weather analysis system that spreads weather analysis and effects over a grided area of interest despite complications of complex terrain and sparse data[8]. The WADIF system was producing asset performance templated on the ground[2,3]; however, in WADIF's present form, Air Avenues of Approach are now being computed. However, TWIST uses the following basic architecture of reasoning across the whole system (See Figure 1).

3.1. Weather Analysis

Since the battlefield weather domain is characterized by large volumes of data that flow from a sparse set of data sources, we have chosen a simple grid of points representing the battle area as the basic data structure. Using this simple approach, a *rule-based reasoning* approach has been used in order to interpolate between data points.
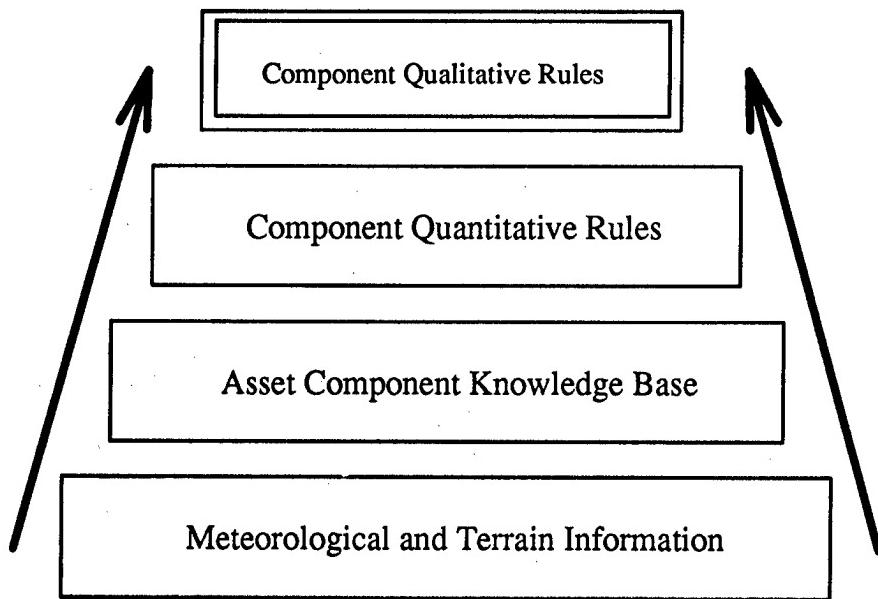
Figure 1: Whole Reasoning System.

Within the rule-based reasoning approach three kinds of rules are used: 1) Quantitative Rules - that translate numerical thresholds to value; 2) Qualitative Rules - that specify contribution of station data to other points within the grid; and 3) Quantitative/ Qualitative Rules - that integrate quantitative and qualitative results.

Within the weather analysis system, Mercury, the weather grid, for example, may support interpolation across variables within each cell representing factors such as surface conditions, cloud conditions, fog, and approximated wind vectors. This is done by taking surface reports and heuristical rules from the rule base and spreading the data across the whole grid. The heuristics allow a more intelligent spreading of data then using only objective analysis[8].

3.2. Weather/Terrain Effects

Using the weather grid just computed and applying information about terrain data for the same area, weather and terrain effects can be twisted together to get more of a picture of the desired area. Moreover, using separate grid structures for terrain, and weather interpolations within these information domains allow independent and low-cost responses to individual queries and allow analysis of effects from integrating grid information together[9].

3.3. AIPB Processing

When a query concerning AIPB processing is given to the system, the system seeks to combine both terrain and weather effects information with doctrinal constraints. In order to create the rules needed for the constraint processing, one must first understand the basic AIPB operational processing requirements. Study has been done in aviation deployment[7], air attack[5], and air defense[4], in order to understand the doctrinal rules of operation for AIPB. From these observations, heuristics can be generated for creating relationship trade-offs. For example, in analyzing an area of interest in order to produce possible air avenues of approach, there is a relationship between the path of fight of the asset (currently this is rotary-wing aircraft) and the amount of fuel used to travel this path. There are times that the path will be longer in length but at the same time safer because of where the asset travels. Each of these trade-offs are considered *parameters* to the system.

Within the AIPB process, parameters are considered to be of two types: 1) independent and 2) dependent. The independent parameters are:

A. Line of Sight - computing visibility of attacking aircraft.
B. Landuse - how does this landuse help, hinder or not effect the choices of attack.
C. Weather - how does the known weather affect the mission.
D. Air Defense - where are the air defenses and where can they move to.

With these parameters the emphasis is on accurate spreading across the whole grid. The amount of time taken to compute is not as important as the accuracy of results.

The dependent parameters are:

A. Start Location - where that attacking aircraft starts from.
B. Target Location - the location of target desired.
C. Fuel Consumption - the amount of fuel available and how important is it to be saved.
D. Risk Factor - how *risky* is the path to travel.
E. Target Zones - the attack area around the target.

With each of these parameters, computation time is more important then the 'perfect' answer. Each of these factors can not be done until the actual mission assessment is performed.

4. FUTURE REASONING IN TWIST

As one can see, in the current architecture, rules and heuristics play a large part in the processing of the system. In the future, we would like to make TWIST even more powerful and be able to process questions that can not be done with just rule-based reasoning. Therefore a new architecture is being evaluated.

The proposed architecture has multiple layers (terrain, weather, decision support, and other constraints) of grid style processing elements. Each layer has processing elements which have both within layer (intra-layer) connections and lateral (inter-layer) connections. The weights for in layer connections (grid weights) are initially loaded from a cost matrix that is either precomputed from mission independent information or from a current cost matrix made up of independent/dependent mission information. The weights between the lateral connection can be learned and/or predefined in certain cases depending on task. The weights between the layers are setup by functional relationships; for example, a weather layer has a functional relationship to terrain layer. These functional relationships are defined by a set of functional weighted links between the layers that are either loaded or learned.

As we see in Figure 2, each individual layer's activations are represented by spatially oriented variables. The set of weights which defines the matrix (grid) relationships within the layer is loaded onto that layer. For example, the current weather, and terrain information is imposed on those layers, and the decision layer is loaded later after information over time has been observed. This allows spatial questions to be addressed across a single layer. The single layer also can address questions within that realm of information; that is, the terrain layer can address questions relating to mountains, valleys, etc.

These layers also have functional relationships between each other. The relationships are defined by a set of functional weighted links between the layers. The terrain layer is the layer which tries to fuse information from all the other layers; that is, this layer takes into account all the 'effects' from the layers above.

INFORMATION FUSION USING NEURAL NET STYLE ARCHITECTURE
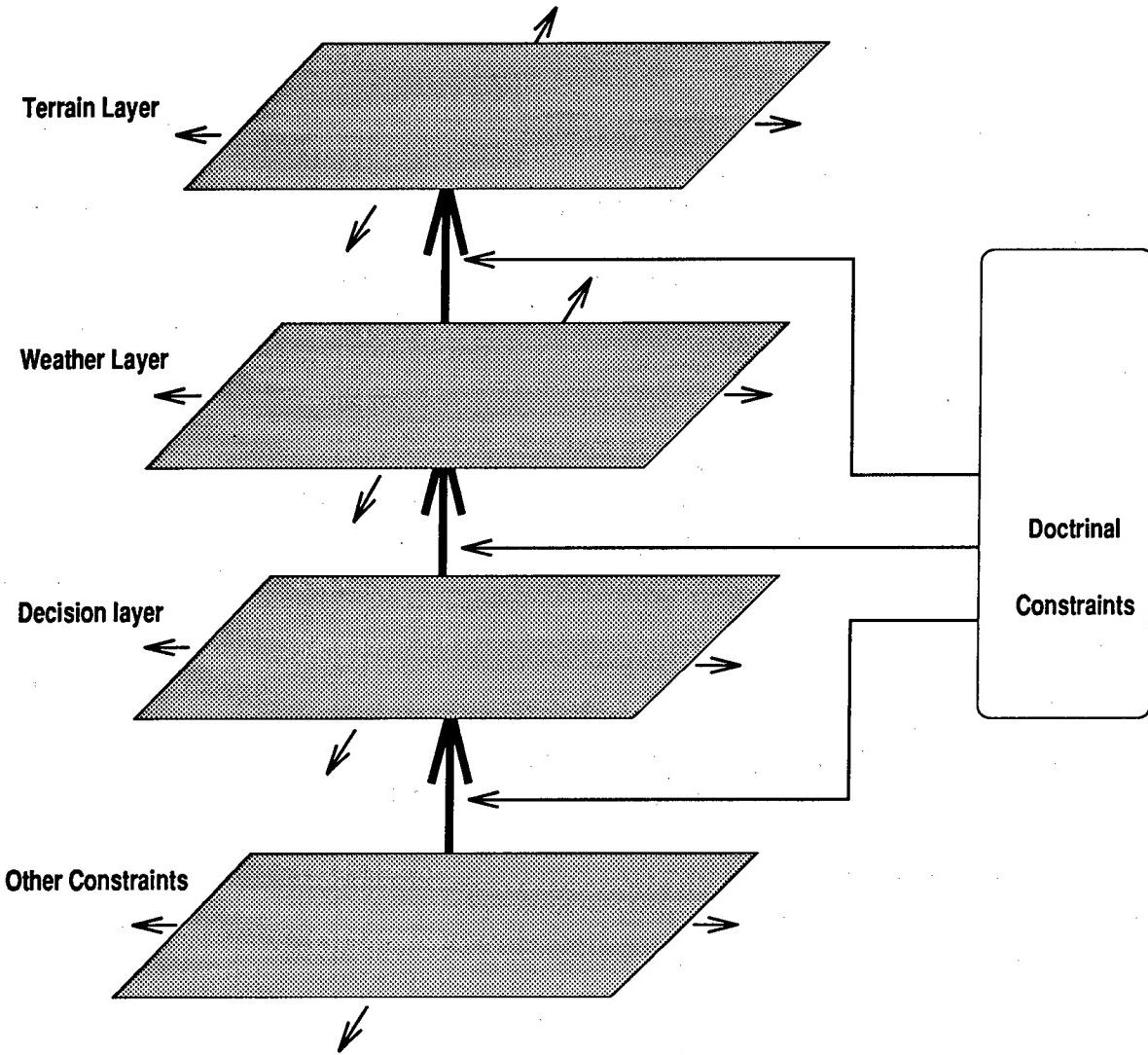
Figure 2: Future TWIST Architecture.

Figure 3 looks more closely at the functional relationships between the layers. For a particular task the set of weights which defines the relationship between the layers are loaded for every pair of layers onto the functional weighted (inter-layer) links. Given a task to be solved, first there exist a set of weight matrices related to the task. These weight matrices represent the functional relationships between the different layer and eventually to the task.

LINK MANAGEMENT INTERCONNECTIONS
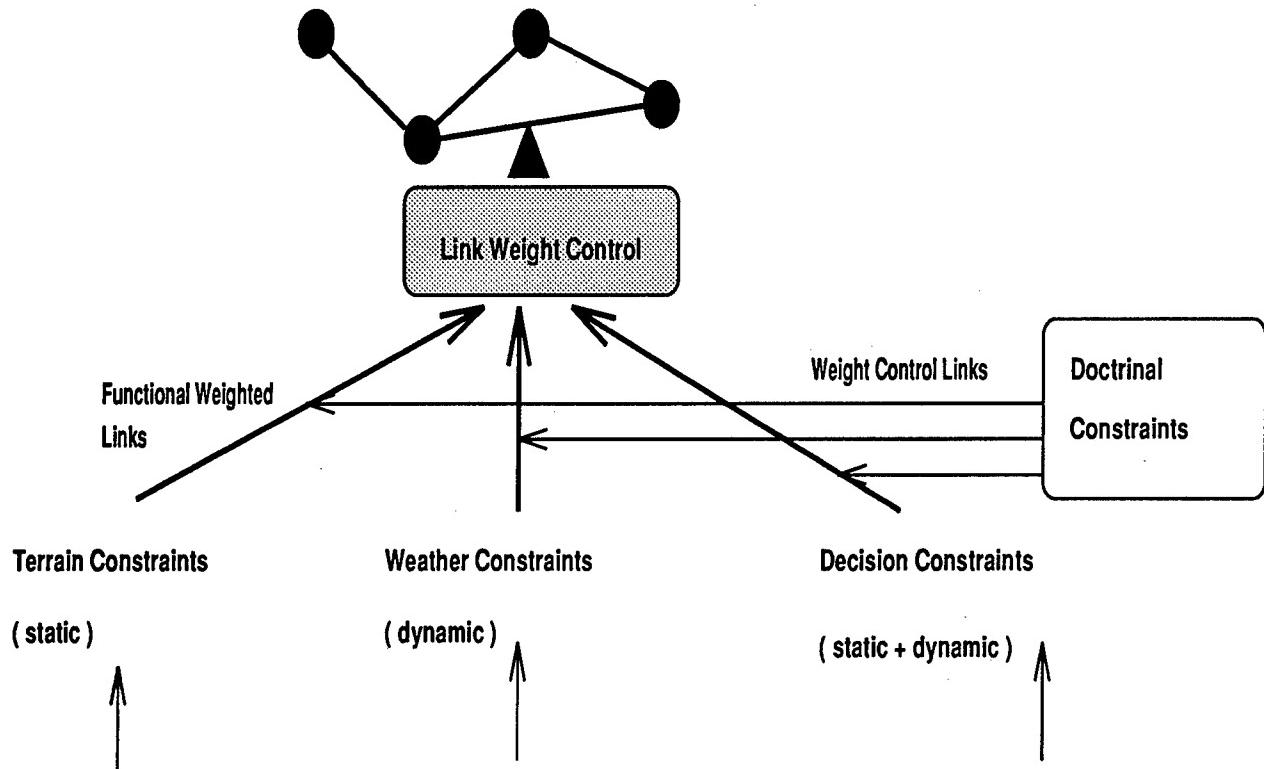
Figure 3: Relationship Links.

For example for asset movements, we will have weight matrices defining the relationship between the weather, and terrain. Also we can have a set of weights between the weather layer and the decision support layer.

When terrain, current weather, and decision information is imposed on the layers, the activations from these layer represent the current weather, terrain, and decision for the whole network. These activation from the layers then interact with each other through the functional weight matrix related to asset movement issue. The interaction of activations through these weight matrix decides upon a set of activations for the terrain layer, where the intra layer connection strengths of terrain layer are mapped according to the fused activation from other layers. This strength represents the cost function in the spatial dimension for asset movement which was derived form combining weather, terrain, decision and their functional relationship to each other with asset

movement task in mind.

How do we develop these functional weight matrices which are task specific? Well, that is where the doctrine constraints come into picture and are represented through the cost matrices. These constraints effect the functional relationships between the layers. They hold basic relationship information between the weather, terrain and other decision dependent parameters. For assess movement, the strategy of moving assets from one place to another applied to the functional weight links by these basic relationships. These doctrine constraints can be learned by the network by presenting prototypical situations or they can be encoded in the form of rules.

This architecture can be used for adding a different or new layer. This will only require a new set of intra layer weight matrices to be loaded for the added layer, and for a suitably set of functional relationships to be added between the new layer and the layers that already exist.

CONCLUSIONS

It is the intent of this work to twist together terrain analysis and weather analysis in order to support the AIPB process. The techniques used allow the process to be automated in order to increase efficiency and effectiveness. As more constraints are recognized, different kinds of reasoning techniques are being evaluated for use with is process. It is our desire to give as much automated support as possible for the integration of terrain, weather and doctrine information (data) within the AIPB process.

ACKNOWLEDGMENT

REFERENCES

1. Brown, R.C., and J.E. Harris, 1990: The United States Army's Proof-of-Concept Integrated Meteorological System. In <u>Proceedings of the Tenth Annual EOSAEL/TWI Conference</u>, Las Cruces, NM, pp. 228-235.

2. Coombs, M.J., and H.D. Pfeiffer, 1993: <u>Research in Information Fusion for Battlefield Intelligence: Final Report</u>, U.S. Army Atmospheric Sciences Laboratory, White Sands Missile Range, NM.

3. Eskridge, T., 1992: <u>WADIF: An Expert System for Fusing Weather and Doctrinal Information Used in the Intelligence Preparation of the Battlefield</u>, CR-92-0034-1, U.S. Army Atmospheric Sciences Laboratory, White Sands Missile Range, NM.

4. FM 44-100, 1988: <u>U.S. Army Air Defense Operations</u>, U.S. Army Headquarters, Washington, D.C.

5. FM 90-4, 1987: <u>U.S. Army Air Assault Operations</u>, U.S. Army Headquarters, Washington, D.C.

6. Luger, G.F., and W.A. Stubblefield, 1993: <u>Artificial Intelligence Structures and Strategies for Complex Problem Solving</u>, Redwood City, CA: Benjamin/Cummings.

7. Planning Guide, 1993: <u>U.S. Army Aviation Deployment For Contingency Operations</u>, U.S. Army Headquarters, Washington, D.C.

8. McWilliams, G.B., 1991: Research and Development Plan: Real-Time Weather/Terrain Exploitation. In <u>Proceedings of the 2nd Workshop on IPB Weather and Terrain Templating</u>, Computing Research Laboratory, New Mexico State University, Las Cruces, NM.

9. McWilliams, G.B., 1992: Integrating Battlefield Weather and Terrain Data for IPB Through Automated Techniques. In <u>Proceedings of the 1992 Battlefield Atmospherics Conference</u>, Fort Bliss, TX., pp. 405-410

10. McWilliams, G.B., and S.F. Kirby, 1992: Weather and Terrain Analysis For Aerial Intelligence Preparation of the Battlefield. In <u>Proceedings of 1992 Battlefield Atmospherics Conference</u>, Fort Bliss, TX.

11. Pfeiffer, H.D., and E.J. Burlbaw, 1993: The Use of An Intelligent Interface For the Predictive Technology Database. In <u>Proceedings of Predictive Technology Symposium, 1993</u>, Orlando, FR, pp.31-37.

Operational Short-range Forecast Model for Battlescale Area

Teizi Henmi and Robert E. Dumais, Jr.
Battlefield Environmental Directorate
U.S. Army Research Laboratory

and

MSgt Timothy J. Smith (USAF)
Operating Location N, HQ Air Weather Service

White Sands Missile Range, New Mexico 88002-5501

ABSTRACT

U.S. Army Research Laboratory (ARL) has developed an operational short-range (12 hours) forecast model system which is suitable for battlescale (< 500 km x 500 km) area. This forecast system utilizes as input data USAF Global Spectral Model analysis and 12 hour forecast field output data which are regularly transmitted through the Automated Weather Distribution System, and a mesoscale meteorological model HOTMAC (Higher Order Turbulence Model for Atmospheric Circulation). Three-dimensional time-dependent forecast fields of wind speed and direction, temperature and moisture are computed and graphically displayed using a workstation computer. This operational forecast model systems will become a major part of the Integrated meteorological System (IMETS) Block 2 software.

The performance of this operational forecast model system will be demonstrated at the conference.

1. INTRODUCTION

The U.S. Army is mainly concerned with meteorological conditions, within the space of 500 km x 500 km x 10 km or less, and within the period of 24 hours or less. Battlefield Environmental Directorate of the U.S. Army Research Laboratory (ARL) has developed an operational meteorological forecast model system suitable for the above spatial and temporal requirements for the Integrated Meteorological System (IMETS).

The IMETS is currently receiving the forecast and analysis fields of meteorological variables produced from the US Air Force Global Spectral Model (GSM) through the Automated Weather Distribution System (AWDS). Forecast and analysis fields of GSM are used to initialize HOTMAC calculation, and also assimilated into model calculation.

Higher Order Turbulence Model for Atmospheric Circulation (HOTMAC) has been selected and used as an initial model for prognostic calculation. HOTMAC has been used extensively at the ARL, and can simulate the evolution of locally forced circulations due to surface heating and cooling over meso-β and γ scale areas. HOTMAC is numerically stable and easy to use, and thus suitable for operational use.

The purposes of the present paper are to describe the Army's operational meteorological forecast system, and to show the capability of the system.

2. MESOSCALE MODEL

The basic equations for HOTMAC are the conservation equations for mass, momentum, potential temperature, mixing ratio of water vapor, and turbulence kinetic energy (Yamada and Bunker, 1988).
The potential temperature equation was modified (Yamada and Bunker, 1989) so that the deviation of potential temperature from that of the large-scale flow at an initial state was solved. This modification was to maintain stable numerical simulations and realistically predicted wind fields when HOTMAC was applied to simulate air flows over complex terrain with strong wind shear and temperature inversion (Yamada and Bunker, 1988). The large scale temperature was allowed to vary with height, and assumed to be uniform in the horizontal directions.

Also referred to as a "second-moment turbulence-closure model", HOTMAC is based on a set of second-moment turbulence equations closed by assuming certain relationships between unknown higher order turbulence moments and the known lower-order moments. HOTMAC can be used under quite general conditions of flow and thermal stratification: methods for turbulence parameterization are more advanced than those in simple eddy viscosity models. The present model, which is referred to as the Level 2.5 model (Mellor and Yamada, 1982), solves a prognostic equation for turbulence kinetic energy only; the remaining second-moment turbulence variables such as standard deviations of wind components, and heat and momentum fluxes, are solved from a set of algebraic equations.

The present model assumes hydrostatic equilibrium and uses the Boussinesq approximation. Therefore, in theory, the model applications are limited to flows where the local acceleration and advection terms in the equation of vertical motion are much smaller than the acceleration due to gravity (hydrostatic equilibrium), and temperature variations in the horizontal directions are not too large (Boussinesq approximation). This assumption is probably satisfied with a horizontal grid spacing greater than 5 km. The only way to assure these assumptions is probably to repeat the simulations with a non-hydrostatic, non- Boussinesq mesoscale model and compare the results with the present results. It is very

complicated and almost impossible to construct a non-Boussinesq turbulence closure model.

Surface boundary conditions were constructed from the empirical formulas of Dyer and Hicks (1970) for nondimensional wind and temperature profiles. The temperatures in the soil layers were obtained by solutions of the heat conduction equation. Appropriate boundary conditions were the heat balance at the soil surface and specification of the soil temperature at a certain depth. The lateral boundary values were obtained by integration of the corresponding governing equations except that variations in the horizontal directions were neglected. Parameterization of tall canopy effects on wind and radiation has been studied (Yamada, 1982): these effects are included in the present model.

The governing equations were integrated by use of the Alternating Direction Implicit method (Richtmyer and Morton, 1967). A time increment was chosen to be 90 % of the minimum value of $\Delta x_i/U_i$, where Δx_i is a grid spacing and U_i the velocity component in the i-th direction (Courant-Freidrich-Lewy criterion). The integration time increment is also limited by the propagation speed of gravity wave which is computed based on the potential temperature gradients. In order to increase the accuracy of finite-difference approximations, mean and turbulence variables are defined at grids which are staggered in both the horizontal and vertical directions. Mean winds, temperature, and water vapor vary most with height near the surface. In order to resolve these variations without introducing an excessive computational burden, nonuniform grid spacing is used in the vertical direction.

3. INITIALIZATION AND ASSIMILATION METHODS

GSM uses normalized pressure sigma=p/p$_s$ for a vertical coordinate. Thus, meteorolgical variables are calculated on constant pressure surfaces. Model-computed values of horizontal wind components, temperature, dew-point depression and geopotential height on mandatary pressure levels are currently communicated every 12 hours to IMETS through AWDS.

HOTMAC uses z^*, defined in the following, for a vertical coordinate:

$$z^*=\overline{H}\frac{z-z_g}{H-z_g} \tag{1}$$

where z^* and z are the transformed and Cartesian vertical coordinate, respectively; z_g is ground elevation above sea level; and H is the material surface top of the model; and $\overline{H}$ is the corresponding height in the Cartecian coordinate. For simplicity,

H is defined as

$$H=\overline{H}+z_{gmax} \tag{2}$$

where z_{gmax} is the maximum value of z_g.

Because different vertical coordinates are used in GSM and HOTMAC, the following two procedures are taken to use GSM output data for initialization of HOTMAC:

    1. Horizontal interpolations of wind components (u,v), temperature, mixing ratio, and geopotential height from GSM grid-points to HOTMAC grid points on constant pressure surface. Barnes' method (1964) is used for horizontal interpolation.

    2. Vertical interpolations of the variables from constant pressure to z^{*} surfaces at HOTMAC grid-points, using a linear interpolation method.

    Large scale variations of meteorological variables calculated in the above are incorporated into the model equations by a "nudging" or "Newtonian relaxation" method (Hoke and Anthes, 1976).

    By adding nudging terms, the equations of horizontal wind components are modified as:

$$\frac{\partial U}{\partial t}=F_1+C_n(U_t-U) \tag{3}$$

$$\frac{\partial V}{\partial t}=F_2+C_n(V_t-V) \tag{4}$$

The equations of potential temperature deviation and mixing ratio are written with nudging terms as:

$$\frac{\partial \delta\theta}{\partial t}=F_4+C_n(\delta\theta_{obs}-\delta\theta) \tag{5}$$

$$\frac{\partial q}{\partial t}=F_4+C_n(q_{obs}-q) \tag{6}$$

572

F_1, F_2, F_3 and F_4 are the terms found in HOTMAC equations (Yamada and Bunker, 1989). C_n is the nudging coefficient, and a constant value of 5×10^{-4} is employed. $\delta\theta$ is the deviation of potential temperature from an initial potential temperature, and q is water vopor mixing ratio. U_t and V_t are "target" wind components for the corresponding wind components U and V, respectively.

For a 12 hr forecasting, both the current analysis and the 12 hr forecast fields from GSM are analysed by the above method, and hourly data are generated by a linear interpolation between two time periods.

As shown schematically in Figure 1, the model starts spin-up computation four hours before the start of forecast initiation. At one hour before the initiation of forecast computation, the first hourly analysis fields data are read in and assimilated by using the nudging method for one hour. After that, the next hourly data are read in at one hour ahead of forecast time and assimilated for one hour. This process is repeated for entire 12 hour period.

3. TARGET WIND

Target wind components U_t and V_t are derived as follows: The equations of motion with the target wind under no frictional force can be written as,

$$\frac{\partial U}{\partial t} = f(V - V_g) + C_n(U_t - U) \tag{7}$$

$$\frac{\partial V}{\partial t} = -f(U - U_g) + C_n(V_t - V) \tag{8}$$

The solutions of the above equations at infinite time are given by

$$U = \frac{fC_n(V_t - V_g) + f^2 U_g + C_n^2 U_t}{C_n^2 + f^2} \tag{9}$$

$$V = \frac{-fC_n(U_t - U_g) + f^2 V_g + C_n^2 V_t}{C_n^2 + f^2} \tag{10}$$

Letting U and V approach to U_{obs} and V_{obs} respectively and solving for U_t and V_t, we obtain the following equations:

$$U_t = U_{obs} - \frac{f}{C_n}(V_{obs} - V_g) \tag{11}$$

$$V_t = V_{obs} + \frac{f}{C_n}(U_{obs} - U_g) \tag{12}$$

Here, U_{obs} and V_{obs} are the observed wind components, and U_g and V_g the geostrophic wind components. The formulas for U_g and V_g can be found in Yamada (1981) and Yamada and Bunker (1989). U_t and V_t are, in general, different from the corresponding large scale wind components. Observed winds may be used as target winds if the Coriolis force is absent or if the observed winds are identical to the geostrophic winds. In all other cases, if only the observed winds are used in the nudging, the solutions will generally be different from the observations.

The physical meaning of the target winds is that the solutions of the equations of motions with the target winds become identical to the observed winds in the absence of frictional effects. Thus, modeled winds should become in good agreement with observations in the layers above the boundary layer where frictional effects are negligible. In the boundary layer, on the other hand, frictional effects are significant due to atmospheric turbulence and the nudging terms play relatively minor roles. In summary, the nudging terms enforce the the modeled winds to match with observations in the free atmosphere, but they play relatively minor roles in the boundary layer.

Comparisons in the simulated wind fields found by nudging to the target wind components U_t and V_t and by nudging to the observed wind components U_{obs} and V_{obs} were conducted (Henmi and Yamada, 1993), and it was shown that nudging to the target wind components produced better agreement between simulated and observed upper winds than nudging to the observed wind components.

4. APPLICATION TO NEW MEXICO

This forecasting system has been operational over the domain covering the state of New Mexico since the spring of 1993. Figure 2 shows terrain elevation distribution in the area covering 950 km x 950 km. latitude and longitude of the southwest corner of the large area are, respectively, 32 N and 112 W. The area within the square covers 500 km x 500 km, and forecast computation has been conducted over this area. Meteorological variables are calculated at 51 x 51 x 21 grid points.

The output of GSM are reported on grid points spaced 381 km apart

apart on the mandatory pressure surfaces, as marked by * in the figure. Therefore, only a few grid points (2 points in this case) of GSM can be contained in a battlescale model domain. In order to cover this shortcoming, three-dimensional objective analysis of GSM output are made over the area covering 950 km x 950 km, and the data over 500 km x 500km are used for forecast computation.

Examples of forecast computation are shown in Figs.3 & 4 and Table-1. Forecast computation for this case was intialized at 1700 local standard time (l.s.t) of October 2 1993, and continued till 0500 1st of October 3 1993.

Figure 3 shows surface wind vector distribution at 0500 1st of October 3. Complicated wind vector distribution due to surface cooling can be depicted along slopes.

Vertical distributions of wind direction, speed, temperature, and dew point at White Sands Missile Range at 0500 of October 3 are shown in Figure 4. Temperature inversion, and wind direction shift in the boundary layer in early morning hour can be seen.

Table 1 shows temperatures, dew points, wind direction and speed at different pressure heights (surface, 850 mb, 700 mb, and 500 mb) at different locations (El Paso, WSMR, and Albuquerque) in the model domain.

5. IMPROVEMENTS AND FURTHER STUDIES

(A) Using all available observed meteorological data, forecast skill of the forecast system will be evaluated. Available data include upper and surface data taken at the NWS stations, and SAMS aand profiler data taken at WSMR.

(B) HOTMAC has a numerical scheme for nested grid(s) computation which allows interaction between a large scale and small scale grids. Currently, we are studying the feasibility of nested grid computation for operational use. When the computational speed of computer is upgraded, the nested grid model will be installed.

6. REFERRENCES

Barnes, S. L., 1964: A technique for maximizing details in numerical weather map analysis, J. App. Meteor. , 3, 396-409.

Dyer, A.J. and B.B. Hickes, 1970: Flux-Gradient Relationships in the Constant Flux Layer, Quart J. Roy Meteor. Soc., 96, 715-721.

Henmi,T. and T. Yamada, 1993: Simulation of the Project WIND Phase I Data: Application of the nudging method for incorporation of large-scale wind flow, submitted to Mon. Wea. Rev.

Hoke, J.E. and R.A.Anthes, 1976: The Initialization of Numerical Models by a Dynamic-Initialization Technique, Mon. Wea. Rev., 104, 1551-1556.

Mellor G. L., Yamada T., 1982: Development of a Turbulence Closure Model for Geophysical Fluid Problems, Rev Geoph. Space Phys., 20, 851-875.

Richtmyer, R. D. and K. W. Morton, 1967: Difference Methods for Initial-value Problems, Second Ed., Interscience Publishers, J. Wiley and Sons, New York, 405 pp.

Yamada, T., 1982: A numerical model study of turbulent airflow in and above a forest canopy, J. Meteoro. Soc. Japan, 60, 439-454.

Yamada, T. 1983: Simulations of Nocturnal Drainage Flows by a $q^2 l$ turbulence closure model, J. Atmos. Sci., 40, 91-106.

Yamada T. and S. Bunker, 1988: Development of a Nested Grid, Second Moment Turbulence Closure Model and Application to the 1982 ASCOT Brush Creek Data Simulation, J. of Appl. Meteor., 27, 562-578.

Yamada T. and S. Bunker, 1989: A Numerical Study of Nocturnal Drainage Flows with Strong Wind and Temperature Gradients, J. Appl. Meteor., 28, 545-554.
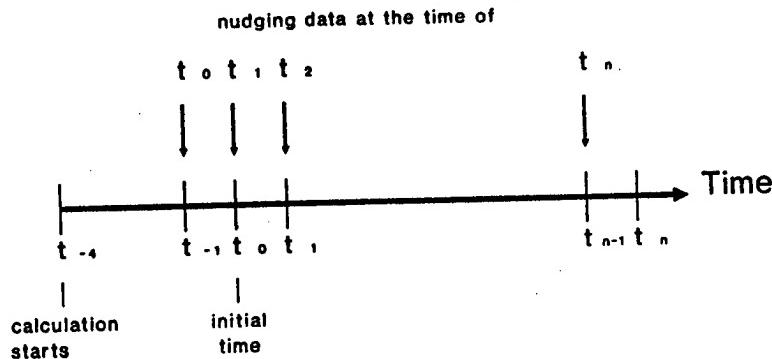
Figure 1. Schematic diagram showing model the timings of model initialization and nudging of GSM data.

CONTOUR FROM 400.00   TO 4000.0   CONTOUR INTERVAL OF 200.00   PT(3,3)= 1194.0
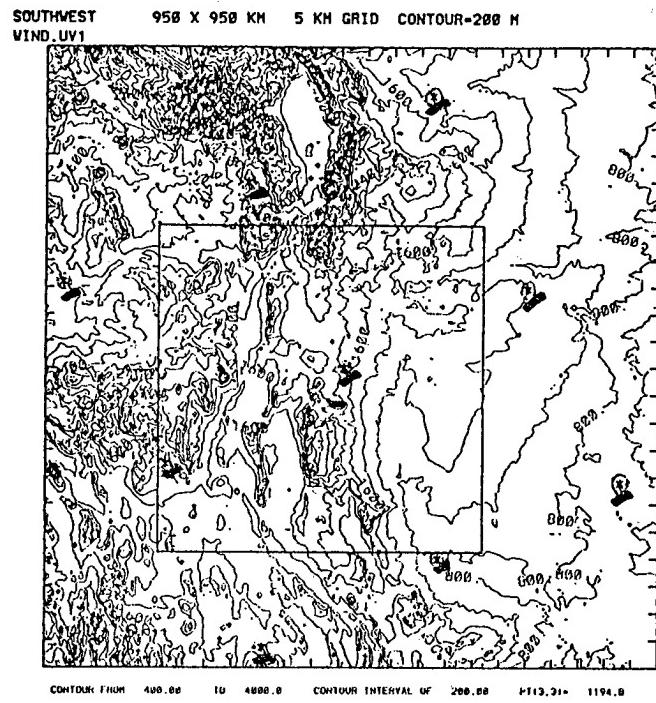
Figure 2. Model domain and locations of GSM grids (marked by *) over terrain elevation contours. Large area covers 950 km x 950 km, and small area 500 km x 500 km.

CONTOUR FROM 600.00   TO 3400.0   CONTOUR INTERVAL OF 200.00   PT(3,3)= 1524 MAXIMUM VECTOR
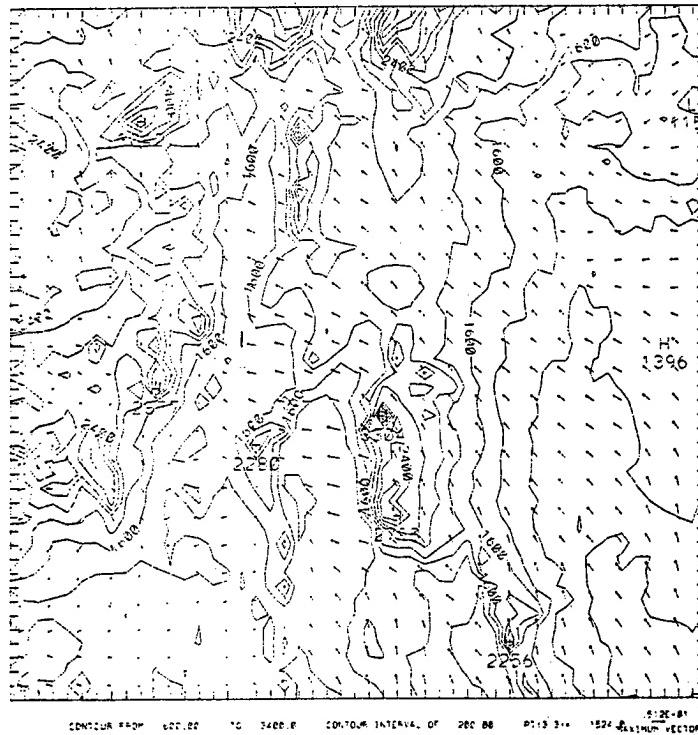
Figure 3. Surface wind vector distribution over model domain, 12 hour forecast at 0500, October 03 1993.
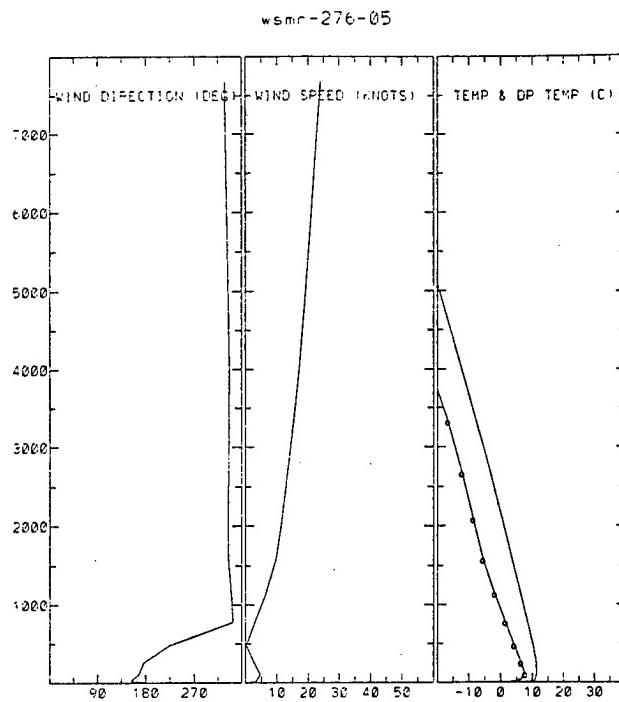
Figure 4. Vertical distributions of wind direction and speed, temperature, and dew point, 12 hour forecast at 0500, October 03 1993.

	ELPS	WSMR	ALBQ
Temp. (F) at Surface	40.2	40.0	38.0
Temp. (F) at 850 mb	53.2	52.1	*****
Temp. (F) at 700 mb	36.3	35.8	37.3
Temp. (F) at 500 mb	4.1	4.1	5.7
R. H. (%) at surface	59.5	58.6	20.8
R. H. (%) at 850 mb	75.5	73.1	*****
R. H. (%) at 700 mb	51.2	50.7	32.2
R. H. (%) at 500 mb	45.5	44.8	29.0
W.S, (kts) at surface	4.4	3.1	6.2
W.D, (deg) at surface	154.5	178.3	118.4
W.S, (kts) at 850 mb	5.7	3.4	*****
W.D, (deg) at 850 mb	198.6	162.7	*****
W.S, (kts) at 700 mb	9.5	10.3	9.5
W.D, (deg) at 700 mb	334.6	337.2	296.9
W.S, (kts) at 500 mb	17.9	18.0	12.1
W.D, (deg) at 500 mb	332.9	336.1	354.8

Table 1. Forecast temperature, relative humidity, wind direction and speed at different pressure levels at different locations, 12 hour forecast at 0500, October 03 1993.

Session II Posters

SIMULATION AND MODELING

Thermal Properties of Soils

Henry Rachele, Frank V. Hansen, Arnold Tunick
Battlefield Environment Directorate
US Army Research Laboratory
White Sands Missile Range, NM 88002-5501

Lisa Manguso
New Mexico State University
Las Cruces, NM 88003

Abstract

Semi-empirical formulations are presented that were designed for
estimating the volumetric heat capacity, thermal conductivity, and
thermal diffusivity of soils. The soil classifications used are
based on the United States Department of Agriculture textural
scheme, which, in turn, is related to more basic soil taxonomy
definitions. The equations that evolved are basic, and hence are
suitable for general applications, even though they were designed
for use in an energy balance model. The energy balance model, in
turn, is used to produce estimates of sensible and latent heat
fluxes used for estimating atmospheric turbulence effects on
optics and acoustics in the planetary boundary layer.

1. Introduction

The formulations presented in this paper are patterned after
material presented in Campbell (1985). Material on soils and their
classification is based on a number of publications as referenced below.
Soil classification systems can be traced back to the Great Soils Groups
of the late 19th century. In the United States this initial scheme has
evolved into a six category ranking labeled as order, suborder, great
group, subgroup, family and series, and is known as the soil taxonomy
system and is the worldwide standard. The basic taxonomy classifications
have been established by the US Department of Agriculture's Soil
Conservation Service (SCS) (1960, 1967, 1975) and is a ten category
scheme. The United Nations through its Food and Agriculture Organization
(FAO) and the United Nations Economic, Social, and Cultural Organization
(UNESCO) has also developed a universal world wide soils order scheme
based upon the SCS soils taxonomy. A cross-classification method between
the two soil taxonomies has been suggested by Hansen (1993), fig. 1a.
Included in Hansen's scheme are the relationships between the FAO-UNESCO
soil orders and the SCS textural classes, fig. 1b, which we shall use in
this effort.

FIGURE 1a. Cross-classification system between FAO-Unesco
soils categories and USDA classifications (Hansen, 1993)
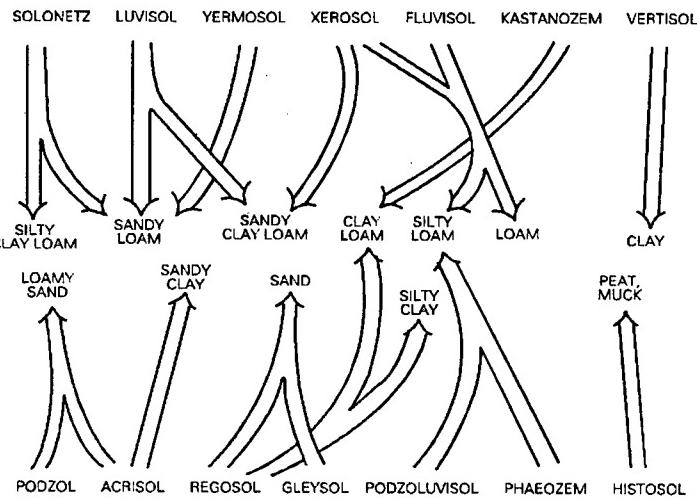
FIGURE 1b. Cross-classifications between FAO-UNESCO
soil categories and SCS textural classifications. (Hansen, 1993)

582

The textural class approach is the easiest to understand and use, since soils are classified according to the percentages of sand, silt, and clay that make up the individual soils. The SCS classification scheme, alternatively, is based on particle size (diameter, d) and not on chemistry such that:

Clay	$d < 0.002$ mm
Silt	$0.002 \le d < 0.05$ mm
Sand	$0.05 \le d < 2.0$ mm

Table 1 gives approximations of the volume fraction of sand, ϕ_{sd}, silt, ϕ_{st}, and clay, ϕ_c, that make up the soil types using the textural class approach. The values in table 1 come from the Soil Conservation Service's soils textural triangle, figure 2.

TABLE 1
Volume Fractions of sand, silt, clay
for each of the 12 textural classes of soils

Soil Type	ϕ_{sd}	ϕ_{st}	ϕ_c
Loam	0.40	0.40	0.20
Sand	0.90	0.06	0.04
Silt	0.01	0.93	0.06
Loamy Sand	0.82	0.08	0.10
Sandy Loam	0.60	0.26	0.14
Silty Loam	0.20	0.70	0.10
Silty Clay Loam	0.10	0.56	0.34
Clay Loam	0.32	0.35	0.33
Sandy Clay Loam	0.57	0.16	0.27
Sandy Clay	0.52	0.06	0.42
Silty Clay	0.06	0.47	0.47
Clay	0.25	0.20	0.55

The volumetric specific heat of soil materials are patterned after DeVries (1963) as shown in table 2, from Campbell (1985).

TABLE 2
Thermal Properties of soil materials (after DeVries, 1963 and Campbell, 1985)

Material	Density Mg m^{-3}	Specific heat J g^{-1} K^{-1}	Thermal Conductivity W m^{-1} K^{-1}	Volumetric sp. heat MJ m^{-3} K^{-1}
Quartz	2.66	0.80	8.80	2.13
Clay minerals	2.65	0.90	2.92	2.39
Organic Matter	1.30	1.92	0.25	2.50
Water	1.00	4.18	0.57	4.18
Air (20 °C)	0.0012	1.01	0.025	0.0012
Ice	0.92	1.88	2.18	1.73

Fig. 2 USCS soil textural class triangle. Each of the 12 textural classes is defined by the percentages of grain sizes within a given soil
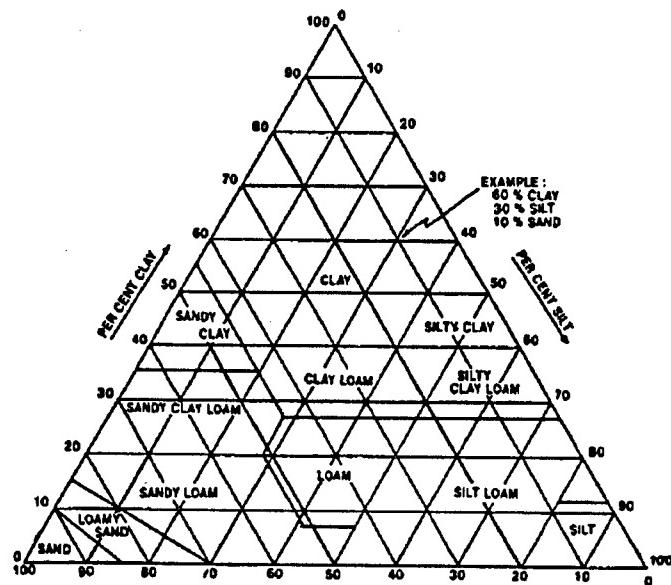
The basic form of the thermal conductivity of soil depends on its bulk density, water content, quartz content and organic matter. For soils of low water content sand, silt, and forest litter all have similar thermal conductivities. For soils with high water content the thermal conductivity of the solid phase becomes more important. For most soils the thermal conductivity changes rapidly and non-linearly with increase of water content, until, at higher water contents the changes of thermal conductivity with water content is strongly linear. The volumetric water content for soils for the three cases of saturation, field capacity, and wilting point is shown in fig. 3 (Hansen, 1993).

Fig. 3. Volumetric water content for soils for cases of saturation, field capacity, and wilting point (from Hansen, 1993)

584
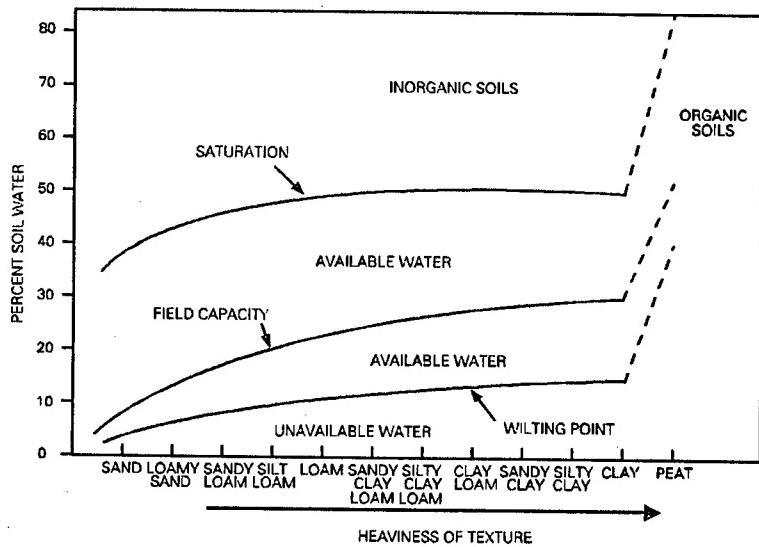
Saturation is defined as the condition where all air spaces within the soil are filled with water. At saturation, water content is the same value as porosity for the given soil. Wilting point is a function of the soil moisture tension and is the amount of water in the soil below which plants are unable to draw moisture from the soil (Van Wijk and DeVries, 1963).

2. Equations for Volumetric Specific Heat

We write the equation for volumetric specific heat of soil as:

$$C = C_{sd}\rho_{sd}\phi_{sd}\phi_s + C_{st}\rho_{st}\phi_{st}\phi_s + C_c\rho_c\phi_c\phi_s$$
$$+ C_o\phi_o\rho_o + C_w\rho_w\phi_w + C_a\rho_a\phi_a \tag{1}$$

where:

C=volumetric specific heat
C_{sd}=specific heat of sand
ρ_{sd}=density of sand
ϕ_{sd}=volume fraction of sand
ϕ_s=volume fraction of sand plus silt plus clay
C_{st}=specific heat of silt
ρ_{st}=density of silt
ϕ_{st}=volume fraction of silt
C_c=specific heat of clay
ρ_c=density of clay
ϕ_c=volume fraction of clay
C_o=specific heat of organic matter
ρ_o=density of organic matter
ϕ_o=volume fraction of organic matter
C_w=specific heat of water
ρ_w=density of water
ϕ_w=volume fraction of water
C_a=specific heat of air
ρ_a=density of air
ϕ_a=volume fraction of air

Since $C_{sd} = C_{st}$, $\rho_{sd}=\rho_{st}$ and $C_a\rho_a\phi_a$ is very small compared to the other terms of eq (1), we can write:

$$C = C_{sd}\rho_{sd}\phi_s(\phi_{sd} + \phi_{st}) + C_c\rho_c\phi_c\phi_s + C_o\phi_o\rho_o + C_w\rho_w\phi_w \tag{2}$$

For any given soil, C is a function of ϕ_s, ϕ_o, and ϕ_w since ϕ_{sd}, ϕ_{st}, and ϕ_s are known, and $C_{sd}\rho_{sd}$, $C_c\rho_c$, $C_o\rho_o$ and $C_w\rho_w$ are fairly well known, see table 2.

Hence, we can write:

$$C = f(\phi_s, \phi_o, \phi_w) \tag{3}$$

Figure 4 shows how the volumetric heat capacity, C, varies as a function of water content, ϕ_w, for different values of ϕ_s and ϕ_o for loam soil. Other soils produce similar curves. We found when examining figure 4 that C varies linearly with ϕ_w, so that for a given value of ϕ_s a family of curves resulted by varying ϕ_o. Since C is a linear function of ϕ_w we can write:

$$C = a + b\phi_w \tag{4}$$

where:
$$a = f_a(\phi_s, \phi_o) \tag{5}$$
and:
$$b = f_b(\phi_s, \phi_o) \tag{6}$$

We found that for different soils "a" was a linear function of ϕ_s and ϕ_o. The coefficients of ϕ_s and ϕ_o have very small variations for the soils considered, so we used average values of 2.195 and 2.496 respectively as the coefficients in our final equation. In determining "b" we found it to be uniformly 4.18 in all cases. Hence, eq (4) can be written as:

$$C = 2.195 \, \phi_s + 2.496 \, \phi_o + 4.18 \, \phi_w \tag{7}$$

These results, equation 7, are significant, showing that the volumetric specific heat can be computed for any of the 12 soil types.

Fig. 4. Volumetric specific heat for loam soil where $\phi_s = .5$ for solid lines and $\phi_s = .7$ for dashed lines.
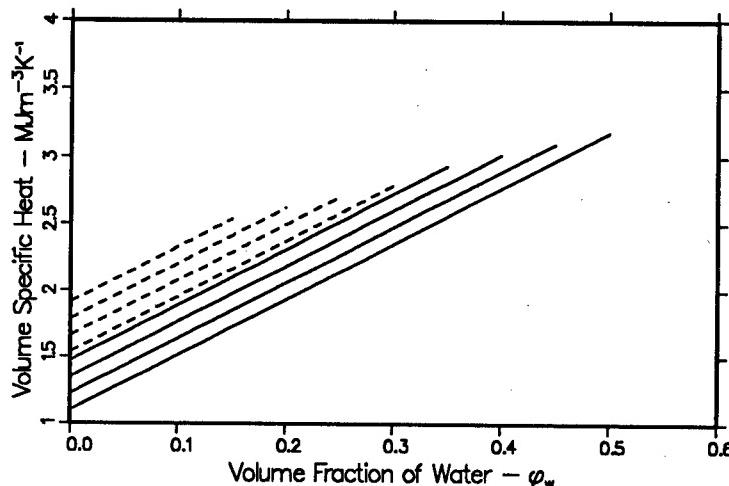
3. Thermal Conductivity Equation

The equation we selected for computing thermal conductivity is presented in Campbell (1985). The constants A, B, C, and E were determined by McInnes (1981), and D was determined by DeVries (1963). We found it necessary to make a few notation changes so that the thermal constants symbols are consistent with the volumetric heat formulations. The modified thermal constant expression is

$$k_s = A + B\phi_w - (A-D) \, e^{(-(c\phi_w)^E)} \tag{8}$$

where:

$$A = \frac{(0.57 + 1.73\phi_q + 0.93\phi_m)}{(1.0 - 0.74\phi_q - 0.49\phi_m)} - 2.8\phi_s^*(1.0 - \phi_s^*) \tag{9}$$

586

$$B = 2.8 \phi_s^*$$ (10)

$$C = 1.26 \phi_c^{-1/2}$$ (11)

$$D = 0.03 + 0.7 \phi_s^{*2}$$ (12)

$$E = 4.0$$

$\phi_c = \phi_m = \phi_s (1.0 - \epsilon)$
ϵ = percentage of ϕ_s (in decimal) quartz
ϕ_q = volume fraction of quartz = $\epsilon \phi_s$
ϕ_s = volume fraction of sand, silt, and clay
$\phi_s^* = \phi_q + \phi_m + \phi_o$
ϕ_w = volume fraction of water
ϕ_o = volume fraction of organic material

In order to evaluate eq (8) one must know the volume fraction of quartz in addition to the volume fraction of sand, silt, and clay for a given soil. The volume fractions ϕ_s and ϕ_o must be consistent with values used to compute the volumetric specific heat.

Figures 6a through 6e show computed thermal conductivities compared to available data. It must be noted here that data containing thermal conductivities of textural class soils is rare or not easily accessible. Thermal conductivity data for soils with measured quartz content is even harder to find.

4. Thermal Diffusivity Equation

In accordance with Campbell (1977) we compute the thermal diffusivity as the ratio of thermal conductivity to the volumetric specific heat, ie.

$$K = \frac{k_s}{VSH}$$ (13)

5. Units

From table 2 we note that density has units of Mg m^{-3}, specific heat as J g^{-1} K^{-1}, thermal conductivity as W m^{-1} K^{-1}, and volumetric specific heat as M J m^{-3} K^{-1}, where:

M = mega, or 10^6
g = grams
m = meters
J = Joules
W = Watts
K = degrees Kelvin
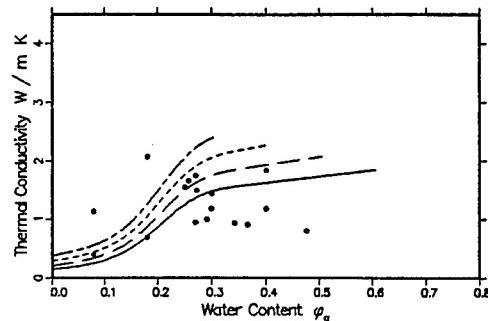
(6 a)
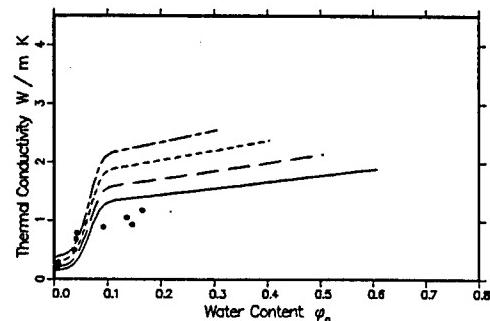
(6 b)
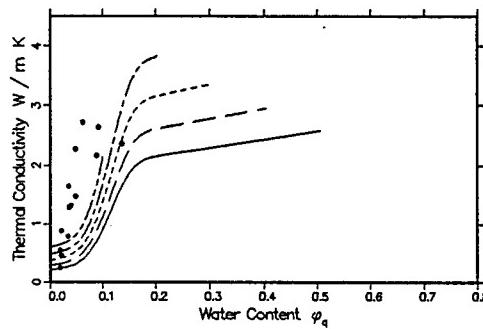
(6 c)
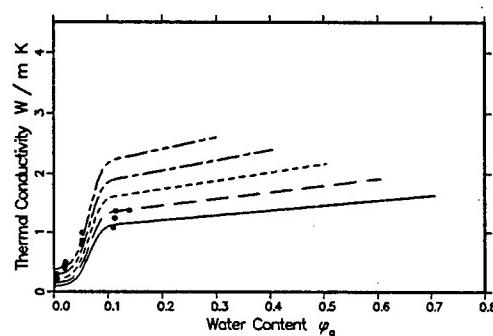
(6 d)

Figure 6
Comparisons of modeled values of thermal conductivity vs.
data. Mulitple line indicate varying values for ϕ_s, volume
fraction of solid material.
a) clay: $\phi_q=0$; b) sand: $\phi_q=0.75$;
c) sandy loam: $\phi_q=0.6$
d) sand: $\phi_q=0.12$
(data points from Farouki, 1982)
e)clay: unknown quartz content
(data points from Ingersoll, 1988, Jumikis, 1977)
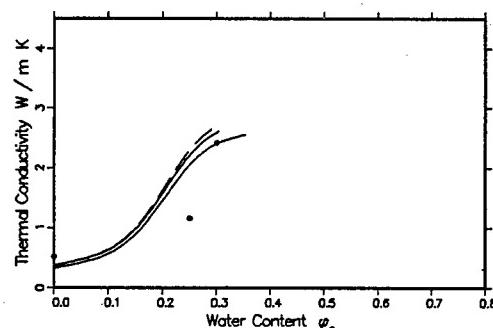
(6 e)

Since the thermal diffusivity is computed from eq. (13) the units of K
are:

$$\frac{Wm^{-1}K^{-1}}{MJm^{-3}K^{-1}} = Wm^2 M^{-1} J^{-1} \tag{14}$$

Since $W = J\ s^{-1}$, then the units of K can be written as $M^{-1}\ m^2\ s^{-1}$, when
using the values in table 2. The basic units, however, are $m^2\ s^{-1}$. For
some applications we have required the diffusivity in m^2hr^{-1}. This can be
obtained by multiplying $M^{-1}m^2s^{-1}$ by 3600.

588

6. Model Evaluation

Campbell (1985) presents thermal conductivity, k_s, as a function of volumetric water content, ϕ_w, for sand, silt loam, and forest litter, see fig. 7. The sand case was defined for $\phi_q = 0.3$, where $\phi_s = 0.6$, and silt loam as $\phi_q = 0$ with $\phi_s = 0.47$.

In Campbell (1977) thermal diffusivity, K, is also presented as a function of ϕ_w, see fig. 8. Two of the curves show the variation of K for sand where $\phi_s = 0.60$ and 0.40. One curve shows the variation of K for clay where $\phi_s = 0.40$. The last curve is for peat.
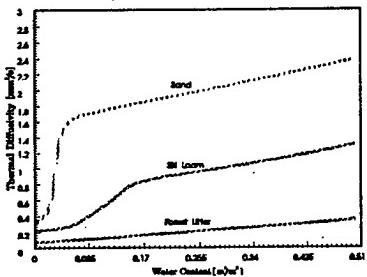
Figure 7. Thermal conductivity of sand, silt loam and forest litter (after Campbell, 1985).
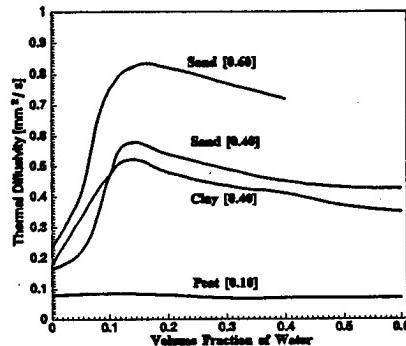
Figure 8. Thermal diffusivity curves for sand, clay, and peat (after Campbell, 1977)

The equations for thermal conductivity, k_s, presented in this report were used to compute values for the same cases as shown in figure 7. Figure 9 shows our computed values for thermal conductivity superimposed on Campbell's values.
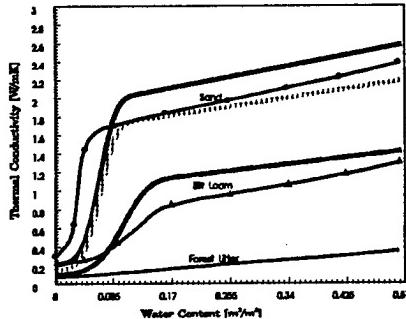
Figure 9. Computed values of thermal conductivity superimposed on Campbell's curves from figure 8.

CONCLUSIONS

To the best of our knowledge, the relationships between soil taxonomies and textural classes in figures 1a and 1b and the expression for volumetric specific heat given in equation 7 are unique and original. The equations used in this modeling attempt give us the best fits for soil thermal constants which are fundamental in engineering approximations of the soil heat flux portion of the Rachele-Tunick (1993) radiation and energy balance model. Data needed to fully evaluate the thermal constants for the various soils are far from complete. Nevertheless, for those limited cases used in this study we found

reasonable agreement between data and formulations developed in this
paper. A particular problem surfaces when trying to evaluate the effects
of quartz on thermal conductivity since quartz content of soils does not
seem to be a routine measurement taken in energy balance and
meteorological field tests. As such, the equations used in this model
are subject to refinement as additional data become available.

REFERENCES

De Vries, D.A. 1963. "Thermal Properties of Soils" in Physics of the
Plant Environment. Ed. W.R. Van Wijk. North-Holland Publishing Co.,
Amsterdam.

Campbell, Gaylon S. 1977. An Introduction to Environmental Biophysics.
Springer-Verlag, New York.

Campbell, Gaylon. S., 1985. Soil Physics with Basic - Transport Models
for Soil-Plant Systems, Elsevier Science Publishing Co. Inc. New York.

Farouki, Omar, 1982. Evaluation of methods for calculating soil thermal
conductivity. CRREL Report 82-8. US Cold Regions Research and
Engineering Laboratory. Hanover, NH.

Hansen, F. V., 1993. Soils, Internal Report (in publication), US Army
Research Laboratory Battlefield Environment Directorate, White Sands
Missile Range, NM 88002-5501.

Ingersoll, J. G., 1988. 'Analytical Determination of Soil Thermal
Conductivity and Diffusivity," in Transactions of the ASME: Journal of
Solar Engineering. Vol. 110. pp. 306-12.

Jumikis, Alfreds R., 1977. Thermal Geotechnics. Rutgers University
Press, New Brunswick, NJ.

McInnes, K.J., 1981. Thermal conductivites of soils from dryland wheat
regions of Eastern Washington. M.S. Thesis, Washington State University,
Pullman.

Soil Conservation Service, 1960, Soil Classification, A Comprehensive
System, Seventh Approximation, U.S. Department of Agriculture,
Washington, D.C.

Soil Conservation Service, 1967, Soil Survey Laboratory Methods and
Procedures for Collecting Soil Samples, U.S. Department of Agriculture,
Washington, D.C.

Soil Consevation Service, 1975, Soil Taxonomy = A basic system of soil
classification for making and interpreting soil surveys, U.S. Department
of Agriculture, Washington, D.C.

Van Wijk, W.R. and D.A. De Vries, 1963. "The Atmosphere and the Soil" in
Physics of the Plant Environment. Ed. W.R. Van Wijk. North-Holland
Publishing Co., Amsterdam.

MADONA: AN INTERNATIONAL HIGH-RESOLUTION METEOROLOGY AND DIFFUSION FIELD STUDY

Ronald M. Cionco   and   John H. Byers
US Army Research Laboratory
Battlefield Environment Laboratory
White Sands Missile Range, NM 88002

ABSTRACT

The multi-nation, high-resolution, meteorology and diffusion field study over non-uniform areas (MADONA) was conducted by scientists from the United States, United Kingdom, Germany, Denmark, Sweden, and The Netherlands at Porton Down, near Salisbury, Wiltshire, UK during September and October 1992. MADONA was composed of meteorological data collection and diffusion experiments using smoke, sulphurhexaflouride (SF_6), and propylene gas during unstable, neutral, and stable atmospheric conditions in an effort to obtain terrain-influenced meteorological fields, dispersion, and concentration fluctuation measurements using specialized sensors and tracer generators. Thirty-one days of meteorological data were collected during the period 7 September through 7 October and 27 diffusion experiments were conducted from 14 to 23 September 1992. Puffs and plumes of smoke and SF_6 were released simultaneously for most of the experiments to gauge the resultant diffusion and concentration behavior. Simulations of airflow and diffusion over the MADONA topography were made with a variety of models. In particular, wind fields and wind-related parameters were simulated with BED's high resolution wind model. A tally of the various data gathering activities indicates that the execution of MADONA was highly successful. Preliminary use of the data sets is showing the high quality and depth of the MADONA data base.

1. INTRODUCTION

During September and October 1992, scientists from six nations conducted a field study[1] of high-resolution Meteorology And Diffusion Over Non-uniform Areas (MADONA) in the south of England. MADONA was composed of meteorological data collection and diffusion experiments using smoke, sulphurhexaflouride (SF_6), and propylene gas during unstable, neutral, and stable atmospheric conditions in

an effort to obtain terrain-influenced meteorological fields, dispersion, and concentration fluctuation measurements.

Scientists from the United States, United Kingdom, Germany, Denmark, Sweden, and the Netherlands joined together to design and conduct a series of meteorological studies and diffusion experiments. The primary goal was to collect a comprehensive high-resolution data base using specialized sensors and tracer generators for model evaluation.

The following organizations participated in MADONA: US Army Research Laboratory (formerly the Atmospheric Sciences Laboratory), USA Dugway Proving Ground, UK Chemical and Biological Defence Establishment, UK Meteorological Office, UK University of Manchester Institute of Science and Technology, German Military Geophysical Office, German Aerospace Research Establishment, German WWDBW at Munster, Denmark's Riso National Laboratory, Sweden's National Defence Establishment, and The Netherlands' TNO Defence Research Establishment.

A portion of the MADONA data base is used herein to provide exposure to the data base as well as a general analysis of the effect of variable terrain on wind flow and transport and diffusion during changing atmospheric stability conditions. The influence of meso- and microscale flows on the wind field, temperature, turbulence, and the mixed layer will also be examined during the course of our studies. These interactions are crucial for predicting and understanding the meteorology, transport, and diffusion in complex terrain domains.

2. THE MADONA FIELD STUDY

2.1 SITE DESCRIPTION

The MADONA field site is located at the Chemical and Biological Defence Establishment (CBDE) on Porton Down, near Salisbury, Wiltshire, UK (Fig 1 inset). The topography of the area is gently rolling terrain with a ridge running southwest to northeast with higher terrain at each end. Battery Hill is located to the southwest of the ridge and Tower Hill is to the northeast. Directly to the west of the ridge is the lowland area of the Bowl where most experiments were conducted. Total relief for the test area is 100 meters ranging from 80 meter northwest of the Bowl and to 180 meters near the Breck east of the Bowl. Figure 1 provides a view of the geography of the field study domain while Figure 2 depicts the topography, from digitized elevation data, for CBDE proper.

2.2 FIELD STUDIES AND EXPERIMENTS

Thirty one days of meteorological data were collected during the period 7 September through 7 October. Nine days of diffusion experiments were conducted from 14 to 23 September 1992 consisting of 27 different configurations. More intense and detailed fast

Figure 1.

Geographic location of CBDE
(■ denotes location of
  Salisbury, England)
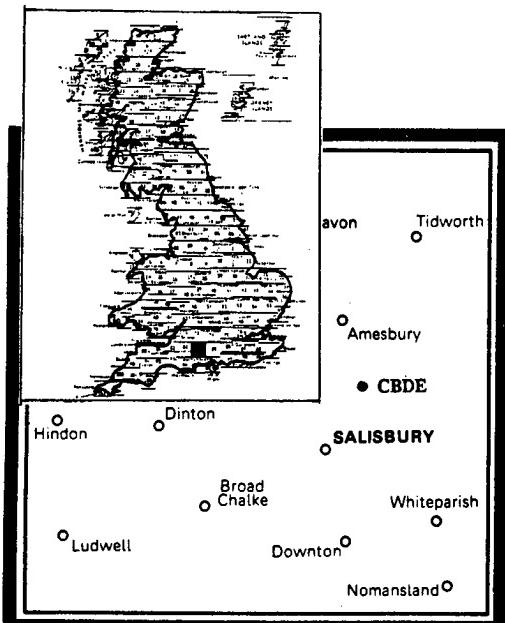
Figure 2

MADONA topography, Porton Down
5 Km x 5 Km
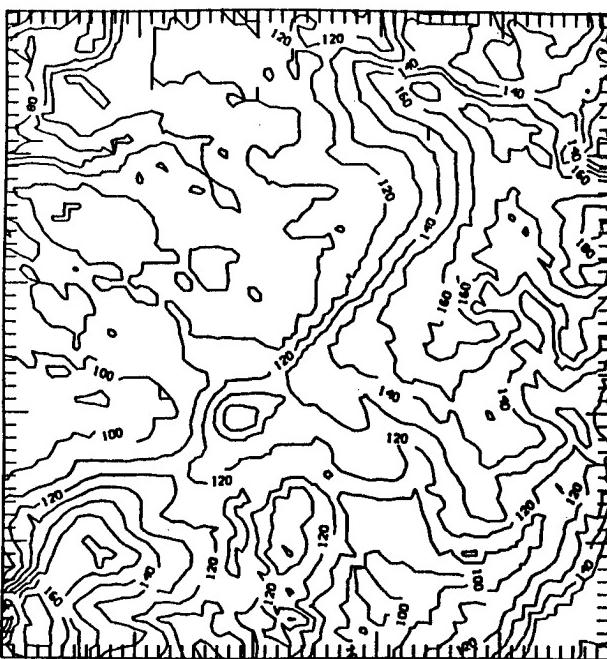
response micrometeorological data sets were collected during the study period to complement the diffusion data base. Traditional upper air and weather station measurements as well as synoptic charts were also archived during the experimental days. Each day, smoke and gas tracers were released during a four hour time frame as the atmosphere evolved from unstable afternoon to neutral and then to stable evening conditions. Eighty-four (84) instantaneous puffs and eight continuous releases were made in a complementary manner to suit the test conditions.

2.3 DAILY WEATHER DESCRIPTION

Daily weather conditions during the study period were generally partly cloudy to overcast skies with the majority of the trials having winds of 5 m/sec or less. Three experiments were conducted with wind speeds of 5 to 10 m/sec as well. Wind directions were mostly from the southwest, next southeasterly, once from the northwest and once from the east. Temperatures were mainly in the 10 to 15 Centigrade range. Synoptically, fast moving troughs passed through the area almost on a daily basis occasionally giving way to high pressure influences from the continent. Light rain occurred once during the experiments while thunderstorms came quite close on another occasion. In general these conditions did not halt our studies. We were unable to release smoke and tracers for only one experimental day (#4) because of weather, i.e. prolonged unsteady wind direction conditions.

2.4 FIELD SENSORS AND EQUIPMENT

High resolution and standard microscale, boundary layer, and synoptic meteorological sensors and equipment were deployed along with fast response concentration and diffusion real-time detectors and sensors. Table 1 lists the field equipment, sensors, and techniques that were used during the study.

TABLE 1.

Type of equipment and sensors used during MADONA.

NR	TYPE	HEIGHT	LOCATION
METEOROLOGICAL SENSORS:			
15	Wind Speed/Direction sets	10 m	Multiple sites
1	Weather Station system:	2-10 m	Met Field
	WS, WD, T, P, HUM, RAD, PREC	10 m	
1	Upper Air system	to 500 mb	Larkhill site
1	Boundary Layer Sonde,	to 500 mb	B C* Road site
	with two level temp & wind	2 & 10 m	
1	Doppler Sodar,	to 300 m	B C* Road site
1	WS/Wdir 2-level tower	10 & 30 m	Tower #2, Bowl
2	Sonic Anemometer/Thermometer	7 m	B C* Road site
2	Sonic Anemometer/Thermometer	2,4,6,8 m	Stop Butt site
	Profile system		HS site
1	Sonic Anemometer/Thermometer	2 m	Met Field
1	Temperature Profile system	0.5,2,4,6,8 m	Stop Butt site
1	Fiber Optics Quartz Thermo-meter Profile system	2,4,6,8 m	HS site
DIFFUSION SENSORS AND EQUIPMENT:			
1	Smoke Plume generator	1 m	Numerous sites
1	Smoke Puff 'generator'	2.3-3 m	Numerous sites
1	SF6 Source with plume/puff	1 & 3 m	Numerous sites
1	Propylene Gas source	0.5-2 m	Met Field
1	LIDAR,	1 m	Bowl sites
1	Visio-ceilometer	1 m	Bowl sites
1	LIDAR, RASCAL system	2 m	Bowl sites
1	SF6 Flame Photometer system	1 m	Mobile in Bowl
1	UVIC system, 5 sensors	2 m	Met Field
1	Video Imaging system	1.5 m	Numerous sites
1	Aerial camera system (aircraft)	var.	Airborne
SURVEY DEVICE:			
1	GPS site survey system	Hand-held	All sites

* B C means Bursting Chamber (Road Site)

594

2.5 METEOROLOGICAL STUDIES

Meteorological studies of the following nature were conducted: a.) to document the behavior of the horizontal and vertical structure of the boundary and surface layers of the study domain on the synoptic, mesoscale, microscale, and the turbulence scale as a function of time and space; b.) to characterize the terrain effects upon the boundary layer meteorology occurring during experimental periods; and c.) to run real-time, high-resolution simulations on-site during each of the experimental days.

Meteorological measurements collected during the field study documented the time histories and diurnal cycles of local variations of the synoptic variables, the vertical structure of the boundary layer, and the horizontal wind speed and direction. Figure 3 locates the sites of various meteorological sensors. This spatial placement of the 14 surface stations (M1-8 & 10-14) insured that microscale motions could be resolved and documented and that these data would be usable to support model simulation, test, and comparisons along with the other measurements. A fifteenth wind set (M-9) was installed at 30m on Tower 2 to provide dual measurements at 10 and 30m. Other sensors such as sonic anemometers (S), doppler sodar (D), and the boundary layer sonde (B) were clustered in the plume transport domain. Figure 4 presents a time history of wind speed and direction measurements made at the M-1 station on CBDE. Plotted are wind speed, wind direction, and their standard deviations from 1100, JD265 to 1400, JD266.

Figure 3	Figure 4
Locations of meteorological sites	Time history of M-1 wind speed & direction and their standard deviations
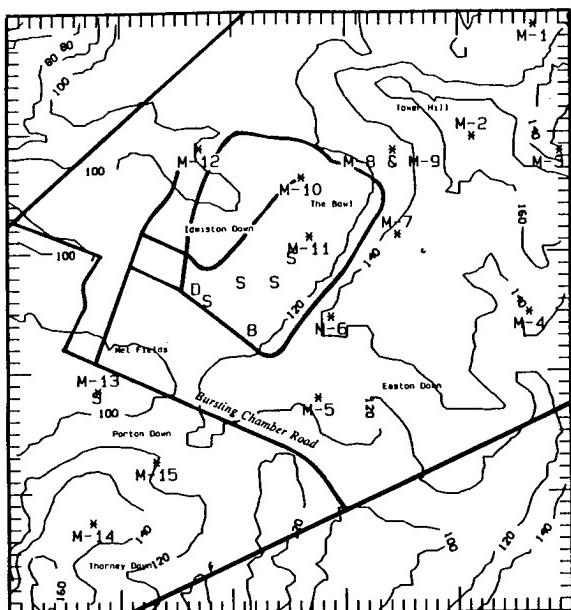
595
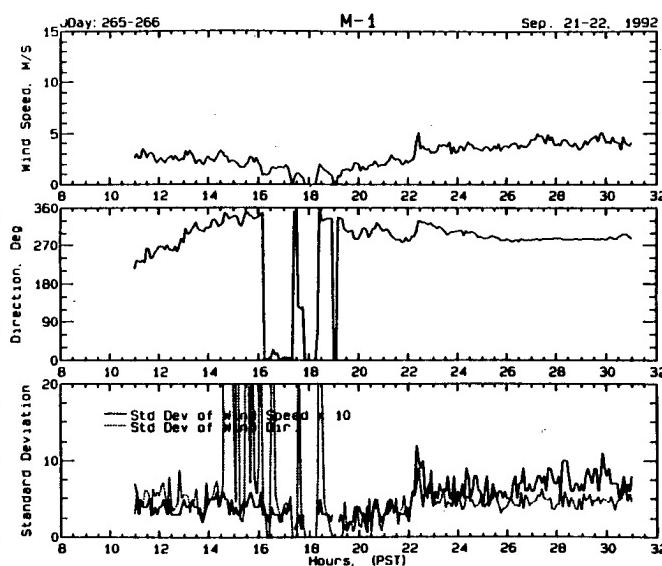
Measurements of the horizontal mean wind fields of station M-1 depict the spatial variability of the wind direction and speed in Figure 5 for a specific period, Julian Day 265, HR 2240. An example of a wind rose of wind direction and speed for one station is presented in Figure 6 from the measured speed and direction data. Figure 7 provides calculated values of the resultant mean wind speed and direction, temperature, friction velocity, virtual temperature, heat flux, the turbulent kinetic energy, and the Obukov length based upon turbulence measurements of u,v,w, and temperature using 3-D sonic anemometer-thermometer single level units. Note that the vertical lines and bars indicate the start, occurrence, and stop of puff and plume release periods between 1200 and 1830 hours. Vertical profiles of wind speed and temperature from other sonics systems at two different sites (Stop Butt and HS) in the plume travel area produces vertical structures such as those given in Figure 8.

Figure 5
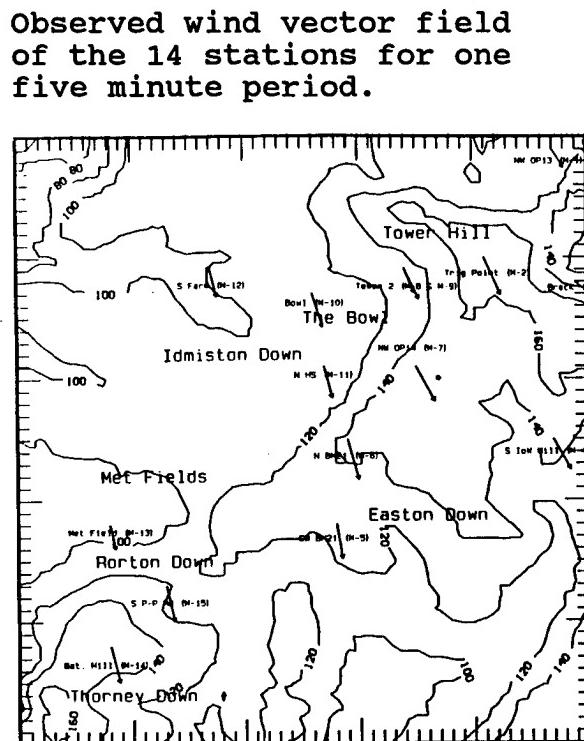
Observed wind vector field
of the 14 stations for one
five minute period.

Figure 6

Wind rose derived from
observed speed & direction.

596
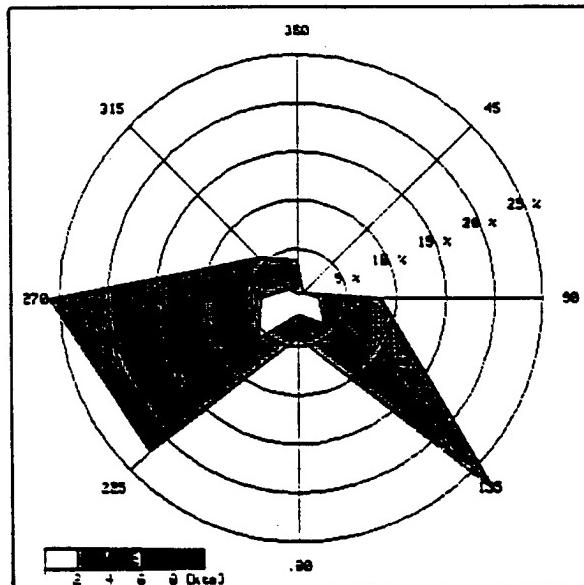
Figure 7

Micrometeorological parameters
calculated from the observed
sonic anemometer data at a
single level

Figure 8

Mean temperature and wind
vertical profiles from the
sonic anemometer profile
tower at Stop Butt
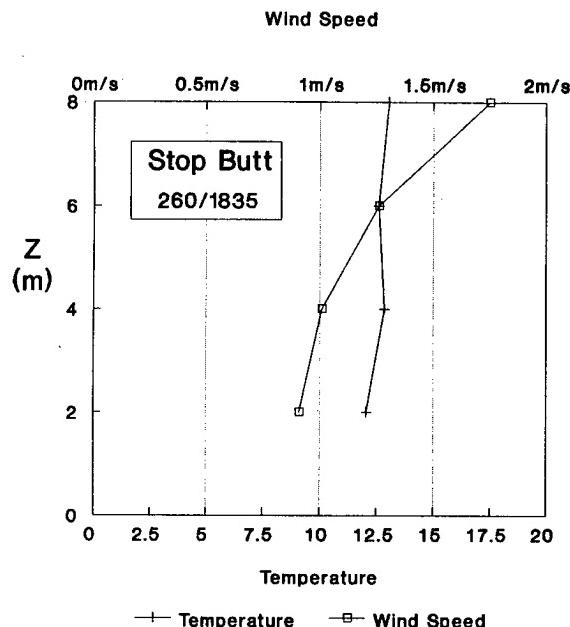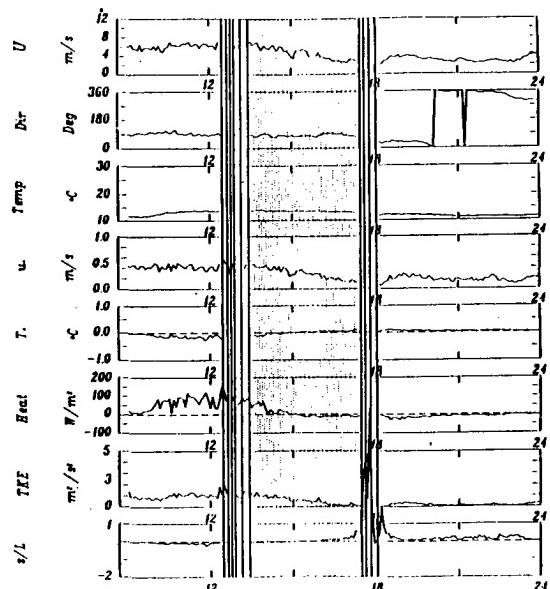
2.6 DIFFUSION AND CONCENTRATION FLUCTUATION EXPERIMENTS

Puffs and plumes of smoke and SF_6 were released separately and simultaneously for these experimental activities. In the Met Field some distance from the smoke generators, propylene gas was also disseminated up to distances of 500 m for detection of the gas ions and for the measurements of these concentrations.

2.7 PLUME AND PUFF BEHAVIOR

Both continuous and instantaneous plumes were released during the experiments to gauge the diffusion behavior and complement each others efforts. Plumes were generated by mixing measured amounts of ammonium hydroxide and silicon tetrachloride to make a dense, white cloud of ammonium chloride and silicon dioxide. Figure 9 shows an aerial view of a continuous smoke plume. Mixing these two materials by explosive means generated puffs of discrete size and duration. Figure 10 is also aerial view of a smoke puff detached from its source. SF_6 gas was also mixed with the plumes and puffs for a reference to the smoke measurements. A second example of a puff at ground level is shown exhibiting some shear in its vertical dimension in Figure 11.

597

Figure 9   Figure 10

Example of continuous smoke   Example of an instantaneous
plume traversing the Bowl   smoke puff detached from the
area (aerial view)   source point (aerial view)
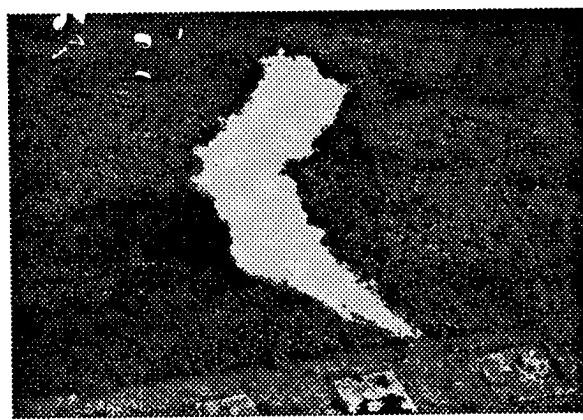
2.8   CONCENTRATION FLUCTUATIONS

Several means were used to detect, sense, and characterize the
state of aerosols and their fluctuations with space and time. Two
LIDAR, one visio-ceilometer, and one SF_6 real-time flame photometer
were deployed in the bowl area. For the detection of propylene
gas, a set of five ion concentration sensors (UVIC) were used
during near field experiments. Turbulence measurements, of course,
were collected and calculations were made to complement and support
these high-resolution phenomena being studied (See Figure 7
again). Note that each Lidar and ceilometer were basically
positioned to be normal to smoke plume and puff centerline travel.

One Lidar was positioned to sense the smoke concentrations
every three seconds with three meter accuracy. Figure 12 displays
the concentration slices with time (seconds) and with the
centerline noted showing that the plume had some meander and
varying values every few seconds. A cross-section of the mean
concentration distribution (in relative units) along the cross wind
distance versus height is presented in Figure 13 as a result of the
above slices through the smoke plume. An example of the SF_6
concentration values across a plume width within a smoke cloud is
given in Figure 14 as the flame photometer was transported normal
to the plume mounted on a moving vehicle. Note that the plume is
about 300m wide. The side-looking visio-ceilometer produce
relative mass values along the centerline of the smoke plume shown

598

Figure 11

Example of instantaneous smoke
puff exhibiting shear in the
vertical (ground level view)
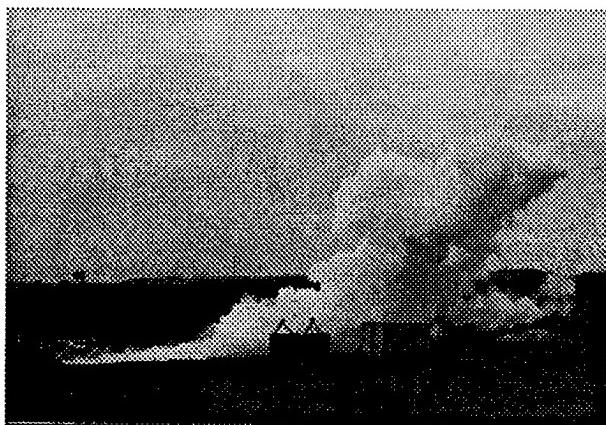
Figure 12

Lidar cross-section slices
of a continuous smoke plume
right to left with time
along the center line
reference.
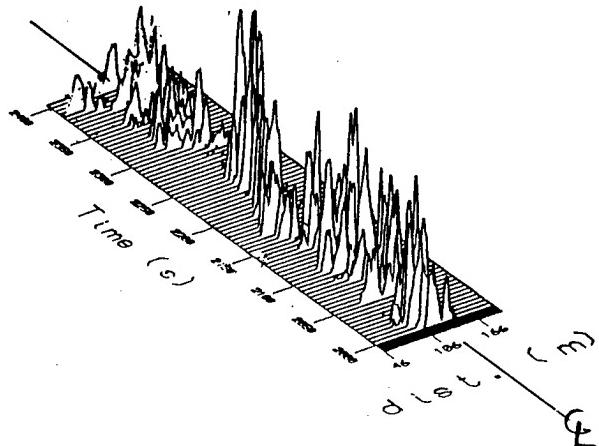
Figure 13

Isoplethes of Lidar mean concen-
tration versus cross-wind
distance and height in relative
units also defining the plume
width
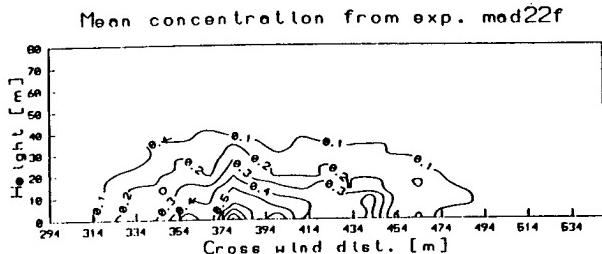
Figure 14

SF$_6$ concentration versus
traversing distance
measured from a moving
vehicle; concentration
in vpb units

599
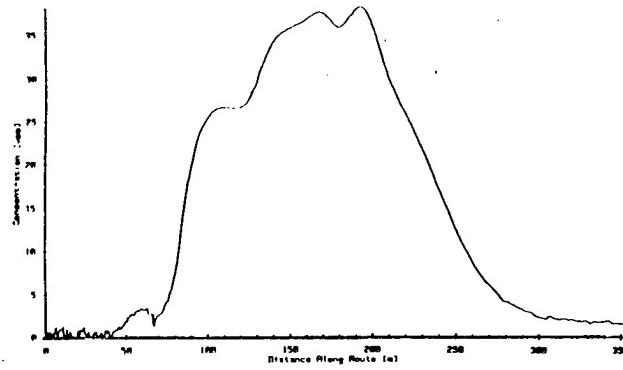
here in Figure 15. The smoke was first sensed shortly after 1530 hours and continued to be detected for the duration of the release. The second Lidar unit produced another type of 'picture' of the smoke cloud every few seconds. Figure 16 displays an instantaneous map of the smoke cloud as the diagonal striped area in the center of the frame against the distant hillside shown as the dark band positioned diagonally from the lower left corner extending toward the upper right corner as background. With several ways of detecting and measuring concentrations of smoke and SF_6 in the same plumes and puffs, more definitive characteristics and behavior of the instantaneous and mean concentrations can be more firmly established.

Figure 15

Figure 16

Visio-ceilometer concentrations in relative mass units along center line; note the arrival of the smoke plume at about 1530 hrs
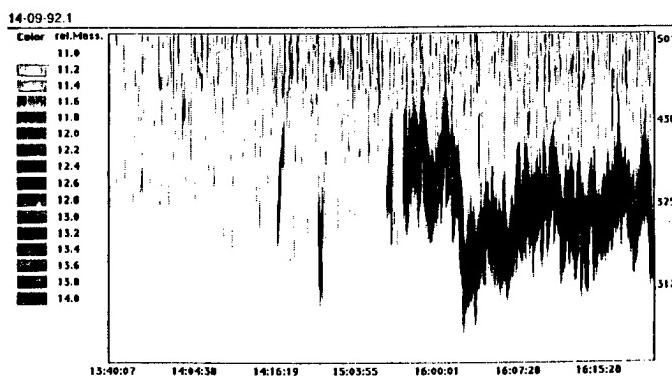
Second Lidar measurements that map the smoke cloud (diagonal stripes) against the hill side (black band)
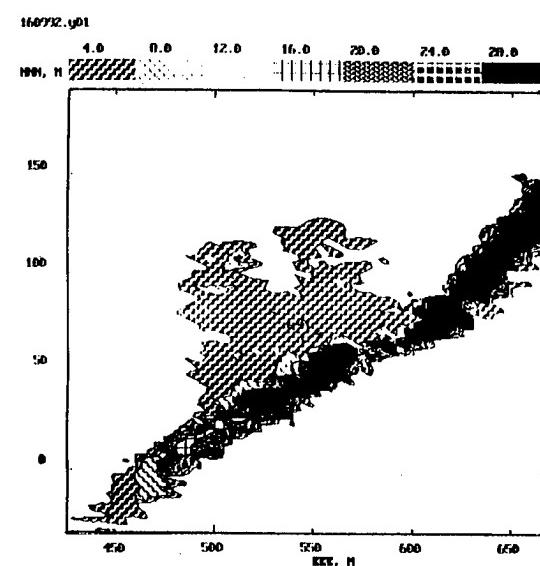
3. HIGH-RESOLUTION SIMULATIONS AT MADONA

Simulations of airflow and diffusion over the MADONA topography were made with a variety of models on-site and in real-time. Wind fields and wind-related parameters were simulated with high resolution wind models such as HRW,[2] Ball and Johnson[3,4], and LINCOM[5].

HRW code was run 40 times during the ten experimental days. Simulations of wind and temperature fields are presented in Figure 17a-b for southwesterly flow on Julian Day 259, 1737 hours. Similar wind field simulations by the Ball and Johnson code, shown

in Figure 18, for easterly flow of another day were also made on-site. The LINCOM wind flow model/code was run to provide wind vector fields as are shown in Figure 19a to drive its complementary diffusion code for JD260 and other days. The RIMPUFF code[6] was used to calculate transport and diffusion of smoke and gas tracer aerosols in the deformed wind fields of the CBDE domain. Figures 20a-b depict a series of numerous 10 minute puff dispersion patterns for a 5 hour period. In Figure 20b, the derived integrated concentrations over the same period are shown.

Additional analyses of the terrain effects upon the airflow were attempted[7] which define areas of adverse and favorable impacts upon the aerosols released at MADONA. Figures 21a and 21b present the simulated streamline analysis and an effects analysis depicting light impact upon the travel and behavior of the smoke/SF_6 plume being maintained in the Bowl area at 1737 hours on Julian Day 259. A more significant impact of a severe nature is shown to exist for the light southerly wind flow of Julian Day 261 at 1415 Hours in Figures 22a and 22b. There are only a few areas where a plume could travel more than 300 to 400 m before its speed or direction would be modified in a disruptive manner. This example was run for Day #4 verifying that it would have been difficult to maintain a steady plume and constant positioning of the Lidar systems for a successful experiment. After numerous attempts, plume and puff releases were canceled for Day #4.

Figure 17a

Streamlines of the wind are simulated by the HRW code, JD259, for a 5 km x 5 km domain with 100 m grid resolution

Figure 17b

Temperature field is simulated by the HRW code, JD259, for a 5 km x 5 km domain with 100 m grid resolution

DAY .259, 1737 HOURS
PROJECT MADONA HRW-PORTON WINDSPEED-STREAMLINES

DAY .259, 1737 HOURS
PROJECT MADONA HRW-PORTON POTENTIAL TEMPERATURE
CONTOUR FROM 206.00 TO 209.40 CONTOUR INTERVA OF .4000
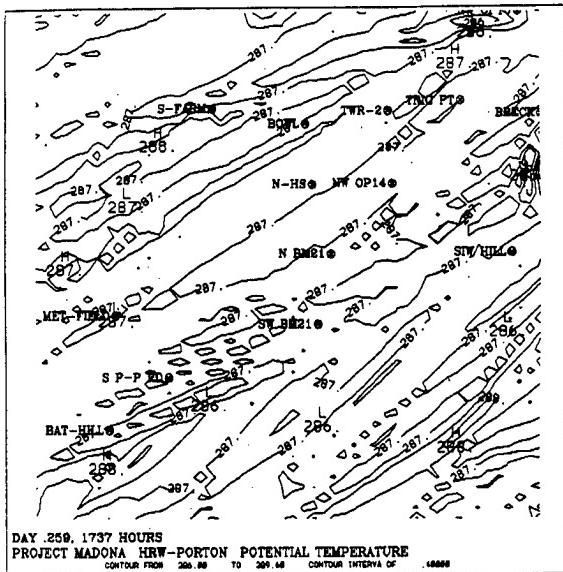
Figure 18

Wind vector field simulated by the Ball & Johnson code
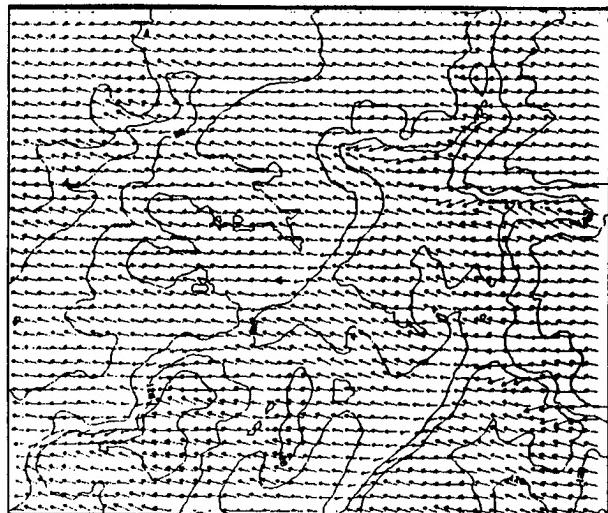
Figure 19

Wind vector field simulated by the LINCOM code
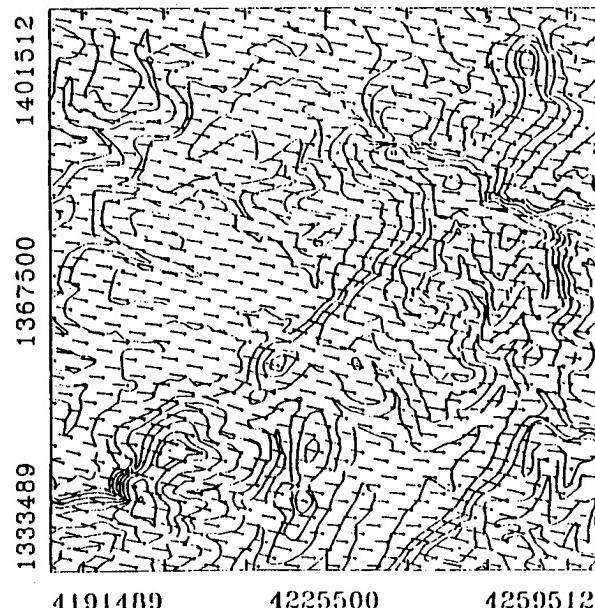
Figure 20a

RIMPUFF code diffusion solution of multiple 10 minute puffs over a period of 5 hours
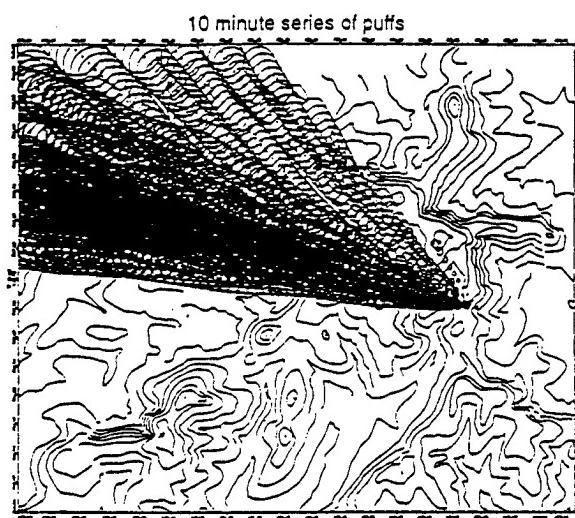
Figure 20b

RIMPUFF code solution of integrated concentration contours for the same 5 hour period
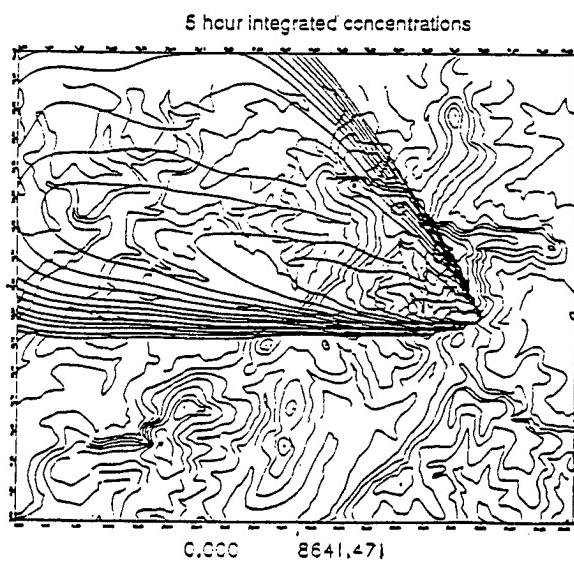
Figure 21a   Figure 21b

HRW wind streamline simulation and adverse impact analysis:

Julian Day 259, 1737 hours
Direction = 240 deg
Speed = 5.5 m/s

Difference in Speed   Difference in Direction

< 10%		< 10 Deg
> 10% < 50%		> 10 < 30 Deg
< 50%		> 30 Deg

Figure 22a   Figure 22b

HRW wind streamline simulation and adverse impact analysis:

Julian Day 261, 1415 hours
Direction = 180 deg
Speed = 1 m/s

Difference in Speed   Difference in Direction

< 10%		< 10 Deg
> 10% < 50%		> 10 < 30 Deg
< 50%		> 30 Deg

603
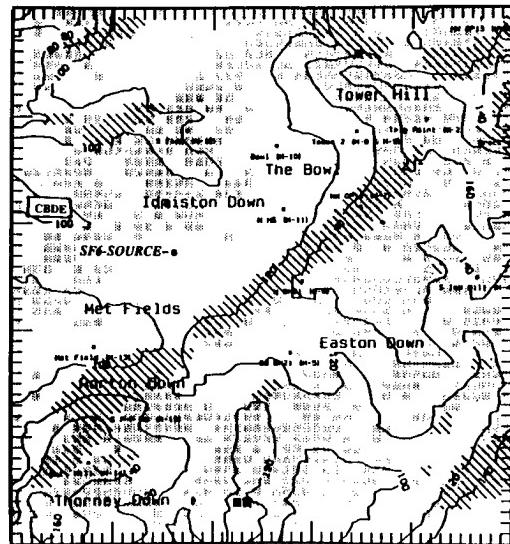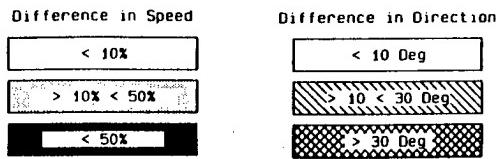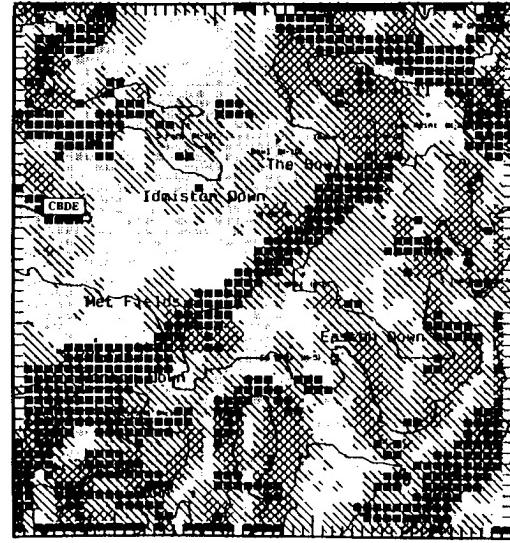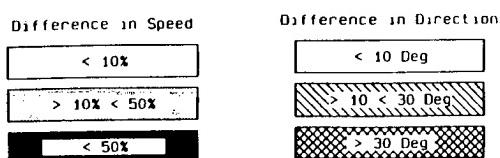
SUMMARY

A tally of the various data gathering activities indicates that the execution of MADONA was highly successful. See Table 2 for a measure of the data base. In addition to the nine experimental days, 21 pre- and post-experimental days of continuous surface layer winds were collected so that the evolution of the wind behavior could be documented for in depth analysis and simulation. More specifically during the nine experimental days, the following grand totals of data were amassed: 186 hours of doppler sodar boundary layer data, 40 boundary layer sonde profiles, 186 hours of fast response turbulence, 84 events of smoke puffs - 39 of which contained SF_6, 17:13 hours of smoke/SF_6 plumes, nine propylene events, and at least 40 on-site real-time model simulations of the flow fields. Preliminary use of the data sets shows the high quality and depth of the MADONA data base. These data sets are being processed and prepared for residency on CD-ROM media.

REFERENCES

1. MADONA Cooperators, 1992: TRIAL MADONA: Meteorology and Diffusion Over Non-uniform Areas Test Plan, UKCBDE, Porton Down, UK.

2. Cionco, R. M., 1985: Modeling Wind Flow and Surface Layer Profiles over Complex Terrain and Within Vegetative Canopies, Forest-Atmosphere Interactions, Editors: B. A. Hutchison and B. B. Hicks, D. Reidel Publishing Co., The Netherlands.

3. Ball, J., and S. Johnson, 1978: Physically-based High Resolution Surface Wind and Temperature Analysis for EPAMS, Report ASL-CR-78-0048-1, USA Atmospheric Sciences Laboratory, WSMR, NM.

4. Weber, H. and W. aufm Kampe, 1992: Das Programmsystem "HEARTS" (Hazard Estimation after Accidental Release of Toxic Substances), Annalen der Meteorologie 27, Duetsche Meteorologen-Tagung 1992, Selbstverlag des Deutschen Wetterdientes, ISSN 0072-4122, Offenbach am Main.

5. Santabarbara, J. S., T. Mikkelsen, R. Kamada, G. Lei, and A. Sempreviva, 1993: LINCOM Wind Flow Model, Riso-R-Report (EN), Meteorology and Wind Energy Department, Riso National Laboratory, Roskilde, Denmark.

6. Thykier-Nielson, S., and T. Mikkelsen, 1993: RIMPUFF User Guide, Version 33 (PC), Meteorology and Wind Energy Department, Riso National Laboratory, Roskilde, Denmark.

7. Cionco R. M. and J. H. Byers, 1993: On Analyzing Wind Effects That May Impact Adversely Upon CB/Obscuration Activities, Proceedings of the 1993 CB Modeling and Simulation Conference, US Army Edgewood Research, Development, and Engineering Center, MD.

TABLE 2.

SUMMARY OF THE MADONA HIGH-RESOLUTION EXPERIMENTS AND STUDIES

DAY	DATE	SFC LYR	BDY LYR	UA SND	TURB	SMOKE PUFF/PLUME	SF6 PUFF/PLUME	PROPYLENE	HRW SIMS
1	14 SEP	24 HR	4 HR	4	4 HR	7 /2:20 HR	- /2:20HR	-	4
2	15 SEP	24 HR	4 HR	4	4 HR	9 /2:00 HR	- /2:00HR	YES	4
3	16 SEP	24 HR	10 HR	4	10 HR	15/ -- HR	15/ -- HR	YES	4
4	17 SEP	24 HR	24 HR	4	24 HR	--/ -- HR	--/ -- HR	YES	4
5	18 SEP	24 HR	24 HR	4	24 HR	4 /1:28 HR	--/1:38HR	YES	4
6	19 SEP	24 HR	24 HR	4	24 HR	14/1:05 HR	--/1:05HR	YES	4
7	20 SEP	24 HR	24 HR	4	24 HR	9 /1:40 HR	2 /1:40HR	YES	4
8	21 SEP	24 HR	24 HR	4	24 HR	6 /3:07 HR	10/3:07HR	YES	4
9	22 SEP	24 HR	24 HR	4	24 HR	5 /1:30 HR	5 /1:30HR	YES	4
10	23 SEP	24 HR	24 HR	4	24 HR	14/4:03 HR	7 /4:03HR	YES	4
TOTALS		240 HR	186 HR	40	186 HR	84+/17:13HR	39/17:13HR	9 EXP	40 SIMS

A METHOD FOR VISUALIZING THE EFFECTS OF TERRAIN AND WIND

UPON BATTLEFIELD OPERATIONS

Ronald M. Cionco and John H. Byers
U.S. Army Research Laboratory
Battlefield Environment Directorate
White Sands Missile Range, NM 88002

ABSTRACT

A successful battlefield operation requires an understanding of the interaction of the surface winds with the underlying terrain. To aid in this understanding, a method was developed and implemented on a personal computer for analyzing and visualizing the effects of the terrain and wind upon the objectives of an operation or activity. Simulated wind fields, produced by our battle-scale High Resolution Wind (HRW) model, are analyzed and the presence and locations of areas that may be impacted upon due to the scenario's terrain configuration and resultant wind effects are depicted in a graphical format. The simulated wind fields are compared to the initialization fields and a given set of criteria to produce the final analysis of where and to what degree the operation or activity may be affected adversely or favorably. Examples are given for pre-study and real-time analyses of the MADONA Field Study, which depict light, moderate and severe impact upon the diffusion experiments.

1. INTRODUCTION

When planning military tactics or during the battle itself, commanders consider knowledge about the current local meteorological conditions and terrain. Although knowledge about the terrain is usually readily available, adequate meteorological data are frequently not accessible to the commander. Available data may not be current, accurate, or of a high enough resolution to be of any value. Sometimes data may be adequate, but the commander receives it in a form which makes it difficult to quickly understand and interpret correctly.

To aid in making decisions, the commander must have this information presented in such a manner that will allow him to

quickly visualize and understand the effects of the wind and terrain upon the operation. Knowing their impact with some level of confidence would ensure more effective and precise deployment of CB aerosols, smoke, troops or equipment. Even if the meteorological and terrain data are clearly and concisely available, it is often difficult for the commander to make a realistic assessment of their effects and impact upon the operation. Sometimes these assessments are made somewhat subjectively or intuitively. This method may be adequate for many instances, but more often than not, meteorological conditions in the more remote portions of the battlefield may not be what is expected, thus making this technique inaccurate and ineffective.

A more definitive method for projecting, quantifying, codifying and interpreting the impact of meteorology and terrain is needed to help the commander make the most intelligent and effective decisions. Such a method was developed and implemented on a high performance lap-top personal computer. The technique was used to help plan diffusion experiments conducted during the recent MADONA Field Study[1] in the United Kingdom. It is currently being used to analyze data from these tests and to help validate wind and diffusion models.

Although the Adverse Impact Method (AIM)[2], described herein, was specifically developed for the MADONA Field Study experiments, it can be adapted to fit a variety of tactical situations. It can be a useful tool in planning for war games and modeling. It can be developed as a decision aide for simulated or actual battles, to determine the impact, either adverse or favorable, of the terrain and meteorological conditions upon the tactical maneuvers being considered. Since the program runs on a lightweight portable system, and requires only a few minutes to run, it is ideally suited for tactical use. Additionally, the wind model requires only a minimum of one upper air sounding and surface measurements at one location to initialize the computation. This level of instrumentation is representative of what would be available in a typical battlefield scenario.

In order to adapt and use AIM in a tactical application the following tasks must be accomplished:

(1) Select a micrometeorological model/code, appropriate for Army-scale battlefield scenarios.
(2) Simulate high-resolution wind fields for a typical battlefield activity.
(3) Analyze terrain and thermal effects upon the wind and other meteorological variables.
(4) Establish typical battlefield "operational" criteria to classify and further identify areas of impact.
(5) Develop a visualization technique to interpret and depict the impact analyses.
(6) Analyze impact areas for adverse and favorable effects upon the battlefield activity.

A commander can then interpret the impact analysis results for his own customized usage and assessment information.

2. APPLICABLE MODELS

AIM uses a microscale model to simulate wind and other meteorological parameters over the area of interest. Several Army-scale micrometeorological models are available at the Battlefield Environment Directorate[3]. Two of these models which analyze flow over complex terrain are considered for this analysis: (1) the High Resolution Wind Model/Code (HRW)[4], and (2) the Canopy-Coupled Surface Layer Model/Code, (C-CSL)[4]. HRW provides simulated horizontal wind and temperature fields over an Army-scale area of 5 km by 5 km. The C-CSL model couples the same HRW surface layer flow to canopy flow for a similar domain. This meteorological coupling adds vertical structure to the simulated horizontal fields and recovers flow within the canopy. For the MADONA experiments, the HRW model/code was chosen to provide the simulated (meteorological) fields for AIM.

The impact analysis is developed to identify and quantify the degree and character of the impact terrain and meteorology have upon a given activity. It does so by applying operational criteria to the resultant effect of the initial field versus the simulated field from the HRW model/code.

3. MICROMETEOROLOGICAL MODEL

HRW is a 2-dimensional, diagnostic, time independent model that simulates the wind flow over a gridded area of 5 km by 5 km with a spacial resolution of 100 meters. The code is initialized with single values of surface layer wind speed, wind direction, temperature, and an estimate of buoyancy by applying these values at each grid point in the computational array. Simulation results are obtained by a direct variational relaxation of the wind and temperature fields in the surface layer. The solution is reached when the internal constraint forces imposed by the warped terrain surface, thermal structure and requirement for flow continuity are minimized. The procedure makes use of Gauss' Principle of Least Constraints which requires these forces to be minimized in order to satisfy the equations of motion. When applied to the surface layer, this procedure also requires the use of empirical wind and temperature profiles.

Computational domain size can actually range from 2 km by 2 km to 20 km by 20 km, with grid resolutions of 40 meters to 400 meters respectively. Note that for MADONA simulations a domain/area of 5 km by 5 km is used exclusively. The vertical thickness of the computation layer is designed to be 1/10th the magnitude of the grid size. A grid size of 100 m therefore produces simulated fields at the 10 m level.

3.1 MODEL INPUT REQUIREMENTS

Initialization of the model can be accomplished with as much, or as little meteorological data that are available. The model inputs include surface layer values of wind speed, wind direction, and temperature as well as temperature-height and pressure-height profiles to estimate the surface domain's buoyancy. Similar surface layer and additional upper air soundings in the computational area can also be used for initialization, but they are not necessary.

Detailed terrain and vegetation/land-use information in a digital format are also required inputs to the model. For the application described herein, an Army-scale area (5 km by 5 km) with a grid size of 100 meters is used for all simulations. Terrain elevation is required at each grid point within the area. Vegetation/land-use height and type are also required at the same resolution.

3.2 MODEL SIMULATION OUTPUT

Model/code output is in the form of listings and binary random access archive files containing simulated values for the wind and temperature as well as other meteorological parameters. Values are computed for each grid point within the domain. The following simulated x,y fields are computed at the top of the 10 m level: (a) u and v wind components, (b) potential temperature, (c) friction velocity (stress), (d) wind power law exponent, (e) Richardson Number, and (f) vertical impaction velocity.

4.0 APPLYING HRW FOR THE MADONA FIELD STUDY

The MADONA Field Study is a series of concurrent meteorological measurements and diffusion experiments conducted during September of 1992 at the Chemical and Biological Defence Establishment (CBDE) at Porton Down, near Salisbury, United Kingdom. The acronym MADONA means Meteorology And Diffusion Over Non-uniform Areas.

During the initial stages of the design phase of the MADONA Field Study, it was apparent that in order to be able to plan the locations for the tracer generators and the receptors/sensors for collecting data, some knowledge of wind flow and its effects over the local Porton Down area was needed. The HRW model/code was selected to simulate the micrometeorological fields over approximately the same area as the proposed study site. With the aid of these simulations, preliminary decisions were made concerning the placement of the generators and sensors. Additionally, it was used to provide an estimate of what conditions might be encountered during the test period. During MADONA, simulations were made for each diffusion experiment.

4.1 FIELD ENVIRONMENT

Figure 1 depicts the simulation area which encompasses the larger part of the study area. The terrain shown was digitized and used for all the MADONA simulations made with the HRW program. The area is characterized by gently sloping terrain with a low, grassy, bowl-shaped area in the central region. This, in fact, is referred to as the Bowl which is where most of the CB/O activities take place at the CBDE. To the east of the Bowl is a gently sloping ridge, culminating with several forested hills. South of the Bowl are more forested hills, farmlands, and scattered houses. West and northwest of the Bowl are scattered farmlands, villages and the administrative buildings and laboratories of the CBDE.

4.2 THE SCENARIO

In conducting these experiments, the location of the CBDE facilities was a major factor in determining where to set up the smoke generators. It was mandated that smoke released during the experiments should not reach the area of the CBDE Headquarters and facilities. It was also considered undesirable to have smoke penetrating the neighboring farmlands.

Initially a planning decision was made to locate the generators along Bursting Chamber Road, which is located along the southwestern edge of the Bowl, because the prevailing wind for the area during September is from the southwest. This would allow the plume to flow away from the critical areas, and through the Bowl for an optimum distance, before reaching the ridge.

A uniform wind field was used to initialize the HRW model with the magnitude and direction of the wind being different for each scenario. An example initial wind field is shown in Figure 2.

Figure 3 illustrates the final simulated wind field from the HRW model. While it is visually easy to determine that the simulated wind direction changed considerably, it is difficult to quantify how much it changed. Also the wind speed changes are difficult to analyze visually. By overlaying the final simulated wind field with the initial field, as shown in Figure 4, the locations of wind direction changes become clearly evident, and could actually be measured if desired. The wind speed changes remain difficult to detect visually.

Originally implemented as a mainframe application, the HRW code was modified for use on a high performance portable PC and transported to the MADONA Field Study where 40 simulations were run "real-time". For these experiments, simulations were run as data became available real-time from the most recent upper air sounding and the local surface station. These simulations were next prepared as input information to the impact analysis method.

FIGURE 1

MADONA Terrain - CBDE, U. K.
5 km x 5 km
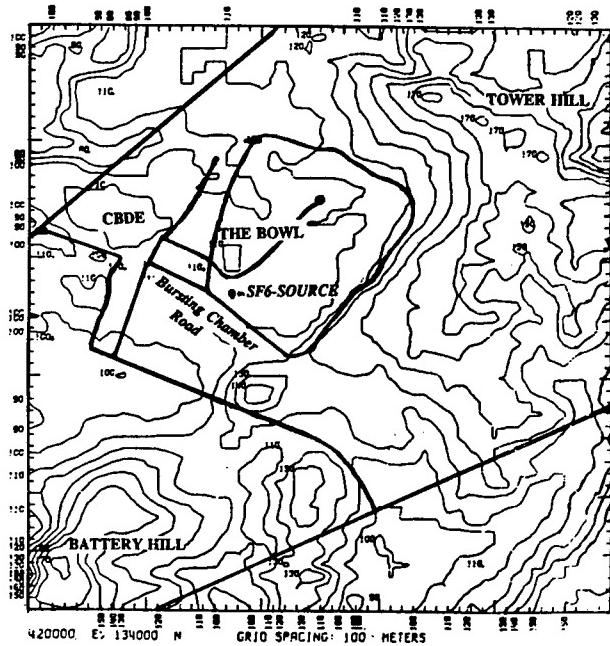
FIGURE 2

Uniform Initial Wind Field
VE=5.1, VN=2.2, Buoy=-5.4
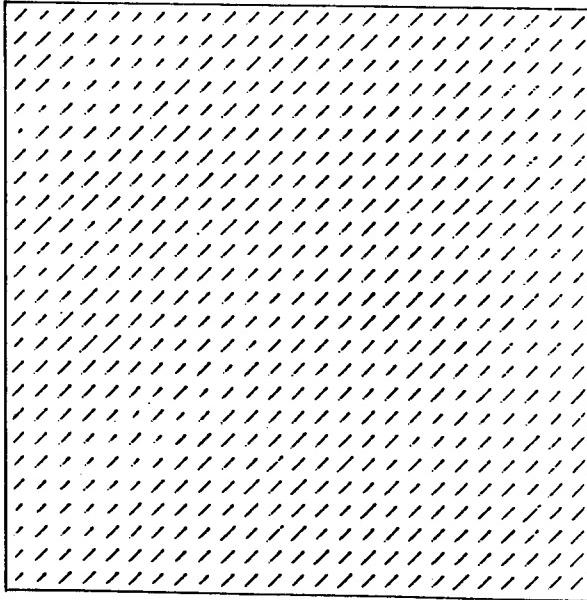
FIGURE 3

Simulated High Resolution Wind
Vector Field.
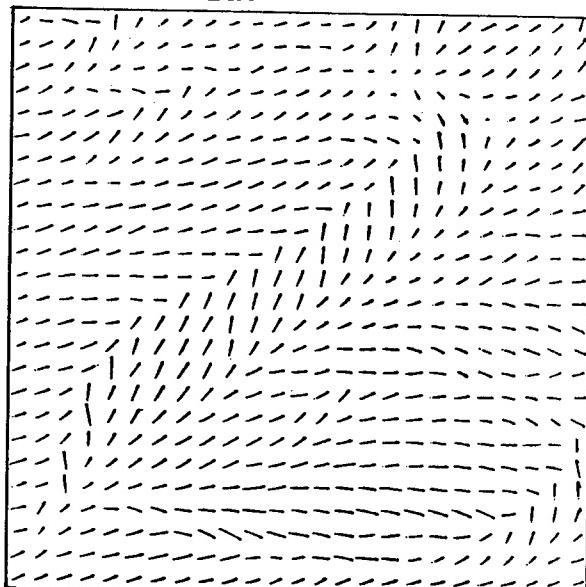
FIGURE 4

Visualization of Wind Direction
Effects.
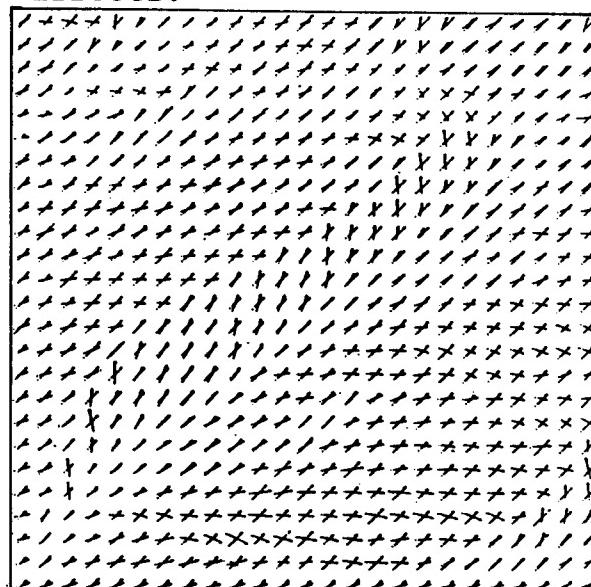
5.0 ADVERSE IMPACT METHOD

Analysis of the pre-MADONA HRW simulations led to the development of the Adverse Impact Method (AIM) described here.

5.1 THE METHOD

For this application, the method involves analyzing the terrain effects upon the wind simulations. The components of the adverse impact analysis are defined to determine the change in conditions due to the simulation:

$$\text{EFFECT} = \text{FINAL SIMULATED FIELD} - \text{INITIAL FIELD} \tag{1}$$

More specifically, we can dissect the wind speed and wind direction effects before we obtain the total effect. The wind speed effect (E_{ws}) is the difference between the values for the final simulated wind speed field (S_s) and the initial wind speed field (S_i):

$$E_{ws} = S_s - S_i . \tag{2}$$

Similarly, the wind direction effect (E_{wd}) is the difference between the values for the final simulated wind direction field (D_s) and the initial wind direction field (D_i):

$$E_{wd} = D_s - D_i . \tag{3}$$

An assessment of the TOTAL EFFECT can be made visually by first evaluating the WIND SPEED EFFECTS and the WIND DIRECTION EFFECTS separately, then examine the combined effect of the two difference fields together.

To quantify the wind effects, a set of adverse impact criteria must be established. For our case, the following criteria are used to define three impact levels:

(a) Impact wind speed and wind direction are considered to be LIGHT if:

$$E_{ws} < 10\% \text{ of } S_i, \quad \text{and} \quad E_{wd} < 10° \text{ of } D_i \tag{4}$$

(b) Impact wind speed and wind direction are considered to be MODERATE if:

$$E_{ws} \text{ is } 10\% \text{ to } 50\% \text{ of } S_i, \tag{5}$$

and

$$E_{wd} \text{ is } 10° \text{ to } 30° \text{ of } D_i \tag{6}$$

(c) Impact wind speed and wind direction are considered to be SEVERE if:

$$E_{ws} > 50\% \text{ of } S_i, \quad \text{and} \quad E_{wd} > 30° \text{ of } D_i \tag{7}$$

When adapting this technique to other applications, these criteria should be tailored to fit your needs or situation.

5.2 GRAPHICAL TECHNIQUE

A computerized graphical technique is developed to aid the analysis. Thus, after finding the differences between the simulated and the initial fields, these criteria can be applied to the individual values at each grid box within the domain. Then color-coded maps showing the impact levels of the wind effects can be constructed. The impact can then be quickly and easily assessed, if the terrain features of the study area are added to these maps. If more information is needed, the vector or streamlines field of the area can also be overlaid on the map. To illustrate the TOTAL IMPACT several effects can be overlaid onto one map.

This graphical analysis technique is particularly effective if implemented on a PC computer such as that used at the MADONA Field Study. With the computer, the color-coded wind speed and wind direction maps can be analyzed individually or together, and the terrain, vectors, or streamlines can easily be added by overlaying each data field on the map one at a time.

Several monochrome examples of this graphical scheme are shown for the "real-time" MADONA simulations. Although they are not quite as effective as the color version, they are still quite useful for this type of analysis.

6. APPLICATION OF THE ADVERSE IMPACT METHOD TO THE MADONA REAL-TIME WIND SIMULATIONS

To illustrate AIM, several simulations made during the MADONA Field Study are selected to represent examples of various levels of impact.

EXAMPLE 1: LIGHT IMPACT shown in Figure 5
Julian Day 259 1737 GMT Sept. 16, 1992

For this day's experiments, the smoke generators were set up along the Bursting Chamber Road which is located at the southwestern edge of the Bowl area. This location was chosen to take advantage of the southwesterly flow and allow the plume to follow a long fetch of approximately 2.5 km across the Bowl before reaching the gently rising terrain at the edge of the ridge. Smoke-detecting LIDAR units were set up in the Bowl and on the ridge to monitor the plume. Overcast conditions persisted throughout this day, with some light precipitation being observed for short intervals of time. At the time of this simulation, slightly unstable conditions existed. The initial wind speed was 5.5 m/s and the wind direction was 240 degrees.

The simulation indicates only small areas where the wind speed and wind direction would have a moderate impact. These areas

FIGURE 5

EXAMPLE 1 - LIGHT IMPACT
Streamlines/Adverse Impact Areas
Julian Day: 259   Time: 1737
Direction: 240 Deg   Speed: 5.5 m/s

Difference in Direction	Difference in Speed
< 10 Deg	< 10%
> 10 < 30 Deg	> 10% < 50%
> 30 Deg	< 50%
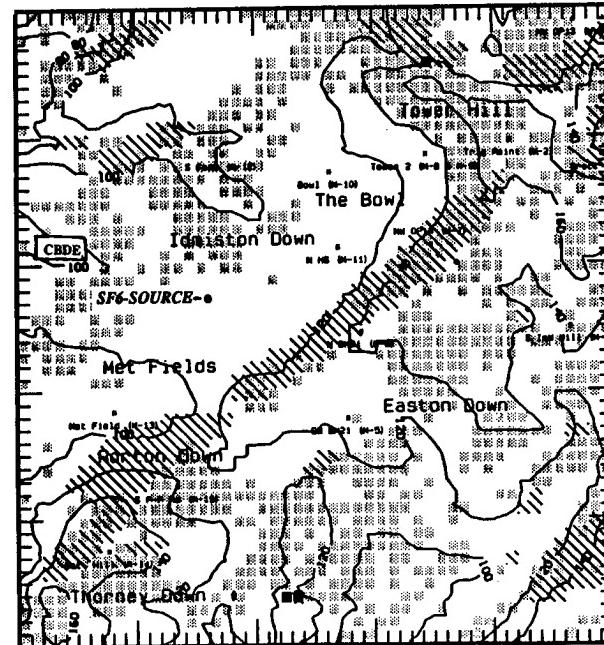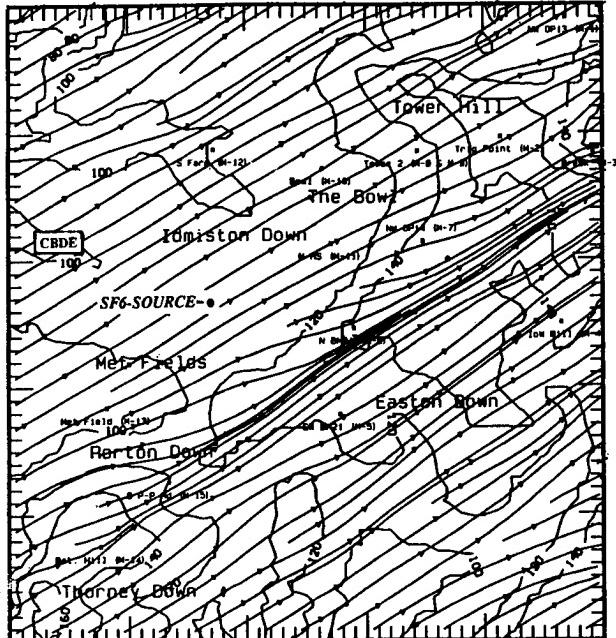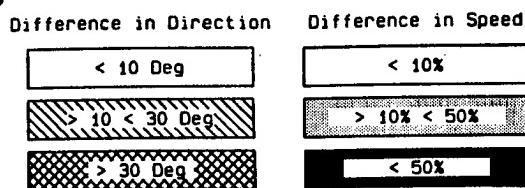
FIGURE 6

EXAMPLE 2 - MODERATE IMPACT
Streamlines/Adverse Impact areas
Julian Day: 262   Time: 1310
Direction: 255 Deg   Speed: 4.0 m/s

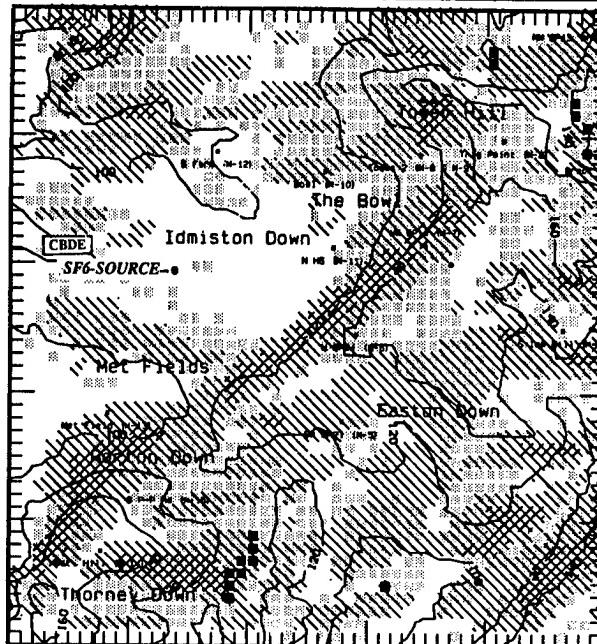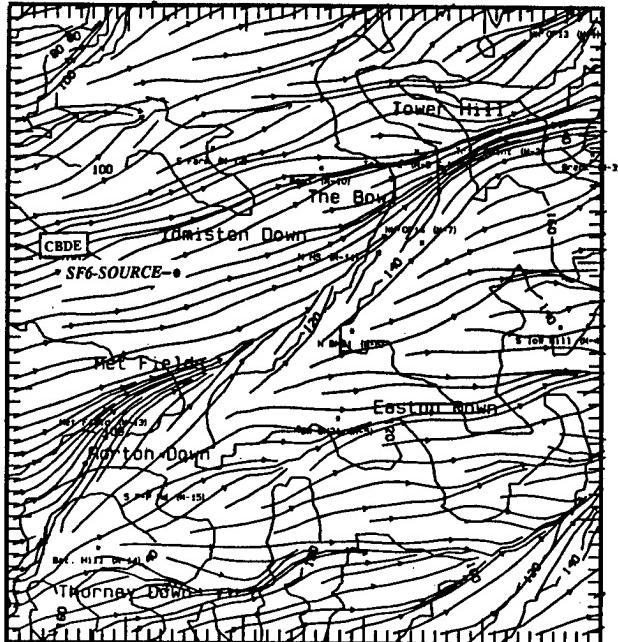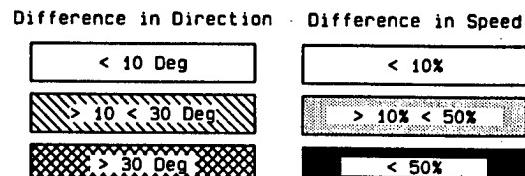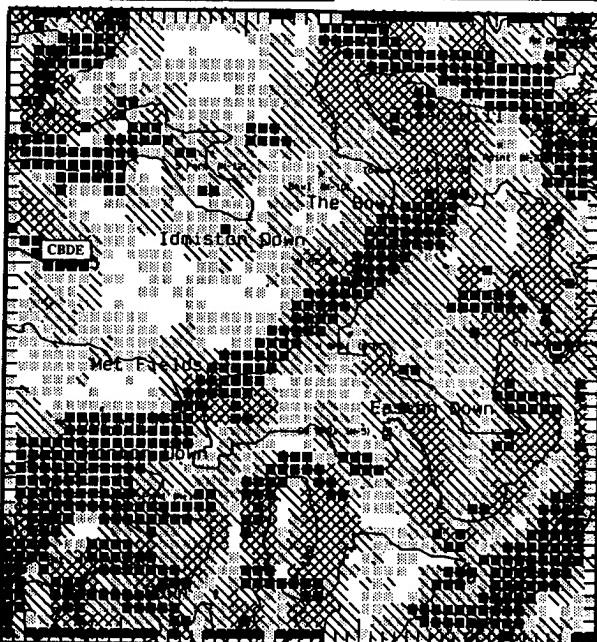| Difference in Direction	Difference in Speed
< 10 Deg	< 10%
10 < 30 Deg	> 10% < 50%
> 30 Deg	< 50%
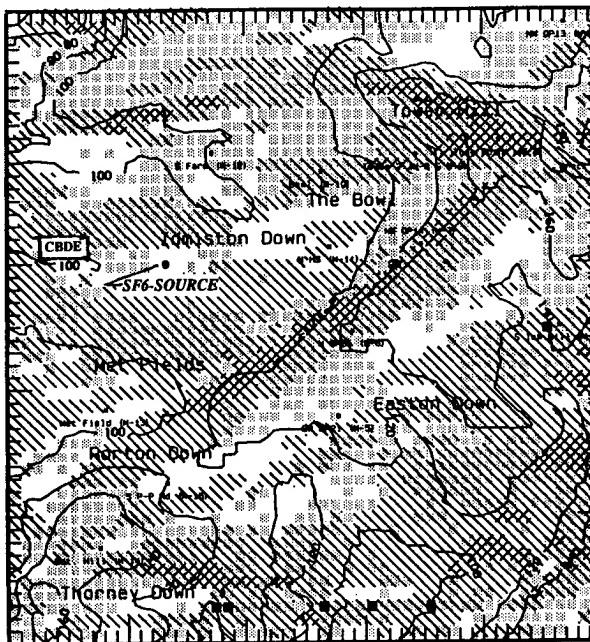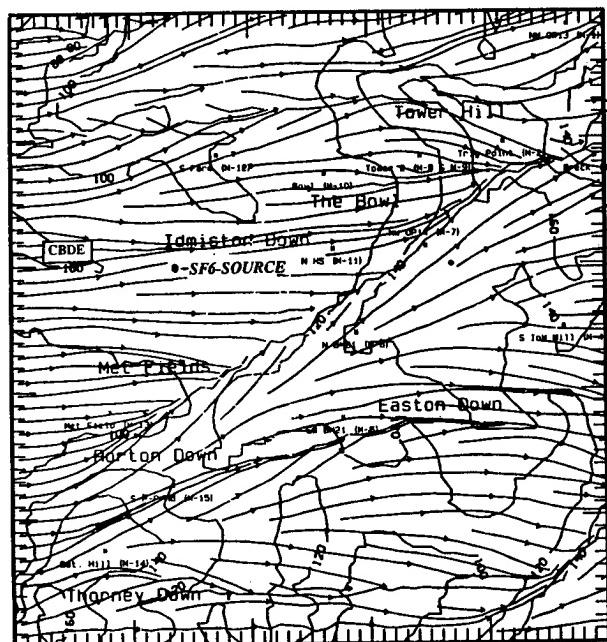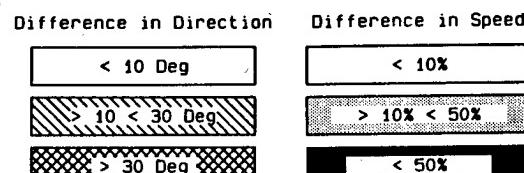
include a narrow band along the ridge, the top of Battery Hill and the higher elevations north of Tower Hill.

When considering the study area as a whole, there are practically no adverse areas that would impact upon test activities. The location chosen for the release of smoke appears to be a good choice. In fact, practically any site in the Bowl area would be good, since the wind speed and wind direction effects are depicted as light in the entire area. The simulation indicates that, except for the slightly high wind speed, conditions appear to be good for releasing smoke in the planned experiment area. During the actual experimental period, continuous smoke was released for a long period of time and a compact plume was maintained for a long distance before it began to diffuse at the northeastern edge of the Bowl. The instantaneous plumes (puffs) released at the same site pulled apart and quickly dissipated after the initial explosion.

EXAMPLE 2: MODERATE IMPACT shown in Figure 6
          Julian Day 262 1310 GMT Sept. 19, 1992

In this example, the release point for the smoke was moved farther north along the western edge of the Bowl and almost due west of the M-7 site. This location presumed the westerly wind would allow a fetch of about 1 1/2 km for the plume to travel before reaching the edge of the ridge. The weather for this day was typified by cloudy, nearly neutral surface heating conditions and occasional light scattered showers in the area. The initial wind speed and wind direction values for the simulation were 4.0 m/s and 255 degrees.

When compared to Example 1, the initializing conditions for example 2 are very similar, with the wind speed for example 2 being 1.5 m/s lighter and the wind direction is 15 degrees more westerly. The adverse effects, however, appear to be much more significant in this simulation. Along the path of the plume, the simulation indicates, primarily, a moderate adverse impact area, with severe wind direction effects at higher elevations near a forested area of the ridge. The wind streamline plot indicates an unchanging flow along the trajectory up to the top of the ridge, where some convergence is indicated.

The site chosen for the generators was an optimum location, as even more adverse impact of the wind effects are indicated in adjacent areas to the north and south. Most other areas appear not suited for a test.

In the field, the smoke plume released shortly after this time traveled close to the ground across the Bowl for about 1.7 km and then continued up the ridge through plantation of trees and beyond. This continuous plume was maintained for about 30 minutes as light rain soon began to fall and made data collection difficult.

EXAMPLE 3: LIGHT TO MODERATE IMPACT shown in Figure 7
            Julian Day 262 1449 GMT Sept. 19, 1992

     Approximately 1 1/2 hours after the time of the simulation for
Example 2, the wind direction changed to more southwesterly and
decreased to 3 m/s. The plots for the adverse impact simulation for
this case indicate that a wide area of light wind effects impact
has opened up in the area of the Bowl. This area includes the site
where the generators were located. This simulation indicates that
conditions might have been much better for an experiment anywhere
in the bowl, than during the time of example 2. Moderate impact
areas are observed immediately to the south of the Bowl, along the
ridge and hill tops. Several severe areas are indicated at the
highest elevations. Though no experiments were conducted at this
time, this may have been a good time for releasing smoke since the
rain terminated shortly before this time.

EXAMPLE 4: SEVERE IMPACT shown in Figure 8
            Julian Day 261 1415 GMT Sept. 18, 1992
            NO TEST CASE

     This simulation indicates severe adverse wind effects in large
areas throughout the entire domain. The field notes show this was
a NO TEST day. Generators were set up at the southern edge of the
Bowl along Bursting Chamber Road to take advantage of the southerly
flow. Although an attempt to release "puffs" was made, the
experiments were aborted because of a dependable wind speed and
wind direction could not be maintained. The simulation verifies
this to be a correct decision. The initial wind speed and wind
direction for this simulation was 1.0 m/s and 180 degrees. As would
be expected for these conditions, the streamline plot indicates
meandering winds twisting and turning and flowing from the south.
The adverse impact plot indicates virtually no contiguous area
large enough that would be suitable for a valid test.

EXAMPLE 5: MODERATE TO SEVERE IMPACT shown in Figure 9
            Julian Day 267 1735 GMT Sept. 24, 1992
            BAD CHEMICAL SITUATION

     For this day, the generators were set up at a site in the
northwestern part of the test area near the western edge of the
Bowl almost due west of the Tower-2 site. For this simulation, the
initial wind speed and wind direction were 2.5 m/s and 250 degrees
and slightly unstable conditions. Very close to the time of this
simulation, the stability conditions appeared to cross through the
transition from unstable, to neutral, and then to stable.

     As can be seen from the adverse impact plot of this
simulation, a large part of the domain indicates moderate to severe
wind effects. The area where the experiment were conducted, looks
particularly hazardous, with severe wind direction effects
throughout most of the plume's trajectory. Wind speed effects in
the same area range from moderate in the lower elevations to severe

FIGURE 7

EXAMPLE 3: LIGHT TO MODERATE IMPACT
Streamlines/Adverse Impact Areas
Julian Day: 262   Time: 1449
Direction: 250 Deg   Speed: 3.0 m/s

Difference in Direction   Difference in Speed

< 10 Deg   < 10%

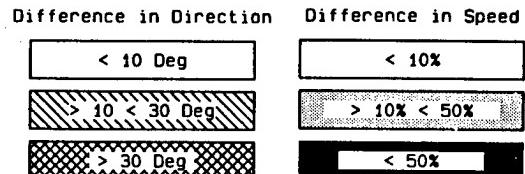> 10 < 30 Deg   > 10% < 50%

> 30 Deg   < 50%

FIGURE 8

EXAMPLE 4: SEVERE IMPACT-NO TEST CASE
Streamlines/Adverse Impact Areas
Julian Day: 261   Time: 1415
Direction: 180 Deg   Speed: 1.0 m/s

Difference in Direction   Difference in Speed

< 10 Deg   < 10%

> 10 < 30 Deg   > 10% < 50%

> 30 Deg   < 50%
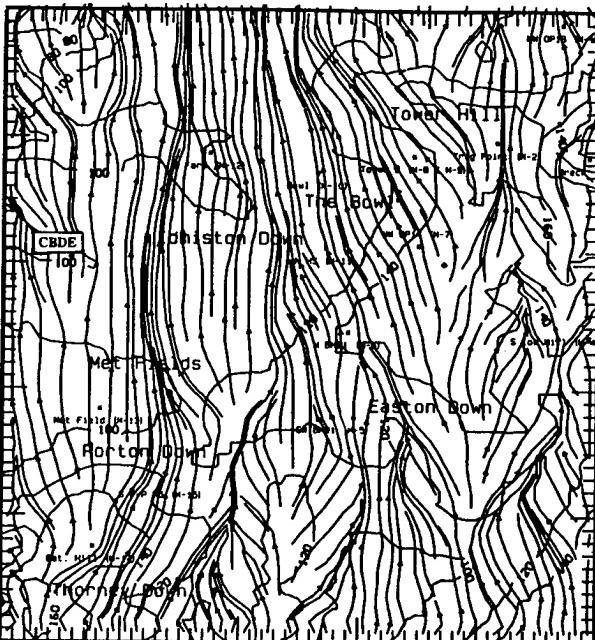
in the forested area on top of Tower Hill to add to the hazardous conditions.

If the scenario had been real-life and harmful chemicals had been released, this simulation may be a good example of a bad chemical situation because wind speed and wind directions were so variable throughout the trajectory of the plume. Observations from an experiment conducted close to the simulation time verify this. The smoke released from an instantaneous "puff" was observed to travel eastward, over the ridge to a concrete target at the top of the hill. It was at this point the cloud reversed its direction, travelled down the hill and settled in the Bowl area stagnating near the release point.

FIGURE 9

EXAMPLE 5: MODERATE TO SEVERE IMPACT
Streamlines/Adverse Impact Areas
Julian Day: 267   Time: 1735
Direction: 250 Deg   Speed: 2.5 m/s

619
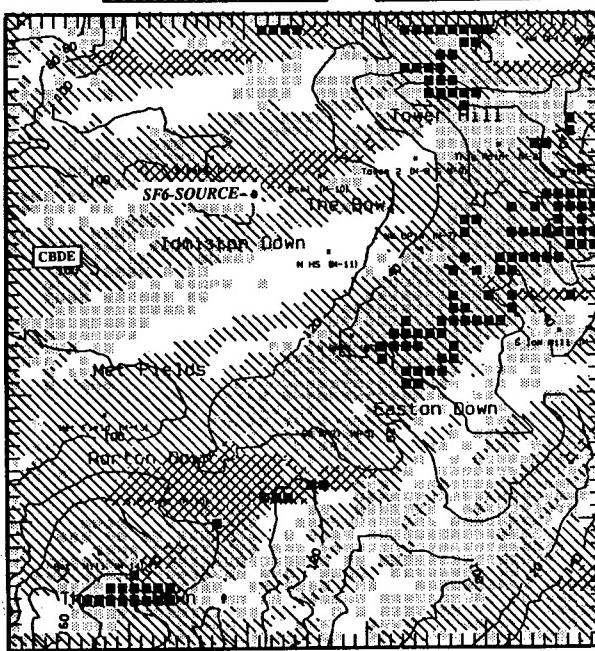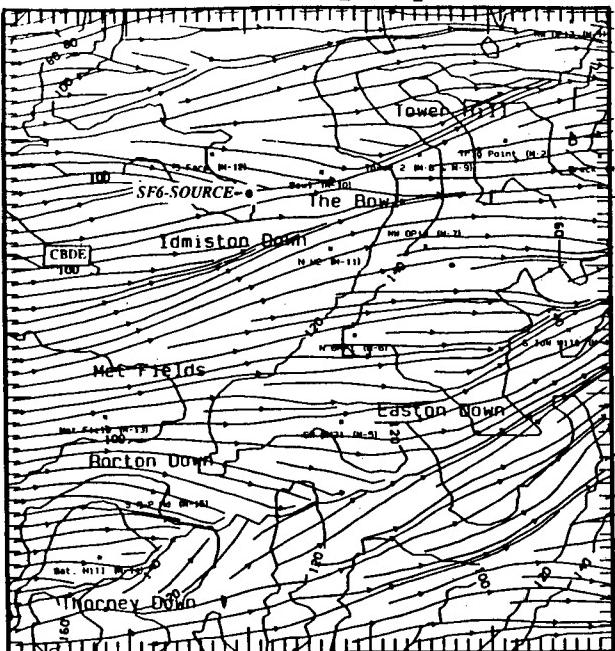
CONCLUSIONS

The Adverse Impact Method (AIM) described here is a simple, yet effective, method of quickly analyzing the impact, adverse or favorable, of winds or other parameters upon activities conducted over and on a land area, roughly the size of a typical battlefield. In order for the method to be effective, several conditions must be satisfied:

1.   Some reliable estimate or simulation of the meteorological conditions in the area of interest is needed. In this case BED's High Resolution Wind Model is used to simulate the meteorological conditions. Other models may be better suited for different applications, but whatever is used should take into account the effects of complex terrain upon the meteorology. Also, data used to initialize the model should be representative of the area modelled.

2.   AIM is based upon the analyzing of the differences between the simulated and initial meteorological fields over the area of interest and applying a set of criteria which quantifies these difference values into three distinct levels: light, moderate and severe. The criteria adopted for this analysis must be correctly defined to fit the specific application.

3.   The impact levels must be codified and presented to the commander in a form that is quickly and easily understood. This is accomplished in this application by overlaying a color-coded map of areas of the impact levels with plots of the terrain features and wind streamlines. This seems to be very effective, but as mentioned above, the visualization scheme should be adapted to fit the specific requirements of the application.

4.   In order to take full advantage of the impact assessment, results must be available quickly, so that near real-time conditions are reflected in the solution. Additionally, AIM should be able to be implemented in an adverse environment such as might be experienced in a typical battlefield. The method used for MADONA fulfills this condition. The HRW model, which was implemented on a high-performance 486 laptop PC, requires only a few minutes to simulate a 5 km by 5 km area. The graphics capability of the computer's active matrix color screen allows the wind speed and wind effects maps to be generated almost instantaneously and analyzed separately or together with the wind vectors, streamlines and terrain.

As shown by the MADONA solutions, AIM has proven to be a useful tool for pre-test planning and on-site real-time analysis purposes. Because it can be implemented on a small computer and is simple and quick, this method can also be useful to the commander as a decision aid for tactical operations.

ACKNOWLEDGEMENTS

REFERENCES

1. Cionco, R. M. and J. H. Byers, 1993: MADONA: An International High-Resolution Meteorology and Diffusion Study, Proceedings of the 1993 Battlefield Atmospherics Conference, sponsored by the U.S. Army Research Laboratory - Battlefield Environment Directorate, White Sands Missile Range, NM 88002.

2. Cionco, R. M. and J. H. Byers, 1993: On Analyzing Wind Effects That May Impact Adversely Upon CB/Obscuration Activities, Proceedings of 1993 CB Modeling and Simulation Conference, sponsored by U.S. Army ERDEC, Aberdeen Proving Ground, MD, p 331-345.

3. Cionco, R. M., 1989: Mesometeorological and Boundary Layer Modeling for the Army, Proceedings of the DOD Environmental Technical Exchange Conference on Mesoscale Phenomena (ETEC), Laurel, MD., sponsored by the Office of the Director of Defence, Research and Engineering, p 249-260.

4. Cionco, R. M., 1985: Modeling Wind fields and Surface layer Profiles over Complex Terrain and Within Vegetative Canopies, Forest-Atmosphere Interactions, B. A. Hutchison and B. B. Hicks, Editors, D. Reidel Publishing Co., Netherlands.

5. Chemical and Biological Defence Establishment Staff et al, 1992: TRIAL MADONA: Meteorology And Diffusion Over Non-uniform Areas (Test Plan), UK CBDE, Porton Down, Nr Salisbury, UK.

COMPARISON OF OPTICAL TURBULENCE MODELS FOR FORECAST APPLICATIONS

Montie M. Orgill
Kenneth P. Freeman
Roger E. Davis

Science and Technology Corporation
White Sands Missile Range, NM 88002, USA

Robert Endlich
U.S. Army Atmospheric Sciences Laboratory
White Sands Missile Range, NM 88002, USA

ABSTRACT

Four optical turbulence models have been evaluated and compared to determine which offers the best potential for producing 12- to 24-hr forecasts of the time variation of C_n^2 near the surface. The models tested include a statistical regression model, a meteorological bulk model, and two comprehensive energy balance models (Kunkel-Walters and Rachele-Tunick) developed at White Sands Missile Range. The statistical model and the Rachele-Tunick energy balance model use operational meteorological variables usually available from daily forecasts. The other two models require more elaborate instrumentation, measurements, and computations for parameters such as temperature and humidity gradients, soil moisture, cloud cover, and other quantities that are more difficult to forecast. All models require an estimate of future wind conditions near the surface.

A comparison of the models using 16 test periods and data from a White Sands Missile Range database indicated that all models do not give consistent results when applied to different time periods, although all can give good results at times. The energy balance models look promising but require more effort in getting correct input conditions. The bulk and Kunkel-Walters energy balance models exhibit occasional signs of computational instability because of the complexity of their algorithms and input conditions. The Rachele-Tunick energy balance model provides reasonable daytime C_n^2 time variations but lacks a nighttime algorithm. The regression technique outperformed the other techniques slightly and may be improved if combined with other analysis techniques such as neural nets.

1. INTRODUCTION

Small-scale fluctuations in the refractive index of air, known as optical turbulence, affect various types of electro-optical sensing systems. A measure of the strength of these fluctuations is the refractive index structure parameter, C_n^2. This parameter is highly variable and can exhibit a range of several orders of magnitude in the course of a day within the atmospheric boundary layer. The ability to predict C_n^2 for periods on the order of minutes or hours is important for various electro-optical sensing operations. The techniques used for making predictions must be able use input parameters that are not difficult to measure but are still representative enough to provide reasonably accurate predictions of optical turbulence.

A number of different methods or models have been developed for computing C_n^2 for the purpose of estimating image degradation or electro-optical system performance. These models differ from each other in physical and mathematical complexity. They also use different input parameters to estimate fluctuations in temperature and water vapor, which appear to be the primary factors in optical turbulence. Some methods include parameters to treat aerosols, which can cause image degradation by radiation scattering. The purpose of this paper is to investigate four models for estimating C_n^2 and to evaluate which models are more appropriate for making 12- to 24-hr predictions of this parameter.

The four models used for this evaluation were (1) an adaptation of a statistical regression method used by Sadot and Kopeika (1992), which uses basic meteorological parameters and an aerosol parameter to estimate C_n^2; (2) a bulk meteorological method of Andreas (1988), which uses basic measurements of wind, temperature, and humidity and their respective scales to estimate C_n^2; (3) the energy balance method of Kunkel and Walters (1983); and (4) the energy balance technique of Rachele and Tunick (1992). A brief description of each model is presented in the next section.

2. BRIEF DESCRIPTION OF MODELS

The Sadot and Kopeika (SK) statistical regression method relies on a polynomial regression correlation between C_n^2, temperature, relative humidity, windspeed, and solar flux. In their development of the model, Sadot and Kopeika reported a correlation coefficient of over 90%. On this basis, we developed a similar regression equation using the same parameters but with a White Sands Missile Range (WSMR) database. This regression equation is

$$C_n^2 = a_1 W + b_1 T + c_1 RH + c_2 RH^2 + c_3 RH^3 + d_1 WS + d_2 WS^2 + d_3 WS^3 + e \tag{1}$$

where W is the temporal hour weight (an estimator of insolation); T is temperature; RH is relative humidity; WS is windspeed; and a_1, b_1, c_1,...... e are numerical regression coefficients.

The Andreas bulk meteorological method requires measurement of pressure, windspeed, and gradients of temperature and humidity. The refractive index structure parameter is then calculated from the relationship

$$C_n^2 = z^{-\frac{2}{3}} g(\zeta) (A^2 T_*^2 + 2ABT_* Q_* + B^2 Q_*^2) \tag{2}$$

where z is height; $g(\zeta)$ is the Wyngaard-Andreas universal function; A and B are functions that depend on pressure, temperature, and wavelength of electromagnetic radiation; and T_* and Q_* are scales equivalent to the vertical fluxes of sensible heat ($\overline{wT}$) and latent heat ($\overline{wq}$). The functions A and B are different for visible, infrared, radio, and millimeter wavelengths (Andreas, 1988a; b). The scales T_* and Q_* are essentially constant with height in the atmospheric surface layer (~ 50 m).

The scales T_*, Q_* and U_* (equivalent to the vertical flux of momentum and used elsewhere in the computation) are estimated from measurements of windspeed and gradients of temperature and humidity and are obtained by an iterative solution of the following equations:

$$T_* = \frac{k\Delta T}{\left[\ln\left[\dfrac{h}{z_t}\right] - \Psi_h\left[\dfrac{h}{L}\right]\right]} \qquad (3)$$

$$Q_* = \frac{k\Delta Q}{\left[\ln\left[\dfrac{h}{z_q}\right] - \Psi_h\left[\dfrac{h}{L}\right]\right]} \qquad (4)$$

$$U_* = \frac{kU_h}{\left[\ln\left[\dfrac{h}{z_0}\right] - \Psi_m\left[\dfrac{h}{L}\right]\right]} \qquad (5)$$

where k is the Von Karman constant (~ 0.4); h is reference height; L is the Monin-Obukhov length; ΔT is temperature gradient; ΔQ is humidity gradient; U_h is reference windspeed; Ψ_m and Ψ_h are diabatic influence functions for momentum and heat; z_t and z_q are roughness lengths for temperature and humidity, respectively; and z_0 is roughness height.

Andreas (1988) indicates that z_t and z_q can be estimated from

$$\ln\left[\frac{z_s}{z_0}\right] = b_0 + b_1\ln(R^*) + b_2(\ln R^*)^2 \qquad (6)$$

where z_s is either z_t or z_q and $R^* = U_* z_0/\nu$. The quantity ν is the kinematic viscosity of air. The coefficients b_0, b_1, and b_2 are functions of temperature, humidity, and Reynolds roughness number.

The Kunkel and Walters model (called FRCST by the authors) employs the surface energy balance equation for estimating the sensible and latent heat fluxes and ground temperature, and then calculates C_n^2 from the following empirical relation from Wesely (1976):

$$C_n^2 = \left[\frac{C_T^2 A^2 P^2}{T_a^4}\right]\left[1 + \frac{0.03}{B}\right]^2 \qquad (7)$$

In Eq. 7, C_T is the temperature structure parameter, which is a function of height, stability, friction velocity, and sensible heat flux; A is a function of temperature, pressure, and wavelength ($\sim 79 \times 10^{-6}$ K mbar^{-1}); P is atmospheric pressure; T_a is the reference temperature; and B is the Bowen ratio or the ratio of surface sensible heat flux to surface latent heat flux.

The FRCST model solves the energy balance equation to obtain the surface fluxes of heat and water vapor and then calculates the ground surface temperature by utilizing the force restore method, the Crank-Nicolson numerical method, and several iterative computations to obtain solutions for C_n^2 (Deardorff, 1978). Two versions of this model are available. The first version (FRCST) is the

original prediction computer code for estimating optical turbulence near the surface up to 24 hr. The second version, which we have called FRCST2, is a modified version of the original code and is diagnostic in nature. Only the second version was used in this analysis because the first version requires an extensive modification in the wind forecast subroutine. The FRCST2 code was further modified for this analysis to produce the version, used for this analysis, that we have called KW2.

The Rachele and Tunick (RT) model uses a direct iterative approach to solve the energy balance equation

$$R_N = H + L'E + G_s \tag{8}$$

where R_N is the net radiative flux, H is the turbulent sensible heat flux, L'E is the latent heat flux due to surface evaporation, and G_s is the flux of heat into (or out of) the soil. The authors use a variety of empirical and theoretical concepts to estimate the components in the energy balance equation for clear skies and dry soil and then include the option to modify their results for cloudy skies and different soil conditions. The model only calculates optical turbulence for the daytime period between the morning and afternoon neutral events. The nighttime portion is under development.

The RT model calculates optical turbulence from the following expression:

$$C_n^2 = bK_h \epsilon^{-\frac{1}{3}} \left[\frac{\partial \eta}{\partial z} \right]^2 \tag{9}$$

In Eq. 9, b is the Obukhov-Corrsin constant (3.2), K_h is the turbulent exchange coefficient for heat, ϵ is the energy dissipation rate, and $\partial\eta/\partial z$ is the gradient of the mean refractive index. The expression used in the model for $\partial\eta/\partial z$ is based on Andreas (1988) for visible wavelengths and is

$$\frac{\partial \eta}{\partial z} = 10^{-6} \frac{\partial \theta}{\partial z} \left\{ -M_1(\lambda) \frac{P}{T^2} - 1.61[M_2(\lambda) - M_1(\lambda)] \frac{PQ}{T^2} \right\} + 1.61 \times 10^{-6} \frac{\partial Q}{\partial z} [M_2(\lambda) - M_1(\lambda)] \frac{P}{T} \tag{10}$$

where M_1 and M_2 are wavelength-dependent parameters, P is atmospheric pressure, T is reference temperature, Q is specific humidity, and $\partial\theta/\partial z$ and $\partial Q/\partial z$ the vertical gradients of potential temperature and specific humidity.

3. DATA INPUT AND EXPERIMENTAL METHODOLOGY

The test data were obtained from the U.S. Army Atmospheric Research Laboratory (ARL) Directed Energy Database, which has C_n^2 data from scintillometers measured over 1-km horizontal paths and from temperature difference probes at single sites. In the evaluation of the computer codes, 16 days were selected for the comparisons (Table 1). These days were based on input data availability and the season of the year.

The input data for the RT energy balance model consisted of Julian day, height, time of neutral event, temperature at neutral event, pressure, temperature, relative humidity, windspeed, soil parameter, cloud cover, cloud density factor, and height of principal cloud base. These data were provided at 15- or 30-min intervals from the morning to evening neutral event. The computer code was first run for clear conditions to obtain the optical air mass parameter. A cloud density factor was then obtained from sky cover, an estimate of the opaqueness of the sky, and optical air mass. A second run of the program provided the final time series of C_n^2.

626

TABLE 1. TEST DAYS USED IN MODEL EVALUATION

Season	Julian Day	Date
Winter	338	4 December 1987
	029	29 January 1987
	039	8 February 1989
	040	9 February 1989
	041	10 February 1989
	044	13 February 1989
Spring	122	2 May 1989
	123	3 May 1989
	124	4 May 1989
Summer	197	16 July 1987
	225	13 August 1987
	228	16 August 1987
	229	17 August 1987
Fall	292	18 October 1988
	293	19 October 1988
	319	14 November 1988

TABLE 2. OPTICAL TURBULENCE MODEL REQUIREMENTS

Data Type	Model			
	SK	Andreas	KW	RT
Date/time/location	Temporal Hr	No	Yes	Yes
Temperatures	Yes	Yes	Yes	Yes
Humidity	Yes	Yes	Yes	Yes
Cloud info.	No	No	Yes	Yes
Pressure	No	Yes	Yes	Yes
Winds	Yes	Yes	Yes	Yes
Upper-air info.	No	No	Yes*	No
Soil parameters	No	No	Yes	Yes
Aerosols	Yes**	No	No	No

* KW2 version does not require upper-air data.
** The present WSMR version of the SK model does not include aerosols.

627

The input data for the SK model consisted of 15-min temperature, relative humidity, and windspeed. We used Sadot and Kopeika's temporal hour weights instead of the solar radiation for time intervals throughout the 24-hr period. A simple program calculated the temporal hour weights. A Quattro Pro© spreadsheet program was then used to obtain regression equations for C_n^2 for the different test periods using Eq. 1. Correlation coefficients varied between 0.60 and 0.93. A plot of the C_n^2 results from the various regression equations indicated some negative C_n^2 values, especially during the nighttime periods and around the morning and evening neutral events. A more general regression equation was developed by averaging the independent variable coefficients from the four best regression equations. This equation was then used to predict C_n^2 for all of the test periods. Results were not satisfactory because of the high frequency of negative C_n^2 values. We then formed average regression equations for each season and used these to predict C_n^2 for the test periods of each season. Autocorrelations were then computed between calculated and observed C_n^2.

The input data for the Andreas bulk model consisted of temperature at reference height, surface and layer temperature, pressure, vapor pressure, windspeed, roughness length, and radiation wavelength (visible, infrared, millimeter, and radar). These input data were provided at 15-min intervals with the exception of roughness length and wavelength. Calculations were made for the visible band with the wavelength approximately 0.55 μm. The roughness lengths for temperature and humidity were obtained from Eq. 6 since a relation was not available for desert conditions. These values are not correct for our conditions and a better estimate is needed. After a series of test runs, it appeared necessary to put limits on the stability factor z/L in order to limit inherent computational instabilities.

The input data for the KW2 energy balance model consisted of Julian day, maximum and minimum temperature, and an estimate of the surface and 20-cm-deep soil moisture. Windspeed, dewpoint, and pressure were obtained from the database at 15-min intervals and cloud conditions and daytime mixing heights were interpolated from hourly values into 1-min values. The KW2 model also requires data files on sunrise and sunset times and climatological mixing or inversion heights.

A number of modifications were made in the KW2 code in order to include better resolution in cloudiness and humidity and in solar and long-wave radiation. The original FRCST code maintains a constant nighttime boundary-layer height of 50 m in one portion of the code. In the version used for this analysis, the nighttime portion of the code was changed to allow for a more natural growth in this height. The nighttime boundary layer height (NBLH) was expressed as

$$ NBLH = He \; erf\left[\frac{t}{\tau_r}\right] \tag{11} $$

where He is an equilibrium boundary-layer height that depends on the total nocturnal cooling, geostrophic wind, roughness, and other factors (Stull, 1993), τ_r is the response time, and t is the time since the evening neutral event. The quantity τ_r may vary from 1 to 2 hr and He from 55 to 373 m. In the cases considered in this phase of work, He = 200 m, τ_r = 120 min, and t was incremented at 15-min intervals during the time from the evening neutral event to the development of a daytime unstable boundary layer.

A summary of the general input data requirements is shown in Table 2. Each model was run using the appropriate data from each time period. Thus the models were run in a diagnostic and not a predictive mode for this analysis. Therefore, the analysis was really a comparison of the models' various computational algorithms and how they responded to the various input parameters.

628

4. RESULTS

A comparison of the model C_n^2 results for two days is shown in Figs. 1 through 4. The figures show the 24-hr variation of C_n^2 as represented by observed 8-m scintillometer data from WSMR and the 24-hr C_n^2 computed by the various models. The 24-hr wind speed variation for the time period covered by the data is also shown in the figures for reference.

The SK, KW2, and RT models provided fairly good results during the daytime (Figs. 1, 2, and 3). The SK regression equation method had a tendency to produce negative C_n^2 values during the nighttime and near the neutral events (as shown by missing points in the logarithmic plots of Fig. 1) but usually performed adequately during the daytime.

The KW2 model results are shown in Fig. 2. The code exhibited occasional computational instability (high peaks in C_n^2) just after the morning neutral event and before the afternoon/evening neutral event (see, for example, Fig. 2a at approximately 1600 hr). This model appears to simulate the time of the neutral events approximately, but the magnitude is usually incorrect. Kunkel and Walters (1983) have shown that C_n^2 is sensitive to windspeed, the soil parameter $\rho_s c_s$, and the soil moisture content. In the KW2 code, the value of the product $\rho_s c_s$ has been changed from a fixed value to a value explicitly calculated from soil moisture parameters. The surface and 20-cm soil moisture values were not known and a number of trial runs using different combinations of soil moisture parameters were necessary to obtain results comparable to the observations. Thus the vertical soil moisture gradient appears to be an important parameter for estimating the optical turbulence with this model. The windspeed sensitivity is more apparent during the nighttime hours and is difficult to isolate during the day.

An attempt to include a correction for cloudiness in the down-welling long-wave radiation equation did not seem to improve the results significantly and in most cases made the correlations between model and observed C_n^2 poorer. This result may not be too surprising because Kondratyev (1969) indicates that empirical equations of down-welling long-wave radiation can be used only in a statistical sense (i.e., as average values). This limitation exists because the radiation is not a unique function of either the air temperature or water vapor pressure near the earth's surface or of cloud amount.

The RT energy balance model was rather consistent in providing a reasonable daytime diurnal curve of the optical turbulence (Fig. 3b). The present version is quite limited, however, since it does not allow input of data within an hour of the neutral events. The model requires data input on clouds and soil conditions. Even with correct cloudiness input, however, it still cannot predict the correct C_n^2 for some time periods, such as happened on Julian day 122 (Fig. 3a). Another characteristic of the results from this model is that on several days the C_n^2 maximum decreased too rapidly toward the evening neutral event as compared to actual conditions. In addition, the results from the model are very sensitive to a soil moisture factor that has to be estimated from ground and weather conditions.

The Andreas model results are shown in Fig. 4. The algorithm exhibited computational instability and this problem affected the overall results. Uncertainty in the temperature and humidity roughness factors for desert conditions may have been a contributing factor. The model did not predict the neutral events very well, either missing them altogether or over- or under-predicting the magnitude. The calculated optical turbulence also appeared sensitive to very low (< 1 m s^{-1}) and high (5 m s^{-1}) windspeeds.
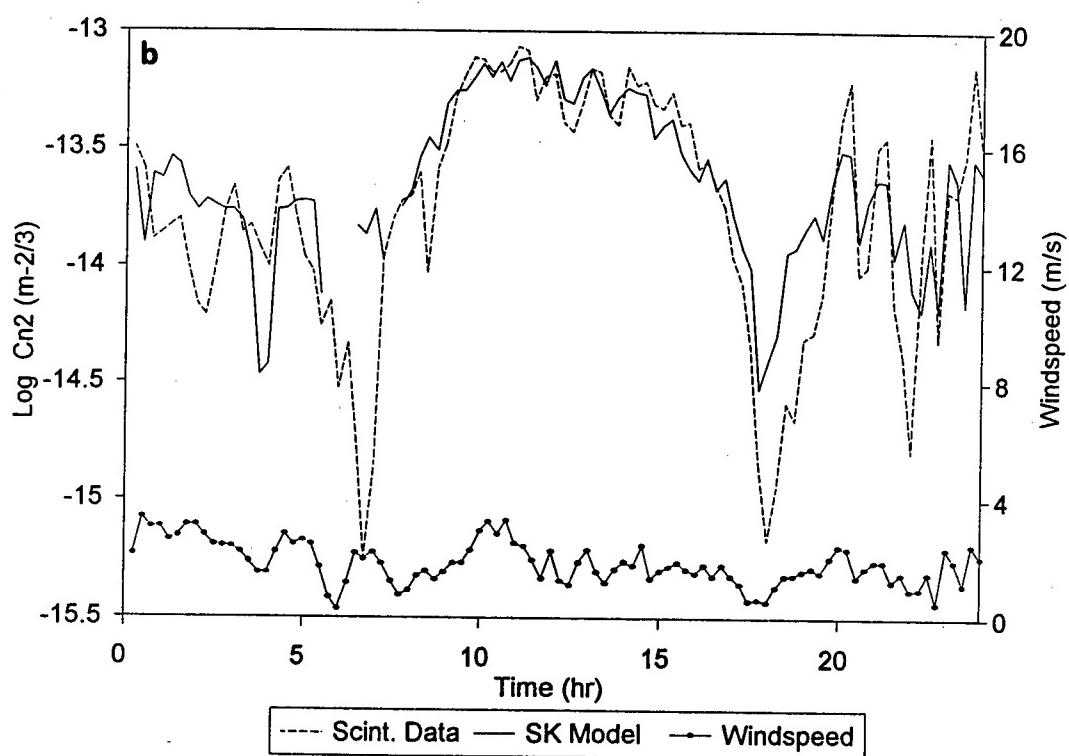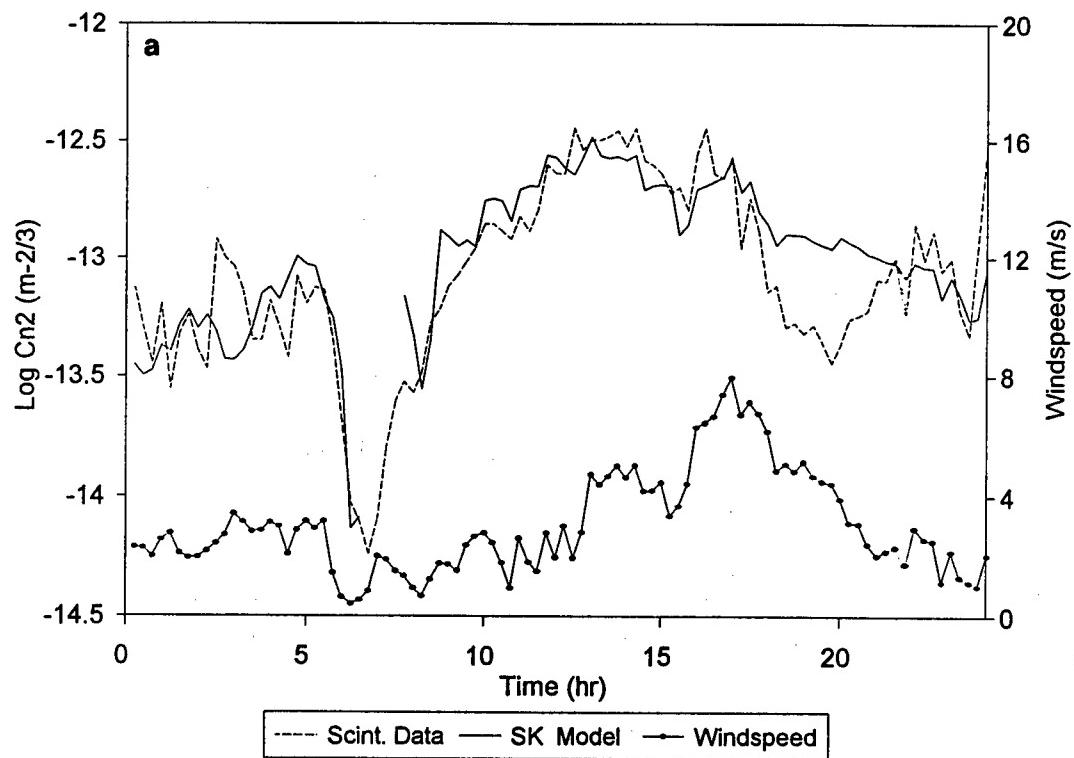
Figure 1. Examples of C_n^2 values from the Sadot/Kopeika statistical regression model compared with scintillation and windspeed data. a: Julian day 122; b: Julian day 228.
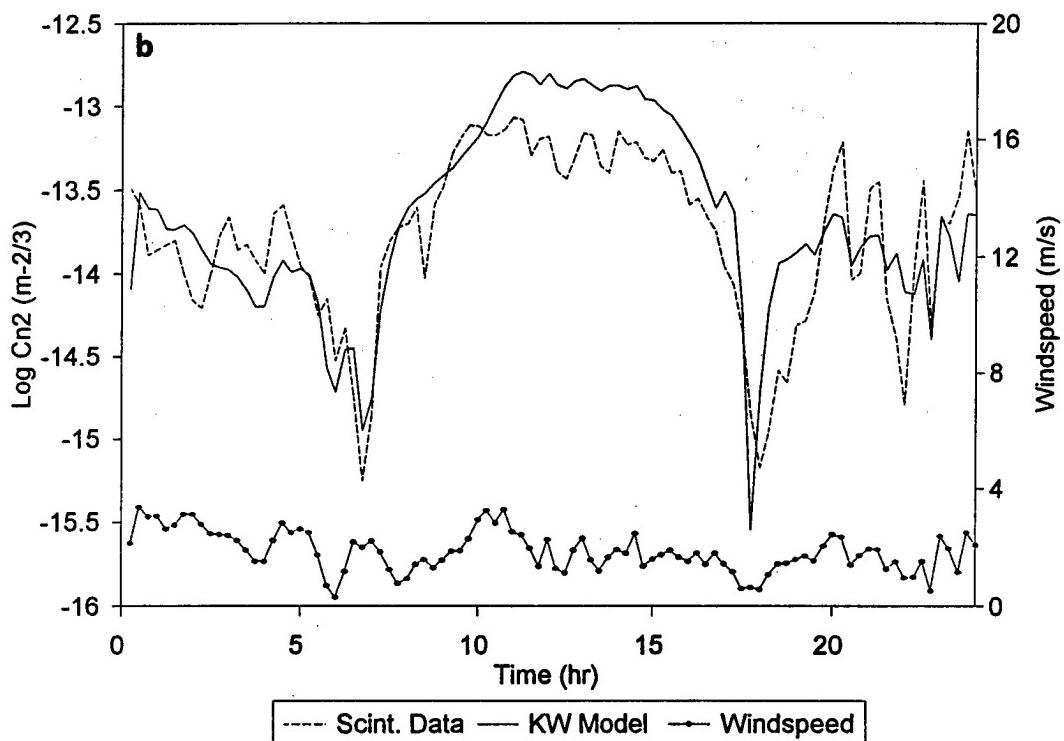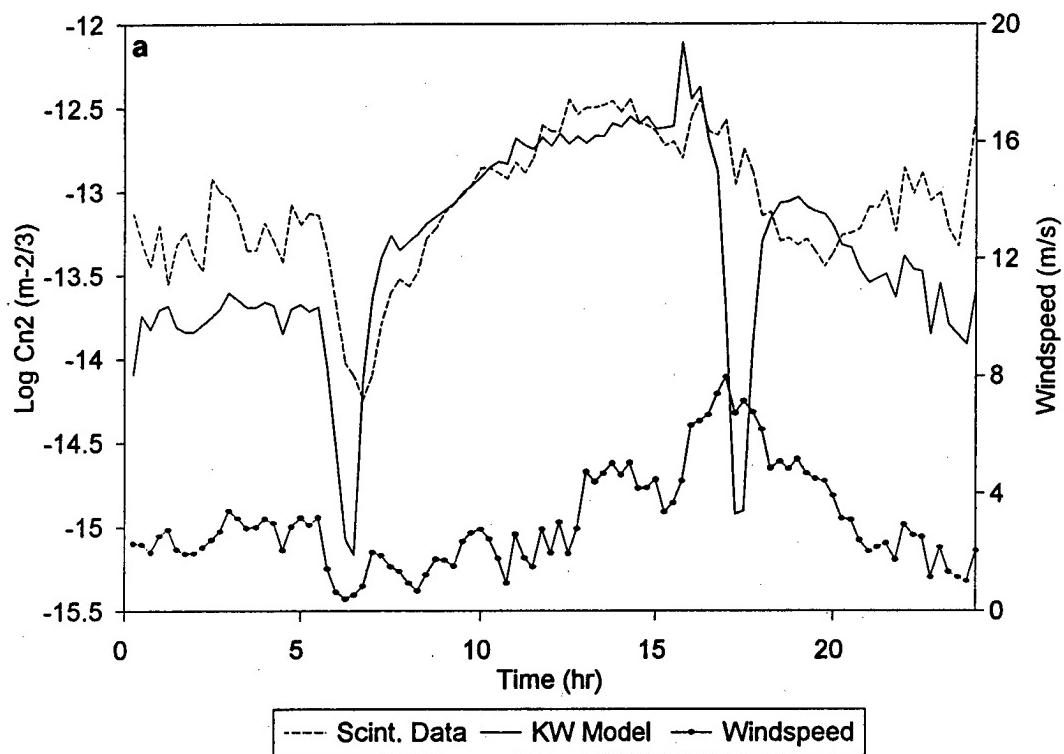
Figure 2. Examples of C_n^2 values from the Kunkel/Walters energy balance model compared with scintillation and windspeed data. a: Julian day 122; b: Julian day 228.
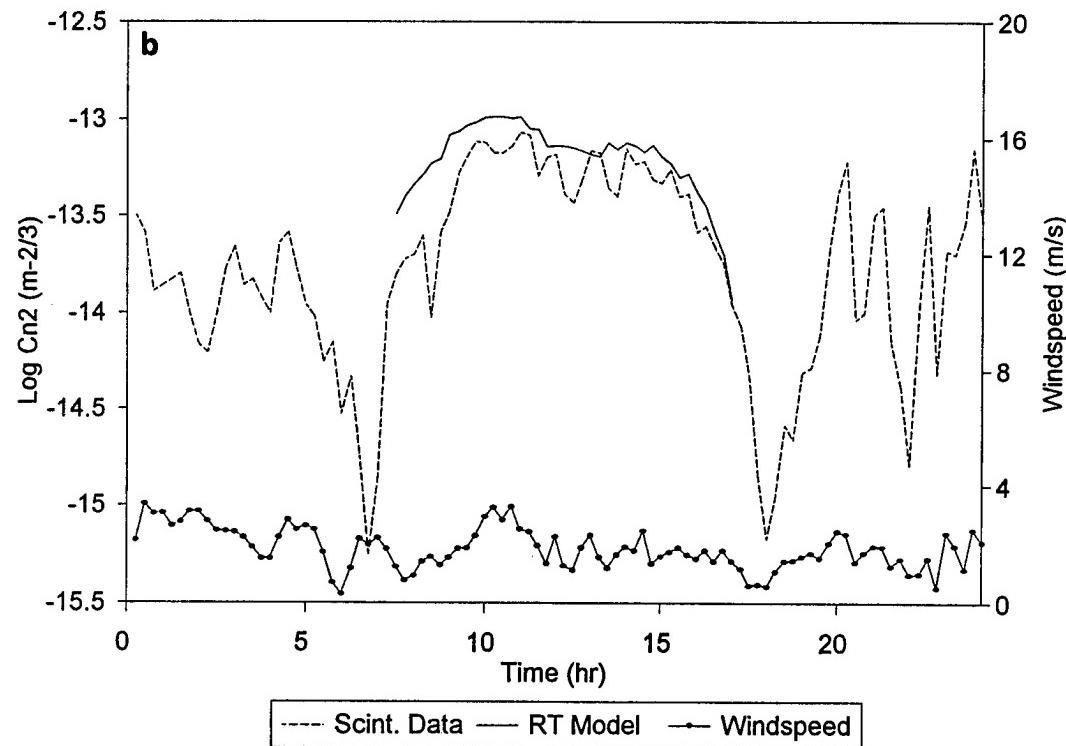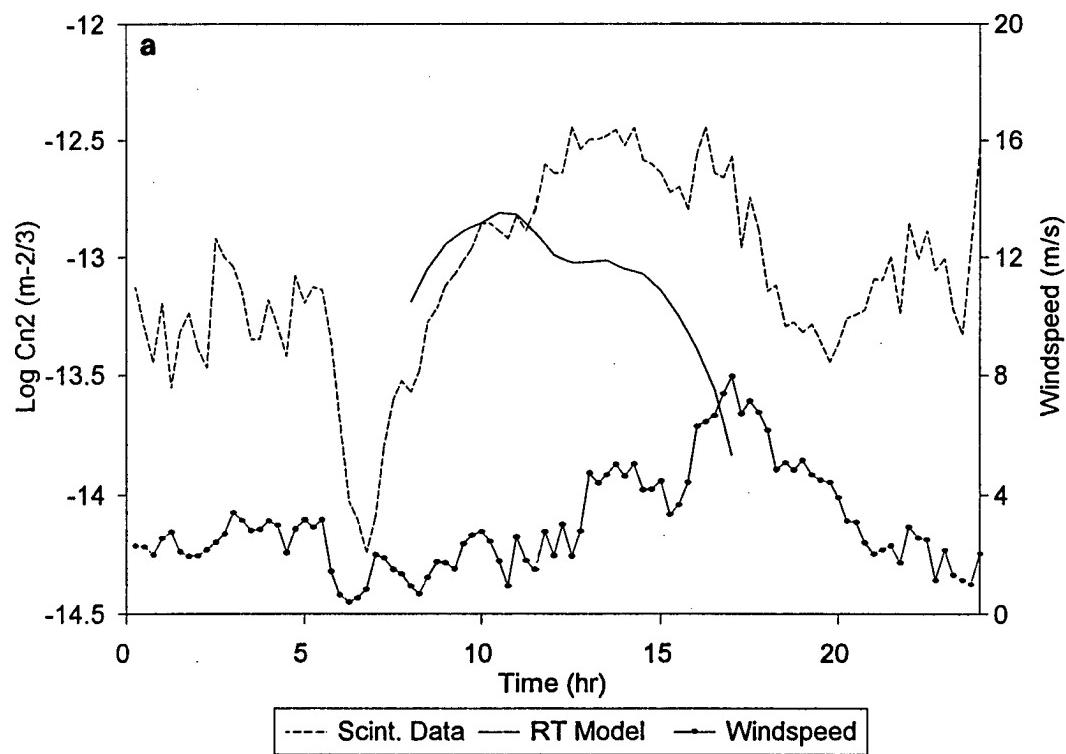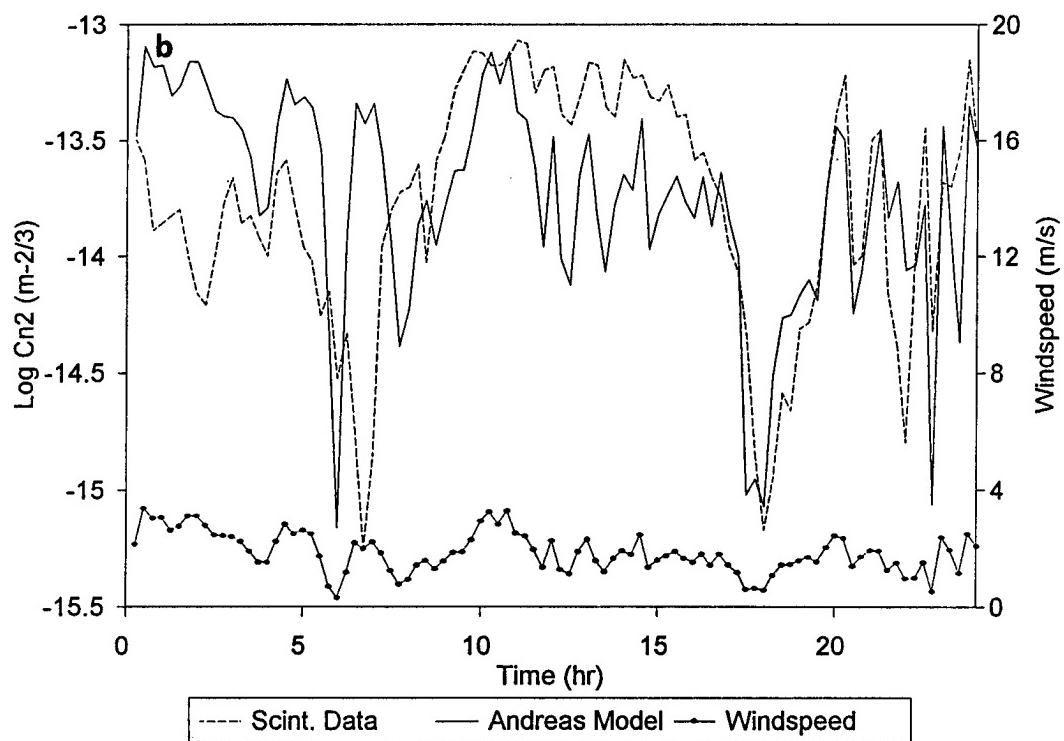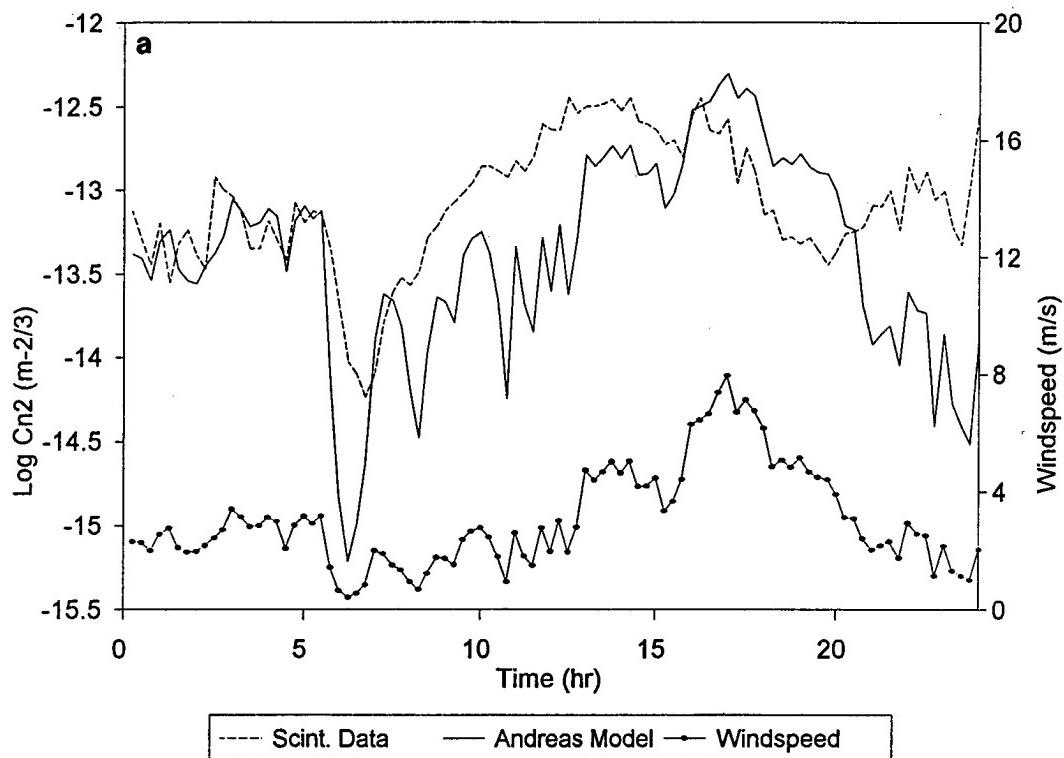
631

Figure 3. Examples of C_n^2 values from the Rachele/Tunick energy balance model compared with scintillation and windspeed data. a: Julian day 122; b: Julian day 228.

Figure 4. Examples of C_n^2 values from the Andreas bulk meteorological model compared with scintillation and windspeed data. a: Julian day 122; b: Julian day 228.

Another comparison of the model results is provided through autocorrelation coefficients between the computed and observed C_n^2 for each time step during a test period. The autocorrelation is computed by

$$Cor = \frac{Cov(O,M)}{\sigma O_i \sigma M_i} \tag{12}$$

where Cov (O,M) denotes the covariance between O and M, defined as follows:

$$Cov(O,M) = \sum_{i=1}^{n} \frac{(M_i - \overline{M})(O_i - \overline{O})}{n} \tag{13}$$

The quantity O_i denotes a particular data item at time i for the observed data, and M_i is the equivalent data item for the model data. The quantities $\overline{O}$ and σO_i denote mean and standard deviation of O_i, $\overline{M}$ and σM_i are the corresponding parameters for the model data, and n is the number of data observations. The autocorrelation coefficients for the four models and sixteen test periods are shown in Table 3.

An examination of Table 3 for all four models shows that they did not perform in a consistent manner, with autocorrelations varying from -0.36 to 0.89. In fact, the models were not even consistent during consecutive days. The best overall results were obtained from the SK, RT, and KW2 computations, with slight differences among them. The correlations for the SK model varied from 0.04 to 0.89. The SK regression method, when used over several days, however, tended to produce negative C_n^2 values for nighttime and evening periods. It also may not predict the neutral events on a consistent basis. Nevertheless, this method appeared to simulate the daytime period just as well as the other models, with an overall average daytime autocorrelation of 0.64.

The correlations for the Andreas bulk model varied from -0.02 to 0.66, indicating that this technique gave variable results because of the problems mentioned above. The overall average autocorrelation was 0.34, the poorest of the four models. The KW2 correlation results varied from 0.20 to 0.84, with an average of 0.51. The KW2 results were also divided into daytime and nighttime periods. Generally, correlations were higher for the daytime periods (0.52 compared to 0.38).

The daytime correlations for the RT model varied from -0.36 to 0.84 with an average of 0.56. This result is comparable to the daytime KW2 overall correlation of 0.52. This model is computationally stable and provided reasonable daytime C_n^2 values for many of the days.

5. CONCLUSIONS AND FUTURE WORK

Four optical turbulence models have been evaluated for predicting C_n^2 at one level (8 m) over a 24-hr period. The SK polynomial regression model is one of the simplest to use, since it requires only four input parameters. This fact also weakens the method, however, because important physical parameters are not considered. The method also produces negative values of C_n^2, especially during early-morning and nighttime periods. The method could probably be improved by adding additional parameters and using a combined neural net and statistical regression technique.

The energy balance models, KW2 and RT, provide fairly reasonable results for the daytime period but require more extensive data inputs. The present RT model does not predict the optical turbulence for the nighttime and additional work is required to add the appropriate algorithm. The KW2 model tends

to be computationally unstable at times, making it difficult to get consistent results from one day to the next. The KW2 is also the more complicated model, requiring detailed input data from temperature, humidity, pressure, wind, mixing and inversion heights, sunrise and sunset times, and soil moisture. It is the only model that provides an output file of the vertical profile of C_n^2 for different time periods, however. Other versions of this model need to be updated with a better wind input subroutine.

The Andreas model also exhibited computational instability, adversely affecting the results. In addition, this model did not predict neutral events with much accuracy, either as to time or as to turbulence level.

All four models could be used in a predictive mode if the appropriate input data could be provided by predictions. Continued examination of these models and additional refinements are necessary to improve the prediction capability for C_n^2. The statistical model, perhaps improved by using a neural net approach and additional parameters, promises to provide a quick and simple computation based on standard meteorological inputs derived from readily available forecast models (with the exception of aerosols). The energy balance models require more input data, which are not so easily obtained from forecast models. In particular, soil and cloudiness parameters are required, and their prediction would add uncertainty to longer-range forecasts of C_n^2. Also, the original Kunkel and Walters FRCST code requires upper-air observations.

TABLE 3. MODEL AUTOCORRELATIONS

Date	SK (Daytime)[*]	RT	Andreas	KW2	KW2 Daytime	KW2 Nighttime
Winter						
87338	(0.49)	0.70	0.53	0.43	0.32	0.45
87029	0.04	0.59	0.06	0.28	0.67	-0.06
89039	(0.87)	0.84	0.65	0.26	-0.05	0.03
89040	0.89	0.47	0.24	0.69	0.48	0.71
89041	(0.70)	0.77	0.33	0.84	0.90	0.73
89044	0.39	0.61	0.25	0.20	0.28	0.04
Spring						
89122	(0.50)	-0.36	0.46	0.66	0.59	0.16
89123	0.68	0.58	-0.02	0.50	0.50	-0.10
89124	0.67	0.30	0.64	0.71	0.72	0.07
Summer						
87197	0.89	0.65	0.05	0.82	0.73	0.33
87225	0.71	0.71	0.45	0.21	0.05	0.70
87228	(0.73)	0.81	0.25	0.80	0.79	0.55
87229	(0.32)	0.74	0.44	0.12	0.07	0.58
Fall						
88292	(0.65)	0.40	0.07	0.69	0.85	0.51
88293	(0.89)	0.40	0.66	0.58	0.68	0.36
88319	(0.60)	0.82	0.38	0.20	0.14	-0.35
Averages	(0.64) 0.61	0.56	0.34	0.51	0.52	0.38

[*] Values in parentheses are for daytime values; others are for the full 24-hr period.

REFERENCES

Andreas, E.L., 1988a: Estimating C_n^2 over snow and sea ice from meteorological quantities. *SPIE Optical, Infrared, and Millimeter Wave Propagation Engineering*, **926**, 258-267.

Andreas, E.L., 1988b: Estimating C_n^2 over snow and sea ice from meteorological data. *J. Opt. Soc. Am.* **A,5**(4), 481-495.

Deardorff, J.W., 1978: Efficient prediction of ground surface temperature and moisture, with inclusion of a layer of vegetation. *J. Geoph. Res.*, **83**(C4), 1889-1903.

Kondratyev, K.Y., 1969: Radiation in the atmosphere. *International Geophysics Series*, Vol. 12, Academic Press, New York.

Kunkel, K.E., and D.L. Walters, 1983: Modeling the diurnal dependence of the optical refractive index structure parameter. *J. Geoph. Res.*, **88**(C15), 10,999-11,004.

Rachele, H., and A. Tunick, 1992: Energy balance model for imagery and electromagnetic propagation. *Proceedings, 1991 Battlefield Atmospherics Conference*, Atmospheric Sciences Laboratory, U.S. Army Laboratory Command, White Sands Missile Range, New Mexico, 251-260.

Sadot, D., and N.S. Kopeika, 1992: Forecasting optical turbulence strength on the basis of macroscale meteorology and aerosols: models and validation. *Optical Engr.*, **31**(2), 200-212.

Wesely, M.L., 1976: The combined effect of temperature and humidity fluctuations on refractive index. *J. Appl. Meteor.*, **15**(1), 43-49.

APPLICABILITY OF MESO-SCALE AND TERRAIN EFFECTS MODELS FOR BATTLEFIELD ENVIRONMENTS

H. Weber and W. aufm Kampe

German Military Geophysical Office
Mont Royal, D-56841 Traben-Trarbach

In order to produce scenarios for battlefield environments there is a need for realistic wind data. Both wind fields for shorter episodes as well as the statistical frequency distribution for a specific location are required. This holds for different aspects of environmental protection and disaster preparedness as well. Actual data from weather stations in the area or output from a routine forecast model is not always available or its representativity is not sufficient (e.g. in heavily structured terrain). The applicability of meso-scale and terrain effects models to derive synthetic wind roses for structured regions is demonstrated for different situations.

Introduction

Climatological wind roses are commonly used to evaluate the expected environmental effects of wind on materiel and operations. Applications are manifold and range from studies on the assessment of the threat from chemical or biological attacks or judging the probability of successfully sustaining a smoke screen to planning operations of airborne mobile forces. In the field of civil engineering the applications range from the siting of chemical plants producing toxic substances to merely estimating the annoyance from odors emitted by refuse dumps. The field of wind energy production is another example for the application of wind roses.

Specific stations are selected for the purpose of providing 'representative' data for the specific domains involved. Such stations are, however, not very numerous and frequently far apart. Additionally, the question as to what is 'representative' for a specific region is not easily answered. The individual appearance of a measured wind rose is determined by phenomena on very different scales ranging from synoptic effects to micro-meteorological influences. The reason for this is generally the terrain. While large scale terrain features such as the distribution of land and sea have a major impact on the synoptic scale, local hills and valleys including the distribution of vegetation will strongly influence the micro-meteorological scale. Therefore a measured wind rose does not allow the deduction of the dominant effects

of different scales in a given domain. It is therefore very difficult to find a measured wind rose which is truly representative for a problem related to a specific scale at a given point.

Numerical models of varying sophistication are available, which are capable of simulating the effects of structured terrain on the wind field. An attempt is made here to use such models in producing synthetic wind roses for arbitrary points in a structured terrain with the aim of arriving at a better indication of areas in which the strongest deviation from a 'representative' wind field are to be expected and will lead to adverse impacts on planned operations.

Resolution of Terrain in Models

The intention of the first series of figures is to visualize the effects of increasing resolution on terrain features and to convey an idea of how terrain is experienced by models in different scales.

Figure 1 shows the terrain used in GMGO's routine weather forecast model, the BLM /1/. It has a resolution of about 60 km and covers central Europe. The area extracted is about 400 km x 300 km and appears rather smooth in the enlargement. A resolution of 5 km (Figure 2) shows, however, that there are some very dominant terrain features in this region (e.g. the Hunsrück and Eifel Mountains in the SW corner bounded to the east by the wide upper Rhine Valley). Again the enlargement of an area of about 25 km x 20 km appears very smooth in this resolution.

Figure 3 shows that again we find a strong relief if we look at the area with a resolution of 200 m. Major features are the Mosel Valley running from the SW to NE with its many tributaries.
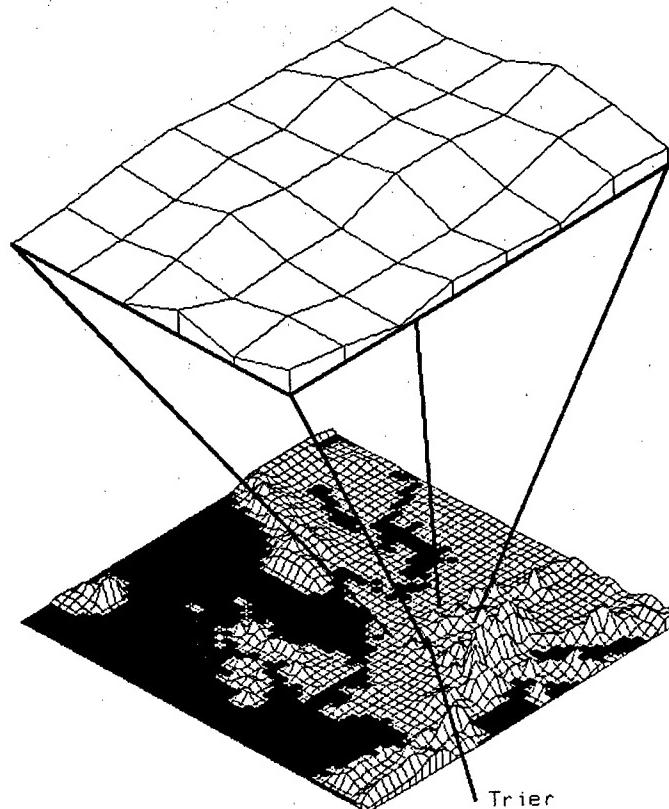
Figure 1: Terrain used in routine forecast model BLM at GMGO.

Figure 2: Extracted area from Figure 1 with a resolution of 5 km. Area extracted here is 25 km x 20 km.

Eifel
Trier
Rhine Valley
Hunsrück

Weather Station
Trier
Eifel
Hunsrück
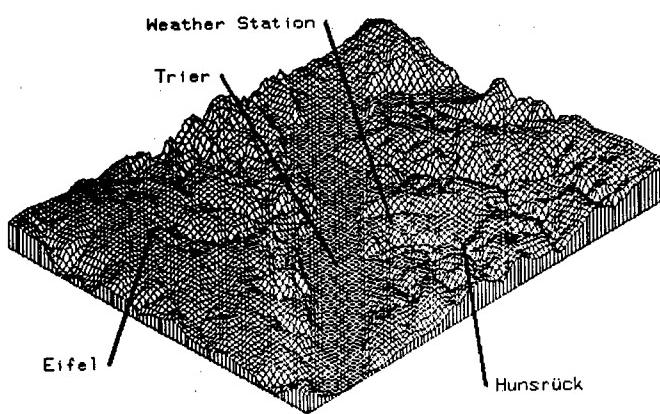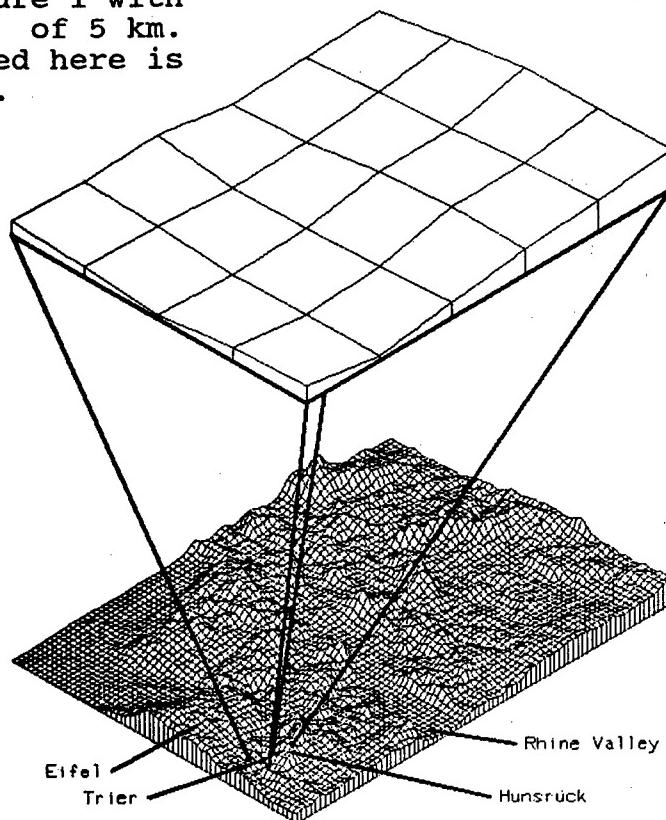
Figure 3: Area extracted from Figure 2 with a resolution of 200 m.

Representative Wind roses

Figure 4 shows a wind rose of measured data from the weather station near Trier on the slopes of the Mosel River marked in Figure 3. This wind rose shows strong channeling effects which can be attributed to the local terrain features of the valley. A measurement on the ridge of the Hunsrück Range to the south would undoubtedly produce quite a different wind rose, but we are lacking a station here. It would be desirable to be able to use a model to simulate the different local effects and thus substitute for a station. Figure 5 shows the wind rose for Trier as produced by the BLM Model for the same time period as in Figure 4. As can easily be seen the results are quite different. This can be attributed to the insufficient resolution of the terrain in the BLM as described above.

Figure 4: Wind rose measured at Trier Weather Station.

Therefore a modified version of the terrain effects model by Ball and Johnson /2/ was used with a grid spacing of 1 km to produce synthetic wind roses for a region around Trier. Besides a wind input this model requires a parameter charac-
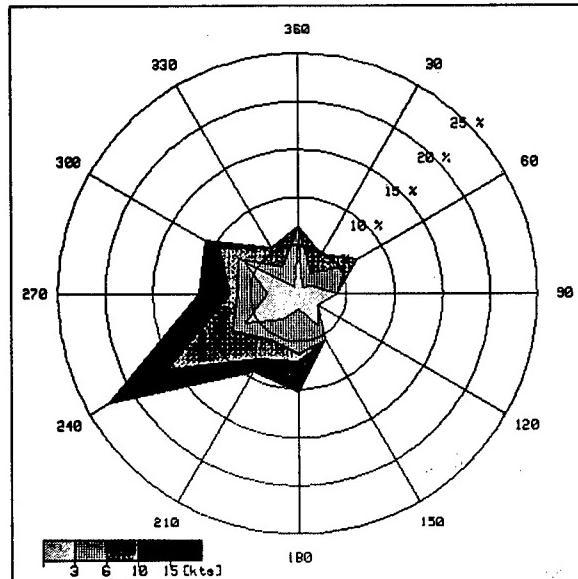
Figure 5: Wind rose produced by the BLM model.

Figure 6: Wind rose derived from large scale pressure gradients

642
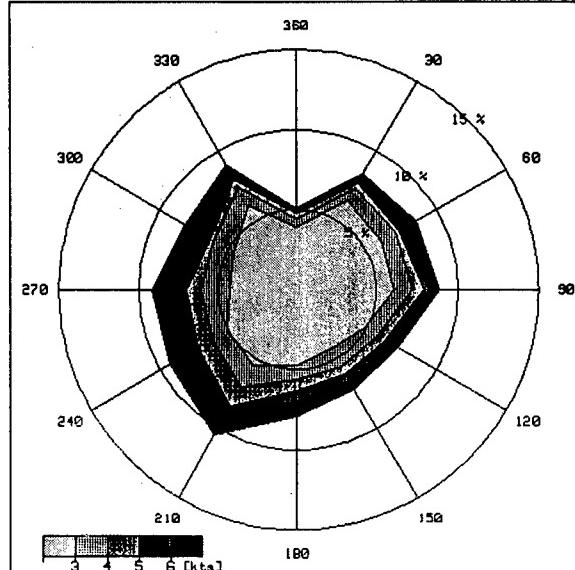
terizing the atmospheric stability. The wind input was derived from large scale pressure data as a quasi geostrophic wind. This wind was reduced to the 10 m level using an empirical procedure developed at GMGO and described in a thesis presented at the University of Trier by Seher in the field of wind energy /3/. This wind rose is shown in Figure 6. Figure 7a and 7b show the corresponding wind roses for unstable and stable conditions. The stability categories were determined using synoptic data.

Based on the stable wind rose a number of runs of the Ball and Johnson Model were carried out to produce the 'rose garden' shown in Figure 8. A run was produced for every 10° from 10° to 360° and each of 5 wind speed categories. Each run was weighted proportionally to the occurrence of its individual combination in the input wind rose (Figure 7b). Using these weights and all runs a wind rose is created at each grid point. The wind roses are shown only for every fourth grid point together with the height contours of the terrain.

The difference between the local wind roses is considerable as was to be expected. The results are plausible with respect to the input made to the model. For example at the bottom of the Mosel Valley the wind roses indicate the occurrence of cross winds. These are caused by the downslope winds under stable conditions. However, the wind roses calculated for the vicinity of the weather station on the hills adjacent to the valley do not show the pronounced channelling effect so characteristic for the measured wind rose (Figure 4). This may
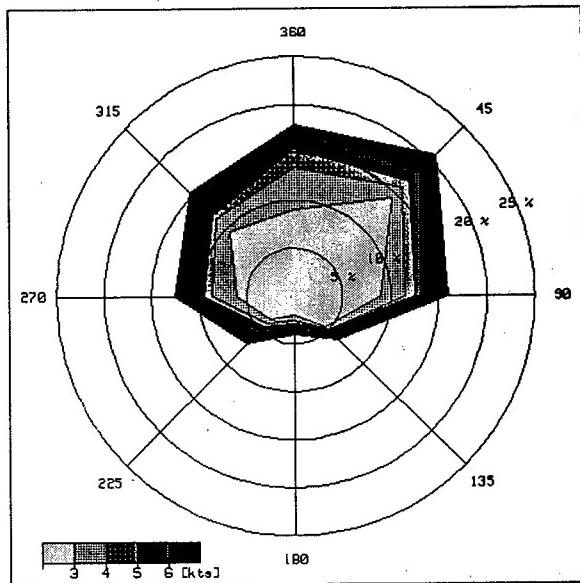
Figure 7a: Wind rose derived from large scale pressure gradients for unstable conditions
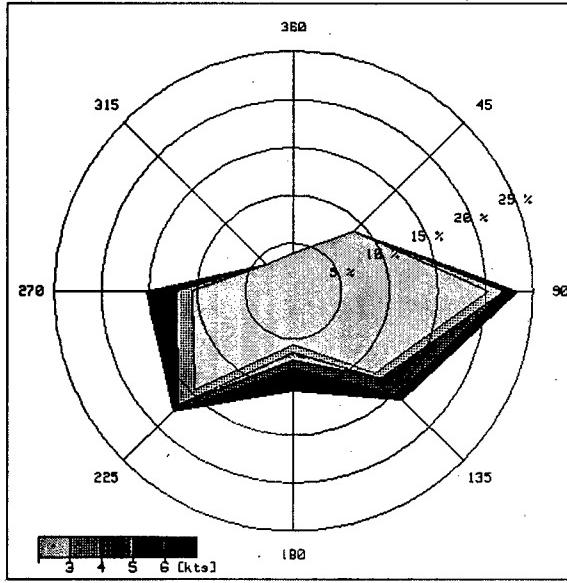
Figure 7b: Wind rose derived from large scale pressure gradients for stable conditions
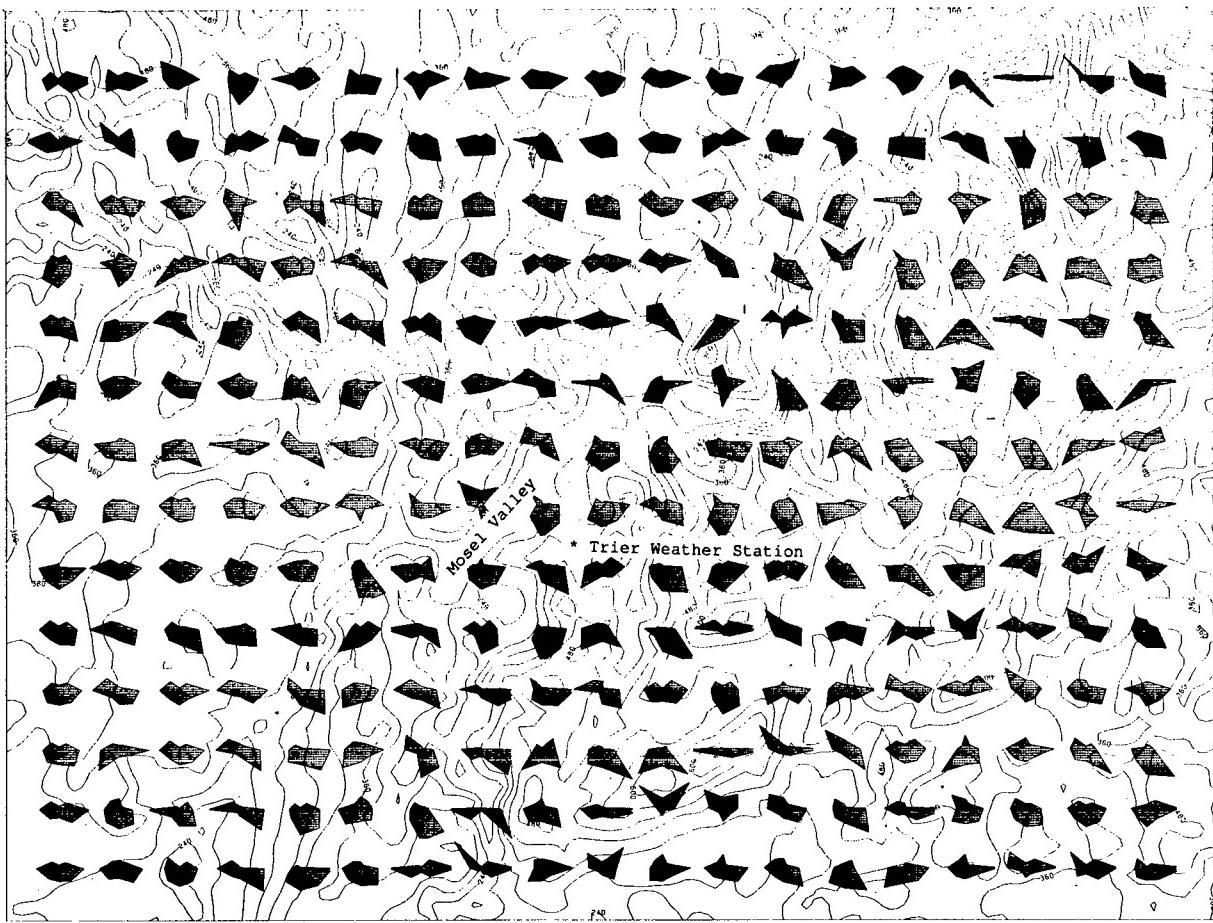
Figure 8: 'Rose Garden' of synthetic wind roses for an area of 80 km x 60 km around Trier using a resolution of 1 km.

be due to the fact that the model physics used here are not suitable for the scale applied. Other models are currently being tested at GMGO, but at present are not operational to a point where they could be run for comparison.

Comparison of Synthetic and Measured Wind Roses

The above results (Figure 8) clearly show that there is a need to compare synthetic wind roses with actual data measured at different points in a structured terrain. This is not possible in the region used in the above examples for lack of weather stations. An ideal set of data for this purpose was compiled during the MADONA field study carried out at CBDE in Porton Down, UK in 1992. This data has yet to be released, but preliminary results made available to the participants during the trial are used in the following for comparison with model results.

Again the Ball and Johnson Model is used now with a grid spacing of 100m. Figure 9a shows 15 wind roses derived from

644
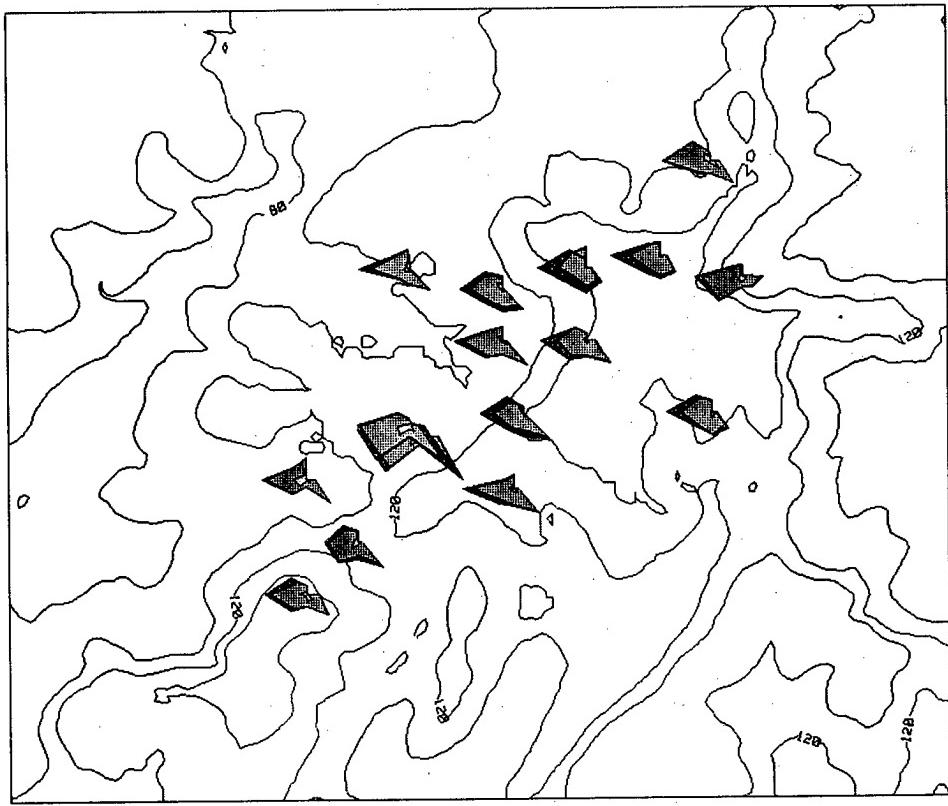
Figure 9a: Wind roses from measured data of the MADONA Trial
for unstable conditions.

measured data under unstable conditions during the 10 day trial
period. Figure 9b shows the analogous results for stable
conditions. The model results were produced using wind roses
measured at a relatively well exposed and undisturbed site near
the center of the plot. They are shown separately in Figure
10a and 10b. Figures 11a and 11b present the resulting
synthetic wind roses for the 14 remaining locations.

The agreement between synthetic and measured wind roses is
not absolutely convincing at first sight for each wind rose,
but a closer look at some of the features is more promising.
In the unstable situation (Figure 9a) almost all wind roses
except the one used as input to the model have a rather smooth,
slightly NW-SE elongated shape. This is also true for the
synthetic case (Figure 11a). Looking at the stable situation
(Figure 9b and 11b), and restricting ourselves to the 2 wind
roses furthest to the northeast, we find that the fact that the
wind rose furthest to the north resembles the input wind rose
while the other one shows stronger terrain effects is also
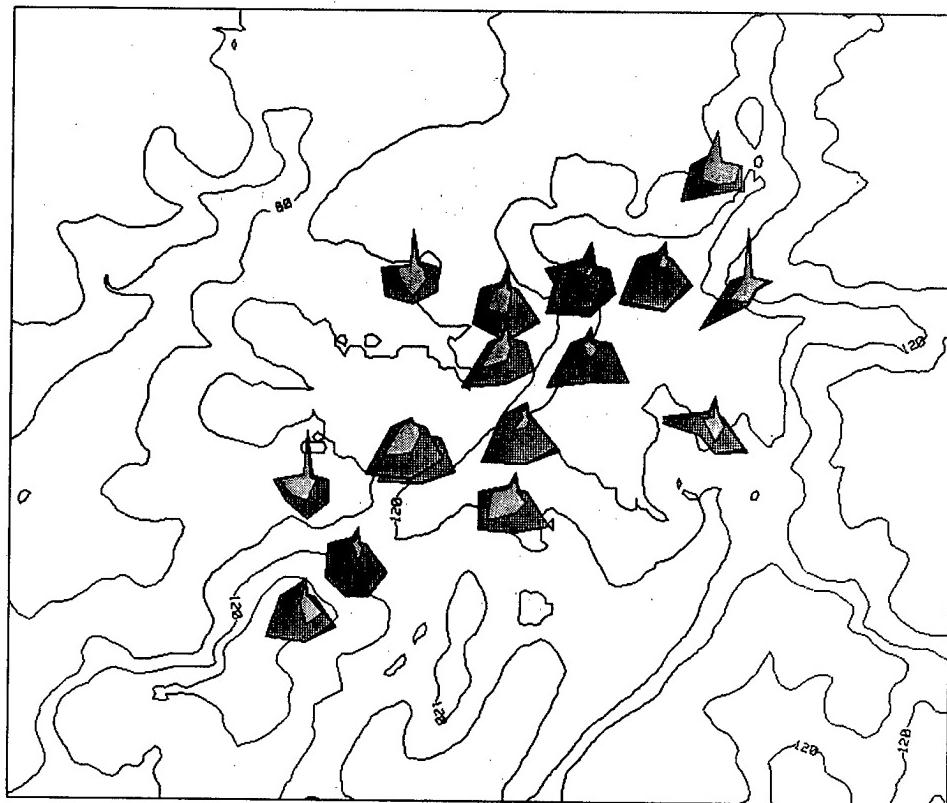
Figure 9b: Wind roses from measured data of the MADONA Trial for stable conditions.
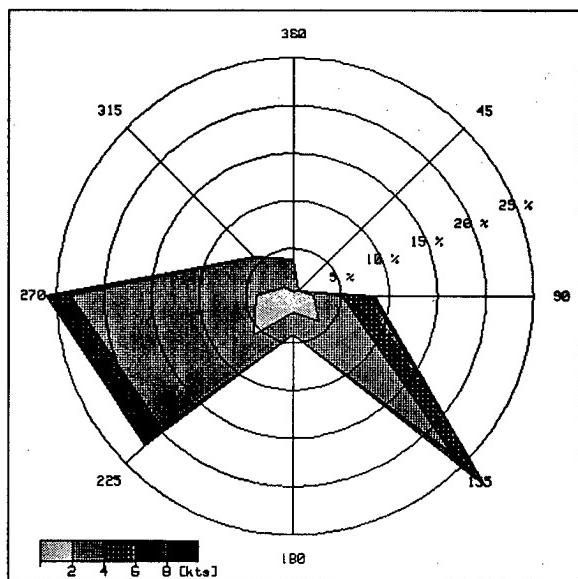

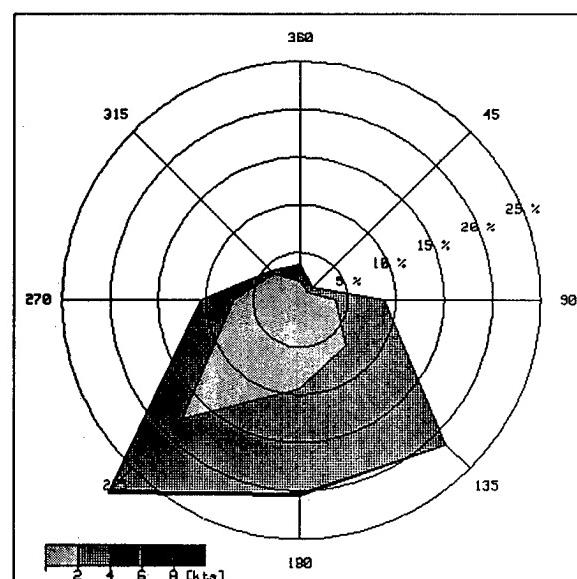Figure 10a: Input wind rose for unstable model run

Figure 10b: Input wind rose for stable model run
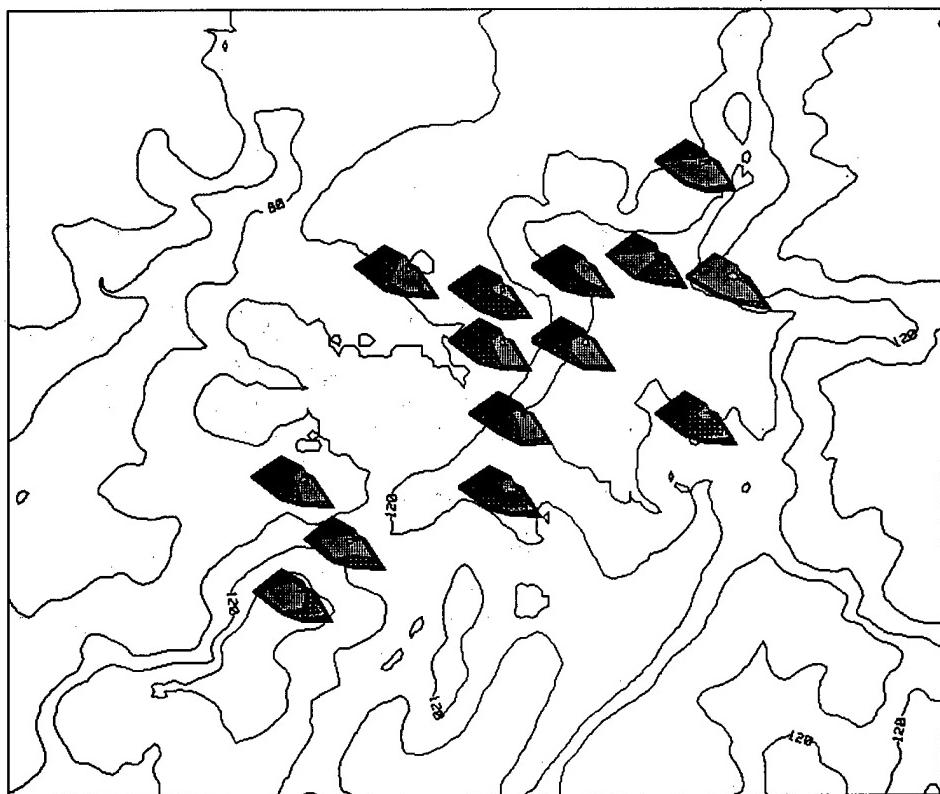
Figure 11a:
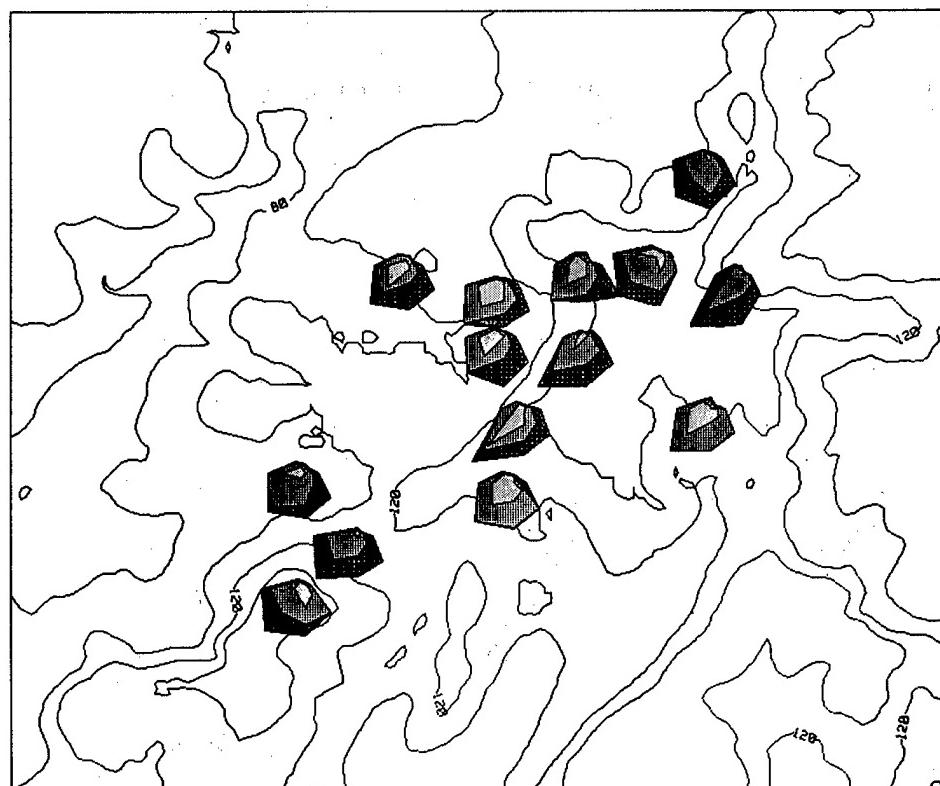
unstable

Figure 11b

stable

Figure 11: Wind roses calculated for the MADONA Trials.

647

reproduced in the synthetic case. In general the model tends to overestimate

the wind speed and smooth peaks as expressed by the larger areas with darker gray shades in Figures 11a and 11b as compared to Figures 9a and 9b.

It must be kept in mind that the results shown here are only based on a 10 day period of measurements. When the complete data set covering a whole month is released a more detailed investigation will be carried out.

CONCLUSIONS

It was shown that there is a need for producing synthetic wind roses to assist in planning operations and conducting studies both to substitute for lacking measured data in structured terrain and to investigate effects related to specific scales. An example of a field of synthetic wind roses is given which shows marked differences in the structure of the wind roses at different locations. A comparison with actual data from field trials shows that further developments are necessary that may lead to more sophisticated models in order to achieve acceptable results.

REFERENCES

/1/ T. Prenosil, H.G. Becker, Das "Boundary Layer" Modell des Geophysikalischen Beratungsdienstes der Bundeswehr. Fachliche Mitteilungen Nr 211, Amt für Wehrgeophysik, Traben-Trarbach, January 1990, ISSN 0342-6025

/2/ J.M. Lanicci, H. Weber, Validation of a Surface Layer Wind Flow Model Using Climatology and Meteorological Tower Data From Vandenberg AFB, California, AFGL-TR-86-0210, Environmental Research Papers, No. 963, Air Force Geophysics Lab. Hanscom AFB, Massachusetts, 1986

/3/ U. Seher, Untersuchung der Effizienz von Windenergie im Raum Trier. Masters Thesis, University of Trier, 1992

A MODERN GRAPHICAL USER INTERFACE
FOR LEGACY FORTRAN CODE

Dick Larson
Physical Science Laboratory
New Mexico State University
Las Cruces, New Mexico

The modern computing world is embracing the Graphical User Interface, e.g., MS Windows for the PC platform, System 7 for the Mac and the X-Windows standard for Unix. But the scientific community has a lot of still valuable FORTRAN code for which the interface is non-graphical. Our group wanted to port several large FORTRAN models from a command line oriented Unix platform to a MS Windows PC. Goals for the port were (1) to take advantage of a Graphical User Interface without having to write our own interface in C or C++, and (2) to avoid having to rewrite the FORTRAN code into some other language. We met the first of these goals by using an off-the-shelf, commercial MS Windows software product, MS Access, as a user interface to our data base of Radiosonde profiles and Radiometer field data. The user of our software employs Access' easy-to-use graphical interface to select the Radiosonde profiles to be ingested by a FORTRAN Radiative Transfer Model. Then Access' programming tool, Access Basic, passes these Radiosonde profiles to the FORTRAN model by calling the Model as a MS Windows DLL (Dynamic Link Library). Compiling the FORTRAN code as a DLL requires very little modification to the code, causes it to function as a single executable program together with the commercial database software and satisfies our second goal for the port, that we not have to rewrite the code.

1.0 INTRODUCTION

The Graphical User Interface is an important part of our modern computer environment. Computer users have begun to use Mac, MS Windows, and X Windows applications that offer, for example, the ability to display more than one window at a time within which graphically depicted options can be selected by clicking a mouse button, that offer on-line help by clicking on a pull-down menu item, and that offer ease of use and learning because the interface is consistent from application to application. In the PC world, sales of Windows software recently surpassed those of DOS software and nine out of the top ten PC manufacturers now include Windows with their systems.[1]

Microsoft estimates that it has sold over a million copies of MS Windows per month since the product was introduced in April of '92. That's an installed base of over 30 million copies.[2] Popularity of this magnitude means that your customers and your boss are likely soon to become familiar with the Windows computing environment - if they haven't already. And this is likely to mean that they will want the programs you write to run in the Windows environment. Far from being merely a burden to you, the developer, this means that your program will be easier for them to learn to use because they will be familiar with all its Windows' conventions.

Fine, new programs can easily be written to run under Windows. But what about old, and still useful, FORTRAN programs prevalent in the scientific community? It would be much too expensive to rewrite very large FORTRAN programs in some newer language. The solution to the problem of bringing these still useful, large FORTRAN programs into the modern GUI computer environment is to use a mixed language approach wherein just the user interface aspects of the program are re-written in a newer language that supports the GUI of the target operating system, e.g., MS Windows, while the computationaly intensive aspects remain in FORTRAN.

This paper describes our experience with this approach: what we tried, what we learned along the way, and what we hope to do in future. But first here are some of the advantages we see in the GUI and, as we see it, the role of FORTRAN in the future of computing.

2.0 ADVANTAGES OF THE GRAPHICAL USER INTERFACE

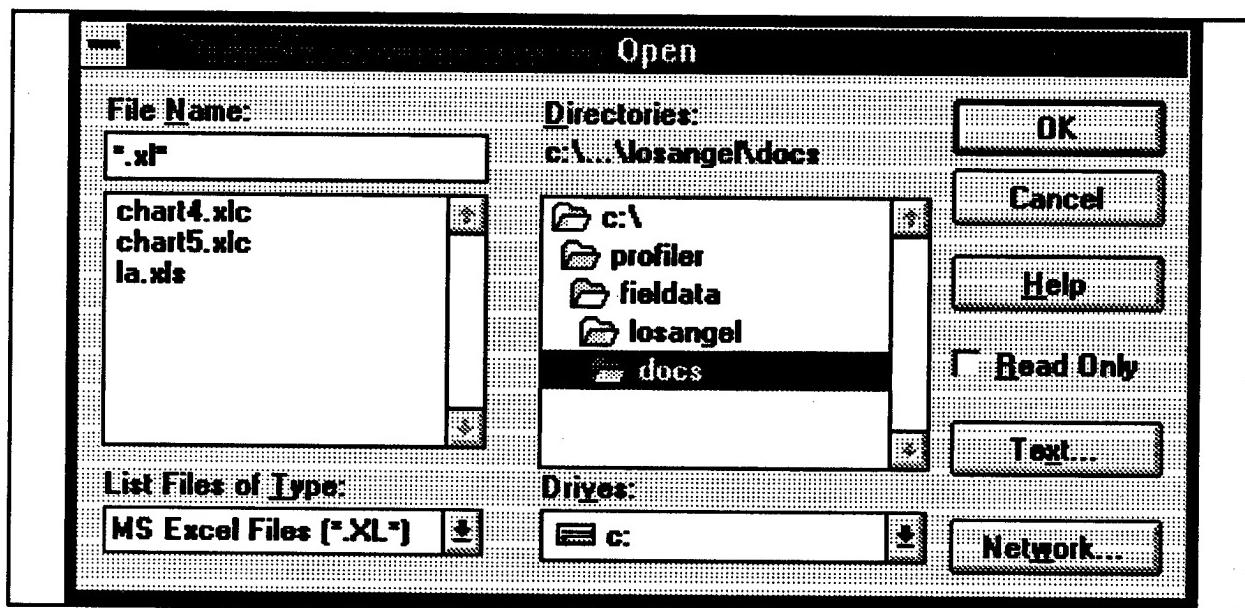The greatest advantage of a GUI may well be the conformity it enforces in the

Figure 1 Microsoft's Common Open File Dialog Box

interface of every program that is written for it. Users, having learned how to use one

Windows program, can use much of what they have learned about how to interact with that program to help them learn how to interact with a new Windows program. Almost all Windows programs, for instance, have a menu bar at the top of the application's main window with at least the pull-down menu items "File," "Edit," and "Help." The "File" item usually has sub-menu items under it of "Open," "Close," and "Print." Clicking on the "Open" sub-menu item usually brings up the common Open File dialog, the code for which. by the way, is available to programmers in Microsoft's COMMDLG.DLL included with every copy of MS Windows 3.1. No doubt you've seen this dialog. The screen shot of Figure 1 is of Microsoft Excel's common Open File dialog.

The point is that any application that reads a file from the operating system, is likely to allow the user to select which file to open using this exact dialog box - so the user will know how to open a file no matter which Windows program he is using.

Minimizing user frustration with the user interface, and increasing the ease of use would cover most of the rest of the advantages we see in the GUI. For instance, were a FORTRAN program to want the user to supply a file name within a traditional non-graphical user interface, the user would have to type the file name correctly without any visual clue, like that in the figure above, as to the correct full directory path or the correct spelling of all the directories on the path or the file name. Frustration may well be the result if the user mistypes the file name. Some of the great user interface devices that Windows supplies can be seen in the overcrowded dialog of Figure 2, a screen shot of Windows 3.1's Main group, Control Panel sub-group, Desktop dialog.

This dialog contains a drop-down list box for selecting from among the Patterns available; there are check boxes; there are control buttons for "OK," "Cancel," and "Help" which most dialog boxes have - to support the earlier point that Windows programs enforce a conformity in the user interface; there are Spin Controls for specifying the Delay in Minutes and the Sizing Grid's Granularity and Border Width and the Icons Spacing; there are Radio Buttons for Wallpaper, Center or Tile; and there is a Slider Bar to select the Cursor Blink Rate. It's fun to use these graphical devices and is likely to increase the functionality and decrease the frustration of a program's user interface.

3.0 ROLE OF FORTRAN IN A GRAPHICAL USER INTERFACE ENVIRONMENT

FORTRAN was written during the '50s. It has a command line oriented user interface (user usually enters his input at the prompt a line at a time). Actually, part of the value of FORTRAN in the 40 years of its existence has been just this operating system independence - FORTRAN code could be easily ported from a Unix machine to a VAX or to a PC FORTRAN compiler. As long as an operating system could support the command line interface (all can) the FORTRAN program was portable. But, given the powerful attractions of the graphical user interfaces built into today's modern operating systems, applauding FORTRAN for its simplicity is somewhat like
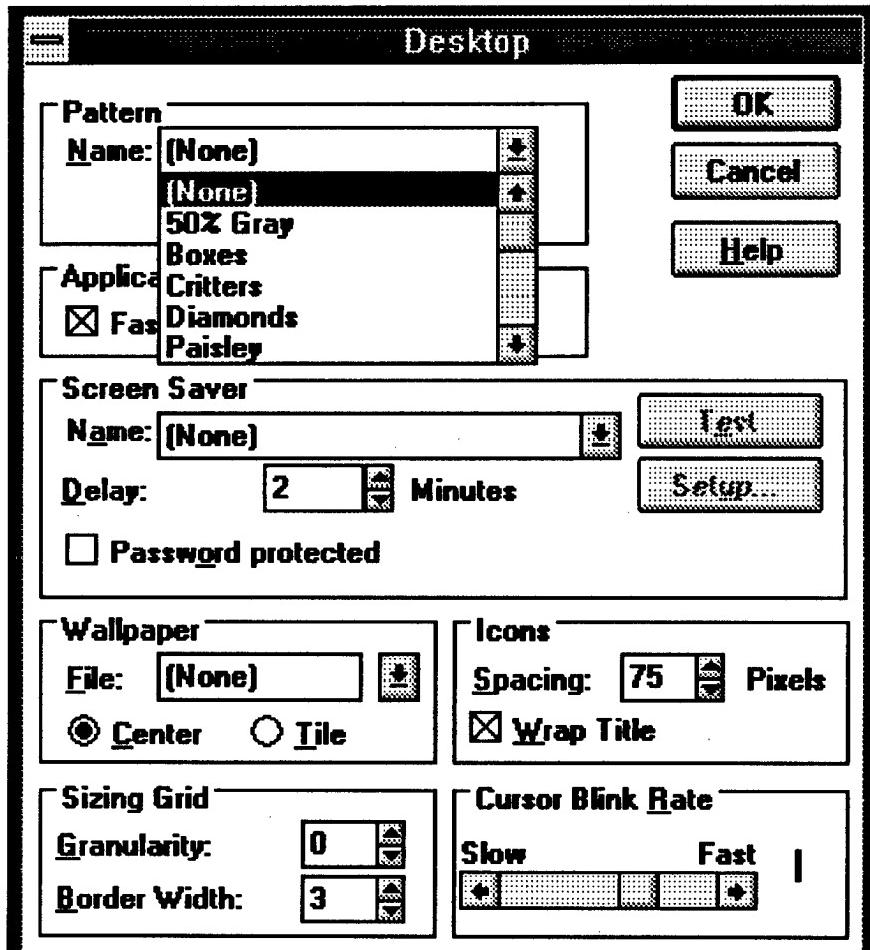
Figure 2 Main; Control Panel; Desktop Dialog

applauding an idiot for his simplicity.

Some of the best of the scientific community's efforts to enhance FORTRAN's command line interface have been the use of the input card order independent scheme in the EOSAEL libraries. And the use of a full page, character oriented (25 lines by 80 columns) interface by some of PSL's programmers in ARL projects (see the discussion of the "User Interface Shell" in Spalding and Weems).[3] Though these were good efforts, the great value and the coming predominance of the GUI, these FORTRAN user interfaces should be brought into the modern GUI environment.

Small FORTRAN programs can be rewritten in a recent language that supports the target GUI, for example Microsoft's Visual Basic or C or C++ in the PC world. But large FORTRAN programs would prove too expensive to completely rewrite in a new language. And FORTRAN has continuing strengths that make it still valuable. There's the already mentioned strength of its simplicity that allows code to be easily ported to new computers and operating systems. This simplicity also comes as a plus for the non-programmer mathematician or physicist who appreciate not only the simplicity but also that FORTRAN is still an excellent language for performing the FORmula TRANslation of mathematical and physical models for which it was designed. Also its math routines and intrinsics have been well tested - fast and efficient - over the past 40 years.

The computer industry has come to see the future role of FORTRAN as a back end compute intensive language in a mixed language scheme with a GUI oriented language providing the user interface.

"In the future when we move into Windows, we will probably have to move toward mixed applications," John said. "We will have the interactive code in C and then call on FORTRAN subroutines."

This programming approach, using the best of both worlds, seems to be part of the future of FORTRAN, according to Sunil Alagade, product manager for Microsoft Corp.'s FORTRAN PowerStation. "We are seeing this with a lot of our users," Alagade said. "FORTRAN is used for the number-crunching at the back end with Visual Basic at the front end." [4]

This mixed language scheme is exactly what we suggest for legacy FORTRAN programs that are too large to rewrite. As an aside, new scientific code might well best be written in one of the object oriented languages such as C++ or SmallTalk. These languages offer tremendous advantages and are, certainly in the case of C++, ready for heavy use in real application development today.

4.0 MOVING FORTRAN CODE TO A GRAPHICAL USER INTERFACE ENVIRONMENT

This section of the paper describes our FORTRAN to GUI experiences.

4.1 ARL'S MICROWAVE RADIOMETRIC PROFILER DATA ANALYSIS SYSTEM

Our data analysis system consists of a collection of graphics and statistical tools tailored to the analysis of RAOB (balloon-borne met instrument data) and Radiometric data. Central to the system, also, is a data base of RAOBs from sites throughout the world, 3 to 10 years of RAOBs for each site. Our most numerically intensive FORTRAN model, a radiative transfer model, ingests a RAOB and computes the radiation that a ground-based microwave radiometer would measure in an atmosphere characterized by the RAOB profile. The model is numerically intensive because of the double integration over the entire profile required to calculate the cumulative effect of radiation for each height layer upon the layer(s) just below it. The model makes good use of FORTRAN's math libraries, especially the trigonometric and complex routines. And the model is too large to economically convert to a newer language: it consists of 28 subroutines and a total of about 5300 lines of code. So this FORTRAN program was an excellent candidate for the mixed language approach currently favored by the computer industry.

4.2 THE GRAPHICAL FRONT END

Much of the required user input for the radiative transfer model is needed to select RAOB(s) to process from the data base: a site number or range of numbers is required as is a date or range of dates. If we could use our data base program, with its Windows graphical interface, to select the desired RAOBs and somehow get these RAOBS into our FORTRAN model, we'd have a first cut at a front end. Our data base program is Microsoft's Access. The screen shot of Figure 3 is of Access' graphical Query by Example grid, showing the selection of RAOBs for site number 31, where DateTime is between 9/01/93 and 9/30/93.
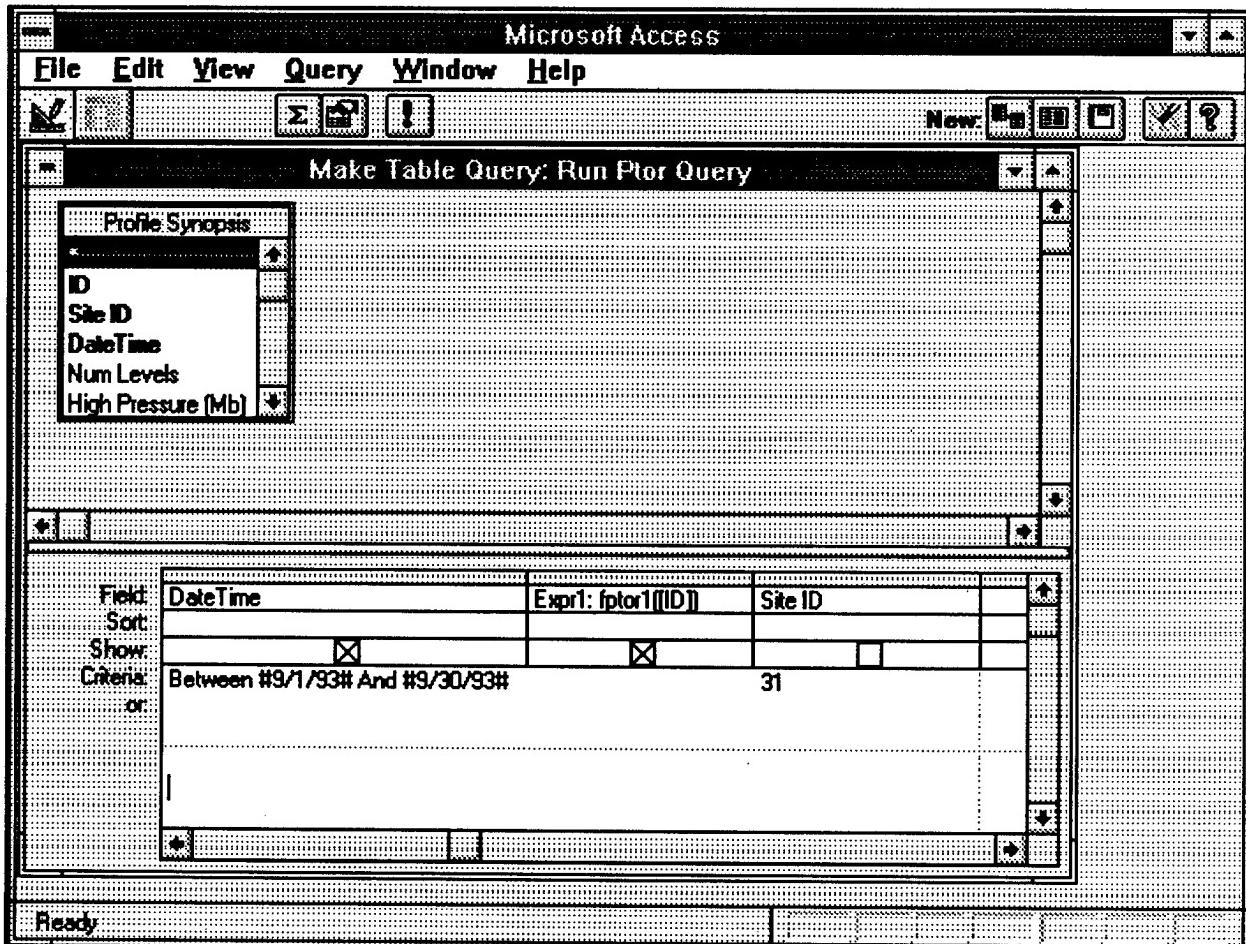
Figure 3 Microsoft Access' Query by Example grid

The depicted query gives us the RAOBs we want. We next need to pass the RAOBs to the FORTRAN model. We did this in Access Basic (a version of Microsoft's Visual Basic with data base extensions) the language that comes with Access. From Access Basic, calling the FORTRAN DLL (described below) requires only that the DLL be declared, e.g.,

```
Declare Sub ptordll Lib "c:\profiler\programs\ptor\ptor.dll"
(Height As Single, Temp As Single, Pres As Single, RelHum As
Single, NumRecs As Long, Tbs As Single, NumTbs As Long,
dwCldFlg As Long, dwIntegLiqWtr As Long, sngTrans As Single)
```

Where this has to be a single, long line. An example code snippet with the actual call to the FORTRAN DLL is:

654

```
Set Q = db.OpenQueryDef("Select Top of StdAtm")
    Q![Enter a Max Height (Km):] = Height(NumRecs)

    Set DataRecs = Q.CreateDynaset()
    I = NumRecs + 1
    Do Until DataRecs.EOF
        Height(I) = DataRecs![Normalized Height]
        Pres(I) = DataRecs![Normalized P]
        Temp(I) = DataRecs![Normalized Temp]
        RelHum(I) = DataRecs![Normalized RH]
        Debug.Print Height(I), Pres(I), Temp(I), RelHum(I)
        I = I + 1
    DataRecs.MoveNext
    Loop
    NumRecs = I - 1
    DataRecs.Close

    wCountProfiles = wCountProfiles + 1
    Debug.Print wCountProfiles, ProfileID, NumRecs

    ptordll Height(1), Temp(1), Pres(1), RelHum(1), NumRecs,
Tb(1), NumTbs, dwCldFlg, dwIntegLiqWtr, sngTrans
```

Where the last line is the call to the radiative transfer model. You can see the RAOB being passed down (height, temperature, pressure, relative humidity) and the Brightness Temperature, "Tb(1)," (computed measure of radiation that the radiometer would "see") being passed back up.

4.3 THE FORTRAN BACK END

We connected the graphical front end to the FORTRAN back end with the Dynamic Link Library feature of MS Windows. This feature allows whole libraries of useful common code routines to be called by any Windows program. These libraries are not linked to a developer's code during the link phase of the traditional edit, compile, link cycle. Instead, the libraries need only be present on a Windows PC when the developed program is run - they are dynamically linked to the program at run time. This is the way, for instance, that the earlier mentioned common Open File dialog (within the COMMDLG.DLL, see Figure 1) is made available to all Windows programs.

We created our DLL using Microsoft's FORTRAN 5.1 compiler. We named it PTORDLL for the Profile TO Radiance DLL. A screen shot from FORTRAN 5.1's Programmer's Work Bench, Initial Build Options menu is shown in Figure 4 with the option selected to build a Windows DLL.
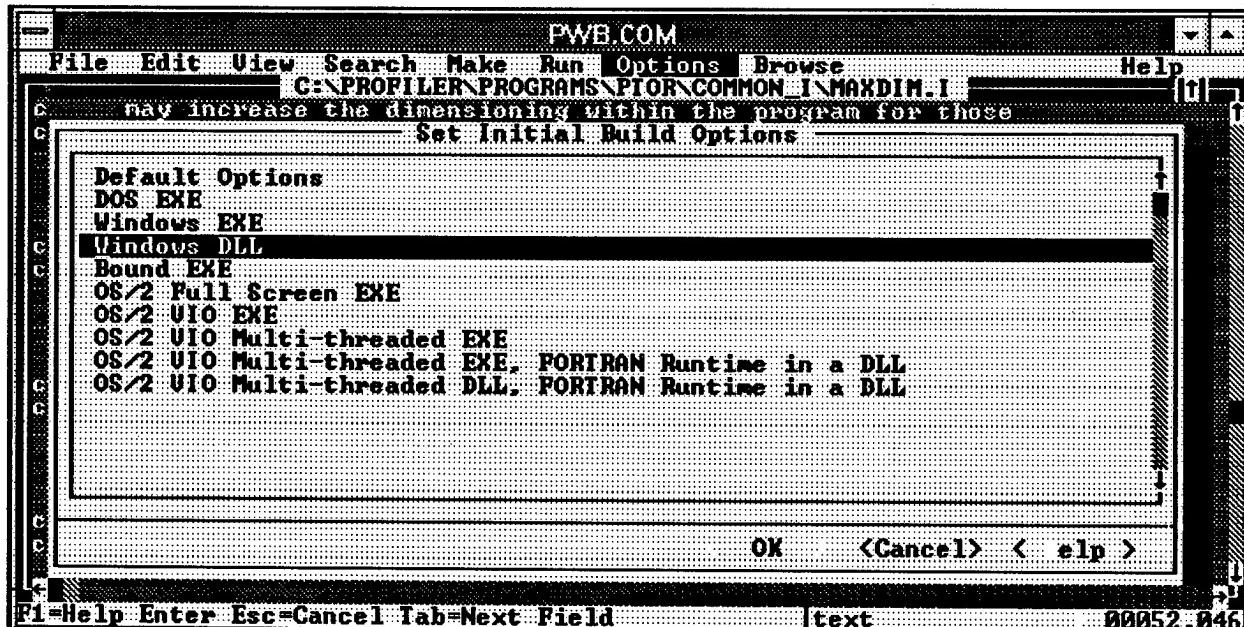
655

Figure 4 Microsoft's FORTRAN 5.1 Programmer's Work Bench, Initial Build Options

4.4 WHAT WE LEARNED; PROBLEMS WE ENCOUNTERED

It's not quite as simple as this presentation might indicate: there are some complexities in the FORTRAN makefile relating to the process of building a DLL and I seem to have to completely exit and reenter Access between each invocation of the DLL lest I not be able to call the DLL a second time. But, I feel confident that I can eventually codify the complexities and find solutions to the problems.

Also problematic is that the present Access - DLL solution provides a front end to only the data base aspects of the user interaction. Non-database parameters must still be written into an input file that the FORTRAN DLL reads when it runs. This unfinished state of affairs begs for the use of Visual Basic which will allow us to graphically collect these parameters as well from the user through some of the great visual devices depicted in the dialog of Figure 2. Visual Basic will give us all those visual devices and more and will, like the Access Basic, allow us to call the radiative transfer code as a DLL.

Though we followed the industry mandate that the user interface be separated from the core of the code base to the extent that we provided user interface for the data base parameters, I forgot to consider another important aspect of the user interface. This was the error handling. I'd been accustomed in my FORTRAN programming to have each routine do its own error checking, following the mandate for cohesive, independent routines, to issue an error message, and to stop the entire program after any sufficiently lethal errors. But DLL's mustn't just shut the whole program down, their calling Windows program expect control to return from the library routines. Newer languages, such as Visual Basic, have error handling built into the

656

language - each subroutine handles the errors for which the programmer has set error traps and passes up errors to calling routines that then may trap the error. So one of the things we'll have to do with our FORTRAN code, is to emulate this behavior - errors detected within a subroutine will have to set an error flag which can be passed back to the calling subroutine, passed up through the calling chain in the FORTRAN DLL, back up into the Windows program that called the DLL. Finally, in the calling program, the error return codes will have to be examined for every detectable error within the whole of the DLL, an appropriate error message issued, and the appropriate response for that error made from the calling program - which can present the error and the response to the user in the graphical environment.

4.5 FUTURE DIRECTIONS

In the short term, i.e., have already started, surely there will be money and time to complete the effort, we'll move the graphical front end to Visual Basic from Access Basic. This move extends the user interface to other than data base parameters. And we'll lose none of the data base functionality because Access Basic 3.0 now comes with the Access engine, so we'll have full access to the data base of RAOBs from within Visual Basic.

Visual Basic allows us to write a stand-alone Windows program so that we can take advantage of even more of the Windows features. We hope to include every functionality of the Profiler Data Analysis System under the main menu of the Windows program such as loading RAOBs or field radiometer measurements from binary or ASCII files into the data base or calling the Profile TO Radiance radiative transfer model. Also, we look forward to using the "Help" menu item common to all Windows programs. We'd like to keep our documentation up to date and on-line as a hypertext Windows Help File, accessible from the menu.

In the longer term, i.e., if there is enough time and money, we'll move to versions the Windows applications we're using (Access, Visual Basic, FORTRAN) that run natively under the recently released Windows NT operating system. We're running the Windows 3.1 (16-bit) applications currently under NT, but native (32-bit) apps promise to be much more stable and much faster on the same hardware. These applications will not only be able to take advantage of NT's flat memory model, but they will be preemptively multitasking and will take advantage of multithreading, i.e., they will be more efficient than current programs and they will never crash the entire operating system as current Windows programs can.

A future direction for the computer industry that could bear on our effort and others like it, is Client/Server Computing. The separation that we experimented with here, between the user interface and the core functionality of the program may well be widened in future. Whereas our separation of these two components was performed upon the same hardware platform, a Client/Server separation is likely to run a program's user interface upon the powerful client machine on your desk, but interact over the network with an even more powerful shared computer. The compute

intensive aspects (the FORTRAN DLL to use our experiment as an example) would run on the shared, server computer. It is likely also that you will have a server data base computer upon which the data base queries are run. So an implementation of our experiment in a Client/Server scenario might well have all three of these components: the user interface would run on a desktop client machine, the compute intensive aspects of the code might well be in some other language (FORTRAN DLL or C++) running on a powerful floating point processing (RISC) machine, and the data base queries would run on a data base machine optimized for fast disk access so that the data might be searched as quickly as possible.

5.0 CONCLUSIONS

Moving our FORTRAN application to the MS Windows GUI environment was, on the whole, successful - we're using the resulting code on a daily basis in our work. We utilized the good programming principle of a separation between the user interface and the core functionality of the program. We implemented this separation in a mixed language approach: the user interface was done in Access Basic and the core functionality was maintained in FORTRAN code in which the program was originally written. We feel that others of our FORTRAN programs could benefit from this mixed language approach and suspect that the scientific community might want to bring their FORTRAN programs into a graphical user interface environment utilizing some of the same techniques and tools.

ACKNOWLEDGEMENT

REFERENCES

1. Knorr, Eric: "Windows scores again." *PC World.*, Jan 1993 v11 n1: p13.

2. Scheier, R., Ferranti, M.: "Cut-rate, 'Window-less' version of OS/2 due for release next month." *PC Week* 18 Oct 93 Vol 10 N41, p1,16.

3. Spalding, J.B., Weems, D.C.: "Tactical Decision Aid Software Design on the ALBE Testbed Computer." *Proceedings of the 1991 Battlefield Atmospherics Conference.* PSL-91/62 Mar 92. p435-444.

4. Crowley, Aileen: "Tenacious FORTRAN finds a way in the '90s" *PC Week* Sep 27, '93 p123.

FIELD TEST RESULTS OF A FORTRAN MODEL
USED TO PREDICT SURFACE AND SUBSURFACE TEMPERATURES

Tommy B. Davis
New Mexico State University
Las Cruces, New Mexico 88003 USA

ABSTRACT

The coupled surface energy budget (CSEB) model is used to predict temperatures of various terrain, giving 24 h profiles; this application is useful in modeling infrared backgrounds for target acquisition purposes. The model was tested in Bushland, Texas (located in the Texas panhandle), in cooperation with the U.S. Department of Agriculture, in May and July of 1992. Comparison of measured and calculated temperatures led to improved modeling and good agreement between measured and calculated subsurface temperature curves.

1. INTRODUCTION

A sample program input file is shown in figure 1. Atmospheric data inputs include pressure, temperature, humidity, cloud type, cloud cover, wind speed, and (optional) incoming solar radiation. Other inputs include surface orientation specifications, initial temperatures at selected depths, terrain-dependent constants (the terrain of the test area was Pullman clay loam soil), and surface moisture content. The coupled surface energy budget (CSEB) model calculates temperatures in two dimensions: depth and one horizontal dimension. Accordingly, the input file allows one to specify number and width of horizontal sections and subsections as well as number and depth of vertical layers and sublayers. The model of the Bushland test area was divided into 36 subsections and 15 sublayers. The total width of the modeled area was 42 m and the total depth of the modeled area was 30 cm. For comparison, measured temperature data were recorded at depths of 0, 2, 4, 6, 10, 15, 20, and 30 cm. The input file also includes bottom, left, and right boundary conditions as well as vegetation parameters for the area modeled (there was no vegetation at the Bushland site). Detailed information on CSEB was obtained from DeAntonio.[1] All the Bushland raw data were obtained from Tunick et al.[2]

```
Bushland, Tx. Day 139, 1992.
CONT        5.          6.          1.          1.          0.01
ATMO      897.          5.        200.
HRLY        0.         14.4        89.        0.0         0.8         0.
HRLY        1.         13.2        96.        0.0         1.3         0.
HRLY       13.         22.9        43.        0.1         2.0         0.
HRLY       24.         14.6       100.        0.0         2.8         0.
DALA      139.         35.2
SORI        1.          0.          0.
SORI        2.          0.          0.
SORI        3.          0.          0.
SORI        4.          0.          0.
SORI        5.          0.          0.
SORI        6.          0.          0.
INIT        0.         14.0
INIT        2.         19.6
INIT        6.         21.2
INIT       15.         22.0
INIT       29.         20.8
SURF        1.          0.93        0.87        0.0
SURF        6.          0.93        0.87        0.0
LAYR        1.          2.          2.
LAYR        2.          6.          2.
LAYR        3.          6.          2.
LAYR        4.          8.          2.
LAYR        5.          8.          2.
SECT        1.       1200.        200.
SECT        2.        600.        100.
SECT        3.        300.         50.
SECT        4.        300.         50.
SECT        5.        600.        100.
SECT        6.       1200.        200.
BLOK        1.          1.          0.60        0.04
BLOK        1.          2.          0.60        0.04
BLOK        1.          3.          0.60        0.04
BLOK        1.          4.          0.60        0.04
BLOK        1.          5.          0.60        0.04
BLOK        1.          6.          0.60        0.04
BLOK        2.          1.          0.60        0.04
BLOK        2.          2.          0.60        0.04
BLOK        2.          3.          0.60        0.04
BLOK        2.          4.          0.60        0.04
BLOK        2.          5.          0.60        0.04
BLOK        2.          6.          0.60        0.04
BLOK        5.          1.          0.60        0.04
BLOK        5.          2.          0.60        0.04
BLOK        5.          3.          0.60        0.04
BLOK        5.          4.          0.60        0.04
BLOK        5.          5.          0.60        0.04
BLOK        5.          6.          0.60        0.04
BBND        1.          0.         20.8
BBND        6.          0.         20.8
LEFT        1.         -1.          0.
LEFT        5.         -1.          0.
RGHT        1.         -1.          0.
RGHT        5.         -1.          0.
VEGI        1.          0.
VEGI        6.          0.
```

Figure 1. Sample input file for CSEB.

2. TEST RESULTS

Figure 2 shows 24-h measured temperature curves at Bushland for Julian Date 139, 1992 (May). The depth with which each curve corresponds is indicated in the legend. In all figures, legend names that include a "0" indicate surface temperatures, names that include a "2" indicate temperatures at the 2-cm depth, and so forth. All temperatures were measured at the same horizontal location. Note the large temperature gap between the first and second layers and the delay in attainment of maximum temperature as depth increases.

Figure 3 shows data from the initial run of CSEB for this day. As one can see, the initial and maximum surface temperatures are much lower than those measured, and the lower layer temperatures do not show proper diurnal variation. Figure 4 shows the result of a CSEB run in which measured values of incoming solar radiation (insolation) were placed in the input file rather than allowing the program to calculate these values. Note the increase in maximum temperature at all depths and the diurnal variations at the lower depths. A new problem, however, arose in that the gap between the first and second layer temperatures is too small.

Figure 5 shows the results of a CSEB run for day 139 where the input file used measured values of insolation and also more accurate values of thermal diffusivity and thermal conductivity. Diffusivity and conductivity values are moisture dependent for soils, with a relatively small amount of moisture causing a large increase in values.[3] Since day 139 was 1 week after irrigation, the surface was dry, while at the 2-cm depth the saturation level was just over one-tenth. Thus a thermal diffusivity value of 0.09 cm^2/min was used at the surface, while a value of 0.35 (same units) was used at the 2-cm and subsequent depths. A thermal conductivity value of 0.04 cal/min/cm/K was used at the surface, while a value of 0.18 (same units) was used at the 2-cm and subsequent depths.

As one can see from figure 5, use of these values created a significant gap between the first and second layer temperatures; lower diffusivities and conductivities at the first layer meant that the diurnal surface temperature changes had a reduced effect on the second layer. Note that the calculated temperature curves accurately show the delay in attainment of peak temperature with increasing depth.
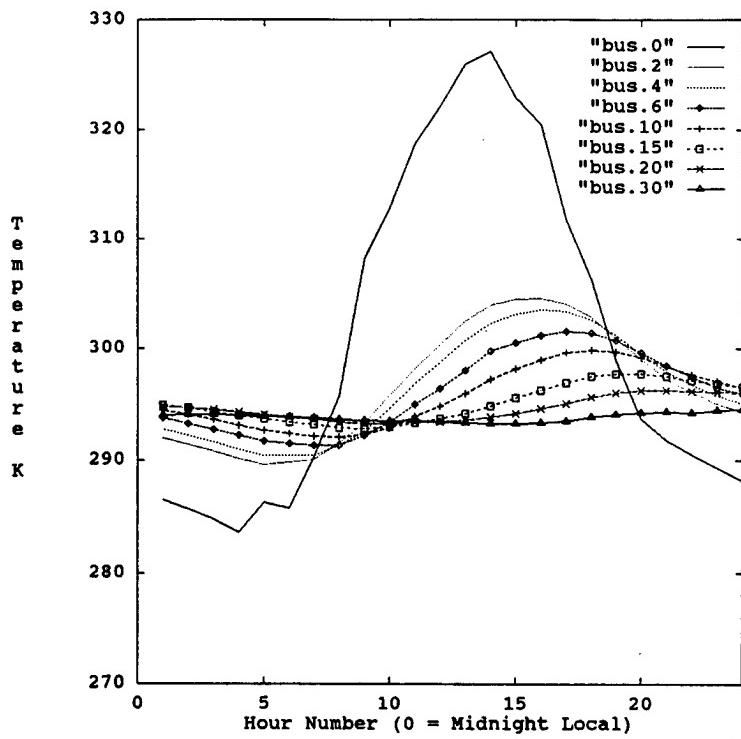
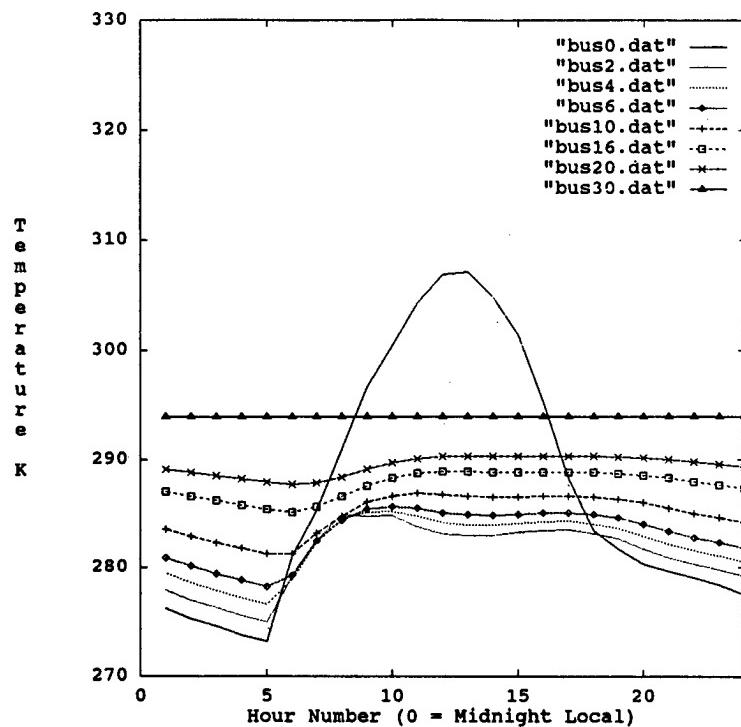**Figure 2. Measured temperatures, Bushland, day 139, 1992.**

Figure 3. Output from initial program run, Bushland, day 139, 1992.
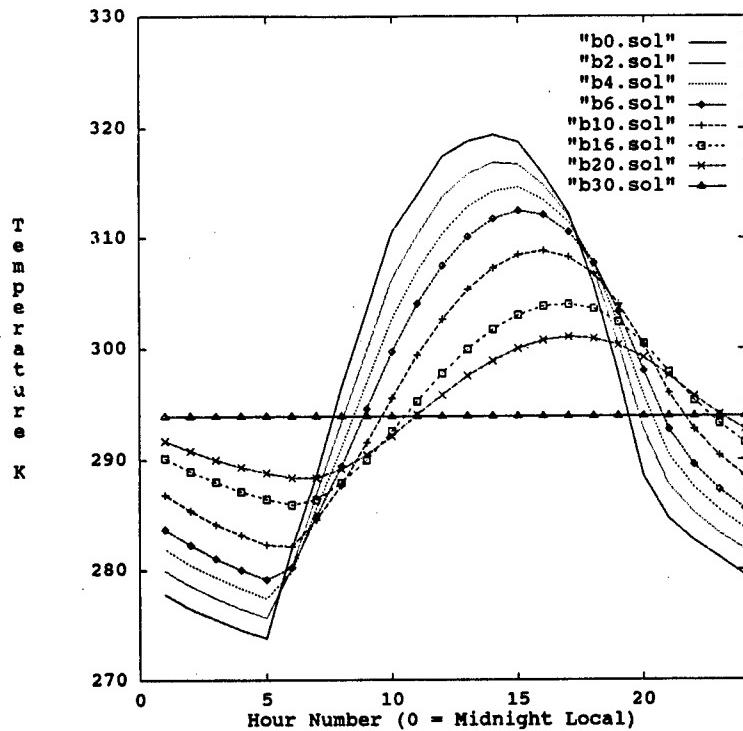
Figure 4. Program output - measured insolation used - Bushland, day 139, 1992.
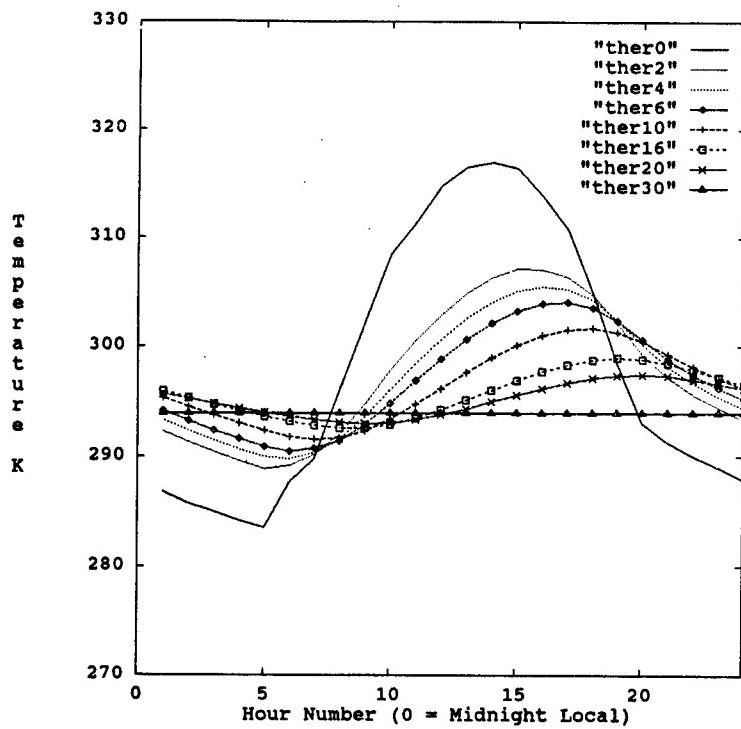

Figure 5. Program output - more accurate thermal constants - day 139, 1992.

3. CONFIRMATION AND CONCLUSION

Further correlation of temperature gap and moisture dependence of thermal constants was found by looking at data from day 192, 1992 (July). It rained the previous evening and continued to drizzle into the morning. Therefore, the surface and first sublayer contained a similar amount of moisture. When temperatures were calculated for this day, the same values of thermal conductivity and thermal diffusivity were used at the surface and first sublayer. Figure 6 shows the measured and figure 7 shows the calculated temperature curves for this day. Note that there is now only a small gap between the first and second layer temperatures in both figures. The larger thermal constants used at the first layer caused the diurnal variations of this layer to have an increased effect on the calculated temperatures of the second layer, thus reducing the gap between layers.

Measured and calculated curves have been generated for two other Bushland test dates (Julian days 133 and 196, 1992). These plots are not presented here because of space constraints, but are similar to day 139 in that the surface contains less moisture than the first sublayer. Once again, moisture dependence of the thermal constants yielded a significant temperature gap. Measured rather than calculated values of insolation provided more accurate calculated temperatures. For all 4 days, the average of the maximum percent error of the surface temperature is 2.2 percent.
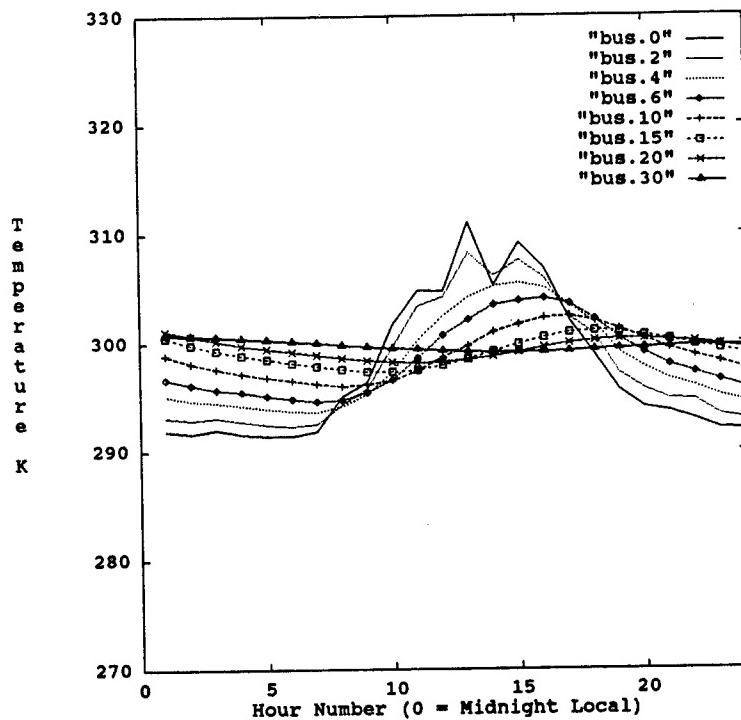
Figure 6. Measured temperatures, Bushland, day 192, 1992.
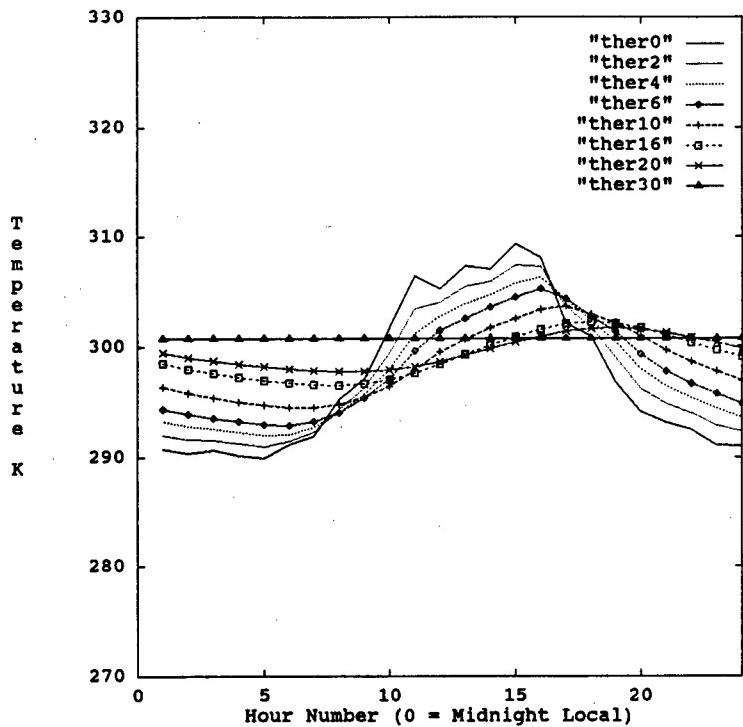
Figure 7. Program output - thermal constants same all layers - day 192, 1992.

The model will be improved (automated input of thermal constants, a more accurate method of calculating solar insolation, and refinement of a program version that accounts for diurnal evaporation) and the program versions will then be used to yield temperatures for a variety of terrain and atmospheric conditions.

REFERENCES

1. DeAntonio, Michael D., 1991, A Two-Dimensional Model of Coupled Surface Energy Balance, New Mexico State University, Las Cruces, NM.

2. Tunick, Arnold, Terry A. Howell, and Jean L. Steiner, 1993, REBAL '92 - A Cooperative Radiation and Energy Balance Field Study for Imagery and E.M. Propagation, Battlefield Environment Directorate, U.S. Army Research Laboratory, White Sands Missile Range, NM 88002. In preparation.

3. Rachele, Henry, Frank V. Hansen, Arnold Tunick, and Lisa Manguso, 1993, Thermal Properties of Soils, Battlefield Environment Directorate, U.S. Army Research Laboratory, White Sands Missile Range, NM 88002. In preparation.

THREE-DIMENSIONAL EXTENSION OF THE CIRRUS TECHNIQUE

Max P. Bleiweiss
U.S. Army Research Laboratory
White Sands Missile Range, NM 88002

Kenneth C. Payne, Thomas A. King and Steven J. LaMotte
Physical Science Laboratory
New Mexico State University
Las Cruces, NM 88003

Recent attempts to realistically model smoke/obscurant clouds for use in simulations causes one to suggest using real clouds in both real and artificial scenes. For real clouds to be used, everywhere in the field-of-view (for two-dimensional work), it is required that the two-dimensional distribution of aerosol concentration (or some function thereof), aerosol radiance, and path radiance due to scattered radiation be known. Except for the Atmospheric Transmission Large-Area Analysis System (ATLAS), there is no way to arrive at those quantities experimentally. In the far-infrared, for most of the aerosols used for screening purposes, the last parameter is thought to be of secondary importance and may be ignored in both the acquisition of that data by ATLAS and in the obscured scene generation. The technique that allows the use of real clouds in these scenes is called CIRRUS (Clouds, IR, Real, for Use in Simulations). The insertion of two-dimensional clouds into two-dimensional scenes has been demonstrated previously and will be reviewed. The work described here will emphasize the hybridization of the two-dimensional cloud to a three-dimensional cloud to allow more versatility in inserting the "real" cloud into a wider variety of scenes. A video tape has been prepared, for viewing, which demonstrates several examples of these hybrid clouds.

INTRODUCTION

In a previous paper (Bleiweiss, et.al., 1993), the basic CIRRUS technique was described: the ATLAS technique for extracting an aerosol cloud from a scene was reviewed and the procedure for inserting that cloud into another scene was described. Basically, ATLAS uses a simple equation of radiative transfer to determine the transmittance and path radiance of the cloud in a scene through knowledge of the two-dimensional distribution of scene radiance with and without the cloud present. CIRRUS uses this same equation to act on a scene whose two-dimensional distribution of radiance is known. The ATLAS-determined values of transmittance and cloud radiance complete

the list of variables which are required to create a new scene with the cloud present. It is to be emphasized that neither CIRRUS nor ATLAS are "cut and paste" operations. Current work in progress is suggesting that the scattering component of the path radiance may be more significant than assumed earlier which may, subsequently, cause modifications to the current CIRRUS technique; discussion of that work is left for a future paper (Bruce, et.al., 1994). In any case, for the present, the scattering component is assumed to be smaller that the blackbody radiation of the cloud and to be constant in space and time.

Also discussed previously, were some of the reasons for attempting simulations, in general, and the desirability and utility of using real clouds versus artificial clouds, in particular. In order that real clouds be as amenable to use in simulations as the available artificial clouds, the two-dimensional ATLAS clouds must somehow be extended to become a three-dimensional cloud. The subject of the current paper is how this may be accomplished. Various techniques are described (and examples of their application shown) which can be applied to the two-dimensional cloud to achieve different three-dimensional distributions of transmittance in space. Of the many distributions available to vary the transmittance along the line of sight (LOS) using the known path-integrated transmittance values, the one which is used here is a Gaussian distribution. The width of the distribution is some arbitrary number; however, this value may eventually be tied to a dispersion parameter as used in transport and diffusion modelling. For example, depending on how far downwind the ATLAS measurements are made, the width of the distribution will vary accordingly and the value will also vary from upwind to downwind depending on the width of the field of view being used for ATLAS. When the full three-dimensional distribution of the cloud is known through measurement, as is proposed and described elsewhere (Bleiweiss, et.al., 1992), then it will not be necessary to resort to these "hybrid" schemes. However, until that time, the methods described here should prove to be useful. The equation used to "distribute" the path-integrated transmittance along the LOS is:

$$f(y) = \frac{1}{\sigma\sqrt{2\pi}} e^{-\frac{(y-\mu)^2}{2\sigma^2}}$$

with μ being the position along the LOS where the peak of the distribution is located and σ being the standard deviation of the distribution. In some of the hybrid clouds presented below, σ has been allowed to vary with x (downwind position) but not with z (vertical position). In other demonstrations, below, μ is allowed to vary with downwind position but not in the vertical.

The next section will discuss various aspects of this "hybridization" which allow a cloud to meander, be viewed from various LOSs, etc. and ways in which cloud parameters may be

estimated upwind and downwind from the original field of view (FOV) used by ATLAS. Several examples of this processing are shown. A video which demonstrates the temporal progression of these clouds and other animations is shown in the oral presentation. A summary and conclusion and the future direction of the current work closes the paper.

HYBRIDIZATION TECHNIQUES

Present hybridization techniques which convert the two-dimensional cloud into a three-dimensional cloud can be divided into three different kinds of modifications of the two-dimensional ATLAS maps. These are defined by the "obstacles" presented to the two-dimensional cloud as attempts are made to insert it into a three-dimensional scene:

cloud meander (lateral -- along the LOS in the crosswind direction): a real cloud meanders away from and towards the viewer as the wind direction changes and as the cloud moves around terrain features,

cloud meander (vertical): the cloud, when inserted into a new scene, may need to move over terrain features,

cloud thickness: a real cloud is not constrained to a two-dimensional plane any more than it is constrained to flow perpendicular to the LOS; different methods to distribute the path integrated transmittance along the LOS are required.

These three modifications allow a fully three-dimensional cloud to be formed. Of course, the situation can be made as complicated as desired; however, compromise between "realism" and speed of computation must be made to allow the process to be more amenable to regular use. This three-dimensional cloud can then be viewed along different LOSs such as from an elevated platform or other "impossible" LOSs with much more realism than assuming that the real cloud is constrained to the plane. Also, in simulations, the cloud may move through a distribution of objects such as a forest with more realism than before. The next several figures are used to demonstrate these various phenomena.

The cloud chosen to operate on and demonstrate these ideas is an aluminum cloud, disseminated by generator, during Smoke Week XII. One particular frame is used throughout this discussion as the primary two-dimensional cloud which is manipulated to create the three-dimensional cloud. Panel A of Figure 1 shows a gray-scale coded transmittance map of the cloud, constrained by the field of view of the ATLAS imager. This map is in a plane perpendicular to the ATLAS LOS. Below this, in panel B, is a top view of this same cloud (transmittance integrated along the vertical LOS) whose transmittance in the

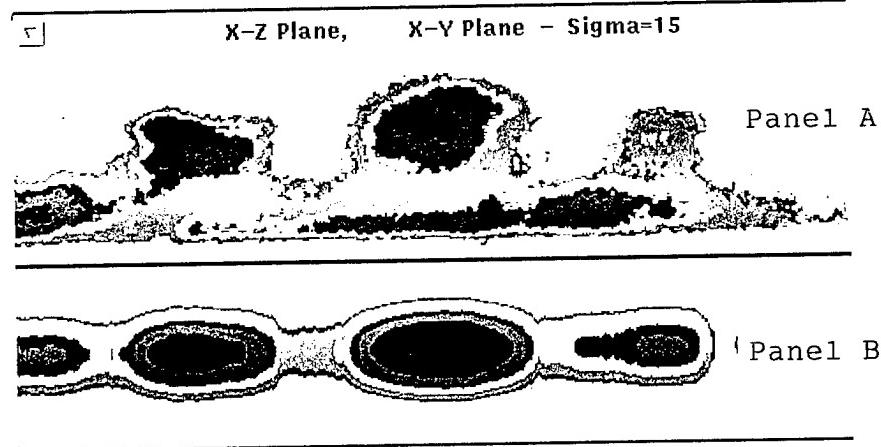**X–Z Plane,   X–Y Plane – Sigma=15**

Panel A

Panel B

Figure 1.   The effect of distributing the aerosol along the LOS with a Gaussian distribution whose standard deviation is the same everywhere in the map (15 in arbitrary units) and seen from the original position (Panel A) and from the top-down position (Panel B).   Both panels represent the path integrated transmittance as seen from the respective view points.
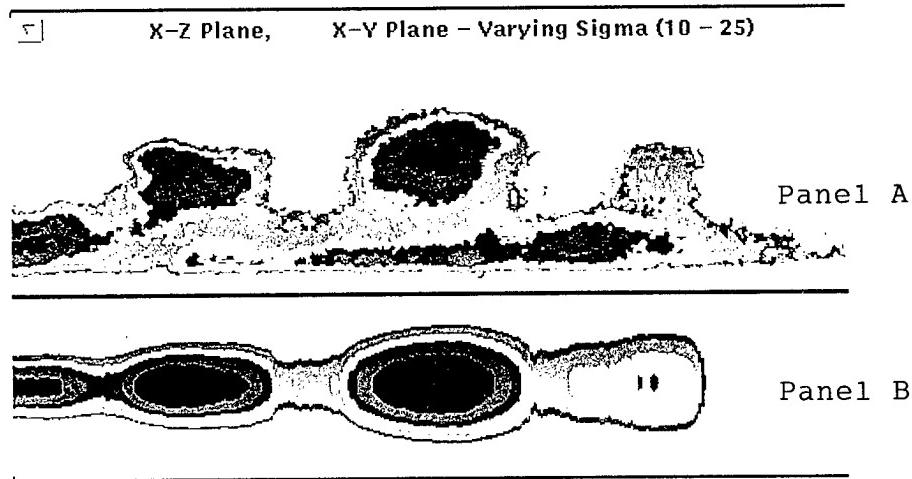

X–Z Plane,   X–Y Plane – Varying Sigma (10 – 25)

Panel A

Panel B

Figure 2.   Modification to the ATLAS map in a manner similar to that in Figure 1 except that the standard deviation of the distribution along the LOS (Y) has been allowed to vary from left to right (along X) in a linear fashion -- the value in arbitrary units is 10 at the left hand edge and 25 at the right hand edge. The value is held constant in the vertical direction (Z).   Panel A is the original map and Panel B is the modified map as seen from above.

Panel A

Panel B

Figure 3. The ATLAS map has had its ground track made to meander in a sinusoidal fashion with constant frequency and amplitude in the downwind direction (x). This is the same three-dimensional distribution as shown in Figure 2. Panel A is the original map and Panel B is the top view.

Panel A

Panel B

Figure 4. The original map modified in a manner similar to that shown in Figure 3 except that the amplitude and frequency of the sine curve is allowed to vary along the ground track. Panel A is the original map and Panel B is the top view of the new three-dimensional distribution, integrated along the vertical LOS.
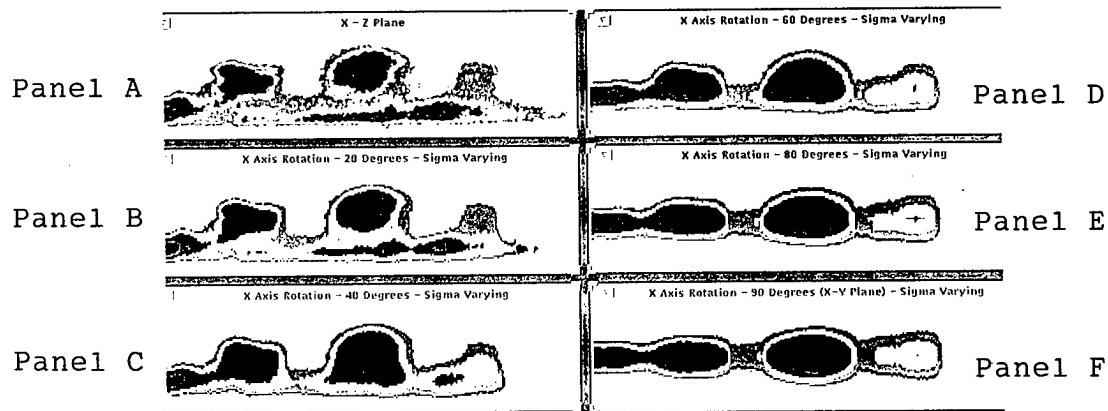
Figure 5. The three-dimensional distribution of the ATLAS map as shown in Figure 1 seen from different points of view: the viewpoint is perpendicular to the mean flow (along the Y-direction and perpendicular to the X-direction) and the observer moves up and over the cloud until the view is top down. (The depression angle increases from Panel A to Panel F.)

(This figure was not available at press time.)

Figure 6. This figure is similar to Figure 5 except that the viewpoint varies from left to right instead of from horizontal to vertical.

(This figure was not available at press time.)

Figure 7. The extension of the FOV left and right (upwind and downwind) from the original FOV is shown here. The effect on several successive frames is demonstrated.

crosswind direction has been distributed along the LOS using a Gaussian distribution -- the integral of this distribution is the path-integrated transmittance seen in the original map and the standard deviation of that distribution is whatever is desired (in this case, 15 voxels). In this figure, the standard deviation is constant throughout the map for all LOSs. The x-z plane shown in Figure 1A is 500 voxels long (x), and 140 voxels high (z). The "along the LOS" direction (y) is 100 voxels deep. In real life, a voxel is approximately 25 cm on a side. Figure 2 illustrates how the same cloud segment appears when the standard deviation is allowed to increase in the downwind direction (left to right) in a linear fashion. The affect of lateral meander is shown in Figure 3 where the cloud's ground track has been allowed to vary in a sinusoidal fashion with constant amplitude and frequency perpendicular to the original LOS (in this Figure, the standard deviation is also allowed to vary as in Figure 2) and in Figure 4, the frequency and amplitude of this sine wave are allowed to vary along the track of the cloud -- an infinite number of variations are possible; the problem is one of choosing those which best emulate the environment being simulated. Figure 5 illustrates varying points of view of the cloud as the observer moves from the horizontal LOS, perpendicular to the mean cloud motion, to progressively more vertical LOSs (remaining perpendicular to the motion) until the observer is in a top-down viewing position. Figure 6 is similar to Figure 5 except that the observer moves left and right of the original position. One obvious problem with these hybrid clouds can be seen in the comparison between the horizontally-viewed cloud and the top down presentation -- there is structure and/or "noise" and variability in the real cloud that is not present in the hybrid cloud. It remains to be determined whether or not this shortcoming (if it is indeed a shortcoming) can, reasonably, be overcome. The originals of these figures which are used in the oral presentation are in color which explains the unusual gray-scale shading presented here.

673

Still another manipulation of this cloud allows estimation of the cloud's character upwind, before it comes into the FOV and downwind, after it leaves the FOV. For this particular cloud, the centroid of several features in the cloud were tracked with time (frame-to-frame) and their position in the FOV noted. Over a short time interval (several tens of seconds), the features seemed to move with relatively constant speed across the FOV with little or no vertical motion. The minimum transmittance of these features did appear to increase -- as expected -- as they moved downwind. Much more work will be required to investigate these properties more fully and ascertain their universal existence. Use of this knowledge results in the series of panels of Figure 7 which shows "extended" frames at ten second intervals over a period of 30 seconds. The reader can determine the relative veracity of this particular technique. [Figure 7 was not available at press time; however, it was presented in the oral presentation.].

Were the practice of tomographic analysis realized as was alluded to earlier, then all of these manipulations would not be necessary as the full three-dimensional field of the aerosol would be known. Albeit, in the interest of producing an immediate utility, what has been presented here may prove useful even when the aerosol cloud tomography is regularly used.

CONCLUSIONS

The modification of a real aerosol cloud from the currently available two-dimensional results to a three-dimensional "hybrid" cloud has been demonstrated. The cloud, originally constrained to a two-dimensional plane perpendicular to the LOS, has been distributed in the crosswind direction (along the LOS) using the equation of a Gaussian distribution. The standard deviation in this equation can vary in the upwind and downwind direction as well as in the vertical direction in any manner desired. The ground track was allowed to meander along simple and complicated paths to emulate variations in wind direction and/or movement around terrain (or other) obstacles. The FOV of the observer was extended upwind and downwind using experimentally determined values for the speed with which the cloud structure moves through the FOV. It remains to insert these hybrid clouds into three-dimensional scenes. This will be accomplished with an upcoming joint effort between ARL and the U.S. Army Topographic Engineering Center. Future efforts will also attempt to more realistically model the diffusion and transport of the cloud as it moves through the FOV and over and around terrain features.

ACKNOWLEDGEMENT

REFERENCES

Bleiweiss, M.P., K.C. Payne, and T.A. King, 1993: CIRRUS -- A Technique for Inserting Real Smoke/Obscurant Clouds in Real or Simulated Scenes, In Proceedings of the Smoke/Obscurants Symposium XVII, U.S. Army Chemical Research Development and Engineering Center, Aberdeen Proving Ground, Maryland 21010.

Bleiweiss, M.P., R. Howerton, K.C. Payne, and T.A. King, 1992: A New Technique for Visualizing Three-Dimensional Flow in the Atmospheric Boundary Layer, In Flow Visualization VI, Proceedings of the Sixth International Symposium on Flow Visualization, October 5-9, 1992, Yokohama, Japan, Y. Tanida and H. Miyashiro, eds., Springer-Verlag, Berlin, Heidelberg.

Bruce, D., M.P. Bleiweiss, R.E. Davis, T.A. King, and K.C. Payne, 1994: Measurement of the Scattering Component of Smoke Cloud Radiance, in preparation.

PC-BASED COMPUTER PROGRAMS FOR ULTRAVIOLET PROPAGATION AND SPECTRAL DISCRIMINATION ANALYSIS

J.B. Gillespie, David L. Rosen, and Stan R. Niles
Army Research Laboratory
AMSRL-BE-W
White Sands Missile Range, NM 88002-5501

ABSTRACT

In the last few years ultraviolet technology has undergone a renewed interest--primarily in the problem areas of fluorescence standoff detection of biological agents and pollution, UV solar blind spectral region imaging, communications, potential for detection of illicit drugs, and combat identification. Modeling and simulations for these applications require UV propagation codes for atmospheric propagation, spectral discrimination analysis programs for fluorescence, and diagnostic codes for systems analysis. We have developed a set of user friendly PC-based codes to perform the above functions. Our UVTRAN propagation model has been recast into a PC windows environment and has been rewritten in Visual BASIC. Our factor analysis rank annihilation and diagnostic codes are in FORTRAN and have had front end menuing added to them for ease of use. These three codes are set up in a computer demo with a slide show of descriptive text and plotted results showing the applicability of the models. The codes have been compared to experimental data for validity of the models.

INTRODUCTION

The U.S. Army Research Laboratory has an ultraviolet propagation research program at the Battlefield Environment Directorate. This program includes both an experimental laboratory research effort and a theoretical modeling effort. The research is designed primarily to support remote chemical sensing, particularly biological agent aerosols utilizing laser induced fluorescence. However, the research is also being applied to UV imaging, UV transmissometry, and to problems such as combat identification of friendly troops and mine detection. The work described below is the modeling aspect of the UV program and includes three models: UVTRAN 3.0, FARA, and OVERLAPD all interactive and written to operate in a windows 3.0 or higher IBM PC environment. These models were originally written in FORTRAN to be research grade computer codes. They have been rewritten in Visual Basic and compiled to run on an IBM compatible PC. Visual Basic provides a Microsoft Windows environment with interactive pop up windows. All three models have built in defaults for all parameters. These can be easily changed and changed values will stay set during the session until the user enters a new value. The defaults can be changed permanently by modifying the Visual Basic source code provided and recompiling.

Modeling research has been aimed at propagation of ultraviolet radiation (e.g. UVTRAN, our UV transmission and lidar model), spectral discrimination (such as our FARA model), simulations of lidar and electrooptic systems, and analysis techniques for experimental data (such as OVERLAPD, our Overlap Index model). An Applied Optics paper was recently published in which we showed the applicability of UV lidar to detection of a constituent in the presence of an interferant that had a strong overlapping fluorescence spectrum.

UVTRAN 3.0 for Windows Transmission and Lidar Model

UVTRAN is an atmospheric transmission code for calculating transmission through the atmosphere for wavelengths from 200 nanometers to 700 nanometers. It can not be used for wavelengths longer than 700 nm because no water vapor band model is included. It is also for visibilities of about 50 km and less; since the quasi-empirical aerosol that is used was based on low visibility measurements. Uvtran also contains a lidar calculation code that can be used to estimate lidar returns for elastic scattering (Mie) and for fluorescence returns. The lidar portion also includes a sky radiance calculation and has six laser lines built in. The transmission code is low resolution--the same as Lowtran. The user has the options of using the standard atmosphere for Ozone and trace gases or can change the values if measurements indicate that higher or lower values are present. Horizontal, vertical, or slant paths can be selected. A complete description of the original calculational capabilities is available in the UVTRAN documentation for the DOS version and in the 1989 Applied Optics paper by Patterson and Gillespie.

UVTRAN 3.0 calculates UV and visible wavelength transmission and LIDAR return values. It requires input of wavelength(s), visibility, range, zenith angle, altitude above sea level, and concentration of gaseous absorbers. The program will output either transmission or expected LIDAR return together with an estimate of the sky background. The model is very fast and very user-friendly. It is modular and can easily be changed by editing the modules of the Visual Basic code which is supplied. The output is listed to screen and options include printing the output to printer or to a disk file.

FARA 1.0 for Windows Spectral Discrimination Model

Many researchers investigating standoff biological detection concentrate on the method of UV fluorescence lidar.[1] Fluorescence spectroscopy is a method that is very sensitive and specific to pure compounds. However, fluorescence spectra of biological materials and aerosols are broad and devoid of line structure. The spectrum from a mixture of compounds is hard to interpret because the fluorescence spectra of the components often overlap.[2][3] Prominent features of the individual components are hidden in a mixture, although the overall spectrum may still be unique in

theory. For example, the spectrum of a microorganism may sometimes overlap the spectrum of dust and smoke in the environment. In an actual application, the spectrum of the organism may have been measured in a laboratory while the spectrum of the dust and smoke are unknown. This paper describes a program, FARA, for interpreting fluorescence spectra in mixtures that we developed using factor analysis-rank annihilation.

An excitation-emission matrix (EEM) is much more specific than a one dimensional fluorescence spectrum. An EEM is fluorescence intensity as a function of both the excitation and the emission wavelengths. Consider the EEM of three hypothetical materials: compound 1 (whose 3-D normalized plot is shown in Fig. 1), compound 2 (shown in Fig. 2), and a mixture of compound 1 and compound 2 in a concentration ratio of 1:2 (shown in Fig.3). The EEM of compounds 1 and 2 overlap but peak at different wavelengths. The mixture peaks at the same emission-excitation wavelength pair (340 nm - 260 nm) as compound 2. Although the peak of compound 1 is hidden, the reader may distinguish a shoulder that indicates its' presence. However, the reader probably couldn't determine the intensity of in compound 1 in the mixture due to the overlap with compound 2. If the EEM of compound 2 was not available for subtraction, one would find the visual discrimination of compound 1 almost impossible. Program FARA distinguishes between these spectra.

Factor analysis-rank annihilation compares the EEM from an unknown with the EEM from the spectrum of a known compound using eigenanalysis techniques. The objective of this technique is to calculate concentration of known compound in unknown sample. It only requires a laboratory standard from the known compound, not the EEM of any other component in the unknown. The algorithm does not need the EEM of any background component. Instead, it uses as a constraint the independence of the normalized emission spectrum on excitation wavelength for a pure compound or fluorescing center. It decomposes the EEM of the unknown's EEM by singular value decomposition (SVD), calculates the rank (i.e., number of nonzero singular values that are not due to random noise) of the unknown's EEM, determines the presence or absence of the known compound using the overlap index,[4] [5] and then calculates the concentration relative to the concentration of a laboratory standard.[6] The rank of the unknown's EEM is equivalent to the number of fluorescing components in the sample.

Sometimes the user can increase accuracy by using a priori information. The accuracy of the calculated rank often varies under different experimental conditions. The overlap index only requires one excitation and one emission spectrum from the EEM of the standard, although the standard EEM contains many other one dimensional spectra. The factor analysis-rank annihilation algorithm for calculating nonzero concentration calculates incorrect values if the known compound is absent from the unknown.[7]

The program is designed for a Windows environment, with user

friendly features such as pop-up menus. The user enters the names of two files containing the EEM for the standard and the unknown. These input files consist of three columns: the emission wavelength, the excitation wavelength, and the fluorescence intensity. The program discards the wavelength information, forms a data matrix from the intensity data, then calculates and displays the singular values of the data matrix. The rank of the unknown's EEM are estimated by searching for the largest ratio between adjacent singular values.[8] A list of singular values are displayed to help the user judge the accuracy of the estimated rank. The user can enter a better estimate for rank if one is available. The program then chooses the most intense emission spectrum and excitation spectrum from the standard EEM. The user can override this choice of spectra. FARA calculates an overlap index for the unknown's EEM as compared to the two standard EEM spectra. The program or user decides, using the overlap index, whether the known compound is present (nonzero concentration) in the unknown or not (zero concentration). If the compound is present, the user enters the rank of the standard EEM. The program then calculates the nonzero concentration of the unknown relative to the standard's concentration.

OVERLAPD the Diagnostics Model

For spectral discrimination of fluorescence spectral which have several different fluorescing compounds present, the OVERLAPD model may be utilized. This model uses an overlap index algorithm to compare spectra in a similar way that a correlation coefficient is used. The overlap index method works under conditions when the sample spectra contain the presence of unknown compounds. In the absence of noise this algorithm can be derived from Bessel's inequality. If the overlap index, p, is equal to one then the calibrant is in the mixture. If $0 < p < 1$, then the calibrant is not in the mixture. If noise is present then a more complicated criteria is required. If $p = 0$, the substance is absent. If p is exactly 1 then the substance is present. If p is between 0 and 1 then some criterion must be set for probability of detection. This criterion has a default value built into the model, and this value can be changed by the user. This model contains UVTRAN (both the transmission and lidar parts) and the FARA algorithm in addition to the overlap index diagnostic. It also contains a Poisson noise simulation so that the effects of random noise can be determined. OVERLAPD therefore can be used to perform sophisticated fluorescence lidar simulations. The windows version has a variety of pop up windows with practical defaults for the user. Presently much of the inputs must be entered as data files. This is handled by Visual Basic menu windows.

MODEL REQUIREMENTS

UVTRAN 3.0, FARA, and OVERLAPD require Microsoft Windows version 3.0 or later to run. A runtime module, VBRUN100.exe, must be present for the models to execute outside of Visual Basic, this

module has been supplied with UVTRAN 3.0. The performance of the three UV models will vary from PC to PC. Processing speed will vary depending on the processing power of PC and on the number of application open within the Windows environment.

CLOSING REMARKS

This collection of three UV models constitute a complete set for UV atmospheric propagation research: a transmission model, a lidar model, a spectral discrimination model, and a diagnostic/simulation model. These models are simple and fast on a PC and are very easy to use in a Microsoft Windows environment. Further enhancements are currently is process: adding pop up help windows and on screen plotting capability.

These Visual Basic models and user guides are available on floppy diskettes from the authors. UVTRAN is also in the EOSAEL Library and is available for either PC or mainframe computers in FORTRAN or for the PC windows environment in Visual Basic.

REFERENCES

1. Measures, R., 1984, Laser Remote Sensing (Wiley, New York).

2. Rosen, David L. and James B. Gillespie, 1989, "Atmospheric extinction effect on analysis of UV fluorescence signatures," Appl. Opt. 28, 4260-4261.

3. Rosen, David L., and James B. Gillespie, 1992, "Fluorescence Lidar Detection with Shot Noise and Sky Radiance," Appl. Opt. 31, 4214-4223.

4. Ho, C. N., G. D. Christian, and E. R. Davidson, 1980, "Application of the Method of Rank Annihilation to Fluorescent Multicomponent Mixtures of Polyatomic Hydrocarbons," Anal. Chem. 52:1071.

5. Ho, C. N., G. D. Christian, and E. R. Davidson, 1978, "Application of the Method of Rank Annihilation to Quantitative Analyses of Multicomponent Fluorescence Data from a Video Fluorometer," Anal. Chem. 50:1108.

6. Rosen, David L., and James B. Gillespie, Algorithms for Spectral Discrimination of Fluorescence Lidar Returns Degraded by Atmospheric Extinction ASL-TR-0297.

7. Lorber, A., 1984, "Quantifying Chemical Composition from Two Dimensional Data Arrays," Anal. Chim. Acta 164:293.

8. Rosen, David L. and James B. Gillespie, 1989, Algorithms for Analyzing Laser-Induced Fluorescence Spectra ASL-TR-0240, 18-21.
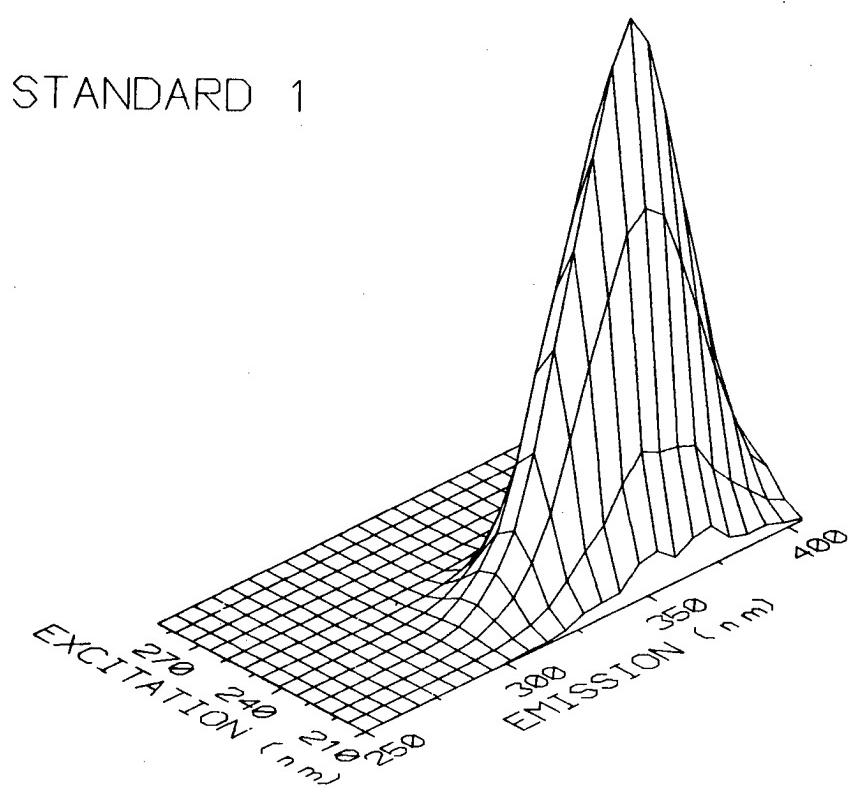
681

STANDARD 1

Figure 1. EEM Fluorescence Spectrum of Standard 1.
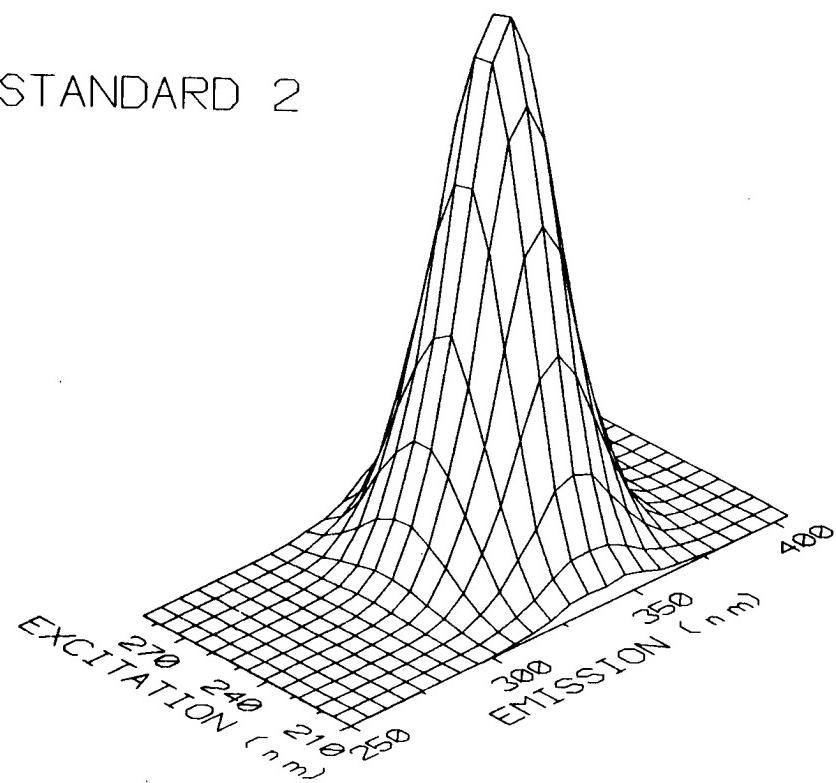
STANDARD 2

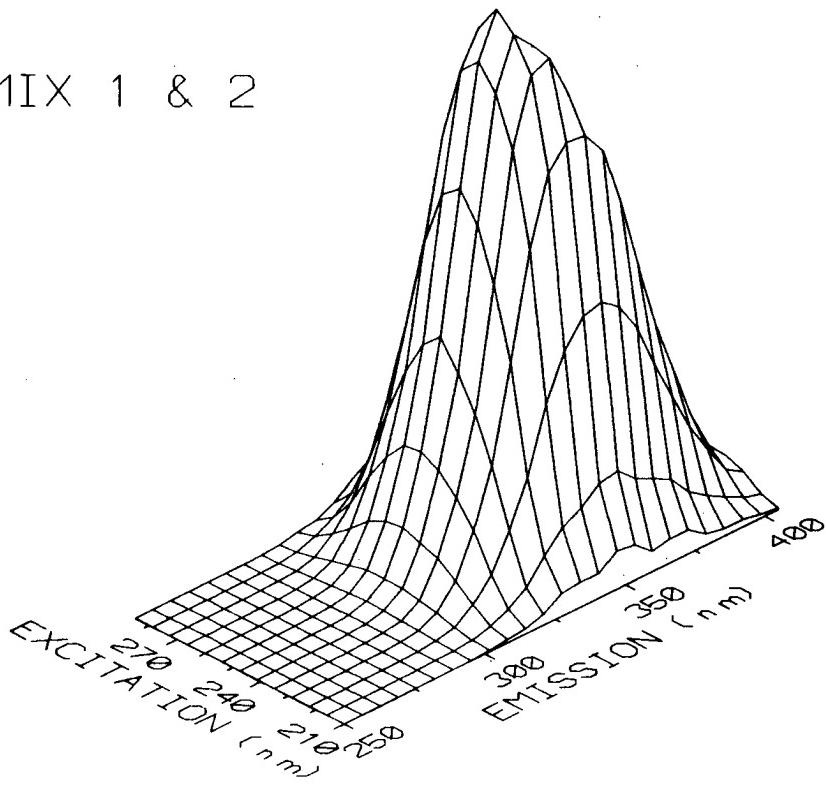**Figure 2. EEM Fluorescence Spectrum of Standard 2.**

MIX 1 & 2

Figure 3.   Fluorescence EEM Spectrum of
a Mix of the Spectra for Standards 1 and 2

Battlefield Atmospheric Simulation of Transport and Diffusion
Over Complex Terrain, Urban Areas, and Military Vehicles:
Simulations of Mesoscale and Urban Structure Flows in
Generalized Coordinates Using the AIRFLOS LES Model

Ronald E. Meyers, Keith S. Deacon
US Army Research Laboratory
Battlefield Environment Directorate
White Sands Missile Range, NM 88002, USA

ABSTRACT

The Air Flow Over Structures (AIRFLOS) model has been developed to calculate
fluid flow over complex objects of military significance. The model solves the
Navier-Stokes equations for laminar and turbulent flow and provides four
dimensional (x,y,z,t) fields of velocity, pressure, temperature, concentration, and
other scalars. AIRFLOS has been developed in generalized coordinates which can
be conformed to tanks, ships, complex terrain, buildings, and other complex
geometric structures. The model runs on advanced unix workstations and
supercomputers including the CM-200, CM-5, Cray-YMP, and KSR-1. AIRFLOS
can be used to solve complex problems in many fields including those in
meteorology, air pollution, NBC defense, and oceanography. The model physics,
numerics, and applications are discussed.

1. Introduction

The Air Flow Over Structures (AIRFLOS) computer code has been developed to calculate the velocity, temperature, humidity, and pressure fields over and through complex geometry. In order to calculate the flow over complex structures the model was developed in generalized coordinates. The Jacobian transformations were computed by finite difference discretization to achieve development efficiency in the modeling of flows over alternative geometries. Grids nodes are defined over and around the complex structures. A file containing the grid coordinates and cells inside the structures is used by the AIRFLOS computer program to calculate the coordinate transformations. For large eddy simulations (LES) the AIRFLOS model is completely self scaling. While the generality of the computer code introduces extra computations, its flexibility of coordinates allows better resolution of complex terrain and structures, and achieves commonalty of code for diverse applications. The AIRFLOS computer model is modular and has been run on advanced work stations such as from SGI, Stardent, HP and DEC, massively parallel computers such as the CM2, CM5 and KSR, and the Cray 2 super computer. High degrees of parallization and vectorization is able to achieve great efficiency on parallel and vector computers.

Since AIRFLOS has had success modeling flows over complex structures, it was desired to modify the AIRFLOS computer code and run simulations to indicate its potential for urban and mesoscale meteorological modeling. Since many meteorological flows are influenced dramatically by reasonably small changes in temperatures affecting buoyancy and stability, a test of the model to simulate drainage flow was considered In this paper we demonstrate the capability of the model to calculate temperature driven meteorological flows, and indicate the direction of future development for the model for these applications.

AIRFLOS has been applied to AMADEUS, Brush Creek, and Project WIND mountain valley complex terrain. A nighttime case was simulated for two hours in which cooling terrain was used to drive the flow by cooling near by air. In the following sections the AIRFLOS model equations are reviewed, the solution methodology is described, and results are presented. It is shown that the model incorporates the requisite physics for simulating temperature effects in complex terrain and predicts generally observed features at the AMADEUS, Brush Creek and Project Wind sites. In addition short duration flows over multiple building complexes were simulated, and the generally expected features of wake and vortex generation were observed.

2. Model Formulation

2.1. Model Equations

For this simulation in accord with simulations of Leone and Lee (1987), the Boussinesq form of the momentum equations was used.

$$\frac{\partial u}{\partial t} + u\frac{\partial u}{\partial x} + v\frac{\partial u}{\partial y} + w\frac{\partial u}{\partial z} = \frac{\partial}{\partial x}\left(K_H\frac{\partial u}{\partial x}\right) + \frac{\partial}{\partial y}\left(K_H\frac{\partial u}{\partial y}\right) + \frac{\partial}{\partial z}\left(K_V\frac{\partial u}{\partial z}\right) - \frac{\partial \pi}{\partial x}$$

$$\frac{\partial v}{\partial t} + u\frac{\partial v}{\partial x} + v\frac{\partial v}{\partial y} + w\frac{\partial v}{\partial z} = \frac{\partial}{\partial x}\left(K_H\frac{\partial v}{\partial x}\right) + \frac{\partial}{\partial y}\left(K_H\frac{\partial v}{\partial y}\right) + \frac{\partial}{\partial z}\left(K_V\frac{\partial v}{\partial z}\right) - \frac{\partial \pi}{\partial y}$$

$$\frac{\partial w}{\partial t} + u\frac{\partial w}{\partial x} + v\frac{\partial w}{\partial y} + w\frac{\partial w}{\partial z} = \frac{\partial}{\partial x}\left(K_H\frac{\partial w}{\partial x}\right) + \frac{\partial}{\partial y}\left(K_H\frac{\partial w}{\partial y}\right) + \frac{\partial}{\partial z}\left(K_V\frac{\partial w}{\partial z}\right) - \frac{\partial \pi}{\partial z} +$$

$$+ \frac{\left(\theta - \bar{\theta}\right)}{\theta_0} g$$

The current model runs were presented without the coriolis force so that initial interpretation of drainage effects would not be confounded by more complexity.

The continuity of mass is given by the incompressibility condition:

$$\frac{\partial u}{\partial x} + \frac{\partial v}{\partial y} + \frac{\partial w}{\partial z} = 0$$

The potential temperature equation is used to account for the effects of changing pressure with height in the atmosphere.

$$\frac{\partial \theta}{\partial t} + u\frac{\partial \theta}{\partial x} + v\frac{\partial \theta}{\partial y} + w\frac{\partial \theta}{\partial z} = \frac{\partial}{\partial x}\left(K_H\frac{\partial \theta}{\partial x}\right) + \frac{\partial}{\partial y}\left(K_H\frac{\partial \theta}{\partial y}\right) + \frac{\partial}{\partial z}\left(K_H\frac{\partial \theta}{\partial z}\right)$$

2.2. Boundary and Initial Conditions

Boundary and initial conditions were applied similarly to simulations at all three complex terrain sites to simulate onset of nighttime drainage conditions. The initial velocities were set to zero. A slight inversion of $+2°$ per kilometer height

was applied from sea level to 4 km. Terrain elevation heights were used at the bottom boundary. The terrain height data is presented in a table.

The velocity components were set to zero on the bottom boundary terrain and on the upper boundary at 4 km. The temperature on the bottom boundary was cooled at a rate of 1° C per hour. On the sides of the grid constant flux boundary conditions were established for momentum and reflection for potential temperature. No explicit boundary conditions were placed on the pressure, rather the pressure was allowed to adjust to satisfy the imposed velocity and temperature boundary conditions.

2.3. Grid

Since AIRFLOS is written in generalized coordinates, variable gridding could be used. The grid consisted of 16 vertical layers for each simulation over complex terrain, and a horizontal grid is presented in the terrain table. The first two layers had uniform vertical spacing, and the thickness of layers doubled until a thickness of 160 meters was reached. The remaining layers were interpolated uniformly from that level to the top at 4 km. Specific grid data for each run is presented in the terrain grid data table. Horizontal spacing was uniform in these runs since we wanted to evaluate the sensitivity of flow calculations to discretization errors in vertical transformations first.

3. Results

3.1. Amadeus

Drainage over AMADEUS terrain was simulated by cooling the ground under initially still air. The horizontal grid consisted of 51 by 51 nodes and the first grid layer was 10 meters above the complex terrain.

Initial forcing pushed cool air down the steep walls of the canyon sides. As cool air pools in the originally stagnant valley, gravity flow is eventually established down the center of the valley until it exits through the valley bottom. Horizontal flow at fixed levels above the terrain is observed to be converging into the valley depressions, and diverging over as it runs over ridges, both as expected. Flow from the two valleys at brush creek also run together.

Observations from Dr. R. Coulter's high resolution three dimensional minisodar in the valley center shows wind speeds of about 1.5 meters per second at 10 meters above the terrain, in agreement with the simulations. It is expected that

to prevent the simulation wind speeds from going beyond that, more information from the boundary conditions is needed on the surrounding flow. Appropriate canopy and surface drag needs to simulated at higher resolution or modeled by conventional means. Surface layer parameterizations have been included in other simulations, and these will be reported on in future papers. All in all these simulations were extremely good, and definitely o establish the potential of AIRFLOS to model temperature driven meteorological flow.

The diffusion and transport of a continuous tracer cloud down the valley was simulated and is included in a figure. Concentration is clearly transported down the valley, taking the turns of the valley and it is confined by the canyon walls

3.2. Brush Creek

The overall drainage flow developed over the simulated 2 hours. It was characterized first by cross valley flow of the cooling air, in contact with the terrain, down the banks of the valley. As cooler air collected in the valley it steered in the down valley direction. At higher elevations a very small up stream circulation developed, being somewhat inhibited by the zero upper boundary conditions. It is believed that the back circulation higher up was caused by the lower pressure caused by the vacating of the heavier air as it moved downward. As the cold air drained to the bottom of the valley, it displaced some warmer air which was forced upward. Some air flowed in at the top of the valley and at higher elevations of terrain boundary and out flow occurred down valley and at lower elevations of the terrain boundary. The flow was substantially decoupled in the vertical due to the low turbulence of stable nighttime conditions. The vertical eddy diffusivity was calculated consistent with the Leone and Lee eddy diffusivity parameterization calculations. Stream lines were calculated after two hours of simulation in order to estimate the effects of the transport and diffusion releases. The above described phenomena was easily observed in such simulations.

3.3. Project WIND

Drainage was simulated over the Project Wind complex terrain. Experiments in Project Wind over four seasons are reported by Cionco, the Chief Scientist for the Army project. A 200km by 200km area was simulated at two different horizontal resolutions, using 5km and 10km horizontal resolutions respectively.

Both flows showed the generally observed drainage off of the mountains slopes into the broad valley. Of course the higher resolution run provided much more

detail and more flow consistency. These runs are a precursor to more detailed simulations throughout the diurnal cycle.

3.4. Urban Structures

The AIRFLOS LES model has simulated the neutral flow over complexes of buildings. A five second simulation has been made of flow over a complex of 16 buildings and extended runs have been made over a five building complex. The results show vortex structures, street canyon circulations, separated flows and return circulations. These computations were carried out on the CM5 at the US ARMY High Performance Super Computer Center at the University of Minnesota. Future work will include more complete simulations of urban areas with comparisons against data. Comparisons will include flow through and around individual structures and urban complexes. Meteorological field fluxes and transport and diffusion will be emphasized in the comparisons.

4. Conclusions

AIRFLOS model simulates temperature driven drainage flow in complex terrain in accordance with generally observed drainage features. Because of the generalized coordinates approach of the model, the same model can be used with a variety of terrains and structures and can provide a detailed meteorological simulation of the effects need for transport and diffusion prognostic simulations. While the simulations were very good, improved realistic mesoscale simulations could result from inclusion of canopy physics, especially drag properties.

While the current results were driven by cooling of the ground, more elaborate runs have been made throughout the diurnal cycle and include radiation considerations. Solar radiation driven mesoscale prognostic simulations will be reported elsewhere.
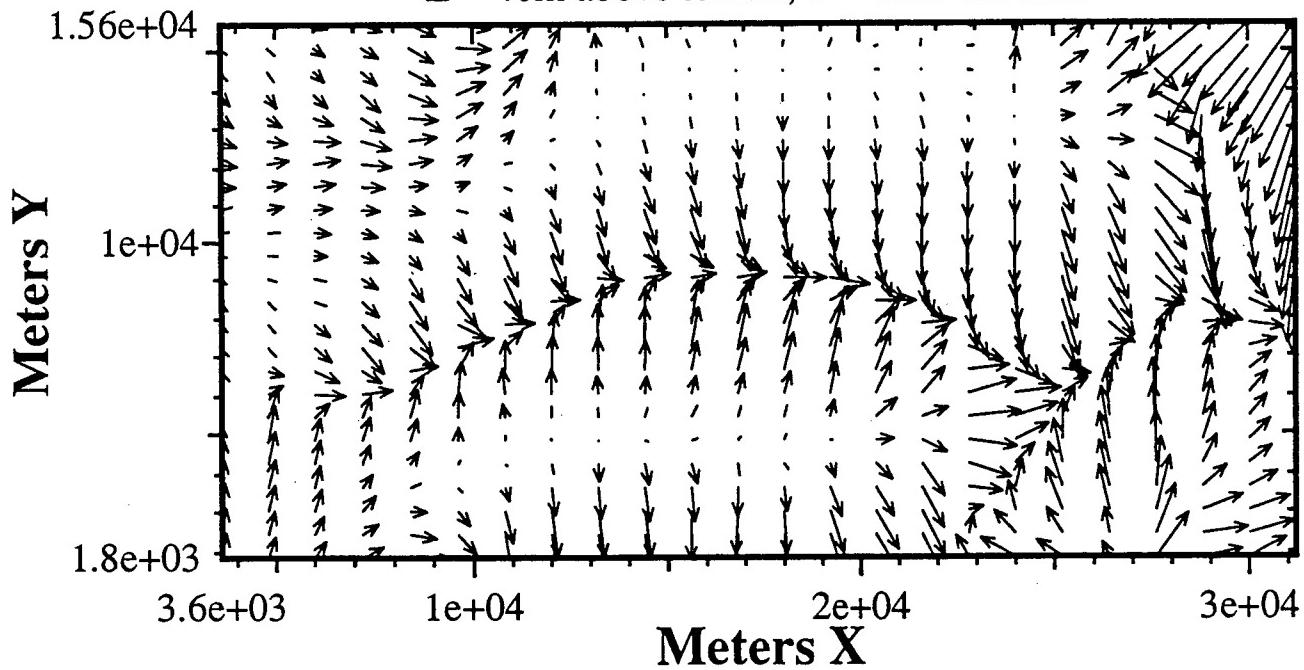
AIRFLOS Wind Vectors, AMADEUS Terrain

Z = 10m above terrain,   T = 5000 seconds
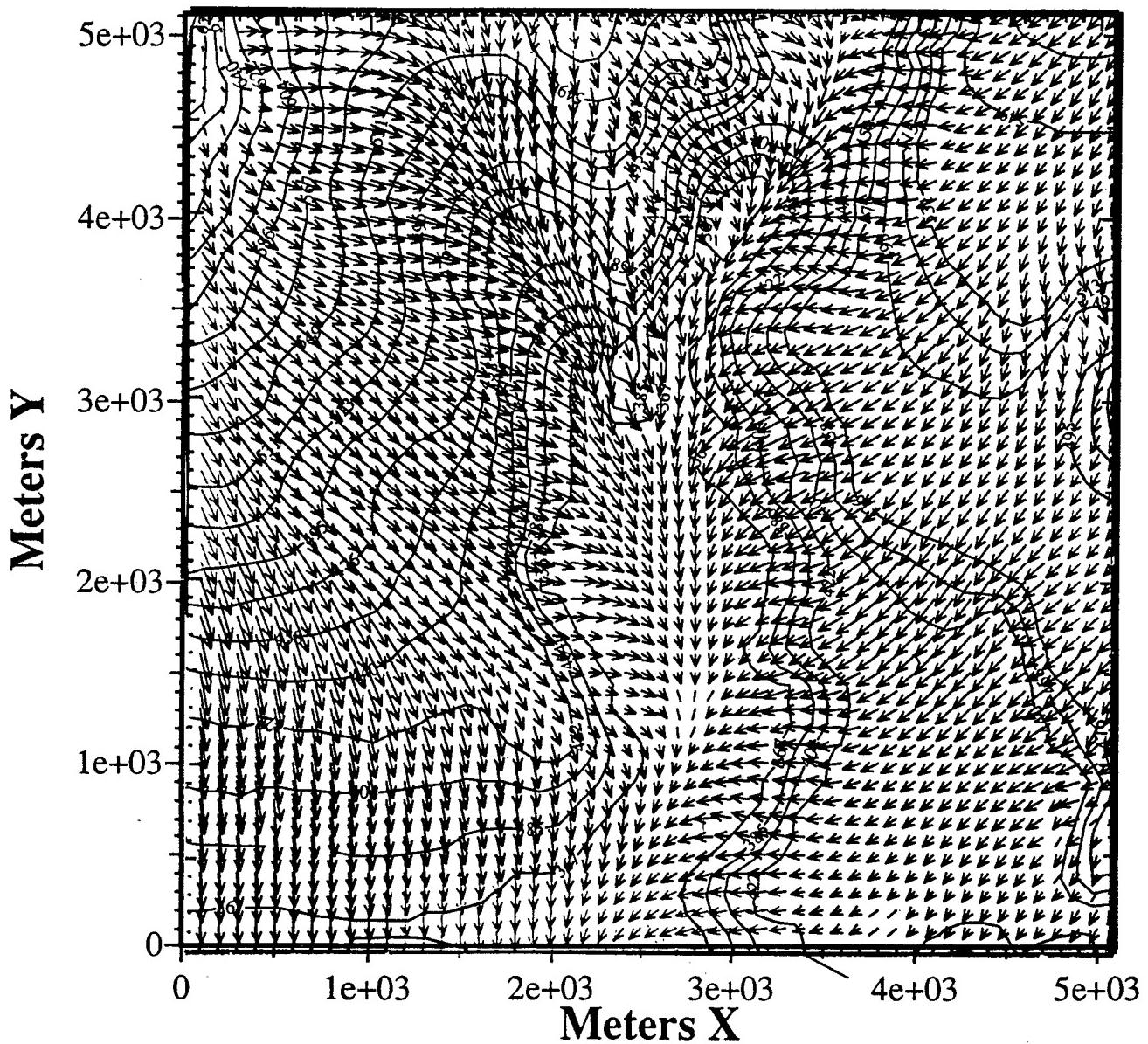
AIRFLOS Wind Vectors, Brush Creek Terrain

Z = 40m above terrain, T = 8000 seconds
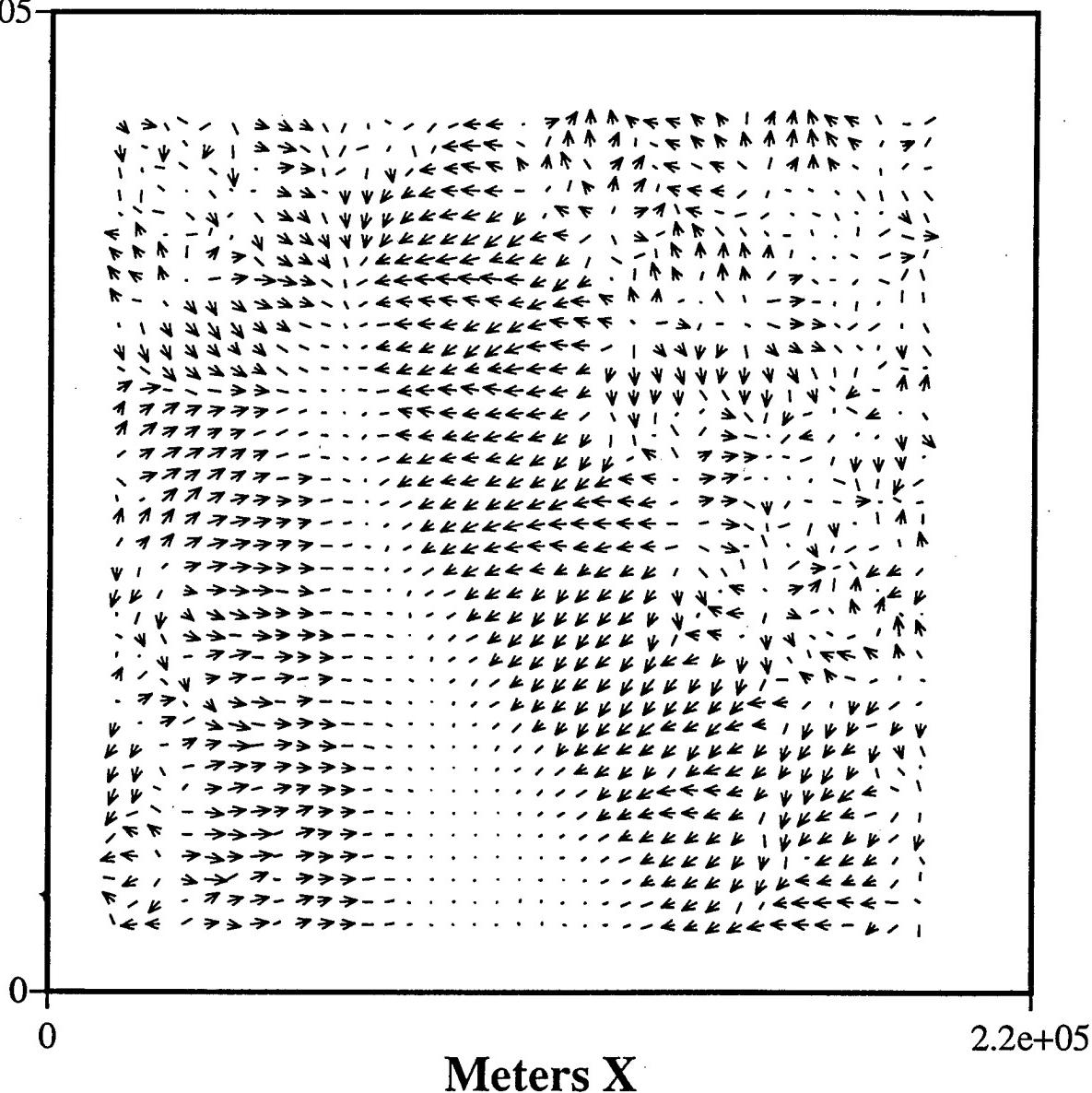
AIRFLOS Wind Vectors, Project Wind Terrain

Z = 10m above terrain,　　　　T = 24000 seconds

Meters Y

Meters X

AIRFLOS

Ronald E. Meyers

Keith Deacon

CN2

EASY-TO-USE OPTICAL PROFILE FUNCTION PROGRAM FOR MODELING EXTINCTION AND BACKSCATTER COEFFICIENTS IN LOW STRATUS CLOUDS AND SUBCLOUD REGIONS

Neal H. Kilmer
Physical Science Laboratory, New Mexico State University
Las Cruces, New Mexico 88003-0002

Henry Rachele
U.S. Army Research Laboratory, Battlefield Environment Directorate
White Sands Missile Range, New Mexico 88002-5501

ABSTRACT

A largely theoretically-based microphysics model developed by the authors was used with Mie efficiency factors to simulate vertical profiles of extinction and backscatter coefficients for 2376 combinations of input parameters and wavelength. These extinction and backscatter coefficient profiles were fit with the Rachele-Kilmer (RK) optical profile function to simplify subsequent computations. Use of a computer program for computing the extinction and backscatter coefficient profiles is described. The purpose of this paper is to publicize this easy-to-use, widely available program, RKOPF, which features the RK optical profile function. Results for a few selected input sets are shown.

1. INTRODUCTION

For various applications, including optimization of the design and operational capability of electro-optical systems for use in the lower atmosphere and possible inclusion in wargaming, it is helpful to have quantitative knowledge of the vertical structure of extinction, backscatter, and absorption. This understanding is needed for sensors operating at various wavelengths of electromagnetic radiation. To expedite research on such vertical structure, the former U.S. Army Atmospheric Sciences Laboratory (ASL) (currently the Battlefield Environment Directorate of the U.S. Army Research Laboratory) has conducted field experiments and supported development of vertical profile models. Field data (including measurements from Project Meppen 80) were collected in Germany. These data included drop sizes and number measured at various heights in the presence of moist haze, fog, and very low stratus clouds. These vertical profiles of drop size distributions were then used as input (assuming the drops were pure water) for Mie calculations,[1] resulting in vertical profiles of extinction, backscatter, and absorption coefficients for wavelengths of 0.55, 1.06, 4.0, and 10.6 μm. Analysis of data from an electro-optical viewpoint led to development of empirical vertical profile models.

Vertical profiles of extinction coefficients (σ) have been approximated (in many ASL studies) by a double exponential function[2-4] of height (z) above ground level; that is,

$$\sigma = A \exp [B \exp (Cz)] , \tag{1}$$

where A, B, and C are constants with appropriate values for the case being approximated. In the past, the values of A, B, and C have been determined empirically by fitting data collected from a limited number of specific locations. The Heaps version of an empirical

model (the double exponential form) was coupled with a U.S. Air Force model that includes drop size distribution expressions by Shettle and Fenn,[5] resulting in the vertical extinction profile model currently in the XSCALE module of EOSAEL.

In addition to the empirically developed electro-optical models, ASL opted to develop a theoretically based microphysical model that together with Mie theory would produce extinction, backscatter, and absorption coefficients. The resulting model, the Rachele-Kilmer microphysics model (hereafter designated the RK model), is described in a detailed technical report.[6] The current RK model is based on the concept that a cluster of drops embedded in a mass of moist air rises from a reference height to the top of a cloud. Even when a Cray supercomputer is used, a run using the full RK model in a high-accuracy research mode for a single combination of input values often requires at least several minutes of CPU time. To make reasonable approximations of some of the full RK model results more readily available, we have used a comparatively simple function, which can be calculated very quickly on a mainframe computer or a 486 PC with a math coprocessor.

The purpose of this paper is to publicize an easy-to-use, widely available computer program, RKOPF, which features this relatively simple continuous function, the RK optical profile function, which is discussed in section 3. This program can be executed easily to simulate vertical profiles of extinction and backscatter coefficients in low stratus clouds and subcloud regions representative of worldwide conditions for various combinations of air mass type, maximum liquid water content, and surface level temperature, relative humidity, and visibility. The extinction and backscatter coefficient profiles were simulated for eight wavelengths (0.55, 1.06, 3, 4, 5, 8, 10.6, and 12 μm). All constants required to evaluate the RK optical profile function for the given combinations have been placed in computer-accessible storage for use by computer program RKOPF for performing the calculations. Since the printing of a previous paper,[7] the definition of the RK optical profile function has been extended, and the number of combinations of input values for which fitting constants are available has been increased to include many cases with simulated cloud top heights of 1000 meters, with many of these having simulated cloud base heights greater than 300 meters. An easy procedure for using computer program RKOPF to approximate extinction and backscatter coefficient profiles is summarized in this paper, and results for a few selected sets of input values are shown.

2. MODEL CONCEPT

Execution of the RK microphysics model requires an estimate of the cloud top height; dry particle chemistry; air mass type (maritime, rural, or urban); and reference level (2 m above ground level) values of temperature, pressure, relative humidity, and visibility. The relative humidity, visibility, and air mass type are required to define the Shettle-Fenn[5] bimodal lognormal distributions, which are used to define the reference level drop size distributions. In this work, each of these distributions is truncated to omit drops that would form from condensation nuclei having radii less than 0.004 μm.

Our approach is to compute Shettle-Fenn drop size distributions at the reference level for different combinations of relative humidity, visibility, and air mass type. Each of these drop size distributions then varies with height in accordance with the thermodynamics of an ascending cluster. For each air mass type, one nucleus type is selected from the ten samples reported by Hänel and Lehmann[8] such that the dry particle chemical composition is consistent with what would be expected for condensation nuclei in an air mass of that type. For each of 33 systematically selected combinations of reference level Shettle-Fenn parameters, three values of the reference level ambient air temperature (0, 15, and 30 °C) are used. The estimated cloud top height, which also can

be varied using the full RK model, is chosen to be 500 m above ground level if the relative humidity at the reference height is 90 percent or greater and 1000 m above ground level for the combinations in which the reference height relative humidity is 80 or 85 percent. The pressure at the reference level is always set at 1000 mbar (1 mbar = 1 hPa) since the drop size distribution is not sensitive to pressure changes. However, we have found that the distribution in the cloud varies with the liquid water content of the cloud. Hence, input parameters are also varied to make the maximum liquid water content approximately 50, 75, and 100 percent of the quasi-adiabatic values. (In this work, a "quasi-adiabatic" simulation is near adiabatic, differing from truly adiabatic by allowing small amounts of entrainment and diffusion from outside the ascending sphere.) The 33 reference level combinations of Shettle-Fenn parameters, 3 choices of maximum liquid water content, and 3 choices of temperature lead to 33 x 3 x 3 = 297 drop size distribution profiles. Applying Mie theory then enables calculation of 297 extinction coefficient profiles and an equal number of backscatter coefficient profiles for each of 8 wavelengths. The fitting method indicated in the next section is used in determining the RK optical profile function constants for approximating each of the 297 x 8 x 2 = 4752 resulting profiles. Fitting constants have been determined for all of the 4752 cases.

3. THE RK OPTICAL PROFILE FUNCTION

The following function, eq. (2), is designated as the "RK optical profile function," where σ is the extinction coefficient. For backscatter, σ is replaced with the backscatter coefficient β.

$$\sigma = \sigma_1 \left(\frac{\sigma_2}{\sigma_1} \right)^{\left(\frac{z - z_1}{z_2 - z_1} \right)^{N(z)}} \tag{2}$$

In this equation, z is the height above ground level. The form of this function guarantees an exact match at z_1 and z_2. We use this function in two pieces. For the lower piece, the subscript 1 refers to the reference height, and the subscript 2 refers to the height of the hinge point, which defines the boundary between the two pieces. For the upper piece, the subscript 1 refers to the height of that same hinge point, and the subscript 2 refers to the height of the "highest forced match" near the top of the cloud. The hinge point typically is chosen to be the inflection point at or near the base of the cloud on a $\ln \sigma$ or $\ln \beta$ versus z curve (where ln represents "natural logarithm of") defined by RK model data. Both pieces are described according to eq. (2) but have different values for the constants and may have different functional forms to describe N(z). N(z) is a function of z and is represented by one of these three equations:

$$N(z) = \exp \left(\sum_{n=0}^{N_E} E_n z^n \right) \tag{3}$$

$$N(z) = \sum_{n=0}^{N_E} E_n z^n \tag{4}$$

$$N(z) = A_o + c_1 z + c_2 z^2 + 2 \sum_{n=1}^{N_A} A_n \cos\left[\frac{2\pi n(z - z_{F1})}{z_{F2} - z_{F1} + 1} \right]$$

$$- 2 \sum_{n=1}^{N_B} B_n \sin\left[\frac{2\pi n(z - z_{F1})}{z_{F2} - z_{F1} + 1} \right] \tag{5}$$

in the range $z_{F1} \leq z \leq z_{F2}$. In these three equations, A_o, the A_n values, the B_n values, the E_n values, c_1, c_2, z_{F1}, and z_{F2} are constants. The terms involving c_1 and c_2 are included in eq. (5) so that the rest of the function — the part that is to be fit using Fourier analysis — would join smoothly from end to beginning like one cycle of a truly periodic function would do.

The definition of the RK optical profile function has been extended to include eq. (4). If the natural logarithm of $N(z)$ is to be submitted for polynomial fitting, as would be done if $N(z)$ is to be calculated using eq. (3), then the maximum extinction or backscatter coefficient value must occur at the maximum z (height) of a piece, as can be seen from taking the natural logarithm of both sides of eq. (6) below. This requirement poses no problem for fitting lower pieces, and eq. (3) is used routinely with $N_E = 3$ in approximating lower pieces of both extinction and backscatter coefficient profiles. However, in some of the profiles simulated using the full RK microphysics model, the maximum value occurs so far below the top of the cloud that ending the calculated profile at that maximum would be undesirable. When $N(z)$ itself is to be a polynomial, as defined in eq. (4), then the $N(z)$ profile to be fitted can be calculated even for an extinction or backscatter coefficient profile that has its maximum value somewhere other than at the end of a piece.

Equation (2) was solved for $N(z)$ as a function of z and σ simulated by the RK model. The resulting expression for $N(z)$ is

$$N(z) = \frac{\ln\left(\dfrac{\ln \sigma - \ln \sigma_1}{\ln \sigma_2 - \ln \sigma_1} \right)}{\ln\left(\dfrac{z - z_1}{z_2 - z_1} \right)} \tag{6}$$

Again, σ is replaced with β for backscatter. Using a vertical profile of $N(z)$ thus obtained, $N(z)$ or $\ln N(z)$ versus z data were fitted as indicated.

When polynomial fitting is used for $\ln N(z)$ versus z data in the upper piece for profiles in the series for which the cloud top height is 500 m, the height at which the maximum extinction or backscatter coefficient between 440 and 492 m, inclusive, above ground level occurs is often used as the height of "highest forced match." When Fourier analysis is used to fit $N(z)$ versus z data in the second piece, each resulting series of Fourier coefficients is truncated to retain only the lowest-frequency components. The number of Fourier constants retained, $N_A + N_B + 1$, is always much less than the number of RK modeled height levels (data points), $z_{F2} - z_{F1} + 1$, used in the Fourier analysis. N_A and N_B usually are both either 15 or 17, leading to 31 or 35 Fourier constants, respectively, besides the two quadratic constants. Some of the worst fits are improved by individual treatment.

A recently-added alternative is fitting N(z) versus z data for the upper piece by using a higher-degree polynomial (typically a twelfth-degree polynomial). The RKOPF (approximate) values of the extinction or backscatter coefficient in the upper piece would then be generated using N(z) calculated according to eq. (4). Since N(z) itself (not its logarithm) is being fitted, the fitting curve can, and often does, extend closer to the top of the cloud than does the height of the maximum value of the extinction or backscatter coefficient in a profile, thus making a more nearly complete profile available to the user.

Weighting of data points, based on the effect of propagation of small errors in calculated values of the dependent variable fitted using polynomials, has been used to improve fits with eq. (4). To analyze error propagation, consider an arbitrary function $f(x)$. If there is an error δ in x, then the calculated function value including the propagated error is $f(x + \delta)$.

The ratio of error in the calculated function value to the error in x is $\dfrac{f(x + \delta) - f(x)}{\delta}$.

If the error is sufficiently small, then this ratio may be approximated by

$$\lim_{\delta \to 0} \frac{f(x + \delta) - f(x)}{\delta} = \frac{df(x)}{dx} . \tag{7}$$

From this consideration of error propagation, each data point used in polynomial fitting of an upper piece was given a relative weight equal to the absolute value of the first partial derivative of the RK optical profile function with respect to N(z). Since z was assumed to be known exactly, the part of the total derivative with respect to z was not considered. This algebraic expression for this partial derivative was obtained from eq. (2):

$$\frac{\partial \sigma}{\partial N(z)} = \sigma_1 \exp \left[\left(\frac{z - z_1}{z_2 - z_1} \right)^{N(z)} \ln\left(\frac{\sigma_2}{\sigma_1} \right) + N(z) \ln\left(\frac{z - z_1}{z_2 - z_1} \right) \right]$$
$$\times \ln\left(\frac{\sigma_2}{\sigma_1} \right) \ln\left(\frac{z - z_1}{z_2 - z_1} \right) \tag{8}$$

For every one of 24 extinction coefficient profiles used in a test, a goodness-of-fit statistic indicated that a better fit was obtained when upper piece data points were weighted in this manner (compared against unweighted fit results). Sometimes lower piece data points were also weighted; however, each of their relative weights was the absolute value of the first partial derivative of the RK optical profile function with respect to ln N(z), since the exponential of a polynomial is still used as N(z) for each lower piece. (This partial derivative may be obtained by multiplying the right hand side of eq. (5a) by N(z).) When lower piece data points were weighted thusly, further improvement was realized for only 10 of the 24 test cases (compared with results for the first piece unweighted and the second piece weighted). Therefore, it was decided that first piece weighting be used for only the extinction coefficient profiles for which first piece weighting leads to additional improvement in a goodness-of-fit statistic. The mechanism used for fitting weighted data includes generating a matrix that contains the weights, values of the dependent variable, and values of z (height) raised to powers one through the degree of the polynomial to be determined. The latter are submitted as independent variables — one for each power of z — in a multivariate linear regression model to be fit via fast Givens transformations using IMSL software.

Both eqs. (4) and (5) are used in fitting backscatter coefficient profiles in the series that has been simulated using a cloud top height of 1000 m as input to the full RK model.

This series includes all of the RKOPF profiles for which the reference height relative humidity is 80 or 85 percent. A number of "highest forced match" values are tried for both types of fits in this series, with the one leading to the best value of a goodness-of-fit statistic usually being accepted. Values of a goodness-of-fit statistic are calculated for fits resulting from both of these methods for backscatter coefficient profiles in this series. The fitting constants are retained for whichever method leads to the better goodness-of-fit value for a given profile, and the corresponding calculation method would be used whenever an RKOPF user requests that profile. When both of these methods were tried for the same profiles, the eq. (4) (polynomial) expression was selected approximately 57 percent of the time, and the eq. (5) (quadratic plus Fourier series) expression was selected approximately 43 percent of the time.

The range typically chosen for fitting ln $N(z)$ versus z data by polynomial in the upper piece is from the second height level at or above the hinge height (noting that a perfect match is forced at the hinge height) to a level somewhat below the height of "highest forced match." The range used for fitting $N(z)$ (not its logarithm) versus z data in the upper piece is from the second height level at or above the hinge height to a level approximately 1 m below the height of "highest forced match."

After fitting constants are determined, they are available for convenient use to calculate $N(z)$ values, which in turn are used in eq. (2).

4. COMPUTER PROGRAM FOR EVALUATING THE RK OPTICAL PROFILE FUNCTION

The computer program RKOPF (RK optical profile function) is designed for interactive use and prompts the user at each step. Stored fitting information is located, applied in calculations, and used to determine whether eq. (3), (4), or (5) is to be used to calculate $N(z)$ for the second piece. The fitting information is stored in computer-accessible storage at White Sands Missile Range. Computer users with network access can use this program by using telnet to access the curie.arl.army.mil computer (internet address 192.67.8.5), logging on as rkopf (all lower-case letters), and using rkopf (again all lower-case letters) as the password. The RK optical profile function is programmed into the user computer program.

The first set of user choices is employed to determine which set (or sets) of fitting constants is to be applied. The user is to indicate each of these choices by entering an integer corresponding to the number of the desired choice. First, the user is presented with a choice of three air mass types (maritime, rural, and urban) and is asked to select one. Near a coastline with wind blowing in from the ocean, a maritime air mass would be the appropriate selection. In a city, an urban air mass would be appropriate. Inland and not near a city, a rural air mass would be appropriate. Next, the user is asked to choose one of five values (80, 85, 90, 95, or 99 percent) for the relative humidity at the reference height. If 95 percent is chosen, the user is informed that the visibility at the reference height is set automatically at 5 km. If one of the other relative humidity values is chosen, the user is asked to select the visibility at the reference height from the two or three available choices. The user is then presented with a choice of three reference height ambient air temperatures (0, 15, and 30 °C) and asked to choose one. The user is then prompted to select the desired value for the maximum liquid water content in terms of a percent (50, 75, or 100 percent) of the quasi-adiabatic (100 percent) value that would be obtained if all of the other input parameters were the same. The choice of this percent is left up to the discretion of the user. It is suggested tentatively that the 100 percent value be tried for night, the 75 percent value from sunrise to noon, and the 50 percent value from noon to sundown. The user is then asked to choose one of the eight available wavelengths. This set of selections is completed when the user indicates the type(s) of

profile(s) desired (profile(s) of the RK optical profile function to approximate the extinction coefficient in km^{-1}, backscatter coefficient in km^{-1} sr^{-1}, or both, with or without the associated N(z) profile(s)).

The next set of user responses enables the user to define some details about the profiles he/she is to receive. If "both" is selected in the last choice above, this set of choices is repeated for the second profile. The user is prompted for the name of each file that is to contain profile data and is to respond by entering a character string. Unless the PC version of the program is being used, this name will appear on the first line of the file created. The program reveals the height limits of validity of the calculated profile. The user may accept these as the bounds of the profile to be calculated, or he/she may specify some range within the range of validity by entering two real numbers (not necessarily integers). Since the RK optical profile function is continuous, function values can be calculated for any desired height spacing, as long as all of the heights are within the range of validity. Therefore, the user may specify the height spacing desired for output data. When prompted to do so, the user is to enter a real number (not necessarily an integer). To avoid creation of unreasonably large data files, this height spacing should be greater than 0.1 m.

The one, two, or four profiles requested are written as ASCII files readable by a Fortran program. The first line of each file created contains the file name specified by the user. (However, the PC version omits this first line as unnecessary, since the actual file name would be identical to the user-specified name if the latter is within the length allowed by the operating system.) If the RKOPF program on the curie.arl.army.mil computer has been accessed by logging in as "rkopf" (as would be done by someone who does not have an account on that computer), then any files created using this program would be sent by electronic mail to the user. If more than one file is mailed, then the recipient could identify each file by the name on the first line. The second line, in 3i5 format, gives the number of data points and two small integers, which can be ignored or interpreted by some software as the line type and symbol type requested for a plot. The rest of each output file contains the data and uses one line for each data point. Each of those lines may be read as free format and contains the value of the requested function followed by the height in meters above ground level for which this function is calculated.

5. RESULTS

RK optical profile function constants were determined by using simulated extinction or backscatter coefficient profiles one at a time. When the RK optical profile function was used for extinction coefficient profiles, agreement of calculated curves with RK model curves generally appeared very good, even when N(z) was calculated according to eq. (3) for the entire profile. For RK model extinction coefficient profiles that appeared wavy, fitting curves calculated according to eq. (3) appeared to be reasonably smoothed curves.

Third-degree polynomials were not nearly as successful in fitting ln N(z) when N(z) was to be approximated according to eq. (3) for upper pieces of backscatter coefficient profiles. Many RK model backscatter coefficient profiles and some RK model extinction coefficient profiles showed enough structure that we decided not to eliminate it by smoothing. Instead, we successfully fitted N(z) for upper pieces of many profiles with a polynomial of higher degree (twelfth degree was typical) or the sum of a quadratic expression and truncated Fourier series to obtain constants for use with a combination of eqs. (2) and either (4) or (5). We found that the goodness of fit depends largely on the number of terms used. Also, the goodness of fit often varies widely with small changes in the height of "highest forced match." Enough terms were used to retain the major oscillations as well as the trends in the profiles. Figure 1 shows an example for which

N(z) was calculated using a tenth-degree polynomial. This figure includes the full RK microphysics model extinction coefficient profile for a wavelength of 0.55 μm as a solid line and an RK optical profile function fitting curve as a dashed line. Figure 2 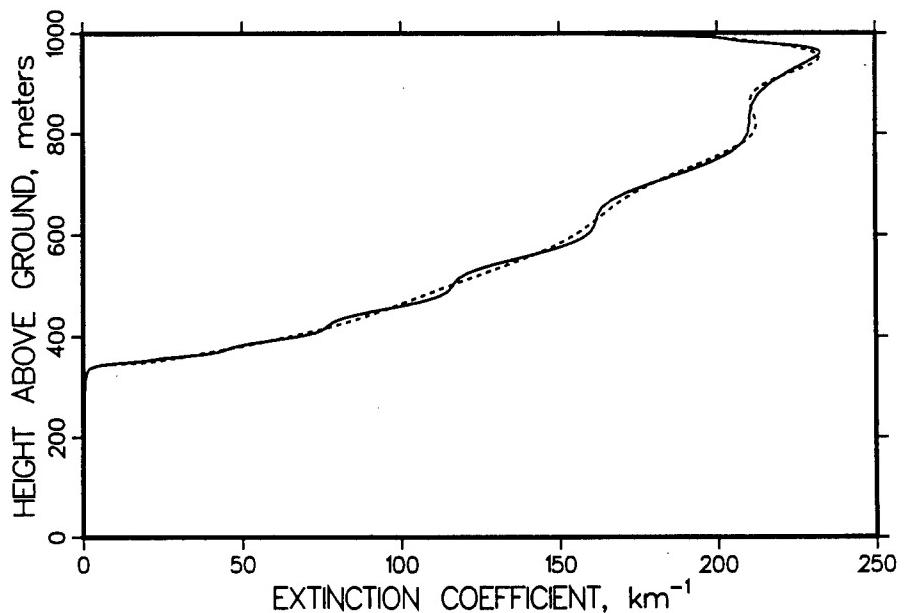shows an example for which N(z) was calculated using a twelfth-degree polynomial. That figure includes a full RK microphysics model backscatter coefficient profile for a wavelength of 1.06 μm as a solid line and an RK optical profile function fitting curve as a dashed line.

Figure 1. An extinction coefficient profile simulated for a wavelength of 0.55 μm using full RK model (solid line) and then approximated using RK optical profile function with a tenth-degree polynomial (dashed line).
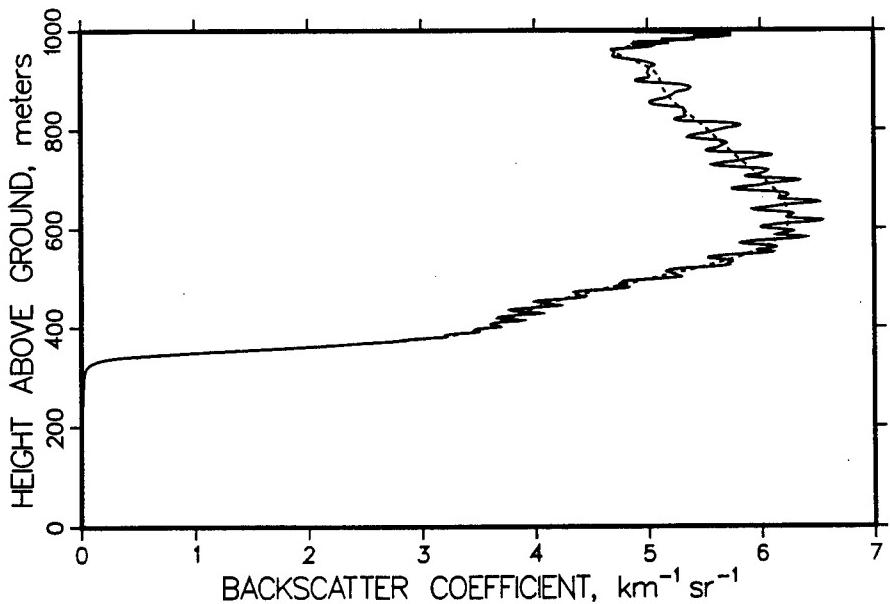
Figure 2. A backscatter coefficient profile simulated for a wavelength of 1.06 μm using full RK model (solid line) and then approximated using RK optical profile function with a twelfth-degree polynomial (dashed line).

702

Out of the 4752 sets of RK optical profile function constants generated in this study, a few sets were chosen for simulating profiles to use in this paper to illustrate results. Effects on calculated RK optical profile function extinction coefficient profiles from varying the maximum liquid water content and reference level relative humidity are shown in figs. 3 and 4 for a wavelength of 0.55 μm.
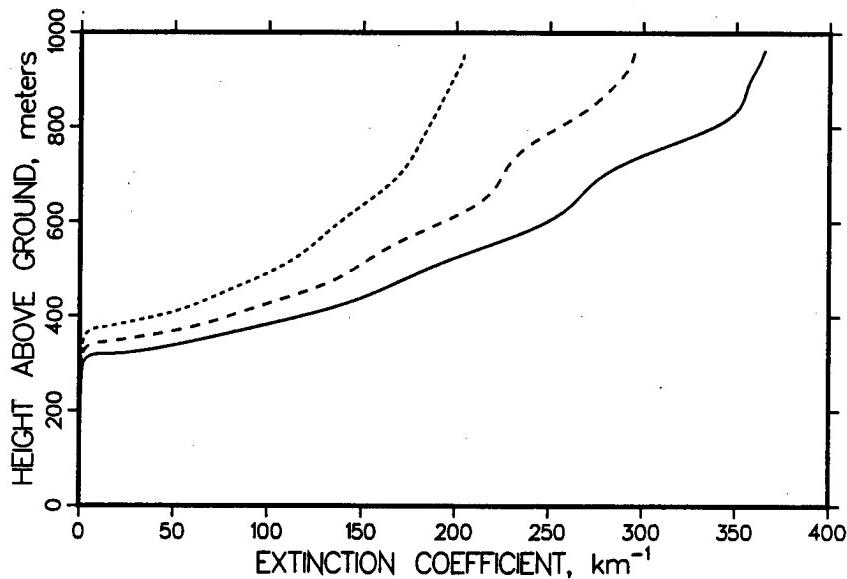
Figure 3. Effect of maximum liquid water content — 100 percent (solid line), 75 percent (medium-length dashes), and 50 percent (short dashes) of quasi-adiabatic — on extinction coefficient profiles calculated using RK optical profile function for a wavelength of 0.55 μm.
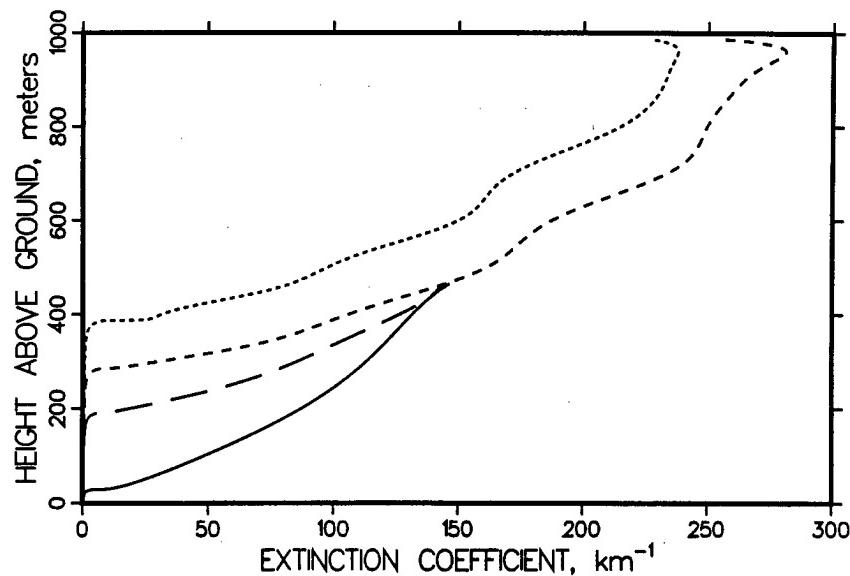
Figure 4. Effect of reference level relative humidity — 80 percent (short dashes), 85 percent (medium-length dashes), 90 percent (long dashes), and 99 percent (solid line) — on extinction coefficient for a wavelength of 0.55 μm according to RK optical profile function.

Some vertical profiles of β simulated using the full RK model are wavy or contain short-range fluctuations, while other such profiles simulated using different input values with the same model for identical wavelengths are smooth. Having a smaller number of droplets in the initial (reference height) drop size distribution seems to increase the tendency to generate wavy β profiles. Two cases, both of which had been simulated using the full RK model for a maritime air mass and quasi-adiabatic liquid water content, were studied thoroughly. One case, which was called "k1", was simulated using reference height (2 m above the surface) input values of 90 percent for the relative humidity, 2 km for the visibility, and 0 °C for the ambient air temperature. This case initially had many more drops per cubic centimeter than the other case, which was called "k14" and which was simulated using reference height input values of 99 percent for the relative humidity, 10 km for the visibility, and 15 °C for the ambient air temperature. When the initial drop concentration for the case (k14) having the smaller drop concentration was increased greatly, much smoother β profile curves resulted. On the other hand, when the initial drop concentration for the case (k1) with the larger drop concentration was decreased greatly, β profile curves exhibited increased waviness or/and very short-range fluctuations. Examples of these effects are shown for a wavelength of 4 μm in figs. 5 and 6, in which the unaltered case results are plotted as solid lines and the results after greatly altering the drop concentration are plotted as dashed lines. (σ profiles usually were smooth, but even some σ profiles exhibited some waviness for small drop concentrations.) In contrast, the in-cloud portions of liquid water content profiles for these cases were insensitive to greatly changing the initial drop concentration.
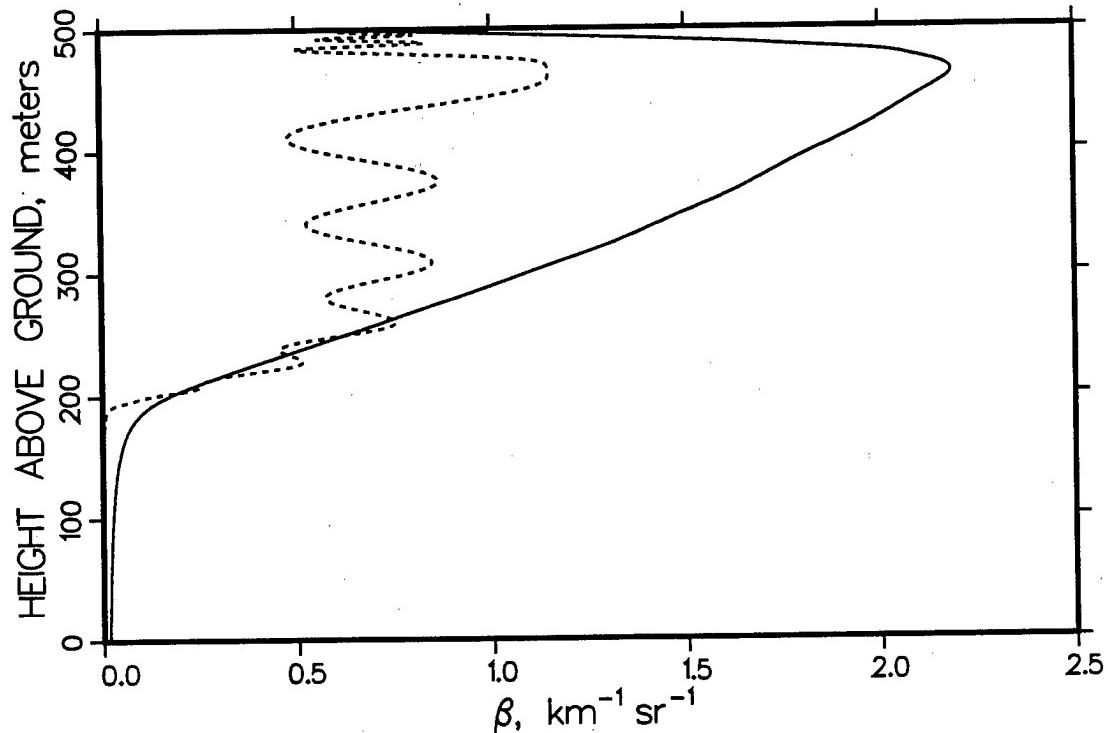

Figure 5.   Effect of initial drop concentration on backscatter coefficient profiles simulated for a wavelength of 4 μm using full RK model: The solid line represents unaltered case k1, and the dashed line represents the same case except that the initial drop concentration is divided by 16.86.
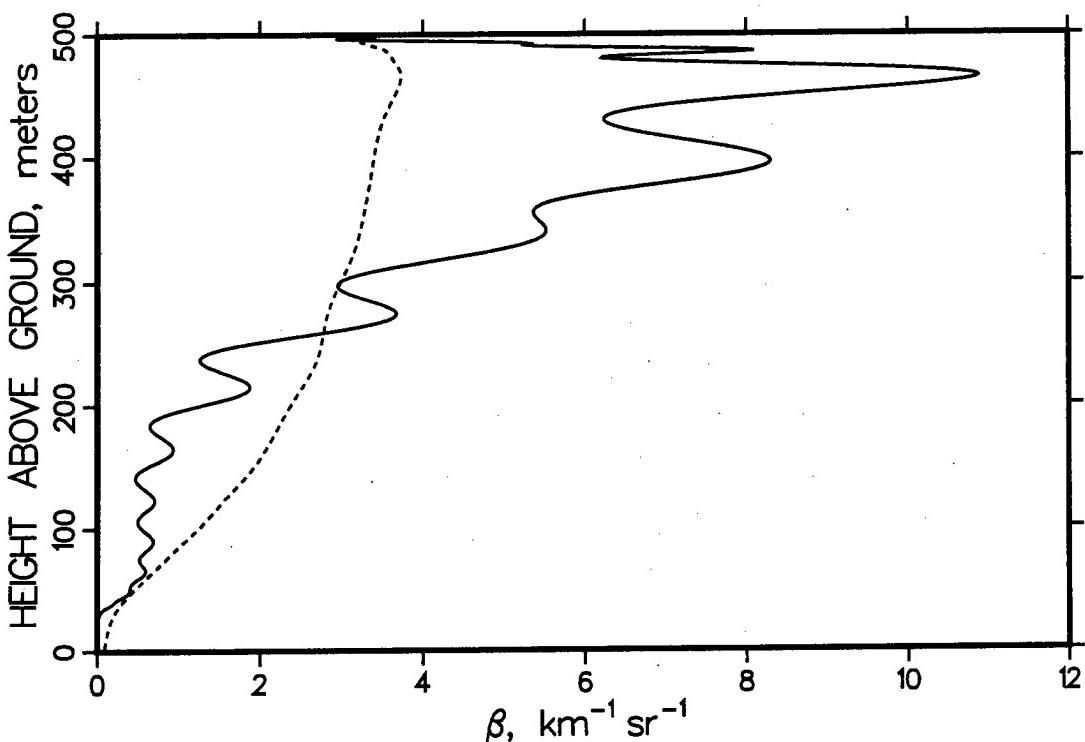
Figure 6. Effect of initial drop concentration on backscatter coefficient profiles simulated for a wavelength of 4 μm using full RK model: The solid line represents unaltered case k14, and the dashed line represents the same case except that the initial drop concentration is multiplied by 16.86.

As part of this investigation, cumulative distribution functions of simulated (RK model) drop size distributions expressed as geometric cross-sectional area were plotted. Examples of in-cloud results are shown for cases k1 (dashed line) and k14 (solid line) for a height of 252 m above ground level in fig. 7. Geometric cross-sectional area was selected because that quantity is multiplied by Mie efficiency factors to calculate σ and β. For relatively small drop concentrations, many of the cumulative distribution functions were very steep in the center, showing that most of the total geometric cross-sectional area often was contributed by drops in a relatively narrow size range. That situation leads to a greater tendency of relative minima and maxima in Mie efficiency factor functions of drop radius to lead to the production of waves and short-range fluctuations in vertical profiles of β. On the other hand, the cumulative distribution functions for larger drop concentrations sloped more gradually, showing that drops in a relatively wide size range were contributing most of the total geometric cross-sectional area. The latter situation leads to a greater tendency of relative minima and maxima in Mie efficiency factor functions of drop radius to be smoothed out in β profiles.

Vertical profiles of simulated (RK model) drop radii also were plotted. Results are shown in fig. 8 for the unaltered case k1 and in fig. 9 for the unaltered case k14. For the cases studied, a large gap between radii of (apparently nonactivated and activated) drops in the cloud region tended to be associated with relatively small drop concentrations, and a smaller gap tended to be associated with relatively large drop concentrations. When a large gap occurred, drop size classes appeared to be bunched together near the upper drop size boundary of the gap. Having so many of the size classes bunched together in
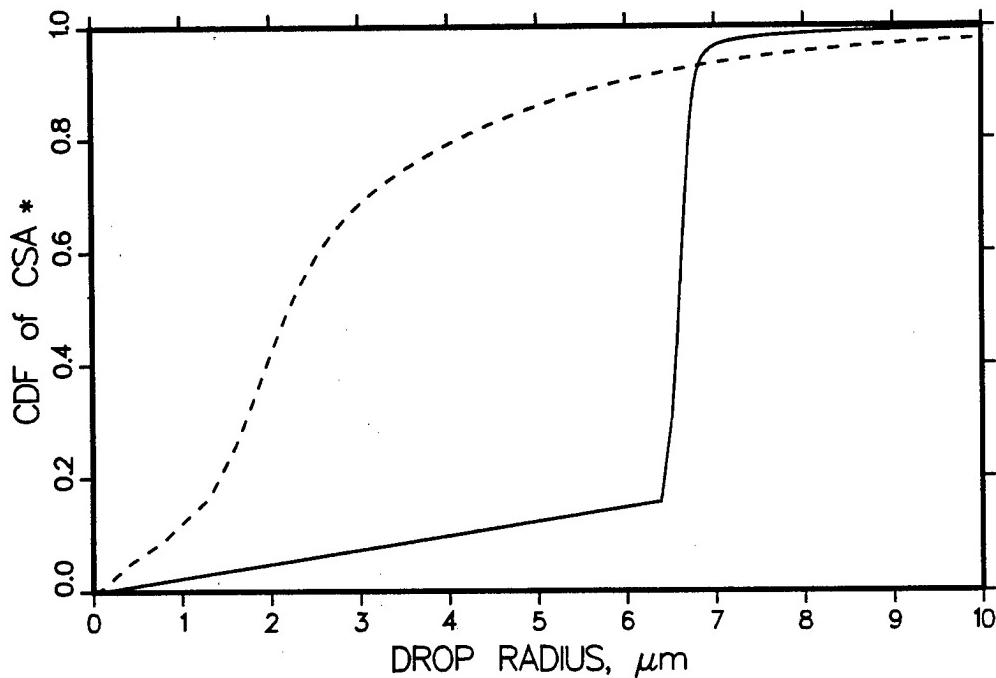
Figure 7. * Cumulative distribution functions (normalized) of total cross-sectional
area of droplets calculated from data simulated for a height of 252 m using
full RK model: Dashed line represents a case (k1) having a much larger
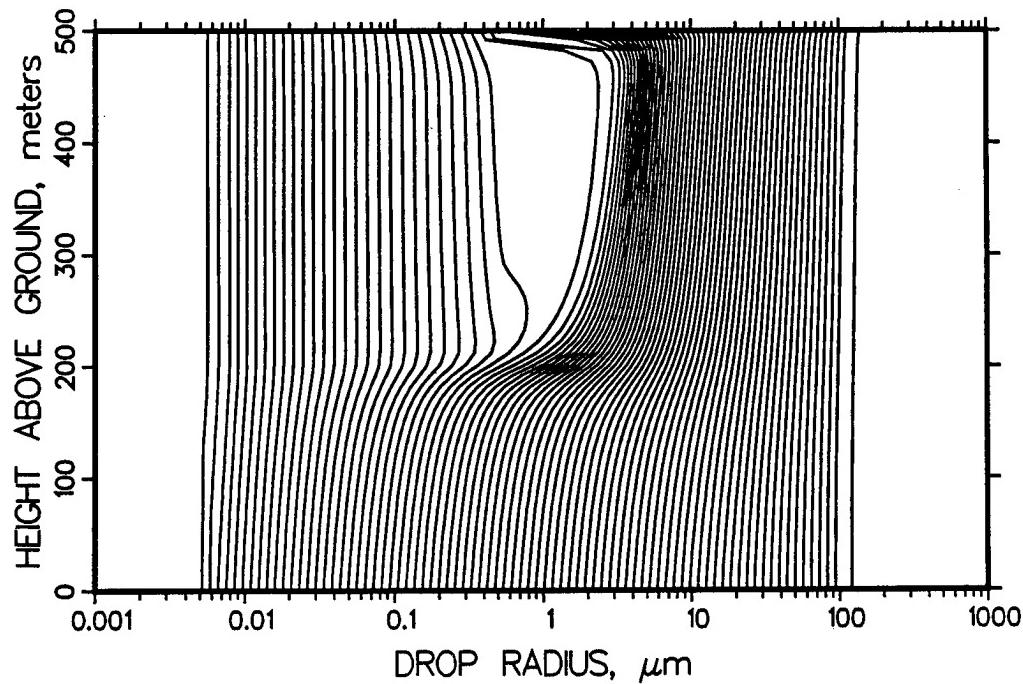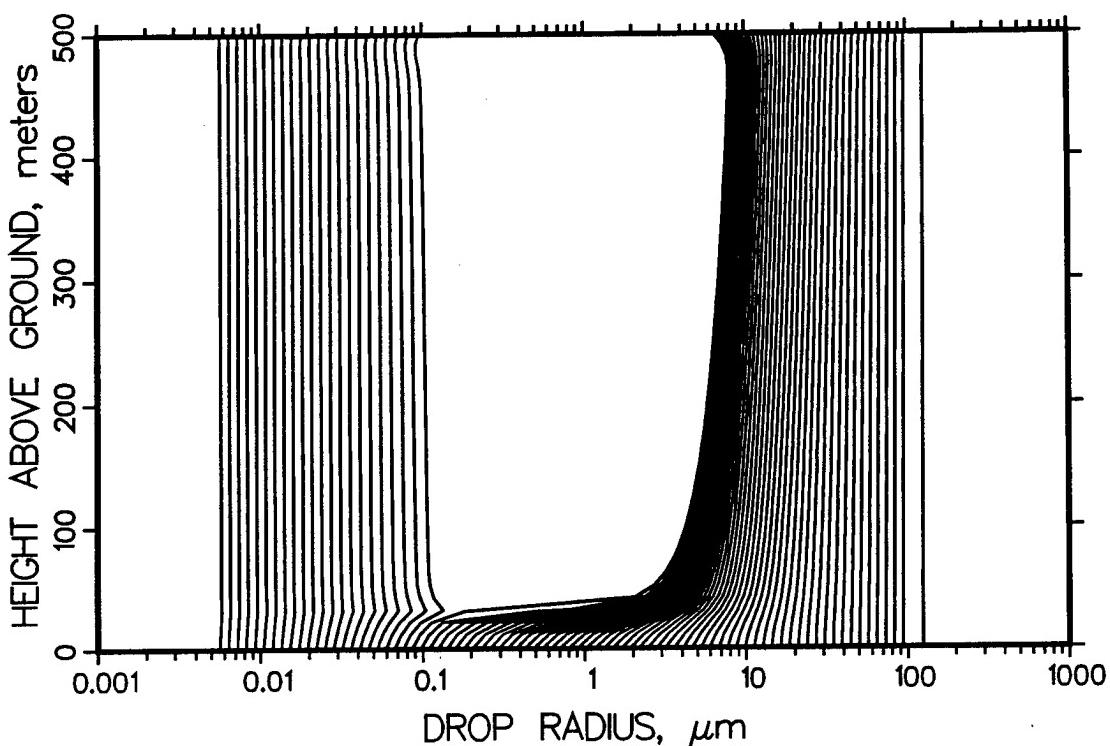drop concentration than the case (k14) represented by the solid line.

Figure 8. Vertical profile of drop radii for all 80 size classes from simulation
using the full RK model for case k1, which has a much larger initial
drop concentration than the case represented in fig. 9.

706

Figure 9. Vertical profile of drop radii for all 80 size classes from simulation
using the full RK model for case k14, which has a much smaller initial
drop concentration than the case represented in fig. 8.

such a small drop size range often leads to β profiles being affected significantly by
fluctuations in Mie efficiency factors; whereas a much more even distribution of drop
sizes tends to lead to β profiles being well smoothed. Using a much smaller initial drop
concentration for a simulated (RK model) case that otherwise corresponded to case k1 led
to a larger in-cloud gap and some cumulative distribution functions of geometric
cross-sectional area that exhibited steeper vertical portions compared with the unaltered
k1 case. On the other hand, using a much larger initial drop concentration for a simulated
case that otherwise corresponded to case k14 led to a smaller in-cloud gap and
cumulative distribution functions of geometric cross-sectional area that sloped more
gradually compared with the unaltered k14 case.

CONCLUSIONS

The authors have developed a theoretically based low stratus cloud/subcloud model,
which is documented elsewhere.[6] Drop size distribution data simulated using this model
are used with Mie efficiency factors to simulate vertical profiles of extinction and
backscatter coefficients for a variety of atmospheric conditions that can occur worldwide.
This model was used in this study to generate extinction and backscatter coefficient
profiles that vary with air mass type, maximum liquid water content, and reference level
values of temperature, relative humidity, and visibility. These profiles were then fitted
individually with the RK optical profile function. To determine values of the constants in
eq. (3), (4), or (5) for each combination of RK microphysics model input and wavelength,
a fitting procedure was used with vertical profiles of the extinction or backscatter
coefficient from the full RK microphysics model and Mie calculations.

Constants for the RK optical profile function were determined for 2376 simulated extinction coefficient profiles and 2376 simulated backscatter coefficient profiles. These fitting constants have been stored in computer-accessible storage, and a program has been written for easy interactive use in calculating simulated profiles for any of the cases for which results have been stored. Network users can access and use this program via telnet. Use of this program is outlined in section 4 of this paper. Proper execution of this program produces profiles that are in excellent agreement with the essence of profiles (this sometimes implies smoothing) produced by using the complete RK microphysics model.

We propose that the RK optical profile function and model-generated values of its fitting constants be considered for possible worldwide application. We invite anyone with network access to try this function by accessing the curie.arl.army.mil computer (internet address 192.67.8.5) using telnet, logging on as rkopf (using lower-case letters), and then using that same word as the password.

ACKNOWLEDGMENT

The authors appreciate the work done by Gregory N. Whitfield, Michael S. Paz, Lyndal D. Frye, and Brian A. Seylar of the Physical Science Laboratory. They used the full RK model many times to determine self-consistent sets of values to use as input and obtained most of the full RK model extinction and backscatter coefficient profiles used in this study. They have helped considerably in the creation of a very large number of plots. Further, Mr. Whitfield, Mr. Frye, and Mr. Seylar have helped in some of the curve fitting. The authors also appreciate the work done by Robert Flanigan and Tom Crow of the U.S. Army Research Laboratory to facilitate making the RKOPF program available to many more potential users without compromising system security.

REFERENCES

1. Miller, A., 1983: Mie Code Agaus 82. ASL-CR-83-0100-3, U.S. Army Atmospheric Sciences Laboratory,[9] White Sands Missile Range, NM 88002.

2. Heaps, M. G., 1982: A Vertical Structure Algorithm for Low Visibility/Low Stratus Conditions. ASL-TR-0111, U.S. Army Atmospheric Sciences Laboratory,[9] White Sands Missile Range, NM 88002.

3. Rachele, H., and N. H. Kilmer, 1991: A Derivation for Determining Double Exponential Liquid Water Content and Extinction Profiles from Discrete Data. ASL-TR-0290, U.S. Army Atmospheric Sciences Laboratory,[9] White Sands Missile Range, NM 88002.

4. Kilmer, N. H., and H. Rachele, 1992: Analytic Functions for Modeling Vertical Profiles of Extinction in and Beneath Very Low Stratus Clouds. In Atmospheric Propagation and Remote Sensing, Anton Kohnle and Walter B. Miller, eds., Proceedings SPIE, 1688, 132-143.

5. Shettle, E. P., and R. W. Fenn, 1979: Models for the Aerosols of the Lower Atmosphere and the Effects of Humidity Variations on Their Optical Properties. AFGL Technical Report AFGL-TR-79-0214, Air Force Geophysics Laboratory, Hanscom AFB, MA 01731.

6. Rachele, H., and N. H. Kilmer, 1992: Unified Very Low Stratus Cloud/Subcloud Microphysics Model. ASL-TR-0309, U.S. Army Atmospheric Sciences Laboratory,[9] White Sands Missile Range, NM 88002.

7. Kilmer, N. H., and H. Rachele, 1993: An Optical Profile Function for Modeling Extinction and Backscatter Coefficients in Very Low Stratus Clouds and Subcloud Regions. In Proceedings of the 1992 Battlefield Atmospherics Conference, 33-42, Battlefield Environment Directorate, U.S. Army Research Laboratory, White Sands Missile Range, NM 88002.

8. Hänel, G., and M. Lehmann, 1981: Equilibrium Size of Aerosol Particles and Relative Humidity: New Experimental Data from Various Aerosol Types and Their Treatment for Cloud Physics Application, Contributions to Atmospheric Physics (Beiträge zur Physik der Atmosphäre), 54(1), 57-71.

9. Currently U.S. Army Research Laboratory, Battlefield Environment Directorate, White Sands Missile Range, NM 88002-5501.

COMBAT-INDUCED ATMOSPHERIC OBSCURANT (CIAO) SYSTEM

Scarlett D. Ayres and Robert A. Sutherland
Battlefield Environment Directorate
U.S. Army Research Laboratory
White Sands Missile Range, New Mexico 88002-5501

Kathy R. Hansen, Spencer C. Newland, and Steven J. LaMotte
Physical Science Laboratory
New Mexico State University
Las Cruces, New Mexico 88003

ABSTRACT

The combat-induced atmospheric obscurants (CIAO) system is a prototype computer-based modeling and simulation system designed to demonstrate the impact of advanced high-resolution atmospheric models in force-on-force wargame simulations. Current wargames use low-resolution atmospheric models that tend to ignore some of the more realistic effects due to the battlefield environment and weather that could prove to be significant on the wargame outcome. In the past this limitation was necessary because of computer limitations and because of the nonavailability of appropriate atmospheric models. The goal of the research behind the CIAO system is to determine the impact of the use of advanced high-fidelity, high-resolution, atmospheric models on the outcome of simulated battles. The system as now configured employs the combined arms and support task force evaluation model as the baseline wargame model with scenarios supplied by the Training and Doctrine Command wargaming community. Atmospheric models include high-resolution wind models treating complex terrain, obscuration models treating contrast and electromagnetic wave propagation, radiative transfer models treating the energy balance, and material transport models treating aerosols and chemicals. In this paper we describe the workings of the CIAO system and the candidate models.

1. INTRODUCTION

The objective of the combat-induced atmospheric obscurants (CIAO) project is to determine the impact of advanced atmospheric modeling technologies on such metrics as

weapon kill statistics and loss-exchange ratios (LER) when integrated into modern combat wargame simulations. This involves developing and testing a (computer/graphics) system for quantitatively demonstrating the impact of high fidelity atmospherics simulations on high level wargame outcomes. The CIAO system is the prototype. In order to maintain compatibility with the simulation language currently used by the Training and Doctrine Command (TRADOC) analysis community, the CIAO system is programmed in the simulation language SIMSCRIPT. The CIAO system is also capable of treating atmospheric models as subroutines programmed in either FORTRAN or "C." System hardware is compatible with current TRADOC technology wherever possible. The TRADOC force-on-force wargame simulation model, the combined arms and support task force evaluation model (CASTFOREM), along with postprocessing software, is the backbone of the CIAO system. Other capabilities include high-resolution graphics aids to highlight effects of aerosols/obscurants and terrain on the complex battlefield.

2. TECHNICAL DESCRIPTION OF CIAO SYSTEM

2.1 Hardware

The CIAO system includes a SUN SPARCstation 10 workstation with a 19-in color monitor, two superSPARC processors, one 1.05-Gbyte internal disk drive, one 3.5-in internal floppy disk drive, one 128-Mbyte RAM, one 1.05-Gbyte external disk drive, one 5-Gbyte 8-mm tape drive, and one 644-Mbyte CD-ROM. There is also an auxiliary SUN SPARCclassic computer system consisting of a 16-in color monitor, a 24-Mbyte RAM, and a 207-Mbyte interval disk drive. Auxiliary input/output hardware includes a 300 DPI 24-bit true color printer and a 300 DPI 24-bit true color scanner.

2.2 Software

The operating system is a SUN Solaris-2.0 that is similar to UNIX and provides multiprocessor support. The CASTFOREM is written in SIMSCRIPT; however, the system can also support atmospheric models as subroutines written in either FORTRAN or C. Compilers for all three languages have been acquired. The SUN Systems Answerbook and NeWSprint software were acquired for the purpose of providing a system reference book and postscript printing capabilities to the color printer, respectively.

3. TECHNICAL DESCRIPTION OF CIAO MODELS

3.1 The CASTFOREM Model

3.1.1 General Description

The CASTFOREM is a high-resolution, two-sided, force-on-force, stochastic, event-sequenced, systemic simulation model of a combined arms conflict.[5] It is the current model used for representing tactics through the use of decision tables and embeds an expert system for battlefield control. Battle orchestration up to the battalion level is accomplished

strictly through the use of decision tables. Combat can last up to 90 min and normally represents an area of 20 km by 20 km. The model provides extensive line of sight (LOS) calculations along various observer-to-target directions accounting for terrain elevation and vegetation. In addition to LOS calculations, the model accounts for intervening atmospheric conditions that can include effects of combat-induced obscurants. Digitized terrain is included but is not, at present, coupled to the meteorological conditions. The original CASTFOREM assumes homogeneous weather that is considered constant in time and space.

The CASTFOREM contains a postprocessor that enables users and modelers to generate statistical output from single and multiple replications of the battle scenario. This output is critical to users for their analysis of study results. Current CASTFOREM postprocessor capabilities include analytic packages that can generate output for the following: commander kills, directed energy negations, engagement opportunities, kills/range, net usage, plots on losses, smoke, suppression, and other areas.

3.2 The High Resolution Wind (HRW) Model

3.2.1 General Description

The HRW model is a micro-alpha scale, two-dimensional, surface layer wind and temperature model of high resolution.[3] The model supplies high-resolution calculations of surface layer wind, temperature and turbulence parameters at selected grid points over a limited area taking into account both the terrain topography and thermal structure. HRW can model an area as large as 20 by 20 km. This area may be divided into as many as 50 by 50 cells. The resolution of this model ranges from 60 to 400 m, but it is generally applied with a resolution of 100 m. HRW is based on applying a special variational form of Gauss' principle of least constraints to the mass and momentum conservation accounting for the terrain configuration and thermal forcing.[2] According to this principle, the equations of motion are satisfied when the internal constraint forces acting on a system are minimized. Results are obtained by a direct variational relaxation of wind and temperature fields in the surface layer to minimize the constraints imposed by the terrain, thermal structure, and the requirement for flow continuity. For each grid point in the area of interest, the values for the wind components and potential temperature, as well as the computed values for the impaction vertical motion, friction velocity, Richardson's number, and the exponent for the wind power law-profile are provided.

The HRW program requires, as input, a previously archived terrain data base that includes the effective terrain elevation, surface roughness, vegetation height, and vegetation type, as well as minimum meteorological parameters such as the initial wind vectors, a temperature profile, and a surface heating parameter. HRW was designed to use limited meteorological input data but detailed terrain data.

3.2.2 Potential Benefits

Although CASTFOREM does include terrain elevation in LOS calculations there is no coupling of the terrain with the wind flow. Thus in the current version of the model, the wind is treated as constant with no variation in either speed or direction in the horizontal plane. However, terrain effects can cause a nonlinear inertial character of the flow interacting with the terrain surface. Terrain sheltering and channeling, wakes, and flow separation are features of wind fields in complex terrain. The HRW model will be used to determine wind fields that, in conjunction with other models like SANDIA, ONION SKIN and atmospheric biological and chemical (ABC) can treat effects that terrain-induced wind fields can have on the modern battlefield.

3.3 The SANDIA Model

3.3.1 General Information

The SANDIA model is a highly parameterized smoke obscuration model, based in part on results from the more comprehensive combined obscuration model for battlefield induced contaminants (COMBIC) model.[1] The model treats obscurant clouds as binary entities, that is, as either completely opaque or completely transparent in either of five electro-optical bandpasses from the visible through infrared.[7] The approach is to use all mathematical or modeling techniques available to produce the best possible representation of smoke clouds in terms of easy to use simple polynomial or exponential expressions.[8] The primary outputs of the SANDIA model are coefficients and scaling parameters that are used in the polynomials and exponential expressions to model the length, width, height, and the vertical centroid of discrete battlefield smoke or dust clouds. The user needs only these final expressions and does not need to perform numerous repetitions involving numerical path integrations through the smoke cloud as is required in the more comprehensive COMBIC model. Speed and simplicity are traded for accuracy in the detailed representation of individual smoke sources. The underlying methodologies in SANDIA and COMBIC are much the same, differing only in degree of sophistication. The main advantage of SANDIA, besides speed in computation, is that the effects of complex windfields such as those supplied by HRW are easily accommodated in the transport of the obscurant.

3.3.2 Potential Benefits

The SANDIA model does not obtain the same degree of accuracy as the COMBIC model currently being used in CASTFOREM. Yet, there are two main benefits in using SANDIA over COMBIC: (a) it executes faster than COMBIC, and (b) it can be assimilated with the HRW model to examine the effects of terrain modified wind fields on smoke. In the current CASTFOREM, COMBIC does not model wind fields; it models smoke blowing from one direction only with constant speed (speed does vary with height). The CIAO system can use HRW and SANDIA to determine if terrain channeling or sheltering can affect the results of the battlefield. The SANDIA model cannot be used to determine if

flow separation (around a hill) affects the statistics, since the user has output from SANDIA to model a single geometric shape for the smoke source. The more advanced ABC model described later is needed to compute the flow of smoke around structures.

3.4 The ONION SKIN Model

3.4.1 General Information

The ONION SKIN model is an extension of the SANDIA model described in the previous paragraph and uses the same general approach. With ONION SKIN, however, the smoke clouds are resolved into layers representing various thresholds of optical thickness, whereas SANDIA considered only one central region representing a single optical thickness threshold.

3.4.2 Potential Benefits

The most obvious benefit of the ONION SKIN approach is that the clouds can be played at a higher resolution than SANDIA without much loss in computational speed. The other advantage is that the cumulative effects of multiple clouds can be treated with ONION SKIN, whereas only the binary option for a single cloud can be used with SANDIA. As with SANDIA, the ONION SKIN approach can be made much more compatible with complex wind models such as HRW.

3.5 The LASS Model

3.5.1 General Description

The large area screening systems (LASS) applications model was originally developed for use in research on the effectiveness of smoke screens deployed over large fixed and relocatable military installations.[4] The model serves as a tool for the assessment of smoke screens (employed with other techniques of camouflage, concealment, and deception) as an electro-optical countermeasure against low-level nap-of-the-earth attack by high-performance aircraft. The outputs of the model are symbolic maps displaying the direct and diffuse components of scene transmission as affected by a large-area smoke screen. The model can be exercised with various optional inputs to determine the effects of solar angle, solar flux density, sky radiance, and surface albedo, etc. The model is logically divided into two distinct parts, one that applies the Gaussian diffusion approximation to compute obscurant concentration path length (CL product) and another that applies the plane-parallel approximation to compute target-background contrast. The plane-parallel approximation implies a smoke screen of large horizontal extent that is a reasonable approximation for a large-area smoke screen. The model is capable of treating inhomogeneities in the smoke screen as long as they represent only small perturbations. The transport and diffusion algorithms are similar to those employed in other obscuration models differing only in minor detail. The radiative-transfer algorithms, however, are unique in the use of the extensive radiative-transfer tables originally published by

715

Van De Hulst that are used together with novel scaling algorithms to account for effects of single and multiple scattering along arbitrary slant path and horizontal lines of sight. The model treats scattering processes only and is thus restricted to visible and near-infrared regions where absorption and thermal emission are negligible. The obscurant phase function is taken to be of the Henyey-Greenstein form and can account for various degrees of anisotropic scattering as well as isotropic scattering. The model accounts for scattering of the direct solar beam, uniform diffuse skylight, and diffuse reflection from the underlying (earth) surface.

3.5.2 Potential Benefits

Models like CASTFOREM directly relate transmission to electro-optical system performance and smoke effectiveness by considering the following generally accepted expression for modeling the total signal incident at an observer location.

$$S(\vec{r}) = S(\vec{r}_o) T + S_p(\vec{r}) \tag{1}$$

where $S(\vec{r})$ is the optical signal received by an observer at $(\vec{r})$ from a target at $(\vec{r}_o)$. The transmission (T) includes effects of both scattering out of the path plus absorption along the path. In equation (1) the second term is the path radiance (S_p) which accounts for scattering of ambient radiation (sun, sky) into the path of propagation or emission along the path, or both.

For nonthermal sensors, the target acquisition probability is related to the direct transmission and the contrast X at the sensor's aperture through the use of the calculated contrast transmission to account for path radiance as

$$X = \left[\frac{1}{1 + (\frac{B_s}{B_b}) (\frac{1}{T(R)} - 1)} \right] X C_o \tag{2}$$

where B_b is background intensity, B_s is path radiance (sometimes called "sky" intensity for a horizontal path), C_o is the target-to-background contrast, and $T(R)$ is the direct transmission over the range denoted by R. In equation (2) the first factor in brackets in referred to as the "Contrast Transmission."

The probability of acquisition may be calculated by using the following integral expression

$$P_a = \frac{1}{\sqrt{2\pi}} \int_{-\infty}^{\frac{(n-\acute{n})}{\sigma}} \exp(-x^2/2)\, dx \qquad (3)$$

where $\acute{n}$ is the number of resolvable cycles across the target for an acquisition probability of 50 percent, and σ is the standard deviation of the number of resolvable cycles across the target.

In CASTFOREM the contrast transmission is approximated by using a single constant value for the ratio B_s/B_b, sometimes referred to as the "sky-to-ground" ratio that is usually required as input by the user. Furthermore, the expression of equation (2) is valid only for the case of horizontal propagation and requires modification for treating the general slant path scenario. Using the LASS radiative transfer algorithms we will be able to overcome both of these limitations by directly computing the contrast transmission as a function of position and viewing direction. The potential benefits of using a more realistic value for the contrast transmission has been reported in a previous paper by Lee et al. (1991).

3.6 The REBAR Model

3.6.1 General Information

The REBAR model accounts for the aerosol-induced "radiative damping" that can alter the local atmospheric stability and the vertical profiles of temperature and humidity and hence alter electromagnetic wave propagation.[9] The aerosols act in two ways: (a) to diminish either by scattering or absorption the amount of radiation reaching the surface and thus altering the surface energy balance, and (b) to increase atmospheric absorption and thermal emissions and thus alter radiative heating and cooling rates in the boundary layer. The REBAR model is an integrated set of aerosol related, radiative, energy balance, stability and turbulence programs to help assess the effects of aerosols on the local meteorology. REBAR will assist in the analysis of atmospheric stability and turbulence structure in the local environment when aerosols are introduced into the atmosphere.

3.6.2 Potential Benefits

A large area smoke screen that lasts a long time can significantly depress the surface irradiance and drive the Pasquill stability towards neutral conditions. Since the rise and diffusion of smoke is critically dependent upon the stability class, this can in turn affect smoke operations. The REBAR model is the first attempt to model this important aspect of large area smoke screens. The CIAO system will use the REBAR model to determine impacts on the battlefield cause by radiative damping. Since neutral conditions are often

717

ideal for smoke deployment and a desired smoke screen can be maintained with less smoke, it is expected that there will be significant reductions in the amount of smoke inventory used.

3.7 The Atmospheric Biological and Chemical Simulation (ABCSIM) Model

3.7.1 General Information

The ABCSIM model was developed by Ron Meyers and his colleagues to provide near-real-time calculations and visualizations of airborne concentrations, dosages, and ground contamination resulting from a nuclear, biological, and chemical (NBC) attack.[6] The model calculates diffusion in space and time in changing wind fields over complex terrain. The model requires as input select meteorological cases, source characteristics, and location. These are provided by the CASTFOREM wargame scenario. The model works on virtually all particle size distributions and vapors resulting from NBC agent releases. To calculate the NBC agent transport and dispersion accurately from all altitudes, we developed a new diffusion scheme that is accurate and can also adapt to the changing meteorological fields. The adaptive numerical scheme was necessary to achieve maximum efficiency for any given level of accuracy. The detailed meteorological fields needed for the transport and diffusion calculations over complex terrain and military structures are computed by AIRSIM, their four-dimension first-principles meteorological code that predicts meteorological fields down to the resolution of meters.

3.7.2 Potential Benefits

In the real modern battlefield, NBC agents can pose a real threat to personnel and military operations. The threat can range from troops temporarily out of action to significant military losses. Recent wars in the Mideast have highlighted concern over the possible use of NBC agents. For the United States (U.S.) to maintain a tactical advantage in such an event, the training and doctrine community must asses the impact of NBC agents on the battlefield. ABCSIM in combination with the CASTFOREM wargame can determine the impact, thus leading to improved doctrine in NBC events.

4. BASELINE HIGH-RESOLUTION SCENARIO

The baseline scenario to be used for CIAO testing is the TRADOC high-resolution scenario (HRS) 3.5. It depicts a balanced task force defending against first echelon tank requirements. Blue tactics will use the air-land battle doctrine. The red force structure represents combat systems projected to be in the field by the year 2000. Terrain contours showing elevation are illustrated in figure 1. The area covered is 20 km by 20 km. Attack lasts 48 min and occurs at dawn in Germany. The red tank army (TA) opposite the sector in which this scenario takes place is conducting a front supporting attack. The tank division depicted in HRS 3.5 is conducting the TA main attack. This division is in the TA's first echelon and attacks along two axes to defeat blue defensive positions in the vicinity of

Rothenkirchen. Its subsequent objective is Lauterbach. Only the northern axis of this division is depicted in the scenario. The northern axis consists of one tank regiment as the first echelon. The U.S. armored division conducts a main battle area defense with a brigade task force (TF) forward as a covering force and two brigades on line comprising the main battle area. Upon completion of the covering force operation, the brigade TF conducts a rearward passage of lines and becomes the division reserve.
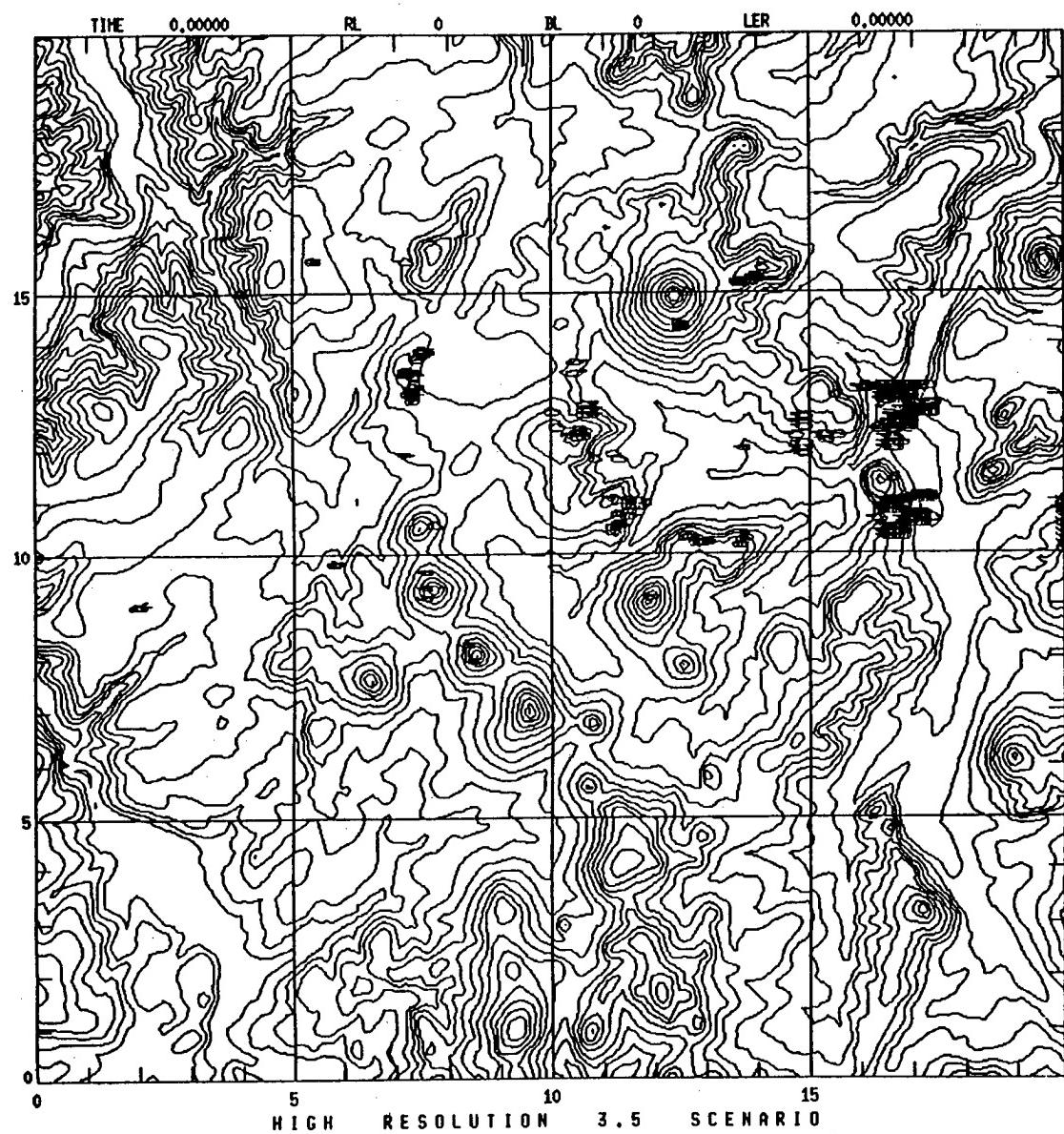

Figure 1. Terrain elevation for high-resolution 3.5 scenario.

719

References

1. Ayres, S. D., and S. DeSutter, 1993: "Combined Obscuration Model for Battlefield Induced Contaminants (COMBIC) Users Guide." In preparation, U.S. Army Research Laboratory, Battlefield Environment Directorate, White Sands Missile Range, NM 88002-5501.

2. Ball, J. A., and S. A. Johnson, 1978: "Physically Based High Resolution Surface Wind and Temperature Analysis for EPAMS." ASL-CR-78-0043-1, U.S. Army Atmospheric Sciences Laboratory, White Sands Missile Range, NM 88002-5501.

3. Ball, J. A., and S. A. Johnson, 1992: "Notes on the Preliminary HRW Code." In preparation, U.S. Army Research Laboratory, Battlefield Environment Directorate, White Sands Missile Range, NM 88002-5501.

4. JTCG/ME, 1985: "Standards For Large-Area Screening Systems (LASS) Modeling." 61 JTCG/ME-85-4, Joint Technical Coordinating Group for Munitions Effectiveness, U.S. Army Materiel Systems Analysis Activity, Aberdeen Proving Ground, MD.

5. Mackey, D. C., D. S. Dixon, K. G. Jensen, T. C. Loncarich, and J. T. Swaim, 1992: "CASTFOREM (Combined Arms and Support Task Force Evaluation Model) Update-Technical Documentation." TRAC-WSMR-TD-92-011, U.S. Army TRADOC Analysis Command, White Sands Missile Range, NM 88002-5501.

6. Meyers, R. E., 1993: "Atmospheric Biological Chemical Simulation Model." In preparation, U.S. Army Research Laboratory, Battlefield Environment Directorate, White Sands Missile Range, NM 88002-5501.

7. Sutherland, R. A., and D. E. Banks, 1986: "Smoke Modeling In the Trasana Wargames-The Comprehensive Smoke Study." In Proceedings of the Smoke Symposium X, Volume 1, DRCPM-SMK-T-001-86, Aberdeen Proving Ground, Maryland 21005, 1:259-268.

8. Sutherland, R. A., 1993: "SANDIA Draft Documentation." In preparation, U.S. Army Research Laboratory, Battlefield Environment Directorate, White Sands Missile Range, NM 88002-5501.

9. Yee, Y. P., R. A. Sutherland, H. Rachele, and A. Tunick, 1993: "Effect of Aerosol Induced Radiative Interactions on Atmospheric Stability and Optical Turbulence." In Proceedings of the International Society for Optical Engineering Atmospheric Propagation and Remote Sensing II, Bellingham, Washington 98227-0100, 1968:192-203.

10. Lee, M. E., S. J. LaMotte, 1991 "Influence of Battlefield-Induced Obscurants and Atmosperic Effects on High-Resolutions Combat Simulations." In Proceedings of Battlefield Atmospherics Conference, U.S. Army Research Laborator,, Battlefield Environment Directorate, White Sands Missile Range, NM 88002-5501, pp 94-104.

AN ATMOSPHERIC DATA BASE STRUCTURE, VISUALIZATION METHODOLOGY, AND DATA EXCHANGE TECHNIQUES

Rene' M. Smith, Thelma A. Chenault
U.S. Army Battlefield Environment Directorate
WSMR, New Mexico, USA

ABSTRACT

Data base structures and visualization methodology that enables scientists to access, understand and use atmospheric data efficiently are presented. Also presented are user and programmer documentation which facilitate data input and post-processing. Finally, this paper outlines a data-exchange method to allow users to run specific data base applications on data retrieved from the data base.

The data base structure for the Atmospheric Joint Acoustic Propagation Experiment Database (AJAPED) is graphically presented. This data base contains atmospheric and acoustic data from the Joint Acoustic Propagation Experiment (JAPE) conducted in July, 1991, at the Dusty Infrared Test (DIRT) Site, White Sands Missile Range, New Mexico. Visualization methodology techniques include a menu-driven atmospheric profile generation and digitized retrieval of acoustic data. Software development which support atmospheric model verification/validation will be demonstrated. This software provides raw data input to the data base, menu-driven access to data in multiple formats and media, and profile graphing. Commercial data-exchange software has been implemented which allows users to access selected functions of the data base with a stand-alone process, i.e., data base application distribution. This technique can be implemented to give users access to data on CD Roms at their own personal computer and/or workstation.

I. INTRODUCTION

Atmospheric model verification/validation is highly dependent on using real field data. It is important to exchange field data in a format that supports the scientist developing the model. The data base developed for this paper is a structure which can be used with other field-obtained data. It is therefore the purpose of the authors to show

the advantages and flexibility of merging commercially obtained data base software with a graphing package and customized programs written in-house.

Paradox Version 3.5, by Borland International was the chosen data base software. This package is a relational data base, and was used with a C Engine that was purchased separately. The C Engine was used to interface the data base information and C programs. Another optional package was the Paradox Runtime Release 3.5. Runtime provided the ability to distribute limited Paradox applications, free from copyright infringements. This abiltiy was greatly enhanced by the addition of C programs interfacing with Dplot, a government developed graphics package written by David Hyde, of Waterways Experimental Station (Authors note: David Hyde has recently released another version of his graphics package which runs under Windows.) Dplot is a menu-driven program which will perform analysis of graphs, to include least-squares fitting, zooming on selected regions, integrating the area under the curve, and much more. Dplot is a stand-alone graphing package. C programs were developed to interface with Dplot and Paradox. This enables scientists to select the data base information needed and have it put directly in a Dplot graph format.

II. DATA BASE STRUCTURE

The field data utilized is not of primary interest, however, a brief overview of the data is necessary to enhance understanding. The data examined in this paper is from the JAPE, conducted at the DIRT Site, White Sands Missile Range, New Mexico. It consists of atmospheric characterization measurements during an 18 day period of July, 1991. The data were grouped by the particular instrument or tower collecting the information. All statistics were arranged chronologically before input into the data base structure.

Data were obtained from eight different locations on the DIRT Site, representing a coverage of approximately 400 square meters. Table 1 lists the instrumentation types used in this test.

TABLE 1
Instrumentation Types Used in AJAPE Data Base.

Data Type	Instrument
A0 Sodar	Remtech A0 Sodar
10m TACS	Tactical Atmospheric Characterization System 10 meter Tower
30m TACS	Tactical Atmospheric Characterization System 30 meter Tower, 1 and 15 minute Averaged Files

(Continued on next page)

722

TABLE 1 (Continued from previous page)
Instrumentation Types Used in AJAPE Data Base.

Data Type	Instrument
30m Thermistor	30 meter Thermistor
PA2 Sodar	Phased Array 2 Sodar
PAMS	Portable Atmospheric Met System 1 and 15 minute Averaged Files
Radar	Radar Profiler High and Low Resolution
RASS	Radio Acoustic Sounding System
Tethersonde	Tethersonde
UHF Wind Profiler	Wind Profiles High and Low Resolution
Upper Air Profiles	Profiles Made From a Composite of Data

There were five different towers collecting 10 meter TACS data. The data in ASCII form was approximately 31 megabytes. The raw record and field breakdown of the data is given in Table 2.

TABLE 2
Raw Record and Field Breakdown of Data.

Data Type	Records	Fields per Record
A0 Sodar	16,692	11
10m TACS		
East Tower	32,364	16
Foothill	16,990	16
Hilltop	15,450	16
North Site	28,609	16
West Tower	28,710	16
30m TACS		
1 min Ave.	5,794	39
15 min Ave.	389	39
30m Thermistor	146,464	7
PA2 Sodar	13,410	11
PAMS		
1 min Ave.	18,047	26
15 min Ave.	3,842	26
Radar		
High Resolution	2,825	7
Low Resolution	2,825	7

(Continued on next page)

TABLE 2 (Continued from previous page)
Raw Record and Field Breakdown of Data.

Data Type	Records	Fields per Record
RASS	1,116	4
Tethersonde	2,607	10
UHF Wind Profiler		
High Resolution	2,900	7
Low Resolution	2,975	7
Upper Air Profiles	1,056	20

A graphical representation of the data base structure is shown in Figure 1. Paradox Runtime starts the application. The Paradox Engine 2.0 together with the C programs provide an interface between the data base information and the graphing and output operations.

FIGURE 1
Graphical Representation of Data Base Structure.
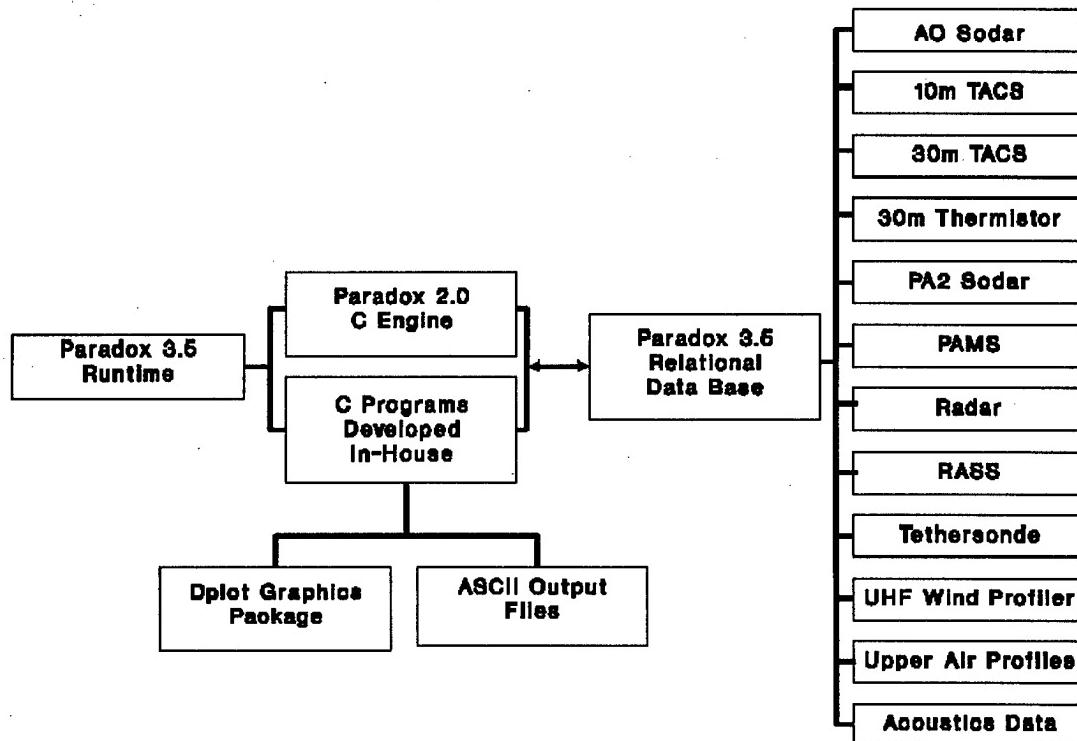
Data searches were performed using Julian day and decimal hours as the key fields. This eliminated the need to sort through the data by the slower method of using Julian day, hours, minutes and seconds. Since the test was run by trials, a key table was introduced to provide the starting and ending times and a description of each trial.

III. VISUALIZATION METHODOLOGY

In order to provide the maximum support to scientists developing models, a simple but powerful tool was needed to enable visualization of data. When the scientist reviews data for potential input into a model, it is helpful to see if it is applicable for validation purposes. Usually when a scientist receives test data for model validation or verification, he only receives raw data in a non-standard format. This means the scientist must either use the data and later decide if it conforms to his needs or he must reformat the raw data to fit into an analysis package. Inclusion of a government developed menu-driven graphics package allows for easy previewing of raw data.

The use of a graphing package and the selection of the data posed continuity problems which were best overcome with a C interface program used in conjunction with the Paradox Software. The overall goal was to provide fast-effective review of data, this meant that after a scientist selects data for visualization, he needed to be able to view it easily with Dplot. A menu-driven search program was written in C that will search the data by trial or by time and output it in a format to be used in Dplot. Menu-driven code was chosen as the most user-friendly way to approach the analysis problem. This reduced the time used by scientist to learn the graphing/selection tools.

A limited amount of acoustics data were added to the data base because of space requirements. However, selected acoustics data can be run through Dplot using the C interface. This facility is only available for users requesting this type of data.

IV. SOFTWARE DEVELOPMENT

New options can easily be added to the C code which interfaces between Paradox and Dplot. This type of flexible development allows the possiblity of user-specific applications. Output routines developed in C code give the user the option of writing files in ASCII or delimited ASCII. Since the user decides which selected data are written to the file, this opens the door for expedient use of the information.

The raw data input into the data base structure were a one-time only process. That is, since the data base is test-specific, there are no new data being added after the conclusion of the test. Data were collected and input to the data base structure using a given ASCII import facility of Paradox. Time conversions to decimal hour and Julian day were accomplished with C programs run on the original data.

Data output is the final stage of the scientist's analysis process. After previewing the data base information, he may wish to export the data for use in his model. This process is concluded in the same menu-driven mode used to build profiles for graphing. This is another of the selections available through C programs written with the use of the Paradox C Engine.

V. DATA-EXCHANGE SOFTWARE

The software developed for this application and the data itself can be written to CD Roms. This will allow a user having a PC equipped with a CD Rom reader to have a large stand-alone data base application. The entire application requires about 35 Megabytes of space, therefore it is best suited for workstations or for 486 PC's and above. Once on a PC or workstation, the data within can be exported in smaller ASCII files if necessary. The whole process is a stand-alone application of the larger original data base housed at the Army Research Laboratory (ARL).

VI. CONCLUSIONS

The ability to distribute data with stand-alone data base applications and graphing capabilities provides a unique opportunity for scientists. The goal is to provide maximum support for scientists developing, verifying, and validating atmospheric or acoustic models. With this in mind, we have set up a process whereby we can allow the scientist to expediently visualize, analyze, and manipulate the data.

The atmospheric field data employed in this data base is not indicative of the only type of data applicable. It is the hope of the authors that the structure be utilized for other field test data, specifically, applications that require large data sets. Mastering the exchange of this data will improve the overall performance of scientists and experimenters alike, and save time and resources in the model verification and validation process.

REFERENCES

Bruce, Thomas A., 1992. *Designing Quality Databases with IDEF1X Information Models*, Thomas A. Bruce. Published by Dorset House Publishing, New York, NY.

Curtice, Robert M., Jones, Paul E., 1982. *Logical Data Base Design,* Van Nostrand Reinhold Company, New York, NY.

Defense Technical Information Center, 1992. *Technical Report Summaries*, Defense Technical Information Center, Alexandria, Virginia, B/Computer Graphics/DTIC B-061307.

Flores, Ivan, 1981. *Data Base Architecture,* Van Nostrand Reinhold Company Inc., New York, NY.

Hyde, David, 1993. Personal Communication.

Kennedy, Bruce W., 1991. *Joint Acoustic Propagation Experiment Project Summary,* The Bionetics Corporation, Las Cruces, New Mexico.

Okrasinski, Richard, 1993. Personal Communication.

MEASUREMENT OF THE INTERMITTENCY IN THE INERTIAL SUB-RANGE OF THE ATMOSPHERIC WIND VELOCITY SPECTRUM

W. Peterson, D. Garvey, T. Chenault, R. Smith, and D. Littell
U.S. Army Research Laboratory
White Sands Missile Range, NM 88002

ABSTRACT

This effort was undertaken to investigate the inertial sub-range intermittency on the Kolmogorov Universal Equilibrium Theory (U.E.T.) by analyzing measurements of small scale wind velocity fluctuations in the atmosphere. Measurements were taken on a tower at White Sands Missile Range. The wind speed was detected with hot film sensors 2 mm long and 0.152 mm diameter at 4 m above the ground. The data were collected at 6000 Hz and then decimated to 1000 Hz for analysis. From these measurements probability densities and moments up to the fourth order were obtained from the velocity fluctuations of the wind in the atmosphere ($Re > 10^4$). Skewness and kurtosis were also obtained from the probability densities. The results of the analysis of these data are compared to Kolmogorov's refined theory and the β-model for intermittency. Probability densities are compared to the Kolmogorov's predictions of log normality. The β-model takes into account that the eddy packing fraction decreases with eddy size, while the U.E.T. assumes that the eddies are evenly distributed and space filling within the inertial sub-range. An important parameter of the β-model is the fractal dimension of the space in which the turbulence is embedded. The analysis of the data in general verifies the prediction of Kolmogorov's refined theory and the β-model. It also agrees in general with the results of previous investigators.

1. INTRODUCTION

This paper discusses some experimental observations and comparisons with existing theories of the probability density and moments of increments of the

fluctuating wind velocity in the inertial subrange in high Reynolds number (Re~10^6) turbulent flow. The term increment means the difference in values of the wind velocity measured at two points separated by a distance r. Conflicting theories for the moments (structure functions) have been discussed by Van Atta and Chen (1970), Wyngaard and Pao (1971), and others. No theoretical predictions for the probability density are available.

Van Atta and Chen (1970) have measured structure functions of the turbulent velocity fluctuations in the atmospheric boundary layer over the open ocean, and the results were compared with theoretical predictions for separations in the inertial subrange. They found that the results of the measured fourth-order structure function was in good agreement with Kolmogorov's (1962) modified theory. Here we shall make a similar comparisons with some data obtained in the atmospheric boundary layer over a desert setting and discuss measured moments with predictions of theories and previous measurements.

2. THEORETICAL RELATIONS

Kolmogorov's Theory

According to Kolmogorov's Universal Equilibrium Theory (U.E.T), 1941, in the inertial subrange the so called structure functions of order n are given by the expression:

$$\langle (u-u')^n \rangle = C_n (\varepsilon r)^{(\frac{n}{3})} \qquad (1)$$

where r is the separation distance of two points, u and u' are the components of the fluctuating velocity at the two points in the direction of separation, ε is the mean rate of dissipation of kinetic energy, and C_n are universal constants. The angle brackets in Equation (1) denote ensemble averaging. Kolmogorov found the value of C_3 to be -4/5. The value of the remaining C_n have not been determined theoretically. The expression (1) applies only to separations in the inertial subrange $l_0 < r < L_0$, where l_0 is the inner scale where dissipation of eddies begin due to viscous effects and L_0 is the length scale of the energy containing eddies. A further consequence of Equation (1) is that the skewness

$$S = \frac{\langle (u-u')^3 \rangle}{\langle (u-u')^2 \rangle^{(\frac{3}{2})}} \qquad (2)$$

and the kurtosis

$$K = \frac{\langle (u-u')^4 \rangle}{\langle (u-u')^2 \rangle^2} \qquad (3)$$

must be constant for $l_0 < r < L_0$. The magnitude of the skewness can be related to C_2 by the relation

$$S = \frac{-4}{5} C_2^{(\frac{-3}{2})} \qquad (4)$$

Since 1941 investigators have noted on theoretical and experimental grounds high Reynolds numbers turbulence is intermittent, that is, irregular and patchy. It had become clear that the energy associated with small eddy sizes is very unevenly distributed in space. Kolmogorov (1962) did refine his original U.E.T. and Equation (1) is replaced by the expression,

$$\langle (u-u')^n \rangle = \hat{C} \varepsilon^{(\frac{n}{3})} r^{(\frac{n}{3})} \left(\frac{L_0}{r} \right)^{(\frac{n(n-3)\mu}{18})} \qquad (5)$$

where the $\hat{C}_n$ are now not absolute constants. We note that the modified theory gives n^{th} order moments which vary like $r^{n/3 - \mu n(n-3)/18}$ rather than $r^{n/3}$. μ is taken to be a universal constant. The modifies expression for the skewness and kurtosis factors are

$$S = \frac{-4}{5} \hat{C}_2^{(\frac{-3}{2})} \left(\frac{L_0}{r} \right)^{(\frac{\mu}{6})} \qquad (6)$$

$$K = \frac{\hat{C}_4}{\hat{C}_2^2} \left(\frac{L_0}{r} \right)^{(\frac{4\mu}{9})} \qquad (7)$$

β-Model of Intermittency

A basic assumption of Kolmogorov's U.E.T is that the cascade of eddies in the inertial range are evenly distributed and space-filling. It is known, however, that at high Reynolds number turbulent eddies become less space-filling and distributed as the cascade progresses.

A phenomenological model of intermittency called the β-model has been developed (Frish, etc., 1978). The key assumption is that turbulent scales within the inertial range fill only a fraction of the total space. The model is dynamical in the sense that it takes into account inertial range quantities such as velocity amplitudes, eddy turnover times, and energy transfer. This gives more physical insight than the traditional approach based on probabilistic models of the dissipation (Monin and Yaglom, 1975).

The β-model leads in an elementary way to the concept of a dimension D which is the fractal dimension of the space in which the turbulence is embedded (Mandelbrot, 1974). Thus, the β-model is intrinsically geometric in nature, and relates the smaller eddy packing fraction to a reduction in the effective dimension of the turbulence. For three-dimensional turbulence it has been found that μ in Equation (5) is related to D by the relationship

$$\mu = 3 - D \qquad (8)$$

Statistical information entropy (Fujiska and Mori, 1979) arguments have been used to deduce a value for D. The value found was D=2.6. Thus, in intermittent turbulence, the effective dimension D is less than three, so the eddies should be though of as a flat ribbon-like structure, rather than spheres. Measurements of μ have been reported (Monin and Yaglom, 1975) and indicate $\mu \approx 0.4 - 0.5$. This is reasonably close to the theoretically predicted value of 0.4 for D = 2.6.

Because of the uncertainty in μ, observations of velocity fluctuations were obtained and from these μ was determined directly by using structure functions of these fluctuations. It is the purpose of this paper to report these observations and analyses.

3. OBSERVATIONS

Observations were made on White Sands Missile Range, New Mexico at Greg Site, during 7 October 1992. Greg Site is a desert setting in southern New Mexico. Conditions were dry with few clouds and the air temperature was approximately 24° C. during the daytime. The fluctuating component of the turbulent velocity field in the mean wind direction was measured at a height 4 meters above ground level with a single vertically oriented hot-film wire 0.015 cm diameter and 0.2 cm long. The hot-wire operated in a constant temperature mode using TSI 124-60 anemometer and the anemometer output was calibrated in a wind tunnel over a variety of wind speeds. A boom arrangement placed the hot-film probe about 2 meters to the side of the tower. This allowed an acceptance angle of about 180° for the mean wind speed. During the time period of the measurements there was a northerly wind of 4-6 meters per second.

The hot-wire signal was digital taped recorded with a TEAC RD200T data recorder. The data recorder has a sampling rate of 6,000 Hz and a low pass filter of 2,500 Hz. The uninterrupted data runs were about 30 minutes to allow for an adequate sample size (Van Atta and Chen, 1970).

4. DATA ANALYSIS

The digitized wind speed at 6,000 Hz was decimated to 1,000 Hz for analysis. The decimated data gave 1.8×10^6 samples for a 30 minute data run. Wind speed differences were computed using every second sample as the initial point of the 30 minute data run. Taylor's frozen turbulence hypothesis in the form r=ūt was used to interpret the measured time delay, t, as a spatial separation r. ū is the mean wind speed. The probability density functions, structure functions, skewness factor, kurtosis factor were computed for the velocity differences (Δu) using the 30 minute data periods.

5. RESULTS

An example of wind velocity at 1,000 samples per second is shown in Figure 1. The highly intermittent nature of the wind speed is evident with bursts of high-frequency fluctuations. Probability density functions were computed for a number of intervals ranging from a separation interval of two data samples to a separation interval of 4,096 data points, corresponding to spatial separations in the range from 1.35 cm to 27.7 m, respectively. A total of 900,000 velocity differences were used to compute each of the probability density functions shown in Figure 2 for various values of separation distance r. σ is the standard deviation of Δu. The probability densities shown in Figure 2 are very far from Gaussian, having a shape characteristic of a strongly intermittent random variable (Van Atta and Chen, 1970). The probability of very small values of Δu normalized with the standard deviation ($\Delta u/\sigma$) and values of $|\Delta u|/\sigma$ greater than about 3 is considerably greater than would be expected for a Gaussian distribution. The probability of intermediate values is smaller. For large values of $\Delta u/\sigma$ the probability of large negative values is greater than for large positive values. Hence, all the odd moments, such as the skewness of the velocity difference and the third-order structure functions are negative.

As the separation distance increases, the probability density of the velocity difference continuously approaches the Gaussian distribution. It appears likely that for even larger separations, the probability density of Δu will approach even closer to the Gaussian distribution, and the skewness associated with the tails of the density function will disappear.

Examples of measured second-order and fourth-order structure functions are shown in Figure 3. The separation distance r in terms of L and the mean wind speed ū is

$$r = 2^L \frac{\overline{u}}{1000} \qquad\qquad \textbf{(9)}$$

The line with circles represents the original theory of Kolmogorov and the solid line is the refined theory. The data in Figures 3(a) and 3(c) are fairly well fitted by Kolmogorov's refined theory, Equation 5, for μ equal to 0.5 (Van Atta and Chen, 1970). For r less than about 2 cm (L=2) the data deviates from the inertial subrange relation, $<(\Delta u)^2> \sim r^{11/9}$ and $<(\Delta u)^2> \sim r^{11/9}$, as expected in the viscous range. For r greater than about 1.20 m (L=8) the data again deviates from the inertial subrange relationship. The inertial subrange will be taken between r=2 cm and 1.20 m corresponding to L=2 and 8, respectively. Figures 3(b) and 3(d) are a regression of the logarithm of the second and fourth-order structure functions on L. Values of the structure function for L between 2 and 8 were used in the regression fit. Figure 3(b) has a slope of 0.22265 for the regression on L. This corresponds to a slope of 0.7396 on r, giving μ a value of 0.65 or D=2.35. From Figure 3(d), the fourth-order structure function, the derived value of μ is 0.42 or D=2.58. Four 30 minute sets of data were analyzed from the field test. Values of μ were derived for each set of data using Equations (5) and (7). Equation (5) was used for the second and fourth-order structure function and Equation (7) was used for the kurtosis. The average value of μ derived from each of the methods are given below.

Average Values of μ

$<(\Delta u)^2>$	$<(\Delta u)^4>$	Kurtosis
0.51	0.45	0.35
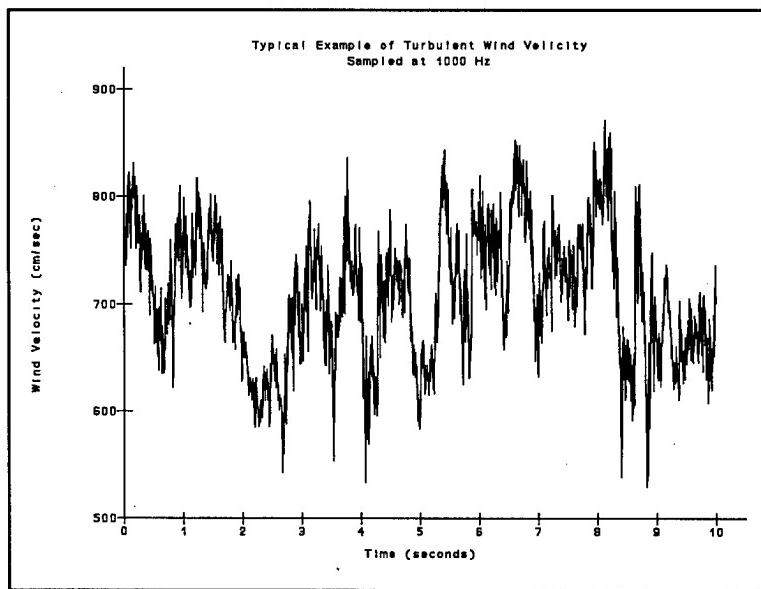
Figure 1.

Figure 2a.

Figure 2b.

Probability Densities of The Velocity Difference
For R equal 43.22 cm.

Figure 2c.

Probability Densities of The Velocity Difference
For R equal 172.90 cm.
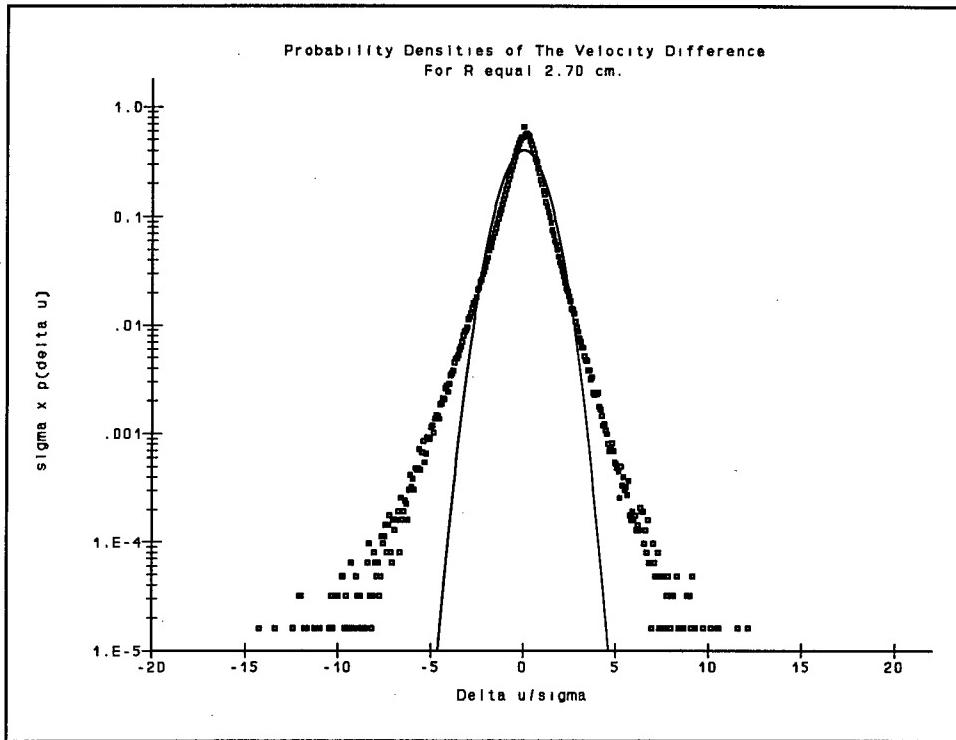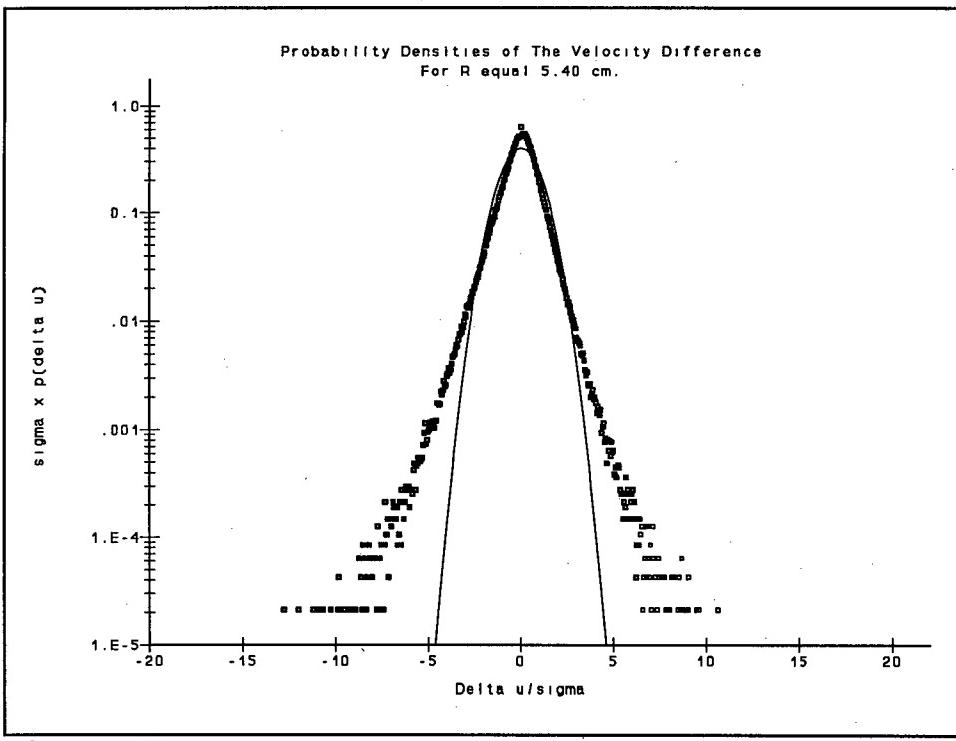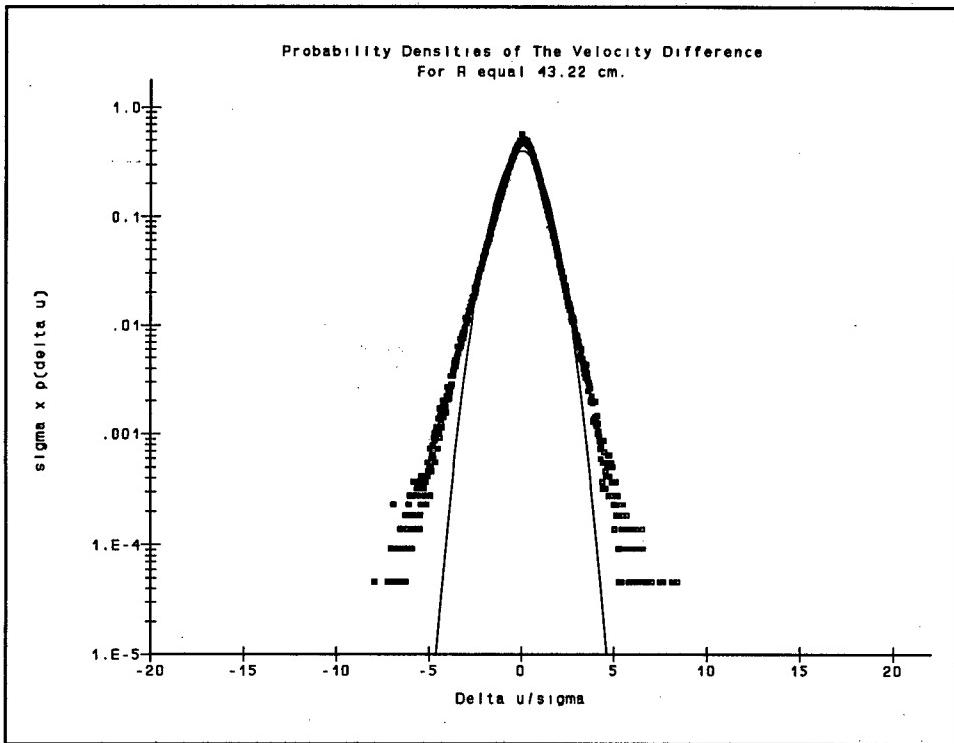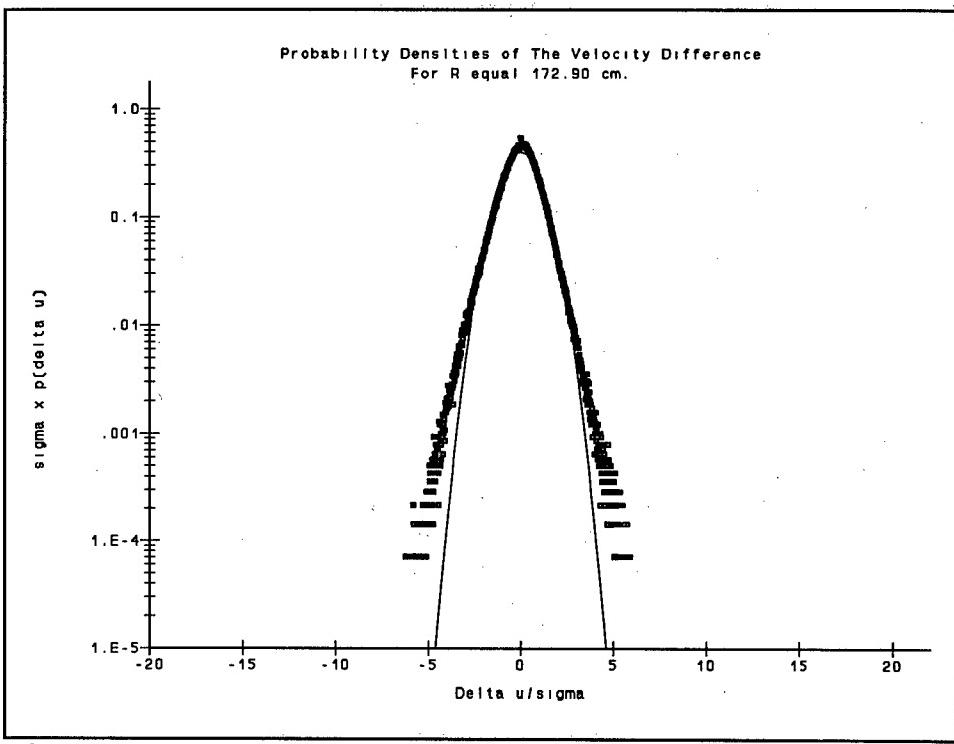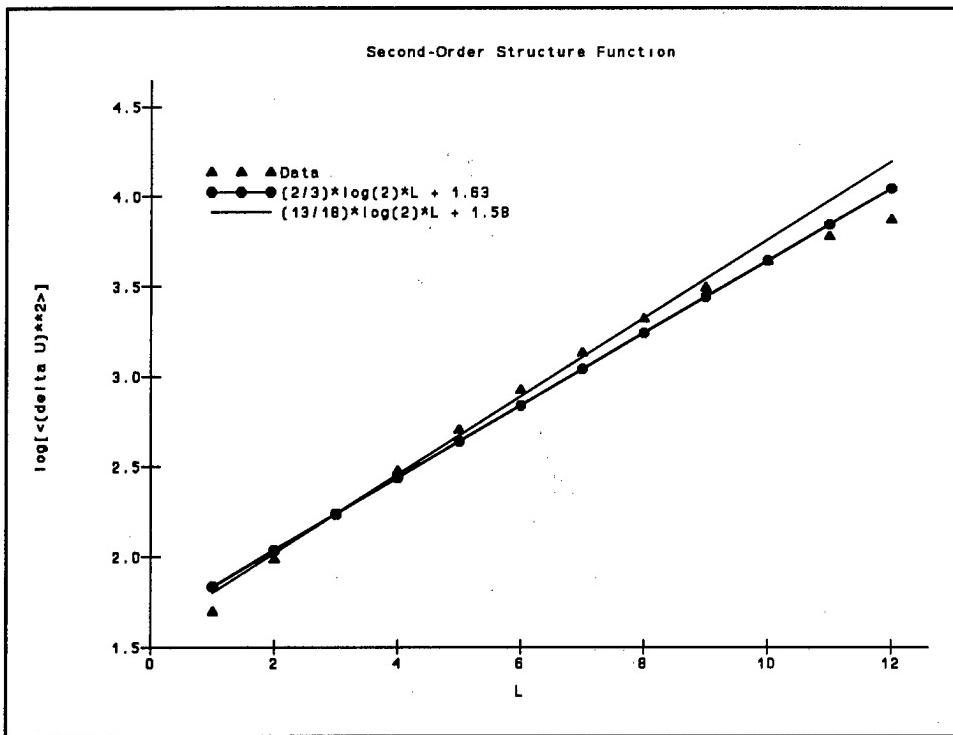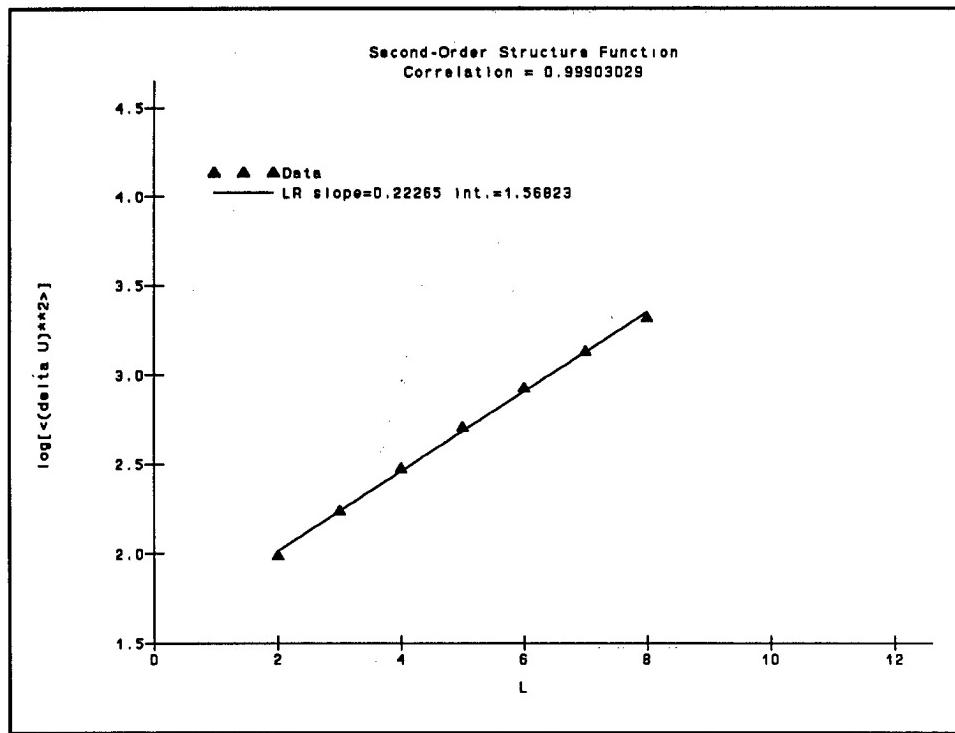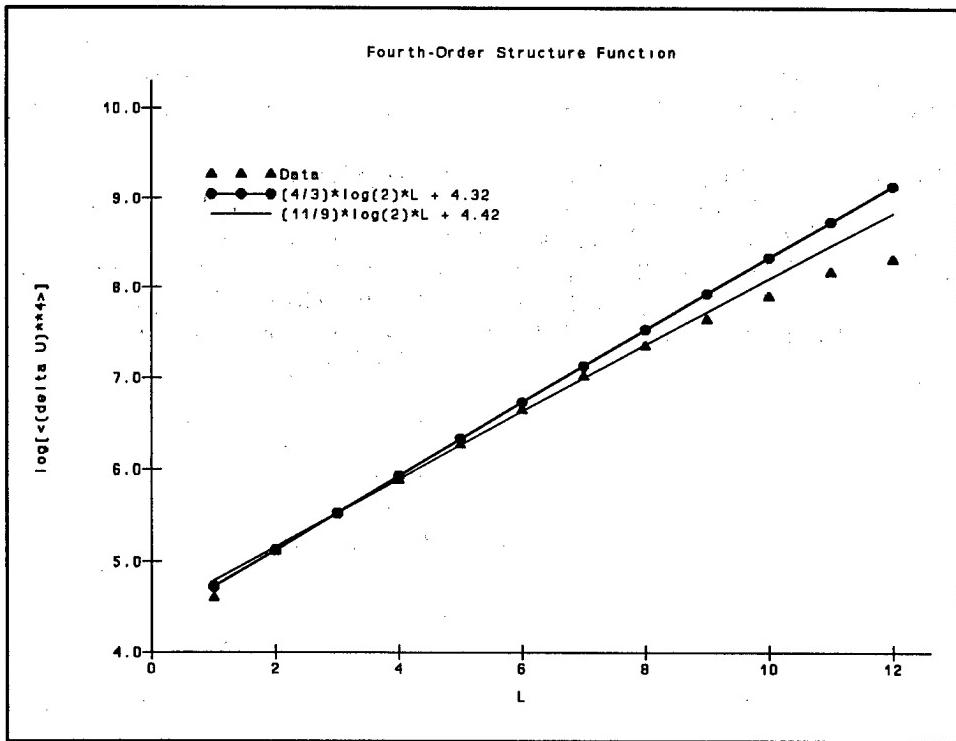
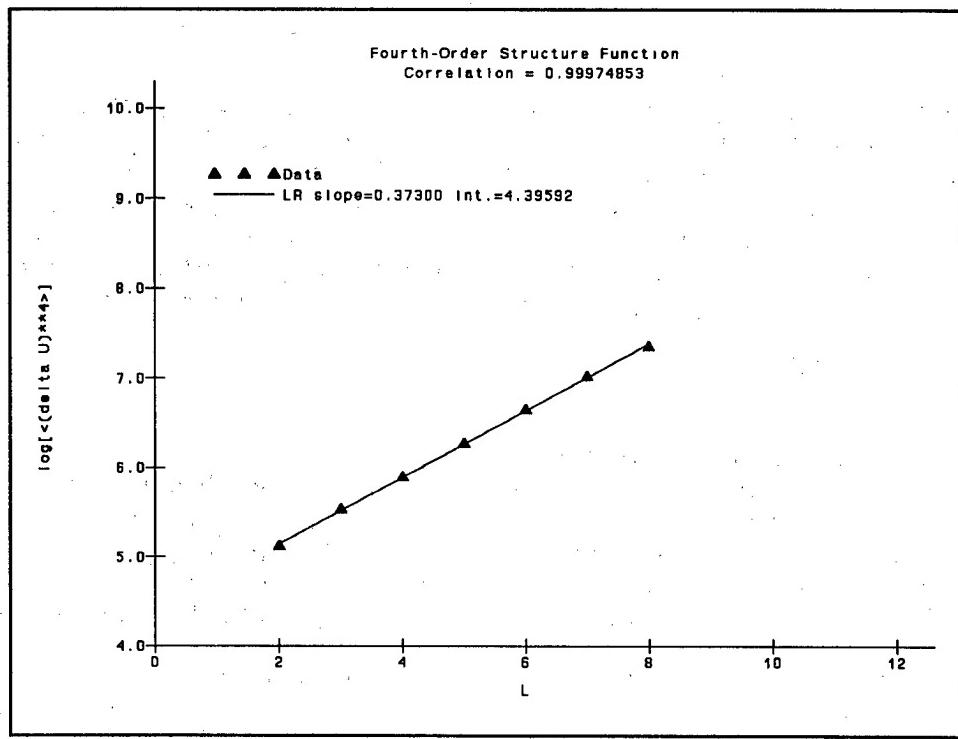Figure 2d.

Figure 3a.

Figure 3b.

Figure 3c.

Figure 3d.

6. CONCLUSIONS

The probability density of the increments of the velocity flucuations in the inertial subrange show a very distinct non-Gaussian behavior. This is inconsistent with the Gaussian assumption of the original Kolmogorov theory. The non-Gaussian behavior of the probability density can be attributed to the intermittency of the fluctuations in the atmospheric wind velocity. Measured second and fourth-order structure functions do not vary with separation as predicted by Kolmogorov's original theory, but are consistent with the behavior predicted by the modified theory. The average value of μ derived from second and fourth-order structure functions and the kurtosis are in agreement with previous experiments and the results predicted by the β-model.

REFERENCES

Frisch, U., Pierre-Louis Sulem, and Mark Nelkin, 1978: A Simple Dynamical Model of Intermittent Fully Developed Turbulence. J. Fluid Mech. 87, part 4 719 -736.

Fujisaka, H. and H. Mori, 1979: A Maximum Principle for Determining the Intermittency Exponent μ of Fully Developed Steady Turbulence, Prog. Theo. Phys. 62, 54-60.

Kolmogorov, A.N., 1941: The Local Structure of Turbulence in Incompressible Viscous Fluids for Very Large Reynolds Numbers. C.R. Acad. Sci. U.S.S.R. 30, 301-305.

Kolmogorov, A.N., 1962: A Refinement of Previous Hypotheses Concerning the Local Structure of Turbulence in a Viscous Incompressible Fluid at High Reynolds Number. J. Fluid Mech. 13, 82-85.

Mandelbrot, B., 1974: Intermittent Turbulence in Self-Similar cascades: Divergence of High Moments and Dimension of the Carrier, J. Fluid Mech. 62, part2, 331-358.

Monin, A.S. and A.M. Yaglom, 1975: Statistical Fluid Mechanics, Vol. II, MIT Press, Cambridge, Massachusetts, Chapter 25.

Van Atta, C.W. and W.Y. Chen, 1970: Structure Functions of Turbulence in the Atmospheric Boundary Layer Over the Ocean. J. Fluid Mech., Vol. 44, Part 1, pp. 145-159.

Wyngaard, J. C., and Y. H. Pao, 1971: Some Measurements of the Fine Structure of Large Reynolds Numbers Turbulence. In Proceedings of a Symposium on Statistical Models and Turbulence, University of California, San Diego, 384-401.

Session III Posters

ATMOSPHERIC SENSING

NEURAL NETWORK RETRIEVAL OF ATMOSPHERIC PARAMETERS FROM METEOROLOGICAL SATELLITES USING TOVS DATA

Donald D. Bustamante and Arthur W. Dudenhoeffer
Physical Science Laboratory
New Mexico State University
Box 30002, Dept. 3548
Las Cruces, New Mexico 88003-0002

and

James L. Cogan
U. S. Army Research Laboratory
Battlefield Environment Directorate
White Sands Missile Range, New Mexico 88002-5501

Remote sensing of atmospheric profiles using meteorological satellite data can supplement conventional data, particularly in areas of missing and sparse coverage. Tactical and strategic decisions are based on weather-related decision aids and models which require meteorological information for the area of interest. The availability of additional data serves to improve the quality of these products. This study introduces the use of artificial intelligence methodologies to the problem of retrieving atmospheric profiles from meteorological satellite data. Backpropagation neural networks have been used to retrieve thermal and dew point profiles from near-polar, sun-synchronous meteorological satellite data obtained from the TIROS Operational Vertical Sounder (TOVS). This paper discusses the collection and processing of data using a satellite receiver system, the use of backpropagation neural networks in retrieving the atmospheric profiles, the creation of training data sets for the networks, and the results obtained from the networks.

INTRODUCTION

Remote sensing involves the detection, collection, processing, and analysis of information from electromagnetic energy to detect and measure an object's characteristics without being in physical contact with the object.[1,2] Data obtained by remote sensing are affected by the sensors used, atmospheric effects, and the characteristics of the object being observed. Typically, remote sensing models include

743

response functions which attempt to correct for these factors. Remote sensing models often contain inverse problems of the nature O = f(x) + g(x), where O is the observed quantity, f(x) is the sensor response function, and g(x) is the random noise in f(x). The solution of this equation becomes ill-posed when no solution exists, the solution is non-unique, or the solution is unstable (depends continuously on the data).

This study introduces the use of artificial intelligence methodologies to the problem of retrieving atmospheric profiles from meteorological satellite data. Backpropagation neural networks have been used to retrieve thermal and dew point profiles from near-polar, sun-synchronous meteorological satellite data obtained from the TOVS.

TIROS-N Satellite Series

The TIROS-N satellites are near polar orbiting satellites operated by the National Environmental Satellite Service of the National Oceanographic and Atmospheric Administration. These satellites provide data used for meteorological and environmental monitoring. Their orbits are not geostationary; consequently, the orbital position and path coverage will vary depending upon the orbital parameters of the individual satellites.

The TOVS instrumentation consists of the High Resolution Infrared Radiation Sensor (HIRS/2), the Stratospheric Sounding Unit (SSU), and the Microwave Sounding Unit (MSU). The HIRS/2 is a 20 channel sensor, mostly infrared, which is used for vertical temperature profiles, atmospheric water content, and ozone measurement. The SSU is a 3 channel sensor which measures the radiation emitted by carbon dioxide at the top of the earth's atmosphere. The MSU is a 4 channel Dicke radiometer which measures the 5.5 mm oxygen band. Detailed specifications may be found in the literature.[3,4]

TOVS data received by the instrumentation are processed, and vertical profiles of temperature, moisture, and other products are produced. Presently, the TOVS Export Package algorithms developed by the University of Wisconsin are being used to retrieve these profiles. The thermal profile retrieval is based on a physical solution of the radiative transfer equation and represents a Fredholm integral of the first kind. An initial guess for the thermal profile is selected from a database of profiles and is used to constrain the problem so that the profile may be computed.[5] The method requires *a priori* knowledge and significant computing power. Similarly, dew points are determined from atmospheric moisture profiles by computing the relative humidity as a function of an initial estimate, computed radiances for the initial guess, and the use of a water vapor weighting function.

METHODOLOGY

Data Collection

Data collected by the U. S. Army Research Laboratory Battlefield Environment Directorate's (ARL/BED) SeaSpace System include the HIRS/2 data. Profiles obtained using the TOVS Export Package are also retrieved and transferred to the ARL/BED Upper Air Database.

Data were collected from July through October 1992 for the sites shown in Table 1. The pass coverage of the TIROS satellite did not permit collection of data for all the sites on a daily basis. In particular, the pass data for Bethel, Hall Beach, Port Hardy, and Primrose were sparse.

TABLE 1
Data Collection Sites (July - October 1992)

Location	Longitude	Latitude
Bethel	-161.80	60.78
Dayton	- 84.20	39.90
Dugway	-112.93	40.20
Ft. Riley	- 96.77	39.05
Ft. Sill	- 98.40	34.65
Ft. Huachuca	-110.35	31.60
Hall Beach	- 81.25	68.78
Midland	-102.11	31.95
North Omaha	- 96.02	41.37
Oklahoma City	- 97.60	35.40
Port Hardy	-127.37	50.68
Primrose	-110.05	54.75
Tucson	-110.93	32.12
White Sands Missile Range	-106.48	32.37
Yuma	-114.40	32.85

The geographical distribution of the sites is shown in Figure 1.

FIGURE 1
Geographical Distribution of Data Collection Sites
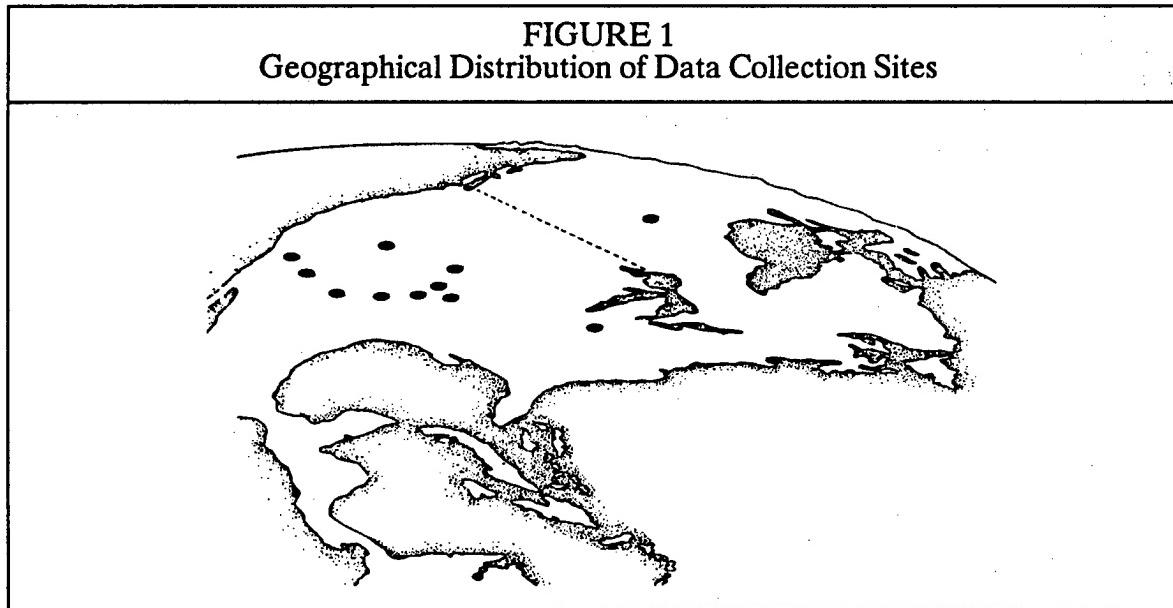
These sites were selected based on the following criteria: (1) sites are on the North American continent; (2) sites are away from the coast; (3) sites are not located in the Rocky Mountains; (4) sites represent various latitudes; and (5) satellite pass coverage such that sufficient data can be collected for use by the neural network.

Data Processing

The TOVS data available for this study are from the HIRS/2 channels only. (The results obtained using additional TOVS channels will be reported in a future paper.) HIRS/2 data collected by the Seaspace System are processed to produce HIRS/2 radiance files that include the following: satellite zenith angles, solar zenith angles, scatter phase angles, and sun reflection angles. The ARL/BED Upper Air Database contains soundings, including those derived using the TOVS Export Package, and is queried for each site to extract sounding data which will be used as "truth" when training the neural network.

Neural Networks

A neural network consists of individual neurons (or processing elements) such as that depicted in Figure 2. Each neuron in a neural network acts as an independent processing element. Inputs and interconnection weights are processed by a summation function (typically a weighted summation) to yield a sum that is passed to a nonlinearity called a transfer function (typically a sigmoid). The output of the nonlinearity is the output of the neuron.

FIGURE 2
Formal Neuron

X = Input
w = Weight
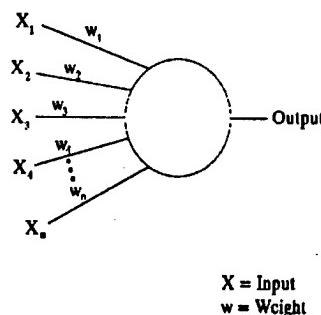
A neural network may consist of multiple layers of neurons interconnected with other neurons in the same or different layers. A neuron's connection topology with other neurons may vary from fully connected to sparsely or even locally connected. Each layer is referred to as either an input layer, a hidden layer, or an output layer.

Neural networks must "learn" how to process input before they can be utilized in an application. The process of training a neural network involves adjusting the input weights on each neuron such that the output of the network is consistent with the

desired output. This involves the development of a training file, which consists of data for each input node and the correct or desired response for each of the network's output nodes. Once the network is trained, only the input data are provided to the network, which then "recalls" the response it "learned" during training.

The backpropagation paradigm trains a neural network using a gradient descent algorithm in which the mean square error between the network's output and the desired output is minimized. This creates a global cost function which is minimized iteratively by "backpropagating" the error from the output nodes to the input nodes. Once the network's error has decreased to less than or equal to the specified threshold, the network has converged and is considered to be trained.

Neural Network Architecture

The neural network should be capable of retrieving atmospheric profiles using data obtained from the SeaSpace System. These data consist primarily of earth-centered radiances and geographical coordinates. Optionally, the system can provide satellite zenith angles, solar zenith angles, scatter phase angles, and sun reflection angles. These angles could possibly be used to handle temporal variations such as satellite pass time, season, etc. Additionally, site elevation data would be useful in developing the profiles. These data, shown in Table 2, were used in the input layer of both networks.

TABLE 2 Inputs to the Neural Network	
Node	Input Data
1	HIRS Channel 1 Radiances
.	.
.	.
.	.
19	HIRS Channel 19 Radiances
20	Latitude
21	Longitude
22	Satellite Zenith Angle
23	Solar Zenith Angle
24	Scatter Phase Angle
25	Sun Reflection Angle
26	Elevation

The neural network is designed to output the thermal and moisture profiles of the atmosphere at the Mandatory Levels shown in Table 3. These requirements establish the number of output nodes for each of the networks; the temperature network has 16 output nodes corresponding to the 1000 to 10 mb values and surface values, respectively. The moisture network has 7 output nodes corresponding to the range from 1000 to 300 mb and surface values, respectively.

The neural networks were developed using a commercial neural network development environment, NeuralWare's NeuralWorks Professional II. The thermal

network had 26 input, 30 hidden, and 16 output nodes. The dew point network had 26 input, 30 hidden, and 7 output nodes.

Neural Network Training

The data were randomly partitioned into training and recall data sets. Table 4 shows the number of training and recall vectors used for each site. No usable data were available for Bethel and Hall Beach. Because of the small number of data sets available for Port Hardy and Primrose, these sets were used in training but not in recall. The neural network training utilized the overall total of 592 data sets shown in Table 4.

TABLE 3		
Desired Neural Network Outputs		
Pressure (mb)	Temperature (C)	Dew Point* (C)
1000	Y	Y
850	Y	Y
700	Y	Y
500	Y	Y
400	Y	Y
300	Y	Y
250	Y	
200	Y	
150	Y	
100	Y	
70	Y	
50	Y	
30	Y	
20	Y	
10	Y	
Surface	Y	Y

* Dew points retrieved for surface to 300 mb only

Temperature and dew point values for pressure heights below the surface are not meaningful, and are not available in the Upper Air Database. Initial studies used an unrealistically large constant value to denote meaningless data, but the use of these large values unfavorably biased the network results near the surface.[6] Subsequently, the values of temperature and dew point for the surface were used as placeholders for pressure heights below the surface.

TABLE 4
Number of Data Vectors Used for Training and Recall

Site	Training	Recall
Bethel	0	0
Dayton	20	4
Dugway	70	18
Ft. Riley	43	11
Ft. Sill	54	12
Hall Beach	0	0
Ft. Huachuca	59	13
Midland	54	12
North Omaha	34	9
Oklahoma City	48	12
Port Hardy	12	1
Primrose	12	1
Tucson	60	15
White Sands Missile Range	65	15
Yuma	61	15
Overall Total	592	138

Neural Network Implementation

The root-mean-square error (RMS Error) of the output layer was used to monitor the training of the network. The network was trained continuously, and the RMS error monitored. Once the RMS error of the network decreased to its minimum, the training process was stopped. The network was then tested with the recall data set (i.e. independent data set), and the RMS errors for the retrievals determined. A C language implementation of the neural network recall functionality is used in the final implementation.

RESULTS

The data obtained from the SeaSpace System were partitioned into two groups: a training set and a recall set. The training data set, which consisted of randomly selected data for each site was presented to the network during its training phase. The recall set, which was not used in training, was presented to the trained networks. The network results were compared with the soundings from the TOVS Export Package, and the RMS Error was computed at each of the mandatory levels using the following equation:

$$\text{RMS Error} = \left[\frac{\Sigma(O_{net} - O_{tovs})^2}{n} \right]^{\frac{1}{2}}$$

where O_{net} = output of the neural network for a mandatory level
O_{tovs} = output of the TOVS Export Package for a mandatory level

n= number of soundings in the recall set

Thermal Profiles

The temperature network was tested using the temperature recall data set described earlier, and the results plotted as RMS temperature error (C) as a function of pressure height (mb) for each of the mandatory levels. The results are shown in Figure 3. The plots depict the overall performance of the network, as well as the performance of the network using data from each of the individual sites.

The RMS error is minimal at higher altitudes, as would be expected from satellite data, since the sensor is probing from the upper atmosphere to the surface. Errors tend to increase closer to the Earth's surface, which is also consistent with satellite data. Some sites, e.g. Dugway, display pronounced changes at the tropopause. Tropopause identification and effects are difficult to discern across all the data and particularly in the plot of the overall network performance due to the fact that the height of the tropopause varies as a function of latitude as well as a variety of meteorological factors. Tropopause identification for a given site may be difficult due to these factors, as well as the fact that the TOVS sensor weighting functions peak at particular levels within the atmosphere, which may or may not be coincident with the level of the tropopause.

Taken over all individual sites, RMS errors vary from a low of less than 1 to 4 C. Typically, the RMS error is in the range of 2 to 3 C. These errors are comparable to those reported for the TOVS Export Package.[5] Due to differences in methodologies (i.e., RMS errors for the networks and Standard Error/Bias for the TOVS Export Package), and the fact that the error values for both methods are a function of atmospheric conditions, an absolute comparison between the two methods is difficult. Future work will include other sources of "truth" data such as radiosondes in order to better compare the neural network results.

Dew Point Profiles

Figure 4 shows plots of the dew point RMS error (C) for pressures between 850 mb and 300 mb. Data were not available for higher altitudes. The overall RMS error decreases from 7.4 C at 850 mb to 4.1 C at 300 mb. Taken over the individual sites, the error varies generally from a low of approximately 2 C to a high of about 10 C. Typically it is in the range of 3 to 8 C. Thus the error computed for dew point is roughly twice that for temperature.

The differences in graphical results for the various sites are not easy to interpret. The fact that the dew point errors are roughly twice as large as the temperature errors suggests that a different neural network architecture should be tried for dew point. As with temperature, the utilization of alternative sources of "truth" data would be helpful in training the network.

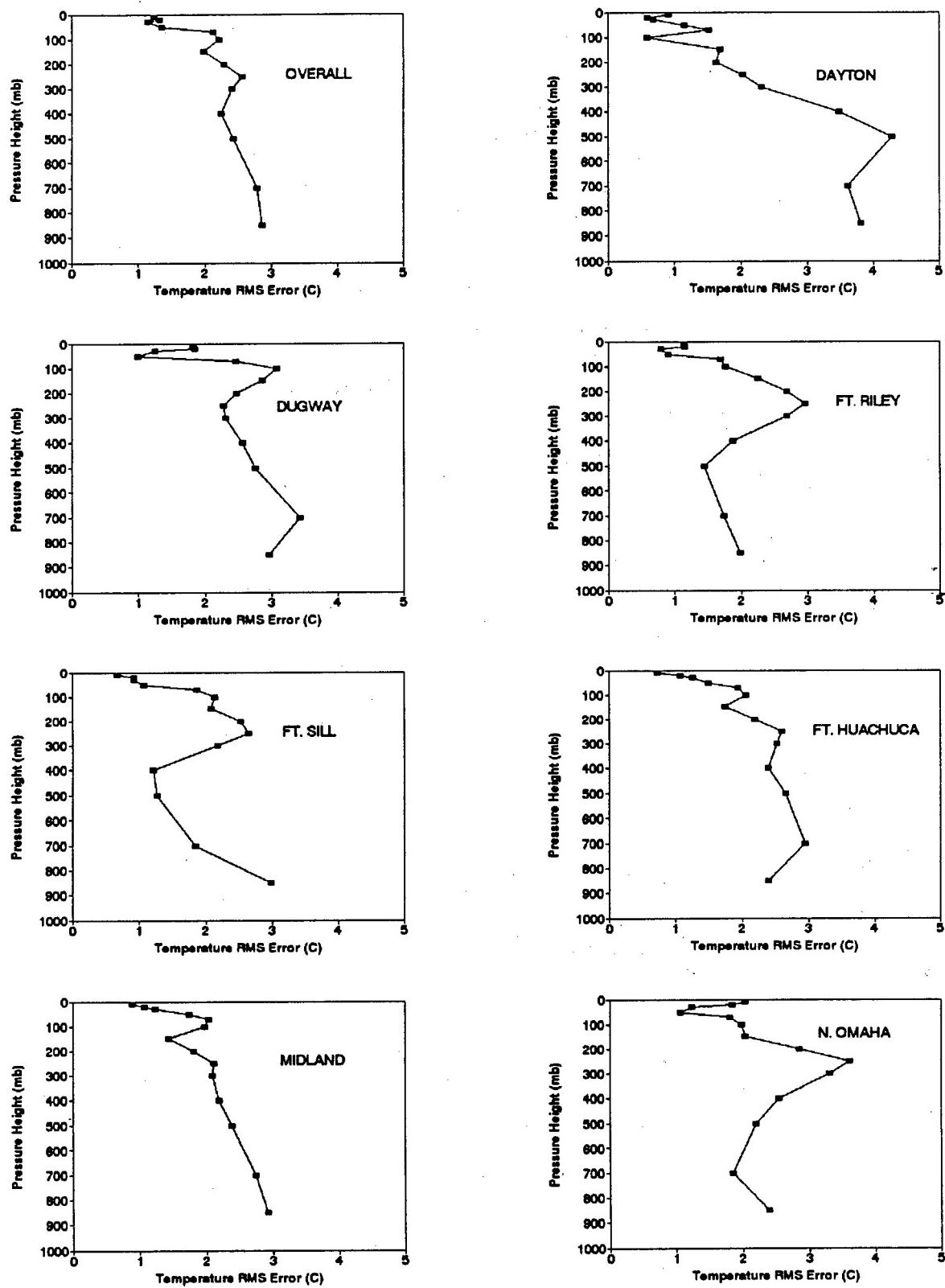FIGURE 3 - Thermal RMS Error Profiles from Neural Network

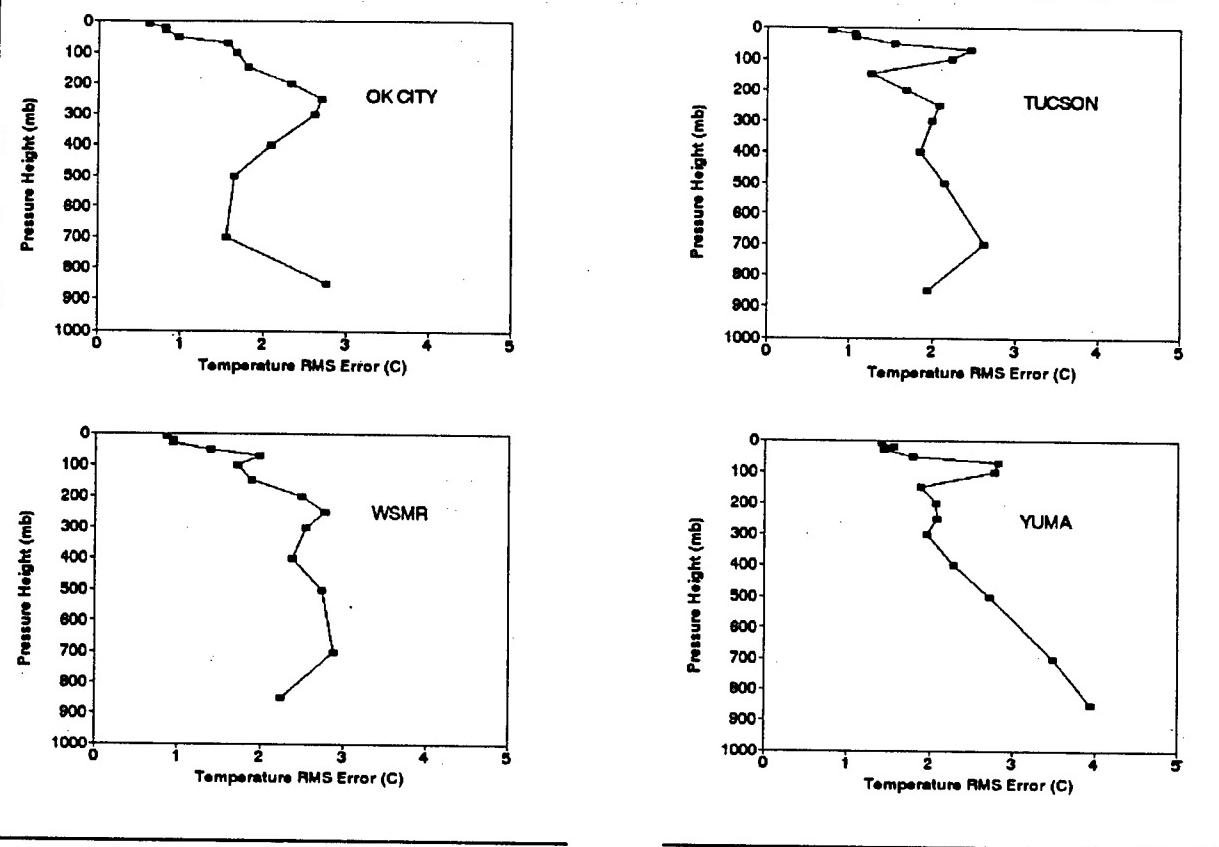# FIGURE 3 -Thermal RMS Error Profiles from Neural Network (Continued)

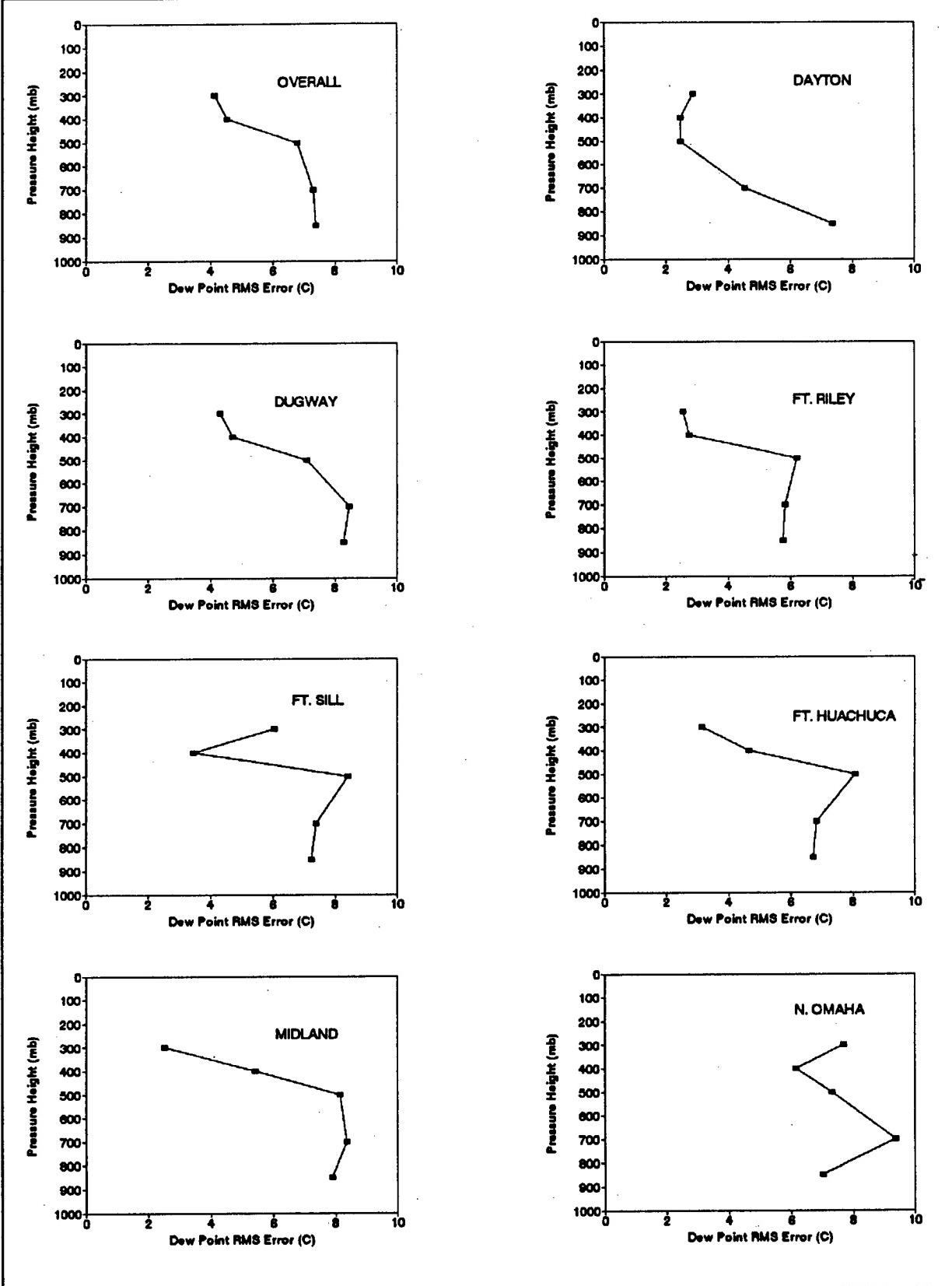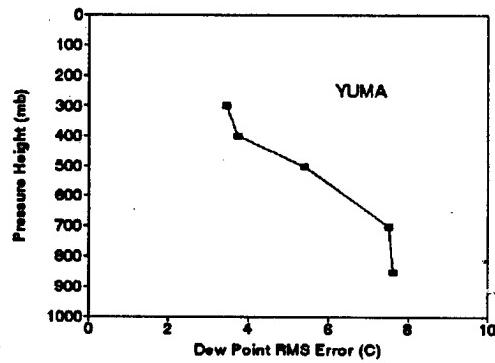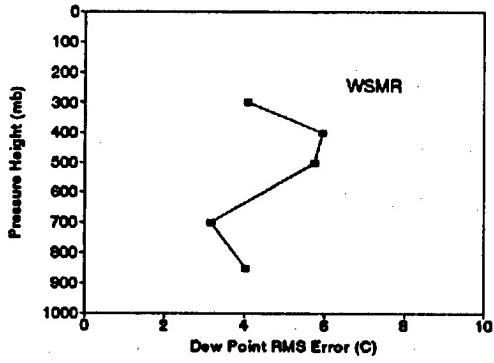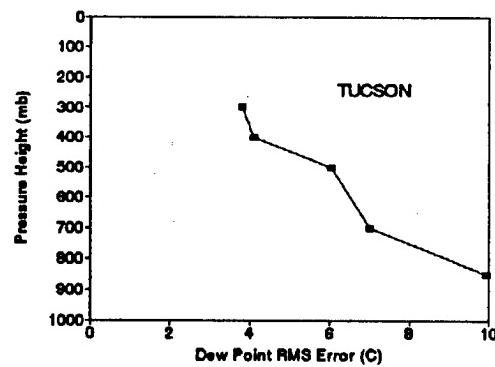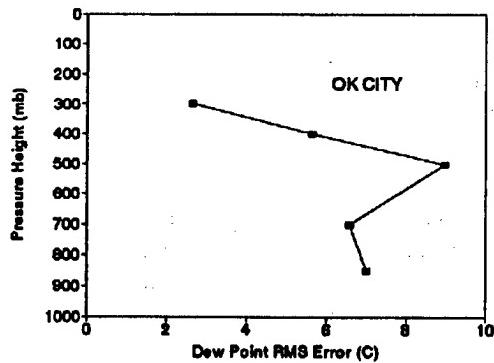Figure 4 - Dew Point RMS Error Profiles from Neural Network

FIGURE 4 - Dew Points RMS Error Profiles from Neural Network (Continued)

CONCLUSIONS

This study demonstrates that neural networks may be successfully applied to the problem of retrieving atmospheric parameters from meteorological satellite radiances. This approach is computationally more efficient, and does not require the *a priori* information (such as climatological databases) required by the TOVS Export Package.

The results demonstrate that thermal profiles with RMS Errors of less than 4 C (Typically < 3 C) can be obtained from the trained neural network. As expected, the accuracy of the thermal profiles is greatest at higher altitudes. Dew point profile RMS Errors vary from 2 C to 10 C, but are more difficult to interpret.

Additional data are needed to test the networks' capabilities. Additional temporal coverage should include year-round data in order to train the networks to incorporate seasonal effects into their results. The incorporation of angular information (solar zenith angle, satellite zenith angle, scatter phase angle, and sun reflection angle) will provide seasonal clues to the network during the training process.

This study compares the neural network results against the conventional algorithm used in the TOVS Export Package. Comparisons of the neural network results should also be made against other types of "truth", such as data obtained from radiosonde measurements.

ACKNOWLEDGMENT

REFERENCES

1. Sabins, Floyd F., Jr., 1978. *Remote Sensing Principles and Interpretation*, W. H. Freeman and Company, San Francisco.

2. Colwell, Robert N., Ed., 1983. *Manual of Remote Sensing*, Volumes I and II, The Sheridan Press.

3. Schwalb, Arthur, 1979. *The TIROS-N/NOAA A-G Satellite Series, Washington*, D. C., National Oceanic and Atmospheric Administration, NOAA Technical Memorandum NESS 95.

4. Barnes, James C. and Michael D. Smallwood, 1982. *TIROS-N Series Direct Readout Services Users Guide*, Washington, D. C., National Oceanic and Atmospheric Administration.

5. Smith, W. L., H. M. Woolf, C. M. Hayden, A. J. Schreiner, and J. M. LeMarshall, 1983. "The Physical Retrieval TOVS Export Package," *First International TOVS Study Conference*, Igls, Austria, 29 August - 2 September, 1983.

6. Bustamante, Donald D., Arthur W. Dudenhoeffer, and James L. Cogan, 1992. "Neural Network Retrieval of Atmospheric Profiles from TOVS Radiances," *Artificial Intelligence Research in Environmental Sciences*, Monterey, CA, 27-29 October 1992.

ENVIRONMENTAL MONITORING
WITH THE MOBILE ATMOSPHERIC SPECTROMETER TESTBED

Frank T. Kantrowitz, Raymond A. Dise, and Dale U. Foreman
U.S. Army Research Laboratory
Battlefield Environment Directorate
White Sands Missile Range, New Mexico 88002-5501 USA

William M. Gutman and Troy D. Gammill
Physical Science Laboratory
New Mexico State University
Las Cruces, New Mexico 88003 USA

ABSTRACT

In response to growing international environmental concerns, government management policy has substantially broadened the role of the Department of Defense to include an Army mission of environmental stewardship resting on the pillars of conservation, compliance, prevention, and restoration. Investigators at the Battlefield Environment Directorate (BED) and the Physical Science Laboratory (PSL) are using the mobile atmospheric spectrometer (MAS) as a large-scale testbed for research within the compliance pillar. The status of each of the following endeavors is described in detail.

● An infrared library of approximately 10,000 gases is now part of the MAS inventory. One of six available search algorithms can be used in conjunction with this library to determine the presence of these trace gases.

● A BED computer algorithm for determining concentrations of selected pollutants has been ported from a mainframe computer to an MS-DOS compatible platform. This program, which is capable of monitoring at the parts per billion (ppb) level, is called PCGAS. Work is underway on an enhanced version called PCGAS-PLUS that will allow for the rapid determination of concentrations of over 150 man-made gases.

● A computer algorithm for determining vertical profiles of temperature and gas concentrations (originally developed by the U.S. Air Force Phillips Laboratory, Geophysics Directorate) has also been converted for use on MS-DOS computers. Beta testing of this program is underway.

• The real-time transmittance modeler (RTTM) was fielded for the first time during 1993. Meteorological data are acquired from a small tower, and selected met parameters are input into an MS-DOS version of the Phillips Laboratory MODTRAN transmittance program. Simulated moderate resolution transmittance over any reasonable pathlength is possible. Near-real-time plotting of simulated transmittance data is also possible. These simulated data provide insight as to meteorological effects on clear air infrared transmittance.

1. INTRODUCTION

Historically, the mobile atmospheric spectrometer (MAS) team has participated in countermeasure obscurant tests such as the SMOKE WEEK Tests,[1] munition characterization tests such as the Pine Bluff Arsenal Phosphorus Munition Trials, aircraft signature characterization in support of Project Long Jump, support of the development of the Free Electron Laser Facility, and research at the High-Energy Laser Systems Test Facility (HELSTF). Recently, the team has become involved in an effort that will lead to the characterization of a variety of rocket plume signatures. These tests will involve three modes: static firings, sled-borne trials, and free-flight missions.

In response to growing international environmental concerns, government management policy has substantially broadened the role of the Department of Defense to include an Army mission of environmental stewardship resting on the pillars of conservation, compliance, prevention, and restoration. Investigators at the Battlefield Environment Directorate (BED) and the Physical Science Laboratory (PSL) are using the MAS as a large-scale testbed to develop algorithms and methodologies that address environmental monitoring issues. Plans are underway for the development of a dual-use "MAS in a suitcase." These plans entail the use of a portable, tripod-mounted spectrometer with 0.26-m optics and a 0.52-m collimated source. While this portable system will enhance the defense-related mission of the MAS, the Sadtler spectral libraries will permit <u>identification</u> of approximately 10,000 gases, and PCGAS-PLUS will permit the <u>determination of the concentrations</u> of over 150 gases. With these research tools, the following environmental studies will be possible.

• Monitoring gaseous pollutants in urban environments, landfills, and toxic waste dumps.

• Determining greenhouse gas concentrations in ambient air.

• Performing fence post identification of emissions from industrial facilities.

• Monitoring air quality at chemical agent storage facilities.

2. THE MAS TESTBED TODAY

The key components of the MAS are a Fourier transform spectrometer (FTS) and a 0.8-m Coudé telescope. The MAS FTS consists of a scanning Michelson interferometer

758

with associated optics, control electronics, and a dedicated computer system. Depending upon the detector, beamsplitter, and source in use, the spectrometer can cover a segment of the spectral region from about 700 to 20,000 cm^{-1} (0.5 to 14 μm). The instrument is capable of spectral resolution as high as 0.04 cm^{-1}. The usual MAS sources are a quartz-halogen lamp and a temperature controlled blackbody that can reach 1000 °C. In either case, the radiation is collimated with a 1.54-m searchlight. The blackbody is the source of choice for most of the mid-infrared (IR) region, while the lamp provides better performance for wavelengths shorter than 2 μm. Therefore, the near-IR and mid-IR regions require different sources and only one region can be optimized at a time. The MAS Coudé-mounted telescope is a classical Cassegrain telescope consisting of a 0.8-m parabolic primary and a 0.15-m-diameter hyperbolic secondary mirror.

3. IDENTIFICATION OF TRACE GASES

A set of search algorithms for the identification of unknown trace gases makes up a part of the MAS inventory. These algorithms are available from Mattson Instruments[2] and, in conjunction with Sadtler spectral libraries, provide excellent results. The procedure is accomplished as a mathematical comparison of the unknown spectrum to approximately 10,000 spectra in a set of spectral libraries. Best matches are those spectra that have the lowest calculated match value. Match values are calculated by comparing each unknown file data point to its corresponding library file data point using one of six search-comparison algorithms. The algorithms may be described mathematically as follows:

- Absolute difference:
$$M_{adf} = \sum \; | \; s_i - r_i \; |$$

This algorithm emphasizes peak heights. Results may be inconclusive when the unknown spectrum has a sloping or offset baseline.

- Squared difference:
$$M_{sdf} = \sum (s_i - r_i)^2$$

This algorithm, as a least squares metric, tends to weight the peaks in the unknown spectrum more heavily than in case 1. The net effect tends to minimize the effects of a noisy baseline. Results may be inconclusive when the unknown spectrum has a sloping or offset baseline.

- Absolute derivative:
$$M_{adr} = \sum \; | \; \Delta s_i - \Delta r_i \; |$$

This algorithm emphasizes peak positions more than peak heights. This emphasis tends to minimize the effect on the match value when the unknown spectrum has a sloping baseline or broad spectral features.

- Squared derivative:
$$M_{sdr} = \sum (\Delta s_i - \Delta r_i)^2$$

This algorithm emphasizes peak positions and weights them more heavily than the absolute derivative algorithm. This algorithm also reduces the effect of a sloping or offset baseline in the unknown spectrum.

- Euclidean vector distance: $\qquad M_{euc} = \sum | s_i^2 - r_i^2 |$

This algorithm calculates the match value as the sum of vector differences. For each data point, two vectors are projected, one from the zero-zero coordinate to the unknown data point and the other from the zero-zero coordinate to the corresponding library file data point. The vector difference is then determined. If the unknown spectrum is a mixture, the compounds may appear in the results. The algorithm may produce inconclusive results for sloping or offset baselines and for spectra that are not mixtures.

- Correlation coefficient: $M_{cco} = \dfrac{[\sum xy - ((\sum x_i \bullet \sum y_i)/N)]}{[(\sum x_i^2 - (\sum x_i \bullet \sum x_i)/N) \bullet (\sum y_i^2 - (\sum y_i \bullet \sum y_i)/N)]^{\frac{1}{2}}}$

This is a linear regression algorithm. It can account for baseline drift and differences in scaling. Because the match value is a correlation coefficient, the results are not a measure of best fit, but are instead absolute values with statistical significance,

where

M_{xxx} = match value

s_i = normalized intensity value of unknown data point

r_i = normalized intensity value of library data point

N = number of data points

In two separate tests, small quantities of acetone and methanol were released near the **MAS** spectrometer. The results are displayed in figures 1 and 2. In both cases the correlation coefficient search algorithm correctly determined the "unknown" gas. In figure 1, "A" is the "unknown" spectrum collected by the **MAS** spectrometer; "B," "C," and "D" are candidate spectra. It may be noted that for spectra "A," "B," and "C," peaks 1, 2, 3, and 4 match. While some noise exists in the field data, sharp features in peaks 1 and 4 are readily apparent. In figure 2, spectra labelled "A" and "B" possess great similarity (peaks 1, 2 and 3) while spectra "C" and "D" are decidedly different. Features "Y1," "Y2," and "Y3" are in regions where the atmosphere is opaque due to water vapor (Y1 and Y3) and carbon dioxide (Y2) absorption. The ratioing of near zero amplitude data tends to yield an unstable solution. This results in the noise observed in these regions.
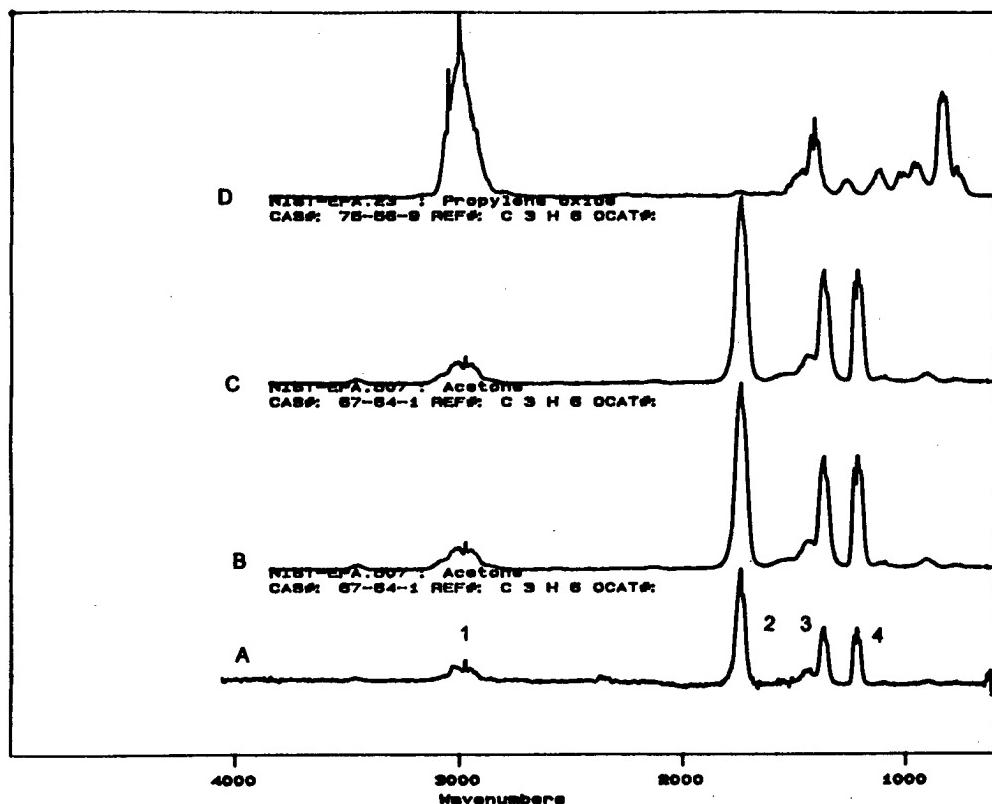
Figure 1. Identification of acetone.

4. DETERMINATION OF GASEOUS ATMOSPHERIC CONSTITUENT CONCENTRATIONS

The horizontal path algorithm[3] employed in the data analysis was suggested by Matise[4] after development by Haaland et al.[5,6] The BED version of the algorithm was originally written for use on a Digital VAX computer. It has now been ported to an MS-DOS platform and is called PCGAS. Reference spectra are generated for water vapor (H_2O), carbon dioxide (CO_2), methane (CH_4), carbon monoxide (CO), and nitrous oxide (N_2O) using FASCODE 3[7,8] and the 1992 HITRAN compilation.[9,10] PCGAS accesses the 31-gas HITRAN database. PCGAS-PLUS will use the 150-gas Hanst spectral library and a computationally more efficient algorithm.

PCGAS performs as follows: A family of transmittance spectra is converted into absorbance spectra and the area under selected spectral lines is measured for each reference species and each concentration. By relating all of the spectral information present in the reference spectra of a trace gas to that of the unknown sample and by appropriately fitting the baseline, one can detect trace gases. Four least squares methods incorporating different baseline assumptions are used. The symbols used in the least squares analysis are displayed in table 1.

761
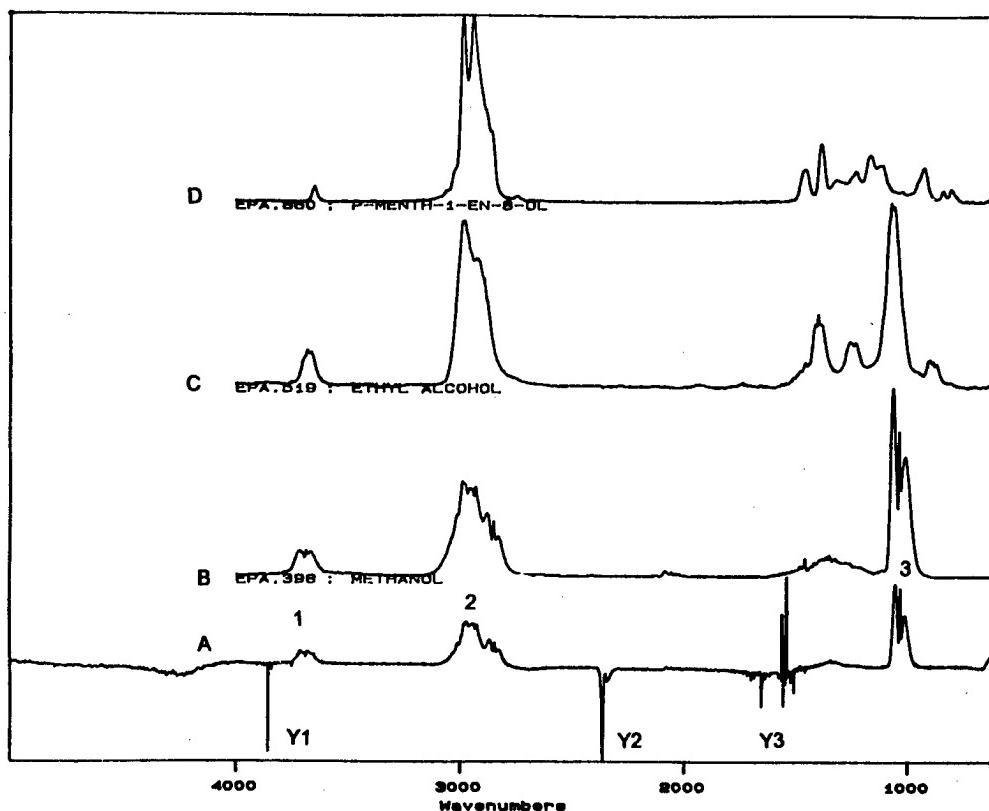
Figure 2. Identification of methanol.

Table 1. Symbols used in Least Squares Analysis

A_{si} = sample absorbance at frequency i.

A_{ri} = reference absorbance at frequency i.

k   = ratio of sample and reference concentration.

v_i = frequency.

a, b = terms pertaining to linear baseline assumption.

e_{si} = noise at frequency i.

p   = subscript indicating values pertaining to a particular peak.

4.1 Method 1. Baseline zero or known

$$A_{si} = (k \bullet A_{ri}) + e_{si}$$

4.2 Method 2. Linear Baseline

$$A_{si} = a + (b \bullet v_i) + (k \bullet A_{ri}) + e_{si}$$

4.3 Method 3. Different Linear Baseline over Each Peak

$$A_{spi} = a_p + (b_p \bullet v_{pi}) + (k \bullet A_{rpi}) + e_{spi}$$

Thus, the assumption made is of possibly different linear baselines within each peak.

4.4 Method 4. Negligible Baseline Shift Between Successive Data Points

$$\Delta A_{si} = (k \bullet \Delta A_{ri}) + e_{si}$$

The differences considered are only those within a peak. Since this model is of the same form as that for method 1, the least squares estimate of k is identical, except for ΔA's replacing the A's.

FTS transmittance measurements were made over a 0.255-km path at White Sands Missile Range, New Mexico, during September 1993. A Mattson Nova Cygni high-resolution field spectrometer was used in this experiment. Data were taken in the 2000 - 3000 cm^{-1} spectral region at 0.125 cm^{-1} point spacing. The infrared source for this test was a 1,000 °C blackbody. The transmitting optics used a 1.54-m searchlight. The results of selected retrievals are displayed in table 2.

Table 2. Measured Concentrations

	Retrieved	Retrieved	Retrieved	Expected
Date:	15 Sep 93	16 Sep 93	17 Sep 93	
H_2O	7.4 torr	8.9 torr	4.9 torr	(7.7, 10.2, 4.9 torr)*
CO_2	346.0 ppmv	336.0 ppmv	326.0 ppmv	350.000 ppmv†
CO	0.159 ppmv	0.166 ppmv	0.151 ppmv	0.150 ppmv†
N_2O	0.324 ppmv	0.323 ppmv	0.332 ppmv	0.320 ppmv†
CH_4	1.53 ppmv	1.49 ppmv	1.43 ppmv	1.3 - 1.7 ppmv‡

*As derived from the MAS meteorological station
†Accepted worldwide average[11]
‡1.7 ppmv worldwide average[11]; 1.3 ppmv in a desert environment[12]

In general, the arbitrarily selected lines displayed in figures 3 through 7 are in good agreement with FASCODE. The MAS data show more structure and a slight shift in extrema. The MAS H_2O data for 16 September 1993 are 13 percent lower than the water vapor content measured with the meteorological station. The CO_2 retrievals exhibit a 20 ppmv drift. The N_2O lines used proved to be very weak and difficult to measure. Since the measurements were made in a desert environment, the methane concentration is, as expected, lower than the accepted worldwide average. Data drift need to be examined. To improve statistical analysis, more spectral lines will be accessed in the next version of the algorithm.
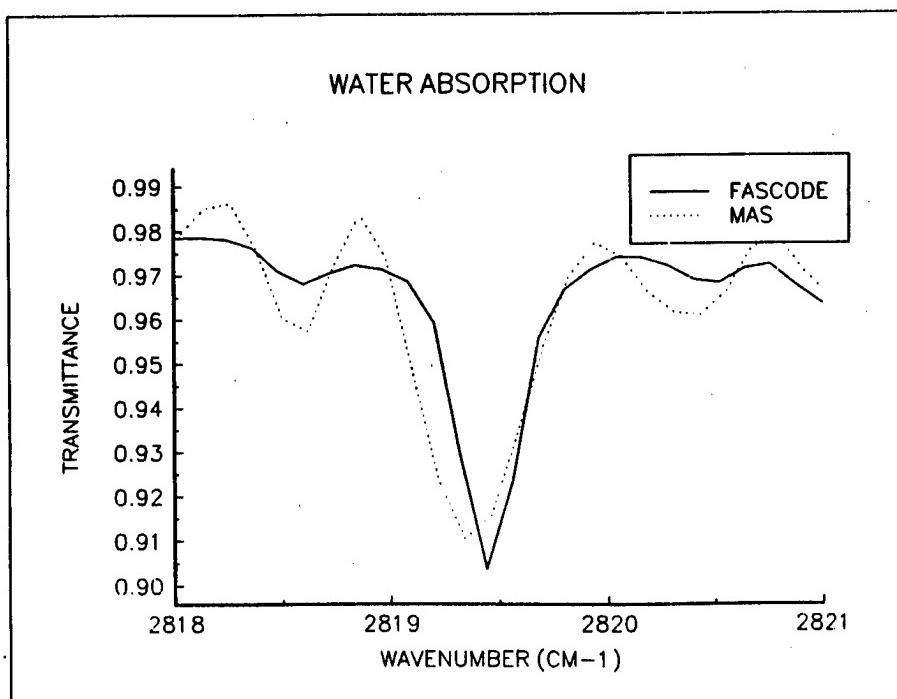
Figure 3. Comparison of MAS data and FASCODE simulation near an H_2O line.

5. VERTICAL PROFILING OF TEMPERATURE AND GAS CONCENTRATIONS

The vertical retrieval algorithm under study was developed by Atmospheric and Environmental Research, Incorporated, for Phillips Laboratory, Geophysics Directorate.[13] The present retrieval approach assumes that an accurate forward model is available. FASCODE is currently used as the forward model because of its flexibility and accuracy. A principal liability of using an accurate line-by-line code such as FASCODE is the computational cost of performing the calculation. A nonlinear method of physical least squares (PLS) is used to retrieve the atmospheric state parameters (temperature, gas concentration) from radiance measurements.
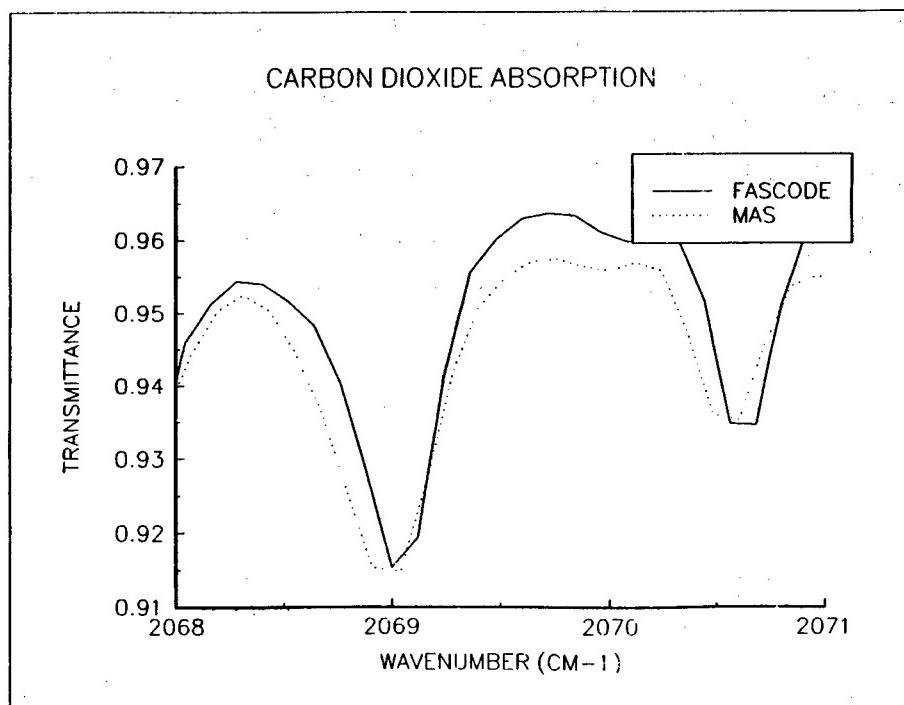
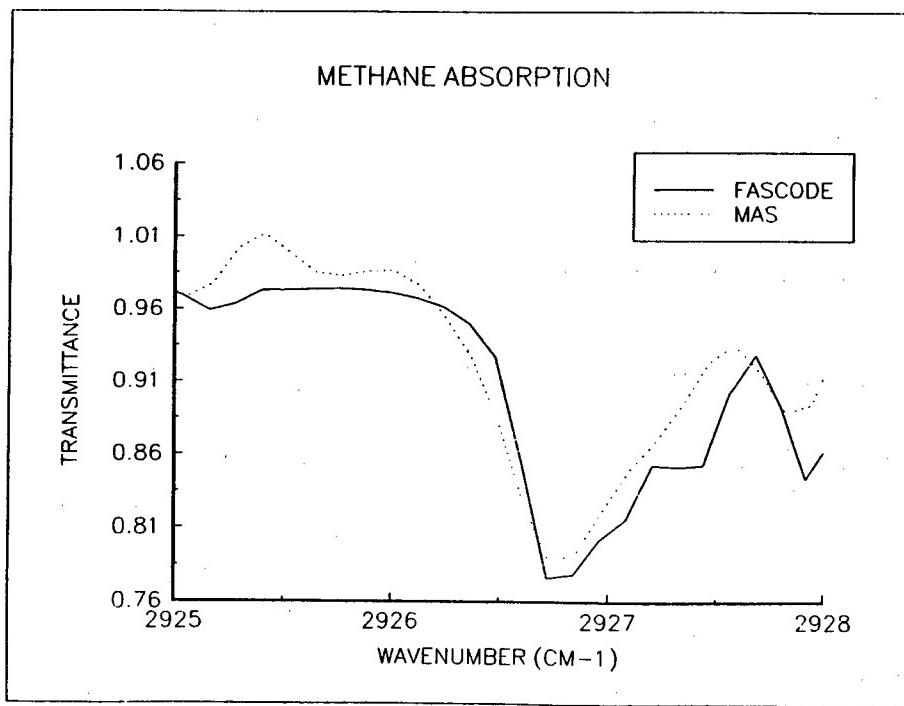**Figure 4.** Comparison of MAS data and FASCODE simulation near a CO_2 line.

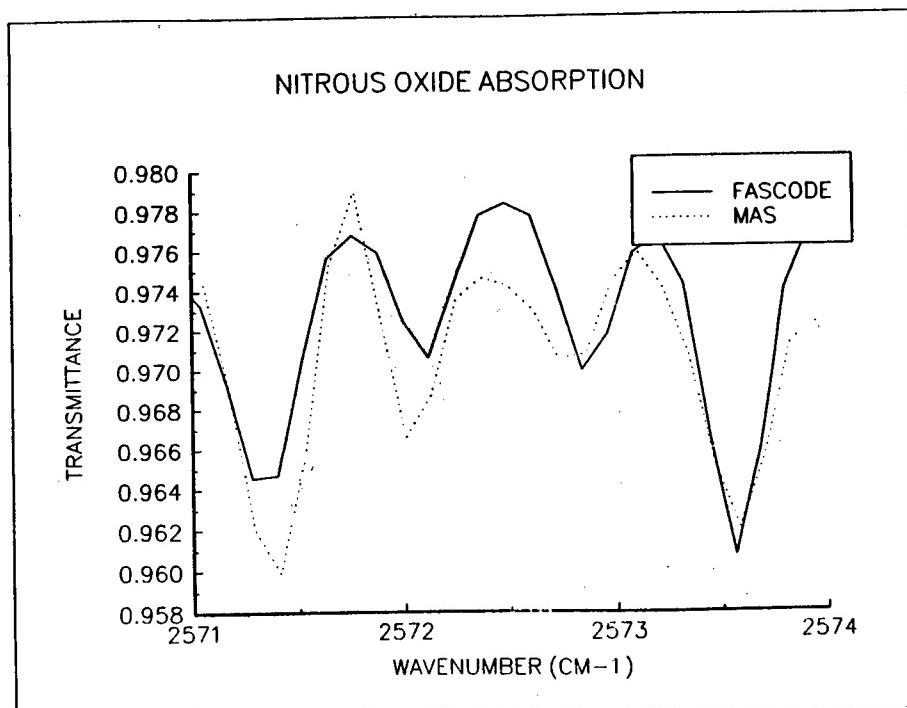**Figure 5.** Comparison of MAS data and FASCODE simulation near a CH_4 line.

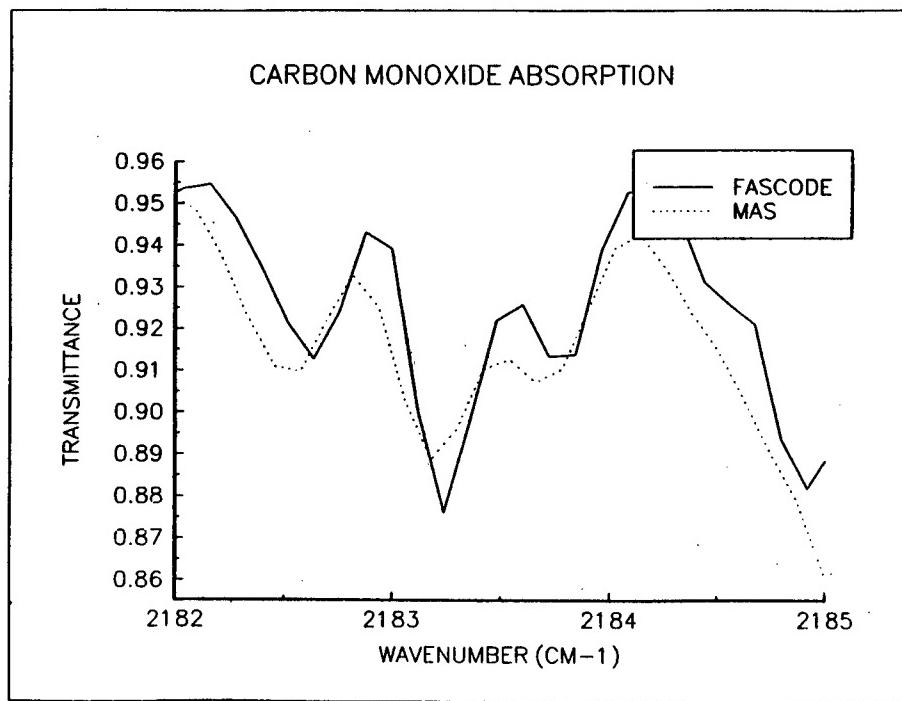**Figure 6. Comparison of MAS data and FASCODE simulation near an N₂O line.**

Figure 7. Comparison of MAS data and FASCODE simulation near a CO line.

The problem of retrieving atmospheric state parameters, x, is posed in terms of minimizing the square of the differences between observation and the forward model $F(x)$ such that the variance, σ^2, given by

$$\sigma^2 = \sum W_i [R_i - F_i(x)]^2$$

is a minimum. W_i is the weight for the ith observed radiance, R_i.

The customary approach to the solution of this problem involves adding a penalty function, $x^T \acute{\Gamma} x$, (T denotes matrix transposition) to σ^2, obtaining

$$\sigma^2 = [R - F(x)]^T W [R - F(x)] + x^T \acute{\Gamma} x$$

The penalty function serves two important roles in the PLS retrieval method. Retrievals of this type are often associated with poorly posed problems. In the case of poorly posed problems the covariance matrix, in the absence of the penalty function ($\acute{\Gamma} = 0$), is ill-conditioned and determinant is near zero. This precludes the determination of a stable inverse. The second role of the penalty function is to control the step size and direction of the iteration.[14, 15]

For the maximum likelihood method

$$\acute{\Gamma} = S_x^{-1}$$

with S_x as the error covariance of the first guess and

$$W = S_R^{-1}$$

with S_R the error covariance of the measurements.

The retrieval is obtained by iterative implementation of the relation

$$x^{n+1} = x^n + (K^T \bullet W \bullet K + \acute{\Gamma})^{-1} K^T \bullet W \bullet r^n.$$

The radiance residuals, r^n, are given by

$$r^n = R - F(x^n)$$

with x^0 as the first guess. The matrix K represents the Jacobian of the forward model with respect to the state parameters, obtained from finite forward differences.

$$K = [F(x^0 + \delta x) - F(x^0)]/\delta x$$

At this time only simulations have been performed. Figures 8, 9, and 10 show simulated temperature profiles from ground level to 8 km. Figure 8 is for a case where the first guess is identical to the simulated temperature profile. Figure 9 is for a first guess that is 2 K (at each layer) higher than the simulated profile. Figure 10 exhibits a first guess that is 4 K above the simulated profile. By the time the first guess is 4 K from the simulated profile at each layer, the algorithm provides large error bars. MAS investigators have noted a spectral dependency on retrieval accuracy. Currently, the forward model operates in the 690 - 740 cm^{-1} region with a point spacing of 0.1 cm^{-1}. The spectral region under investigation will be shifted to determine which region provides the most accurate results.
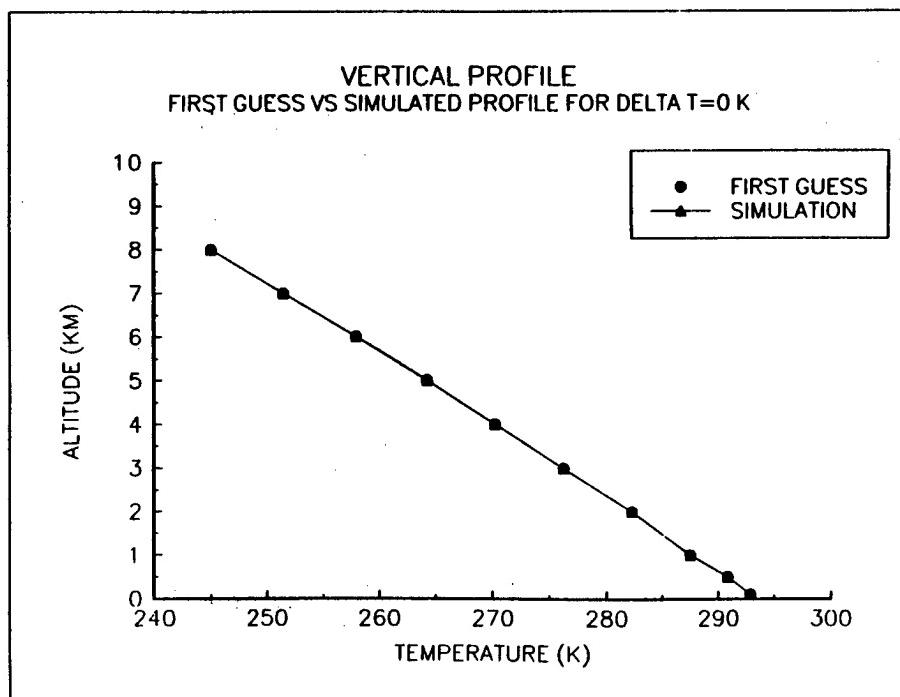

Figure 8. First guess versus profile for delta T = 0 Kelvin (per layer).
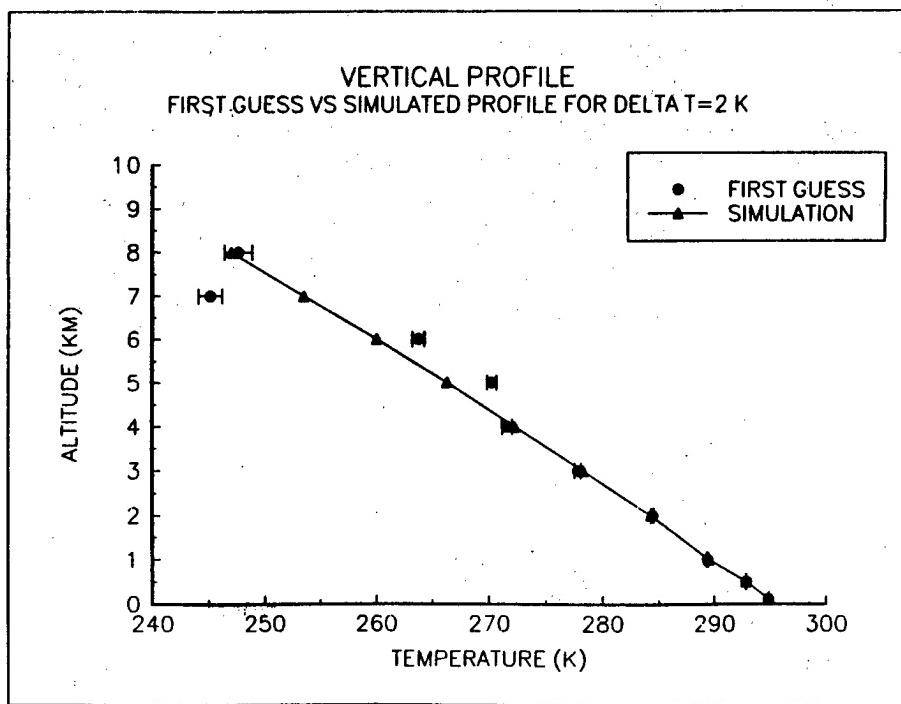
Figure 9. First guess versus profile for delta T = 2 Kelvin (per layer).
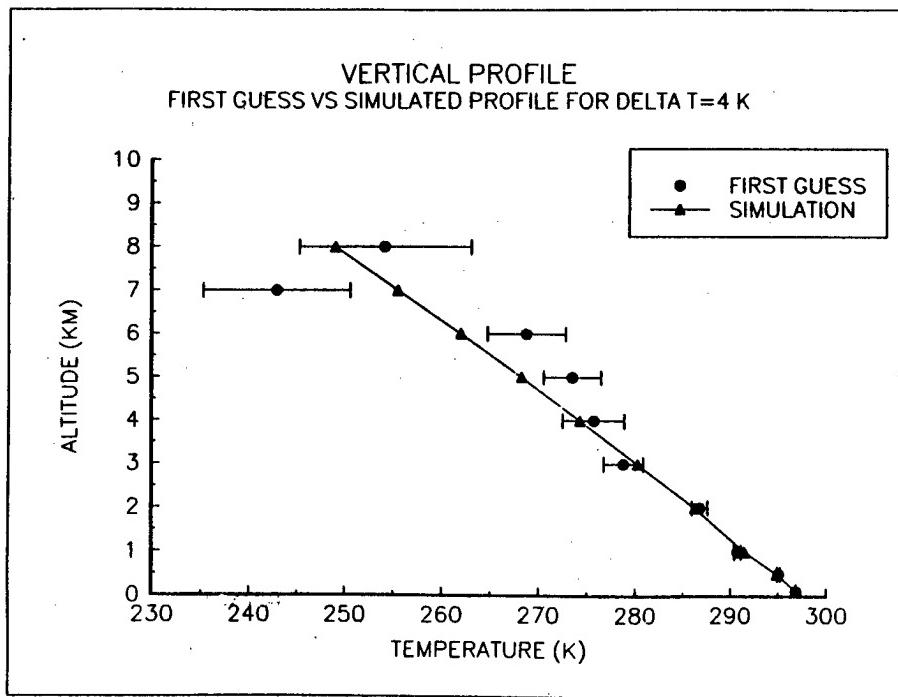

Figure 10. First guess versus profile for delta T = 4 Kelvin (per layer).

This testbed program has yet to evolve into a viable, computationally efficient algorithm and to provide more accurate data for higher altitudes (~ 30 km). After the mechanics of a mature algorithm become understood, actual radiance data will be collected. The measurement procedure will be as follows: A spectrum of a liquid nitrogen (LN_2) bath will be taken. This is, in effect, the radiance of the system optics since the radiance from the LN_2 is negligible. Next a spectrum of a low temperature blackbody will be taken, followed by a spectrum of the sky emissions. Subtracting the system radiance from both the sky and blackbody radiance will leave the ratio of the sky radiance to the low temperature blackbody radiance. These data will be calibrated by multiplication with the Planck function for the blackbody temperature. A calibration stand with an alignment source and the LN_2 bath are shown in figure 11.

Figure 11. Spectrometer with calibration stand.

Mathematically stated:

$$L_{calibrated\ sky} = \frac{(\ L_{raw\ sky} - L_{system}\ )}{(\ L_{raw\ blackbody} - L_{system}\ )} \bullet P_{blackbody}$$

where

$L_{calibrated\ sky}$ = calibrated sky radiance.

$L_{raw\ sky}$ = raw sky and system radiance.

L_{system} = raw radiance from system optics.

$L_{raw\ blackbody}$ = raw blackbody radiance.

$P_{blackbody}$ = Planck function for the blackbody.

6. REAL-TIME TRANSMITTANCE MODELER (RTTM)

The Real-Time Transmittance Modeler (RTTM) was fielded for the first time during 1993. Temperature (degrees Celsius), pressure (millibars), relative humidity (percent), dew point temperature (degrees Celsius), wind speed (meters per second) and direction, solar loading (watts per meter^2), and visibility (kilometers) data are acquired from a small tower; and selected meteorological parameters are input into an MS-DOS version of the Phillips Laboratory MODTRAN transmittance program. Transmittance over any reasonable path length and for spectral resolutions as fine as 1.0

Figure 12. Meteorological tower with MAS in the background.

μm are possible. Near-real-time plotting of transmittance data is also possible. These simulated data provide insight as to meteorological effects on clear air infrared transmittance. The current tower, with the MAS as a backdrop, may be seen in figure 12. In the drive for miniaturization, we hope that a small tripod-mounted version of the present meteorological tower will be fielded soon.
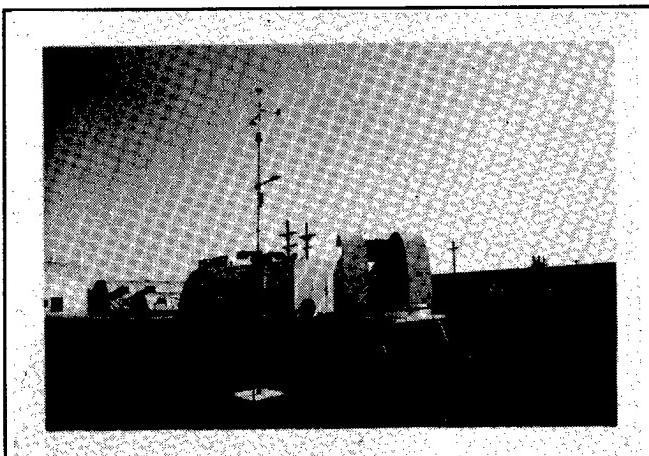
7. CONCLUDING REMARKS

Investigators at BED and PSL are using the MAS as a large-scale testbed for research within the air quality compliance pillar. A large spectral library and search algorithms are available for identification of trace gases. A BED computer algorithm called PCGAS is capable of monitoring gas concentrations at the ppb level. Field trials showed the need to improve statistics by the addition of more spectral lines accessed by the algorithm. Work is underway on an enhanced version called PCGAS-PLUS that will allow for the rapid determination of concentrations of over 150 man-made gases. Beta testing of a Phillips Laboratory vertical retrieval algorithm is underway on an MS-DOS platform. Real-time modeling of atmospheric transmittance is progressing with the RTTM. Miniaturization of the meteorological tower is the next step in the evolution of this system.

Plans are underway for the development of a dual-use "MAS in a suitcase." While this portable system and methodologies under development will enhance the defense-related mission of the MAS, this portable system will also be capable of environmental monitoring of gaseous pollutants in urban environments, landfills and toxic waste dumps, fence post identification of emissions from industrial facilities, and monitoring air quality at chemical agent storage facilities.

REFERENCES

1. Kantrowitz, F. T., W. M. Gutman, T. D. Gammill, and J. V. Rice, 1993, "High Resolution Spectroscopy At Smoke Week XIV," Proceedings of the Smoke/Obscurants Symposium XVII, Johns Hopkins University, Laurel, MD.

2. Enhanced FIRST™ (Fourier Infrared Software Tools) User's Manual, 1991, Analytical Technology, Inc. (ATI), Mattson Division, Madison, WI 53717.

3. Kantrowitz, F. T., et al., 1991, "An Algorithm For The Retrieval of Atmospheric Constituent Concentrations," Proceedings of the Battlefield Atmospherics Conference, U.S. Army Atmospheric Sciences Laboratory, White Sands Missile Range, NM 88002-5501.

4. Matise, B., private communication, Optimetrics, Inc.

5. Haaland, D. M., and R. G. Easterling, 1980, "Improved Sensitivity of Infrared Spectroscopy by the Application of Least Squares Methods," Appl. Spectros., 34(5):539-548.

6. Haaland, D. M., R. G. Easterling, and D. A. Vopicka, 1985, "Multivariate Least-Squares Methods Applied to the Quantitative Spectral Analysis of Multicomponent Samples," Appl. Spectros., 39(1):73-84.

7. Clough, S. A., F. X. Kneizys, E. P. Shettle, and G. P. Anderson, 1986, Atmospheric Radiance and Transmittance: FASCOD2, Sixth Conference on Atmospheric Radiation, Williamsburg, VA.

8. Kantrowitz, F. T., 1990, A VAX/VMS/GKS Format Version of the Fast Atmospheric Signature Code (FASCODE 2) with Comparisons to ASL Field Spectroscopic Data, ASL TR-0269, U.S. Army Atmospheric Sciences Laboratory, White Sands Missile Range, NM.

9. Rothman, L. S., et al., 1987, The HITRAN Database: 1986 Edition," Appl. Opt., 26(19):4058-4096.

10. Park, J. H., L. S. Rothman, C. P. Rinsland, H. M. Pickett, D. J. Richardson, and J. S. Namkung, 1987, Atlas of Absorption Lines From 0 to 17,900 cm^{-1}, NASA Reference Publication 1188, NASA Langley Research Center, Hampton, VA.

11. Anderson, G. P., S. A. Clough, F. X. Kneizys, C. H. Chetwynd, and E. P. Shettle, 1986, AFGL Atmospheric Constituent Profiles (0-120 km), AFGL-TR-86-0110, Air Force Geophysics Laboratory, Hanscom, MA.

12. High Energy Laser Propagation Handbook, 1984, ASL TR-0148, U.S. Army Atmospheric Sciences Laboratory, White Sands Missile Range, NM.

13. Isaacs, R.G., S. A. Clough, R.D. Worsham, J.L. Moncet, B.L. Lindner, and L.D. Kaplan, 1990, Path Characterization Algorithms for FASCODE, GL-TR-90-0080, Air Force Geophysics Laboratory, Hanscom, MA.

14. Levenberg, K., 1944, "A Method for the Solution of Certain Nonlinear Problems in Least Squares," Quart. Appl. Math., 2(2):164-168.

15. Marquardt, D., 1963, "An Algorithm for Least-Squares Estimation of Nonlinear Parameters," SIAM J. Appl. Math., 11(2):431-441.

A Generic Method for Earth Locating Data Scanned From Satellites

Steve McGee
Physical Science Laboratory
Las Cruces, NM 88003, USA

Dr. James Cogan
Battlefield Environment Directorate, U.S. Army Research Laboratory
White Sands Missile Range, New Mexico 88002-5501, USA

ABSTRACT

In the battlefield environment, meteorological data from inaccessible regions can be crucial. Remote sensing systems including satellite borne instrumentation can obtain and disseminate this information. Data sets scanned from satellite sensors must be earth located before synoptic meteorological display systems or atmospheric models may include them. Many different solutions to earth location exist which are specific to a particular satellite. By using independent orbital prediction and previously existing algorithms, the METSAT software, developed for the U.S. Army Research Laboratory, Battlefield Environment Directorate, contains a generic solution applicable to many meteorological and other types of satellites. This paper presents this generic method of earth location, describes the necessary orbital prediction data, and demonstrates the results of this method as applied to the Automatic Picture Transmission data from NOAA satellites.

INTRODUCTION

In recent years, technological improvements have increased the role of satellites in providing real-time remotely sensed meteorological data to tactical users. Many inexpensive and mobile meteorological satellite receiving systems are now available. The METSAT software was developed for the U.S. Army Research Laboratory Battlefield Environment Directorate to provide analysis and display of Automatic Picture Transmission (APT) data from NOAA satellites. To accomplish this it was necessary to apply algorithms to geo-reference or 'earth locate' the data. The problem of earth location is not inordinately difficult to solve, but many different analysts have developed many different solutions leading to inconsistencies, duplicated effort and specific software.

Earth location can be divided into two steps. The first step is predicting the position and velocity of the satellite with respect to an earth centered Cartesian coordinate system. The second step is to solve for the earth surface intercept of the instrument scanner at an angle with respect to the satellite. The METSAT software uses the Simplified General Perturbation (SGP) models of

Hoots and Roehrich to predict the satellite position and orientation and a generalized intercept solution by Puccinelli to provide an independent generic solution.

ORBITAL PREDICTION

NORAD tracks all resident space objects and applies an orbital model to generate general perturbation element sets. A user may then apply the inverse of the same orbital model to these element sets in order to predict the position and velocity of a given object at a given time. Hoots and Roehrich developed the latest model for near-Earth satellites known as the SGP8 model. It includes improved solutions for the effects of gravitation and high atmospheric drag.

Due to the efforts of Dr. T.S. Kelso, the element sets are now available to users outside of NORAD. The element sets are sometimes referred to as the Two Line Elements (TLE) because of the standard format in which they appear. Other models may accept the NORAD element sets but because the elements are generated by SGP8, only applying SGP8 can provide the best orbital predictions. Hoots and Roerhrich facilitated this by providing an SGP8 algorithm written in FORTRAN.

SOLVING FOR SCANNER EARTH INTERCEPT

Puccinelli developed a concise solution to the intercept problem which requires: the position of the spacecraft; the velocity of the spacecraft; the orientation of the scanner with respect to the spacecraft yaw, pitch and roll axes; and any rotations of the spacecraft about the yaw, pitch and roll axes. SGP8 provides the position and velocity of the spacecraft. The NOAA and other satellites have yaw control mechanisms to minimize variation about the yaw pitch and roll axes. For METSAT software, these values are assumed to be zero. This leaves only the function of the scanner orientation about the spacecraft with time. This isolates the system dependence to the scanner function. Puccinelli provided a FORTRAN algorithm of his solution called LOCATE.

APPLICATION

For the METSAT software, SGP8 and LOCATE were converted to the C programming language and used with a function which specifies the orientation of the scanner with time. The NOAA APT data is transmitted as an image from the satellite perspective as shown in **Figure 1.** The METSAT software earth locates the image and displays it in a Mercator projection as shown in **Figure 2.**
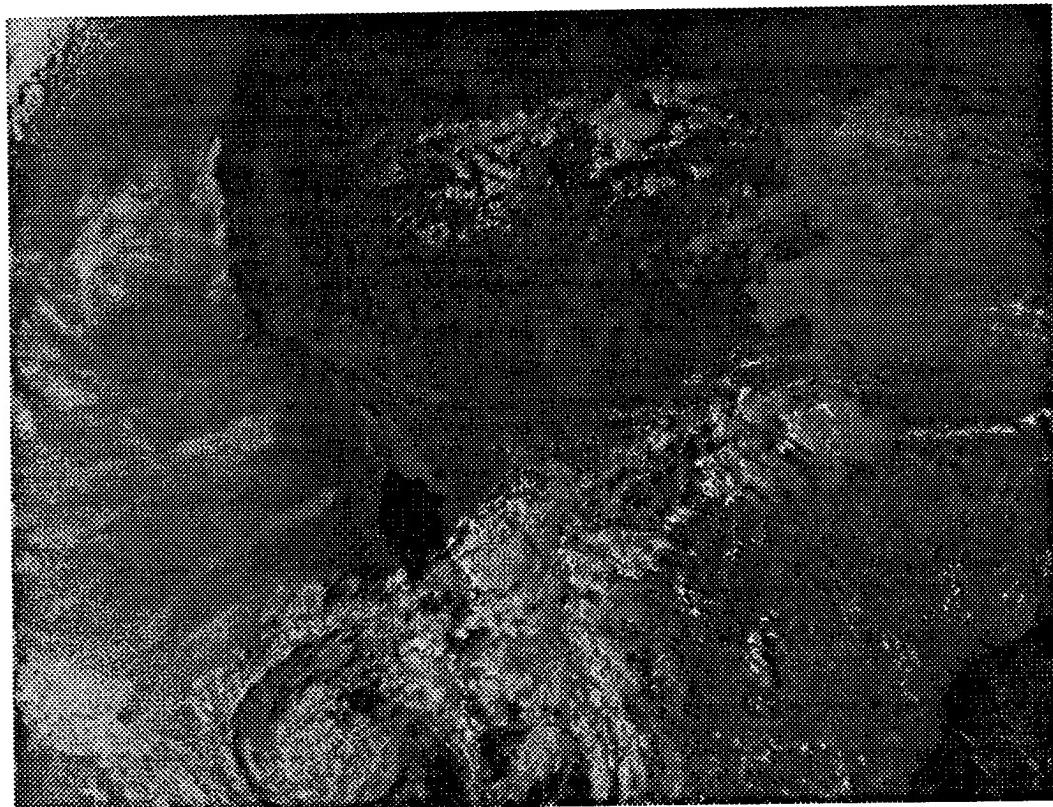
Figure 1. September 1993, APT image from NOAA 11 as captured in satellite perspective.
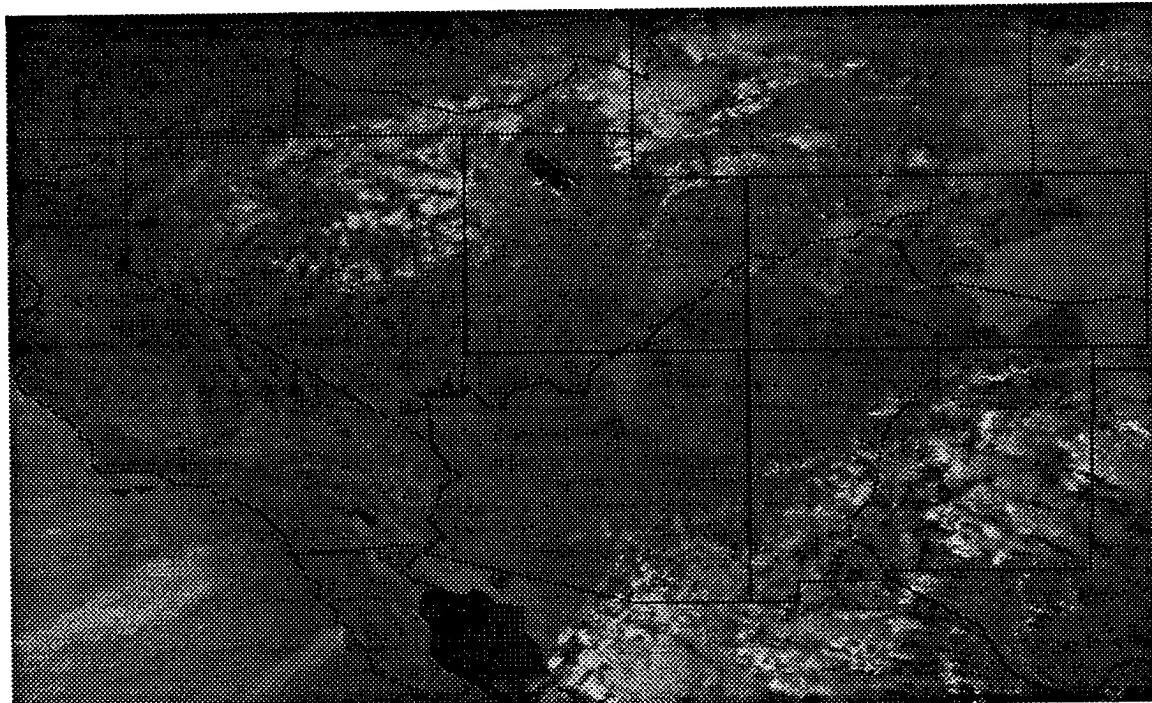

Figure 2. The same image as in **Figure 1.** earth located to a Mercator projection by using the METSAT software.

CONCLUSIONS

By using the SGP8 orbital model and relatively recent orbital element sets, one can accurately and independently predict the position and orientation of orbiting satellites. By using LOCATE, one may then earth locate scanned data. This solution is suitable for data from any satellite with the addition of a function describing the scanner orientation with respect to the spacecraft as a function of time.

ACQUIRING INFORMATION

The Two Line Element data are available via telephone modem on the **Celestial Bulletin Board (513)427-0674**.

Sites with Internet access can retrieve the element sets via anonymous ftp from **archive.afit.af.mil**. The element sets and other information are found in the **pub/space** directory.

Weather satellite element sets and information are distributed via electronic mail to subscribers of the wxsat mailing list. To subscribe to this list, send an email message including your complete email address, and a request for subscription to **wxsat-request@ssg.com**.

For a copy of SGP8 and LOCATE in the C programming language, send an email message request to **smcgee@psl.nmsu.edu**

REFERENCES

Hoots, Felix R. and Roehrich, Ronald L., 1980: Models for Propagation of NORAD Element Sets, Spacetrack Report Number 3, Office of Astrodynamics, Peterson Air Force Base, CO.

Moik, Johhanes G., 1980: Digital Processing of Remotely Sensed Images, National Aeronautics and Space Administration, Washington, DC.

Puccinelli, Edward F., 1976: Ground Location of Satellite Scanner Data, Photogrammetric Engineering and Remote Sensing, Vol. 42, No. 4, April 1976, pp 537-543.

DEVELOPMENT OF A LABORATORY TECHNIQUE FOR DETERMINING THE FLUORESCENCE EFFICIENCY FOR A SINGLY LEVITATED DROPLET

J.B. Gillespie, Stan R. Niles, and David Ligon
Army Research Laboratory
AMSRL-BE-W
White Sands Missile Range, NM 88002-5501

ABSTRACT

Fluorescence is the technique of choice for remote standoff detection of biological agents dispersed in the atmosphere. It is also used for detection of environmental pollution. In order to model the anticipated fluorescence radiation from an atmospheric plume of aerosol, a quantity called the fluorescence photon yield, or fluorescence efficiency, is required. We have developed a laboratory technique to levitate a single micrometer sized particle electrodynamically in a device called a spherical void levitator and perform measurements that enable the determination of the fluorescence efficiency. Development of the technique required determining the size, absorption, density, and fluorescence spectra of a droplet of known composition and fluorescence efficiency and collecting the total emitted fluorescence. Observations were made on several particles of different sizes and different concentrations of fluorescing substance. Data indicate that this is a difficult measurement to perform, but that fluorescence efficiency can be inferred for spherical droplets. Further measurements will be performed to examine the potential for irregularly shaped particles of unknown composition.

INTRODUCTION

The U.S. Army Research Laboratory has a Chem/Bio research effort to support remote standoff detection of biological aerosols. As part of this effort, an experimental laser spectroscopy laboratory has been developed for characterization of fundamental properties of airborne particles. One aspect of this research involves studies of fluorescence properties of single, micrometer size particles. The optical and fluorescence properties of the aerosol particles is essential for modeling of ultraviolet fluorescence lidar--the technique of choice for remote sensing of biological agents. This type of technology also has application in areas of pollution detection, detection of oil spills, detection of clandestine drug facilities, and agricultural research. The objective of this present work is to develop a technique in which the fluorescence quantum yield of a single micrometer size particle can be determined using a spherical void levitator as an electrodynamic particle levitation device.

BACKGROUND

Fluorescence is the emission of light upon the absorption of radiation from a light source. A photon of with a wavelength λ_1 is incident on a molecule. The molecule absorbs the photon and is excited from its ground state to some vibrational level in the first electronic state. The molecule nonradiatively decays to the ground state of the first electronic state and then emits a photon of wavelength λ_2 as it decays to some vibrational state in the electronic ground state; this last transition is fluorescence. The molecule finally decays nonradiatively to the lowest vibrational level in the ground state. The emitted photon has less energy, thus a longer wavelength, λ_2. The following facts can be stated about fluorescence: (1) Fluorescence is always at a longer wavelength than the exciting light, a phenomenon known called the Stokes shift. (2) Fluorescence spectra have band structures-- generally broad and devoid of line structure, and even though fluorescence may be used to identify a specific substance, most fluorescence spectra look very similar. (3) Fluorescence can be excited by various sight sources but lasers and arc lamps are the most common. (4) And finally, the great majority of fluorescent substances are excited by ultraviolet light.

THEORETICAL BACKGROUND

For fluorescence to occur, light must be absorbed. This leads to the concept of fluorescence efficiency, which is now described as fluorescence yield or quantum yield and is defined as the ratio between the number of photons emitted as fluorescence and the number of photons incident on the system. For a bulk medium absorption of light by atoms or molecules is governed by the Beer-Lambert law which can be written as

$$I = I_0 \, e^{-\epsilon c l} \qquad \qquad (1)$$

where ϵ is the molar extinction coefficient in liters per mole per centimeters, c is the concentration in moles per liter, and l is the length of the absorption cell in centimeters. To obtain the molar extinction coefficient of a bulk material one collects intensity measurements from spectra of several concentrations of material, takes the log of Equation (1), and plots intensity versus concentration. The extinction coefficient is then the slope divided by the path length. This information is required for the fluorescence efficiency calculation.

The fluorescence yield is defined by

$$\phi = N_e/N_a \qquad \qquad (2)$$

where N_e is the number of emitted photons and N_a is the number of absorbed photons. Fluorescence intensity is given by

$$I_f = I_0 (1 - e^{-\epsilon cl}) \phi \qquad (3)$$

If ϵcl is small Equation 3 can be approximated by

$$I_f = I_0 \epsilon cl \phi \qquad (4)$$

Absolute determination of fluorescence is difficult; so one generally determines fluorescence yields relative to some standard. In that case the following Equation is used

$$\phi = \frac{\epsilon c_s I I_{os}}{\epsilon c I_s I_0} \phi_s \qquad (5)$$

where I is the fluorescence efficiency, I_0 is the source intensity, and the subscript s stands for the quantities respect to the standard compound. For a practical procedure, a situation in which spectra are collected, one uses the formula

$$\phi_s = \phi_r \frac{A_{s,\Delta\lambda} \; a_s \; I_{0,s}}{A_{r,\Delta\lambda} \; a_r \; I_{0,r}} N \qquad (6)$$

where A is the area under a fluorescence emission curve, a is the absorbance (which is ϵcl), I is the source intensity, N is the refractivity correction for the solvent if the standard and sample have different solvents, and the subscripts s,r,0, and $\Delta\lambda$ refer to sample, reference, initial, and wavelength bandwidth respectively.

EXPERIMENTAL

Fluorescein, a laser dye, was selected as a substance to use in developing our technique because it is a relatively well-known fluorescing substance and can be put into glycerin, the substance we use to create levitated droplets. A spherical void levitator trap was coated with barium sulfate white reflectance standard so that it would act as an integrating sphere to collect fluorescence

779

emitted at all angles. A barium sulfate baffle was inserted into the trap to block direct view of the particle by the detector. A schematic of the trap is shown in Figure 1. A DC voltage is placed across the end caps of the trap and an AC voltage is placed on the isolated center ring. The droplet containing the dye is electrically charged as it enters the trap and is levitated by the electric fields. The particle is placed in the center of the trap by adjusting the voltages. A schematic of the experimental setup is shown in Figure 2. A CW helium cadmium laser operating at a wavelength of 442 nm and an intensity of 12 mW was used as the light source. The fluorescence emitted from the particle was observed using a fiber optic cable and piped into a spectrometer that was interfaced to an IBM PC compatible computer. Both photomultiplier tube and optical multichannel analyzer (with photodiode array) were used as detectors in the experiments. The laser light was chopped and a lock-in amplifier was used on the signal.

For the first part of the experiment, measurements were made on glycerine as a bulk substance and as a mixed substance of fluorescein and glycerine. The spectra are shown in Figure 3. The fluorescein spectrum peaks at 530 nm while the glycerine spectrum peaks about 510 nm; however, the spectra are relative presentations--the fluorescein mixture is actually about 20 times as intense as the glycerine neat sample; this is obvious if one looks at the relative noise of the two spectra. The absorbance of a sample of 2.5 x10^{-4} molar was measured by a transmission through a cuvette of 1 centimeter path length containing the mixture and applying Equation 4. Equation 6 is then used to determine the fluorescence yield, using published literature values.

The second part of the experiment is considerably more difficult and involves levitating a droplet 13.8 micrometers in radius of the glycerine - fluorescein mixture and determining its spectra. This was done using the procedures described by Essien et al.[1] The particle was irradiated with the 442 nm laser light from the helium cadmium laser for a period of several minutes. For the final measurements a diode array was used and data were averaged over one minute. The spectra are shown in Figure 4. The fluorescein had a tendency to bleach if exposed for long time exposures; this will distort any efficiency measurements. The structure seen on the spectra are probably real since the signal was strong compared to the noise. The structure is probably due to morphological effects since the droplets are spherical. To use Equation (6) to determine the efficiency entails using a reference efficiency (such as determined experimentally in part 1 of the experiment) and then measuring the areas under the curves for the two measurements. The absorptivity for the reference was also obtained by the transmission measurement; however one must infer an equivalent value for the droplet using the Mie absorption cross section. This value is obtained using the elastic scattering of the 442 nm light. By letting the particle evaporate over a period of hours and monitoring the scattering at 90°, the particle radius

and its complex refractive index can be determined. The absorption cross section can then be calculated.

COMMENTS

In the preliminary measurements made thus far, little difference is seen between the bulk values and the droplet values; however there are some differences when the particle goes through resonances. This is expected since all our particles were very large (13.8 micrometers radius). Enhancements due to particle effects are expected to occur for smaller particles. This will be examined in future work.

The intent of this research is to develop a technique to determine fluorescence yields for single particles, primarily those that do not exist as bulk materials such as pollens, clays, biological spores, etc. Our research will include measurements on these types of common aerosol particles since these will be interferents to ultraviolet lidar remote stand off detection.

REFERENCES

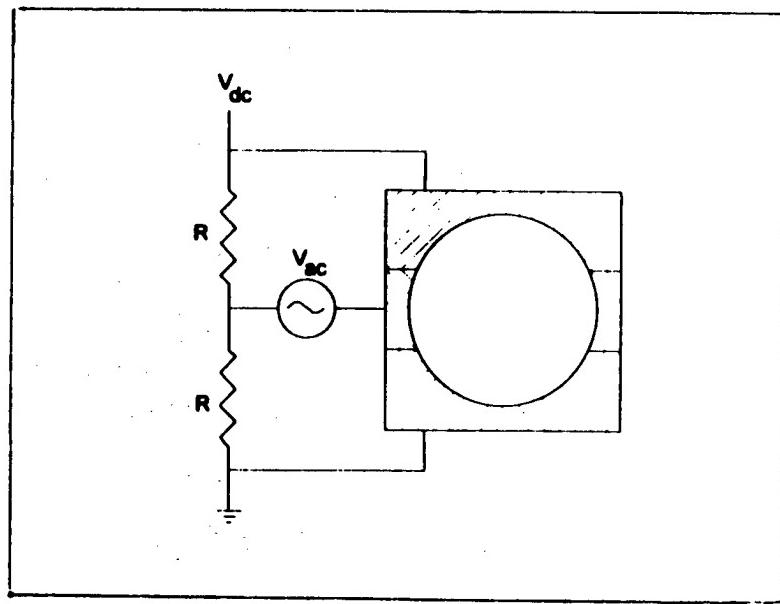1. Essien, M., J.B. Gillespie, and R.L. Armstrong, Appl. Opt. 31, 2148 (1992).
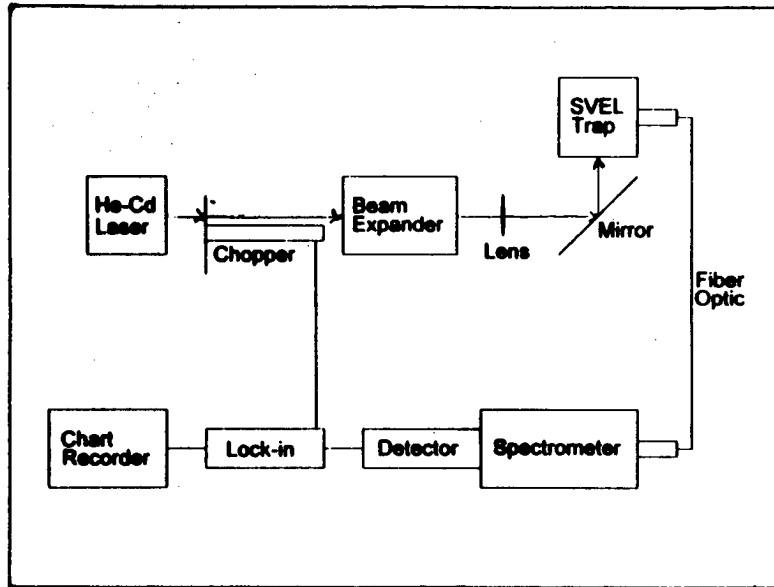
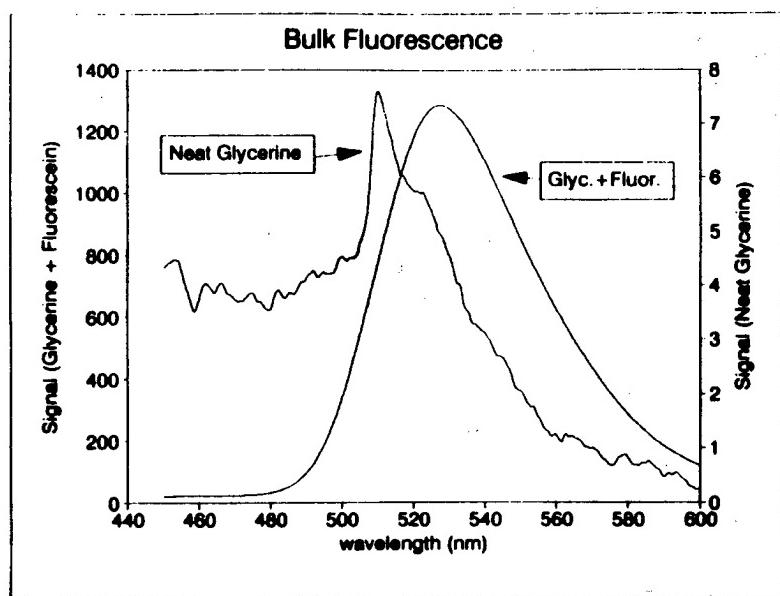Figure 1. Spherical Void Levitator Trap

Figure 2. Experimental Setup

Figure 3. Spectra of bulk samples of Glycerine and of Fluorescein
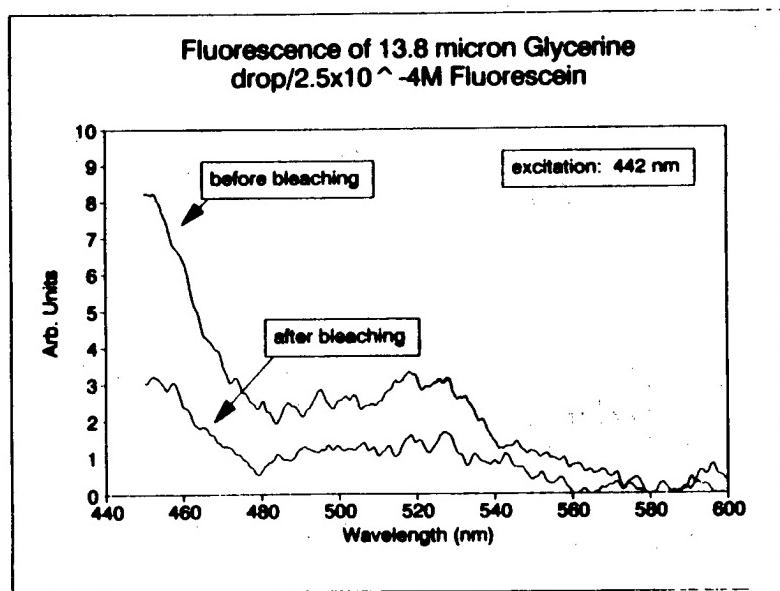

Figure 4. Fluorescence Emission Spectra of a Fluorescein-doped Glycerine Droplet

NEURAL NETWORKS FOR
VEHICLE DETECTION AND CLASSIFICATION

Gilles BUREL & Jean-Yves CATROS

Thomson CSF, Laboratoires Electroniques de Rennes,
Avenue de Belle Fontaine, 35510 Cesson-Sévigné, France

Abstract

Automatic classification of vehicles on infra-red images is a hard image processing problem. Because it is difficult to use a pattern recognition method based on models, an alternative approach, based on learning by example, is investigated. The approach involves neural network techniques. Experimental results show that classification rates around 92% can be obtained with a training base of 1000 examples.

1 Introduction

Recent experiments concerning detection and classification of vehicles on infra-red images are presented. Classical approach to pattern racognition is usually based on structural analysis and comparison with models. However, because of noise level, and relatively impredictable target signature, pattern recognition is much more difficult on infra-red images than on images of the visible domain. Hence, an alternative approach, based on learning by example, is proposed in this paper. The approach involves two neural network techniques (Multi-Layer Perceptron, and Learning Vector Quantization), which are described in sections 2 and 3. Section 4 describes the method for vehicle classification, and provides experimental results. In section 5, an extension of this method to detection of vehicles is proposed.

2 The Multi-Layer Perceptron

The Multi-Layer Perceptron is a popular neural network model, which has been succesfully used in a variety of image processing and pattern recognition applications. The Multi-Layer Perceptron is trained by the backpropagation algorithm [3]. An example of such a neural network structure is shown on figure 1. The neuron model is shown on figure 2. It is a weighted summator followed by a non-linear function. First, the neuron's potential X_j is computed as weighted sum of its inputs O_i: $X_j = \sum_i W_{ij}O_i$. Then, the neuron's output O_j is computed as a non-linear function of its potential: $O_j = F(X_j) = tanh(X_j)$. Adding special neurons, called "threshold neurons", whose output is always 1, improves the performances of the network.
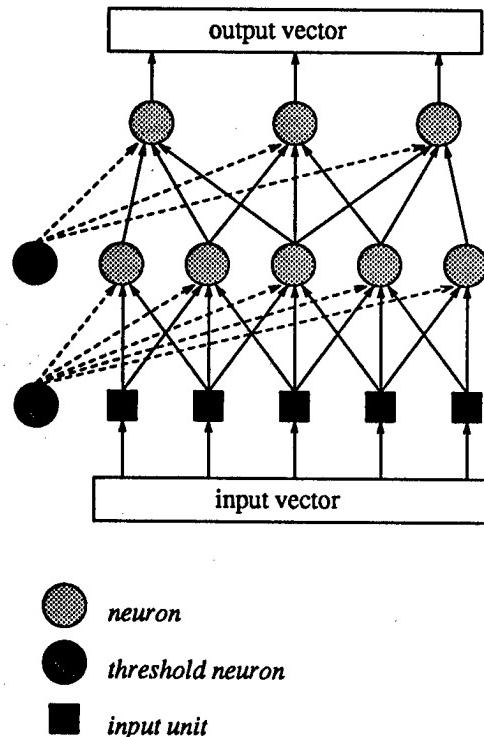

Figure 1: *An example of Multi-Layer Perceptron*

For instance, for a 3 classes problem, there are 3 neurons on the output layer (one for each class), and the desired output values are:

$$(+1, -1, -1) \quad \text{for class 1}$$
$$(-1, +1, -1) \quad \text{for class 2}$$
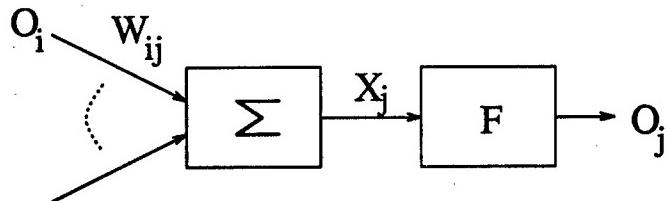$$(-1, -1, +1) \quad \text{for class 3}$$

Figure 2: *The neuron model*

Let us note E the mathematical expectancy. The learning algorithm adjusts the weights in order to provide correct outputs when examples extracted (in a random order) from a training set are presented on the network input layer. To perform this task, a mean square error is defined as:

$$e_{MS} = E\{e_S\}$$

where

$$e_S = \sum_{output\ neurons} \frac{1}{2}(obtained\ output\ -\ desired\ output)^2$$

Let us note $g_{ij} = -\dfrac{\partial e_S}{\partial W_{ij}}$, S_j the desired outputs, and O_j the obtained outputs. It has been proved [3] that $g_{ij} = \delta_j O_i$, where $\delta_j = (O_j - S_j)F'(X_j)$ when j is on the output layer, and $\delta_j = \left(\displaystyle\sum_{successors(j)} \delta_k W_{jk} \right) F'(X_j)$ when j is on another layer. Since the examples are extracted in random order (and provided that the training set is significant), the gradient of e_{MS} can be approximated by low pass filtering of g_{ij} :

$$\bar{g}_{ij}(t) = (1 - \beta)g_{ij}(t) + \beta\bar{g}_{ij}(t - 1)$$

The backpropagation algorithm performs a gradient descent according to:

$$\Delta W_{ij}(t) = -\alpha\bar{g}_{ij}(t)$$

Once learning is achieved, the network can deal with new data. For classification, the neuron whose output value is the highest determines the class.

A confidence measure (between 0 and 1) can also be defined as :
$$confidence = \tfrac{1}{2} (\ highest\ output\ -\ second\ highest\ output\ )$$

3   Learning Vector Quantization

Learning Vector Quantization is a neural network algorithm proposed by Kohonen [2], which involves 2 main steps:

- Unsupervised representation of the data, using the Topological Maps model.

- Supervised fine tuning of the neural network.

3.1   The Topological Maps

The Kohonen network, also known as the "topologic maps model", is inspired from a special structure found in some cortex areas (fig 3). The neurons are organized in layers, and, inside a layer, each neuron sends excitatory connections towards its nearest neighbours, and inhibitory connections towards the other neurons. All neurons receive the same inputs from the external world.
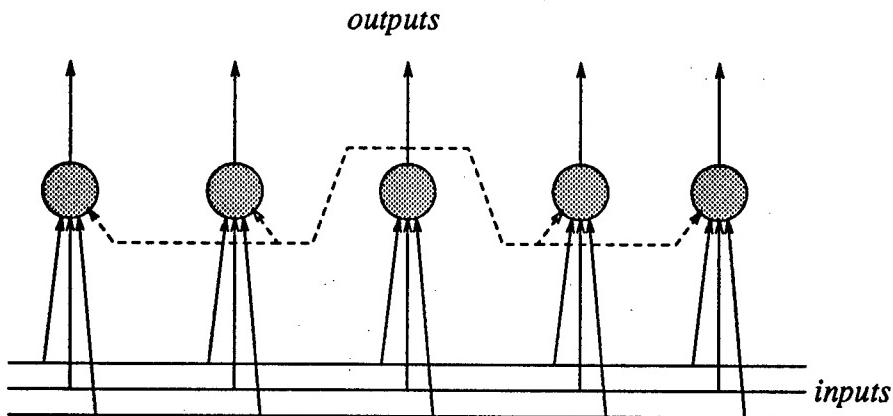

Figure 3: *The topologic maps model (1D)*

Kohonen simulated the behaviour of this kind of neural network [1], and showed that it can be approximated by the following algorithm. Let us consider a network with M neurons, and let us note K the number of inputs, and $\vec{x} = [x_1, x_2, ..., x_K]^T$

an input vector. The input vectors are extracted from a set $\mathcal{A}$, called "the learning set". This set contains $card(\mathcal{A})$ vectors. Each neuron is characterized by a vector of weights $\vec{W_j} = [W_{1j}...W_{Kj}]^T$, where j is the index of the neuron. In response to an input vector $\vec{x}$, the neuron such that the quadratic distance $\|\vec{W_j} - \vec{x}\|^2$ is minimal is called the winner. We will note O_j the output of neuron j:

$$O_j = \|\vec{W_j} - \vec{x}\|^2 = \sum_{i=1}^{K} (W_{ij} - x_i)^2$$

The learning algorithm is the following (t is the iteration index, and T is the total number of iterations):

1. $t = 0$
   Initialization of the weight vectors $\{\vec{W_1}, \vec{W_2}, ..., \vec{W_M}\}$

2. $n = 1$
   Let ρ be a random permutation of the set $\{1, 2, ..., card(\mathcal{A})\}$

3. Presentation of the vector $\vec{x}(\rho(n))$ on input.

4. Computation of neurons outputs O_j

5. Determination of the winner (neuron k which provides the lowest output)

6. Modification of the weights according to:

$$\Delta \vec{W_j} = \alpha_{jk}(t).[\vec{x} - \vec{W_j}]$$

7. $n = n + 1$
   If $n \leq card(\mathcal{A})$, go to (3)

8. t=t+1
   If $t < T$ go to (2)

The coefficients $\alpha_{jk}(t)$ are of the form $\alpha(t, d(j, k))$. The distance d defines the dimension of the network. For 1D networks arranged in ring, such as the one we used for our application, we have $d(j, k) = min(|j - k|, |M - j + k|)$. We propose to use:

$$\alpha_{jk}(t) = \alpha_0 e^{-\frac{d^2(j,k)}{2\sigma_t^2}}$$

The constant α_0 is called "the learning rate". Kohonen suggests values around 10^{-1}. The standard deviation σ_t decreases with t according to an exponential rule:

$$\sigma_t = \sigma_0 \left(\frac{\sigma_{T-1}}{\sigma_0}\right)^{\frac{t}{T-1}}$$

It is clear that, at each step, the winner and its neighbours will move their weights in direction of the input vector $\vec{x}$. Hence, the network's dynamics could be seen as the result of an external force (adaptation to input vectors), and an internal force (the neighbourhood relations, that force nearby neurons to have close weights). Kohonen validated his algorithm on speech data, and showed that the neurons organize their weights in order to become representative of phonemes. Furthermore, topological relations are preserved (close neurons react to close phonemes).
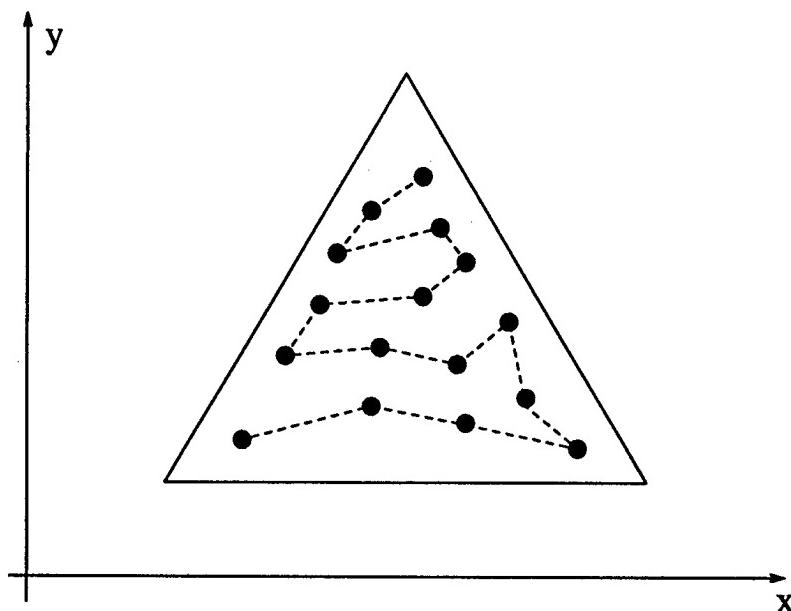

Figure 4: *Self-organization inside a triangle*

Properties of Kohonen's algorithm may be illustrated on a simple example. Let us assume that the input vectors are of dimension 2, and that their components are coordinates of a point randomly selected inside a triangle. Each neuron has two weights, so we can represent it by a point in the 2D plane. Figure 4 shows the network state after learning. Hence, the neural network, that can be seen as a one dimensional curve, has performed an approximation of a 2D domain (the triangle).

Kohonen's algorithm may be easily generalized to higher network's dimensions. For example, a 2D network is shown on figure 5.
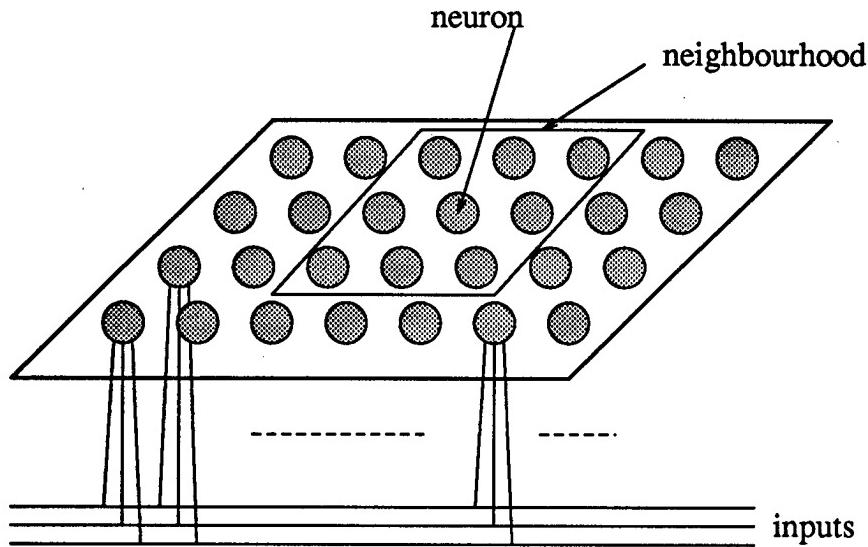
Figure 5: *Topologic maps model (2D)*

3.2 Supervised fine tuning of the neural network

Starting from a topological map which has converged, a class is assigned to each neuron by majority voting (among the examples for which this neuron is the winner). Then, the network is tuned in order to improve its classification accuracy. Kohonen has proposed 3 methods (LVQ1, LVQ2, LVQ3) for fine tuning. LVQ2 is supposed to be an improved version of LVQ1, and LVQ3 an improved version of LVQ2, although, for some applications, LVQ1 may provide the best results.

3.2.1 LVQ1

The examples are presented randomly and, for each example, the weights of the winner (j) are tuned as below (c is the class of the example):

- $\Delta \vec{W}_j = \alpha(\vec{x} - \vec{W}_j)$ if $c = j$

- $\Delta \vec{W}_j = -\alpha(\vec{x} - \vec{W}_j)$ if $c \neq j$

791

3.2.2 LVQ2

Let us note j the winner, and k the next-to-nearest neuron. Let us note also $d_j = ||\vec{x} - \vec{W_j}||$ and $d_k = ||\vec{x} - \vec{W_k}||$. If the class assigned to k is the same as the class of $\vec{x}$, and is different to the class assigned to j, and if $d_k < s\ d_j$ ($s \simeq 1.2$), then:

- $\Delta \vec{W_j} = -\alpha(\vec{x} - \vec{W_j})$

- $\Delta \vec{W_k} = \alpha(\vec{x} - \vec{W_k})$

3.2.3 LVQ3

If the class assigned to k is the same as the class of $\vec{x}$, and is different to the class assigned to j, and if $d_k < s\ d_j$ ($s \simeq 1.2$), then:

- $\Delta \vec{W_j} = -\alpha(\vec{x} - \vec{W_j})$

- $\Delta \vec{W_k} = \alpha(\vec{x} - \vec{W_k})$

If $\vec{x}$, j, k, belong to the same class, then:

- $\Delta \vec{W_j} = \alpha(\vec{x} - \vec{W_j})$

- $\Delta \vec{W_k} = \alpha(\vec{x} - \vec{W_k})$

4   Classification

Classification of vehicles on infra-red images leads to serious difficulties, due to the following variabilities:

- The background is unknown.

- The meteorological conditions are uncontrolled.

- The orientation of the vehicle with respect to the camera is unknown.

- The including frame provided by a detector is approximate, hence there may be slight variations of the apparent size of the vehicle.

These variabilities are taken into account by creating a large training base, containing various vehicles in many orientations, with many backgrounds and environmental conditions. Furthermore, to take into account the fact that the including frame is approximate, slight homotheties are performed on the examples of this data base.

The image to classify is normalized in mean and variance, in order to obtain some insensibility with respect to camera gain. Then it is normalized in size, because the input size of a neural network is fixed. For our experiments, this size was 24x16 pixels.

Six classes of vehicles have been defined: helicopter, truck, and four classes of tanks. A data base of 945 images of vehicles has been created to train the neural network. A second data base of 1407 images of vehicles has been created to test the generalization capabilities of the neural network (these images are not used for training).

Two kinds of neural networks have been compared:

- A 3-layer perceptron (384 + 15 + 6 neurons), trained by the backpropagation algorithm

- A LVQ network (384 inputs, 32 neurons). The LVQ1 method for fine tuning has been used.

The obtained generalization rate is:

- 92% with the 3-layer perceptron

- 89% with the LVQ network

The required training time (on a Sun workstation) is 10 hours for the 3-layer perceptron and 30mn for the LVQ network. Classification of a normalized image requires 385x15+16x6 = 5871 multiplications with the 3-layer perceptron, and 384x32 = 12288 multiplications with the LVQ network.

The conclusion is that the performances of these neural networks are quite similar (92% and 89%), but the MLP is twice faster at recognition. However, since the

training time required by the LVQ network is 20 times lower than the training time required by the MLP, the LVQ network should be used preferently if one wants to compare quickly the interest of new training bases.

Figure 6 shows the weights of the LVQ network after training. Although the weights are difficult to interpret, one may recognize patterns similar to helicopters, trucks, and tanks by careful examination of this image.
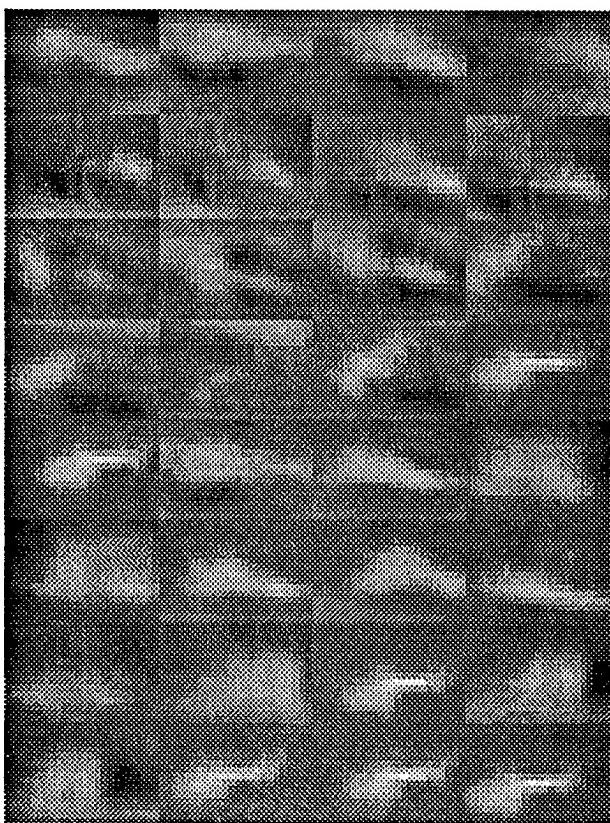

Figure 6: *Weights of the LVQ network*

5   Detection

The approach may be extended to vehicle detection by considering that detection is some kind of classification problem, where the classes are "vehicle" and "background". However, a specific difficulty must be stressed: we do not know the distance between the vehicle and the camera. Hence, the apparent size of the vehicle

on the image is unknown.

The proposed approach consists in scanning the image at various resolutions. For each location and size of the scanning window, the window content is normalized in mean and variance, then normalized in size, and finally propagated through a neural network. The neural network provides a class (vehicle or background), and a confidence associated to this decision.

All the local decisions are then fused to suppress multiple detections at close spatial locations. To achieve this task, we search for the strongly overlapping detections. Two detections are considered as strongly overlapping if the center of one window is included in the other window. For such configurations, we suppress the detection which has the lower confidence.

For experimentation, we have created a training base of 4647 images (1407 images of vehicles and 3240 images of backgrounds). It is good to have more backgrounds than vehicles in the training base, in order to keep the false alarm rate at a low level. MLP and LVQ networks provide comparable results. On a typical test sequence showing 3 tanks moving at various distances, the 3 vehicles are detected almost on each image of the sequence, while two or three false alarms may appear stealthy. Since the location of these false alarms seem to be almost random, they might be suppressed by temporal analysis.

6   Conclusion

An approach to vehicle detection and classification on infra-red images has been proposed in this paper. The approach is based on learning by example and neural network techniques. Concerning classification, 6 classes have been defined: helicopter, truck, and 4 classes of tanks. A neural network has been trained to recognize these classes independently of vehicle orientation and environment conditions. Two kinds of neural networks have been compared: the multi-layer perceptron and Kohonen's learning vector quantization. Experimental results obtained on 1400 examples show that a classification rate of 92% can be expected. An extension of this approach for detection purpose has been proposed. The image is analysed by multi-resolution scanning. For each resolution and each window location, the content of the window is normalized in size, average brightness, and contrast. Then, it is propagated through a neural network, which provides a decision ("vehicle" or "background") and a confidence measure. All the decisions are then fused across the various resolutions in order to suppress multiple detections at the same location. The fusion is based on analysis of confidence.

References

[1] T. Kohonen, "Self-Organization and Associative Memory", Springer-Verlag, 1984

[2] T. Kohonen, "The Self-Organizing Map", Proc. of IEEE, vol 78, n° 9, pp 1465-1481, September 1990

[3] D.E. Rumelhart, G.E. Hinton, R.J. Williams, "Learning internal representations by error backpropagation", In Parallel Distributed Processing, D.E. Rumelhart and J.L. Mc Clelland, Chap 8, Bradford Book - MIT Press - 1986

COMPARISON OF RADIOMETER, RASS, AND RADIOSONDE GENERATED VERTICAL PROFILES OF ATMOSPHERIC TEMPERATURE

by

Edward M. Measure
Teddy L. Barber

U. S. Army Research Laboratory, Battlefield Environment Directorate, WSMR, NM, 88002.

and

Randall J. Hulsey
Dick R. Larson

Physical Science Laboratory, New Mexico State University, Las Cruces, NM 88004

ABSTRACT

The Army Research Laboratory is developing a Mobile Atmospheric Profiler system to measure important atmospheric parameters from the surface to 30 kilometers. Several technologies are available for measuring the crucial atmospheric temperature profiles, This paper presents results of simultaneous measurements using two promising remote sensing technologies, namely, the microwave radiometer and the Radio Acoustic Sounding System, with radiosonde measurements.

1. INTRODUCTION

The Army Research Laboratory is currently developing a Mobile Atmospheric Profiler, designed to provide vertical profiles of important atmospheric parameters with a compact, highly mobile system. One of the most crucial such parameters is atmospheric temperature. In order to achieve the objectives of mobility and timeliness of temperature data with a minimal logistical tail, we intend to rely on a mixture of satellite and surface based remote sensing technologies.

The radiosonde balloon has a long data cycle and requires extensive logistical support. Satellite measurements lack accuracy near the surface (where the unknown brightness of the Earth's confuses their radiometry). Two surface based remote sensors appear to have the capability to fill the resulting data gap: microwave radiometry and the Radio Acoustic Sounding System (RASS).

RASS was invented in the early 1970's (North et. al., 1973) and has been developed over the past 20 years by groups around

the world. The idea behind RASS is to use radar to measure the speed of an upward propagating acoustic pulse, and deduce the virtual temperature of the path from the measured speed of sound.

$$c = (p\gamma/\rho)^{1/2} = (R_d T_v \gamma)^{1/2} \qquad (1)$$

where

c = The speed of sound

p = atmospheric pressure

ρ = atmospheric density

γ = adiabatic constant

R_d = gas constant for dry air = R/m_d

R = universal gas constant

m_d = average molecular mass of dry air

T_v = virtual temperature

2. OBJECTIVE

The series of measurements described in the present paper were undertaken to address whether ground based radiometry or RASS (or both together) can provide satisfactory temperatures in the lower atmosphere. In particular: (1) Does one of the two (radiometry or RASS) have a clear performance advantage over the other? (2) Are their capabilities redundant, or are both required for the total mission?

2. APPARATUS USED

The radiometer used in the measurements was the Army Research Laboratory (ARL) Passive Microwave Temperature Profiler (PMTP) which was built for the ARL by the Jet Propulsion Laboratory of the California Institute of Technology. The PMTP measures sky brightness temperatures at 51.07 GHz, 53.88 GHz, 55.29 GHz, and 57.45 GHz. In the operating mode used here it makes a series of measurements with the antenna directed at elevation angles of 9, 15, 25, 40, and 90 degrees, and intersperses each series of measurements with a measurement of an internal target. During these measurements, the radiometer was located at the Profiler Test Facility at White Sands Missile Range, New Mexico. The PMTP will be incorporated in the initial Mobile Profiler System Prototype.

The RASS used was also located at the Profiler Test Facility. The RASS, which is based on a 924 MHz wind radar with a peak power of 1 kilowatt, is a trailer mounted mobile system

which will be incorporated into the Mobile Profiler System Prototype.

The simultaneous radiosonde observations were launched from the Oasis Site at White Sands Missile Range, located about four miles from the other two instruments.

3. THEORY AND OPERATING PRINCIPLES OF THE INSTRUMENTS

The radiosonde is a balloon borne instrument package which makes periodic measurements of pressure, temperature, and humidity. The measurements are transmitted by radio to a ground station. Altitude is inferred by integrating the pressure equation from the surface.

The radiometer measures downwelling radiation at 4 microwave wavelengths at elevation angles of 9, 15, 25, 40 and 90 degrees. Each measurement is effectively a measurement of an altitude-weighted average over the temperature profile of the atmosphere. Because the altitude weighting functions are known (at least in approximation), the temperature profile can be retrieved from the microwave radiance measurements.

The basis of behind the operation of the RASS is the dependence of the speed of sound on the virtual temperature. Sound waves are propagated upward and radar waves are reflected from the propagating sound waves. The doppler shift of the reflected radar signal yields the speed of propagation of the sound waves, from which the atmospheric virtual temperature at the location of the sound wave can be deduced.

4. MEASUREMENT PROGRAM

Two series of results are shown in the following section. The first series represents data taken at WSMR during the summer of 1992. The second series consists of data taken in Los Angeles, California during September of 1993. In the intervening period, the noise rejection algorithms of the RASS were extensively altered (reference)

5. RESULTS

The results of these comparisons are shown in three types of graphs. The first and second of these types are three way comparisons of values given by the three types of measurement versus height above the surface. Type one shows comparisons from the surface to 20 kilometers. Type two show the same comparisons from the surface to two kilometers, and were so chosen to better illustrate the performance of the RASS, measures (at most) to 1,3 kilometers. The third graph type compares 5 successive RASS measurements, to show the stability (or lack thereof) of the RASS measurements. All temperatures shown are virtual temperatures.

The most striking aspect of the results of the comparisons we made is the highly variable performance of the RASS. In several of the comparisons, the RASS performance is outstanding through its range of availability. In several others it is notably poor. There don't seem to be intermediate cases for the RASS.

All of radiometer profiles track the radiosonde observations up to 20 kilometers, except for a few cases where the radiosonde observations do not go that high. RASS height coverage is very variable, since values are shown only where the RASS algorithms were able to compute temperatures. In no case do the RASS temperatures go above 1.3 kilometers. In several cases RASS temperatures were found at only one or two heights.
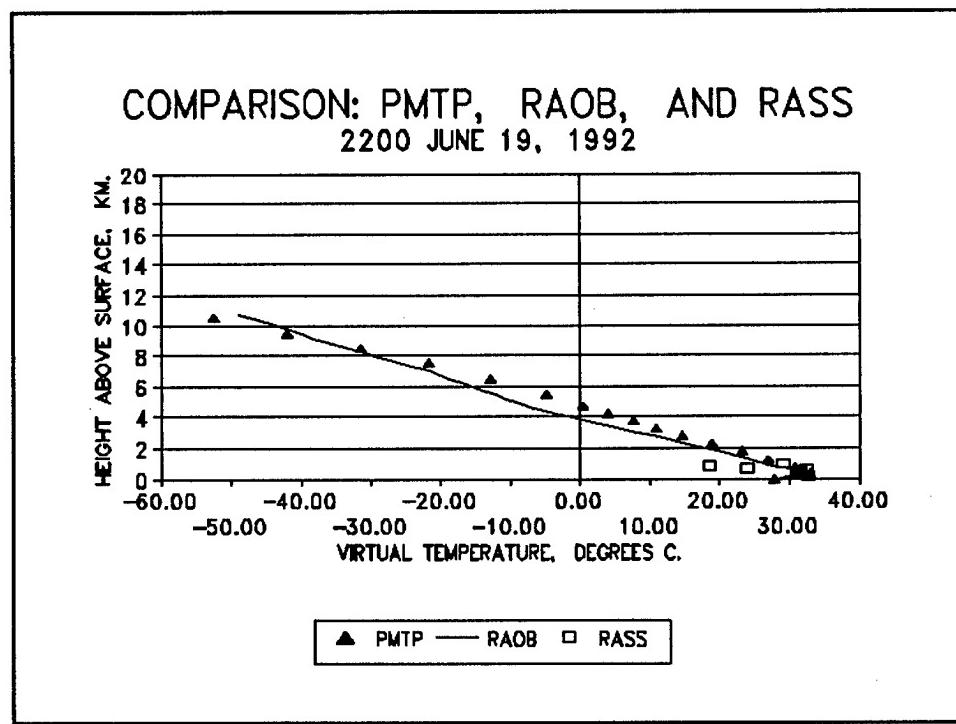

Figure 1. Three way comparison of RASS, Raob, and PMTP.
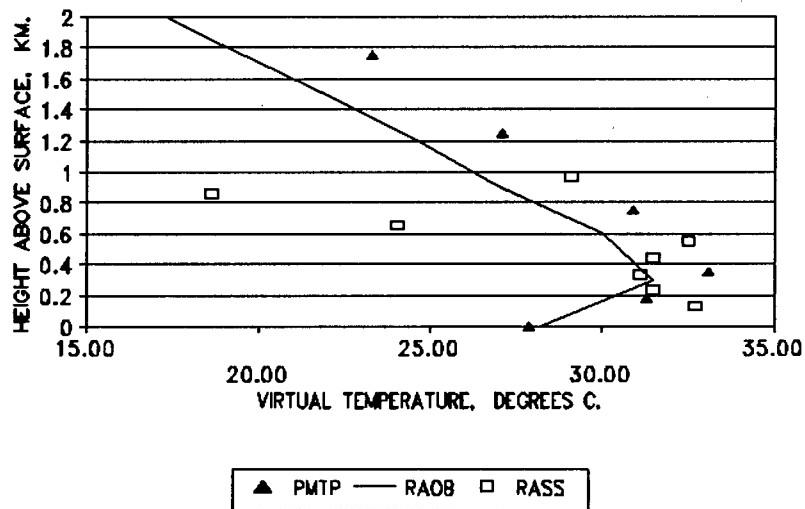
Figure 2. Comparison at lower levels.

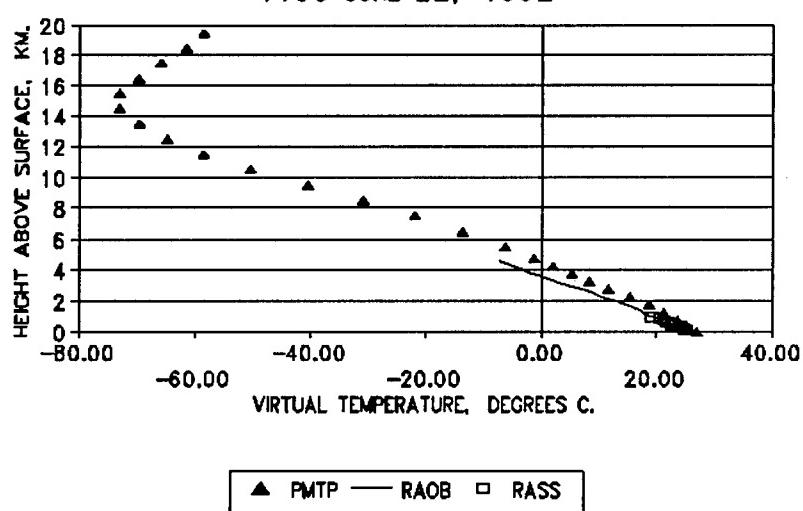**Figure 3.** Three way comparison of RASS, Raob. and PMTP.
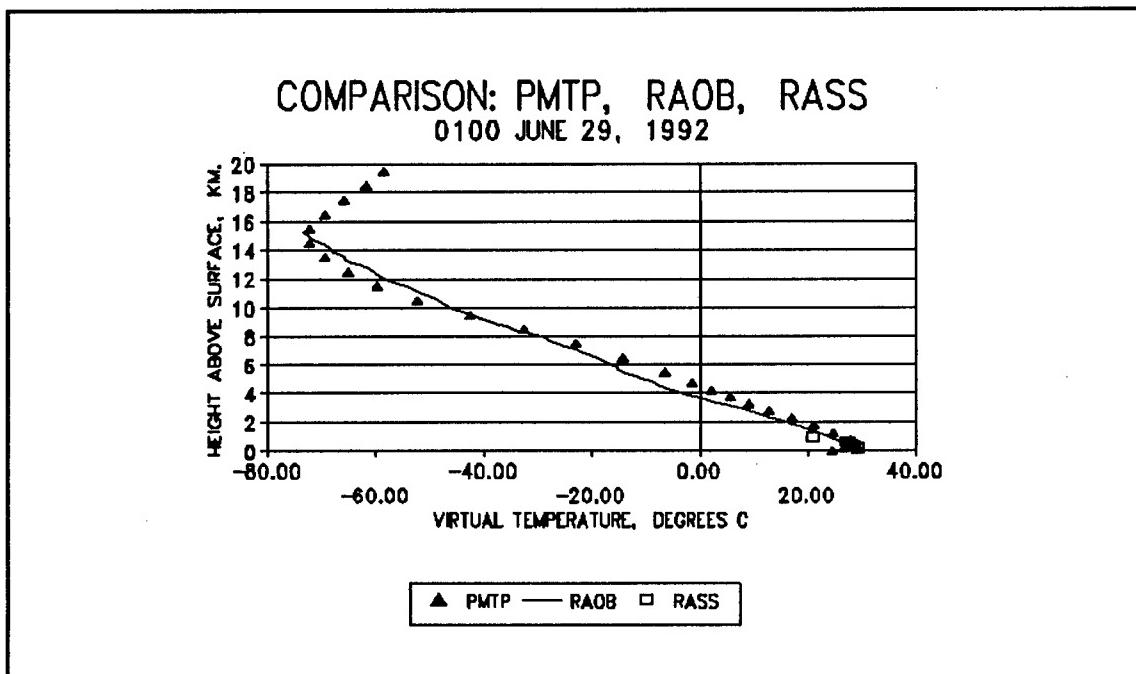
Figure 4. Three way comparison of PMTP, Raob, and RASS.
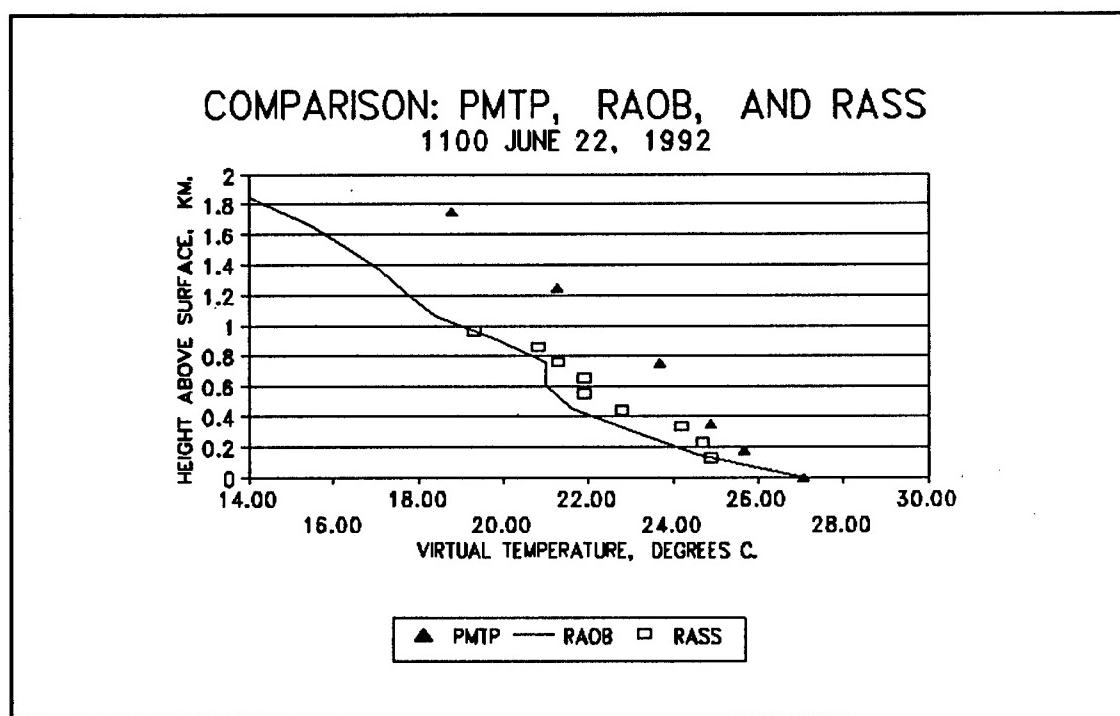
Figure 5. Comparison at lower levels.
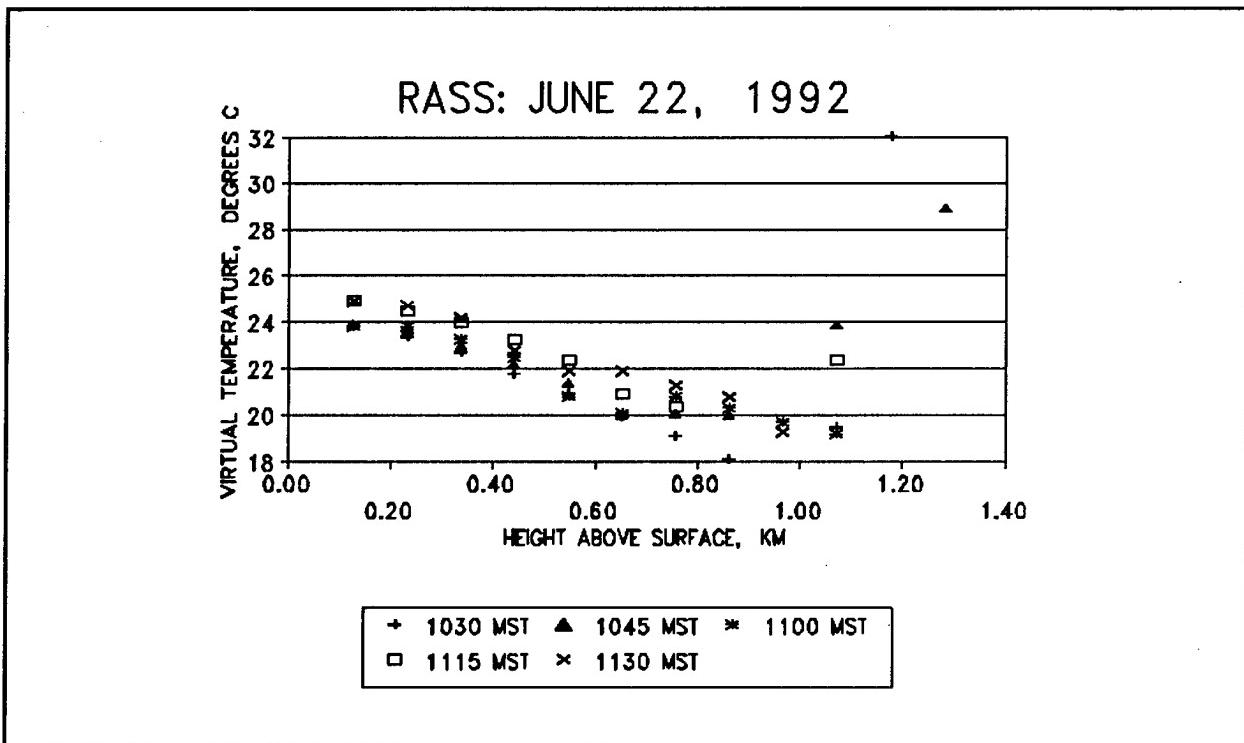
Figure 6. RASS values at 15 minute intervals.
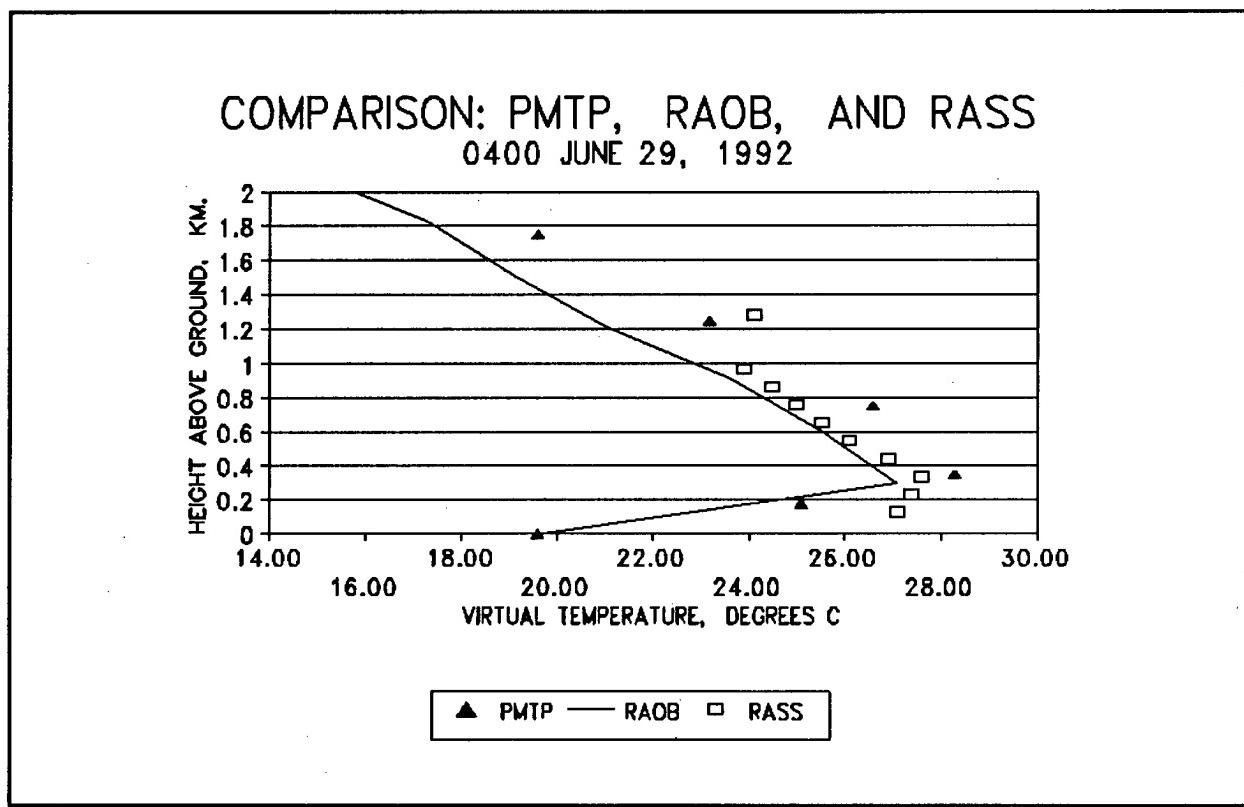
Figure 7. Comparison of PMTP, Raob, and RASS Tv.
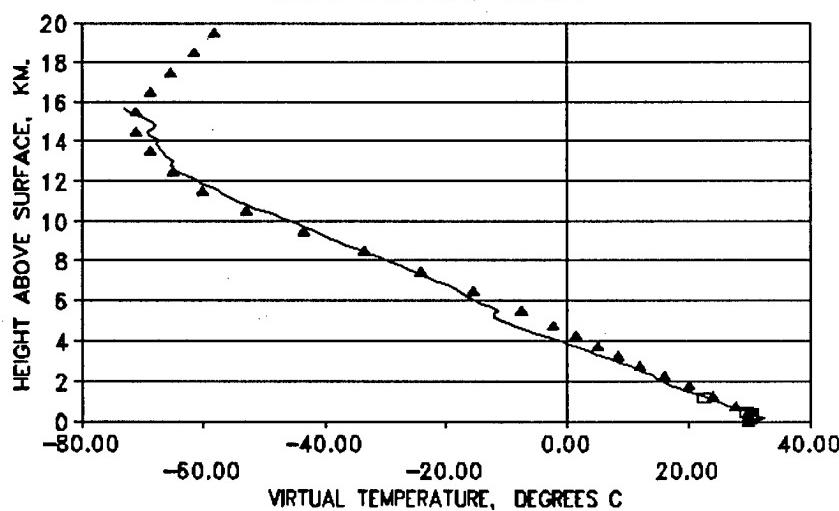
Figure 8. Three way comparison of PMTP, Raob, and RASS.

Figure 9. Lower 2 kilometers comparison of same data as Fig. 8.

Figure 10. 1993 Data. RASS vs Raob.
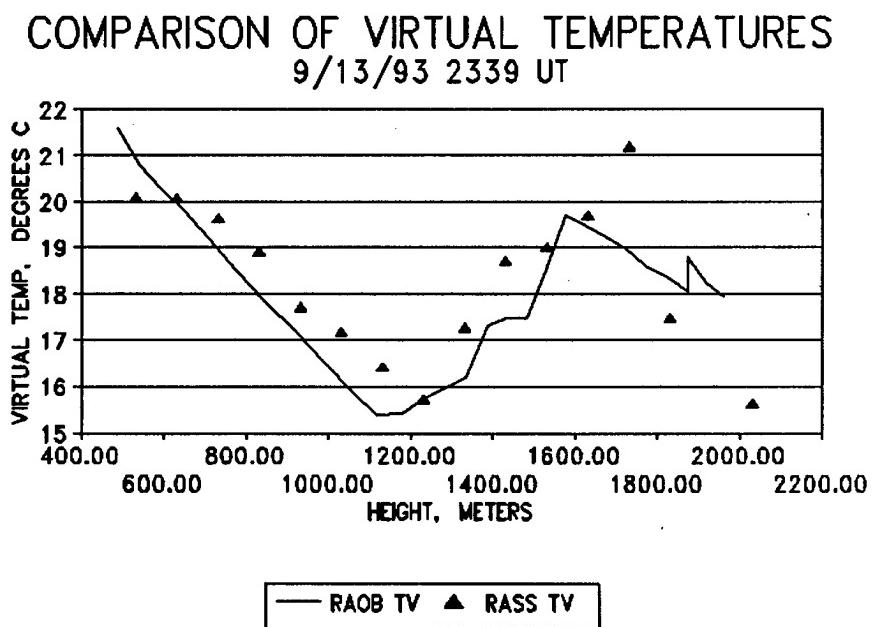
Figure 11. 1993 Data. RASS versus Raob.
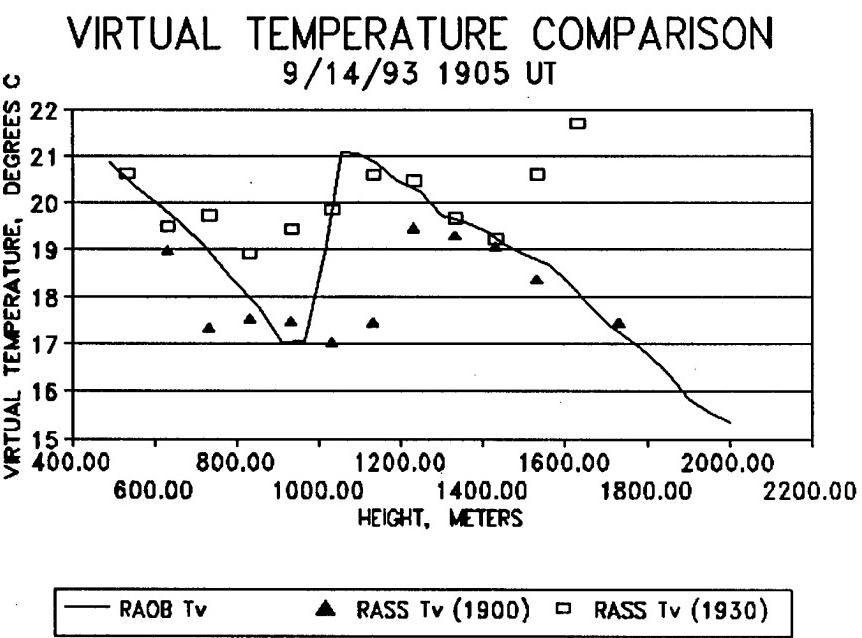
Figure 12. 1993 Data. RASS versus Raob.
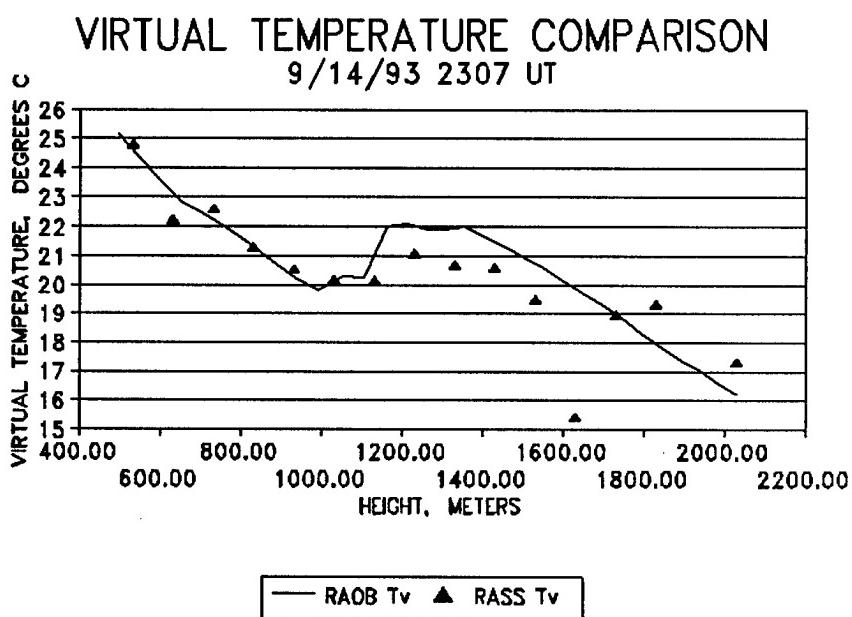
Figure 13. 1993 Data. RASS versus Raob.

REMOTE MEASUREMENTS OF THE DENSITY OF BATTLEFIELD VISUAL OBSCURANTS
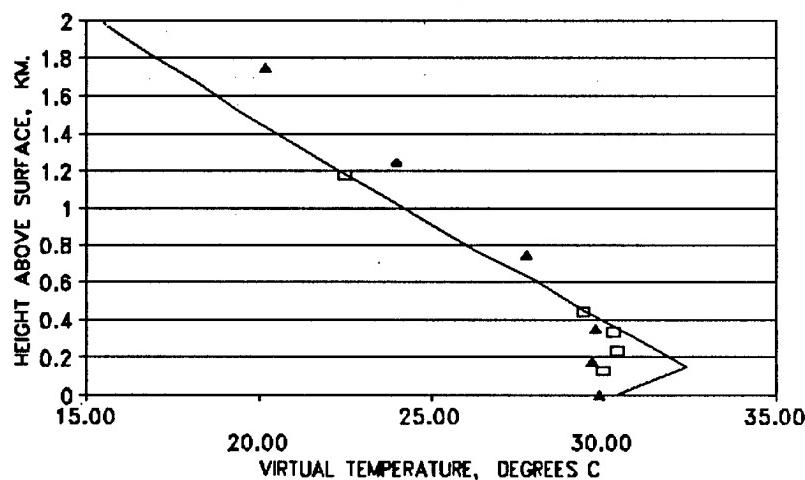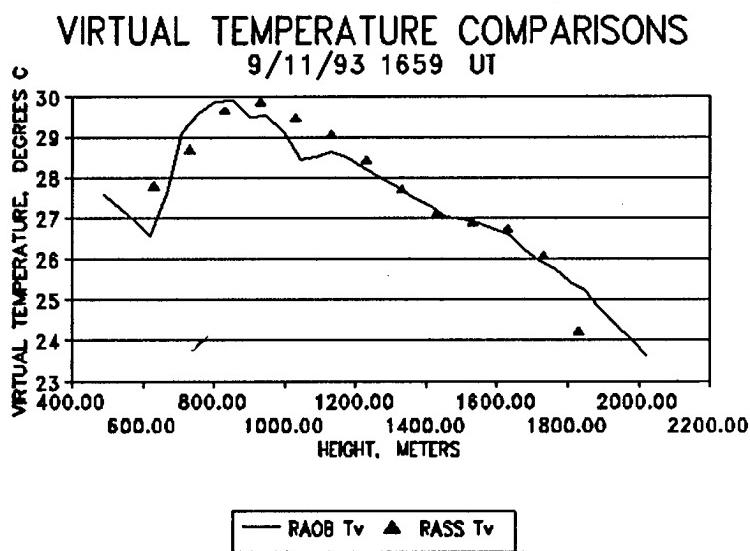
Radon B. Loveland
Department of Physics
New Mexico State University
Las Cruces, New Mexico 88003

Raul Gonzalez
and
Jill C. Thompson
U.S. Army Research Laboratory
Battlefield Environmental Directorate
White Sands Missile Range
New Mexico 88002

Ascencion Acosta
Department of Electrical Engineering
New Mexico State University
Las Cruces, New Mexico 88003

ABSTRACT: Particle density may be measured remotely using a lidar if certain conditions can be met. The results of observation of the particle density of certain obscuring munitions are presented and compared with data from nephelometers.

INTRODUCTION: Smoke densities along a given path are currently measured using an array of light scattering detectors operating in a digital mode.(ARL/PSL Nephelometer array) The technique is, in principle, an absolute measurement and is elegant in conception. However, the devices invade the space in which the measurement takes place and are limited in dynamic range by the requirement that on the average there must be less than one particle in the sample volume of the nephelometer.

The lowest practical limit is one particle per time interval of interest. The invasive nature of the measurement implies that measurements cannot be made directly in the region of interest such as a radar beam.

The lidar has several advantages over the nephelometer array.
It has higher data rate.
It has higher spacial resolution than the present nephelometer array.
It has a larger sample volume which makes data more statistically meaningful.

The lidar beam can be placed in close proximity to the radar beam and in fact they may cross in the region of interest. The ARL/BED Mobile Lidar System (MLS) can be operated at 10 Hz. and make measurements over a 1 kilometer path with a resolution of about 2 meters with the present system. The maximum path length is in practice dictated by the size of the reference target available. The entire path is not available but most of it is. This corresponds in principle to an array of slightly less than 500 nephelometers. In order to use the for this purpose a target which is optically stable over the data taking period and which is sufficiently large to encompass the beam, is required.

In addition, at our current level of knowledge about multiple scattering we must confine ourselves to conditions of modest attenuation so that the single scattering approximation is adequate. The MLS does not provide an direct measure of particle density for particles of arbitrary shape and size and nonrandom orientation. It may be calibrated against a suitable reference. In this work the lidar is calibrated against the nephelometer array.

DESCRIPTION OF EXPERIMENT:

For Trial 13747 the MLS beam was aligned parallel to the nephelometer line about 5 meters north and approximately .8 meters higher than the nephelometer line. The beam was terminated at 1005 meters by the target described in the section entitled "Description of the MLS"

The locations of the nephelometers in terms of the MLS coordinate system are shown in Fig. 1.
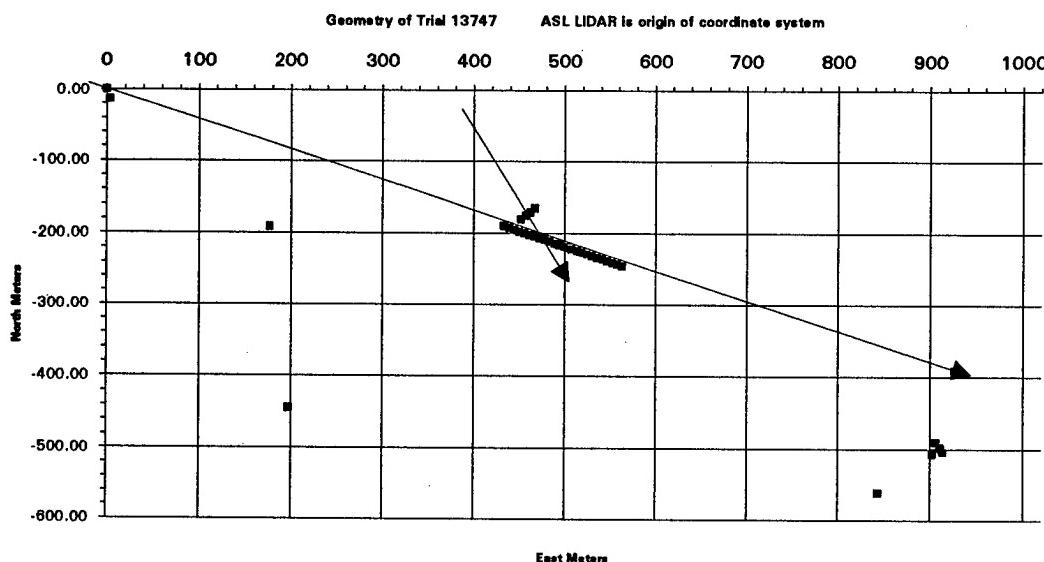
Fig. 1 Geometry of lidar and nephelometers

The nephelometers are displaced approximately 7 meters from the lidar line of sight. They are approximately .8 meters below it and about 5 meters above the ground. In Fig. 1 the small arrow is in the direction of the average wind vector during the trial. The wind speed average at the height of the lidar beam is about 5 m/s. at 330 degrees. The four small squares just above the

nephelometer line are the locations of the munitions detonations. The other squares represents locations of other artifacts that are not relevant to the results.

DESCRIPTION OF MLS:

The MLS as presently configured is a limited pointing capability lidar tailored for participation in battlefield obscurant tests and for vertical measurements. It must be aligned along a given path and has no facilities for simultaneous motion of the transmitted and received beams. As configured for these tests it operated at 532 nm. The subsystems are described below.

OPTICAL SOURCE:

The optical source consists of a laser with a harmonic generator, a beam separator and a 3X beam expander.

LASER SPECIFICATIONS:

Spectra Physics Model GCR-11 YAG laser with harmonic generator Model HG-2
Operating repetition rate 10 PPS (other settings available)

Output wavelengths nanometers	Max. energy per pulse Joules	Pulse width nanoseconds
1064	.320	8-9
532	.155	6-7
355	.70	5-6
266	.35	4-5

Nominal beam divergence is about 1 milliradian.

BEAM EXPANDER:

Galilean telescope with fused silica entrance lens and objective, 3X magnification. The combination of the beam expander and the laser permits the laser beam divergence to be adjusted from large values to about .3 milliradians at 1 Km. The laser beam divergence was set at about .5 milliradians for the test.

TELESCOPE AND OPTICAL TRAIN:
TELESCOPE:
Newtonian
.406 M diameter primary
1.22 M focal length
.304 M width primary turning mirror

OPTICAL SHUTTER:

The optical shutter consists of a PLZT (Lead Zirconate) element and crossed polarizers. The polarization of the light passing through the PLZT is rotated by the application of a 500 volt pulse. The transmission through the shutter is about 25% for randomly polarized light when it is open and is about 3 orders of magnitude lower when closed.

DATA ACQUISITION SYSTEM:

For these tests the output of the photomultiplier tube was fed to an Analog Devices Model 382 logarithmic amplifier. This was connected to a LeCroy Model 8828 Analog to Digital converter who's output was formatted by a LeCroy Model 6010 controller and sent to a PC over an IEEE-488 link.

LOGARITHMIC AMPLIFIER:

Analog Modules 382
Input impedance 50 Ohms

Input Dynamic Range	-200 μV. to -2V. (degraded linearity over the range +200 μV. to +2V.)

Rated dynamic range 80 dB
0.5 dB rated linearity

Response	DC- 3 ns rise time , fall time : 5 nS to about. 20 dB down 20 nS to 40 dB down 40 nS to 60 dB down
Output	Drives 50 Ohms , non inverting Offset typically 1 mv. Max. output : -.5V +0.6V. Linear with dB input , typ. 6.0 mV/dB for -ve input 7.9 mV/dB for +ve input
Linearity	+ or - .5 dB maximum deviation from plot of dB Volts input versus volts output, measured over at least 70 dB.

ANALOG TO DIGITAL CONVERTER:

LeCroy Model 8828D
Available Sampling increments, 5, 10, 20, 40, 80,160, 320 nS and external clock.

CALIBRATION:

The system lidar constant is provided by observation of a 1.22 meter square calibrated target placed at approximately one kilometer range. For proper calibration the majority of the beam must be reflected by the target.

The target used is made of SS304 stainless steel which has been sandblasted with coarse sand. The target was calibrated by measuring samples of the same material sandblasted at the same time with the same media. The reflectivity measurements were made with a Varian "Cary 14" Spectrometer. The target diffuse reflectance at 532 nm is .44 .

LIDAR RETURN INVERSION:

Unless the transmission losses though the obscurant are very small, it is necessary to perform an inversion of the lidar return to obtain backscatter. The return from the stable target permits this operation to be carried out by means of a simple iterative process which is the subject of another paper in preparation.

The results of the inversion may be compared with the raw lidar return in fig. 2 below.

Tr 137   1726 +6.7 sec relative backscatter and raw data
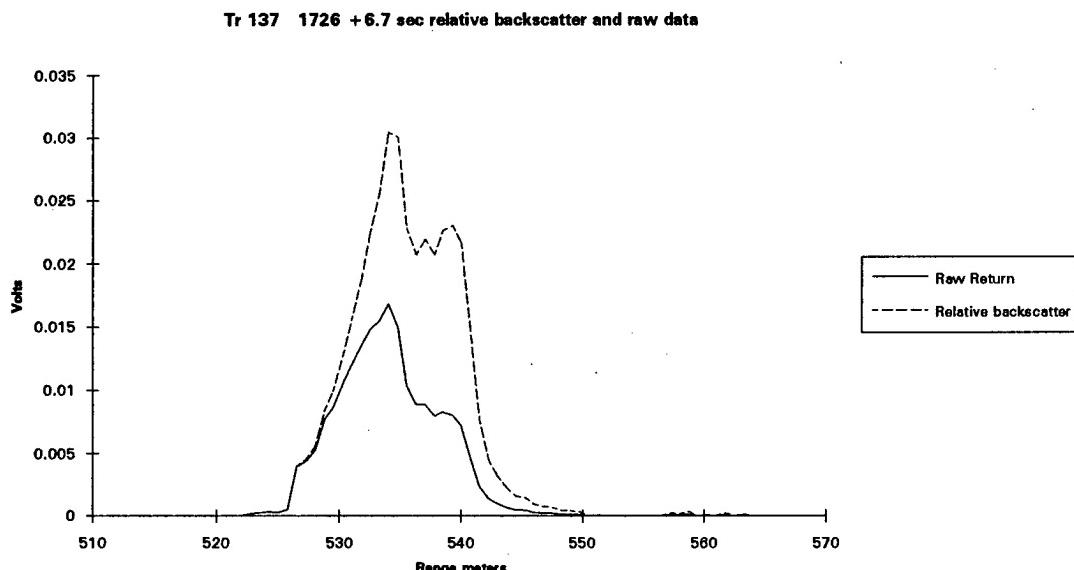
Fig. 2   Relative backscatter and raw lidar return at 6.7 seconds after 1726

COMPARISON OF SAMPLE VOLUMES:

The Nephelometer sample volume per unit time consists of an approximate cylinder whose crossection is approximately .38 cm^2 (1) and whose length is determined by the wind velocity and the sampling interval. For Trial 13747 the wind velocity was approximately 4 meters/sec. and the sampling interval was .2 seconds. The sample volume for this set of conditions is .   0.0000304 meters^3 per sampling interval per nephelometer.

The corresponding sample volume for the LIDAR with the beam expander attached is a cylinder .75 meters long and .0177 meters^2 (the beam diameter at 500 meters is about .15 meters) . This is 0.013 meters ^{3} . The normal sampling interval is .1 seconds. The sample volume of the lidar is along the range direction which is in these experiments more or less perpendicular to the wind drift. The LIDAR output is a "snapshot" with an exposure of a few nanoseconds and does not need the wind information in order to determine the sample volume.

811

The vastly different sample volumes and orientations make comparisons of data difficult if the data has spacial variations which are small with respect to the spacing of the nephelometers. For the trial discussed in the in this paper this is indeed the case. Fig. 3 shows pronounced "blobs" of visual obscuration whose shapes approach the response of the lidar to a singularity.
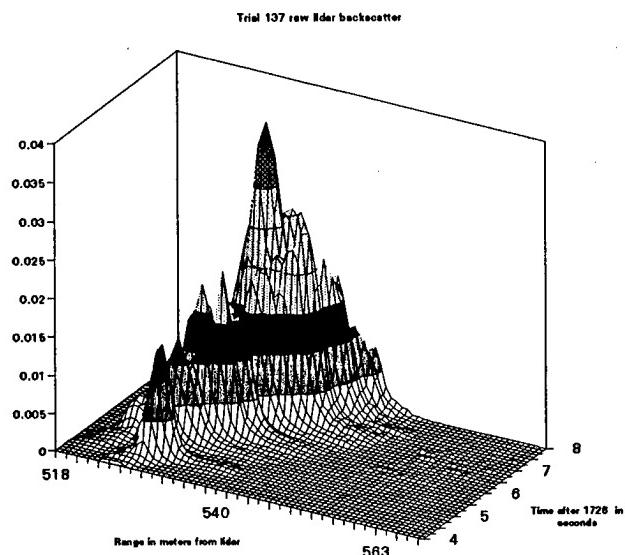
Fig. 3 Raw lidar backscatter

In view of this, it was concluded that the best method of calibrating the lidar would be to compare the observation of the total number of particles estimated to have passed through the nephelometer in 20 seconds with the corresponding summation of the backscatter data. For Trial 13747 the sum of the nephelometer CL's (concentrations along the line) is 184,474. The corresponding sum from the lidar is 11.215. using this assumption the calibration factor for the lidar is 16448. This factor has been applied to the data in fig. 4 which may be compared with data from the nephelometers in fig. 5
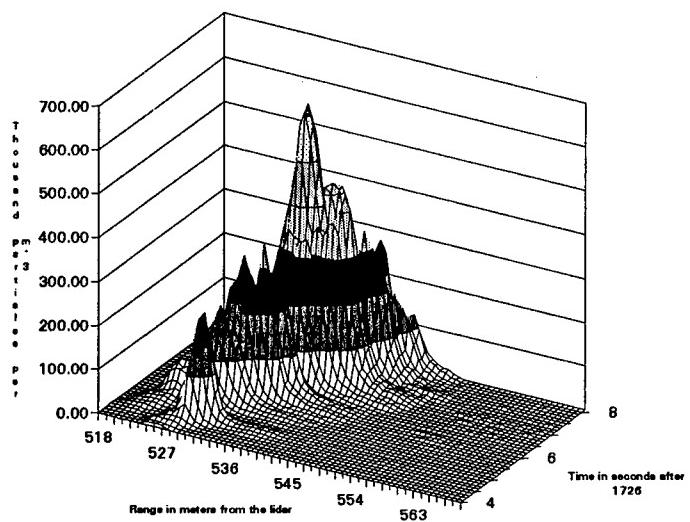
Fig. 4 Particle density as observed by the lidar.
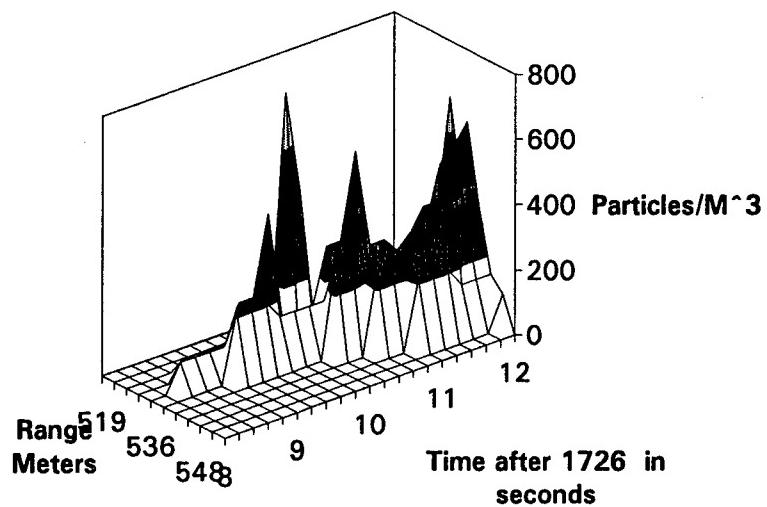
Figure 5   Particulate density as observed by the nephelometer.

CONCLUSION:

If a stable reflector is available which encompasses the laser beam and if the density of the obscurant is small enough so that the single scattering approximation is appropriate then relative particle density can be inferred from the relative backscatter coefficients arrived at by inverting the lidar return. This data can be converted to particle density by calibration against a suitable reference. This calibration requires that the ratio of backscatter to particle density is a constant.

The MLS can provide data which would require several hundred Nephelometers on 2 meter spacing.

The data rate available with the present equipment is higher than that available with the current nephelometer.

The larger sample volume of the MLS implies a greater statistical validity for the acquired data.

The data rate and resolution of the lidar for this application could be significantly improved with equipment which is available "off the Shelf".

BIBLIOGRAPHY:
Spence ,Tony and Pratt,James   (Obscurant Concentration Measurement System) OCDMS Data Report for MAGIC DRAGON TEST June 1992 ,   PSL report #93/67   Sept. 93)

Session IV Posters

ATMOSPHERIC ASSESSMENT

AN EVALUATION OF THE APRF ACOUSTIC SOUNDER AS RELATED TO THE FM-CW CALIBRATION PROCESS

John R. Hines, Scott A. McLaughlin, Frank D. Eaton
US Army Research Laboratory,
AMSRL-BE-E, WSMR, NM 88002-5501

David Vaello
Radian Corporation,
Austin, TX 78720-1088

ABSTRACT

A Doppler acoustic sounder system is used at the Atmospheric Profiler Research Facility to supplement/augment the facility's wind and refractive index structure parameter (C_n^2) measurement capability. The measured winds are used to bridge between the point sensing 150 m tower and either the 404 or 924 MHz wind profiler. In addition, C_n^2 derived from the reflected returned power is used to link the high resolution C_n^2 profile generated by the FM-CW Radar to surface measurements to effect the required calibration. This paper addresses the comparison of wind and C_n^2 measurements from the acoustic sounder, the 150 m instrumented tower and a tethered balloon system. The procedure using the measured acoustic sounder C_n^2 profile to extend and calibrate the FM-CW C_n^2 profile near the surface is discussed.

1. INTRODUCTION

The Army's Atmospheric Profiler Research Facility (APRF), located at White Sands Missile Range, NM, is designed for atmospheric research in the planetary boundary layer and up through the lower stratosphere. The APRF incorporates unique and specialized remote sensing measurement and analysis techniques to provide high resolution (spatial and temporal) profiles of wind, refractive index structure parameter (C_n^2) and virtual temperature. An array of surface and tower-mounted instrumentation as well as balloon borne instrumentation are available which supplement the specialized APRF equipment. A full description of all sensors and systems is available from the authors. An aerial view of the APRF complex is shown in Figure 1. The APRF includes as major systems a large (150-m diameter) aperture 50-MHz profiler, a 404-MHz NOAA Demonstration Network profiler, a 924-MHz boundary layer profiler, an acoustic sounder (sodar) and a FM-CW radar.

Each of the APRF wind-profiling radars (50, 404 and 924-MHz) uses three antenna beams to measure the radial speed component along the axis of each beam. One beam of

each system is directed vertically while the other two are directed off axis. The speeds along the oblique axes represent the contributions of the horizontal wind and the vertical motion. Therefore, a profile of the horizontal wind (components or speed and direction) estimate is derived upon removal of the vertical motion at each altitude spacing. Each profiler incorporates a specific altitude spacing, minimum/maximum altitude coverage above ground level (AGL), and operational cycle period as shown in Table 1.

One unique APRF product results in an integrated high resolution (spatial & temporal) wind profile derived through the selective combination of several independent and quality controlled wind profile segments generated by each of the APRF profilers. A 100 to 200-m gap exists between the minimum acceptable profiler altitude wind measurement and the available surface/tower-mounted point-sensor measurement. A Doppler sodar is successfully used at the APRF to bridge this resultant data gap and thus permit a link between the integrated remote profiler measurements and those derived from the surface and tower-mounted sensors.

In addition, the APRF's unique ultra-high resolution FM-CW Radar profiles the refractive index structure parameter (C_n^2) from 150-m to its maximum sensing altitude (2000-10000 m). The radar's inherent near-field operational characteristics precludes a continuous measurement to the surface. Sodar C_n^2 derived from the measured reflected returned power can be used to link the high resolution C_n^2 profile generated by the FM-CW to surface/tower measurements and thus contribute to the required near-field calibration.

Table 1. Key Profiler Features

Feature	50-MHz	404-MHz	924-MHz
Manufacturer	Tycho Tech.	Unisys	NOAA/ERL
Altitude Spacing (m AGL)	150	375[*]	100
Minimum/Maximum Altitude (m AGL)	2000/18480	500/8500	127/4027
Cycle Period (sec)	180	360	90
Typical Averaging Interval (min)	60	60	30

[*] low mode only

2. INSTRUMENTATION

The instrumentation used in the study includes a Sodar (sound detection and ranging), a 152-m and 20-m meteorological tower, a tethered balloon system, a 404 MHz and 924 MHz wind profiler, and a FM-CW Radar. Each type of instrumentation is discussed separately.

2.1 Sodar

The sodar used is an Echosonde model three-axis monostatic system manufactured by Radian Corporation. The three antennas have 1.5-m diameter apertures. The sodar is

typically operated at 1850 Hz and 250 W transmitted power using a 125 ms pulse length. Acoustic energy is directed 18° from the zenith toward the north and east, and vertical, thus permitting the three components of the wind vector to be resolved. Doppler derived winds are averaged over 15 min in 20 range gates, 25-m steps. Backscatter or reflected returned power measured by the vertical antenna (for deriving $C_T{}^2$) is averaged every 30 sec in 200 range gates to obtain C_n^2 from 50-700 m AGL.

Most sodar displays, typically as time-height maps, have been used to identify atmospheric features or patterns such as produced by drainage flows, frontal passages, circulation, storms or wave activity as well as diurnal variations. Some researchers obtain calibrated C_T^2 values from sodars by comparing the backscattered signals to in situ measurements of C_T^2 taken on towers. Calibration of this sodar is accomplished by relating received signal power including gains and efficiencies of the various acoustic system components to C_T^2, similar to the method used for calibrating radar returns. The troublesome problem of "excess attenuation," caused by forward beam scatter by the atmospheric turbulence and beam refraction by a horizontal wind, is not addressed. The accuracy of this calibration method is usually checked against the results determined from in situ microthermal (spatial temperature) measurements.[1]

The measured C_T^2 values are converted to the optical index of refraction structure parameter C_n^2 values by:

$$C_n^2 = C_T^2 \left[(79 \times 10^{-6}) \frac{P}{T^2} \right]^2$$

where:

P = ambient pressure (mb), and
T = ambient temperature (°K)

2.2 Tower Systems

A 152-m steel triangular mast tower is located near the APRF where eight levels of UVW anemometers (RM Young) and C_T^2 probes (ARL developed spatial temperature sensor) are measured. The C_T^2 device use two fine wire tungsten temperature probes mounted with a 0.2-m separation. Full details of the balanced D.C. bridge and associated electronics are available from the authors. Wind components or speed and direction are derived and averaged over 15 min. Optical C_n^2 is obtained using the relationship above coupled with pressure and temperature measurements from each level and usually averaged over a 15 min period. Radar C_n^2 is calculated using a method described by Eaton et al. (1988)[2].

A 20-m scaffold-type tower is located adjacent to the 50-MHz radar profiler. Two levels of C_T^2 (4 and 20 m) are obtained from identical instrumentation as that used on the 152-m tower. In addition, two path-averaging optical scintillometers (Lockheed model 4-L) are used at these two levels to provide a direct measurement of optical C_n^2. The sources for the double-ended scintillometers are located at 330 and 1000 m horizontal distances, respectively. See Table 2 for selected key features.

2.3 Tethered Balloon System

A tethered balloon system used provides in situ measurements of ambient temperature, humidity, pressure, wind speed and direction, and C_T^2. Measurements are taken in different modes: slow ascent and descent, rapid ascent or descent to altitudes of interest and sensing

for a few minutes at each altitude, or maintaining the sensing package at an altitude for approximately one-half hour.

The system is a boundary layer sounding system manufactured by Atmospheric Instrumentation Research, Inc. (A.I.R.) with the exception of the C_T^2 sensor. The sounding system sensor package, Tethersonde, measures dry-bulb and wet-bulb temperatures using precision matched thermistors, barometric pressure by a temperature compensated aneroid sensor, wind speed using a 3-cup anemometer, and wind direction with a magnetic compass. Spare channels are available for specialized instrumentation such as the C_T^2 sensor. C_T^2 is measured by an ARL developed sensor using two fine wire tungsten temperature probes mounted with a 1-m separation and a miniaturized electronics package similar to that used on the tower system. All parameters are averaged over a 15 min period. Optical and radar C_n^2 are calculated identically as previously described. Refer to Table 2 for selected features.

Table 2. Key Tower and Tethersonde $C_T{}^2$ Features

Feature	152-m Tower	20-m Tower	Tethersonde
Manufacturer	RM Young ARL	RM Young ARL	A.I.R. ARL
Altitude Spacing (m AGL)	7,22,37,52, 67,90,120, 152	4,20	N/A
Minimum/Maximum Altitude (m AGL)	point	point	0-2000
Cycle Period (sec)	10	10	10
Typical Averaging Interval (min)	15	15	15

The data is telemetered to an Atmospheric Data Acquisition System (ADAS) for data acquisition and real-time computation. A blimp-shaped balloon, either 5.25 m^3 or 7.50 m^3, is used to lift the sounding package. A line connects the balloon to a winch with variable speed for controlling the package altitudes.

2.4 404-MHz and 924-MHz Wind Profiler

The 404-MHz wind profiler used is a NOAA Demonstration Network model three-axis system manufactured by UNISYS. This system is one of 31 identical profilers deployed about the central part of the United States by the National Weather Service to evaluate profiler effectiveness and operation. The phased-array antenna, 170 m^2, directs three beams vertically. Through a 6-min sequential operation cycle, the reflected return power along two oblique beams tilted at a 16° angle from zenith and a vertical beam is measured to derive the horizontal wind field at specific gated spacings. The minimum acceptable altitude measured by the 404-MHz profiler is 500-m.

The 924-MHz wind profiler used is a boundary layer model three-axis system fabricated by NOAA-Wave Propagation Laboratory. This system is similar to the LAP-4000, currently available through Radian Corporation. Three micro-strip antenna panels, approximately 10 m^2

total, directs three beams vertically. Through a 90-sec sequential operation cycle, the reflected return power along two oblique beams tilted at a 15° angle from zenith and a vertical beam is measured to derive the horizontal wind field at specific gated spacings. The minimum acceptable altitude measured by the 924-MHz profiler is 200-m. Refer to Table 1 for selected key features.

2.5 FM-CW Radar

The FM-CW radar used is a unique ultra-high resolution C_n^2 system manufactured by Radian Corporation. The radar is designed for studying the boundary layer and lower troposphere phenomena. State-of-the-art technology is incorporated throughout enhancing the temporal and spatial resolution and allowing for a more precise calibration. The highly linear FM sweep is generated with a frequency synthesized source. All data collection, system calibration, and processing is performed in real-time. The characteristics of the FM-CW radar; high resolution, ultra sensitivity, accurate calibration and sensing near the ground, are crucial for modern experimental programs in the boundary layer.

As shown in Figure 2, the FM-CW radar system consists of two trailers, one for the data processing/electronics equipment, the other for the antennas. The two identical ten-foot diameter antennas, one transmitting and one receiving, are mounted on a fully steerable mount. The antennas can be directed vertically (or lower, e.g. slant path measurements) for high resolution backscatter profiling. The radar uses a phased-locked-loop digital frequency synthesizer to obtain a highly linear, very low noise 200-MHz sweep over 50ms as a "sawtooth" wave centered at 2.9-GHz. The final amplifier is a traveling-wave-tube (TWT), with a continuous 220W output. The radar sweeps and takes data continuously, processing all data real-time using an Analogic 16-bit Analog-Digital-Convertor coupled to a Analogic Array Processor combined with a Hewlett-Packard (HP) 1000 minicomputer. Data is written to tape or disk, graphically to video screens, and in a color FAX type display to a HP PaintJet. The FM-CW RF and data flow diagram is shown in Figure 3. The electronic calibration is performed by taking an attenuated known sample of the transmitted signal, delaying it in a electro-acoustic delay line (equivalent to a target at 675-m), and coupling it into the receiver. Thus the system can be calibrated from the receiver forward, including the digital signal processing, by using this test signal and the resultant output. The gain of the r-f preamplifier, antennas, and attenuation of the cable assemblies is measured to complete the calibration. Table 3 displays some of the key FM-CW radar features.

Absolute calibration of the FM-CW radar system for the far field is necessary to relate returned signal power to radar C_n^2. The far field calibration procedure is discussed in Eaton et al. (1993)[3].

The antenna autocorrelation term accounts for the changing overlap of the transmit and receive beams due to the bistatic side-by-side arrangement of the two antennas. This correction is calculated from the autocorrelation function of the two identical antenna patterns. For ranges less than about 500-m, correct C_n^2 calibration depends strongly on accurate knowledge of the antenna autocorrelation. Below approximately 100-m, the weighting function goes to zero. However, the weighting function uses the antenna far-field patterns, and thus is only valid above about 180-m. The weighting function is currently applied to the data below 180-m to improve data clarity for review purposes. An empirical correction for low altitudes is necessary utilizing C_n^2 measurements taken from a calibrated sodar, tower measurements, and a tethered balloon.

821

Table 3. Key Features of the FM-CW Radar

Feature	Value
Operating Frequency/Wavelength	2.9 GHz, ± 100 MHz / 10 cm
Minimum/Maximum Altitude (m)	150 / 1000 to 10000
Spatial Resolution (m)	1 to 10
Temporal Resolution (sec)	6 to 12
Number of Gates	1024
Antenna Type Antenna 3 dB Beamwidth	parabolic 2.7°
Minimum Detectable Signal	-165 dBm

3. RESULTS AND DISCUSSION

Examples of boundary layer wind speed and wind direction profiles are shown from measurements taken with a 924-MHz profiler, a sodar and a fixed 152-m tower under daytime and nighttime conditions. The daytime measurements include occasions of desert-floor generated convective-plume interference to the 924-MHz profiler vertical beam correction algorithm. The nighttime measurements may include errors induced by bird and insect migrations as detected by the 924-MHz profiler. Five examples of APRF system comparisons are shown in Figures 4 through 8. Figure 4 depicts the diurnal variation of wind (speed and direction) as measured with a 924-MHz profiler and tower-mounted anemometers. Volume averaged anemometer data agree reasonably well with the data from the lowest gate of the 924-MHz profiler. Figures 5 and 6 depict vertical profiles of wind speed and wind direction as measured with a 924-MHz profiler and a sodar. Under low wind speed conditions, the sodar and 924-MHz profiler data agree moderately well. Figure 7 depicts vertical profiles of wind speed and wind direction as measured with a 924-MHz profiler and a 404-MHz profiler. Both systems appear to depict the measured wind shift quite well. Figure 8 depicts the diurnal variability of wind (speed and direction) at a fixed height (150-m) as measured by the sodar (volume-averaged) and an anemometer. On occasion, sodar and tower wind data agree quite well up to 150-m AGL and beyond. From these data examples, it is evident that the apparent gap in the APRF integrated wind profile can be filled.

An example of radar backscatter (radar reflectivity) as measured with the FM-CW radar is shown in Figure 9. An example of temperature induced backscatter as measured with the sodar is shown in Figure 10. Complex atmospheric wave structures were detected by both systems.

Figure 11 depicts the diurnal variability of C_n^2 at a fixed height (91-m) as measured by the sodar and the 152-m tower on 23 Oct 91. Figure 12 depicts the diurnal variability of C_n^2 at a fixed height (23-m) as measured by the sodar and the 152-m tower on 15 Jan 92. The two profiles compare reasonably well. These results show excellent agreement in C_n^2 by intercomparisons using different measurement techniques (sodar, tower, and tethersonde). These data are necessary for providing empirical C_n^2 calibrations in the near field using the FM-CW Radar techniques.

4. REFERENCES

Forbes, F. F., E. S. Barker, K. R. Peterman, D. D. Cudaback, and D. A. Morse, 1985. High-Altitude Acoustic Soundings. *Conference Workshop on the Effects on the Environment on Systems Performance at the 1985 Technical Symposium East*, Arlington, VA, 8-10 Apr 1985, SPIE vol. 547, pp. 75-85.

Eaton, F. D., W. A. Peterson, J. R. Hines, K. R. Peterman, R. E. Good, R. R. Beland, and J. H. Brown, 1988. Comparisons of VHF Radar, Optical and Temperature Fluctuation Measurements of C_n^2, r_o and θ_o. Theoretical and Applied Climatology, vol 39, pp. 17-29.

Eaton, F. D., S. A. McLaughlin, J. R. Hines, J. J. Drexler, D. B. Soules, J. Qualtrough, 1993. Variability of Atmospheric Turbidity and the Refractive Index Structure Parameter (C_n^2). *Battlefield Atmospherics Conference*, 30 Nov 1993.
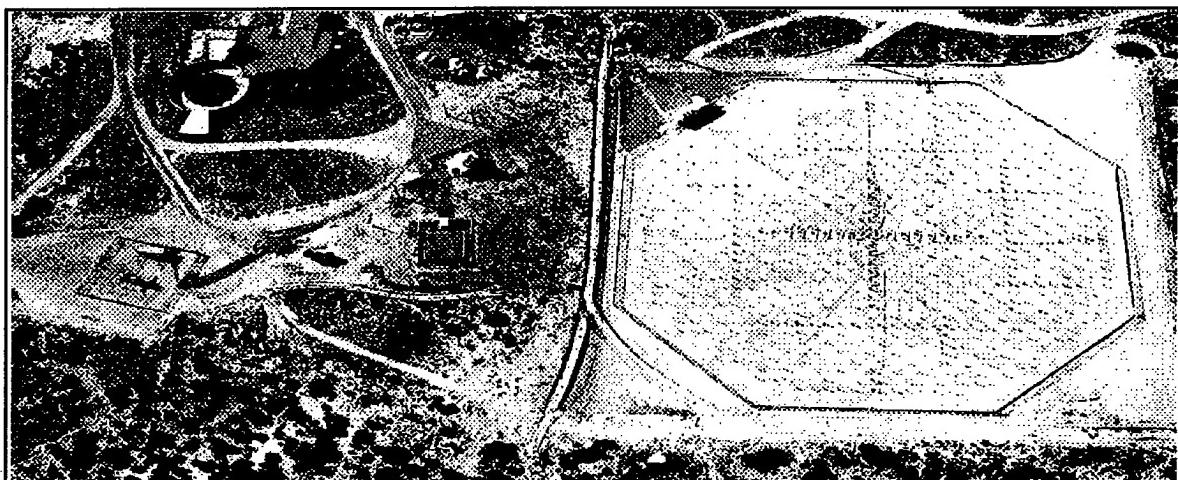
Figure 1. Aerial view of the Atmospheric Profiler Research Facility. The FM-CW radar is located at the extreme left; the 50 MHz is right-center.
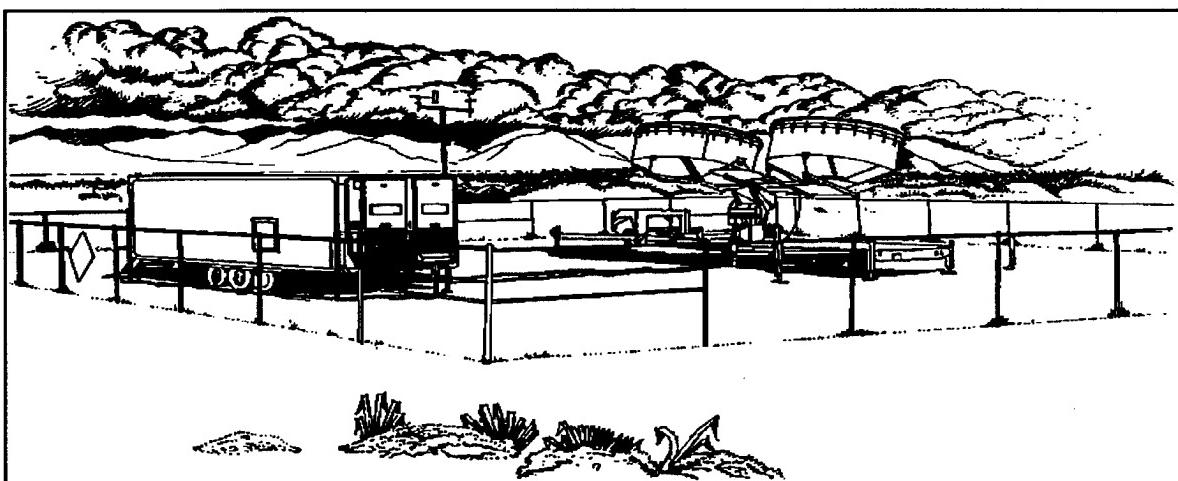
Figure 2. Artist sketch of the ARL FM-CW radar.
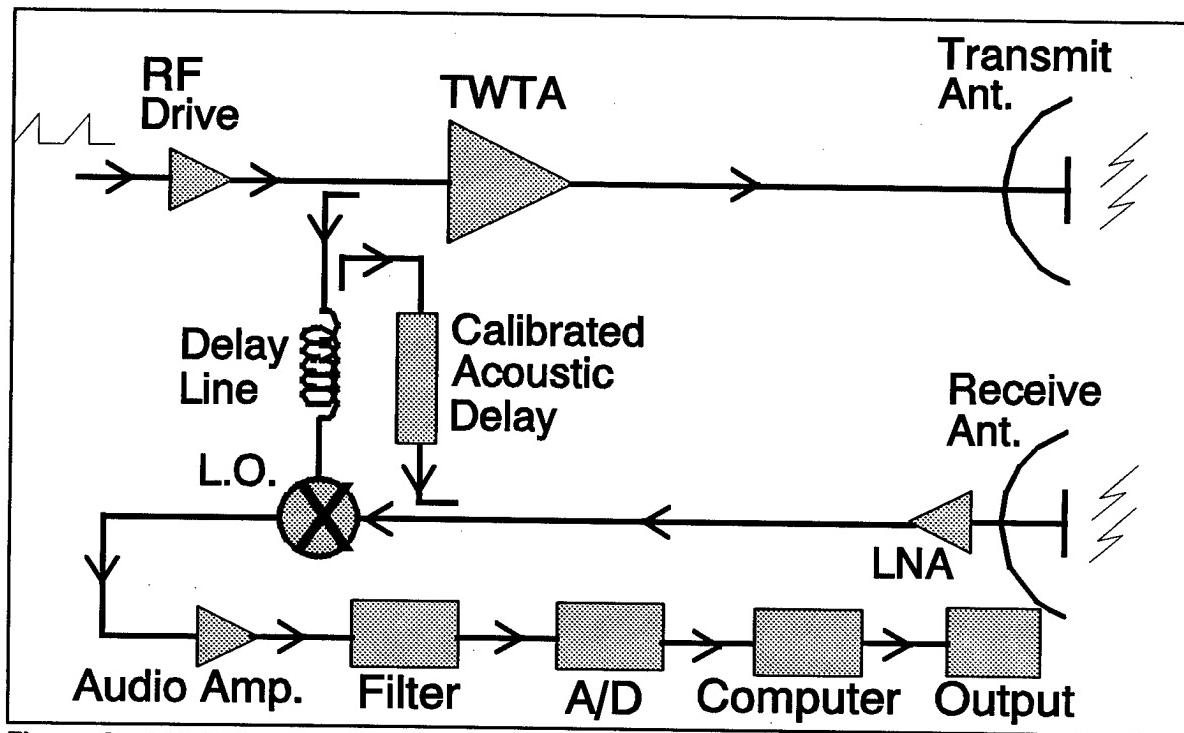
Figure 3. FM-CW radar RF and data flow diagram.
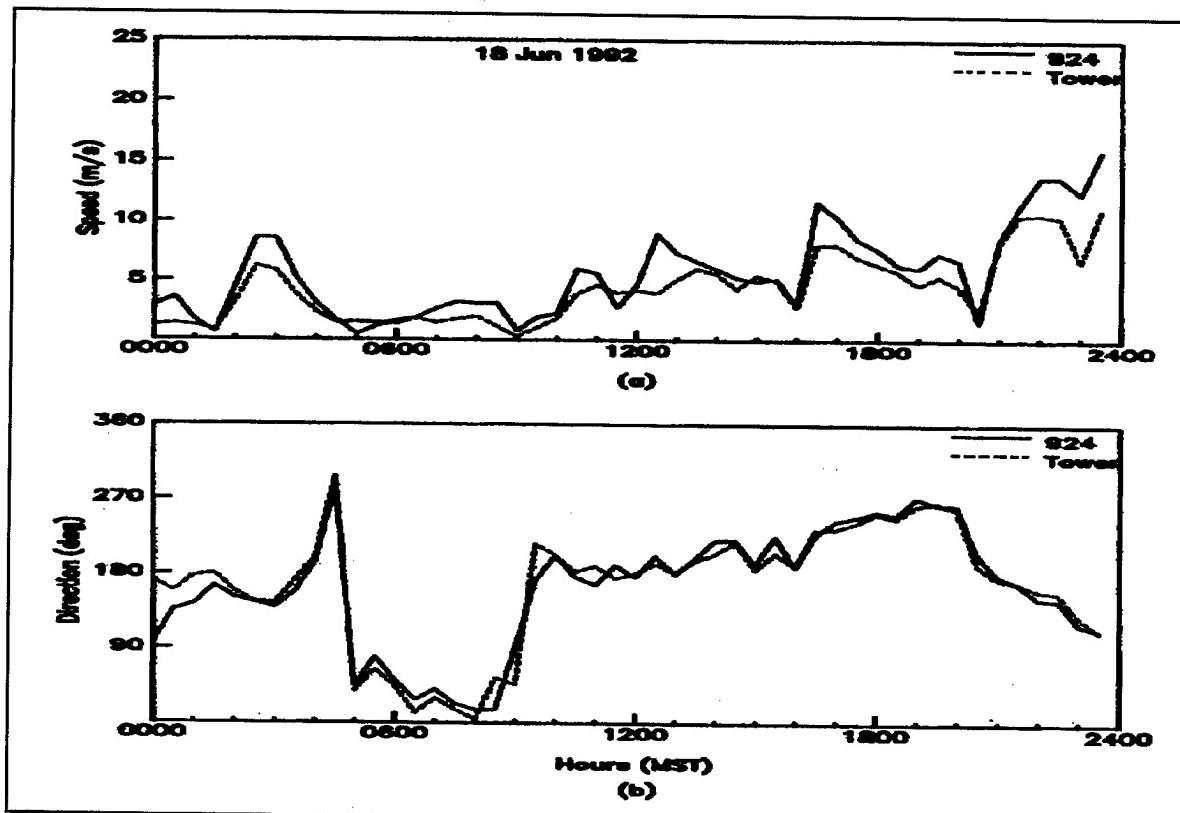
Figure 4. Diurnal variation of (a) wind speed and (b) wind direction as measured with a 924-MHz profiler at 120-m AGL and tower-mounted anemometers at 90, 120, and 150-m AGL on 18 Jun 92 (15-min averages).
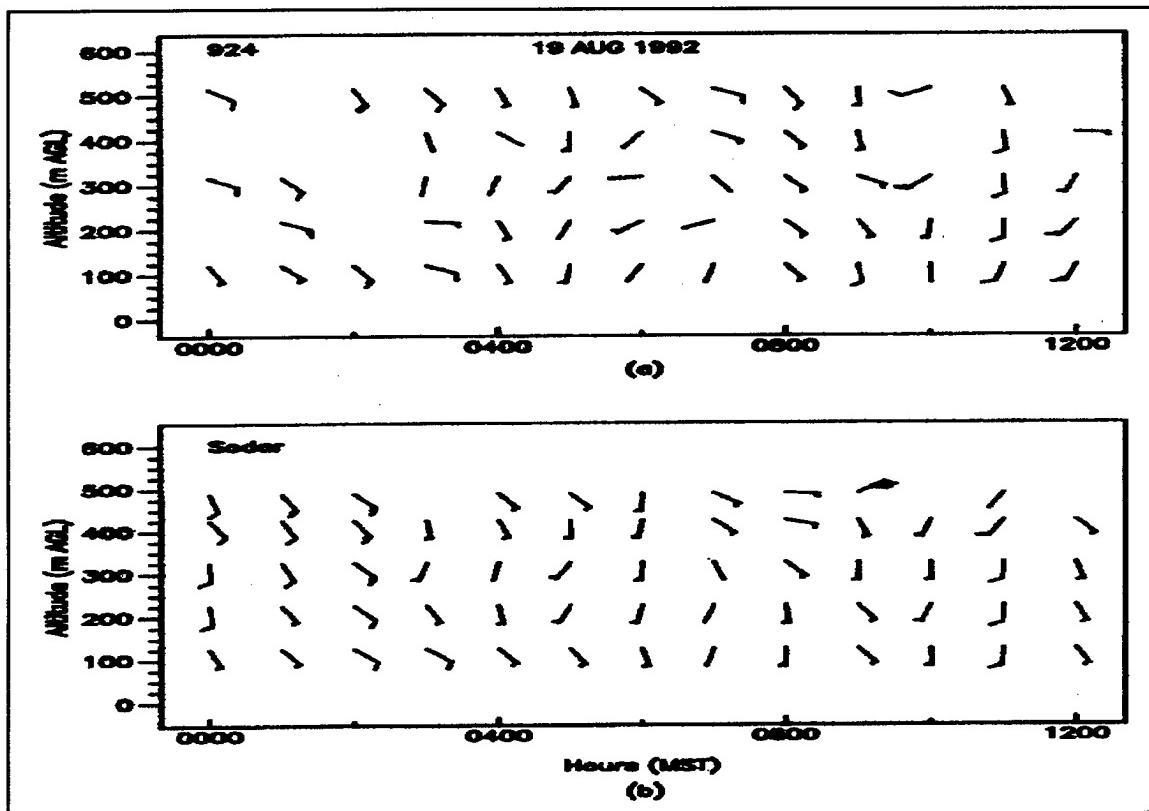
Figure 5. Vertical profiles of wind speed and wind direction, as measured with (a) a 924-MHz profiler and (b) a sodar, APRF site, 0000 to 1200 MST, 19 Aug 92 (15-min averages).
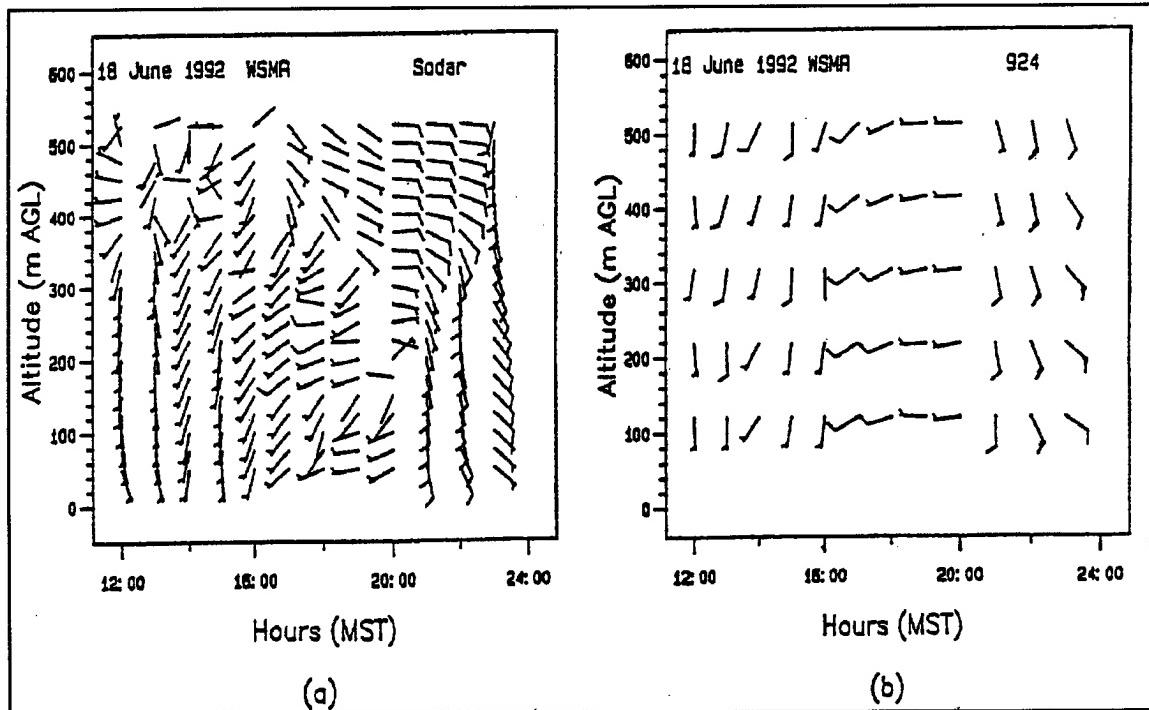
Figure 6. Comparative horizontal wind measurements from the (a) sodar and (b) 924 MHz profiler.
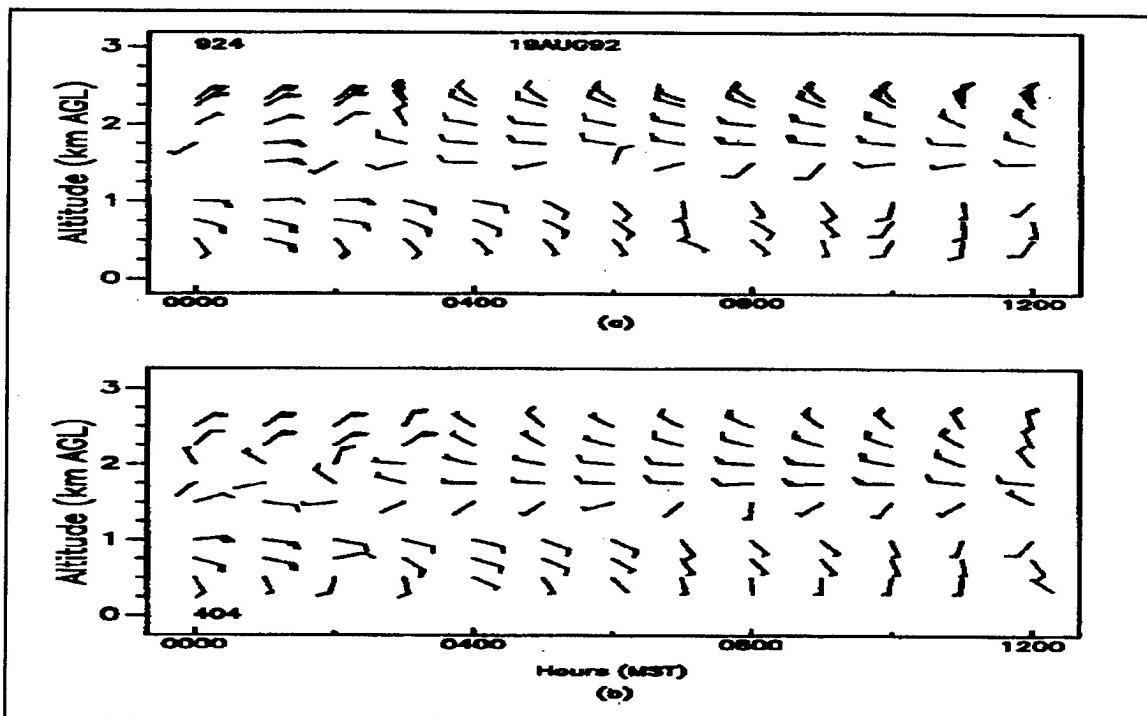
Figure 7. Vertical profiles of wind speed and wind direction, as measured with (a) a 924-MHz profiler and (b) a 404-MHz profiler, APRF site, 0000 to 1200 MST, 19 Aug 92 (1-hr averages).
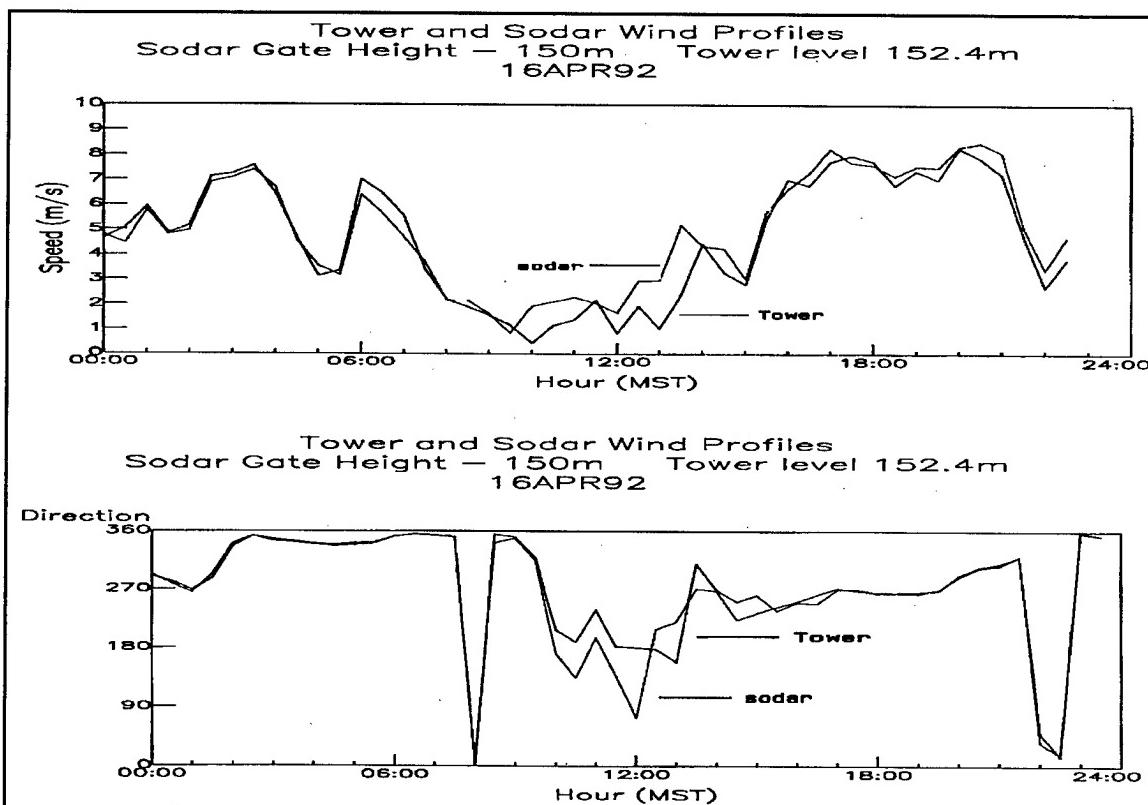
Figure 8. Diurnal variability of wind (speed and direction) at a fixed height (150-m) as measured by a anemometer and a sodar, 16 Apr 92.
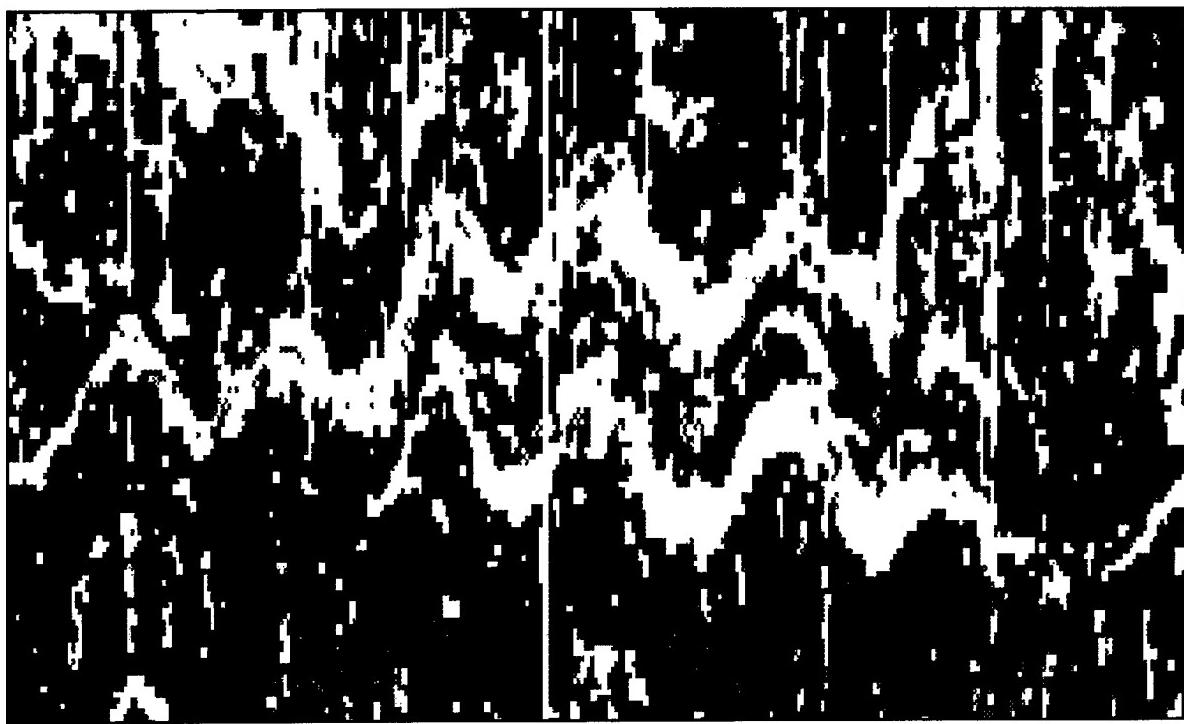
Figure 9. FM-CW radar measured atmospheric wave activity between 0730 and 0820 GMT on 27 Oct 92 at the APRF.
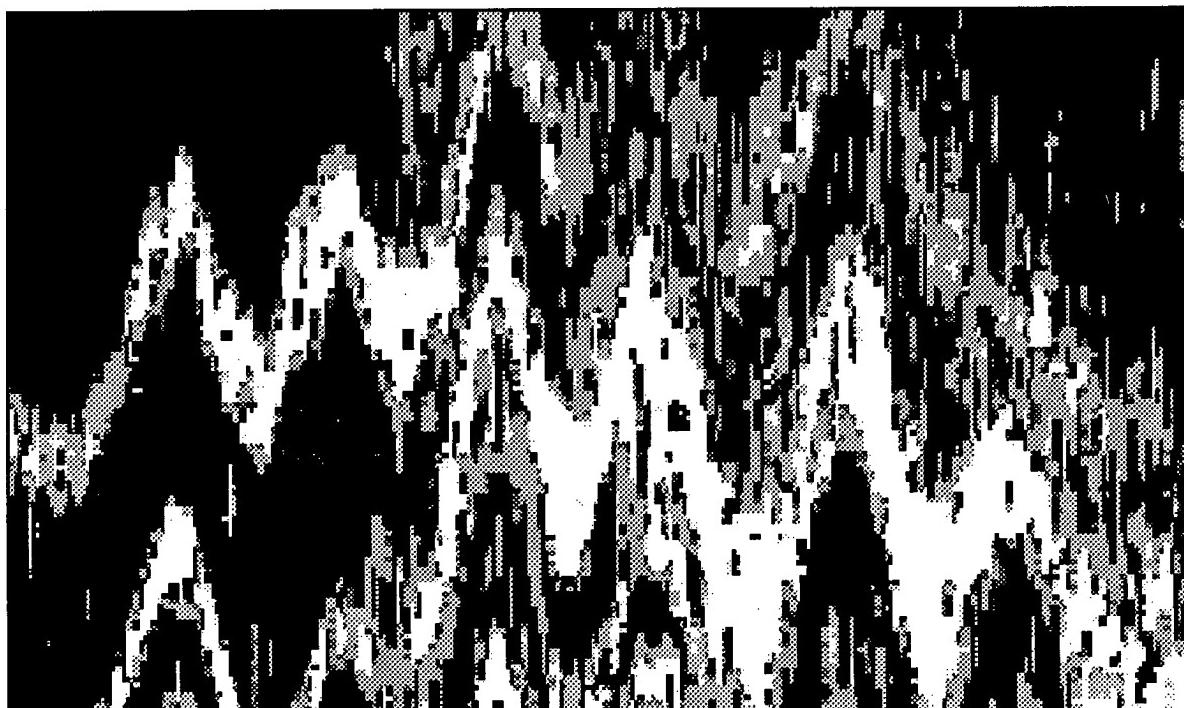
Figure 10. Acoustic sounder measured atmospheric wave activity between 0730 and 0820 GMT on 27 Oct 92 at the APRF.
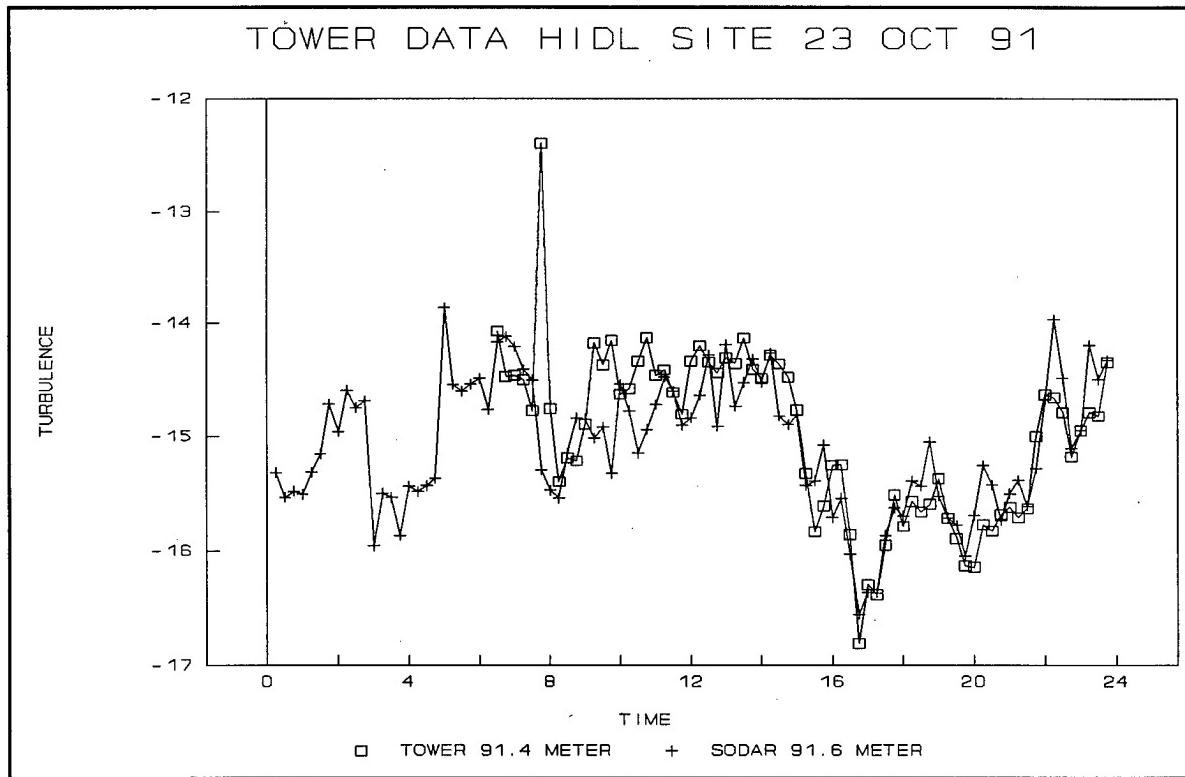
Figure 11. Diurnal variability of C_n^2 at 91-m as measured by the sodar and a point C_T^2 sensor on the 152-m tower, 23 Oct 91.
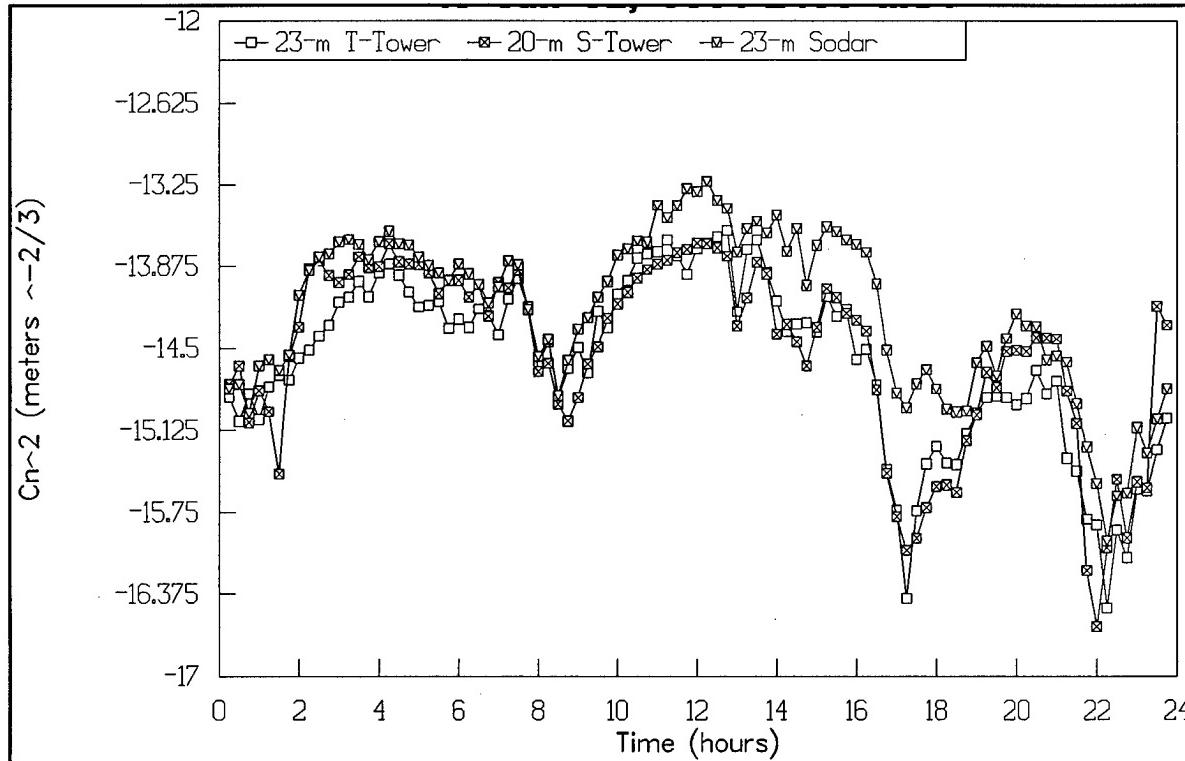
Figure 12. Diurnal variability of C_n^2 at 23-m as measured by the sodar and a point C_T^2 sensor on the 152-m tower, 15 Jan 92.

CHARACTERIZATION OF THE WIND FIELD AT AERIAL CABLE TEST CAPABILITY SITE

R. J. Okrasinski
Physical Science Laboratory
New Mexico State University
Las Cruces, New Mexico, 88003-0002, USA

R. O. Olsen
Battlefield Environment Directorate
U.S. Army Research Laboratory
White Sands Missile Range, New Mexico 88002-5501, USA

ABSTRACT

The U.S. Army is building a new test facility in the north central part of White Sands Missile Range called the Aerial Cable Test Capability. It will consist of a cable, approximately five kilometers long, hung several hundred meters above a test range. Targets will be either suspended or dropped from a trolley moving along the cable during various battlefield simulations. In the winter and spring of 1992, several months of atmospheric data were collected by four meteorological towers and a Doppler sodar deployed in the area. Results of an analysis of the wind data are presented to show the characteristics of the wind field and to help decide which meteorological instrumentation should be installed at the facility for operational support.

1. INTRODUCTION

A new facility, known as the Aerial Cable Test Capability (ACTC), is being installed on White Sands Missile Range. It will consist of an cable, approximately 5 km long, hung several hundred meters above the ground. During various battlefield simulations, targets will be either suspended or dropped from a trolley moving along the cable. The trolley will be capable of accelerations to approximately 150 knots by gravity or up to 500 knots by rockets. Trolley and target combined may weigh up to 7000 pounds.

The ACTC will be used for approximately 400 tests per year. About 20% of the tests will involve a missile firing from a ground-based launcher toward a suspended target, and the remainder will

FIGURE 1

Conceptual Operations at Aerial Cable Test Capability[1]
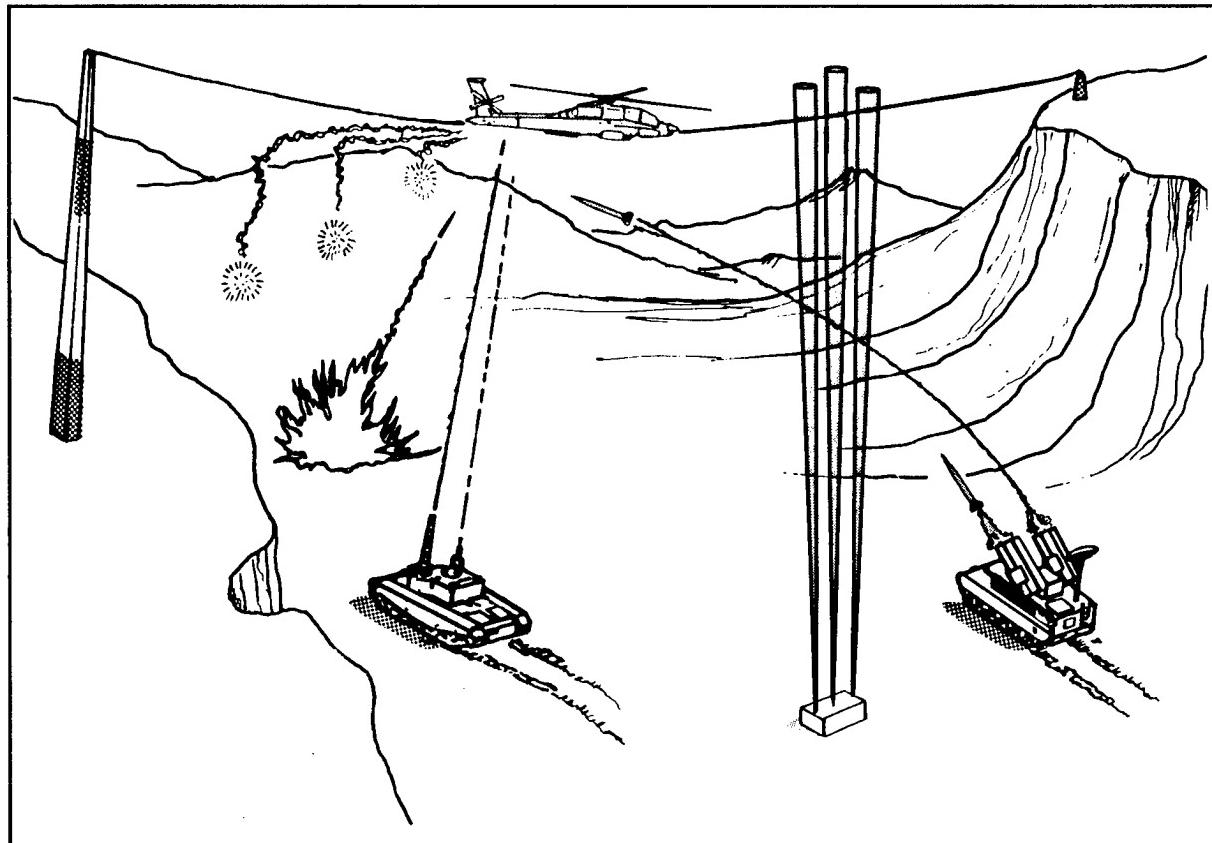
involve items dropped from the trolley to simulate airborne delivery. An artist's conception of a test using a suspended target is shown in Figure 1. An optional remote sensor, measuring winds between the surface and cable, is pictured in the lower right side of the diagram. Using the cable will be much faster and less expensive than flying remotely controlled targets or dropping material from aircraft.

The ACTC will be located approximately 8 km northeast of Mockingbird Gap in the north central part of White Sands Missile Range. The upper anchor of the cable will be at Jim Site on the crest of the Oscura Mountains at 2530 m above mean sea level (msl), and the lower anchor will be in the Little Burro Mountains at 1830 m msl. The missile impact area occupies the valley floor in between which slopes from 1700 m to 1330 m msl. Vegetation in the area is typical of the southwestern U.S. desert. A more detailed description of the ACTC and its surrounding area is given in the environmental impact statement.[2]

During the winter and spring of 1992, four meteorological towers and a Doppler sodar were deployed by the U.S. Army Research

Laboratory to measure surface and upper-air winds in the vicinity of the new facility. In this paper, a statistical summary of the collected wind data is presented to show the characteristics of the wind field and to help decide which meteorological instrumentation should be installed at the ACTC for operational support.

2. INSTRUMENTATION AND DATA COLLECTION

2.1 SAMS

Surface data were collected by four Surface Atmospheric Measurement Systems (SAMS). Each SAMS consists of a 10-m mast instrumented with standard meteorological sensors. One mast was situated near the upper anchor at Jim Site (2576 m msl), and two others were deployed at Yaw Line (1646 m msl) and Little Burro (1591 m msl) in the valley to the east. Yaw Line was located near the center of the valley, and Little Burro was situated at the western end, closer to the lower anchor. The remaining tower, at Mockingbird Gap (1633 m msl), was several kilometers southwest of the area on the opposite side of the Little Burro Mountains.

Two-meter wind speed and direction, measured at each tower by a wind vane and a propeller anemometer, were processed by SAMS reduction programs to calculate one-hour averaged wind speeds and directions and one-hour peak wind gusts for each hour of the day. This information was available for the Yaw Line, Jim Site, and Little Burro stations between February 1 and April 30, 1992 and for Mockingbird Gap between February 1 and June 23, 1992.

2.2 SODAR

Upper-air wind data were collected by a phased-array Doppler sodar. This device remotely measures wind parameters using acoustic sounding. One vertical and two tilted beams are transmitted upward. Changes in the acoustic refractive index caused by temperature fluctuations scatter some of this energy back to the antennas. Doppler shifts in the backscattered signals determine the radial wind velocity along each beam. These velocities are then used to calculate horizontal wind speeds and directions. Wind data can be measured at heights between 50 m and several hundred meters above the surface continuously for several days without human attention.

The sodar was situated near Yaw Line from February 19 to March 31, 1992 and was powered by a solar panel. Solar powering proved unsuccessful, however, so the sodar was moved to Mockingbird Gap, where hard power was available, and operated there from April 15 to May 26, 1992 and again from June 17 to June 23, 1992. Fifteen-minute averaged wind data were collected at 15 heights, 50 m apart, from 50 m to 750 m above the surface.

FIGURE 2

Scalar Average Wind Speed Versus Time of Day

WHITE SANDS MISSILE RANGE
FEBRUARY 01 — APRIL 30, 1992
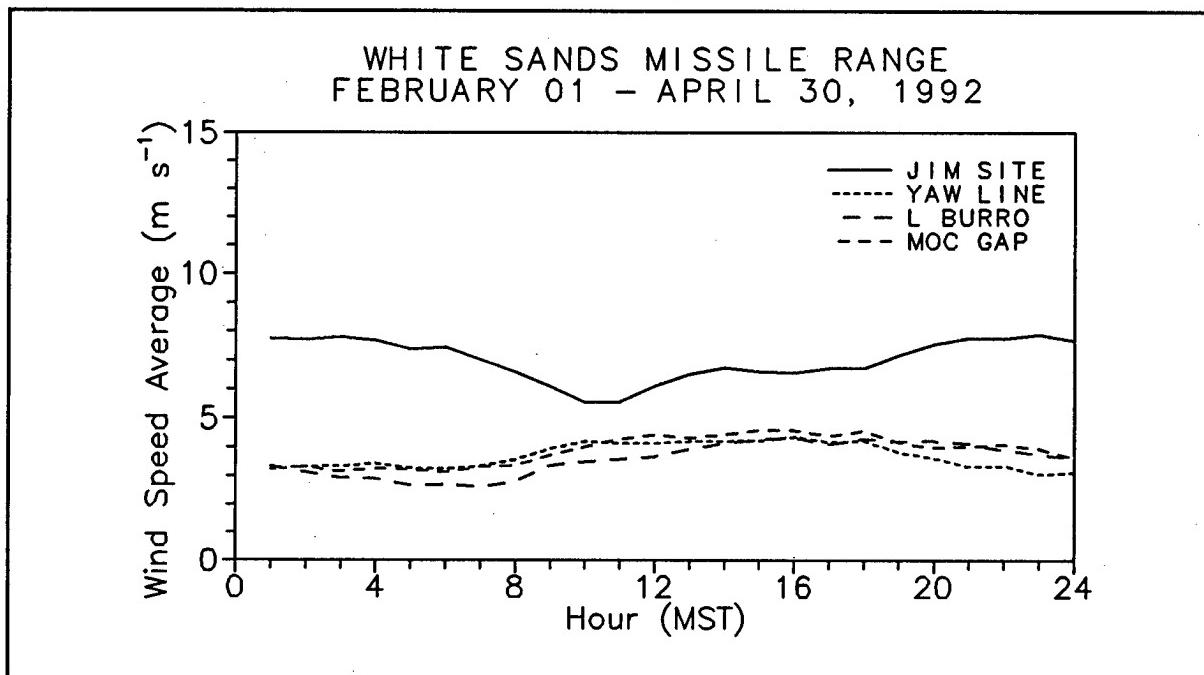
3. SAMS DATA ANALYSIS

Surface winds at the future ACTC were statistically characterized using the one-hour data collected during February, March, and April at the four SAMS stations. Scalar average wind speeds and peak wind gusts, calculated for each hour of the day, are plotted in Figures 2 and 3. Average wind speeds at the three valley locations were comparable, ranging from about 3 m s^{-1} in the morning to 4-4.5 m s^{-1} during late afternoon. The average Jim Site winds, at the upper anchor, were between 5.5 m s^{-1} and 8 m s^{-1}. Unlike the other three stations, these winds were highest in the late evening and early morning and lowest during late morning. The highest wind gusts at the four stations ranged from 15 m s^{-1} to 39 m s^{-1}.

Frequency distributions of wind speed and direction were also computed and are shown in Figure 4 and Table 1, respectively. Table 1 also contains the scalar mean wind speeds and maximum and minimum wind speeds for each of the eight wind direction categories. Again, wind speed statistics for the three valley sites were comparable, but the Jim Site winds were higher. There was somewhat less agreement in wind direction. Most of the Jim Site winds were from the southwest to northwest. The Yaw Line winds were most frequently from the north and southeast. The Little Burro winds were more evenly distributed, but most frequently blew from the southwest, and the Mockingbird Gap winds

FIGURE 3

Highest Wind Gust Versus Time of Day

WHITE SANDS MISSILE RANGE
FEBRUARY 01 – APRIL 30, 1992
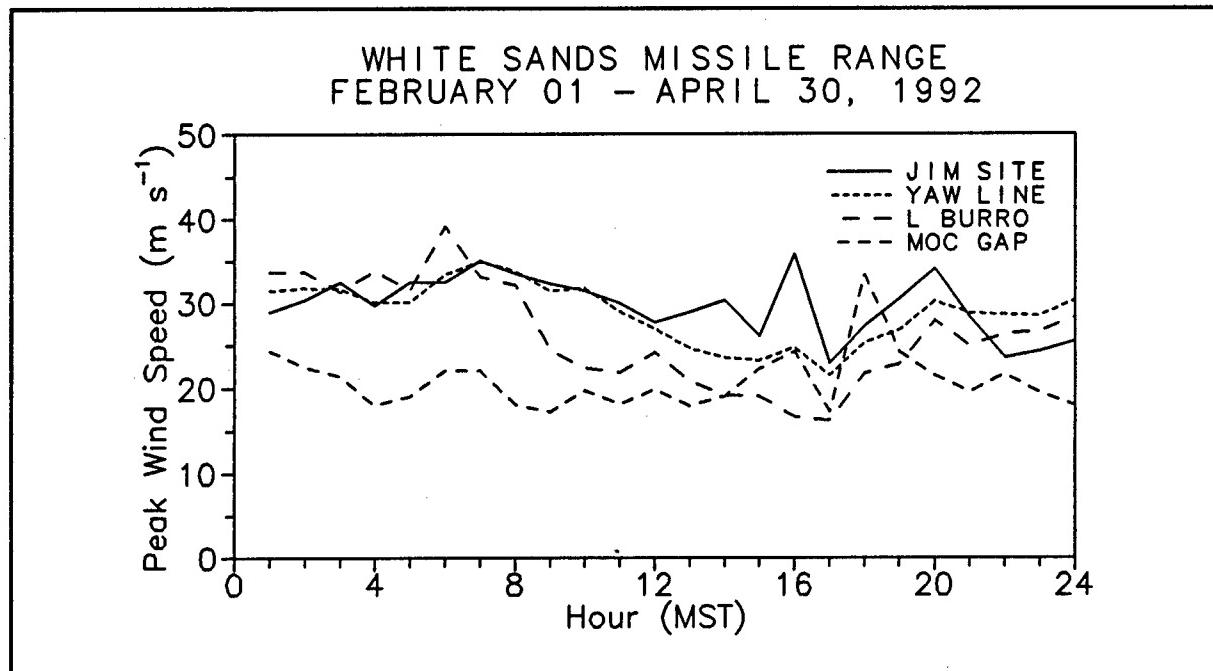
FIGURE 4

Frequency Distribution of Wind Speed

WHITE SANDS MISSILE RANGE
FEBRUARY 01 – APRIL 30, 1992
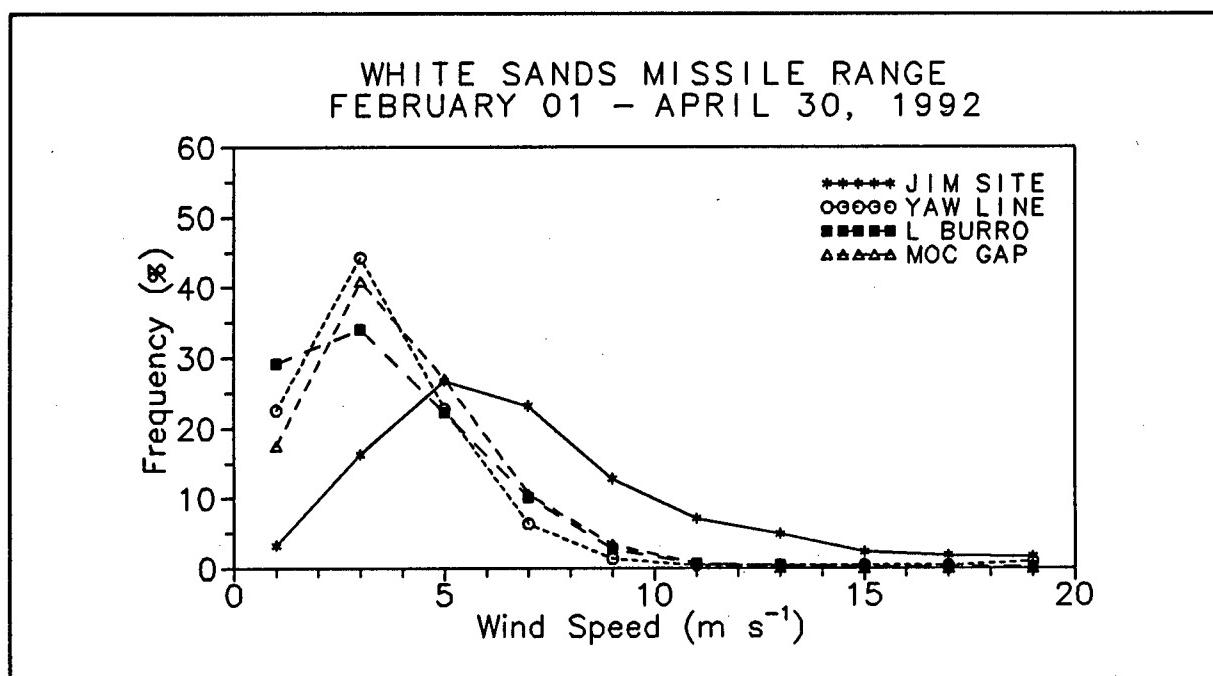
TABLE 1

SAMS Wind Data Statistics

DIRECTION	FREQ (%)	WIND SPEED $(m\ s^{-1})$		
		MEAN	MAX	MIN

JIM SITE

DIRECTION	FREQ (%)	MEAN	MAX	MIN
N	3	5.4	11.2	1.0
NE	6	8.9	26.8	1.3
E	5	8.3	20.7	1.6
SE	2	5.3	12.3	1.1
S	16	5.3	11.0	1.2
SW	26	6.7	19.8	.9
W	24	7.8	20.3	1.3
NW	18	7.6	19.6	.6

YAW LINE

DIRECTION	FREQ (%)	MEAN	MAX	MIN
N	22	3.8	13.3	.4
NE	8	6.8	20.5	.5
E	6	3.1	17.9	.3
SE	26	2.8	7.5	.4
S	12	3.6	8.6	.7
SW	4	3.3	6.5	.6
W	8	3.6	9.0	1.0
NW	14	3.9	9.2	.6

LITTLE BURRO

DIRECTION	FREQ (%)	MEAN	MAX	MIN
N	9	3.2	8.6	.3
NE	9	5.0	17.6	.5
E	12	3.9	18.4	.4
SE	12	3.4	19.2	.4
S	14	3.3	10.3	.4
SW	21	3.7	10.0	.3
W	10	3.0	10.1	.5
NW	13	3.3	10.1	.6

TABLE 1 (Continued)

SAMS Wind Data Statistics

DIRECTION	FREQ (%)	WIND SPEED (m s^{-1})		
		MEAN	MAX	MIN

MOCKINGBIRD GAP

DIRECTION	FREQ (%)	MEAN	MAX	MIN
N	24	4.3	11.1	.6
NE	3	2.7	7.3	.8
E	3	5.6	12.4	.8
SE	4	3.1	8.6	.9
S	22	3.9	10.5	.6
SW	20	3.3	10.2	.6
W	8	3.9	10.0	.5
NW	15	4.2	10.0	.5

were primarily from the north, south, and southwest. The strongest average winds were from the northeast at Jim Site, Yaw Line, and Little Burro, and from the east at Mockingbird Gap. The highest one-hour averaged wind was 26.8 m s^{-1} from the northeast at Jim Site.

4. SODAR DATA ANALYSIS

Figure 5 shows the percent 15-minute averaged wind data successfully collected by the sodar as a function of height when it was operated at Yaw Line using solar power between February 19 and March 31 and after it was moved to Mockingbird Gap on April 15 and run on hard power. The diagram illustrates the great improvement in sodar functioning after it was relocated. Wind data were successfully measured at least

FIGURE 5

Percent Sodar Wind Data Collected
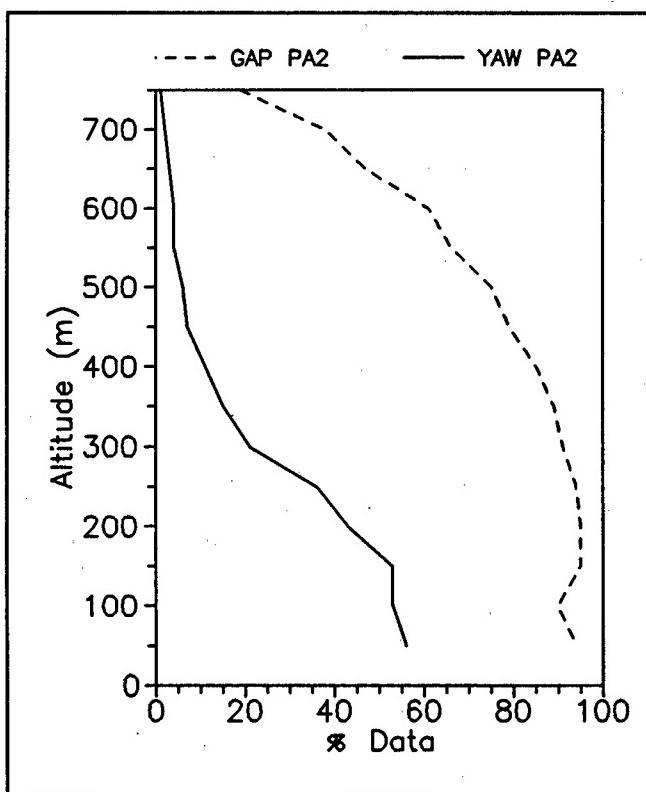
TABLE 2

Statistics of Sodar Wind Data Collected at Mockingbird Gap

DIRECTION	FREQ (%)	WIND SPEED (m s^{-1})		
		MEAN	MAX	MIN
50-300 M				
N	5	7.2	27.8	.0
NE	3	5.5	20.5	.2
E	6	4.8	25.1	.1
SE	30	4.6	13.8	.0
S	18	5.9	28.2	.1
SW	9	5.0	18.7	.2
W	10	6.5	17.8	.1
NW	18	5.1	28.5	.1
350-600 M				
N	6	7.7	27.9	.1
NE	4	4.5	21.0	.1
E	6	5.0	25.0	.1
SE	17	5.1	14.7	.0
S	27	6.5	28.5	.2
SW	14	4.7	23.6	.3
W	13	6.1	20.4	.1
NW	13	5.8	28.6	.0

75% of the time at Mockingbird Gap at heights up to 500 m.

Using the Mockingbird Gap measurements, wind direction frequencies, scalar mean wind speeds, and maximum and minimum wind speeds were calculated for eight wind directions. The results are listed in Table 2 for data collected between 50 m and 300 m and 350 m and 600 m.

Wind speed statistics for the two layers are similar. Mean sodar wind speeds ranged between 4.7 m s^{-1} and 7.7 m s^{-1}. The highest average winds were from the north, and the strongest 15-minute averaged wind was 28.6 m s^{-1} from the northwest. The wind direction frequencies at the two heights were also comparable. In the lower layer, however, the most common direction was southeast, but southerly winds were more frequent between 350 m and 600 m.

FIGURE 6

Jim Site and 400-m Sodar Average Wind Speed Versus Time of Day

400M SODAR AND JIM SITE
APRIL 16-30, 1992
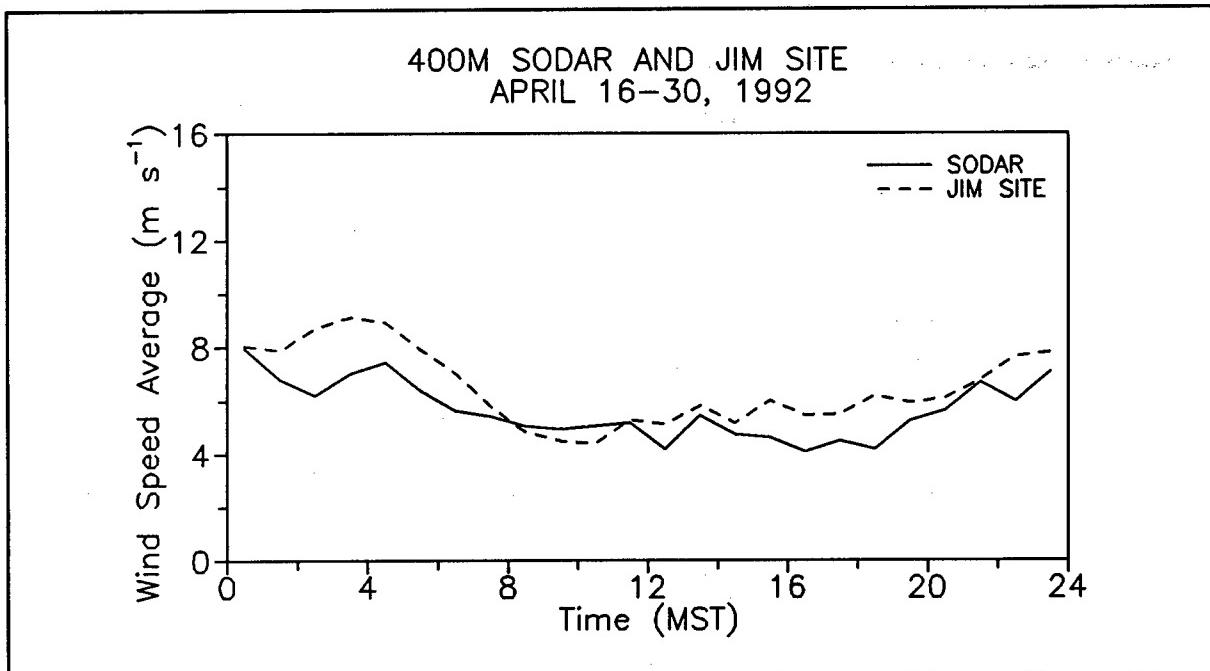
5. COMPARISON OF SAMS AND SODAR DATA

To determine how well the Jim Site SAMS measurements agree with winds expected above the valley floor at the height of the cable, they were statistically compared with conjunctive 400-m sodar data collected at Mockingbird Gap between April 16 and 30. The 15-minute averaged sodar measurements were first averaged over each hour to match the temporal resolution of the SAMS data. Using the two one-hour averaged data sets, scalar average wind speeds for each hour of the day and frequency distributions of wind speed and direction were then computed. The results are plotted in Figures 6-8. Agreement between the sodar and SAMS wind speeds was fairly good, but there were some differences in wind direction. Compared to the Jim Site measurements, the sodar winds were more frequently from the south and less frequently from the southwest and west.

FIGURE 7

Frequency Distribution of Jim Site and 400-m Sodar Wind Speeds

400M SODAR AND JIM SITE
APRIL 16-30, 1992
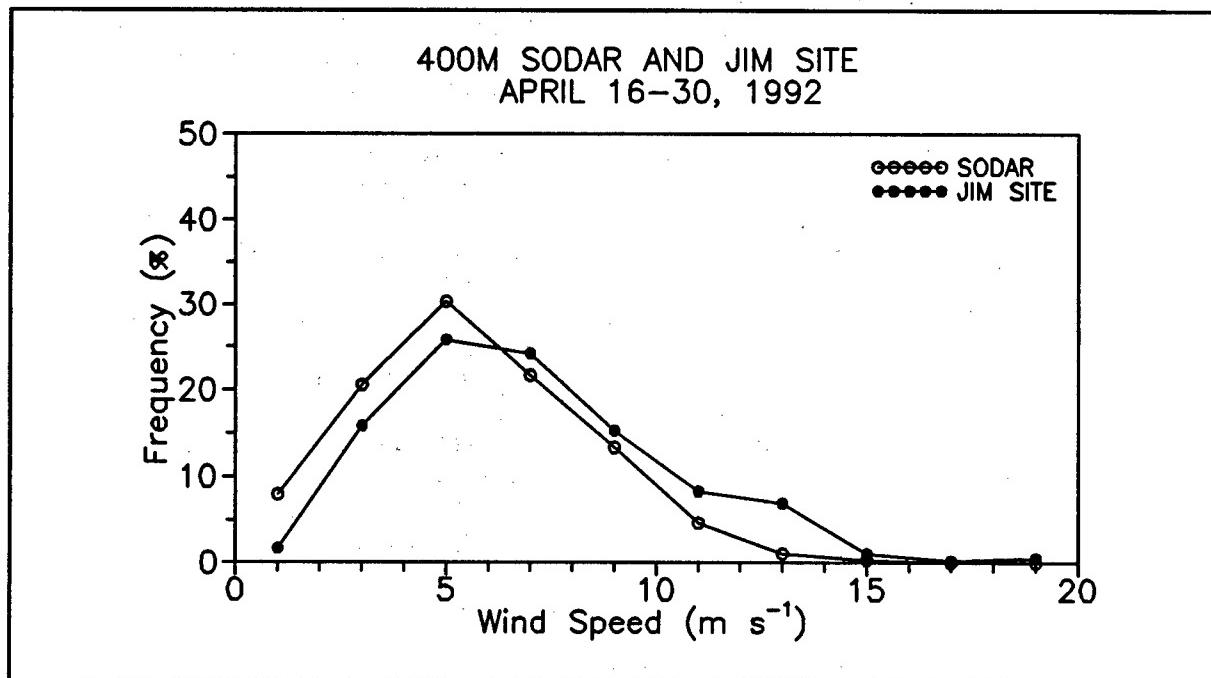
FIGURE 8

Frequency Distribution of Jim Site and 400-m Sodar Wind Directions

400M SODAR AND JIM SITE
APRIL 16-30, 1992
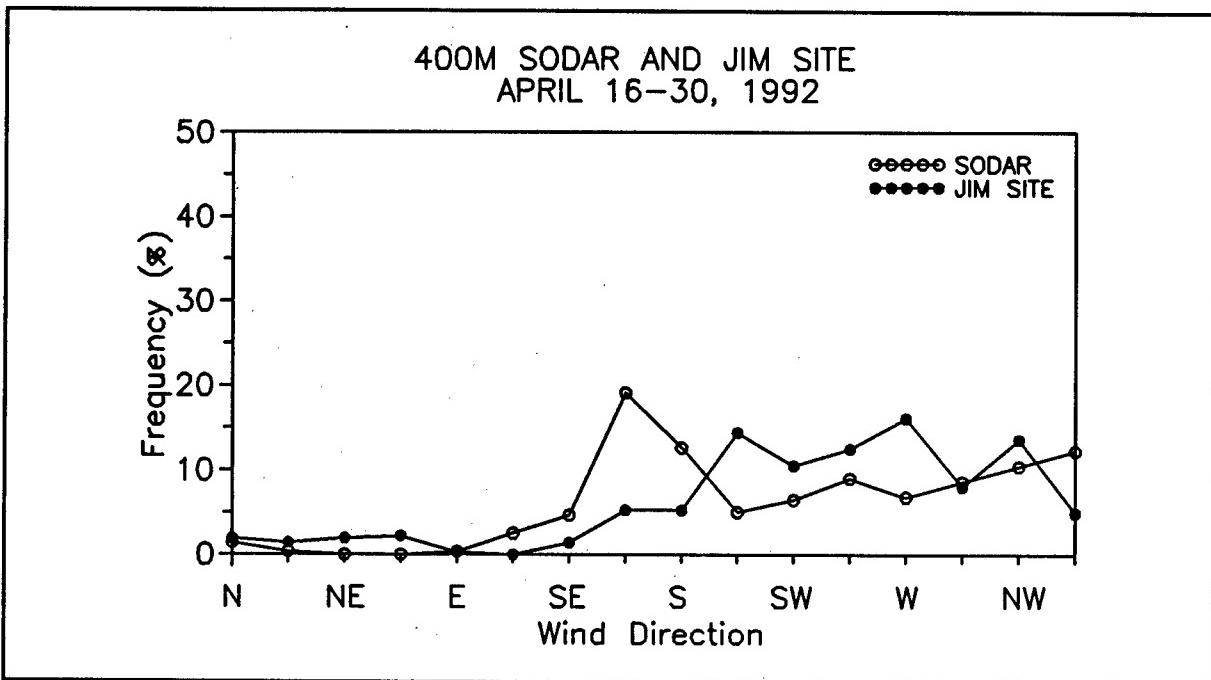
6. CONCLUSIONS

There was good agreement in wind speed among the three SAMS stations situated in the two valleys and poor agreement between the valley stations and the station at the upper anchor of the cable. The wind speeds measured at the latter were comparable with concurrent 400-m sodar data, although there was less agreement in direction. Based on this analysis, it is recommended that a surface station be placed at Jim Site to determine the wind loading on the cable. If wind direction data at the cable or wind data between the cable and valley floor are required, a surface station and an upper-air sensing system, preferably situated in the valley below the cable, should be installed. The upper-air data could be provided by the sodar used in this study. It collects wind data at regular height intervals up to several hundred meters above the surface continuously for several hours or days without human attention. During the 52 days it was operated at Mockingbird Gap, 15-minute averaged wind data were successfully collected every 50 m between 50 m and 500 m above the surface at least 75% of the time. The sodar must be operated off a generator or hard power, however, because solar powering was found to be unfeasible.

ACKNOWLEDGMENTS

REFERENCES

1. WSMR Aerial Cable Briefing. Sandia National Laboratories, Albuquerque, New Mexico, 23 January 1990.

2. *Aerial Cable Test Capability Final Environmental Impact Statement*. Department of the Army, White Sands Missile Range, New Mexico, 10 October 1991.

ASSESSMENT OF THE PERFORMANCE OF RASS SYSTEMS AT WHITE SANDS MISSILE RANGE

John Hines
Battlefield Environment Directorate
U.S. Army Research Laboratory
White Sands Missile Range, New Mexico

and

Wayne Flowers, Glenn Hoidale, Elaine Santantonio[1]
Science and Technology Corporation
White Sands Missile Range, New Mexico

ABSTRACT

Although there have been a number of studies assessing the performance of various wind-profiling radars, there have been relatively few studies of the performance of the Radio Acoustic Sounding System (RASS), often associated with the wind-profiling radars to measure virtual temperature. The RASS capability has been added to 50-, 404-, and 924-MHz wind profilers located at White Sands Missile Range. Following a discussion of the principle of RASS temperature measurement, the height coverage and limitations of each of the three RASS systems are presented. Finally, virtual temperature profiles obtained with the three RASS units are compared to those computed from radiosonde data from a site 6 km from the profiler complex. Based on data acquired during the spring and summer of 1992, the correlation coefficient between the RASS data associated with the 924-MHz wind profiler and the corresponding radiosonde data was 0.93 and the root mean square error was 1.6 °C.

1. INTRODUCTION

The U.S. Army Research Laboratory's (ARL) Battlefield Environment Directorate is developing an integrated system for the continuous measurement of tropospheric vertical profiles of temperature that are tailored to ARL requirements. One portion of the system consists of 50-, 404-, and 924-MHz wind-profiling radars, each equipped with a Radio Acousic Sounding System (RASS) to measure virtual temperature. The three RASS systems are located at the Atmospheric Profiler Research Facility (APRF) complex at White Sands Missile Range (WSMR), New Mexico (Hines et al., 1993) and were brought on line beginning in April of 1992.

One requirement was to assess the accuracy of the virtual temperature data. Previous studies by May et al. (1989) and Martner et al. (1993) have shown rms differences between radiosonde measurements and RASS measurements to be about 1.0 °C under a variety of meteorological conditions and have stated that under ideal conditions a precision of 0.2 °C is achievable.

The purpose of this paper is to compare the composite RASS vertical profile of virtual temperature to the virtual temperature profile computed from the corresponding radiosonde run. Comparisons with

---

[1] Currently affiliated with CDSI, WSMR, NM

rawinsonde data at WSMR are useful since the rawinsonde measurements are, by historical precedent, the current standard. At WSMR, however, the closest rawinsonde release point is 6 km from the APRF complex and the frequency of aperiodic releases is low. To mitigate the effects of this spatial separation, periods in 1992 and 1993 were selected for comparison during which the wind field over the WSMR air shed was uniform and both RASS and Oasis radiosonde data were available.

The radiosonde runs selected from 1992 for comparison were limited by data availability to those runs previously used for rawinsonde/924 wind comparisons (Flowers et al., 1993a). Nineteen radiosonde runs beginning on 2 April were included in the comparison. Examination of the availability of radiosonde data from Oasis and RASS data from the APRF complex during April, May, and June 1993 revealed few days during which there were simultaneous radiosonde data from Oasis Site and RASS data from all three profiler systems.

2. VIRTUAL TEMPERATURE

The virtual temperature is the temperature that dry air would have if it had the same pressure and density as a given sample of moist air. Thus, the virtual temperature always exceeds the air temperature. The difference is very small in dry air, but can exceed 3 °C in very moist tropical air. For the dry conditions usually prevailing over south-central New Mexico, the difference between the virtual temperature and air temperature is usually very small.

The following expression was used to compute the virtual temperature from the radiosonde measurements of air temperature and moisture:

$$T_v = (1 + 0.61q)T_a \tag{1}$$

where

$$
\begin{aligned}
T_v &= \text{virtual temperature} \\
T_a &= \text{air temperature} \\
q &= \text{specific humidity of the air}
\end{aligned}
$$

The specific humidity, q, is given by

$$q = \frac{w}{1 + w} \tag{2}$$

where

$$
\begin{aligned}
w &= w = 0.622\,\frac{e}{p - e} = \text{mixing ratio} \\
p &= \text{atmospheric pressure} \\
e &= \text{vapor pressure}
\end{aligned}
$$

The vapor pressure is computed from the Goff-Gratch formulation.

3. SITES

The APRF complex is situated on the floor of the Tularosa basin about 1220 m above mean sea level (MSL)) some 10 to 15 km east of the north-south oriented San Andres, San Augustin, and Organ Mountains. Individual mountain peaks extend as high as 1500 m above the basin floor. The radiosondes were released from Oasis Site, which is located about 6 km south southwest of the APRF complex.

4. INSTRUMENTATION

Selected characteristics of the three RASS systems are listed in Table 1. Detailed range gate information has been documented elsewhere (Flowers et al., 1993b).

Table 1. RASS Characteristics for the Three Radar Profilers

Characteristic	50 MHz	404 MHz	924 MHz
Acoustic frequency (Hz)	110	900	2100-2183
Acoustic power: total electrical input (W)	2400	125	50
Acoustic beam width (deg)	60	18	8

4.1 50-MHZ PROFILER

The 50-MHz RASS system has 64 gates, spanning the height range from 4200 to 13650 m AGL. Antenna problems precluded acquisition of reliable data below 5 km AGL, however, and weak signal strength generally precluded acquisition of reliable data above about 12 km AGL. In addition, the higher the wind speed (May, et al., 1989) and the dryer the atmosphere, the less data are acquired (Hatch, 1993). The RASS 1-min temperature data are acquired over a span of several minutes at approximately half-hour intervals.

4.2 404-MHZ PROFILER

The 404-MHz RASS system has 22 gates, spanning the height range from 500 to 5750 m AGL. Due to side-lobe problems caused by the surrounding mountains, there are currently no data above 2750 m AGL. RASS virtual temperature data represent 1-min averages acquired at 6-min intervals.

4.3 924-MHZ PROFILER

The 924-MHz profiler has 12 gates extending from 127 to 1283 m AGL. Data from the higher range gates are often missing or discontinuous due to low signal return. Virtual temperature data represent 5-min averages acquired at half-hour intervals.

4.4 RADIOSONDE

Although radiosonde data are acquired from a number of sites at WSMR, only those from Oasis Site were used in this study since that release point is the closest to the APRF complex. The rise rate of the balloon is approximately 300 m min^{-1}. Therefore, it requires about 40 min after release for the radiosonde package to reach an altitude of 12 km, the approximate upper limit of data acquisition with the 50-MHz RASS system. Temperature, pressure, and humidity data are aquired every 10 s of the ascent.

5. DATA SELECTION

During 1992, RASS data were only available from the 924-MHz profiler system. For statistical comparisons of the 1992 data, the samples were paired as closely as possible temporally and spatially. The RASS data were reported as 6-min averages before 5 June 1992 and 3-min averages after that date. Radiosonde air temperature and moisture data were reported every 10 s as the balloon rose. The RASS data were paired temporally with the radiosonde data by selecting the averaging period that most overlapped the first 1300 m of the radiosonde flight.

Radiosonde data were matched to RASS data with respect to gate height. Radiosonde temperature readings reported within the upper and lower boundaries of any given RASS gate were averaged and paired with the RASS temperature from that gate. Paired temperature readings whose difference exceeded 10 °C were eliminated before the data were subjected to statistical evaluation. Few data points were eliminated by this quality control, and those that were eliminated were invariably the highest reported RASS temperature value.

In the case of the WSMR 1993 RASS data, an intercomparison of virtual temperature data from the three RASS systems was not practical because the ranges of overlap were so small. In the case of the 50- and 404-MHz systems, the overlap was only 750 m (5000 to 5750 m AGL) and in the case of 404- and 924-MHz systems the overlap was again about 750 m (500 to 1250 m AGL). Therefore, for those Oasis Site radiosonde flights that were accompanied by nearly concurrent virtual temperature data from all three RASS systems, the composite RASS vertical profile of virtual temperature was compared to the virtual temperature profile as computed from the corresponding radiosonde run.

From 30 March 1993, when a new 924-MHz wind profiler was installed at the APRF complex, until 30 June 1993, there were 21 radiosonde releases from Oasis Site for which there were corresponding RASS data from all three radar profiler systems. These releases are identified in Table 2.

For the 1993 data, the 50-MHz RASS data are averages over several minutes taken at intervals of 30 min or so, the 404-MHz RASS data are 1-min averages taken at 6-min intervals, the 924-MHz RASS data are 5-min averages taken at 30-min intervals, and the radiosondes take about 40 min to ascend from the surface to 12 km AGL. The RASS data are paired temporally with the radiosonde data by selecting the averaging period that most closely overlaps the portion of the radiosonde flight that pertains to that RASS system.

Radiosonde data were matched to RASS data with respect to gate height. Radiosonde temperature readings that were within ±50 m of the midpoint of any given RASS gate were paired with the RASS temperatures from that gate.

Table 2. **Radiosonde Releases from Oasis Site for Which There Were Virtual Temperature Data from All Three Profiler Systems**

Date (1993)	Radiosonde Release Times (MST)		
May			
13	0803	1409	
14	0923	1323	1400
18	1345	1747	
26	0630		
27	1020		
June			
3	0356		
5	0758	1335	
9	0355	1255	
10	1050	1254	
11	1258		
14	0400		
15	0359	1137	
17	035		

6. DATA COMPARISON

The root mean square error (MSE), the Pearson product-moment (correlation) coefficient ρ, the regression slope and y intercept, and the paired Student's t-test probability were determined for each of the 19 periods in 1992, using paired values from each gate as repeated samples. Analysis indicates that these data are from normally distributed populations and thus the t-test is a valid test. The t statistic, the t probability, and the Wilcoxon probability were computed for each data set. Standard least-squares regression was used rather than the median of least squares regression, since significance tests indicated that parametric statistics were appropriate.

We used the standard null hypothesis that the differences between means of the paired profiler speed populations are not significantly different from zero and tested for the significance of this hypothesis. If a 5% significance level is chosen as the measure of rejection (at least a 5% chance the results are not random), then the probability (Prob > $|t|$) is compared with 0.05. If the probability is greater than 0.05, then the null hypothesis is not rejected. To put it slightly differently, the probability is the observed significance level, the probability that the observed difference in means between the two populations would occur if, in fact, the difference in means of the populations is not significantly different from zero.

A summary of these comparison statistics for 1992 is shown in Table 3. From the table we see that the data set taken as a whole shows a correlation coefficient of 0.93. Although the correlation is high, there is the rather troubling offset in the data summary of about 5 °C. The existence of the offset is further corroborated by the results of the t-test given in Table 3, which indicate that on the whole the mean difference between the two populations is nonzero, as well as the differences for about half of the individual data sets.

845

Table 3. Statistical Summary of the 924-MHz Profiler RASS and Radiosonde Temperature Data Comparisons for the Uniform Wind Field Days

Date (1992)	Time (MST)	Root MSE	ρ	m	b	Prob > |t|
2 Apr	0158	0.16	0.97	0.51	8.82	0.0002
7 Apr	0657	0.59	0.71	0.25	11.91	0.0438
12 Apr	1133	2.03	0.91	1.52	-9.17	0.3100
15 Apr	0700	0.32	0.93	0.63	6.32	0.1484
22 Apr	0730	1.83	0.48	0.38	11.20	0.2959
30 Apr	0057	0.49	0.62	0.29	17.67	0.0054
19 May	1258	0.58	0.96	0.55	11.90	0.0101
27 May	1255	0.41	0.98	0.61	8.26	0.6526
3 Jun	1056	1.53	0.97	1.41	-10.40	0.8953
10 Jun	0156	0.32	0.96	1.00	0.26	0.1680
19 Jun	0006	0.86	0.96	3.78	-81.40	0.8654
30 Jun	1257	0.14	0.99	0.25	24.27	0.4552
1 Jul	0706	0.96	0.45	0.26	20.11	0.0278
2 Jul	0630	0.85	0.91	1.06	-0.20	0.0116
9 Jul	0655	0.45	0.98	1.03	0.94	0.0001
24 Jul	0659	0.36	0.97	1.07	0.75	0.0001
12 Aug	0655	1.08	0.53	0.42	12.65	0.0001
13 Aug	0700	0.30	0.87	0.40	13.54	0.0004
24 Aug	0529	0.07	0.89	1.06	0.53	0.0001
Composite		1.62	0.93	0.83	4.89	0.0001

Vertical profiles of the virtual temperature, virtual temperature differences, and regression lines from the 19 radiosonde runs in 1992 and the corresponding 924-MHz RASS data are shown in Figs. 1 and 2. The data in Fig. 1 demonstrate the relatively good agreement typically observed in the 1992 data between the 924 RASS and the radiosonde under apparently uniform wind field conditions, although, as illustrated in Fig. 2, the topmost profiler points frequently diverged the most from the balloon data. A scatter diagram of the composite 1992 intercomparisons is shown in Fig. 3, where the above-mentioned offset in the data is easily discernable, since the bulk of the points lie to the left of the $m = 1$, $b = 0$ line.

Composite profiles from the 924-, 404-, and 50-MHz profilers compared to the radiosonde data for two runs from 15 June 1993 are shown in Fig. 4. These sample flights show a generally good correlation. The outlier points in the profiler data should be eliminated after the data are subjected to the quality control algorithms (Weber and Wuertz, 1991) currently under development by Hines and Parker (1993). Development of summary statistics for the 1993 data will be feasible when the quality control algorithms have been fully implemented.

7. CONCLUSIONS

Under uniform wind field conditions the profiler RASS data yield temperatures that correlate highly with radiosonde data, although it is necessary to apply the appropriate regression formula to obtain temperatures that correspond exactly. Quality control algorithms currently under development are expected to reduce significantly the problem of outliers currently observed in the raw data.

Figure 1. Comparison of virtual temperatures under apparently uniform wind field conditions from RASS (APRF Site) and radiosonde (Oasis site). (a) vertical temperature profiles, (b) vertical temperature difference profiles, (c) regression line.

Temperature Profiles 02 July 1992

QC: eliminate paired samples with absolute difference > 10 deg C
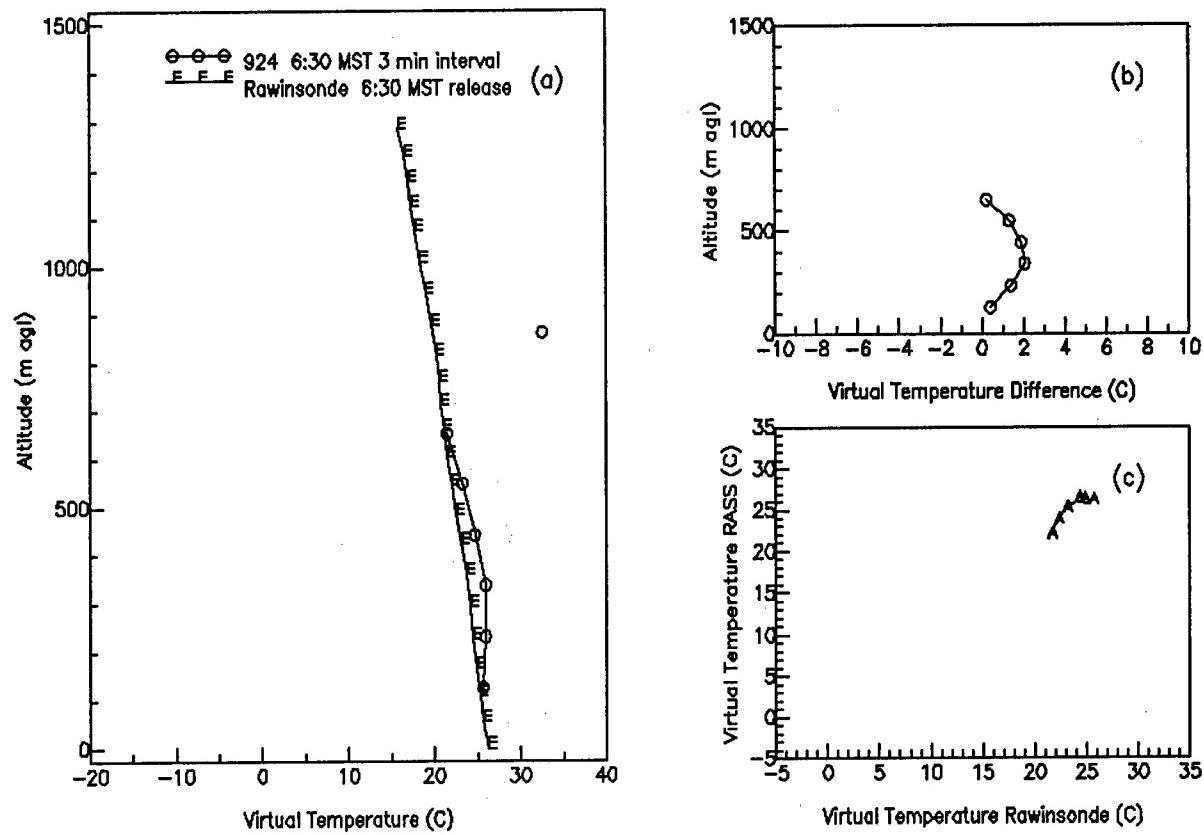
Figure 2. Comparison of virtual temperatures under apparently uniform wind field conditions from RASS (APRF Site) and radiosonde (Oasis Site): (a) vertical temperature profiles, (b) vertical temperature diference profiles, (c) regression line.

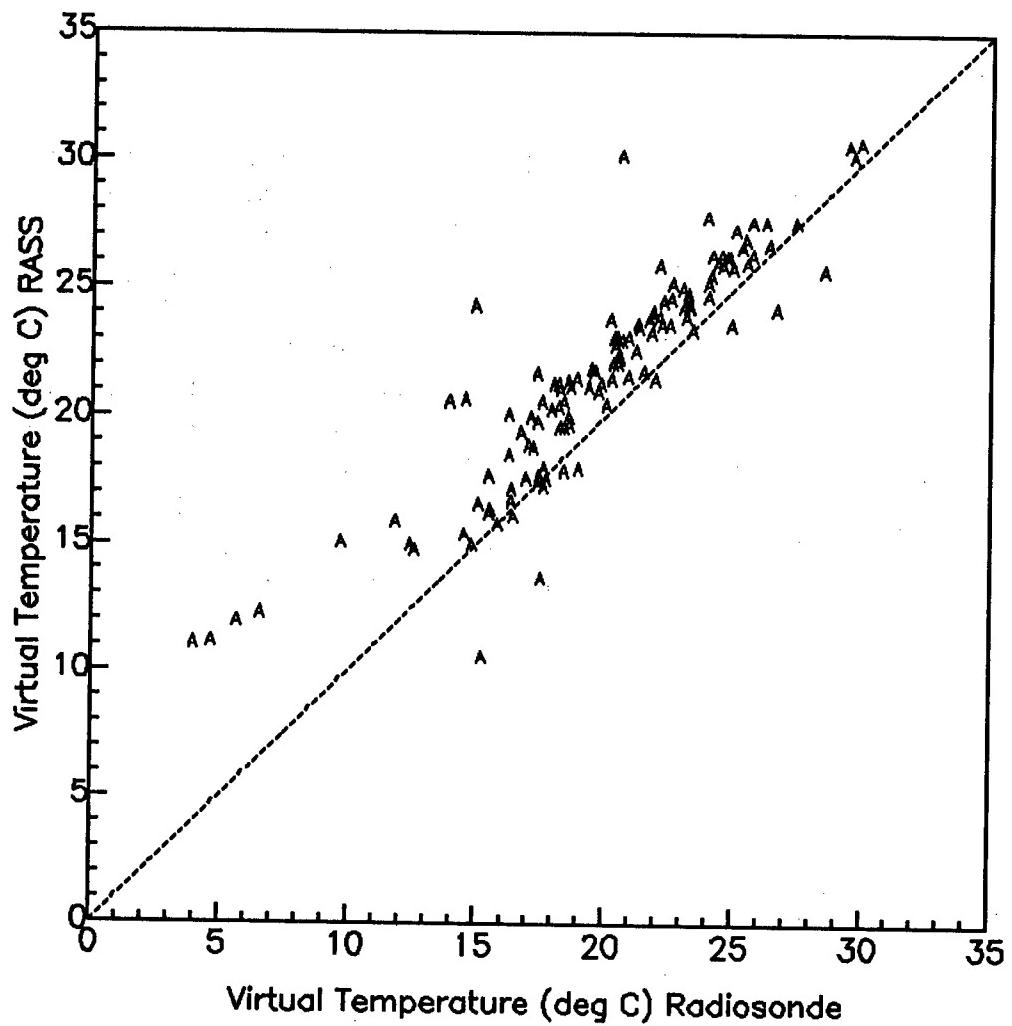**Figure 3.** Scatter plot of virtual temperature data based on 924-MHz RASS (APRF Site) and radiosonde (Oasis Site) data from the 1992 apparent uniform wind field days, with m = 1, b = 0 line superimposed.
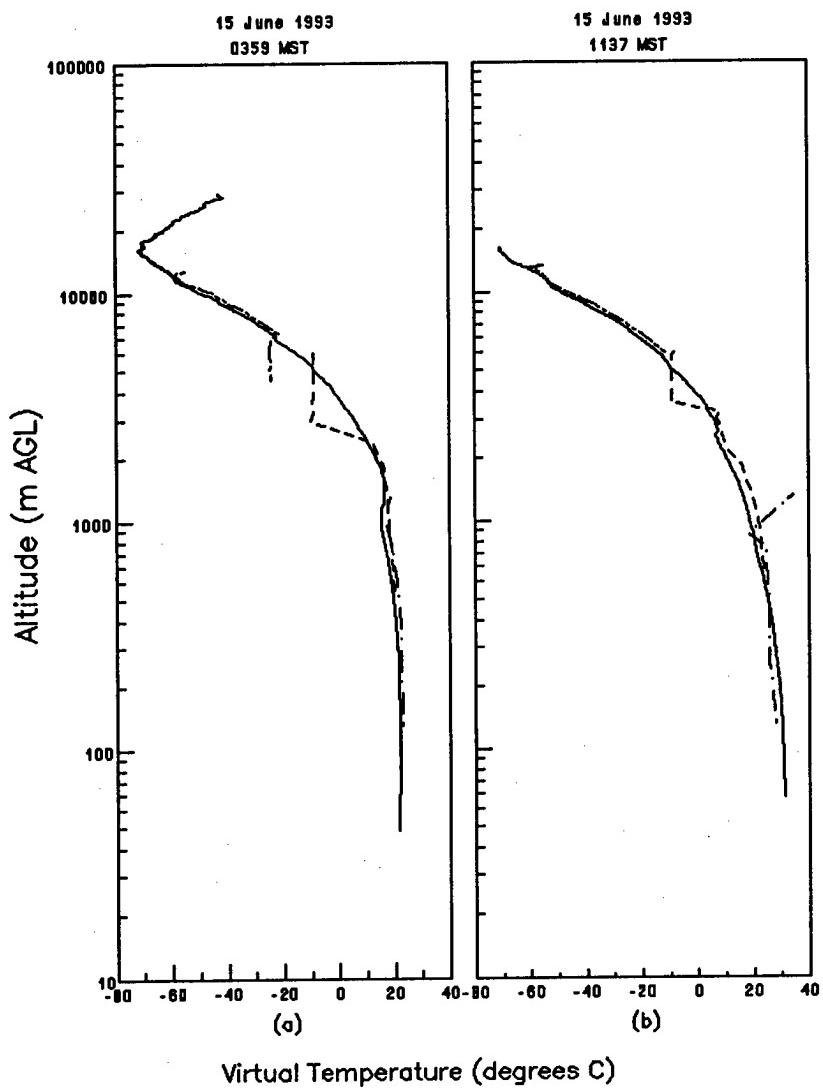
Figure 4. Vertical profiles of temperature as computed from the 924 ($\cdot$ — $\cdot$ —), 404 (– – –), and 50 (– – –) MHz RASS profilers, APRF Site; and radiosonde (———) Oasis Site, WSMR, 1993.

REFERENCES

Flowers, W., L. Parker, G. Hoidale, E. Santantonio, and J. Hines, 1993a: *Evaluation of a 924-MHz Wind Profiling Radar*. Final Report. Science and Technology Corp. and the U. S. Army Research Laboratory, White Sands Missile Range, NM.

Flowers, W., L. Parker, E. Santantonio, G. Hoidale, J. Hines, F. Eaton, W. Hatch, and S. McLaughlin, 1993b: *Relative Accuracies of Wind, Virtual Temperature, and Cn**2: Profiler Measurements at the Atmospheric Profiler Research Facility (APRF), White Sands Missile Range, New Mexico*. Draft Report. Science and Technology Corporation and the U. S. Army Research Laboratory, White Sands Missile Range, New Mexico.

Hatch, W.H., 1993: An Attempt to Correlate RASS Coverage with Wind Speed and Relative Humidity, *These Proceedings*.

Hines, J.R., F.D. Eaton, W.H. Hatch, and S. McLaughlin, 1992: The U.S. Army Profiler Facility: A Preliminary View. *Proceedings of the Atmospheric Propagation and Remote Sensing Conference*, SPIE Vol. 1688, 225-236.

Hines J., and L. Parker, 1993: Assessment of the Performance of Wind Profilers at White Sands Missile Range. *These Proceedings*.

Martner, B.E., D.B. Wuertz, B.B. Stankov, R.G. Strauch, E.R. Westwater, K.S. Gage, W.L. Ecklund, C.L. Martin, and W.F. Dabberdt, 1993: An Evaluation of Wind Profiler, RASS, and Microwave Rasiometer Performance. *Bull. Am. Met. Soc.*, **74**, 599-613.

May, P.T., K.P. Moran, and R.G. Strauch, 1989: The accuracy of RASS temperature measurements. *J. Appl. Meteorol.*, **28**, 1329-1335.

May, P.T., R.G. Strauch, K.P. Moran, and W.L. Ecklund, 1990: Temperature sounding by RASS with wind profiler radars: A preliminary study. *IEEE Trans. Geosci. Remote Sens.*, **28**, 19-28.

Weber, B.L. and D.B. Wuertz, 1991: *Quality control algorithm for profiler measurements of winds and temperatures*. NOAA Tech. Memo. ERL WPL-212, National Oceanographic and Atmospheric Administrtion, Boulder, Clolrado.

Weber, B.L., D.B. Wuertz, D.C. Law, S.S. Frisch, and J.M. Brown, 1992: Effects of small-scale vertical motion on radar measurements of wind and temperature profiles. *J. Atmos. Ocean. Technol.*, **9**, 193-209.

Weber, B.L., D.B. Wuertz, D.C. Welsh, and R. McPeek, 1993: Quality controls for profiler measurements of winds and RASS temperatures. *J. Atmos. Ocean. Technol.*, **10**, 452-464.

CLOUD FREE LINE OF SIGHT MODEL DIFFERENCES

Kenneth E. Eis, Thomas H. Vonder Haar, John M. Forsythe and Donald L. Reinke
STC-METSAT
Fort Collins, Colorado, U.S.A.

ABSTRACT

The weather community has historically supported a variety of the DoD's cloud modeling requirements with two generic data sets: mean cloud cover statistics, and cloud-free-line-of-site (CFLOS) calculations. Each of these data sets can be broken down into specific program applications. An example of the CFLOS tool is the C-Cloud-S model. The major mean cloud cover database currently used by the DoD is the RTNEPH .

These models served the strategic simulations and modeling communities well. Recently, military and geopolitical requirements forced war planners to "think tactical". Consequently, simulations and wargaming must be done at a higher fidelity. Questions are changing from -- What is the cloud cover over Baghdad? to -- What is the cloud cover over the Iraqi Intelligence Headquarters? CFLOS applications use two assumptions that make them inaccurate. First, cloud fields, on average, have correlation lengths of several hundred kilometers. Secondly, clouds can be treated as isotropic and spatially invariant. The first assumption is not supported by the data. The second, is never true, but represents the limitation of any model's resolution. This paper outlines some of the considerations involved in the CFLOS process including grid spacing and cloud structure.

1.0 BACKGROUND

CFLOS values can be calculated in two different ways. The most widely used method was detailed by Hering (Hering 1990) and (Allen and Malick 1983). Their approach is to use a conditional probability based on elevation angle t and the *in-situ* cloud cover value s. Hering gives Allen and Malick's equation as:

$$P_r(s,t) = (1 - s(1 + 3s)/4)^{(1+(0.55-s/2)\tan(t))} \tag{1}$$

Note: (Henderson-Sellers and McGuffie 1990) corrected the 1-s(1+3s)/4 term to 1/4 s(1+3s).

Hering caveats Equation 1 by indicating that this method does not take into account cloud cover variations. In fact, this statistical method of computing CFLOS is only an approximation of the real cloud fields that result in a cloud free line of site (CFLOS). In effect, this means the CFLOS computation is always made from a single cloud cover value s, even if higher resolution cloud structural information is available. This method also makes a fundamental assumption that there is a smoothly varying spatial autocorrelation function where $\rho_d = \exp(-d/D)$. d is the distance along the line of site, D is the sky cover relaxation distance that Hering assumes to be 500 km and ρ_d is the correlation coefficient.

CFLOS values, based on this equation and using different elevation angles (t) are shown in Figure 1. Note that due to the statistical nature of the CFLOS process, the line of site probabilities are all smoothly decreasing values which is not the case for real clouds. Reinke (Reinke 1992) has developed high resolution cloud climatologies that show that the correlation distances are much shorter than 500 km for much of the land surfaces and near geographic features such as mountains, shore lines, and ocean currents.

Figure 1 - CFLOS vs. Elevation Angle
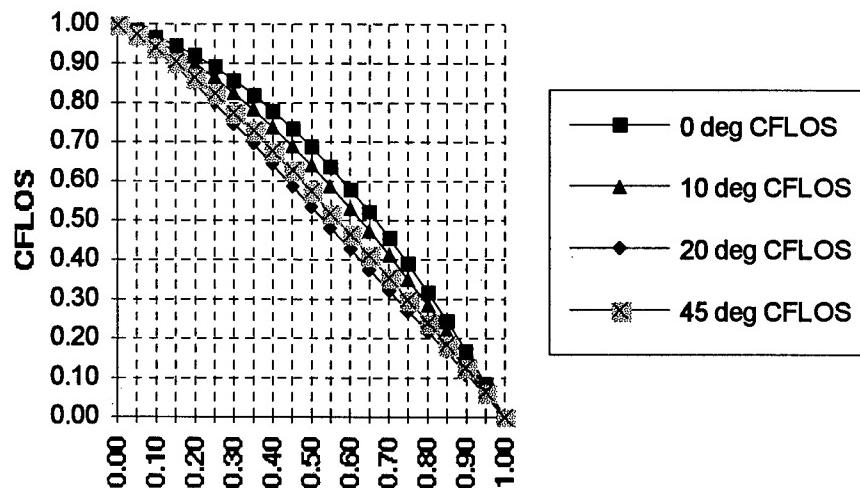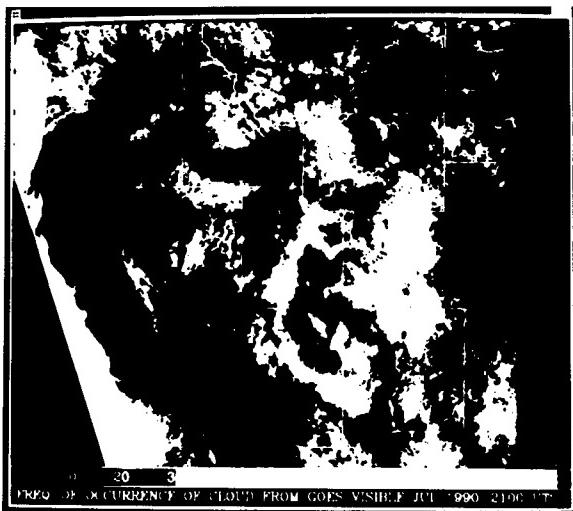
Figure 2. Cloud frequency composite from the GOES satellite for July 1990,
2100 UTC.

Figure 2 shows the probability distribution for cloud ceilings based on GOES
imagery averaged for a month of data. Note that there are many areas where
gradients in cloud distribution probability are large over distances of less than 250 km.
A recent study of cloud interval length (Reinke et. al., 1993) is illustrative of the issue.

Florida 2200UTC, Day 119 - Figure 3
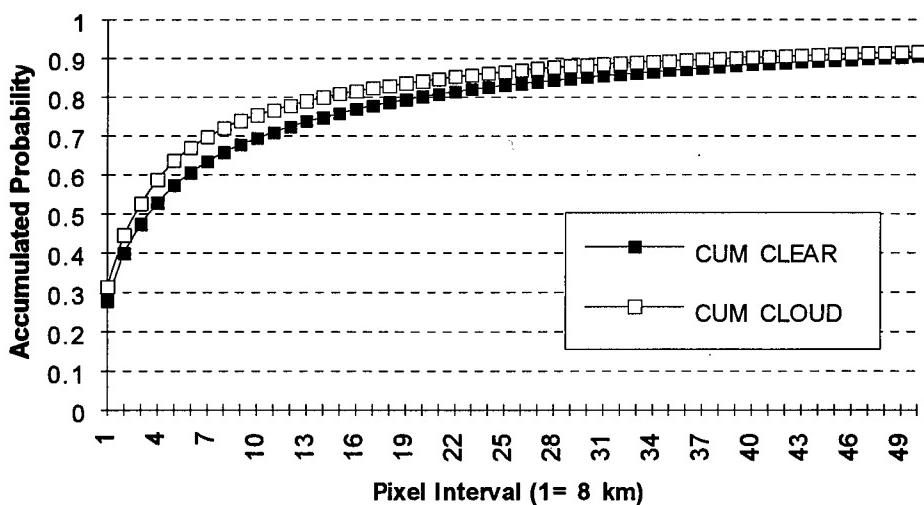
This analysis took a cloud/no cloud image, derived from a GOES-7 image and
produced an accumulated cloud and cloud-free interval histogram. More than 80
percent of the cloud intervals are of less than 20 km in length. Clear intervals,
although longer, as still predominately less than 20 km. The intervals were even more
sharply defined by intervals of less than 20 km (2.4 pixels) for the New Mexico area

855

where many cloud features are anchored to terrain. In terms of correlation length discussed by Burger (Burger, 1985), the 99 percent correlation length is less than one pixel in image distance. Using Burger's equation (4) where:

$$\rho(s) = 1 - (12/\pi) * s + s^2 \quad 0 \le s \le 1 \tag{2}$$

where s=s'/Λ, s' is the distance in km and Λ is the wavelength in km. $\rho(s)$ is the correlation function and s is the scale distance. Making the same assumptions as Burger (that the wavelength equals 340 km) and solving the equation for various s' distances yields the following graph:

Correlation vs Distance
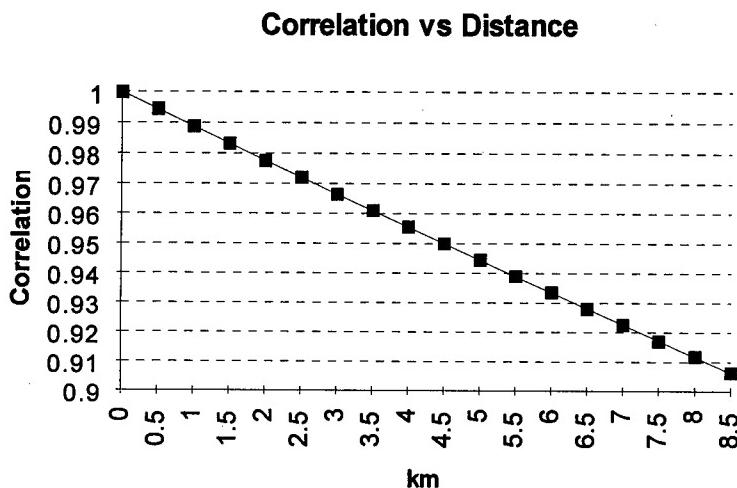
Figure 4. Correlation Length vs. Distance

At 8 km this treatment yields a correlation of ~0.91. Based on the interval study where over 35 percent of all correlation lengths are equal or less than 8 km, this correlation length does not appear correct. Clearly a relaxation interval of 500 km (or the 340 km used by Burger) is at least an order of magnitude too large.

2.0 ANOTHER CFLOS METHOD

Another method of determining CFLOS is to measure it directly using the basic definition of CFLOS. At a given elevation angle t, the CFLOS is the slant distance from a given target location to the nearest cloud. Probability of CFLOS can be accumulated over different times, azimuths, months, or conditional climatology.
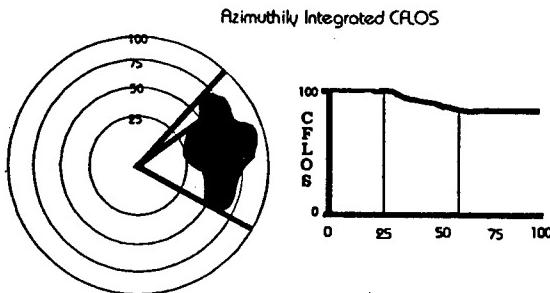
Figure 5. Direct Probability of CFLOS method integrated azimuthly.

With a high resolution cloud field where the cloud tops and bases are known, CFLOS can be measured directly as illustrated above. Here a cloud/no cloud slice of a three dimensional data base is interrogated and displayed for a given elevation angle. Distances from the site in question to a user-selected outer distance are azimuthly integrated for cloud obscuration. The azimuthal integration is then repeated at intermediate distances out to a user-defined outer range and CFLOS tables are accumulated for a given time and month, to produce a CFLOS probability data set. The azimuthal integration can be eliminated to produce an azimuthly dependent table as well.

3.0 COMPARISON OF THE TWO METHODS

Visibility Considerations: The basic cloud cover value determined by surface and satellite observation methods will vary. One of the problems already discussed is the sky dome geometric consideration that has been covered extensively in the literature. Another consideration is visibility. Surface observations are restricted by terrain, buildings, and most importantly, the prevailing visibility at the point of observation. When observers have visibilities greater than 30 km, they tend to over estimate the percentage of the sky dome covered with cloud. This effect biases s, the mean cloud cover used to seed the CFLOS algorithms when a location and date are provided and the algorithm assigns a climatological cloud value to the independent variable s in the CFLOS probability algorithm.

Cloud Structure Impacts: C_Cloud_S and other PCFLOS tools are based predominantly on surface data, and to some extent on azimuthly smoothed Nimbus -7 data. Smoothing the clouds by averaging over all azimuths introduces a progressively larger error in the CFLOS probability as the grid spacing increases. As we have **The most significant effect of this illustration is that CFLOS probabilities for a given mean cloud freeness at a given distance from target can vary in excess of 20 percent due just to the distribution of those clouds within the area of treatment.**

already discussed, clouds have a pronounced non-isotropic probability structure over

857

distances much smaller than 350 km. Most PCFLOS algorithms, in order to minimize computational and data storage requirements assume cloud cover distributions are isotropic. The model developers recognize this limitation, but were required to make these assumptions in order to fit the constraints of a PC-based application or because of the lack of a high resolution data set.

This cloud structure issue can be broken down into two different effects. The first is a theoretical issue based solely on how the distribution of clouds effects CFLOS. This effect is illustrated in the following experiment.
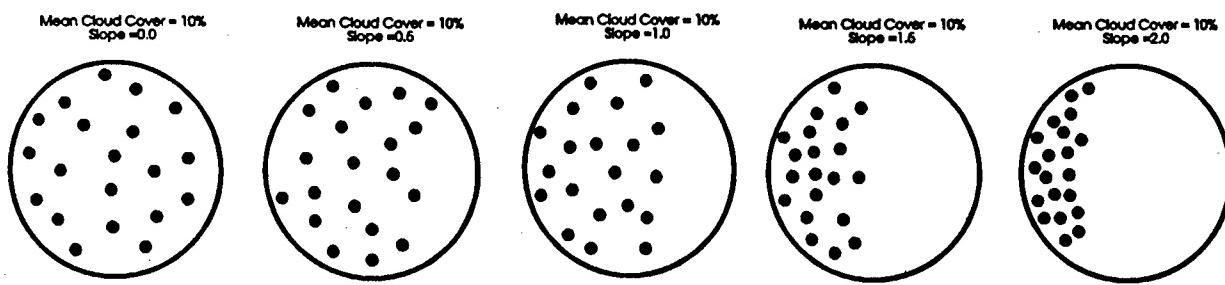
Figure 6. Cloud distribution of various cloud structures

The five "pizza" graphs (Figure 6) show a series of 100 km radius circles populated by 5 km circular clouds. In each instance the total cloud cover is 10 percent. In the first figure the clouds are randomly distributed across the entire 100 km radius. In each successive circle the clouds are progressively constrained by a linear probability distribution of increasing slope. The effect is to move from a purely random cloud pattern to a more structured cloud pattern.

We ran 9 Monte Carlo simulation runs against each of these probability distributions and computed the azimuthly averaged CFLOS probability for each. Additionally, we ran the same simulations given 10, 20, and 30 percent cloud-free values (see Figure 7). Note that the purely random cloud patterns or synthetic patterns give more pessimistic CFLOS values than the more structured cases until the mean cloud cover (s) exceeds 30 percent. Also note that the CFLOS probabilities cross. This odd behavior was also noted in our analysis of real cloud data. The reason for the crossing in the simulation values is due to two competing effects in the CFLOS extraction. First, as the clouds are moved to a more densely packed structure, the totally cloud free azimuths increase from zero to approximately 220 degrees of arc. This increases the cloud free probability. Secondly, the region of cloudiness becomes more densely packed and the probability of having any CFLOS through this region decreases. The most significant effect of this illustration is that CFLOS probabilities for a given mean cloud freeness at a given distance from target can vary in excess of 20 percent due just to the distribution of those clouds within the area of treatment. Lastly, as the probability density change bunches up the clouds there is a higher probability of clouds occurring closer to the target location. A cloud close-in obscures a more solid angle thus lowering the CFLOS probability.

CFLOS for Mean Cloudiness = 0.10

CFLOS for Mean Cloudiness = 0.20

CFLOS for Mean Cloudiness = 0.30
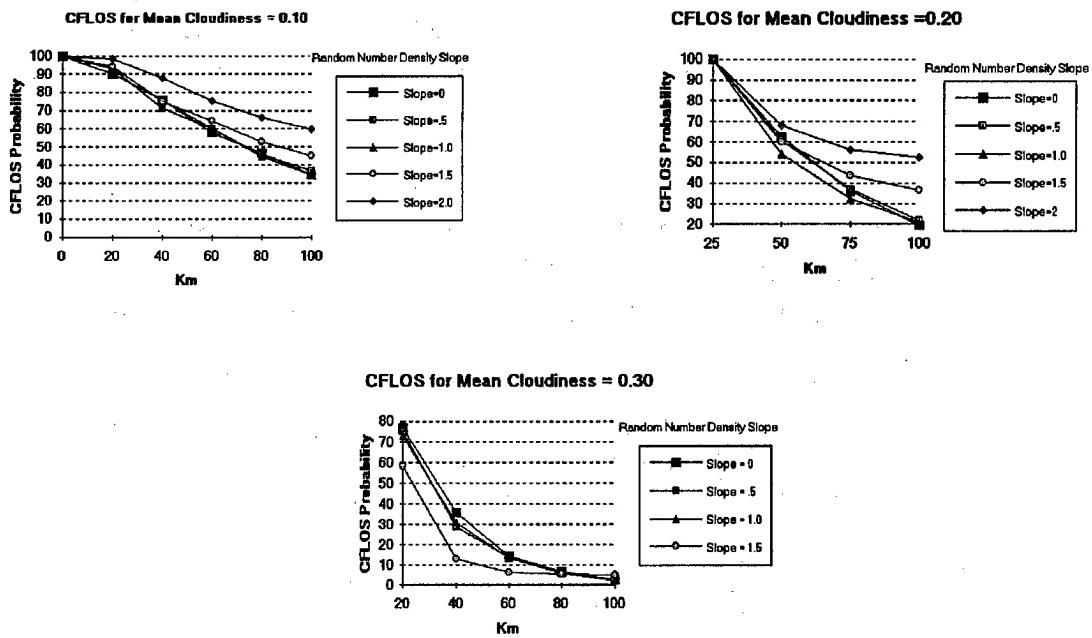
Figure 7. CFLOS behavior as cloud structure changes from random to organized.

Period of Record: The conventional CFLOS approaches use multi-year databases to compute the probability statistics. Our CFLOS can also be accumulated over multiple years but to-date we have only performed a single year analysis. The following graphs show a seven year monthly average variance for two ISCCP (270 km by 270 km) regions. The x axis is the Julian Day for the monthly period. The repeated x axis labels show the same monthly periods for consecutive years. Note the high variance in the Iraq 1200 values. For instance the January values (001 x labels) vary between 17 and 54 percent mean cloud cover. This high variance illustrates two problems. First, if you pick any single year to base a CFLOS analysis on, you are likely to have other years contradict your results. Secondly, taking the mean value for (s) will also give you a non-representative value because of the high variance of the data. This effect also shows up in the Korean data but to a lesser extent with January values varying between 46 and 53 percent.

Korean 0600 UTC ISCCP Total Cloud Cover

Iraq 1200 UTC ISCCP Total Cloud Cover

Figure 8. Mean cloud cover (7 years) in Korea at 0600 UTC
and Iraq at 1200 UTC.

4.0 TWO DIMENSIONAL VS. THREE DIMENSIONAL SIMULATIONS

Most CFLOS discussions, including the papers by Hering and Allen, mentioned in the background section of this paper, use the elevation angle t as the independent variable. We have set t to a constant and concentrated on the azimuth angle and the mean cloud cover s. We did not do a three dimensional treatment because the geometries would have been too complex and unnecessary to illustrate our point.   The mapping of a vertical cloud to CFLOS probability values was developed by (Eis et al., 1993). Note in this example the elevated observer is able to look over the cloud obscuration so the probability of seeing for this single cloud example varies between 100, zero and 100 percent at a given altitude as we vary the distance.

Figure 9. Vertical treatment of cloud-free-line-of-sight - probability vs. cloud
geometry.

5.0 CONCLUSION

PC-based applications like C-Cloud_S are powerful, user friendly tools for many applications within the DoD. Unfortunately, CFLOS algorithms, based on isotropic and spatially invariant assumptions over distances greater than 20 km will provide erroneous results for applications that require high fidelity answers where the underlying cloud probability structures do matter. On the other hand, the CFLOS computations that we have developed are dependent upon massive amounts of high resolution cloud imagery that are just now becoming available. Many of the CFLOS customers will have to undergo a paradigm shift when we respond to the question about the probability of CFLOS over Baghdad by asking them, " from what direction?"

The underlying assumption, that cloud fields, within a limited area of interest (say 340 km) are isotropic and spatially invarient also impacts other cloud scene generators. Fractal cloud scene generators assume that the cloud fields they are creating are self similar and therefore isotropic and spatially invarient. This is not true on any scale down to a few kilometers. As a result, the synthetic cloud scenes generated by fractal methods are realistic looking but might not represent a true cloud pattern in regions of large cloud probability gradients.

6.0 REFERENCES

Burger, C.F, 1985: World Atlas Of Total Sky-Cover. AFGL/TR-85/0198, AFGL, Atmospheric Sciences Division, Hanscom AFB, Massachusetts, 112 pp.

Eis, Kenneth E., 1992: High-resolution cloud climatologies. Proceedings of the Battlefield Atmospherics Conference at Fort Bliss in El Paso, Texas, December 1-3, 1992. (METSAT, Inc. Technical Report No. 92-111)

Eis, Kenneth E., T.H. Vonder Haar, J.M. Forsythe, T. Wong and D.L. Reinke, 1993: RAPTOR transmissivity and cloud climatology study. Final Report to LLNL for Subcontract #B208922 under Prime Contract #W-7405-ENG-48 and METSAT, Inc. Report No. 93-101.

Henderson-Sellers, A. and K. McGuffie, 1990: Are cloud amounts estimated from satellite sensor and conventional surface-based observations?. Int. J. Remote Sensing, 11, 543-550.

Hering, W. S. 1990: Probability Estimate of Cloud-Obscured Line-of-Sight. GL-TR-90-0204, AFGL, Air Force Systems Command, Hansom AFB, Massachusetts, 7 pp.

Reinke, D.L., T.H. Vonder Haar, C.L. Combs and S.Q. Kidder, 1992: Satellite cloud composite climatologies: a new high-resolution tool in atmospheric research and forecasting. Bull. Amer. Meteor. Soc., 73, 278-285.

CLIMATOLOGICAL AND HISTORICAL ANALYSIS OF CLOUD FOR ENVIRONMENTAL SIMULATIONS (CHANCES)

Donald L. Reinke, Thomas H. Vonder Haar, Kenneth E. Eis, John M. Forsythe,
and D. Neil Allen
STC-METSAT
Fort Collins, Colorado, USA

ABSTRACT

Clouds have been identified as one of the most significant deterrents to mission success for a wide range of Air Force systems and missions. Past research by *STC*-METSAT has identified High-Resolution Satellite Cloud Climatologies (HRSCC's) (Eis, 1992) as the optimum cloud cover product available today for meeting these requirements. Our research under a DoD SBIR Phase I has supported these findings and identified a technique for producing this unique and innovative product. However such a product is technically challenging. In an SBIR Phase II we will build a prototype global HRSCC that will require special processing of over 300 gigabytes of digital imagery, composed of over 70,000 satellite images.

Our Phase II effort will produce a global, 1-year, 5 km resolution HRSCC product. It will be produced at a higher spatial and temporal resolution than the current DoD cloud product, using almost 2 orders of magnitude more data than the RTNEPH. More importantly, we will provide the DoD with a global cloud climatology that is more accurate and more reliable than previous global nephanalysis products from any other source.

Both our HRSCC product, and the algorithms we propose to use for producing it, have been published in scientifically reviewed, journal papers (Reinke, *et al.*, 1992 and Rossow, *et al.*, 1991).

This paper and related presentation will provide an overview of the data archive and processing, and resultant "CHANCES" database that will be produced during our two-year SBIR Phase II.

1.0 INTRODUCTION

The "Cloud Problem"

Clouds have been identified as one of the most significant deterrents to mission success for a wide range of Air Force systems. In the Joint Chiefs of Staff report MJCS 154-86, clouds were identified as the highest priority atmospheric science research element and the USAF/XOW No. 2 Geophysical Requirement is improved cloud data handling and analysis. DESERT STORM planners started the air campaign, at least partially based on cloud climatologies. They were surprised by the cloudiness encountered by the actual combat sorties. The RTNEPH, used by the planners, was found to be optimistically biased because its dependence on inaccurate surface observations.

Impact of Clouds on Military Operations

The R&D requirement for high-resolution cloud climatologies is well documented, but the Persian Gulf conflict additionally identified an operational need for a comprehensive historical record of satellite-derived cloud information. Unfortunately, it was not available. Real-time observations of clouds were described as "barely adequate", however theater commanders did not have a climatological database to use for strategic planning or execution over data-sparse or data-denied regions. Colonel Gerald Riley, keynote speaker at the 1991 Conference on Cloud Impacts on DoD Operations and Systems (CIDOS-91), emphasized how difficult it was to provide cloud cover forecasts for Desert Storm. As the Staff Meteorologist for General Horner during the Gulf operation he was not able to provide a high-resolution satellite-based cloud climatology. In his opinion, such a product would have had a significant impact on planning and execution of the air campaign. Such a database can now be built.

Today, it is even more vital that DoD meteorological support include comprehensive cloud climatology data. With the Air Force becoming a "deployable" force (vs. a deployed force), it is essential that the forces know what type of meteorological conditions to expect in the theater of operations. Weather support, like military force, must be capable of immediate projection to any place on earth. This new cloud climatology data described in this paper can be used for all phases of air and ground, operations from deployment to theater operations. Reconnaissance, target acquisition, post-strike assessment, environmental support, and engineering operations will all be impacted by clouds and related meteorological events. Geopolitical trends indicate future conflicts will require military activities to be localized, regional operations where weather support tailored to strategic large-scale operations will be inadequate.

The Value of a New Cloud Database for Simulations

The DoD is required to assess the impact of the environment on new systems before they enter the acquisition process. This requirement has now received a renewed emphasis on having an accurate global cloud database to test system performance against. In short, clouds are a "show stopper" for systems requiring visual or infrared target acquisition. Since these requirements have been identified, much has been learned about the analysis of clouds from satellite imagery. Unfortunately, we are still operating with a very limited satellite-derived cloud database!

Our Phase I work demonstrated that the current state of the art in cloud simulations can be improved significantly. Two important points that should be made from the Phase I investigation: a) The current cloud database, the Real-Time NEPHanalysis (RTNEPH) is based primarily on surface observations, and has a resolution of 46 km, and b) The PCFLOS models are also surface observation based, and are based on 200 km intervals. The Phase I results show that approximately 90% of the cloud intervals are less than 10 km (i.e., the mean size of a cloud element) (see Figure 1). Thus both the RTNEPH and, even more so, PCFLOS models based on surface data might not provide a representative measure of the impact of clouds in specific geographic locations.

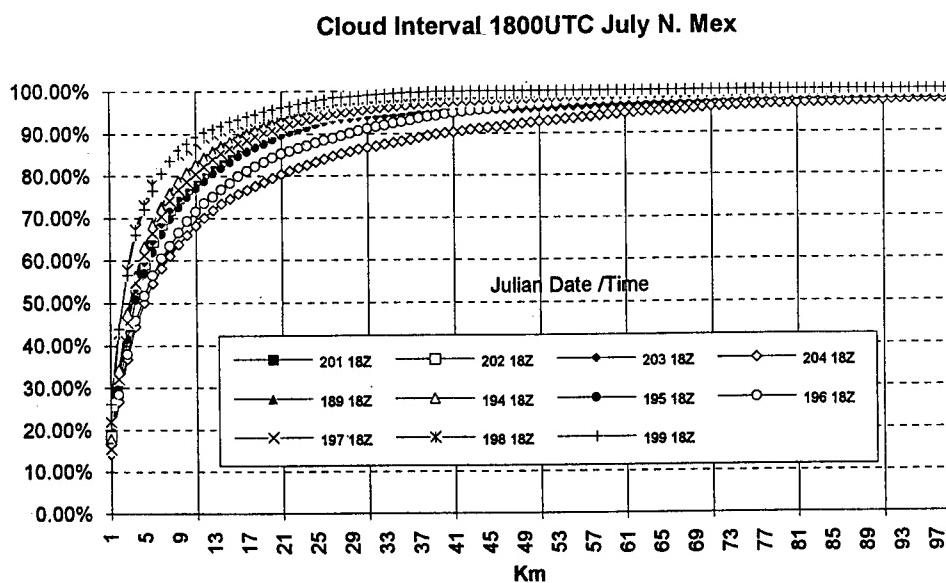**Cloud Interval 1800UTC July N. Mex**

Figure 1. Cumulative frequency of cloud interval at varying resolutions from 11 days of GOES visible imagery in July of 1989.

The development of new or improved weapons systems has forced an even more critical dependence on the accurate representation of clouds during the initial proof-of-concept simulations. The effectiveness of a system that is impacted by clouds can be more accurately demonstrated by knowing the climatological cloud distribution. New stealthy delivery systems may be even more dependent on good cloud climatologies for their optimization and acquisition than the new generation of precision guided munitions. A stealth mission would rely on good design for immunity from radar, but it would rely on clouds to be invisible to infrared detection systems. This new database will provide a tool to measure and assess these systems in the presence of high resolution cloud structures.

2.0 DATA AND DATA PROCESSING

Our SBIR Phase II work will focus on the production of a 1-year, global, 5 km cloud database. The technical challenge is to 1) Produce a one-year cloud database from as many as eight independent satellite platforms, and 2) _Align_ and _Merge_ data from these different satellite systems into a global climatology. Building a 5 km database is a technically challenging task. This type of product has not been produced on either the temporal or spatial resolution that we are proposing to use. Because of this fact, it has the potential to more significantly impact military planning and R&D than any previous environmental database.

Data Sets

All of the satellite imagery to be used in this project will be archived by _STC_-METSAT in Fort Collins, CO.   Satellite data sources are shown in Figure 2.   All satellite imagery will be archived on high-density 8mm tape.

Geostationary satellite imagery

METEOSAT, GOES, and GMS imagery will be archived by the Fort Collins Earthstation at the Cooperative Institute for Research in the Atmosphere (CIRA), Colorado State University.   All geostationary data will be archived at a nominal 5 km resolution, with data archived on both "daily" and "hour" tapes.   Daily tapes will provide imagery from all vehicles on a daily basis. Hour tapes will contain one month of imagery from all vehicles for a given hour (this format allows for more efficient processing of data). Figure 3 shows the global coverage of the current geostationary satellite configuration.

SATELLITE DATA

GOES direct readout via Ft. Collins Earthstation

GOES 4X8 km VIS/IR

DOMSAT / F2R via Ft. Collins

METEOSAT 3 5km VIS/IR

METEOSAT 4 5km VIS/IR

via 8mm from Boulder

DMSP 4 km VIS/IR

via T1 Internet link

GMS 5km VIS/IR

via 8mm from NOAA

AVHRR GAC 4 km multi-channel
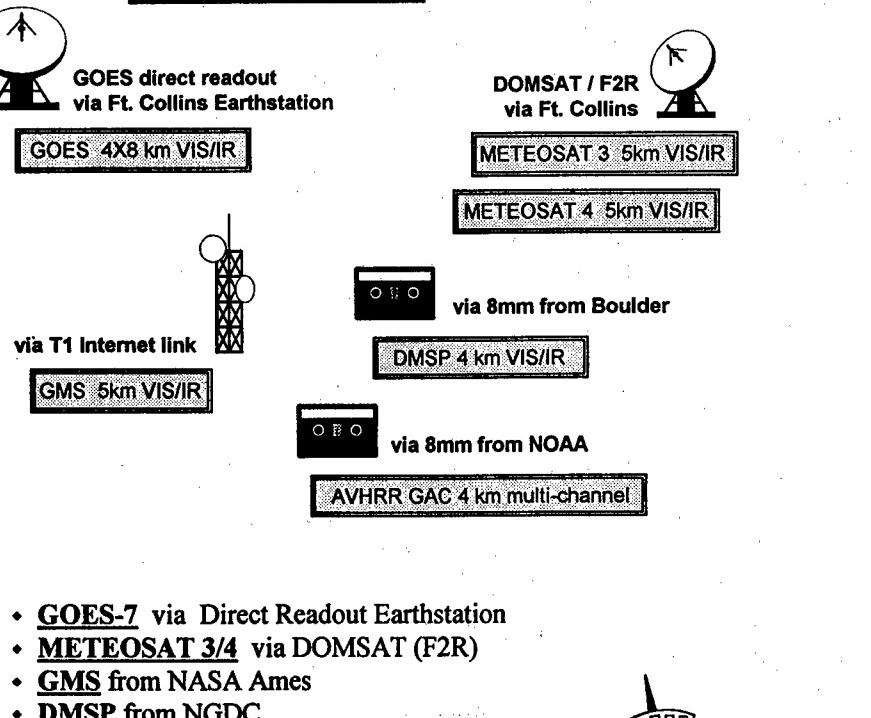
- **GOES-7** via Direct Readout Earthstation
- **METEOSAT 3/4** via DOMSAT (F2R)
- **GMS** from NASA Ames
- **DMSP** from NGDC
- **NOAA AVHRR GAC** from NOAA

STC -METSAT
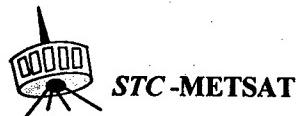
Figure 2. CHANCES satellite data sources.

Four Satellite Coverage

GMS   GOES   MET3   MET4
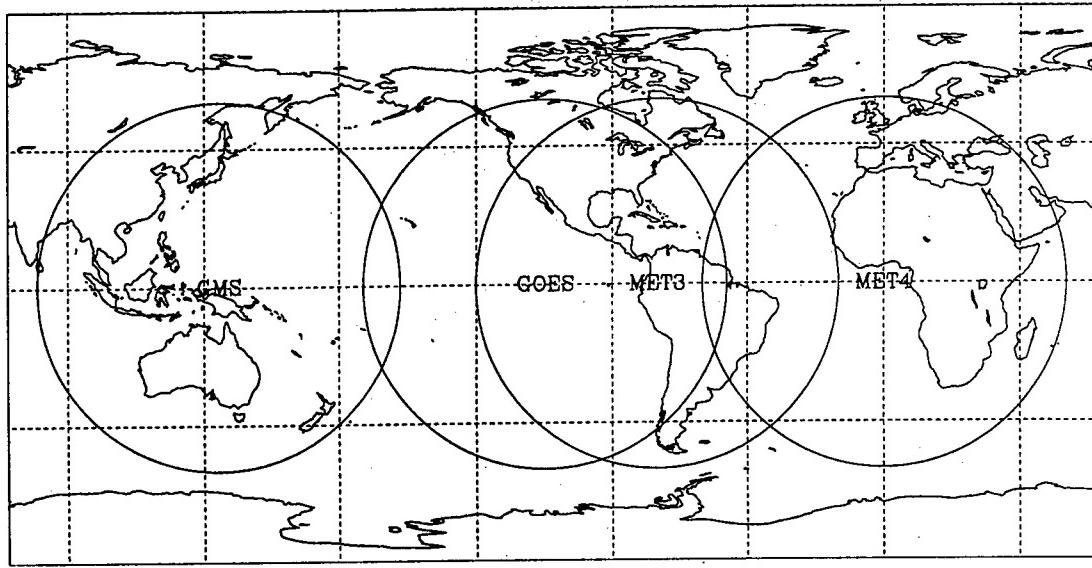
Figure 3. Geostationary Satellite coverage. Circles represent a distance of 60° of latitude from the satellite subpoint.

Polar orbiter satellite imagery

TIROS/AVHRR data will be archived by NOAA on 8mm tape. Data will consist of Global Area Coverage (GAC), 5 channels, at a 4 km resolution.

Digital DMSP OLS smooth data will be archived to 8mm tape by the National Geophysical Data Center (NGDC) in Boulder Colorado. DMSP "smooth" data will be archived at a 2.8 km resolution.

Ancillary data

In addition to the primary satellite data set, a number of ancillary data products will be archived for use in data alignment, calibration, and the cloud/no cloud processing.

Terrain data (topography, water/land boundaries, elevation) - this database will be close to our 5 km product resolution.

Snow/Ice data - this database should be available at approximately 110 km (1 degree), 1 day resolution.

Temperature data - both surface and upper air gridded temperature fields. At this time the plan is to use a 1 degree gridded field (USAF HIRAS database).

Geographic/Soil Type data - required for albedo estimates.

Data Processing

The primary satellite imagery source will be geostationary satellite imagery. The four primary satellites (GMS, GOES-7, METEOSAT 3 and 4) will provide hourly coverage for most of the globe. The data beyond about 60 degrees from subpoint will not be used due to the degraded resolution (see Figure 3). There will also be an area where the INSAT data is not available between GMS and METEOSAT-4 (Figure 3). Polar data from NOAA and/or DMSP will be used to fill in these data voids. Due to orbit overlaps, there will be some time periods where only two of the polar-orbiters will be useful, and periods where three or potentially more might fit into the data set. Polar data overlap will, in most areas, provide frequency coverage almost as good as that provided by geostationary data (particularly over the polar regions). Our intent is to build a solid database from the available geostationary satellite imagery, and fill in the "gaps" with polar data.

Images will be processed to correct for navigation errors (see Figure 4). Geostationary data will be renavigated and aligned to fit a fixed projection. This projection will be based on the nominal subpoint for the analysis period. Remapped imagery will be stored as an "intermediate" product, by individual satellite. Once the

images are aligned and manually quality controlled, they will be sampled to produce an image within the global 5 km resolution grid. A cloud/no cloud processor will produce a binary image for each satellite, then a merge processor will combine the individual binary images using a distance and time weighted scheme where images overlap, to form the final output grid of cloud/no cloud.

The cloud/no cloud algorithm is, at this time, still to be determined, but will be of the class: Bi-Specral, Dynamic Threshold, with time variance, spatial variance, and will use a form of the ISCCP tri-spectral cloud algorithm over snow and ice.

Also undetermined at this time is the projection of the final output fields. It will be either an equal area grid, or fixed 5 km geographic grid. In either case, coordinate transformation utilities will be available to convert to all common grid projections.

SATELLITE IMAGE PROCESSING
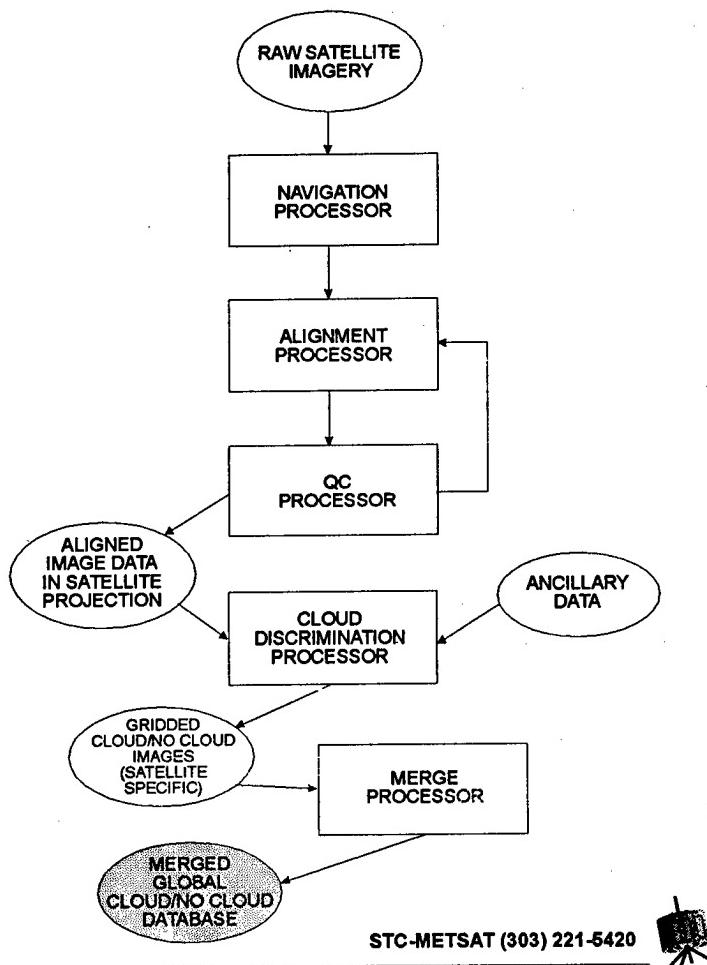

STC-METSAT (303) 221-5420

Figure 4. CHANCES data processing.

3.0 CONCLUSIONS

Perhaps the most significant finding of the early investigations of High-Resolution Satellite Cloud Climatologies (HRSCC's) is the advantage over conventional cloud climatologies. Initial comparisons between standard surface observations and satellite-derived cloud cover indicate satellite-based analysis offer a substantial improvement in accuracy (See related paper in this volume). The initial HRSCC's, produced from geostationary satellites, have revealed details that are not evident in lower resolution products. The HRSCC's have shown the ability to observe and composite azimuthally dependent frequency of occurrence of cloud, and diurnal variability in the frequency of occurrence of cloud. Additionally, the higher resolution satellite data has shown that surface observed cloud cover estimates from synoptic reporting stations may give a very misleading estimate of the frequency (Reinke, et al., 1992). Conventional observations have been the mainstay of DoD climatological cloud databases for decades. We believe it is time to update that database with data from the most comprehensive platform available today -- meteorological satellites.

It is now practical to produce a multi-year satellite cloud climatology to meet many of the technical challenges and documented requirements for a DoD cloud database. Because of new techniques, economical processing systems, and a better understanding of satellite image processing, a database such as CHANCES is now feasible and practical. We believe that this global, 5 km, hourly product will become the standard cloud climatology reference for both the DoD and civilian operations that are impacted by clouds.

4.0 ACKNOWLEDGMENTS

5.0 REFERENCES

Eis, K. E., 1992: High-Resolution Cloud Climatologies, proceedings 1992 Battlefield Atmospherics Conference, Fort Bliss, TX. 151-160.

Reinke, D.L., C.L. Combs, S.Q. Kidder, and T.H. Vonder Haar, 1992: Satellite Cloud Composite Climatologies: a new tool in atmospheric research and forecasting. Bull. Am. Meteor. Soc., 73, No. 3, Mar., 278-285.

Rossow, W.B., L.C. Gardner, J.P. Lu., and A.W. Walker. 1991: International Satellite Cloud Climatology Project (ISCCP) Documentation of Cloud Data WMO/TD - No. 266, World Meteorological Organization, Geneva, 76 pp. plus 3 appendices.

Session V Posters

MITIGATION AND EXPLOITATION

AN OVERVIEW OF THE ATMOSPHERIC AEROSOLS AND OPTICS DATA LIBRARY (AAODL)

John N. Crain
Science and Technology Corporation
Las Cruces, New Mexico 88001, USA

Fidel Tibuni
U.S. Army Research Laboratory
White Sands Missile Range, New Mexico 88002, USA

ABSTRACT

Jointly sponsored by the U.S. Army Research Laboratory (ARL) and the U.S. Army Edgewood Research, Development, and Engineering Center (ERDEC), the primary goals of the Atmospheric Aerosols and Optics Data Library (AAODL) are to validate, quality control, organize, archive, and distribute to the user community data acquired in Government-sponsored smoke and aerosol tests. For more than a decade the AAODL has provided a central source of data for researchers in areas that include obscuration modeling, wargaming, weapon system development, and sensor performance. The purpose of this presentation is to provide an overview of the data library and how it may be used by the smoke/obscurants research community. The overview will include a brief description of the historical development of the AAODL with emphasis on the significant enhancements of recent years, as well as a detailed summary of its current state and information necessary for users who wish to gain access to the AAODL.

1. ORIGIN AND PURPOSE

Initiated in 1982, the Atmospheric Aerosols and Optics Data Library (AAODL) has become a valuable tool for a broad range of research. Sponsored jointly by the U.S. Army Research Laboratory (ARL) and the U.S. Army Edgewood Research, Development, and Engineering Center (ERDEC), AAODL is a centralized depository for field test and laboratory data. The computer and data center are located at the Science and Technology Corp. (STC) branch office in Las Cruces, NM.

The AAODL provides consistent, quality-controlled data sets. The data include a wide variety of quantities measured in Government-sponsored field tests, meteorological tests, and laboratory tests. These quantities include physical, chemical, or radiative properties of obscurants, micrometeorological measurements, and supporting information about the tests or experiments in which the data were acquired. Uses of the data include electro-optical system development, munition development, tactical decision aid development, wargaming, modeling, test development, evaluation, training and education.

The computerized portion of the AAODL currently resides on a SUN/UNIX Ethernet system implementing the Oracle® relational DBMS. Additional microcomputers are also tied into the network, giving the ability to transfer data using a variety of media.

2. DESCRIPTION OF THE AAODL

The AAODL consists of two major types of archived information. The core of the library is an online computer-accessible set of databases containing quality-controlled data and derived quantities. Supporting and supplementing this computerized data library is a collection of printed documentation and data, magnetic data tapes, videotapes, and field test documentation. The online library uses a relational database management system (DBMS). An annually published AAODL library bulletin keeps the user community informed about recent additions to the database library and other topics of interest to the researcher concerned with the battlefield environment.

Users can obtain data from the AAODL either by submitting a request for the data or by accessing the AAODL directly. Data can be sent to users in hard-copy or electronic format. The data library can be accessed directly either by modem or in-house at the Las Cruces facility. Dial-up use is most appropriate for browsing the database library and identifying data sets that are relevant to a particular task. In-house use is best suited to large data transfers or complex analyses. In addition to the information contained in the database library, data analysis tools exist for the in-house user. These tools can be used to manipulate data sets with the help of AAODL personnel.

3. THE AAODL USER'S GUIDE

The AAODL User's Guide provides an introduction to the contents and use of the database library. With this document, the user should be able to access databases within the library, determine the location of data sets, and perform routine data extractions.

The user's guide includes both descriptive sections and how-to sections with examples. The guide describes in general terms the structure and content of the computerized AAODL database library. This description gives the user enough information to begin a search for desired data. The guide also provides an elementary introduction to the structure of a relational database (as used in the AAODL), and explains how the AAODL content fits into this structure. In addition, the guide provides an introduction to the Oracle DBMS and the language used to access it.

Following the descriptive material, the guide provides step-by-step procedures that the user needs to perform for some common data access tasks. These tasks include the following:

- Logging on

- Browsing the DBKEY database, which functions as the library "table of contents," to determine the existence and location of needed data

- Selecting various types of data subsets from a field test database

- Exporting and downloading data

4. ACCESSING THE AAODL

Users may obtain AAODL data in a number of forms. These include the following:

- Hard copy sent by AAODL personnel

- Diskette or tape sent by AAODL personnel

- Information on database library contents obtained by dial-up access

- Data transferred by modem

- Data accessed directly at the Las Cruces facility and transferred to electronic files or hard copy

A number of different approaches may be used for obtaining data in any of these forms, and users can choose any degree of involvement with the database library, from simply requesting that specific data be sent by AAODL personnel to selecting and extracting the data themselves. For example, a user may dial up and browse the library contents, determining which data sets are appropriate for a given project. Then the user can request that these data sets be extracted by AAODL personnel and sent in a specified format. Alternatively, the user may dial up, identify the desired data sets, and then use some simple features of Oracle to create an output file containing the data. If it is small, this output may be sent to the user over the modem. For larger data sets, AAODL personnel may send the data to the user on magnetic media in the requested format.

4.1 USER REQUEST FORMS

The first step in any type of AAODL access is the submission of a user request form. These forms are published in every issue of the AAODL bulletin, and are available upon request from the AAODL Technical Representative. A copy of the user request form is shown in the appendix.

The user may specify what kind of data are needed and what method of access is desired. If in-house use is requested, an appointment will be made and an initial tutorial will be provided, with ongoing assistance as needed. After the request is approved, the next step depends on whether the user has requested in-house or dial-up use.

4.2 IN-HOUSE USE

For in-house users, direct assistance from AAODL personnel and access to additional documentation are available. Also, logging onto the AAODL computer through an in-house terminal offers higher performance than does remote access, as well as the ability to use graphics tools developed for the SUN system to generate plots of data of interest, or to perform image analysis with the AAODL image processing system.

4.3 DIAL-UP ACCESS

If in-house use is impractical, the AAODL currently has Hayes-compatible modems capable of 300-, 1200-, 2400-, or 9600-bps communications. Any user requiring remote access to the AAODL online database library must have a computer with a compatible modem, communications software, and a telephone line. After receiving approval from the Government Technical Representative to access the AAODL, the user will be contacted by the database administrator at the Las Cruces office of STC.

The user will be provided with the necessary telephone numbers, passwords, and other log-in information at that time. AAODL personnel will consult with the user to determine that the proper communications software and hardware are available, perhaps performing preliminary tests to verify communication.

4.4 AAODL BETA SITES

Another method of gaining access to AAODL data is through the establishment of a beta site. The AAODL beta site concept was originated to enable organizations that need frequent access to AAODL data to hold an AAODL database at their sites. Beta sites would receive all or part of the AAODL database library implemented on an Oracle system. This arrangement allows researchers at the beta site to develop their own software for data applications and become familiar with the use of the relational database system.

The beta site concept can improve the efficiency of AAODL data utilization and increase the accessibility of AAODL data to regular users. Once a beta site is established, a user no longer needs to submit user request forms and wait for data transfer every time a new data set is needed. Beta sites are not authorized to release AAODL data outside their organizations.

5. STRUCTURE AND CONTENT OF THE AAODL COMPUTERIZED DATABASE LIBRARY

This section illustrates how the individual AAODL databases are structured using a relational database management system, and provides an outline of the content of the computerized portion of the AAODL database library. The AAODL database library consists of many databases, each containing a set of tables. The library is designed as much as possible so that databases have similar structures. Nevertheless, there are some variations in structure among different databases. Table 1 is a partial list of the databases included in the library.

As an example of what the user may expect to find when accessing a field test database is shown in Fig. 1. This diagram of the Smoke Week IX field test database SMOKE9 shows a fairly common type of database structure. The tables contained in the database and the contents of the columns of the tables are shown schematically.

The DBKEY database serves as the AAODL "table of contents," as it provides the user with a directory of the databases in the computerized portion of the AAODL. By using DBKEY, the user can determine the general content of all the databases and make a preliminary selection of data.

The DBKEY database includes six major tables, shown schematically in Fig. 2. All of these tables give essential general information about the contents of AAODL databases and their tables and columns. The tables included in the database DBKEY are the following:

- DBLIST
- DBINFO
- TRLINFO
- REFS
- VIDEO
- ABBREVS

The following sections describe briefly the contents of these tables.

TABLE 1. PARTIAL LIST OF DATABASE LIBRARY CONTENTS

NAME	TEST NAME	DATE	LOCATION
CRATER	Crater measurements database (formerly "SHOT" database)	Various field tests	
LABDAT	Characteristics of smokes/obscurants from laboratory experiments	Various laboratories	
PHAS2A	Inventory smoke munition test, Phase IIA	23 Sept 77	Dugway Proving Ground, UT
COPGFE	Copperhead ground fog experiment	24 Apr 78	Ft. Ord, CA
DIRT1	Dusty Infrared Test I	2 Oct 78	WSMR, NM
SMOKE2	Smoke Week II	6 Nov 78	Eglin AFB, FL
H3S	High Humidity Hygroscopic Smoke Test	19 Jul 79	Aberdeen Proving Ground, MD
SNOW1	Snow-One	5 Jan 81	Camp Ethan Allen, VT
RPL8A1	Comparison test of grenade smoke: screening, RP, L8A1	1 Jun 81	Dugway Proving Ground, UT
BICT2	Battlefield Induced Contamination Test II	20 Aug 81	WSMR, NM
SMOKE4	Smoke Week IV	2 Nov 81	Redstone Arsenal, AL
DOT1	Dust Obscuration Test I	15 Apr 83	Fort Carson, CO
SNOW3	Snow III-West	19 Dec 84	Grayling, MI
SMOKE7	Smoke Week VII	15 Jun '85	Fort Sill, OK
CECATS	Characterization, Evaluation, and Comparison of Army Transmissometer Systems	2 May 88	WSMR, NM
SMOKE11	Smoke Week XI	20 Feb 89	Valcartier, Quebec, Canada
SMOKE14	Smoke Week XIV	28 Apr 92	Eglin AFB, FL

SMOKE9

GENINFO

TRIAL NUMBER
JULIAN DAY
START TIME, LOCAL
LENGTH OF TRIAL, S
OBSCURANT
FLARES
WINDSPEED
WIND DIRECTION
RELATIVE HUMIDITY
AMBIENT TEMPERATURE
PASQUILL CATEGORY
CLOUD COVER
SOLAR IRRADIANCE
AIR PRESSURE
AIR DENSITY
MUNITION
MUNITION LOCATION

SURVEY

TEST SITE AREA
SYSTEM OR COMPONENT
X, Y, Z COORDINATES
DESCRIPTION OF SURVEY POINT

MET

TRIAL NUMBER
JULIAN DAY
DECIMAL LOCAL TIME
TRIAL ELAPSED TIME, S
RELATIVE HUMIDITY, 2 & 10 M
AMBIENT TEMPERATURE, 2 &10 M
SOLAR FLUX
U, V, W COMPONENTS
    WIND VELOCITY AT
    AT 2,4,8,16, & 20 M LEVELS

LOVIRS1

TRIAL NUMBER
JULIAN DAY
DECIMAL LOCAL TIME
TRIAL ELAPSED TIME, S
TRANSMITTANCE, VISUAL
TRANSMITTANCE, 1.06 UM
TRANSMITTANCE, 3-5 UM
TRANSMITTANCE, 8-14 UM

LOVIRM1

TRIAL NUMBER
JULIAN DAY
DECIMAL LOCAL TIME
TRIAL ELAPSED TIME, S
TRANSMITTANCE, 1.06 UM
TRANSMITTANCE, VISUAL
TRANSMITTANCE, 3-5 UM
TRANSMITTANCE, 8-14 UM

SMART

TRIAL NUMBER
JULIAN DAY
DECIMAL LOCAL TIME
TRIAL ELAPSED TIME, S
TRANSMITTANCE, 1.06 UM
TRANSMITTANCE, VISUAL
TRANSMITTANCE, 3-5 UM
TRANSMITTANCE, 8-14 UM

MPTR

TRIAL NUMBER
JULIAN DAY
DECIMAL LOCAL TIME
TRIAL ELAPSED TIME, S
TRANSMITTANCE IN
    FOUR BANDS AND
    FOR 12 MPTR SOURCES

DPG

TRIAL NUMBER
JULIAN DAY
DECIMAL LOCAL TIME
TRIAL ELAPSED TIME
TRANSMITTANCE IN
    7 WAVEBANDS OVER
    3 LINES OF SIGHT

MIDAS

TRIAL NUMBER
JULIAN DAY
DECIMAL LOCAL TIME
TRIAL ELAPSED TIME, S
CLOUD DIMENSION AND
    LOCATION PARAMETERS

ATLAS

TRIAL NUMBER
JULIAN DAY
LOCAL TIME OF MAP
ELAPSED TRIAL
    TIME OF MAP

NEPH

TRIAL NUMBER
JULIAN DAY
DECIMAL LOCAL TIME
TRIAL ELAPSED TIME
CONCENTRATION DATA FROM
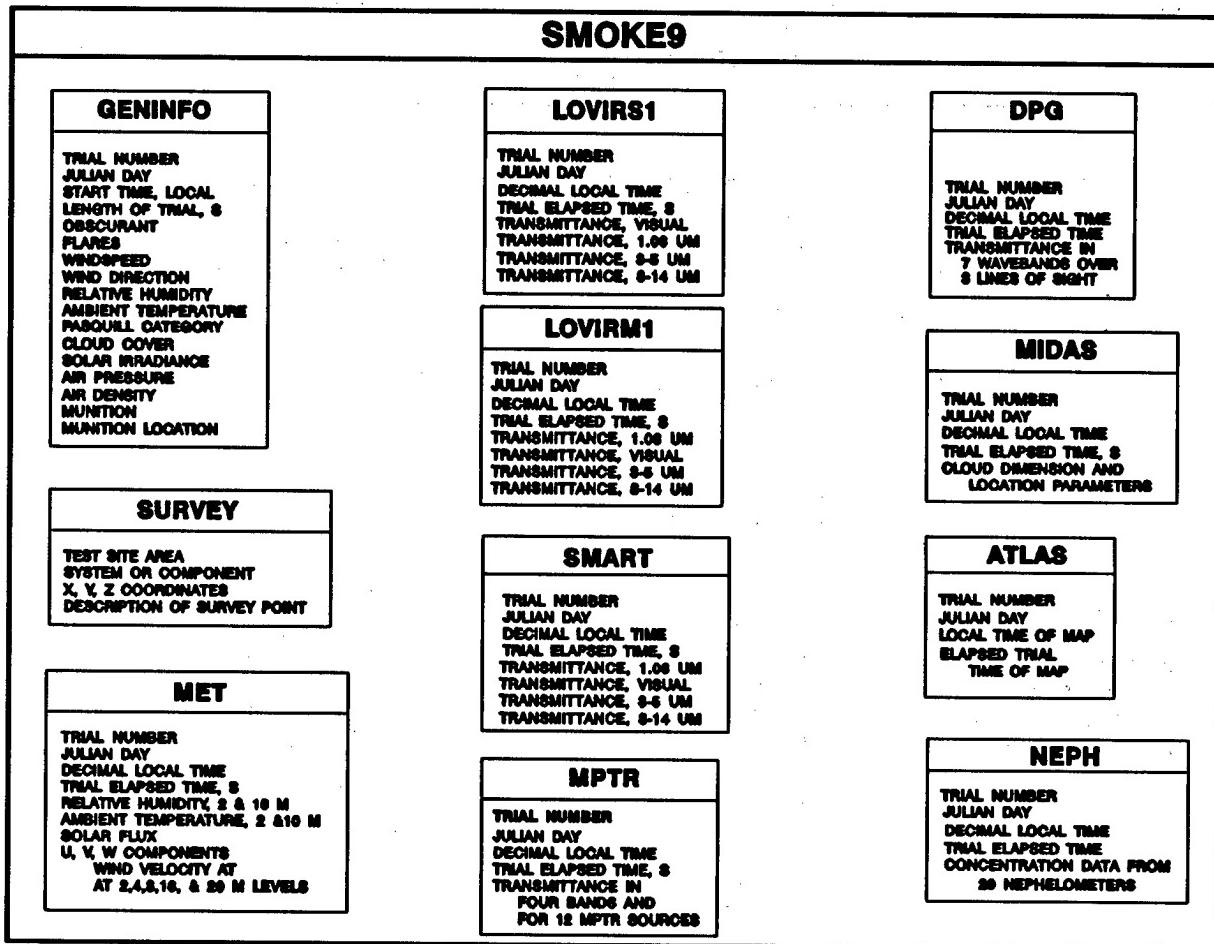   20 NEPHELOMETERS

Figure 1. Smoke Week IX database structure.

DBKEY

DBLIST
- Database
- Test
- Date
- Location
- Type
- Sponsor

DBINFO
- Database
- Participating Organization
- Type of Data
- Media
- Table Names
- Total Rows
- Total Columns
- Point of Contact
- Data Classification
- Quality Code

TRLINFO
- Database
- Trial Number
- Date
- Munition
- Obscurant

REFS
- Database
- Documentation Information

VIDEO
- Test Name
- Tape Date
- Instrumentation/ System
- Trial Number(s)
- Point of Contact
- Color or B/W
- Wavelength
- Tape Format
- Videotape Library Number
- Comments

ABBREVS
- Abbreviation
- Type of Abbrev.
- Definition

Figure 2. Tables of DBKEY database.

5.1.1 DBKEY Table DBLIST

The table DBLIST gives a list of the databases in the entire AAODL data library. The columns in this table tell the user what type of test or data-gathering effort contributed the data, the date and location of the effort, and the sponsoring organization. Table 1 in the previous section was generated by selecting certain columns from DBLIST.

A list of the columns found in DBLIST is shown below.

ID	NAME	TYPE	COMMENTS
1	DBNAME	CHAR	Database name
2	TESTNAME	CHAR	Full name of test
3	TESTTYPE	CHAR	Type of test, e.g., field, lab, etc.
4	STARTDATE	DATE	Starting date of test
5	ENDDATE	DATE	Ending date of test
6	LOCATION	CHAR	Where the test was conducted
7	SPONSOR	CHAR	Test sponsor

5.1.2 DBKEY Table DBINFO

The table DBINFO gives detailed information about all of the data in the AAODL data library. Information is cataloged for data that have been incorporated into databases in the electronic data library, as well as for data that exist in another form, such as hard copy or videotape. This information includes the types of data that are included and the type of media used to record the data. For data that are part of the computerized database library, the column DBTABLE gives the name of the table within the computerized AAODL database that contains the data. If the data are not recorded in the computerized portion of the database, this entry is null.

A list of the columns in DBINFO is shown below.

ID	NAME	TYPE	COMMENTS
1	DBNAME	CHAR	Database name
2	PARTORG	CHAR	Name of participating organization
3	DATATYPE	CHAR	General type of data acquired
4	MEDIA	CHAR	Type of media, hard copy or electronic
5	DBTABLE	CHAR	Name of database table, if any
6	TROWS	NUMBER	Total number of rows in the database (all tables)
7	COLS	NUMBER	Total number of columns in the database (all tables)
8	POC	CHAR	Point of contact, if known
9	CLASS	CHAR	Security classification of data set
10	QCODE	CHAR	Quality code of data, if determined

5.1.3 DBKEY Table TRLINFO

Another table in the database DBKEY that can be of great help to the user in identifying data needed is TRLINFO. This table, used to catalog the information in the databases containing field test data, gives the date, identification number, munitions, and obscurants for every trial in every field test

880

represented in the AAODL database library. The user can find out the conditions for each trial and what database it belongs to. For example, this information allows users to pick out data for trials using a particular munition or obscurant.

A list of the columns in TRLINFO is shown below.

ID	NAME	TYPE	COMMENTS
1	DBNAME	CHAR	Database name
2	TRLDATE	DATE	Trial date
3	TRL	CHAR	Trial identification
4	MUNITION	CHAR	Type of munition(s) used
5	OBSCURANT	CHAR	Type of obscurant(s) used

5.1.4 DBKEY Table REFS

The DBKEY table REFS gives, for each database, the names and publishing information, where relevant, for any written reports that relate to the data. This information may include field test or laboratory reports, data analysis papers, raw data reports, and other supplementary information.

The two columns in the table REFS are the database name and bibliographic information relating to the database. There may be more than one entry for a given database.

5.1.5 DBKEY Table VIDEO

The VIDEO table contains information about imagery recorded at various field tests and submitted to the AAODL videotape library. Users requiring imagery may identify specific videotapes for AAODL personnel to copy for them. The AAODL also has hardware and software with the ability to "grab" single frames and perform image processing.

A list of the columns found in VIDEO is shown below.

ID	NAME	TYPE	COMMENTS
1	TNAME	CHAR	Test name (e.g. SMOKE6)
2	YDATE	CHAR	Video tape date
3	INST	CHAR	Instrumentation/system
4	TRL	CHAR	Trial number(s)
5	POC	CHAR	Point of contact
6	COLOR	CHAR	Videotape type: color or B/W
7	WAVELEN	CHAR	Wavelength of instrument
8	FMAT	CHAR	Videotape format
9	NMBR	CHAR	Videotape library number
10	ANNOT	CHAR	Additional comments

5.1.6 DBKEY Table ABBREVS

The table ABBREVS gives the definitions of abbreviations used in DBKEY. Many of these abbreviations are the same as those used in the data tables in the individual databases; for example, the DBKEY table TRLINFO uses the same abbreviations for munitions and obscurants that are used throughout the data library.

A list of the columns of the ABBREVS table is shown below.

ID	NAME	TYPE	COMMENTS
1	TYPE	CHAR	Type of abbreviation
2	ABBREV	CHAR	Abbreviation used in database
3	DEFN	CHAR	Definition of abbreviation

6. CONCLUDING REMARKS

The AAODL has made steady progress from the time of its establishment twelve years ago. As the battlefield atmospherics research community has evolved, the AAODL has grown to meet new requirements. Improvements in computer hardware and software are regularly made to provide better access and more efficient data archival procedures. These improvements are reflected in the growing number of researchers and organizations that are taking advantage of the services provided by the AAODL.

AAODL USER REQUEST FORM

Complete and mail this form to   Director   Control # _____
                                     U.S. Army Research Laboratory
                                     ATTN: AMSRL-BE-A (Mr. Fidel Tibuni)
                                     White Sands Missile Range, NM 88002-5501
                                     (505) 678-1801 (phone)   (505) 678-8822 (fax)

Name and Address of Requester   _____

                                    _____

                                    _____

                                    _____

Contract No. (if applicable)   _____

Telephone   _____(Commercial)   _____(AV) _____(FTS)

Deliver to ("same as above" if applicable)_____

                                    _____

                                    _____

Required Delivery Date   _____

Data and/or Analyses Requested _____

_____

_____

_____

Format_____

Transfer Medium_____

. . . .

MAILING LIST UPDATE INFORMATION

Please fill in this form if we do not have your correct mailing information.

☐Following is my address correction   ☐Please add the following name(s) to the
                                                         mailing list

_____   _____

_____   _____

_____   _____

☐Please remove my name from your list.   ☐Please send a copy of the USER'S GUIDE.

_____
                          (this section to be completed by AAODL personnel)

Authorized by   _____ Signature_____ Date_____

Released by   _____ Signature_____ Date_____

Delivered to_____

THE EFFECT OF RELATIVE HUMIDITY, WIND, AND ATMOSPHERIC STABILITY ON SMOKE MUNITIONS

Edward D. Creegan
U.S. Army Research Laboratory
Battlefield Environment Directorate
White Sands Missile Range, New Mexico 88002-5501 USA

ABSTRACT

The thrust of this effort is to provide fundamental information as to the importance of wind, relative humidity, and atmospheric stability in terms of their effect on the use of smoke munitions. The variation in the number of munitions required to initiate and sustain smoke screens of a desired length and duration for given relative humidity, wind speed, wind direction, and atmospheric stability is examined. The effects of these atmospheric conditions were calculated based on the Electro-Optical Systems Atmospheric Effects Library (EOSAEL) module crosswind integrated concentration (KWIK). The screens are required to reduce the observation and detection of targets in the visible and near-infrared regions. Several munitions are examined under these atmospheric conditions.

1. INTRODUCTION

The function of a smoke screen is to conceal or obscure something so that it cannot be detected or cannot detect anything else. The level of obscuration needed is driven by the wavelength region and threshold level of detection that the screen is intended to counter. Threshold levels of 10% for the visible and near-infrared (IR) regions were empirically derived from data obtained from the Smoke Week VII field test.[2] Smoke munition materials have different "blocking" effects at various wavelengths and as such, the munition type will determine the best screen for the different wavelength regions.

The screen exists in the atmosphere and is subject to both the positive and negative effects caused by different atmospheric conditions. The atmospheric conditions, as well as the size of the screen, will affect the amount of time the screen remains in the atmosphere. In order to make a screen function, the forces in the atmosphere that affect it must be accounted for correctly.

The Electro-Optical Systems Atmospheric Effects Library (EOSAEL) module crosswind integrated concentration (KWIK) computes the number of munitions necessary to meet screen size and duration requirements for the given parameters of detection threshold and wavelength region. KWIK also requires the munition expenditure calculation to include the atmospheric quantities of wind direction, wind velocity, Pasquill category, and relative humidity (RH).

The wind speed and wind direction are required to evaluate the cloud transport and diffusion calculation. The wind will affect both the direction and the velocity of the screen. This effect can be counter balanced by starting the smoke screen in an advantageous position.

The Pasquill category is a relative measure of the stability of the air mass and will determine how the screen will grow and travel in the atmosphere. The rate of smoke cloud expansion and the concentration of smoke within the cloud is very sensitive to the Pasquill stability category. The atmospheric stability close to the ground depends mainly on net solar radiation and wind speed. Incoming radiation depends on the solar altitude angle, which is a function of the time of day, season of the year, and location on the earth (latitude and longitude). The amount of cloud cover and its height above the ground (ceiling) will also influence solar radiation. The six Pasquill stability categories (A-F) are shown in table 1.[6]

Table 1. Category Descriptions

Pasquill Category	Description
A	Extremely unstable
B	Unstable
C	Slightly unstable
D	Neutral
E	Slightly stable
F	Stable

Relative humidity reflects the density and size distribution of water particles in the air. The yield factor and mass extinction coefficient for both munitions are dependent on the relative humidity.[5,4,1]

2. METHOD

The geometry used for the calculations was a single line-of-sight (LOS) over a 2 km horizontal east-west path with a 1 m terrain roughness length. The visibility was 10 km and no significant weather was included. KWIK was used to calculate the number of munitions necessary to create smoke screens 200 m long and lasting 5 min at the required threshold level of 10%. This was done for both munitions in the visible and near-IR wavelength

regions. Headwind and crosswind cases were examined with relative humidities of 20%, 50%, and 80% for all Pasquill categories (A-F).

Wind velocity is divided within each Pasquill category (shown in table 2) conforming with previous work.[3] For this effort however, the wind velocities within each Pasquill category was averaged to yield a single data point for every Pasquill category in each case.

Table 3. Wind Speed per Pasquill Category (knots)

Pasquill Category	Description
A	2-5
B	3-6
B	6-10
C	0-8
C	9-10
C	11-15
D	6-10
D	12
D	16
E	4-5
E	6-9
F	1-3
F	4-5

The munition expenditure rates were then converted to an effectiveness of arbitrary units with the larger number indicating a better performance.

The trends resulting from the different atmospheric conditions were then plotted and examined in terms of the degradation they had on the smoke screen.

3. PLOTS

The figures show the headwind and crosswind cases for each wavelength region. Within each Pasquill category (A-F) (RH is shown).
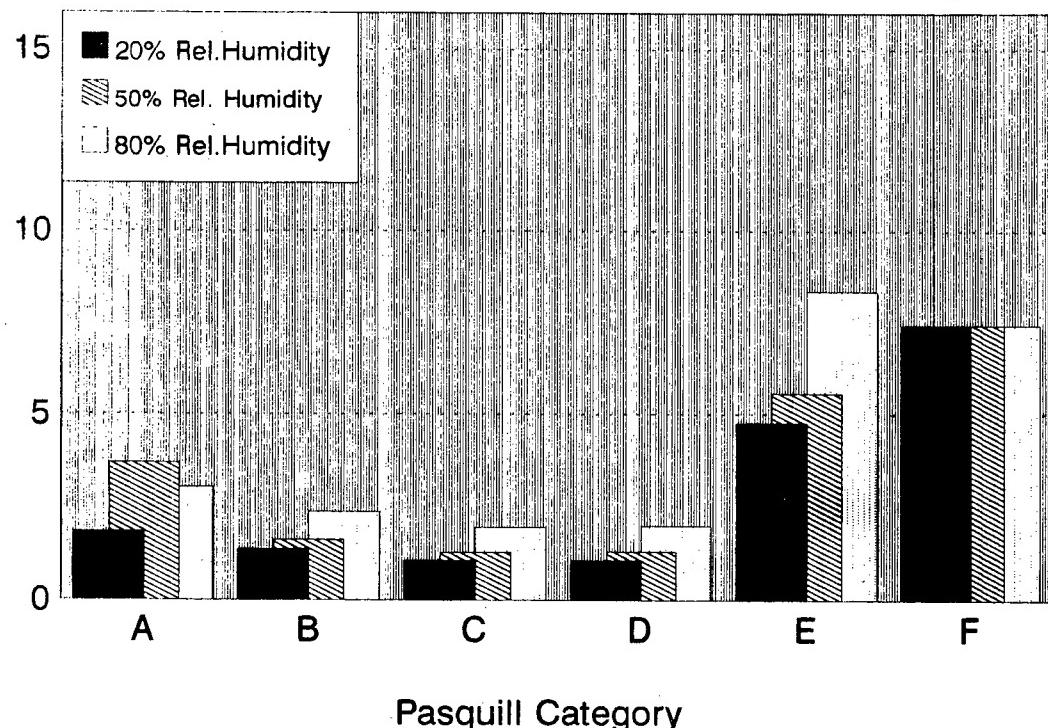
Figure 1. Munition type A - head wind, visible wavelength.
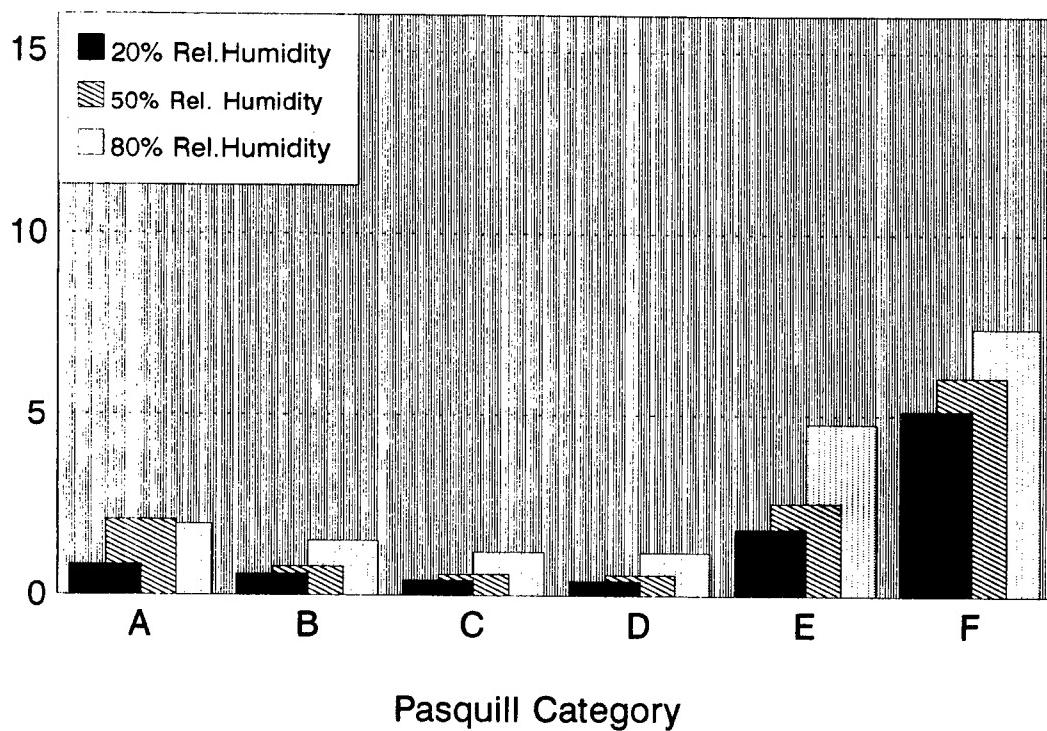
Figure 2. Munition type A - head wind, near-IR wavelength.
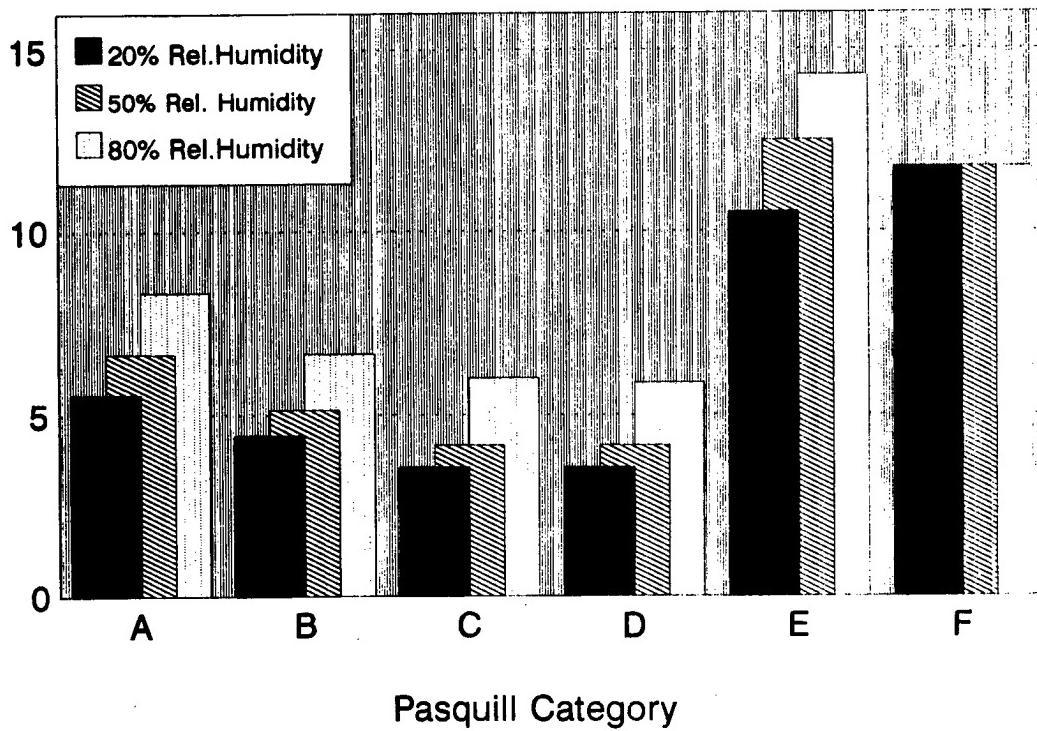
Figure 3. Munition type A - cross wind, visible wavelength.
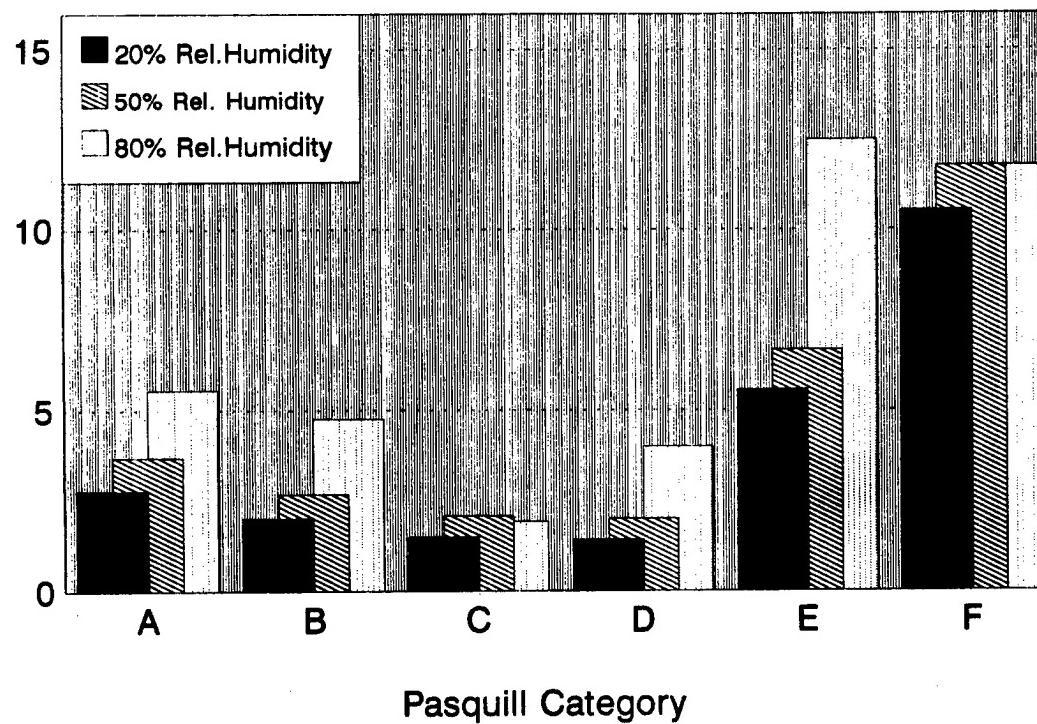
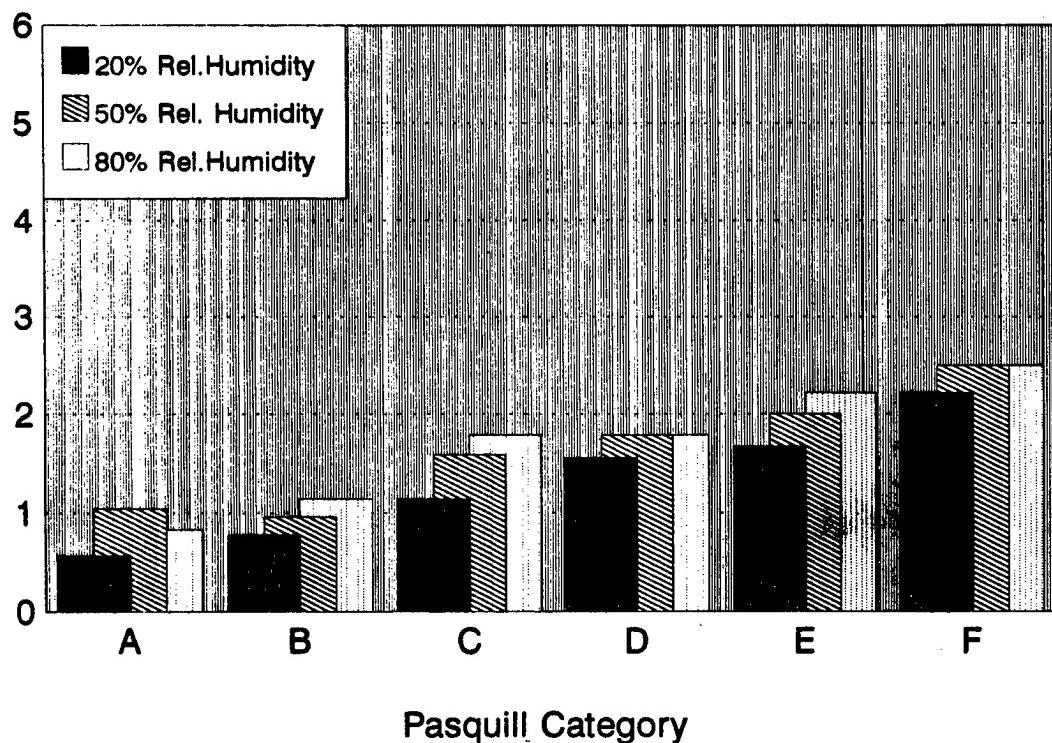**Figure 4. Munition type A - cross wind, near-IR wavelength.**
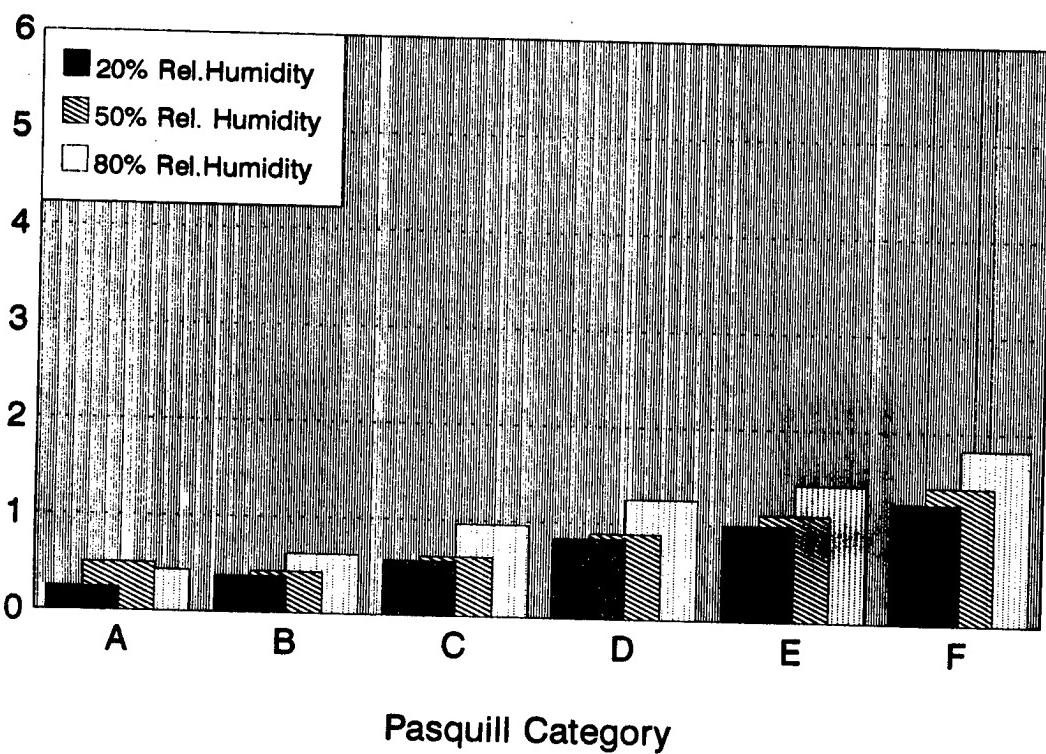
Figure 5. Munition type B - head wind, visible wavelength.

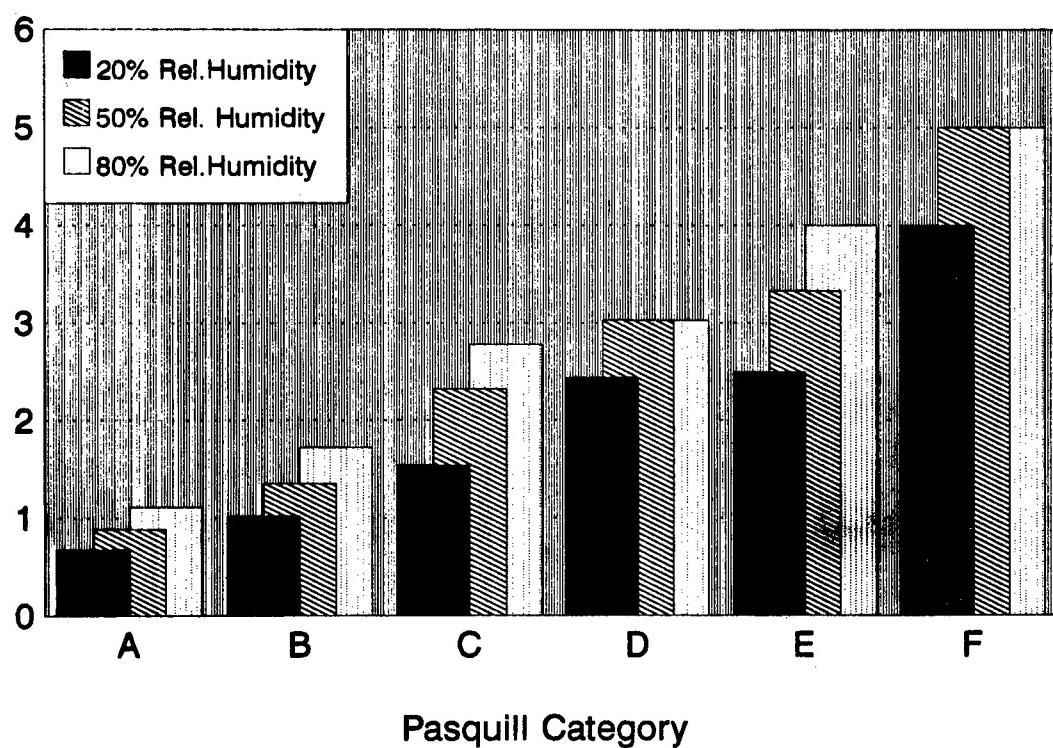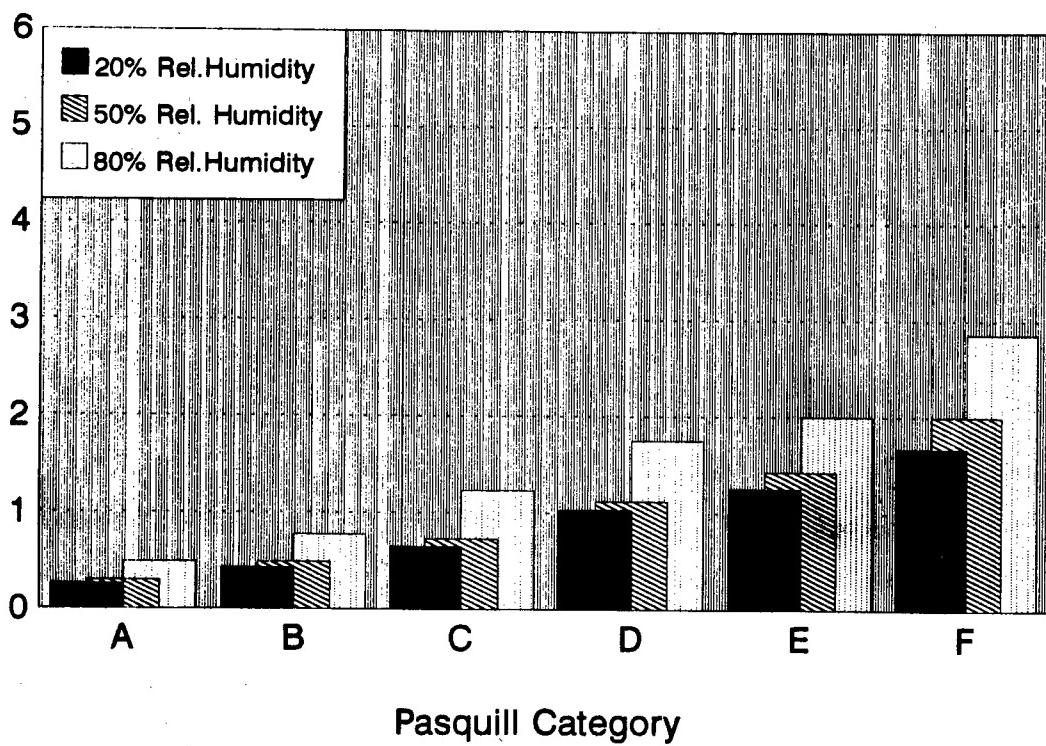**Figure 6. Munition type B - head wind, near-IR wavelength.**

Figure 7. Munition type B - cross wind, visible wavelength.

Figure 8. Munition type B - cross wind, near-IR wavelength.

4. RESULTS AND CONCLUSION

Both munitions were more effective in the visible wavelength region than the near IR, probably by choice of the materials in the smoke.

Munition A:

Pasquill category or the stable atmosphere is the most significant factor considered here in the deployment of the smoke munition. Also, the stable categories (E-F) have lower wind velocities than the less stable ones (C-D). The unstable cases A and B have low wind velocities and were also more effective than the stable and neutral cases that had higher wind velocities.

Next, the wind direction is a unique factor in smoke munition use because the crosswind case can be partially countered by KWIK's upwind adjustment calculation. In the headwind case, the smoke screen is blown clear of the LOS too quickly.

Relative humidity is still a strong factor in smoke munition use because it drives both the mass extinction coefficient and the yield factor; the higher the relative humidity the more effective the munition was within each Pasquill category in almost all cases.

The conditions most advantageous for smoke screen use are a stable air mass, with low wind speed, a crosswind rather than a headwind and a large relative humidity.

Munition B:

The stable air mass is the strongest factor in all the cases and the wind velocities within each case did not have an effect like they did for categories A and B with munition A.

The ability to compensate for the crosswind case makes the wind direction an important consideration in smoke use.

The relative humidity appears to have a threshold in the near IR region above which the effectiveness increases rapidly.

The effects discussed here are only a few of the many parameters known about the atmosphere and are among the most significant for the arena of smoke munitions.

REFERENCES

1. Pena, Ricardo, 1987, "EOSAEL 87 Volume 13 A Munition Expenditures Module KWIK." ASL-TR-0221-13, U.S. Army Atmospheric Sciences Laboratory, White Sands Missile Range, NM 88002-5501.

2. Pena, Ricardo, 1986, "Smoke Munition Expenditures: FM6-40 Versus KWIK Model." ASL-TR-0206, U.S. Army Atmospheric Sciences Laboratory, White Sands Missile Range, NM 88002-5501.

3. Pena, Ricardo, 1991, "Smoke Expenditure Tables For M825, M116, and M110 Munitions." ASL-TMR-0008, U.S. Army Atmospheric Sciences Laboratory, White Sands Missile Range, NM 88002-5501.

4. Sutherland, Robert A., 1983, "Determination and Use of the Hanel Growth Factors for Modeling Hygroscopic Aerosols." Internal Report, U.S. Army Atmospheric Sciences Laboratory, White Sands Missile Range, NM 88002-5501.

5. Hoock, D. W., R. A. Sutherland, and D. Clayton, 1984, "EOSAEL 84 Combined Obscuration Model for Battlefield-Induced Contaminants, COMBIC." ASL-TR-0160-11, U.S. Army Atmospheric Sciences Laboratory, White Sands Missile Range, NM 88002-5501.

6. Pasquill, F., 1974, Atmospheric Diffusion. Second edition, John Wiley and Sons Inc., New York.

THE INTEGRATED WEATHER EFFECTS DECISION AID: A YEAR LATER

David P. Sauter and Robert R. Lee[1]
U.S. Army Research Laboratory
Battlefield Environment Directorate
White Sands Missile Range, NM 88002-5501 USA

Wilbert G. Maunz, Carl H. Chesley, and Andrew R. Spillane
Science and Technology Corporation
Hampton, VA 23666 USA

ABSTRACT

The integrated weather effects decision aid (IWEDA) is a software tool to provide weather effects on Army operations, systems, and subsystems in a tactical environment. An initial version of IWEDA was demonstrated at the 1992 Battlefield Atmospherics Conference (BAC). Since then, beta-testing of the product has been completed by staff weather officers at Fort Hood, Texas. A number of additional capabilities have also been added to IWEDA since the 1992 BAC (for example, a "What-If" module and on-line help). Work is currently progressing on version 2.0 of the software. Interest in IWEDA throughout the Army has been very high.

1. INTRODUCTION

Future command, control, communication, and intelligence (C^3I) systems will harmonize operational and tactical planning of battlefield functional areas (BFAs) by communicating on local and wide-area networks. A new weather effects tactical decision aid (TDA) is intended to reside on these separate BFA nodes that will receive weather data from the integrated meteorological system (IMETS). This TDA will allow the commander and his staff to consider weather and its effects while planning operations and engagements.

---

[1]Current affiliation is with Operational Support Facility - NEXRAD, 1200 Westheimer, Norman, OK 73069

The Battlefield Environment Directorate of the U.S. Army Research Laboratory is developing an integrated weather effects decision aid (IWEDA) software program that will be used to assess the effects of environmental impacts. The responsibility and requirements for assessing environmental effects through weather decision aids (WDAs) is contained in an Army/Air Force joint regulation. The regulation states that the Army is responsible for providing weather effects information to the Air Weather Service, including weather elements and their weather effects critical threshold values, whereas the Air Force is responsible for providing weather decision aid information in general formats such as favorable, marginal, or unfavorable. These WDAs (using green, amber, and red color codes, respectively) are based on operating limitations (critical values) provided by the Army.

Weather always has had and always will have an impact on operations, equipment, and personnel. However, the current weather support precludes planners from being informed of weather impacts *before* the adverse conditions appear. Problems exist in the definition and validation of critical values applied to various operations. Since Army field manuals contain critical values for a number of mission operations without reference to systems, the basis of these critical values is not known. Hence, no obvious vertical connection exists between these published values and specific systems that might be related to the operations.

2. THE IWEDA CONCEPT

The IWEDA program will identify and classify weather effects on equipment, operations, and personnel. IWEDA knowledge bases keep track of systems (for example, M1s, TOWs (tube launched, optically tracked, wire guided), Cobras, personnel), weather parameters (such as temperature, wind, and visibility), and the effects that these parameters have on each system. The user can group different systems into various "operations" during the program setup. After this initial setup, IWEDA evaluates all missions and systems for weather effects and displays rows of missions and columns of times that are color coded favorable, marginal, or unfavorable depending on which missions are affected by current or forecast environmental parameters. In addition, IWEDA can display regions of weather effects as map overlays and provide information concerning the specific causes of weather effects via an explanation facility. Currently weather parameters are entered manually by the user. Weather effects regions are then displayed on a manually generated geographic "map." Eventually the weather data will be automatically ingested via IMETS; and realistic color maps with geographic, cultural, and terrain features will be utilized. This product will reduce the time currently required to assess pertinent weather effects.

Primary users of IWEDA will be Army users, commanders, staff principals/planners, and the staff weather officer (SWO). IMETS will collect the environmental data from various sources and provide these data to drive IWEDA. The role of the SWO will be to ensure that the environmental database in IMETS is current and complete, to generate WDAs to determine the impacts that may occur if and when weather conditions change, and

to brief the tactical commander on the WDAs. With IWEDA on the user's standard workstation (which contains a complete knowledge base of equipment and weapon systems), the program will serve to encourage the user to be more reactive to potential weather impacts and to take the timely and necessary actions to minimize environmental effects on systems and/or operations.

The IWEDA software program can be considered a shell that consists of three distinct parts: weather decision aids, user interface, and data interaction. The WDA component can be further subdivided into traditional algorithmic aids and advanced intelligent aids. The latter consists of an *expert system inference engine*. The data interaction requirements between the IWEDA software and other hardware systems containing IWEDA input data are not explicitly addressed in this paper. The question of "push-pull" of environmental data between IMETS and IWEDA must be addressed in the IMETS concept of operation.

3. KEY DESIGN ATTRIBUTE

The vertical connectivity or linking between mission operations and systems/ subsystems is the key factor that makes IWEDA an extremely useful and effective tool. By taking three separate modules (weather effects matrix, tactical weather effects messages, and consolidated weather effects decision aid) and vertically linking them, IWEDA captures their individual strengths, thereby encapsulating the IWEDA expert system. Vertical connectivity allows the user to determine the basis or rationale of critical values and to visualize how the effects impact the mission. Vertical connectivity also supports the WDA process by allowing the user to trace a weather impact on a mission or operation down to the contributing impact on an individual system or subsystem. The IWEDA program will permit the user to query the system and learn *where*, *what*, *when*, and *why* a mission operation and/or a system is or is forecast to be degraded. This capability will be possible because IWEDA is based upon the vertical connectivity of systems and subsystems with simple defined battlefield mission operations.

CONCLUSIONS

An initial version of IWEDA was taken to Fort Hood, Texas, SWOs for beta testing in August 1993. Preliminary reaction to IWEDA at Fort Hood has been very favorable. Near-term enhancements to IWEDA include the completion of a "What-If" module (to allow the user to immediately see the effects of changes to meteorological parameter values or systems), a graphics and text print capability, and the inclusion of an interactive rule editor. Longer term plans include incorporating algorithmic TDAs (for example, for smoke planning or night vision goggles usage) and the porting to UNIX/XWindows in preparation for IMETS hosting and IMETS weather data ingest.

APPENDICES

AUTHOR INDEX

APPENDIX A

```
╔═══════════════════════╗
║       AGENDA          ║
╚═══════════════════════╝
```

Tuesday, 30 November 1993

0730   **REGISTRATION**
        (Coffee & Tea)

0830   Welcome
        Administrative Announcements
        Introduction of Keynote Speaker

0900   Keynote Address
        Mr. Richard Vitali, Special Assistant to the Commander, U.S. Army Material Command

1000   **BREAK** (Refreshments)

```
╔═══════════════════════════════════════╗
║   SESSION I:  Battle Weather Data     ║
╚═══════════════════════════════════════╝
```

1030   Session I Introduction

1040   Battlefield Weather Data Support for the Army
        Lt Col Douglas C. Pearson, David G. Biggar and *Edward L. Bensman*, Headquarters First
        Weather Group

1100   Combat Weather System (CWS)
        Capt Robert E. Hardwick, HQ AWS/PMA

1120   Weather Data Requirements for State-Of-The-Ground Terrain Analysis
        Franz E. Westermeier, U.S. Army Engineer School

1140   Mobile Profiler System Improvements to the Met Error Contribution of the Artillery
        Error Budget
        Abel J. Blanco and *James Cogan*, U.S. Army Research Laboratory

1200   **LUNCH**

1340   Computer-Assisted Artillery Meteorology System Design
        John B. Spalding, Natalie G. Kellner and *Kerry H. Williamson*, New Mexico State
        University; *Robert S. Bonner*, U.S. Army Research Laboratory

1400   Effects on a Proposed CAAM (Computer Assisted Artillery Met) Model on the Impact
        of the MLRS
        Edward M. D'Arcy, U.S. Army Research Laboratory

1420   TAMDE-The Variability of Weather Over an Army Division Size Area
        John T. Grace, U.S. Army Research Laboratory

1440   Techniques for Measuring Turbulence Parameters for Atmospheric Acoustics
John M. Noble, U.S. Army Research Laboratory

1500   Fluctuations of Acoustic Signals Scattering by an Ensemble of Turbules
George H. Goedecke and *Michael D. DeAntonio*, New Mexico State University;
Harry J. Auvermann, U.S. Army Research Laboratory

1520   Poster Introductions

1545   **BREAK** (Refreshments)

1600   **POSTER SESSION**

1730   **ADJOURNMENT**

Wednesday, 1 December 1993

SESSION II: Simulation and Modeling

0800   Session II Introduction

0810   Obscuration Modeling for Material Developers and Trainers
COL Robert E. Thornton, U.S. Army Chemical School, TRADOC Smoke Integration Proponency Office

0830   Simulating 3D Phenomena of Smoke and Cloud on Synthetic and Real Sequences of Images
Laurent Blondé, Philippe Bordes and *Jean-Christophe Dusseux*, Thomson-CSF/LER, France

0850   Effects of Nonuniform Aerosol Forward Scattering on Imagery
David H. Tofsted, U.S. Army Research Laboratory

0910   Hazard Prediction and Assessment Capability and the OMEGA System
LTC Mark E. Byers, Defense Nuclear Agency; *David P. Bacon*, Science Applications International Corporation

0930   **BREAK** (Refreshments)

1000   Development of the Model of Atmospheric Chemical Hazards for Theater Missile Defense
Ronald E. Meyers, Keith S. Deacon and *Donald Durack*, U.S. Army Research Laboratory

1020   Overview of the Long-Range Overwater Diffusion (LROD) Experiment
James F. Bowers, U.S. Army Dugway Proving Ground

1040   Airflow Indices and Characteristics Within and Above Regular and Irregular Roughness Domains
Brian L. Orndorff and *Ronald M. Cionco*, U.S. Army Research Laboratory

Wednesday, 1 December 1993

1100 The Radiative Energy Balance and Redistribution (REBAR) Program
Young P. Yee and *Robert A. Sutherland*, U.S. Army Research Laboratory; *Roger E. Davis,*
Stephen W. Berrick and *Montie M. Orgill*, Science and Technology Corporation

1120 A Functional Relationship Between Backscatter and Extinction in Very Low Stratus
Clouds and Associated Subcloud Regions
Henry Rachele, U.S. Army Research Laboratory; *Neal H. Kilmer*, New Mexico State
University

1140 **LUNCH**

SESSION III: Atmospheric Sensing

1300 Session III Introduction

1310 Battlefield Atmospheric Soundings: Test Results from a Technical Demonstration
Mobile Profiler System
James L. Cogan, U.S. Army Research Laboratory; *Bob Weber* and *Melinda Simon*,
National Oceanographic and Atmospheric Administration

1330 Analysis of Bi-Spectral Obscurant Trials at Smoke Week XV
Roger E. Davis and *Ronald Catherson*, Science and Technology Corporation

1350 LARDS-A Low Altitude Rocket/Dropsonde with GPS Windfinding
David B. Call, A.I.R., Incorporated

1410 Near-Ground Seeing Measurements
James J. Drexler and *David B. Soules*, Lockheed Engineering and Sciences Company;
Frank D. Eaton, Scott A. McLaughlin and *John R. Hines*, U.S. Army Research
Laboratory

1430 An Attempt to Correlate RASS Coverage with Wind Speed and Relative Humidity
William H. Hatch, U.S. Army Research Laboratory

1450 **BREAK** (Refreshments)

1500 **POSTER SESSION**

1700 **ADJOURNMENT**

1800 **BANQUET**

Thursday, 2 December 1993

SESSION IV: Atmospheric Assessment

0800 Session IV Introduction

0810   The Dirty Battlefield Environment
        Alice L. C. Ruf, James A. Dawson, Lucinda Griner and *Brian Matkin*, Dynetics,
        Incorporated

0830   Analysis of Infrared Backround Scenes from the Grayling I SWOE JT&E Field Test
        Max P. Bleiweiss, U.S. Army Research Laboratory; *Michael Rollins* and *Charles Chaapel*,
        Science and Technology Corporation

0850   Microphone Wind Noise: Is It Really Caused By Wind?
        David H. Marlin, U.S. Army Research Laboratory

0910   Short Term Forecasting for Artillery Using Time Series of Meteorological Data
        Fernando Caracena and *Hui Xue Zhang*, National Oceanographic and Atmospheric
        Administration

0930   **BREAK** (Refreshments)

1000   Measuring/Analyzing Crosswinds Along a High Energy Laser Beam Path
        Gail Tirrell Vaucher, Science and Technology Corporation; *Robert W. Endlich*, U.S.
        Army Research Laboratoy; *Elaine Santantonio*, Science and Technology Corporation

1020   Variability of Atmospheric Turbidity and the Refractive Index Structure Parameter
        (C_n^2)
        Frank D. Eaton, Scott A. McLaughlin and *John R. Hines*, U.S. Army Research
        Laboratory;
        James J. Drexler, David B. Soules and *John Qualtrough*, Lockheed Engineering &
        Sciences Company

1040   Assessment of the Performance of Wind Profilers at White Sands Missile Range
        John R. Hines, U.S. Army Research Laboratory; *Linda Parker*, Science and Technology
        Corporation

1100   Satellite Analysis of Kuwaiti Oil Smoke Plumes
        Jan L. Behunek, John M. Forsythe, and *Thomas H. Vonder Haar*, STC-METSAT

1120   Remote Sensing of Visibility Over Monterey Bay
        Arunas Kuciauskas and *Andreas Goroch*, Naval Research Laboratory

1140   **LUNCH**

```
SESSION V:  Mitigation and Exploitation
```

1300   Session V Introduction

1310   A Review of Model Evaluations for TARGAC
        Patti Gillespie, U.S. Army Research Laboratory

1330   Evaluation of Target Acquisition Model "TARGAC" Using "BEST TWO" Observer
        Performance Data
        Piet Bijl and *J. Mathieu Valeton*, TNO Institute for Human Factors, The Netherlands

1350   Methods for Representing the Atmosphere in Interactive Scene Visualizations
        Donald W. Hoock, U.S. Army Research Laboratory; *John C. Giever*, New Mexico State
        University

1410   Comparison of the BEAMS 2.2 Radiative Transfer Algorithm with Other Radiative
        Transfer Methods
        Sean G. O'Brien, New Mexico State University

1430   Computer Modeling of Timelines and Tactics for Use of the XM81 Grenade
        Joseph L. Manning and *William G. Greenleaf*, Computer Sciences Corporation;
        Jeffery S. Moore, U.S. Army Edgewood RD&E Center

1450   Integrated Weather Effects Decision Aid (IWEDA)
        Carl H. Chesley, Andrew R. Spillane and *Wilbert G. Maunz*, Science and Technology
        Corporation; *Franklin Niles, Robert Lee* and *David Sauter*, U.S. Army Research
        Laboratory

1510   Configuration Management for the Technology Exploitation Weather Testbed
        John R. Elrick, U.S. Army Research Laboratory

1530F   **WRAP-UP**
        Awards - Photos

1600   **ADJOURMENT**

SESSION I POSTERS: Battle Weather Data

Modeled Climatology
Capt Robert J. Falvey, U.S. Air Force Environmental Technical Applications Center

Lockheed MeteoStar™ Model LEADS (Lockheed Environmental Analysis and Display System)
Meteorological Workstation Demonstration
Robert L. Scheinhartz and *T. Steven Barker*, Lockheed Missiles & Space Company, Incorporated

Integration of a Heat Strain Prediction Model with Army Weather Data Resources
William T. Matthew, U.S. Army Research Institute of Environmental Medicine;
Richard E. McNally, Science Applications International Corporation; *Gary B. McWilliams* and
Steve F. Kirby, U.S. Army Research Laboratory; *Heather D. Pfeiffer*, New Mexico State University

Forecasting Clear Air Turbulence Using a Single Sounding
Jeffrey E. Passner, U.S. Army Research Laboratory

Two Recent Climatological Data Initiatives at USAFETAC
Capt Christopher A. Donahue, U.S. Air Force Environmental Technical Applications Center

Evaluation of Low-Level Turbulence Indices on a Mesoscale Grid
Capt David I. Knapp, Robert Dumais and *MSgt Timothy J. Smith*, U.S. Army Research Laboratory

Development of Rule-Based Techniques for the Management of Meteorological Message Dissemination in the Computer-Assisted Artillery Meteorology System
Arthur W. Dudenhoeffer and *Donald D. Bustamante*, New Mexico State University

Time and Space Weighted Computer Assisted Artillery Message
Abel J. Blanco, Edward Vidal and *Sean D'Arcy*, U.S. Army Research Laboratory

Wind Field Variability in the CAAM (Computer Assisted Artillery Met) Model Validation
Juan R. Quezada, John T. Grace and *Abel J. Blanco*, U.S. Army Research Laboratory

TWIST: Reasoning Within the Combined Mercury and WADIF Systems
Heather D. Pfeiffer, New Mexico State University

An Extrapolation Technique for Determining Temperature Distributions in the Battlefield Environment
Brian T. Davis, New Mexico State University

Operational Short-Range Forecast Model for Battlescale Area
Teizi Henmi and *Robert E. Dumais, Jr.*, U.S. Army Research Laboratory

SESSION II POSTERS: Simulation and Modeling

Thermal Properties of Soils
Henry Rachele, Frank V. Hansen and *Arnold Tunick*, U.S. Army Research Laboratory; *Lisa Manguso*, New Mexico State University

MADONA - An International High-Resolution Meteorology and Diffusion Field Study
Ronald M. Cionco and *John H. Byers*, U.S. Army Research Laboratory

A Method for Visualizing the Effects of Terrain and Wind Upon Battlefield Operations
Ronald M. Cionco and *John H. Byers*, U.S. Army Research Laboratory

Comparison of Optical Turbulence Models for Forecast Applications
Montie M. Orgill, Kenneth P. Freeman and *Roger E. Davis*, Science and Technology Corporation; *Robert Endlich*, U.S. Army Research Laboratory

Applicability of Meso-Scale and Terrain Effects Models for Battlefield Environments
Harald Weber, German Military Geophysical Office, Germany

A Modern Graphical User Interface for Legacy FORTRAN Code
Dick Larson, New Mexico State University

Field Test Results of a FORTRAN Model Used to Predict Surface and Subsurface Temperatures
Tommy B. Davis, New Mexico State University

Three-Dimensional Extension of the CIRRUS Technique
Max P. Bleiweiss, U.S. Army Research Laboratory; *Kenneth C. Payne, Thomas A. King* and *Steven J. LaMotte*, New Mexico State University

PC-Based Computer Programs for Ultraviolet Propagation and Spectral Discrimination Analysis
James B. Gillespie, David L. Rosen and *Stan R. Niles*, U.S. Army Research Laboratory

Battlefield Atmospheric Simulation of Transport and Diffusion Over Complex Terrain, Urban Areas, and Military Vehicles
Ronald E. Meyers and *Keith S. Deacon*, U.S. Army Research Laboratory

Easy-To-Use Optical Profile Function Program for Modeling Extinction and Backscatter Coefficients in Low Stratus Clouds and Subcloud Regions
Neal H. Kilmer, New Mexico State University; *Henry Rachele*, U.S. Army Research Laboratory

Combat-Induced Atmospheric Obscurants (CIAO) System
Scarlett D. Ayres and *Robert A. Sutherland*, U.S. Army Research Laboratory; *Kathy R. Hansen* and *Steven C. Newman*, New Mexico State University

An Atmospheric Data Base Structure, Visualization Methodology, and Data Exchange Techniques
R. Smith and *Thelma Chenault*, U.S. Army Research Laboratory

Measurement of the Intermittency in the Inertial Sub-Range of the Atmospheric Wind Velocity Spectrum
William A. Peterson, D. Garvey, Thelma Chenault, R. Smith and D. Littell, U.S. Army Research Laboratory

```
SESSION III POSTERS:  Atmospheric Sensing
```

Neural Network Retrieval of Atmospheric Parameters from Meteorological Satellites Using TOVS Data
Donald D. Bustamante and *Arthur W. Dudenhoeffer*, New Mexico State University; *James L. Cogan*, U.S. Army Research Laboratory

Environmental Monitoring with the Mobile Atmospheric Spectrometer Testbed
Frank T. Kantrowitz and *Raymond A. Dise*, U.S. Army Research Laboratory; *William M. Gutman* and *Troy D. Gammill*, New Mexico State University

A Generic Method for Earth Locating Data Scan by Satellite
Steve McGee, New Mexico State University

Development of a Laboratory Technique for Determining the Fluorescence Efficiency for a Singly Levitated Droplet
J.B. Gillespie, Stan R. Niles and *David Ligon*, U.S. Army Research Laboratory

Neural Networks for Vehicle Detection and Classification
Gilles Burel and *Jean-Yves Catros*, Thomson CSF, Laboratoires Electroniques de Rennes, France

Comparison of Radiometer, RASS, and Radiosonde Generated Vertical Profiles of Atmospheric Temperature
Edward M. Measure, U.S. Army Research Laboratory; *Teddy L. Barber* and *Dick R. Larson*, New Mexico State University

Remote Measurements of the Density of Battlefield Visual Obscurants
Radon B. Loveland and *Ascencion Acosta*, New Mexico State University; *Raul Gonzalez* and
Jill C. Thompson, U.S. Army Research Laboratory

SESSION IV POSTERS: Atmospheric Assessment

An Evaluation of the APRF Acoustic Sounder As Related to the FM-CW Calibration Process
John R. Hines, Scott A. McLaughlin and *Frank D. Eaton*, U.S. Army Research Laboratory;
David Vaello, Radian Corporation

Characterization of the Wind Field at Aerial Cable Test Capability Site
Richard Okrasinski, New Mexico State University; *Robert Olsen*, U.S. Army Research Laboratory

Assessment of the Performance of RASS Systems at White Sands Missile Range
John R. Hines, U.S. Army Research Laboratory; *Elaine Santantonio, Glenn Hoidale* and
Wayne Flowers, Science and Technology Corporation

Cloud Free Line of Sight Model Differences
Kenneth E. Eis, Donald L. Reinke, John M. Forsythe and *Thomas H. Vonder Haar*, STC-METSAT

Climatological and Historical Analysis of Cloud for Environmental Simulations (CHANCES)
Donald L. Reinke, Thomas H. Vonder Haar, Kenneth E. Eis, John M. Forsythe and *D. Neil Allen*,
STC-METSAT

SESSION V POSTERS: Mitigation and Exploitation

An Overview of the Atmospheric Aerosols and Optics Data Library (AAODL)
John N. Crain, Science and Technology Corporation; *Fidel Tibuni*, U.S. Army Research
Laboratory

The Effect of Relative Humidity, Wind, and Atmospheric Stability on Smoke Munitions
Edward D. Creegan, U.S. Army Research Laboratory

The Integrated Weather Effects Decision Aid: A Year Later
David Sauter and *Robert Lee*, U.S. Army Research Laboratory; *Wilbert G. Maunz, Carl H. Chesley*
and *Andrew R. Spillane*, Science and Technology Corporation

Army Weather and Environmental Critical Value Relational Data Base
Charles Warnick, U.S. Army Intelligence Center

APPENDIX B

LIST OF ATTENDEES

A

Mr. Joseph Andrese
U.S. Army Research Laboratory
AMSRL-SL-CM
APG, MD 21010-5423
Tel: 410/671-2045
Fax: 410/671-3471

Dr. Harry J. Auvermann
U.S. Army Research Laboratory
Battlefield Environment Directorate
AMSRL-BE-M
WSMR, NM 88002-5001
Tel: 505/678-4224
Fax: 505/678-2432

LCDR Gary Ayers
Naval Research Laboratory
TOWS Program Office
Code 7410, Bldg 1105
Stennis Space Center, MS 39529-5004
Tel: 601/688-4760
Fax: 601/688-4605

Ms. Scarlett D. Ayres
U.S. Army Research Laboratory
Battlefield Environment Directorate
AMSRL-BE-E
WSMR, NM 88002-5501
Tel: 505/678-4350
Fax: 505/678-2631

B

Dr. Walter D. Bach, Jr.
Army Research Office
P.O. Box 12211
Research Triangle Park, NC 27709-2211
Tel: 919/549-4247
Fax: 919/549-4310

Mr. Teddy L. Barber
Physical Science Laboratory
P.O. Box 30002
Las Cruces, NM 88003-0002
Tel: 505/522-9380
Fax: 505/522-9434

Mr. T. Steven Barker
Lockheed Austin Division
Org. T2-30, Bldg 320
6800 Burleson Road
Austin, TX 78744
Tel: 512/386-1190
Fax: 512/386-1730

CDR Wesley A. Barton
COMNAVMETOCCAM
1020 Balck Boulevard
Stennis Space Center, MS 39529-5005
Tel: 601/688-4892
Fax: 601/688-5332

CAPT Edward L. Bensman
1st Weather Group
1 WEAG/WSOT
Bldg 130, Anderson Way
Fort McPherson, GA 30330-5000
Tel: 404/752-3299
Fax: 404/752-2744

Mr. John R. Benton
U.S. Army Topographic Engineering Center
Artificial Intelligence Division
Bldg 2592
Fort Belvoir, VA 22060
Tel: 703/355-2717
Fax: 703/355-3176

Mr. Jack Berndt
Science Applications International Corp
626 Towne Center Drive, Suite 205
Joppa, MD 21085
Tel: 410/679-9800
Fax: 410/679-3705

Mr. Abel J. Blanco
U.S. Army Research Laboratory
Battlefield Environment Directorate
AMSRL-BE-W
WSMR, NM 88002-5501
Tel: 505/678-3924
Fax: 505/678-3385

Mr. Max P. Bleiweiss
U.S. Army Research Laboratory
Battlefield Environment Directorate
AMSRL-BE-A
WSMR, NM 88002-5501
Tel: 505/678-3504
Fax: 505/678-3822

Dr. Marie L. Boeck
The Aerospace Corp
P.O. Box 92957
Los Angeles, CA 9009-2957
Tel: 310/336-5879
Fax: 310/336-1812

Mr. Robert S. Bonner
U.S. Army Research Laboratory
Battlefield Environment Directorate
AMSRL-BE-W
WSMR, NM 88002-5501
Tel: 505/678-6662

Mr. James F. Bowers
U.S. Army Dugway Proving Ground
STEDP-MT-M
Dugway Proving Ground, UT 84022-5000
Tel: 801/831-5101
Fax: 801/831-5289

Mr. Harry Lee Brano
46 Weather Flight
601 W Choctawhatchee Avenue, Suite 60
Eglin AFB, FL 32542-5719
Tel: 904/882-5960
Fax: 904/882-3341

Ms. Jan Breeden
USAFSTC
220 7th Street NE
Charlottesville, VA 22901
Tel: 804/980-7870
Fax: 804/980-7699

Dr. Ralph J. Brewer
OptiMetrics, Inc.
106 E. Idaho, Suite C
Las Cruces, NM 88005
Tel: 505/523-4987
Fax: 505/525-1775

Dr. Douglas R. Brown
U.S. Army Research Laboratory
Battlefield Environment Directorate
AMSRL-BE
WSMR, NM 88002-5501
Tel: 505/678-1227
Fax: 505/678-1230

MAJ Raymond C. Brown
HQ USMC (ASL-44)
2 Navy Annex
Washington, DC 20380-1775
Tel: 703/614-1835
Fax: 703/614-2131

Mr. Robert C. Brown
U.S. Army Research Laboratory
Battlefield Environment Directorate
AMSRL-BE-S
WSMR, NM 88002-5001
Tel: 505/678-4334
Fax: 505/678-2053

Dr. Dorothy A. Bruce
U.S. Army Research Laboratory
Battlefield Environment Directorate
AMSRL-BE-A
WSMR, NM 88002-5501
Tel: 505/678-5524
Fax: 505/678-8822

Mr. Brain R. Bullard
Science and Technology Corp
555 Telshor Boulevard, Suite 200
Las Cruces, NM 88011
Tel: 505/521-4353
Fax: 505/522-9062

Mr. Chuck Busick
ASTRO/Science and Technology Corp
5321 Riggs Road
Gaithersburg, MD 20882
Tel: 301/926-5496
Fax: 301/926-5306

Mr. Donald D. Bustamante
Physical Science Laboratory
New Mexico State University
P.O. Box 30002
Las Cruces, NM 88003
Tel: 505/522-9209
Fax: 505/522-9434

Mr. John H. Byers
U.S. Army Research Laboratory
Battlefield Environment Directorate
AMSRL-BE-E
WSMR, NM 88002-5501
Tel: 505/678-3951
Fax: 505/678-2053

C

Mr. David B. Call
Atmospheric Instrumentation Research Inc
8401 Baseline Road
Boulder, CO 80303
Tel: 303/499-1701
Fax: 303/499-1767

Dr. Fernando Caracena
NOAA-Environmental Research Laboratory
RIE/FSI
325 Broadway Street
Boulder, CO 80303
Tel: 303/497-6269
Fax: 303/497-3329

Mr. Ernest A. Carroll
Pacific-Sierra Researach Corp
1401 Wilson Boulevard, Suite 1100
Arlington, VA 22209
Tel: 703/516-6105
Fax: 703/524-2420

Mr. Mogens Caspersen
Danish Defence Research Est.
Ryvergs alle 1
P.O. Box 2715
DK2100 Copenhagen, Denmark
Tel: 45 3927 2233
Fax: 45 3120 3315

Mr. Ronald Catherson
Science and Technology Corp
555 Telshor Boulevard, Suite 200
Las Cruces, NM 88011
Tel: 505/521-4353
Fax: 505/522-9062

Dr. S.J. Caughey
UK Meteorological Office
London Road, Bracknell
Berkshire, RG12 2SZ, United Kingdom
Tel: 44 344 85 6298
Fax: 44 344 85 6979

Dr. Pin-Chou Chen
The Aerospace Corp
P.O. Box 92957-M3/716
Los Angeles, CA 90009-2957
Tel: 310/336-7442
Fax: 310/336-8943

Ms. Thelma A. Chenault
U.S. Army Research Laboratory
Battlefield Environment Directorate
AMSRL-BE-A
WSMR, NM 88002
Tel: 505/678-6579
Fax: 505/678-4449

Mr. Carl H. Chesley
Science and Technology Corp
101 Research Drive
Hampton, VA 23666-1340
Tel: 804/865-0467
Fax: 804/865-8721

Mr. Prasan Chintawongvanich
Physical Science Laboratory
New Mexico State University
P.O. Box 30002
Las Cruces, NM 88003-0002
Tel: 505/522-9142
Fax: 505/522-9389

Mr. Ronald M. Cionco
U.S. Army Research Laboratory
Battlefield Environment Directorate
AMSRL-BE-S
WSMR, NM 88002-5501
Tel: 505/678-5210
Fax: 505/678-2053

Dr. James L. Cogan
U.S. Army Research Laboratory
Battlefield Environment Directorate
AMSRL-BE-W
WSMR, NM 88002-5501
Tel: 505/678-2094
Fax: 505/678-0343

MAJ Robert M. Cox
HQ DNA/SPWE
6801 Telegraph Road
Alexandria, VA 22310
Tel: 703/325-1282
Fax: 703/325-0398

Mr. John N. Crain
Science and Technology Corp
555 Telshor Boulevard, Suite 200
Las Cruces, NM 88011
Tel: 505/521-4353
Fax: 505/522-9062

Mr. Edward D. Creegan
U.S. Army Research Laboratory
Battlefield Environment Directorate
AMSRL-BE-W
WSMR, NM 88002-5501
Tel: 505/678-4684
Fax: 505/678-8366

D

Mr. Edward M. D'Arcy
U.S. Army Research Laboratory
Battlefield Environment Directorate
AMSRL-BE-W
WSMR, NM 88002-5501
Tel: 505/678-3523
Fax: 505/678-3385

Mr. Sean D'Arcy
U.S. Army Research Laboratory
Battlefield Environment Directorate
AMSRL-BE
WSMR, NM 88002
Tel: 505/678-1184

Mr. Francis Danielian
Army Procurement, DGA/SEFT
18, Rue du Docteur Zamenhof
92131 Issy-Les-Moulineaux Cedex, France
Tel: 33.1.40.95.35.51
Fax: 33.1.40.95.31.01

Mr. Lyle L. Dauber
U.S. Army Edgewood RD&E Center
SCBRD-ENM
APG, MD 21010-5423
Tel: 410/671-6571
Fax: 410/671-2082

Dr. Roger E. Davis
Science and Technology Corp
555 Telshor Boulevard, Suite 200
Las Cruces, NM 88011
Tel: 505/521-4353
Fax: 505/522-9062

Mr. Tommy B. Davis
4322 Santa Rita
El Paso, TX 79902
Tel: 505/521-1135

Dr. Adarsh Deepak
Science and Technology Corp
101 Research Drive
Hampton, VA 23666
Tel: 804/865-1894
Fax: 804/865-1294

Mr. John Devore
Visidyne, Inc.
5951 Encina Road, Suite 208
Goleta, CA 93117-2211
Tel: 805/683-4277
Fax: 805/683-5377

Mr. Alwin Dimmeler
Research Institute for Optics (FGAN-FFO)
Schloss Kressbach
72072 Tuebingen, Germany
Tel: 7071-709145
Fax: 7071-709270

Dr. Nathan Dinar
Israel Institute for Biologial Research
Department of Mathematics
P.O. Box 19
70450 Ness-Ziona, Israel
Tel: 972-8-381440
Fax: 972-8-401404

CAPT Christopher A. Donahue
USAFETAC/SYT
859 Buchanan Street, Rm 306
Scott AFB, IL 62225-5116
Tel: 618/256-4107
Fax: 618/256-3772

Mr. James J. Drexler
Lockheed Engineering & Sciences Co
P.O. Box 189
WSMR, NM 88002
Tel: 505/678-4735
Fax: 505/678-7388

Dr. Arthur W. Dudenhoeffer
Physical Science Laboratory
New Mexico State University
P.O. Box 30002
Las Cruces, NM 88003
Tel: 505/522-9343
Fax: 505/522-9434

Mr. Robert E. Dumais, Jr.
U.S. Army Research Laboratory
Battlefield Environment Directorate
AMSRL-BE-W
WSMR, NM 88002-5501
Tel: 505/678-4650

E

Mr. Frank D. Eaton
U.S. Army Research Laboratory
Battlefield Environment Directorate
AMSRL-BE-E
WSMR, NM 88002-5501
Tel: 505/678-3956
Fax: 505/678-7623

Mr. David P. Edwards
GTE Govt Systems
81717 La Tienda
Box 5027
Westlake Village, CA 91359-5027
Tel: 818/706-5444
Fax: 818/706-5050

Dr. Harry Edwards
Defence Research Agency
MTC4(C), Fort Halstead, Sevenoaks
Kent, TN14 7BP, United Kingdom
Tel: 0959 532222
Fax: 0959 53900

Mr. Doyle S. Elliott
U.S. Army Research Laboratory
Artillery Meteorology Team
AMSRL-BE-W
WSMR, NM 88002-5501
Tel: 505/678-3838
Fax: 505/678-3385

Mr. John R. Elrick
U.S. Army Research Laboratory
Battlefield Environment Directorate
AMSRL-BE-W
WSMR, NM 88002-5501
Tel: 505/678-3691
Fax: 505/678-3385

Mr. Robert Endlich
U.S. Army Research Laboratory
Battlefield Environment Directorate
AMSRL-BE-A
WSMR, NM 88002-5501
Tel: 505/678-6297
Fax: 505/678-4449

Dr. Bernard F. Engebos
U.S. Army Research Laboratory
Battlefield Environment Directorate
AMSRL-BE-M
WSMR, NM 88005-5501
Tel: 505/678-1489
Fax: 505/678-8366

Ms. Joanne M. Esparza
Physical Science Laboratory
New Mexico State University
P.O. Box 30002
Las Cruces, NM 88003-0002
Tel: 505/522-9117
Fax: 505/522-9389

F

CAPT Gary R. Faltinowski
Space and Naval Warfare Systems Command
(PMW 165-14)
2451 Crystal Drive, Room 301
Arlington, VA 22245-5200
Tel: 703/602-3187
Fax: 703/602-1535

CAPT Robert J. Falvey
USAFETAC
Simulations and Techniques Branch
859 Buchanan Street, Rm 311S
Scott AFB, IL 62225-5116
Tel: 618/256-5412
Fax: 618/256-3772

Dr. Michael W. Farmer
The Bionetics Corporation
500 S. Main, Suite 900
Las Cruces, NM 88001
Tel: 505/527-5623
Fax: 505/527-5633

MAJ Richard Fleming
USAIC&FH/SWO
ATZS-CDI-W
Fort Huachuca, AZ 85613
Tel: 602/538-6472
Fax: 602/533-5045

Mr. Wayne Flowers
Science and Technology Corp
555 Telshor Boulevard, Suite 200
Las Cruces, NM 88011
Tel: 505/521-4353
Fax: 505/522-9062

MSGT Bryan Folk
HQ Air Weather Service
102 W. Losey Street, Room 105
Scott AFB, IL 62225
Tel: 618/256-4911
Fax: 618/256-6300

Mr. John R. Fox
U.S. Army Research Laboratory
Battlefield Environment Directorate
AMSRL-BE-M
WSMR, NM 88002-5501
Tel: 505/678-2110
Fax: 505/678-2432

Dr. K. Patrick Freeman
Science and Technology Corp
555 Telshor Boulevard, Suite 200
Las Cruces, NM 88011
Tel: 505/521-4353
Fax: 505/522-9062

G

Mr. Joseph Gamson
U.S. Army Research Laboratory
AMSRL-CP-PE
2800 Powder Mill Road
Adelphi, MD 20783-1145
Tel: 301/394-3557
Fax: 301/394-2591

Mr. Dennis Garvey
US Army Research Laboratory
Battlefield Environment Directorate
AMSRL-BE-E
WSMR, NM 88002-5501
Tel: 505/678-5677
Fax: 505/678-2053

Mr. John C. Giever
Physical Science Laboratory
New Mexico State University
P.O. Box 30002
Las Cruces, NM 88003-0002
Tel: 505/522-3280

Dr. James B. Gillespie
U.S. Army Research Laboratory
Battlefield Environment Directorate
AMSRL-BE-W
WSMR, NM 88002-5501
Tel: 505/678-6609
Fax: 505/678-2432

Dr. Patti Gillespie
U.S. Army Research Laboratory
Battlefield Environment Directorate
AMSRL-BE
WSMR, NM 88002-5501
Tel: 505/678-1817
Fax: 505/678-8366

Ms. Melanie Gouveia
Hughes STX
109 Massachusetts Avenue
Lexington, MA 02173
Tel: 617/862-0715
Fax: 617/863-2357

Mr. John T. Grace
U.S. Army Research Laboratory
Battlefield Environment Directorate
AMSRL-BE-W
WSMR, NM 88002-5501
Tel: 505/678-6509
Fax: 505/678-0343

Mr. William G. Greenleaf
Computer Sciences Corporation
4815 Bradford Drive
Huntsville, AL 35805
Tel: 205/837-7200
Fax: 205/837-7200

Dr. William M. Gutman
Physical Science Laboratory
P.O. Box 30002
Las Cruces, NM 88003-0002
Tel: 505/522-9573
Fax: 505/522-9434

H

Dr. Patrick E. Hagerty
FMC Corp
Armament Systems Division
4800 E. River Road
Minneapolis, MN 55421-1498
Tel: 612/572-4787
Fax: 612/572-4978

MSGT Frank J. Hall
Det 4, HQ AWS/XTE
Bldg 91027
595 Independence Road
Hurlburt Field, FL 32544-5618
Tel: 904/884-6754
Fax: 904/884-5503

CAPT Stephen C. Hallin
ESC/XRC
50 Griffiss Street
Hanscom AFB, MA 01731-1624
Tel: 617/271-8621
Fax: 617/271-4683

Mr. G. Michael Hardaway
U.S. Army Topographic Engineering Center
CETEC-GL-VA
7701 Telegraph Road
Fort Belvoir, VA 22060-5546
Tel: 703/355-3852
Fax: 703/355-3176

Mr. James E. Harris
U.S. Army Research Laboratory
Battlefield Environment Directorate
AMSRL-BE-W
WSMR, NM 88002-5501
Tel: 505/678-4207
Fax: 505/678-0343

Mr. William H. Hatch
U.S. Army Research Laboratory
Battlefield Environment Directorate
AMSRL-BE-E
WSMR, NM 88002-5501
Tel: 505/678-1561
Fax: 505/678-7623

Dr. Teizi Henmi
U.S. Army Research Laboratory
Battlefield Environment Directorate
AMSRL-BE-W
WSMR, NM 88002-5501
Tel: 505/678-3519
Fax: 505/678-8366

Ms. Joyce Henry
U.S. Army Tradoc Analysis Center
ATRC-WEA
WSMR, NM 88002
Tel: 505/678-4789
Fax: 505/678-5104

Mr. Richard F. Himebrook
U.S. Army Research Laboratory
AMSRL-CP-PE
WSMR, NM 88001-5501
Tel: 505/678-4917
Fax: 505/678-2432

Mr. John R. Hines
U.S. Army Research Laboratory
Battlefield Environment Directorate
AMSRL-BE-E
WSMR, NM 88002-5501
Tel: 505/678-1561
Fax: 505/678-7623

Dr. Donald B. Hodges
Hughes STX Corporation
109 Massachusetts Avenue
Lexington, MA 02173
Tel: 617/862-0713
Fax: 617/863-2357

Mr. Benjamin Holberg
U.S. Army Research Laboratory
AMSRL
WSMR, NM 88002-5501
Tel: 505/678-8846
Fax: 505/678-8846

Dr. Donald W. Hoock
U.S. Army Research Laboratory
Battlefield Environment Directorate
AMSRL-BE-S
WSMR, NM 88002-5501
Tel: 505/678-5430
Fax: 505/678-8366

Ms. Karen L. Hutchison
Physical Science Laboratory
New Mexico State University
P.O. Box 30002
Las Cruces, NM 88003-0002
Tel: 505/522-9412
Fax: 505/522-9434

J

Mr. Ray Jablonski
U.S. Army Edgewood RD&E Center
SCBRD-RTM
APG, MD 21010-5423
Tel: 410/671-3566
Fax: 410/671-3523

Mr. Jeffrey Johnson
U.S. Army Research Laboratory
Battlefield Environment Directorate
AMSRL-BE-A
WSMR, NM 88002-5501
Tel: 505/678-3569
Fax: 505/678-4449

Mr. Jerry Johnson
Science and Technology Corp
101 Research Drive
Hampton, VA 23666
Tel: 804/865-0467
Fax: 804/865-8721

Mr. Mark R. Jourdan
USAE Waterways Experiment Station
CEWES-HE-E
3909 Halls Ferry Road
Vicksburg, MS 39181-6199
Tel: 601/634-3525
Fax: 601/634-2986

K

Mr. Terrence A. Kanka
The MITRE Corp
M/S Z421
7525 Colshire Drive
McLean, VA 22102
Tel: 703/883-7204
Fax: 703/883-1230

Dr. Hadassah Kaplan
Israel Institute for Biologial Research
Department of Mathematics
P.O. Box 19
70450 Ness-Ziona, Israel
Tel: 972-8-381440
Fax: 972-8-401404

Mr. Dennis Kasparek
Science and Technology Corp
555 Telshor Boulevard, Suite 200
Las Cruces, NM 88011
Tel: 505/521-4353
Fax: 505/522-9062

Ms. Natalie Kellner
Physical Science Laboratory
New Mexico State University
PO Box 30002
Las Cruces, NM 88003-0002
Tel: 505/522-9288
Fax: 505/522-9389

Mr. Bruce Kennedy
Physical Science Laboratory
P.O. Box 30002
Las Cruces, NM 88005
Tel: 505/522-9289
Fax: 505/522-9389

Dr. Neal H. Kilmer
Physical Science Laboratory
New Mexico State University
PO Box 30002
Las Cruces, NM 88003-0002
Tel: 505/522-9495
Fax: 505/522-9389

Mr. Thomas A. King
Physical Science Laboratory
New Mexico State University
PO Box 30002
Las Cruces, NM 88003-0002
Tel: 505/678-1488
Fax: 505/678-4198

Mr. William Klein
Science and Technology Corp
555 Telshor Drive, Suite 200
Las Cruces, NM 88005
Tel: 505/521-4353
Fax: 505/522-9062

Mr. Walter G. Klimek
U.S. Army Research Laboratory
AMSRL-SL-CO
APG, MD 21010-5423
Tel: 410/671-2260
Fax: 410/671-3471

Mr. Arunas P. Kuciauskas
Naval Research Laboratory
7 Grace Hopper Avenue
Monterey, CA 93943-5502
Tel: 408/656-4784
Fax: 408/656-4769

L

Mr. Peter F. Lambeck
Optimetrics, Inc.
2107 Laurel Bush Road, Suite 209
Bel Air, MD 21015
Tel: 410/569-0293
Fax: 410/569-0295

Mr. Steven Lamotte
Physical Science Laboratory
New Mexico State University
P.O. Box 30002
Las Cruces, NM 88003-0002
Tel: 505/678-4419
Fax: 505/678-2053

Mr. Dick R. Larson
Physical Science Laboratory
New Mexico State University
P.O. BOX 30002
Las Cruces, NM 88003-0002
Tel: 505/522-9383
Fax: 505/522-9389

Mr. Martin E. Lee
U.S. Army Research Laboratory
Battlefield Environment Directorate
AMSRL-BE-W
WSMR, NM 88002-5501
Tel: 505/678-3514
Fax: 505/678-0342

Dr. Patrick Lhomme
French DOD
SEPT, 18 rue du Dr Zamenhof
92131 Issy-les-Doulineaux, France
Tel: 33-1-40-95-38-35
Fax: 33-1-40-95-31-01

Mr. David W. Linden
Simulation Technologies, Inc.
PO Box 7009
Huntsville, AL 35807
Tel: 205/876-4204
Fax: 205/955-7376

Mr. Dewitt F. Littell
U.S. Army Research Laboratory
AMSRL-BE-W
WSMR, NM 88002-5501
Tel: 505/678-6664

Mr. Radon B. Loveland
New Mexico State University
Department of Physics, Dept 3D
Box 30001
Las Cruces, NM 88003-0001
Tel: 505/646-3831
Fax: 505/646-1934

M

Mr. Mat V. Maddix
U.S. Army Missile Command
AMSMI-RD-GC-T
Bldg 5400
Redstone Arsenal, AL 35898-5254
Tel: 205/876-2339
Fax: 205/876-6799

MAJ John T. Manfredi
HQ AWS/XTX
102 West Losey Street
Room 105
Scott AFB, IL 62225-5206
Tel: 618/256-4721
Fax: 618/256-6306

Ms. Lisa Manguso
New Mexico State University
Las Cruces, NM 88003
Tel: 505/678-6826

Mr. Joseph L. Manning
Computer Sciences Corporation
4815 Bradford Drive
Huntsville, AL 35805
Tel: 205/837-7200
Fax: 205/876-4301

Mr. David H. Marlin
U.S. Army Research Laboratory
Battlefield Environment Directorate
AMSRL-BE-M
WSMR, NM 88002-5501
Tel: 505/678-5447
Fax: 505/678-8366

Mr. William T. Matthew
U.S. Army Research Institute
of Environmental Medicine
SGRD-VE-EMB
Kansas Street
Natick, MA 01760-5007
Tel: 508/651-5140
Fax: 508-651-5298

Dr. Robert A. McClatchey
PL/GPA
29 Randolph Road
Hanscom AFB, MA 01731-3010
Tel: 617/377-2975
Fax: 617/377-8892

Mr. Steve J. McGee
Physical Science Laboratory
New Mexico State University
P.O. Box 30002
Las Cruces, NM 88003-0002
Tel: 505/522-9100
Fax: 505/522-9434

Mr. Scott A. McLaughlin
U.S. Army Research Laboratory
Battlefield Environment Directorate
AMSRL-BE-E
WSMR, NM 88002
Tel: 505/678-3956
Fax: 505/678-7623

Mr. Richard E. McNally
Science Applications International Corp
626 Towne Center Drive, Suite 205
Joppa, MD 21085
Tel: 410/679-9800
Fax: 410/679-3705

Dr. Edward M. Measure
U.S. Army Research Laboratory
Battlefield Environment Directorate
AMSRL-BE-W
WSMR, NM 88002
Tel: 505/678-3307
Fax: 505/678-3384

Dr. Robert E. Meredith
Optimetrics, Inc.
3115 Professional Drive
Ann Arbor, MI 48105
Tel: 313/973-1177
Fax: 313/973-1199

Mr. William H. Mermagen Sr.
U.S. Army Research Laboratory
AMSRL-CI
APG, MD 21005-5067
Tel: 410/278-6639
Fax: 410/278-5075

Mr. Ronald E. Meyers
U.S. Army Research Laboratory
Battlefield Environment Directorate
AMSRL-BE-S
WSMR, NM 88002-5501
Tel: 505/678-4037
Fax: 505/678-4393

Mr. Richard J. Mezan
U.S. Army Materiel Systems
Analysis Activity
AMXSY-GC
APG, MD 21005-5071
Tel: 410/278-2274
Fax: 410/278-2778

Mr. Arnold B. Michels
Naval Oceanographic Office
Code N541
Stennis Space Center, MS 39529
Tel: 601/688-4317
Fax: 601/688-4569

Prof. David R. Miller
U. of Connecticut c/o U.S. ARL
AMSRL-BE-E
WSMR, NM 88002-5501
Tel: 505/678-3042
Fax: 505/678-2053

Mr. Noah Montoya
US Army Research Laboratory
Battlefield Environment Directorate
AMSRL-BE-E
WSMR, NM 88002
Tel: 505/678-1561
Fax: 505/678-7623

Ms. Mary Beth Morris
Naval Surface Warfare Center
Code J41
Dahlgren, VA 22440-5000
Tel: 703/663-4781
Fax: 703/663-4977

N

Mr. Ronald J. Nelson
Science and Technology Corp
12452 Towner N.E.
Albuquerque, NM 87112
Tel: 505-275-6663
Fax: 505/275-6663

Dr. Frank E. Niles
US Army Research Laboratory
Battlefield Environment Directorate
AMSRL-BE-S
WSMR, NM 88002-5501
Tel: 505/678-3721
Fax: 505/678-8366

Mr. Stan Niles
U.S. Army Research Laboratory
Battlefield Environment Directorate
AMSRL-BE-W
WSMR, NM 88002-5501
Tel: 505/678-3834
Fax: 505/678-2432

Mr. John M. Noble
U.S. Army Research Laboratory
Battlefield Environment Directorate
AMSRL-BE-M
WSMR, NM 88002-5501
Tel: 505/678-3751
Fax: 505/678-8366

O

Dr. Sean G. O'Brien
Physical Science Laboratory
New Mexico State University
P.O. Box 30002
Las Cruces, NM 88003-0002
Tel: 505/521-9560
Fax: 505/522-9389

Mr. Richard J. Okrasinski
Physical Science Laboratory
New Mexico State University
PO Box 30002
Las Cruces, NM 88003-0002
Tel: 505/522-9496
Fax: 505/522-9389

Mr. Robert Olsen
U.S. Army Research Laboratory
Battlefield Environment Directorate
AMSRL-BE-M
WSMR, NM 88002
Tel: 505/678-1939
Fax: 505/678-8366

Dr. Montie M. Orgill
Science and Technology Corp
555 Telshor Boulevard, Suite 200
Las Cruces, NM 88011
Tel: 505/521-4353
Fax: 505/678-9062

Mr. Brain L. Orndorff
U.S. Army Research Laboratory
Battlefield Environment Directorate
AMSRL-BE-E
WSMR, NM 88002
Tel: 505/678-1803
Fax: 505/678-2053

Mr. William M. Oseles
Technical Solutions, Inc.
P.O. Box 1148
Mesilla Park, NM 88047
Tel: 505/524-2154
Fax: 505/525-5801

Dr. Clem Ota
Science and Technology Corp
555 Telshor Boulevard, Suite 200
Las Cruces, NM 88011
Tel: 505/521-4353
Fax: 505/522-9062

P

Mr. Leander Page, III
HQDA, Office of the Deputy Chief of
Staff for Intelligence
DAMI-POI
Washington, DC 20310-1067
Tel: 202/695-5509
Fax: 703/697-8849

Mr. Jeffrey E. Passner
U.S. Army Research Laboratory
Battlefield Environment Directorate
AMSRL-BE-W
WSMR, NM 88002-5501
Tel: 505/678-3193
Fax: 505/678-0343

Dr. H.T.A. Pentecost
Defence Research Agency
Fort Halstead
Sevenoaks, Kent, TN14 7BP, United Kingdom
Tel: 44-959-532222
Fax: 44-959-532970

Dr. William A. Peterson
U.S. Army Research Laboratory
Battlefield Environment Directorate
AMSRL-BE-A
WSMR, NM 88002-5501
Tel: 505/678-1465
Fax: 505/678-4449

Dr. Ronald Pinnick
U.S. Army Research Laboratory
Battlefield Environment Directorate
AMSRL-BE
WSMR, NM 88002-5501
Tel: 505/678-5634

CMSGT Robert W. Platt
Det 4, HQ AWS/XTE
Bldg 91027
595 Independence Road
Hurlburt Field, FL 32544-5618
Tel: 904/884-5493
Fax: 904/884-5503

Mr. Bradley Poore
U.S. Army Research Laboratory
Battlefield Environment Directorate
AMSRL-BE-A
WSMR, NM 88002
Tel: 505/678-5504
Fax: 505/678-2976

R

Mr. John W. Raby
U.S. Army Research Laboratory
Battlefield Environment Directorate
AMSRL-BE-A
WSMR, NM 88002-5501
Tel: 505/679-5078
Fax: 505/678-5228

Mr. Henry Rachele
U.S. Army Research Laboratory
Battlefield Environment Directorate
AMSRL-BE-S
WSMR, NM 88005-5501
Tel: 505/678-6687

Mr. Phil Raihl
U.S. Army Research Laboratory
Battlefield Environment Directorate
AMSRL-BE-W
WSMR, NM 88002-5001
Tel: 505/678-4539

LT COL John R. Roadcap
PL/WE
3550 Aberdeen Avenue, SE
Kirkland AFB, NM 87117-5776
Tel: 505/846-4722
Fax: 505/846-4934

2LT Paul A. Roelle
DET 31, 1WEAG USAF
Fort Polk, LA 71459-6250
Tel: 318/531-2015

Mr. Jaap Rogge
Royal Military Academy
PO Box 90154
4800 Rg Breda, The Netherlands
Tel: 31 76 273172
Fax: 31 76 273534

Dr. Michael Rollins
Science and Technology Corp
555 Telshor Boulevard, Suite 200
Las Cruces, NM 88011
Tel: 505/521-4353
Fax: 505/522-9062

Dr. David L. Rosen
U.S. Army Research Laboratory
Battlefield Environment Directorate
AMSRL-BE-W
WSMR, NM 88002-5501
Tel: 505/678-1490
Fax: 505/678-3385

Mr. Robert Rubio
U.S. Army Research Laboratory
Battlefield Environment Directorate
AMSRL-BE-A
WSMR, NM 88002-5501
Tel: 505/678-3331
Fax: 505/678-4449

Ms. Alice L.C. Ruf
Dynetics, Inc.
P.O. Drawer B
Huntsville, AL 35814-5050
Tel: 205/922-9230
Fax: 205/922-9255

S

Mr. Randall Safier
Teledyne Continential Motors
General Products
640 Seminole Road
Muskegon, MI 49441-4720
Tel: 616/780-5573
Fax: 616/780-5656

Ms. Barbara Sauter
U.S. Army Research Laboratory
Battlefield Environment Directorate
AMSRL-BE
WSMR, NM 88002-5501
Tel: 505/678-2840
Fax: 505/678-2432

Mr. David P. Sauter
U.S. Army Research Laboratory
Battlefield Environment Directorate
AMSRL-BE-M
WSMR, NM 88002-5501
Tel: 505/678-2078
Fax: 505/678-8366

Mr. Robert Scheinhartz
Lockheed Austin Division
Org. T2-30, Bldg 320
6800 Burleson Road
Austin, TX 78744
Tel: 512/386-2855
Fax: 512/386-1730

Mr. Luke Scott
Night Vision & Electronic
Sensors Directorate
AMSEL-RD-NV-VISP
Fort Belvoir, VA 22060
Tel: 703/704-1766
Fax: 703/704-1753

Dr. Mary Ann Seagraves
U.S. Army Research Laboratory
Battlefield Environment Directorate
AMSRL-BE-W
WSMR, NM 88002-5501
Tel: 505/678-1339
Fax: 505/678-3385

Mr. Ted Sekula
GTE Government Systems Corporation
Westlake Operations
31717 LaTienda Drive
Box 5027
Westlake Village, CA 91359-5027
Tel: 818/706-5333
Fax: 818/706-4001

Mr. Harry D. Selsor
Naval Research Laboratory
TOWS Program Office
Code 7410, Building 1105
Stennis Space Center, MS 39529-5004
Tel: 601/688-4760
Fax: 601/688-4605

Mr. Jose M. Serna
Physical Science Laboratory
New Mexico State University
P.O. Box 30002
Las Cruces, NM 88003-0002
Tel: 505/522-9333
Fax: 505/522-9434

Dr. Richard Shirkey
U.S. Army Research Laboratory
Battlefield Environment Directorate
AMSRL-BE-M
WSMR, NM 88002-5001
Tel: 505/678-5470
Fax: 505/678-8366

Cpt Brad Smith
ODDDRE
E&LS
3080 Defense Pentagon
Washington, DC 20301-3080
Tel: 703/695-9604
Fax: 703/693-7042

Mrs. René Smith
U.S. Army Research Laboratory
9496 Luna Vista Drive, Sp. 3
Las Cruces, NM 88001
Tel: 505/678-6780
Fax: 505/678-4449

MSST Timothy J. Smith
OL-N, HQ AWS, c/o U.S. Army Research Lab
AMSRL-BE-W
WSMR, NM 88002-5501
Tel: 505/678-8148
Fax: 505/678-0343

Dr. David B. Soules
Lockheed
PO Box 189
WSMR, NM 88002
Tel: 505/678-7917
Fax: 505/678-7388

Dr. John B. Spalding
Physical Science Laboratory
New Mexico State University
P.O. Box 30002
Las Cruces, NM 88003-0002
Tel: 505/524-8029
Fax: 505/522-9389

Dr. Andrew R. Spillane
Science and Technology Corp
101 Research Drive
Hampton, VA 23666-0000
Tel: 804/865-0467
Fax: 804/865-8721

Mr. Ralph Steinhoff
U.S. Army Research Laboratory
Battlefield Environment Directorate
AMSRL-BE-A
Bldg 1622/1646
WSMR, NM 88002-5501
Tel: 505/678-4481

Dr. Thomas J. Sullivan
Lawrence Livermore National Laboratory
PO Box 808, L-262
Livermore, CA 94550
Tel: 510/422-1838
Fax: 505/423-4908

Mr. Robert A. Sutherland
U.S. Army Research Laboratory
Battlefield Environment Directorate
AMSRL-BE-E
WSMR, NM 88002-5501
Tel: 505/678-4520
Fax: 505/678-2432

T

Mr. Charles S. Taylor
U.S. Army Field Artillery School/DCD
ATSF-TA
Fort Sill, OK 73503
Tel: 405/351-2352
Fax: 405/351-4802

Dr. Rastsilav J. Telgarsky
Technical Solutions, Inc.
P.O. Box 1148
Mesilla Park, NM 88047
Tel: 505/524-2154
Fax: 505/525-5801

Mr. Dennis Thomson
Pennsylvania State
Meteoroogy Department
503 Walker Bldg
University Park, PA 16802
Tel: 814/865-0478
Fax: 814/865-3663

COL Robert E. Thornton
U.S. Army Chemical School
TRADOC SIPO
ATZN-CM-ASP
Fort McClellan, AL 36205-5020
Tel: 205/238-5654
Fax: 205/848-4615

Mr. Jeff Todd
Dynetics, Inc.
P.O. Drawer B
Huntsville, AL 35814-5050
Tel: 205/922-9230
Fax: 205/922-9255

Mr. David H. Tofsted
U.S. Army Research Laboratory
Battlefield Environment Directorate
AMSRL-BE-M
WSMR, NM 88002-5501
Tel: 505/678-3039
Fax: 505/678-2432

Mr. Andrew R. Tooth
Sowerby Research Centre
British Aerospace
FPC 267
PO Box 5
Filton, Bristol, United Kingdom
Tel: 44 272 363095
Fax: 44 272 363733

Mr. Philippe Tourtier
THOMSON-CSF/LER
Avenue de Belle-Fontaine
Cesson-Sevigne, 35510, France
Tel: 33 99.25.43.36
Fax: 33 99.25.43.34

Mr. James Troung
U.S. Army Topographic Engineering Center
Fort Belvoir, VA 22060
Tel: 703/355-3852
Fax: 703/355-3176

Mr. Arnold D. Tunick
U.S. Army Research Laboratory
Battlefield Environment Directorate
AMSRL-BE-S
WSMR, NM 88002-5501
Tel: 505/678-4832
Fax: 505/678-2053

Mr. Jonathan D. Turton
UK Meteorological Office
London Road, Bracknell
Berkshire, RG12 2SZ, United Kingdom
Tel: 00 44 344 85 6991
Fax: 00 44 344 85 6967

LTC Charles W. Tuttle III
CAC Staff Wether Officer
ATZL-CAW-E
Fort Leavenworth, KS 66027-5300
Tel: 913/684-4897
Fax: 913/684-3654

V

Mr. J.M. Valeton
TNO Institute for Perception
PO Box 23
3769 ZG Soesterverg, The Netherlands
Tel: 31 3463-56239
Fax: 31 3463-53977

Ms. Gail T. Vaucher
Science and Technology Corp
555 Telshor Drive, Suite 200
Las Cruces, NM 88011
Tel: 505/521-4353
Fax: 505/522-9062

Mr. Don Veazey
U.S. Army Research Laboratory
Battlefield Environment Directorate
AMSRL-BE
WSMR, NM 88002-5501
Tel: 505/678-1225
Fax: 505/678-1230

Mr. Joseph J. Vervier
U.S. Army Edgewood RD&E Center
SMCBRD-TD
APG, MD 21010-5423
Tel: 410/671-5501
Fax: 410/671-3484

Mr. Edward Vidal, Jr.
U.S. Army Research Laboratory
Battlefield Environment Directorate
AMSRL-BE-W
WSMR, NM 88002-5501
Tel: 505/678-1184
Fax: 505/678-3385

Mr. Richard Vitali
U.S. Army Research Laboratory (AMC)
2800 Powder Mill Road
Adelphi, MD 20783-1145
Tel: 202/394-1600
Fax: 202/394-5187

MAJ John A. White III
U.S. Army Special Operations Command
AOWX(SWO)
Fort Bragg, NC 28307-5203
Tel: 910/432-2981
Fax: 910/432-1074

W

Mr. Joseph M. Wall
U.S. Army Research Laboratory
Weapons Technology Directorate
AMSRL-WT-WF
Bldg 1121
APG, MD 21005
Tel: 410/278-9798
Fax: 410/278-8829

Mr. Charles Warnick
USAIC&FH
ATZS-CDI-W
Fort Huachuca, AZ 85613-7000
Tel: 602/538-6647
Fax: 602/533-5054

Mr. Harald Weber
German Military Geophysical Office
Mont Royal
56841 Traben-Trarbach, Germany
Tel: 49 6541 18345
Fax: 49 6541 18296

Mr. Michael E. Wells
Wells Consulting, Inc.
3812 Glenmont Drive
Fort Worth, TX 76133
Tel: 818/292-2378
Fax: 818/292-2378

Mr. Franz E. Westermeier
U.S. Army Engineer School
ATSE-DAC-MCG
Fort Leonard Wood, MO 65473-6650
Tel: 314/566-0131
Fax: 314/563-7950

Dr. Alan E. Wetmore
U.S. Army Research Laboratory
Battlefield Environment Directorate
AMSRL-BE-S
WSMR, NM 88002
Tel: 505/678-5563

Y

Mr. Jimmy Yarbrough
U.S. Army Research Laboratory
Battlefield Environment Directorate
AMSRL-BED
WSMR, NM 88002
Tel: 505/678-3792

Mr. Young P. Yee
U.S. Army Research Laboratory
Battlefield Environment Directorate
AMSRL-BE-E
WSMR, NM 88002
Tel: 505/678-6468
Fax: 505/678-2053

Z

COL Karl Zeller
USAF/XOW (MA)
3717 NCR 2SE
Bellvue, CO 80512
Tel: 303/498-1238
Fax: 303/498-1010

AUTHOR INDEX